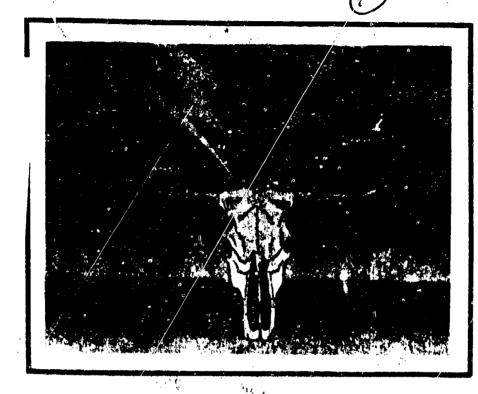
AD A 135100



# 8th INTERNATIONAL AEROSPACE and GROUND CONFERENCE

LIGHTNING and STATIC I
ELECTRICITY

OCT 2 4 1983

LIGHTNING TECHNOLOGY ROUNDUP

June 21-23, 1983

This document has been approved for public release and sale; its distribution is unlimited.

For Worth Taxes, U.S.A.

186 10 12 178

TE FILE COPY

# Technical Report Documentation Page

<b></b>			
1. Report No.	2. Government Accordion No. A135100	3. Recipient's Catalog No	) <b>,</b>
DOT/FAA/CT-83/25	1133100	1	
4. Title and Subtitle		5. Report Date	
Time and destrine			
		June 1983	
INTERNATIONAL AEROSPACE AND	GROUND CONFERENCE ON	6. Performing Organization	n Code
LIGHTNING AND STATIC ELECTRI	TCT # I		A N .
		8. Performing Organization	n Kapari Ita.
7. Author(s)		1	
		ì	
		10. Work Unit No. (TRAIS)	<del></del>
9. Performing Organization Name and Address	69	IV. Werk Unit No. (1 KAIS)	,
Federal Aviation Administrat	tion	1	
Technical Center		11. Contract or Grant No.	
	T 08405		
Atlantic City Airport, New .	dersey 00405		
		13. Type of Report and Pa	ried Cevered
12. Spensoring Agency Name and Address		7	
NATIONAL OF THE PARTY OF THE PA	nation Crown (NTCC) of the	1	
National Intersgency Coordin	uacton Group (MICG) of cue	<b>1</b>	. 1
National Atmospheric Electr	icity Hazards Protection	Conference Pub	
Program	-	14. Sponsoring Agency Co	de
rrogram		1	
		<u> </u>	
19. Supplementary Notes			
			\7.4 6.4
The NICG consists of member	s from the U.S. Air Force, U	.S. Army, U.S. Nav	vy, NASA,
NOAA, and the FAA.	•	-	
14. Abstract			
Anna a second landa	n of papers presented at the	1983 Internations	al Aerospace
LWIS LEBOLT IR & COMBITATIO	n or papers presented at the		
	The purpose framework and the purpose of the purpos		
and Ground Conference on Li	ghtning and Static Electrici	ty, held at the Fo	ort Worth
and Ground Conference on L1	ghtning and Static Electrici	ty, held at the Fo	ort Worth
and Ground Conference on Li	ghtning and Static Electrici xas. June 21-23, 1983. It i	ty, held at the Fo ncludes papers co	ort Worth oncerning
and Ground Conference on Li Hilton Hotel, Fort Worth Te lightning phenomenology, 11	ghtning and Static Electrici was, June 21-23, 1983. It i ghtning characterization, mo	ty, held at the Fo ncludes papers co deling and simulat	ort Worth oncerning tion, test
and Ground Conference on Li Hilton Hotel, Fort Worth Te lightning phenomenology, 11	ghtning and Static Electrici was, June 21-23, 1983. It i ghtning characterization, mo	ty, held at the Fo ncludes papers co deling and simulat	ort Worth oncerning tion, test
and Ground Conference on Li Hilton Hotel, Fort Worth Te lightning phenomonology, 11	ghtning and Static Electrici xas. June 21-23, 1983. It i	ty, held at the Fo ncludes papers co deling and simulat	ort Worth oncerning tion, test
and Ground Conference on Li Hilton Hotel, Fort Worth Te lightning phenomenology, li criteria and techniques, an	ghtning and Static Electrici xas, June 21-23, 1983. It i ghtning characterization, mo d protection of both Airborn	ty, held at the Fonciudes papers condeling and simulate and Ground Systems	ort Worth oncerning tion, test ems.
and Ground Conference on Li Hilton Hotel, Fort Worth Te lightning phenomenology, li criteria and techniques, an This conference was sponsor	ghtning and Static Electrici xas, June 21-23, 1983. It i ghtning characterization, mod protection of both Airborn ed by the NICG in concert wi	ty, held at the Forncludes papers condeling and simulate and Ground Systems the the Florida Inc	ort Worth concerning tion, test eas.
and Ground Conference on Li Hilton Hotel, Fort Worth Te lightning phenomenology, li criteria and techniques, an This conference was sponsor	ghtning and Static Electrici xas, June 21-23, 1983. It i ghtning characterization, mod protection of both Airborn ed by the NICG in concert wi	ty, held at the Forncludes papers condeling and simulate and Ground Systems the the Florida Inc	ort Worth oncerning tion, test ems. stitute of
and Ground Conference on Li Hilton Hotel, Fort Worth Te lightning phenomenology, li criteria and techniques, an This conference was sponsor Technology and in associati	ghtning and Static Electrici xas, June 21-23, 1983. It i ghtning characterization, mod protection of both Airborned by the NICG in concert will on with the Institute of Electrical xas and the state of Electrical xas and the state and the st	ty, held at the Forncludes papers codeling and simulate and Ground Systems the the Florida Inductrical and Electrical	ort Worth oncerning tion, test ems. stitute of ronic
and Ground Conference on Li Hilton Hotel, Fort Worth Te lightning phenomenology, li criteria and techniques, an This conference was sponsor Technology and in associati Engineers. SAE-AE4 committe	ghtning and Static Electrici xas, June 21-23, 1983. It i ghtning characterization, mod protection of both Airborn ed by the NICG in concert will no with the Institute of Electrician the United Kingdom Civil	ty, held at the Forncludes papers condeling and simulate and Ground Systems the Florida Insectical and Electrical Authority	ort Worth concerning tion, test ems. stitute of ronic
and Ground Conference on Li Hilton Hotel, Fort Worth Te lightning phenomenology, li criteria and techniques, an This conference was sponsor Technology and in associati Engineers. SAE-AE4 committe	ghtning and Static Electrici xas, June 21-23, 1983. It i ghtning characterization, mod protection of both Airborned by the NICG in concert will on with the Institute of Electrical xas and the state of Electrical xas and the state and the st	ty, held at the Forncludes papers condeling and simulate and Ground Systems the Florida Insectical and Electrical Authority	ort Worth concerning tion, test ems. stitute of ronic
and Ground Conference on Li Hilton Hotel, Fort Worth Te lightning phenomenology, li criteria and techniques, an This conference was sponsor Technology and in associati Engineers. SAE-AE4 committe	ghtning and Static Electrici xas, June 21-23, 1983. It i ghtning characterization, mod protection of both Airborn ed by the NICG in concert will on with the Institute of Electrician the United Kingdom Civil	ty, held at the Forncludes papers condeling and simulate and Ground Systems the the Florida Insectical and Electrical Authority	ort Worth concerning tion, test ems. stitute of ronic
and Ground Conference on Li Hilton Hotel, Fort Worth Te lightning phenomenology, li criteria and techniques, an This conference was sponsor Technology and in associati Engineers, SAE-AE4 committe	ghtning and Static Electrici xas, June 21-23, 1983. It i ghtning characterization, mod protection of both Airborn ed by the NICG in concert will on with the Institute of Electrician the United Kingdom Civil	ty, held at the Forncludes papers condeling and simulate and Ground Systems the the Florida Insectical and Electrical Authority	ort Worth concerning tion, test ems. stitute of ronic
and Ground Conference on Li Hilton Hotel, Fort Worth Te lightning phenomenology, li criteria and techniques, an This conference was sponsor Technology and in associati Engineers. SAE-AE4 committe	ghtning and Static Electrici xas, June 21-23, 1983. It i ghtning characterization, mod protection of both Airborn ed by the NICG in concert will on with the Institute of Electrician the United Kingdom Civil	ty, held at the Forncludes papers condeling and simulate and Ground Systems the the Florida Insectical and Electrical Authority	ort Worth concerning tion, test ems. stitute of ronic
and Ground Conference on Li Hilton Hotel, Fort Worth Te lightning phenomenology, li criteria and techniques, an This conference was sponsor Technology and in associati Engineers. SAE-AE4 committe	ghtning and Static Electrici xas, June 21-23, 1983. It i ghtning characterization, mod protection of both Airborn ed by the NICG in concert will on with the Institute of Electrician the United Kingdom Civil	ty, held at the Forncludes papers condeling and simulate and Ground Systems the the Florida Insectical and Electrical Authority	ort Worth concerning tion, test ems. stitute of ronic
and Ground Conference on Li Hilton Hotel, Fort Worth Te lightning phenomenology, li criteria and techniques, an This conference was sponsor Technology and in associati Engineers. SAE-AE4 committe	ghtning and Static Electrici xas, June 21-23, 1983. It i ghtning characterization, mod protection of both Airborn ed by the NICG in concert will on with the Institute of Electrician the United Kingdom Civil	ty, held at the Forncludes papers condeling and simulate and Ground Systems the the Florida Insectical and Electrical Authority	ort Worth oncerning tion, test ems. stitute of ronic
and Ground Conference on Li Hilton Hotel, Fort Worth Te lightning phenomenology, li criteria and techniques, an This conference was sponsor Technology and in associati Engineers, SAE-AE4 committe	ghtning and Static Electrici xas, June 21-23, 1983. It i ghtning characterization, mod protection of both Airborn ed by the NICG in concert will on with the Institute of Electrician the United Kingdom Civil	ty, held at the Forncludes papers condeling and simulate and Ground Systems the the Florida Insectical and Electrical Authority	ort Worth oncerning tion, test ems. stitute of ronic
and Ground Conference on Li Hilton Hotel, Fort Worth Te lightning phenomenology, li criteria and techniques, an This conference was sponsor Technology and in associati Engineers, SAE-AE4 committe	ghtning and Static Electrici xas, June 21-23, 1983. It i ghtning characterization, mod protection of both Airborn ed by the NICG in concert will on with the Institute of Electrician the United Kingdom Civil	ty, held at the Forncludes papers condeling and simulate and Ground Systems the the Florida Insectical and Electrical Authority	ort Worth oncerning tion, test ems. stitute of ronic
and Ground Conference on Li Hilton Hotel, Fort Worth Te lightning phenomenology, li criteria and techniques, an This conference was sponsor Technology and in associati Engineers, SAE-AE4 committe	ghtning and Static Electrici xas, June 21-23, 1983. It i ghtning characterization, mod protection of both Airborn ed by the NICG in concert will on with the Institute of Electrician the United Kingdom Civil	ty, held at the Forncludes papers condeling and simulate and Ground Systems the the Florida Insectical and Electrical Authority	ort Worth oncerning tion, test ems. stitute of ronic
and Ground Conference on Li Hilton Hotel, Fort Worth Te lightning phenomenology, li criteria and techniques, an This conference was sponsor Technology and in associati Engineers. SAE-AE4 committe	ghtning and Static Electrici xas, June 21-23, 1983. It i ghtning characterization, mod protection of both Airborn ed by the NICG in concert will on with the Institute of Electrician the United Kingdom Civil	ty, held at the Forncludes papers condeling and simulate and Ground Systems the the Florida Insectical and Electrical Authority	ort Worth oncerning tion, test ems. stitute of ronic
and Ground Conference on Li Hilton Hotel, Fort Worth Te lightning phenomenology, li criteria and techniques, an This conference was sponsor Technology and in associati Engineers, SAE-AE4 committe	ghtning and Static Electrici xas, June 21-23, 1983. It i ghtning characterization, mod protection of both Airborn ed by the NICG in concert will on with the Institute of Electrician the United Kingdom Civil	ty, held at the Forncludes papers condeling and simulate and Ground Systems the the Florida Insectical and Electrical Authority	ort Worth oncerning tion, test ems. stitute of ronic
and Ground Conference on Li Hilton Hotel, Fort Worth Te lightning phenomenology, li criteria and techniques, an This conference was sponsor Technology and in associati Engineers. SAE-AE4 committe	ghtning and Static Electrici xas, June 21-23, 1983. It i ghtning characterization, mod protection of both Airborn ed by the NICG in concert will on with the Institute of Electrician the United Kingdom Civil	ty, held at the Forncludes papers condeling and simulate and Ground Systems the the Florida Insectical and Electrical Authority	ort Worth oncerning tion, test ems. stitute of ronic
and Ground Conference on Li Hilton Hotel, Fort Worth Te lightning phenomenology, li criteria and techniques, an This conference was sponsor Technology and in associati Engineers. SAE-AE4 committe	ghtning and Static Electrici xas, June 21-23, 1983. It i ghtning characterization, mod protection of both Airborn ed by the NICG in concert will on with the Institute of Electrician the United Kingdom Civil	ty, held at the Forncludes papers condeling and simulate and Ground Systems the the Florida Insectical and Electrical Authority	ort Worth oncerning tion, test ems. stitute of ronic
and Ground Conference on Li Hilton Hotel, Fort Worth Te lightning phenomenology, li criteria and techniques, an This conference was sponsor Technology and in associati Engineers. SAE-AE4 committe	ghtning and Static Electrici xas, June 21-23, 1983. It i ghtning characterization, mod protection of both Airborn ed by the NICG in concert will on with the Institute of Electrician the United Kingdom Civil	ty, held at the Forncludes papers condeling and simulate and Ground Systems the the Florida Insectical and Electrical Authority	ort Worth oncerning tion, test ems. stitute of ronic
and Ground Conference on Li Hilton Hotel, Fort Worth Te lightning phenomenology, li criteria and techniques, an This conference was sponsor Technology and in associati Engineers. SAE-AE4 committe	ghtning and Static Electrici xas, June 21-23, 1983. It i ghtning characterization, mod protection of both Airborn ed by the NICG in concert will on with the Institute of Electrician the United Kingdom Civil	ty, held at the Forncludes papers condeling and simulate and Ground Systems the the Florida Insectical and Electrical Authority	ort Worth oncerning tion, test ems. stitute of ronic
and Ground Conference on Li Hilton Hotel, Fort Worth Te lightning phenomenology, li criteria and techniques, an This conference was sponsor Technology and in associati Engineers. SAE-AE4 committe	ghtning and Static Electrici xas, June 21-23, 1983. It is ghtning characterization, moded protection of both Airborn and by the NICG in concert without the Institute of Electrical Education Civil and the United Kingdom Civil and the United Culham Laboratory	ty, held at the Foncludes papers codeling and simulate and Ground Systems the Florida Instriction and Electrical and Electrical Authority	ort Worth oncerning tion, test ems. stitute of ronic
and Ground Conference on Li Hilton Hotel, Fort Worth Te lightning phenomenology, li criteria and techniques, an This conference was sponsor Technology and in associati Engineers. SAE-AE4 committe	ghtning and Static Electrici xas, June 21-23, 1983. It i ghtning characterization, mod protection of both Airborn ed by the NICG in concert will on with the Institute of Electrician the United Kingdom Civil	ty, held at the Foncludes papers codeling and simulate and Ground Systems the Florida Instriction and Electrical and Electrical Authority	ort Worth oncerning tion, test ems. stitute of ronic
and Ground Conference on Li Hilton Hotel, Fort Worth Te lightning phenomenology, li criteria and techniques, an This conference was sponsor Technology and in associati Engineers, SAE-AE4 committe Aircraft Establishment, Far	ghtning and Static Electrici xas, June 21-23, 1983. It is ghtning characterization, moded protection of both Airborn and by the NICG in concert without the Institute of Electrician with the Institute of Electric the United Kingdom Civil Insborough, Culham Laboratory	ty, held at the Foncludes papers codeling and simulate and Ground System the Florida Institute and Electrical and Electrical Aviation Authority	ort Worth oncerning tion, test ems. stitute of ronic y, Boyal
and Ground Conference on Li Hilton Hotel, Fort Worth Te lightning phenomenology, li criteria and techniques, an This conference was sponsor Technology and in associati Engineers, SAE-AE4 committe Aircraft Establishment, Far	ghtning and Static Electrici xas, June 21-23, 1983. It i ghtning characterization, mo d protection of both Airborn ed by the NICG in concert wi on with the Institute of Ele e, the United Kingdom Civil rasborough, Culham Laboratory	ty, held at the Forncludes papers codeling and simulate and Ground System the Florida Instituted and Electrical and Electrical and Electrical Aviation Authority	ort Worth oncerning tion, test ems. stitute of ronic y, Boyal
and Ground Conference on Li Hilton Hotel, Fort Worth Te lightning phenomenology, li criteria and techniques, an This conference was sponsor Technology and in associati Engineers, SAE-AE4 committe Aircraft Establishment, Far	ghtning and Static Electrici xas, June 21-23, 1983. It i ghtning characterization, me d protection of both Airborn ed by the NICG in concert wi on with the Institute of Ele e, the United Kingdom Civil nsborough, Culham Laboratory  16. Dismission See Document is through the	ty, held at the Foncludes papers codeling and simulate and Ground System that the Florida Inctrical and Electrical Aviation Authority	U.S. public linformation
and Ground Conference on Li Hilton Hotel, Fort Worth Te lightning phenomenology, li criteria and techniques, an This conference was sponsor Technology and in associati Engineers, SAE-AE4 committe Aircraft Establishment, Far  17. Key Weeds Phenomonology Lightning Locators	ghtning and Static Electrici xas, June 21-23, 1983. It i ghtning characterization, me d protection of both Airborn ed by the NICG in concert wi on with the Institute of Ele e, the United Kingdom Civil nsborough, Culham Laboratory  16. Dismission See Document is through the	ty, held at the Foncludes papers codeling and simulate and Ground System that the Florida Inctrical and Electrical Aviation Authority	U.S. public
and Ground Conference on Li Hilton Hotel, Fort Worth Te lightning phenomenology, li criteria and techniques, an This conference was sponsor Technology and in associati Engineers, SAE-AE4 committe Aircraft Establishment, Far  17. Key Weeds Phenomonology Lightning Locators 'P' Static and Corona	ghtning and Static Electrici xas, June 21-23, 1983. It i ghtning characterization, me d protection of both Airborn ed by the NICG in concert wi on with the Institute of Ele e, the United Kingdom Civil nsborough, Culham Laboratory  16. Dismission See Document is through the	ty, held at the Forncludes papers codeling and simulate and Ground System the Florida Instituted and Electrical and Electrical and Electrical Aviation Authority	U.S. public linformation
and Ground Conference on Li Hilton Hotel, Fort Worth Te lightning phenomenology, li criteria and techniques, an This conference was sponsor Technology and in associati Engineers, SAE-AE4 committe Aircraft Establishment, Far  17. Key Words Phenomonology Lightning L-cators	ghtning and Static Electrici xas, June 21-23, 1983. It i ghtning characterization, me d protection of both Airborn ed by the NICG in concert wi on with the Institute of Ele e, the United Kingdom Civil nsborough, Culham Laboratory  16. Dismission See Document is through the	ty, held at the Foncludes papers codeling and simulate and Ground System that the Florida Inctrical and Electrical Aviation Authority	v.S. public linformation
and Ground Conference on Li Hilton Hotel, Fort Worth Te lightning phenomenology, li criteria and techniques, an This conference was sponsor Technology and in associati Engineers, SAE-AE4 committe Aircraft Establishment, Far  17. Key Werde Phenomonology Lightning L.cators 'P' Static and Corona Lightning Simulation	ghtning and Static Electrici xas, June 21-23, 1983. It i ghtning characterization, me d protection of both Airborn ed by the NICG in concert wi on with the Institute of Ele e, the United Kingdom Civil nsborough, Culham Laboratory  16. Dismission See Document is through the Service, Spi	ty, held at the Foncludes papers codeling and simulate and Ground System that the Florida Instituted and Electrical and Electrical and Electrical Aviation Authority available to the National Technical ingfield, Virgini	U.S. public l Information
and Ground Conference on Li Hilton Hotel, Fort Worth Te lightning phenomenology, li criteria and techniques, an This conference was sponsor Technology and in associati Engineers, SAE-AE4 committe Aircraft Establishment, Far  17. Key Words Phenomonology Lightning Locators 'P' Static and Corona	ghtning and Static Electrici xas, June 21-23, 1983. It i ghtning characterization, me d protection of both Airborn ed by the NICG in concert wi on with the Institute of Ele e, the United Kingdom Civil nsborough, Culham Laboratory  16. Dismission See Document is through the	ty, held at the Foncludes papers codeling and simulate and Ground System that the Florida Inctrical and Electrical Aviation Authority	v.S. public l Information
and Ground Conference on Li Hilton Hotel, Fort Worth Te lightning phenomenology, li criteria and techniques, an This conference was sponsor Technology and in associati Engineers, SAE-AE4 committe Aircraft Establishment, Far  17. Key Words Phenomonology Lightning Locators 'P' Static and Corona Lightning Simulation  19. Seconty Classif. (of this report)	ghtning and Static Electrici xas, June 21-23, 1983. It i ghtning characterization, me d protection of both Airborn ed by the NICG in concert wi on with the Institute of Ele e, the United Kingdom Civil nsborough, Culham Laboratory  16. Dismission Ste Document is through the Service, Sp:	ty, held at the Foncludes papers codeling and simulate and Ground System that the Florida Instituted and Electrical and Electrical and Electrical Aviation Authority available to the National Technical ingfield, Virgini	U.S. public l Information
and Ground Conference on Li Hilton Hotel, Fort Worth Te lightning phenomenology, li criteria and techniques, an This conference was sponsor Technology and in associati Engineers, SAE-AE4 committe Aircraft Establishment, Far  17. Key Werde Phenomonology Lightning L.cators 'P' Static and Corona Lightning Simulation	ghtning and Static Electrici xas, June 21-23, 1983. It i ghtning characterization, me d protection of both Airborn ed by the NICG in concert wi on with the Institute of Ele e, the United Kingdom Civil nsborough, Culham Laboratory  16. Dismission See Document is through the Service, Spi	ty, held at the Foncludes papers codeling and simulate and Ground System that the Florida Instituted and Electrical and Electrical and Electrical Aviation Authority available to the National Technical ingfield, Virgini	U.S. public l Information

Form DOT F 1700.7 (8-72)

Reproduction of sampleted page outhorized

## COMPONENT PART NOTICE

THIS PAPER IS A COMPONENT PART OF THE FOLLOWING COMPILATION REPORT:

(TITLE): International Aerospace and Ground Converence on Lightning and

Static Electricity (8th): 'Lightning Technology Roundup,' held at

Fort Worth, Texas on 21-23 June 1983.

(SOURCE): Federal Aviation Administration, Atlantic City, NJ. Technical Center.

TO ORDER THE COMPLETE COMPILATION REPORT USE AD-A135 100

THE COMPONENT PART IS PROVIDED HERE TO ALLOW USERS ACCESS TO INDIVIDUALLY AUTHORED SECTIONS OF PROCEEDINGS, ANNALS, SYMPOSIA, ETC. HOWEVER, THE COMPONENT SHOULD BE CONSIDERED WITHIN THE CONTEXT OF THE OVERALL COMPILATION REPORT AND NOT AS A STAND-ALONE TECHNICAL REPORT.

THE FOLLOWING COMPONENT PART NUMBERS COMPRISE THE COMPILATION REPORT:

AD#:	•	TITLE:
AD-P002	161	Storm Electricity Research in Oklahoma: An Overview.
AD-P002	162	Atmospheric Electricty Hazards Protection Program.
AD-P002	163	Lightning Problems Encountered in Large Electronics Installations and their Solution.
AD-P002	-	Lightning Activity Observed in Upper and Lower Portions of Storms and Its Relationship to Storm Structure from UHF (Very High Frequency) Mapping and Doppler Radar.
AD-P002	165	Some Spatial and Temporal Relationships between Lightning and Storm Structure and Evolution.
AD-P002	166	Damage of RFC Surface Layers by Electrostatic Charging.
AD-P002	167	Relative Importance of Electromagnetic Shield Violations,
AD-PU02	168	Topological Grounding Anomalies.
AD-P002	169	Protection against Lightning Surge Voltage. C. Communication Lines and Power Lines.
AP-P002	170	Frequent Failure of Lightning Arresters at the Satpure Thermal Power Station, India: Preliminary Results of Field Observations.
AD-P002	171	Jorrelated Measurements of UHF Radar Signatures, RF Radiation, and Electric Field Changes from Lightning.
AD-P002	172	Relationships between Lightning Occurrences and Radar Echo Characteristics in South Florida.
AD-P002	173	Climatological Characteristics of Lightning over South Florida and their Correlation with Radar Activity.
AD-P002	174	Modelling of Direct-Strike Lightning Coupling by a Transfer Function Technique.
AD-P002	175	Some Results and Limitations of Prony Analysis of In-Flight Lightning Data.

# COMPONENT PART NOTICE (CON'T)

AD#:	TITLE:
AD-P002 176	A Modeling System for Conducted Transient Analysis.
AD-P002 177	Lightning Protection Zones for Rocket Launch Complexes.
AD-P002 178	Relations of the Flashover Voltage Vorsus the Velocity of the Moving Electrode.
AD-P002 179	Static Discharge and Triggered Lightning.
AD-P002 180	Laboratory and Field Observations Related to Ice Particle and Aircraft Charging in Convective Storms.
AD-P002 181	Inside the Cone of Protection.
AD-P002 182	Earth Electrodes for Grounding NEMP Type Lightning.
AD-2002 183	Improved Grounding System for Mountain Top Radio Sites.
AD-P002 184	Electrical Resistivity of Concrete in the Foundation Earth.
AD-P002 187,	Electrostatic Voltage Sensors for Helicopter Dischargers.
.01.	The transmission of the against an work. The Milling against Decision bear the
AD-P002 188	Detection and Ranging of Electric Charged Helicopters.
AD-P002 189	A Realistic Approach to Aircraft Lightning Protection.
AD-P002 130	Correlation of Space Shuttle As-Built Atmospheric Capatilities
	With Known Atmospheric Conditions that Produce Lightning.
VD-5007 181	Atmospheric Electricity Threat Definition for Aircraft Lightning Protection.
AD-P002 192	Lightning Strikes to Aircraft of the German Federal Armed Forces.
AD- P002 193	Recent Lightning Induced Voltage Test Technique Investigations
AD-P002 194	NASA F-106B Lightning Ground Tests.
AD-POO2 195	Induced Transients in a Simulated Lightning Test of the
1,2 100,2 100,	Fly-by-Wire Jaguar Aircraft.
AD-P002 196	Introcloud Lightning Streamer Modeling Based upon In Situ Balloon Measurements.
AP-2002 197	Propagation, of Discharge, Channel Inside the Cloud. at to
	14 g - 11
AD-P002 198	Electromagnetic Measurements of Lightning Attachment to Aircraft.
AD-P002 199	Airborne Measurements of the Risetimas in Lightning Recurn Stroke Fields.
AD-P002 200 -	Lightning Field Spectra Obtained form Airborne Measurements.
AD-P002 201	Ground Evaluation of an Airborne Lightning Locator System.
AD-P002 202	A Wideband Airborne/Ground Lightning Flash Location System.
AD-P002 203	Wideband Magnetic Direction Finder Networks for Locating Cloud-to-Ground Lightning.
AD=P002 204	Airborne and Ground-Based Lightning Electronic and Magnetic Fields and VHF Source Locations for a Two-Stroke Ground Flash.
AD-P002 205,	Lightning Flash Density Versus Altitude and Storm Structure from Observations with UHF- and S-Band Radars.
AD-P002 206	The Effects of New Tochnology Trends on Aircraft Lightning Vulnerability and the Capability to Identify Technology Deficiencies.

# COMPONENT PART NOTICE (CON'T)

AD#:		TITLE:
AD-P002	207'	· Unprotected Radome Lightning Tests and Implications to
AD-1002	207	Keular Airframe Designs.
AD-P002	208	Errors in Lightning direction Finding by Airborne Crossed Loops.
AD-P002	209	Electrostatic Theory Applied to Helicopter Discharging.
AD-P002	210	Advance Testing of Lightning Protection Schemes for Composite Main Rotor Blades (Helicopter).
AD-P002	211	Nanosecond Resolution of E. H. and I. in Aircraft Lightning Test Riss.
AD-P002		Full-System Tests Using the Sandia Lightning Simulator.
AD-P002	213	Lightning Interaction with USAF Aircraft.
AD-P002	2.14	Usage of the SYSCAP II Circuit Analysis Program to Determine Semiconductor Failure Threshold Levels caused by Lightning/EMP Transients.
AD-P002	215	The Submicrosecond Structure of Lightning Radiation Fields.
AD-P002		A Solution for the Electromagnetic Fields Close to a
		Lightning Discharge
AD-P002	217	Tropical Lightning: Electromagnetic Characterization C.O.P.T.
		81 Experiment (Tropical Deep Convection).
AD-P002	218	The Effect of Propagation on Electromagnetic Fields Radiated by Lightning.
AD-P002	219,	Performance of the Sandia Lightning Simulator during F-14A and F/A-18 Aircraft Lightning Tests.
AD-P002		An Impulse Generator to Simulate Lightning Effects on Aircraft.
AD-P002	221	Measurements and Theoretical Analysis of a Full Scale NEMP Type Lightning Simulator for Aerospace Vehicles.
AD-P002	222	Updating the McAir Lightning Simulation Laboratory.
AD-P002	223	Vulnerability Assessment of Electrical/Electronic Subsystems
		and Equipment to Atmospheric Electricity.
AD-P002		Monitors for Upset Dotection in Computer Systems.
AD-P002		Lightning Protection Devices for High Frequencies Equipments.
AD-P002	226	Development of a Human Electrostatic Discharge Model in
		Relation to Electronic Systems,
AD-P002		Fast Field Changes Produced by Positive Ground Strokes.
AD-P002		On the Oscillating Bipolar Return Stroke Current.
AD-P002		P-Static Flight Evaluation of a Large Jet Andernftdrops.
AD-P002		Electric Charging by Impact of Hailstones and Raindrops.
AD-P002		The Effects of Precipitation Static and Lightning on the Airborne Reception of LORAN-C.
AD-P002		Digital System UpsetThe Effects of Simulated Lightning-Induced Transients on a General Purpose Microprocessor.
AD-P002		Lightning Protection Design and Lightning Threat Flight Clearance of a Fly-by-Wire Flight Control System for an Unstable Aircraft.
AD-P002		Upset Experimentation in Computer-Based Systems.
AD-P002		Conditions Conducive to Lightning Striking an Aircraft in a Thunderstorm.
AD-P002	236	Lightning Initiation in Thunderclouds.
AD-2002	237.	The Orgin of Thunderstorm - Electricity.
		·

# COMPONENT PART NOTICE (CON'T)

AD#:	TITLE:
AD-P002 238	Aerospace Vehicles Charging by Thruster Plumes.
AD-P002 239	Allocation of Protection against the Effects of Lightning on Electronic Systems.
AD-P002 240	The Lightning Spark Barrier.
AD-P002 241	Protecting the World's Largest Commercial Helicopter from Atmospheric Hazards.

Access	ion Fo	ì.		
NTTS	GRA&I		E.	
A 1	'AB			
T' 1 . "				
J = -1	Cunti	) II		
B/				
Pistr	bution	n/ _		
Ave1	lab411	cy (	eclos	
	15 i #	and	/or	f .
1400	Spec	ial		
A 1				
141				



# 1983

# **INTERNATIONAL**

# AEROSPACE AND GROUND CONFERENCE

ON

# LIGHTNING AND STATIC ELECTRICITY



June 21 - 23, 1983

Fort Worth, Texas

LIGHTNING TECHNOLOGY ROUNDUP

## CHAIRMAN'S MESSAGE



Welcome to the Eighth International Aerospace and Ground Conference on Lightning and Static Electricity. This years theme, "LIGHTNING TECHNOLOGY ROUND UP," reflects the coalensence of the many technological functions, from phenomenology to the lightning hardening of both Aerospace and Ground Systems. The lightning community has come a long way from the days of remote, lonely mountain top research with crude homemade instruments. The advent of modern high technological data retrieval and analysis systems has "OPENED THE DOOR," and provided the scientific world with the tools needed to unlock the mysteries associated with lightning.

Protection criteria for future electronic systems, has been seriously impacted through the expanded use of microelectronics, increased data transfer rates being employed in state-of-the-art digital systems and reduced shielding provided by advanced technology composite materials has provided the ultimate challenge to every discipline within the lightning community.

Problems associated with lightning activity are certainly International and have no geographical boundaries. This conference is truly international with approximately 25 percent of the papers being presented by international participants. This provides you with an opportunity to learn new concepts, exchange ideas, discuss new and controversial ideas and have informal discussions and conversations with your colleagues.

The technical program has been organized to offer something to both the new engineer as well as the established research scientist. I would like to express my appreciation and thanks to the many talented people who have worked so hard to make this a successful conference. This includes the conference speakers, session Chairmen and organizers, advisors, and last but certainly not least, the Conference steering committee and all their staff.

Nickolus O. Rasch Conference Chairman The Eighth International Aerospace and Ground Conference on Lightning and Static Electricity is sponsored by the National Interagency Coordination Group (NICG) in concert with the Florida Institute of Technology, and in association with the Institute of Electrical and Electronic Engineers, SAE-AE4 committee, the United Kingdom Civil Aviation Authority, Royal Aircraft Establishment, Farnsborough, Culham Laboratory.

## **APPRECIATION**

The NICG Conference Committee expresses its appreciation to the Federal Aviation Administration, Technical Center, Atlantic City Airport, New Jersey for its assistance in preparation and printing this program.

**KEYNOTE SPEAKER**Mr. C. R. (Tex) Melugin, Jr.



C. R. (Tex) Melugin, Jr., Director of the Federal Aviation Administration's Southwest Region, assumed his present position July 29, 1979. Headquartered in Fort Worth, Texas, he directs the activities of the Federal Aviation Administration in Arkansas, Louisiana, New Mexico, Oklahoma and Texas.

A veteran of 22 years of service with the FAA, Tex began his career as an aviation specialist at the FAA's Aeronautical Center, Oklahoma City. He later became the chief pilot and general manager for all Washington-based FAA aircraft. In 1965 he was named special assistant to the Deputy Administrator and a year later became manager of Washington National Airport. Named deputy director of Flight Standards Service in 1972, he remained in this position until 1975 when he became director of the FAA's Central Region.

# Committee Chairpersons



Chairman Nick Rasch FAA, Technical Center (609) 641-8200 x1144



Vice Chairman/Treasurer Joe Fisher U.S. Navy (202) 692-7788



Ground Systems
Chuck Andrasco
FAA, Headquarters
(202) 426-3585



Helicopters
Dave Albright
U.S. Army
(314) 263-1726



Aircraft & Aerospace Felix Pitts NASA Langley Research Center (804) 827-3681



Meteorology Don MacGorman NSSL (405) 360-3620



Lightning Locators
Jim Foster
U.S.Navy Engineering
Development Center
(201) 323-7636



Simulation Larry Walko USAF Flight Dynamics Laboratory (513) 257-7718



Military Sector Bill Walker Naval Air Development Center (215) 441-3054



Commerical Sector J. Reed FAA, Technical Center (609) 641-8200 x1137



International Liaison Garry DuBro USAF Flight Dynamics Laboratory (513) 257-7469



Guests Program Marsha Moe



Conference Coordinator
Walt McKerchan



Conference Assistant Tony Barile FAA, Technical Center (609) 641-8200 x1145



Technical Editor Henrietta Gilbert FAA, Technical Center (609) 641-8200 x1154



Conference Assistant Mike Glynn FAA Technical Center (609) 641-8200 x2491

Phenomonology Andy Revay Florida Institute of Technology (305) 723-3701

# **Contents**

Session 1A: Plenary Session Introduction: Nick Rasch, Conference Chairman FAA Technical Center, Atlantic City, N. J.

Welcome: The Honorable 'Bob Bolen'
Mayor
Fort Worth, Texas

Key Note Speaker: Tex Melugin Director, Southwest Region Fort Worth, Texas

## Session 2A:Plenary

Chairman: N. Rasch, FAA Technical Center, Atlantic City Airport, NJ

Storm Electricity Research in Okiahoma-an Overview	1-1
D. Rust, W. R. Taylor, D. R. MacGorman, S. J. Goodman, R. T. Arnold, V. Mazur (National Severe Storm Lab)  Atmospheric Electricity Hazards Protection (AEHP) Program	2-1
Rudy Beavin (Wright Patterson AFB)  Lightning Problems Encountered in Large Electronic Installations and Their Solutions  Samuel Crowford (Ford Agreement & Communication) (Co.(2))	3-1
Samuel Crawford (Ford Aerospace & Communication's Cc/p.)	
Session 3A: Phenomenology Chairperson: D. Rust, NSSL (NOAA), Norman, Oklahoma	
Lightning Activity Observed in Upper and Lower Portions of Storms and its Relationship to Structures, from VHF Mapping W. Taylor (National Severe Storm Lab)	4-1
Some Spatial and Temporal Relationships between Lightning and Storm Structure and Evolution D.R. MacGorman, W. Taylor, S. J. Goodman, R. T. Arnold, V. Mazur (National Severe Storm Lab)	5-1
Improved Estimates of the Area Density of Cloud-to-Ground Lightning over the United States Michael Maier, J. M. Piotrowicz (Lightning Location and Protection, Inc.)	6-1
Session 3B: Aircraft and Aerospace Lightning Modeling and Analysis Chairman: D. Levine, Goddard Space Flight Center, Greenbelt, Maryland	
Damage of RFC Surface Layers by Electrostatic Charging	7-1
D. Konigstein (Hochschule Der Bundeswehr) Relative Importance of EM Shield Violations	8-1
W. Graf, E.F. Vance (SRI International)	
Topological Grounding Anomalies W. Graf, I. E. Nanevicz (SRI International)	9-1
Session 3C: Ground System Protection Chairman: M. Huddleztot, Georgia Institute of Technology, Atlanta, Georgia	
Chairman. M. Huddiettol., Georgia metitute of Fechnology, Atlanta, Georgia	
Lightning and Transient Protection of Radio Systems S. Lundquist, R. Hogberg, K. G. Lorstrand (Instituted for Hogsponnings/orskning)	10-1
C. Eunoquies, A. Hogoerg, A. C. Evietrana (montated for Hogopolinings)	11-1
Protection Against Lightning Surge Voltages on Communication Lines and Power Lines J. L. Ter Haseborg, H. Trinks (German Federal Armed Forces University)	
Frequency Failure of Lightning Arresters at Satpura Thermal Power Station, India: Preliminary Regults of Field Observations	12-1
M. A. Selvam, G. K. Manohar, L. T. Khemoni, P.C.S. Devarc, G. A. Monin, A. S. R. Murty, V. R. Murty, (indian Institute of Tropical Meteorology)	

## Session 4A: Phenomonology Chairman: P. Rustan Wright Patterson AFB, Dayton Ohio

Correlated Measurements of UHF Radar Signatures, RF Radiation and Electric Field Changes from Lightning Vladistav Mazur, D. M. LeVine (University of Oklahoma)	13-1
Relationship Between Lightning Occurrences and Radar Echo Characteristics Over South Florida and Their Correlation With Redar Activity	14-1
P. E. Lopez, R. L. Holle, W. L. Hiscox (NOAA) Climatological Characteristics of Lightning Over South Florids and Their Correlation with Padar Activity	15-1
P. E. Lopez, R. L. Holle, W. L. Hiscox (NOAA)	
Session 4B: Aircraft and Aerospace Lightning Modeling Chairman: J. Birken Department of Defense, (NAV Air) Washington, DC	
Modeling of Direct-Strike Lightning Coupling by a Transfer Function Technique	16-1
D. Auckland, J.A. Birken (Syracuse Research Corp.)  Some Results and Limitations of Prony Analysis of In-Flight Lightning Data  T. Trost (Texas Tech. University)	17-1
Coupling of Natural Atmospheric Interference through Apertures J. Hamm, W. Graf, E. F. Vance (SRI International)	18-1
Session 4C: Ground System Protection Chairman: M. Huddleston, Georgia Institute of Technology, Atlanta Georgia	
A Modeling System for Conducted Transient Analysis	19-1
Thomas Mahoney (Harris Corp.) Lightning Protection Zones for Rocket Launched complexes	20-1
K. Pinckney, A. Murakami (USAF, Norton Air Force Base) The MLRS Lightning Protection Program John Robb, G. Edlin (Lightning Transients Research Institute)	21-1
Session 5A: Phenomenology Triggered Lightning Chairman: A. Few, Rice University, Huston Texas	
A Contribution to the Analysis of Triggered Lightning: First Results Obtained During the Trip 82  Experiment*	<b>2</b> 2 1
P. Laroche (Office National d'Etudes et de recherches aerospatiales) Relations of the Flashover Voltage Versus The Velocity of the Moving Electrode, Simulation of the Rocket Triggered Lightning	23-1
Y. Nagal, T. Koide, K. Kinoshita (Sagami Institute of Technology) Static Discharge and Triggered Lightning Heinz Kasemir (Colorada Scientific Corp.)	24-1
Session 5B: Aircraft and Aerospace Flight Enviroment I Chairman: J. Moe, General Dynamics, Fort Worth, Texas	
Laboratory and Field Observations Related to Ice Particle and Aircraft Charging in Convective Storms	25 <sup>,</sup>
J. Hallett,C. P. R. Saunders (Desert Research Institute) Lightning Attachment Patterns and Flight Conditions Experienced by the NASA F-106B Airplane	26-1
Bruce Fisher, A. Plumer (NASA-Langley Research Center, Virginia) Inside the Cone of Protection	27-1
J. Stahamann (Kennedy Space Center)	
Session 5C: Ground Systems Ground Installations Chairman: W. Peele, SCEEE St. Cloud, Florida	
Earth Electrodes for Grounding NEMP Type Lightning	28-1
D. Millard (Georgia Institute of Technology) Improved Grounding System for Mountain Top Radio Sites	29-1
L. Watts (Federal Emer. Management Agency)  Electrical Resistivity of Concrete in the Foundation Earthing  A. Vorgucici (University of Nis)	30-

# Session 6A: Helicopter Electrostatics Chairman: J. Mast, Bell Helicopter, Fort Worth, Texas

Electrostatic Voltage Sensors for Helicopter Dischargers	31-
Owen Tranbarger (Southwest Research Institute) Electrostatic Voltage Sensors for Helicopter Dischargers	31-
B. M. Duff (Southwest Research Institute)	
Electrostatic Charging Occurring in a Vortex Trailed from the Tip of a Lifting Surface Henry R. Velkoff, J. Dougherty (Ohio State University)	32-
Detection and Ranging of Electric Charged Helicopters	33-
H. Trinks, J. L. ter Haseborg (Technical University Hamburg-Harburg)	
Session 6B: Aircraft and Aerospace Flight Environment ii Chairman: J. Mye, General Dynamics, Fort Worth, Texas	
Chairman, J. M. Ve, General Dynamics, Port Worth, Texas	
Intracloud Lightning Streamer Modeling Based Upon in Situ Balloon Measurements G. L. Weinstock (Mcl`onnell Aircraft Co.)	34-
Correlation of Space Shuttle As-Built Atmospheric Capabilities with Known Atmospheric Conditions that Produce Lightning Tim Fitzsimmons (McDonnell Douglas Tech. Services Comp., Inc.)	35-
Atmospheric Electricity Threat Definition for Aircraft Lightning Protection  B. G. Melander (Boeing Military Airplane Co.)	36-
Lightning Strikes to Aircraft of the German Federal Armed Forces	37-
Wilfried Ziegle: (ERPROBUNGSSTELLE Der BUNDESWIEHR) Session 6C: Aircraft and Aerospace Full-Scale Simulation	
Chairman: B. Burrows, Culhan Laboratory, Oxfordahire, England	
Effects of Simulated Lightning Current on the Tensile Strength of Graphite/Epoxy	38-
Mr. William Howell (NASA-Langley Research Center, Virginia	20
Recent Lightning Induced Voltage Test Technique Investigations  Mr. Keith Crouch (Lightning Technology Institute, Massachusetts).	39-
NASA F-106B Lightning Ground Tests	40-
B. Heady (McDonnell Aircraft Co.)	44.
Induced Transients in Simulated Lightning Testing of the Fly-by-Wire Jaquar Aircraft J. Bishop, R. Evans (Royal Aircraft Establishment)	41-
Session 7A: Phenomenology Lightning Streamer initiation Chairman: A. Few, Rice University, Houston, Texas	
The Streamer-Leader Transition in Uniform Fields	42-
Dr. J. A. Bicknell (University of Manchester, Institute of Science and Technology)	
Intractional Lightning Streamer Modeling Based Upon in Situ Balloon Measurements G. Byrne, A. A. Few, M. F. Stewart, M. E. Weber (Rice University)	43-
Propagation of Discharge Channel Inside the Cloud	44-
P. P. Pathak (University of Roorkee, India)	
Session 7B: Aircraft and Aerospace Flight Environment Chairman: G. DuBro, Flight Dynamic Lab, Dayton, Ohio	
Electromagnetic Measurements of Lightning Attachment with Aircraft P. L. Rustan, B. Kuhman, J. Reazer, J. Showalter (Air Force Wright Aero Lab)	45-
Airborne Measurements of the Risctimes in Lightning Return Stroke Fields	46-
P. L. Rustan, B. Kuhman, J. Reazer, G. DuBro (Air Force Wright Aero Lab)	
Lightning Fields Spectra Obtained from Airborne Measurements W. P. Geren (Boeing Company)	47-
Session 7C: Locators - Lightning Locators	
Chairman: R. Bont, Atlantic Scientific Corp, Indian Harbour Beach, Florida	
Ground Evaluation of an Airborne Lightning Locator System	48-
W. Lewis, A. Barile, N. Rasch (FAA Technical Center)  A Wideband Alrborne/Ground Lightning Flash Location System	49-
E. Coleman (Naval Air Development Center)	70
Wideband Magnetic Direction Finder Networks for Locating Cloud-to-Ground Lightning R. Binford, L. Byerley, E. Krider, M Mier, A. Pifer, M. Uman (Lightning Location and Protection, Inc.)	50-

# Session 8A: Phenomenology Lightning Flash Distribution Chairman: D. Mac Gorman, NSSL (NOAA), Norman, Oklahoma

Airborne and Ground Based Lightning Electric and Magnetic Fleids and VHF Source Locations  for A Two Stroke Ground Flash	51-1
M. Uman, E. P. Krider, (Lightning Location and Protection, Inc.)	
Lightning Flash Density Versus Altitude and Storm Structure from Observations with UHF and 'S' Band Radar	52-1
V. Ladislav Mazur, R. T. Arnold, (University of Oklahoma)	
Lightning Shockwave Effects on Aircraft Fuel Vent Lines	53-1
T. Lee, J. Robb (Lighting and Transient Research Institute)	
Session 8B: Aircraft and Aerospace Full Scale Simulation and Test Techniques Chairman: I. Mendel, IIT Research Institute, Chicago, Illinois	
The Effects of New Technology Trends on Aircalift Lightning Vulnerability and the Capability to lidentify Technology Deficiencies	54-1
D. Auckland, J. Birken, R. Wallenberg, SRC, (Syracuse, New York) Unprotected Radome Lightning Tests and implications Keviar Airframe Design D. Aukland (Despression of News)	5 <i>5-</i> 1
D. Aukland (Department of Navy) <b>An Overview of the F-14A and F/A-18A Lightning Tests*</b> R. Perla, C. Esterbrook, J. Birken (EMA, Denver, Colorado)	56-1
Session 8C: Lightning Locators Chairman: R. Bent, Atlantic Scientific Corp., Indian Harbour Beach, Florida	
Errors in Lightning Direction Finding by Airborne Crossed Loops L. Parker (Lee W. Parker, Inc.)	6 <b>7-1</b>
UHF Interferometric Imaging of Lightning	5 <b>8</b> -1
P. Richard, G. Labaune (Office Nat'l e'Etudes et dt Recherches Aerospatiales)	
Mechanical Force Damage Resulting From Lightning Strike C. Jones, G. Reid (Culman Lab)	59-1
Session 9A: Helicopter Lightning Protection Chairman: G. Parkinson, United Aircraft Co., Stratford, Connecticut	
Electrostatic Theory Applied to Helicopter Discharging Robert V. Anderson (Naval Research Lab)	
	60-1
The Lightning and Electrostatic Control Effort for Apachy AH-64 Helicopter	61-1
H. Hoffart, G. A. Booth (Hughes Helicopter) Advance Testing of Lightning Protection Schemes for Composite Main Notor Blades J. Haseltine (Westland Helicopters Limited)	<b>62-</b> 1
Session 9B: Aircraft and Aerospace Simulation Facilities Chairman: L. Walko, USAF Flight Dynamics Lab, Daytor., Ohio	
Nanosecond Resolution of E. H. and I. in Aircraft Lightning Test Rigs B. J. C. Burrows (Culham Laboratory)	63-1
The Sandia Lightning Simulator	64-1
James C. Bushnell (Sandia National Lab) Full System Tests Using the Sandia Lightning Simulator Robert White (Sandia National Lab)	85-1
Hopert Willie (Sandia Hational Lab)	
Session 9C: Aircraft and Aerospace Test and Protection Chairman: H. Knoller, Lockheed Aircraft Co., Northridge, California	
Lightning Interaction with USAF Aircraft John C. Corbin (ASD/ENACE)	66-1
Component Lightning Test for the AFTI/F-15 Digital Fly-by-Wire System R. T. Zeitler, K. G. Wiles (General Dynamics)	67-1
Usage of the Sys cap II Circuit Analysis Program to Determine Semi-conductor Fallure Threshold Levels caused by Lightning/EMP Translents C. T. Kleiner, D. Rusher (Rockwell International)	68-

# Session 10A: Phenomenology Lightning Electromagnetic Characterization Chairman: M. Uman, University of Florida, Gainsville, Florida

The Submicrosecond Structure of Lightning Radiation Fields Philip Krider, E. D. Weldman (University of Arizona)	68-1
A Sciution for the Electromagnetic Fields Close to A Lightning Discharge  D. LeVine, R. Meneghini (Goddard Space Flight Center, NASA)	70-1
Tropical Lightning: Electromagnetic Characterization C.O.P.T. 81 Experiment (Tropical Deep Convection)	71-1
Z. C. Leteinturier, J. Jamelin, M. LeBoulch (National Telecommunications Research Center) The Effect of Propagation on Electromagnetic Field Radiated by Lightning Robert L. Gardner (Mission Research Corporation)	72-1
Session 108: Aircraft and Aerospace Simulation Facilities Chairman: L. Walko, USAF Flight Dynamics Lab, Dayton, Ohio	
Performance of the Sandia Lightning Simulator during F-14A and F/A-18 Aircraft Lightning Tests Ronald I. Ewing (Sandia National Lab)	
An Impulse Generator to Simulate Lightning Effects on Aircraft	73-1 74-1
E. Gockenbach, M. Modrusan, H. Sutter (EMILE, Haffely and Company)	/ <del></del> ·
Measurements with Theoretical Analysis of a Full Scale NEMP Type Lightning Simulator for Aerospace Vehicles	75-1
J. Robb, R. Perala (Lightning Transient Lightning Institute) Updating the McAir Lightning Simulation Laboratory	76-1
E. H. Schulte (McDonnell Airplane Company)	70-1
Session 10C: Aircraft and Aerospace Test and Protection Chairman: H. Knoller, Lockheed Aircraft Co. Northridge, California	
Vulnerability Assessment of Electrical/Electronic Subsystems and Equipment to Atmospheric Electricity	77-1
Jack Lippert (AFWAL/FIEA)  Monitors for Upset Detection and Computer Systems  A. Davidoff, M. Schmid, R. Traff, G. Masson (John Hopkins University)	78-1
Lightning Protection Devices for Very High Frequency Equipments	<b>79</b> -1
Jean Pierre Simi (les cables de Lyon) Lightning Tests of an Electronic Engine Control with Associated Wiring J. Robb, D. Loncrini, H. Ogasian, P. Geren (Lightning and Transients Research Institute)	80-1
Session 11A: Phenomenology Lightning Electromagnetic Characterization Chairman: M. Uman, University of Fiorida Gainesville, Fiorida	
Development of a Human Electrostatic Discharge Model in Relation to Electronic Systems W. Byrne (SRI)	
	81-1
Fast Fleid Changes Produced by Positive Ground Strokes M. Ishil, J. Hojo, T. Kawamura (University of Tokyo)	82-1
On the Oscillating Bipolar Return Stroke Current T. Takeuti, N. Takagi, M. Nakano (Nagoya University)	83-1
Session 118: Aircraft and Aerospace 'P' Static and Corona Chairman: J. Boulay, Office National d Etudes et ed Recherches Aerospatiales, France	
P-Static Flight Evaluation of a Large Jet Transport	84-1
Charles H. King (Boeing Airpiane Co.) Electric Charging by Impact of Halistones and Raindrops	85-1
H. Trinks, J. L. ter Haseborg (Technical University Hamburg-Harburg)	JU 1
The Effects of Precipitation Static and Lightning on the Airbo∗ne Reception of LORAN-€ James D. Nickum (Ohio University)	86-1

## Session 11C: Aircraft and Aerospace Test and Protection Chairman: J. Corbin, USAF Flight Dynamics Lub, Dayton, Otio

Digital System Upset-The Effects of Simulated Lightning-Induced Transients on a General Microprocessor	Purpose
Celeste M. Belcastro (NASA-Langley Research Center)	
	87-1
Lightning Protection Design and Lightning Threat Flight Clearance of a Fly-by-Wire Flight Control System for an Unstable Alcoraft	88-1
P. A. Doggett, I. P. MacDiarmid (British Aerospace P.L.C.)	
Upset Experimentation in Computer Based Systems Dr. G. Masson	89-1
Session 12A: Phenomenology Lightning Changing Mechanism Chairman: J. Robb, Lightning and Translent Research Institute, St Paul Minnesota	
Conditions Conducive to Lightning Striking an Airplane in a Thunderstorm J. Gerlach, V. Mazur, B. Fisher (Goddard Space Flight Center)	90-1
Lightning Initiation in Thunderclouds J. Latham (UMIST)	91-1
The Origin of Thunderstorm-Electricity  A. Puhringer (E'EKTROTECHNIK der Technischen Universität DRESDEN)	92-1
Session 12B: Alreraft and Aerospace 'P' Static and Corona Chairman: J. Nanevicz, Stanford Research Institute, Menio Park, California	
Aerospace Vehicles Charging by Thruster Plumes	93-1
H. Trinks (Technical University Hamburg) Laboratory and In-Flight Evaluation of Passive Dischargers	94-1
J. L. Boulay (Office National d'Etudes et de Rocherches Aerospatiales)	•
Session 12C: Aircraft and Aerospace Test and Protection Chairman: J. Corbin, USAF Flight Dynamics Lab, Dayton, Ohio	
Allocation of Protection	95-1
E. F. Vance, J. E. Nanevicz, W. Graf, J. Hamm (SRI International)	
The Lightning Spark Barrier Mike Amason, M. C. Hofmisiter (McDonnell Douglas Corporation)	
96-1 Protecting the World's Largest Commercial Helicopter from Atmospheric Hazards	97-1
G. A. Heiderscheidt (Boeing Vertol Company)	67-1

STORM ELECTRICITY RESEARCH IN OKLAHOMA: AN OVERVIEW

W. David Rust, William L. Taylor, Donald R. MacGorman National Severe Storms Laboratory, Norman, OK 73069

Roy T. Arnold University of Mississippi, Oxford, MS 38677

Stephen J. Goodman
NASA/Marshall Space Flight Center, Huntsville, AL 35812

Vladislav Mazur Cooperative Institute for Mesoscale Meteorological Studies, Norman, OK 73019

The National Severe Storms Laboratory and other agencies and institutions have collaborated on storm studies in which electrical and meteorological phenomena are compared and individual lightning characteristics are studied. We have found that lightning is usually associated with higher radar reflectivities from precipitation and often extends downwind from the main updraft into lower reflectivities. Lightning activity appears to be distributed vertically with a bimodal distribution having peaks between about 4-6 and 11-13 km. The upper peak is in lower reflectivities and strongly associated with divergent winds at the top of the storm. Lightning of significant horizontal extent (tens of kilometers) appears to be common in Great Plains storms. In-cloud progression speeds vary during a flash with maximum speeds averaging about 100 km/s. Lightning flashes that lower positive charge to ground may pose unusual threats because they can occur in very weak reflectivities, tend to propagate long distances, usually contain continuing current, have fast risetimes during their return stroke, and appear to have very high peak currents.

#### INTRODUCTION

In 1978 the National Severe Storms Laboratory began coordinated measurements of the electricity, dynamics, and precipitation associated with the large and often severe thunderstorms that form over the Great Plains of the United States. This research effort has incorporated cooperative studies with several groups, including universities and other U.S. government agencies.

In the central United States, large and often severe storms typically occur during the spring and early summer, although they do occur during other months as well. The spring storms are typified by rapid motion across the terrain (speeds of >15 m/s), large hail (>3 cm in diameter is not unusual), strong surface winds (often >30 m/s), high cloud tops (often >15 km), intense updrafts, and mesocyclones, and sometimes tornadoes. They occur in squall lines or in isolation and can be of the multicall or supercell type (1).\* These characteristics are a challenge to effective study of severe storms and their electrical behavior. Our goal is to develop an understanding of relationships

 $^{\aleph}$ Numbers in parentheses designate references at the end of paper.

between electricity and co-existing dynamics and precipitation in severe storms. Examples of these interrelationships and of phenomena related to lightning hazards will be presented here.

#### INSTRUMENTATION

Measurements of electrical phenomena are made with both fixed and mobile facilities (Fig. 1). The fixed facilities include a lightning discharge mapping system that allows three dimensional location of VHF radiation sources (30-80 MHz) from lightning (2) at rates of up to 1.6x104 per second and out to a range of about 70 km. Electric field changes, AE, are measured with field change sensors (3) that have 0.7 us rise times and decay time constants τ of 10 s and 100 μs (or 1 ms in the present version). The longer T allows the entire flash to be characterized by its field change, while the faster T is used to study waveform detail in return strokes, K-changes, etc. Other parameters we measure include the atmospheric electric field, optical transients from lightning, location of cloud-to-ground (CG) flashes within about 400 km (Fig. 2), corona current, and precipitation current. Documentation of clouds and lightning are made with television, movie, and cameras. Both Doppler and conventional radars are utilised to acquire echoes

from lightning. Additional information is obtained from meteorological soundings of the atmosphere and a surface network that records corona, wind, pressure, temperature, and humidity.

A van has been equipped as a mobile laboratory to measure most of the electrical parameters mentioned above. Use of a mobile laboratory creates logistical problems, but placing instrumentation in a relatively fixed position within the severe storm, in particular, beneath the precipitation-free cloud base (see asterisk in Fig. 3), provides the possibility of making quantitative electrical measurements in this key region (4). In tornadic storms, the region is characterized by a strong, inflowing lowlevel wind that flows into the rotating updraft, called the mesocyclone (sometimes visible as a lowered, rotating cloud base called the wall cloud). If they occur, strong tornadoes form under the wall cloud. Because of previous work on the correlation of visual, severe-storm cloud features with Doppler radar analyses, the documentation of visual features of these storms

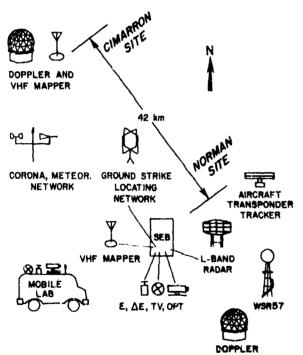


Figure 1. NSSL storm electricity research facilities are at Norman and Cimarron. The two major fixed sites are at Norman and Cimarron. These two both have a VHF lightning mapping system and a 10-cm wavelength Doppler radar. The main recording site for storm electricity parameters in Norman is the storm electricity building (SEB). The University of Niesissippi/NSSL mobile laboratory carries much of the same instrumentation as used at the SEB. The L-band (23-cm wavelength) radar is used exclusively to acquire schoes from lightning.

allows us to infer gross storm dynamics with which to correlate electrical activity even when storms occur outside the Doppler radar data acquisition area. Mobility also increases substantially the number of severe storms that are studied each season.

Radar information on storms is obtained with one conventional and two Doppler, 10-cm wavelength radars. One Doppler is located at NeSL and the other 42 km to the northwest. This arrangement forms a primary dual-Doppler data acquisition area that is about 200 km in length and is aligned from southwest to northeast (5) along the predominant direction of movement of springtime storms. Dual Doppler data are usually

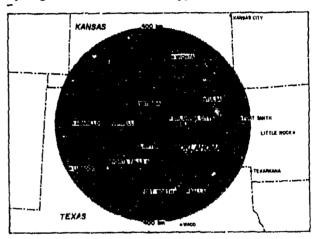


Figure 2. Cloud-to-ground strike location network. The four squares denote site locations, which are about 100 km apart. The nominal range of detection is within a radius of about 400 km of NSSL. All sites are capable of detecting both positive and negative flashes to ground.

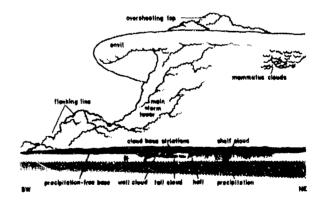


Figure 3. Sketch of typical tornadic storm as viewed from the southeast. The region south of the wall cloud (marked with an asterisk) is generally precipitation free and is the preferred close-in observational location. The horisontal dimensions of the sketch are compressed, and the downshear anvil that can extend more than a 100 km (toward the NE) is not shown.

obtained by coordinated scanning up through a selected storm region. Each tilt sequence through the storm region usually takes 4 to 5 min. Single Doppler information, i.e., only one component of velocity, can be obtained at ranges greater than 300 km.

Logistic support and guidance for storm intercept, balloon launch, and aircraft crews are provided with a radio communications network. Aircraft can be controlled and tracked at the NSSL Doppler facility making possible real-time assessment of precipitation, turbulence, and lightning, which aids the selection of desired flight paths.

#### **OBSERVATIONS**

Severe Storm, 20 June 1978, Central Oklahoma

Although only single Doppler data up to midstorm level (7 km) were obtained and only a few flashes were mapped, this storm is significant because it demonstrates that it is indeed feasible to correlate lightning with storm dynamics and precipitation. The storm was a severe, non-tornadic, supercall thunderstorm. The storm contained a mesocyclone circulation and produced four funnel clouds, hailstones up to 6 cm in diameter, and surface wind gusts in excess of 35 m/s. Details of the observations made on this supercell have been reported by Goodman et. al. (6). The evolution of this storm during our observations is consistent with the general aspects of the mature and dissipating phase of a supercell life cycle (7) and the entire evolution of a mesocyclone life cycle (8).

Results of this study are constrained by the following: 1) a small number of lightning flashes were mapped; 2) many mapped source locations were at higher altitudes than the radar data; 3) all but one of the mapped flashes occurred during the dissipating phase of the supercell life-cycle; and 4) there is uncertainty in the precise location and intensity of the updraft because only limited single Doppler radar data are available. Limitations notwithstanding, some useful insights and relationships can be inferred for the collapse stage of the storm:

- Many of the mapped sources were in the vicinity of cyclonic wind shear associated with the updraft.
- 2) The mapped sources produced by CG flashes were more closely associated with the mesocyclone position at storm mid-levels than were the mapped sources from intracloud (IC) flashes.
- 3) Mapped sources from both IC and CG flushes were distributed over large horizontal distances (approximately 20 km), and the vertical and horizontal extents of regions encompassing the mapped sources for individual IC and CG flushes were highly variable.

- 4) Many mapped sources occurred near the reflectivity core of the storm. Some mapped sources occurred in regions of the storm having a reflectivity factor of at least 50 dBZ. This agrees with observations reported by Rust et al. (9).
- 5) The mapped sources were spatially and temporally associated with the development of the updraft. The number of mapped sources in the immediate vicinity of the mesocyclone decreased as it decayed, and a new region to the south of the mesocyclone became electrically active, as indicated by an increase in the number of mapped sources as a reflectivity core and region of cyclonic shear formed nearby.

Squall Line, 6 June 1979

We examine one group of cells (sustained, identifiable radar reflectivity cores) within a squall line that developed during midafternoon. Our analysis covers this storm as it approached the laboratory from the west during 1640-1708 CST. It was categorized as severe because it had produced large hail and straight-line winds in excess of 25 m/s. but there was neither a mesocyclone nor tornado.

We located 342 flashes within this storm between 1640 and 1708 CST. Of these flashes, 149 were CG, giving an IC:CG ratio of 1.3:1. Using our lightning strike locating system, we mapped the CG strike locations onto radar reflectivity contours at a height of 5 km. The modian value of reflectivity at 5 km above the strike points was 40 dBZ. About 75% of all flashes struck beneath reflectivities of ≥20 dBZ. In general, the strike point does not indicate the location of the intracloud position of these flashes because of the significant horizontal propagation that is common for flashes in such storms. Flashing rates, while not extreme, were high, with averages of 5 per minute for CG flashes and 12 per minute for all flashes.

From the dual-Doppler radar data, we have derived estimates of all three wind velocity components. The VHF mapped source locations tended to occur in regions of weak updraft (<10 m/s), often adjacent to regions of downdraft. The lightning generally stretched from the reflectivity cores and strong updrafts downwind within the storm. Few VHF sources were within cores of reflectivity in excess of 45 dBZ.

We also have examined radar-determined paramaters to correlate with flashing rates. Maximum reflectivity and maximum inferred updraft speed are shown in the lower portion of Fig. 4, with the number of lightning flashes plotted in the upper portion of the figure. The plots are partitioned into 4-min intervals that coincide approximately with the dual-Doppler data acquisition periods. There is an interesting apparent correlation of the trends in updraft, reflectivity, and total flashing rate in the 16-20 min interval.

Note also that throughout the entire period, the maximum updraft speed and the total flashing rate change in the same direction. The lightning activity is characterized by a slight decrease in CG flashes and a large increase in IC activity during the last interval analyzed. A determination of whether these apparent correlations are characteristic of large storms awaits additional analyses of other storms.

Flash Density in Squall Line, 20 May 1980

We have used our radars for location of lightning in storms at long ranges (10,11). Although radar techniques are particularly useful at long ranges from the observing site, lightning outside the radar beam is, of course, not observed. During a squall line on 20 May 1980, we used on L-band radar (23-cm wavelength) with an antenna beam width of 2.5° in aximuth and a cosecant squared vertical pattern and observed 1055 flashes during a 46 min period. The ICrCG flash ratio was at least 40:1. With our Doppler radar, we also recorded the precipitation in four

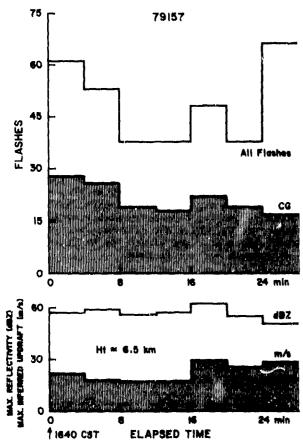


Figure 4. Lightning activity and storm parameters, 6 June 1979. The radar data are from a dual Doppler analysis for a height of 6.5 km. The trend in the total number of flashes, i.e., both CG and IC, per 4-min. interval is the same as for the maximum inferred updraft velocity.

cells, one growing and then dissipating and the other three still growing at the end of the observation.

From these data we infer the following about lightning in squall lines: 1) the maximum number of flashes may not coincide spatially with the highest precipitation reflectivity, 2) there is a tendency for most lightning to have at least some portion of each flash near the leading edge of the precipitation core, and 3) throughout the electrically active life of cells there are flashes that are shorter and longer than 20 km; as a cell develops and lightning activity increases, shorter ones predominate; as a cell dissipates, the shorter flashes diminish and the longer ones dominate the activity.

#### Spatial Extent of Lightning

Several investigators have reported the existence of long, horizontal flashes (see e.g., 12,13,2,3,10). We are finding that long flashes are common in Oklahoma storms; flash length is apparently associated with storm cloud size. An example of how two different systems, radar and VHF mapping, map the same long flash is shown in Fig. 5. The flash is first observed in the L-band radar beam at about 75 km, just beyond the range of the VHF mapping system. The total length of the lightning activity mapped with the two systems is >100 km.

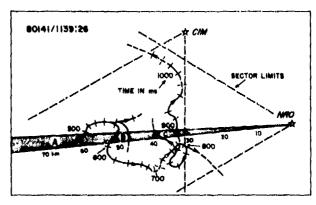


Figure 5. Lightning flash mapped with VHF and L-band radar, 20 May 1980 at 1139:26 CST. The shaded area is the radar beamwidth; the long dashed lines denote the VHF mapping sectors from Norman and Cimarron. The line with cross tice is the path of the center of the discharge obtained from the VHF mapping. Arrows indicate the direction of progression. Dashed line segments represent uncertain portions of the path. The cross true are every 20 ms, labeled each 100 me after 1139:28.000. A, B, and C mark the opinaidence in range and time as mapped with both systems. In addition to the main part of the flash, there were other discharge paths that moved in various directions. They stopped radiating prior to the end of the flash.

## In-Cloud Progression Speed of Lightning

Estimates have been made of the progression speed of discharges within clouds using various mapping techniques (e.g., 2,14). Taylor (9) mapped flashes in Oklahoma and found typical speeds of about 60 km/s. We also have used L-band radar to measure radial progression speed. Shown in Fig. 6 is an example of a lightning flash whose extent is >30 km. Notice that the flash progresses toward the radar (labeled fast) and then seems to stop for several milliseconds before moving forward again. This appears to be a typical pattern in radar data for the development of a flash. Using this radar technique, we have measured in cloud progression speeds as high as 250 km/s, with the average being about 100 km/s.

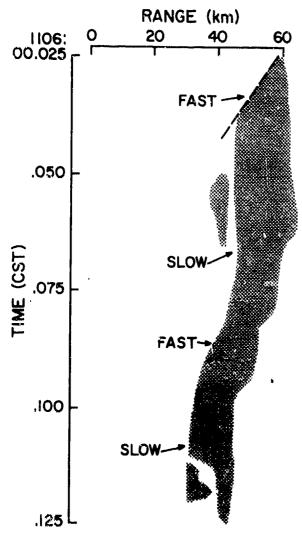


Figure 8. Range-time variation of radar scho from IC lightning, 20 May 1980. At any time the width of the shaded region shows the total range extent of the lightning scho within the antenna beam.

#### Vertical Distribution of Lightning

Lightning is found at all heights within storms, but there appear to be preferred heights where most activity occurs. Details are being presented in other papers at this conference (e.g., Taylor, MacGorman et al., Mazur et al.). Previously, we (9) have presented VHF mapping data that suggest CG flashes tend to begin and have their center of activity slightly lower than IC flashes. The median discharge height for the CG and IC flashes studied was 4.3 km and 5.9 km, respectively. Furthermore, when we have plotted all VNF mapped sources versus height, we find a bimodal distribution with peak activities between about 4-6 km and 11-13 km in Oklahoma, small severe storms (Fig. 7). We have observed this same sort of bimodal vertical distribution near Wallops Island, Virginia where we used a vertically scanning radar to locate lightning. During penetrations of the upper part of the Virginia storms with the NASA F106, it was possible to maximize the number of strikes to the aircraft by flying at the height of the upper maximum in the lightning activity.

#### Positive CG Flashes

Flashes that lower positive charge to ground (+CG) have been documented by several investigators. Most of the studies prior to the late 1970's were of flashes to tall structures (see, e.g., 15). In these studies it was noted that positive flashes, while numbering only a few percent of all CG flashes, often had very large peak currents. These flashes were termed triggered because tall structures were involved. Positive CG have also been thought to occur naturally, i.e., not triggered by tall structures.

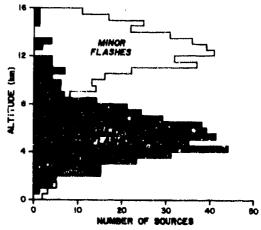


Figure ?. Altitude distribution of number of mapped VHP impulse sources from flashes during a non-severe storm, 19 June 1980. This type of bimodal distribution has been observed in several Oklahoma storms. The major flashes are those IC and CG generally observed, while the minor flashes are apparently smaller sime intracloud flashes that dominate the activity in the upper part of the storm.

This was confirmed in 1978 by Takeuti, Brook, and their colleagues (16) who reported that most CC flashes that occur in winter storms over the Japanese coast are positive. As a result, we began looking for +CG flashes in Oklahoma during spring storms. We have found that indeed, +CG flashes are present during severe storms and squall lines and may pose unusual threats to aviation.

We pre ent here our analysis of 31 confirmed CG's that were positive. We have observed +CG flashes to emanate from specific regions of severe storms as indicated in Fig. 8. Depicted in the figure is the classical supercell thunderstorm, which contains an intense convective region, shear, large anvil, and rotation. Of the CG flashes we observed within isolated severe thunderstorms, only negative charge has been lowered to ground by flashes within the heavy precipitation regions. Those from under the upshear anvil on the back of the storm and from the downshear anvil near the main storm tower can lower charge of either polarity, but usually lower negative charge. Of the few flashes we have observed to emanate from wail clouds, we

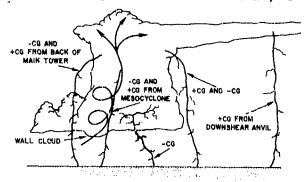


Figure 8. Observed locations of CG flashes based on observations of 31 confirmed +CG and numer-cus -CG flashes in several isolated, severe storms.



Figure 9. Electric field change for +CG flash, 20 May 1980 at about 1913:33 CST. SA denotes that the instrument had a 10 s decay time (see instrumentation section in text). The return stroke is labeled R. This flash was observed to emanate from the down shear anvil of a storm shortly after a wall cloud formed.

have documented two that were positive. Nearly all of the flashes to ground from the downshear anvil and well away from the storm tower have been positive. Most of the +CG flashes that we have observed have emerged from high in the storm, the notable exception being those from the wall cloud.

Single-stroke +CG flashes, which are the vast majority of positive flashes, have a rather typical but not unique electric field change (Fig. 9). Usually the flash shows substantial preliminary activity (240 ms average) followed by a return stroke whose amplitude averages about one-tenth the total field change. The presence of continuing current is suggested by the large, slow field change after the return stroke. Since our initial analysis of the thirty-one +CG flashes, we have obtained simultaneous electric field. optical, photographic, and television data for a fet other +CG flashes. An example is shown in Fig. 10. The field change is typical. A large ELF radiation pulse occurs at the time of each return stroke. The electric field waveform (Fig. 11) shows a zero-to-peak risetime of about 4 μs. Shorter +CG return-stroke risetimes have been observed, with the fastest in the submicro-

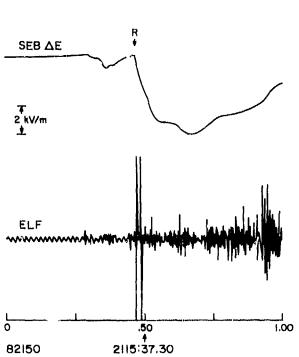


Figure 10. Electric field change,  $\Delta E$ , and ELF waveform for +CG flash recorded at the SEB, 30 May 1982. The time arrow denotes time at the center of the scale with full scale being 1.0 s. The return stroke is labeled R and is coincident with the first large ELF pulse that also shows the return stroke lowered positive charge (the second ELF pulse is an instrumental artifact). The amplitude calibration for  $\Delta E$  is snown.

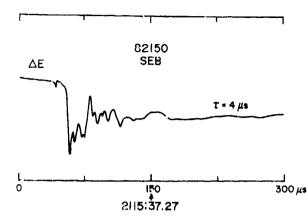


Figure 11. Electric field waveform for flash shown in Fig. 10. The zero-to-peak time, τ, for this return stroke is about 4 μs.



Figure 12. Streak-film photograph of +CG flash described in Figs. 10 and 11. Continuing ourrent is evident from the continuous smearing of luminosity. It lasts for about 60 ms; the associated continuing current field change can be seen in Fig. 10 from R to the first 'break' in the curve.

second range (17). The flash shown here was captured on TV and with a streak camera (Fig. 12). Notice the blurred channel luminosity that verifies continuing current is present as indicated by the field change. The four +CG flashes for which we have streak camera or TV images show the presence of continuing current. Based on the high percentage of single-stroke +CG flashes that have similar field changes and these few with confirmed continuing current, we suspect that continuing current is a common occurrence in +CG flashes.

We have obtained photographs of two +CG flashes clearly showing downward branches, thus indicating downward leader propagation. Of the +CG flashes we have observed in Oklahoma storms, we have no evidence of upward propagation, which would be indicative of tall structure triggering. Thus it appears as if these +CG flashes occur

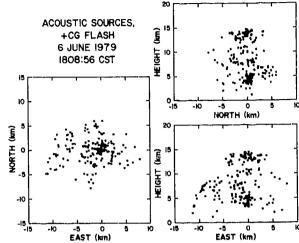


Figure 13. Map of thunder acoustic sources for +CG flash. Coordinates are relative to NSSL. The major part of the flash was nearly directly overhead with significant discharge activity extending to a height of about 15 km. The freezing level was at about 4 km.

naturally to the relatively flat terrain in the Oklahoma area.

Not only do we find +CG flashes in the mature and late stages of supercells, but we also observe them on the back side of squall lines. In fact, our recent observations suggest that squall lines may produce more +CG flashes than isolated storms. In squall lines the +CG flashes appear to propagate very long distances before coming to ground.

We have mapped the locations of acoustic sources from two +CG flashes using the thunder technique for mapping lightning channels described by Few (18) and Teer and Few (13). Shown in Fig. 13 are the reconstructed thunder source locations for one of six positive flashes that occurred in an 8-min period on 6 June 1979 following the passage of the more intense part of the squall line over NSSL (this is the same squall line described in an earlier section). The flash was observed to come to ground to the west. From a time-to-thunder measurement, we infer it struck earth about 8 km away. Many thunder sources in both flashas were located at or just above the freezing level, approximately 4 km above ground (or 4.7 km MSL). There were, however, a significant number of sources above 10

Data from our Cimmaron Doppler radar show that the acoustic sources lower than about 5 km were located in reflectivities of <17 dBZ, while those above 10 km were located in even weaker reflectivities. This flash was about 30 km from the closest large precipitation core of >50 dBZ, and it was on the back side of the squall line.

There are several aspects of +CG flashes that we feel need further study to ascertain whether these flashes may pose an unusual threat

#### to aviation. They include:

- the presence of very fast return stroke risetimes
- 2) the presence of large peak currents
- 3) the frequent occurrence of continuing current in the return stroke channel
- the tendency for these flashes to be in low reflectivity regions, which can appear innocent on radar, and
- 5) their very large spatial extent.

#### CONCLUDING REMARKS

We believe that several aspects of our research are relevant to lightning hazards to aviation. Study areas that we are currently addressing include: 1) procedures for real-time guidance of research aircraft, 2) the location of lightning relative to storm features in different storm types, 3) techniques for warnings to ground operations, 4) lightning location relative to turbulence within storms, 5) peak currents in channels of both -CG and +CG flashes, and 6) assessment of whether +CG flashes pose unusual hazards.

Progress is being made, and we invite other interested investigators to join us in continued and increased collaborative efforts.

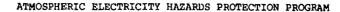
#### ACKNOWLEDGMENTS

Our work is supported in part by the Severe Storms and Local Weather Research Office of the National Aeronatucis and Space Administration, the Atmospheric Sciences Program of the Office of Naval Research, the Atmospheric Sciences Grant Programs Section of the National Science Foundation, and the National Oceanic and Atmospheric Administration.

#### REFERENCES

- K. A. Browning, "Hail: The structure and mechanisms of hailstorms," A Review of Hail Science and Hail Suppression, Meteor. Monogr., No. 38, Ed. by G. B. Foote and C. A. Knight, Amer. Meteor. Soc., Boston, Mass., 1-39, 1977.
- W. L. Taylor, "A VHF technique for spacetime time mapping of lightning discharge processes," J. Geophys. Res., 83, 3575-3583, 1978.
- P. R. Krehbiel, M. Brook, and R. McCrory, "An analysis of charge structure of lightning discharges to ground," J. Geophys. Res., 84, 2432-2456, 1979.

- 4. R. T. Arnold and W. D. Rust, "Initial attempt to make electrical measurements on tornadic storms by surface intercept," Preprints, 11th Conf. Severe Local Storms, Amer. Meteor. Soc., Boston, Mass., 320-325, 1979.
- R. A. Brown, D. W. Burgess, J. K. Carter, L. R. Lemon, and D. Sirmans, "NSSL dual-Doppler radar measurements in tornadic: A preview," <u>Bull</u>. <u>Amer. Meteor. Soc., 56,</u> 524-526, 1975.
- S. J. Goodman, D. R. MacGorman, R. J. Doviak, W. D. Rust and W. L. Taylor, "Spatis! and temporal characteristics of VHF emissions from lightning in a severe Oklahoma thunderstorm," <u>J. Atmos. Sci.</u>, submitted for publication, 1982.
- L. R. Lemon and Charles A. Doswell, III,
   "Severe thunderstorm evolution and mesocyclone structure as related to tornadogenesis," Mon. Wea. Rev., 107, 1184-1197,
  1979.
- D. W. Burgess, V. T. Wood, and R. A. Brown, "Mesocyclone evolution statistics," Preprints, 12th Conf. Severe Local Storms, Amer. Meteor. Soc., Boston, Mass., 422-424, 1982.
- W. D. Rust, D. R. MacGorman, and R. T. Arnold, "Positive cloud-to-ground lightning flashes in severe storms," <u>Geophys. Res.</u> <u>Letters</u>, <u>8</u>, 791-794, 1981.
- E. W. Szymanski and W. D. Rust, "Preliminary observations of lightning radar echoes and simultaneous electric field changes,"
   <u>Geophys. Res. Letters, 6</u>, 527-530, 1979.
- V. Mazur and W. D. Rust, "Lightning propagation and flash density in squall lines as determined with radar," J. Geophys. Res., accepted for publication, 1983.
- M. H. Ligda, "Lightning detection by radar," <u>Bull. Amer. Meteor. Soc.</u>, 31, 279-283, 1950.
- T. L. Teer and A. A. Few, "Horizontal lightning," J. Geophys. Res., 79, 3436-3441, 1974.
- D. E. Proctor, "VHF radio pictures of cloud flashes," J. Geophys. Res., 86, 4041-4071, 1981.
- K. Berger, "The earth flash," <u>Lightning</u>, <u>1</u>,
   R. H. Golde (Ed.), Academic Press, London,
   119-190, 1977.
- T. Takeuti, M. Nakano, M. Brook, D. J. Raymond, and P. Krehbiel, "The anomalous winter thunderstorms of the Hokuriku coast," J. Geophys. Res., 33, 2385-2394, 1978.
- W. D. Rust, D. R. MacGorman and R. T. Arnold, "Positive cloud-to-ground lightning flashes in severe storms," Geophys. Res. Letters, 8, 791-794, 1981.
- A. A. Few, "Lightning channel reconstruction from thunder measurements," J. Geophys. Res., 75, 7517-7523, 1970.



Rudy C. Beavin, Jack R. Lippert, and 't Jayme E. Lavoie

Air Force Wright Aeronautical Laboratories

#### ABSTRACT

The Flight Dynamics Laboratory of the Air Force Wright Aeronautical Laboratories (AFWAL/FIEA) is administering an Advanced Development Program (ADP) with support from other Government Agencies; e.g., members of the National Interagency Coordination Group (NICG); to design and demonstrate Atmospheric Electricity Hazards Protection (AEHP) for advanced technology A/C. The prime Contractor for the AEHP program is the Boeing Military Airplane Company (BMAC). The fifty-four (54) month (Technical Performance) Air Force Contract was initiated on 1 April 1982.

The two-Phase AEHP Program will consist ( a twenty-one (21) month Phase One for Protection Definition and thirty-three (33) month Phase Two for Effectiveness Demonstration. During the AEHP program, the electromagnetic (EM) environment resulting from aircraft (A/C) interaction with Atmospheric Electricity (AE) r e.g., Lightning and Precipitation Static, will be defined and the impact of that environment on electrical/electronic subsystems and equipment assessed. Tradeoffs will then be exercised to prescribe AEHP concepts which are compatible with protection required against other EM threats/ e.g., EMI, NEMP. From the candidate protection concepts available, optimized AEHP schemes for various classes of vehicles; e.g., Fighters, Transports/Bombers, Helicopters, and Missiles, will be specified. The effectiveness of the protection provided will be demonstrated through ground based AE simulation utilizing full-scale A/C and operating electrical/electronic subsystems and equipment employing appropriate AEHP concepts. The AEHP Program will emphasize timely information distribution and participation by interested organizations and personnel.

This paper provides an overview of the AE threats defined for the AEHP Program and presents an outline of the effort planned for the AEHP Contract Program. It is the intent of the Air Force management office for the AEHP Program to maintain communication with the technical community in order to more effectively direct Program investigations and encourage the timely transfer of results. Constructive criticism of AEHP Program activities is encouraged to insure effective application of Program resources.

#### INTRODUCTION

The AEHP Advanced Development Program enjoys the application of financial and Program resources by an assembly of Military/Civilian Agencies. This support is suggested on the Logo for the ADP shown as Figure 1. The Flight Dynamics Laboratory of the Air Force Wright Aeronautical Laboratories (AFWAL/FI) provides the ADP office for interagency coordination and AEHP Program direction. Other Federal Military Agencies contributing to the Program include other Air Force Laboratories and the Aeronautical Systems Division, as well as the Army, the Navy Air Systems Command and the Defense Nuclear Agency. In addition, the Federal Aviation Administration and the National Aeronautics and Space Administration are participating in the Program. The Boeing Military Airplane Company (BMAC) is the Prime Contractor for the Program. The National Interagency Coordination Group (NICG) for the National AEHP Program meets annually to review the work accomplished, underway and planned by various Agencies to encourage a coordinated application of Federal resources for AEHP investigations.



Figure 1 - AEHP ADP LOGO

In addition to the Agencies identified in the AEHP Logo, the National Sever, scorms Laboratory of the National Ocear graphic and Atmospheric Administration (NOAA/NSSL) is also a member of the NICG.

The first Phase of the AEHP Program will result in the definition of balanced protection concepts to provide confidence for all-weather application of advanced avionic and structural concepts in military and civilian scenarios. Balanced protection concepts which are appropriate for each of four classes of A/C; e.g., Fighters, Transports/Bombers, Helicopters, and Missiles will be provided. This Phase was initiated on 1 April 1982 and is scheduled to extend through December 1983 (21 months). During Phase One of the Program, the electromagnetic environments incident on A/C electrical/electronic systems will be defined and appropriate protection schemes defined. The balanced protection identified will provide appropriate protection for flight/mission critical elements of modern A/C when operated in the AE threat(s) defined. In order to achieve this result, the interaction of AE environments with modern A/C structures(s); e.g., Advanced Composite Materials, Lexan, high resistance metals; must be determined to characterize the AE associated threat incident on advanced electrical/electronic elements; e.g., Fly-by-Wire, Power-by-Wire, et al. Appropriate hardening schemes will then be designed to assure confident operation of flight/mission critical elements under AE threat conditions. The hardening employed will include a balanced set of: system, power, and information shielding; passive/active system protection; et al. The AEHP concepts prescribed will also be evaluated for their contribution to protection against other EM threats; e.g., EMI, NEMP; and protection concepts against the latter will be considered for incorporation in the final AEHP schemes specified. Finally, Phase One will provide an updated definition of the procedures to be employed in Phase Two to demonstrate the effectiveness of the AEHP provided through application of the Interim Design Guides derived from the Phase One investigation.

Currently, Phase Two is anticipated as having a January 1984 start with the technical investigations program being completed by October 1986 (33 months). During that period, it is planned to configure modified YUH-61 Helicopter and F-14 test beds with representative advanced electrical/electronic systems and advanced structural concepts to demonstrate the effectiveness of the balanced AEHP defined during Phase One. The test bed A/C, together with protected electrical/electronic systems representative of A/C of the 1990's will be subjected to interaction with simulated lightning flashes which will be representative of the AE threat determined during the ADP. The results of these tests will be evaluated and

appropriate adjustments made to the protection schemes employed. In addition to the demonstration of balanced protection effectiveness, techniques for qualification of protection and continued assessment of the integrity of the AEHP provided will be identified and demonstrated.

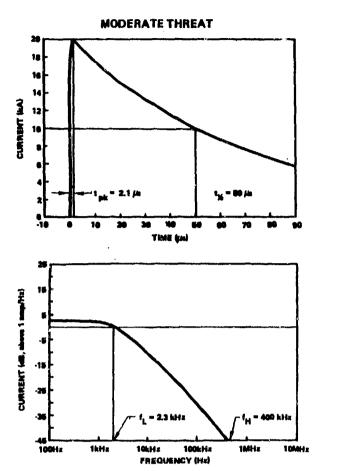
The AEHP ADP invites contributions from the aerospace technical community to improve the effectiveness of the Program and aid transition of Program results to aerospace system application. Your constructive criticism of the AEHP Program is encouraged. Continuing interactions will improve the quality of the AEHP Program and yield a maximum return on the Program investment.

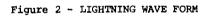
#### PHASE ONE (I)

The AEHP ADP is configures as a two Phase effort with Phase I being directed toward the development/design of effective AEHP for the four classes of flight vehicles displayed in Figure 10, i.e., Fighters, Transports/Bombers, Cruise Missiles, Helicopters.

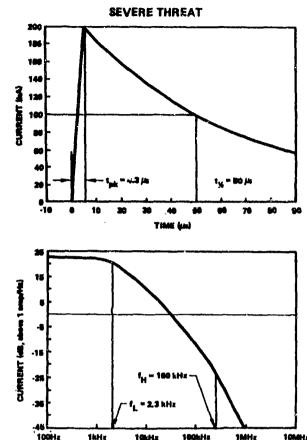
Atmospheric Electricity Threat - The electrical threat environment associated with atmospheric electricity phenomena has had recent intense investigations. This Program will continue through the Summer of 1983 with lightning attachment experiments planned by both NASA (LaRC) and AFWAL (FIESL). The results of these and other investigations will be afforded close scrutiny during the AEHP ADPO and appropriate adjustments to the AE environment made for the Program, when warranted. For the present, the historical data bases for Lightning and P-Static environments have been examined, including near-term investigations, and an Atmospheric Electricity Hazards Threat Environment Definition report prepared.

Atmospheric Electricity Threat Definition - The characterization of the atmospheric electricity threat environment imposed on flight and mission critical electrical/electronic elements aboard A/C is important for the AEHP Program. The initial definition of both lightning and precipitation static associated electrical environments for A/C has been taken from the technical record. In the case of precipitation static, the literature base has been examined, and the significant threat parameters with their range of magnitudes noted for inclusion in the atmospheric electricity threat characterization. There appears to be no need for additional exploration to define the precipitation static electrical environment at the A/C surfaces. For the lightning case however, although an appropriate initial characterization has been achieved for use during Phase I of the AEHP Program, both existing and new data will continue to be evaluated for contribution to the characterization of the lightning threat.





For defining the initial characterization of the lightning threat which will be considered during the AEHP ADP, the "best" available data has been employed. This characterization will be reviewed and revised, as necessary, as "new" data becomes available. The "initial" threat is based on three major sources of lightning current measurement which have an adequate statistical base; e.g., Berger in Switzerland, Garbagnati in Italy, and Uman, Weidman and Krider in the United States. From these measurements there is sufficient evidence to demand the increase of the prior accepted lightning maximum rate of current rise by a factor of two which has been included in the initial characterization of the AEHP threat wo A/C.



The "initial single stroke lightning threat has been characterized by double exponential current waveforms (Figure 2). The severe threat for the AEHP Program has a maximum rate of rise of 200 ka/µs with a peak current of 200kA, a falltime to half-peak value of 50µs, and an action integral of 1.5 x 10 Å -sec. The moderate threat has a 20kA peak current with a maximum rate of rise of 50kA/µs, a fall-time to half-peak value of 50µs and an action integral of 1.5 x 10 Å -sec. These parameters are shown in Table 1. Moderate and severe lightning flashes consist of multiple strokes of the nature shown in Table 1. Lightning flash characteristics are shown in Table 2.

FREQUENCY (Hz)

Airborne lightning characterization programs have been conducted by both NASA and AFWAL/FIESL which assist with evaluation of

TABLE 1 - LIGHTNING PARAMETERS

	PEAK CURRENT	PEAK RATE-OF-RISE	ACTION INTEGRAL		
Moderate:	20kA	5 ж 10 <sup>10</sup> амря/вес	$1.5 \times 10^4 \text{ amp}^2$ -sec		
Severe:	200kA	$2 \times 10^{11}$ amps/sec	$1.5 \times 10^6 \text{ amp}^2$ -sec		

#### TABLE 2 - LIGHTNING FLASH CHARACTERISTICS

O Duration of induced transient

50 - 500us

Inter-stroke time interval

10 - 100 ms

Time duration of lightning event

2 sec maximum

Number of strokes

Undefined (>50 recorded)

lightning current models and will lead to confirmation or adjustment of the current lightning characterization being employed. FIESL has also conducted Rocket-Triggered Lightning (RTL) experiments from Mt Baldy in New Mexico and further RTL investigations are planned for Florida in Summer 1983. Additional programs planned for this summer by both Groups are expected to contribute significantly to this effort. To assure that the AEHP ADP is afforded full benefit from these continuing investigations, resources have been provided for data analysis and model/characterization adjustment under the AEHP Program.

With the attachment of lightning flashes to A/C or the incidence of electromagnetic fields from nearby lightning events, as well as with charge accumulation resulting from precipitation static, currents and fields will be experienced at the surface of A/C. The waveform of this energy, as well as the magnitude of energy transferred to elements inside the A/C will be affected by A/C geometry and material. Various computer codes have been evaluated to determine the characteristics of the threat at the circuit/element station in an A/C as the result of transfer functions and coupling effectiveness. Among codes which have been applied are WIRAMT, THREDE, SRC-2D, as well as PRESTO/TRAFFIC. It is anticipated that the SRC-3D code may also be available for use in the AEHP Program.

These codes have made possible the prediction of fields and currents to be experienced during lightning simulation tests with the ALCM and YG-16 plus F-16 mock-up test beds. These predictions will be evaluated during tests to be conducted in Summer of 1983. In addition, the codes developed and demonstrated during Phase I will be applied to other test beds during Phase II and will be available for application during A/C - Lightning interaction analyses.

Electronic Susceptibility - Opportunities to perform extensive data acquisition/processing and effect flight and propulsion control, and extend navigational and communication capabilities, as well as effect sophisticated weapons employment, and other benefits have been afforded by recent/anticipated electronic concepts. However, the effective application

of avionics employing these concepts demands that appropriate protection against Atmospheric Electricity Hazards be supplied. Preparatory to identifying appropriate protection concepts, evaluating their effectiveness and performing system trades to determine effective balanced protection schemes for various classes of A/C scenario and associated avionics, the susceptibility of various electronic elements to upset/damage from electrical environments associated with Atmospheric Electricity - A/C interaction must be determined. The interest of the AEHP ADP is in providing effective protection for flight/mission critical electrical/electronic systems of the 1990's, anon. Many of the devices/systems of interest will not be available for direct investigation, but from the historical record and consideration of system/device trends both upset/damage mechanisms and tolerance may be projected. Such a consideration then aids in delimiting the protection which must be afforded against the threats of interest.

As a first step in determining the protection which must be afforded, the historical record has been examined to identify damage mechanisms for various types of semiconductors and other components. The sensitivity to upset has been assessed from manufacturer's data sheets and the necessity of testing to evaluate system upset effects noted. Some device upset evaluation by lightning transient testing will also be performed to assist in system upset consideration. To guide work in this area, flight and mission critical subsystems/equipment for A/C have been identified (Table 3). Many components required for these subsystems/ equipment will be individually tested in bench-tests, while others will be employed in test-bed evaluations, (Table 4). In addition to components employing current technology, new technology is also being tracked to establish a projection of A/C electrical/electronic subsystems trends. New component technology concepts; e.g., bubble memories, CCD, VLSI; are shown in Table 5. In addition, bench testing has been performed on representative electronic components/subsystems.

Since digital systems are very sensitive to upset, as well as employ components with low damage thresholds, it is important that a representative digital system be tosted/

TABLE 3 - FLIGHT/MISSION CRITICAL SUBSYSTEMS/EQUIPMENT

		• •	
TYPE OF SYSTEM	BENCH TEST	ANALYZE	EMP ANALYSIS AVAILABLE
Communication	ARC-190	ASC-19	ARC-164
Control & Display	MSIP Control (Honeywell)	ARV-50A	ASQ-176
EW			ALR-20 ALQ-153
System Integration	AP-101C (IBM)		AYK-17
Identification			KIT-1A APX-101
Flight Control		F-16 FCC (Bendix)	
	F-18 FCC (G.E.)		
Engine Control	Pratt & Whitney Ham-Std 2037		
Electrical Power	Sundstrand KC-135 Sunstrand (767/767)		AC Voltage Regulator DC Voltage Regulator
Fuel Management			KC-135 Capacitive Probe (B-52)
Navigation	Commercial ILS (Bendix)	Carousel INS (Bendix)	ARN-118
		ARN-14	ARN-108
Target Acquisition			ASQ-151 AVQ-HUD

## TABLE 4 - RECOMMENDED COMPONENTS FOR TEST

DEVICE P/N	DEVICE TYPE	MFG	QTY	UNIT PRICE
BPK70-4 (1)	Bubble Memory	Intel	2	370.00
7220-1 (1)	Bubble Memory Controller	Intel	10	64.00
F2642DC (2)(1)	CCD Memory, 65K - NMOS	Fairchild	10	38.50
MCM2801C	EEPROM 16 x 16 - NMOS	Motorola	10	9.00
D2806 - 4	EEPROM 2K x 8 - HMOS-E	Intel	10	29.50
MCM2708C	EPROM 1024 x 8 NMOS	Motorola	10	6.20
TMS3716CL	EPROM 2K x 8 - NMOS	Motorola	10	4.50
IM6654IJ6	EPRCM 512 x 8 - CMOS	Intersil	10	14.55
MC14034BCP	Commercial Universal Bus Register (8 bit)-CMOS	Motorola	10	2.90
8748 (3)	Microprocessor (8 bit) MMOS	Intel	10	24.00
SN5420J	Nand Gate - Dual 4 Input TTL	Texas Instr.	10	. 84

TABLE 4 - RECOMMENDED COMPONENTS FOR TEST (CONTINUED)

DEVICE P/N	DEVICE TYPE	MFG	QTY	UNIT PRICE
MC10101L	Nor Gate - Quad 2 Input ECL	Motorola	30	.75
MC10501L	Nor Gate - Quad 2 Input ECL (Militar)	Motorola	10	2.80
CD4011BCN	Nand Gate - Quad 2 Input - CMOS	RCA	30	.30
MC14011BAL	Nand Gate - Quad 2 Input - CMOS (Military)	Motorola	10	.62
			182	\$2735.00

TABLE 5 - COMPONENT TECHNOLOGIES IN FLIGHT AND MISSION CRITICAL AVIONIC SYSTEMS

		VHSIC	VLSI	CMOS	GaAs	COLOR	FIBER OPTICS	BUBBLE MEMOKY	ccs	SAW
1.	COMMUNICATIONS	x	x	x	x		х			x
2.	CONTROLS & DISPLAYS	x	x			x			x	
з.	ELECTRONIC WARFARE	x	x	x	x					
4.	SYSTEM INTEGRATION	x	x	x	x		x	x		x
5.	IDENTIFICATION	x	x	x	x			x		x
6.	FLIGHT CONTROL	x	x	x	x		x			
7.	NAVIGATION	x	х	x	x		<b>x</b> .			x
8.	TARGET ACQUIS. AND STRIKE	x	x	x	x					
9.	ELECTRICAL POWER		x	x	x	x				
10.	ENGINE CONTROL	x	x	x	x		x			
11.	FUEL MANAGEMENT	x	x	<b>x</b> ·	x		x			

evaluated during Phase I of the AEHP ADP. In addition to damage tolerance testing which is being performed, considerable attention is being focused on digital system upset. Results from testing of a representative digital control system(s); e.g., computer control system with a twisted shielded pair data bus; should be available in subsequent Program reports. In addition, the impact of AE transients on a color CRT display system suitable for use as an A/C display module is planned to be evaluated under representative operating conditions. A part of the testing is planned to include the observations of the types of disturbances that occur and their effect(s) on operator interpretation and reaction.

Vulnerability Assessment - This requires a substantial degree of experimental work. The main purpose is to obtain generic data on the susceptibility of components/subsystems in various generalized configurations when subjected to the defined lightning threat. This investigation is being accomplished via two different test beds (YG-16, ALCM) at two different facilities (BMAC, Sandia).

The YG-16 test bed consists of an advanced composite forward fuselage section mated to a mock-up representing the remainder of the F-16 aircraft. The forward fuselage is 78% GR/EP with some aluminum support structure. The

mock-up is sheet aluminum over a wood frame in the general F-16 shape to preserve electrical lengths and resonances appropriate for the fighter aircraft. The entire test bed is supported above the ground plane by nonconducting wood bracing. A picture of the YG-16 test bed is shown in Figure 3.

The YG-16 test series is designed to: a. Characterize the induced transients in aircraft wiring due to lightning attachment to the aircraft. b. Determine upset and damage sensitivities of advanced technology subsystems when exposed to moderate level lightning environments. c. Provide low level CW and moderate level pulse test data for comparison with analytical calculation.

Of the two test techniques employed, the Swept Continuous Wave (Swept CW) technique injects a low level current onto the aircraft skin/structure and measures the output voltage/current at wiring/equipment stations as a function of frequency. This results in definition of thetransfer functions in the frequency domain which may be used to determine coupling effectiveness and as an analytical tool. The other technique, pulse injection, applies a unipolar current impulse to the aircraft with response measurements taken in the time domain. This test generates information concerning susceptibility levels and interaction mechan-

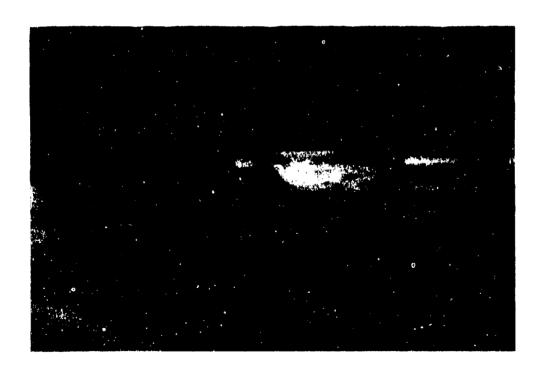


Figure 3 - YG-16 TEST BED

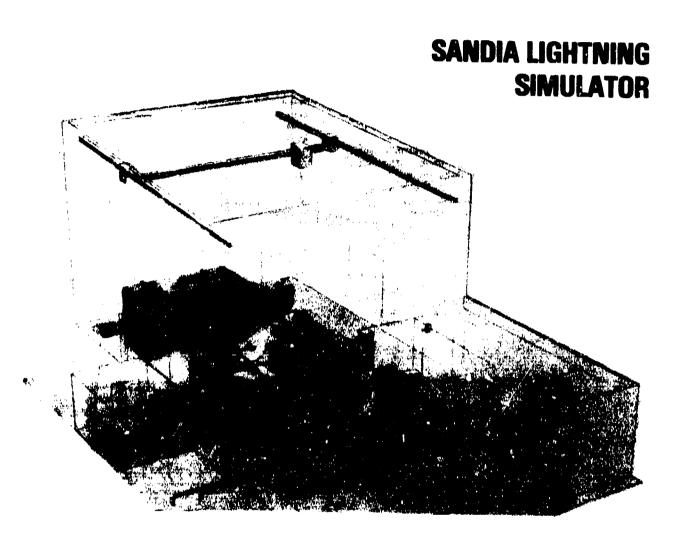


Figure 4 - SANDIA LIGHTNING FACILITY

isms. The pulse waveform used is the moderate level threat representation defined as a double exponential current waveform with the following parameters:

- a. Peak Current 10kA
- b. Peak Rate of Rise 5 x 10 10 A/sec.
- c. Action Integral 1.5 x  $10^{11} \lambda^2$ -sec.

Three levels of complexity are structured into the YG-16 test series: a. Simple, point to point wiring configurations with no operat-

ing subsystems. b. Generic installation of wiring with dummy loads which are electrically representative of advanced avionics. c. An operating subsystem with an airborne computer, appropriate power, control, and display equipment. The information gained from these tests feeds into protection concept development/tradeoff.

The Air Launched Cruise Missile (ALCM) test bed is a prototype version of the production AGM-86B which has undergone skin panel modification/removal and cable shield alteration to yield generic data for general missile configurations. This test series is being conducted at the Sandia Lightning Facility in

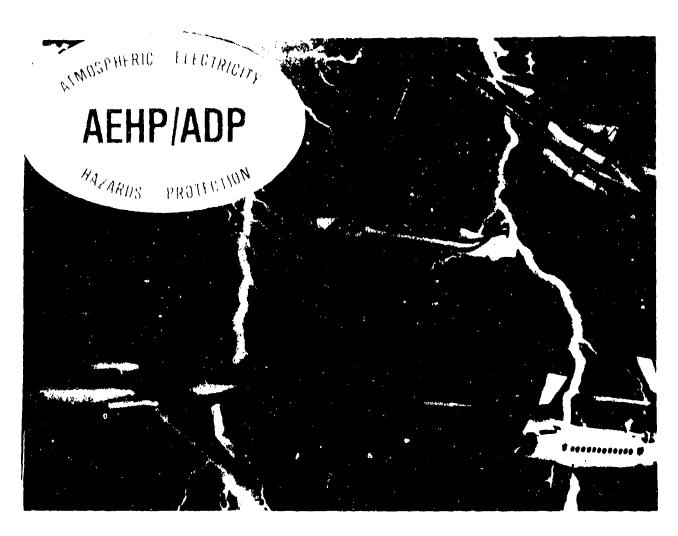


Figure 5 - REPRESENTATIVE A/C

Albuquerque N.M., which is shown in Figure 4. This facility is capable of subjecting the ALCM to current waveforms corresponding to the defined severe lightning threat:

- a. Peak Current 200kA
- b. Peak Rate of Rise 2 x 10 11 A/S
- c. Action Integral 1.5 x 10<sup>6</sup> A<sup>2</sup>-8

This severe threat coupled to a vehicle as small as the ALCM will provide a very strong current density on the vehicle to assess the impact of an extreme lightning current threat.

The objectives of the ALCM test series are as follows: a. To characterize the EM coupling paths from the lightning attachment point to mission critical equipment interfaces; b. To determine stress levels at selected equipment from various pulse levels; c. To determine upset and damage effects of simulated full threat lightning current pulses on operating avionics. The information gained will comple-

ment that from the YG-16 test series for use during Task V efforts.

Protection Evaluation/Tradeoffs - The objective of this Task is to evaluate and establish practical, effective protection concepts. These concepts will minimize cost, weight, power, reliability/maintainability requirements. The Task V trade study is to develop a specification for balanced protection for advanced (1990-95) airframes and associated electronic/electrical systems.

Protection concepts are being considered for each of four different classes of flight vehicles: Fighter, large Transport/Bomber, Helicopter; and, Cruise Missile (Figure 5). The trade studies will be primarily analytical but, when required, concepts will be evaluated experimentally on the YG-16 test bed to determine hardness effectiveness. At completion of Task V, the protection concepts will have been developed and evaluated parametrically. This information will then be assembled and correlated into the interim design criteria and used as the basis for the Phase II plans for full

scale demonstration of these protection concepts.

Interim Design Criteria - Near the conclusion of Phase I, Interim Design Criteria for Atmospheric Electricity Hazards Protection will be provided to the Aerospace Community for review and comment. It is important that the results of this ADP are effectively communicated to A/C and Systems producers so the AEHP concepts resulting from the ADP may have an early introduction to the Military/Commercial A/C fleets. Comments/suggestions from the Aerospace Community are encouraged throughout the ADP. Periodic presentations to Government/ Industry are planned for the April time period of each year during the Program to increase the transfer of technology. During these periodic interactions, as well as through meetings/ publication for troatment of special issues, the AEHP ADP will communicate findings/ uncertainties to the Aerospace Community. Through this mechanism the ADP hopes to continue productive interactions with Government/ Industry.

#### PHASE TWO (II)

In Phase II the effectiveness of the AEHP Interim Design Criteria and initial ARNP concepts will be demonstrated on A/C test beds using ground- based Atmospheric Electricity Simulators. At this time it is contemplated that the test beds to be used will be derived from a YUH-16 Helicopter and an F-14 A/C. basic vehicles will likely be extensively modified through application of advance composite and other poorly conducting materials as vehicle surface cover, as well as installation of electrical/electronic systems employing operational concepts representative of those anticipated for the 1990's. It is believed that this procedure will permit the evaluation of many electrical/electronic system protection concepts, including structural aspects and local shielding, as well as AEH tolerant electrical concepts, in configurations which are representative of those which will be encountered in future A/C of the four classes being considered; e.g., Fighters, Transports/ Bombers, Cruise Missiles, and Helicopters. The details of the Phase II Program to be conducted will be documented as part of the Phase I activity on the AEHP Contract.

Phase II is expected to be initiated in January 1984 with active investigation completed by October 1986 and the documentation of the AEHP Program continuing into early FY87. A product of Phase II will be finalized AEHP design concepts following adjustment from the initial design concepts produced in Phase I, as demanded by user critique and findings/actions from the demonstration activities of Phase II. Another product from Phase II will be documentation/demonstration of procedures for initial qualification of AEHP concepts for A/C

and procedures for evaluating the continuing integrity of the AEHP provided to A/C while in the operational inventory. Work is under way, both with AFWAL/FIESL and with Lightning Transients Research Incorporated (LTRI), chrough the AEHP Prime Contractor, BMAC, to define procedures/equipment which are appropriate for demonstration of AEHP concepts and initial qualifications of System and A/C protection. FIESL, BMAC and other organizations are also addressing the continuing assessment of protection integrity. Finally, during Phase II, the relationship of AEHP to protection against other electromagnetic threats; e.g., EMI, NEMP, Radar, et al; will continue to be explored. Where possible, consolidated design concepts will L : documented, but where advised the need for explicit protection outside the spectrum of protection provided by AEHP will be noted.

#### CONCLUSION

Through the Program planned for the Atmospheric Electricity Hazards Protection (AEHP) Advanced Development Program (ADP), the AE threat environment incident on A/C and the resulting threat at specific A/C stations will be documented. Then, appropriate AEMP design concepts will be identified for A/C electrical/ electronic systems representative of Military/ Civilian air vehicles of the 1990's. The effectiveness of these concepts for providing the AEHP required will be demonstrated and procedures documented for assessing the effectiveness/integrity of AMHP on-board operational A/C. Your review of efforts under the ARHP ADP and constructive comments are encouraged.

# LIGHTNING PROBLEMS ENCOUNTERED IN LARGE ELECTRONICS INSTALLATIONS AND THEIR SOLUTION

Samuel R. Crawford, Senior Engineering Specialist Ford Aerospace and Communications Corporation, Sunnyvale, California

ABSTRACT

The deleterious effects of lightning discharges due to inter/intra-cloud discharge on large distributed electronics installations (observed over a number of years) range from momentary disruption in performance to catastrophic destruction of site components.

A model is developed which gives ground level electric field intensity. The effects of this electric field on overhead power lines, including the influence of the soil characteristics on the effect of the lightning electromagnetic pulse (LEMP) is presented. The results of voltages induced in long cables by LEMP on the components of the installation is also discussed.

A history of implementation procedures for distributed electronic installation and methods of mitigating these results are presented.

THE PHENOMENON OF LIGHTNING has been a constant and continuing threat to large electronic installations which are distributed over a significant area, e.g., acres or a radius of thousands of feet. Since the introduction and extensive use of semiconductor devices with their inherent sensitivities to transient energy and voltage, this threat from the effects of lightning has increased many-fold. It has been demonstrated on any number of occasions that lightning can effectively cripple such an installation without a direct discharge to the installation or to any point on the earth or nearby structure.

A particular interest in the consideration of the vulnerability to lightning of such an installation is the effects of inter and intra-cloud discharges\* and the intensity of the electro-magnetic fields generated by these discharges. Electric field intensities of thousands of volts per meter at ground level have been computed as well as measured and their effects have been obrand as a result of a discharge as small as a few thousand amperes peak occurring at a height of one or two kilometers. These fields can induce potentials of catastrophic levels in power and signal lines interconnecting the elements of a large distributed electronic installation.

The effects of these inter and intra-cloud discharges as well those of the direct and nearby strikes on elements of the installation (such as outside plant cables and electronic circuits connected to these cables) will be discussed using the experience at several sites for illustration. Both the time and frequency domains are considered in the accompanying analysis to illustrate the effects of lightning-induced phenomena on bandwidth limited devices and on wideband devices that are subjected to a time-distributed pulse of lightning energy.

Several techniques of mitigating the effects of both ground-to-cloud cloud-to-cloud (or intra-cloud) and lightning discharges **V111** ba described. The effectiveness of these protection techniques is reported in terms of experience in actual implementation at sites subject to high lightning activity and high-remistivity earth.

#### CASE HISTORIES

Some case histories are now given of the effects of lightning activity at a few typical installations around the world. This reveals, typically, the damaging effects of lightning on the station's performance.

CASE I - A large installation in New England. This site normally experiences a high level of lightning activity during the summer and early autumn months. The station is built on a granite shelf, and, accordingly, the ground resistivity is quite high in the order of one-half megohmcentimeter. Often when a thunderstorm occurred in the vicinity, some damage would be suffered by the station electronics. This damage varied from momentary outages of primary power to the catastrophic destruction of station components. Seldom would there be any evidence of a direct strike to any part of the station where a strike did occur, it usually would be found that items such as antenna towers of heights of 200 to 400 feet had been struck. On those occasions when a direct strike was determined to have occurred, it was the system components related to those towers that had suffered damage. It was subsequently determined that the most prevalent damage to the instal-lation resulted from the effects of inter/intra-cloud lightning discharges inducing hesardous potentials into the power distribution system. This problem was solved by the installation of large surge suppression devices into the power system at the point where the power was fed in the buildings comprising the station.

CASE II - An electronic installation on the island of Oshu distributed with elements as far as 5500 feet apart. On one occasion, more than 120 LSI components of the station suffered catastrophic damage during a lightning storm. No evidence of a direct strike could be found, but someone remembered having seen a great display of cloud-to-cloud lightning activity over the ocean about three miles to the south of the station and apparently parallel to the cable interconnecting the two most remote elements of the station. Though it was never proven, this cloud-to-cloud lightning phenomenon seems to be the most logical culprit to blame for the damage, as no evidence to the contrary

was ever identified.

<sup>\*</sup>These discharges account for at least 75% of all lightning activity.

CASE III - A similar installation in the Indian Ocean with distributed elements about 1000 feet awart and in an area of high soil resistivity. At this latitude, about 90% of the lightning activity is inter/intra cloud in nature. The clouds occur at a very low altitude, at times coincident with the altitude of the station. During one thunderstorm the station suffered a direct strike to one of the antenna radones. The radone was grounded to a short (1-meter) ground red in soil of very high resistivity, while the antenna enclosed within the radome was connected to an excellent, chemically enhanced, low resistance (0.3 ohms) earth ground located some 50 meters away near an equipment building. The lightning energy, seeking the easiest route to the earth, found it by ignoring the radome ground connection and jumping from the radone frame to the antenna reflector. From there it was conducted through cables to the low resistance ground at the equipment building. The lightning current flowing in the ground cable parallel to the route of the various signsl, control and power lines to the antennas induced a high potential pulse in these latter lines which resulted in catastrophic failure of a number of critical antenna components. As a result, the entire station capability was lost for several days.

CASE IV - A West Coast electronic installation that includes a 15-meter antenna with a nutating sub-reflector in a Cassegrain-like configuration. The antenna feed horn projected some four meters from the center of the reflector toward the subreflector. A heater blanket was installed at the end of the feed horn to insure that the window at the end of the feed was always clear of ice and snow when operating in frigid environments. This feed horn was within the of cones-of-protection the subreflector support legs and braces and to that of a number of air terminals. A depot repair team on a semi-annual visit to the station found this heater blanket charred and hanging in shreds. The circuit breaker intended to provide for power line fault protection for this heater, had not tripped and was found to be functioning normally. It was concluded that the only way in which the heater blanket could have failed in such a totally catastrophic manner, with the circuit breaker remaining in the ON position, was that the blanket

had suffered a direct lightning discharge. This conclusion was supported by the fact that the azimuth bearings of the antenna mount showed some evidence of minor pitting as a result of arcing that took place, presumably when the lightning current was seeking earth.

These examples tend to point out the capricious nature of lightning. The solutions given to lightning protection problems later in this paper are based on statistical and logical behavior expected of lightning but very often the unexpected will happen and lightning will perform in a totally "illogical" manner. As an example, consider the case of a Yagi television antenna struck by lightning at a residence in Indiana. The television receiver to which that antenna was connected suffered only a burned out speaker voice coil. Other than that, there was no damage to the receiver — a perfect example of lightning caprice.

#### THE LIGHTNING PHENOMENON

The mechanism for the generation of lightning has not been universally agreed upon. It is usually held, however, that it is a thermo-dynamic process and the freezing and melting of water must be involved. A charge separation known as the Workman Reynolds effect takes place during freezing that results in the development of a potential the magnitude of which is a function of the volume of water involved (1)\*. There must also be a convection process within the cloud ensuring a continuation of the freezing and melting process (Fig. 1). Since the freezing and melting process take place at separately discrete altitudes, a potential buildup can result between these Ciscrete altitudes and the mechanism for a lightning discharge is created. This is an oversimplification of the process. There can be many convection column generators within a storm cell and many storm cells within a thunderstorm.

The natural consequences of the generation of these ultimately huge potentials are (a) the conditions are established for the oscurrence of an intra-cloud discharge, and (b) a potential of opposite polarity is developed on the surface of the earth

<sup>\*</sup>Numbers in parentheses designate References at end of paper.

beneath the cloud mass by a process of electrostatic induction (Fig. 2). Thus the stage is set for both ground-to-cloud and cloud-to-ground discharges. The particular polarities developed in the cloud and on the ground in this process are a function of the impurities (particularly ammonia) contained in the cloud water.

Inter/intra-cloud discharges are thought to take place between individual storm cells in the same or different clouds and are initiated when a conductive path, that can be enhanced by ionization, is established between these cells (Fig. 3).

discharges Ground-to-cloud initiated when the potential between a storm cell cloud and the earth reaches a level near breakdown and a downward moving leader is launched toward the earth (Fig. 4). The leader moves in steps at a velocity of about one-third the velocity of light. This leader, in its progress toward earth, leaves behind it an ionized channel (Fig. 4a). The leader approaches the earth or some object on the earth to within the "striking distance" \*\* (Fig. 4b). At this striking distance a violent surge of current called the "return stroke" is initiated from the ground to the cloud along the ionized path created by the stepped leader (Figure 4c). This current typically reaches a peak value of 10,000 to 200,000 amperes within 10 microseconds, and then tapers off to 50% of the peak value in about 50 microseconds or longer. This discharge causes a readiustment of the charge distribution within the cloud such that subsequent return strokes are initiated along the still-existing ionised path a few milliseconds Statistically, later. there are usually 4.12 return strokes in one pyrotechnic display of lightning. These appear to a viewer as a single flash because of the persistence of vision and the short time required for their occurrence. The greatest number of return strokes which have been observed (using a special camera known as a Boyes camera developed for this purpose) is 46 - observed on the Empire State Building in New York City.

\*\*Striking distance is the distance across which the potential between the tip of the leader and the earth or object will break down via the conductivity of the air for the mext stage of development of the discharge.

discharges Cloud-to-ground ATA auch then ATO rarer the ground-to-cloud type. They Are believed to develop 1n the rain-producing portion of the storm cell cloud as a result of a mechanism not thoroughly understood. It has been observed that these discharges carry positive charges to the earth while a ground-to-cloud discharge does the opposite. These discharges are usually directed at tall structures and quite often branch to more than one structure for the same discharge.

THE PROBABILITIES OF A DIRECT STRIKE TO A STRUCTURE

The probability that structures of distributed electronic large installation will be subjected to the damaging effects of a discharge to or from the ground is a vital concern in the design of its lightning protection system. N. Cianos and E. T. Pierce in paper "A Ground-Lightning their Environment for Engineering Usage" (2)\* have given us' some empirical methods for determining such a probability. Their work cites the probability. results of the investigation of many others and probably represents the state-of-the-art of lightning effects prediction as of August 1972. A cookbook procedure based on this work will be presented in the following discussion.

- a) Determine the annual isokaurenic level, Ty (number of days per year on which thunder is heard). This information can be obtained from a number of sources. The author uses the "USAF Handbook for Geophysics" but for a finer, more timely cut at this data, the nearest FAA control tower log is a good source of reliable lightning data.
- b) Determine the mean duration of a thunderstorm in hours from:

$$D = 0.9 \times T_y^{0.3} \tag{1}$$

c) Determine the number of flashes per storm, Fg. The conclusion that Pierce and Cianos reached was that the average flashing rate per storm is 3 per minute, regardless of the storm locale in the world. This is 180 flashes per hour so that Fg becomes:

$$F_s = D \times 180$$
 flashes per storm (2)

d) Determine the flashing

density, Fd. ? a storm area. The "thundery" area in the vicinity of an observing station has been determined to be 500 square kilometers - an empirical value for any place in the world. The flashing density Fd thus is given by the relation:

 $F_d = F_s/500$  flashes per storm per square kilometer. (3)

e) The fraction of these flashes which involve contact with the earth or an object on the earth is a function of the latitude of the installation and is (emperically) given as:

$$p = 0.1 [1 + (\lambda/30)^2]$$
 (4)

where  $\lambda$  is the latitude in degrees and p is the fraction of F<sub>d</sub> which is ground-to-cloud or cloud-to-ground (Fig. 5).

f) The flashing density which involves contact with earth or an object on it is then:

 $F_g = p \, x \, F_d \ \, \text{discharges per storm} \\ \text{per square kilometer}$ 

(5)

g) Determine the attractive radius around an object of height h (meters) in which lightning is attracted to the object. This radius is determined by the empirical equation:

$$r_a = 80\sqrt{h} (e^{-ah} - e^{-bh}) + 400 (I - e^{-ch2}) \text{ meters}$$
 (6)

where h = height of structure in meters

 $a = 2 \times 10^{-2} m^{-1}$   $b = 5 \times 10^{-2} m^{-1}$  $c = 10^{14} m^{-2}$ 

h) Calculate the attractive area encompassed by the attractive radius in square kilometers:

$$A_n = \pi \times r_n^2 \times 10^{-6} \tag{7}$$

 The number of discharges to the structure per storm, assuming a uniform distribution of flashes over the storm cell is:

$$N_s * F_g \times A_g$$
 discharges , per storm. (8)

j) The number of strikes to the structure on an annual basis is  $S_V = N_S \times T_V \tag{9}$ 

There are subtleties in the above analysis capable of a more precise determination but, in view of the caprices of lightning, little is to be gained from greater precision.

#### THE CONE-OF-PROTECTION

The majority οf lightning protection philosophies for structures are predicated on the provision of an terminal (lightning rod) which reaches above the height of the structure and is provided with a down conductor that electrically connects the air terminal to earth. The air terminal is supposed to intercept a direct strike and carry the current harmlessly into the ground. In performing this task the device the device provides so-called "cone-of-protection" around the structure within which there is no from a strike. The danger cone-of-protection concept was first proposed by Joseph Louis Gay-Lussac (of gas-law fame) in 1823. He defined the protected volume to be a cylinder equal in diameter to twice the height of the air terminal. Since that time number of configuration and height-to-diameter ratios have been used. Even today, U.S. and British Standards and regulations, both civil and military, skip about a cone angle of 30, 45 and even 60 degrees. The cone-of-protection model used herein is somewhat more rigorously and logically based than that revealed in the literature or regulatory values cited above.

This model is derived as follows. The majority of ground strikes are initiated from the ground and proceed to the charged cloud from the ground object up. for the initialisation of such a strike is the stepped leader. This is a path of ionisation (about 100 paths) which originates at the The motivating phenomenon which originates at charged cloud and proceeds toward the ground in steps as described earlier. For each step there is, as Benjamin called it in 1767, a This striking Franklin "striking distance". distance is a function of the polarity of the cloud (Fig. 6). The breakdown gradient is about 3 kV/cm for a positively polarized stepped leader. Consider now the model illustrated in Figure .7. The stepped leader head at Point A is located such that the striking distance, dsA, is equidistant from a potential standpoint, from the air terminal or lightning protection tower and the earth and it may

initiate a main discharge from either the earth or the tower. Realistically, discharge will the probably be initiated from the point source of the tower rather than the flat surface of the earth because of higher differential voltage gradient around a point source. the stepped leader head were at point A', it would most certainly initiate a discharge from the tower and would have done so before it reached A, because the striking distance locus has been penetrated. If, on the other hand, the stepped leader arrived at A" it would initiate a discharge from the ground, the distance being at or under the striking distance to the earth and beyond the striking distance to the From point A, anything which is within the shaded area, the border of which represents the locus of striking distances from A, will not be the target of a main discharge. This shaded area, then, represents the cone-of-protection. Consider now a second stepped leader at B, having a higher potential, and, consequently having a greater striking distance dsg. Note that the resulting cone-of-protection is greater in extent than that developed in the case of stepped leader A because striking distance is greater. Thus, the size of the cone-of-protection actually developed about the lightning tower is a linear function of the potential which drives the stepped leader.

#### LIGHTNING MODEL ANALYSIS

In the cookbook discussion for determining the threat of a direct strike to a building, it becomes apparent after examining a few examples that the threat of a ground-to-cloud discharge is minimal until the height of the object being considered approaches 100 meters. It is now appropriate to determine the effect of an inter/intra cloud discharge on a typical installation.

A knowledgeable analysis of the effects of lightning can be performed by assuming a specific forcing function or model for both ground-to-cloud and inter/intra cloud discharges which approximates an active lightning discharge. If lightning protection is designed for the worst-case threat of current amplitude (which may occur less than 0.1 percent of the time), the facility could be expected to be extremely costly, and yet the worst-case threat

might never occur during the useful life of the installation. On the other hand, the use of a lower threat level based on a higher probability of occurrence would lead to a less costly protection scheme but also would yield a more vulnerable installation because of the lower degree of protection afforded. Accordingly, a threat level representing that Most often encountered in electrical storms has been selected for the model. For the ground-to-cloud discharge, the model used is that described by Dr. M. A. Uman in his book, "Lightning" (3)\*. For the inter/intra cloud discharge, a similar model will be employed, modified by data given by D. Mackeras (4)\*.

THE LIGHTNING MODEL - The parameters of lightning currents in the time and frequency domains are of specific interest in any analysis which determines the threat imposed by lightning. These are defined by the lightning model.

The time domain model will point out the maxima of current and rate-of-change of current to which the model will be subjected. The frequency domain model will point out vulnerabilities in frequency-sensitive portions of the system. Both the ground-to-cloud and inter/intra cloud discharges will be modeled herein for comparison of magnitudes, rise times and energy distribution by frequency.

Time Domain Model - Zither the ground-to-cloud or the inter/intra cloud types of discharges currents can be modeled in the time domain by:

$$I(t) = I0 \left( e^{-\alpha t} - e^{-\beta t} \right) + I, e^{-\gamma t}$$
 (10)

where,

I(t) = instantaneous current of time, t

In a factor determining the peak current

α = function largely controlling rise time

β = Junction largely controlling decay rate

y = function describing decay time beyond the

50% point
I1 = factor of decay
current

Uman (3)\* has assigned representative values to the factors for a ground-to-cloud discharge as follows:

(a) Initial Stroke

Io = 3x104 amperes

 $I_1 = 2.5 \times 10^3$  amperes

 $\alpha = 2x10^4 \text{ sec}^{-1}$   $\beta = 2x10^5 \text{ sec}^{-1}$  $\gamma = 10^3 \text{ sec}^{-1}$ 

#### (b) Subsequent Strokes

 $I_0 = 10^4$  amperes  $I_1 = 2.5 \times 10^3$  amperes  $\alpha = 1.4 \times 10^4$  sec<sup>-1</sup>  $\beta = 6 \times 10^6$  sec<sup>-1</sup>  $\gamma = 10^3$  sec<sup>-1</sup>

Mackeras (4)\* points out that the inter/intra cloud discharges tend to have, on the average, a longer rise time and decay time and a peak current approximately one-third that of a ground-to-cloud stroke. Accordingly, a time domain model for the inter/intra cloud discharge will be used having the following parameters:

#### (a) Initial Stroke

 $I_0 = 10^4$  amperes  $I_1 = 1.5 \times 10^3$  amperes  $\alpha = 4 \times 10^4$  sec<sup>-1</sup>  $\beta = 2 \times 10^5$  sec<sup>-1</sup>  $\gamma = 10^3$  sec<sup>-1</sup>

#### (b) Subsequent Strokes

 $I_0 = 3 \times 10^3$  amperes  $I_1 = 10^3$  amperes  $\alpha = 2 \times 10^4$  sec<sup>-1</sup>  $\beta = 2 \times 10^6$  sec<sup>-1</sup>  $\gamma = 10^3$  sec<sup>-1</sup>

A further difference between the ground-to-cloud and the inter/intracloud discharges lies in the number of discharges per lightning event. The mean number of discharges per event for a ground-to-cloud event is 4.12, while that for an inter/intracloud event is 1.28 to 1.69, depending on whether it is a high-altitude or low-altitude event, respectively. The low-altitude event will be used for the model in this discussion as being the worst case for consideration.

In the subsequent analyses, the last term of the above expressions,  $I_1 \in \mathcal{I}^1$ , has been eliminated since its contribution is primarily to the decay well beyond the 50 percent point and it introduces a false factor giving a finite current,  $I_1$  at t = 0, which is totally unrealistic. The presence of this factor contributes only a small perturbation to the energy spectrum (less than 10%). The time domain characteristics of the four phenomena for which parameters are given above (without the  $I_1 \in \mathcal{I}^1$  factor) are given in Figure 8.

Frequency Domain Model - The distribution of the energy contained in these discharges in the frequency

domain is used to determine the vulnerability of frequency sensitive portions of threatened electronics. In order to determine this distribution, a Fourier transform of the type:

$$I(\omega) = \int_{-\infty}^{+\infty} I(t) e^{-j\omega t} dt$$
 (11)

is made. When this integration is performed for the time domain current equations, the real part of the frequency domain current becomes:

$$|I(\omega)| = I_0 \sqrt{(\omega^4 + \omega^2(\alpha^2 + \beta^2) + \alpha^2\beta^2)}$$
 (12)

These frequency domain currents for both ground-to-gloud and inter/intra cloud discharges are plotted in Figure

Squaring this expression will yield a quantity which is proportioned to the power at any value of frequency:

$$P(\omega) = I_0^2 = \frac{(\beta - \alpha)^2}{\omega^4 + \omega^2 (\alpha^2 + \beta^2) + \alpha^2 \beta^2}$$
 (13)

o£ The numerical value expression is equal to the power in watts if the current were filtered in a bandpass filter of unit bandwidth (1 Hz) centered at frequency f, and which had a characteristic impedance of one ohm. A complete derivation of the above is given by Dr. William E. Waters (a co-investigator in Case I the C3I installation in New England) 1n his recent reference text. "Electrical Inductions from Distant Current Surges\* (5)\*. He also calculated the vertical and horizontal electric field intensities at a height of one meter above the earth's surface 1n the vicinity of a model inter/intra-cloud discharge of 10,000 amperes having a length of one kilometer, a height of one kilometer and an orientation parallel to the earth's surface (Fig. '10). These field intensities, which are plotted in Figures 11 and 12, are calculated for a plane one meter above a flat earth and include the effects of the proximity of the earth to this plane. These effects are absorption of some of the energy into the earth and reflection of the remaining energy back toward the plane. The earth effects are a function of the dielectric constant and resistivity of the earth as well as frequency and polarisation of the incident wave. The mathematics involved in deriving

the magnitudes of these factors is very tedious and is best performed on a digital computer. It is sufficient to say, in this instance where the energy in lightning lies mostly in the low-frequency region, that the reflection coefficient is more than 90% and the phase of the reflected wave is nearly 180° out of phase with the incident wave over a broad range of frequencies. At the one meter plane, therefore there 1 = considerable cancellation of the magnitude of the incident wave which is, as stated above, taken into consideration in the plots of Figures 11 and 12. In the calculation of the reflection coefficient,

$$R = \frac{1 + i\chi}{1 - i\chi} \quad \chi = \sigma/\omega \epsilon \tag{14}$$

The reflection phase angle is determined as:

$$\angle R = \pi - \sqrt{2/\chi} \tag{15}$$

Waters has used a frequency of 4 kHz which is the median of the energy spectrum for lightning for the particular model employed.

Even with this large cancellation figure from reflection factored into the calculation, it can be seen from these plots that there is a high probability of producing an induced voltage of hazardous magnitude in a conductor lying in or within a few meters of the reference plane. The result of this induced voltage is potential catastrophic damage to the equipment to which the conductor is connected.

FAILURE ANALYSIS USING MODELS - As an example of the catastrophic damage which can occur, return to the New England example where the damage scenario now can be now cited as follows:

- a) A 12-KV primary line several miles long was the source of power for the installation.
- b) This line was equipped with lightning arrestors at about every five poles.
- c) These particular arrestors have a flashover potential of 45 KV a level easily attained by exposure of a length of the line to the type of inter/intra cloud discharge described in paragraph 6.1.2.
- d) The potential of the 120-volt feeders from substations located at elements of the installation was raised by a proportional amount, or (45/12) x 120 = 450 volts.

e) The output of five-volt power supplies feeding many of the solidstate electronic units of the installation were thereby raised by the same ratio from 5 volts to 18.75 volts. This occurred within a time period less than the time constant of the typical power supply regulators (which averages about 80 microseconds); thus the regulators could not respond rapidly enough to protect against this transient. Catastrophic failures therefore occurred in many solid-state modules as a result of the largely induced veltage. Many other modules may have been stressed in such a manner that their MTBFs were significantly reduced.

#### PROTECTION METHODS

While the threat made by the lightning to large distributed electronic installations is severe. regardless of the type of discharge, there are, fortunately, means of mitigating this threat - or rather, the statistically derived threat. Little can be done to protect against the capricious unpredictable threat within any practical, cost-effective realm. For example, to return to the of the discharge to television antenna described earlier does the fact that the speaker was catastrophically destroyed justify providing protection for all TV receiver speakers? Certainly not, because statistically this particular failure would hardly ever recur. We are concerned only with the types of damage which can predictably occur in the two basic types of lightning discharges - the ground-to-cloud discharge and the inter/intra cloud discharge.

PROTECTION AGAINST GROUND-TO-CLOUD DISCHARGES - The most common method of protection against the ground-to-cloud discharge is the air terminal/ down conductor/sarth ground system. This. mystem was invented by Benjamin Franklin to provide an easy path to the earth for the lightning current from some wate distance above the object to be protected. Some argue that the lightning rod (common name for air terminal) has, as its primary Purpose. the reduction of potential gradient in the vicinity of the rod in order to lessen the probability of a strike. The air terminal is often provided with a pointed tip to ensure a high potential gradient in its vicinity. The gradient reduction in the vicinity of the object being protected is microscopic in extent compared to the entire lightning complex. Consequently, the principal function of the lightning rod is what Franklin supposed it to be - to provide a solid conductive path to earth for any lightning energy which threatens the structure being protected.

Air Terminals - This protection system includes an air terminal which extends to a higher elevation than the object being protected in order to provide the cone-of-protection about the object. It is not always practical to provide an air terminal high enough to provide the cone-ofprotection about any object. Consider for example the Vehicle Assembly Building at the Kennedy Space Center. To provide such protection, an air terminal would be over 500 feet above the roof of that structure. This concept was not considered to be practical for this building. Instead, the roof of that building is covered with many 3-foot air terminals to provide a virtual protection zone. The main requirement is that there be a point source device elevated above the surface to be protected.

Down Conductors - The design of down conductors often requires some ingenuity. Certain rules are recommended to prevent damage from arising by virtue of the high current carried down this conductor. Some of these are:

The conductor must be large a) enough to carry the magnitude of current anticipated for the expected length of time without melting. Because of the thermal inertia of most metals, the size of the conductor is not required to have an adequate cross-sectional area great enough to carry the large magnitude of currents on a steady-state basis. The conductor must be large enough, however, not to be heated to its melting point over the duration of the discharge, say 100 microseconds. Where the conductor is attached to nonmetallic and inflammable structural members, its temperature rise from the current must not approach the ignition point of the structural material too closely. In the type of structures which usually house the elements of distributed electronic systems, cable of #4/0 AWG bare multistrand copper cable is usually used. For one or two story structures this is probably an overkill, but it is certainly safe.

b) The down conductor should not change direction more than 900 in any one bend, and the bending radius should not be less than 23 centi-The reason for this is that a meters. large discharge current generates a very strong magnetic field which tends to straighten any conductor through which it flows. The installation of such a conductor with too large an angle or too tight a bending radius will cause the down conductor to virtually tear itself apart in an effort to become straight when fulfilling its function as a high current carrier.

c) Care must be taken in the placement of down conductors with relation to portions of electronic circuit cables because of induction effects from the lightning current. The combination of the fast rise time (di/dt) and the peak magnitudes of the lightni gurrent which could be in the dow onductor (10,000 - 200,000 can create an intense, amperes) rapidly changing magnetic field around the down conductor. The voltage which could be induced as a result of this changing magnetic field into ANY conductors that parallel the conductor could be catastrophic even though the two conductors separated by everal meters. For example, supposes a down conductor and a signal line were parallel for a distance of five meters and separated by a spacing of three meters, such that their mutual inductance over that distance 0.1 microHenry. WAS the down Consider, also, that conductor was carrying a lightning current which peaked at 30,000 amperes in 10 microseconds. The peak voltage induced into the signal line by the lightning current would be:

$$e = -m \frac{di}{ds} = 300 \text{ volts}$$
 (16)

This level of voltage would certainly be catastrophic to most solid state circuits having no protection.

d) The placement of down conductors should be such that the conductor down not pass within 6 meters of metallic masses because of the possibility of side flashes. Where this cannot be avoided, it may be feasible to extend a small branch wire from the down conductor to the metal mass and make it a part of the grounded lightning protection system.

e) Structural steel may be used as a down conductor if it is accessible for making a ground connection.

f) Ideally, two down conductors should be provided from each air terminal and these down conductors should be separated by a considerable distance or even on opposite sides of the structure.

Zarth Connections - The design of grounds (earth connections) for the termination of the down conductors can be one of the most major problems of establishing protection from groundto-cloud lightning. Too often this portion of the protection system is implemented by driving a one or two into the ground and meter rod connecting the down conductor to the rod without any consideration given to the soil composition or the grounding of the electronics, power and facility items of the installation. Consider first the soil composition problem. The most relevant characteristic of the soil in the making of a ground connection is its resistivity. resistance of a single vertical rod of length, 1 cm, radius a cm placed in a medium of resistivity of p ohn-cm is:

$$R = \frac{p}{2\pi \ell} [\ln \frac{4\ell}{2} - 1]$$
 (17)

The maximum resistance of a lightning ground (arbitrarily) should not exceed 20 ohms. To achieve this resistance with a 2-foot (60.96cm) rod 3/4 inch in diameter (radius = 0.9525cm), soil with a resistivity of 1686 ohm-cm would be required. Unfortunately, soils with this resistivity are rare. The average resistivity around the United States is probably more like 25,000 ohm-cm. Accordingly, it is sometimes necessary to make the earth connection with longer rods, multiple rods and, in very shallow soils, even long-wire counterpoises. There is an extensive bibliography on making earth connections (6)\* and (7)\*. It cannot be emphasized enough that an essential preliminary to the design of an earth connection is a measurement of the resistivity to a depth consistent with the maximum rod length which might be employed.

Another significant point is the relationship of the lightning-earth connection to that used for power. equipment and technical facility In all soils items. with resistivity of 10,000 ohm - centimeters or more, it is imperative that the lightning ground and the singlepoint ground for the installation be either common or interconnected. The obvious reason for this consolidation of earth connections is to prevent a differential voltage between equipment and conducting portions of the building which can result from hazardous voltage gradients produced between their grounds by the lightning current in the soil. These gradients can run to thousands of volts/meter in high resistivity soil. The impact of the hazards to personnel and equipment that could be produced by these gradients occurring between strucural members and equipment cannot be stressed too strongly.

PROTECTION AGAINST INTER/INTRA-CLOUD DISCHARGES - The threat of inter/intra cloud discharges has received little attention in lightning literature, nonetheless, such discharges been the actual cause of many equipment failures blamed on groundto-cloud lightning. The threat is serious; in fact it is so serious that the New England installation discussed earlier went through a period of shutting down operations when the National Weather Advisory indicated that a thunderstorm was approaching. During the summer months thunderstorms are frequent and severe, with the result that there was much lost time, either by defensive shut- down or by catastrophic failure of components if no shutdowns had been made. Since the protective methods described below have been implemented, the defensive procedure shutdown has been abandoned. The installation DOM operates. safely and continuously during thunderstorms.

The principal threat from inter/intra cloud activity is the voltage induced in outside plant cables, be they either power or signal cables. One characteristic of signal cables in a lightning environment is that the shielding effectiveness (SE) of braid type shields, such as those used in the typical shielded cable or coaxial cable, becomes quite low as the frequency decreases into the audio region. A typical cable shield, which might have a shielding effectiveness of 35 dB at 100 kHz, may have an SE of less than 10 dB at one kHs. In addition, burying such cables is of little useful protection against the lightning affects of induced transients. For most soils, the skin depth over the lightning spectrum is typically tens or even hundreds of meters, with the result that the SE of the earth at a practical depth of burial is quite small. Therefore, it appears that the most cost-effective measure which can be taken against the threat of inter/intra cloud lightning are (a) containment of long cables in

welded iron pipes, and (b) suppression of the induced energy at the ends of the cables. Suppression must be accomplished in such a manner that it does not interfere with the transmission of either signals or power over the cables. This means that any protective device used cannot be of the linear energy absorptive type but must be a non-linear voltageor current-limiting device that will become active only if a predetermined maximum is exceeded. Typical of the devices used in this application are variators, sener diodes, gas diodes, filters and hybrid devices including two or more kinds of devices.

Some of the devices and their lications and limitations are applications discussed below.

a) Varistors - These devices have a resistance which is a function of the inverse of the applied voltage. In a transient protection - These voltage. In a transient protection application, if the voltage across the device increases, the varistor resistance decreases to limit the voltage to a safe level. Unfortunately, this voltage limiting is inadequate since there is no clear clamping ceiling on it, and it may also act too slowly.

b) Zener Diodes - These diodes are very useful as clamping devices.
When a rener diode reaches its avalanche point, any attempt to increase the applied voltage will result in more current through the diode. The avalanche point can be very accurately controlled in the manufacturing process. For lightning protection a bipolar or back-to-back configuration form is necessary because the polarity of an induced transient voltage may be of either sign. One manufacturer (General Semiconductors, Inc.) has a product line of polarized and bipolar zeners called Transzorbs\*, that Vere developed specifically for protection against the effects of electromagnetic pulse (EMP). The Transzorb has a response time of less than one nanosecond. Because it is constructed with a junction of relatively large area. it can dissipate large quantities of energy over the short time period usually taken by lightning or RMP events. The Transzorb is limited in application by the high which interelectrode capacitance results from the large area of the junction. It cannot be used on circuits where this capacitance across the circuit would affect the characteristics of the signal. This

can be offset by using high frequency diodes in series with the device, or, where possible, placing it at the end of a quarter wave stub if high of a quarter wave stub if if frequencies are involved. applications where many circuits For AFO involved, in telephone subscriber line circuits, the Transzorbs are packaged in a DIP configuration, four to a package.

c) Gas Diodes These usually consist of two electrodes in a Glass envelope which has evacuated and filled with an inert gas such as neon or argon. The tube has an ignition voltage and a somewhat lower steady-state voltage at which conduction starts and tends to be maintained. The ignition voltage and steady-state voltage are a function of the kind of gas, gas pressure and the electrode spacing. This device is often used in lightning protection applications where the steady state voltage drop is greater than the normal operating voltage of the circuits protected. The major disadvantages are that the higher ignition voltage is usually well above the steady state level and the potential clamping action 1. potential clamping action is relatively slow. Protected circuits may, therefore be subjected to a higher level of the transient before the gas reaches ignition.

These devices are usually limited to a steady state level of from 70 volts to 300 volts; therefore their use is generally in power circuits and not for protection of low-level solid state circuits. In addition, they are coulomb limited, presumably because of erosion of the electrode material through continued discharge. Accordingly, their useful life is limited and they must be replaced periodically in order to maintain a continuing level of protection. Surge protection systems using gas diode devices were used in the New England installations discussed in this paper for power line protection with very satisfactory results.

d) Filters - Filters can be used for protection against the effects of lightning to a limited degree. Their application is found mainly where they are not required to meet the full burst of the impulse but rather are needed to suppress frequency components of the induced lightning

<sup>\*</sup>Transsorb is a registered trademark of General Semiconductor, Inc., Tempe, Arizona.

voltage which might cause functional disruption of electronic systems, e.g., an unwanted computer halt. Typical applications are the use of low-pass filters in power supply feeders or in high-pass filers in control lines. In all filter applications, one must assume that there is other protection in the system to preclude the development of voltages on the filters which would exceed the breakdown level of any of the filter components.

e) Hybrid Devices **Hybrid** devices are those which include two or more of the protective devices described above. The combination of devices is dictated by the specific requirements for the system or because of the inadequacies of one of the devices combined. For example, a gas diode is often used in combination with a Transsorb. The gas diode has a relatively slow response to transient and requires a voltage above the protection level for ignition. The Transmorb, on the other hand, while responding very rapidly to limit the voltage applied to a circuit, is limited in the amount of energy it can dissipate. If the two devices are combined as shown in Figure 13 with an inductor to form a hybrid circuit, the combination can provide adequate protection throughout the entirety of a strong lightning-induced transient. The Transsorb conducts the instant the threshold is exceeded, the inductor helps to develop the ignition voltage for the gas diode and the gas diode, then can handle the induced voltage during the decay period of the transient. This hybrid device is particularly effective in protecting circuits against the more rapid rise time transients encountered in EMP. Other hybrid circuits may incorprate filters with gas diodes and/or sener diodes for specialized applications portions of the frequency spectrum must be inhibited.

#### SUPPLARY AND CONCLUSION

Large distributed electronic systems such as area traffic control systems, plant process control systems, satellite ground communication and tracking systems and plant branch telephone exchange systems are at the mercy of lightning induction phenomena unless properly protected.

Most installations are traditionally protected against the effects of ground-to-cloud lightning discharges. The basic principles for this type of protection, which were begun by Men Franklin, have been expanded upon to meet the more stringent protection requirements for solid state circuitry.

The threats imposed upon solid state circuitry by inter/intra cloud lightning discharges have been printed out in this paper. These threats have not received much attention in the past, yet they are probably more serious than the threats imposed by the ground-to-cloud direct strike Inter/intra phenomena. aloud discharges account for the highest percentage of lightning activity and they produce electromagnetic fields capable of inducing catastrophic potentials of thousands of volts in any portion οf . distributed electronic system.

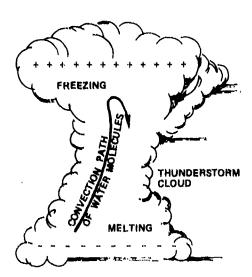
Protection measures against the inter/intra cloud discharge phenomenon, may be designed using the following procedure:

- a) Determine the lightning threat Use isokaurenic maps, FAA weather data or local weather bureau information calculate the inter/intra cloud activity from equation (4) [inter/intra cloud fraction c [uals (1 p)].
- b) Determine the vulnerabilities of the system Given worst-case threats as shown in Figures 11 and 12, determine the hazard potential produced by those threats, with due consideration given to the shielding effectiveness of encapsulation, the apparent shielding realized from balanced circuits and any other threat-mitigating factors.
- c) Determine the catastrophic failure voltage levels of the circuits associated with the vulnerable portions of the system.
- d) Assign protective devices to the circuits in accordance with their vulnerability as determined in (c).

Protective measures thus developed and implemented will protect these systems against the majority of inter/intra cloud discharges. In addition, these measures will afford protection against some of the caprices of ground-to-cloud discharges, both direct and nearby.

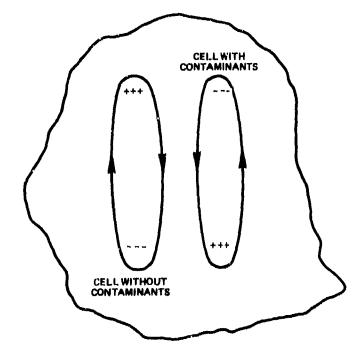
#### REFERENCES

- 1. E. J. Workman, "The Production of Thunderstorm Electricity", Journal of the Franklin Institute, Philadelphia, Pa.: Franklin Institute Press. June 1967.
- N. Cianos and E. T. Pierce, "A Ground-Lightning Environment for Engineering Usage", Stanford Research Institute Project 1834, Henlo Park, Ca: August 1972.
- Martin A. Uman, "Lightning", New York, N.Y.: McGraw Hill, 1969.
- 4. D. Mackeras, "A Comparison of Discharge Processes in Cloud and Ground Lightning Flashes", Journal of Geophysical Renearch, Washington, D.C.: American Geophysical Union, February 15, 1968.
- 5. W. E. Waters, "Electrical Induction From Distant Current Surges", Eaglewood Cliffs, N.J.: Prentice Hall, 1982.
- 6. E. D. Sunde, "Earth Conduction Effects in Transmission Systems", New York. N.Y.: Dover Publications, 1968.
- 7. S. R. Crawford, "Grounding of Large Electronic Systems, FAA/Georgia Institute of Technology Grounding Workshop and Lightning Protection Seminar, Final Report, Report No. FAA-RD-75-106, Atlanta, Ga.: May 1975.



NOTE: POLARITY MAY CHANGE WITH VARIOUS CONTAMINANTS AND THEIR CONCENTRATION

Fig. 1 - Lightning development with a cloud

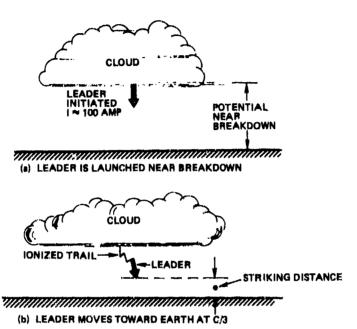


AS CONVECTION PROCESSES CONTINUE WITHIN CELLS, POTENTIALS BETWEEN CELLS CONTINUE THROUGH CHARGE SEPARATION - COULD TAKE PLACE BETWEEN CELLS IN DIFFERENT CLOUDS. EVENTUALLY STRIKING DISTANCE WILL EXCEED PHYSICAL DISTANCE AND A DISCHARGE WILL RESULT





Fig. 2 - Cloud-to-earth charge induction



CLOUD

MAIN DISCHARGE
10 - 200 K AMPS
FOLLOWS LEADER TRAIL.

STRIKING DISTANCE

(c) MAIN DISCHARGE INITIATED WHEN LEADER
PASSES WITHIN STRIKING DISTANCE

Fig. 4 - Stages of development in a ground-to-cloud discharge

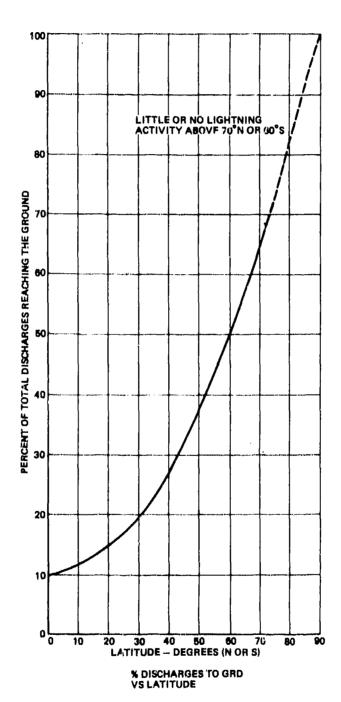


Fig. 5 - Variation of lightning activity type with latitude

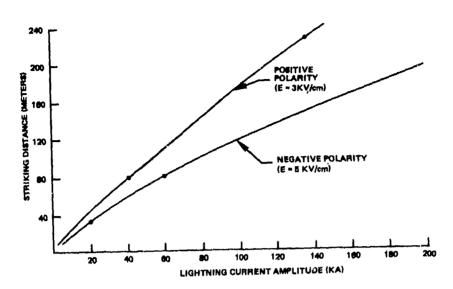


Fig. 6 - Striking distance for positive and netgative charges

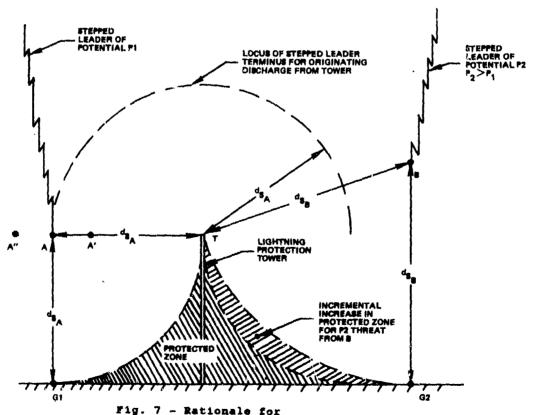


Fig. 7 - Rationale for cone-of-protection

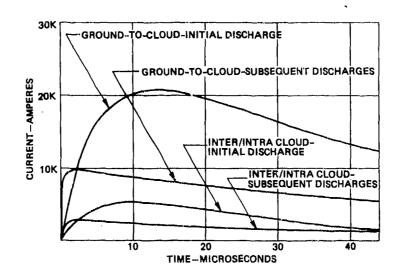
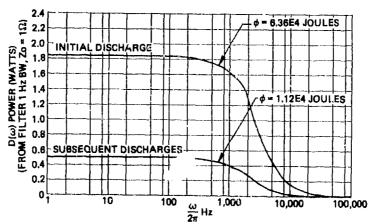
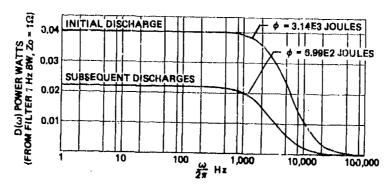


Fig. 8 - Time domain characteristics of lightning models



Frequency Domain Characteristics of Ground-to-Cloud Lightning Model



Frequency Domain Characteristics of Inter/Intra Cloud Lightning Models

Pig. 9 - Frequency domain lightning currents

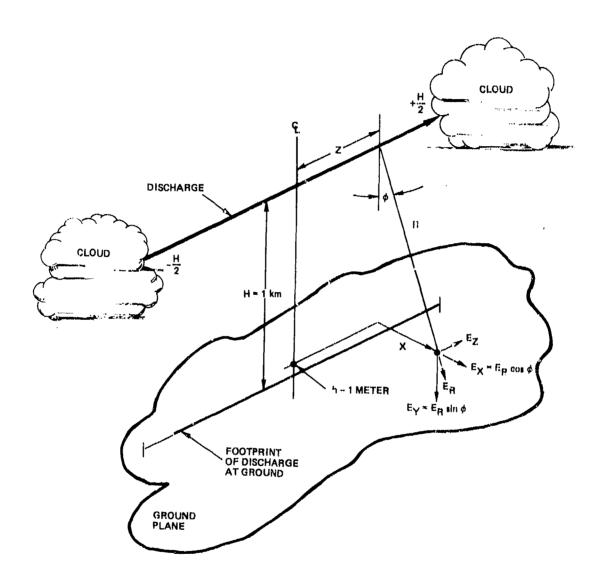
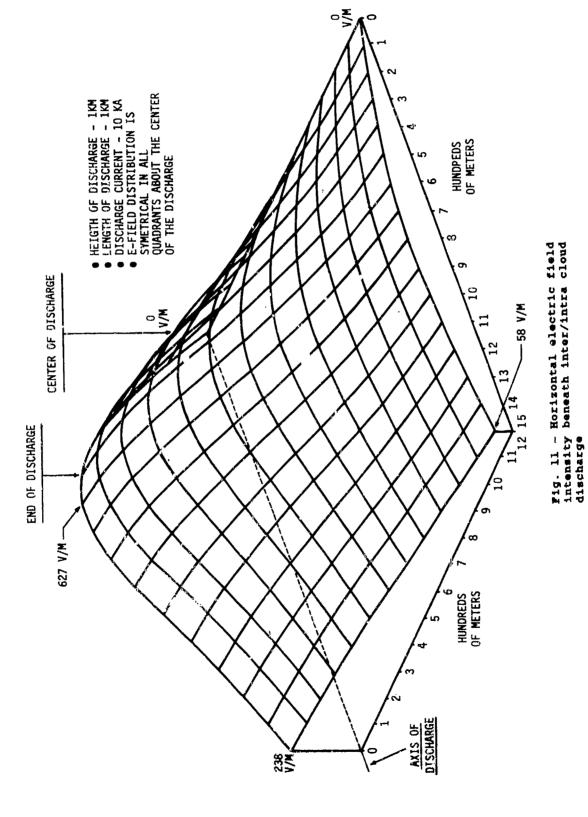


Fig. 10 - Inter/intra cloud discharge model



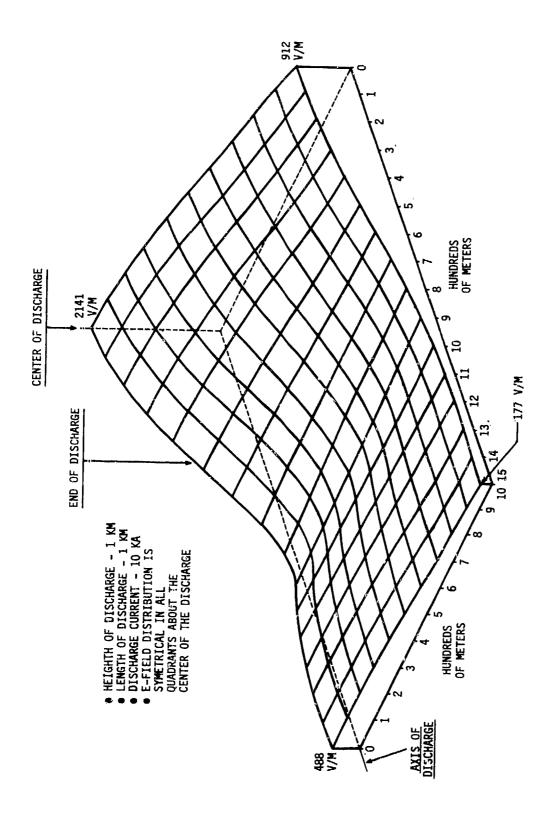


Fig. 12 - Vertical electric field intensity beneath inter/intra cloud discharge

3-21

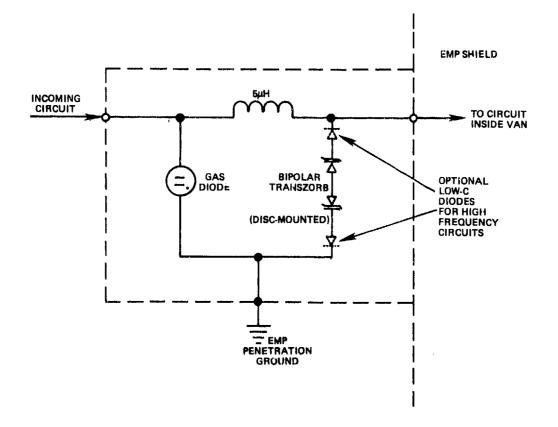


Fig. 13 - Typical hybrid protection device



# LIGHTNING ACTIVITY OBSERVED IN UPPER AND LOWER FORTIONS OF STORMS AND ITS RELATIONSHIP TO STORM STRUCTURE FROM VHF MAPPING AND DOPPLER RADAR

William L. Taylor W. David Rust Donald R. MacGorman Edward A. Brandes

National Severe Storms Laboratory 1313 Halley Circle Norman, Oklahoma 73069

Space-time mapping of VHF sources reveals lightning processes for cloud-to-ground (CG) and for large intracloud (IC) flashes are confined to an altitude below about 10 km and closely associated with the central high reflectivity region of a storm. Another class of IC flashes has been identified that produces a splattering of small sources within the main electrically active volume of a storm and also within a large divergent wind canopy at the top of a storm. There is no apparent temporal association between the small high altitude IC flashes occurring almost continuously and the large IC and CG flashes sporadically occurring in the lower portions of storms.

#### INTRODUCTION

Relating lightning location with storm reflectivity and internal wind structure is one of our major efforts within the Storm Electricity Group at the National Severe Storms Laboratory. Definitive results in this field require good data obtained simultaneously with our dual VHF lightning mapping stations, dual 10-cm wavelength Doppler radars, and supportive data from many other storm electricity sensors for documentation of lightning type.

MacGorman and Taylor (1)\* recently presented the superposition of VHF sources for individual flashes with radar reflectivity and the vertical distribution of VHF sources. Rust, Taylor, and MacGorman (2) discussed the complexity of lightning, the spatial characteristics of flashes and the progression speeds of IC flashes resulting from use of the VHF mapping technique. The association of VHF sources with radar reflectivity and storm winds and with the radar reflectivity of a storm with a mesocyclone was presented by Rust et al. (3). In all of these results, only the prominent major flashes with big field changes and large numbers of VHF signals were selected for study. Analyses consisted of utilizing the signals produced by each flash during a short period of time, usually less than on a second. An active storm producing six major flashes

\*Numbers in parentheses designate references at end of paper.

per minute would result in having analysis performed during less than 10 percent of the storm time period. Although a background of small, minor flashes, each containing only a few VHF sources, was evident primarily at high altitudes during the process of selecting data for the various analyses, these minor flashes were not considered sufficiently important for study.

P0021

Four thunderstorms passed within our VHF and Doppler radar mapping areas during 19 June 1980. These were small marginally severe storms and were not very active electrically as evidenced by infraquent major flashes. Because of this, the minor flashes at high altitude seemed to be of more relative importance to the overall electrical activity of the storms. Consequently, all lightning activity detected by the VHF mapping system for both major and minor flashes associated with these storms was analyzed. This report presents spatial relationships between major and minor flashes and the precipitation and wind in those four Oklahoma storms.

#### INSTRUMENTATION

NSSL operates two recording sites to observe simultaneously the VHF radio frequency signals produced by lightning and to obtain Doppler radar data for the accompanying storms. The main site at Norman is part of the NSSL research facility. The other site, Cimarron, is located about 42 km northwest of Norman.

This configuration forms a primary dual-mapping data acquisition area that is shaped approximately as a figure 8 with the long axis aligned from southwest to northeast.

The VHF mapping technique uses a wideband (30-80 MHz) system capable of resolving 16,000 electromagnetic impulse signals per second. The sources of these signals are probably from the extremely short-term changes in the current moment that are spatially distributed along lightning flash channels within the cloud. Time difference of arrival of these signals at a pair of horizontally spaced autennas and a pair of vertically spaced antennas define, respectively, azimuth and elevation angles to individual signal sources. An antenna spacing of 13.74 m combined with careful amplitude threshold adjustments and fast emitter-coupled logic circuitry provide a measura of signal arrival-time differences between the antennas with an error of less than ±0.4 ns. This relates through simple trigonometric formulations to an angular accuracy of ±0.5°. A network of horizontally spaced antennas allows a 60° azimuthal sector of signal acceptance to be adjusted in 30° increments. (Recently the sector was expanded to 120°.) A real-time monitor at each station provides an azimuthelevation display of all lightning signals within the sector limits to allow tracking and interpretation of lightning activity. Additional details of this instrumentation are presented by Taylor (4) and by MucGorman and Taylor (1).

The simultaneously observed azimuth and elevation directions and signal arrival times recorded digitally on magnetic tape at our two stations are used in post analysis to determine through triangulation the three-dimensional location of the lightning element producing each received sig: 1. The arrival times. measured to 16 s relative accuracy between stations, are used to identify signals for processing. To assure that only those signals that were produced by a common source are selected for analysis, it is required that the location of the source obtained through triangulation must fall within the hyperbolic region defined by the gross difference in arrival time of the signal at the two stations. A sizable portion of the signals observed at either station do not survive this selection process. For those that do survive, the sources of signals are defined by using the 0.5° accuracy intrinsic to each site.

Dual Doppler rader data are obtained by coordinated scans up through a selected storm. Sector limits, antenna rotation speads, elevation increments and other selectables are programmed into the radar controls. Each tilt sequence takes 4-6 minutes depending on storm size and range. More information on the scanning technique and details on the data synthesis to provide storm structure and dynamics are presented by Ray et al. (5).

Electric field changes are measured with sensors of the type described by Krehbiel et al. (6). These devices have microsecond rise times and exponential decay time constants of 10 s and 100  $\mu$ s. Changes in the electric field accompanying a lightning flash are used to identify cloud-to-ground flashes and determine the number of strokes.

#### OBSERVATIONS AND RESULTS

#### Storm Overview

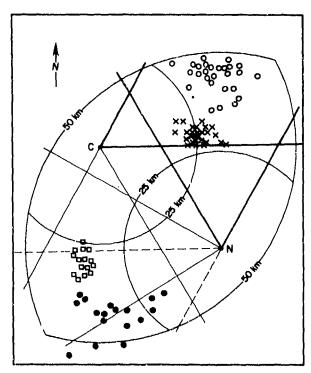
Deep convection began on 19 June 1980 to the southwest of Norman around 1930 CST and several storms developed in Central Oklahoma during the next two and one half hours. Both Doppler and Storm Electricity data were collected on these storms, but they were outside the nominal range of the VHF mapping system.

Rawinsonde observations were taken at three sites in central Oklahoma during periods 2015-2100 and 2215-2300. Environmental winds were generally from the east at \$\times\$1 km heights, veering through south at 2 km and from the west at heights from 3 to 16 km. Wind speed averaged 10 m s<sup>-1</sup> at \$\times\$6 km, increased to 30 m s<sup>-1</sup> at 10-12 km and then decreased at greater heights. The temporature was 0°C at 4.8 km height, -20°C at 7.6 km, -30°C at 9.0 km, and -40°C at 10.4 km during the first period. The same temperatures were shifted about 0.1 km higher during the second period.

At 2214, a storm about 50 km north of Norman had become electrically active, and all sensors were focused on this new storm area and hereafter referred to as storm I. The Norman (N) VHF mapping sector was set for 330°-30° and the Cimarron (C) sector for 30°-90° as shown in Fig. 1 by the heaviest lines. The approximate centers of all major flashes observed from storm I are indicated by open circles.

Shortly after our observations on storm I began, we became aware that storm II was becoming electrically active. The approximate centers of the major flashes from storm II are shown in Fig. 1 by X's. As the storm moved southward, some of the flashes occurred at azimuths greater than the 90° sector limit for Cimarron. It was decided not to rotate the 60° observing sector to accommodate all of the storm II flashes because to have done so would have prevented further lightning flash observations of storm I.

Lightning activity in storm I and storm II ceased at about 2247, and we turned our attention to a developing storm about 40 km to the west of Norman. Flashes from this storm III are shown in Fig. 1 by open squares. VHF mapping sectors were at 240°-300° for Norman and 150°-210° for Cimarra. Electrical activity within this storm terminated about



Straight lines radiating out from C (Cimarron) and N (Norman) are asimuthal sector limits explained in text.

2321, and shortly thereafter lightning activity began to the south of storm III whereupon the Norman sector was changed to 210°-270°. Although the flash centers for this last observational period are very scattered, as shown in Fig. 1 by the solid circles, we catagorize these as having their origin in storm IV. Lightning activity in this storm slowly decreased and finally ceased after about 2359.

#### Lightning Activity as a Function of Time

The altitudes of all VHF sources located by triangulation for storm I are plotted as a function of time in Fig. 2. Altitude of each source is computed relative to ground level which is 0.4 km above MSL. The CG (cloud-to-ground) and large IC (intracloud) flashes are very conspicuous since the sources for each flash occur in a short span of time (usually less than 0.5 s) and in the figure are distributed in vertical columns of pluses (+). Only twelve or fifteen flaches are obvious at first glance, but other smaller flashes producing only a few sources distributed along vertical lines can be recognized by angling the figure

back and aiming with the eye up through increasing alritudes.

Storm I was undoubtedly electrically active prior to the beginning of our observations as evidenced by the relative high density of sources already attained by 2214. There was a steady decrease in electrical activity for the major IC and CG flashes in the lower part of the storm, as well as for the minor IC flashes and individual sources scattered throughout the storm, starting at about 2222 until the last source was produced just prior to 2245.

The time distribution of major flashes for storm II, presented in Fig. 3, is almost a mirror image of that for storm I. Electrical activity in storm II grew very slowly through 2238. A period of relatively steady activity then continued until 2246, after which the lightning abruptly ended. The last VHF source in storm II occurred about two minutes after the last source in storm I.

As seen in Fig. 4, storm III was the least active of the four storms. We probably did not observe the initial lightning in this storm. The general trend of activity did not vary greatly during this storm although there was a minimum near 2303, followed by a peak between 2307-2311, and finally the last source was mapped just prior to 2322.

Twenty seconds after termination of atorm III, storm IV became active as seen in Fig. 5. Initial lightning began approximately 24 km south of the final activity in storm III. The first mapped source occurred at 12.5 km altitude and was just less then one minute before the first major flash. Activity generally decreased with time. Unlike the other three storms, the minor flashes at altitudes above 10 km decreased in rate more rapidly than the major and minor flashes at lower altitudes.

The general characteristics of the arrangement of sources in altitude as a function of time for these four storms presented in Figs. 2-5 are very similar. Very few sources ansociated with the major flashes are observed at an altitude above 10 km and most seem to terminate at 8 km or less. All sources resulting from minor flashes are scattered in altitude and time throughout the storm but tend to concentrate in the upper regions centered at about 12 km. A minimum in the number of lightning sources is just discernible meandering between 8-10 km altitude as time progresses. Also, some fine structure in the altitude-time distribution of sources is evident at the higher altitudes suggesting that the altitude of lightning activity may increase or decrease in an organized manner. Changes in the fine structure of source altitude versus time is most clearly shown in storm I, Fig. 2 and the latter part of storm II, Fig. 3.

When we examine the last eight minutes of storm IV, we find that apparently the high altitude minor flashes are moved down with

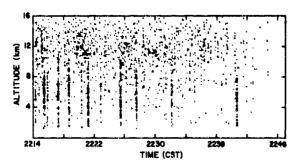


Figure 2. Altitude of all VHF sources versus time for Storm I.

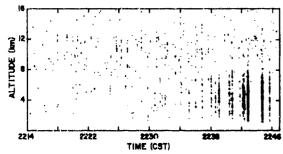
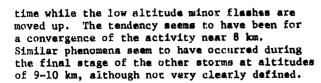


Figure 3. Altitude of all VHF sources versus time for Storm II.



#### Major and Minor Flashes

Major flashes are those that produced >30 VHF signals at each mapping station. The most prominent flashes produced several hundred signals, whereas the median number for all major flashes was 80. Minor flashes are those that produce 25 VHF signals but <30 at each mapping station. Only about 25 percent of all recorded signals were converted to lightning source locations and mapped in 3-D. Some signals were eliminated by the data selection process mentioned previously; others were not obscrved either because they were outside the sector limits of one of the stations or because they did not exceed the amplitude threshold of one of the stations. Consequently, some minor flashes are represented by a single plus symbol in Figs. 2-5.

Detecting CG flashes was accomplished by recognizing the stepped characteristics on the electric field changes that occurred simultaneously with the VHF signals. A step change in the electric field is produced for each return

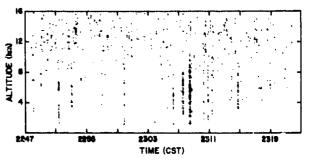


Figure 4. Altitude of all VHF sources versus time for Storm III.

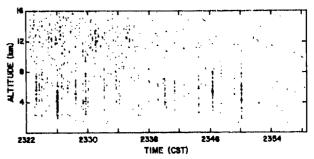


Figure 5. Altitude of all VHF sources veruss time for Storm IV.

stroka in a CG flash. Because of the range to some flashes coupled with interference from other storms, it was not possible to accurately determine the number of strokes in each CG flash, but we do feel confident that we have properly identified the CG flashes. The number of IC flashes was determined solely from the mapping data. Table I shows the lightning activity for each storm.

Table I

Major lightning flash activity for each storm

Storm No.	Number of all flashes	Number of CG flashes	Percent CG	Total Storm Time
I	27	9	33%	31 min
II	28	9	32%	33 <b>mi</b> n
III	15	3	20%	34 <b>mi</b> n
IV	17	4	24%	36 min
Totals	87 .	25	29%	134 min

The percentage of flashes that are CG is about what we usually encounter for Oklahoma storms, yet the flashing rates are far below

those usually observed (3). There was an average of only 0.65 major flashes per minute throughout the observing period. If we group storms I and II into a storm complex, since they occurred concurrently, the actual flashing rate for that period was 1.67 min<sup>-1</sup>. The rate for storms III and IV, which were consecutive, was only 0.46 min<sup>-1</sup>. The most active five—minute period for an individual storm occurred between 2238-2243 for storm II when the overall flashing rate was 2.2, and the CG flashing rate was 1.2 min<sup>-1</sup>.

The absence of a high flashing rate for the major flaches in these storms led to the realization that a background of small flashes existed primarily at high altitudes. These small, minor flashes seemed to be of much more relative importance in the overall electrical activity in these storms than we had ascribed to them in our previous studies. An analysis of the azimuth-elevation data of the minor flashes observed at each station reveals that each of these flashes involved a relatively small region of the storm. During the first eight minutes of storm I, selected because it was one of the more electrically active periods during these observations, the average size in the horizontal plane of all minor flashes was 9 km2. The average size of the major IC and CG flashes for all four storms were, respectively,  $28 \text{ km}^2$  and  $48 \text{ km}^2$ . Thus, the size of the average minor IC flash was substantially smaller than the major IC and considerably smaller than the major CG.

There were 12 major flashes during this pariod, i.e., 9 IC and 3 CG, and 210 minor flashes. A 3:1 ratio in the major IC to CG activity is near the average we observed for these storms. The ratio of minor to major flashes, for which we have analyzed no other data for comparison, is greater than 17:1. The flashing rates of the minor flashes varied from 18 to 36 min<sup>-1</sup> and averaged 26 min<sup>-1</sup>. This gives an average time separation between flashes of 2.3 s. Time separations, however, are log normally distributed with a median of 1.4 s and a standard deviation of ±20 log 2.5 giving a -10 value of 0.56 and a +10 value of 3.5 s.

#### Altitude Distribution of Lightning

Let us now examine the altitude distribution of the mapped VHF sources for our four storms as shown in Figs. 6-9. The lower, shaded distribution in each figure comprise the major flashes, i.e., those containing >30 VHF signals. Minor flashes are represented in the unshaded distribution with the tail end of the distribution at low altitudes passing through the shaded area.

No altitude discriminants were employed in categorizing the flashes, only the number of sources in each flash was used. Thus, to start the selection process, all mapped sources occurring during the active period of a major flash, sometimes extending beyond a second in duration, were counted as part of the flash.

Some sources from minor flashes were undoubtedly included in this period. Most major flashes occurred at lower altitudes, but a few flashes at high altitude satisfied the count criteria and were counted as major flashes, e.g., the one in storm II at 2225:42, recognized as a short vertical line of pluses centered at 11 km. These sources at high altitude caused the distribution of major flashes to tail off slowly with height. The sources occurring at all other times throughout the storm not designated as a major flash were counted in the minor flash category. There were a few small flashes at low altitudes that produced only a few sources and these caused the distribution of the minor flashes to tail off at low elevations.

Most lightning sources in the major flashes occurred at 4-6 km altitude, while the minor flashes showed maximum occurrence at 11-13 km. Large differences in the altitude distributions of flashes in storm I and storm II are evident in Fig. 6 and Fig. 7. Although these storms occurred concurrently, the most active period of lightning occurred prior to 2222 for storm I and after 2238 for storm II. When we smooth the altitude distributions by eye, we find that the source altitudes in storm II for the major flashes were 2.5 km lower, and for the minor flashes were 1.0 km lower, than those observed in storm I. In addition, the relative number of minor flashes in storm II was very small. Altitude distributions in storms III and IV were very similar, as shown in Fig. 8 and Fig. 9, and only slight differences in the relative number of sources are apparent. For this group of four storms, about the same number of VHF sources was produced by lightning activity above 8 km as below that Altitude.

#### Lightning Relative to Precipitation and Winds

It is very difficult to produce an easily understandable composite of lightning activity and Doppler radar derived storm parameters. We delve into this part of our results by presenting the analyses performed, an example of results obtained by combining lightning location, precipitation and horizontal wind parameters for one storm, and discussion of the general associative characteristics among these parameters for the other three storms.

VHF sources occurring during each radar tilt sequence were partitioned into 1 km height increments and mapped separately for major and minor flashes. Radar data were synthesized to give reflectivity contours, horizontal wind vectors and vertical wind speeds for each 1 km height. Upon comparing the lightning data with the radar derived storm parameters for each height, it was found that the location of lightning sources conforms best with the radar reflectivity contours at 5 km height for major flashes, and with the divergent horizontal wind pattern at 13 km height for minor flashes. There seemed to be

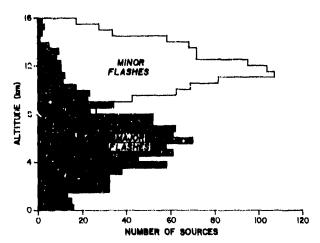


Figure 6. Altitude distribution of VHF sources for Storm I.

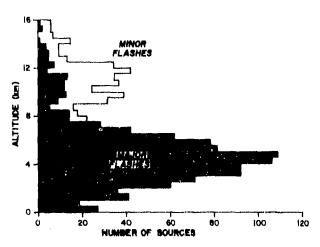
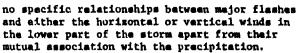
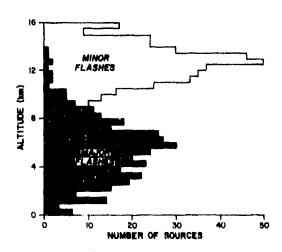


Figure 7. Altitude distribution of VHF sources for Storm II.

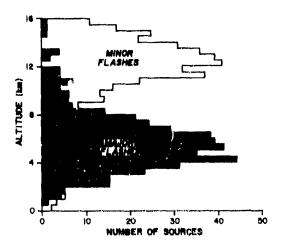


At the sacrifice of structural detail and secondary relationships, lightning locations and radar derived parameters are presented for only the two heights where associations appear the strongest. The essential aspects of this study, therefore, are presented in the examples shown in Figs. 10 and 11, which are representative of all data collection periods for the four storms.

Superposed onto the plan view of the 40 and 50 dBZ reflectivity contours and the streamlines of horizontal winds at the 5 km altitude are the VHF sources of major flashes occurring at all altitudes as indicated in Fig. 10. The radar sector scan extended from



Storm 8. Altitude distribution of VHF sources for Storm III.



Storm 9. Altitude distribution of VHF sources for Storm IV.

2222 to 2227 whereas the lightning activity was summed over the period 2219-2227. Upon eliminating 20 percent of the most widely scattered sources within the view presented in Fig. 10, we find that 80 percent of all sources are contained in the shaded area and 50 percent are within the more darkly shaded portion. It is clear that the lightning sources were concentrated in the high reflectivity core of this storm. The horizontal winds tended to curve through the main lightning activity area with indications of slight convergence. The main updraft core for this part of the storm was centered at 4 km west and 41 km north of Norman and encompassed an elougated region oriented SW-NE, which is parallel to the axis between the centers of the 50 dBZ cores within the shading and the major axis of the shaded area containing 50 percent of the VHF

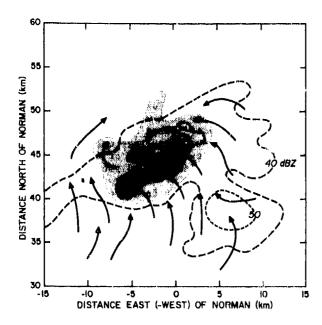


Figure 10. Plan view of VHF soruces of major flashes at all altitudes superposed onto the 40 (long dashed lines) and 50 (short dashed lines) dBZ reflectivity contours and horisontal wind streamlines at 5 km altitude. The total shaded area contains 80% of all mapped sources, while 50% are within the darker shading.

sources. Updraft speed was between 10 and 20 m·s<sup>-1</sup> at this level, but exceeded 20 m·s<sup>-1</sup> above 6 km sititude.

This storm complex was actually composed of two high reflectivity regions whose centers were separated by about 10 km. We refer to them as cell A containing the lightning activity and call B located to the southeast of the other cell and containing no lightning during this period. Cell A at this 5 km altitude shows three areas of 50 dBZ reflectivity. At lower altitudes, these areas merged into a single larger 50 dBZ cora. The central 50 dBZ reflectivity core continued upward to 9 km altitude as a single 50 dBZ core and thence to 14 km as a single 20 dBZ core. Very little vertical shear in the horizontal wind was found in the structure of this cell. A line running vertically through the core centers at each kilometer interval would have to deviate horizontally only 2 km between ground and 14 km altitude. Cell B contained only 40 dBZ reflectivity at very low altitudes, became a single 50 dBZ core from 2 km through 6 km, split into two 50 dBZ cores at 7 km, extended up to about 10 km as dual 40 dBZ cores, and became unidentifiable at higher altitudes.

A quantitative description of Cell A at the 5 km attitude in the Storm I complex indicates the three small areas where the

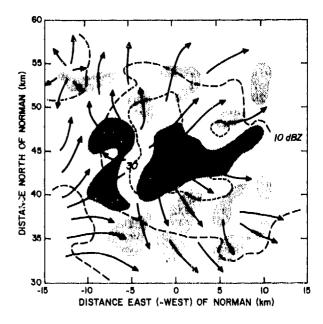


Figure 11. Plan view of VHF sources of minor flashes at all altitudes superposed onto the 10 (long dashed lines) and 30 (short dashed lines) dBZ reflectivity contours and horisontal wind streamlines at 13 km altitude. The total shaded areas contain 80% of all mapped sources, while 50% are within the darker shading.

reflectivity is >50 dBZ totaled about 19 km², and the area of reflectivity >40 dBZ totaled 180 km². Twenty-five percent of the VHF sources was within the >50 dBZ reflectivity areas. The VHF source density within the >50 dBZ areas was three times greater than that in the >40 dBZ area which contained 85 percent of the sources. The darkly shaded portion in Fig. 10 containing half the VHF sources covered an area of 30 km² and produced a source density twice that found in the total shaded area covering 94 km².

Minor flashes at all altitudes are superposed onto the 10 and 30 dBZ reflectivity contours and streamlines of horizontal winds at 13 km in Fig. 11. The plan view distribution of minor flash sources was very patchy and distributed over a much larger total area than for the major flashes. When we tried to represent the main electrically active region by again eliminating 20 percent of the most widely scattered sources, no single region of conentration was found. Therefore, thirteen separate areas that contain 80 percent of the sources are shown in Fig. 11. Fifty percent of the sources is contained in the two darker shaded areas.

Although lightning sources from these minor flashes seem to be scattered around the center of the 30 dBZ core of the storm, the

sources are not well aligned with the 30 dBZ contour and many sources are in regions where the reflectivity is less than 10 dBZ. It seems more likely, therefore, that the sources are closely allied with the divergent, outflowing winds at the top of the storm as indicated by the streamlines. There may be also a slight tendency for source generation near regions of interaction between convective cells, such as the confluent zone between outflow from storm I and storm II in the lower left corner of Fig. 11 (in a region along a line from coordinates -4 and 33 km to -9 and 46 km).

Additional quantitative information about Storm I at the 13 km altitude indicates the areas of reflectivity >30 dBZ and >10 dBZ were, respectively, 78 km² and 364 km². Thirty-three percent of the VHF sources was observed in the >30 dBZ reflectivity area and 67 percent was in the >10 dBZ reflectivity with corresponding VHF source density ratios between the regions of about 2:1.

During succeeding observational periods, in storm I, relationships between lightning and radar derived structural parameters continued similarly to that just described. After about 2228, Call A decreased in lightning activity and Call B became more active.

Now, in more general terms, we examine the other three storms. The data for the early stage of storm II are not complete because some of the storm structure was outside the sector scans of the Doppler raders and for the late stage some of the lightning activity occurred outside the VHF mapping sector limits. Nevertheless, enough of the main reflectivity region and the central portions of lightning activity was observed to conclude that the relationships between lightning and storm structure were similar to that in storm I. Vertical shear in the storm structure was again found to be very small. Storm II was also multicellular, having two or three cells varying from 6-10 km apart depending on the altitude and time of observation. The cell cores were >50 dBZ and generally only 10 dBZ greater in reflectivity than the background region in which they were imbedded. Major flashes were associated with the central area of the calls. Minor flashes at high altitude were located in the divergent horizontal winds outflowing toward the east from updrafts associated with reflectivity maxima.

The first lightning activity in storm III was not distributed around the main 50 dBZ reflectivity region but displaced downwind and to the north. A small 40 dBZ cell developed about 6 km north of the main reflectivity core. While the main cell moved southeastward at 9 m·s<sup>-1</sup>, the newly formed small cell moved northeastward at 15 m·s<sup>-1</sup>. The updraft speed in the small cell was only 10 m·s<sup>-1</sup> as compared with 35 m·s<sup>-1</sup> for the main cell. The small cell structure was evident only below about 7 km. The major flashes at low levels were located near the core of the small cell, where the VHF sources were very dense, and between the two cells, where the sources were dispersed over a slightly larger

region. Minor flashes were consistently located in the divergent horizontal winds in the upper part of the main cell, but only in the outflow region toward the northeast, which was above and to the east of the small cell.

The small cell never penetrated upper levels of the reflectivity complex in storm III. Maximum reflectivity in this cell was only 40 dBZ and the core of reflectivity leaned at an angle of about 30° toward the east. The large cell attained a maximum reflectivity in excess of 60 dBZ. The core of the cell tilted toward the southwest with a maximum inclination of 45° between 3-8 km heights and a total tilt from ground to top or about 20°.

Relationships between lightning activity and storm structure in storm IV cannot clearly be defined as yet because the synthesis of radar data has not been completed. But from the analysis of radar scans obtained at the beginning of the storm and during the period 2337-2343, we can see that this storm was comprised of three or four cells with 8-16 km separation between cores. Major flash sources tended to concentrate near large, high reflectivity cores, in regions where the horizontal winds were converging and between the smaller cells that were only well defined at low sittitudes. Minor flashes tended to concentrate over the main core of the storm complex, around the center of the divergent horizontal winds in the upper part of the storm, and generally toward the east in the stronger outflowing winds.

#### Summary and Conclusions

We have analyzed the VHF mapping and dual Doppler radar data for four storms occurring in Oklahoma during an approximate two hour period on 19 June 1980. VHF source altitudes as a function of time show the altitude characteristics of major and minor flashes as the storms evolve. First-time data show considerable lightning activity to 16 km altitude in storms. The low occurrence rates of major flashes in these storms aid in characterizing the minor flashes. Altitude distributions of mapped VHF sources show bimodal scructure, with minor flashes occupying the higher altitude mode and major flashes the lower mode.

Many strong similarities exist among the four storms encompassed in this work, although important differences are also evident. Strong gust fronts were reported from storms I and II, and large hail and damaging winds were observed from storms III and IV. A single, high reflectivity core in excess of 50 dBZ usually dominated each storm, but multicellular structure was also apparent. Although these storms were relatively small, they were all classified as severe.

Lightning characteristics were very similar in terms of flashing rate, altitude distribution, and relationship with storm structures. We feel confident, therefore, that these storms are typical of relatively small nonsevere and marginally severe thunderstorms found in the Great Plains area of the United States.

Our major conclusions are: 1) There is a class of small IC flashes that produces a splattering of VHF sources in a large canopy over the main electrically active region of a storm to an altitude of 16 km or more. 2) The minor flashes produce almost a continuum of lightning activity centered at 11-13 km altitude and have no apparent temporal association with the major flashes sporadically occurring in the lower portions of storms. 3) Major flashes concentrate within or near to high reflectivity regions at mid levels in a storm, . 4) Major flash activity is centered at 4-6 km altitude and seldom produces sources above 10 km altitude. 5) Structure in the altitude-time distribution of VHF sources suggests that lightning activity may be closely associated with upward and downward convective plumes and tends to avoid a region between about 8-10 km altitude that closely corresponds with an environmental temperature of about -30°C. 6) The locations of VHF sources indicate lightning activity may concentrate either in a single high reflectivity region, between two high reflectivity cells, in divergent horizontal winds in the upper part of a storm, or in regions of horizontal wind interaction between cells.

We have shown that in some storms comparable lightning activity, as measured by the number of VHF sources, can occur in the upper regions of a storm and at low altitudes. Since each VHF source results from a radio signal produced by a change in the vertical current moment of some lightning process, we may have a means to estimate the electric current budget of a storm through VHF observations. The high altitude lightning may be the manifestation of processes coupling the charge in the upper portion of a storm to the atmosphere. The discharge mechanism involved remains to be determined. Other aspects of high altitude lightning yet to be determined involve the chemical compounds produced by the lightning and injected into the upper troposphere and lower stratosphere, the impairment to derecting CG flashes from space and the hazard to aircraft operating in the upper portion of storms.

#### ACKNOWLEDGEMENTS

We are indebted to our many co-workers at NSSL who helped in the collection and reduction of electrical and radar data used in this study, and to numerous others whose continual help keeps the Storm Electricity Group an important research unit in this field. Particular thanks to Joan Kimpel for illustrations and to Joy Walton and Sandra McPherson for typing. This work was supported in part by the Severe Storms and Local Weather Research Office of the National Aeronautics and Space Administration.

#### REFERENCES

- D. R. MacGorman and W. L. Taylor, "Lightning Location Relative to Storm Structure in an Oklahoma Thunderstorm", <u>Preprints</u>, 11th Conf. Severe Local Storms, Kansas City, Mo., Am. Meteor. Soc., Boston, Mass., October 2-5, 1979.
- W. D. Rust, W. L. Taylor, and D. MacGorman, "Preliminary Study of Lightning Location Relative to Storm Structure", AIAA Journal, 20 (3), March, 1982.
- 3. W. D. Rust, W. L. Taylor, D. R. MacGorman, and R. T. Arnold, "Research on Electrical Properties of Severe Thunderstorms in the Great Plains", Bull. Am. Meteor. Soc., 62 (9), September, 1981.
- W. L. Taylor, "A VHF Technique for Space-Time Mapping of Lightning Discharge Processes", J. Geophy. Res., 83 (C7), July, 1978.
- P. S. Ray, R. J. Doviak, G. B. Walker, D. Sirmans, J. Carter, and B. Bumgarner, "Dual-Doppler Observations of a Tornadic Storm", J. Appl. Meteor. 14, December, 1975.
- P. R. Krehbiel, M. Brook, and R. A. McCrory, "An Analysis of Charge Structure of Lightning Discharges to Ground", J. Geophy. Res., 84, May, 1979.

### SOME SPATIAL AND TEMPORAL RELATIONSHIPS BETWEEN LIGHTNING AND STORM STRUCTURE AND EVOLUTION



## AD P002165

D. R. MacGorman and W. L. Taylor National Severe Storms Laboratory/NOAA/ERL, Norman, OK 73069

A. A. Few Dept. of Space Physics and Astronomy, Rice University, Houston, TX 77251

We have used a number of systems to study relationships between lightning and and other storm parameters. Instrumentation includes a system for locating cloud-to-ground lightning strike points, an acoustic lightning mapper and a VHF (30-80 MHz) lightning mapper to study the structure and location of lightning, and S-band radar to provide other storm data. Several characteristics of the reconstructed lightning have been relatively constant: (1) lightning structure is usually predominately horizontal; (2) lightning tends to occur preferrentially in certain altitude ranges that are only a few kilometers thick and above the O°C isotherm; (3) it tends to occur near, but not necessarily inside, cores of high reflectivity (945 dBZ), and it often connects with regions of relatively weak reflectivity downstream from stronger reflectivity and updraft cores. Other relationships are also discussed.

(aprox. 5)

#### INTRODUCTION

Several techniques have been used to locate various segments of a lightning flash. Krider et al. (1)\* located the strike point of a cloud-to-ground flash by direction finding from the initial rise in the magnetic field change produced by lightning. Krehbiel et al. (2) located equivalent charge centers neutralized by ground flashes. Szymanski and Rust (3) employed radar to locate lightning echoes within a stationary radar beam.

More detailed lightning structure has been provided by acoustic and VHF techniques for mapping lightning. Few (4) and Few and Teer (5) map lightning structure from thunder recorded by an array of microphones with baselines of 30-100 m. Proctor (6) uses an array of antennas separated 10-15 km for mapping lightning from its VHF radiation. Lhermitte and Krehbiel (7) also used a large array (the LDAR system at Kennedy Space Center) to map lightning from VHF radiation. Taylor (8) uses an array of antennas separated by 13.7 m to determine the azimuth and elevation of VHF signals; two arrays were used to determine the three dimensional location of the source of a signal by triangulation.

We have used three of these location techniques to study lightning in Colorado and Oklahoma: the direction finding technique for locating ground strikes and the acoustic and VHF techniques for mapping lightning structure. Data are also available from S-band radar to correlate with the lightning data. In this

relationships between lightning and storm structure and kinematics in several storms. A case history of a different group of storms that occurred consecutively on one day is presented by one of the authors in another paper at this conference.

paper, we present an overview of our study of

#### INSTRUMENTATION

#### Colorado Storm.

A detailed analysis of the Colorado storm has been presented by MacGorman (9) and MacGorman et al. (10). Lightning flashes from this storm were mapped using the acoustic technique described by Few (4) and Few and Teer (5). The direction of arrival of a thunder impulse at an array of microphones is determined by the propagation time between microphones, measured to an accuracy of 1 ms using a cross-correlation analysis. The acoustic ray defined by this direction is then retraced through the atmosphere to its source. Range to the source is determined from the propagation time between occurrence of the lightning, detected by its electric field change, and arrival of the thunder impulse at the array. Source locations are computed from all processes in a lightning flash that produces analyzable thunder at the array. However, since acoustic propagation time is long compared to the duration of lightning, the relative times at which different acoustic sources were generated by a lightning flash are not determined in the acoustic analysis.

Radar reflectivity data for the Colorado storm were obtained from a narrow beam, 10.7 cm radar operated approximately 50 km from our site

<sup>\*</sup>Numbers in parentheses designate references at the end of the paper.

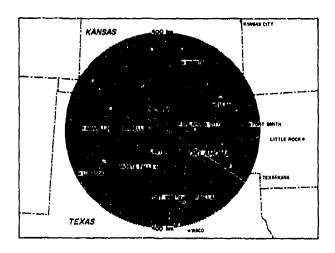


Figure 1. NSSL lightning ground strike locating system. The location of each of the four stations is indicated by a black square. The baselines that are indicated by solid black lines range from 80 km to 110 km. Shading denotes the nominal area coverage of the system.

by the National Center for Atmospheric Research (NCAR) as part of the National Hail Research Experiment. During the summer that the acoustic experiment was in Colorado, radar data was collected by scanning rapidly in azimuth while the elevation angle was slowly increased. Scanning through the storm usually required 5-6 minutes in the case we studied.

#### Oklahoma Storms.

The VHF technique employed in Oklahoma uses two arrays of antennas separated by 42 km to map lightning from VHF radiation in the 30-80 MHz band. At each array, fast logic circuitry measures the azimuth and elevation angles of a VHF impulse to an accuracy of 0.5°. Later computer analysis identifies corresponding impulses at the two arrays and triangulates to locate sources in three dimensions. This technique is discussed in detail by Taylor (8).

In addition to the VIIF mapping system, the National Severe Storms Laboratory (NSSL) has also operated a direction finding system (1) for locating lightning ground strikes. Four stations are connected to a central processor as shown in Figure 1. Each station includes a crossed-loop antenna, electric field antenna, and microprocessor, which are used to reject intracloud lightning, determine the direction to a lightning strike, and transmit the strike data to a central processor at NSSL. When the central processor receives coincident data from two or more stations, it triangulates to locate the strike points and records the data on magnetic tape. All four stations have been modified to locate ground flashes that lower positive charge

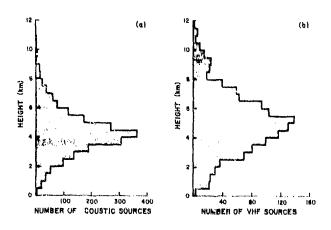


Figure 2. The vertical distribution of lightning locations in each 0.5 km increment of height. (a) Acoustic sources are from thirtyfive lightning flashes during a storm in Colorado on 25 July 1972. The OOC isotherm measured by soundings in clear air was at approximately 3.5 km above ground level and 5.0 km MSL. (b) VHF sources are from forty-two flashes during a storm in Oklahoma on 1 June 1978. The O<sup>O</sup>C isotherm was at approximately 4 km above ground level and 4.4 km MSL.

in addition to those that lower negative charge. We currently are evaluating the performance of the modification.

Radar data for the Oklahoma storms were obtained with one or both of the two Doppler radars operated by NSSL and co-located with the VHF lightning mapping sites. Each radar has a 0.8° beamwidth and operates in the S-band (10.5 cm wavelength for one and 11.0 cm for the other). Radar data were collected by scanning in azimuth at a constant elevation and stepping through a series of elevation angles. A series of scans through a storm was normally completed within five minutes.

#### LIGHTNING AND STORM DATA

#### Lightning geometry.

The acoustic and VHF mapping techniques locate points on lightning channels from different properties of the lightning, so there may be systematic differences in the reconstructed lightning structure from each. In our limited sample, however, several characteristics of lightning have appeared similar in maps from both techniques. For example, reconstructed lightning structure has been predominantly horizontal. A visual examination of reconstructed intracloud structure shows that the horizontal extent is usually larger than the vertical extent; predominantly vertical discharges, such as one might expect between two localized charged regions in

a vertical dipole, have been the exception rather than the rule. Predominantly horizontal structure has also been observed by acoustic and VHF techniques in several other storms, as reported by Proctor (11), Taylor (8), Bohannon (12), Winn et al. (13), and Teer and Few (14). However, the acoustically reconstructed structure of lightning was primarily vertical in a small storm investigated by Christian et al. (15).

In addition to being predominantly horizontal, lightning flashes during the 10-30 min periods we studied tended to cluster about preferred altitudes that were above the 0°C isotherm. Figure 2 shows the vertical distribution of computed sources in two storms. The peak in both distributions occurs near 5.5 km MSL, which is above the 0°C isotherm in the two storms. The thickness of the distrib wis at half the maximum number of sources is . km and 4 km. respectively, for the distributions shown in Figures 2a and 2b. A thickness of 2-4 km at half maximum is typical of the storms we have observed. Using a different lightning mapping technique, Krehbiel et al. (2) also observed stratification: the equivalent negative charge neutralized by cloud-to-ground lightning in one storm was stratified between environmental temperatures of -9°C and -17°C. MacGorman et al. (10) report on three other storms in different geographic regions in which the vertical distribution of lightning had two peaks, each with a vertical thickness at half maximum of 2-4 km. Taylor (16) reports a similar bimodal distribution in four Oklahoma storms he has recently analyzed.

#### Cloud-to-ground lightning in tornadic storms.

A number of observers have reported that cloud-to-ground lightning appeared to be suppressed during tornadoes, e.g., (17) and (18). Most of trass reports have been subjective, but Gunn (15 : ported a lack of ground flashes in electric and recordings made near the Blackwell-Udall tornado. More recently, Orville (20) reported that a medium range ground strike locating system in central Oklahoma located little ground strike activity near the Lawton tornado of 10 April 1979, but located considerable activity in other parts of the storm that were about the same range from the locating system as the tornado. We have analylzed ground strike data from 22 May 1981, when there was an outbreak of tornadoes within our ground strike locating network in Oklahoma. We have concentrated thus far on a tornado that occurred from 1852-1927 CST near Binger, Oklahoma, and was the severest tornado to occur on that day (F4 on the Fujita scale, which ranges from F0 to F5).

Figure 3 shows variations in the lightning ground strike rates for each 5 min period during the active lifetime of the storm. Included in the histogram are all strikes that were located anywhere in the storm, which had horizontal

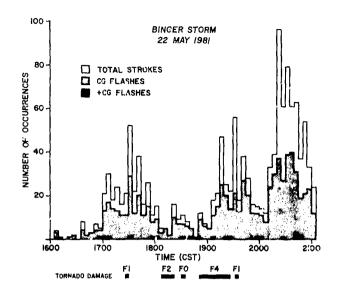
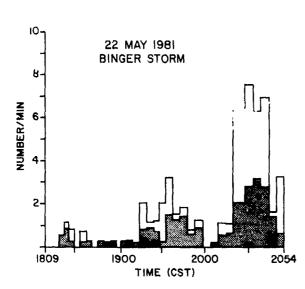


Figure 3. Lightning ground strikes for each 5 min. period in a tornadic storm on 22 May 1981. The bars beneath the time line indicate time of tornadoes. Each tornado is labelled with its Fujita scale rating, which ranges from FO for light damage to F5 for heaviest damage. The shaded middle trace indicates total number of flashes, including both positive and negative flashes.

dimensions of 40-60 km on the radar display. There were several tornadoes of varying severity in this storm. No obvious suppression of lightning ground strikes is characteristic of tornadoes in the histogram. A significant decrease in the ground flash rate occurred during the F2 tornado, but there was a significant increase during the F4, Binger tornado. The average number of strokes per flash did increase, however, between 2010-2100 CST, after the tornadic stage ended. The fraction of flashes that lower positive charge was generally larger before and during tornadoes, although the positive flash rate increased somewhat after the tornadic stage ended.

Since most of the earlier reports had been near tornadoes, we also analyzed the data by restricting the area of interest to the vicinity of the largest tornado. We compared the ground strike rate variations with the strength of the mesocyclone (the parent circulation of tornadoes within the storm), as measured by cyclonic shear in the horizontal wind at the 6 km level. Figure 4 shows the resulting histogram, which includes only strikes within 10 km of the mesocyclone center. The ground strike rate is lower as cyclonic shear in the mesocyclone increases due to stronger rotation, and the rate increases when the cyclonic shear decreases. Again in this case, the fraction of flashes lowering positive charge was largest before and during the tornado, and the number of strokes per flash increased



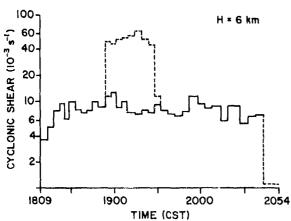


Figure 4. Lightning strike rate characteristics versus cyclonic shear at the 6 km level for the storm that produced the Binger tornado. Cyclonic shear was calculated from the azimuthal shear in the single Doppler radial winds for the mesocyclone, which has a characteristic horizontal dimension of a few kilometers. The dashed line in the bottom trace indicates cyclonic shear on the tornadic scale, usually 1 km. The top histogram gives lightning strike rate characteristics. Solid bars denote positive cloud-to-ground flashes. Shading denotes total number of ground flashes, including both negative and positive flashes. The top trace on the histogram indicates number of strokes.

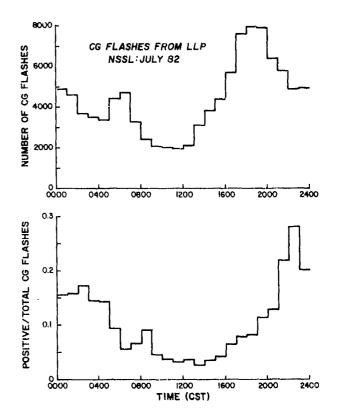


Figure 5. Diurnal variation in number of positive ground flashes during July 1982. The top histogram shows the total hourly count for all ground strikes, both positive and negative, during July. the lower histogram shows the fraction of these that are positive.

after the tornado ended and the mesocyclone was dissipating.

#### Diurnal variation of positive ground flashes.

As discussed in more detail by Rust et al. (21) at this conference, cloud-to-cloud lightning flashes that lower positive charge to ground may be more hazardous than the usual flashes that lower negative charge; they may have larger peak currents, have currents of longer average dura-tion, and occur in regions of storms where one would normally expect few, is any, lightning To understand better the conditions under which positive ground flashes occu examined the diurnal variation of postiv strikes located by our ground strike 1 cating system. Shown in Figure 5 is lightning ' ike data for the month of July 1982. The top istogram, variations in the total hourly count of ground strikes of both polarities, is about what one would expect from the diurnal variation in the convective growth of storms during July in Oklahoma. The pattern of the diurnal variation in the fraction of flashes that are positive,

shown in the lower histogram, is similar to the variation in total lightning strikes, but the minimum is broader and the peak occurs 2-3 hr later in the evening. This indicates that conditions in July are more conducive to positive ground flashes later in the life of storm systems.

#### Lightning location relative to storm structure.

In three storms for which we have radar and lightning mapping data, lightning was usually closely associated with regions of sustained high reflectivity. Part of the reconstructed structure of a flash was often near these regions of high reflectivity, but in two storms, it tended to avoid the cores of strongest reflectivity (greater than 45-50 dBZ). Lightning often stretched from near these cores to an area with reflectivities of less than 30 dBZ. As new regions of high reflectivity formed, a region of lightning activity also formed near the new

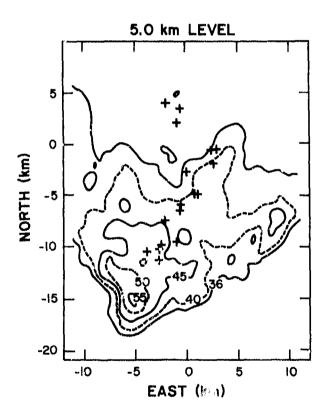


Figure 6. Acoustically reconstructed structure for a lightning flash at 1720:29 Mountain Standard Time (MST) superimposed on radar reflectivity contours from a Colorado storm on 25 July 1972. Computed thunder sources with heights of 4.5-5.5 km are plotted as "+"; sources at other heights are not shown. Radar reflectivity contours, labeled in dSI and shown at a height of 5.0 km, are derived from a series of radar scans at 1718-1723 MST.

reflectivity core. An example of a lightning flash occurring near, but not inside a high-reflectivity core is shown in Figure 6 from a Colorado storm. In the 35 flashes mapped from this Colorado storm, there were very few thunder sources located in reflectivities higher than 45 dB2 and none located in reflectivities higher than 50 dBZ. Since the fraction of the storm having reflectivities higher than 45 dBZ was also small, this observation is significant primarily in suggesting that high reflectivity cores are not the preferred location for lightning that some theories of storm electrification would lead us to expect.

With Boppler radar data available for the Oklahoma storms, we were able to relate the location of lightning with the measured winds within the storm. In a storm on 1 June 1978, the reconstructed locations of VHF sources tended to be concentrated in and near regions of cyclonic shear deduced from single Doppler measurements, as shown in Figure 7. These regions were inferred to be in the vicinity of updrafts from the reflectivity structure of the storm and from the cyclonic shear signature (22).

For a storm on 6 June 1979, dual Doppler radar data were used to derive estimates of all three components of wind. As shown in the example in Figure 8, the reconstructed VHF source locations in this storm tended to occur in regions of weak updraft (<10 m/s) and were also often adjacent to regions of downdraft. Regions having vertical updraft velocities greater than 10 m/s were south and southeast of

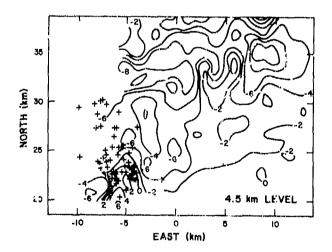


Figure 7. VHF source locations for a flash at 1515:36 CST superimposed on radial Doppler velocity contours from an Oklahoma storm on 1 June 1978. Velocity data are shown in m/s at a height of 4.5 km from a series of radar scans at 1512-1519 CST. Positive velocities indicate radial motion outward from the origin. Each "+" is the plan location of a VHF source calculated to be 4-5 km above ground by the mapping analysis.

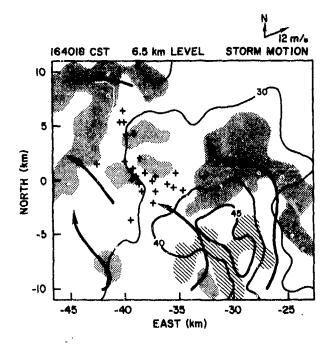


Figure 8. VHF source locations for a flash at 1640:18 CST superimposed on radar data from an Ohlahoma storm on 6 June 1979. Radar data are shown at a height of 6.5 km from a series of radar scars at 1630-1633 CST. Contour lines indicate reflectivity in dBZ. Arrows indicate streamlines in the horizontal wind after storm motion is subtracted. Potted shading indicates areas of downdraft (mostly \$\leftsigma\$n/s). Striped shading indicates areas having updrafts greater than 10 m/s. the remaining area of the figure has updrafts of \$\leftsigma\$ 10 m/s. Each calculated VHF source location 5-7 km above ground is ploxted as "+".

the lightning. After storm motion was subtracted from the horizontal wind, horizontal streamlines at the level of the lightning generally flowed from the reflectivity cores and strong updrafts back toward the lightning.

#### DISCUSSION AND SUMMARY

While the number of storms for which lightning mapping data have been analyzed is still relatively small, it has been consistently observed that lightning tends to be stratified above the 0°C isotherm, occurring most frequently within a 2-4 km thick layer. Furthermore, lightling has tended to occur near cores of high reflectivity (545 dEZ), often connecting with regions of relatively weak reflectivity (in some cases 20 dGZ or less). However, there has been some variation in the details of the location of lightning relative to reflectivity cores. In two of the storms presented in this paper, reconstructed lightning was clearly outside, but

near, the cores, but in other reports (7 and 16), it was concentrated in and around higher reflectivities. There have also been some differences in the preponderance of horizontal or vertical lightning structure. While most of the lightning we have observed and much of the lightning observed elsewhere (e.g., 8, 11, 12, and 14) have been predominantly horizontal, vertical lightning coes occur and can dominate the activity of some storms (15).

There have been only three storm studies that included both lightning mapping data and dual Doppler synthesis of the three-dimensional wind field: the one presented in this paper, Taylor et al. (8), and Lhermitte and Krehbiel (7). In both the Oklahoma studies, lightning tended to occur in regions of weak updraft. Lhermitte and Krehbiel (7) concentrated on the initial VHF source located for each flash. They found that initial VHF sources tended to occur above reflectivity cores and were in the upper part of the main updraft and in adjacent regions on the upshear side of the updraft where there was an upper level downdraft. It was also reported that many of the VHF sources occurred in the anvil, where vertical velocities should be weak.

In tornadic storms, we have found relatively few cloud-to-ground flashes in the vicinity of tornadoes. When lightning strikes from the whole storm were considered, however, there was no obvious relationship between flash rates and tornadoes. It is interesting that before and during tornadoes the fraction of ground flashes lowering positive charge was higher and the average number of strokes per flash was lower. More data is needed to determine whether these tendencies are sufficiently regular and identifiable to be useful aids for tornado warnings. More analysis is also needed to confirm and fully explain the tendency for the positive ground flash rate to peak 2 to 3 hours later than the total ground flash rate in summer storms.

For aircraft penetrating a thunderstorm, we have found that there is no region of the storm safe from lightning, even if we ignore the possibility that aircraft may trigger flashes where none would have occurred otherwise. As discussed by Rust et al. (21), we have seen lightning even in the anvils of storms, tens of kilometers from reflectivity cores. Furthermore, there is considerable variability in the features of storms associated with the most concentrated lightning. It may be possible, however, to learn to identify regions of a storm where the probability of strikes to aircraft is low or where lightning is less damaging, such as, possibly, the upper region of minor discharges discussed by Taylor et al. (16).

#### **ACKNOWLEDGMENTS**

We would like to thank the staff of the National Severe Storms Laboratory, who makes it possible for us to carry out our research.

Particular thanks are due Joy Walton, Evelyn Horwitz and Joan Kimpel for their help in the preparation of this paper. This research has been funded in part by the Severe Storms and Local Weather Research Office of the National Aeronautics and Space Administration, the Atmospheric Sciences Section of the National Science Foundation, and the postdoctoral research associate program of the National Research Council.

L. W. Vollas aprilament

#### REFERENCES

- E. P. Krider and R. C. Noggle, "A gated, wideband magnetic direction finder for lightning return strokes," J. Appl. Meteor., 15, 301-306, 1976.
- P. R. Krehbiel and R. A. McCrory, "An analysis of the charge structure of lightning discharges to ground," J. Geophys. Res., 84, 2432-2456, 1979.
- E. W. Szymanski and W. D. Rust, "Preliminary observations of lightning radar echoes and simultaneous electric field changes," Geophys. Res. Letters, 6, 527-530, 1979.
- A. A. Few, "Lightning channel reconstruction from thunder measurements," J. Geophys. Res., 75, 7517-7523, 1970.
- A. A. Few and T. L. Teer, "The accuracy of acoustic reconstructions of lightning channels," J. Geophys. Res., 79, 5007-5011, 1974.
- D. E. Proctor, "A hyperbolic system for obtaining VHF radio pictures of lightning," J. Geophys. Res. 76, 1478-1489, 1971.
- R. M. Lhermitte and P. R. Krehbiel, "Doppler radar and radio observations of thunderstorms," IEEE Trans. on Geoscience Electronics, GE-17, 162-171, 1979.
- W. L. Taylor, "A VHF technique for spacetime mapping of lightning discharge processes," J. Geophys. Res., 83, 3575-3583, 1978.
- D. R. MacGorman, "Lightning location in a storm with strong wind shear," Ph.D Dissertation, Rice University, Houston, Texas, available from University Microfilms International, Dissertation Copies, P.O. Box 1764, Ann Arbor, Michigan 48106, 1978.
- 10. D. R. MacGorman, A. A. Few and T. L. Teer, "Layered lightning activity." J. Geophys. Res., 86, 9900-9910, 1981.
- 11. D. E. Proctor, "VHF radio pictures of cloud flashes," J. Geophys. Res., E6, 4041-4071,

- J. L. Bohamnon, "Infrasonic pulses from thunderstorms," M.S. Thesis, Rice University, available from Rice University Library, P.O. Box 1892, Houston, Texas 77251, 1978.
- W. P. Winn, C. B. Moore, C. R. Holmes and L. G. Byerley, III, "Thunderstorm on July 16, 1975, over Langmuir Laboratory: A case study," J. Geophys. Res., 83, 3079-3098, 1978.
- T. L. Teer and A. A. Few, Horizontal lightning. J. Geophys. Res., 79, 3436-3441, 1974.
- H. Christian, C. R. Holmes, J. R. Bullock, W. Gaskell, A. J. Illingworth and J. Latham, "Airborne and ground-based studies of thunderstorms in the vicinity of Langmuir Laboratory," Quart. J. Roy. Meteor. Soc., 106, 159-174, 1980.
- 16. W. L. Taylor, W. D. Rust, D. R. MacGorman and E. A. Brandes, "Lightning activity observed in upper and lower portions of storms and its relationship to storm structure from VHF mapping and Doppler radar." In this volume, 1983.
- R. P. Davies-Jones and J. H. Golden, "On the relation of electrical activity to tornadoes," J. Geophys. Res., 80, 1614-1616, 1975.
- C. R. Church and B. J. Barnhart, "A review of electrical phenomena associated with tornadoes," <u>Preprints</u>, 11th Conf. Severe Local Storms, Amer. Meteor. Soc., Boston, Mass., 337-342, 1979.
- R. Gunn, "Electric field intensity at the ground under active thunderstorms and tornadoes," <u>J. Meteor.</u>, <u>13</u>, 269-273, 1956.
- 20. R. E. Orville, M. W. Maier, F. R. Mosher, D. P. Lylie and W. D. Rust, "The simultaneous display in a severe storm of lightning ground strike locations onto satellite images and radar reflectivity patterns."

  Preprints, 12th Conf. Severe Local Storms, Amer. Meteor. Soc., Boston, Mass., 448-451, 1982.
- 21. W. D. Rust, W. L. Taylor, D. R. MacGorman, R. T. Arnold and S. J. Goodman, "Storm electricity research in Oklahoma: An overview." In this volume, 1983.
- L. R. Lemon and C. A. Dostell, III, "Severe thunderstorm evolution and mesoscyclone structure as related to tornadogenesis,"
   <u>Monthly Wea. Rev.</u>, 107, 1184-1197, 1979.



Extract

# OF CLOUD-TO-GROUND LIGHTNING OVER THE UNITED STATES

Michael W. Maier Lightning Location and Protection, Inc. Tucson, Arizona

and

Jackie M. Piotrowicz NOAA/NHRL Coral Gables, Florida

**ABSTRACT** 

A key element for any successful and cost-effective lightning protection design is an accurate estimate of the frequency of direct lightning strikes to ground. For example, an effective protection system for an electric power transmission line in Florida (an area of high lightning incidence) would be far too costly and not accessary for an area such as California (an area of low lightning incidence). In order to estimate the frequency of lightning strikes the local area density of lightning flashes to ground, i.e. the number of strikes per unit area per month or per year, must be known. In the USA, ground flash density is often assumed to be a relatively simple function of the mean number of thunderstorm days per month or per year. Many design handbooks give formulas which relate ground flash density to thunderstorm days, but no formula is generally accepted as standard. All too often, the actual lightning strike incidence is considerably different from the lightning strike projections based on the thunderstorm day statistics. The resulting over or under design of light. In protection systems ultimately leads to greater costs.

Here we show that the thunderstorm duration statistics are a much better indicator of true ground flash densities than the number of thunderstorm days. Maps of mean annual ground flash density are presented which have been inferred from long term thunderstorm duration observations. The thunderstorm duration data were obtained by the relatively dense network of existing aviation weather reporting stations. Approximately 450 stations are used, each with an uninterrupted 30 year period of record. The station density available here is essentially twice that of any previous thunderstorm frequency analysis of the United States.

Our analyses show that maximum annual ground flash densitios of  $18,\,\mathrm{km}^2$  are found in the western interior of Florida from Naples to Cross City. High flash density values (>  $12/\mathrm{km}^2$ ) are found over much of the Florida peninsula, the Florida panhandle, and westward through the southern gulf states to eastern Texas. A large area of flash densities >  $8/\mathrm{km}^2$  are found over most of Oklahoma, Kansas, Missouri, Arkansas, Louisiana, Mississippi, and Tennessee. High flash densities (>  $8/\mathrm{km}^2$ ) in the western states are limited to south central Colorado, northeastern New Mexico, northern Arizona and extreme southeastern Arizona. Pronounced flash density minima are found over the southern half of Texas and in the southeastern states from central Alabama northeastward through western Virginia. Most of the western and northeastern states have flash densities <  $4/\mathrm{km}^2$ . Maps of the 95% and 5% probability flash density values are also presented. Verification of these maps awaits a nationwide direct measurement program or successful practical application.

This paper was not available for incorporation into this book. Therefore, it will be published at a future date.

ELECTROSTATIC CHARGING
D. Königstein

Hochschule der Bundeswehr Hamburg Holstenhofweg 85, 2000 Hamburg 70

#### **ABSTRACT**

Painted RFC-material has been tested by extremly high electrostatic charging. Charge densities reached some hundreds of nanocoulombs per square centimeter on thin surface layers. The resulting high field strength in the dielectric leads to an electric breakdown with or without mechanical damage depending on material thickness and the conductivity of any grounded layer next to the surface.

The time-dependent development of the entire local charge distribution was monitored by a computer-controlled measuring system. In any case, there was little influence of a damaged point on the discharging or recharging process.  $\kappa$ 

INSULATING SUPERFICIAL LAYERS on aircraft parts may cause electrostatic problems, because they are able to store electrostatic energy. If the electric breakdown field strength of the layer is reached, a discharge to the metallic panel or the conductive layer will occur. If the surface field strength is high enough there will be a flashover to a grounded point.

In order to find out whether a breakdown will occur and how the influences on the charging process are, several RFC samples were tested. The base materials were GFRP, CFRP, and Aramid, covered with or without a conductive layer and different surface coatings of 0.02 to 0.23 mm thickness. Methods and results are described in this paper.

#### ELECTROSTATIC CHARGING OF A THIN LAYER

CHARGING OF SURFACE IN FLIGHT - A value for the maximum charging rate to an exposed surface during a typical flight was given by J.E. Nanevicz (1)\*. He reported a charging rate of about 250  $\mu$ A/m² at a speed of 490 m/s. At higher speed, this value may be exceeded (2). What happens to an insulating superficial paint layer of thickness d is illustrated in Fig. 1. The chargedensity  $\sigma$  increases linearly with time and is directly proportional to the rate of current I per considered area A. Using the value mentioned above, we get eq. (1):

$$\sigma = \frac{I}{A} \cdot t = \frac{25 \text{ nC}}{\text{cm}^2 \cdot \text{s}} \cdot t, \qquad (1)$$

The field strength in the insulating layer  $E_1$  increases following eq. (2):

$$E_1 = \frac{\sigma}{\varepsilon} = \frac{I}{A \cdot \varepsilon} \cdot t.$$
 (2)

If we assume a relative permittivity  $\epsilon_r$  = 5, the rising rate of field strength is

$$\frac{E_{1}}{t} = 56.5 \frac{kV}{cm \cdot s} \tag{3}$$

For this assumptions, the electric breakdown field strength  $E_b$  of a usual paint material will be reached in a few seconds. The electric energy  $W_e$ , stored in an area A increases with material thickness d and follows eq. (4):

$$W_{e} = A \cdot \frac{\sigma^{2}}{2\epsilon} d \qquad (4)$$

For a charge density of 25 nC/cm<sup>2</sup> and a thickness of 0.02 mm 1,4·10<sup>-6</sup> Ws of energy is stored on a square-centimeter of surface, for d = 0.2 mm and  $\sigma = 250$  nC/cm<sup>2</sup> this value increases to 1,4·10<sup>-3</sup> Ws/cm<sup>2</sup>.

ARTIFICIAL CHARGING - The artificial charging was done by means of high voltage corona. The principle of the arrangement is shown in Fig. 2. With a charging voltage of up to 30 kV it was possible to create charging currents of up to 250  $\mu A$ . As the test samples had a size of 200 x 200 mm, a charging rate higher than under flight conditions was possible. The test objects were fit into the grounded holder of the charge distribution measurement system to make it possible to start measurement immediately after charging (5 s) without handling the sample.

MEASUREMENT OF THE LOCAL CHARGE DISTRIBUTION – The measurement of surface charges  $\sigma$  on an insulating layer has to be done by the static electric field. The measuring system is described more in detail in a preceding paper (3). The relation between the field strength E in the air gap a between the probe and the charged layer, and the charge density  $\sigma$  is given by eq. 5:

$$\sigma = \varepsilon_0 E \left( 1 + \frac{\pi}{c!} \varepsilon_r \right) \tag{5}$$

It is important to realize that high surface charge densities may have relatively low fields if the measuring distance is high, compared to the thickness of the layer.

The principle of operation and the performance data of the measuring system are shown in Fig. 3. The field strength in a distance of 1.16 mm of the charged insulator surface is measured by means of an active capacitive probe. It is mounted in a brass housing which can be moved by the stapping motors of a plotter mechanism. This allows computer-controlled positioning of the probe and storing of the field strength values.

The usual distance between two different measuring positions was 2 mm and the size of the test objects was 200 x 200 mm. Thus 10 000 charge values are collected during one run, which takes two minutes. The measured data are stored simultaneously on magnetic tape. The measuring program and the storage capacity of the tape allow up to ten successive runs during the discharging process without manual interaction. Thus, the time-dependent development of the whole local charge distribution can be monitored.

Numbers in parentheses designate References at end of paper.

TEST RESULTS

DESCRIPTION OF TEST-OBJECTS - Fig. 4 shows a cross-section of the different test sample layers. Two additional aluminium samples, one with surface paint the other with priming paint, were used for comparison. A carbon filled conductive paint was used on sample 1.2, 2.2, 2.5 and 3.1. For this material a resistance per square mesh of 5 to 10  $k\Omega$  is given by the manufacturer. Other samples had a conductive layer of aluminium-mesh (2.3, 2.4). A special method of manufacturing a conductive layer was used for sample 3.3. In this case some of the fibre-layers of the aramid material were treated with carbon powder resulting in a resistance per square mesh of approx. 100  $\mbox{M}\Omega$  . The CFRP can be considered conductive.

All samples were metallized for grounding on the back-side, any conductive layer was connected. The surfaces of the grounded layers are marked in Fig. 4, to make clear, that only the layers above can be charged electrostatically. Thus the interesting thickness of the charged layer varies from 0.02 to 1.43 mm.

Breakdown Field Strength - The electric breakdown field strength Eb of the insulating layers was tested with a sphere electrode in direct contact to the surface. It was found to be in the range of 500 to 1000 kV/cm for the surface paint and the priming paint. Layers with a thickness of 0.23 mm and more (2.1, 3.2, 1.1) could not be measured, as flashover occurs before volume breakdown.

Specific Resistivity - As demonstrated in (3) interpretation of the time-dependent development of the initial charge on a surface gives more meaningful values for the specific resistivity than conventional methods. Assuming an exponential decay between measuring runs, it is possible to define a discharging time constant  $\tau$ :

$$\tau = \frac{\Delta t}{\ln \frac{Q_0}{Q_1}}.$$
 (6)

Δt: time difference between runs

Qo: charge measured before Q1: measured charge

The specific resistivity py of the charges layer is given by eq. 7:

$$\rho_{\mathbf{V}} = \frac{\tau}{\varepsilon_{\mathbf{0}} \varepsilon_{\mathbf{r}}} \tag{7}$$

if the discharging current flows mainly through the insulator volume. The values were in the range of some 10<sup>14</sup>  $\Omega cm$  to some 10<sup>16</sup>  $\Omega cm$  rising with time.

LOCAL CHARGE DISTRIBUTION AT DIFFERENT CHARGING VOLTAGES

Charging below Breakdown - Fig. 5 shows a typical charge distribution with a charging voltage low enough not te exceed the breakdown fieldstrength of the charged layer. The charge distribution depends only on the arrangement of the corona needles. The discharging process appears to be uniform over the entire surface, there is

no significant influence of the earthed rim. That means the main part of the discharging current is flowing through the volume of the

insulating layers and not across the surface.

Charging above Breakdown - Fig. 6 shows a typical charge distribution with several points of electrical breakdown. The charge distribution is dependent now on the limitation of charge density due to the material. The tested samples were able to store up to 240 nC/cm<sup>2</sup> on the surface coating. Using eq. (2) this means a field strength in the insulator of 540 kV/cm. This is in good agreement with the measurements of breakdown field strength. Nearly each one of the samples had some points of damage due to electric discharge of a limited area into this point. The size of this area varied between less than 1 cm<sup>2</sup> and up to 50 cm<sup>2</sup>. As the spark energy of equally charged layers is increasing with the thickness, the thin samples had a lot of hardly visible small holes with less than 0.1 mm diameter, caused by a spark energy of about 0.1 mWs. Charged layers with a thickness in the range of 0.13 to 0.23 mm showed holes of up to 0.7 mm diameter, caused by energies of about 10 mWs.

Four effects of discharging were observed: 1. Charge limitation due to breakdown field strength, no visible holes. This 'soft' breakdown was the only effect observed on sample 3.3 with a conductive layer of very high resistivity. Apparently in this case the local discharge energy was always low enough, not to make any damage to the paint layer.

 Microdischarges of a very small area of about 1 cm<sup>2</sup>, small hardly visible holes of less than 0.1 mm diameter. This effect was observed on all samples with a thickness below 0.20 mm, except sample 3.3. The related energy is about 0.1 mWs, the charge about 200 µC.

 Surface streamer, discharging a certain portion of the charged surface (about 50 cm² at the sample size of 200 x 200 mm and the used charging method), visible holes of up to 0.7 mm diameter. This effect was observed on some samples with a thickness above 0.13 mm. It is related to a charge of some microcoulombs and an energy above 10 mWs.

4. flashover across the surface occurs on layers of relatively high thickness. For this reason sample 1.1 and 3.2 could not be charged to their volume breakdown voltage.

Most of the points of discharge, that can be localized in Fig. 6 are due to microdischarges. One point at x = 107 mm, y = 47 mm is a point of damage due to an observed surface streamer. As it is not easy to determine the exact location of it from the three-dimensional graphic presentation, Fig. 7 shows the same charge distribution with lines of equal field strength. In addition, the measured field strength at y=47 mm is plotted together with a picture of the damaged surface paint. It is remarkable that only the nearest vicinity of the punctured hole remained uncharged. This influence is even smaller for points of microdischarges.

TIME-DEPENDENT DEVELOPMENT OF THE SURFACE CHARGE - The digital storage of all measured data allows evaluation of interesting data such as total surface charge Q, maximum charge density  $\vartheta$ , discharging time constant  $\tau$ , and volume resistivity  $\rho_V$ . These values are plotted versus time in Fig. 8 for two different samples, one with low charging voltage and no breakdown of the surface layer, the other with higher charging voltage and local points of electrical breakdown.

There is no significant difference between the discharging curves, just the absolute values are greater for the high charging voltage. The time dependent development of the material constants  $\tau$  and  $\rho_V$  are nearly identical. These facts were true for all measured samples. There is only a limited influence of a damaged point on the discharging process of the entire surface.

#### SUMMARY

Electrostatic charging of thin insulating superficial paint layers applied on the conductive structure, lightning or p-static protection system of aircraft parts can lead to mechanical damage due to electrical breakdown. For layers of less than approx. 0.25 mm thickness the effects can be tested on small samples of the interesting material.

The energy of the discharge and consequently the resulting damage is increasing with:

1. The breakdown field strength of the paint, 2. The thickness of the insulating layer,

3. The conductivity of the conductive layer next to the surface.

In any case, there was little influence of a damaged point on the discharging or recharging process of the entire surface. The graphic presentation of charge distribution showed that only the nearest vicinity of a punctured hole re-

mained uncharged.

Interpretation of the time-dependent development of the initial local charge distribution gave values for the specific resistivity in the range of some  $10^{14}$  to some  $10^{16}$   $\Omega$ cm. These values seem to be more meaningful than the results of conventional methods and are much too high to prevent electrostatic charging.

#### CONCLUSIONS

To prevent electrostatic charging of the protective paint layer, the paint should have a true volume resistivity of less than  $10^{10}~\Omega cm$  resulting in a discharging time constant of 0.01 s. A way to keep the stored energy low could be to reduce the electric breakdown field strength of the paint.

A conductive layer for pure p-static protection should not be of high conductivity. It is sufficient to keep the resistance per square mesh in the range of 100  $M\Omega$  to gain a good

damping of discharge currents.

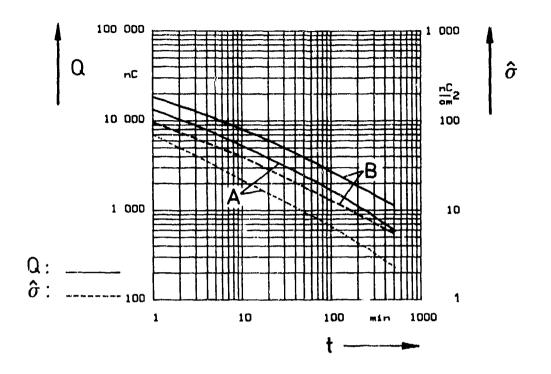
#### REFERENCES

1. J.E. Nanevicz, "Flight-Test Studies of Static Electrification on a Supersonic Aircraft". Lightning and Static Electricity Conference, 14-17 April 1975 Proceedings.

2. J.E. Nanevicz and E.F. Vance, "Studies of Supersonic Vehicle Electrification". Lightning and Static Electricity Conference, 9-11 December

1970, pp. 73-88.

3. D. Königstein, "Local Charge Distribution and Development on Insulating Surfaces". International Aerospace Conference on Lightning and Static Electricity, Oxford, 23-25 March 1982, Proceedings report E 8.



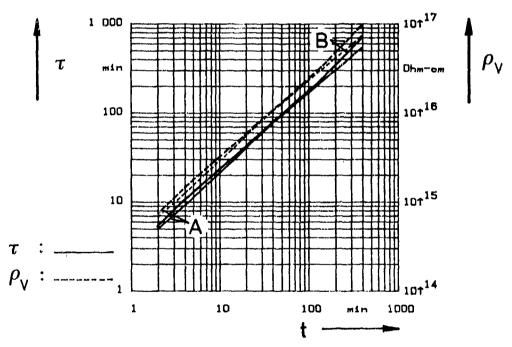
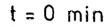


Fig. 8 - Discharging curves of two different samples:
A: Sample 2.1, d = 0.23 mm, charging voltage + 10 kV (see Fig. 5)
B: Sample 2.3, d = 0.18 mm, charging voltage + 30 kV (see Fig. 6)

- Q: Total surface charge
- θ: Maximum charge density
   τ: Discharging time constant
   ρ<sub>V</sub>: Volume resistivity derived from τ



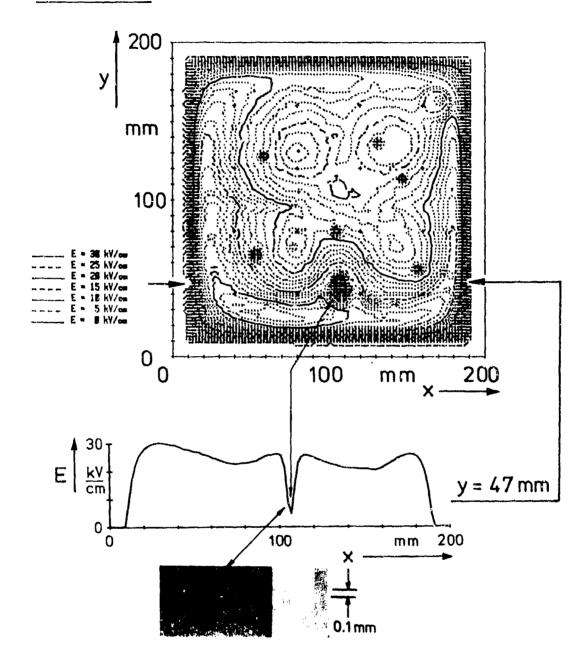


Fig. 7 - Charge distribution of Fig. 6 with lines of equal field strength and cross-section at point of damage

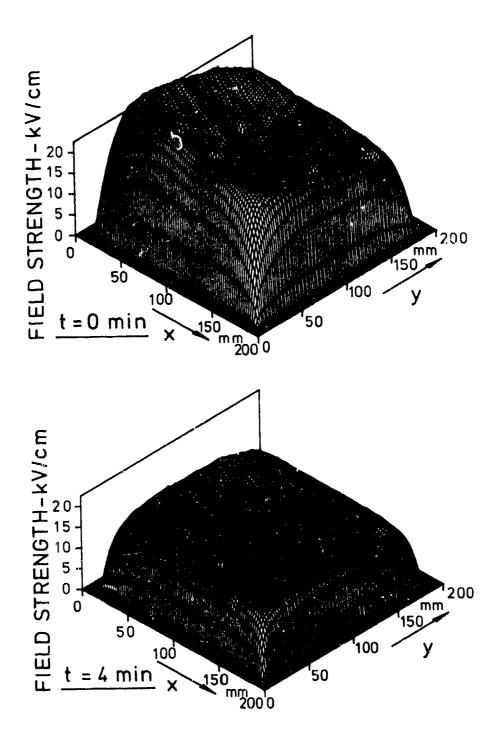


Fig. 6 - Typical local charge distribution with several points of electrical breakdown (sample 2.3, d = 0.18 mm, charging voltage: + 30 kV)

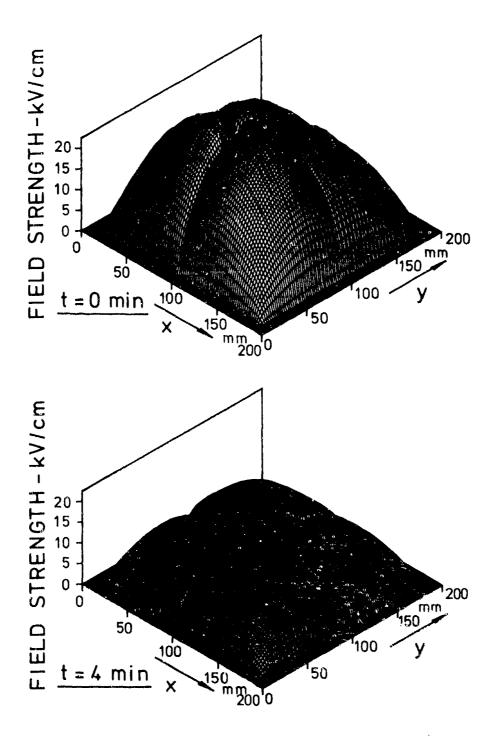


Fig. 5 - Typical local charge distribution without breakdown at t=0 and t=4 minutes (sample 2.1, d=0.23 mm, charging voltage: +10 kV)

	0.17	[ <u></u> ]		۵.		Ara	Ara.	7
	1.33	םר סר		۵			Ara.	₩°
E		[]		۵			Ara.	7,
- 0,1 mm -	0.02						CFK	C L
	0,13	DI		۵.	Al-m	GFK	C T X	20   20   20   2 日
	0.18			<u>a</u>		Al-m	CFK X	0
10 Ze	0.13	10		<u>a</u>			SF	2
d lay	0,23	<u></u>	-	۵_			S, Y	<u></u>
mmm : surface of grounded layer d [mm] = thickness of charaed layer =	0,21	0-		a.			GFK SFR	7
ace of	1,43	<u></u>	) <b>3</b>	۵			GFK	
d [mm] = thickness	0,03	DL	· · · · · · · · · · · · · · · · · · ·				- Y	0
d [mm]	0,05 0,03	۵				7. Manufall (1994)	₹_	CO

Fig. 4 - Cross-section of the different test sample layers

Ara.Rufl: carbon-powder filled a.

Al-m: alu.-mesh

Al: aluminium

GFK: GFRP CFK: CFRP

LL : conductive paint

P : priming paint

DL: surface paint

Ara. : aramid

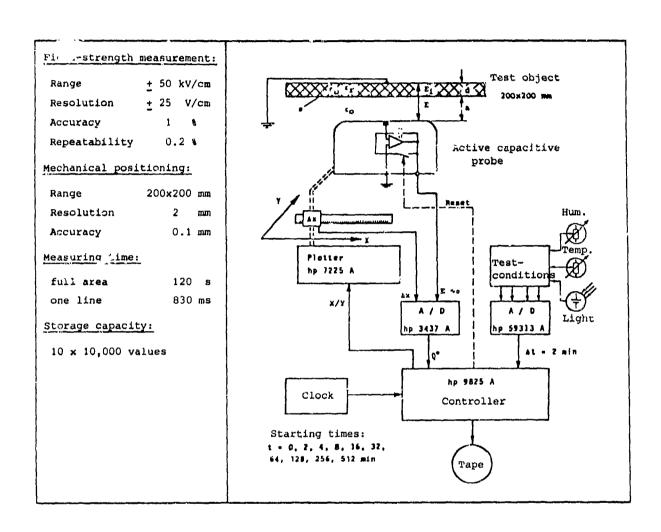


Fig. 3 - Principle of operation and performance data of the measuring system

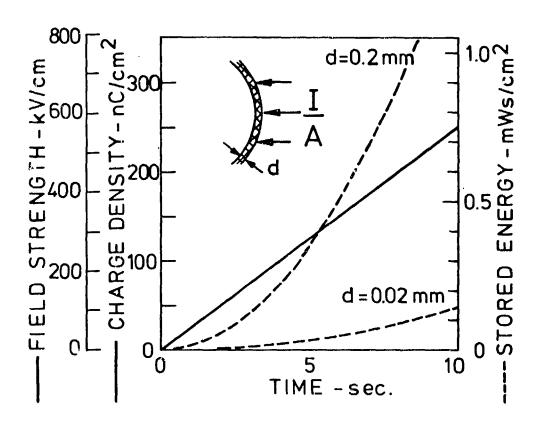


Fig. 1 - Surface charge density  $\sigma$ , density of stored energy  $W_e$ , and field strength  $E_i$  in an insulating layer of thickness d charged by I/A = 250  $\mu$ A/m² ( $\epsilon_r$ =5)

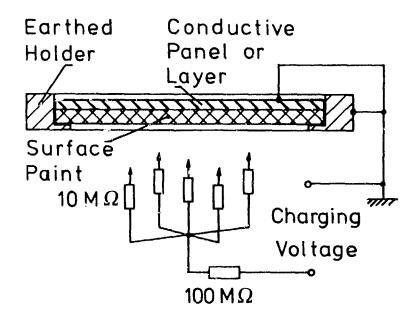


Fig. 2 - Principle of corona charging arrangement (not to scale)

### AD P002167

RELATIVE IMPORTANCE OF ELECTROMAGNETIC SHIELD VIOLATIONS

 $\leftarrow$ 

W. Graf, J. Hamm, E. F. Vance SRI International, Menlo Park, California

ABSTRACT

In the topological approach to hardening systems against lightning, a barrier that is effectively impervious to electromagnetic energy is placed between the source of interference and the system to be protected. To be impervious, the barrier must form a topologically closed surface. The ideal barrier can never be achieved in practice, but it is not necessary. The three categories of compromise are, in order to importance, penetrations, apertures, and diffusion. Diffusion is almost always negligible (unless the metal walls consist of foils), and wire penetrations are almost always by far the worst compromise. Thus, an otherwise excellent barrier may be compromised by one untreated penetration. The compromise may go undetected until a major portion of the lightning current flows on the barrier near the compromise. At that time, it will become quite evident that the barrier is not sufficiently impervious to electromagnetic energy. Lightning, from an interference point of view, is a broadband electromagnetic phenomenon, and therefore practices that are adequate at low frequencies or dc will not be satisfactory for lightning protection. Examples of such practices include cable shields terminated in pigtails, grounding conductor penetrations, and apertures with a wire penetration. We have performed several simple laboratory experiments to demonstrate quantitatively the effects of those practices. The experiments lead to the conclusion that the simple compromises mentioned above limit the effectiveness of the barrier by many orders of magnitude. That is, although the ideal barrier cannot be achieved, the practical barrier can be improved substantially by avoiding the most obvious compromises. The topological approach provides simple guidance to identify the compromises in an otherwise closed barrier.

LIGHTNING CAN BE one of the most harsh sources of transient interference. The severe direct strike, while rare, produces large electromagnetic stresses on the outer levels of the system in the form of large charge and current densities and large induction fields. If lightning attaches to exposed conductors such as power or signal cables or antenna wires, extremely large currents are driven into the system on these conductors. The effects of lightning are awesome, and elements of systems that are valuable because of cost, need, or other measure of value must be protected from the stresses of lightning. In this paper, we discuss the effects of lightning on internal circuits or equipment: we will not discuss the blast and heating phenomena that occur at the exterior attach point of a direct strike.

Protection against the electromagnetic effects of lightning may be thought of as establishing an electromagnetic barrier between the lightning and the protected space. (1)\* Thi barrier must be sufficiently impervious to waves propagating through space and to waves propagating along conductors (e.g., wires and cables). A truly impervious barrier could be made with a closed, perfectly conducting surface, but in order to use the protected space we must usually compromise the conducting surface by passing power and signal cables through it and by perforating it to allow heat dissipation, etc. In addition, it is impracticul to make aircraft skins and equipment cases from superconducting materials -impractical and unnecessary, since the shielding properties of practical shields are usually limited by the penetrating conductor and aperture compromises rather than by the finite conductivity of the shield material. In this paper, we will discuss the relative importance of the compromises and discuss some practical bounds on the amount of protection needed -- we will explain what is meant by "sufficiently impervious."

#### BARRIER ELEMENTS

Consider first a closed shield made of thin, finitely conducting metal (e.g., aluminum). It can be shown that the maximum open-circuit voltage induced on a wire inside a 10-m diameter spherical aluminum shell, 0.5 mm thick, by a 20-kA direct strike (entering one pole and leaving the other) is about 2 or 3 V. The exact value iepends on the decay time assumed for lightning and on the contact spot/size assumed for lightning attachment (see Appendix; for a 1-cm diameter spot size, the induced voltage is 1.8 V if the exponential decay time constant is 10 µs; 2.8 V is induced if the decay time constant is much larger than 10 µs. If the spot diameter is reduced to 2 mm, the induced voltage

increases by about 20%). In all of these cases, it has been assumed that the aluminum shell remained intact (i.e., the stroke did not melt out a hole). Furthermore, the rise time of the induced voltage is about 3 µs, even if a zero rise time strike current is impressed on the exterior of the shield.

Thus the closed, thin aluminum shield reduces the lightning transient to a small, slowly varying voltage induced on a large internal circuit. Since systems frequently generate transients larger than those induced by lightning, a closed, thin aluminum shield would adequately protect most interior circuits and equipment. In practice, however, the shield is not closed. An all-aluminum aircraft skin, for example, has inperfections such as wiring for external lights and cables in some exposed areas such as wings and radomes, and windows, doors, joints, and other apertures that can seriously compromise the skin as an electromagnetic shield against lightning.

Suppose, for example, that lightning attaches to the wiring on a navigation light on the wing tip or on the radar in the nose. These wires or cables are routed to the interior of the aircraft; hence, lightning current delivered to these wires can propagate through the shield without attenuation unless a filter or other surge limiter is installed. The filter or surge limiter thus behaves as the barrier element for the penetrating ware; it may be considered to close the shield about the wire (out-of-band for the filter or above a threshold for the nonlinear surge arrester), or it may be viewed as a barrier to currents propagating on the wire. Without the barrier element, however, it is apparent that the penetrating wire is a 0-dB compromise of the shield -- the wire current (hence the magnetic field) is the same inside the shield as it is outside the shield, as illustrated in Figure 1. The barrier element, a filter or nonlinear surge limiter, prevents most of the exterior wire current from entering the protected volume.

Evidently, the imperfect conductivity of the shield material is not a very important compromise unless the conductivity is quite poor (e.g., bare graphite-epoxy composite), or the shield is very thin (foil), or slowly varying (low-frequency) interior magnetic fields are important. On the other hand, conductors that penetrate the shield are very severe (0-dB) compromises. Somewhere in between, are apertures such as windows, doors, riveted joints, etc. The effects of apertures are discussed in a companion paper. (2) Here we will merely observe that the coupling through an aperture to interior circuits depends on aperture size, external current density, and internal circuit proximity to the aperture. will also give an example of coupling to an

<sup>\*</sup>Numbers in parentheses designate References at end of paper.

internal wire in the 10-m diameter spherical shell.

For a circular aperture of radius r in a flat surface (or a surface whose radius of curvature is much greater than r), the open circuit voltage induced on a wire crossing the aperture is(3)

$$V \approx \mu_0 r_0 \frac{dJ}{dt}$$

where J is the current density that would be present if the aperture were covered with a perfect conductor, and  $\mu$  is the permeability of vacuum (or air). The induced voltage is greatest for the rapidly changing (high-frequency) current density, where, as it will be recalled, the shield excluded the fast changing part of the lightning transient and allowed only the slowly varying fields to diffuse through the wall.

If the circular aperture is 90 degrees from the stroke attack point on the 10-m diameter sphere, as illustrated in Figure 2 for aperture number 1, a rate of rise of  $2 \times 10^{10}$  A/s will induce about 18 V in a wire crossing just behind a 30-cm diameter aperture. As the aperture is moved closer to the stroke attach point, the current density and the induced voltage increase. When the center of the aperture is 3 aperture radii (45 cm) from the stroke attach point, the induced voltage is about 200 V. If the interior wire is moved away from the aperture, or if the aperture is subdivided into many small apertures, the induced voltage is reduced.

Thus, although the voltage induced in the internal circuit through an aperture is significant, its effect is much smaller than the penetrating wire or cable, where the voltage is limited only by the insulation strength of the wire. In addition, only the low energy leading edge of the transient is effective in inducing voltages through apertures, whereas the entire transient is carried through the wall on an insulated penetrating conductor. Finally, small apertures do not individually permit much interaction between the shield currents and interior circuits. Thus, for example, the discontinuities at riveted joints do not account for large aperture coupling -- the ohmic resistance of the joints is often more important than the aperture leakage.

However, a large number of small apertures can allow significant voltages to be induced in internal circuits. From the formula above, one hundred 3-cm diameter apertures (all aligned with the internal wire) would have the same effect as the one 30-cm diameter sperture (if the same current density existed at each aperture). One hundred 3-cm apertures has the same area as or 30-cm aperture; hence the saventage of sundividing large apertures is not evident in this case. This is because it was assumed that the hundred small apertures were in a roy along the wire path so that the wire was

maximally coupled to each small aperture. When a large aperture is subdivided into n small apertures, this situation does not occur. Instead, only one row, containing roughly  $\sqrt{n}$  small apertures, is maximally coupled to the wire, so that the coupling through the subdivided aperture is roughly  $1/\sqrt{n}$  times the coupling through the one large aperture. Subdivision is therefore an effective means of improving the barrier in apertures such as ventilation and natural lighting openings.

Converting the apertures into waveguides beyond cutoff is even more effective than subdividing, but it requires considerable space on one side of the shield or the other. It is more common to subdivide and use waveguide beyond cutoff on the smaller aperture; this requires less space, since a small opening requires only a short waveguide. Thus, the effective barrier elements for apertures are perforated sheet, wire mesh (if the wire crossings are in good contact), and waveguides beyond cutoff.

The complete electromagnetic barrier is thus composed of shielding material (metal sheet or plate), wire and cable elements such as filters, surge limiters, isolators, and aperture treatments such as wavegulds beyond cutoff or perforated sheet. A shield without the complement of wire and aperture barriers may offer little protection against large electromagnetic sources such as lightning. Conversely, filters, surge limiters, etc., installed on wires without a shield (or without adequate bonding to the shield) may not be very effective, because these devices cannot exclude all of the electromagnetic field guided by the wire. Therefore, the wire treatments are essential for the shield to porform well, and the shield is essential for the wire treatments to function properly. Large apertures, or large numbers of small apertures, can also degrade the performance of a shield or barrier. Hence, attention must also be given to apertures. In this regard, it is noteworthy that screens or meshes are in reality large collections of apertures; hence "shields" made of open mesh tend to be very leaky at high frequencies.

#### COMMON BARRIER VIOLATIONS

As noted above, the most serious violation of the barrier is the insulated penetrating conductor, since it carries exterior electromagnetic waves directly into the protected space. Equipment designers who are serious about controlling transient interference may use line filters on power leads and balanced circuits with high common-mode rejection, or some other effective barrier element, on the signal leads. However, it is surprising how often systems designers violate the shield with penetrating conductors. This may be because the four barrier shapes illustrated in Vigure 3 are not recognized as being topologically the sameeach one is simply a closed surface separating the interior from the exterior. Hence, it is

であるではある

not unusual to see the cable shield opened so that the core conductors exit one part of the shield and reenter another part of the shield. Some of these are illustrated in Figure 4.

We performed some simple experiments to demonstrate the effectiveness of topological cable shield terminations. The frequency range of the experiments was chosen to reflect the broadband nature of many transient interference sources, as discussed in the previous sections.

Two small instrumentation boxes, made of discast aluminum, were separated by a distance of 2 m. Each contained a simple "circuit" (Figure 5a) consisting of a resistor equal to the characteristic impedance of the coaxial cable (RG62/U) used to connect the two boxes.

Box No. 1, on the left in the figure, was driven with current  $I_1$  by a 50  $\Omega$  source. Box No. 2 was considered to be the receiving unit, and current  $I_2$  was measured with a Textronix CT-1 current probe. Note that Box No. 1 was insulated from the ground plane, while Box No. 2 was connected to it.

In practical cases, both boxes would be connected to the ground plane. A varying magnetic field produced by an interfering source then would induce an emf and, therefore, a current in the loop formed by the cable shield, the ground plane, and the shield terminations. If the shield is not terminated at one end to interrupt the loop current, the same emf would be induced in the center conductor of the coaxial cable. The setup in Figure 5a is equivalent to the practical case in that the test source drives a current directly on the cable shield. Therefore, any conclusions drawn from these experiments regarding shield terminations also apply to the case where magnetic fields interact with the loop and induce a shield current.

We measured I<sub>2</sub> as a function of frequency from 100 kHz to 50 MHz. This range is broad enough to cover both low-frequency and high-frequency effects. (A few of the measurements were extended down to 20 kHz to verify extrapolation of the data shown in the figures.)

The effects of three different cable shield terminations are shown in Figure 5b. The ratio  $I_2/I_1$  is plotted in decibels as a function of frequency. Resonance effects dominate above 10 MHz; the data should be interpreted only below that frequency. Curve 1, which shows the case for the cable shield terminated only at the source with a 10-cm pigtail, indicates that the current  $\mathbf{I}_2$  in the receiving circuit is equal to the source current  $\mathbf{I}_1$ . A straightforward analysis at dc confirms that this is expected. However, curve 1 implies only that the shield provides no electrodynamic shielding; the cable shield still would provide electrosustic protection. It is clear, though, that such an arrangement provides no protection against interference.

The second case (curve 2) involves pigtails at both ends of the cable shield. Shielding is effective for the length of the cable, and interference leaks into the receiving circuit

only at the two pigtails. The slope of the curve is 20 dB per decade, which indicates that the dominant effect is inductive coupling (which is proportional to frequency).

For the third case (curve 3), BNC connectors were used. Only a small dependence on frequency can be seen (below 10 MHz; above that frequency the resonance effect dominates). This small frequency dependence probably is caused by leakage through the holes in the braided shield.

It is instructive to compare curves 2 and 3 at various frequencies. At very low frequencies (extrapolated to the left in the figure), there is no difference between pigtails and BNC connectors. Thus, if the only concern is power line or other low frequencies, the shield termination could be chosen according to considerations other than transient EMI. However, at 100 kHz, the peripheral shield termination is almost 10 dB better, and at 5 MHz it provides well over 30 dB more attenuation than the pigtails.

The type of shield termination used often reflects the operating frequency band of the circuit or systems involved; such considerations do not account for the possibility of high-frequency or transient interference, because such interference is considered to be outside the frequency band to which the circuit or system would normally respond. Nevertheless, such a circuit can be interfered with or even damaged if the level of interference is high enough, as is the case for lightning and EMP.

A similar set of experiments was conducted with a shielded twisted pair replacing the coaxial cable (Figure 6a). In this case, only the shield terminations at the receiving end were varied; at the source end the shield was terminated with an rf connector, as shown in the figure. Measurements again were taken over the band 100 kHz to 50 MHz. Figure 6b shows the results obtained with the various terminations.

The curves lead us to conclusions similar to those discussed above. With no shield termination, current I2 is essentially independent of frequency; pigtails and rf connectors are the same at low frequencies, but differ at high frequencies. Note that in the first four cases only the common-mode current has been measured. Case No. 5 shows the differential-mode current for a balanced configuration. The figure shows that the balanced configuration offers more attenuation than any other of the practices shown, up to at least 5 MHz in this case. (In some cases, it may be difficult to balance a circuit at high frequencies.) At low frequencies, a balanced circuit, even without the shield termination, offers 20 dB more attenuation than any of the unbalanced cases with shield termination. The poorest performance is obtained with an unbalanced load and no shield termination (Case 1). In this case, the use of a shielded twisted pair provides no benefit (beyond electrostatic protection) over the use of a single wire.

#### CONCLUSIONS

The most severe compromise of electromagnetic barriers is the insulated penetrating conductor. It is also one of the more common compromises because of the way interconnecting cables and cable shields are installed and "grounded." In addition, the common-mode rejection of a balanced pair, an excellent barrier technique, is often foiled by deliberately unbalancing the terminations by grounding one side. We have demonstrated that topological and electromagnetically correct treatment of cable shields and twisted pairs provides great improvement over the improper grounding schemes frequently used. These laboratory demonstrations are consistent with the effects estimated for simple geometry and elementary topology concepts. In general, the cost of using proper shield treatments is smallto-nil, and the cost of using balanced, rather than unbalanced, grounding of balanced circuits is probably negligible once this requirement is incorporated into equipment specifications. In the meantime, the cost of using a twisted shielded pair but not benefitting from its most important characteristic -- its common-mode rejection - is probably substantial.

#### APPENDIX---SPHERICAL SHIELD ANALYSIS

A spherical metal shell of radius a and thickness d is assumed to have a current I flowing in one pole and out the other, as illustrated in Figure A-1. The radius of the current attachment spot on the surface of the sphere is A. A wire attached to the inside surface of the sphere (behind the current spot) runs along a diameter to the opposite side. The open-circuit voltage induced in this wire is calculated.

By analogy with cylindrical shield theory, the incremental transfer impedance of a ring of shield add in length is  $^{(4)}$ 

$$dZ_{T} = dR \frac{\gamma d}{4(nh) \gamma d}$$

where dR is the dc resistance of the ring in the  $\theta$  direction, and  $\gamma$  is the propagation factor in the metal. The dc resistance dR is

$$dR \approx \frac{ad\theta}{2\pi a \sigma ds in\theta}$$

and

$$R = 2a R_{a} \int_{\Delta/a}^{\pi/2} \frac{d\theta}{\sin \theta} = 2a R_{a} \ln \tan \frac{\theta}{2} |_{\Delta/a}^{\pi/2}$$

$$\approx 2a R_{a} \ln \frac{2a}{\Delta} \qquad (\Delta << a)$$

where R<sub>a</sub> is the dc resistance of a cylinder of radius a, thickness d, and length 1 m.

The voltage induced on the pole-to-pole wire

$$V = IZ_T = I 2a 1n \frac{a}{\Delta} R_a \frac{\gamma d}{sinh\gamma d}$$

in which R yd/sinhyd is the transfer impedance of a cylindrical shield of radius a and thickness d. The induced voltage waveforms have been obtained for cylindrical shields excited by exponential current waves. (4) Hence, if we assume an exponential lightning current, we can infer the induced voltage waveforms from Figures 5 and 6, Reference 4. Table A-1 below gives the peak voltage and rise time (10-90%) for a 20-kA exponential current with different exponential decay time constants, current attachment spot size, and shield radius.

#### REFERENCES

- K. F. Casey, "Low Frequency Electromagnetic Penetration of Loaded Apertures," IEEE Transactions EMC, Vol. EMC-23, No. 4, pp. 367-376 (November 1981).
- J. Hamm, W. Graf, and E. Vance, "Coupling of Natural Atmospheric Interference Through Apertures," International Conference on Lightning and Static Electricity, Fort Worth: Texas (21-23 June 1983).
- 3. E. F. Vance, "Coupling to Shielded Cables,"
  John Wiley & Sons, pp. 112-119 (1978).
- 4. E. F. Vance and F. M. Tesche, "Shield Topology in Eightning Transient Control," Symposium on Lightning Technology, NASA Langley Research Center, Hampton, Virginia (22-24 April 1980).

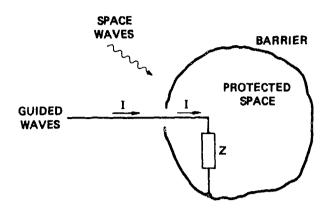


Fig. 1 - Barrier compromised by an untreated conductor

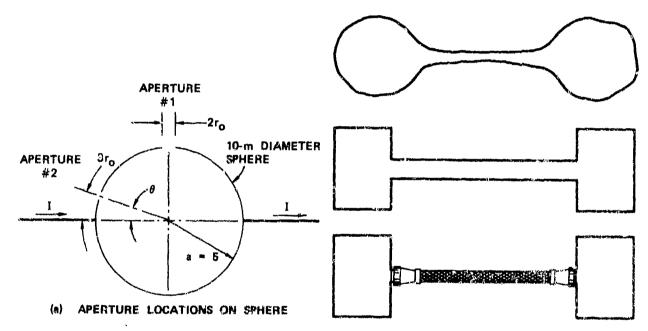


Fig. 3 - Four topologically equivalent barriers

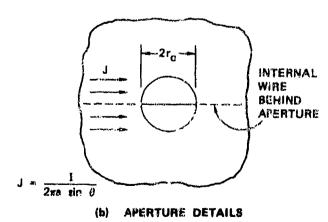


Fig. 2 - Aperture details for sample analysis

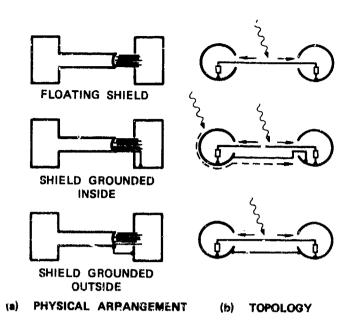


Fig. 4 - Common shield violations

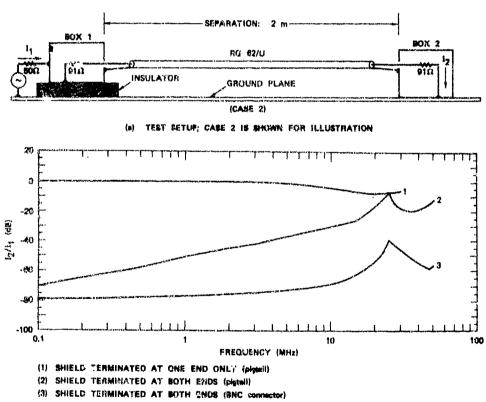
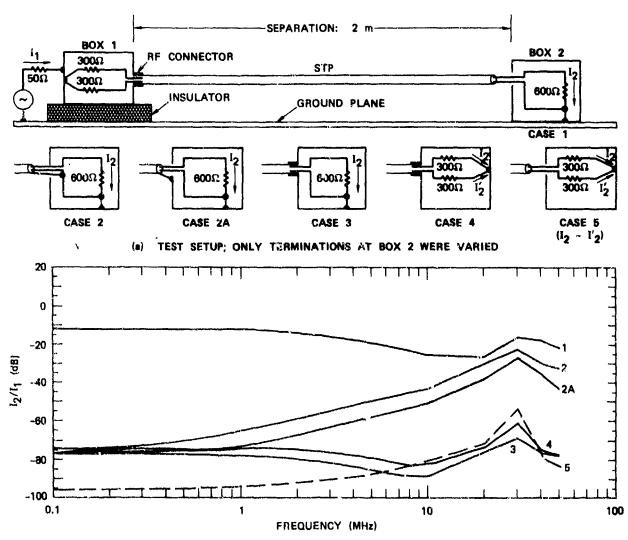


Fig. 5 - Experiments with copylal cable (RG62/U)



- (1) NO SHIELD TERMINATION
- (2) PIGTAIL, INSIDE
- (2A) PIGTAIL, OUTSIDE
- (3) RF CONNECTOR, UNBALANCED
- (4) RF CONNECTOR, BALANCED
- (5) NORMALIZED DIFFERENTIAL CURRENT (no shield termination)
  - (b) NORMALIZED CURRENT  $I_2$  (surve 5 shows the normalized differential current  $I_2 I_2'$ )

Fig. 6 - Experiments with shielded twisted pair

## AD P002168

TOPOLOGICAL GROUNDING ANOMALIES



W. Graf and J. E. Namevicz SRI International, Menlo Park, California

ABSTRACT

Two principal anomalies found in current grounding practices are discussed: The ground conductor penetrating a shield, and a grounded but open shield. Good grounding practices are simple when viewed from the topological viewpoint. A system is divided into different zones, each separated from the other by an electromagnetically impervious barrier, and each zone has its own ground system. Because lightning is a broadband phenomenon, the separation of the zones must also be achieved over a broadband if a system is to be protected against the effects of lightning. It is well understood that aircraft avionics systems do not require a connection to earth to be protected against lightning. This is much less recognized for ground equipment and ground facilities. Here, the practice of connecting the signal reference ground to the earth electrode has serious consequences (in the event of a lightning strike) for the equipment connected to it, unless the ground rod has zero impedance. In the topological approach, such a connection is only permitted if the grounding conductor does not penetrate the barrier surfaces that separate the different zones of the system. Experimental data to support this approach are discussed.

WHEN A COMPLEX SYSTEM such as a new computer is delivered to a customer, the field engineer frequently spends one or more days working with the system—moving grounds from place to place—until he comes up with the magic arrangement that renders the system self—compatible. After the first local thunderstorm often he must return to continue working his magic until the system also becomes hardened to externally—generated transients. Questions naturally arise as to why ground connections should be so critical to the proper functioning of the system and why it is so difficult to design and install the ground system properly the first time.

In considering this problem, it appears that much of the difficulty is caused by deviating from modern topological interference control principles (1,2)\* in the design of the grounding system. A consequence of the deviation is that the grounding system is thereby forced to perform inappropriate functions and to meet standards almost impossible to achieve. Furthermore, it appears that these deviations frequently are a consequence of the perception that somehow grounding, bonding, and shielding intertwined and that together constitute the array of techniques available to the EMC engineer. Actually the proper roles of grounding and bonding hav little to do with interference control design that they should not be considered interference control tools. course, poor bonding or the improper application of grounding can compromise an otherwise good design. In this paper, we will discuss topological interference control techniques, the role of grounding in their application, and how improperly applied grounding can degrade system immunity to lightning and other forms of broadband interference.

BASIC TECHNIQUES AVAILABLE FOR INTERFERENCE CONTROL

In its most elementary form an interference control problem reduces to a source of interference, a potential victim, and the intervening space and structure as shown in Fig. 1. If the source can be eliminated or if the victim can be rendered immune, the problem is solved. Generally, however, as in the case of lightning, the engineer is powerless to affect the source. Similarly, the sensitivity of the victim usually cannot be changed appreciably. Thus, one is left with modification of the coupling path as the primary viable interference control technique.

Fig. 2 shows the three general methods by which electromagnetic waves emanating from the source can be prevented from coupling to, and interacting with, the victim:

- The separation between the source and victim is made infinite (Fig. 2a).
- (2) The sensitivity of the victim is

orthogonal (i.e., cross polarized) to the source (Fig. 2b).

(3) The source and the victim are separated by an electromagnetically impervious barrier (Fig. 2c).

All passive interference control techniques that do not operate directly on the source rely on one or more of these methods. Separation and orthogon/Alization can, in fact, he incorporated into the barrier concept. Therefore, of the three listed concepts, the barrier concept is the most fundamental one, and is the one we will consider here. (The ideal conditions listed above are only approximated in practice, but this does not detract from the utility of these concepts since perfect isolation is rately needed.)

For practical reasons, it is found that the barrier cannot be a closed, flawless shield. In general, the shields will have imperfections such as those illustrated in Fig. 3. The penetrating conductor guides waves to the interior of the barrier, and the aperture and the joint in the shield also allow excitation of the interior.

Thus, the designer must devise ways to close off the openings and imperfections in the shield to achieve an impervious barrier. An example of a fruitful way of thinking about the problem is shown in Fig. 4. In Fig. 4(a), the surge limiter in its normal condition allows current flow unimpeded along the penetrating conductor to the protected circuit. If a surge occurs that exceeds the threshold voltage, the surge arrester fires and closes the barrier as shown in Fig. 4(b), and diverts the surge current to the outside surface of the shield. Accordingly, a surge arrester may be thought of as a device that closes the barrier when the signal amplitude on a penetrating conductor exceeds a predetermined level. Similarly, a filter may be thought of as a device that closes the barrier at all frequencies outside the Conceptually, the barrier is an passband. electromagnetically closed surface composed of a number of various elements, e.g., filters, surge limiters, metal meshes, joint bonds, etc., in addition to the metallic shield.

The various elements of a typical barrier are shown in Fig. 5. Here, the principal natural boundary of the barrier is defined by the metal case of the system. Bonding is applied at the joint, and the circular opening is filled with one of several possible aperture treatments to assure closure of the surface. An appendage system is included in the barrier by connecting the two systems with a closed The penetrating conductor is treated using a filter, limiter, and/or isolator. It is very important to note that the ground wire has not been allowed to penetrate the barrier. Instead, the external ground is connected to the exterior of the case. Internal ground

\*Numbers in parentheses designate References at end of paper"

connections are returned to the interior of the case. In this way, noise currents induced on the external ground by lightning and other transient sources are not carried to the interior of the barrier.

For a number of reasons, it is not desirable to achieve all of the required isolation between the source and the victim by means of a single, high-performance barrier, especially when isolation of 60 dB or greater is required. Usually, it is preferable to use two or more less perfect barriers nested one inside the other as indicated in Fig. 6. Here, the outer barrier is defined by the skin of the aircraft. The second barrier level is the equipment cabinet, and the third barrier level is a shielded box within the cabinet. The successive barriers enclose progressively more benign topological zones ranging from the harsh environment in the untreated region of Zone 0 to the triply-shielded environment of Zone 3.

Penetrating conductors are treated at every level, and great care is taken to prohibit ground conductors from penetrating barrier surfaces.

#### GROUNDING ANOMALIES AND THEIR CONSEQUENCES

Many grounding anomalies and interference problems result from expecting the grounding system to perform inappropriate functions substantially beyond its capability. The development of grounding practices evolved in connection with consideration of safety for personnel, equipment, and buildings. The National Electric Code (NEC) definition of grounding is as follows:

"Grounding: A conducting connection, whether intentional or acccidental, between an electric circuit or equipment and the earth, or to some conducting body that serves in place of the earth."

Note that grounding does not necessarily involve a connection to earth. For example, systems in the aircraft of Fig. 6 operate quite well when the aircraft is airborne and the earth connection is broken even when the aircraft is struck by lightning and its potential is raised to millions of volts.

Standard functions of grounding are shown in Fig. 7. By conducting away fault currents in (a), the ground system protects personnel from shock or electrocution. In (b), the ground system prevents the accumulation of static charge on elements of a facility thereby avoiding shock to personnel or damage to that might otherwise components Finally, in (c), the ground overstressed. system reduces the differences in potential between the objects constituting a facility. It should be noted that these functions of a system are achieved in grounding topologically zoned system of Fig. 6. However, ground wires do not cross topological zones but are generated anew on each side of the barrier.

Grounding gradually began to be associated

with the additional role of interference control sometime after World War II. Today many engineers believe that they can "ground out" interference. In this same context, they feel that a shield should be "grounded" when, in fact it should be closed.

Some of these attitudes stem from certain of the misconceptions regarding ground systems illustrated in Fig. 8. In (a) we see that the ground system cannot be expected to prevent potential rise. A practical ground system has a non-zero impedance (ohms or tens of ohms) so that the currents associated with a lightning stroke will raise the potential of the external ground terminal to thousands of volts. Even nearby lightning produces substantial pulses in the ground terminal. Thus, any system whose proper functioning depends on a zero-impedance ground connection is doomed to failure. Such a design is also entirely inappropriate because the systems of the aircraft of Fig. 6 operate perfectly well with an infinite-impedance earth connection when the aircraft is airborne.

In Fig. 8(b), we note that the ground system cannot provide an infinite current sink for noise signals originating within the system. Here, again, the non-zero impedance of the ground connection and of the grounding system wiring implies that noise currents within the system can generate substantial voltages on the grounding system.

Finally, in Fig. 8(c), we observe that simple grounding of the source does not control interference at the victim. As is discussed in a comparison paper (3), the "grounding" of shields to control interference is better considered as an effort to "close the barrier" around the victim system.

One of the consequences of permitting a ground conductor to penetrate the barriers surrounding a system is illustrated in Fig. 9. From the foregoing discussion, we note that the ground wire cannot be treated as a benign entity capable of extracting all of the noise from a system. Instead, it must be recognized as a conductor that can carry noise from the harsh exterior environment to the interior. Thus, topologically, the penetrating ground conductor transforms the doubly-shielded volume into an unshielded volume.

A further consequence of an ill-conceived grounding system is shown in Fig. 10. Here, we note that the "signal reference ground" has been brought out through one or more layers of shielding and connected to the facility ground rod. Also connected to the ground rod are the power neutral (white wire) and the safety ground (green wire). Switching the power circuits within the facility induces transients in the power ground wiring. Since the ground is not an infinite current sink, a portion of the transient current will flow on the signal reference ground directly to the low-level circultry within the system. Essentially, the grounding system of Fig. 10 serves to collect the transien(: generated within the system and apply them to the most susceptible circuits.

grounding Some common1y encountered anomalies are illustrated in Figs. 11(a), (c), and (e). In Fig. 11(a), the building shield is violated by routing a separate ground wire from the equipment cabinet to the earth electrode outside the building, thus contaminating the building environment. More serious violations are illustrated in Figs. 11(c) and (e); in these examples, swall-signal ground (signal common) is connected to a conductor exposed to the raw outside environment. Although such grounding arrangements have been used, they have been the source of much objectionable interference in digital systems -- at least upset and often The correct shielding and grounding damage. topology is illustrated in Fig. 11(b), where it is seen that no grounding conductor penetrates a An alternative such as that system shield. shown in Fig. 11(d) can be used to correct the severe violation of Fig. 11(c), but this is usually a more expensive and less reliable Another acceptable alternative is shown in Fig. 11(f), in which the grounding conductor is continuous through both shields but the hole through which the conductor passes is filled by welding, brazing, or soldering the conductor to the shield material. As in the case of the filtered ground penetration, there is no particular advantage to the continuous conductor fused to the shields; hence, these methods are not usually recommended. Irrational applications of single-point grounding such as those illustrated in Fig. 11(c) have caused equipment damage and high upset rates during The grounding arrangement of thunderstorms. Fig. 11(e) was found to be a probable cause for upset in an EMP environment in a weapon system.

To quantify the degree to which a barrier may be degraded by penetrations, a set of experiments was conducted using the setup illustrated in Fig. 12. A chamber, roughly a cube 2.5 m on a side, made of mild sheet steel 0.8-mm thick was used to establish an arbitrary but well-defined electromagnetic barrier. The seams were bolted together with an equivalent overlap of about 2 cm. The chamber was set up 13 cm above a ground plane of aluminum sheets riveted together. The wall thickness of the chamber was approximately five times the skin depth at 1 MHz. The average shielding effectiveness as measured by the amplitude reduction of a double exponential driving pulse was about 60 dB. While this is not a highperformance barrier, it is perfectly adequate for the experiments described below.

The chamber was driven near the center of one side wall, with the return conductor connected to the center of the opposite wall and the ground plans. A high-voltage pulse generator was used to produce a driving pulse with a rise time of about 40 ns and a decay time of about 2 µs so that it had adequate spectral energy in the HF band to simulate modern lightning models.

Many different sensors could have been used to measure the response on the inside of the chamber. We used the largest loop that could be installed in the chamber. The rationale for this choice of sensor was that it produces a response at least as large as could be obtained on a system conductor in the chamber. Both open-circuit voltage and short-circuit current (peak value) were measured.

To simulate a penetrating ground conductor, the return lead was connected to the inside of the wall using pigtails of various lengths as is detailed in Table 1. In (a), a small pigtail with a radius of 5 cm was used. The peak value of the short-circuit current induced in the test loop in this configuration was 25 mA, whereas in the basic configuration it was only 5 mA. The open-circuit voltage increased only by a factor of 2, but a large amount of ringing (presumably due to direct coupling between the pigtail and the loop) made an exact reading impossible. The resonance could not be excited when the return conductor was connected to the outside of the chamber, that is, when the barrier was closed.

The dependence of the induced signal strength on the length of the pigtail was investigated using the configurations of (c), (d), and (e) of Table 1. The results of the measurements for these five configurations with a test loop are presented in the table.

The results shown in Table 1 should be interpreted with caution; the numbers represent typical losses in performance, but, of course, they are dependent on the geometry of the entire experiment. However, they can be taken as being indicative of the degree to which a shielded system can be degraded by penetrating ground conductors.

#### SUMMARY AND CONCLUSIONS

Historically, grounding systems were evolved for reasons of personnel safety, and they served primarily to tie together the components making up a system to protect personnel from shocks resulting from static charge accumulation or from ground fault currents. More recently. grounding has emerged as an interference-control technique. Although the application of improper grounding procedures can degrade an otherwise vell-designed system, grounding should not be as an interference-reduction thought of technique. For example, one should not expect a grounding system to "ground out" interference. In fact, grounding systems designed with this serve as "interference premise generally distributors" within a facility.

It is possible to design facilities highly immune to lightning interference by applying modern topological zoning concepts. It in necessary to prohibit the penetration of a barrier by an untreated conductor to maintain integrity of these facilities. Unfortunately, designers frequently consider the ground wire to be at least benign and possibly endowed with magic powers, so that it is allowed to thread its way through all levels of the This procedure is entirely facility. inappropriate; each shielded region (topological zone) should have a separate grounding system making contact with both the inner and outer shield defining the zone. This approach allows the grounding system to perform its safety function, and it also prevents the distribution of noise from one topological level to the other on the grounding system.

#### REFERENCES

- E. F. Vance, "Electromagnetic-Interference Control," "IEEE Trans. on Electromagnetic Compatibility," Vol. EMC-22, No. 4, November 1980.
- 2. W. Graf and E. Vance, "A Topological Approach to the Unification of Electromagnetic Specifications and Standards," "Proc. of the IEEE 1982 National Aerospace and Electronics Conference," May 1982.
- 3. W. Graf, J. Hamm, and E. F. Vance, "Relative Importance of Electromagnetic Shield Violations," International Aerospace and Ground Conference on Lightning and Static Electricity, June 21-23, 1983.

Table 1 - Loss of Shielding Effectiveness Due to Conductor Penetration (Open-circuit voltage  $V_{\rm oc}$ , and short-circuit current  $I_{\rm sc}$  are shown for loop 1)

	Experime	Vec	I <sub>sc</sub>	
'a.	Basic Configuration	70.	80 mV	5 m.A.
b.	Pigtail 5 cm Radius	Side	150 mV	25 mA
c.	Pigtail 1 m Long	Drive Side	2 V	200 mA
d.	Pigtail 2 m Long	Grou	16 V	0.6 A
e.	Pigtail 4 m Long		>16 V	1.5 A

The setup is shown schematically. Only the location of the ground return is varied. In all but the first experiment the driver was connected to the outside of the shield and the return to the inside of the shield as shown.

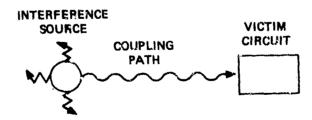


Fig. 1 – Schematic characterization of the interference coupling process

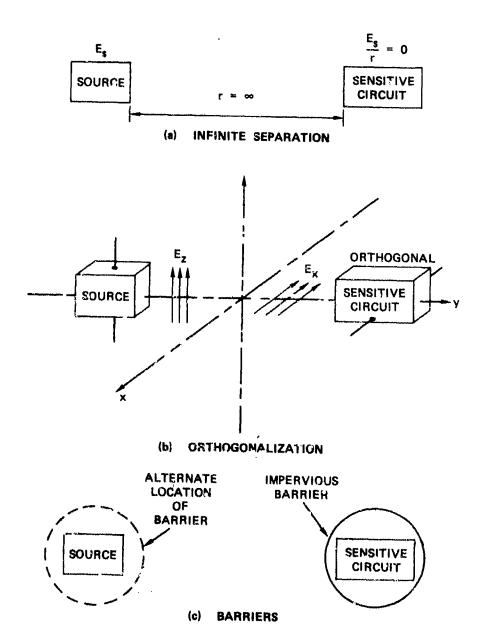


Fig. 2 – Methods of eliminating the interaction of an interference source with a sensitive circuit

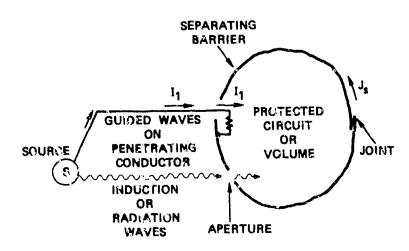


Fig. 3 - Typical imperfections in a practical barrier

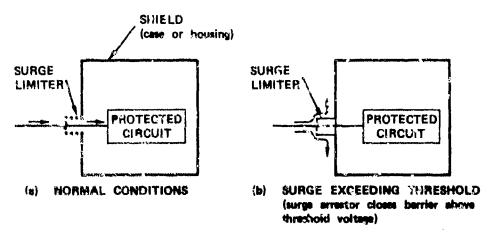
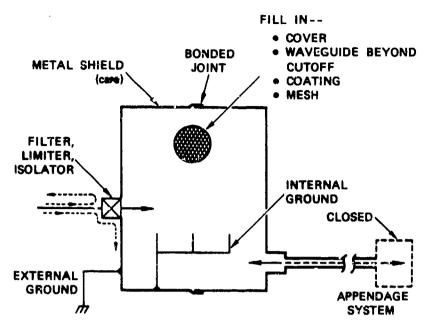


Fig. 4 - Concept of closing berrier  $\epsilon \lambda$  a povetration



高中 いきこれおかけ、小女女の南京の大きのはない

Fig. 5 - Elements of a typical closed electromagnetic barrier

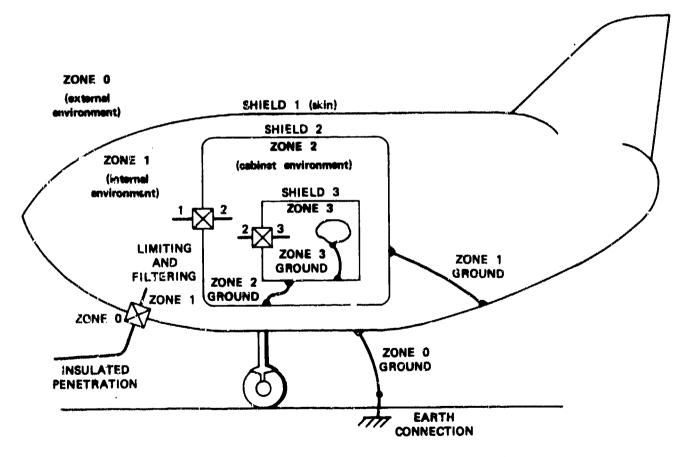
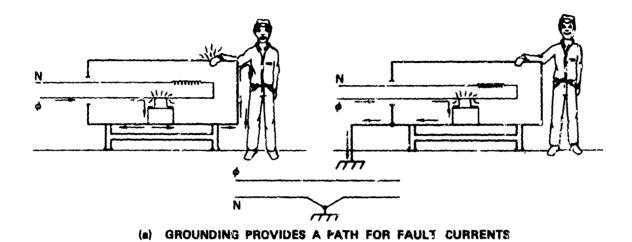
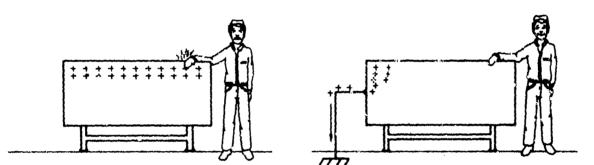
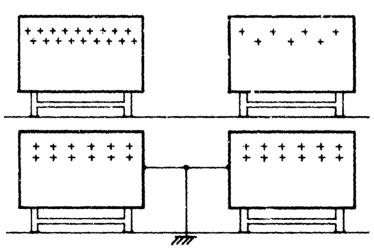


Fig. 6 - Environmental zones in a complex facility such as an aircraft



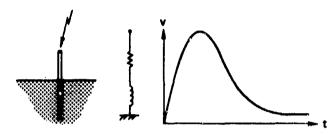


#### (b) GROUNDING PREVENTS STATIC CHARGE BUILDUP

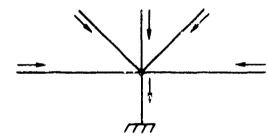


(c) GROUNDING CAN EQUALIZE POTENTIALS OF NEARBY OBJECTS

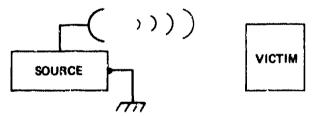
Fig. 7 - Appropriate functions for a grounding system



(a) GROUNDING CANNOT PREVENT POTENTIAL RISE

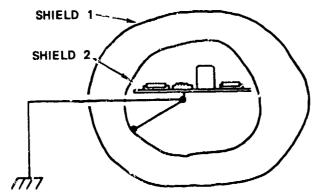


(b) GROUNDING CANNOT PROVIDE INFINITE CURRENT SINK



(e) GROUNDING SOURCE OR VICTIM STRUCTURE DOES NOT CONTROL INTERFERENCE

Fig. 8 - Some popular misconceptions regarding grounding



PENETRATING GROUND CONDUCTOR TRANSFORMS
DOUBLY SHIELDED VOLUME . . .

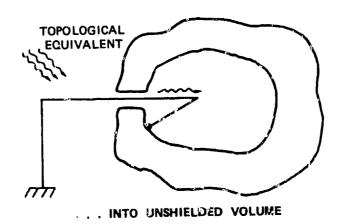


Fig. 9 - Penetrating ground connector from the topological point of view

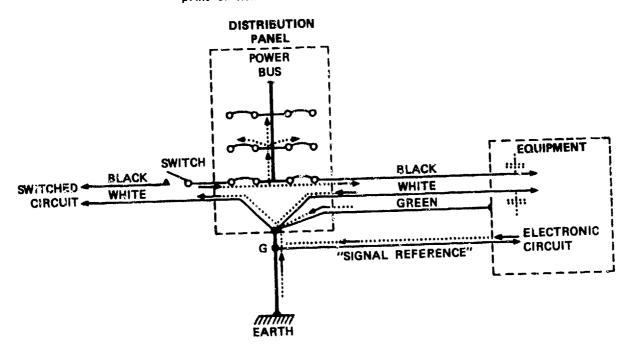


Fig. 10 - Interference distribution through an ill-conceived grounding system

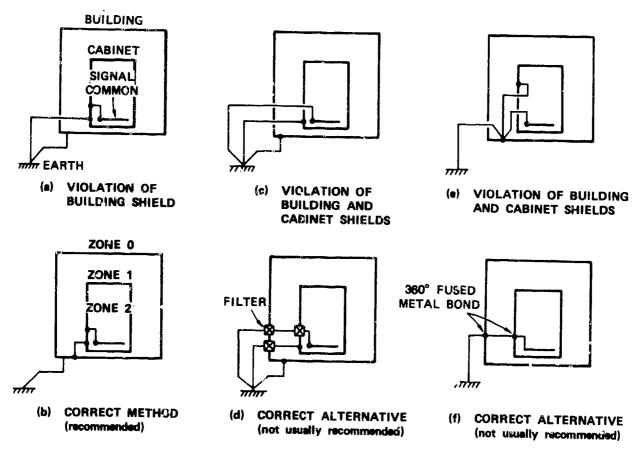


Fig. 11 - Typical grounding anomalies encountered in practice and some correct alternatives

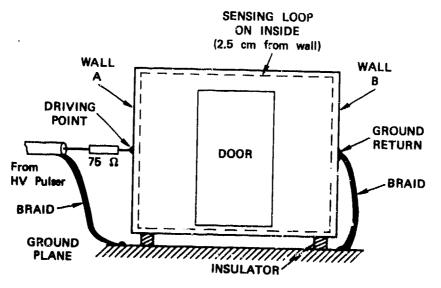


Fig. 12 - Test setup for penetration experiments

Lightning and Transient Protection of Radio Systems

Ву

Prof. S. Lundquist Institute of High Voltage Research Uppgala University, S-755 90 Uppsala, Sweden

#### ABSTRACT

Protection of important radio systems against electromagnetic transients from lightning discharges and nuclear explosions (NEMP) nowadays is more or less a standard procedure. However, the problem of coordinating different protective measures and selection of the most suitable components still are problems deserving further studies. Tests have therefore been performed to evaluate some important parameters of individual components and of radio systems for frequencies up to 75 MHz. At the testing both standard test pulses as well as fast rising pulses in the nanosecond range has been used. Gas discharge tubes, cables etc. have been tested separately and as part of a system. In this way it is possible to study the effect of different counterpoise and grounding systems, different cable lengths and different locations of the cables as well as the location and properties of gas discharge tubes and semiconductor protection elements on the amplitude and energy of the transient reaching the sensitive parts of the system. The results are also used to estimate the necessary intervals for routine maintenance and to predict the MTBF for faults caused by lightning. A technique for field tests in actual installations will also be discussed.

This paper was not available for incorporation into this book. Therefore, it will be published at a future date.



## AD P002169

PROTECTION AGAINST LIGHTNING SURGE VOLTAGES ON COMMUNICATION LINES AND POWER LINES

J. L. ter Haseborg\* and H. Trinks\*\*

\*German Federal Armed Forces University Hamburg, Holstenhofweg, Hamburg, Germany

\*\*Technical University Hamburg-Harburg, Hamburg, Germany

ABSTRACT

Sensitive electronic systems are shielded against electromagnetic interferences (lightning, EMP). The shielding efficiency is reduced by field coupling through apertures and particularly by feeding of interfering currents through cable entries. In case these cables are connected to the inputs of electronic devices, the surge voltages may disturb or even destroy these devices or single electronic components, particularly semiconductors.

Special passive protection circuits for communication and power lines against lightning- and EMP-induced surge voltages are developed. The edge steepnesses of the applying surge voltages show values of 2kV/us (lightning) up to 2kV/ns (EMP).

いいときのできるがは、大きなないのできる

CONCERNING PROTECTION CIRCUITS AGAINST surge voltages it is necessary to distinguish between circuits, connected into communication lines, and such, connected into power lines. For both types of protection circuits a definite threshold voltage is required. In case of communication lines the protection circuits additionally have to show a minimum insertion loss, in order to guarantee a largely non-attenuated transmission of the information signals. Particularly for frequencies higher than 5 MHz it is difficult to realize a protection circuit with a low threshold voltage in consideration of an also low insertion loss. Concerning protection circuits, connected into power lines, these circuits have to show the characteristic to transmit electrical power from the power supply to the load.

Not only a protection against lightning surge voltages (edge steepness about 2kV/µs) is required, but also against EMP-surge voltages (edge steepness up to 2...10kV/ns) (1)\*,(2),(6). Measurements have shown that in many cases it can be assumed that EMP-pulses, coupled into transmission lines, have rise times of the order of microseconds. In addition, there are some applications where the edges of lightning- and EMP-pulses, coupled into electronic systems, are attenuated only slightly, e.g. antenna inputs.

Concerning the response of protection circuits the difference between lightning and EMP-surge voltages, applying these circuits, will be shown.

In case the spectrum of the interference does not overlap with the frequency range of the communication signals (s. Fig. 1) it is not problematical to realize a suitable band-pass filter. However, in the other case the frequency ranges mentioned are overlapping, and therefore nonlinear protection circuits with definite threshold voltages are necessary as shown in Fig. 2.

#### TEST EQUIPMENT

In case of edge steepnesses up to 10kV/ns of the applying surge voltage it is very difficult to realize measurements at protection circuits concerning comparatively low threshold voltages u2(t). In order to obtain reproducible measurement results with a sufficient precision a special and accurate shielding of the measurement circuit is necessary as shown schematically in Fig. 3. A 1800:1 frequency-calibrated high voltage attenuator probe is used for measuring output voltages u2(t) of the protection circuit. The registration of the signals is performed by means of a 400 MHz storage oscilloscope.

The transmission characteristics of protection circuits, on principle, of any two-port network are described by the s-parameter. In this case the simparameter and the magnitude of the simparameter are of special interest. By means of the simparameter - represented in a Smith chart - for an arbitrary frequency the input \*Numbers in parantheses designate References at end of paper

impedance and the reflection coefficient of a two-port network can be determined. The magnitude of the s21-parameter is the insertion loss of the two-port network. A network analyzer, as shown in Fig. 4, is used for measuring the s11- and s21-parameter. In this case it is required to realize a measurement of the insertion loss down to values of -0.5dB with a resolution of + 0.1dB. Therefore, a computer-controlled network analyzer is used which enables, by means of a special software, an automatic calibration and a consideration of the frequency-dependent loss of feed lines and internal connections.

#### DESIGN CONCEPT OF THE PROTECTION CIRCUITS

Concerning the protection against surge voltages, in certain cases the application of gas arresters is sufficient. As shown in Fig. 5 and mentioned in (1),(2) the dynamic threshold voltage is dependent on the edge steepness of the applying surge voltage. Fig. 5 shows the response of an arrester with the static threshold voltage U<sub>stat</sub> = 230V. The following values, concerning the dynamic threshold voltage, were obtained:  $U_{dyn} \simeq 900V$  for  $du_1/dt \simeq 2kV/\mu s$  and  $U_{dyn} \simeq 1750V$  for  $du_1/dt \simeq 5kV/ns$  (3),(4). In many cases these values are still too high and an additional protection is required. Fig. 6 shows a generalized block diagram of a protection circuit which consists of a coarse protection and a fine protection. The coarse protection contains gas arresters and the fine protection special suppressor diodes (E). Coarse and fine protection are decoupled by a series impedance. Starting from this block diagram, protection circuits against lightning- and EMP-induced surge voltages on lines and cables are developed for different applications.

#### MEASUREMENT RESULTS

In oder to guarantee a reliable operating of the protection circuits a sufficient decoupling between coarse and fine protection is necessary. The decoupling is dependent on a suitably proportioned series impedance (ohmic resistor and/or inductance) and on an optimal arrangement and shielding of the electronic components. The decoupling is required for both, the protection circuits for communication lines and the protection circuits for power lines. Particularly the discharge currents of the arresters generate magnetic fields with high amplitudes and extreme edge steepnesses. These magnetic fields may induce interfering voltages Ui. Starting from a realistic discharge current of an arrester, applied with a lightning- or EMP-induced surge voltage, the following approximation is valid, I =  $2cm^{2a}$ : max =  $2cm^{2a}$ : max =  $2cm^{2a}$ :

$$U_{\dagger} = N \frac{d\phi}{dt} \sim N \cdot A \cdot \mu \frac{dH}{dt} \sim N \cdot A \cdot \mu \cdot \frac{1}{2\pi r} \frac{d\dot{\dagger}}{dt} \sim 800V \qquad (1)$$

where Ia max is the maximum discharge current, Ui the open-circuit voltage of a loop with the area A and r the distance between the axis of the arrester and the center of the loop. (In this example the axis of the arrester and the loop form a plane). In order to show the influence of an insufficient shielding of the arresters on the response of a protection circuit, Fig. 7 shows measurements for a) a sufficient shielding of the arresters and b) a shielding with apertures (insufficient shielding). Concerning an insufficient shielding it is evident that an influence on the response u2(t) (Fig. 7b) appears during the first 10ns (marked by an arrow), that means during the response of the arresters. According to the oscillograms of Fig. 7, in case of Fig. 7a a peak value of 20V and in case of Fig. 7b a peak value of 150V was measured.

In the following two different protection circuits for special applications are shown and discussed. In Fig. 8 the block diagram and response of a protection circuit for symmetrical telephone transmission lines are represented. Because of the low frequencies of the communication signals (f < 5kHz) the problem concerning the insertion loss of this protection circuit is of secondary significance. The test pulse of Fig. 8 has an edge steepness of 5 kV/ns. In consideration of this comparatively high value of 5 kV/ns the peak pulse voltage (s. arrow in Fig. 8) only shows a value of about 25V. The pulser with the surge voltage  $u_1(t)$  is connected to the protection circuit as shown in Fig. 8, and the response voltage u2(t) is tapped off at the corresponding output terminals. This is the "worst case" because generally a common-mode excitation is valid in case of lightning- and EMP-induced currents on lines and cables. Concerning the edge steepness of the applying surge voltage the "worst case" is assumed, too, for in the most cases - particularly in low frequency multiconductor transmission lines - edge steepnesses of the order of some kV/ns are attenuated to values down to some  $kV/\mu s$ . Fig. 9 shows a photo of a protection circuit, installed on a printed-circuit board, for two symmetrical telephone channe's. The other type of protection circuit is a coaxially constructed device for high frequency transmission lines (characteristic impedance  $Z_L \approx 50\Omega$ ). It is difficult to develop protection circuits with a low threshold voltage in consideration of a minimum insertion loss for frequencies f > 5 MHz. An insertion loss shown in Fig. 10a is useless because a value of e.g. -50dB for 70 MHz is unacceptable. By means of special diodes as shown in Fig. 10b it is possible to reduce these values. In order to realize values for an insertion loss al < 2dB for frequencies up to 70 MHz a special coaxially constructed protection circuit is developed (s. photo of Fig. 11, Prototype PCC 100/1.25). Fig. 12 shows the block diagram which consists of a coarse protection and a multistage fine protection (fine protection FPI and fine protection FPII). The response (Fig. 12) is valid for an

edge steepness of the applying surge voltage of du<sub>1</sub>/dt $\simeq$ 5kV/ns. Generally, the first peak value (s. arrow in Fig. 12b) is dependent on the edge steepness, this value will be lower in case of lightning surge voltages (du<sub>1</sub>/dt $\simeq$ 2kV/ $\mu$ s). The measured 50 $\Omega$ -insertion loss (magnitude of s21-parameter) and the magnitude of the measured reflection coefficient |r| at the input of the protection circuit PCC 100/1.25 as a function of the frequency are represented in Fig. 13.

#### SUMMARY AND CONCLUSIONS

It has been shown that it is impossible to realize a universal protection circuit for all applications. There are considerable differences between circuits for low frequency and such for high frequency transmission lines. The main characteristics, concerning protection circuits for power lines, are a low threshold voltage and a special series impedance, which is proportioned for currents of several ampere up to several hundred ampere.

For the excecuted measurements an edge steepness of the applying surge voltage  $du_1/dt \simeq 5 kV/ns$  was valid. Since the response is largely dependent on the edge steepness, the maximum peak threshold voltages in case of lightning surge voltages (edge steepness  $du_1/dt \simeq 2 kV/\mu s$ ) are below the peaks obtained in case of EMP-surge voltages (edge steepness  $du_1/dt \simeq 5 kV/ns$ ).

The research work in conjunction with the industry is going on. The activities concern the development of protection circuits for special applications particularly for telecommunications.

#### **REFERENCES**

1. J.L. ter Haseborg, H. Trinks, "Protection Against Lightning and EMP Surge Voltages by Means of Gas Arresters and Special Diodes". Nuclear EMP Meeting. Albuquerque. New Moxico. May 24-28. 1982

Meeting, Albuquerque, New Mexico, May 24-28, 1982 2. J.L. ter Haseborg, H. Trinks, "Protection Circuits for Suppressing Surge Voltages with Edge Steepnesses up to 10 kV/ns". 5th Symposium on electromagnetic compatibility EMC, Zurich, March 8-10, 1983

3. P.A. Merz, "Lightning and NEMP Surges on Gas Arresters. A Computation Procedure for the Transient Response". 4th Symposium and Technical Exhibition on Electromagnetic Compatibility, Tunich March 19-12, 1991

Zurich, March 10-12, 1981
4. H. Wik, W.H. Kapp, A. Eggendorfer, W.Jöhl, W. Buchmann, "Measurements and Application of Secondary Surge Arresters for the Purpose of NEMP Protection". 4th Symposium on Electromagnetic Compatibility. Zurich. March 10-12, 1981

THE STATE OF THE PARTY OF THE P

tic Compatibility, Zurich, March 10-12, 1981
5. O. Melville Clar, R.D. Winters, "Feasibility Study for EMP Terminal Protection". U.S. Army Material Command, Harry Diamond Laboratories Electromagnetic Effects Laboratory Washington, D.C., report number TPD 003, AD 909267, March 1973

6. W. Nobis, E. Pivit, "Lightning Protection of Mobile Ground Systems". International Aerospace Conference on Lightning and Static Electricity, Oxford-England, March 23-25, 1982

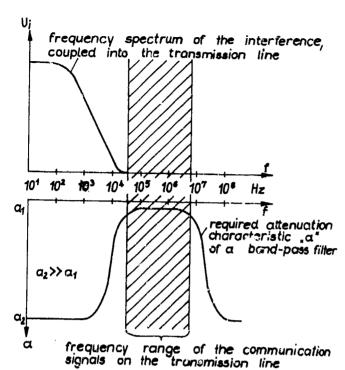


Fig. 1 - Required attenuation characteristic of band-pass filters against low frequency interferences, coupled into transmission lines

shielding,

H.V. allenuator probe

EMP-pulser

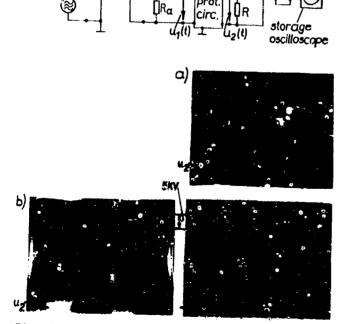


Fig. 3 - Test equipment for measuring the response u.(t) of protection circuits a) du\_1/de\2kV/us, lightning surge voltage b) du\_1/de\2kV/ns, EMP-surge voltage

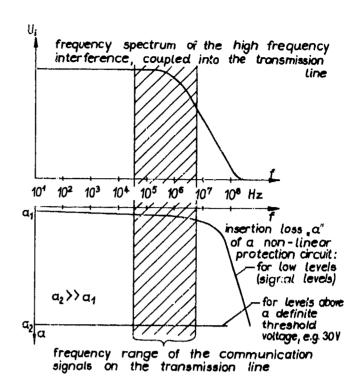


Fig. 2 - Required attenuation characteristic of protection circuits against EMP - and lightning - interferences, coupled into transmission lines

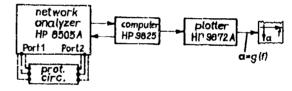


Fig. 4 - Test equipment for measuring the  $s_{11}\text{-}$  and  $s_{21}\text{-}\text{parameter}$ 

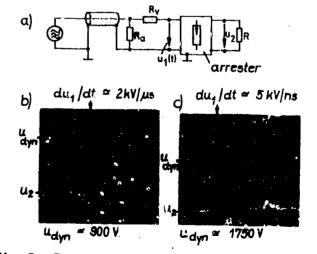


Fig. 5 - Pesponse  $u_2(\tau)$  of gas arrester with static threshold voltage  $U_{stat} = 230 \text{Y}$ , "\$\forall \text{marks} the response, a) circuit diagram edge steepness of applying surge voltage: b)  $du_1/dt \approx 2kV/\mu s$  (lightning) c)  $du_1/dt \approx 5kV/ns$  (EMP)

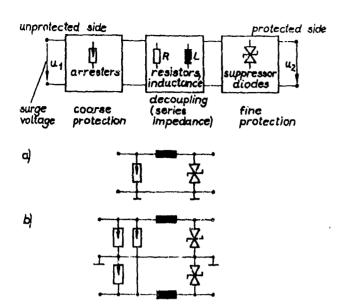


Fig. 6 - Generalized block diagram of protection circuits against lightning- and EMP-induced surge voltages on lines and cables

a) elementary protection circuit for unsymmetrical lines

b) elementary protection circuit for symmetrical

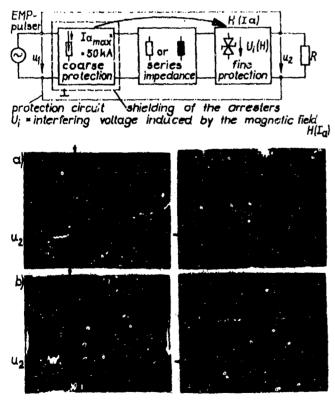


Fig. 8 - Block diagram of symmetrical protection circuit and response  $u_2(t)$  (edge steepness of surge voltage  $du_1/dt \simeq 5kV/ns$ )

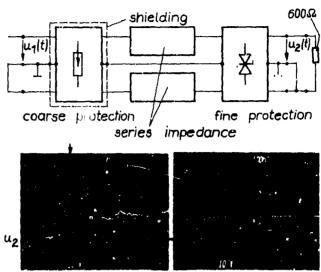


Fig. 7 - Influence of an insufficient shielding of arresters on the fine protection,  $\frac{1}{2}$ du<sub>1</sub>/dt∝5 kV/ns

a) u<sub>2</sub>(t): sufficient shielding b) u<sub>2</sub>(t): shielding with apertures, influence marked by arrow

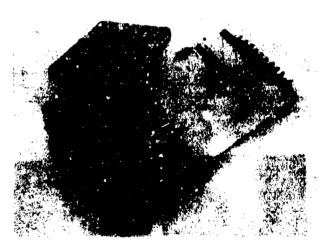


Fig. 9 - Photo of the protection circuit PCS 2/20 for two symmetrical telephone channels, installed on a printed-circuit board

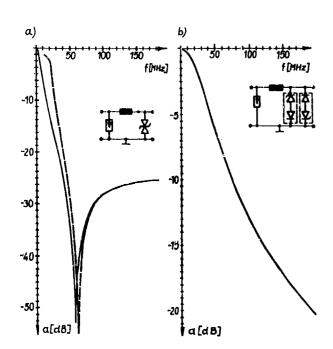


Fig. 10 -  $50\Omega$ -insertion loss, solid curve: measurement; dashed curve: computation

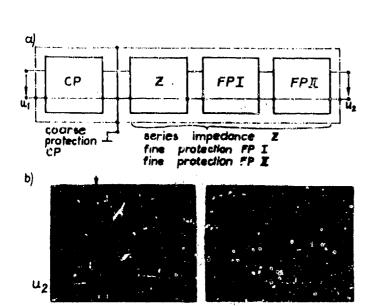


Fig. 12 - Block diagram and response  $u_2(t)$  of the coaxially constructed protection circuit PCC 100/1.25, (edge steepness of surge voltage  $du_1/dt \approx 5kV/ns$ )

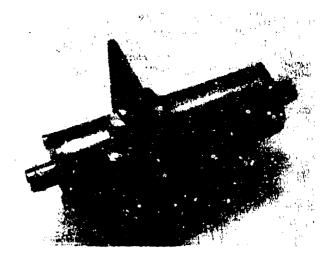


Fig. 11 - Photo of the coaxially constructed protection circuit PCC 100/1.25

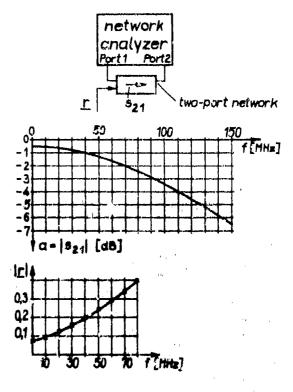


Fig. 10 - The magnitude of  $s_{21}$ -parameter (500-insertion loss "a") and magnitude of reflection coefficient  $|{\bf r}|$  as a function of the frequency



# AD P002170

TREQUENT FAILURE OF LIGHTNING ARPESTERS AT THE SATPURA THERMAL POWER STATION, INDIA: PRELIMINARY RESULTS OF FIELD OBSERVATIONS

A. Mary Selvan, G. K. Manchar, L. T. Khemani, P. C. S. Devara, G. A. Momin, A. S. R. Murty, and Bh. V. Ramana Murty Indian Institute of Tropical Meteorology, Pure, India

ABSTRACT

Surface observations were undertaken around the 722.5 MW Satpurs thermal power station, Madhya Pradesh, India, for investigating the possible reasons for frequent failure of lightning arresters.

The observations made have indicated unusually high negative electric fields (up to -8 kg/m) during fair weather conditions and also very high concentrations of particulate pollutants (up to  $2000\,\mathrm{m}^3$ ) in the downwind region. The high negative electric fields are attributed to the very high concentrations of particulate pollutants released into atmosphere from stacks.

A new theory for the generation of static electricity in the atmosphere has been proposed. The theory can explain the atmospheric electrical phenomena like intense electrification of dust storms, lightning activity associated with volcano erruptions and vary high electric fields in plumes emitted from power plant stacks. Also, it may have useful applications in the prediction and mapping of electric fields in the environment of space vehicle launching sites, super thermal power plants and explosive testing/storage sites.

The failure of the lightning arresters is attributed to the fatigue caused by the continuous flow of surge currents through the arresters. When these currents exceed a critical value the resealing function of the arresters may be affected resulting in their failure.

FREQUENT FAILURE OF LIGHTENING ARRESTERS installed at the 722.5 mW Satpura thermal power station located at Sarni (220 07' N. 78º 10' E, 436.4 ASL), Madhya Pradesh, India has been reported. At the request of the Madhya Pradesh State Electricity Board, the Institute undertook field observational programmes during July 1981, October 1981 and May 1982. Measurements of atmospheric electric field, point discharge current, raindrop charge, selected meteorological parameters, atmospheric gaseous and particulate pollutants and Aitken nuclei were carried out. The o observations indicated unusually high negative electric field during fair weather conditions and also very high concentrations of the gaseous and particulate pollutants in the immediate vicinity

of the thermal power plant.

Intense electrification of dust raised in sand storms was reported by several investigators. Negative potential gradients as high as 10 KV/m were observed during dust storms (1)\*. Potential gradients observations made close to a dust devil suggested that the dust cloud behaved like an inverted thunder cloud with negative charges. Measurements made at Beni-Abbes in the Northern Sahara indicated electric fields up to 15 KV/m in the dust cloud the polarity corresponding to the charges carried by the dust particles in the air. Similar effects ware also reported from the measurements made in Japan and in Nigeria (2,3). Erupting volcances are often accompanied by lightning and thunder (4). However, the physical mechanism for charge generation in dust clouds is not yet understood. Aircraft measurements made around large coal fired power plants in USA showed that particulates which escaps even the most efficient pollution convrol devices are highly charged and result in negatively charged plumes which are detectable electrically as far as 80 km downwind from the source (5). Electric field as high as 19 KV/m, only an order of magnitude less than typically found in a thunderstorm were detected in the plume emitted from an electrostic precipitator equipped Aircraft measurements made around thermal power plant/urban industrial complexes in India showed that the thermal, microphysical electrical and chemical conditions in the downwind regions are altered by the waste heat, moisture gaseous/particular pollutants emitting from stacks (6,7,8).

The above observations indicate that the unusually high negative electric fields noted during fair weather conditions in the downwind region of the Satpura thermal power plant could be due to the presence of highly charged

\*Numbers in parentheses designate References at end of paper. particulate pollutants released into the environment from the stacks. The above effect is more marked due to the low efficiency of the mechanical dust collectors installed in Units 1-5 of the thermal power plant (Fig.1). The high negative electric field observed in the environment of the thermal power station would cause fatigue to lightening arresters due to continuous surge currents passing through the arresters. Under certain conditions when the surge currents exceed certain value the resealing function of the arresters may be affected resulting in the failure of the arresters.

In this paper, a new mechanism has been proposed for the generation and maintenance of fair weather electric field and for the generation of static electricity in the atmosphere. The theory relating to the new mechanism and the results of the field observations are

presented below.

#### DETAILS OF THE THERMAL POWER PLANT

The thermal power station is located at Sarni in the forest region of Madhya Pradesh. It is surrounded by hills and the major rainy season is the summer monsoon (June-September). The winds in the lower troposphere are southwesterly and the normal annual rainfall is 121 Cm.

The present total capacity of the power plant is 722.5 MW. It consists of 7 Units (Fig.1.). Units 1 to 5 are of capacity of 62.5 MW each. Units 6 and 7 are of 200 MW and 210 MW respectively. Mechanical dust collectors are installed in Units 1-5 and electrostatic pracipi tators in Units 6 and 7. Units 1-5 have stacks of height 50 meters each, Units 6 and 7 have a common stack of height 160 meters. The efficiency of the mechanical dust collectors (Units 1-5) is about 80% and that of the electrostatic precipitators is about 98.5%. On the average about 90 x 103 Kg/hr of coal is burnt for the power generation.

### **OBSERVATIONS**

Observations of (i) atmospheric electric field, (ii) point discharge current, (iii) raindrop charges, (iv) rain fall intensity, (v) gaseous pollutants (SO<sub>2</sub>, NH<sub>3</sub>, NO<sub>2</sub>, O<sub>3</sub>), (vi) wind speed and direction, (vii) temperature, and (viii) humidity were recorded during the field programmes. The details of measurements of parameters of (i) to (vi) were described elsewhere (9,10). Parameters at (vi) to (viii) were measured using standard meteorological instruments.

The above measurements were carried out at (i) Sites 1 and 2 (upwind),

(ii) Site 3 near the stacks, and (iii)

Site 4 (downwind).

The dust load (TSP) in the vicinity of the power plant is very high. This is due to the hills located around the power plant whose height varied between 50 and 200 meters and the fly ash released from the stacks is unable to get dispersed. A photograph of the stacks and the plume is shown in Fig.2. The location of the lightning arresters is shown in Fig.3.

#### RESULTS

The diurnal variation of the vertical electric field at the surface based on the observations made under fair weather conditions in the upwind (Site 1) and downwind (Site 3) regions is shown in Fig.4. The electric field is negative and also unusually high (up to -8 KV/m). The maximum value of the electric field was as high as -8 KV/m when the plume from the stiacks was overhead. The electric field in the upwind region (Fig.4) is lower in magnitude (+200 V/m to -100 V/m) and almost tends to approach the undisturbed positive fair weather electric field. The point discharge current in the downwind varied between -0.1 and -1.4 µA. No detectable point discharge current was observed in the upwind region.

Similarly the concentrations of the gaseous and particulate pollutants are significantly high in the downwind regions. The maximum concentrations ( $\mu g/m^3$ ) of the total suspended particulates (TSP), SO<sub>2</sub> and NO<sub>x</sub> in the upwind and downwind respectively are 775,23,10,

and 2067, 149 and 12.

## NEW MECHANISM

A new mechanism for the generation and maintenance of fair weather electric field is proposed in the following.

The physical mechanism envisaged basically considers upward transport of large ions (charged particles/aerosols) from surface layer to higher levels. This gives rise to an aerosol current (IA) since the surface aerosols, by and large, carry positive charges. The upward transport of aerosols from surface to higher levels takes place due to the vertical mass exchange between the troposphere and the ionosphere. Similarly downward transport of negatively charged small ions from higher levels to lower levels takes place due to the vertical mass exchange. The vertical mass exchange takes place by a chain of eddies through the gravity wave feedback mechanism as explained below.

The atmospheric planetary boundary

layer contains large eddies (vortex rolls). The turbulent oddies originating from surface friction are contained as internal circulations along the envelopes of the large eddies. The circulation speed of turbulent eddies is several times that of large eddy. Microscale-fractional-condensation occurs in turbulent eddies even in an unsaturated environment. The turbulent eddies get amplified in the vertical by the latent heat released during the microscale-fractional-condensation. Thus the turbulent eddies are a continuous source of buoyant energy input for the sustenance and vertical growth of large eddies (11).

Theory indicates (12) that for a large eddy which is 10 times bigger in size than the turbulent eddy, the increase in the circulation speed of the large eddy is 25 per cent of the increase in the circulation speed of the turbulent eddy. The turbulent eddy fluctuations result in vertical mixing of the large eddy volume with overlying air. The fractional dilution by volume of the large eddy is equal to 0.45 for large eddies of size 10 times larger than the turbulent eddies. The dilution increases with decrease in large eddy size. Hence, it follows that large eddies of size R>10r

can alone exist as identifiable entities.

The buoyant production of turbulent kinetic energy (T.K.E.) by the microscale-fractional-condensation is maximum at the crest of the large eddies and results in the warming of the large eddy volume. The turbulent eddies at the crest of the large eddies are identifiable by a microscale-capping-inversion which rises upwards with the convective growth of the large eddy in the course of the day (Fig.5). This is seen as the rising inversion of the day time planetary boundary layer in the acheeonde records.

boundary layer in the echosonde records.

As the parcel of air corresponding to the large eddies rises in the stable environment, Brunt Vaisala oscillations are generated. These oscillations will give rise to gravity waves. The frequency of the Brunt Vaisala oscillations is equal to

 $N_{B} = \frac{g}{\theta_{V}} \cdot \frac{d\theta_{V}}{dg} \tag{1}$ 

where g is the acceleration due to gravity, where virtual porential temperature and dew/dz is the virtual potential temperature lapse rate in the microscale-capping-inversion. Thus the rising large eddy generates a continuous spectrum of atmospheric gravity waves (11).

atmospheric gravity waves (11).

The evidence for the generation of continuous spectrum of Brunt Vaisala eddies in the atmosphere can be seen from the turbulence spectra of wind and temperature observations. The slope of the

turbulence spectra is slightly steeper tham -5/3 (-1.6667). Theoretically the slope of the Brunt Vaisala addy spectrum can be derived as follows.

As explained earlier turbulent eddies are a continuous source of buoyant energy input for the vertical growth of large eddies. Hence, for a decadic wave-length range of eddies, the spectral slope (S) is given by

$$S = -\lambda n \left( S_{\underline{L}} / S_{\underline{A}} \right) \tag{2}$$

where  $S_L$  is the spectral density of the turbulent kinetic energy in the vertical direction for the large eddy and S for the turbulent eddy.

For wind the following expressions can be written

$$S_L = \frac{1}{4} (4/3) \pi R^3 W^2$$
 (3)

$$S_{n} = \frac{1}{4} (4/3) \pi r^{3} w^{2}$$
 (4)

where W and w are respectively the vertical velocities of the large and turbulent eddies. The spectral slope (S) is given by

$$S = -\epsilon n \left\{ \frac{R^3}{r^3} + \frac{W^2}{w^2} \right\}$$
 (5)

The value of S is ~1.8037 for a decadic wave-length range since W = 0.25w as shown earlier. The spectral slope for temperature may be shown to be the same as that for wind.

The slope of the spectrum of the Brunt Vaisala eddies is in agreement with the slope of the turbulence spectra for wind and temperature observations. Thus the physical mechanism envisaged for the generation of gravity waves is consistent.

It is postulated that vertical mass exchange takes place by a chain of eddies (gravity waves) extending from the lower troposphere to the ionospheric levels. As already pointed out the existence of the chain of eddies and the microscale-capping-inversion layers in the atmospheric planetary boundary layer can be seen from the echosonde records. At higher levels the eddy systems get amplified due to decrease in atmospheric density. The presence of the microscalecapping inversion layers at higher levels was noticed in the MST radar observations (13). Another observational evidence for the presence of the eddy systems (waves) at higher levels (about 80 km) is formation of noclucent clouds. The eddy systems described above are vertically propagating gravity waves exclusively of buoyancy type and these waves are respon-sible for the vertical mass exchange between the troposphere and the ionoaphere (14).

The vertical mass exchange by the gravity wave feedback mechanism results in the upward mransport of positively

charged large ions (serosols) and downward transport of negatively charged small ions as explained earlier. This would give rise to an aerosol current which can be represented as follows:

$$I_{A} = \frac{0.5V}{t} (N_{+} + + N_{-} + + n_{+} + + n_{-} +) e$$
 (6)
where

v = volume of the turbulent eddy

N = the large ion concentration and

n = the small ion concentration
t = circulation time period of the

turbulent eddy

e - electronic charge

As the concentration of large ions in the atmosphere is about 10,000 per cm<sup>3</sup> and that of small ions is 0.1 per cm<sup>3</sup> (17), I<sub>A</sub> is 5 orders of magnitude larger and is in the opposite direction to the conventional air-earth conduction current I, which is  $10^{-12}$  A per m<sup>2</sup>.

It is now postulated that IA is responsible for the generation of fair weather electrical field (F) instead of the global thunderstorm activity.

It is generally believed that the global thunderstorm activity is responsible for the maintenance of the fair weather atmospheric electric field since the observations show a simultaneous peak in the global fair weather electric field and thunderstorm activity. However, it has not been proved conclusively that the required number of thunderstorms occur at any time over the globe to maintain the fair weather electric field.

Schmidt (15) and Bauer (16) postulated the existence of the atmospheric currents 105 times larger and of opposite direction to the conventional air-earth conduction current in order to explain the variations in the horizontal geomagnetic field (H). However, there is no observational evidence for the Schmidt-Bauer currents. The serosol current (IA) proposed in the present paper is nothing but what has been visua-lised by Schmidt-Bauer. These currents occur over turbulent length-scale of about 200 m and hence could not be detected during single point observations. Indeed, the IA current has been actually observed in the telegraph wires along the mountain slopes in certain locations (17). The new mechanism proposed can thus also provide the physical explanation for the observed variations in the horizontal geomagnetic field (H)

One of the observational evidences for the vertical mass exchange as the generation mechanism for the atmospheric electric phenomenon is described below

The measured values of air-earth current density are found to be only

half of those obtained by computing the air-earth current density using the atmospheric electric field and conductivity values (18). This apparent discrepancy in the values of air-earth conduction current obtained by the above two methods can be explained as follows.

The atmospheric electrical conductivity (λ) measured by conventional methods

can be expressed as

$$\lambda = (n_{\perp}w_{\perp} + n_{\perp}w_{\perp})e \tag{7}$$

where n is the small ion concentration, w its mobility and a the electronic charge. Hence the air-earth conduction current (Ip) computed as the product of the atmospheric electric field (F) and the conductivity is given as follows.

In the direct method, the conductivity is obtained as the inverse of the atmospheric relaxation time i.e., time taken for the potential of a charged conductor to drop to 1/eth (e = base of natural logarithms) of its initial value by atmospheric conduction. In this case the charge leakage occurs by conduction due to small ions. The number of small ions available for conduction is only half of the total number available since the other half of the small ion concentration is involved in turbulent vertical mixing due to vertical mass exchange.

Thus the conductivity  $(\lambda p)$  measured by the direct method =  $\lambda/2$ . Hence the air-earth current (Ip) measured by the direct method =  $F.\lambda/2 = Ip/2$ . Thus the observed discrepancy between the direct and indirect methods of determination of the air-earth conduction current density

is explained.

APPLICATION OF NEW MECHANISM TO STATIC ELECTRIFICATION IN THE ATMOSPHERE

It was shown earlier that the atmospheric aerosol current IA is expressed as

 $I_A = \frac{0.5V}{t} (N_+ + N_- + + N_+ + + N_- +) e$ As a result of this aerosol current let there be an accumulation of an excess

positive space charge o at any level A as compared to that at the lower level B. Also, let oA and oB represent the space charge densities at A and B respectively.

The potential difference dr generated between the two levels A and B due to their unequal space charge densities can be expressed as follows.

 $dF = \frac{\sigma A - \sigma B}{\sigma} = \frac{\sigma}{\sigma}$ (10)

where so is the permittivity of free space. The potential gradient in the space between AB = dF/dz, where dz is the vertical distance of separation between

A and B. This potential gradient is conventionally taken to be positive when o is positive. Thus negative potential gradients are associated with an excess negative space charge overhead.

The vertical mass exchange resulting from the gravity wave feedback mechanism can also explain many of the observed phenomenon e.g., intense electrification of dust storms like Harmattan dust (1), lightning activity following volcano eruption (4) and very high electric fields in plumes emitted from power plant stacks (5,6).

The magnitude of the static electricity generated in the atmosphere is dependent on the intensity of the surface frictional turbulence, convective activity and dust load in the atmosphere. The new theory proposed for the generation of static electricity in the atmosphere will have useful applications in the prediction and mapping of electric fields in the environment of space vehicle launching sites, super thermal power plants and explosive testing/ storage sites.

#### ACKNOWLE DCEMENT

The facilities for undertaking the field observational programmes at the Satpure thermal power plant were provided by the Madhya Pradesh State Electricity Board.

#### REFERENCES

1. A.I.I.Ette, "The Effect of the Harmattan Dust on Atmospheric Electric Parameters." J. Atmosph. Terr. Phys.,

33, 295-300, 1971.
2. D.J. Harris, "Atmospheric Electric Field Measurements in Northern

Nigeria during the Dry Season." J.Atmosph. Terr. Phys., 33, 581-588, 1971.
3. E.O. Oladiran, "Results of Twenty Years of Atmospheric Electricity Research at Ibadan." PACEOPH, Basel, 120,123-135, 1982.

"Volcanic Lightning."

4. C. Pounder, "Volcanic Lightning."
Weather, 35, 357-360, 1980.
5. W.E. Cobb, B.R. Caldwell and D.L.
Wellman, "Aircraft Elect" 'c Field Measurements in Coal-Fired P wer Plant Plumes." EOS Transactions, Amer. Geophys.

Union., 60, No.18, 271, 1979.
6. A. Mary Selvam, A.S.R. urty,
R. Vijayakumar and Bh.V. Ramana Murty, "Electrical and Microphysical Measurements in the Environment of a Thermal Power Station." Atmos. Environ., 10,

957-962, 1976.

7. A. Mary Selvam, A.S.R. Murty, S.K. Paul, R. Vijayakumar and Bh.V. Ramana Murty, "Airborne Electrical and Microphysical Measurements in Clouds in Maritime and Urban Environments." Atmos. Environ. 12 1097-1101. 1978.

Environ., 12, 1097-1101, 1978.

8. L.T. Khemani, G.A. Momin, M.S.
Naik, A. Mary Selvam and Eh.V. Ramana
Murty, "Thermal, Microphysical and
Chemical Conditions in an Urban Environment." Proc. VIII International Conf.
Cloud Physics., Clermont-Ferrand, France
15-19 July 1986, 153-156, 1980.

Cloud Physics., Clermont-Ferrand, France, 15-19 July 1980, 153-156, 1980.

9. A. Mary Selvam, G.K. Manohar, L.T. Khemani and Bh.V. Ramana Murty, "Characteristics of Raindrop Charge and Associated Electric Field in Different Types of Rain." J. Atmos. Sci., 34, 1791-1796, 1977.

10. L.T. Khemani, G.A. Mumin, M.S.

10. L.T. Khemani, G.A. Mumin, M.S. Naik, R. Vijayakumar and Bh.V. Ramana Murty, "Chemical Composition and Size Distribution of Atmospheric Aerosols Over the Deccan Plateau, India." Tellus, 34,

151-150, 1982.

11. A. Mary Selvam, A.S.R. Murty and Bh.V. Ramana Murty, "Surface Frictional Turbulence as an Agent for the Maintenance and Growth of Large Eddies in the Atmospheric Planetary Boundary Layer." Sixth Symposium on Turbulence and Diffusion, AMS, Boston, USA, 22-25 March 1983

March, 1983. 12. A.A. Townsend, "The Structure of Turbulent Shear Flow." Cambridge Univ. Press. Cambridge, 113-130, 1956.

13. J. Rottger, "Structure and Dynamics of the Stratosphere and Masosphere as Revealed by VHF Radar Investigations." PAGEOPH, Basel, 118, 494-527, 1980.

14. A. Mary Selvam, A.S.R. Murty and Bh.V. Ramana Murty, "Dynamical Interaction Between the Troposphere and Stratosphere." Proc. Regional Scientific Conf. Tropical Meteorology, Japan, 18-22 Oct. 1982. 11-12. 1982.

1982, 11-12, 1982. 15. A. Schmidt, "The Problem of Vertical Electric Currents." Z.Geophys., 1, 281-284, 1924.

16. L.A. Bauer, "On Vertical Electric Currents and the Relation Between Terrestrial Magnetism and Atmospheric Electricity." Terr. Magn. Atmos. Elect., 25, 145-162, 1920.

17. H. Israel, "Atmospheric Electricity." Vol.II, Israel Program for Scientific Translations Ltd., IPST No.1996,

Jerusalem, 1973.

18. J.M. Rosen, D.J. Hofmann, W. Gringel, J. Berlinski, S. Michonowski, Y. Morita, T. Ogawa, and D. Olson, "Results of an International Workshop on Atmospheric Electrical Messurements."

J. Geophys. Res., 87, 1219-1227, 1982.

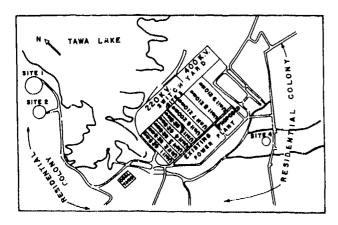


Fig. 1 - Location of the Satpura thermal power plant and observational sites



Fig. 2 - Plume emitting from stacks

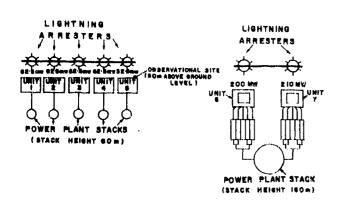


Fig. 3 - Location of lightning arresters

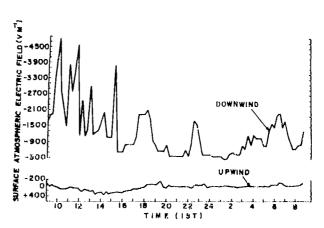


Fig. 4 - Atmospheric electric field in the upwind and the downwind regions of the power plant

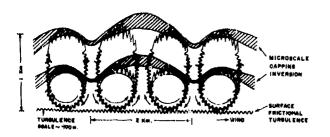


Fig. 5 - Large eddies (vortex rolls) and turbulent eddies in the atmospheric planetary boundary layer (PBL). The turbulent eddies are contained as internal circulations along the envelop of the large eddy. The microscale-capping inversion forms at the crest of the large eddies and rises upwards with the growth of the large eddy



# Correlated Measurements of UHF Radar Signatures, RF Radiation, and

Electric Field Changes from Lightning



D. M. Le Vine

AD P002171

Goddard Space Flight Center

Greenbelt, MD 20771

Vladislav Mazur

Cooperative Institute for Mesoscale Meteorological Studies

University of Oklahoma

Morman, OK 73019

#### ABSTRACT

During Storm Hazards - 82, simultaneous measurements were made of radar schoes, fast and slow field changes and RF radiation from lightning near the Wallops Flight Facility. RF radiation and radar schoes were also obtained during periods when the NASA FlO6 research aircraft was struck by lightning. These data are presently being used to better understand the electrical processes which occur during strikes to the aircraft. Preliminary conclusions based on data obtained in 1982 varify that the events recorded aboard the sircraft occurred during lightning but also indicate that they occur with surprising frequency very early in the flash.

DURING THE SUMMER, 1982, simultaneous measurements of radar echoes and electromagnetic radiation from lightning were made at the Wallops Flight Facility (WFF), Wallops Island, Virginia. These measurements were part of the Storm Hazards experiment. The electromagnetic fields were measured with fast and slow field change systems and also with radio receivers tuned to several frequencies between 3 and 300 MHz, and the radar measurements were made using the very high resolution UHF radar maintained at the Wallops Flight Facility. Measurements were made to support flight experiments with the NASA F106 research aircraft, and data were collected during several storms during which the aircraft was struck by lightning. Data were also obtained during local thunderstorms not perturbed by the aircraft. The objective of these measurements were to aid in the interpretation of data collected by the F106 and also to learn more about the physics of lightning.

During the Storm Hazards experiment in 1982, electromagnetic radiation was obtained during 45 "strikes" to the aircraft and correlated radiation and radar echoes were obtained for more than 30 events. These cases indicate that the data obtained by the aircraft occurred during lightning discharges and that the events recorded on the aircraft tend to occur quite early in the flash.

#### INSTRUMENTATION

The electric field change systems employed in these measurements are broad bandwidth devices designed to record changes that occur in the electric field at the ground during a lightning flash. They were based on a design by Krider [1]\* and consisted of flat plate antennas followed by an integrator which compensates for the capacitive response of the antenna and also provides gain [1,2]. The integration time constant is chosen to be long compared to the time scale of events of interest. Two systems, similar except for the time constant, were used. The time constant for the "slow" electric field change system was about I second and about I millisecond for the "fast" field change system. The slow electric field change system has a frequency response from near d.c. to a few kilohertz and measures the quasi-static electric fields at the ground due to changes in charge in the cloud [2]. The fast electric field change system has a frequency response from near a kiloherts to several MHz and is designed to record radiation from the sharp transients that occur during lightning events such as return strokes and stepped leaders. The signal from this system normally is recorded with a high-speed digital sample and hold

\*Numbers in parentheses designate References at end of paper.

device (Biomation Model 8100 waveform recorder) capable of sampling at selectable rates up to 108 samples/second and storing 2000 samples per record.

At frequencies above a few MHz, rediation was monitored using d.c. coupled A.M. radio receivers. Measurements at 3 MHz and 30 MHz were made using a fixed tuned receiver developed for lightning research at the Georgia Institute of Technology [3]. These receivers were used with vertical whip antennas mounted on the ground. At frequencies between 30 MHz and 300 MHz the radiation from lightning was recorded using commercially available radio receivers (Watkins Johnson models WJ-997 and WJ 8730) which were modified to provide d.c. coupled output. Disk-cone antennas were used at these frequencies. These receiving systems were designed to operate at a bandwidth of 300 kHz.

The electronics for both the RF receivers and the electric field change systems were housed in the Spandar Radar Facility at the Wallops Flight Facility and the antonnas were mounted a few hundred feet from the building on the flat grassy lawn between Spandar and the UHF radar. A pair of flat plate antennas were also mounted on the roof of the Spandar Facility and were generally used to obtain fast field changes.

The radar used in these studies to detect the ionised channels created by lightning discharges is a UHF radar which operates at 430 MHz and has an antenna 60 feet in diameter. The radar transmits a pulse 1 µs long once every 3 ms. The antenna beam at this frequency is about 2.5 degrees wide and the range resolution with this pulse is 150 meters. At 100 km this radar scatters from a resolution volume about 4 km high, 4 km wide and 150 meters deep (range). The radar could be slaved to a C-band tracking radar which followed the aircraft during flights. Thus, the aircraft could be continually kept in the resolution volume of the radar as it moved through the storm which allowed the radar to see lightning channels which developed near the aircraft.

Data from all instruments were recorded on a strip chart recorder and also on analogue magnetic tape using an Ampax model PR-2200 instrumentation tape recorder. The data recorded on tape included the signals from the fast and slow field change systems, the output from the radio receivers, and the video output from the radar. In addition, to obtain more bandwidth, the fast field changes were recorded digitally using a Biomation 8100 waveform recorder. The waveform recorder was operated in its pre-trigger mode in which the memory stores data before and after the triggering

signal, and the system was set to trigger when the input exceeded a preset threshold. When the waveform recorder was triggered, a pulse was sent to the magnetic tape and strip chart to aid in correlating these events with the other data. After a trigger digital data stored in the Biomation memory were dumped rapidly into a buffer and the waveform recorder was re-armed. The time required to complete this cycle was less than 2 ms and up to 10 of the 2000 word memory units could be stored in the buffer. Once the buffer was full, or the lightning flash ended, the buffer was transferred to digital tape. An internal clock kept track of the time between triggers and allowed the time between events to be determined with an accuracy of better than  $10~\mu\text{s}$  . The radar data were recorded on magnetic tape and on the strip chart, but for purposes of processing, it was also recorded on a modified video cassette recorder with about 500 kHz bandwidth. The radar video was recorded on the cassette for each pulse plus the time code and a reference pulse which was used when playing the data back for display on an oscilloscope. The data to be presented here were obtained by making video TV images from the oscilloscope display. In doing so, 30 radar pulses were averaged to form one video frame.

DATA

Figures 1-3 show data collected during a lightning flash which occurred at about (23 hrs 17 min 27 sec) on August 17, 1982, during a storm close to the Wallops Flight Facility. Figure 1 is a strip chart summary of all the data collected for this flash. It shows radiation at 3, 30, and 139 MHz, the fast and slow field changes, the pulses from the digital waveform recorder and the raw radar data. The slow field change for this flash consists of a series of abrupt downward steps typical of cloud-to-ground flashes [2]. Three steps can be seen on close examination, suggesting a cloud-to-ground flash with three return strokes. This is corroborated by the fast field change system which produced three distinct pulses. The RF radiation is quite strong at each frequency during this flash with peaks clearly evident during the return stroke phase of the flash, although strong radiation peaks also occur before and after this portion of the flash. Although strong RF radiation during return strokes is to be expected [4], it is not uncommon to find strong RF radiation in other portions of the flash [5], and in fact, there is evidence to suggest that the strongest RF radiation is associated with intra-cloud processes and not return

strokes [6].

As mentioned above, the fast field changes were also recorded using the Biomation waveform recorder and digital interface described in the preceding sections. The waveform recorder was set to trigger on large negative pulses for this experiment and to take data at a rate of .05 us/sample. The waveform recorder was triggered four times during this flash. Three of these coincide with the pulses recorded on the strip chart from the fast field change system. The other event appears to have occurred early, before the first return stroke. The waveforms recorded during these four triggers are shown in Figure 2. The Biomation recorded 100 µs of data each time it triggered (2000 samples x .05 us/sample). These data were plotted on a strip chart from the digital tape to obtain Figure 2. Although the amplitude in V/m 1) not accurately known for these radiation fields, the relative amplitude between events is correctly displayed in the figure. Also, although the time is only correct to the synchronization accuracy of the time code generator (about 50 µs), the relative time between events is accurate to better than 10 us. The first event in Figure 2 (23 hrs 17 min 26.841 sec) is a sequence of regular pulses typical of radiation from stepped leaders preceding first return strokes [1,7]. The same periodic train of pulses can also be seen preceding the second event in Figure 2 (23 hrs 17 min 26.890 sec). This second event has a shape which is typical of radiation from first return strokes [8,9,10,11]. It possesses an initial ramp-like portion followed by a sharp rise to peak and then an irregular decay back toward zero which is typical of first return strokes. The third event (23 hrs 17 min 26.946 sec) is something of a surprise because it also has the characteristics of a first return stroke, whereas one would have expected to have seen a waveform more like the last one. As will be shown below, the radar data during the early phase of this flash indicates ionized channels in two different locations and developing about 60 ms apart, suggesting that in this flash the second return stroke may not have followed the path of the previous stroke but ionized its own channel. The last event is small but has a shape commonly encountered in subsequent return strokes [8,11].

Figure 3 is a sequence of photographs showing the radar signal received during this flash. Each photograph represents the average of 30 radar returns. They are photographs of the video (TV) frames made from an oscilloscope display of the data on the cassette recorder. The vertical axis is intensity of the scattered signal (power) and the horizontal axis is distance in kilometers. The first frame

(23 hrs 17 min 26.87 sec) shows the rader return prior to the beginning of the lightning flash. The second frame shows the radar return just after the flash has begun (i.e., the first evidence of an echo appears). The spike to the right of center in the photograph is from the lightning channel. One frame (photograph) was made every 30 ms and the times on the figures indicate the time when the data was recorded to within about 30 ms. The frames shown have been selected from a great many to illustrate the stages that the echo went through in the course of this flash. There were several frames of data between the first photograph (23 hrs 17 min 26.87 sec) and the second (23 hrs 17 min 26.94 sec) shown here. The echo was first discernable at about (23 hrs 17 min 26.90 sec) but the photograph shown here (two frames later) was chosen for display because it shows the echo more clearly. About two frames (60 ms) after the first echo appears, a second echo appeared in a different location and is shown in its fully mature form in the frame made at (23 hrs 17 min 27.05 sec). The fast field changes also indicate about 60 ms between the first two return strokes (Figure 2). This second echo percists for several tenths of a second broadening and changing shape somewhat, whereas the first echo disappears quite soon after it appeared. Toward the end of the flash, a third echo (illustrated by the frame at 23 hrs 17 min 27.33 sec) appeared. It occurs well after the return stroke phase of this flash is over and coincides well with the large burst of RF radiation evident in Figure 1 in the late stages of the flash. This third echo is short-lived, and has disappeared by about (23 hrs 17 min 27.43 sec). All evidence of ionized channels eventually ends at (23 hrs 1? min 27.60 sec) about 640 ms after the flash began. This duration corresponds well with the duration of the flash as determined from the record of RF radiation in Figure 1. After the flash is over, the radar return again has the form shown in the first frame in Figure 3.

The combination of radar echoes, RF radiation, and electric field changes paint a clearer picture of this flash than either set of data could provide alone. This flash appears to have been a cloud-to-ground discharge with three return strokes, the first two following their own (different) paths, and the third being a subsequent stroke most likely following the path of the second return stroke. In addition, toward the end of this flash, what appears to be a strong intra-cloud event took place somewhat displaced from either return stroke

The summer of 1982 was the first time that coordinated measurements of UHF radar echoes

and radiation fields from lightning had been tried at WFF, and all instrumentation problems weren't solved until late in the summer. However, several good examples were obtained during storms on August 11 and August 17 which are now being analyzed. One objective of this analysis is to compare cloud-to-ground and intra-cloud flashes to see if quantitative differences in their echo structure can be identified and we hope to report results of these studies in the near future.

#### DATA COORDINATED WITH AIRCRAFT

During the summer of 1982, data was also collected during storms penetrated by the NASA F106 research aircraft. Unfortunately, most of these storms were too far from the Wallops Flight Facility to obtain slow electric field changes, and equipment problems with one system or the other prevented simultaneous records of fast field changes and radar echoes to be obtained at times when the aircraft was struck by lightning. However, simultaneous records of RF radiation and radar echoes were obtained on several flights and yielded good data on occasions when the aircraft reported "strike". This data is described below.

Our objective in this initial study was to examine times when the instrumentation on the aircraft was triggered to see if, in fact, these events corresponded to the occurrence of lightning and to see if this lightning was in any way unusual. The trigger times of the modified Biomation waveform recorder aboard the aircraft were selected as the definition of the event. Then the records of RF radiation and radar echoes were examined at these times. Figure 4 is an example of radiation received at 3 MHz during flight #34 on July 30, 1983. About 40 seconds of data is shown near (19 hrs 55 min 28.75 sec) when the aircraft reported a Biomation trigger. The trigger occurred at the very beginning of the strong flash shown in the middle of the figure. The fact that the aircraft trigger occurred early in the flash was typical of the RF data collected during 1982 [12]. Figure 5 is a histogram made from 45 events which correlated with RF radiation at WFF. It shows the location of the aircraft events measured from the beginning of the flash and plotted as a percentage of the duration of the flash. The beginning and duration were determined from the RF radiation at 3 MHz. It is clear from the figure that the Biomation triggers tended to occur early on the flash. It was most probable to find the aircraft event in the first 10-20% of the flash and the mean was about 29%.

The UHF radar was also operating on July 30 and recorded an echo during the event shown in Figure 4. The first four frames of radar data for this flash are shown in Figure 6. The sharp pulse in the first frame (19 hrs 55 min

29.7 sec) is the radar return scattered from the aircraft just before the flash began. In the second frame (19 hrs 55 min 29.8 sec) the outline of an echo from lightning can be seen superimposed on the return from the aircraft. This echo becomes more distinct and grows in amplitude and spatially in the succeeding frames. The interesting feature of the radar echo is that it appears to begin right at the location of the aircraft. This was not always the case as is evident in Figure 7 which shows the first four frames of the radar return during flight #37 on August 6, 1982, during an event at about near (19 hrs 50 min 04 sec). In this case, the radar indicates a channel which developed several kilometers from the aircraft and then grew in spatial extent to eventually include the resolution volume in which the aircraft was located. Of more than 35 events recorded during the summer of 1982, (i.e. aircraft events during which there were both RF radiation and radar echoes) less than 10% were nearby flashes of the form shown in Figure 7. The overwhelming majority had echo patterns such as that shown in Figure

A final example of data recorded during the aircraft flights is shown in Figures 8 and 9 for a flash recorded at about (22 hrs 34 min 48 sec) on August 9, 1982, during flight #40. The aircraft recorded an event at (22 hrs 34 min 47.86 sec) and Figure 8 shows the RF data at 3 MHz and 30 MHz recorded at this time as well as the unprocessed radar video signal. This example was obtained from magnetic tape by playing the data back at slow tape speed to obtain very high time resolution. This was done with most events to clearly show the detail of the radiation signal. The radar echo began at about (22 hrs 34 min 47.67 sec) for this flash and persisted for about 550 ms until about (22 hrs 34 min 48.22 sec). The beginning of the echo is apparently associated with the large pulse of RF radiation occurring in the center of the flash. On several occasions, the beginning of the radar echo was associated with large pulses in the RF radiation. This flash is somewhat unusual in that the radar echo and aircraft event occur in the middle of the flash. It is also unusual in that the duration of the KF radiation is quite long, about 1.5 seconds. There is a strong possibility that this is not one flash, but rather two overlapping flashes (the RF system is omni-directional and therefore receives radiation from all storms within range of the system at the same time). For example, in 18 cases of good quality, high time resolution data studied so far, the RF signal divided naturally into two quite distinct classes: flashes whose duration was less than one second (the average was .67 sec), and those

whose duration was greater than one second (average = 1.85 seconds). Most examples (67%) were in the first category. The length of the flashes in the second category strongly suggests overlapping flashes. The interesting feature of these two classes is that in every one of the former (short flashes) the radar echo and aircraft event occurred right at the very beginning of the flash, on the average within 70 ms of the first noticeable RF radiation. In the second class (very long flashes) the radar echo sud aircraft event occurred on the average 0.60 seconds from the beginning of the RF radiation. The implication is that the events recorded aboard the aircraft occur toward the beginning of the flash with even more frequency than indicated in Figure 5. This is so because the histogram was obtained using all flashes, including those of the second class, and these may very well have been overlapping flashes with the aircraft event actually occurring at the beginning of one them.

#### CONCLUSION

The combination of radar echoes from lightning channels and the electric field changes and radiation at radio frequencies from the flash promise to offer improved insight into the structure of lightning. Those data are presently being used to help understand the lightning which occurs during strikes to the NASA FlO5 research aircraft as part of Storm Hazards. Preliminary conclusions based on data obtained during 1982 verify that the events recorded on the airplane occurred during lightning flashes, but also indicates that they occur with surprising frequency very early in the flash.

#### ACKNOWLEDGEMENT

This data would not have been possible without the patience and help of B. J. Wilson of the Georgia Institute of Technology and the staff at the Spandar Radar Facility. This work was funded in part by NASA Grant #NCC5-600.

#### REFERENCES

- 1. E. P. Krider, C. D. Weidman, and R. C. Noggle, "The Electric Fields Produced by Lightning Stepped Leaders, J. Geophys. Res., 82, 951-960, 1977.
- 2. M. A. Uman, Lightning, McGraw-Hill, 1969.
- 3. D. M. Le Vine, et. al., "The Structure of Lightning Flashes HF-UHF: September 12, 1975. Aclanta. Georgia." NASA X-953-76-176.
- 1975, Aclanta, Georgia, "NASA X-953-76-176.
  4. D. M. Le Vine, "The Spectrum of Radiation from Lightning", IEEE International Symposium on Electromagnetic Compability, pp. 249-253, October 1980.
- 5. D. M. Le Vine, "The Temporal Structure of RF Radiation from Lightning," NASA TM-78113, April 1978.
- 6. D. M. Le Vine "Sources of the Strongest RF Radiation from Lightning", J. Geophys. Res., Vol. 85, (#67) pp. 4091-4095, July 1980.
- 7. E. P. Krider and G. J. Radda, "Radiation Field Waveforms Produced by Lightning Stepped Leaders", J. Geophys. Res., Vol. 80. (#18), pp. 2653-2657. June 1975.
- Vol. 80, (#18), pp. 2653-2657, June 1975. 8. C. D. Weidman and E. P. Krider, "The Fine Structure of Lightning Return Strokes Waveforms," J. Geophys. Res., Vol. 83, (#C12), pp. 6239-6247, December 1978.
- (#C12), pp. 6239-6247, December 1978.
  9. C. Guo and R. P. Krider, "The Optical and Radiation Field Signatures Produced by Lightning Return Strokes," J. Geophys.
  Res., Vol 87, (#C11), pp. 8913-8922, October 1982.
  10. Y. T. Lin, M. A. Uman, and J. A. Tiller,
- R. D. Brantley, W. H. Beasley, E. F. Krider, and C. D. Weidman, "Characterization of Lightning Return Stroke Electric and Magnetic Fields from Simultaneous Two-Station Measurements," J. Geophys. Res., Vol. 84 (C10), pp. 6307-6314, 1979.
- 11. J. A. Tiller, M. A. Uman, Y. T. Lin, R. D. Brantley, and E. P. Krider, "Electric Field Statistics for Close Lightning Return Strokes Near Gainseville, Florida," J. Geophys. Res., 81, 4430-4434, 1978.
- 12. D. M. Le Vine, "R.F. Radiation from Lightning Correlated with Aircraft Measurements During Storm Hazards-82," NASA TM-85007, March 1983.

## AUGUST 17, 1982 23 HRS 17 MIN 27 SEC

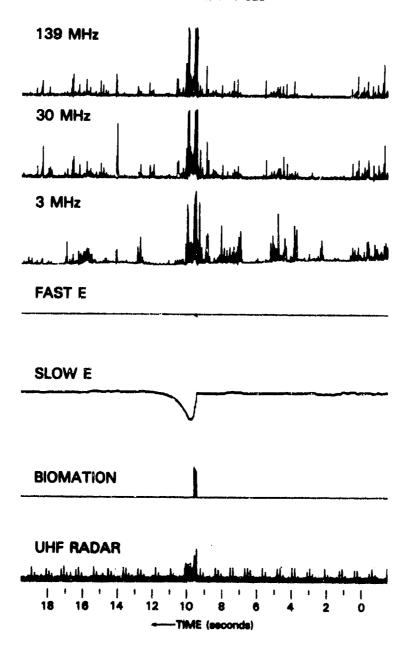


Fig. 1 - Strip chart record showing data collected on August 17, 1982, at about (28 hrs 17 min 27 sec) during a storm close to the Wallops Flight Facility, Wallops Island, VA

# AUGUST 17, 1982 23 HRS 17 MIN 27 SEC

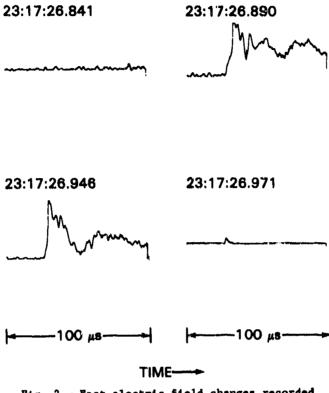


Fig. 2 - Fast electric field changes recorded on the Biomation waveform recorder on August 17, 1982 during the lightning flash shown in Figure 1. The Biomation sampling rate was .05 ms/sample

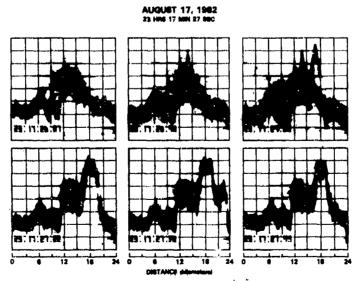


Fig. 3 - Rapresentative frames showing UHF radar data obtained on August 17, 1982, for the flash shown in Figure 1



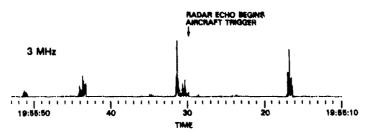


Fig. 4 - A strip chart record of radiation at 3 MHs recorded on July 30, 1983, during flight #34. The aircraft recorded an event at (19 hrs 55 min 29.75 sec)

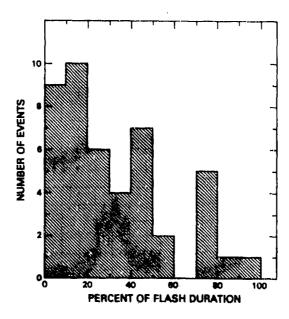


Fig. 5 ~ Histogram showing the occurrence of events recorded aboard the aircraft measured from the beginning of the lightning flash and plotted as a percentage of the duration of the flash. Flash duration was determined from records of RF radiation at 3 MHz

#### JAJLY 30, 1982 10 HR6 96 HRH 20 SUC

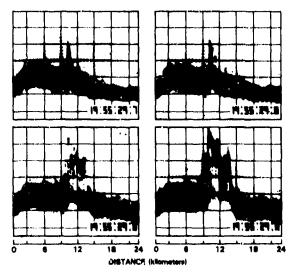


Fig. 6 - The first four frames of UHF radar data at the beginning of the flash on July 30, 1982, shown in Figure 4

#### AUGUST 6, 1982 19 HRS 90 HRI 04 SEC

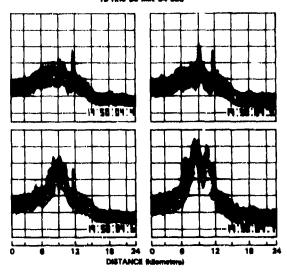


Fig. 7 - The first four frames of UMF radar data for a flash on Amgust 6, 1982, during flight #37 which started near the aircraft and then spread to include it

#### AUGUST 9, 1982 22 HRS 34 MIN 46 SEC

AIRCRAFT TRIGGER RADAR ECHO STARTS



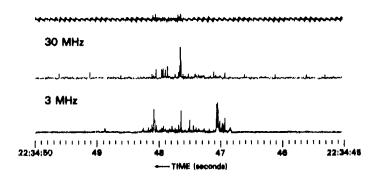


Fig. 8 - Example of RF radiation and UNF radar echo data for a flash on August 9, 1982, during flight #40. The aircraft reported an event at (22 hrs 34 min 47.80 sec). The UHF radar echo began at (22 hrs 34 min 47.66 sec)

. 0

#### AUGUST 9, 19612 22 HRS 34 NR 47 SEC

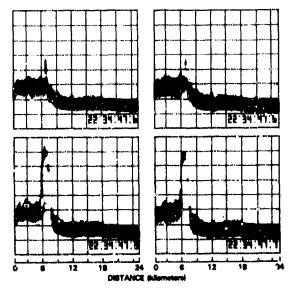


Fig. 9 ~ The first four frames of processed UHF radar data for the lightning flash on August 9, 1982, shown in Figure 8



RELATIONSHIPS BETWEEN LIGHTNING OCCURRENCES AND RADAR ECHO CHARACTERISTICS IN SOUTH FLORIDA

Ronald L. Holle, Raul E. Lopez and William L. Hiscox

Weather Research Project Environmental Research Laboratories National Oceanic and Atmospheric Administration Boulder, Colorado 80303

#### ABSTRACT

Locations of cloud-ground lightning flashes were recorded during 1978 in south Florida; concurrently, radar data were digitized over a wide variety of meteorological conditions. Analyses show that a sharp difference exists between the frequency distributions of 1) radar cells (reflectivity maxima) associated with lightning flashes, which peaked at 46 dBs, and 2) cells without lightning, which peaked at 18 dBs. Similar results also apply for an area several kilometers around a flash, and indicate that only 20% of the radar data (above 30 dBs) accounted for nearly 70% of the collocated lightning. Other results specifying time relations, cell areas, and number of flashes are also described.

LIGHTNING AND RADAR DATA were collected during the summer of 1978 in south Florida as part of a study of the modification potential of convective clouds during FACE, the Florida Area Cumulus Experiment (1, 2). The analyses of convection in this area as part of FACE have lead to a significant growth in knowledge of storms over interior Florida on scales ranging from individual clouds to large-scale environmental influences and interactions (3). In the process of studying precipitation in this area, characteristics of the radar and lightning data have become known well enough to make detailed studies of, and comparisons between these two data sets. While the electrical behavior of Florida clouds has been reported for the Kennedy Space Center area (4, 5, 6), there have not been extensive studies of how lightning flashes relate to radar reflectivity characteristics using large samples. In this paper, detailed relationships hetween a large number of cloud-to-ground flashes and several radar parameters in the vicinity of the flash or echo are presented. In a companion paper in these proceedings (7), flash populations are stratified by synoptic-scale regimes for the same data set as described here. Based on experience from analyzing data sets in detail for south Florida, this pair of papers shows how flash and precipitation echo phenomena relate to each other on several scales; these studies appear to have no precedent, especially in view of the large sample sizes analyzed for the present study.

### DATA ANALYSIS METHODS

INTRODUCTION - Radar data were digitally recorded from the WSR-57 radar operated by the National Hurricane Center in Coral Gables, Florida (Fig. 1). Base scans were made by this radar at a typical elevation angle of 0.5°. The cloud-to-ground lightning data were collected by two direction finders manufactured by Lightning Location and Protection, Inc. (8, 9). To determine the appropriate way to match the radar and lightning data collected during FACE-2, several aspects of the accuracy of both systems must be considered. In general, the raw radar data consist of average reflected power values from truncated pie-shaped sections which gradually widen with distance away from the radar. The lightning data consist of point values of flash location which decrease in accuracy with distance from the two antonnas.

RADAR DATA CHARACTERISTICS - The WSR-57 radar at Coral Gables has a two-degree conical beam and a gatelength of 927 m. Close to the radar, fictitious returns are received due to anomalous propagation and ground targets; therefore, data within 31 km were not included in the study. At this distance, the beam is less than 1 km in diameter. About 150 km away the radar beam attains a diameter of 5 km, and a radar data point corresponds to the volume of a 2° truncated cone of 5 km diameter in vertical cross section, but only 927 m in radial depth. Another factor to consider as the rising level of the center of the radar beam with distance. For this reason, it was decided to limit the study area to about 150 km where the beam's height of less than 3 km did not become an excessively important factor in a study with large samples. It should be noted that the terrain in south Florida is flat and does not exceed 10 m above sea level in the region. A convenient A convenient point of reference for the outer range was chosen to be the northeast corner of the FACE target area (Fig. 1), which is located 144 km from the radar. Radar data were considered, then, in the 31 to 144 km range from the radar. Within this range, the raw radar data consist of reflectivity values for regions that have horizontal areas ranging from about 1 km by 1 km at the closest range to 1 km by 5 km at the far-

thest range.
LIGHTWING DATA CHARACTERISTICS - In 1978, one of the Lightning Location and Protection, Inc. (LLP) direction finders was located south of the center of the target area, and the other was rear Clewiston on the north edge of the target area (Fig. 1). Each direction finder has a random error of ±0.87\* from the detected azi-This value has been determined from a series of ground truth studies of LLP sensors in various locations. Other non-random but apparently small errors may also have occurred for which no objective corrections were made. When the two direction finders were in the configuration used in 1978, the result is an error around each ground strike location that varies from less than 1 km in radius in a north-south region between the two detectors, to about 2 km in radius over the remainder of the area out to 144 km from the radar. The region of error is circular in most of the area but becomes more elliptical between the direction finders.

"Numbers in parentheses designate References at end of paper.

MATCHING OF RADAR AND LIGHTNING DATA - At the northeast corner of the target area at 144 km, the raw radar bin represents information over approximately a 1 by 5 km region, and the lightning direction finder data indicate flashes in a circular or elliptical area with a diameter of up to 4 km around the recorded flash loca-If a much larger area were used, the tion. width of the radar bin would exceed 5 km and the radar beam's center would be over 3 km above the ground; in addition, the random errors in the lightning data become larger. However, a larger area also increases the sample size. In conreducing the analysis range to closer trast. than 144 km decreases the sample size. And, the lightning data accuracy would not improve since the direction finders were located 80 to 130 km west and northwest of the radar. Some results will be presented to show how the relationships are affected if smaller ranges are used.

The raw radar data were recorded with positions that have been found in previous FACE studies to be somewhat in error in azimuth and gatelength from day to day. Corrections were obtained by matching lightning flashes with the radar data; different corrections were introduced and the one that maximized the match was The assumption was made that the best match occurred when the highest average reflectivity was associated with all of the lightning flashes for the day. Every flash was associated with a radar bin of the scan nearest in time. On most days, the azimuth correction was 2 to , and occasionally 6 to 8°, for the best matches, always in the same direction. gatelength was adjusted by a few meters per bin on most days; this represented a total of a few km in radial position when accumulated at the farthest range. These corrections are similar in magnitude to the results found by other FACE researchers when matching radar bins to rain gage and aircraft cloud penetaration data, although the daily values are not identical. There was a tendency for poorer matches when lightning activity was light.

#### RADAR CELLS RELATED TO LIGHTNING

INTRODUCTION - The individual convective elements of a thunderstorm have variable sizes. durations, intensities, and other parameters depending on the activity of the cloud. These individual convective elements correspond to radar echo cells. For these analyses, a radar echo cell has been defined as an area en-Compassing a maximum in reflectivity relative to the surrounding returns. Any time when there is a raw rader bin (or a group of contiguous bins) whose reflectivity is greater than all sur-rounding returns, a cell has been identified. The cell's area is found by examining the surrounding lower reflectivities out from the maximum until the reflectivity reaches a trough and starts to increase again, or until the boundary of the echo is reached. An echo may contain one or more cells.

RADAR CELLS AND LIGHTNING FLASHES DISTRIB-UTED BY REFLECTIVITY - The initial results to consider are comparisons of lightning and radar reflectivity distributions within these objectively-determined radar cells. Figure 2 shows frequency distributions of peak radar reflactivity for cells without lightning (dashed line) and with lightning (solid line) within their different areas. The distribution of cells without lightning has a peak frequency at 18 dBz, while the distribution for the cells with lightning present peaks sharply at 46 dBz. Cells with lightning do not have weak reflectivity very often, but usually have peak values above 36 dBz. The drop in the number of lightning-associated cells with high reflectivities is more dramatic than the rise from weaker returns. However, rather few cells have reflectivities above 50 dBz.

The preceding results have indicated a sharp difference between the reflectivity distributions of cells with and without flashes. These two curves can be combined by calculating the percentage of all cells at each reflectivity value that have lightning associated with them. Figure 3 shows such a result on another day in 1978 in terms of the probability of the presence of lightning associated with different peak reflectivities. There is a very low probability of a cell having lightning when its peak reflectivity is below 30 dBz, then the probability increases rapidly to over 50% at 50 dBz, followed by an abrupt decrease beyond 52 dBz. With regard to this Jecrease, it is not clear whether lightning activity in south Florida is less common for strong returns because lightning flashes are not associated with heavy rainfall, or the sample of one day has very few strong echoes and the result occurs by chance. Other rainy days in 1978 have been analyzed and show a rather similar distribution, so that the first option is more likely to be the reason.

KADAR ČELL CHARACTERISTICS RELATED TO LIGHTNING - The number of flashes per cell is shown in Fig. 4 to be rather invariant for cell reflectivities less than 44 dBz, then the number rapidly increases. This number of flashes is for the time of the radar sweep and 2.5 minutes on either side.

The frequency of lightning increases with the size of the radar cell rather steadily (Fig. 5). Very few of the large number of cells with areas under 50 km² have lightning associated with them, however, the percentage rises to over half when the cell is larger than 150 km².

A brief analysis of the nature of these radar cells on 16 August 1979 indicates that lightning was associated with only 0.2% of new cells. All other types of cells, consisting of mergers, splits, continuations, etc. had lightning over 4% of the time. These figures imply that lightning is associated with cells in a way that is dependent on duration, which will be explored later in more detail.

INTRODUCTION - The discussions of cell results in the previous section have shown welldefined relationships between lightning flashes and radar reflectivities in the same locations at individual times. The objective analysis of large numbers of cells, however, is very complex. For this reason, only one day has been considered for each study in the preceding section, and not much time variation has been taken into account. However, although the cell with variable area is a better measure of the convective element, a simpler method has been used to analyze a large sample of radar echoes for relationships between lightning and the adjacent

area surrounding the flash.

For this study of the reflectivity surrounding a flash, the term "local area" is used to distinguish it from the radar cell. Recall from earlier discussions that radar data are nonuniform with range, varying from 1 km by 1 km at the nearest distance to 1 km by 5 km at the farthest distance. The radial depth of the radar bin is fixed at 927 m. To equalize this effect, the "raw radar bins" were used to construct 1 km by 5 km "composite radar bins." number of raw bins that were used varied with range from the radar. The combination was chosen to attain an area as close to a 5 km The method involved a width as possible. decision about which of the following was closer to 5 km: 1) the individual raw radar bin, 2) the raw radar bin plus a pair of bins on either side, or 3) the bin plus two pairs of bins on either side. The reflectivity of the composite radar bin was calculated by averaging the values of the smaller raw radar data bins, including zeroes. The resolution of the reflectivity data is rendered much less range-dependent by this method, and is equivalent to that at 144 km from the radar.

To study the association of lightning with radar reflectivities, the 1 by 5 km composite radar bins were assembled into an area of 5 km by 5 km around the composite radar bin containing the flash. The radial distance from the flash to the edge of the "local area" is then between 2 and 3 km in most cases.

LOCAL AREAS AND LIGHTNING FLASHES DISTRIB-UTED BY REFLECTIVITY - When local areas are distributed by reflectivity, Fig. 6 shows a very similar result for 15 days compared to Fig. 2 for the radar cells of one day. These 15 days are all GO days from the FACE program when operations were conducted (2), and include mostly moderate-rainfall days. On the left is the distribution of all local areas regardless of lightning activity; the maximum percentage frequency occurs at 18 dBz. On the right is the distribution of reflectivities of the 6726 local areas which contained a flash. The most frequent reflectivity value of lightning-associated areas is at 46 dBz (13%), while there is also a maximum at 0 dBz on the far left side (15%).

The drop in the number of lightning-associated areas at higher reflectivities is quite sharp, as in Fig. 2 for cells. The same large difference is apparent between distributions because of the presence of a flash. In both distributions, the maximum reflectivity value among the 5 composite bins that make the local areas were considered. The local radar areas were considered in an overlapping mode, provided at one raw radar bin had nonzero reflectivity. A total of over one million values were used to calculate the distribution of all local areas containing an echo in Fig. 6 for 15 days in 1978. The radar scan was associated with flashes occurring in the 5 minutes following the scan.

Some of the lightning flashes coincided with local areas that had no reflectivity values in any bins. Figure 6 shows the frequency of echoless flashes to be 15% for all 15 days combined, however, the percentage varied from day to day. In Fig. 7, less than 10% misses were found on days with large lightning counts when radar echoes were presumably larger. Over 20% of the flashes were outside of echoes on other which tended to be on days with low lightning activity. It should be mentioned that over the 15 days, 85% of the lightning flashes are found in local areas with nonzero reflectivity, so that the analysis and matching pro-

cedures are working quite well.

The range dependency of the relationship betweeen lightning and reflectivity is shown in Fig. 8. Closer to the radar (solid line), the distribution of lightning-associated reflectivities peaks at 48 dBz, while farther out it peaks at 44 to 46 dBz. That is, the more distant echoes tended to be weaker, however the general shape of the distribution is maintained. The change in the distribution is not large, however, and indicates that the choice of the nominal 5 by 5 km area has minimized range dependency while allowing data to be combined over a rather broad area to increase the sample size.

In contrast, when raw radar bins are preserved ower a wide area, very significant range effects dominate the results (Fig. 9). These data consist of a raw radar bin, and its adjacent 8 raw radar bins, regardless of size. A lightning flash which is associated with any of the 9 bins is considered to be in the neighborhood of the central bin. Recall that analyses in Fig. 6 were made from 31 to 144 km (78 mmi); Fig. 9 considers that region in two parts plus another outer range section. On the right half of the diagram, from 31 nml (57 km) to 50 nml (93 km), flashes occurred most often at 46 dBz for these raw radar bins. At farther ranges, the distributions of radar bins with flashes shift to lower values and become rather flat. That is, close to the radar there is a peaked distribution, while farther out, flashes occurred rather evenly across a wide range of reflectivities. On the left half of the diagram, a peaked distribution of radar bins 4. E. A. Jacobsen and E. P. Krider, "Electrostatic Field Changes Produced by Florida Lightning." Journal of the Atmospheric Sciences, Vol. 33, 103-117, 1976.
5. J. M. Livingston and E. P. Krider, "Electric Fields Produced by Florida Thunderstorms." Journal of Geophysical Passanch Vol

Journal of Geophysical Research, Vol.

83, 385-401, 1978. 6. D. J. Jordan and M. A. Uman, "Variations of Light Intensity with Height and Time from Subsequent Return Strokes." Transactions of the American Geophysical Union, Vol. 61, 977, 1980.

R. E. Lopez, R. L. Holle and W. L. "Climatological Characteristics of Hiscox, Lightning over South Florida and Their Correlation with Radar Activity." Preprints of the International Conference on Lightning and Static

Electricity, Fort Worth, June 1983.

8. E. P. Krider, R. C. Noggle and M. A.

Uman, "A Gated, Wideband Magnetic Direction
Finder for Lightning Return Strokes." Journal

of Applied Meteorology, Vol. 15, 301-315, 1976.
9. E. P. Krider, R. C. Noggle, A. E. Pifer and D. L. Vance, "Lightning Direction Finding Systems for Forest Fire Detection." Bulletin of the American Meteorological Society, Vol. 61, 980-986, 1980.

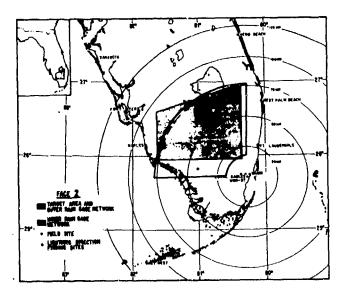


Fig. 1 - Location of analysis area for radarlightning studies is shown by the annulus with a dark outline to the northwest from 16 to 144 km away from the WSR-57 radar located in Coral Gables. Lightning direction finders in 1978 were positioned in the southern portion of the analysis region, and a short distance south of Clewiston

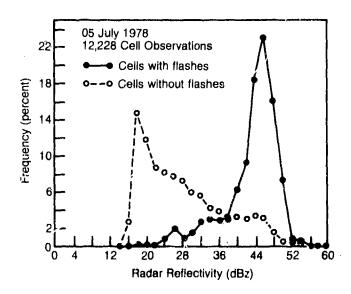


Fig. 2 - Distribution of radar cells on 5 July 1978 according to the maximum reflectivity (dBz) in the cell. Solid curve shows the distribution when cells had at least one flash in the area of the cell within 2 1/2 minutes of the radar scan, while the dashed plot shows the distribution without flashes

without flashes applies at all ranges, but the highest value steadily shifts to lower reflectivities. This represents a shift in the raw radar data with range and indicates the need to

take the distance bias into account.

PROBABILITY OF FLASHES DISTRIBUTED BY RE-FLECTIVITY - The probability of a local radar area having a flash is shown for these days in Fig. 10. The probabilities were computed as the ratio between the number of local areas with lightning in a given reflectivity range and the total number of local areas in that reflectivity range. Similar to the cell results (Fig. 3), there is a low frequency of flashes until the local area's maximum reflectivity exceeds 44 dBz. The probability decreases again above 50 dBz.

Cumulative percentages (Fig. 11) show that only 5% of the local radar areas are associated with 50% of the lightning, and those reflectivities are in excess of 40 dBz. It takes only 20% of the radar data (above 30 dBz) to account for nearly 70% of the lightning. In the upper right is seen a vertical line which represents the remaining 15% of the lightning flashes which are

rom a practical standpoint, the concentration of flashes at high reflectivities holds promise for a number of applications. In order to assess the lightning hazard, the stronger (but not the strongest) echoes are most important in south Florida. If a nowcast or forecast can be made of these echoes, then the lightning activity is also quantifiable. On a daily basis, the amount of echo over 30 or 40 dBz is a starting point to consider for lightning activ-

TIME VARIATIONS OF REFLECTIVITY RELATIVE TO FLASH - All of these local area results have been for time-coincident data; in this case, the radar scan was associated with flashes occurring in the 5 minutes following the scan. It is also interesting to consider the association between the flash and the radar reflectivity at the same fixed location before and after the flash. In Fig. 12, the average reflectivity in the local area (upper solid line) is indicated to be near its maximum value at or 5 minutes before the The average reflectivity at the flash location is much weaker when the flash locations are examined 15 or 20 minutes earlier, and 10 minutes or more later than the flash. The differences between reflectivities near the time of the flash are probably not important. In fact, when the average reflectivity is calculated with zero dBz values included, the average reflectivity has a peak at the time of the flash rather than 5 minutes earlier (Fig. 12). The lower line on Fig. 12 shows a minimum of 7% of the flashes without echoes at and 5 minutes after the time of the flash, and much higher frequencies earlier than the flash time. The asymmetry in echoless flashes could be explained by an increase in the size of thunderstorms after flashes, while they were small barore the

flashes. Since these results are for a fixed area at the location of the flash, the light-ning-producing storm's motion may affect the interpretation, as well as growth of the storm. For better time relationships, tracking radar cells is a more precise approach.

#### SUMMARY

The detailed analyses of large volumes of radar and lightning data from the summer of 1978 in south Florida have indicated strong relationships in space and time between several relevant They have been limited to WSR-57 parameters. base-scan radar data and cloud-to-ground lightning flashes. Quite similar conclusions were reached both with radar cells and local areas a few km around the flash. Namely, most lightning flashes are coincident with radar reflectivity peaks in the 40 to 50 dBz range, compared to the bulk of radar returns having weaker values. A strong decrease in likelihood of lightning was identified above 50 dBz. Lightning flashes are associated with the highest reflectivities and lowest frequencies of echoless local areas within 5 minutes of the flash. Also, larger cells had a higher probability of lightning. More extensive analyses of all of these features are planned on the radar cell scale with a view toward assessing the probabilities of flashes given the cell size and maximum cell reflectivity. When the age of a cell also is taken into account, it may be possible to nowcast the likelihoood of lightning as radar echos develop, grow, and evolve. The well-behaved nature of the Florida results also indicates that similar analyses should be pursued in very different locations to assess the extent to which these relationships are widely applicable.

ACKNOWLEDGEMENT - The authors gratefully recognize the contributions of Mr. Michael Maier, now of Lightning Location and Protection, Inc., of Tucson, Arizona for the design, installation and operation of the mapping system in south Florida during FACE and his advice and interest in the analysis of the data described in

this report.

#### REFERENCES

1. W. L. Woodley, "Precipitation Results from a Pyrotechnic Cumulus Seeding Experiment." Journal of Applied Meteorology, Vol. 9, 242-257, 1970.

2. W. L. Woodley, J. Jordan, A. Barnston, J. Simpson, R. Biondini and J. Flueck, "Rainfall Results of the Florida Area Cumulus Experiment." Journal of Applied Meteorology, Vol. 21, 139-164, 1982.

3. J. B. Cunning, R. L. Holle, P. T. Gannon and A. I. Watson, "Convective Evolution and Merger in the FACE Experimental Area: Mesoscale Convection and Boundary Layer Interactions." Journal of Applied Meteorology, Vol. 21, 953-977, 1982.

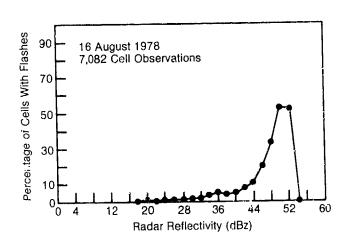


Fig. 3 - Percent of cells on 16 August 1978 with at least one lightning flash in the area of the cell within 2 1/2 minutes of the radar scan according to the maximum reflectivity (dBz) in the cell

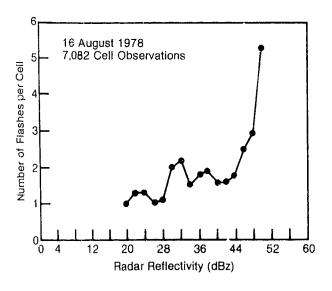


Fig. 4 - Number of lightning flashes per radar cell on 16 August 1978 in the cell area within 2 1/2 minutes of the radar scan according to the maximum reflectivity (dBz) in the cell

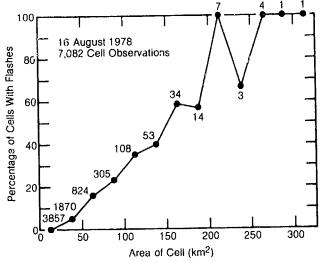
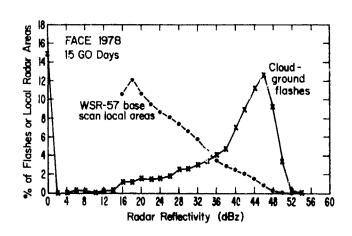


Fig. 5 - Percent of radar cells with lightning flashes in the cell area within 2 1/2 minutes of the radar scan according to the area  $(km^2)$  of the cell. Small numbers indicate the number of cells in each area increment of 25 km<sup>2</sup>



· 人名英格兰人名英格兰人名

Fig. 6 - Distribution of local areas on 15 operations (GO) days in FACE 1978 according to the maximum reflectivity (dBz) in the local area surrounding the lightning flash. Solid line shows distribution when local areas had at least one flash within 5 minutes after the radar scan, while the dashed plot shows the distribution of all local radar areas on all days

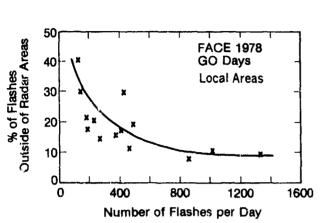


Fig. 7 - Percent of total flashes during a day which were located outside local radar reflectivity areas as a function of the total number of flashes per day for 14 FACE GO days

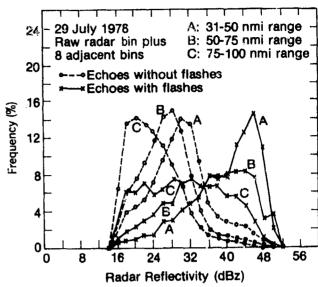


Fig. 9 - Distribution of reflectivity (dBz) of raw radar bins for three ranges relative to the radar (Fig. 1) on 29 July 1978. Distributions are divided into raw radar bins and their adjacent 8 bins with and without flashes for the 5 minutes after the radar scan

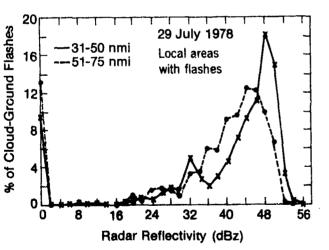


Fig. 8 - Distribution of local areas with flashes on 29 July 1978 according to the maximum reflectivity (dBz) in the local area surrounding the lightning flash within 5 minutes after the radar 5can. Distributions are shown for the inner half of the analysis area (solid line) relative to the radar (Fig. 1) from 31 to 50 nmi (57 to 93 km) and the outer half (dashed) from 51 to 75 nmi (93 to 139 km)

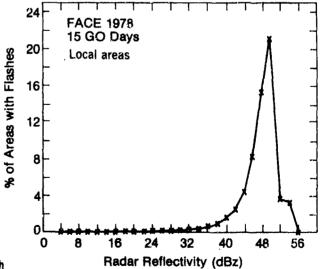


Fig. 10 - Percent of local areas on 15 FACE days having at least one lightning flash in the local area, within 5 minutes after the radar scen, according to the maximum reflectivity (dBz) in the local area surrounding the lightning flash

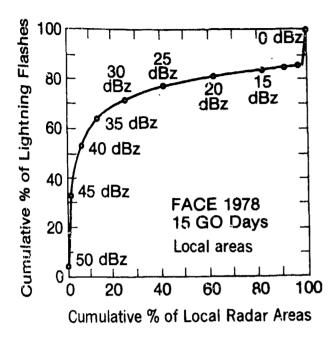


Fig. 11 - Cumulative percent of local areas with lightning flashes related to cumulative percent of local radar areas for the same data as shown in Fig. 10

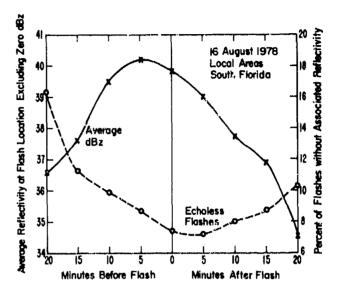


Fig. 12 - History of radar parameters at the location of each flash on 16 August 1978 before and after the flash (flash is at time 0). The average reflectivity (solid line) of local areas at the positions of all flashes is shown up to ± 20 minutes from the event and scaled on the left side. The percent of flashes without echoes (dashed line) is scaled on the right side

# AD P002173

 $\rightarrow$ 

CLIMATOLOGICAL CHARACTERISITCS OF LIGHTNING OVER SOUTH FLORIDA AND THEIR CORRELATION WITH RADAR ACTIVITY

Raul E. Lopez, Ronald L. Holle and William L. Hiscox

Weather Research Program
Environmental Research Laboratories
National Oceanic and Atmospheric Administration
Boulder, Colorado 80303

#### ABSTRACT

The analysis of lightning, radar, and sounding data for two summer months in south Florida has shown that there is a relationship between the degree of cloud-to-ground flash activity during the day and certain combinations of meteorological parameters detected early in the morning before significant convection develops. In general, it appears that clouds tend to be better flash producers (per unit area) under conditions of suppression of convection and light winds. As the atmosphere becomes disturbed, the clouds (although greater in numbers) tend to be less intense in their lightning activity.

FOR MANY APPLICATIONS, it is extremely important to have advance knowledge of the degree of lightning activity to be expected over a region in the next 12 to 24 hrs. Until now, there has been very little guidance to enable the meteorologist to predict lightning activity with any Recently, however, with significant accuracy. the development of reliable cloud-to-ground (C-G) lightning detectors, enough data are becoming available from some regions to identify the meteorological factors that determine the degree of lightning activity over a certain area and during a specified period of time. One such region has been south Florida. Extensive C-G lightning flash data were collected daily during July and August of 1978 using two direction finders. The data were collected as part of the Florida Area Cumulus Experiment (FACE). Simultaneous with the lightning observations, digitized radar information and atmospheric soundings were recorded.

The objective of this paper is to use those data sets from 1978 to identify the principal meteorological regimes that are associated with different degrees of C-G flash activity. The basic analysis strategy consists of using the FACE lightning and radar data to stratify the days by groups according to their degree of flash activity, and then employing the corresponding early morning soundings to determine the meteorological flow regimes that are typically present, and how they are associated with the different lightning groups.

#### DATA AND ANALYSIS PROCEDURES

LIGHTNING DATA - A description of FACE 1978 has been published elsewhere (1, 2, 3). An overview of that experiment is also included in a companion paper in these proceedings (4). The C-G lightning data were collected by two direction finders (DF) manufactured by Lightning Location and Protection, Inc. (LLP) (5, 6). The locations of the two DF are indicated in Fig. 1. During 1978 the two direction finders were aligned north to south in the middle of the Penninsula. The data from the direction finders were analyzed with a computer program that produces, by triangulation, point values of C-G flash location. The accuracy of these locations decreases with distance from the two antennas. Each direction finder has a random error of ±0.87° in azimuth. This value has been determined from a series of ground truth studies of LLP sensors in various locations and applies to the FACE direction finders. Other non-random errors may also have occurred for which we have no objective determinations. For the configuration used in 1978, the resultant error around each ground strike ranges from less than 1 km in radius in a north-south region between the two detectors, to about 2 km over the remainder of the area of study (see Fig. 1). The region of error around each strike location is circular in most of the area but becomes more elliptical in the region between the direction finders.

RADAR DATA - The radar information used in this study was obtained with a WSR-57 radar system located in Coral Gables, Florida (see Fig. 1). This radar had a wavelength of 10.53 cm. It had a two-degree conical beam and a gatelength of 927 m. The system was operated continuously from 0800 to 2000 EST during all the days of FACE except for a small amount of downtime due to malfunctions. A full 360° scan covering a range of about 200 km was recorded every 5 min. The WSR-57 was constrained by U.S. National Weather Service (NWS) operational requirements to operate at a low scanning angle; the antenna elevation was 0.5°. The data were digitized and recorded on magnetic tape. All days in July and August of 1978 for which data existed were used. Echoes in the northwestern quadrant covered by the radar were included in the analysis. This region extended from 31 to 144 km (16 to 75 nmi) from the radar (Fig. 1). Only lightning flashes located within this region were used. This area was selected as comprising the best radar data in terms of being free from ground clutter, and the most accurate flash locations.

A series of computer programs was designed to process and analyze the radar data. A detailed description of the data collection and processing methods has been published elsewhere (7). A principal result of those procedures was a set of time series of area covered by echoes at intervals of 5 min. These time series were the basic source of radar information used in this paper.

RADIOSONDE DATA - Radiosondes were released by the NMS at West Palm Beach. The soundings used were taken at 1200 UT (0700 EST). It was felt that a later sounding taken in the afternoon would reflect the changes in the atmospheric structure of the region produced by the convection itself, thus confusing the information about those environmental factors that are conducive to or attending the development of

<sup>\*</sup>Numbers in parentheses designate References at end of paper.

that convection. Use of morning soundings also allows forecasts to be made after relationships are established from past data. Data points were interpolated to every 50-mb interval.

#### DAILY VARIABILITY OF LIGHTNING ACTIVITY

INTRODUCTION - Time series were constructed of the total number of flashes over the region of study during 5 minute intervals. One such time series was prepared for every day in the sample. Figure 2 shows examples of the series for four representative days in 1978 for the period of 0800 to 2000 EST. This is the period when most of the flashes were detected. is a will range of activity among the different days, especially as it refers to the total number of flashes, the maximum number observed, the shape of the series, and its position in time. It would be desirable to be able to predict, based on conventional meteorological data, the characteristics of the expected diurnal cycle of lightning activity. The present study represents a first step to quantify the differences between the activity of the days and to investigate the corresponding differences in

atmospheric sounding parameters.
STRATIFICATION OF DAYS - In this first study it was deemed more important and tractable to investigate the conditions associated with the degree of activity rather than the timing or nature of the diurnal fluctuations. ingly, the maximum number of flashes during any 5 minute period (i.e., maximum 5 min flash rate) was used to classify the days as to their degree of lightning activity. The total number of flashes during the day was also considered, but it gave confusing results when days that had extensive activity during a short period of time were classified together with days that produced fewer flashes at any given time but for a longer period. In addition, due to the presence of randomly occurring data gaps, the number of days for which a maximum number of flashes in a 5 minute period can be obtained is greater than those for which the total number of flashes can

be computed. All days in July and August 1978 for which data existed were ordered from the smallest maximum number of flashes during any 5-minute period to the largest. Figure 3 shows how the 52 days are distributed in relation to each other. The figure shows pictorially the large variability in waily lightning activity that can exist in the region. Motice that some days are extremely quiet (a few flashes in the area) while others are fairly active (up to 86 flashes per 5 min). It is interesting to observe that 80% of the days have a maximum rate that is less than half that of the maximum of 86. Again, as is characteristic of convective phenomena, the majority of days are moderate in the production of flashes, although a few cases can be considerably active.

It is reasonable to infer that the number of flashes during a given period is proportional to the amount of clouds present in the same period. To the degree that that is true, the problem of forecasting maximum lightning activity over a region is reduced to forecasting maximum cloud cover. Figure 4, however, shows that the relationship between echo area and flash rate, although present to some extent, is not universal. The scatterplot of maximum flash rate versus the corresponding radar echo cover shows sufficient scatter to indicate that other effects, besides the amount of convection present, are important in determining the lightning activity. In order to eliminate the dependency on echo area, the maximum flash rate was divided by the corresponding echo area, giving an echo flash intensity figure. The frequency distribution of this new parameter is portrayed in Fig. 5. This distribution can be closely represented as a lognormal distribution. It points to the skewness of flash intensity and to the fact that only a small number of days have intense rates.

It is obviously hopeless to try to understand at this time the myriad factors and complex interactions of factors that specifically determine the degree of C-G flash activity found in any particular day. In this study the basic concern is with the principal meteorological factors and types of flow patterns that are associated with broad classes of flash activity. Accordingly, the new distribution was divided into quartiles, the first one, Q1, represents the 25% of days having lowest flash intensities, Q2, the next 25% more active days, and so on. represents the most active 25% of days. Table 1 shows the average characteristics of each quartile. As mentioned before, there is a large range of flash intensity across these quartiles. In the next sections the sounding data are analyzed to determine which are the principal atmospheric flow regimes present in the region, and how they are associated with the different lightning intensity quartiles.

#### TYPICAL FLOW REGIMES IN SOUTH FLORIDA

A previous study (8) has shown that the degree of development of the diurnal convective activity in south Florida is determined to a large extent by the type of synoptic flow pattern present during the day. It is reasonable to expect that the different flow regimes are also reflected in the degree of lightning activity. The nature of the flow regime is important becasue it determines the type of air mass (i.e., the atmospheric thermodynamic properties) in which the convective clouds are developing in response to the forcing produced by local sea and lake breeze circulations. In addition, the different flow patterns can bring dynamic influences in the form of enhanced forcing or suppression of convection.

In south Florida during the summer, the principal synoptic flow regimes are determined by three main features:

 the position of the Atlantic High in relation to the peninsula

2. the passage of tropical systems

 the passage of mid-latitude perturbations.

In order to describe the overall flow in the region it is convenient to examine the entire wind direction profile. The use of one level or a shallow layer to describe the wind flow can lead to confusing results in view of the often layered nature of the regional circulations and the rapid changes in direction with height. The early morning West Palm Beach soundings used in this analysis were taken close to the area of study. They should be characteristic of the large-scale flow in the region during the development of convective and lightning activity, provided synoptic conditions to not change drastically during the next several hours.

All of the wind direction profiles corre-

All of the wind direction profiles corresponding to the days for which lightning and radar data existed were examined (45 profiles). The individual profiles could be classified (independently of the lightning intensity) into four distinct types. Figure 6 shows the mean wind direction profile for each of the four types. They can be described as follows:

1. Deep easterlies: ESE winds predominate in a deep layer from the surface to 450 mb with very little wind directional shear. Above that level the winds turn gradually to NE.

2. Low level southerlies: SSW winds present in the layer from the surface to 650 mb. Beyond that level the winds turn SE and finally NE above 300 mb.

3. Mid-level westerlies: SSN winds very close to the surface changing to WSN/WNN in the layer 850 - 400 mb. Above that level the winds turn into a northerly direction, finally becoming NE as in all the other profiles.

4. Mid-level northerlies: .NNE winds in a layer from 700 to 500 mb, with sheared layers above and below. In the lower part winds change from SW at the surface to NNE at 700 mb. In the upper layer the winds change from NNE to W, S and NE above 200 mb.

It is shown in the next section that each of these wind profiles corresponds to a different synoptic flow regime to which are associated particular thermodynamic characteristics of the atmosphere. It is also shown how the different atmospheric properties are related to different degrees of convective and lightning activity.

#### METEOROLOGICAL CONDITIONS AND LIGHTNING ACTIVITY

Each quartile of flash intensity was exemined to determine the typical wind profile predominant during those days. It was apparent

that each quartile did not correspond uniquely to a particular wind profile. The same type of profile could be found present among the days of widely different quartiles and one quartile could contain different wind profiles. However, when the soundings were averaged together by quartiles, within wind profile types, characteristic differences were found that gave a consistent picture of the factors determining different degrees of lightning activity.

EASTERLY WIND PROFILE - Figures 7 and 8 contain the average mixing ratio and temperature difference profiles by quartiles for those days having an easterly wind profile. The differences were taken from the mean sounding for all Figure 9 shows the corresponding wind days. speed graph. In all quartiles considerable drying and warming (compared to the means for all days) is present below 500 mb. This is typical of the easterly flow regime and speaks of subsidence and suppression of convection due to the presence of a high-pressure cell in the western branch at the subtropical high north of the area of study (8). Table 2 shows that the area covered by echoes at time of maximum flash rate was, in the mean, smaller during easterly wind days than in other occa: jons when a different wind regime was present.

Q4 days show the deepest and most widespread suppression effects. These days, however, show the most intense lightning activity. Actually, very little deep convection develops as indicated in Table 2; the maximum-rate echo cover has a mean of only  $1.3 \times 10^3 \ km^2$  for those days, which is the smallest for any one group. The wind speed, on the other hand, is considerably lower for that quartile (Fig. 9) than for any other quartile, amounting to only about 4 m/s through most of the layer below 500 mb. Under these conditions of suppression and low wind speeds, the lower atmosphere can become very unstable and produce, after a long period continued surface insolation and soil moisture evaporation, very vigorous isolated thunderstorms. That this is the case is indicated in Table 2; the maximum number of light-ning flashes per 5 min is very high (a mean 5 min rate of 29.6 flashes) in spite of the small amount of echo area. This combination ranks 04 easterly days as the most intensively active of all categories, with 27.9 flashes per 103 km<sup>2</sup>. It is interesting to note that all of the Q4 (or the 25% most active) days have an easterly flow of the type described.

The very inactive days (Q1) also show the signs of subsidence in their mean sounding. Although not as widespread as in the case of Q4 days, the warming and drying are as large or larger, presenting a significant barrier to the development of deep penetrative convection. This condition is reflected in Table 2, where the maximum-rate echo cover has a mean value comparable to the dry days of Q4. The maximum flash rate (and consequently the area intensity) however, is an order of magnitude smaller. The

reason for this dramatic difference is probably linked to the mean wind speed profile of those days (Fig. 9). The winds below 600 mb are about 2 times as fast in Q1 as in Q4. Thus, the advantage of the Q4 days, of accumulating convective energy in the lower layers and producing intense but isolated thunderstorms, is not present in Q1 days.

The intermediately active days of Q2 and Q3 are also intermediate in thermal conditions. The effects of subsidence are not as widespread or as large as in the active or inactive days. Without as severe suppression, echoes are more frequently observed (42% more area at time of maximum rate). The less extensive and weaker suppression should also result in deeper and more active clouds than in the case of Q1. Noth of these factors (increased area cover and deeper clouds) are probably the reason for the relatively large maximum flash rate during those days (Table 2). The flash intensity of the clouds is also higher than the very suppressed days of O1 but is only 40% that of the O4 days.

days of Q1 but is only 40% that of the Q4 days.

In general, the days characterized by a deep easterly flow are suppressed, and the more suppressed the day is (as reflected in the warming and drying of the lower atmosphere), the smaller are the maximum flash rate and the intensity of flashes per unit area. However, in the case of strong suppression and when the wind speed in the lower layers is small, a few very intense isolated thunderstorms are to be expected which can produce a large amount of flashes.

SOUTHERLY WIND PROFILE - This type of wind regime in south Florida is associated with moist tropical air masses coming from the Caribbean or Gulf of Mexico (8). In many cases tropical disturbances are experienced. This wind regime is represented among 3 of the quartiles of lightning intensity.

Figures 10 and 11 contain the mean mixing ratio and temperature difference profiles for the entire group of 10 southerly wind days. The temperature difference curve indicates warming in the upper half of the troposphere compared to the mean of all days. That condition is typically associated with warm core tropical disturbances. The moisture difference is not particularly different from the mean, except for an indication of some excess humidity around 600 mb. The echo cover of 2.8 10 km² associated with the maximum flash rate is rather large in the mean (Table 2).

The individual soundings (not shown) indicate that Q1 (the least intense) days have the largest warming in the upper levels and also the largest echo area cover (Table 2). Q2 days have a smaller warming (indicating less disturbed days) and this is reflected in a smaller echo cover. The 2 days of Q3, however, show a sounding that is 1 to 1.5°C cooler than the mean below 500 mb. That condition would preclude the development of much convection as is reflected in the low echo cover for that quartile (1.4

compared to 2.8 and 3.3 x  $10^3$  km² for Q2 and Q3). The maximum flash rate, however, is roughly the same for all quartiles. Therefore, by unit area, the number of flashes is much higher (Table 2) for the days with the smaller echo cover. It is important to smaller echo q3 days have 50% slower winds below 850 mb than the other two quartiles.

Again we have the interesting result that clouds tend to be better flash producers per unit arez under conditions of suppression of convection and light winds. As the atmosphere becomes disturbed, more clouds can develop but they tend to be less intense in their lightning

activity MID-LEVEL WESTERLIES WIND PROFILE - Eleven days showed wind profiles that were characterized by westerly winds in the layer from 850 to 400 mb (Fig. 6). Aloft, the winds returned to the typical northeasterlies characteristic of the summer in south Florida. Below 850 mb the winds tended to come from the south. These days have the largest echo cover values of all groups (Table 2). The temperature difference profile (Fig. 12) shows cooling in the layer from 450 to 750 mb and warming aloft compared to the mean sounding of all days. The mixing ratio difference (Fig. 13) indicates moister-than-average conditions in the same middle layer. conditions are indicative of large-scale accent in the middle of the atmosphere caused by upperlevel westerly disturbances. In south Florida during the summer, it is frequently observed that short waves in the westerlies produce disturbed conditions which result in enhanced precipitation over the region (8).

Not only are these disturbed days characterized by high precipitation, but also by the production of a large number of flashes. As a group (Table 2) they produce the largest number of flashes in any 5-minute interval in the region (39.5). This large activity is probably due to both the increased total amount of convection and the dynamic and thermodynamic facilitation of deep convection produced by the synoptic disturbances usually present during this type of day. In terms of the maximum intensity of lightning, however, these days rank mediocre, showing in the average only 11 flashes per 10<sup>3</sup> km<sup>2</sup> of echo (Table 2).

できたないのでは、

When these days are considered individually, considerable differences in total activity and intensity are noted. Table 2 shows that the most disturbed days, in the sense of higher echo cover, have the smallest flash production and therefore are the least intense in terms of flashes per unit area (Q1 days). As the area covered with echoes diminisies, the maximum 5-minute total of flashes increases together with the intensity (Q2 and Q3 days). The individual soundings tend to indicate that the area cover is related to the degree of thermal perturbation. Figure 14 shows the mixing ratio profiles for the different quartiles. It can be seen that the days with more widespread rain but

least flash activity, i.e. Q1 days, have a moisture excess of up to 3 g/kg compared to the mean of all days. As the moisture excess diminishes in magnitude and spread (Q2 and Q3), so does the echo cover, while the flash activity increases. Thus, it appears that as in the case of southerly winds, the least disturbed days

produce the most active clouds.

MID-LEVEL NORTHERLY WIND PROFILE - Two days in the sample exhibited a strong sheared profile of wind direction: from southerlies in the low levels, to easterlies and then northerlies in the middle, to wasterlies and then southerlies aloft (Fig. 6). One way in which that pattern of wind directions could result is by having the southwesterly branch of an upper trough over the region with a cyclonic circulation in the middle levels. The temperature difference profile (Fig. 15) shows a remarkably cool region on those days from 750 to 150 mb. A difference of -2.1°C is observed at 650 mb decreasing to -0.75°C at 200 mb. A moist layer is also present from 600 to 800 mb, reaching a maximum difference of more than 2 g/kg (Fig. 16). Table 2 shows that in terms of echo cover those days are mildly disturbed. They show a moderate maximum flash rate (17.5 per 5-min) and a corresponding medium intensity of 10.3 flashes per  $10^3~\rm km^2$ .

OYERALL CHARACTERISTICS OF THE SAMPLE - Three principal groups of days emerge from the sample: suppressed, tropically-influenced, and mid-latitude influenced. The suppressed regime typically consists of days with deep easterly winds and indications of large-scale subsidence. The area covered by echoes at the time of the maximum lightning rate is very small indicating a scanty distribution of convection. The maximum 5-min flash rate and area intensity can be very low, very high, or intermediate depending of the degree of suppression and the speed of

the low-level winds.

The tropically-influenced days generally have winds with a marked southerly component in the lower half of the troposphere. Moist unstable air normally accompanies this flow and tropical disturbances may occur. The area covered with echoes can be considerable depending on the degree of disturbance of the day. The number of flashes per unit echo area is moderately large for the least disturbed days and becomes very small as the echo cover increases.

Days influenced by mid-latitude flows tend to be greatly disturbed, with large echo covers and cool and moist layers at middle levels of the atmosphere. The maximum 5-min flash rates can be rather high, but per unit echo area, the intensity tends to range from moderate to very small as the echo area increases.

### CONCLUSIONS AND OUTLOOK

The analysis of C-G flash data from two summer months in south Florida has shown that there is a considerable variability from day to

day in terms of flash rates and flash intensity (by echo area). This variability is not necessarily related to similar fluctuations in shower area.

However, relationships exist between the daily flash activity and certain combinations of meteorological parameters detected early in the morning before significant convection develops. In general, it appears that clouds tend to be better flash producers (per unit area) under conditions of suppression of convection and light winds. As the atmosphere becomes disturbed, however, more clouds can develop but they tend to be less intense in their lightning activity. A detailed analysis of the sounding data shows that four principal wind flow regimes are typical of south Florida during the summer. Within each regime variations in the degree of convection enhancement or suppression provide the different thermal and dynamic settings that appear to be associated with the different degrees of flash activity.

The present sample is relatively small in view of the large observed variability of lightning activity and flow regimes. Therefore, the establishment of quantitative relationships between different atmospheric parameters and C-G flash activity is presently not warranted. It is hoped, however, that the future analysis of the data from the other available FACE year (1980) will increase the sample size to where multiple correlation analysis could provide useful prediction algorithms. Meanwhile, the results of this study provide insights into the

problem of lightning warnings.

It is the intention of the authors to also repeat these analyzes with data from other climatical regions. Although the same results are not expected, similar basic principles could emerge and help develop a unified understanding of lightning in its relationship to meteorological conditions.

Lastly, this understanding probably cannot be reached without attacking the problem from different scales and studying their interrelationships. Toward that end a study of the relationships between C-G flashes and radar echoes has been started and is reported elsewhere in this Proceedings (4).

### **ACKNOWLEDGEMENTS**

The authors want to express their appreciation to Mr. Michael Maier of LLP for his efforts and foresight in establishing the FACE direction finder network and designing the lightning studies program. His early analyses and software development have also simplified the authors' work considerably. The authors' appreciation is also extended to Mr. David Blanchard of NOAA for his assistance in the processing of the radar data.

### REFERENCES

- 1. W. L. Woodley and R. I. Sax, "The Flor-ida Area Cumulus Experiment: Rationale, Design, Procedures, Results, and Future Course." KOAA Technical Report, ERL 354 WMPO-6, 204 pp, 1976. Available from the Weather Research Program, NOAA, ERL, 325 Broadway, Boulder, Colorado, 80303.
- 2. W. L. Woodley, J. Jordan, A. Barnston, J. Simpson, R. Biondini and J. Flueck, "Rainfall Results of the Florida Area Cumulus Experiment." Journal of Applied Meteorology, Vol.21, 139-164, 1982.
- 3. Cumulus Group Staff, "1978 Florida Area Cumulus Experiment (FACE): Operational Summary and Data Inventory." NOAA Technical Memorandum, ERL NHEML-4, 262 pp, May 1979. Available from the Weather Research Program, ERL, NOAA, 325 Broadway, Boulder, Colorado, 80303.
- 4. R. L. Holle, R. E. Lopez and W. L. Hiscox, "Relationships Between Lightning Occurrences and Radar Echo Characteristics in South Florida." Proc. International Aerospace and Ground Conference on Lightning and Statistic Electricity. June 21-23, 1983. Fort Worth.
- Ground Conference on Lightning and Statistic Electricity, June 21-23, 1983, Fort Worth.

  5. E. P. Krider, R. C. Noggle and M. A. Uman, "A Gated, Wideband Magnetic Direction Finder for Lightning Return Strokes." Journal of Applied Meteorology, Vol. 15, 301-315, 1976.
- of Applied Meteorology, Vol. 15, 301-315, 1976.
  6. E. P. Krider, R. C. Noggle, A. E. Pifer and D. L. Vance, "Lightning Direction Finding Systems for Forest Fire Detection." Bulletin of the American Meteorological Society, Vol. 61, 980-986, 1980.
- 7. R. E. Lopez, D. O. Blanchard, D. Rosenfeld, M. J. Casey, W. L. Hiscox, "FACE-2 Data Reductions and Analyses (Prior to Disclosure of the Treatment Decisions): Part II, S- and C-Band Radar Observations in Support of FACE-2." NOAA Technical Memorandum, ERL, OWRM-7, U.S Department of Commerce, NOAA, Boulder, Colorado, 80303, 267 pp, 1981.
- 8. R. E. Lopez, P. T. Gannon, D. O. Blanchard and C. C. Balch, "Synoptic and Regional Circulation Parameters Associated with the Degree of Convective Shower Activity in South Florida." Submitted to Monthly Weather Review, 1983.

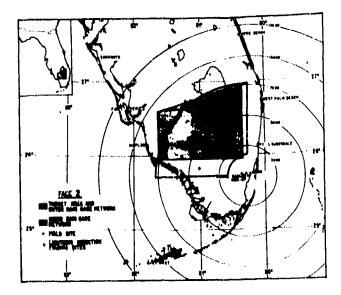


Fig. 1 - Map of south Florida showing region of study (heavy outline), FACE target area (stippled) and the positions of the lightning direction finding sites (diamonds). Range markers refer to the WSR-57 radar located in Coral Gables

Table 2. Flash Characteristics of the Different Flow Regimes as a Whole and by Intensity Quartiles.

		Easterlies	Southerlies	Mid-level Westerlies	Mid-level Northeriles
Number of Days Maximum 5 min Flash Rate		20 21.0	10 19.9	11 39.5	2 17.5
	o Area at Ti <b>me of Max.</b> Rate (10 <sup>3</sup> km²) sh Intensity (per 10 <sup>3</sup> km²)	1.4 17.7	2.8 8.1	3.9 11.0	1.7 10.3
Q1		The transmission of the second se			
	No. Days	5 4,4	5 19.4	1 29.0	0
	Max. Rate Echo Area	1.3	3.3	5.9	m
	Intensity	4.2	5.9	4.9	
Q2					**************************************
	No. Days	2	3	4	2
	Max. Rate Echo Area	17.0 1.8	22.3 2.8	39.8 4.1	17.5 1.7
	Intensity	9.7	8.2	9.6	19.3
Q3	er men fan en flygenn pad fri er geen men en de fan beste fan de fan			<del>,</del>	
,	No. Days	3	2	6	0
	Max. Rate.	22.7 1.9	17.5 1.4	41.0 3.4	
	Echo Area Intensity	11.5	13.5	13.0	
04		tin yangi dagir in sagati menili sagatan da da			· · · · · · · · · · · · · · · · · · ·
•	No. Days	10	0	0	0
	Max. Rate	29.6 1.3		m <b>-</b>	300, 164
	Echo Area Intensity	27.9	~~	~-	ter 44

Table 1. Average Characteristics of Days by Quartiles of Flash Intensity

Quartile	Maximum 5-min flash rates	Corresponding area covered with echoes (10 <sup>3</sup> km <sup>2</sup> )	Number of flashes per unit area at time of maximum activity
1	12.6	2.48	5.1
2	25.3	2.73	9.4
ា	31.7	2.62	12.7
4	27.2	1.15	27.1

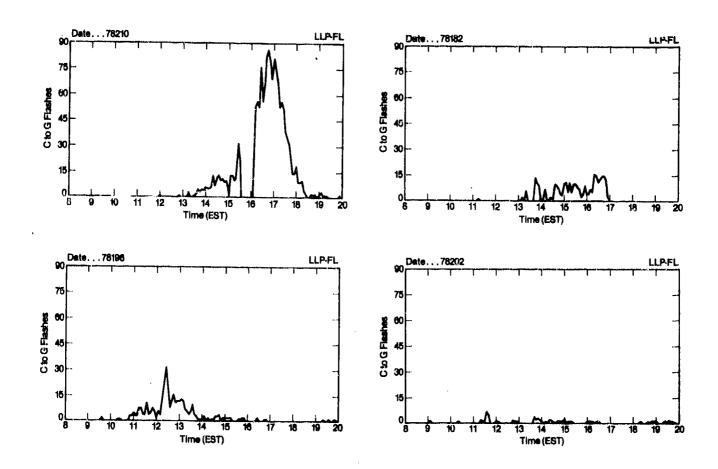


Fig. 2 - Time series of  $5~\rm min~C\text{-}G$  flash rates for the period 0800 to 2000 EST for four typical days in FACE

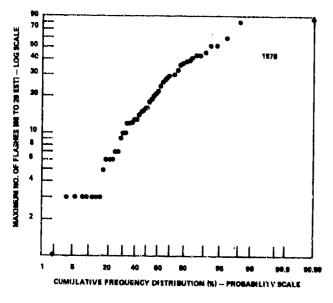


Fig. 3 - Cumulative frequency distribution of 53 daily values of 5 min flash rates in logarithmic/probability coordinates

### RADAR AREA COVERAGE - 10<sup>3</sup>km<sup>2</sup>

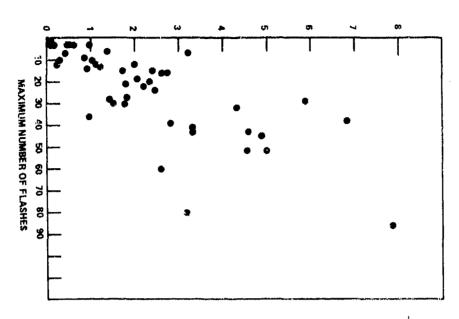


Fig. 4 - Scattergram of the daily values of maximum 5 min flash rate versus the area covered by echoes at the time of the maximum

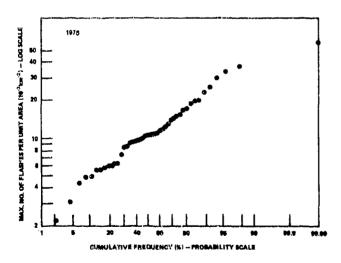


Fig. 5 - Cumulative frequency distribution of the daily values of maximum C-G flash intensity in logarithmic/probability coordinates

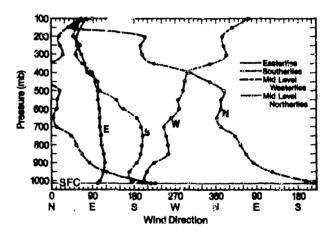


Fig. 6 - Typical wind direction profiles present in the sample of 43 days

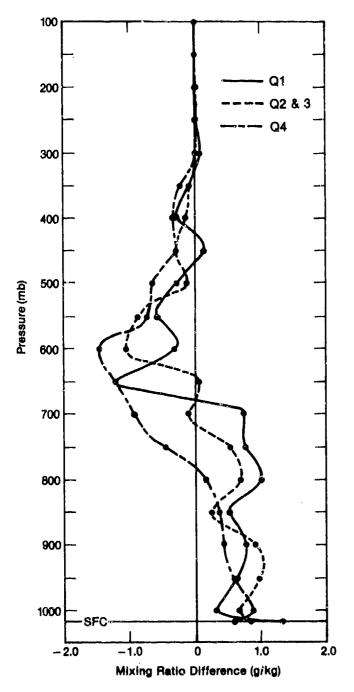


Fig. 7 - Mean vertical profile of mixing-ratio difference for those days having an easterly wind profile by flash-intensity quartiles. The mean sounding for all days in the sample has been used as reference

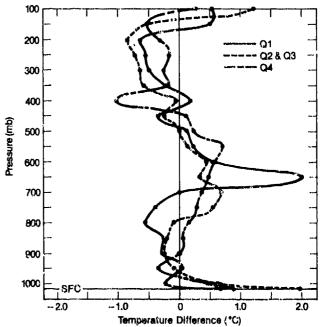


Fig. 8 - Mean vertical profile of temperature difference for those days having an easterly wind profile by flash-intensity quartities. The mean sounding for all days in the sample has been used as reference

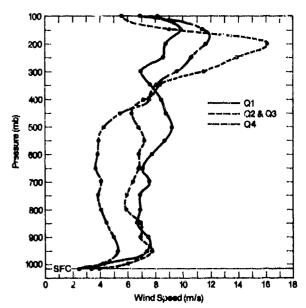


Fig. 9 - Mean vertical profile of wind speed for those days having an easterly wind profile by flash-intensity quartiles

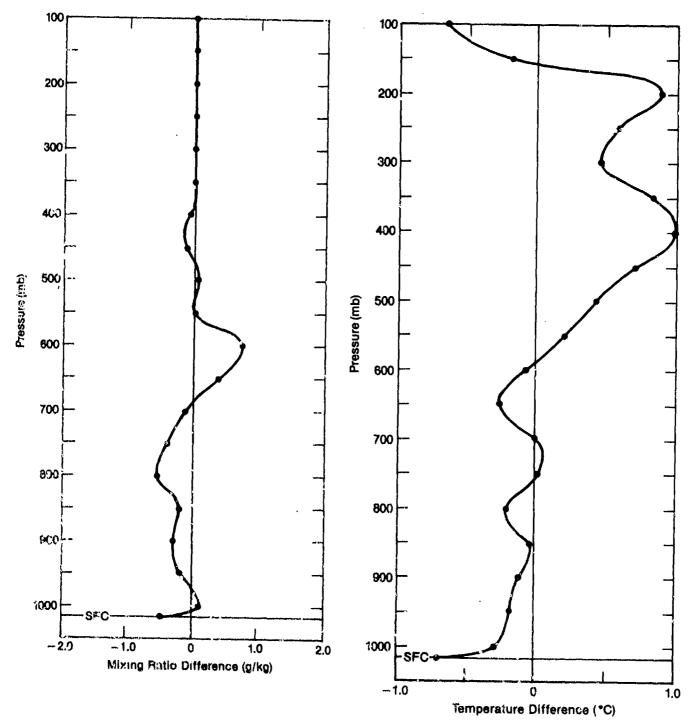


Fig. 10 - Mean vertical profile of mixing-ratic difference for those days having a southerly wind profile. The mean sounding for all days in the sample has been used as reference

Fig. 11 - Mean vertical profile of temperature difference for those days having a southerly wind profile. The mean sounding for all days in the sample has been used as reference

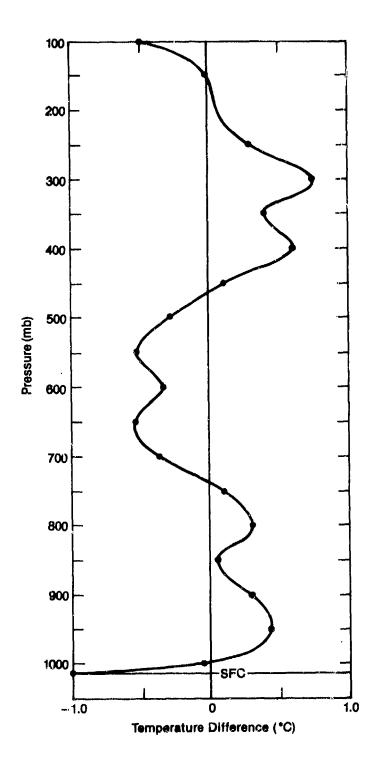


Fig. 12 - Mean vertical profile of temperature for those days having a mid-level westerlies wind profile. The mean sounding for all days in the sample has been used as reference

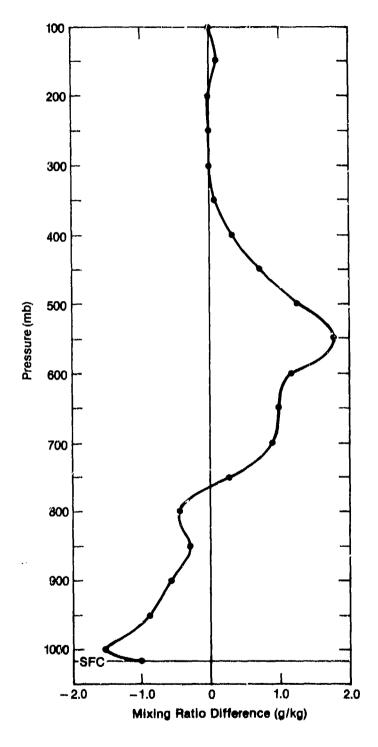


Fig. 13 - Mean vertical profile of mixing-ratio difference for those days having a mid-level westerlies wind profile. The mean sounding for all days in the sample has been used as reference

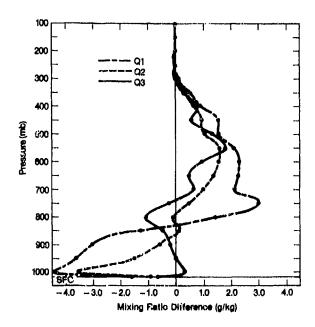


Fig. 14 - Mean vertical profile of mixing-ratio difference by quartiles for those days having a mid-level westerlies wind profile. The mean sounding for all days in the sumple has been used as reference

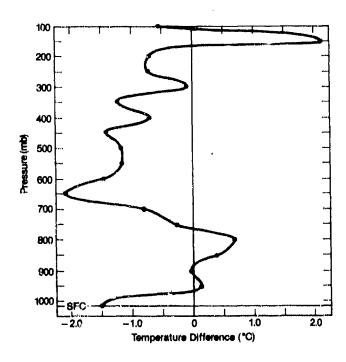


Fig. 15 - Mean vertical profile of temperature for those days having a mid-level northerlies wind profile. The mean sounding for all days in the sample has been used as reference

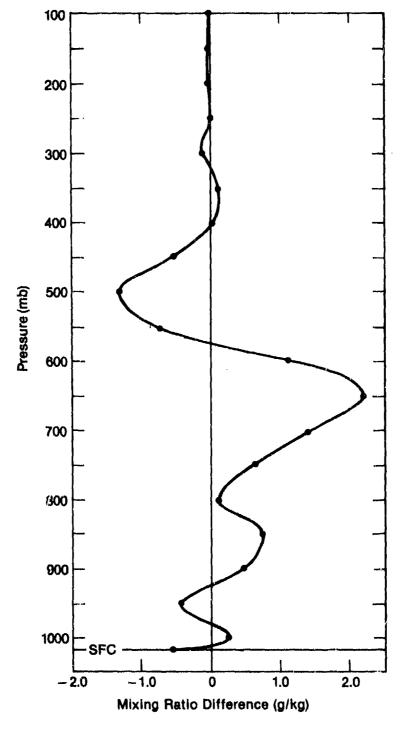


Fig. 16 - Mean vertical profile of mixing-ratio difference for those days having a mid-level northerlies wind profile. The mean sounding for all days in the sample has been used as reference



# AD P002174

MODELLING OF DIRECT-STRIKE LIGHTNING COUPLING BY A TRANSFER FUNCTION TECHNIQUE

D. T. Auckland and R. F. Wallenberg Syracuse Research Corporation, Syracuse, New York J. A. Rirken Naval Air Systems Command, Washington, D. C.

ABSTRACT

A transfer function approach is applied to the problem of lightning coupling into internal aircraft avionic circuits. This approach allows a systematic procedure for determining transient levels induced on interior aircraft circuits due to exterior interference fields such as those caused by nearby or direct-strike lightning. Unique in the approach used here is the use of a triangular patch model for the exterior surface of the aircraft with all points of entry (POEs) closed. A moment method procedure is then used to find the "short circuit" skin current in the frequency domain. This current interacts with all the POEs, described by either measured or theoretically calculated transfer functions, in a secondary interaction problem to create interior penetrating fields. These interior fields are used to derive distributed voltage and current sources which excite a transmission line model of a wire harness or cable bundle. Further levels of coupling are indicated along with their concomitant transfer functions.

### INTRODUCTION

THE GENERAL PROBLEM of analytically determining the susceptibility of interior aircraft avionics circuitry to upset or damage caused by an external electromagnetic threat is inherently complicated. To facilitate the analysis, two principle assumptions concerning the electromagnetic coupling phenomenon are made at the outset:

Linearity of material media

Interaction level decoupling
The meaning of the first assumption is obvious and test results show that it is generally valid for bulk cable current responses. The second assumption means that the aircraft has no effect on the source, the interior compartments have no effect on the external skin currents, and the interior circuits have no effect on the interior fields. It is easy to construct pathological cases for which the second assumption is theoretically invalid. Measured results, however, indicate that for a great many cases, it is a reasonable assumption.

Figure 1 illustrates a marrix of possible interaction levels whore, ar each level, a source interacts with a characteristic to produce a result. Further simplifying assumptions concerning the threat, the external physical detail of the aircraft, and the interior detail of the circuit in question must still be made in order to make the problem tractable. Errors introduced at each characteristic model level combine to cast accumulative uncertainty at each successive result level. Hopefully, careful comparison between computations and measured results will aid in refining characteristic models and reducing result error.

Using the first two assumptions, and working in the frequency domain, one may express the results of level D in Fig.1 by the following equations:

where

V<sub>B</sub>(f), I<sub>B</sub>(f) = Voltage and current transfer function at input of susceptible device (avionics box)

D(f) = Threat driving function

TAC(f) = Band-limited approximation to impulse response of aircraft

T<sub>POE</sub>(f) = Point-of-entry (POE) transtransfer function Z<sub>st</sub> = Material shielding transfer impedance Y<sub>4</sub> = Joint admittance

 $T_C(f)$  = Transfer functions accounting for compartment detail  $T_C^V$ ,  $T_C^{I}$ 

T<sub>T</sub>(f) = Transmission line coupling transfer function including cable shielding

Tp(f) = Avionice box protection function including penetration and circuit protection functions

juxtaposition of functions is illustrated pictorially in Fig. 2. Further detail concerning the above transfer function approach to electromagnetic coupling applied aircraft is given in [1]\* and [2]. of some of the Examples above characteristic transfer functions illustrated pictorially in Fig. 2.

DESCRIPTION OF THE METHOD

The double exponential time function

$$D(t) = A(e^{-\alpha t} - e^{-\beta t}) \tag{2}$$

is often used to model lightning waveforms [3] where the parameters  $\alpha$  and  $\beta$  may be adjusted to change the rise time  $1/\beta$  and fall time  $1/\alpha$  of the lightning raturn stroke. This simple double exponential model is assumed to sufficiently characterize the behavior of the current in

<sup>\*</sup>Mumbers in brackets indicate references at end of paper.

the lightning channel. In this model, the lightning attachment to the aircraft is well underway and the source of the channel is treated as a very high impedance current generator so that the aircraft has no loading effect on the channel.

When a conducting aircraft becomes part of the path of a lightning channel current, a large charge displacement takes place at certain "junction" points on the sircraft where the channel enters and exits. These points are deemed "entry" and "exit" points, where the conventional reference direction of current is implied to denote charge transfer. Here we assume that the entry and exit points are given and that they coincide with nodes in the triangular surface patch model [4, 5, and 6] of the aircraft skin. This will, in fact, be the case when modelling an experimental setup where current injection points are well defined [7]. Further details concerning the computation of direct strike skin currents may be found in [6] and details concerning direct strike test methods may be found in [8, 9, and 10] for operational aircraft.

A widely used and readily available data base which models sircraft skin by surface patches is the so-called NASTRAN data base [11]. An example of this is shown in Fig. 3 for the Black Hawk helicopter. In order to solve for the skin currents by the method of moments, a reduced data base consisting of triangular surface patches is created. Examples of these are shown in Figs. 4 through 7 for the Black Hawk helicopter and F-14 fighter aircraft. Here we have picked various direct-strike entry and exit points and pictorially represented the normalised 1 MHz component of the direct strike skin current density distribution. Vectors are drawn at the centroid of each visible triangular face to indicate the direction of  $Re\{\underline{J}_{\mathbf{g}}\}$ for a particular wt, where the skin current phasor,  $\underline{J}_{\mathbf{S}}$ , is found at each centroid from the coefficients of triangular patch expension at adjacent edges. For the pictures shown here, of was taken to be sero. Current magnitude information may be obtained from Fig. 5 and 7 where numbers from 0 to 9 are printed on each triangular face to indicate the magnitude of the current at that face scaled relative to the maximum current.

At level B of the interaction table the skin currents  $\underline{J}_8$  and charges  $\rho_8$ , which are obtained from  $\underline{J}_8$  by the equation of continuity, drive a model for the particular POE under consideration. This may be a composite avionics bay door, or a joint or

seam in the aircraft skin. For each case, we relate internal sources  $\underline{J}^{int}$ ,  $\underline{M}^{int}$  to  $\underline{J}_{e}$  by:

\* Joints - joint admittance Y4

$$\underline{\mathbf{M}}^{\text{int}} = \mathbf{Y}_1^{-1} \underline{\mathbf{J}}_{\mathbf{S}} \tag{3}$$

 $^{\circ}$  Composite Panels - transfer impedance  $Z_{t}$ 

$$\underline{\mathbf{M}}^{\mathrm{int}} = \mathbf{Z}_{+} \underline{\mathbf{J}}_{\mathbf{S}} \tag{4}$$

 $T_{POE}(f)$  is thus defined by  $Z_t$  or  $Y_j^{-1}$  depending on the POE under consideration. The effects of more than one POE are linearly superposed.

The interior sources radiate in the presence of an interior compartment to produce the interior fields Eint and Hint. The transfer functions TC and TC account for the effect of the compartment detail. An example of the effects of the compartment transfer functions is shown in Fig. 8 where a two-dimensional field mapping of the F-14 cockpit is illustrated for a nose-tail strike.

At successive levels of interaction, the complexity of the problem can exponentially increase if one tries to accurately model the excitation of convoluted masses of cable bundles. Here we assume that a bundle of wires routed from one box to mother within the penetrated compartment of interest may be modeled by a transmission line where a single TEM mode is assumed. The interior fields are used to determine distributed voltage and current excitations along the line so that we may write

$$\begin{cases} v_{\mathbf{g}}(\mathbf{f}) \\ v_{\mathbf{g}}(\mathbf{f}) \end{cases} - \int_{\mathbf{g}=0}^{\mathbf{L}} \quad \begin{cases} c_{\mathbf{g}}^{VI}(\mathbf{f}, \mathbf{f}) & \mathbf{I}_{\mathbf{g}}(\mathbf{f}, \mathbf{f}) + c_{\mathbf{g}}^{VV}(\mathbf{f}, \mathbf{f}) & \mathbf{V}_{\mathbf{g}}(\mathbf{f}, \mathbf{f}) \\ c_{\mathbf{g}}^{II}(\mathbf{f}, \mathbf{f}) & \mathbf{I}_{\mathbf{g}}(\mathbf{f}, \mathbf{f}) + c_{\mathbf{g}}^{IV}(\mathbf{f}, \mathbf{f}) & \mathbf{V}_{\mathbf{g}}(\mathbf{f}, \mathbf{f}) \end{cases} d\mathbf{f}$$

The functions  $G_{\rm B}$  are obtained from a straightforward solution of the transmission line equations using impulsive voltage and current sources.

In some cases, the bulk voltages and currents may be used to define an avionics box protection function  $T_{\rm p}$  given by

$$\begin{bmatrix} \mathbf{r}_{\mathbf{p}}^{\mathbf{I}} \\ \mathbf{r}_{\mathbf{p}}^{\mathbf{V}} \end{bmatrix} = \begin{bmatrix} \mathbf{r}_{\mathbf{B}} \\ \mathbf{v}_{\mathbf{B}} \end{bmatrix} - \begin{bmatrix} \hat{\mathbf{I}}_{\mathbf{B}} \\ \hat{\mathbf{v}}_{\mathbf{B}} \end{bmatrix} (d\mathbf{B}) \quad (6)$$

where  $I_B$  and  $V_B$  are the threshold box current and voltage denage levels, respectively.  $T_{\mathbf{p}}$  gives the additional box protection required against the computed bulk voltage V<sub>n</sub> and current I<sub>n</sub>.

### CONCLUSION

The utility of the above procedure is made apparent when put in the form of a user-oriented design program. Data bases which describe the various frequency domain transfer functions are accessed as needed and can be updated or changed depending upon design constraints. Once the exact location of a cable bundle is described inside the aircraft, as well as all of its associated POEs, induced current and voltage levels may be computed for a given lightning stroke situation. An example of this type of computation for a "generic" cable harness in the nose wheel well of an F-14 aircraft is given in Fig. 9.

#### REFERENCES

- 1. R.F. Wallenberg, D.T. Auckland, and J.A. Birken, "A Transfer Function Approach to Coupling to the Interior of a Composite/Metal Aircraft Based on Triangular Patch Model", IEEE International Symposium on EMC, Santa Clara, September 1982.
- 2. R. Wallenberg, et. al., "Advanced Composite Aircraft Electromagnetic Design and Synthesis", Syracuse Research Corporation Interim Report SRC TR 79-490, Syracuse, New York, April 1980.

3. E.T. Pierce, et. al., "Natural Lightning Parameters and their Simulation in Laboratory Tests", SRI Project 3062, February 1976.

Rao, 4. S.M. "Electromagnetic Scattering and Radiation of Arbitrarily

Shaped Surfaces by Triangular Patch Modelling", Ph.D. Dissertation, University

of Mississippi, August 1980.

5. S.M. Rao, D.R. Wilton, and A.W. Glisson, "Electromagnetic Scattering by Surfaces of Arbitrary Shape", IEEE Transactions on Antennas and Propagation, Vol. AP-30, May 1982, pp 409-418.

6. D.T. Auckland and C.C. Cha, "A Model for Direct-Strike Lightning Excitation of a Conducting Body", IEEE International Symposium on IMC, Santa

Clara, CA, September 1982.

7. FLLASH (Full Level Lightning Aircraft System Hardening) Tests performed on the F-14 and F-18 aircraft at Albuquerque, NM, under the direction of J.A. Birken, Naval Air Systems Command, Spring-Summer 1982.

8. R.A. Perala, "Full Level Lightning Aircraft System Hardening (FLLASH) Test Plan for Lightning Testing of the F/A-18A", prepared for Syracuse Research Corporation under Purchase Order 6008 and Naval Air Systems Command Prime Contract

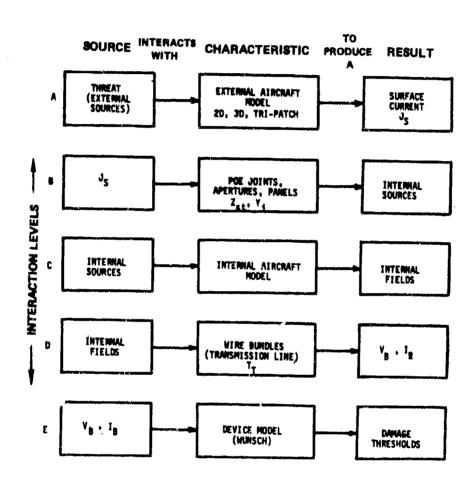
NOO019-82-C-0088, March 1982.

9. R.A. Perala, "Full Level Lightning Aircraft System Hardening (FLLASH) Test Plan for Lightning Testing of the F-14A Aircraft", prepared for Syracuse Research Corporation under Purchase Order 6008 and Naval Air Systems Command Prime Contract NOO019-82-C-0088, February 1982,

10. J.D. Robb and J.D. Herring, "Lightning Tests Sikorsky Black Hawk" prepared by Lightning and Transients Research Institute, 2531 West Summer Street, St. Faul, Minnesota, for Sikorsky Aircraft Company under Purchase Order 208578, January 1980.

11. H.G. Schaeffer, "MSC/MASTRAN Primer, Static and Normal Model Analysis",

Schaeffer Analysis, Inc., 1979.



35

 $\frac{A}{A}$ 

Fig. 1 - Interaction Partition Table

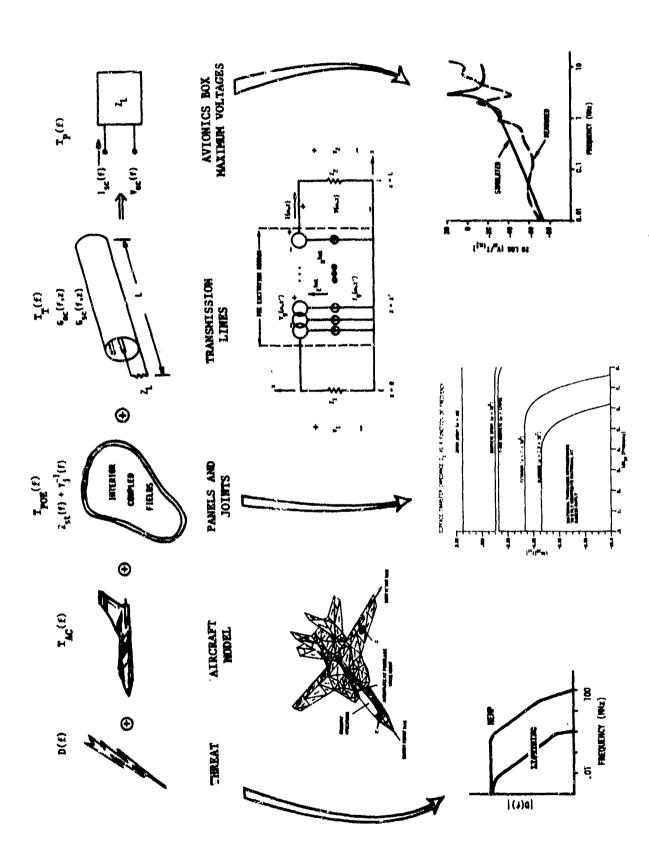


Fig. 2 - Frequency Domain Linear Cascaded Coupling Model

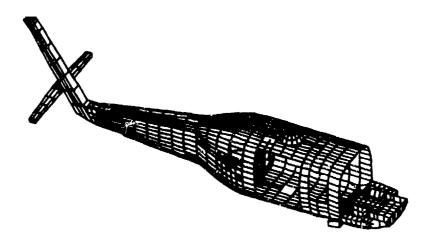


Fig. 3 - NASTRAN External Skin Data Base for Black Hawk Helicopter

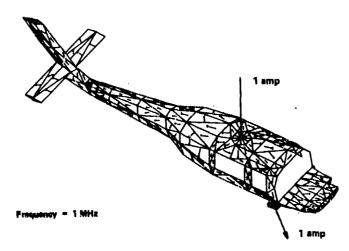


Fig. 4 - Top Oblique View of Black Hawk Showing Surface Currents  $\text{Re}\{\underline{J}_S\}$  for Main Rotor-to-Landing Gear Direct Strike Injection Current of 1 amp at Frequency of 1 MHz

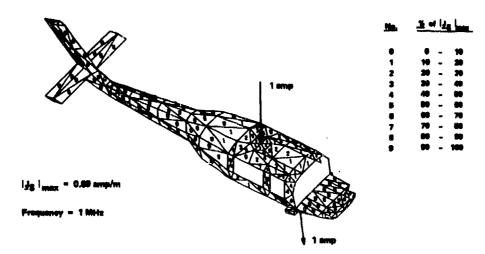


Fig. 5 - Top Oblique View of Black Hawk Showing Magnitudes of Current Vectors in Fig. 4 Scalad Relative to  $\|\mathbf{J}_{6}\|_{\max}$ 

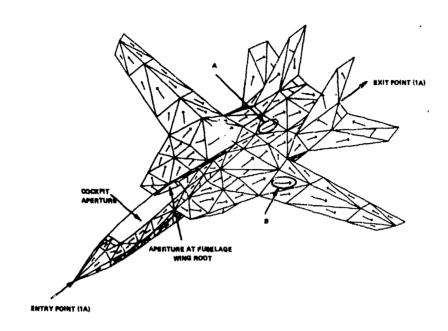


Fig. 6 - Top Oblique View of F-14 Showing Surface Currents  $\text{Re}\{\underline{J}^b\}$  for Nose-to-Tail Injection Current of 1 amp at Frequency of 1 MHz

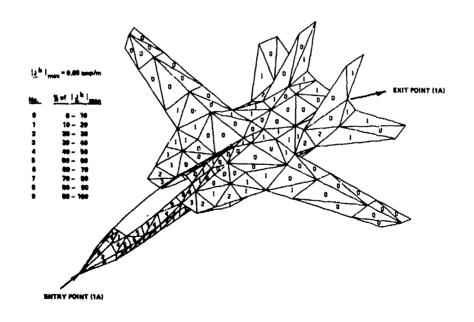
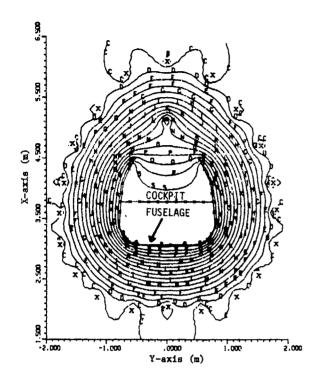


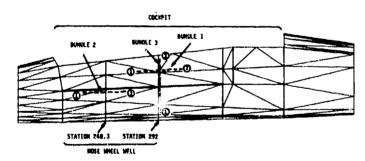
Fig. 7 - Illustration Showing Magnitudes of Current Vectors in Fig. 6 Scaled Relative to  $\left\|\mathbf{J}^{\mathbf{b}}\right\|_{\max}$ 



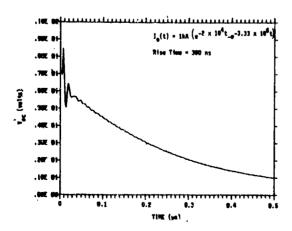
Equipotential lines at cross section of F-14 fuselage station 320 inside aircraft test fixture. The fuselage carries the injected current, which is returned to the generator by return conductors. This is used to estimate field levels inside large apertures and the total inductance of test fixtures.

x's indicate aircraft test fixture return conductors	A ≡ -10V •
$\phi_f = 83.39V$ (potential of fuselage)	S ≡ 80V
φ <sub>r</sub> = -16.61V (potential of return conductor	5V Intervals

Fig. 8 - Field Lines Inside F-14 Cockpit for Nose-Tail Strike



Example of transmission line model applied to F-14 wire bundle coupling in large aperture region. Distributed POE fields are computed by two-dimensional field penetration results.



Open-circuit voltage at terminal 1 of Bundle 2 when Terminal 2 is terminated in  $50\Omega$ .

Fig. 9 - Generic Cable Bundle Results for F-14

## AD P002175

SOME RESULTS AND LIMITATIONS
OF PRONY ANALYSIS OF IN-FLIGHT LIGHTNING DATA

by

T. F. Trost C. D. Turner C.-T. Wen

Electrical Engineering Department Texas Tech University Lubbock, Texas 79409

### ABSTRACT

Recent results have shown that the electromagnetic resonances of an aircraft can be excited by lightning. Each resonance may be characterized by a particular frequency and damping rate, and these two quantities taken together constitute a matural frequencies. One way to determine the natural frequencies is by applying ProLy analysis to waveforms measured during lightning strikes. This involves a numerical termique for fitting a series of damped sinusoids to the measured waveforms.

Electric and magnetic field waveforms recorded on the N.A.S.A E-106B aircraft during lightning strikes have been analyzed using the Prony technique. A number of natural frequencies have been determined, and these are in substantial agreement with the frequencies observed on a laboratory model of the airplane. The process of determining the frequencies is not without difficulties, and some waveforms yield much better results than others.

### INTRODUCTION

The success of the N.A.S.A. storm hazards research program in 1982 has resulted in a large number of direct-strike lightning signstures (1).\* These include time-domain waveforms of aB/at, a D/at, aI/at, and I measured on the F-106B aircraft. Analysis of these waveforms is now underway, and this paper presents the results of a technique, known as Prony's method (2,3), which has been applied to 21 of the 1982 direct-strike waveforms. The technique is used to determine the electromagnetic resonances, or natural frequencies, of the aircraft in the lightning channel. Each natural frequency corresponds to a particular electromagnetic field configuration or mode. The application of Prony's method derives from the singularity expansion method (S.E.M.) of Baum (4) where the fields on an object are expressed in terms of a set of natural frequencies. Prony's method extracts these frequencies from the time-domain waveforms.

Resonance is a fundamental physical phenomenon and represents one of several aspects of an aircraft-lightning interaction which are important areas of study. In the in-flight situation, the resonances of the aircraft modify the fields imposed by the lightning by enhancing the spectral components lying at or near the resonance frequencies. Thus, some knowledge of the resonances is necessary for interpreting the measured lightning data. In addition, the lightning channel plays a role in determining the characteristics of the resonances including their frequencies and damping rates. Thus, detailed studies of the resonances observed during lightning strikes can yield information about the channels. The resonances are not the same, for example, as they would be for the case of a nearby lightning flash or a nuclear EMP, where there is no channel attachment. Of course, the channols have time-dependent and nonlinear properties; our technique does not attempt to investigate these.

Our first attempts at applying Prony analysis to F-106 data were carried out on a rather limited amount of 1980 and 1981 data and have been discussed in a paper at this conference last year (5) and in a report (6). A parallel effort has involved a study of the resonances of a laboratory model of the F-106 (6,7). The present paper deals primarily with the new results obtained from the F-105 in 1982 and briefly mentions the laboratory model results for comparison.

RESULTS FROM THE F-106

APPLICATION OF PRONY ANALYSIS TO IN-FLIGHT WAVEFORMS-Prony analysis is a technique for fitting a given waveform with an-

\*Numbers in parentheses designate references at end of paper.

other waveform consisting of a sum of damped sinusoids. This sum, sometimes called a Prony series, can also be written with complex exponentials. For example,

$$\frac{\partial B}{\partial t} = \sum_{i=1}^{N} R_i e^{s_i t}$$

where the  $s_i$ 's are the complex or "natural" frequencies of the waveform.  $s_i=\sigma_i+j\omega_i,$  where  $\sigma_i$  is the damping rate and  $\omega_i$  is the radian frequency. The  $s_i$ 's are also called "poles" since, if the series were Laplace transformed, the  $s_i$ 's would be poles in the Laplace domain. The  $R_i$ 's are called residues, again from considering the Laplace transform. Since we will be dealing only with real waveforms, the  $s_i$ 's and the  $R_i$ 's must occur in complex-conjugate pairs. All of the  $\sigma_i$ 's are negative. The "order" of the series is N.

Fitting the measured waveform with the Prony series means finding the  $R_i$ 's and  $s_i$ 's. Prony's method of doing this is to first construct a polynomial which has essentially the  $s_i$ 's as its roots, and then to solve for the roots. Last, the  $R_i$ 's are found by equating the Prony series, with  $s_i$  values substituted, to the given waveform at N different times. We have written a FORTRAN computer code to carry out these steps; a detailed description is to be found in Ref. 6.

To run the code on a particular waveform, a value must first be assumed for the order. The code will accept any order up to 36. Thus far, for in-fright lightning waveforms we have used orders in the range 15 to 20. For a given order, N, there are 2N numbers to be determined - N/2 poles with real and imaginary parts and N/2 residues with real and imaginary parts. Thus 2N or more points of the given waveform are needed. Our code always uses exectly 2N waveform points.

We think of the response of the airplane to the lightning, that is, the measured wave-form, as being the result of the convolution of a lightning input waveform with the airplane impulse response. From the S.E.M. we know that the impulse response consists of a sum of damped sinuspids. If the lightning input is also of this form, then one can readily show that so also to the convolution. In this case Prony's method will work well, and the poles (and residues) of the measured waveform are extracted. These poles are the poles of the airplane-and-channel and of the lightning input. However, in the case where the lightning input is not of the damped sinusoidal form, part or all of the measured waveform will not be either. The Prony mnalysis may not be able to fit the measured waveform; it may not be able to extract any poles.

SUMMARY OF RESULTS - Application of the Prony code to the 1982 data has met with some successes and some failures. Out of a total

of 21 waveforms, the code failed to extract poles from 7, and the results from several others are suspect because of the deleterious effect of quantization errors.

The most successful case was waveform B-dot 82-038-02, recorded from the B-dot sensor located on the aft fuselage over the starboard wing. This sensor measures aB/at associated with longitudinal current. The waveform is shown in Fig. 1 (labeled B-DOTL). We interpret this waveform as consisting of a series of several lightning (derivative) pulses with accompanying ringing of the aircraft. The largest pulse, positive-going at about 0.5  $\mu\text{S}$ , and the oscillations following it were chosen for the Prony analysis. An expanded plot of this portion of the waveform (with its Fourier transform) is shown in Fig. 2. Superimposed on it is the Prony fitted or reconstructed waveform. Evidently there were no lightning pulses during the ringing time since the fit is excellent. The RMS error between the measured and the reconstructed waveforms is 6.2%. In general, one must be careful to select a section of waveform or "data window" for Prony analysis where the ringing is undisturbed by lightning pulses, since the Prony code will not give a good fit or good poles if there are delayed input pulses.

The poles extracted from the Fig. 2 waveform are listed in Table 1. For each of the eight poles the table gives normalized values of  $\sigma_1$  and  $\omega_1$ , with the frequency,  $\omega_1/2\pi$ , in parentheses. The normalization was done by dividing by  $C\pi/L$ , where C is the speed of light and L is the length of the F-106, 17.23 m. This yields a normalized w, of unity for a half-wavelength resonance. As can be seen from the table, the actual first resonance, at 0.72, is a bit lower than this. The values in Table 1 are averages and have been obtained in the following way: The code was run for the orders 15, 17, and 19. Orders lower than 15 were found to yield large RMS error. Orders greater than 19 gave low RMS error but the poles became somewhat variable us the method apparently was giving precise file to imperfections in the waveform or sed by small quantization errors and perhaps lightning input fluctuations. For each of the three orders the code was run for three data windows, each displaced from the next by one time increment (10 ns). Corresponding poles from the nine runs were averaged together. A run requires about 2 minutes of minicomputer time, including the time for printing out the poles, the residuen, and the RMS error of fit. By doing multiple runs in this way we can determine the stability of the poles, that is, the amount they change when the order  $\ensuremath{\circ} \mathbf{r}$  the set of waveform points is changed slightly. Only stable poles are considered meaningful.

The spread in the damping rate and in the frequency of each pole is shown in parentheses in the table. These are all stable poles.

As to the meaning of the poles in Table 1, it is clear that poles 2 through 8 are the natural frequencies of the resonant modes of the aircraft-lightning channel system. Their frequencies and damping rates are similar to those of our laboratory model of the F-106 discussed below. Unfortunately, the locations of the attachment points are not known for this strike, so a detailed comparison with the model is not as helpful as it might be. The first pole, which has zero frequency and thus represents a decaying exponential, is not seen on the model and is evidently due to the lightning.

A D-dot waveform (D-dot 82-038-02) was recorded on the F-106 along with the B-dot waveform of Fig. 1. The D-dot sensor is located under the nose of the aircraft and mossures  $\partial D/\partial t + J$  normal to the surface. The contribution, it any, to the recorded waveform from the conduction current J is not known. Only if J=0 is the sensor truly a "D-dot" sensor. The waveform is shown in Fig. 3 (labeled D-DOIF). Notice that the aircraft resonances ride on a slow, positive-going variation which is not present in the B-dot waveform.

The Prony analysis of D-dot 52-038-02 was not quite as successful as for 8-dot. There were only two good orders, in the sense of stable poles and low RMS error of fit, 17 and 18. Figure 4 shows the section of waveform used in the analysis (and its Fourier transform) and the reconstructed waveform for order 18. The error in the fit was 7.4%. Table 2 lists the poles. The values were obtained by averaging the poles from three windows for order 17 and three windows for order 18.

On comparing the poles in Table 1 and Table 2, it is seen that there is quite good agreement. Excluding the first pole, the average difference between corresponding damping rates is 12% and between frequencies, 4%. These numbers are probably good estimates for the accuracies of the pole values since ideally the agreement would be exact. high-frequency poles at 41 and 45 MHz in B-dot were not extracted from D-dot, so their accuracy is less certain than the others. course, the accuracy of any pole is in doubt if its amplitude, that is its residue, is weak. Fortunately, none of the residues of B-dot is very weak, with the weakest only 18dB down from the strongest. The situation for D-dot is not quite as good, with the weakest residue, at 37.5 MHz, being 29dB down.

Some comments are in order regarding the general characteristics of the resonances in the 1982 data. The frequency spectrum in Fig. 2 contains one dominant peak, that of the first aircraft resonance lying at about 6.5 MHz. The Q of the resonance (from the damping rate and frequency in Table 1) is 2.5. Spectra from the other strikes reveal that other, higher frequency resonances sometimes dominate, for example 20 MHz and 41 MHz; and often several of the resonances are present in

roughly equal strength. Some of this variability is probably due to differences in attachment point locations since the various modes would be excited differently depending on the current injection point on the aircraft. In principle, the modes themselves would also change somewhat with attachment point because the channel is part of the overail conductor topology. In practice the mode changes will be small if the channel impedance is large.

In general terms, the poles extracted from the 1982 waveforms can be described as follows: Pole frequencies lie consistently at about 6.5, 13, 20, and 41 MHz and sometimes at about 26, 29, 35, 37 and 44 MHz. The damping rates of the poles generally lie between -.15 and -.35. They are less stable than the frequencies, during consecutive Prony analysis runs on the same waveform. The analysis failed more often on I-dot and D-dot waveforms than on B-dot.

As an aside we note that there are 9 pairs of simultaneously recorded B-dot and D-dot waveforms among the total of 21. Figures 1 and 3 are an example of a pair. The rumaining waveforms are of I-dot. The polarities of all of the 5-dot-D-dot pairs indicate lightning pulses of positive charge flowing

fore-to-aft on the airplane.

The 1-dot waveform shown in Fig. 5 is an example of one for which the Prony analysis failed. Apparently, the waveform contains closely spaced lightning pulses. This interpretation is supported by the frequency spectrum, also shown in Fig. 5. The spectrum contains a strong peak at 15 MHz instead of peaks at the mirplane resonances of 6.5, 20, etc. A current (I) waveform recorded simultaneously revouls that the I-dot pulses are actually the fast changes on the leading edge of a 3.6kA current pulse. The trailing edge is slower and does not have a large enough derivative to register in the I-dot scale. Both I and I-dot were measured on a conductor inside the radome connected between the noseboom and the fuselage.

EFFECT OF WAVEFORM QUANTIZATION-The transient recorders on board the F-106 utilize 6-bit digitization and so quantize the sensor output waveforms into a maximum of 64 levels (36 dB dynamic range). To quantization can be expected to affect the accuracy of the poles extracted by our Prony analysis. order to examine this offect, we have artificially reduced the size of one of the large amplitude waveforms, thus increasing the quantization error, and recalculated the poles. The waveform was B-dot 82-036-02 (Fig. 1), the one giving the best Prony results. It had a peak extent of 31 levels, with 56 peak-to-peak. It was reduced to a peak of just 5 levels, which coincides with the trigger level sutting of the transient recorders. This is the worst-case situation for quantization.

The poles of the reduced waveform are given in Table 3 and may be compared with those in Table 1 for the original waveform. Notice that the frequencies of the poles have been changed only slightly by the quantization, some moving upward and some downward. The damping factor, -.19, of the lowest-frequency, and strongest, mircraft resonance is unchanged. The damping factors of most of the others, however, have been systematically lowered, some by over a factor of 2. The stability of the damping factors is also much worse. Thus, it is seen that the degree of quantization typical of the weakest in-flight waveforms can pretty much destroy the accuracy one would hope to achieve for the damping factors.

COMPARISON WITH RESULTS FROM THE LABORATORY MODEL-An approximate scale model of the F-106 has been tested in our laboratory using fast current pulses applied by wires connected to the model (6,7). B-dot and D-dot fields on the model have been recorded and analyzed with

the Prony code.

Before considering the results from the model, it is worth mentioning the effect that attached wires can have on the poles of an object. The effect was observed by using a simple object, a circular cylinder, in place of the F-106 model. The wires were attached to the ends. The resulting poles were compared with known poles of a cylinder having no wires attached and excited by an incident wave. The differences observed in the poles were that the damping rates were increased considerably and the frequencies just slightly by the presence of the wires.

We now turn to the results obtained from the F-106 model. The model was connected to the wires in four different configurations to simulate four lightning-channel attachment possibilities (6). The values of the resulting poles vary somewhat depending on the configuration; the average frequencies of the poles are 7.5, 13, 19, 24, 29, 35, and 41 MHz. The approximate agreement between these frequencies and the in-flight frequencies given earlier (6.5, 13, 20, 25, 29, 35, 37, 41, 44) makes it clear that the poles in the in-flight duta really are those of the mircraft. It also indicates a certain degree of correctness of the model. The largest discrepancies involve 7.5 MHz, which is a bit high, and 19 and 24 MHz, which are a bit low. These suggest that some refinement to the geometry of the model may be in order. The frequencies 37 and 44 MHz have not been identified as poles of the model, but our present experimental technique does not cause poles in this high-frequency region to be strongly excited. We have concentrated on the low-frequency poles, assuming that these would be the strongest in the in-flight situation. It was somewhat surprising to discover poles excited in-flight right up to the 50 MHz Nyquist frequency.

The damping rates of the poles of the model lie between -.21 and -.49 and so tend to be slightly larger (more negative) than those in Tables 1 and 2. This may be due to the fact that the lightning channel impedance during the 82-038-02 event was larger than the impedance of the wires on the model. Thus the resonance energy was not carried away as quickly by the channel as it is by the wires.

To determine how big an effect the lighthing channel has on the damping, one should look at the poles from nearby strikes where there is no attachment at all and the damping is at a minimum. In our report (6) we presented poles from 1981 nearby strikes and showed that the damping rates were fairly small, -.14 to -.19 for the first pole. However, this is only slightly smaller than the -.17 to -.19 from Tables 1 and 2, so in this case the difference may be insignificant. Thus far, the amount of nearby data is limited, and most is low in amplitude and so may have bissed damping rates due to quantization as discussed above. Additional large amplitude nearby-strike data is needed.

### CONCLUSIONS

The Prony analysis technique can be applied successfully to at least some in-flight waveforms. In this way, natural frequencies of the aircraft-channel system are determined. This is illustrated by the good results for B-dot and D-dot in strike 82-038-02.

The closeness of agreement between the poles of a simultaneously measured pair of waveforms was used as an indication of the accuracy of the poles. For waveforms which are not paired in this way, or for pairs where only one has a successful Prony analysis, the accuracy of the poles is less certain.

Some damping rates extracted from waveforms of low amplitude are inaccurate due to the coarse quantization of the waveforms. This effect was seen by artificially quantizing the B-dot 82-038-02 waveform, re-computing the poles, and comparing with the original poles.

The general characteristics of the first five poles from strike 82-038-02 sre, first, frequencies located at roughly equal intervals between 6.3 and 35 MHz and, second, damping rates all lying between -.19 and -.25 (as seen in Table 1).

### REFERENCES

- 1. M. E. Thomas and F. L. Pitts, "1982 Direct-Strike Lightning Data." N.A.S.A. TM 84626. March. 1983.
- 84626, March, 1983.

  2. E. K. Miller, "Natural Mode Methods in Frequency and Time Domain Analysis." Preprint UCRL-82323, Lawrence Livermore National Laboratory, May 30, 1979.
- 3. S. M. Kay and S. L. Marple, Jr., "Spectrum Analysis-a Modern Perspective." Proc. IEEE, Vol. 69, pp. 1380-1419, Nov. 1981.

- 4. L. B. Felsen, ed., "Transient Electromagnetic Fields." New York: Springer-Verlag, 1976, pp. 129-179.
- 5. T. F. Trost and F. L. Pitts, "Analysis of Electromagnetic Fields on an F-106B Aircraft During Lightning Strikes." Proc. Intl. Conf. Lightning and Static Elec., pp. D5-8-D5-15, March 1982.
- 6. C. D. Turner and T. F. Trost, "Laboratory Modeling and Analysis of Aircraft-Lightning Interactions." NASA CR 169455, Aug. 1982.
- Interactions." NASA CR 169455, Aug. 1982.
  7. T. F. Trost and C. D. Turner, "Transient Electromagnetic Fields on a Delta-Wing Aircraft Model with Injected Currents." Proc. Intl: Conf. Lightning and Static Elec., pp. D5-0-D5-7, March 1982.

### **ACKNOWLEDGEMENTS**

The authors wish to thank G. W. Wood for help with the numerical analysis, and M. E. Thomas for many valuable discussions regarding the F-106 data.

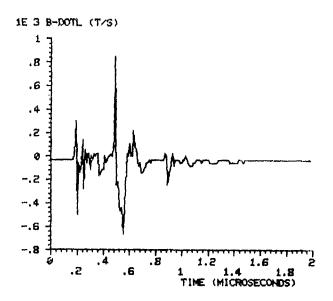
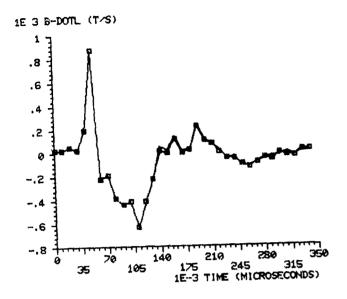


Fig. 1 - B-dot 82-038-02 waveform



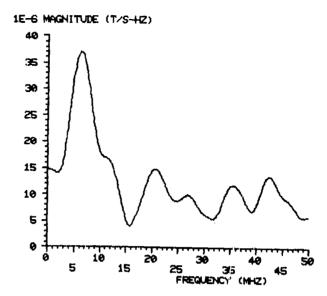


Fig. 2 - Expanded portion of waveform in Fig. 1 (solid line) along with Prony reconstructed version (solid line with squares); magnitude of Fourier transform of expanded portion

Table 1 - Poles of Waveform B-dot 82-038-02

1. 
$$\begin{pmatrix} -.35 \\ (-.23+1.41) \end{pmatrix} \pm j \begin{pmatrix} 0 \\ 0+0 \end{pmatrix} \begin{pmatrix} \text{MHz} \\ 0 \end{pmatrix}$$

2.  $\begin{pmatrix} -.19 \\ (-.18+-.23) \end{pmatrix} \pm j \begin{pmatrix} .72 \\ (.70+.73) \end{pmatrix} \begin{pmatrix} (6.3) \\ (3.5) \end{pmatrix}$ 

3.  $\begin{pmatrix} -.20 \\ (-.18+-.22) \end{pmatrix} \pm j \begin{pmatrix} 1.55 \\ (1.49+1.60) \end{pmatrix} \begin{pmatrix} (13.5) \\ (20.2) \end{pmatrix}$ 

4.  $\begin{pmatrix} -.25 \\ (-.21+-.32) \end{pmatrix} \pm j \begin{pmatrix} 2.32 \\ (2.30+2.36) \end{pmatrix} \begin{pmatrix} (20.2) \\ (3.00+3.29) \end{pmatrix}$ 

5.  $\begin{pmatrix} -.22 \\ (-.15+-.27) \end{pmatrix} \pm j \begin{pmatrix} 3.18 \\ (3.00+3.29) \end{pmatrix} \begin{pmatrix} (27.8) \\ (3.99+4.10) \end{pmatrix}$ 

7.  $\begin{pmatrix} -.14 \\ (-.11+-.20) \end{pmatrix} \pm j \begin{pmatrix} 4.73 \\ (4.69+4.77) \end{pmatrix} \begin{pmatrix} (41.4) \\ (41.4) \end{pmatrix}$ 

5.14 (5.11#5.17)

8.

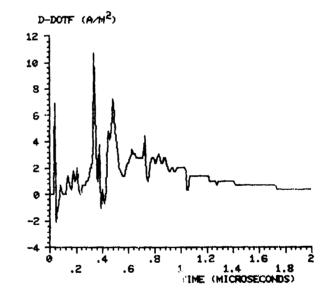
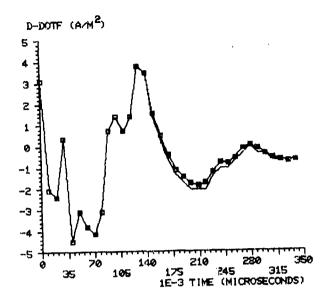


Fig. 3 - D-dot 82-038-02 waveform

(44.9)



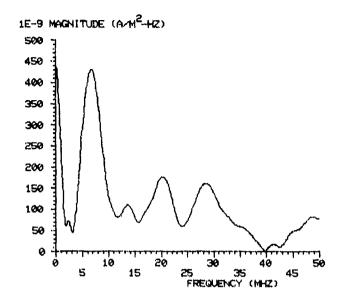
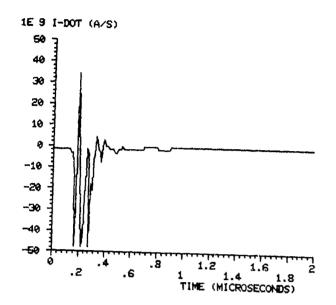


Fig. 4 - Expanded portion of waveform in Fig. 3 (solid line) along with Prony reconstructed version (solid line with squares); magnitude of Fourier transform of expanded portion

Table 2 - Poles of Waveform D-dot 82-038-02

1.	20 (1429)	±j	( 0+0 )	MHz ( 0)
2.	17 (15+19)	±j	.77 (.76~.78)	( 6.7)
3.	19 (16+21)	±j	1.56 (1.54+1.59)	(13.6)
4.	25 (24+25)	±j	2.40 (2.40+2.40)	(20.9)
5.	28 (28+29)	±j	3.24 (3.24+3.25)	(28.3)
6.	17 (13+20)	±j	4.30 (4.27+4.33)	(37.5)



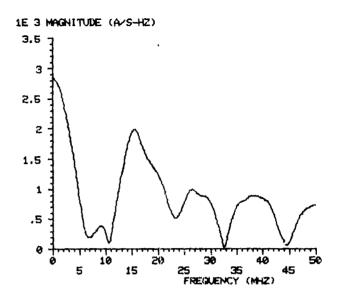


Fig. 5 - I-dot 82-044-02 waveform and magnitude of its Fourier transform

Table 3 - Poles of Quantized 8-dot 82-038-02

	•		44811C1280 B=00C	02-038-02
1.	30 (23+36	s) ±1	(0 + 0)	MHz ( 0 )
2.	19 (15+20	) ±1	( .73 ÷ .76)	( 6.5)
3.	10 (08→18	) <u>+</u> j	1.53 (1.41÷1.57)	(13.3)
4.	15 (11*23	) <u>+</u> j	2.47 (2.34+2.55)	(21.6)
5.	10 (02+18	) ±j	3.13 (3.09+3.15)	(27.3)
6.	27 (~.14+49)	±j	4.05 (3.96+4.18)	(35.4)
7.	14 (03+27)	<u>+</u> j	4.60 (4.4 <del>6</del> ÷4.71)	(40.1)
€.	35 (24+51)	±j	5.44 (5.39°5,53)	(47.4)

a teliar

Coupling of Natural Atmospheric Interference Through Apertures

By

J. Hamm, W. Graf, and E. F. Vance SRI International Menlo Park, CA 94025

### ABSTRACT

The coupling of electromagnetic energy through apertures has received a great deal of attention in recent years. This rejent research has been both theoretical and experimental in nature and has been focussed on the problems associated with apertures which are small compared to a wavelength.

The results of this research can be applied to the problem of determining the transient signals induced on conductors behind an aperture by lightning and static charging. While the problem of determining induced transients in complex systems (such as aircraft or ground-based facilities) cannot be solved exactly, the research of the past few years indicates that upper bounds can be determined for these transients. This paper reviews our recent work on aperture coupling and applies the results to models of airborne and ground-based facilities.

The nature of this recent work is such that reasonable upper bounds can be determined without the use of extensive computer codes. The system designer can determine quickly whether or not a particular aperture presents a problem for electronic systems located behind the aperture. The analysis performed in recent years has been of two different types: transmission line modeling of canonical circuits behind the aperture, and matrix formulation of Maxwell's equations. Both approches lead to relatively straightforward expressions for bounds on transient voltages and currents on conductors behind the aperture. Our laboratory measurements on test aperturer are used to investigate the suitability of these bounds.

The results of this research can also be applied to the problem of generating realistic specifications, standards, and test procedures for certifying systems which must operate in the natural electrical environment.

This paper was not available for incorporation into this book. Therefore, it will be published at a future date.

## A MODELING SYSTEM FOR CONDUCTED TRANSIENT ANALYSIS



### THOMAS L. MAHONEY HARRIS/PRD ELECTRONICS DIVISION

ABSTRACT

A computer simulation system has been developed which facilitates the analysis of electrical/electronic systems. Sponsored by the Naval Air Systems Command to investigate power interface transient problems, the program is called the Navy Power Systems Simulator. The simulator is used as a system engineering tool which generates and processes models of virtually any electrical network. It is simple to use and capable of automatically producing a complex system's steady state or transient output response. An engineering friendly computer interface has been achieved by the extensive use of interactive graphics and menu-driven prompting.

### INTRODUC'TION

PRESENT POWER DISTRIBUTION SYSTEMS, both commercial and military, are directed to satisfying the requirement of their principal customers - typical applications are lighting, heating, and prime power for machinery equipment. In most applications, the effects of transients - lightning, load switching, etc. - are tions, the effects of transients - lightning, load switching, etc. - are generally of small consequence. Little consideration is given to transients below levels which jeopardize the distribution system or to power interruptions of a few minutes or less.

Unfortunately, the recent quantum increase in applications involving semiconductors - especially in the area of volatile computer memory - has resulted in a large sector of user equipment which is extremely sensitive to transient phenomena at the power interface. Filters, transient arrestors, and battery supported Uninterruptible Power Systems (UPS) are now often found at the power interface and attest to the magnitude of the problem.

In particular, the Naval Air Systems Command has become aware of a considerable loss in operating hours on automatic test systems due to powerline transients. Areas of concern included loss of test memory and test aborts by the line monitor. The potential for erroneous indication of test unit failure is also a concern. The cause of these problems was often traced to transients at the power interface.

A clear-cut example occurred in Florida. Lightning strikes were quickly correlated with major interruptions in avionic repair shop operation. Line transient suppressors were installed

and the problem was eliminated. In other locations, the problem sources are not so clear-cut. A thorough analysis was required of the complex systems and variable interface factors. In many cases, complex solutions were indicated to correct the problems. Brute force approaches were soon found to be cumbersome and expensive - the need for a powerful system analysis tool was recognized. NAVAIR responded by sponsoring the development of the Navy Power Systems Simulator (NPSS) Program.

### SIMULATOR SYSTEM CONFIGURATION OVERVIEW

The simulation system is based on, and retains as a core, the Bonneville Power Administration Electromagnetic Transient Program (EMTP). The powerful and flexible EMTP program has been developing in the power systems community since the late 1960's. Over this period it has become quite complex, and to be applied successfully it requires both a computer background and extensive familiarization training (1)\*. The thrust of the development effort for the Naval modeling system was therefore directed to implementation of a "user-friendly" computer interface and of a compatible method of modeling the various user systems involved in the simulation. Interactive graphics and the concept of multi-level input/output modules in system definition served these goals admirably.

On the NPSS only a few hours of instruction in users procedures are required to produce useful outputs. Although the EMTP core runs in FORTRAN, the user friendly design allows operation of the modeling system with no real need

"Numbers in parentheses designate References at end of paper. for formal programming languages. The use of graphic system diagrams provides a familiar engineering oriented interface, while the use of the technically powerful EMPT core provides the tool needed to solve the complex transient effects problems.

The input/output configuration is determined by the placement of the various steady state and transient generator and measuring device symbols. These symbols are introduced during system layout. At the completion of the run, both a precision numeric printout of the system response and a graphic plot on the CRT or graphics printer are available. Depending on the symbols chosen during the system definition, output parameters can be either voltage and/or current amplitudes with independent parameters of either frequency or time (total time and time steps or frequency range and frequency increments are entered as user specified input parameters). The hard copy of a typical layout as it appeared on the graphic screen is shown in Figure B-1, Appendix B.

While the above cited features are aimed at simplifying the engineering task, they cannot replace good engineering. The system augments the skills of the systems engineer, allowing him to execute a more accurate analysis in less time and provides an optimum method of presenting and manipulating data. Thus, the accuracy and completeness of the initial layout and input data are important to the success of the simulation.

### ANTICIPATED APPLICATIONS

PROBLEM ANALYSIS - Simulation of systems known to have high failure rates can establish the transient levels to be expected, highlight design weaknesses, and verify protective schemes and their placement in the system.

NEW SYSTEM DESIGN - Simulation of possible system design configurations and variation of critical parameters or of component locations will provide a much higher success rate with new system layouts and proposed modifications to present systems.

COMPONENT SELECTION - Transient and steady state stress in terms of voltage, current, and power are readily available from system simulations and may be used to specify special characteristics for potentially susceptible components.

PROCUREMENT TRADE-OFF STUDIES - Selection and optimization of the various subsystems for a large scale procurement in terms of cost effectiveness are simplified by simulation and ranking of the various options.

SPECIFICATION DEVELOPMENT - The establishment of optimum limits, preferred design approaches and standards, and of test methods and configurations can generally be accomplished by simulation with considerable savings in engineering effort.

DESIGN VERIFICATION - Simplified and more thorough verification of a design configuration can be accomplished with speed, accuracy, and flexibility by the simulation system.

### COMPUTATION METHODS AND SIMULATION LIMITATIONS

EMTP methods form the computational basis for the NPSS and establish its current limitations. The EMTP also provides elemental modules on which all circuit description must be based. These elemental modules represent a limitation on the simulator's capabilities. The major elements are given in Appendix A.

The fundamental approach of the NPSS is that of network analysis performed in a series of discrete time steps. The graphical input data, based on the elemental modules, are resolved into an ordered set of ordinary differential and algebraic equations. At each time step a system of simultaneous equations, derived by second order trapezoidal-rule integration from the differential and algebraic system, is solved. The solution is accomplished by first placing the simultaneous equations in the nodal-admittance form and applying ordered triangular factorization. Such an approach applied to sparse matrices, as normally encountered in circuit analysis, provides major benefits in conserving computer memory space and reducing run time. This general explanation of the computations is expanded and detailed in references (2) through (5).

Of course, these mathematical considerations are not needed by the systems engineer (modeler) except as they may affect memory space limitations in the computer. The modeler's limit is the amount of fine detail he can implement in his particular model and the basic limitations of network theory. As parasitic characteristics such as skin effect, stray capactance, and lead inductance become noticeable in the hardware configuration, they must also be correctly modeled in the simulation to maintain accuracy. This is easily accomplished at the lower frequencies. However, as the complexity increases, a point will be reached where the circuit analysis approach becomes too cumbersome or too inaccurate to compensate for the benefits provided by NPSS computer simulation. When that judgment is made, other techniques

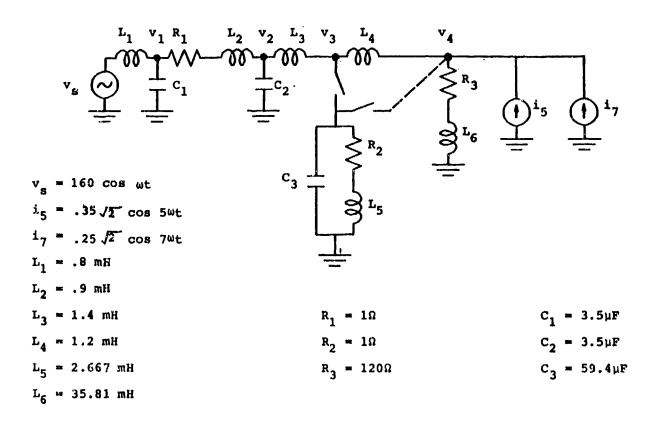


FIG. 1 STEADY STATE HARMONICS ANALYTIC VALIDATION EXAMPLE.

must be sought. Thus, the fundamental limitation is in the network theory of modeling rather than the computational characteristics or methods.

In practice, rounding off and other numeric manipulation result in third to fourth place accuracy in a moderately complex simulation such as Figure 1. There are also various idiosyncrasies of the EMTP program which must be observed, such as connection techniques for grounding and switching elements, etc. However, simple work around procedures are available and are, at worst, a minor nuisance (6). In general, the simulation accuracy is an order of magnitude better than the usual accuracy of the input data that the models are based on. Simulation accuracies of around 0.1 to 1.0 percent are normal.

### NPSS PROGRAM OVERVIEW

GRAPHICS - Once the system data have been assembled and the model configuration sketched, modeling simulation is primarily a graphics effort for the system engineer. The routine consists of withdrawing a basic element (R, C, L, etc.) from a library, positioning it on the model and assigning values and connections to assemble it into the system. All operations are menudriven and can be accomplished in a rapid,

routine fashion. Output of data is even simpler; once the data is requested the axis and data are plotted and automatically scaled for full screen with soom and pseudo-panning capabilities and again menu-driven for ease of operation. A top level system functional is shown in Figure 2.

MODELING FEATURES - Two features have been incorporated which considerably simplify the modeling process, the first of which is the multi-level module concept. At any point in the system definition, a model or subsystem, no matter how complex, may be given a label and treated as a black box or element during further system development. By this method, a complex subsystem may be used in a number of different places in the overall system design by simply inputting its assigned label. In addition, the program tracks all positions of the labeled, black box - if the modeler goes back into the subsystem (black box) detail and makes a change, it will be implemented in every part of the system where that black box or label has been installed. This greatly simplifies changes or updates to a large model.

A second modeling feature facilitates variations studies by making variables within subsystems available at the system

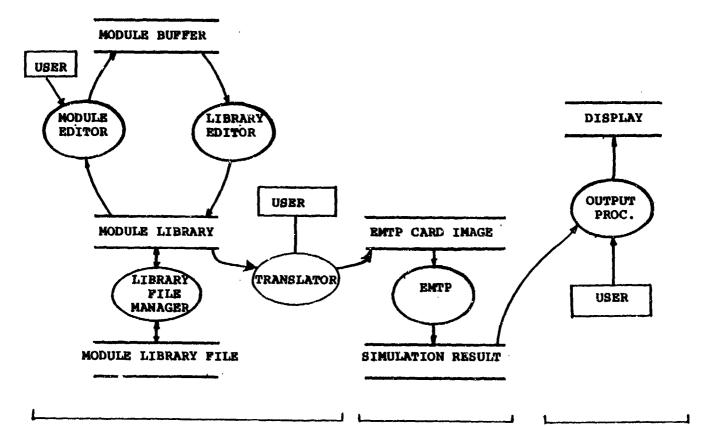


FIG. 2 INPUT PROCESSOR

SIMULATION

OUTPUT PROCESSOR

level. As each element is connected into the circuit, it is given a numerical value or a parameter name. If a parameter name is used and the circuit designated by some label (as if a black box) for connection in a higher level subsystem, the now buried element may be varied simply by assigning values to the parameter name. Thus, the value of an element at the lowest level of circuitry can be brought up through each subsystem level, i.e., made visible as a variable, and controlled at the top system level for variation/sensitivity studies.

LIBRARY - The NPSS library is the filing system for the storage of elemental components as well as complete simulation models. A branching or root system is used to access the various stored data. The transfer of an exact facsimile for assembly in a system being simulated thus becomes a straightforward operation. The elemental model actually remains in the library and can be accessed as often as necessary to generate any number of facsimiles by this copying process. This elemental model may be as simple as a resistor or as complex as an amplifier, control system or an entire installation.

The library is divided into two parts, a collection of elements from the EMTP are considered basic or atomic. Units

in this section may be freely copied but cannot be either deleted or added to by normal operations.

The second section is called the users library. The user stores additional elements in the user library, as required, to complete an immediate modeling task. He may also store particularly useful or generally applicable modules on a permanent basis in this section at his option. The user library is completely under the control of the modeler. He may add, delete, or modify any element or system at will. His only restriction is that the basic elements used in all user library models may consist only of elements copied from the EMTP library. For example, electromagnetic radiation is not part of the network analysis schema. Therefore, the simple dipole will not be found in the EMTP library and cannot be entered in the user library.

GRAPHICS ASSEMBLY - The mechanics of assembling the simulation model is straightforward. Each component is copied from the library to the "Module Buffer" - values or parameter labels and connections are designated and the results reentered in the library. A simple list of commands - define, copy, edit, empty, display - is all that is needed to accomplish the graphics assembly tasks.

TRANSLATOR - The translator performs the tedious and demanding task originally imposed on the modeler by standard EMTP input procedures. Data equivalents or image cards for FORTRAN input cards are automatically generated for each discrete portion of the model. These are then sequenced in decks (concatenation) and held ready to operate the EMTP.

EMTP OPERATION - The EMTP operation is fully automatic with all output data stored and ready for display as required by the Output Processor. For those interested in special function or application of the EMTP alone, it may be accessed directly by the operator. This is accomplished by manually keying the data needed to generate the "image" FORTRAN input rather than relying on the automatic analysis of the graphic model performed by the NPSS.

OUTPUT - Simulation results are output in graphic format with automatic scaling for full-screen display. See Figure 3. In addition, the numeric value of any crosshair selected point can be displayed above the graph. Several steps of 10:1 zoom capability are also provided in either or both horizontal and vertical and enhance accuracy for crosshair readouts. See Figure 4.) In addition, a pseudo-panning capability allows stepping through the enlarged output to observe various points. The zoom and pan capabilities are also available in the model generation mode.

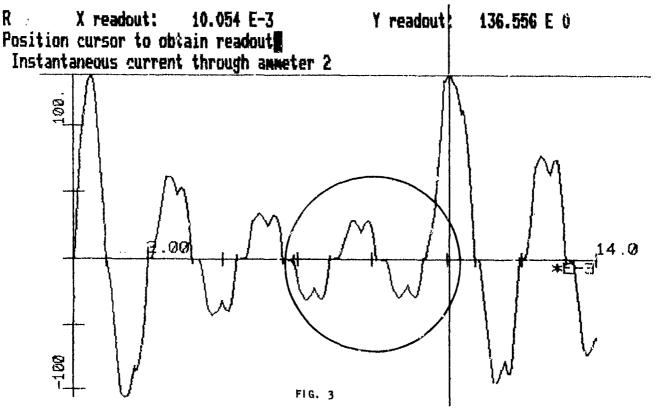
A printer output of the data in tabular form is also available as well as hard copy of the screen displays. The printer output is of greater accuracy and in more detail than the graphics display.

TRANSIENT SIMULATION - A power interface transient simulation is detailed in Appendix B. A direct strike of 20 KA in taken as the input stimulus. The response at the interface with an ATE system was then recorded.

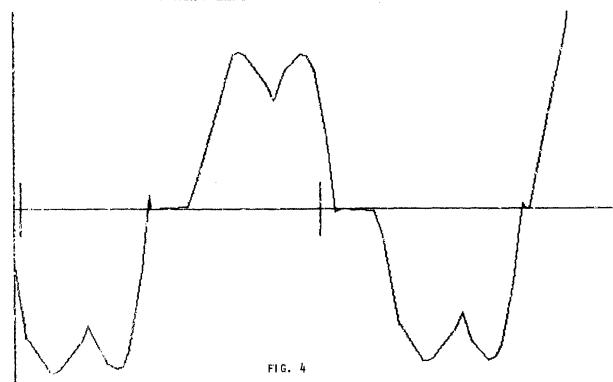
This effort illustrates the stress levels occurring with an average size strike. Further analysis and more evaluation runs are necessary for full definition of the problem and to establish protection recommendations.

### CONCLUSIONS

The use of Naval Power Systems Simulator Model has provided the speed and flexibility needed to thoroughly investigate power system conducted electromagnetic transient problems. This system model approach is a powerful aid in improving design and reducing a major cause of system failure, the powerline conducted transient. Because of the general transient analytic formulation and ease of use for system engineers, we believe it can be applied to a wide range of analytical applications beyond the power interface analysis.



### Zoom Full Restout Next Quit



### ACKNOWLEDGEMENTS

The model was sponsored by AIR 55223D, Naval Air Systems Command. Model development was directed by the Harris/FRD Electronics Division through Dr. F. Alvarado, University of Wisconsin at Madison, and Dr. H. Kwon, Electrocom International Corporation. An operational model is in use by the ATE Power Study Group, Technology Center, harris/PRD, Syosset, New York.

### APPENDIX A

The Transients Program is used to solve the ordinary differential and/or algebraic equations associated with an "arbitrary" interconnection of the following elements:

- 1. imped resistance: R
- 2. Lumped inductance: L
- 3. Lumped capacitance: C
- 4. Multiphase Pi-equivalents, where the preceding scalar R, L, C become symmetric square matrices  $\{R\ ,\ L\ ,\ C\ .$
- 5. Multiphase distributed-parameter transmission lines, wherein propagation time of the line is represented. Distortion. Less and externally-jumped-resistance approximations are evailable, as well as "exact" frequency-dependent representations.

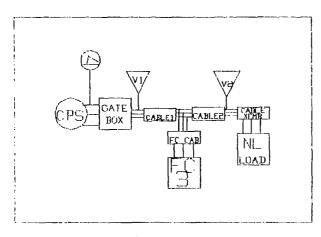
- 6. Nonlinear resistors, where the curve must be single-valued.
- 7. Nonlinear inductors, either with the conventional single-valued characteristic or including hysteresis.
  - 8. Time-varying resistance.
- 9. Switches, used to simulate circuit breakers, lightning-arrestor flashover, or any other network connection change. Diodes and do converter valves are included.
- 10. Voltage or current sources. In addition to standard mathematical functions (sinusoids, surge functions, steps, and ramps), the user may specify sources point-by-point as functions of time, or in FORTRAN, or as defined by TACS (Transient Analysis of Control Systems).
- 11. Dynamic synchronous machines (3-phase balanced design only). The electrical side is represented by Park's (Blondel's) equations, while the mechanical side is modeled as an interconnection of masses, springs, and damping. Arbitrary exciter and governor dynamics can be represented, by connection to TACS.

12. Contro! system dynamics, as are normally represented on differential analyzers (analog computers). This modeling capability goes by the name of TACS. Nonlinear and logical operations may be represented. Input and output may be interfaced with the electric network of the EMTP, providing a hybric representation. All TACS representation is user-patchable, and hence configuration free.

### APPENDIX B

### A TRANSIENT SIMULATION

The first step in the analysis consists of modeling the system configuration. Figure B-1 presents the top level of the distribution-user equipment system. The Central Power Source (CPS) represents a complex submodel containing a 4160-volt, 400-Hz generator and additional sources of



Hit or to exam the diagram:

FIG. B-1

fifth and seventh harmonics. The GATE BOX is a 4160:120 transformer. A high current impulse source of 20 KA with 2 microseconds use time and 100 microseconds decay was applied to the transformer high side as presented in Figure B-2.

The input to the distribution cables is measured at V1, shown in Figure B-3, prior to the strike. Figure B-4 shows the voltage response at this point during and after the strike.

As shown in Figure B-1, there is a cable after the measuring point VI, followed by a harmonic filter (FC3) which is simply a large 400 Hz resonant tank circuit, and a second short cable to the equipment transformer and the equipment represented by NL LOAD (non-linear load). The magnitude of the conducted strike voltage was measured by V2, shown in Figure B-5 before the strike, and shown in Figure B-6 during the strike.

Zoom Full Readout Next Duit THE LIGHTNING STRIKE

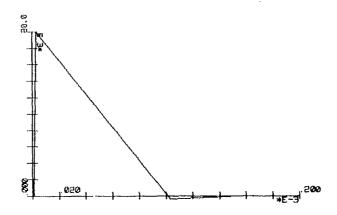
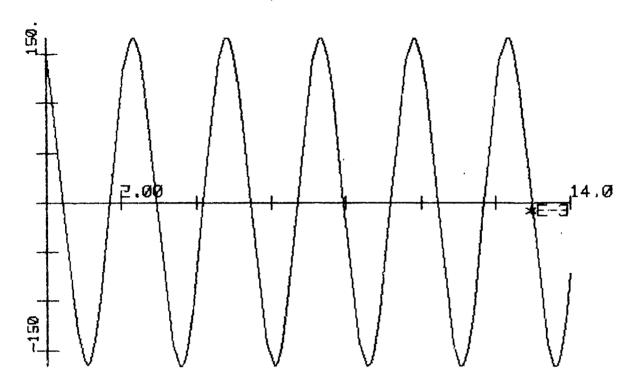
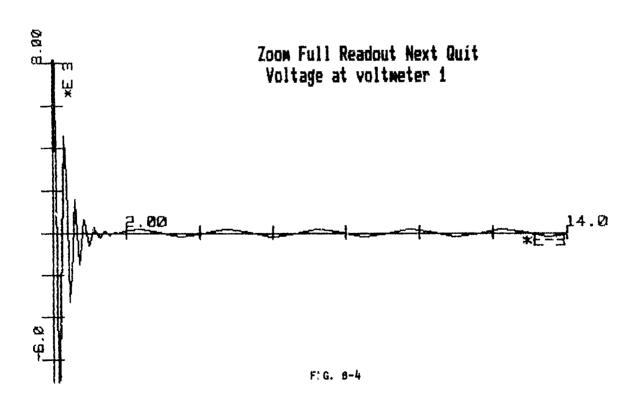


FIG. B-2



Zoom Full Readout Next Quit Voltage at voltmeter 1

FIG. B-3



### Zoom Full Readout Next Quit Voltage at voltmeter 2

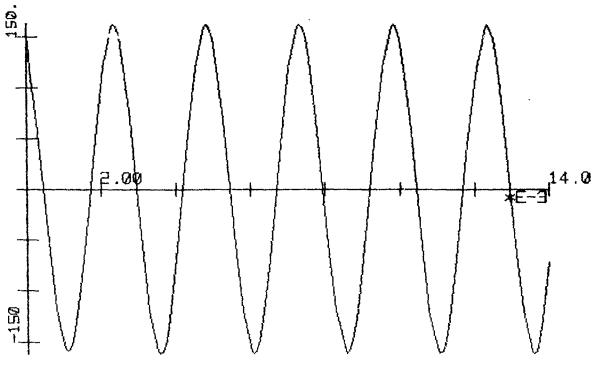


FIG. B-5

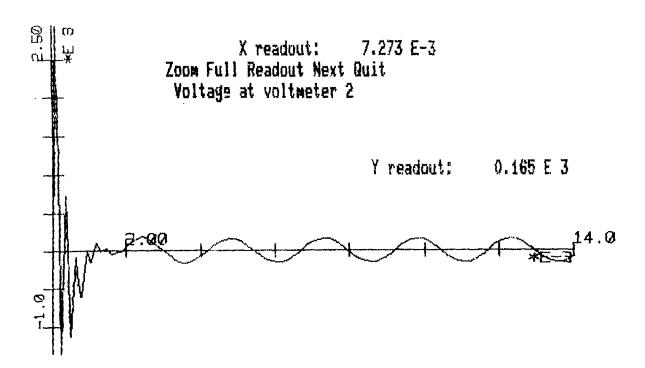


FIG. 8-6

#### REFERENCES

- (1) Electromagnetic Transients Program (EMTP) Reference Manual, Bonneville Power Administration, April 1982 Edition.
- (2) H. W. Dommel, "Digital Computer Solution of Electromagnetic Transients in Single and Multiphase Networks." IEEE Trans., Vol. PAS-88, pp. 388-399, April 1969.
- (3) H. W. Dommel, "Nonlinear and Time-Varying Elements in Digital Simulation of Electromagnetic Transients." IEEE Trans., Vol. PAS-90, pp. 2561-2567, Nov/Dec 1971.
- (4) W. S. Meyer, H. W. Dommel, "Numerical Modelling of Frequency-Dependent Transmission Line Parameters in an Electromagnetic Transient, "rogram." IEEE Trans., Vol. PAS-93, pp. 1401-1409, Sep/Oct 1974.
- (5) W. F. Tinney, J. W. Walker, "Direct Solutions or Sparse Network Equations by Optimally Ordered Triangular Factorization." Proc. IEEE, Vol. 55, pp. 1801-1809, November 1967. Also available in 1967 IEEE PES PICA Conference Record.
- (6) F. L. Alvarado, "Damping Numerical Oscillations in Trapezoidal Integration," EMPT Newsletter; 1981.



LIGHTNING PROTECTION ZONES FOR ROCKET LAUNCH COMPLEXES



A. Murakami and K. R. Pinckney
MSO Norton Air Force Base
J. D. Robb
Lightning and Transients Research Institute

ABSTRACT

This paper examines the "Rolling Ball Theory" of lightning protection zones. It provides support for this theory in terms of the critical gradient time history for lightning rods as described mathematically in terms of a prolate spheroid. The analysis shows how the critical threshold gradient for a sharp object lying below a lightning rod can emit a ground streamer which will move above the lightning rod before the critical gradient is reached on the taller rod. This occurs only if the radius of the lightning rod tip is substantially larger than the radius of objects lying within its zone of protection and this results in defeat of the rod. Also considered is the use of the catenary cable protection system over launch complexes and the need for it.

WHICH OCCURS in the ONE PROBLEM development of lightning protection for rocket launch complexes is the question of the area of validity for protection zones provided by Earlier theories lightning rods. considered historical data from power transmission lines in determining the protected areas from overhead ground wires or single rods. More recent considered the have theories importance of striking distance, the distance at which the step leader connects to ground streamers. This led to a rolling ball theory of lightning rod protection in which a hypothetical ball with a radius equal. striking distance theoretically rolled about a site determine the protection zones. The it contacts points which considered to be possible strike points. Support is given this theory by the examination of lightning rod tip gradients using prolate spheroids mathematically represent to The lightning rod geometry. investigation considers the action of streamers which initiate from low radius points within the protection zone as they climb above the lightning rod before the Lightning rod streamer threshold is reached.

The calculations support the rolling ball theory in defining a greatly reduced protection zone as compared with the classical conic 45 and 60 degree zones of protection.

CHANNEL MECHANISMS AND LIGHTNING LIGHTNING PROTECTION ZONES.

The mechanism for a lightning strike to ground is illustrated in Figure 1. As the lightning (or step leader) approaches the ground, it induces bound charge in nearby ground objects until the critical charge density and related local electric field are exceeded at the tip of any sharp high points in the area. Then

streamers issue from all local high points towards the step leader tip. The streamers can issue from points at the side of the step leader tip as well as from below it as illustrated in Figure 2.

The

fact that streamer can be induced off objects to the side of the step leader as well as below it lead to the rolling ball theory of lightning protection zones, (1)\*, (2). This new theory represents a refinement of the classic 45 and 60 degree zones of protection concepts which have been used for many decades in the protection of power transmission lines.

ground streamer initiates when the step leader reaches 100 to 300 feet above the ground depending upon the intensity of the stroke (or charge density in the channel) and by the geometry of the local terrain below the step leader. When the induced ground streamers come to within about 10 meters of closure with the tip of the step leader, close the streamers multiple | remaining distance. The multiple channels indicate the existence of very high local rates of current rise; otherwise, the first streamer to contact the tip of the step leader would cancel the potential difference and stop the other branch streamers from joining. This multiple channel closure is seen in both natural lightning ground strikes and laboratory simulations of the process as illustrated in Figure 3a and 3b. This multiple branch closure process has also been noted in lightning triggering from the Lightning & Research ship in which Transients four or five channels struck the ship one return stroke from This is suggested simultaneously.

parentheses designate \*Numbers in References at end of paper.

incidentally as a partial explanation for the steep front of the radiated waveform of natural lightning. It is suggested that this is a local effect which does not reflect the return stroke current except at this

point of closure.

At the point of closure, the charge stored along the channel can now flow to ground through the ground streamer and this flow to ground is described as the "high current return stroke." The high current return stroke proceeds up the channel to the cloud charge centers as the charge along the channel progressively dumps into the channel to flow to ground.

The charge in the channel is responsible for the high currents and high current rates of rise, but the total charge stored is relatively low - of the order of a few coulombs. When the high current return stroke reaches the cloud charge centers, the larger charge areas stored in the cloud are tapped and proceed through the channel to ground, but they have generally lower current levels and lower rates of rise than does the high current return stroke.

EXAMINATION OF TIP GRADIENT EFFECTS OF LIGHTNING RODS.

As shown in Figure 4, the streamers will initiate off a lightning rod when the threshhold is exceeded gradient and the threshhold gradient is determined by the incident electric field resulting from an approaching step leader as well as by the height and radius of the tip of the object. This can be conveniently examined mathematically by use of a prolate spheroidal geometry to represent the lightning a close which permits

approximation of the tip gradients.
As illustrated in Figure 4, if an object lies below a more rounded lightning rod tip, the gradient can exceed critical (the point at which ionization initiates), and a streamer will be induced off the lower object the ratios of the two are sufficiently different, a streamer initiated off the lower point may whimb above the height of the protection lightning rod before its critical threshhold gradient is reached and the streamer can continue above the higher rod. The streamer, in effect, now acts as a lightning rod. In this way, objects lying bolow a 60 or 45 degree come of protection may be struck.

The streamer was assumed to have been induced on the lower object because of a sharper radius and it propagated up past the lightning rod before a streamer was initiated on

The gradient amplification factor as a function of the ratio of tip radius to rod height is plotted using the expression for a prolate spheroid as shown in Figure 5.

With a few approximations, the general relationship between the tip radius and the lightning rod height at the streamer initiation threshold may be illustrated. Assuming a velocity of both the step leader and the ground streamer of about one meter per microsecond, the general

relationship may be seen as follows.

As the step leader approaches the ground, the ambient electric field at the ground increases nearly linearly with the step leader linearly movement as the ground electric field is determined primarily by the spacing. Thus, for a 10 meter movement of the step leader, 150 meters above the ground as illustrated in Figure 4, the ground ambient electric field increases 10m/150m or about six percent. Assuming a one meter per microsecond step velocity and double the gradient amplification factor on the lower rod, the electric field on the lower rod in the figure would just rise above the critical electric field threshold to initiate a streamer. In ten microseconds, the streamer would rise above the higher rod and now would be the highest point. The gradient on the higher rod, however, would have increased only six percent and wuld still be only about half Thus the tip radius is in determining protection critical. critical zones and height cannot be considered alone. The rolling ball theory of protection is consistent with strikes to objects below a 45 degree cone of protection and is a more realistic as well as a more conservative approach.

CATENARY WIRE TYPE LIGHTNING PROTECTION

The above arguments support the use of catenary wire protection systems such as used on space shuttle and in effect on power transmission lines (the overhead ground wire). This approach is illustrated in Figure 6 for a rocket launch area. With a wire overhead, much surer

protection is provided than with a rod because of the relatively small

area covered by the rod.

When a wire is supported by an insulated post such as used for Space Shuttle, much better protection is generally provided, as the lightning transients are only magnetically coupled from the lightning current flow in the catenary wire rather than conductively coupled by direct current flow through the launch tower structure.

#### PROTECTION RATIONALE

In discussions of lightning rods the reason for lightning protection needs to be considered in the design installations. protection protection zone which is entirely adequate for a power line, for which a lightning strike means only a temporary loss of power, may not be satisfactory for a rocket because of the possible hazard involved.

purpose of Thus, the protection needs to be considered very carefully in the margins which

are used in the protection.

For power line use, the rolling approach also the quantification of margins provided in terms of the basic Insulation Level (BUL) of the line. (1)This quantification could of course be done with a rocket at the expense of more complex calculations.

#### GECUND POTENTIALS

Also important is the problem of protection of ground personnel. Thus, ground systems have two very different purposes: (a) to minimize the voltages and currents coupled into critical circultry, and (b) to protect ground personnel from the hazard of earth current potentials. The importance of a low resistance and low impedance ground grid for both purposes can hardly be overemphasized.

The ground grid network does not affect the formation of ground streamers as the bound charge and induced streamers are of low enough level that they are easily fed even without ground grids. The earth resistance is usually sufficient. However, once the large lightning strike current begins to flow, only metallic ground grids are sufficient to prevent ground potentials hazardous to personnel.

It may be noted that in Figure

6, the catenary wire outside the fence. is grounded Thus lightning ground currents essentially outside the fence. lightning flow The interior with its ground grid has 109 differential ground potentials and relatively low hazard to personnel. It should be also be noted that induced streamers can still be a hazard unprotected personnel to the fence perimeter anywhere near a lightning strike.

#### STATISTICS

With the 120 degree and degree zones of protection, it Was possible to predict the number of strikes per year from the isokeraunic data (published data on the number of thunderstorm days per year). With the rolling ball theory of lightning protection zones of protection, a corresponding statistical theory is also needed and is being planned for further work.

#### CONCLUSIONS

The following conclusions drawn from the investigations.

o Based on this analysis, the rolling ball protection concept is recommended for use in the protection

design of rocket launch sites.

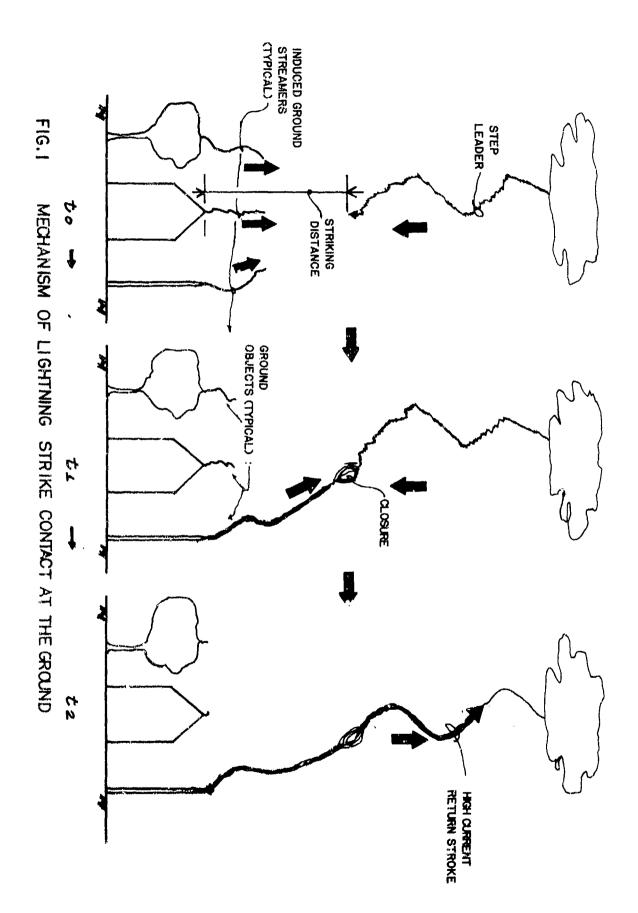
o For protection, the use of catenary wire overhead protection using insulated support howers is recommended for rocket launch sites as a method of obtaining superior protection.

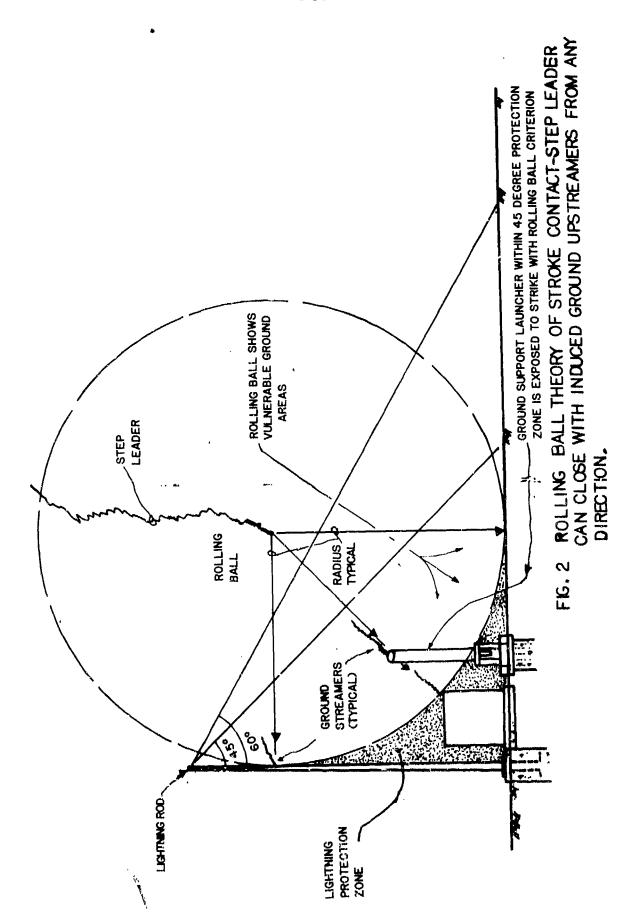
o The importance of providing a good ground grid system for rocket launch complexes for both protection sensitive electronics operation personnal on the site.

#### REFERENCES

R. H. Lee, "Protect Your Plant Against Lightning. " Instruments

and Control Systems, February 1982.
2. "National Fire Prevent Fire Prevention Handbook-1978. "NFFA"., Boston, MA.





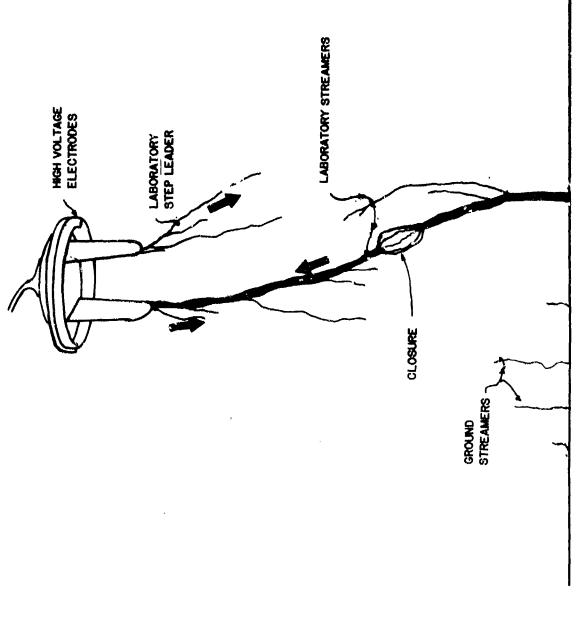


FIG. 3 A SKETCH OF LABORATORY STREAMERS





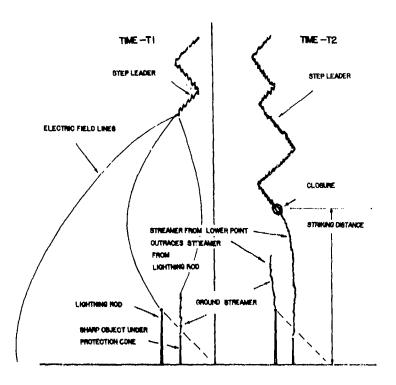
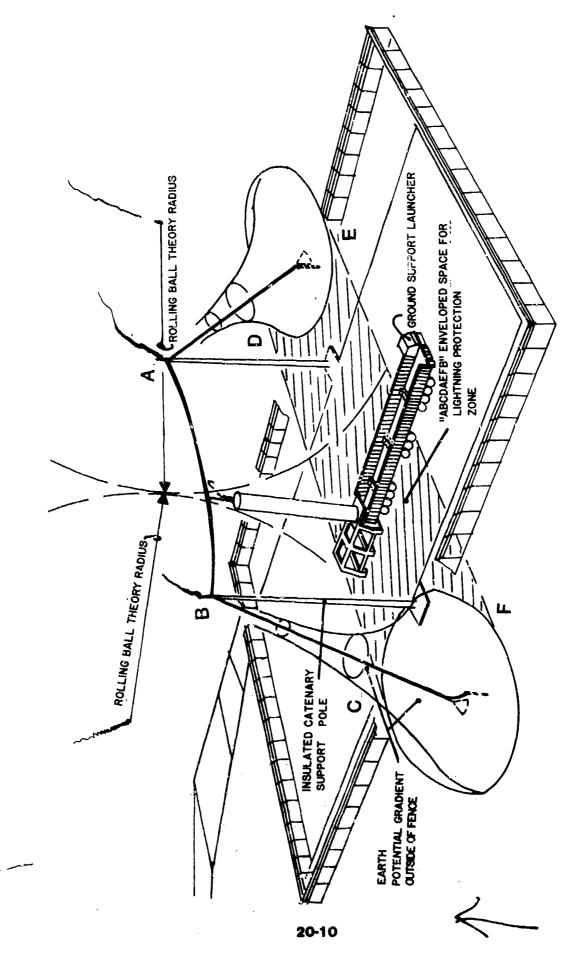


FIG. 4. MECHANISM OF PROTECTION CONE TAILURE

### Company of the Co

Figure 5. Gradient Amplification Factor (Free Space to Tip Electric Field Ratio) as a Function of Rod Length to Tip Radius Patio



LIGHTNING PROTECTION ZONE IN THE CATENARY SYSTEM TO PROTECT A TALL LAUNCHER; ZONE, "A BCDAEFB" ENVELOPED SPACE CONFINED W/ROLLING BALL SPHERES & EARTH SURFACE POT ENTIAL PARABOLOID FIG 6

the second

The MLRS Lightning Protection Program

By

John Robb and G. Edlin Lightning Transients Research Institute

ABSTRACT

The MLRS (Multiple Launch Rocket System) is a U.S. Army system capable of delivering twelve warheads, without reloading, to multiple targets up to twenty wiles in distance in less than one minute. Up to twelve offsets per target may be selected without additional Fire Control System computation. Figure 1 shows the complete vehicle which consists of three major sub-assemblies, i.e., the tracked vehicle built by FMC, the Self-Propelled Launcher Loader (SPLL), and two Launch-Pod Containers (LP/C), each of which holds six rockets with options for various types of warheads.

The MLRS has international significance in that it will be deployed by Armed Forces of the UK, and West Germany.

The MLRS is required to remain safe, from an EED hazards consideration, for specified median and maximum peak current and maximum total charge environments. The rocket motor ignitor EED and its safe/arm and firing circuit are the components applicable to this requirement.

Specific design techniques used to achieve the required hardness are discussed.

Evaluation tests were conducted at the Lightning Transient Research Institute's Miami, Florida facility to demonstrate compliance to specification requirements. Median peak current, maximum peak current, maximum total charge, and near-atrike test results are discussed including corrective measures required to satisfactorily complete one area of the test environment. The four options of corrective measures considered are discussed and rationals is given for the one chosen.

This paper was not available for incorporation into this book. Therefore, it will be published at a future date.

Ephyle)

A Contribution to the Analysis of Triggered Lightning: First Results Obtained During the Trip 82 Experiment\*

Вy

#### P. Laroche

Office National d'Etudes et de Recherches Aerospatiales B.P. 72 - 92322 Chatillon - France Phone: (1) 657.11.60

#### **ABSTRACT**

During the summer of 1982, the Thunderstorm Research International Program, organized at Langmuir Laboratory, Socorro, New Mexico, was Lainy devoted to triggered lightning analysis. Several teams performed related experiments (NMIMT, University of Arizona, WPAFB of USAF, CEA and ONERA).

This paper describes the principles of measurements and comments the preliminary results obtained by the following instruments:

- (a) a coaxial resistive shunt, installed under the attachment point of the lightning channel;
- (b) a UHF interferometer used for locating the sources of electromagnetic radiation associated with the various phases of the lightning stroke, including the pre-breakdown discharges;
  - (c) a set of frequency analysers with 1 s resolutin.

Fourteen cloud-to-ground triggered flashes have been obtained in 1982. A comparison with the results collected during the TRIP 1981 campaign will be presented.

This paper was not available for incorporation into this book. Therefore, it will be published at a future date.

<sup>\*</sup> Research supported in part by DRET (Direction des Recherchers, Etudes et Techniques de la Delegation Generale pour l'Armement).

## AD P002178

RELATIONS OF THE FLASHOVER VOLTAGE VERSUS
THE VELOCITY OF THE MOVING ELECTRODE

 $\rightarrow$ 

Y. Nagai, T. Koide, and K. Kinoshita Sagami Institute of Technology, Fujisawa, Japan

ABSTRACT

It is shown experimentally how the velocity of the moving electrode effects on the flashover voltages between the stationary plane electrode and the moving electrode. In case of stationary electrode system, the space charges produced from the tip of the electrode distribute to relax the strength of the electric field at its point, and prevent the flashover. While the electrode set in motion, it is difficult to suppress the development of the corona or streamer and it becomes easy to lead to flashover, because the tip of the electrode moves always prior to the existing region of space charges. This explains why the lightning is triggered easily by a moving aircraft or a launching rocket carrying a wire connected to the ground.

A METHOD OF TRIGGERING LIGHTNING by launching the rocket carrying a wire which is connected to the earth is one of the most effective method to research the lightning discharge phenomena (1)\*, (2), because it is able to control the striking time and point of lightning, which are hardly to do in case of natural lightning. The height of the rocket which triggers lightning depends on the electric field strength at the launching site (3). The launched rocket with high speed produces some conditions for triggering the lightning: increase of the electric field at the front of the rocket, generation and development of corona or streamer from that point and so on. One of the most important reason for triggering lightning is that the coronas generated at the front of the rocket are not steady stable state, because of the movement of the rocket with high

Based on the above simple conception, it is a purpose of this paper to investigate experimentally how the moving electrode effects on the flashover voltages between the stationary and moving electrodes. The experimental results of this kind may be useful to simulate the lightning strike to the moving aircraft. In our experiment, we rotate the electrode around a point to obtain an appropriate speed (about 200 km/h which corresponds to 50 - 60 m/sec) at the tip of the electrode, instead of moving the electrode along a straight line. Hence, in this paper "the velocity of the moving electrode" means the velocity at the tip of the rotating electrode.

Experimental results using a high potentialized stationary-plane and a grounded moving-needle or -sphere electrodes system show that the increase of the velocity of the moving electrode tends to decrease the flashover voltages in case of application of negative DC voltages to the stationary plane electrode, while the flashover voltage increases gradually in case of application of positive DC or AC voltages to the stationary plane electrode, because of polarity effect of the flashover charactericity.

\*Numbers in parentheses designate References at end of paper.

#### EXPERIMENTAL APPARATUS

The schematic diagram of the experimental apparatus is shown in (Fig. 1). The stationary plane electrode is made of a tin plate with a thickness of 0.4 mm and a diameter of 600 mm, the edge of which is made round, not to generate the corona discharge from the corner of the plate, by soldering the copper pipe with a diameter of 6.0 mm along the adge of the plate and by finishing the edge section with a #240 sandpaper. As the moving electrode we use a brass rod with a diameter of 6.0 mm which is fixed vertically to the rotating axis of the pulley coupled to the motor through a belt. Two kinds of rod are used, one of which is capped by the brass cone with a vertical angle of 8 degrees and the other is mounted with the brass sphere

of a diameter of 10 mm. Hereafter, we call the former as the needle electrode and the latter as the sphere electrode. The length L from the center of the rotation axis to the tip of the moving electrode is 227.0 mm in case of the needle electrode and 223.0 mm of the sphere electrode.

The moving electrode is installed so as that the rotation axis is parallel to the surface of the stationary plane electrode, that is, the surface produced by the rotation of the electrode is perpendicular to that. Attachment of the balance weight to the other end of each rod can make the rotation of the moving electrode be stable and uniform.

Motive force of the moving electrode is transmitted from the DC survo-motor through a rubber belt. The revolution frequency N of the moving electrode is changeable from 0 to about 40 cycles per second by changing the applied voltage to the DC motor. Hence, the velocity at the tip of the moving electrode is changeable from 0 to 55 m/sec, which corresponds to about 200 km/h, because the velocity v at the tip of the moving electrode is obtained by  $v = 2 \pi L N$ .

In this experiment, the gap spacing D between the electrodes is estimated as the smallest distance between the electrodes both in the stationary (v = 0) and moving electrode systems. The high voltage, (A) +DC, (B) -DC, and (C) AC, is applied to the stationary plane electrode, and the moving electrode is always grounded through the rotation axis of the moving electrode.

The experiments are carried out in a dark room to take photographes of the discharge circumstances: corona and flashover phenomenon, by using the ASA 400 film.

#### EXPERIMENTAL RESULTS

In (Figs. 2 and 3) are shown the characteristics of the flashover toltage versus the velocity of the moving electrode in case of using the needle and sphere electrode, respectively. In each figure, (A) is at the conditions of applying +DC voltage to the stationary plane electrode, (B) -DC voltage and (C) AC voltage, respectively. The flashover voltages in all cases of (A), (B), and (C) are represented with the crest values.

In case of the needle electrode, (Fig. 2-(A)) shows that the flashover voltage in nearly constant independent of the velocity of the moving electrode except the gradual increase within a small velocity regions and the case of D=30 mm in which it tends to decrease gradually accompanying with a small variations of it. On the other hand, (Fig. 2-(B)) shows that it increases gradually with the increase of the velocity of the moving electrode, and after reaching the peak voltage it tends to decrease weakly for all of the gap spacing used in this experiment. (Fig. 2-(C)) shows that its charactericity is resembled to that of (Fig. 2-(A)) in case of small gap spacing ( $D \le 20$  mm) as it is

nearly constant independent of the velocity of the moving electrode, and to that of (Fig. 2-(B)) in large pap spacing (D  $\geq$  30 mm) as it increases gradually and after reaching the peak value it decreases weakly.

In case of the sphere electrode, (Fig. 3-(A)) shows that at smaller gap spacing (D 15 mm) the flashover voltage is nearly constant independent of the velocity, but at large gap spacing (D = 20 mm) it increases with the increase of the velocity. On the other hand, (Fig. 3-(B)) shows that at small gap spacing (D =10 mm) it is nearly constant independent of the velocity of the moving electrode. However, in case of large gap spacing (D ≥ 20 mm) it decreases abruptly to lower values than that of the stationary case (v = 0) with increasing the velocity and remains nearly constant values after that. (Fig. 3-(C)) shows that at small gap spacing (D = 10 mm) the flashover voltage is nearly constant, but it increases with the velocity in case of larger gap spacing (D > 20 mm). These tendencies in (Fig. 3-(C)) resemble to that in (Fig. 3-(A)).

The above results show that in the case of applying the negative polarity voltages to the stationary plane electrode the flashover voltage decreases or tends to decrease with increasing the velocity of the moving electrode, inspite of the electrode shape.

#### DISCUSSIONS

The electric field at the tip of the moving electrode used in this experiment is extremelt nonuniform to be concentrated to the tip of the electrode. Increase of the applied voltage to the stationary plane electrode produces a partial breakdown at the tip of the moving electrode and the self-sustaining discharge, corona, is manifested.

In our experiment, as the electrode is rotating around a axis, the tip of the moving electrode approaches to the opposite-side plane electrode or departs from it, alternatively. As the applied voltage across the gap is kept constant, the electric field at the tip of the moving electrode increases in case of approaching to the opposite-side plane electrode and decreases in case of departing from it, and the corona is produced depending on the electrode motion. If the charges emerged from the tip of the moving electrode do not diffuse or disappear quickly, they accumulate along the trajectory of the tip of the moving electrode, then, interrupt the succeeding pour of the charges from the electrode. If the space charges diffuse or disappear quickly, the emerged charges from the moving electrode transverse the gap immediately, and lead to flashover between the gap ensily. This nature is noticed as the "polarity effect" of corona or flashover.

In (Fig. 4) are shown the photographes representing the development of the corona discharge and flashover circumstances in the use of the needle electrode, where the applied voltage between the electrodes is about 80 % value of the flashover voltage. In these figures, the

velocity of the moving electrode is constant of 21.9 m/sec and the rotation of the electrode is clockwise direction as shown in (Fig. 1). The gap spacing D, the corona voltage  $V_{\rm C}$ , which means the voltages at taking the photograph of corona discharge, and the flashover voltage  $V_{\rm f}$  are (A) D = 20 mm,  $V_{\rm C}$  = 18.0 kV and  $V_{\rm f}$  = 21.0 kV at the conditions of applying +DC voltage to the stationary plane electrode, (B) D = 50 mm,  $V_{\rm C}$  = 32.0 kV and  $V_{\rm f}$  = 39.8 kV at -DC, and (C) D = 40 mm,  $V_{\rm C}$  = 30.0 kV and  $V_{\rm f}$  = 37.6 kV at AC, respectively.

In the needle against plane electrode system, the polarity of the needle electrode is inversed to that of the potentialized plane electrode. Hence, when the plane electrode is in positive (or negative), the polarity of the needle electrode becomes negative (or positive). In case of (Fig. 4-(A)), observation of the luminous trajectory of the moving electrode by corona discharge shows clearly that the corona emerged from the tip of the moving electrode ceases to develop toward the opposite-side plane electrode. This characteristic coincides with that of the negative corona in stationary electrode system. On the other hand, in case of (Fig. 4-(3)), the corona is easy to develop toward the opposite-side plane electrode and the diffused type corona, glow-corona, is observed over a fairly broad region within the gap spacing. case of (Fig. 4-(C)), it is shown that the corona circumstances resemble to that in (Fig. 4-(A)).

It is interesting to note that the luminosity of the corona discharge shows brighter at the left hand side from the vertical line through the rotation axis of the moving electrode than that at the right hand side. As the rotation occurs in the clockwise direction, charge quantities emerged from the tip of the moving electrode at approaching to the stationary plane electrode are more than that at departing from

In (Fig. 5) are shown the characteristics of the corona form action versus the velocity of the moving electrode, when the needle electrode with gap spacing of 50 mm and negative BC voltage of 32.0 kV is used, except (Fig. 5-(D)), in which negative DC voltage of 38.8 kV is applied.

At the small velocity of the moving electrode as shown in (Fig. 5-(A)), in which the velocity of the moving electrode is 21.9 m/sec, the corona brightens nearly uniformly along the moving direction of the electrode. However, by increasing the velocity of the moving electrode ((A) v = 21.9 m/sec + (B) v = 35.6 m/sec + (C) v = 42.1 m/sec), the uniformity of corona brightness is diminished and the luminous part of the corona is divided into two parts with inserting a dark space, as shown in (Figs. 5-(B),(C)). These manifestations show that the movement of the electrode makes the space charges concentrate into some narrow region.

As shown in (Fig. 5-(D)), the flashover takes place at the right hand side region from the vertical line through the rotation center. Comparison between (Fig. 5-(C)) and (Fig. 5-(D)) shows that this region corresponds to the boundary of the luminous region of the corona discharges. Hence, it coincides with the boundary of the space charges and so the strong electric field region generated from the space charges.

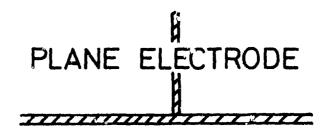
From the above discussions it is concluded that the motion of the electrode effects on the space charges emerged from the electrode, and so the flashover voltages.

#### ACKNOWLEDGEMENT

The authors would like to express their thanks to Prof. Y. Nishida at Utsunomiya University for his kind comments. They also express their thanks to Messrs. N. Tamura and N. Hara for their helpness in experiments.

#### REFERENCES

- 1. M.M. Newman, J.R. Stahman, J.D. Robb, E.A. Lewis, S.G. Martin, and S.V. Zinn, "Triggered lightning strokes at very close range." J. Geophys. Res., vol. 72, pp4761-4764, 1967.
- 2. R. Fieux, C. Gray, and P. Hubert, "Artificially triggered lightning above land." Nature, vol. 257, pp212-214, 1975.
- 3. K. Horii, and S. Sumi, "Flashover characteristics between the plane and the abruply launching rod electrode." Hoden-Kenkyu, No. 89, pp3-8, February 1982 [in Japanese].



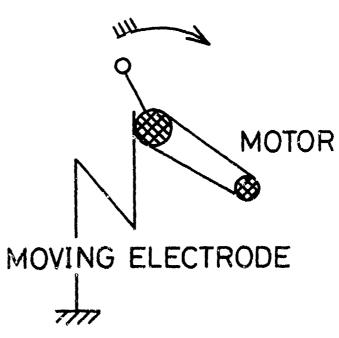


Fig. 1 - Schematic diagram of experimental apparatus

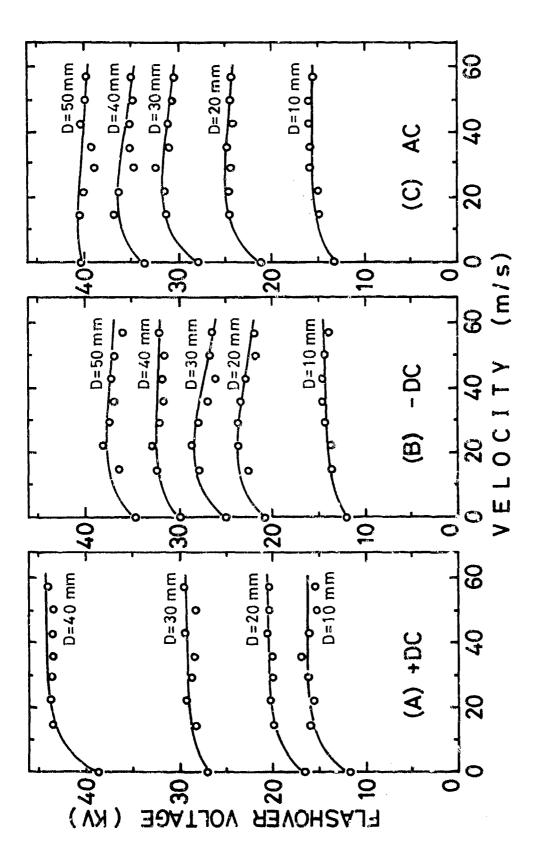


Fig. 2 - Characteristics of the flashover voltage bersus the velocity of the moving electrode in case of needle electrode

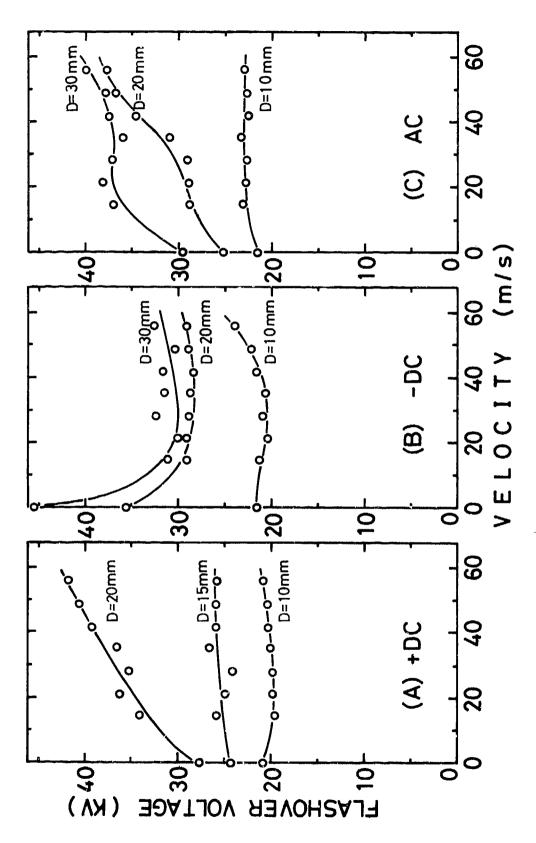
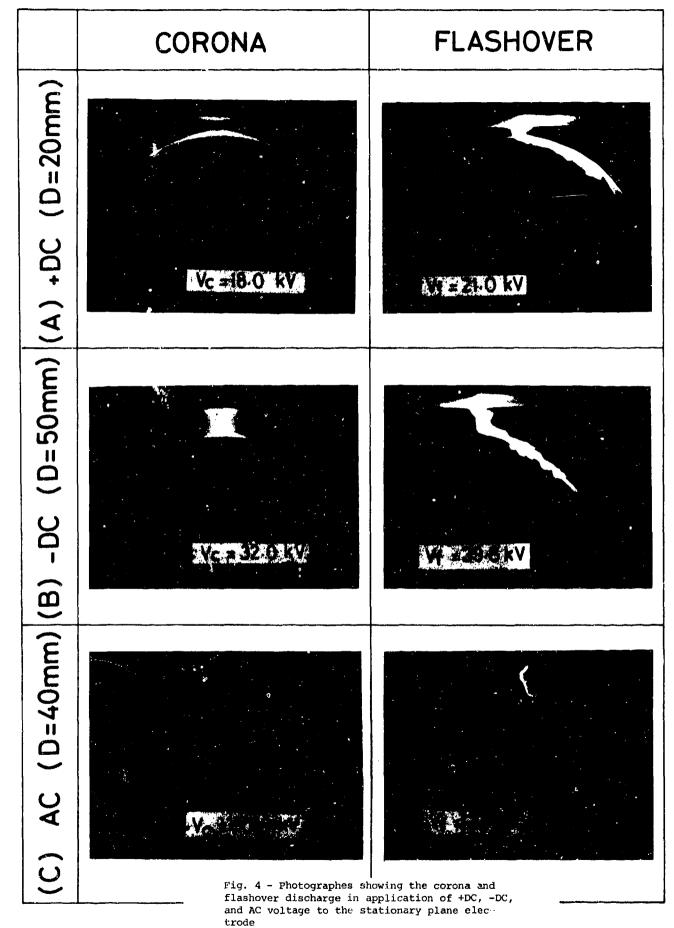
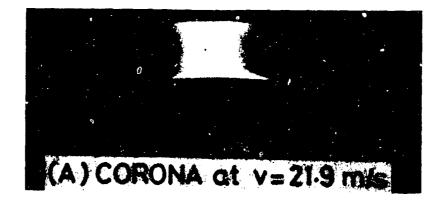
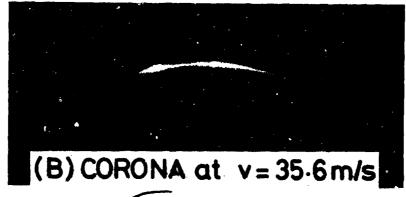


Fig. 3 - Characteristics of the flashover voltage versus the velocity of the moving electrode in case of sphere electrode







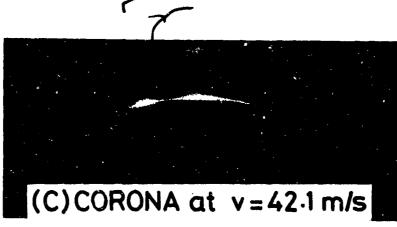




Fig. 5 - Characteristics of the corona discharge state versus the velocity of the moving electrode

23.8

STATIC DISCHARGE AND TRIGGERED LIGHTNING

## AD P002179



Heinz W. Kasemir Colorado Scientific Research Corporation, Berthoud, Colorado

#### ABSTRACT

The mechanism of a lightning discharge as introduced by Schonland(1) and coworkers 1938 is analagous to a spark discharge between two metallic electrodes. Charges are collected by the leader stroke from the negatively charged cloud volume (negative electrode) and carried either to ground (positive electrode) producing a ground discharge or to the positively charged cloud volume producing a cloud discharge. We may call this the unidirectional or charged leader theory. A different mechanism has been suggested by the author, Kasemir (2) 1950, based on a uncharged leader (net charge zero) that works only with induced charge separation in the conductive lightning channel itself. This leader growth to both sides from a nucleus in the high field regions between oppositely charge cloud volumes. One end penetrating into the positive space charge carries negative induction charges and the other end penetrating into the negative space charge region carries positive induction charge. The net charge of the leader is zero. We will call this bi-directional or uncharged leader theory. This leader does not collect cloud charges but uses only the electric field energy provided by the charged cloud for its mechanism. An energy calculation shows that the unidirectional leader requires energy input above that provided by the cloud. Therefore, even beside the unexplained charge collecting mechanism the commonly used unidirectional leader is not a workable physical process. On the other hand, the bidirectional leader does not require charge collection and obtains enough energy from the electric field of the thunderstorm to feed the energy consuming processes of the lightning discharge, such as ionizing and heating the channel production of electromagnetic fields and radiation, etc. Applied to the problem of triggered lightning the bi-directional leader theory furnishes unexpected but far reaching results. For instance, it is shown that all so-called static discharges encountered on an aircraft are triggered lightning. Since triggered lightning outnumbers by far the rather rare hit by natural lightning and since warning devices, danger zones, etc., are quite different for the two types of accidents, a more intense study of the rather neglected triggered lightning is recommended. > An intriguing controversy between pilots and scientists on charge and energy problems of static discharges will be discussed and resolved in this paper. These problems always center on the question: ("Where does the lightning discharge obtain its charges to produce the measured currents or fields, if it is triggered far away from a thundercloud?" These problems are resolved by the uncharged leader theory, which explains that lightning does not have to collect charges from the environment be it a thunder cloud or a volume of clear air. The charges are generated in the lightning channel itself by ionization and then separated in the channel by the induction mechanism.

INTRODUCTION

It is the purpose of this paper to correct a mistake made in the theory of the lightning discharge which may be labelled the cloud charge collecting leader usually known as stepped leader, cloud to cloud, intra cloud, or cloud to air discharge. All these discharges are essentially of the same type. The correction includes the following points. The channel does not carry any net charge collected from the cloud. It works only with induced charges generated inside the channel, separated ty the external cloud field and energy for growth and other energy consuming phenomena is obtained solely from the electric field. From this new point of view we can obtain the answer to many enigmatic problems. All static discharges are lightning triggered by the airplane. Critical objections that the aircraft cannot provide charge nor energy to produce a lightning discharge become irrelevant, since the lightning discharge obtains the energy from the field and manufactures the charges inside its channel by ionization. Charge separation is then accomplished by the field. However the net charge of the channel remains zero. Since the static discharges outnumber by far the rare hit of an airplane by natural lightning a new look at the lightning hazard to airplanes appears to be necessary. The difference between the hit by a natural discharge and a triggered discharge includes occurrence, danger zones and in consequence development of warning devices, direction of research, etcetera. This will be different for the two types of accidents caused by a triggered lightning or by a naturally occurring lightning discharge.

#### THE LEADER STROKE

There are two basically different physical concepts of the leader stroke of a lightning discharge, one introduced by Schonland (1) 1938 and the other one by Kasemir (2) 1950. To follow and comprehend the discussion in this paper it is essential to understand thoroughly the differences between these two concepts.

THE LEADER BASED ON CLOUD CHARGE COLLECTION - Schonland's concept of the stepped leader of cloud to ground discharge has been developed and diversified over the last 48 years. It includes in essence also the different types of cloud discharges, for instance, intra cloud, cloud to cloud, and cloud-air discharge. Detailed descriptions are given in the literature

and text books. Uman (3) 1969, Golde (4) 1977, Volland (5) 1982. Figure la shows a brief sketch of a stepped leader advancing from the cloud to ground. The leader has collected negative charge from the cloud and stored along its channel with a charge per unit length of about q=1C/km. contact with ground is made the negative charge flows into the ground in the return stroke. This process may be repeated several times by a dart leader-return stroke sequence bringing more negative charge to ground, each time discharging new areas of the negatively charged cloud volume by the upward or sideways growing branched lightning channel. After the lightning is terminated a portion of the cloud charges and the charges on the lightning channel have flown into the ground. Figure 1b.

In Figure 1c the same discharging mechanism is shown for an intracloud In this case it is an discharge. upward moving streamer which collects negative charge from the lower part of the cloud and moves it to the upper positive part of the cloud. direction negative to positive is favored by Smith (6) 1957. Ogawa and Brook (7) deduce from field records at the groundin unidirectional descending streamer carrying positive charge downwards Figure 1d. However, in a footnote they mention the possibility of a bidirectional streamer moving upwards and downwards as shown in Figure 2c and

2d.

THE STATE OF THE S

THE LEADER BASED ON INDUCED CHARGES - The leader based on induced charges has been introduced by the Kasemir (2), for the following reasons: The thundercloud has to be considered as an excellent insulator. The cloud charges are immobile and fixed to there place in the time period of a lightning discharge of about one second. They cannot take an active part in the discharge. 2. Even if they are made mobile - Uman (3) suggests for this purpose a break down field extending over a larger region between positive and negative charged cloud volumes - the charges would follow the electric field lines, i.e., they would spread as far apart as pessible, especially if we are dealing There is no with unipolar charge. physical law which makes even mobile negative (or positive) cloud charges concentrate in a lightning channel. This would require energy that cannot be drawn from the cloud. The energy calculation of this problem is discussed in the next section. 3.

hypothetical charge collecting mechanism by a widespread filament system of the lightning has never been explained.

大き 本文書

In the new theory the incization process inside the channel generates a large number of positive ions and elec-A slight shift of electrons along the channel following the external field will create a surplus of electrons at one end of the channel, forming the required negative induced charge, and at the same time leaving at the other end of the channel a surplus of positive ions, generating in this way the required positve induced charge. The net charge of the channel still remains zero. The cloud charge collecting mechanism is completely avoided.

Figure 2a shows the charge distribution on the uncharged stepped leader corresponding to Figure la of the charged leader. Figure 2b shows the charge distribution on the lightning channel after the return stroke - or the dart leader- return stroke sequence is finished. Note here the marked difference between the corresponding Figure 1b, where the lightning channel is completely discharged, and Figure 2b, where the lightning channel carries a maximum of positive charge. When the ground discharge has brought -30 coulomb to ground then +30 coulomb of charge remains on the lightning channel. During the whole discharge the cloud charges haven't moved or participated in the discharge in any way. may mention that Figure 2b shows also the charge distribution of a rocket triggered lightning for a rocket fired from the ground but grounded by a trailing wire. Figure 2c and 2d show the charge distribution at the beginning and at the end of a cloud discharge. Here too the lightning has the maximum charge density on the channel at the end of the discharge. The cloud charges remain at their 'place. In the exact meaning of the word "discharge", neither cloud nor ground discharges "discharge" the cloud. What they do in fact is to transport the opposite charge into the cloud volume. During the life time of the lightning strike this charge is still confined within the lightning channel. actual neutralization between cloud and lightning charge occurs after the lightning is over. This neutralization process may take a minute or more rather than a second or less. After the lightning loses its conductivity and free electrons are attached to air molecules the wir ions will disperse in the neighborhood of the channel,

neutralize oppositely charged cloud elements or attach themselves to neutral cloud elements or precipitation particles. We will end up with a cloud volume containing positive and negative charged cloud elements or precipitation particles. This will cause increased coagulation and result in the rain guah often observed after a lightning discharge. The idea that the lightning causes the rain gush has been promoted for some time by C. Moore. An excellent description of the whole process is given by Moore and Vonnegut (8). It will be difficult to explain this effect for a ground discharge by the charged leader, which just removes negative cloud charge from the lower part of the thundercloud. (see Figure 1b).

#### ENERGY PROBLEMS OF THE LEADER STROKE

Energy calculations are not often applied to lightning or thunderstorm processes. They are, however, quite useful to check if a suggested mechanism is energy consumming or producing lightning should consume thunderstorm energy since in turn the lightning has to provide energy for all the different processes necessary to or connected with its growth. These are mainly ionizing and heating the channel, producing electromagnetic radiation, building a magnetic field, etcetera. In general we may consider the lightning discharge as an energy converter.

ENERGY BALANCE OF THE CHARGED LEADER - To calculate the energy balance of the charged leader we need a mathematical model and a scheme of the calculation. With reference to Figure la we represent the negatively charged volume of the thundercloud by a sphere of radius R filled with negative charge Q of constant charge density  $\rho$ . The leader is represented by a spheroid filled with negative charge  $\mathbf{Q}_1$  with constant charge per unit length q. centerpoint of the leader is positioned at the lowest point of the aphere surface and the long axis is radially directed. We calculate now the electric energy U of the system before the leader has formed and the energy V after the leader has formed to length L. The difference W of U and V

$$V = U - V \tag{1}$$

will tell us if the formation of the leader has consumed energy, U>V, W>O, or if the formation has increased the energy of the system U<V, W<O. The

second result indicates a non workable mechanism and the first result a workable one. U is the energy of the charged sphere. If  $\phi$  is the potential function inside the sphere we integrate the product  $\rho\phi$  over the volume of the sphere. This gives with the factor 1/2 the energy U.

$$U = 4\pi R^5 \rho^2 / 15\varepsilon = 3Q^2 / 4\pi \epsilon R.$$
 (2)

The energy V consists of two terms. First we have after removing the charge  $\mathbf{Q}_1$  from the rim of the sphere the main portion of  $\mathbf{Q}_2$  in the now slightly smaller sphere of radius  $\mathbf{R}_1$ . For the calculation of the energy  $\mathbf{U}_1$  of the smaller sphere we use also Equation (2) replacing  $\mathbf{R}$  by  $\mathbf{R}_1$ .

$$U_1 = 4\pi \epsilon R_1^5 \rho^2 / 15 \epsilon$$
. (3)

Furthermore, we have to concentrate  $\mathbb{Q}_1$  into the spheroid representing the leader. If  $\mathbb{C}_1$  is the capacity of the spheroid and K the concentration energy, we have

$$K = Q_1^2/2C_1.$$
 (4)

From Equation (1), (2), (3), and (4) we obtain the final result

$$W = U - U_1 - Q_1^2 / 2C_1. (5)$$

U-U<sub>1</sub> represents now the energy of a very thin spherical shell charged with the charge  $Q_1$ . We can either make the transition  $R_1 \rightarrow R$  using Equations (2) and (3) or use right away the capacity formula (4) replacing  $C_1$  by  $C = 4 \times \epsilon R$ . C is the capacity of the spherical shell. The result is then

$$W = -Q_1^2(1/C_1-1/C)/2.$$
 (6)

Since C is always greater than  $C_1$ , the energy difference is negative and consequently the charged leader mechanism is not a workable concept. From a physical point of view the result is self evident, since — as mentioned above — the concentration of charge requires always an energy input.

ENERGY BALANCE OF THE INDUCTION LEADER - J. A. Stratton (9) gave in his textbook, "Electromagnetic Theory," under section number 2.13 a theorem on the energy of uncharged conductors in the following verbal and mathematical formulations: "The introduction of an uncharged conductor into the field of a fixed set of charges diminishes the total energy of the field", or expressed in a mathematical formula

$$W = \left\{ \int_{V_0} \varepsilon E^2 dV + \int_{V_1} \varepsilon (E - E')^2 dV \right\} / 2. \quad (7)$$

Wie again the difference of the energy U before and the energy V after the introduction of the conductive apheroid representing the leader of a lightning discharge. E and E' designate the field vestor before and after the body is brought into the field. It shall be understood that Stratton's expression "uncharged conductor's" means that the net charge on the conductor is zero. Induced charges are permitted and present since they are the cause of the diminishing of the field energy. This theorem, mathematically expressed in Equation (7), proves the point we wented to make which is:

The leader mechanism introduced by Kapemir 1950, which is based on an uncharged bidirectional growing channel carrying only induced charges can draw enorgy for its growth and connected energy consuming phenomena from the energy stored in the electric field of a thunderstorm.

We apply now Stratton's Equation (7) to a slim spheroid presenting the leader for the case shown in Figure 2a. The leader is restricted in length so that the cloud field can be assumed constant in the neighborhood of the leader. The equation of the potential function of the uncharged conductive spheroid exposed to a constant electric field is generally known or can be found in any textbook of potential theory or electricity, for instance, 5mythe (10) "Static and Dynamic Electricity." To obtain the field E' and solve the integrals of Equation (7) requires only straightforward calculus. Use partial integration to solve the second integral.

The spheroid has the long axis a, the short axis b, and the eccentricity c. The solution of the first integral  $I_1$  in (7), which has to be taken over the inside of spheroid  $V_{\Omega}$  is

$$I_1 = 4\pi \epsilon E^2 ab^2/6$$
. (8)

The solution of the second integral  $I_2$  taken over the outside of the spheroid is

$$I_2 = 4\pi \epsilon E^2 a^3 (1-b^2 Q_0/ac)/6Q_1$$
 (9)

$$Q_0 = \frac{1}{2} \cdot \ln \frac{a+c}{a-c}$$
;  $Q_1 = \frac{a}{2c} \cdot \ln \frac{a+c}{a-c} - 1$  (9a)

 $\mathbf{Q}_{0}$  and  $\mathbf{Q}_{1}$  are Legendre's Polinomials of

second kind and order 0 and 1. Inserting and combining Equation (8) and (9) in Equation (7) we obtain

 $W = 4\pi \epsilon E^{2} u^{3} (1-b^{2}(Q_{0}-Q_{1})/a^{2})/\epsilon Q_{1}. \quad (10)$ 

or in good approximation for slim spheroids,

 $W = 4\pi \epsilon E^2 a^3/6Q_1$ ; b<<a. (10a)

STATIC DISCHARGE AND TRIGGERED LIGHTNING

We are now in a position to take a new look on lightning strikes to aircraft, static discharges and triggered lightning, and the problems involved in energy and charge supply. Harrison (11) reported on a controversy between pilots and scientists representing observation on one side and theory on the other side. Since the confusion existing about static discharges and triggered lightning cannot be better illustrated than by this discussion, we quote here from a paper of Clifford (12) who gives the following description of the controversy:

"The pilots almost unanimously argeed that there are two distinct types of lightning observed in flight. The most common variety usually occurs while flying in precipitation at temps-ratures near freezing. This type is preceded by a build up of static noise in the communication gear and the presence of corona (St. Elmo's fire) can be observed if the flight is at night. The build up may continue for several seconds before the discharge terminates the static and corona.

The second variety occurs abruptly without warning. It is most likely to be encountered in or near thunderstorms, in contrast to the former variety which is more likely to be experienced in precipitation that has no connection with thunderstorms. Pilots tend to believe that the slow build up type of discharge is not a true lightning strike but rather a discharge of excess charge build up on the aircraft by flying through precipitation. The non-thunderstorm type greatly outnumbers the other. Both kinds can create a brilliant flash and a boom which can be heard throughout the airplane.

The response of the scientists to the pilots' static discharge theory has been universally negative. They insist that insufficient charge can be stored on an aircraft to produce a discharge which looks and sounds like lightning.

Scientists are oven more emphatic that insufficient energy could be contained in such a static charge buildup to produce any visible evidence such as burn marks, pitting or other damage on the aircraft. Yet, the pilots continue to insist that the aircraft is discharging and that the discharges do manifest themselves by bright noisy arcs and (not all pilots are sure about this) visible damage. The controversy has been characterized as a difference in view between scientists of long standing and pilots of long sitting."

This is a remarkable and illustrative description of the problem of the triggered lightning. Scientists who still adhere to the charged leader theory of the natural lightning discharge will have extreme difficulties in solving the charge supply or energy problems of the static discharge. What they obviously don't realize is that the same problem exists with the natural as with the triggered light-Using the uncharged leader nina. theory there is no problem in any of these cases. What the pilots label static discharge is nothing else than a triggered lightning. The energy is furnished from the electric field. It would not matter if the field is produced by a thundercloud, by electrified shower clouds or the debris clouds after a thunderstorm which are known to be highly electrified. Even snowstorms which produce very few natural lightning discharges or non at all generate high electric fields capable of providing the energy of a triggered lightning. The starting nucleus is the airplane itself. Since it is much larger than a precipitation particle it can trigger lightning discharges in clouds where the field is not strong enough for a precipitation particle to do so. The pilots emphasize the point that flying through precipitation close to the zero degree level, or more precisely, through a cloud region containing a mixture of ice and water enhances the possibility of a static discharge. This too, is a valid observation since flying through sleat or wet snow produces very effective triboelectric charging of the aircraft. This charging of the aircraft will not be able to furnish enough charge or energy for a lightning discharge but it will help in the critical atage of converting corona into a lightning As moon as a sufficient discharge. long filement is established the externel electric field can take over and provide the necessary energy for

further growth. This help in starting the discharge furnished by a large nucleus and friction charge will enable the sircraft to trigger lightning in relative weak fields where the ensuing lightning is also weak and it may not be easy to detect marks on the aircraft. However, this may lead to the wrong conclusion that triggered lightning -or static discharges - are generally harmless. This will not be true if the relatively weak leader reaches ground and the aircraft is exposed to the return stroke. Furthermore, not knowing how to differentiate a triggered lightning from a hit by a natural lightning it is a fair conclusion that many lightning discharges triggered in a thunderstorm are mistaken for lightning hits. If the trigger mechanism works in the weaker fields of non-thunderstorm clouds there is not reason to assume that it wouldn't work even better in the stronger fields of thunderstorms. The question here is how to distinguish between a triggered and the hit of a natural lightning. The step leader of a natural lightning has still a velocity of about 10 m/s. A leader coming towards the airplane would bridge 100 meter in 1 millisecond or 1000 meter in 10 milliseconds. This is too short a time for a human eye to focus on or resolve any detail. Therefore the rtatement of the pilots that, "The second variety occurs abruptly without warning," is again correct. streamers emerging from an airplane to meet or intercept a lightning, shown in most drawings of such an event, are certainly not based on observation.

With the exception of the case that the aircraft was already in corona before the lightning hit we have here a simple rule to differentiate the triggered lightning from the hit by a natural lightning.

Triggered lightning (static discharge) is preceded by corona discharge, which lasts long enough to be perceptible by human senses, and which is stopped at the occurance of the lightning discharge. The hit by a natural lightning occurs abruptly without a preceding perceptible corona discharge.

The distinction between the triggered and not triggered lightning variety is important since in accordance with pilots observations the first greatly outnumbers the second type. (Estimatee of the author about: 100 to: '.) Lightning hits can occur almost anywhere inside, underneath or in very close

proximily of a thunderstorm. Triggered lightning is bound to occur in zones of high electric fields inside or in close proximity to the cloud but these zones ere not limited to thunder clouds, they occur also in other non thundering but highly electrified clouds. The two bolts of lightning triggered by the Apollo 12 rocket are the best documented examples of such a situation. The probability of the occurrence of triggered lightning is enhanced by certain types of precipitation. Much effort in laboratory tests, lightning analysis, occurrence, location, and design of warning devices is spent on natural lightning, but surprisingly little effort is directed to the study of triggered lightning, which accounts for the majority of lightning accidents.

LABORATORY EXPERIMENTS OF TRIGGERED LIGHTNING

It has been made clear in the discussion of the preceding sections that triggered lightning is what we may term an electrodeless discharge. That means the discharge channel is not conected or originates at one metallic electrode of a high voltage generator and proceeds to the other electrode. However the discharge may start on a floating metallic or non-metallic nucleus, such as an airplane or a precipitation particle, and use the electric field energy provided by the generator for its growth. The distinctive difference between a spark starting from one electrode and an electrodeless discharge is that the spark has ready access to draw current or charge from the generator, restricted only by the internal resistance of the generator, whereas the electrodeless discharge can draw no current or charge from the generator and is limited to the use of the energy confined in the field. This makes the two types of discharges quite different in mechanism and discharge characteristics. Therefore the spark discharge between two electrodes is not a good model of a leader of a natural lightning nor of a triggered lightning.

It is easy to see that the spark between a pointed electrode and a plate inspired the model of the charged leader. The spark emerges from the pointed electrode, which may have been a piece of wire connected to one terminal of the generator. The other terminal is connected to the plate. The spark easily draws charge from the generator and deposits it along the channel during its growth to plate. Making contact with the plate the spark

will discharge the charge in the channel and the charge of the capacitor of
the generator. Schonland's drawing of
the first leader to ground and the
return stroke shown in Figure la is an
exact transference of the events taking
place during a spark discharge between
two electrodes energized by a charged
capacitor. This picture has set the
mold for the model of the lightning
discharge up to the present time.

The spark between the two electrodes of a high voltage generator has in most cases been the experimental tool to investigate the properties and effects of a lightning discharge. Since the model was in error right at the beginning, the results of these laboratory experiments should be interpreted with caution. Especially all events which require charge or current supply in short time (microseconds) or have a high frequency content (MHz) will be influenced or even dominated by the internal impedance of the generator. The technical resistor, for instance, is a linear circuit elément and technical circuit problems are based on the solution of linear differential equations. The resistance or conductivity of a lightning channel is very definitely not a linear circuit element and the treatment of dynamic lightning problems require the solution of non-linear differential equations. Indiscriminate applications of the telegraph equation to lightning problems, for instance, may lead to Erroneous conclusions. To the knowledge of the author no laboratory experiment has been carried out which reflects the situation of a lightning discharge. However there is an experimental determination of the field necessary to trigger a lightning discharge by the orbiter (space shuttle) Kasemir, Perkins (15) which shows at least the initial stage of a triggered lightning as seen from the point of view of this section - an electrodeless discharge. A model of the orbiter was supported on three teflon posts in a large plate condensor capable of producing static electric fields of maximum 330 kV/m. Figure (3). The distance of the belly of the orbiter to the lower plate was 165 mm and that of the tip of the tail fin to the upper plate 280 mm. dimensions of the upper plate were 5x5 m, and for the lower plate the ground was used, so for all practical purposes, it was an infinite conductive The distance between upper plate. plate and ground was 750 mm so that in the area of the model the field was uniform (with the orbiter absent.) The

main point here is that the orbiter was well insulated from either electrode, i.e., it could not obtain charge or current from the generator. The following measurements were carried out. The voltage at the upper plate was raised until the first small corona discharge appears. In this case it was in a field of 153 kV/m. Then the voltage was raised until the corona was strong enough to be photographed. The drawing in Figure 3 was made when the field was 280 kV/m. In Figure (4) flash over occured in a field of about 304 kV/m.

Figure (4) is the reproduction of a photograph taken on color film. The reproduction of the color photo of Figure (3) doesn't show the corona points at the fucelage of the orbiter and is here replaced by a technical drawing.

There are several interesting comments one can make to this experiment.

1. If the field is kept constant at a value between 153 and 304 kV/m corona is maintained as long as the field lasts. Since corona cannot be sustained out of a charge the airplane has accidentally aquired or out of any charge collected from the air, or from the field generator we have to have at least two corona points on opposite sides of the airplane. One point releases positive charge into the air we call this the positive corons point - and the other one releases negative charge, so that the airplane remains essentially uncharged. There is no demand that the airplane has to deliver charge to the corona points.

2. It is well known that negative corona starts at a slightly lower field than positive corons. In this case the negative corona point will charge the airplane with positive charge. The result is that the field at the positive point is increased until positive corona starts too. At the same time the field at the negative corona point is decreased so that the negative charge release at this point is diminished. This is an automatic balancing effect which keeps the two corons currents equal. A similar balancing mechanism is also effective on a leader stroke which keeps it essentially uncharued.

3. Nore critical than the different corona starting fields is the difference in the exposure of the corona points. It is obvious from Figures (3) and (4) that the corona point at the tail fin of the orbiter is

more exposed, i.e., the field concentration factor there is higher than on any point on the fuselage where the field concentration is weak. This generates many corona points, even at the nose of the orbiter, to counter balance the strong tail fin corona.

4. We may mention here the effect of precipitation or triboelectric This continuous charge charging. supply to the aircraft will cause a certain imbalance in the corona currents. If for instance negative charge is supplied, the current of the negative corona point will get stronger. This will support filement formation (discussed in 5) and may turn corona

into lightning.

5. Flash over is preceded by formation of distinct filaments in the otherwise diffuse corons glow. They are short in length at the beginning, about 5 to 10 cm, and of short duration, about 1/2 seconds. We see here the first sign of the changeover from a cold to a hot discharge, or from diffuse corona to a slim lightning As soon as one of these channel. jumping filaments reaches the upper plate, flash over occurs. Corona glow may reach the upper plate but that causes no flash over and has no visible effect on the form or intensity of the discharge.

6. As soon as flash over occured the discharge ceases to represent lightning since the discharge is now governed by the electric circuit of the generator. The filament may have reached several meter length if not

limited by the upper plate.

7. It will be of interest here to report on an observation made by the author on his many thunderstorm penetration flights during NOAA's (National Oceanic and Atmospheric Agency) lightning suppression progrem. During cloud penetrations at 6 to 10 km altitude in fields of more than 100 Vy/m, numerous alim and weak discharges of about 10 to 30 meter length could be seen in the cloud in a distance up to about 100 or 200 meters from the airplane. These discharges were called flicker discharges or beby lightnings. They were obviously natures attempt to start lightning discharges. They produced no visible strikes on the field records. However the field mills were running on the 300 kV/m range and fields of a few kV/m would not have been visible on the records.

The transition from corona to channel formation is one of the most crucial but practically unexplored aspects in triggered lightning

It may be difficult to research. generate electric fields strong enough and over a long enough distance. may however be possible to use thunderatorm fields at suitable locations either at mountain tops or using high towers. Another approach is to trigger lightning from the ground by a rocket with a trailing wire connected to ground. However the best and most appropriate measurements could be obtained from a suitably equipped air-Since research along these oraft. avenues is still in progress and will be reported on this conference the reader can obtain the newest information from the relevant papers.

#### CONCLUSIONS

Two different mechanism for the leader stroke of a cloud to ground discharge have been suggested. One by Schonland 1938 (1), which will be called "The charged leader," and another one by Kasemir 1950 (2), which will be called, "The uncharged leader."

2. The charged leader collects charges from the cloud, stores them in the channel, and carries these charges to the ground in case of a cloud to ground discharge, or to the oppositely charged cloud volume in case of an

intra-cloud discharge.

3. The uncharged leader does not collect charges from the cloud. produces positive (positive ione) and negative (electrons) charges inside its channel by ionization. These charges are separated in the channel by the external cloud field to form the induced charges according to the minimum energy theorem of physics (Thompson's theorem). Consequently one half of the channel carries positive and the other half negative induced charges. The net charge of the channel is and remains zero. Therefore the label, "The uncharged leader."

4. The charged leader actually discharges the cloud during its lifetime. The uncharged leader carried only negative induced charges into the positive charged cloud volume and positive induced charges into the negative charged cloud volume. During the lifetime of the leader the induced charges remain in or very close to the channel. The actual discharging or neutralizetion of the cloud charges occurs after

the lightning discharge is over.

5. The charged !eader requires energy to concentrate the cloud charges in its channel. This energy cannot be obtained from the cloud mince the charge flow does not follow the field lines produced by the cloud. Consequently there is an energy deficit in the charged leader concept. Furthermore the introduction of the cloud charge collecting mechanism has never been explained or justified. conclusions

The charged leader is not a

workable physical concept.

The formation of the uncharged 6. leader diminishes the energy of the cloud (Stratton's theorem). In other words it liberates energy from the electric field of the cloud and converts it into the energy consuming processes of the lightning channel such as ionization, channel heating, electromagnetic radiation, etceters.

7. The uncharged leader is based on the well-known physical laws or concepts, ionization for producing positive and negative charges inside the channel, and induction for separating these charges into a positive and a negative induced charge on the upper and lower half of the channel. This concept of the uncharged leader can, applied to the problem of static discharges, resolve existing controversies, guide research, and predict or explain the outcome of future experi-

mental results or measurement.

One conclusion of 8. uncharged leader concept is that all statio discharges observed on airplanes are triggered lightning. With the knowledge of the mechanism of a triggered lightning and its characteristios, we have a simple rule to decide if we are dealing with triggered lightning or an accidental hit by natural The triggered lightning is lightnin**g.** preceded by observable corona discharge and the hit by natural lightning is The triggered lightning not. restricted to the zones of high fields in the cloud and the probability of occurrence is enhanced by certain types of precipitation. The triggered lightning is not restricted to thunderstorms but can happen also in non-thunderous electrified clouds including anowstorms. One of the most important future research objectives is the determination of the conditions that convert corona discharge into a lightning channel.

#### REFERENCES

1. B.F.J.Schonland, "Progressive Lightning IV," Proc. Roy. Soc. (A) 164,

132 - 150, 1938

H.W.Kasemir, "Qualitative 2. Vebersicht ueber Potential -, Feld -, und Ladungsverhaltnisse bei einer Blitzentladung in der Gewitterwolke," in "Das Gewitter" by Hans Israel, Akad. Verlage. Gee. Geest and Portig K .- G., Leipzig, 1950

M.A.Uman, "Lightning," McGraw-

Hill Book Company, New York, 1969

4. R.H.Golde, ed. "Lightning I, II," Academic Press, New York, 1977

5. H. Volland, ed. "Handbook of Atmospherics I, II," LRC Press Inc., Boca Raton, Florida, 1982 6. L.G.Smith, "Intracloud

Lightning Discharges," Quart. J. Roy.

Meterol. Soc., 83, 103-111, 1957 7. T.Ogawa, M.Brook, "The Mechanism of the Intracloud Lightning Discharge," J.G.R., Vol. 68, 24, 5141-5154, 1964

8. C.B.Moore, B.Vonnegut, "The Thundercloud," in "Lightning I," ed. R.H.Golde, Academic Press, New York, 1977

Theory," McGraw-Hill Book Co., New York, 1941 J.A.Stratton, "Electomagnetic

10. W.R.Smythe, "Statio and Dynamic Electricity," McGraw-Hill Book Co., New

York, 1950

- 11. H.T.Harrison, "UAL Turbojet Experience with Electrical Discharges," UAL Meteorological Circular No. 57, United Airlines, Chicago, Ill., January 1965
- 12. D.W.Clifford, "Aircraft Mishap Experience From Atmospheric Electricity Hazards." AGARD Lecture Series No., 110. North Atlantic Treaty Organization, 1980

13. D.W.Clifford, H.W.Kasemir, "Triggered Lightning," IEEE, Vol. EMC-

24, No. 2, 112-122, 1982

14. L.W.Parker, H.W.Kasemir, "Airborne Warning Systems for Natural and Aircraft-Initiated Lightning," IEEE, Vol. EMC-24, No. 2, 137-158, 1982

15. H.W.Kasemir, F.Perkins, "Lightning Trigger Field of the Orbiter," NASA, KSC Contract CC 6964A, Final Report, 1978

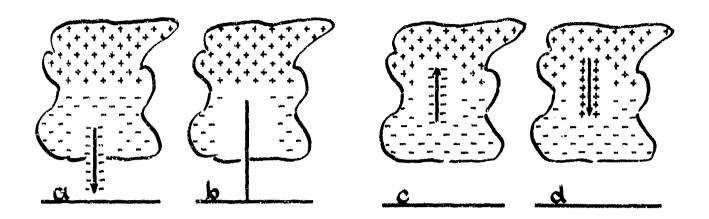


Fig. 1. Charged Distribution on Charged Leader

- N. Stepped leader

- b. After return stroke
  c. Cloud discharge advancing upwards
  d. Cloud discharge advancing downwards

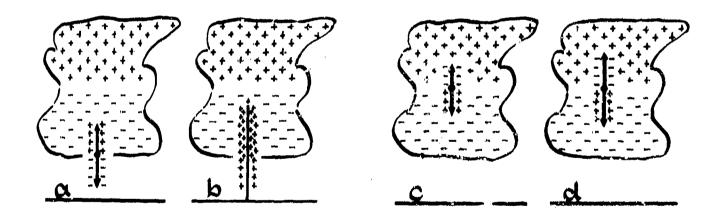


Fig. 2. Charged Distribution on Uncharged Leader

- Stepped leader
- b.
- After return stroke Cloud discharge beginning stage
- d. Cloud discharge end stage

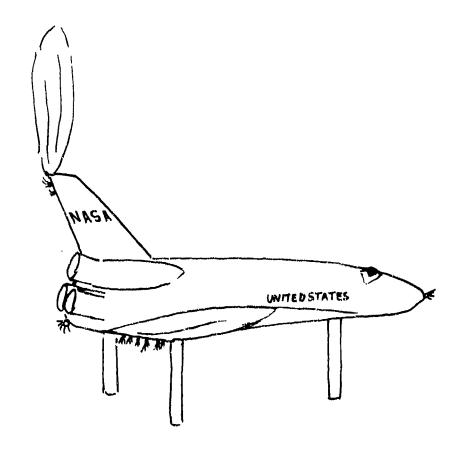


Fig. 3. Corone Discharge on Orbiter

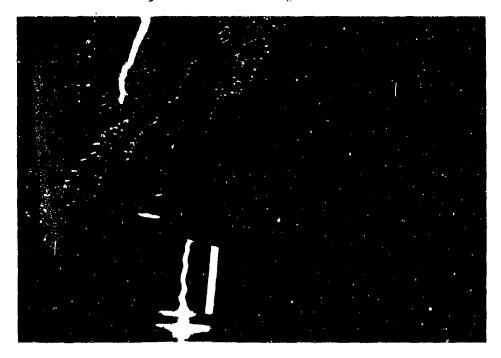


Fig. 4. Flashover on Orbiter

# AD P002180

LABORATORY AND FIELD OBSERVATIONS RELATED TO ICE PARTICLE AND AIRCRAFT CHARGING IN CONVECTIVE STORMS

 $\rightarrow$ 

H. Christian

Marshall Space Flight Center, Huntsville, Alabama
L. Lillie
Aerosystems, Incorporated, Erie, Colorado
C. P. R. Saunders
University of Manchester Institute of Science and Technology
Manchester, United Kingdom
J. Hallett
Desert Research Institute, Reno, Nevada

#### ABSTRACT

Laboratory studies of graupel particle charging in simulated cloud conditions show the need for the presence of ice crystals and cloud water simultaneously except under conditions where secondary ice crystal production occurs, when charging initially occurs in the absence of ice crystals. The magnitude of the charging increases with size of ice crystal, and impact velocity; it is also sensitive to impurities. The magnitude of the charge is also sensitive to temperature and the sign changes between -10 and -20 °C, depending on cloud liquid water content.

Aircraft studies were carried out in Montana convective clouds to test the validity of the extrapolation of the laboratory data to the atmosphere from the viewpoint of generation of charge, electric field, and aircraft charging during cloud penetration.

CIRCUMSTANTIAL EVIDENCE EXISTS for an important role of the ice phase in the separation of electric charge in thunderstorms (1). While the occurrence of lightning from clouds which lie in temperatures entirely above the ice melting point cannot be excluded (a few reports exist), most thunderstorms extend to temperatures well below the freezing point with anvils often as cold as -50°C. Field studies by Kuettner (2) on a mountain observatory on the Zugspitze showed that high electric fields were associated with the precipitation of graupel, ice particles some ma diameter formed by the accretion and freezing of supercooled cloud droplets. This association is further substantiated by the well-known observation by the dramatic increase in radio static commonly observed when an aircraft flies through regions of graupel precipitation; this effect can also be observed in an automobile radio when driving through graupel precipitation. observations have led to laboratory studies which attempt to simulate graupel growth and measure the conditions necessary for the separation of charge. These experiments have been carried out from the viewpoint of elucidating the particular mechanism or mechanisms responsible for the electrification observed in real clouds. paper discusses results of recent laboratory studies, and describes field observations designed to examine the initial electrification of a cloud as the ice phase is beginning to evolve from the viewpoint of relating the two processes. Measurements are also made of the rate of charge of the aircraft as it penetrates such a cloud and collides with the falling graupel particles.

LABORATORY AND FIELD STUDIES: GRAUPEL ELECTRIFICATION

Early simulation studies by Reynolds et al. (3) investigated charge separated during graupel growth simulated by moving small metal spheres through a supercooled cloud. Charge was only reported when the cloud consisted of a mixture of supercooled droplets or ice crystals; no charge was reported during graupel growth in a cloud composed only of supercooled cloud droplets. On the other hand, Hallett and Saunders (4) found that a charge separation sometimes takes place in a supercooled droplet cloud, but only in association with the production of secondary ice crystals during graupel growth, which occurred only under specific conditions at temperatures near -4°C and with a wide cloud drop size distri-Both studies showed that substantial charge separation occurred when ice crystals

(~ 100 um)were produced and collided with graupel particles, without coagulation. Substantial effects were found only with the presence of cloud water and ice crystals together. Takahashi (5) and Jayaratne et al. (6) found that the magnitude and sign of the charge was sensitive to the magnitude of the cloud liquid water content. In particular, the latter study showed that for graupel particles moving through the air at 1 to 2 mm s-1, typical of thunderstorm conditions, a reversal of charge sign occurred with rime +ve and ice crystals -ve at temperatures\_above -20°C for liquid water content of 1g m<sup>-3</sup> and above -10°C for liquid water content of 2g m<sup>-3</sup>. Charge separation for each ice crystal collisionseparation event gave a charge separation of  $\sim 10^{-11}$ C. This value increased by  $\sim X10$  in the presence of impurities typical of atmosphere.

A carryover of these results to the atmosphere poses the question of how frequently the simultaneous presence of graupel, supercooled water and ice crystals occurs, and whether or not such interaction can be predicted. Radar studies of Lhermitte and Krehbiel (7) and Krehbiel et al. (8,9) have shown that regions of -ve charge centers are co-located within well-defined temperature regions below the freezing level. Aircraft penetrations of convective (10,11) show integrated volume charge densities measured on precipitation (graupel) particles growing in similar cloud regions to reach values of 10 km<sup>-3</sup>. Three questions can be posed from these considerations. First, it is necessary to ask how far the charge measurements made in the laboratory can be extrapolated to particle impaction on airacraft, and graupel particle impaction and separation from crystals larger than those used in the laboratory studies. Second, are there localized regions of a convective cloud where the particle type and concentrations are optimum for charge separation. This is suggested by the laboratory studies, since relatively minor changes in crystal size, concentration and liquid water content give rise to significant differences in charge separation. Third, are there regions of particles responsible for local high rates of sircraft charging during cloud penetration. In order to answer these questions, quite Earlier specific measurements are required. measurements (12) showed that the separated charge increased dramatically over the velocity range 4-18m  $s^{-1}$ , approximately as Q  $\alpha$  V<sup>4</sup>. No measurements are available at higher velocities,

and with crystals larger than 100  $\mu m$  to simulate some cloud conditions which occur.

In order to compare the laboratory studies with the atmosphere, it is necessary to measure the charge on individual pecipitation (graupel) particles, along with cloud properties which laboratory studies have shown to be responsible for the charge separation - graupel structure, ice crystal size, cloud water. Simultaneously, it is necessary to measure the electric field to assess the spatial distribution of such charges, together with the aircraft charge during its passage. These measurements were undertaken during the Cooperative Convection and Precipitation Experiment (CCOPE) carried out near Miles City, Montana in 1981.

#### FIELD STUDIES

An Aerosystems\* Aerocommander turbo propaircraft was equipped with instrumentation to measure these quantities, together with other cloud and state parameters. Data was recorded at 1/10 second intervals during cloud passages and in the cloud environment. Specific measurements included:

- (a) Electric field normal to the aircraft (up and down) by two field mills just protruding from the aircraft skin at a position in the center of the fuselage, near the trailing edge of Each unit had two outputs, the wing. sepsitive/insensitive, full scale 2.103v m-1 and 10 V m-1. The aircraft could be calibrated for electric field measurement by charging it in clear air and a form factor determined. The difference values of the two electric field measurements at the same time can be utilized, assuming the aircraft to be an equipotential surface, to give the electric field at infinity, whereas the sum of the fields can give a value of the instantaneous aircraft charge.
- (b) An induction tube, axis facing the direction of flight, with two rings in series through which particles pass sequentially. Some particles impact on the tube to give spurious charge separation; these can be eliminated by examining the passage time between rings and the time constant for decay of the signal.
- (c) Cloud and liquid water content Johnson-Williams hot wire.
- (d) Particle measuring systems. Foreward scattering spectrometer probe, to give cloud droplet size distribution in 3  $\mu m$  bins to 45  $\mu m$  diameter.
- (e) Particle measuring systems 2DC probe to give precipitation particle shapes and concentration for  $\sim 100~\mu m$  to 1 mm.
- (f) Continuous formwar replicator to give a simultaneous record of all cloud and precipitation particles from ~ 5 µm to 2 mm diameter, from which size, shape, degree of riming and phase can be inferred.

PRELIMINARY RESULTS

Penetrations of a cumulus cloud at an altitude of 15,000 ft. at  $-3^{\circ}\mathrm{C}$  with a liquid water content of 0.2g m<sup>-3</sup> and  $-10^{\circ}\mathrm{C}$ , 200-600 µm diameter graupel particles, in a concentration of  $20t^{-1}$ , the electric field was 70 kv/m in the same direction as the fair weather field. The particle charge data showed many small negative charges (average charge  $-3.7 \times 10^{-11}$  C) and Sew large charges (average charge  $+2.9 \times 10^{-10}$  C) with a volume charge density of -1.5 C km<sup>-3</sup>.

Table 1 shows charge particle data from a series of penetrations in growing convective clouds at temperature levels near -10°C to -15°C. Volume charge is typical of thunderstorm values, yet these clouds were at a rather early stage in their evolution. Of interest is that regions exist where particles of one sign dominate, although particles of opposite sign are usually present in ratio approximately 10:1.

Examples of electric field data are shown in Figs. 1 and 2, together with other cloud measurements. The presence of cloud is indicated by the presence of liquid water. This data shows that the upper and lower fields sometimes are tracking (no aircraft charge), but on other occasions they do not track showing buildup of aircraft charge.

A complete analysis of this data will link electric field and aircraft charge with the detail of the ice and water content of the cloud during penetration. The analysis is being undertaken from the viewpoint of finding out whether extrapolation of the laboratory results to atmospheric conditions (large crystals) and higher aircraft speeds are reasonable, or whether some new phenomena in the charging process are at work. The aircraft charging/discharge rate in ice precipitation, compared with ice precipitating in water cloud will be crucial to this analysis.

The physical processes leading to charge separation in these studies is fundamental to our understanding of the cloud electrification process. Although recent studies have shown the presence of a long lasting (hours) contact potential which builds up during rime growth (13), the laboratory studies reported here show a cessation of charging as conditions change over a period of ~ 10s. This could be related to accretion and sticking of crystals on the charged surfaces, and is subject to continuing investigation.

### ACKNOWLEDGEMENT

Laboratory studies were supported by a grant from Meteorology Division, National Science Foundation #ATM79-20399; field studies in Montana by NSF Grant No. ATM802-0415.

<sup>\*</sup>Aerosystems Inc., Erie, CO

- 1. J. Latham, "The Electrification of Thunderstorms." Quart. J. Roy. Met. Soc., 107, 277-298, 1981.
- 2 J. Kuettner, "The Electrical and Meteorological Conditions Inside Thunderstorms." J. Met., 7, 322, 1950.
- J. Met., 7, 322, 1950.
  3. S.E. Reynolds, M. Brook and M.F. Gourley, "Thunderstorm Charge Separation."
  J. Met., 14, 426-436, 1978.
- 4. J. Hallett and C.P.R. Saunders, "Charge Separation Associated with Secondary Ice Crystal Production." J. Atmos. Sci., 36, 2230-2235, 1979.
- 5. T. Takahashi, "Riming Electrification as a Charge Generation Mechanism in Thunderstorms." J. Atmos. Sci., 35, 1536-1548, 1978.
- 6. E.R. Jayaratne, C.P.R. Saunders and J. Hallett, "Laboratory Studies of the Charging of Soft-Hail During Ice Crystal Interactions." Quart. J. Roy. Met. Soc., In Press, 1983.
- 7. R. Lhermitte and P.R. Krehbiel, "Doppler Radar and Radio Observations of Thunderstorms." I.E.E.E. Trans. on Geoscience Electronics, GE 17, 162-171, 1979.
- 8. P.R. Krehbiel, M. Brook and R.A. McCrory, "An Analysis of the Charge Structure of Lightning Discharges to Ground." J. Geophys. Res., 84, 2432-2456, 1979.
- 9. P.R. Krehbiel, M. Brook, R.L. Lhermitte and C.L. Lennon, "Lightning Charge Structure in Thunderstorms." Proc. Int. Conf. Atmos. Electricity, Manchester, In Press, 1980.
- 10. W. Gaskell, A.J. Illingworth, J. Latham and C.B. Moore, "Airborne Studies of Electric Fields and the Charge and Size of Precipitation Elements in Thunderstorms." Quart. J. Roy. Met. Soc., 104, 447-460, 1978.
- 11. H. Christian, C.R. Holmes, J.W. Bullock, W. Gaskell, A.J. Illingworth and J. Latham, "Airborne and Ground-Rased Studies of Thunderstorms in the Vicinity of Language Laboratory." Quart. J. Roy. Met. Soc., 106, 159-174, 1980.
- 12. B.J.P. Marshall, J. Latham and C.P.R. Saunders, "A Laboratory Study of Charge Transfer Accompanying the Collision of Ice Crystals with a Simulated Hailstone." Quart. J. Roy. Met. Soc., 104, 163-178, 1978.
- 13. J.M. Caranti and A.J. Illingworth, "The Contact Potential of Rimed Ice." J. Phys. Chem., In Press, 1983.

Table 1 - Measurements of charge on graupel particles during aircraft traverses of Montans convective clouds, CCOPE 1981

Lower values of charge and numbers of particles in second ring result from particle loss or charging by collision on the walls; Q<sub>1</sub> data does not suffer from this problem. Charge per unit volume of cloud in coulombs per km.  $Q_{\hat{1}}$  - data from first induction ring;  $Q_{\hat{2}}$  - data from second induction ring

CCOPE - 1981

1 C Km <sup>-3</sup>	Ž Ž	72/	.00	-1.67	.023		-1.61	1	17	.03	021		110			74	25	-3.42	084	092	<b>7</b>	.046	.034
			002	-1.69	.077	+ .133	-1.33	<b>70.</b> -	33	.054	-1.89	.25	016	011	035	71	96	-3.46	-1.23	680	9.	.048	.035
	٠ <del>*</del>	9	-	09			71	ð	Ξ	-	M		_			13	2	苏	9	7	<b>-</b>		7
		02/2	.00	1.74			1.63	.26	.24	ş	950.		970°			<b>89</b> ₹	.33	3.45	. 084	.024	.025		.0535
	<b>₽</b>	۲		-	7		_	7	4	7	~		<b>,</b>			-	m	<b></b>		9	7	.046	<b>,-</b> -
		±02/V		8	.023		.02	-15	.07	.07	.035		.015			.008	<b>8</b> 0.	.03		.12	722.	5	.0876
	<b>₩</b>	9	_	52	7	m	**	30	32	m	21	10	21	90	21	35	94	73	15	7	9	4	ĸ
		210	600.	1.93	.022	.170	1.37	.24	ŧ.	.056	.314	.28	.163	.073	.0707	.75	1:1	3.56	.19	\$	407	.029	.0111
	ъ т	9	••	9	Ξ	2	-	92	7	9	<b>~</b>	-	•	m	<b>60</b>	m	9	4	7	12	7	<b>o</b>	<b>C1</b>
		<b>√√10</b> +	700.	0.24	069.	.403	.036	.17	.11	0.11	124	.03	.147	.062	.0671	.041	-14	-	.026	.13	.468	.0779	.0146
	Total Data	Time/Sec	20.5	6.3	16.1	2.45	1.23	4.08	3.13	3.34	3.82	1.65	3.43	2.35	8.3	3.1	#*S	4.1	3.13	2.94	4.5	4.31	0.58
	Data	Inter.	26-230	1-66	24-185	7-27	1-13	3-45	1-32	6-39	7-45	3-20	1-35	9-32	2-85	1-32	4-58	1-42	12-43	8-38	9-63	3-46	5-10
	Actual	Time	154517	190610 -14	184633	194946	15 1895	153334	161337	122610	153905	163846	165934	163233	163552	142956	193345	144443	194930	155220	191728 191910	15500	172445
		<b>~</b>		10.2					. 21												25	53	53
		Oate	7 JUL	11 JUL	11 JUL	11 JUL	12 JUL	12 JUL	12 JUL	17 JUL.	18 JUL	16 JUL	19 JUL	19 JUL	19 JUL	21 JUL	21 3UL	21 JUL	1 AUG	1 AUG	2 AUG	6 AUG	6 AUG

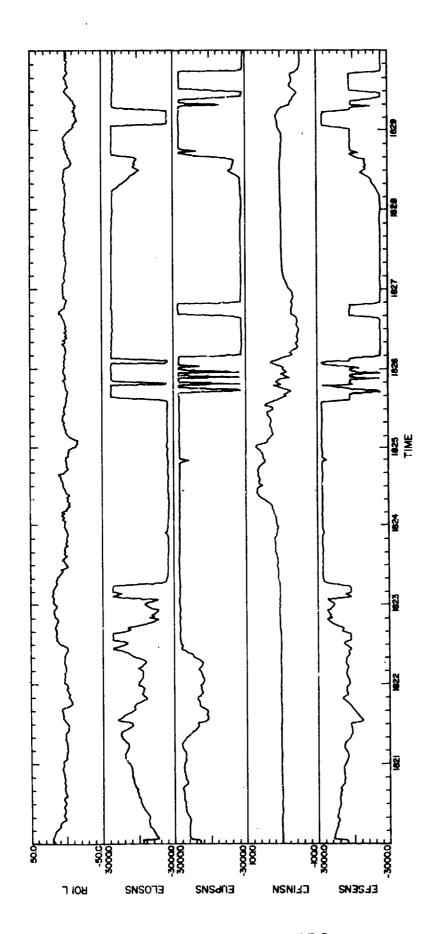


FIGURE CAPTIONS

sensitive channels for electric field, saturating (straight lines) at 1 x 10<sup>3</sup> V m<sup>-</sup>1, EF is net field sensitive, and insensitive, the latter saturating at 10<sup>5</sup> V m<sup>-1</sup>, This flight was in a region of ice particles with low liquid water content (< 0.2g m<sup>-3</sup>). Local times are a wclssa; aircraft speed 100 m s<sup>-1</sup> approximately 6 km per minute.

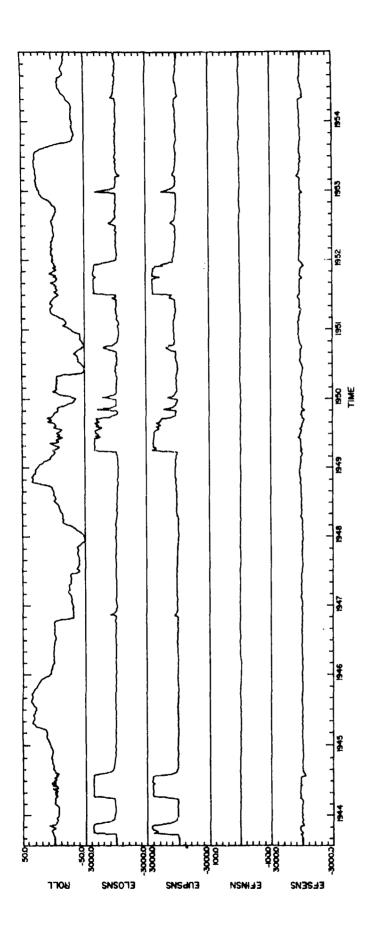


Fig. 2(a). Field measurements in penetrations of a growing cumulus with a little ice - 1 Aug. 1981, Flight 24. Up and down field tracking occurs outside the cloud, but differences in field occurs during penetration (shown by liquid water, top graph). VVS - air vertical velocity, S. Temp - Rosemont static temperature; Theta - potential temperature; Alt - altitude (m)

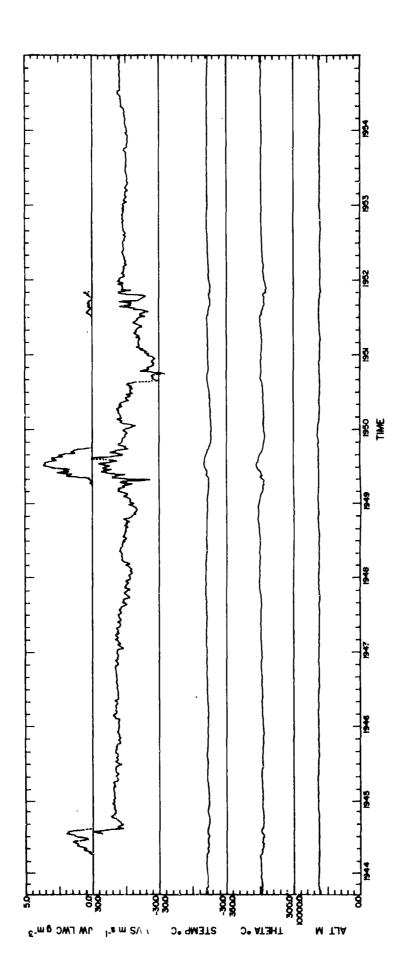


Fig. 2(b). Field measurements in penetrations of a growing cumulus with a little ice - 1 Aug. 1981, Flight 24. Up and down field tracking occurs outside the cloud, but differences in field occurs during penetration (shown by liquid water, top graph). VVS - air vertical velocity, S. Temp - Rosemont static temperature; Theta - potential temperature; Alt - altitude (m)

Explide

## LIGHTNING ATTACHMENT PATTERNS AND FLIGHT CONDITIONS EXPERIENCED BY THE NASA F-106B AIRPLANE

Bruce D. Fisher NASA Langley Research Center

J. Anderson Plumer Lightning Technologies, Inc.

**ABSTRACT** 

During the NASA Langley Research Center Storm Hazards Program, thunderstorm penetrations have been made during three summers by an extensively instrumented F-106B research airplane in order to record direct lightning strike data and the associated flight conditions. The penetrations were made in Oklahoma and Virginia in conjunction with ground-based weather radar measurements by the NOAA-National Severe Storms Laboratory and NASA Wallops Flight Center, respectively. In 1980 and 1981, the airplane received 10 direct lightning strikes each year, with most penetrations occurring near the freezing level. In 1982, 239 penetrations were made during which 153 direct lightning strikes occurred. Most of the penetrations in 1982 were made at higher altitudes and colder ambient temperatures than in 1980 and 1981. Following each flight, the airplane was thoroughly inspected for evidence of lightning attachment, and the individual lightning attachment spots were plotted on isometric projections of the airplane to identify swept flash patterns.

This paper presents samples of the strike attachment patterns that were found, and discusses the implications of the patterns with respect to airplane protection design. The altitudes, ambient temperatures, turbulence and precipitation at which the strikes occurred are also summarized. The significance of these findings with respect to lightning avoidance by airplanes is also discussed. Finally, lightning strikes to several U. S. Air Force airplanes struck during routine operations are discussed in relation to the Storm Hazards flight experience.

This paper was not available for incorporation into this book. Therefore, it will be published at a future date.

# AD P002181

INSIDE THE CONE OF PROTECTION



J. M. Stahmann PRC-1217 , PRC Systems Services Kennedy Space Center, Florida 32899

Although lightning cones of protection and cones of attraction have been used for over 100 years, much confusion still remains as to their effectiveness, particularly as applied to personnel protection. At Kennedy Space Center, a 1:1 cone of protection with a straight side is standard for structure or equipment protection. However, at the launch pad, where a 400-foot lightning lightning rod on top of an insulating mast is used for pad lightning protection, the idea developed that personnel within a 400-foot radius of this mast would be safe from lightning and those outside it would not. Since it is obvious that a person 395 feet (120.4 m.) from the mast is only slightly safer than one at 405 feet (123.5 m.), an investigation was initiated to calculate the probabilities of a person being struck by lightning as he moves closer to the mast inside the cone of protection. Since the risk does not go to zero outside the structure, the risk level can then be estimated.

Golde, Pierce, and others have presented data and probability curves from which the probability of striking a person standing within the cone of protection can be calculated. The striking distance theory, dating back to the time of Ben Franklin, can be used to define a cone of protection with a circular side and the attraction radius about a tower and an individual about 6 feet in height. The striking distance is a function of stroke charge which in turn is realated to stroke peak current.

To arrive at the expected strike frequency, it was necessry to measure the strike frequencies at KSC. Krider and others have found a mean area density of cloud-to-ground lightning at KSC of about 4.645.1 flashes per (km²) per month in the summer. An overall frequency is estimated as about 20 flashes per (km²) per year. With these data, the risk of exposure at various distances from the lightning mast can be calculated. Assuming continuous exposure during thunderstorms, this risk varies from about one strike per person in 1,400 years near the tower to one stroke per person in 300 years at about 400 foot (122 m.).

Since exposure is not continuous, the risk is less for individuals who are only temporarily exposed; however, since many workers may be present, the risk of accident is greater. If a person is exposed to lightning in an open area such as on a gollf course in Florida through one complete storm, the risk of being struck is about the same as being killed in a motor vehicle accident, about once in 4,000 years. In the vicinity of a 400-foot (122 m.) tower, the risk is reduced by a factor of about 33 at a distance of 150 feet (46 m.) from the tower.

(59 kin)

PERSONNEL LIGHTNING PROTECTION outside but near tall structures is a concern at Kennedy Space Center (KSC). Standards relating to the protection of the Shuttle vehicle, equipment, and small nearby structures invoke the 1:1 cone of protection (1)\* with a straight side where the radius of the circle of protection on the ground equals the height of the structure and is centered at the center of the structure. In the case of the lightning mast on the top of the Fixed Service Structure (FSS), the height is about 400 ft. (122 m.) resulting in a circle of protection on the ground with a radius of 400 ft. (122 m.). The immediate question which arises is: "How safe are personnel from the lightning strike hazard inside this circular area?" Obviously, a person just inside this boundary is about as exposed as a person just outside it. Many protection cone shapes have been proposed (1), but none of them function as a shield against lightning. They all describe a geometric probability boundary within which the probability of being struck by lightning is very low. Systematic investigations of the protection afforded by a vertical lightning rod have concluded that no specific protective some could be ascribed with complete confidence (1). It is the purpose of this paper to illustrate how the probabilities of strokes to personnel within, as well as outside, the cone of protection vary and can be estimated so that the risk may be evaluated relative to the penalties or risks involved in not performing a particular activity requiring exposure.

#### BASIC ASSUMPTIONS

The geometrical approach to the solution for the probability of a person being struck by lightning near a tall structure will be used for this analysis. The lightning leader is assumed to progress from uniformly distributed charged regions in the cloud toward the earth in steps until its tip is close enough to strike the ground or a grounded object in one final jump. The height of the leader tip at this critical breakdown point is termed the "striking distance" (1). This concept dates back to Benjamin Franklin (1767). During the process, a streamer also is formed on the structure or other point on the ground and grows toward the leader. The leader and streamer meet at a junction point about 1/3 of the distance from the streamer initiating terminal to the "point of influence" on the stepped leader (2). The stepped leader moves downward in a random manner until it is within striking distance of the ground. The lightning then strikes the closest ground point. typical stroke to the top of the lightning mast on the FSS is shown in Fig. 1 where the striking distance was estimated as about 700 ft. (213 m.).

\*Numbers in parentheses designate References at end of paper.

The fundamental geometry for a tall structure of height H and a striking distance of S. is shown in Fig. 2. All leaders that arrive first at a distance S. from the tall structure when all other distances from it to ground points are greater than S. are assumed to strike the structure. For the calculated results, the height of the FSS mast, which is 400 ft. (122 m.), is the tall structure height. Similarly, it is assumed that all strokes whose leaders arrive first at a distance of S. from a standard 6-ft. (1.83 m.) person will strike the person. As shown in Fig. 2, the result is that, for a particular S., all strokes within a "radius of attraction" R will be attracted to the tall structure or person and therefore cannot reach the ground within this radius. The radius of attraction is a function of the striking distance (3):

$$R = (S_d^2 - (S_d - H)^2)^{\frac{1}{2}}$$

$$R = H((2S_d/H) - 1)^{\frac{1}{2}}$$
(1)

R may also be considered the radius protected by the tall structures against strokes with a particular  $S_a$  to persons or small structures on the ground. The area protected from strikes is a linear function of  $S_a$ :

$$A = \pi H(2S_d - H) \tag{2}$$

and if Sd>>H

 $A \approx 2\pi HS_d$ 

The above formulas hold for  $S_d \stackrel{>}{=} H$ . If  $S_d < H$ , then  $R = S_d$  and  $A = \pi S_d$ .

The striking distance is a function of the charge in the leader tip which, in turn, is related to the peak current, I,, in the return stroke. To take into account the fact that upward streamers from a tall structure may be as long as a few hundred meters (4) and that S, should increase with structure height, the curve giving the largest striking distance for various peak currents was selected for the 400-ft. (122 m.) tower calculations (Golde, Fig. 6) (1). A tower height of less than 150 m. is not likely to trigger lightning with an upward going leader (4). The measurement of the probability of strokes having various peak currents vary widely and a composite of the results of several investigators was used in the next section. The data was divided into 10 deciles of 10 percentiles each and an average striking distance and average peak current was assigned to each decile.

For calculating strikes to a person, a more conservative relationship between striking distance and peak current was used which was expressed by a formula due to Love (1):

 $s_d = 10 I_{pk}^{0.65} m$  (3)

Krider and others (5) have estimated a mean monthly area flash density at KSC over the years from 1974 to 1980 of 12 discharges/km²/month in June, July, and August. The number of cloud-to-ground discharges was estimated as 4.6/km²/month. Using the seasonal distribution of thunderstorms at KSC (6) for extrapolation, the yearly average is about 20 cloud-to-ground discharges/km²/year. This density was used to find the stroke probabilities per year in the next section.

#### RESULTS

In a manner similar to that used in Reference (7), the results of the calculations for a 400-ft. (122 m.) towar and for a 6-ft. (1.83 m.) person are tabulated in Tables 1 and 2. I and S are average values of peak current and average striking distances respectively selected from the curves and formula referenced in the previous section. R is the attraction radius. It is assumed that all strokes of the specified magnitude will be attracted to the tower within that radius and therefore they will not hit the ground or a person on the ground. The estimated stroke density of 20 strokes/km<sup>2</sup>/year is equivalent to 2 x 10<sup>6</sup> strokes/m<sup>2</sup>/year/ decile used for these calculations. The probabilities for each average current in a decile of hitting the tower are summed to obtain the cumulative probability of strokes, below the specified average magnitude, hitting the tower. As the strokes become larger, S and the attraction area increase so that more large strokes are attracted to the tower than small strokes. Small stroke leaders must arrive close to the tower by chance in order to strike it. The estimated cumulative probability for all strokes of 2 per year is about what has been experienced at KSC.

Similar calculations may be made for a 6-ft. (1.83 m.) person. According to the results, an exposed person could attract large strokes from 92 ft. (28 m.) away. If the person raises a 3-ft. (0.915 m.) golf club over his head, increasing his total height to 9 ft. (2.74 m.), the attraction radius increases by 20 ft. to 112 ft. (34.2 m.). As we have shown, where S >>H, the attraction area is proportional to H for a particular S. Therefore, the 50% height increase due to the golf club results in a 50% greater chance of being hit by lightning. This is why it is so important to maintain a low profile on a beach, golf course, or other exposed area.

Tables 1 and 2 show that, as a person moves toward the tower from a distance of about 915 ft. (279 m.), he is initially protected only against the larger strokes which can hit the tower and then against smaller and smaller strokes. At 377 ft. (115 m.) or about 400 ft. (122 m.), a person is protected against strokes =17.6 kA and must wait 294 years, on the average to be struck,

being sure to be exposed to all 97 thunderstorms per year. However, it should be pointed out that the size of the stroke is not of interest to the person being struck. If the person is not near the tower, a person might be struck once every 41.5 years. The probability may be reduced by a factor of 7 by approaching to within 377 ft. (115 m.) of the tower. Finally, at a distance of 150 ft. (46 m.), the probability is reduced to once per 1,364 years, providing a factor of 33 compared to unprotected exposure. Tables 1 and 2 illustrate that the protection gradually increases as the distance from the tower decreases with no sharp boundaries. Currently, the tendency is to reduce to allowed radius of protection where personnel are concerned. For example, Lee (2) suggests a radius of 50 ft. (15.2 m.). It may be more logical to accept the risk in certain circumstances, particularly under the conditions discussed in the next section.

Since the launch pad radius is about 1,500 ft. (457 m.), at a\_cloud-to-ground stroke density of 20 strokes/km²/year, it is estimated that about 13 strokes would hit the launch pad per year. If two hit the FSS mast and one hits the nearby water tower, about 10 strokes/year are left to hit elsewhere on the launch pad.

#### CONDITIONAL PROBABILITIES

So far, we have assumed unrealistic conditions. For example, we have assumed full exposure to all thunderstorms, symmetrical approach from all angles, uniform strike density distribution, and a fixed average ratio between cloud-to-cloud and cloud-to-ground strokes. It is hoped that in the future, we will be able to take advantage of more specific conditions.

It is obvious that no one will be exposed to lightwing in all the storms so that a factor must be introduced to account for exposure time, such as the exposure time divided by the total thunderstorm minutes per year. Using Krider's 107 minutes per storm on the average in the summer (5), by extrapolation, KSC storms would last about 107 minutes  $\times$  97 storms/year  $\approx$  10,000 minutes (about one week)/year. The minutes are not of equal threat value and therefore should be weighted in real time in conformance to the actual storm intensity and locations. Storms are located over the threatened area only a portion of the time. At KSC, thunderstorms generally approach from the westerly directions. If the charged areas can be located and the direction of approach determined, specific probabilities may be calculated. For example, if the charged areas are west of the launch pad, personnel working east of the tower are much less threatened. The cloud-to-ground stroke probability should also be related to charge location. Some storms in Florida produce

almost all cloud-to-cloud lightning which is much less of a threat to personnel, even if located overhead. When we can confidently predict specific conditions, the lightning hazard can be more specifically estimated.

#### CONCLUDING DISCUSSION

While the hazard of being struck by lightning is small, it is comparable to the hazards of being killed by tornadoes, floods, and earthquakes combined. If a person is required to be exposed to the lightning hazard in the vicinity of a call structure, the degree of hazard can be estimated. The concept of striking distance provides a technique, as has been illustrated. While the estimate will vary with the assumptions and data used, it is evident that the probability does not vary suddenly at a particular distance from the tower. However, the probability of being struck does decrease rapidly as the tower is closely approached.

The probability of an individual being killed in an automobile accident is about 24 deaths/100,000 people/year or once in 4,167 years for a person. From the results in Tables 1 and 2, if we assume that an individual is exposed to only one complete Florida storm/year and is located at a distance of 377 ft. (115 m.) from a 400-ft. (122 m.) tower, the person would be struck by lightning every 97 x 294 = 28,518 years since his exposure is reduced to 1/97 of that previously calculated. At the outer 915 ft. (279 m.) distance, the probability would be once every 41.5 x 97 = 4,025 years or about the same chance as being killed in an auto accident. Since, nationally, the chances of being killed by lightning are less than those of being killed by a motor vehicle by a factor of about 500, most people try not to expose themselves to the lightning strike hazard, even for the equivalent of one complete storm per year. Further, from a safety point of view, the probability of any lightning strike to a group of persons is important. This hazard is increased by the number of people exposed.

The hope for reducing the lightning strike hazards in the future lies in our ability to make specific predictions about the location of the thunderstorm charged regions and about the thunderstorm intensity and other characteristics that may be used to accurately predict the strike threat to personnel at specific locations.

#### REFERENCES

- 1. R. H. Golde, "Lightning Conductor." Lightning Vol. 2, Chapter 17, Academic Press, 1977, pp. 545-576.
- 2. R. H. Lee, "Grounding and Lightning Protection." University of South Carolina Notes and References, pp. L1-L25.
- Notes and References, pp. L1-L25.
  3. A. D. Vorgucic, "Condition for Evaluation of the Protecting Zone of the Lightning Rod." FAA/Georgia Institute of Technology Workshop on Grounding and Lightning Protection. FAA-RD-78-83. May. 197
- Lightning Protection, FAA-RD-78-83, May, 1978. 4. N. Cianos, E. T. Pierce, "A Ground Lightning Environment for Engineering Usage." Technical Report No. 1, Stanford Research Institute, August, 1972.
- 5. M. V. Piepgrass, E. P. Krider, C. B. Moore, "Lightning and Surface Rainfall during Florida Thunderstorms." Journal of Geophysical Research, Vol. 87, No. Cl3, December 20, 1982, pp. 11,193-11,201.
- December 20, 1982, pp. 11,193-11,201.
  6. M. J. Changery, "National Thunderstorm Frequencies for Contiguous United States."
  NUREG/CR-2252. November. 1981.
- NUREG/CR-2252, November, 1981.
  7. J. R. Plumer and K. E. Crouch,
  "Lightning Protection for Traffic Control
  Systems." NASA and Public Technology Inc.,
  Report, 1978, pp. 4-8.

Table 1 - Probability of Striking a 400 ft (122 m) Tower

Decile	Tpk	Sd m	R	Area	Decile Probability Strokes/Year	Cumulative Probability Strokes/Year	Years/Strike
0- 10	6.2 kA	46	46	6,648	0.01330	0.01330	75.2
10~ 20	12.9 kA	90	90	25,447	0.05089	0.06419	15.6
20- 30	17.6 kA	115	115	41,548	0.08310	0.14729	6.8
30~ 40	22.7 kA	137	1.36	58,107	0.11621	0.2635	3.8
40~ 50	28.4 kA	161	156	76,454	0.15291	0.4164	2.4
50~ 60	35.2 kA	186	174	95,115	0.19023	0.6066	1.65
60- 70	44.5 kA	217	195	149,459	0.23892	0.8455	1.18
70- 80	57.0 kA	258	219	150,674	0.30135	0.1468	0.872
80- 90	77.0 kA	31.8	ناد	196,350	0.39270	1.5395	0.65
90-100	112.0 kA	380	279	244,545	0.48909	2.0286	0.49

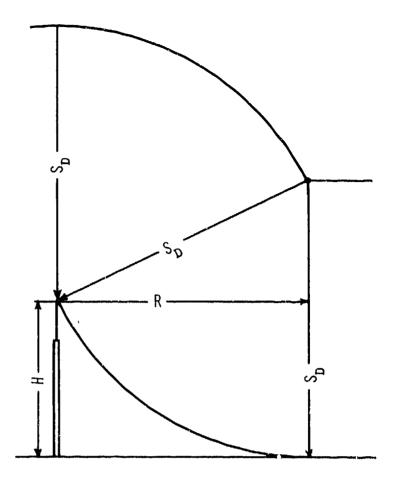
Table 2 - Probability of Striking a 6 ft (1.83 m) Person

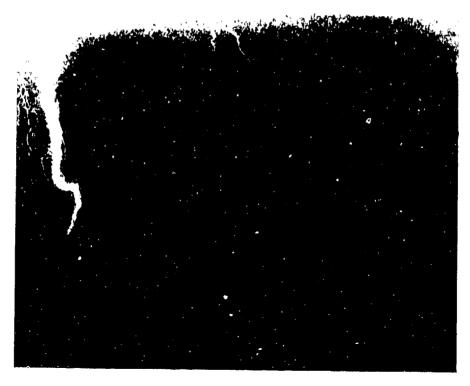
Decile	T <sub>pk</sub>	Sd m	R m	Area m <sup>2</sup>	Decile Probability Strokes/Year	Cumulative Probability Strokes/Year	Years/Strike	
0- 10	6.2 kA	32.7	1,0.8	366	0.000732	0.000732	1,364	
1.0~ 20	12.9 kA	52.7	13,8	598	0.001196	0.001928	519	
20~ 30	17.6 kA	64.5	15.3	735	0.001470	0.003398	294	
30~ 40	22.7 kA	76.1	16.6	866	0.001732	0.005130	195	
40~ 50	28.4 kA	88.0	17.9	1,007	0.002014	0.007144	140	
50 <b>~ 6</b> 0	35.2 kA	101.2	19.2	1,158	0.002316	0.009460	106	
60~ 70	44.5 kA	117.9	20.7	1,346	0.002692	0.012152	82	
70- 80	57.0 kA	138.5	22.4	1,576	0.003152	0.015304	65	
80- 90	77.0 kA	168.4	24.8	1,932	0.003864	0.019168	52	
90~100	112.0 kA	214.8	28.0	2,463	0.004926	0.024094	41.5	

### FIGURE CAPTIONS

Fig. 1 - A typical lightning stroke to the top of the lightning mast, Pad-39A, KSC

Fig. 2 - Geometry for determining the radius of attraction for lightning strokes to a tall structure or person





# AD P002182



EARTH ELECTRODES FOR GROUNDING NEMP TYPE LIGHTNING

David P. Millard Georgia Institute of Technology, Atlanta, Georgia

ABSTRACT

An investigation was conducted into the properties of earth electrode systems over a frequency range covering the NEMP type lightning (rise times faster than 2 microseconds) power spectrum. Since this power spectrum extends well into the VHF region, conventional low frequency (less than 100 Hz) and historic impulse measurement techniques were not adequate to describe the electrode system's response to NEMP type lightning. Therefore, initial emphasis was placed on the development of a measurement technique that could be used to both: (1) Assess the performance of a given ground electrode; and (2) conduct a site survey to determine the best location for ground electrodes. Then the technique was used to evaluate the performance of various common ground electrode configurations (the subject of a companion paper to be published at a later date).

THE RESPONSE OF AN EARTH ELECTRODE to an NEMP type lightning pulse is determined by the properties of the soil and the electrical characteristics of the geometrical particular electrode system configuration. Thus, the first step in establishing an adequate ground is to determine dielectric properties (conductivity, permittivity, and permeability) of the soil. (This step is important because it dictates the geometrical configuration (i.e., number of ground rods, method of interconnection, etc.) required to establish a good ground in a given area.)

Historically, soil parameter identification started with a laboratory analysis of soil samples and then moved to sophisticated on-site analyses of the soils and underlying strata at the planned location. Recent advances in on-site techniques have been made. One of these, the Resonant Linear Antenna Method [1] appears to be the most suitable for NEMP type lightning grounding studies. (The method is accurate over a broad frequency range, is easily transportable, and is generally in use by geophysicists for geological surveying.) From the input admittance and the geometry of a probe antenna, the soil parameters can be calculated. This method requires only a resonant monopole antenna, a signal source covering the desired frequency range, and a display device complete with necessary coaxial voltage and current probes. An adaption of this technique was employed to examine the behavior of selected earth electrodes up to frequencies reflective of fast risetime responses applicable to NEMP type lightning waveforms.

The grounding of power circuits (25-60 Hz) and grounding for lightning protection (impulse) is the primary concern for structures and power Thus, many studies were performed to determine the volt-ampere characteristics of a driven ground rod using direct current or low frequency ( < 100 Hz) alternating current instruments to determine power properties 2]. Impulse generators were used to determine the response to lightning strokes [3].

The typical impulse generator was capable of producing 50 KV and 800 A with a 1 to 2 microsecond rise time. From these tests, a resistive, inductive and capacitive (RLC) model of a ground rod was developed [4] (Figure 1) that reflected the geometry of the rod, the soil parameters, and the climatic conditions at the time of the test.

Within the last several years lightning pulses faster than the traditional 2 microsecond rise time have been recorded [5]. development of a new technique for measuring ground electrode impedances at these extended frequencies was necessary. After careful consideration of existing instrumentation capabilities, it was determined that a technique could be devised to display the response of an electrode system up to 500 MHz which covers the NEMP type lightning and much of the NEMP spectrum (Figure 2). Three different measurement techniques must be used to cover the entire frequncy range from DC up to 500 MHz. frequency ranges covered by each are: (1) low (DC to 100 Hertz), (2) medium (100 Hz to 500 KHz), and (3) high (500 Hz to 50 MHz). The design and construction of a standardized test probe along with a description of the test techniques for these three frequency regions are discussed in the next sections.

#### STANDARD TEST PROBE

A rod of 1.25 cm (0.5 inches) in diameter and 81 cm (32 inches) in length was chosen for the standard test probe. (Brass was used although steel, copper, or any other metal of sufficient strength is adequate.) This length is long enough to provide effective soil contact but not so long as to require extensive work to place the rod in the ground.

An adapter was then constructed to interface the ground rod to the test instruments (see Figure 3). The adapter consists of a tapered coaxial line transition with a male type N connector on the top. The taper maintains 50 ohms impedance down to the point of attachment to the rod. (The impedance characteristics of the connector from

0.5 to 500 MHz are shown in Figure 4.) The adapter is fastened to the ground rod via a threaded connection.

#### HIGH PREQUENCY MEASUREMENTS

The high frequency impedance characteristics of the test probe were measured with the aid of a General Radio 1710 RF Network Analyzer. analyzer was connected to the type N connector as shown in Figure 3, calibrated (Figure 5), and an impedance plot of the probe in earth was photographed (see Figure 6). It is noted that there is a great deal of ringing associated with both the magnitude and phase of the rod impedance. The ringing is due to the non-uniform imaging of the rod with the soil, the inductance and capacitance of the test leads to earth, and the standing waves at the surface [6]. By increasing the reference plane area of the probe, the standing waves and reflections were reduced, yielding a more acceptable plot of the ground rod impedance. The reference plane area was increased by attaching auxiliary grounds and an aluminum plate to the test connector shield (see Figure 7). A series of plots, Figures 8 to 13, were taken with different auxiliary grounds. The figures reveal that the rod impedance ringing decreased and displayed an overall capacitive nature at high frequencies as expected. These results indicated that this approach can be used to determine the impedance of the reference probe up to frequencies of 500 MHz. From this impedance characteristic, determination of the equivalent circuit of the probe can be made

A computer run was made to calculate the input impedance of the equivalent circuit (Figure 1) with the test rod geometry and soil conditions of the particular test area. The input impedance of the ground rod equivalent circuit is given by:

where

$$Z_{L} = R + j \omega L$$

$$Z_{C} = \frac{1}{j\omega C}$$

$$R = \frac{\rho}{2\pi \ell} \ln \frac{2\ell}{a} \text{ ohas}$$

$$L = 2\ell \ln \frac{2\ell}{a} - 10^{-7} \text{ H}$$

$$C = \frac{\epsilon_{L}}{2\ln 2\ell} \frac{10^{-9}}{9} \text{ F}$$

$$\ell = \text{length of rod}$$

$$a = \text{radius of } r \text{ od}$$

$$\rho = 97.67 \Omega \text{ m}$$

$$10 < \epsilon_{L} < 13$$

A graph of the results is shown on Figure 14. For this second order system, the resonant frequency is approximately 15 MHz. The response of the final test configuration (Figure 13) reveals a resonance around 8 to 9 MHz with ringing from 100 to 500 MHz.

#### LOW FREQUENCY MEASUREMENTS

The impedance of an earth electrode at low frequencies is dominated by the properties of the soil. Analytically the resistance of a ground rod can be determined if the soil resistivity,  $\rho$ , and the rod geometry are known, i.e.,

$$R = \frac{\rho}{2\ell} \cdot \ln \frac{2\ell}{a} \text{ ohm} \tag{2}$$

where & = length of the rod and a = its radius.

Experimentally the ground rod resistance was accurately measured by the Fall-of-Potential Method (see Figure 15) [8]. This is a simple voltage drop measurement relating the current injected to the resistance of the ground rod. (The injected current usually has a frequency of 70 to 100 Hz so as not to be confused with stray 60 Hz ground currents.) The ground rod resistance

was found by recording the resistance on a Biddle Meggar-Earth Tester as distance, d (distance between the ground rod and probe  $C_2$ ), was varied. The potential probe,  $P_2$ , must be placed 62% f d, between the ground rod and probe  $C_2$ . By using this method a plot was made of ground rod resistance versus separation distance, d (see Figure 16). From this graph the test ground rod resistance was determined to be 107 ohms.

The four probe technique can also be used to find soil resistivity,  $\rho$ . The resistivity of the soil at the test site was measured using the test setup shown in Figure 17. This resistivity was determined to be 97.67 ohm-meter. With this resistivity, the resistance of the ground rod should be 98.6 ohms, which is within 10% of the Fall-of-Potential Method. (This result is considered to represent reasonable accuracy, given the high degree of dependence of the tests on environmental conditions.)

#### HID-FREQUENCY MEASUREMENTS

The mid-frequency range, 100 Hz to 500 KHz, impedance measurement proved to be the most difficult to obtain because of instrumentation limitations. Most off-the-shelf impedance measuring devices require that the object of the test not be grounded. (Specifically the HP 4800A Vector Impedance Meter has "DO NOT GROUND" printed under the input terminals.) Therefore, measuring the impedance of a grounded rod proved impossible with this type of instrument.

An approach was developed which relied strictly on network theory and the fact that the magnitude of the impedance is equal to the ratio of the magnitude of the voltage across and the current through the rod. Several attempts were made to obtain a suitable measurement. Since most oscilloscopes use "ground" as a reference and have a high impedance input, there was no problem with making voltage measurements on the source end of the ground rod. A problem arose in trying to

measure the current into the ground rod, however.

An HP current probe and amplifier provided just such a solution (see Figure 18). This test setup worked well in measuring the ground rod impedance over the mid-frequency range. The results match the low and high frequency impedance measurement of the rod and allowed measurements of impedance over the low end of the NEMP type lightning spectrum. Figure 19 is a plot of the test probe impedance to ground using the mid-frequency setup. The highest frequencies are compared to the high frequency test and the results are within the measurement error.

The test procedure consisted of varying the frequency of the HP 651A Test Oscillator, while maintaining constant output voltage, and measuring the voltage at the terminal of the ground rod and the current through the lead to the ground rod. The test probe configuration was the same as for the high frequency measurements technique. The ground plate and auxiliary ground points were used to provide an effective reference contact with the soil.

#### SUMMARY

This research has demonstrated how difficult it is to predict and measure the high frequency characteristics of a ground electrode. Without the aid of a network analyzer the impedance of a ground electrode is hard to measure at high frequency. The impedance will vary greatly with the parameters of the soil and the environmental conditions. At high frequencies the coupling mode

The first approach was to measure the voltage drop across a one ohm resistor in series with the ground rod. Problems were encountered when the oscilloscope probe shield was connected to the terminal of the resistor thereby adding another "ground" to the circuit. Attempts were made to isolate the oscilloscope from ground, but this only served to increase the noise in the measurement. Obviously, a method of measuring the current was needed which would provide isolation from ground and provide noise rejection.

An HP current probe and amplifier provided

James G. Biddle Co., Plymouth Meeting, PA 19462

for the earth electrode is capacitive, therefore, the contact area at the ground surface should be as large as possible (relative geometric mean area) to dissipate any transient energy.

#### ACKNOWLEDGEMENTS

This work [9] was sponsored by the Defense Nuclear Agency under RDT&E RMSS Code B3630 80462 G52AAXEX40602 H2590D contract number DNA001-80-C-0294 and performed by the Engineering Experiment Station of the Georgia Institute of Technology, Atlanta, Georgia 30332.

#### KEPERENCKS

- 1. Smith, G. S., and King, R. W. P., "The Resonant Linear Antenna as a Probe for Measuring the In Situ Electrical Properties of Geological Media", <u>Journal of Geophysical Research</u>, Vol. 79, No. 17, June 10, 1974, pp. 2623-2628.
- 2. Curdts, E. B., "Some of the Fundamental Aspects of Ground Resistance Measurements", AIEE Transactions, Communications and Electronics, Vol. 77, No. 39, November 1958, pp. 767-770.
- 3. Gaddy, O. L., "A Simple Method of Measuring Fractional Millimicrosecond Pulse Characteristics," IRE Transactions on Instrumentation, Vol. 1-9, No. 3, December 1960, pp. 326-333.
- 4. Mukhedkar, D., Gervais, Y., and De Jean, J. P., "Modeling of a Grounding Electrode", IEEE Transactions on Power Apparatus and Systems. Vol. PAS 92, No. 1, January-February 1973, pp. 295-297.
- 5. Weidman, C. D. and Krider, E. P., "Submicrosecond Rise Times in Lightning Radiation Fields", Proceedings of the Lightning Technology Symposium, sponsored by the FAA and NASA at NASA Langley Research Center, Hampton, VA, April 22-24, 1980.
- 6. Lee, K. M., and Smith, G. S., "Measured Properties and Insulated Antennas in Sand", IEEE Transactions on Antennas and Propagation, Vol. AP-23, No. 5, September 1975, pp. 664-70.
- 7. Lytle, R. J., "Properties of the Ground Inferred from Electromagnetic Measurements", IEEE Transactions on Antennas and Propagation, Vol. AP-27, No. 6, November 1979, pp. 899-902.

- 8. Denny, H. W., Holland, L. D., Robinette, S. L., and Woody, J. A., "Grounding, Bonding, and Shielding Practices and Procedures for Electronic Equipments and Facilities," Volume 1, Final Report, Contract DOT-FA72WA-2850, Engineering Experiment Station, Georgia Institute of Technology, December 1975, AD A022 332.
- 9. Denny, H. W., Acree, D. W., Melson, G. E., and Millard, D. P., "Supplemental Grounding of Extended EMP Collectors", Georgia Institute of Technology, Engineering Experiment Station, for the Defense Nuclear Agency, 31 January 1982.

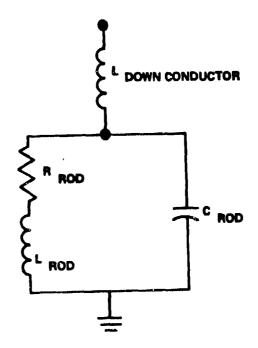
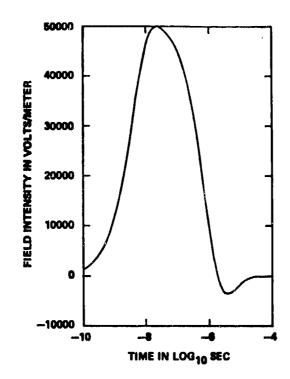


Fig. 1 - Ground rod model.



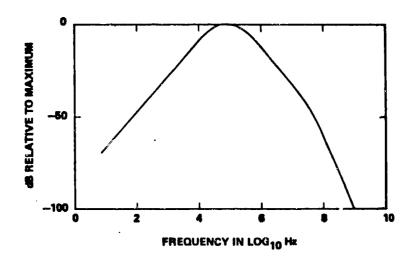


Fig. 2 - NMP time waveform and power spectrum representations.

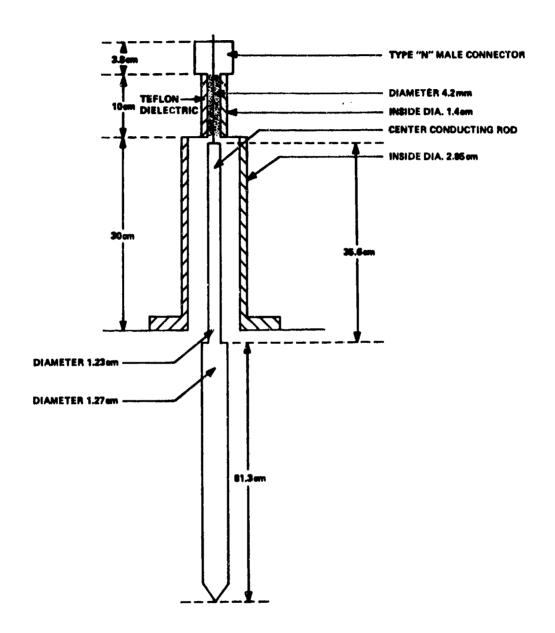


Fig. 3 - Standard test probe details.

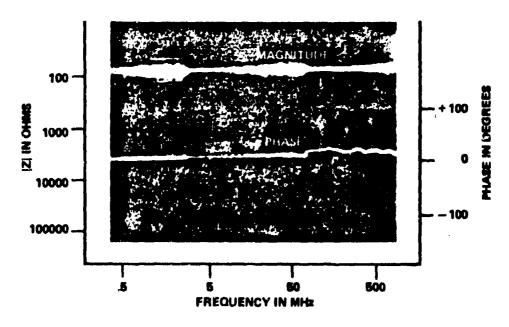


Fig. 4 - Connector input impedance.

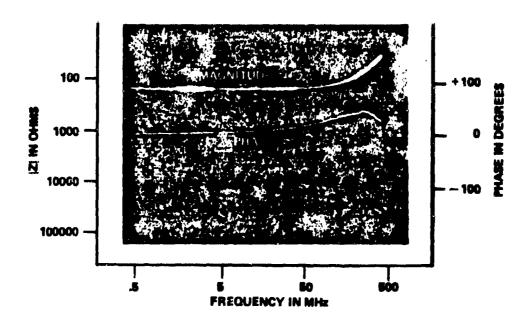


Fig. 5 - Connector output impedance for calibrated 100 ohm load.

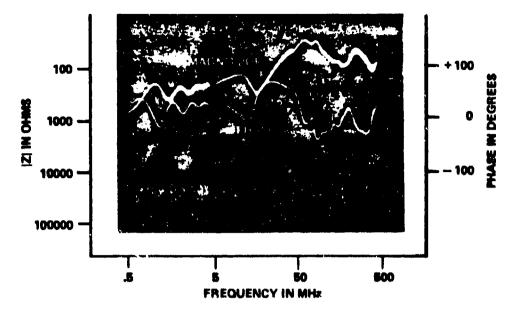


Fig. 6 - Simple ground rod impedance.

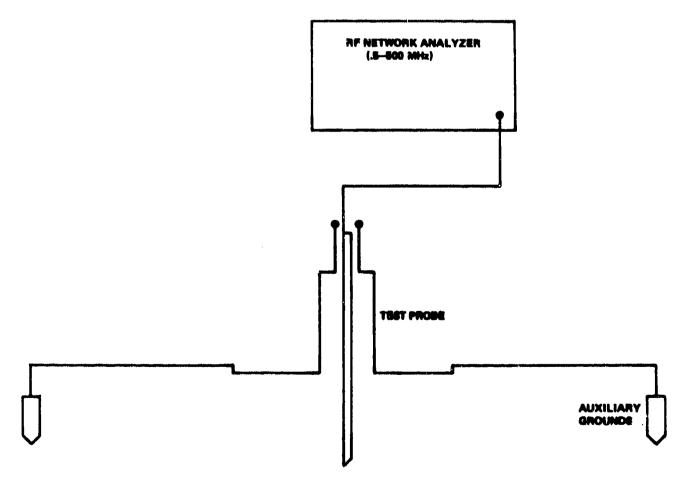


Fig. 7 - Test setup for high frequency seasurements.

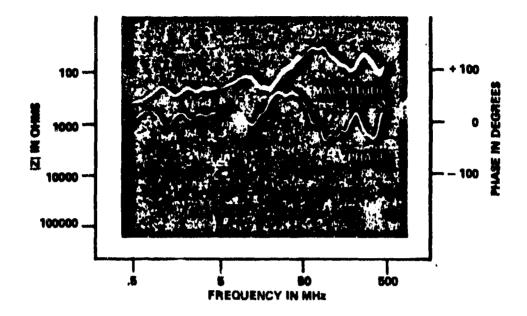


Fig. 8 - Impedance of ground rod and one auxiliary ground.

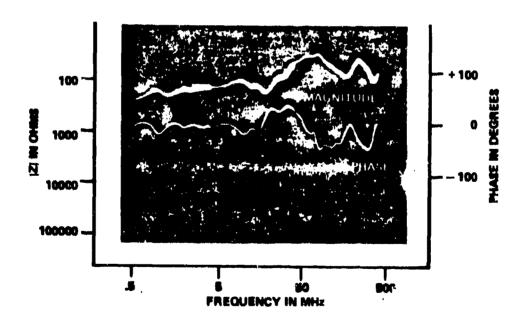


Fig. 9 - Impedance of ground rod and two auxiliary grounds.

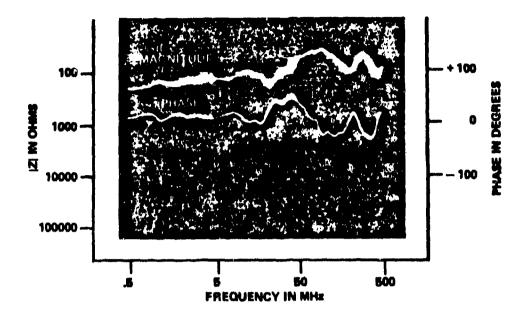


Fig. 10 - Impedance of ground rod and three auxiliary grounds.

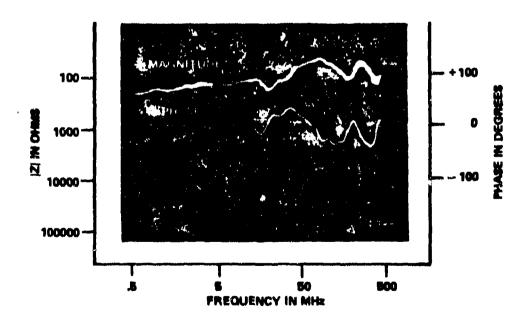


Fig. 11 - Impedance of ground rod and four auxiliary grounds.

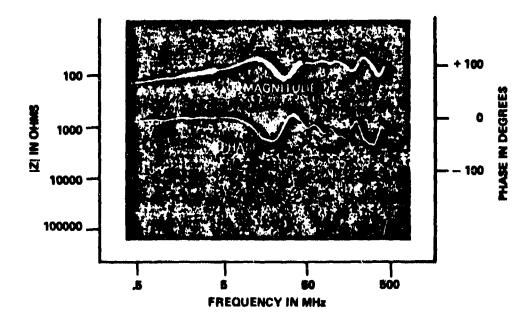


Fig. 12 - Impedance of ground rod, four auxiliary grounds, and an aluminum gournd plate.

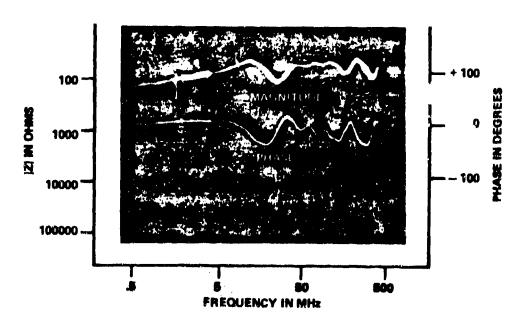


Fig. 13 - Impedance of ground rod, four auxiliary grounds, and a buried aluminum ground plate.

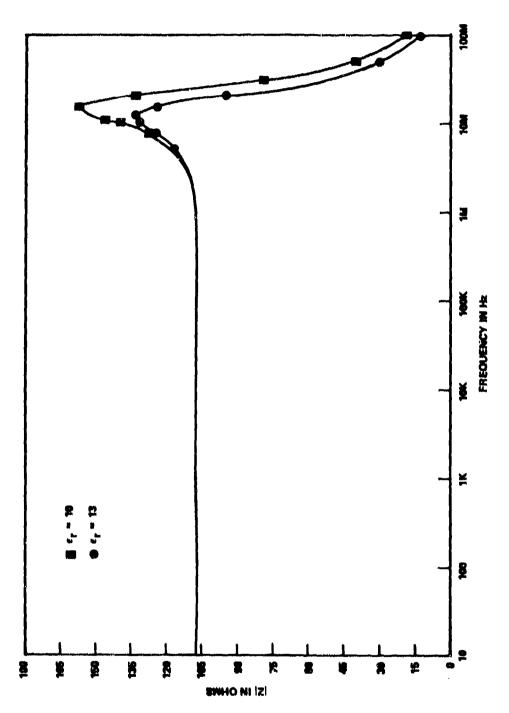


Fig. 14 - Computer simulation of impedance of ground electrode model.

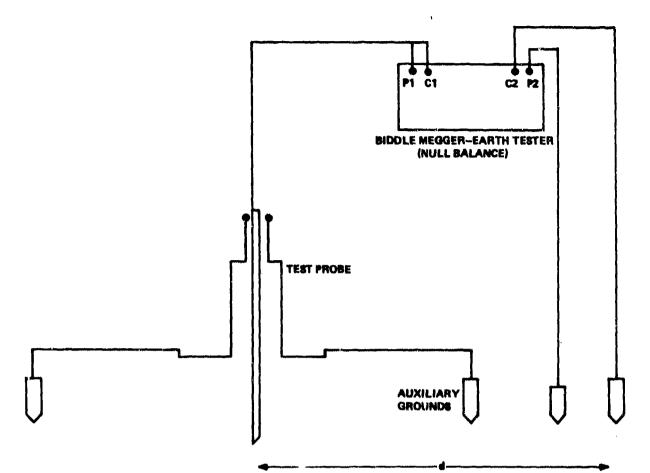


Fig. 15 - Test setup for low frequency measurements.

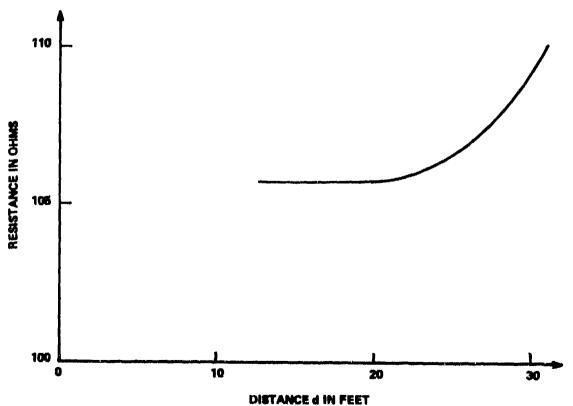


Fig. 16 - Test probe resistance characteristics.

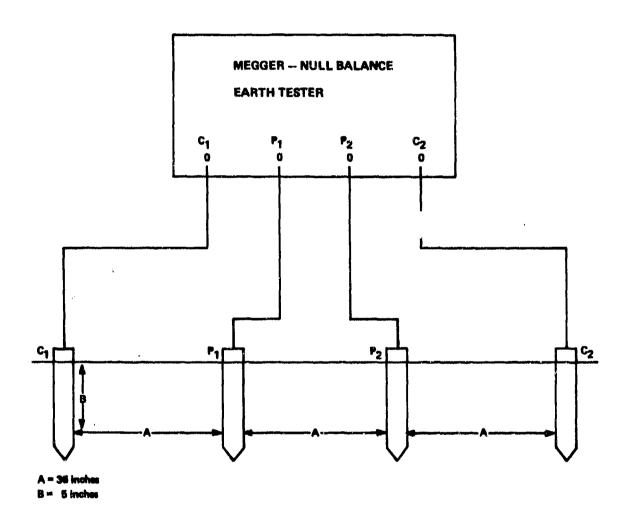


Fig. 17 - Soil resistivity measurement setup.

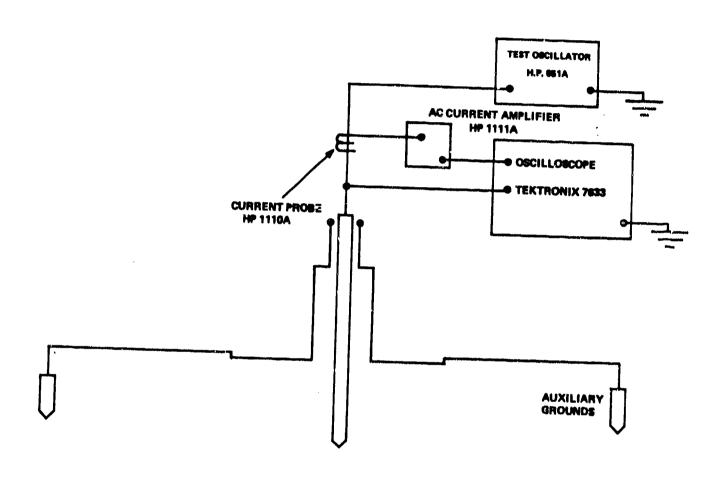


Fig. 18 - Test setup for mid-frequency measure-

Fig. 19  $\sim$  Mid-frequency ground electrode impedance behavior.

# AD P002183

# IMPROVED GROUNDING SYSTEM FOR MOUNTAIN TOP RADIO SITES

LLOYD B. WATTS, PE, ELECTRICAL ENGINEER
Federal Emergency Management Agency, Region VIII,
Denver, Colorado

ABSTRACT

In 1980, Warren R. Jones, IEEE, published a paper on the use of Bentonite (well drillers mud) when installing vertical ground rods. This concept has now been developed to use copper tubing in a lateral trench (radial type ground) that has been backfilled with layers of Bentonite. In the case of mountain top sites, it is usually possible, with machinery, to obtain a trench that is 200 mm (8 in.) to 600 mm (24 in.) deep. In fact, 32 sites in the Utah state radio system are now using this grounding method. Several of these sites are over 3460 M (11, 350 ft.) and are difficult to ground by any method, but during the past two summers, they have been successful in getting a backhoe and dry Bentonite to these locations. In addition to the radial ground, Metal Oxide Varistors (MOV), bipodar zeners and coax tee's (with protectors) are used to complete the protective scheme.

MARK TWAIN IS QUOTED (1)\* AS SAYING:

"A prodigious storm of thunder and lightning, accompanied by a deluging rain that turned the streets and lanes into rivers, caused me to repent and resolve to lead a better life. I can remember those awful thunder-bursts and the white glars of the lightning yet and the wild lashing of the rain against the windowpanes....With every glare of lightning I shriveled and shrank together in mortal terror, and in the interval of black darkness that followed I poured out my lamentings over my lost condition, and my supplications for just one more chance, with an energy and feeling of sincerity quite foreign to my nature. But in the morning I saw that it was a false alarm and concluded to resume business at the old stand and wait for another reminder." Unfortunately, this attitude of wait and see if it happens again still persists among radio maintenance and installation personnel today.

In January of 1981, the entire state of Utah experienced a 5 hour power outage precipitated by a network fluke. The state radio system switched to emergency power smoothly and continued to operate during the outage with only a few problems reported. The key stations in the commercial Emergency Broadcast System EBS also came back on the air within minutes through use of emergency generators. The real trouble began when network power was being restored-voltage and frequency instability caused several microwave sites to fail.

The Utah office of Comprehensive Emergency Management knew that the Federal Emergency Management Agency (FEMA) had been actively engaged in Electromagnetic Pulse (EMP) mitigation for the past 10 years. These efforts had been confined to selected commercial radio stations and Emergency Operating Centers (EOC's) designed to maintain continuity of government during disasters. The EMP protective system developed by FEMA also provides superior lightning protection for critical electronics equipment. The Utah emergency planners also recognized that a reliable state radio network is essential to their functions during all types of disasters. With the spectre of the power outage as motivation to override the Mark Twain syndrome, a project asking for technical assistance in improving reliability of the state radio network was submitted to the FEMA regional office in Denver, Co.

### SITE SURVEYS AND TRAINING

The assistance from FEMA started with site surveys to determine what equipment was install-

\*Numbers in parentheses designate references at the end of the paper. ed, what type station ground was in use and to determine soil conditions on typical mountain topsites. Two seminars were held with state radio maintenance personnel where site survey techniques were discussed along with ground and protector installation methods. Following the system survey, a consolidated bill of materials was developed and ail parts placed on order.

STATION GROUND STILL A PROBLEM -The typical mountain top radio site has always presented a grounding problem and the Utah sites (some above 3460 M-11,352 ft.) were no exception. Fortunately, an article (2) which appeared in IEEE Transactions in 1980 held the solution. This article advocated the use of Bentonito (well drillers mud) as a superior backfill for vertically installed ground rods and noted resistance reductions of 36% when compared to driven rods of similar dimensions.

ADAPTATION TO MOUNTAIN TOPS - The original proposal cited (2) was that a power auger, such as used by utility companies, could go through almost any type of soil or rock and a ground rod could be centered in the hole and then backfilled with Bentonite. This technique is excellent for rods of up to 3.048 meters (10 feet) but is impossible for longer, low resistance, radial type grounding systems which rely on large surface areas in contact with the soil. For mountain top sites, a narrow bucket backhoe is used to dig a 200mm (8 in.) to 600mm (24 in.) deep trench from the radio tower base to accomodate 19mm (3/4 in.) copper tubing about 15.24 meters (50 feet) in length. Where terrain permits, three such trenches are opened with approximately 15 degree separation as they branch from the tower base. In one case it has been necessary to open one trench approximately 61 meters (200 feet) long to accomodate multiple users and to obtain maximum contact with the soil. Following excavation, dry Bentonite (typically a 44mm-11/2 in. layer) is placed in the tranch followed by the copper tubing which is covered with another thin layer of Bentonite and topped with excavated soil. Caution is urged when using Bentonite under areas that will ultimately be paved as it can expand to several times the dry volume when saturated.

BRAZING RECOMMENDED FOR CONNECTIONS
-Where the pieces of tubing come together, they are flattened and brazed (Fig. 1) along with the runs of heavy copper wire to the tower base and station (equipment) ground. Bentonite (Fig. 2) is also used in and around the connection point. In addition to the hydration property of Bentonite, it is highly conductive and noncorrosive. The purpose of the brazing is to assure a strong, low

impedance connection and by enclosing it in a noncorrosive environment, long life is assured.

#### **EQUIPMENT PROTECTION**

A Commence

With a low impedance ground in place the next step toward improved pulse protection and subsequent improved equipment reliability is to install protective devices. These include Metal Oxide Varistor's (MOV's) bi-polar seners and coax connectors with integral solid state surge arresters. A typical site layout (Fig. 3) shows equipment and antennas in the microwave and VHF bands. Radio maintenance personnel were also instructed to ground the outer sheath of all coax cables at least 2 meters (6.5 feet) prior to connection to radio equipment. In most cases this requirement was met at the grounded plate where the coax "T" with integral surge protector was installed. Due to antenna design, the center conductor of the microwave feed coax is relatively immune to transients so microwave protection is limited to grounding of the outer sheath as previously described and protecting the power feed with MOV's. In addition, individual dc power supplies were protected with bi-polar zeners. Very few of the Utah sites have cable pairs to the site but where these do exist, communications gas gaps are installed.

#### ANALYSIS AND TESTING

Testing of these grounds by the remote ground rod method is not practical since the test rods cannot be placed but the relationship given by Warren R. Jones. (2) provides insight as to results expected and achieved to date. The relationship is:

R = Revistance of rod to remote ground <math>p = Soil Resistivity

The increased surface area by using copper tubing is obvious and the use of low resistivity Bentonite further enhances the ground effectiveness in soils over 100 ohms-meter. The use of a radial type ground and selection of protectors is based on FEMA (3) documents concerning EMP protection of command and control functions for government installations.

## CONCLUSIONS

It is still too early to fully assess the improvements in reliability, but the inherent qualities of Bentonite leave little doubt that for the first time, mountaintop radio equipment has a superior ground that is far easier to install and maintain than the doubtful technique of driven rods in loose rock. The Utah Department of Public Safety has already documented considerable reduction in the effects of lightning on the completed sites and to their surprise, a reduction or elimination of intermodulation and Radio Frequency Interference (RFI). Their next step in improving their lightning protection will be to extend tower steel approximately 2 meters (6.5 feet) above the tallest antenna. (Fig. 3). It has been confirmed that the radio maintenance personnol have been making fewer trips to protected sites for repair or equipment replacement.

#### REFERENCES:

- 1. Viemeister, Peter E. (1961) The Lightning Book. Doubleday & Company inc. New York, pp 230. 2. Jones, W.R. (1979). Bentonite Rods Assure
- Ground Rod Installation in Problem Soils, IEEE Transactions on Power Apparatus and Systems, Vol. PAS-99, No. 4 July/Aug. 1980, pp 1343-1348.
- 3. Technical Report, TR-61A (July 1972) EMP Protection for Emergency Operating Centers -Defense Civil Preparedness Agency (now Federal Emergency Management Agency). pp 40-45.



FIG. 1 - Method of brazing copper tubing at common point.

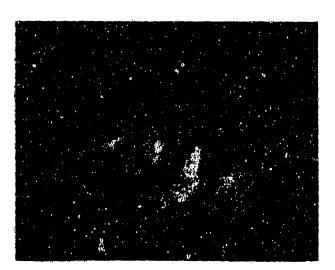


FIG. 2 - Application of Bentonite following brazing of common point.

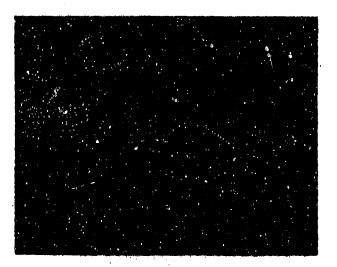


FIG. 3 - Typical radio equipment building and antenna structure.

Aleksandar Vorgučić, D.sc. Electronic Faculty, University of Niš Yugoslavia

 $\rightarrow$ 

#### ABSTRACT

-> The results of many years research of the electrical resistivity change of concrete in conection with different grounding are presented. The eximinations are made under different conditions of moisture and combinations of electrodes. Even for a long period of time, the concrete electrical resistivity increasis permanently. The electrical resistivity increasing of concrete at foundation earth could lead to decreasing of the effectivity of the grounding system. Also, in industries/where static electricity appears, increasing resistivity of concrete floors could have influence in the technological processes

USE OF CONCRETE, in conection with electrical current, every day is more and more frequent. Electrical demands from the concrete, in general, are quite oposite. On one hand concrete should have a high resistivity, when used as isolator, for example for concrete crossties, since this resistivity affects the operation of railroad signal systems. On the other hand concrete should have low resistivity in cases where the concrete is applied in grounding for example in foundation earth.

Foundation earth results as consequence from: 1° using more and more reinforced concrete i.e. using the metal

in the objects, 2° the objects closenes in the setlled places and 3° plastic replacing the metal in the water and other installations used as an additional earth electrodes before.

Recently, very often foundation earth is in use. According to the Codes of many countries concrete foundation provided with the steel reinforcement or with a conductor embeded in the concrete can be used as an earth termination. The advantages of reinforced concrete foundation are: 10 it is cheap to install during building constraction, 20 it is free from intesive corrossion and 30 it binds all art of grounding together i.e. it makes potential equalizing. The long conductors in the concrete i.e. a large dimensions of foundation earth which is in moist soil should ensure low resistance of earthing. But the reports about electrical resistivity of concrete are incomplet and contradictory what makes this matter unclear.

Unlike from electrical, the machanical properties of concrete are well known. "It is considered that the concrete matures for about one manth, and all examinations of strenght of concrete performs at the 28-th day of its age." Fig.1 shows strenght of concrete for a period of five years (1)\*. The main

<sup>\*</sup> Numbers in parentheses designate References at end of paper.

increasing is for the first month. Probably the mechanical mature of concrete for one month, influenced an short term electrical investigation of concrete. But the electrical properties does not follow the mechanical properties.

To make this question clear, author started to investigate the time dependence of electrical resistivity of the concrete. Investigations took more the four years and are steel in the course of.

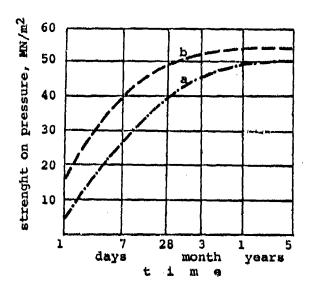


Fig. 1 - Strenght on pressure-time characteristics for concrete from a) normal cement, b) fast-binding cement (1)

From the plenty of results heir would be given some the most important ones without comments. Some reports about this investigations are olready presented (2,3).

#### ELECTRICAL PROPERTIES OF CONCRETE

In this part would be given short data about electrical properties of concrete which are given in literature and got by systematic investigation. Investigation the resistivity of the concrete in past was short-dated. The electri-

cal behaviour of the concrete after longer time is unknown.

Concrete is a system of nonconductive particles of sand or gravel embeded in a conductive cement paste. The resistance of such a composition in general depends from cement paste. The concrete has greater resistance than the cement pasta becouse the current has now longer way between particles of agregat and smaller cross-section of this way. Fig. 2 showes curves the resistivities in function of time for the concrete and cement paste. The measuring of resistivities were after periods of 7, 28 and 90 days. The increasing of resistivity were explaine as effect of continous moist storage (4).

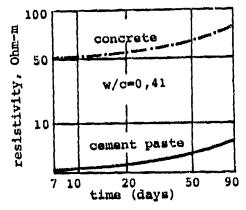


Fig. 2 - Effect of concrete moist storage (4)

"The electrical conductance of set cement pasts and concrete stored under constant conditions generally decreases with age, at least during the first few months. However, the moisture plays an essential part in the decrease in conductivity. The specific resistance of concrete, cured in water for three months, may be less than 10<sup>2</sup> ohms-m, whereas the volume resistivity of well-dreid concrete may attain a value of 10<sup>9</sup> ohms-m at about the same age\* (5).

Fresh cement puste and concrete are

conductors with negative temperature coefficient as the electrolyte. The resistance of hardened cement paste and concrete is less dependent on the temperature.

Water-cement ratio (w/c) by making the concrete influences on the electrical resistivity. "The resistivity of paste having a water-cement ratio of 0,40 was about double that of past having a ratio 0.60" (4).

Table 1 - Effect of water-cement ratio (4)

w/c ratio	Res	ohm-m	
	7 days	28 days	90 days
0.40	10.3	11.7	15.7
0.50	7.9	8.8	10.9
0.60	5.3	7.0	7.6

#### LONG-TIME INVESTIGATION

TEST SPECIMENT for electrical proparties investigation of concrete consist from short metal electrodes embeded in the concrete which is using for foundation. The electrodes are: 10 from zinc coated steel bands (In-electrodes), cross-section area 25x3 mm<sup>2</sup>, 20 from steel rods for the concrete rainforcement, diameter 6 mm (Fe-electrodes) and 30 from copper bands area 20x0,6 mm<sup>2</sup> (Cu-electrodes). All electrodes have the same length of 100 mm. The speciments are the concrete blocks with electrodes in pairs on the same distance of 20 mm under different conditions. The first block with two pairs of Zn electrodes is settled in wet soil as foundation (wet speciment). Second block is the same as the first but in the dry air what corresponds to the concrete columnes and the other concrete constructions on the buildings (dry speciment). The next block with the pairs of Zn, Fe

and Cu electrodes was 1/3 in the water for the first 56 days and than is pulled out and dried in the air (wet-dry speciment). They are 15 measuring pairs of electrodes in concrete blocks under different conditions.

RESULTS OF MEASURING. Measurements on concrete speciments are performed with direct and alternatic current. Direct current used to see phenomenon and influence of polarization potential becouse special the fresh concrete behaves as an electrolyte. To avoid the polarization effects, for resistance measuring alternating current is used.

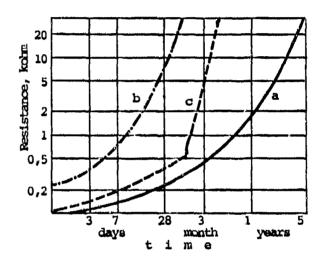


Fig. 3 - Resistance - time characteristics of concrete spaciments a) wet concrete, b) dry concrete, c) wet-dry concrete

Fig. 3 shows the curves resistance changing in function of time:  $1^{\circ}$  between electrodes in a wet concrete, which is in a moist soil (measuring place  $N^{\circ}$  4),  $2^{\circ}$  between electrodes in wet-dry concrete (measuring place  $N^{\circ}$  8) and  $3^{\circ}$  between electrodes in dry concrete (measuring place  $N^{\circ}$  6). The concrete is same and the electrodes configuration are also the same in speciments. The resistance increasing of concrete in functi-

on of age is evident in all cases. Curves of electrical resistivity and mechanical strenght are total different (Fig. 1 and Fig. 3). Increasing the concrete resistance in moist soil is in four years about 300 times from the begining of measurement. Increasing the resistance in dry concrete is about milion times. On the last, humidity of air has big influence.

The resistance jump in wet-dry spacement on 56-th day shows the influence of the current way trough the water. On the 56-th day the wet-dray speciment is pulled from the water.

Now, it should be mentioned some interesting observations.

The spaciments with measuring places  $N^{O}$  6 (dry) and  $N^{O}$  8 (wet-dry) had have the same resistance when on 665-th day had been exposed to water in duration of 15 min. The resistances had rapidly fell of to 11 kohms. With draying on air faster increased resistance in spaciment who was dry. The increasing of resistance for both spaciments are given in table 2.

Table 2 - Increasing of resistance t(days) 1 4 7 11 Spec.  $N^{O}$  6 11 280 550 950 kohms Spec.  $N^{O}$  8 11 93 124 180 kohms

It would be considered the case of two pairs of electrodes in block wet-dry. One pair from the zinc coated steel bands 25 mm wide (Zn) and the other from concrete rainforced steel diameter of 6 mm (Fe). Distance between the electrodes for the both pairs is the same.
Naturally, becouse of greater cross-section area the first pair had lower resistance then other. Some days affter pulling out the block from the water, as is shown on Fig. 4, the situation was changed. Trough the drying, the resis-

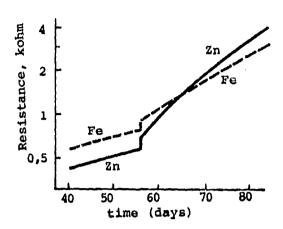


Fig. 4 - Resistance - time characteristics of wet-dry concrete speciment

tance between zinc coated bands was greater than between the steel electrodes. This was not expected becouse the cross-section through concrete between 25 mm wide bands is much greater then between thiner 6 mm steel rods. The behaving is as the effective diameter of steel rods are increased.

Some times the dry block was wetting for some minutes, what should simulate rain. In this cases resistance between electrodes was rapidly folling. With drying resistance was fast increasing. In comparing with the permanent wet concrete, the resistance just affter wetting the dry spacement was greater, but only during the period of nearly four years. After four years such a measuring repeated. Now the resistance on wetted dry block was 19 kohm compared with 30 kohm on the permanent wet blok. Probably this greater resistance on permanent wet concrete is result of the salts rinsing from concrete in permanent presence of water.

#### SUMMARY

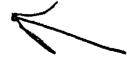
The first long-term electrical resistivity investigations shows that the concrete resistivity increasis permanen-

tly. The increasing of the concrete resistivity is also for the concrete which is permanent in moist soil. The resistance increasing from the begining of measuring in the time more of the four years is: 1° about 300 times for permanent wer concrete and 2° about one milion times for dry concrete.

The increasing concrete resistivity after long period could have: 1° considerable increasing of the grounding resistance of the foundation earth, what could lead to decreasing of the grounding system effectivity and 2° the resistivity increasing of the concrete floors in industries where static electricity appears, what could lead to the technological processes spoiling and the speed reduction of the production.

#### REFERENCES

- 1. A. M. Neville, "Osobine betona" ("Properties of concrete" translation), Gradjevins) > knjiga, Beograd, 1976.
- 2. A. Vorgučić, "Električna otpornost betona vremenska zavisnost" (Electrical resistivity of concrete time dependence), Proc. SMEITJ-GES 80, D. Milanovac, 1980.
- 3. A. Vorgučić, "Električna otpornost betona problemi vezani za tehnološke procese" (Electrical resistivity
  of concrete Problems concerning the
  technological processes), Proc. Scientific assemble in developing textile
  industry, Leskovac, Dec. 1981.
- 4. C. A. Monfore, "The electrical resistivity of concrete", J.Portl. Cem. Assoc. Reaserch and Development Laboratories, May, 1968.
- 5. Anon, "Electrical properties of concrete", Concrete and Constructionnal Engineering, Vol. 58, May, 1963.



# AD P002187

ELECTROSTATIC VOLTAGE SENSORS FOR HELICOPTER DISCHARGERS\*



Oren Tranbarger and Bob M. Duff, Senior Research Engineers, Southwest Research Institute, San Antonio, Texas

#### ABSTRACT

To maintain hovering helicopters at safe energy levels, a noncontacting electrostatic sensor is required to accurately determine the voltage on the sircraft relative to ground and provide proper control data to an active discharger for neutralizing hazardous charging conditions. Analytical model studies of a sphere suspended between two electrified ground planes and surrounded by space charge resulted in a theoretical relationship showing how charge density, excess surface charge, and external electric fields affect the voltage on the sphere. The electrostatic trends predicted from the theoretical analysis were sufficiently verified through independent large-scale laboratory experiments using empirical analysis techniques. From the theoretical and empirical analyses, helicopter charge equilibrium conditions were specified, together with a methodology for determining the electrostatic coefficients of full-scale hovering helicopters. The implications of the investigative program are that active electrostatic discharger systems are now feasible for helicopter applications.

\*The work described in this paper is the result of a project conducted by Southwest Research Institute under the support of the U.S. Army Research and Technology Laboratories (AVRADCOM) at Fort Eustis, Virginia, under Contract No. DAAK51-79-C-0060.

GROUND PERSONNEL who come in contact with cargo hooks lowered from hovering helicopters frequently suffer severe electrical shock capable of striking a man down, injuring fingertips, and splitting fingernails. In past years, considerable research effort has been directed toward the development of noncontacting active electrostatic discharger systems for measuring the voltage buildup on helicopters and reducing this nuisance problem to within safe energy levels. Although electrostatic discharger systems described in the technical literature [1]\* can generate the necessary countercharge for neutralizing the voltage buildup on hovering aircraft, deficiencies in the voltage sensor require additional development work before the voltage on the aircraft relative to ground can be accurately measured.

To fully understand the nature of the voltage sensing problem, the helicopter was approximated in laboratory model studies as a sphere which was suspended in space above the ground, surrounded by space charge, and subjected to an external electric field. Experiments were conducted using a conducting sphere in a specially constructed electrostatic test chamber where bound surface charge, surrounding space charge, and the external electric field could be varied independently to determine the manner in which each parameter affected the voltage on the sphere. Through empirical analysis, these laboratory model studies revealed the voltage on the sphere to be a linear function of the externally applied electric field, surrounding space charge, and the excess surface charge on the model. There is a companion geometric coefficient associated with each voltage parameter. The magnitudes of the coefficients vary as a function of height above the ground. The laboratory model configuration was also analyzed through classical techniques by solving Poisson's equation in a manner suggested by Smythe [2]. Excellent agreement was obtained between the theoretical results and empirical analysis of the laboratory data.

The results of the investigative work into the sensor problem show the necessary conditions for maintaining zero potential on the helicopter and a method for determining the geometric coefficients of full-scale helicopters. It can be concluded that active electrostatic discharger systems are now feasible for helicopter applications. A practical discharger system would require multiple-point electrostatic sensors to measure electric fields and charge density. In a closed feedback system, data from these sensors would be processed by a microcomputer which would calculate the voltage on the helicopter as a function of height and control countercharge generated for neutralizing purposes.

In addition to the technical results of the electrostatic model studies mentioned, this paper describes briefly the electrostatic test chamber used for the model experiments, some of the unique electrostatic instrumentation required for measuring electric fields and space charge, and the construction of the spherical model.

\*Numbers in brackets designate references at end of paper.

#### THEORETICAL ANALYSIS

The potential and electric fields for models which correspond closely to the test chamber have been analyzed theoretically. The results include solutions for a charged sphere between finite size conducting plates, and between infinite conducting plates with a cylindrical space charge region surrounding the sphere.

SPHERE BETWEEN INFINITE PARALLEL PLATES — Before the finite plate problem is considered, the classic problem of a charged sphere between infinite parallel conducting plates is reviewed. The notation used follows that of Morse and Feshback [3] in most cases. The potentials interior and exterior to the sphere may be expressed by the eigenfunction series

$$\psi^{1}(\mathbf{r},\theta) = \sum_{n=0}^{\infty} C_{n} \left(\frac{\mathbf{r}^{n}}{\mathbf{a}^{n}}\right) P_{n}(\cos\theta)$$
 (1)

$$\psi^{a}(\mathbf{r},\theta) = \sum_{n=0}^{\infty} C_{n} \left( \frac{\mathbf{g}^{(n+1)}}{\mathbf{r}^{(n+1)}} \right) \mathbf{P}_{n}(\cos\theta) \tag{2}$$

where:

 $\psi(\mathbf{r}, \theta)$  = the electrostatic potential interior to a sphere of radius a,

 $\psi^{2}(\mathbf{r},\theta)$  = the electrostatic potential exterior to a sphere of radius a,

 $r, \theta, \phi$  = spherical coordinate variables having origin at the center of the sphere,

P<sub>n</sub>(cosθ) = the Legendre function of the first kind of degree n, and

 $C_n$  = the undetermined coefficients.

The condition that the potential be everywhere finite and continuous across the surface of the sphere has been imposed in formulating Equations (1) and (2). In addition, only rotationally symmetric (i.e.,  $\phi$  independent) solutions are considered. Imposing the boundary condition for the normal component of electric field at the surface of the sphere leads to expressions for the model components of surface charge density as

$$a_n(\theta) = C_n \epsilon_0 \frac{(2n+1)}{a} P_n(\cos \theta)$$
 (3)

The capacitance of the sphere is defined as

$$c = Q/V_0 \tag{4}$$

where:

Q = the total charge on the sphere, and

 $V_0$  = the potential imposed upon the sphere.

The total charge is obtained by integration of the surface charge density over the surface of the sphere. Since only the zeroth degree Legendre function has a non zero integral, the capacitance may be written as

$$c = 4\pi a \epsilon_0 C_0 / V_0 \tag{5}$$

where:

a = the radius of the sphere, and

 $\epsilon_0$  = the permittivity of free space.

If the sphere were located in free space, the distribution of charge would be uniform and only  $C_0$  would be non zero. When the sphere is placed between parallel conducting plates, or in fact near any other conductor, the higher order terms exist. The infinite parallel plate geometry is shown in Figure 1.

The boundary conditions which must be met are

 $\psi(\mathbf{r}, \theta) = \mathbf{V}_0$  at all points on the surface and within the sphere,

 $\psi(r,\theta) = V_1$  at all points on the lower plate, and

 $\psi(r,\theta) = V_2$  at all points on the upper plate.

The potentials  $V_0$ ,  $V_1$  and  $V_2$  are assumed to be known and, initially, V<sub>1</sub> and V<sub>2</sub> will be taken as zero. Following the procedure given by Smythe [2], the total potential at the center of the sphere is set equal to V<sub>0</sub> and, since the potential is constant within the sphere, the derivatives of potential of all orders are set equal to zero. The total potential at the center of the sphere is the sum of the potentials due to charges on the sphere and to surface charge on the two plates. Image theory may now be used to replace the two plates by a series of images of the sphere. The potential at the center of the sphere is then obtained by adding to Equation (1) a series of image terms computed from Equation (2). Truncating the eigenfunction series at Nth order, a set of N linear equations is formed by setting the potential equal to V<sub>0</sub> and the first N-1 derivatives of the potential with respect to z equal to zero. After some algebraic manipulation, the resulting equa-

$$\sum_{n=0}^{N} \left\{ C_n \left[ \delta_n^0 + a^{n+1} \sum_{k=1}^{M} (-1)^{(n+1)k} \right] \right\}.$$
 (6)

$$\cdot \left( \frac{1}{(kD + [1 - (-1)^k]z_0)^{n+1}} + \frac{(-1)^n}{(kD - [1 - (-1)^k]z_0)^{n+1}} \right) \right] \right\} = V_0$$

$$\begin{split} &\sum_{n=0}^{N} \left\{ C_{n} \left[ \frac{m! \delta_{n}^{m}}{a^{n}} + \frac{a^{n+1}(n+m)!}{n!} \sum_{k=1}^{M} (-1)^{(n+m)k} (-1)^{n}, \right. \right. \\ &\left. \cdot \left( \frac{1}{(kD + [1-(-1)^{k}]z_{0})^{n+m+1}} + \frac{(-1)^{n}}{(kD - [1-(-1)^{k}]z_{0})^{n+m+1}} \right) \right] \right\} = 0; \end{split}$$

m = 1, 2, ..., N-1

where:

$$\delta_n^m = \begin{cases} 1 & \text{for } n = m \\ 0 & \text{for } n \neq m \end{cases}$$

D = the separation between the plates;

z<sub>0</sub> = location of the center of the sphere; and

M = the number of image terms retained in the computation.

A potential applied to the plates may be included by recognizing that a linear gradient of potential is added in the region between the plates. For a potential  $V_2$  applied to the upper plates, with  $V_1 = 0$ , the potential and its derivative with respect to z are given by

$$\psi(z) = \left(\frac{1}{2} + \frac{z}{D}\right) V_2 \tag{8}$$

$$\frac{\mathrm{d}\psi(z)}{\mathrm{d}z} = \frac{\mathrm{V}_2}{\mathrm{D}} \tag{9}$$

These two terms may then be subtracted from the right-hand sides of Equation (6) and the first of Equations (7) as modifications of the source vector. The solution of this set of linear equations for the coefficients  $C_n$  then allows for computation of the charge density on the sphere using Equation (3). The electric field at the lower plate is also of interest and may be obtained from the potential by adding an appropriate image series to Equation (2). The result may be expressed as

$$E_{n}(y_{n}-D/2) = \sum_{k=0}^{N} C_{n} e^{n+1} (n+1) \sum_{k=1}^{M} \frac{(-1)^{k} P_{n+1}(z_{k}/r_{k})}{r_{k}^{(n+2)}}$$
(10)

where:

$$z_k = (-1)^k [(k-1/2) D + (-1)^k z_0],$$
 and

$$r_k = [y^2 + z_k^2]^{1/2}$$
.

and a recurrence formula for the Legendre functions (Equation (843)) of Reference [4] has been used.

SPHERE BETWEEN THIN OBLATE SPHEROIDS — Since the width of the roof and floor plates of the test chamber are of the order of their separation, the accuracy of an infinite plate model must be examined. For this purpose, the roof and floor are modeled as thin oblate spheroids which, in the limit of zero thickness, become circular disks. The geometry used in this analysis is shown in Figure 2.

Rotational symmetry about the vertical axis is maintained and the spheroidal coordinates  $\xi$  and  $\eta$  are defined [3] by

$$z = b\eta \xi \tag{11}$$

$$x = b\sqrt{(\xi^2 + 1)(1 - \eta^2)}$$
 (12)

Solutions of Laplace's equation appropriate to an oblate spheroid defined by  $\xi = \xi_0$  are

$$\psi^{i}(\xi,\eta) = \sum_{n=0}^{\infty} P_{n}(\eta) [A_{n}P_{n}(i\xi) + B_{n}Q_{n}(i\xi)] ; \xi \leq \xi_{0}$$

$$\psi^{n}(\xi,\eta) = \sum_{n=0}^{\infty} C_{n}P_{n}(\eta)Q_{n}(i\xi) ; \xi \geq \xi_{0}$$
(14)

where:

 $P_n$  = the Legendre function of the first kind;

 $Q_n$  = the Legendre function of the second kind; and  $i = \sqrt{-1}$ 

The requirement that the potential be finite everywhere has been imposed in formulating Equations (13) and (14). Further simplification can be achieved from symmetry considerations. An even charge distribution on the surface of the spheroid must produce a zero electric field (gradient of potential) at  $\xi = 0$ , and an odd charge distribution must produce a zero potential at  $\xi = 0$ . Only  $P_n(i\xi)$  has these properties; thus,  $B_n$  in Equation (13) must be zero. Requiring continuity of potential at the surface of the spheroid ( $\xi = \xi_0$ ) leads to

$$\psi^{1}(\xi,\eta) = \sum_{n=0}^{\infty} A_{n} P_{n}(\eta) \frac{P_{n}(i\xi)}{P_{n}(i\xi_{0})}; \xi \leq \xi_{0}$$
 (15)

$$\psi^{a}(\xi,\eta) = \sum_{n=0}^{\infty} A_{n} P_{n}(\eta) \frac{Q_{n}(i\xi)}{Q_{n}(i\xi_{0})} ; \xi \geq \xi_{0}$$
 (16)

The total potential at any point in space may be written by adding the potential due to the sphere (Equation (1) or (2)) and the potential due to each of the two spheroids (Equation (15) or (16)). The coordinates of a point in space must of course be related to the local coordinate systems used in formulating these equations.

A set of 3N equations for determination of the 3N unknown coefficients must now be formed. The procedure used for the infinite parallel plate problem, i.e., enforcing the value of potential and zero derivatives of potential at the center of each electrode, can be used. This procedure was found, however, to result in poor convergence of the numerical solution. Better convergence was achieved by enforcing the value of the potential at a set of N points on the surface of each electrode.

The computed capacitance of the sphere as a function of height above the lower plate for irree space, infinite parallel plates and finite thin plates of area equal to the actual test chamber roof and floor is shown in Figure 3. It is seen that the capacitance is essentially the same for infinite and finite plates.

The normal component of electric field at the surface of the sphere for different heights above the lower plate is shown in Figure 4. For these computations, the oblate spheroids were taken to have a major diameter which would give a disc area equal to the roof or floor

area of the test chamber, and a thickness of 0.0035 meters. Some of the difference in field strength between the infinite plate and oblate spheroid solutions may be caused by the finite thickness and curvature of the spheroid surface, however, these errors are believed to be small. These results thus indicate that the finite size of the roof and floor electrodes in the rest chamber results in a slightly higher field at the south pole when the sphere is near the floor, as compared to the infinite plate prediction.

SPHERE IMBEDDED IN A SPACE CHARGE REGION — The final problem which has been solved relating to the experimental measurements is that of a sphere between infinite parallel plates and surrounded by a finite diameter cylindrical region containing a uniform space charge density. The geometry used for this solution is shown in Figure 5. The solution for the potential at a point designated by r, due to a volume density of charge  $\rho$ , is given by

$$\psi(\bar{\mathbf{r}}) = \frac{1}{4\pi\epsilon} \iiint_{\mathbf{V}} \frac{\rho}{R} \, \mathrm{d}\mathbf{v}' \tag{17}$$

where:

$$R^2 = [(z-z')^2 + r^2 + r'^2 - 2rr'\cos(\phi - \phi')];$$
 and

 $r,\phi,z$  = the cylindrical coordinate variables. The unprimed variables designate the location of the field point at which the potential is to be determined, while the primed variables are variables of integration. The evaluation of the integral in Equation (17) for a general field point leads to an elliptic integral form. The problem is greatly simplified, however, if only field points along the z axis (r=0) are considered. The potential at any point along the z axis which is produced by a finite cylindrical region of uniform charge density is found to be expressible as:

$$\psi^{c}(z) = \frac{\rho}{2e} \left\{ K(z) - z^{2} + \frac{D^{2}}{4} \right\}; \frac{-D}{2} \le z \le \frac{D}{2}$$
 (18)

$$\psi^{c}(z) = \frac{\rho}{2\epsilon} \left\{ K(z) \mp zD \right\}; |z| > \frac{D}{2}$$
 (19)

where:

the upper sign of Equation (19) is used for  $z \ge D/2$ , and

the lower sign of Equation (19) is used for  $z \le -D/2$ ,

$$K(z) = \left[ \frac{(D/2 - z)}{2} \sqrt{(D/2 - z)^2 + b^2} + \frac{(D/2 + z)}{2} \sqrt{(z + D/2)^2 + b^2} + \frac{b^2}{2} \ln \left| \frac{\sqrt{(D/2 - z)^2 + b^2} + (D/2 - z)}{\sqrt{(D/2 - z)^2 + b^2} - (D/2 - z)} \right| \right]$$

 $\rho$  = the volume density of charge, and

 $\epsilon$  = the permittivity.

Equations (18) and (19) do not give the potential needed, however, since the sphere excludes space charge from its interior.

The existence of the sphere may be accounted for by adding to Equations (18) and (19) the potential produced by a spherical region having a charge density of  $-\rho$ . Evaluating Equation (17) for this spherical region gives

$$\psi^{s}(z) = -\frac{\rho}{2\epsilon} \left( a^{2} - \frac{|z|^{2}}{3} \right); |z| \leq a \qquad (20)$$

$$\psi^{i}(z) = -\frac{\rho}{2\epsilon} \frac{2a^{3}}{3|z|}; |z| \ge a \tag{21}$$

where a spherical coo limite system centered on the sphere has been assumed. The desired potential may now be expressed as

$$\psi(z) = \psi^{c}(z) + \psi^{a}(z - z_{n}) \tag{22}$$

where  $z_0$  is the position of the sphere in the coordinate system of Figure 5. This is still, however, only the potential of a finite cylindrical space charge region with a spherical hole. To obtain the desired solution, the potential produced by charge distribution on the sphere, Equations (1) and (2), and an image series to account for the parallel conducting plates must be added to Equation (22). The solution for the unknown coefficients is than carried out in the same manner as previously for the infinite parallel plate case. The equations which are solved are similar to Equations (6) and (7), with the potential produced by the space charge and its image series subtracted from the right-hand side. The required derivatives of the space charge potentials up to the tenth order are given in Reference [5].

The field strength at the lower place as a function of the radius of the space charge region (without sphere) is shown in Figure 6. The horizontal dashed line in Figure 6 indicates the field predicted by an infinite slab of space charge and the vertical dashed line indicates the radius of the cylinder having the same cross-sectional area as the test chamber. It is seen that the finite size of the chamber produces a field at the center of the lower plate which is about 70 percent of that predicted by the infinite slab model. Figure 7 shows the computed electric field at the south pole (bottom) of the sphere as a function of height above the lower plate for a 5 kV potential on the sphere and various space charge densities.

SUMMARY OF THE THEORETICAL ANALYSIS — The analysis of the charge density and electric field on a spherical conducting body has been expressed as an eigenfunction series, the coefficients in the series being determined by the interaction with external electrodes and external space charge density. The general form of the solution is of interest in relation to empirical formules which have been derived. The potential is first expressed as

$$\psi = \sum_{n=0}^{N} C_n K_n(H, x, y, z)$$
 (23)

where:

K, = the eigenfunctions for the sphere,

H = the height of the sphere above the floor of the test chamber, and

x,y,z =the rectangular coordinate variables.

A set of linear equations is formed by matching the boundary conditions on all electrodes and the solutions for the  $C_n$  may be written as

$$C_{n} = \sum_{m} K_{n-m}^{-1} V_{m}$$
 (24)

where:

 $K_{-1}^{-1}$  = elements of an inverse matrix, and

 $V_m = a$  source vector expressing the boundary conditions.

From Equation (24), the potential may then be expressed as

$$\psi = \sum_{\mathbf{n}} \left( \sum_{\mathbf{m}} \mathbf{K}_{1}^{-1} \mathbf{V}_{\mathbf{m}} \right) \mathbf{K}_{\mathbf{n}}$$
 (25)

$$\psi = \sum_{\mathbf{m}} \left( \sum_{\mathbf{n}} K_{\mathbf{n}}^{-1} K_{\mathbf{n}} \right) V_{\mathbf{m}}$$
 (26)

The term in parentheses in Equation (26) is a function of the geometry only, while the vector  $V_m$  contains the influence of externally applied fields and space charge.

The potential produced by an external vertical electric field  $\mathbf{E}_0$  is

$$V^{E} = -E_{o}z$$

and that produced by a space charge density may be written as

$$V_{\rho} = \rho M$$

where M is a function of the geometry. If the boundary conditions of constant potential V and zero derivatives of potential at the center of the sphere are imposed, Equation (26) may be expanded to show the influence of the different external sources as

$$\psi(x,y,z) = V_0 \left[ \sum_{n}^{N} K_n K_{n0}^{-1} \right] + E_0 \left[ \sum_{n}^{N} K_n K_{n0}^{-1} + \sum_{m}^{M} \sum_{n}^{N} K_n K_{nm}^{-1} - z \right] - \rho \left[ \sum_{m}^{M} \sum_{n}^{N} K_n K_{nm}^{-1} \frac{\partial^m M}{\partial z^m} \Big|_{z=H} + M \right]$$
(27)

Each of the terms in brackets in Equation (27) is a function of the geometry alone and thus the influence of each source may be studied separately.

#### **TEST CHAMBER**

To conduct the laboratory tests, it was necessary to construct a special test facility sufficiently large to accommodate the spherical mode! In addition to the size requirement, the design of the chamber included provisions for generating a large volume of space charge and simulating electric fields typical of the earth's natural electric field in the range of ±100 V/m. For the size requirement, a wooden frame plywood cubical structure measuring 6.2 meters (20.25 feet) on a side was constructed. The roof and floor were comprised of sheet metal ground planes that could be electrified to produce external electric fields around the model. The walls of the chamber were insulated with plastic liner sheets to protect the walls from moisture effects as a result of the manner in which space charge was generated in the chamber. Some of the external and overall construction features of the test chamber can be seen in Figures 8 and 9.

Space charge was generated in a small cubical antechamber measuring 1.8 meters (6 feet) on a side, which is visible in the upper right-hand portion of Figure 8. This was accomplished by a water spray electrification process as shown in Figure 10. In this process, six high-velocity nozzles spray water jets against one side of the antechamber. When the water impacts the walls, minute water droplets are formed, resulting in negatively charged fog and mist. With a corona needle in the middle of the antechamber, the negative charge can be greatly enhanced or reversed and made positive in polarity. With a high-volume blower system, the charged fog and mist in the antechamber were transported through large PVC pipes to the main test chamber. A close-up view of the space charge generating antechamber and the circulation pipes to the main test chamber are shown in Figure 11. Overall, the antechamber was constructed out of plywood and lined with galvanized sheet metal which made the interior chamber walls conducting where the charge was generated. The process described for generating the space charge is the phenomenon associated with tank washing [6] on board supertankers which has been responsible for numerous shiptank explosions.

With the water spray electrification and blower circulation system used for generating space charge, the main test chamber could be filled with charged fog and mist that had a charge density on the order of 7 to 12 nC/m<sup>3</sup>. With the model removed from the test chamber, electric fields measured at the center of the floor ground plane varied from 1.85 to 3.18 kV/m as a result of the space charge filling the chamber.

#### INSTRUMENTATION

In conducting the model experiments, some special electrostatic instrumentation was used to measure electric fields and space charge density remotely from the model and at designated points within the test chamber. The primary instrument used for measuring electric fields was a Monroe Electronics, Inc. Model 171 electric fieldmeter. For remote electric field measurements from the model, the mainframe of the instrument and the electric field sensors were implemented within the model and operated by a rechargeable battery power supply. Readout from the instrument was accomplished through a multichannel fiber optic data link coupled to the output of the fieldmeter instrument.

Charge density measurements on the charged mist and fog within the test chamber were made with a momentarily sampling charge density meter, designed in-house and originally used for shiptank studies conducted for the U.S. Maritime Administration [7]. Making remote space charge measurements from the model required the design of a pneumatically-operated valving mechanism which was also implemented within the model. The output of the sampling valve mechanism was connected through a Nylobrade hose attached to the model. The construction of the on-board sampling valves together with the electric field instrumentation can be seen in Figures 14 and 15, which are more fully described in the following section.

#### MODEL CONSTRUCTION

The spherical model was designed as two hemispherical shells bolted together at the equator. Fiberglass material was used in the construction. A conductive coating was applied to the surface. Three sets of electric field and charge density sensors were implemented around the equator with companion sensors at the north and south poles. The completed spherical model is shown in Figure 12. Overall, the model had a diameter of 1.30 meters (4.28 feet).

Figure 13 shows the method used in suspending the model in the test chamber. A special harness comprised

of polyethylene rope and the insulators shown were required to adequately isolate the model from charge leakage effects that could otherwise occur from other types of harnesses. The three small insulators on the sphere carry the direct load of the internal instrumentation package as well as the weight of the model.

The instrumentation package implemented in the model is shown in Figures 14 and 15. Figure 16 shows the manner in which the hemispherical shells and instrumentation package are assembled. Figure 17 shows the fully operational model with the charge density sampling hose, fiber optic cables, and polyethylene air hoses for actuating the sampling valves and sampling the space charge at various points around the model. The instrumentation package battery supply could-power the model for a good 10-hour period before recharging was necessary. Recharging could be accomplished in an overnight period with an appropriate battery charger connected to a plug mounted on the model.

#### **EXPERIMENTAL TESTS**

There were many experimental tests conducted that cannot fully be described within the scope of this paper; however, two series of experimental tests are described that clearly illustrate how the various electrostatic parameters are related and affect the voltage on the model. During the course of the experimental test efforts, it was determined that external electric fields on the order of ±100 V/m had very little effect on the test results. Laboratory tests with external electric fields are therefore not described in this paper. However, the natural electric field from the earth is a factor considered later in deriving the charge equilibrium conditions for full-scale helicopters. The nature of the tests to be described and the experimental data are first presented without mathematical interpretation. Data analysis is treated separately where empirical techniques are applied to show electric field trends very similar to the results obtained from the theoretical analysis.

FLOOR SENSOR TESTS — The floor sensor tests involved no electrostatic instrumentation on board the model. For this first series of tests, a single electric field sensor was implemented in the floor ground plane at the center of the chamber. Space charge was sampled from a wall port. The model was raised and lowered at the center of the chamber directly above the electric field sensor. The physical arrangement of this test setup is shown in Figure 18. To eliminate external electric fields, the roof and floor ground planes were shorted together. A highvoltage power supply was used to charge the model to a given potential. Excess surface charge imparted to the model in this manner was accomplished through a special charging probe which could be applied to the model surface and then quickly removed. The time constant of the sphere in this first test configuration was greater than two hours. Also, in addition to charging the sphere, a probe connected to ground was used to discharge the excess surface charge when required. Charging and discharging effects were observed under charge-filled and charge-free chamber conditions.

Two tests were conducted when the test chamber was free of space charge. The results of these tests are shown in Tables 1 and 2. The primary differences between these two tests were the charging voltages at which the two tests were conducted. These tests show that no nonlinear corona effects were present during the two tests. Also, the  $\rm E_f/V_s$  ratios in Tables 1 and 2 are comparable and within the expectations of repeatable test results and instrumentation errors.

The third test conducted was aimed at determining the effects of space charge upon the electric field sensor mounted in the floor. Negative space charge was circulated in the test chamber and the sphere was charged to the potentials used in Test \$2 (summarized in Table 2) for the various heights above the floor. During this test, the output of the electric field sensor was recorded on a strip chart. Electric field measurements were also made for the condition when the sphere was discharged to zero potential by momentarily shorting the sphere to ground. The data collected for this third test are shown in Table 3.

The results of these tests show that when the sphere is charged to a potential of +10 kV and suspended at a height of about 2.5 meters (8.2 feet), the electric field at the sensor is zero. At this point, the space charge effects exactly counterbalance the electric fields from the sphere due to excess surface charge. Also, when the sphere is grounded and there are no electric field lines emanating from the model, the presence of the sphere is completely masked by the space charge for heights greater than 2.44 meters (8.0 feet).

The true nature of the space charge effects can further be seen by comparing the electric field data given in Tables 2 and 3. As the sphere is lowered close to the floor sensor, electric fields from the charged sphere predominate over the space charge effects and, conversely, when the sphere is raised above 2.5 meters (8.2 feet), the space charge effects predominate. These data dramatically illustrate that the potential difference on the model is a function of both the space charge surrounding the sphere and the measured electric fields.

ON-BOARD SENSOR MEASUREMENTS — For on-board electrostatic measurements, three electric field sensors were installed in the model at the north pole, equator and south pole. Space charge was sampled from a wall port and directly from the model in two different tests. The test chamber and model configuration for the case where space charge was sampled from a wall port are shown in Figure 19. The first test conducted determined the electric fields as a function of model height in a charge-free test chamber. The test results shown in Table 4 are for different charging potentials on the sphere. The electric field intensities listed under the data columns identified as E, E, and E, refer to the north pole, equator and south pole locations, respectively. In Table 5, the charging potential was held constant as the model height was varied. The results from these two tests indicate a wider variation in the electric fields at the south pole than at the equator or north pole. Also, it can be concluded from these two tests that the south pole sensor data is more significant in inferring the potential of the model.

MINOR MATERIAL

The data presented in Table 6 show the electric fields measured on the model when the test chamber was filled with space charge. In this test, the sphere was charged in the same manner as in Test #1 (summarized in Table 4). Like the floor sensor experiments, the electric fields on the model were altered considerably by the presence of the surrounding space charge.

Several trends are evident in the electric field data as a result of the space charge surrounding the model: (1) As the sphere is lowered from the midpoint in the test chamber, the distance between the north pole and the roof increases, providing volumetric increases in the amount of space charge affecting the electric field sensor at the north pole. As the space charge effects tend to increase the electric fields at the north pole with changes in reduced height, there is also an overall decrease in the electric fields observed due to less surface charge since the charging voltage is reduced; therefore, an increase in one field component and a decrease in the other field component result in a slight overall net decrease in the electric fields measured at the north pole; (2) The electric fields measured at the equator decrease as the sphere is lowered. Large increases in the electric fields at the equator would not be expected from the space charge alone since the distance between the equator sensor and the wall is constant and does not affect the volumetric amount of space charge influencing the sensor; therefore, any changes in the electric field at the equator would be due almost entirely to changes in the excess surface charge on the sphere; (3) Electric fields measured at the south pole decrease as the model is lowered because both space charge and excess surface charge effects are reduced. The space charge effects are reduced with decreasing height since there is less volumetric space charge between the south pole and floor to affect the sensor. The excess surface charge is reduced as the height is lowered because lower charging voltages were used in the tests; and (4) At the midpoint in the test chamber, the electric fields on all the sensors can be considered essentially the same since all the electrostatic parameters are uniformly distributed around the model.

Another observation can be made in comparison with the tests conducted with the floor sensor. In positive space charge had been used together with a positive charging potential on the sphere, zero electric field conditions would have been measured at the south pole at some point where the space charge and excess surface charge effects were equal and opposite.

The data trends shown in Table 6 were also observed again for the case where the full on-board measurement capabilities of the model were used. This included making electric field and space charge measurements directly from the model. Table 7 shows the results of this test. Representative space charge measurements were made at the equator of the model.

## **EMPIRICAL ANALYSIS**

The tests described resulted in discrete data consisting of electrostatic measurements taken at specific heights above the ground plane under varying reference voltages and charge densities. The charging voltages were varied so that the magnitudes of the electric fields were within the measurement range of the electric fieldmeter. The charge densities varied due to the nature of the process used for generating the space charge. In spite of the variations in the electrostatic parameters during the tests, the test data reflect certain trends which can be normalized for general comparison purposes. Since it is obvious from the test data that only linear processes are involved in the interaction of the electrostatic parameters that determine the model potential, the laws of superposition may be applied to the laboratory test data so that the effects of the electrostatic parameters can be separated and independently analyzed.

In applying the laws of superposition to the laboratory test data, any reference point (whether it is on the sphere, in space around the model, the wall of the chamber, or the ground plane) will have a composite electric field intensity that is comprised of: (1) the external electric field, (2) the excess surface charge on the model, and (3) the space charge density of the surrounding medium. This general hypothesis accounts for the case when there can be an external electric field component, although the data presented in this paper only show the effects of surface and space charge. From the model studies, the effects of the external electric field were trivial and are neglected in the empirical analysis. Furthermore, each of the electric field components has a geometric coefficient that varies as a function of the model height. Using computer techniques, the discrete test data can be analyzed to obtain interpolation formulas for the geometric coefficients associated with the surface charge on the model and the surrounding space charge. With computed geometric functions, the empirical analysis results in a family of graphical displays showing the electric fields at the point of reference as a function of model height, voltage and surrounding space charge density.

FLOOR SENSOR — Since the space charge density, the model potential, and the external electric field all produce linear independent effects at the floor sensor, the electric field at the ground plane sensor can be expressed in a general form as

$$E_1 = E_1 + E_2 + E_3 \text{ volts/meter}$$
 (28)

where:

- $E_1 = g_0 E_0$  is the electric field component of the externally applied field; (29)
- $E_2 = -g_1V_4$  is the electric field component caused by the potential on the model surface; (30)
- E<sub>3</sub> = -g<sub>2</sub>o is the electric field component caused by the space charge density surrounding the model; (31)
- $g_0$  = dimensionless geometric coefficient;
- 8<sub>1</sub> = geometric coefficient with units of 1/meter;
- g<sub>2</sub> = geometric coefficient with units of volt-meters<sup>2</sup> per coulomb (Vm<sup>2</sup>/C);

E<sub>0</sub> = the positive external electric field in volts/meter:

V. = the model potential voltage in volts; and

ρ = the space charge density of the surrounding medium in coulombs/m³.

The electric field components given by Equation (28) are vector quantities; however, the electric field sensor can only measure the field component normal to the sensor aperture. Since the sensors are always flushmounted at the measurement surfaces, the equations in this analysis are given in scalar notation.

From Equations (28)-(31), the electric field at the ground plane can be expressed as

$$E_t = g_0 E_0 - g_1 V_1 - g_2 \rho. \tag{32}$$

By neglecting the external electric field component, the sphere potential,  $V_a$ , may be expressed as

$$V_a = -G_1 E_f - G_{2\rho} \text{ volts}$$
 (33)

where:

G<sub>1</sub> = 1/g<sub>1</sub>, a geometric coefficient with units of meters; and

 $G_2 = g_2/g_1$ , a geometric coefficient with units of volt-meters<sup>3</sup> per coulomb (Vm<sup>3</sup>/C).

Thus, from Equation (33), the sphere potential can be calculated by knowing the geometric coefficients  $G_1$  and  $G_2$ , the electric field intensity at the ground plane reference point, and the space charge density surrounding the model. With the form given by Equation (33), the geometric coefficients can be found by the defining relationships given below.

$$G_{i} = -\left[\frac{\mathbf{v}_{i}}{\mathbf{E}_{i}}\right]_{i=0} \tag{34}$$

$$G_2 = -\left[\frac{V_1 + G_1 E_f}{\rho}\right] \tag{35}$$

In determining the geometric coefficients given by Equations (34) and (35), tests must first be conducted in a charge-free test chamber. Under this condition, the sphere is charged to a known potential and the resultant electric fields at the ground plane are measured. Once  $G_1$  has been determined, then the test chamber is filled with a known space charge density and tests are repeated by charging the sphere to a known potential as the electric field intensity is measured at the ground plane. The  $V_o$ ,  $E_f$  and  $\rho$  quantities, together with  $G_1$ , can then be used to calculate the  $G_2$  geometric coefficient.

Once  $G_1$  and  $G_2$  have been derived for various sphere heights, H, then it is possible to calculate the sphere potential for any given electric field and space charge density using Equation (33). From the test data

shown in Tables 1 and 2, the  $G_1$  coefficient was derived by an approximate polynomial series expansion. This function is shown graphically in Figure 20.

The  $G_2$  geometric coefficient for the ground plane configuration was determined from data contained in Table 3. This analysis involved calculations using Equation (35) and the values derived for  $G_1$  shown in Figure 20. A computer analysis of calculated data points for the raw  $G_2$  data showed that a four-term polynomial curve was the best fit. Figure 21 shows a graphical plot of the  $G_2$  function.

From Equation (33), the electric field sensor mounted in the ground plane will have an output given by

$$E_t = -\left[\frac{V_1 + G_2\rho}{G_1}\right] \text{ volta/meter.}$$
 (36)

OF

The electric fields at the reference floor sensor are shown in Figures 22-25 for constant charging voltages of 0, +1, +5 and +10 kV. For each voltage, the space charge density was varied in step values of +50, +30, +10, 0, -10, -30 and -50 nC/m³. Another family of curves could have been plotted for negative sphere potentials. However, as can be seen by the nature of Equation (36), negative sphere potentials would have resulted in curves of the same general shape, but skewed into the positive right half of the electric field plane.

ON-BOARD SENSOR — The measured field strength at the south pole was more sensitive to height variations than data from the sensors at the equator or north pole; therefore, the south pole was selected as the reference point for performing an empirical analysis of the data collected in the on-board instrumentation tests. In the empirical analysis that follows for the south pole reference point, the nomenclature for defining the geometric coefficients is similar to that used for the floor sensor case; however, the characteristics of the derived geometric coefficients are completely different.

The electric field, E, at the south pole can be expressed in a general form as the sum of three field components.

$$E_1 = E_1 + E_2 + E_3 \text{ volts/meter}$$
 (37)

where

 $E_1 = g_0 E_0$  is the electric field component produced by the externally applied field; (38)

 $B_2 = g_1 V_1$  is the electric field component produced by staface charge on the model staface; (39)

 $E_3 = g_{20}$  is the electric field component produced by the space charge surrounding the model; (40)

go = dimensionless geometric coefficient:

g<sub>1</sub> = geometric coefficient with units of 1/meter;

g<sub>2</sub> = geometric coefficient with units of volt-meters<sup>2</sup> per coulomb (Vm<sup>2</sup>/C); E<sub>0</sub> = the positive external electric field in volts/meter;

V. = the model potential in volts; and

 $\rho$  = the space charge density of the surrounding medium in coulombs/m<sup>3</sup>.

In terms of the external electric field, model potential, and the space charge, the electric field at the south pole can be expressed as

$$E_a = -g_0 E_0 + g_1 V_a - g_2 \rho \text{ volts/m-ker.}$$
 (41)

If the external electric field component is neglected, the sphere potential, V<sub>s</sub>, at the south pole is

$$V_{a} = G_{1}E_{a} + G_{2}\rho \text{ volts}$$
 (42)

where:

G<sub>1</sub> = 1/g<sub>1</sub>, a geometric coefficient with units of meters; and

 $G_2 = g_2/g_1$ , a geometric coefficient with units of volt-meters<sup>3</sup> per coulomb ( $V \omega^3/C$ ).

From this relationship, the sphere potential can be inferred by measuring the electric fields at the south pole and the surrounding space charge density once the geometric coefficients,  $G_1$  and  $G_2$ , have been determined. The  $G_1$  and  $G_2$  geometric coefficients can be determined from the expressions shown below.

$$G_1 = -\left[\frac{V_i}{E_i}\right]_{i=0} \tag{43}$$

$$G_2 = -\left[\frac{V_1 - G_1 E_1}{a}\right] \tag{44}$$

To determine  $G_1$ , charging tests are first conducted in a charge-free test chamber. The ratio of the charging voltage to the observed electric field is  $G_1$ . With the  $G_1$  coefficient determined, charging tests are again performed in the presence of space charge in which  $V_i$ ,  $E_i$  and  $\rho$  are known as required for the  $G_2$  calculation defined by Equation (44).

Two charging tests were conducted on the sphere in a charge-free test chamber to obtain data required for the G<sub>1</sub> calculations. The results of these tests are listed in Tables 4 and 5. In the first test the charging potential was varied, while in the second test the voltage was held constant at 1.5 kV. The results of these two tests were averaged together and analyzed for the best curve-fit as shown in Figure 26.

The  $G_2$  geometric coefficient was derived from the data listed in Tables 6 and 7. For Test 3 in Table 6, space charge measurements were made by sampling from a wall fixture. In Test 4, shown by Table 7, space charge sampling was accomplished by the on-board model instrumentation designed for that purpose. The  $G_2$  function

derived from empirically averaged data is shown in Figure 27.

Measurements of the south pole electric field and the surrounding space charge density can be used to infer the model potential by the relationship given in Equation (42). This voltage expression assumes that the voltage on the model is an unknown and is thereby inferred by measurements of the electric field at the south pole and the surrounding space charge density. In the laboratory tests, the sphere voltage and space charge were always known. From Equation (42), the terms can be rearranged as shown below to reflect the electric fields expected at the south pole as a function of the sphere potential and the space charge density.

$$E_{a} = \left[\frac{V_{a} - G_{2}\rho}{G_{1}}\right] \text{ volts/meter.}$$
 (45)

This expression is useful in graphically illustrating the electrostatic phenomena existing at the south pole of the model. By holding the sphere potential, V<sub>s</sub>, constant and adjusting the space charge density in discrete steps, a family of curves for the electric field can be derived whereby the effects of space charge can be clearly illustrated. Equation (45) is plotted in Figures 28-31 for the same charging voltages and space charge densities used for the floor sensor case.

# COMPARISON OF EXPERIMENTAL AND THEORETICAL RESULTS

The analysis of the observed electrostatic test data provides empirical relations from which the electric field at the ground plane and on the sphere may be calculated as a function of height of the sphere above the ground plane. These field strengths may also be predicted based upon the theoretical analysis. Comparison of the experimental and theoretical results is of considerable value both in evaluating the present results and indicating directions for future work. Figures 32 and 33 show the electric field at the ground plane and at the south pole of the sphere, respectively, for the case of 10 kV applied to the sphere. While the general agreement of the theoretical and experimental results is very encouraging, the difference in magnitude of the space charge effect indicates the need for further investigation.

The theoretical predictions shown in these figures were computed from the infinite parallel plate with a finite space charge region model. It is of interest to note that the experimental values for the electric field at the ground plane approach the theoretical value for an infinite slab space charge region. During the tests, charge was found to accumulate on the walls of the test chamber. This wall effect, combined with the finite size of the roof and floor plates, may combine to produce the effect of a larger space charge than considered in the theoretical computations.

In contrast to the electric field at the ground plane, the measured field at the south pole of the sphere was found to be less than the predicted value. One explanation for this difference is probably nonuniformity in the charge distribution within the test chamber. Another probable influence on the measured data is that of instrumentation cables attached to the sphere during measurement. Figure 34 shows a comparison of measured and predicted capacitance of the sphere without space charge in the chamber. The lower values of measured capacitance are probably caused by the instrumentation cables.

#### HELICOPTER ELECTROSTATIC COEFFICIENTS

in the laboratory, under controlled electrostatic conditions, the potential of the spherical model relative to the ground was quantitatively sensed by measuring the composite electric field at a reference point and the surrounding space charge and applying the relevant mathematical calculations. This technique depends upon geometric coefficients that must be used in the voltage sensing equations. Although actual helicopter flight conditions present new problems of scale and complex geometry in comparison with the laboratory model tests, the techniques developed for the model tests can be extended and applied directly to helicopters.

From the empirical and theoretical analyses, the helicopter voltage sensing equation can be generalized as

$$V_{i} = G_{0}E_{0} + G_{1}E_{1} + G_{2}\rho \text{ volts}$$
 (46)

where:

V. = voltage on the helicopter;

En = the earth a natural electric field in volts/meter;

- E<sub>r</sub> = the electric field at a reference measurement point in volts/meter:
- ρ = space charge around the helicopter in coulombe/m³;
- G<sub>0</sub> = the geometric coefficient of the helicopter related to the external electric field in meters;
- G<sub>1</sub> = the geometric coefficient of the helicopter related to the composite electric field measurement at the reference point in meters; and
- G<sub>2</sub> = the geometric coefficient of the helicopter related to the space charge density in volts/meter<sup>3</sup> per coulomb (Vm<sup>3</sup>/C).

From the above expression, the geometric coefficients can be defined mathematically and determined experimentally from practical tests on a helicopter hovering above the ground in the presence of space charge under the influence of the earth's natural electric field. For helicopter testing,

$$G_1 = \frac{\Delta V_i}{\Delta E_r} \Big|_{\rho = \text{ constant}}^{E_0 = \text{ constant}}$$
 (47)

$$G_2 = -G_t \left[ \frac{\Delta E_r}{\Delta \rho} \right] \Big|_{E_0 = \text{constant}}^{V_0 = \text{constant}}$$
 (48)

$$G_0 = \frac{V_s - G_1 E_r - G_2 \rho}{E_0}$$
 (49)

To determine the G, coefficient, the space charge around the helicopter due to triboelectrification and the ionized engine exhaust gases will generally be constant for conditions that can be established for test purposes. With constant space charge conditions and a constant external field from the earth around the aircraft, the hovering helicopter can be charged to some given potential. This potential will result in related electric field measurements at any test point on the aircraft. Following this initial charging test, the helicopter can be charged again a second time to a different voltage which will result in a different electric field measurement at the reference point. Differences between the first and second sequences of measurements provide the difference quantities required in Equation (47). By repeating these charging tests over the range of heights typically used in hovering, the G, coefficient may be completely determined by using curve-fitting techniques to derive practical empirical relationships.

To determine  $G_2$ , a constant voltage is required on the aircraft as the space charge around the aircraft is varied. Variations in the space charge around the aircraft may be accomplished by implementing a space charge generator on board the aircraft or through some other means. Variations in space charge will cause associated variations to occur in electric field observations at the reference measurement test point on the aircraft. Differences in these parameters are the factors required in Equation (48) for calculating the  $G_2$  coefficient when the helicopter is maintained at a constant voltage; for example, by means of a high-voltage power supply on the ground, connected to the aircraft by a wire.

Once the  $G_1$  and  $G_2$  geometric coefficients are determined by best curve-fit empirical analytical relationships, the  $G_0$  coefficient can be found from Equation (49). For these tests, the external electric field component,  $E_0$ , would be measured on the ground by an electric field sensor some distance away from the helicopter. By knowing the earth's electric field and the  $G_1$  and  $G_2$  coefficients, the helicopter would be charged to a known voltage,  $V_s$ , as measurements are made to determine the composite electric field and space charge at the reference measurement point on the aircraft.

The description of the test procedures for determining the geometric coefficients that fully define the electrostatic voltage tensor expression in Equation (46) has been general in nature. There are two factors related to helicopter flight that must be considered in the test procedures before the final voltage expression can be used for making calculations. These include the effects on the geometric coefficients due to: (1) the length of the cargo hook, and (2) variations in the space charge region around the aircraft.

#### **ACTIVE DISCHARGER SYSTEM**

From the voltage sensing expression given by Equation (46), the requirements for electrostatic equilibrium can be defined. If an active discharger system senses the voltage on the aircraft and neutralizes charge buildup, then the aircraft potential, V<sub>s</sub>, must be zero. Then, under equilibrium conditions, the electric field at a reference point must be

$$E_r = -\left[\frac{G_0 E_0 + G_2 \rho}{G_1}\right] \text{ volts/meter.}$$
 (50)

If the discharger system detects an inequality or departure from the conditions required by Equation (50), there will be excess surface charge on the aircraft. This condition will represent an error signal in the control system which can be used to drive the off-flowing current from the discharger to reestablish a minimum error condition.

To accomplish this, an active helicopter discharger system will consist of: (1) the necessary electric field and space charge sensors, (2) an electrostatic discharger system capable of generating off-flowing countercurrent from the aircraft to the surrounding atmosphere at a magnitude at least as great as the on-flowing currents which charge the aircraft, (3) a microprocessor system control unit, and (4) an appropriate readout indicator. These system components would be integrated into a closed-loop control system that senses the electrostatic conditions on the aircraft and determines the necessary discharger operation to control excess charge buildup on the aircraft. The electrostatic conditions on the aircraft must be measured by multiple-point electric field sensors and space charge samplers. Multiple-point electric field sensors are required for resolving the magnitude of the earth's natural electric field component and for accurately characterizing the conditions around a large aircraft.

### CONCLUSIONS

- (1) The electric field measured at any reference point in the test chamber is the sum of three field components related to: (a) the applied external field, (b) the surface charge on the model, and (c) the surrounding space charge. Each of these can be separated by linear superposition laws.
- (2) Separation of the electrostatic parameters in the empirical and analytical analyses of the model show that the geometric coefficients are functions of the test model height.
- (3) The potential on the model (helicopter) can be inferred by measuring the model height, H; the surrounding space charge density,  $\rho$ ; the external electric field component,  $E_0$ ; and the electric field,  $E_r$  at a reference location on the model once the companion geometric coefficients for each parameter have been empirically derived from experimental tests.
- (4) The potential of the spherical model can be determined from electrostatic measurements at the ground plane below the model, at the south pole of the

sphere, or at the end of a simulated cargo hook suspended from the south pole.

- (5) The effects of electric fields within the test chamber in the range of  $\pm 100$  V/m can be neglected without significantly affecting the voltage on the model. With helicopters hovering in flight, the external electric field from the earth can significantly affect the voltage on the helicopter, since the altitudes are generally greater than the test heights used in the model tests.
- (6) If the external electric field component is neglected, the spherical model potential at a given height can be inferred from a single electric field sensor on board the model and a space charge density measurement.
- (7) In general, since the external electric field from the earth cannot be neglected for helicopters hovering in flight, the magnitude of this field component must be measured for voltage computational purposes by the electric field instrumentation on board the aircraft.
- (8) The methodology used for determining the geometric coefficients for the model can be extended and applied directly to full-scale helicopters.
- (9) The empirical relationships developed for inferring the potential on the model were demonstrated to be accurate in representing the data trends of the controlled experimental tests performed in the electrostatic chamber.
- (10) Data from the on-board electric field sensors indicate that the south pole measurements contained more useful information related to height, surface charge, and voltage variations on the spherical model than data from the equator and north pole sensors.
- (11) The presence of surrounding space charge, even for relatively small magnitudes of charge density, will have significant effects upon on-board electric field readings used for voltage sensing instrumentation purposes.
- (12) Under some electrostatic conditions, the electric fields resulting from space charge surrounding the aircraft can cause apparent zero electric field measurements, even though the voltage on the model (aircraft) may be very high. Hence, the space charge density must be measured and used in the potential analysis.
- (13) From the voltage sensor expression derived in the empirical and theoretical analyses, the model (helicopter) voltage will be zero whenever the electric field condition  $E_r = -[G_0E_0 + G_2\rho]/G_1$  is satisfied at a given reference measurement point.
- (14) An automatic feedback control noncontacting electrostatic sensor for helicopters can be developed that would maintain the zero electrostatic field condition on the aircraft as defined below.
- (15) Additional design and development work will be required to produce instrumentation suitable for use with an active electrostatic discharger system in order to operate reliably in the helicopter flight environment and to provide faster response times.
- (16) In the model tests, the G<sub>2</sub> coefficient related to space charge density is well defined because of the physical constraints of the chamber facility. In full-scale helicopter flight conditions, however, the space charge envelope around the helicopter will be dynamic and difficult to define. These variations will affect the value of the

 $G_2$  coefficient in a statistical manner. In contrast to this, the  $G_0$  and  $G_1$  coefficients associated with the external field and the on-board electric field measured at the sensor reference point may be readily determined under full-scale helicopter flight conditions, since these coefficients are not dependent upon surrounding space charge effects. Even with some variations and uncertainty in the  $G_2$  coefficient, the helicopter can be discharged by an active discharger system to energy levels that are quite safe to ground personnel if practical measurements of average space charge density can be made and updated in a timely manner.

(17) The length of the cargo hook is an important parameter that must be considered in future model or full-scale helicopter tests. The suspended cable length will affect the values of the derived geometric coefficients.

(18) Model testing has been an effective means for conducting controlled laboratory experiments for studying the requirements for on-board helicopter voltage sensing techniques.

(19) The theoretical solution obtained for Poisson's equation for a sphere between two parallel plates can be modified to derive first-order approximations of the electrostatic geometric coefficients for actual helicopters by formulating and solving the problem as a sphere above a single image plane representing the earth. In the same manner, the solution techniques can be extended further to include a more complex geometry configuration, such as a prolate spheroid, which more closely resembles the helicopter shape of interest. For complex helicopter geometries, a closed solution of Poisson's equation becomes impractical. In these cases, the electrostatic voltage and field distributions can be found indirectly by computer numerical modeling using integral equation formulations.

#### REFERENCES

- 1. J.B. Solak and G.T. Wilson, "Technology Development Report--Results of Static Electricity Discharge System Tests (Active and Passive)--Heavy Lift Helicopter." Boeing Vertol Company, Report USAAMRDURT-74-22, May 1974.
- 2. W.R. Smythe, "Static and Dynamic Electricity." McGraw-Hill Book Company, Inc., New York and London, 1968.
- 3. P.M. Morse and H. Feshbach, "Methods of Theoretical Physics." McGraw-Hill Book Company, Inc., New York, 1953.
- 4. H.B. Dwight, "Tables of Integrals and Other Mathematical Data." 4th Edition. The Macmillan Company, New York, 1961.
- 5. O. Tranbarger, B.M. Duff and T.E. Owen, "Helicopter Model Studies for On-Board Electrostatic Sensors." Contract DAAK51-79-C-0060, USAAVRAD-COM TR-81-D-26, September 1981.
- 6. G.J. Butterworth, I.E. Pollard, B. Jaffrey, C.J. Mottershead and J.N. Chubb, "Studies of Tank Washing on *British Purpose* During Ballast Voyage from Isle of Grain to Cape of Good Hope, April 7th to May 5th, 1977." UKAEA Culham Laboratory, Abingdon, England, February 1978.

- 7. O. Tranbarger and T.E. Owen, "Bulk Carrier Operations Safety Enhancement Project." Phase III Final Report, Contract DO-A01-78-00-3080, Volume II—Full-Scale Measurements and Model Correlations, Maritime Administration Report No. MA-RD-920-980087, July 1980.
- 8. N. Felici and S. Larigaldie, "Experimental Study of a Static Discharger for Aircraft with Special Reference to Helicopters." *Journal of Electrostatics*, Vol. 9, pp. 59-70, 1980.
- 9. R. Muehleisen and H.J. Fischer, "Electric Charging of Helicopters." Report No. BMVG-FB-78-7, 1978.

Table 1
Test #1 - Charging Potentials and Floor Electric Fields in Charge-Free Test Chamber

Sphere	Charging	Electric Field	
Height	Potential	at Floor Sensor	E/V
H (m)	V <sub>s</sub> (kV)	E <sub>f</sub> (kV/m)	l
0.91	+ 2.5	-8.77	-3,51
1.07	+ 2,5	-5.18	-2.07
1.22	+ 5.0	-6.72	-1,34
1,52	+ 10.0	-7.36	-0.74
1.83	+20.0	-9.17	-0.40
2,13	+20.0	-6.36	-0,32
2,44	+ 20.0	-4.54	-0.23
2.74	+ 20,0	-3.38	-0.17
3.06	+ 20.0	-2,56	-0.13

Table 2
Test #2 - Charging Potentials and Floor Electric Fields in Charge-Free Test Chamber

Sphere Height H (m)	Charging Potential V <sub>a</sub> (kV)	Electric Field at Floor Sensor E <sub>(</sub> (kV/m)	E <sub>t</sub> /V
0.91	+ 2.5	- 9.15	-3.68
1.07	+ 6.0	-10.50	-2.10
1.22	+ 6.0	- 7.06	-1.41
1.62	+ 5.0	- 3.92	-0.78
1.83	+ 10.0	- 4.84	-0.48
2.13	+ 10.0	- 3.36	-0.34
2.44	+ 10.0	- 2.36	-0.24
2.74	+ 10.0	- 1,77	-0.18
3.06	+ 10.0	- 1.30	-0.13

Table 3
Test #3 - Charging Potentials and Floor Electric Fields in Charge-Filled Test Chamber

for  $V_a = V$ ;  $\rho \neq 0$ 

からの 教養の 一般の はまない かんきゅう でき

日本華を見て物に中島記の

Sphere	Space Charge	Charging	Electric Fleid
Height	Density	Potential	at Floor Sensor
H (m)	ρ(nC/m³)	V <sub>s</sub> (kV)	E, (kV/m)
0.91	-6.69_	+ 2.5	- 8.86
1.07	-7.48	+ 6.0	- 9.50
1.22	-6.60	+ 6.0	- 6.19
1.52	-7.06	+ 5,0	- 2.56
1.83	-7.46	+ 10.0	- 3.10
2,13	-7.36	+ 10,0	- 1.50
2.44	-7.17_	+ 10,0	- 0,10
2.74	-7.30	+ 10,0	+ 0.76
3.05	-7.60	+ 10.0	+ 1.30

for  $V_u = 0$ ;  $\rho \neq 0$ 

Sphere Height H (m)	Space Charge Density ρ (nC/m³)	Electric Field at Floor Sensor E <sub>t</sub> (kV/m)
0.91	-6.69	+0.08
1,07	-7.48	+0.21
1,22	6.80	+0.33
1,52	-7,06	+ 0.88
1,83	-7.45	+ 1,50
2.13	-7.36	+ 1.63
2,44	-7.17	+ 1.73
2.74	-7.30	+ 2,05
3.06	-7.60	+ 1.95

Table 4
Test #1 - Charging Potentials and Model Electric Fields in Charge-Free
Test Chamber

for  $V_a = V_0$ ;  $\rho = 0$ 

Sphere Height	Charging Potential	Electric Fields at Model Sensors (kV/m)			
H (m)	V, (kV)	E <sub>n</sub>	E,	E,	
0.91	+1.0	1.90	1,90	4,60	
1.07	+1.0	1.90	1.90	3,30	
1.22	+1.0	2.00	1.80	2,80	
1.52	+1.5	2.70	2.00	3.20	
1.83	+2.0	3.30	3.30	3.00	
2,13	+2.0	3.40	3,30	3.70	
2.44	+2.5	4.00	4.10	4,60	
2,74	+2.5	3.90	4.20	4.60	
3.06	+2.5	3.80	4.20	4.60	

Table 5
Test #2 - Charging Potentials and Model Electric Fields in Charge-Free Test Chamber

for  $V_a = 1.5 \text{ kV}$ ;  $\rho = 0$ 

Sphere Height	Charging Potential	Electric Fields at Model Sensors (kV/m)			
H (m)	V <sub>a</sub> (kV)	En	E	E,	
0.91	+1.503	2.36	2.78	5.62	
1.07	+1.492	2.28	2.69	4.02	
1.22	+1.498	2.27	2.57	3.41	
1,52	+1.500	2.25	2.50	2,82	
1.83	+1.496	2.21	2.40	2.61	
2.13	+1.520	2.25	2.39	2.51	
2.44	+1.514	2.29	2.34	2.53	
2.74	+1.513	2.28	2.33	2.51	
3.05	+1.513	2.31	2.32	2.56	

Table 6
Test #3 - Charging Potentials and Model Electric Fields in Charge-Filled Test Chamber

for  $V_a = V_0$ ;  $p \neq 0$ 

Sphere Height	Space Charge Dansity	Charging Potential			dal
H (m)	ρ (nC/m³)	V, (kV)	E	E,	E,
0.91	-7.33	+1.0	6.60	4.50	4.20
1.07	-7,29	+1.0	6.96	4.85	3.40
1.22	-8.45	+1.0	7.60	5.80	3.25
1.52	-8.18	+1.5	8.80	7.40	4.80
1.83	-7.08	+ 2.0	8.65	7.86	5.60
2.13	-7.14	+2.0	8.75	7.90	6.00
2.44	-7.81	+ 2.5	9.50	8.60	7.20
2.74	-7.63	+2.5	9.00	9.00	7.50
3.06	-7.49	+2.5	8.96	9.06	7.80

Table 7
Test #4 - Measured Sectric Fields on Sphere in Charge-Filled Test Chamber Using Fully Instrumented Model

 $V_a = V_0; \rho \neq 0$ 

Sphere Height	Space Charge Charging Density Potential		Electric Fields at Model Sensors (kV/m)		
H (m)	$\rho_{\rm e}$ (nC/m <sup>3</sup> )	V, (kV)	E <sub>0</sub>	Ε,	E
0.91	-10.04	+1.0	8,20	4,90	4.40
1.07	-10.49	+1.0	8.70	4.96	3.30
1.22	- 9.38	+1.0	7.05	4.75	3.10
1,52	- 8.76	+1.5	8,10	5.80	4,30
1.83	- 9.64	+2.0	9.45	7.30	5.80
2.13	- 3.24	+2.0	8.80	7.00	6.00
2,44	- 8,69	+ 2.5	8.86	7.55	6.70
2.74	- 9.68	+ 2.5	9.00	7.80	7.10
3,05	-10.61	+ 2.5	8.80	8.20	7.40

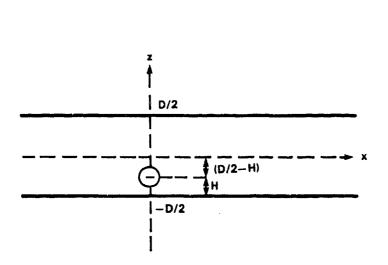


Fig. 1 - Geometry for sphere between parallel plates

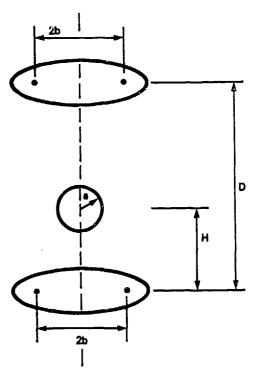


Fig. 2 - Geometry for sphere between oblate spheroids

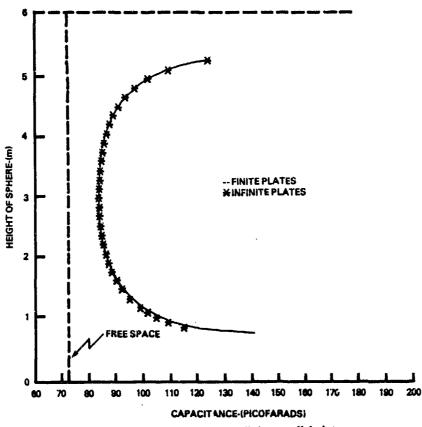


Fig. 3 - Capacitance of sphere - finite parallel plates

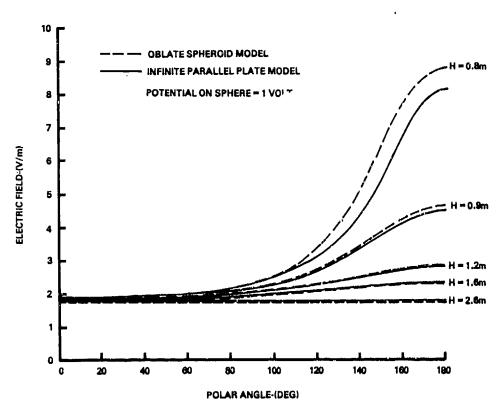


Fig. 4 - Electric field at the surface of the sphere

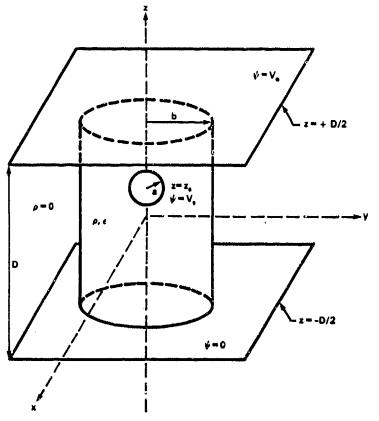


Fig. 5 - Sphere embedded in cylindrical space charge region between infinite parallel plates

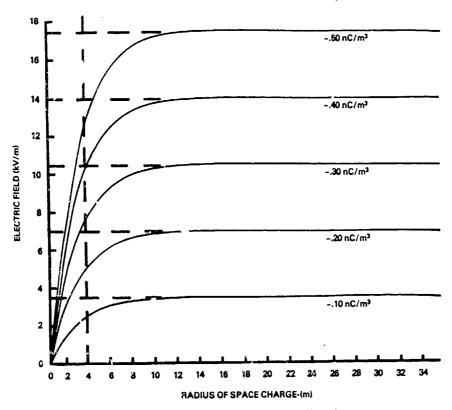
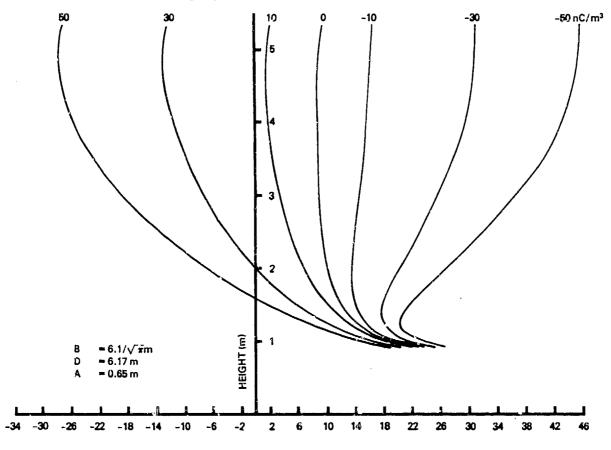


Fig. 6 - Electric field at lower plate vs radius of space charge region



SOUTH POLE ELECTRIC FIELD (kV/m)

Fig. 7 - Electric field at the south pole vs space charge density and height of sphere— $V_a = 5 \text{ kV}$ 

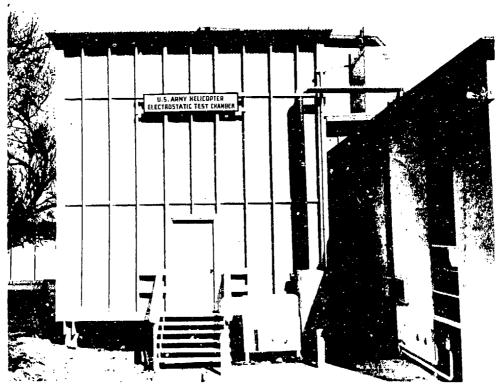


Fig. 8 - Front view of electrostatic test chamber

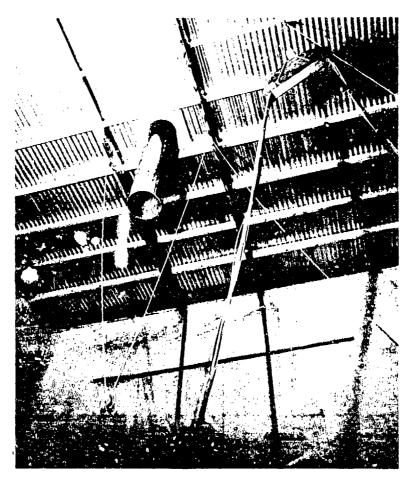


Fig. 9 - Roof ground plane, charge injection pipe, model hoist, and fiber optic bundle

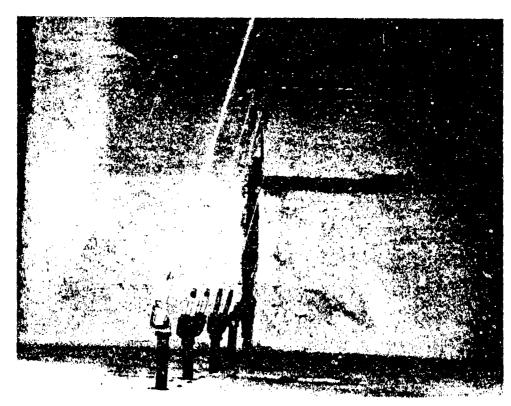


Fig. 10 - Water spray nozzles and corona discharge needle

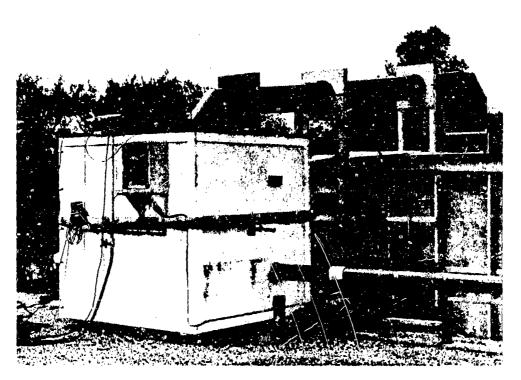


Fig. 11 - Charge generating antechamber



Fig. 12 - Completed spherical model

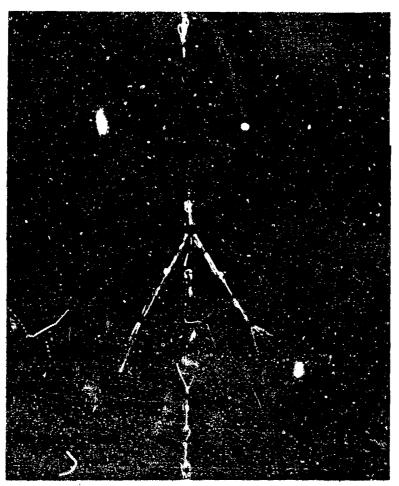


Fig. 13 - Suspension harness and insulators

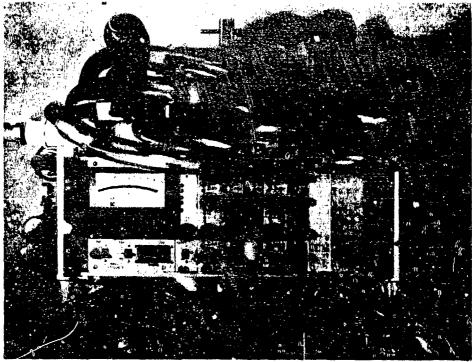


Fig. 14 - Front view of electric fieldmeter and space charge sampling valve assembly

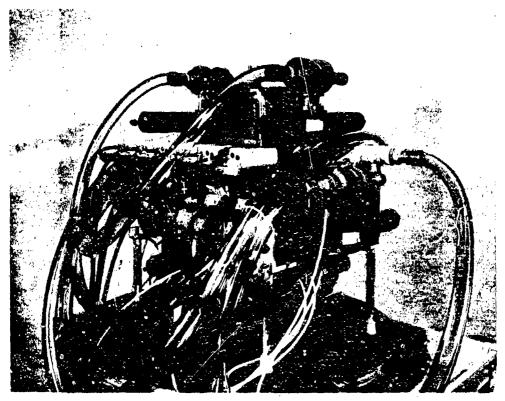


Fig. 15 - Rear view of instrumentation package showing fiber optic transmitters

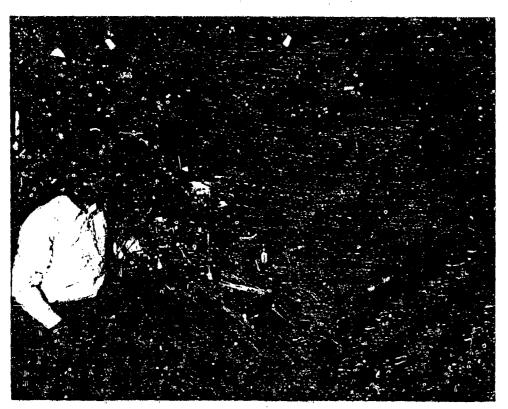


Fig. 16 - Instrumentation package being mounted in model

THE PROPERTY OF THE PROPERTY O

Fig. 17 - Fully operational model

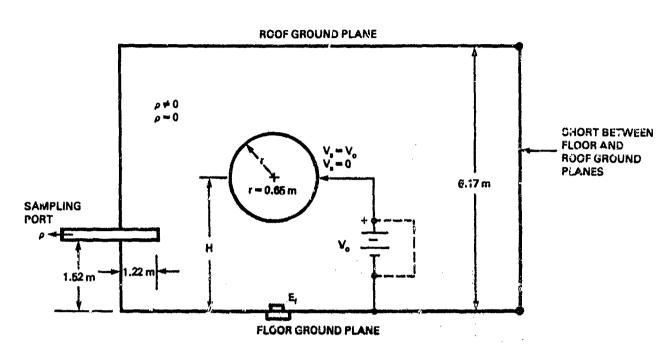


Fig. 18 - Test chamber configuration for floor sensor

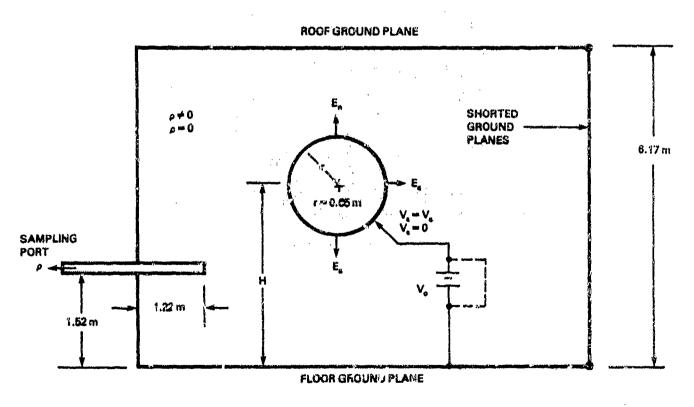


Fig. 19 - Test configuration for on-board electric field measurements

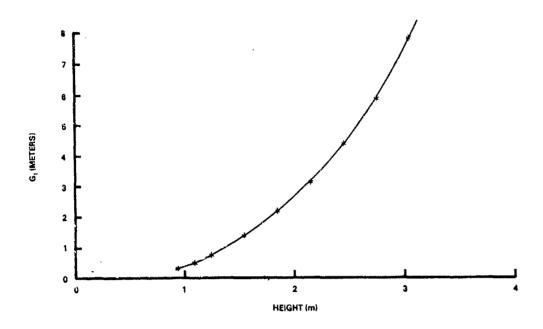


Fig. 20 -  $G_1$  geometric coefficient as a function of height for ground plane sensor

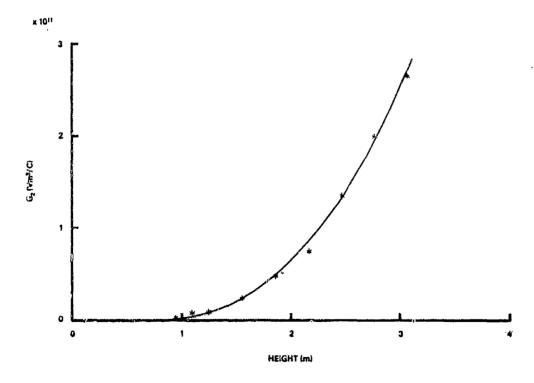


Fig. 21 -  $G_2$  geometric coefficient as a function of height for ground plane sensor

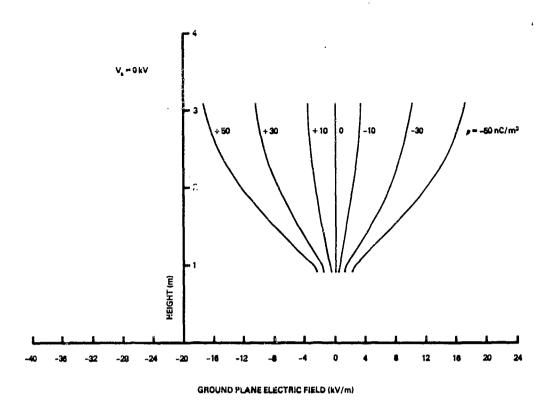


Fig 22 - Ground plane electric fields for sphere at zero potential

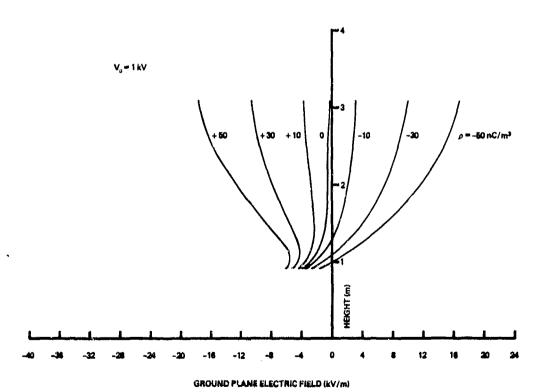


Fig 23 - Ground plane electric fields for sphere at  $+1~\mathrm{kV}$  potential

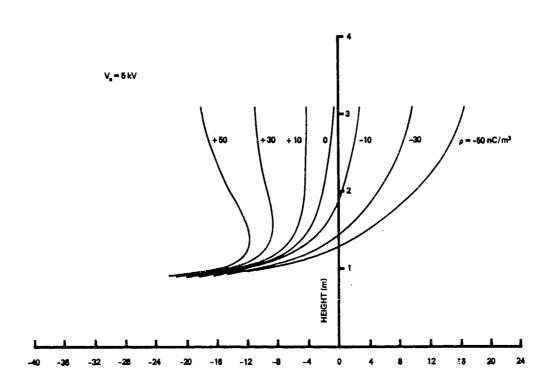


Fig 24 - Ground plane electric fields for sphere at +5 kV potential

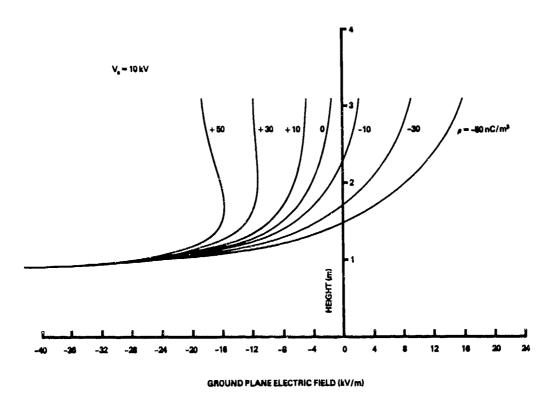


Fig 25 - Ground plane electric fields for sphere at +10 kV potential

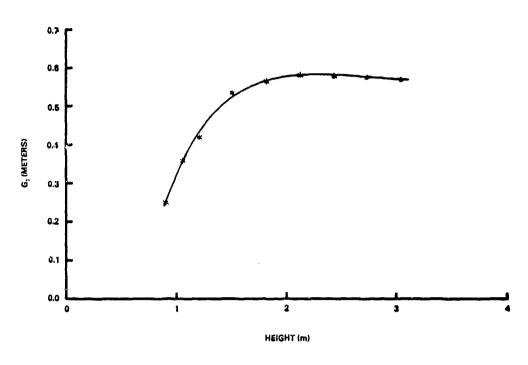


Fig 26 -  $G_1$  geometric coefficient as a function of height for south pole sensor

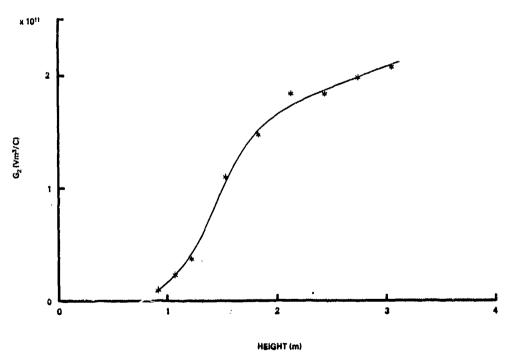


Fig 27 -  $G_2$  geometric coefficient as a function of height for south pole sensor .

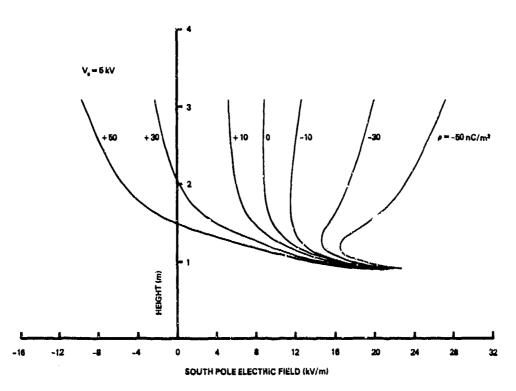


Fig 30 - South pole electric fields for sphere at +5 kV potential

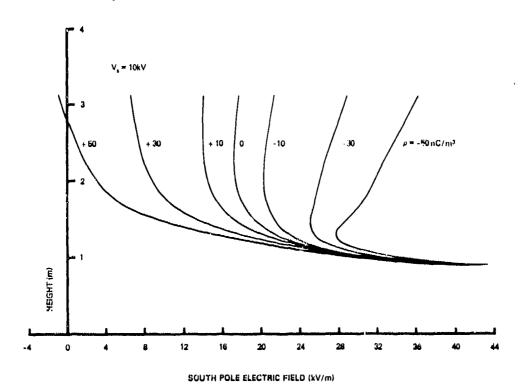


Fig 31 - South pole electric fields for sphere at  $\pm 10 \text{ kV}$  potential

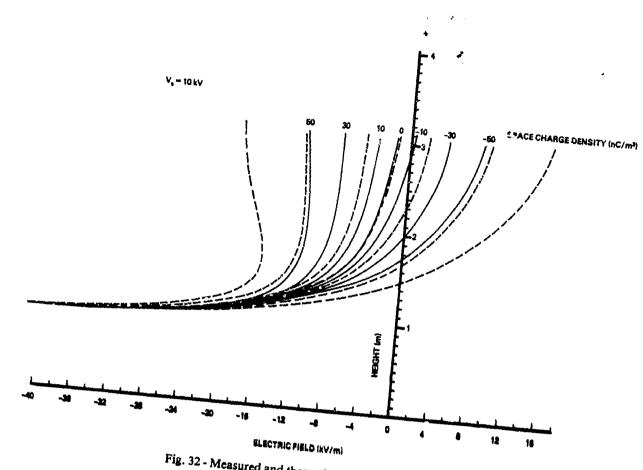


Fig. 32 - Measured and theoretical electric field at the ground plane— $V_s = 10 \text{ kV}$ 

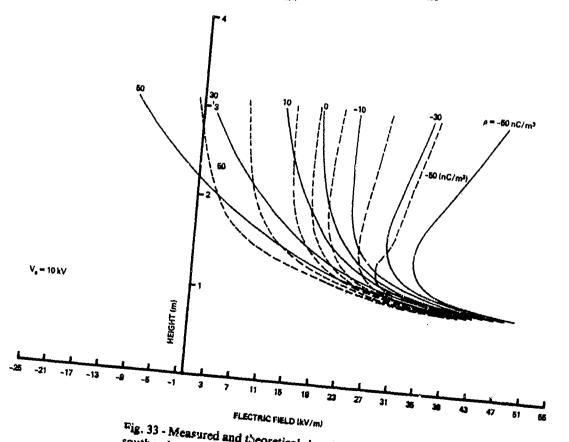


Fig. 33 - Measured and theoretical electric field at the south pole of the sphere— $V_c = 10 \text{ kV}$ 

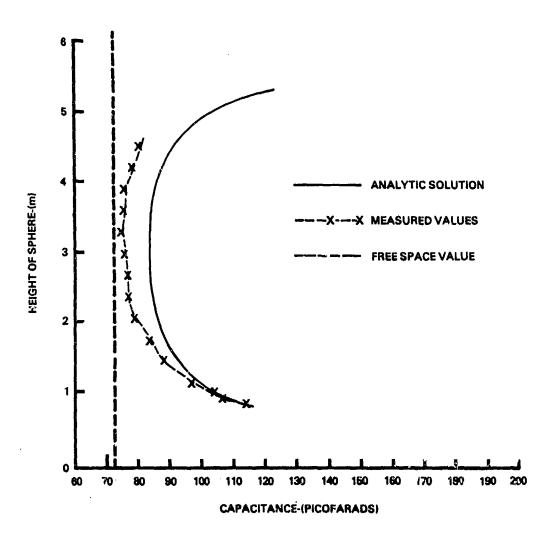


Fig. 34 - Capacitance of sphere between parallel plates—measured and theoretical values

it like

Electrostatic Charging Occuring in a Vortex Trailed from the Tip of a Lifting Surface

Henry P. Velkoff and John W. Dougherty

#### ABSTRACT

Because of the high electrostatic potentials built up on helicopters operating in dusty or dry snow environments, an investigation was undertaken to evaluate what contribution the vortex roll-up at the tip of a rotor blade could make to the rate of charging. If the vortex could generate charge separation and an internal electrical field, then impingement of the vortex with the other surfaces of the helicopter could lead to increased charging rates.

A program was undertaken to investigate the vortex geometry, particle distribution and electric field distribution in a trailing vortex shed from an airfoil tip placed in a dust laden flow. A differential airfoil, positioned in a subsonic wind tunnel, generated the trailing vortex. Dust conditions, typical of helicopter landing zone, were simulated by seeding the wind tunnel flow with P.V.C. plastic pellets, #3 sand, and #120 sand.

A vaned probe was used to measure the vortex geometry. A particle impact probe and a miniature field meter were used to map the particle distribution and electric field distribution across the trailing vortex. Vortex geometry particle distribution and electric field intensity were measured throughout the plane normal to the wind tunnel axis at several locations downstrem from the airfoil.

The particles in the trailing vortex create a quasi-steady electric field with contours of constant electric field similar in appearance to the particle distribution contours. The electric field strength was found to increase nearly linearly with radial distance from the vortex center within the field of measurement.

This paper was not available for incorporation into this book. Therefore, it will be published at a future date.

# AD P002188

DETECTION AND RANGING OF ELECTRIC CHARGED HELICOPTERS

H. Trinks\* and J. L. ter Haseborg\*\*

\*Technical University Hamburg-Harburg, Hamburg, Germany

\*\*German Federal Armed Forces University Hamburg, Hamburg, Germany

ABSTRACT

Helicopters are electrically charged during their flight. The electric charge generates an electric field in the helicopters vicinity which can be measured. By such electric field measurements, the detection and localization of Elying helicopters is possible in principle. Numerous systematical investigations have been performed in connection with different types of helicopters flying over ground-based electric field sensors. Supplementary electric field sensors were telemetric guided in the vicinity of hovering helicopters. The experimental results were compared with theoretical computations about electric field distributions of electric charged helicopters hovering pear trees and buildings.

HELICOPTERS DURING FREE FLIGHT are in a specific electrically charged condition. Numerous experimental and theoretical investigations have been performed to understand the charging and discharging processes in correction with aircraft and helicopters. For many years it has been known that an aircraft operating in an environment containing particulate material such as snow, ice crystals, rain and dust will become electrified. By this effect the potential of the aircraft is increased to a level beyond which corona discharges may occur.

The charging of helicopters gives on the one hand rise to unwanted disturbances. The high potential of helicopters and aircraft may for example lead to the winchman's endangering or to corons-generated interference in aircraft. Numerous reports and publications are known concerning the development of electrostatic discharge systems in connection with different types of helicopters - see e. q. (1,2).

On the other hand the electric charge on helicopters generates an electric field in the helicopters vicinity which can be measured. By such electric field measurements the detection and the localization of flying helicopters is possible in principle. In this connection it is interesting to know the distance up to which the electric field detection of helicopters may be possible even if the helicopter is bovering or flying in the vicinity of trees and buildings.

Concerning charged projectiles and aircraft it is already published how the electric field transported by the flying object provides information by which measuring the position and velo-

city is possible - see e. g. (3,4).

Numerous systematical experimental investigations have been performed in connection with different types of helicopters concerning the charging and the electric distribution in the helicopters vicinity. The experimental results were compared with theoretical computations. The computations deliver quantitative electric field distributions near electric charged helicopters and they take into account electric field disturbances caused by trees and electric charged clouds.

#### EXFERIMENTAL DEVICE

The investigations concerning the electric field in the vicinity of helicopters were conducted during undisturbed free flight, under the influence of external disturbance by tises and buildings and finally during hovering flight over sand, earth and meadows. The most important parameter describing the charging and discharging process is the value of the helicopter's charge. To measure the electric charge without touching the helicopter, special sensors were placed in the vicinity of the flight path of the helicopter. As shown in Fig. 1, the electric charge Q is generated on a sensor when a charge Q passes the sensor. There are two methods to measure the charge generated on the sensor:

i) The sensor is coupled to the input of a charge amplifier. Then the output voltage  $U_{\widehat{\Gamma}\widehat{A}}(t)$  of the charge amplifier is proport-

ional to the charge Q(t) generated on the sensor. 2) The voltage  $U_{R}(t)$  is proportional to the time derivative of Q(t).

Both signals  $U_{r,A}(t)$  and  $U_{r,C}(t)$  are represented in Fig. 1. The mighals were recorded by means of storage oscilloscopes, transient recorders, or magnetic tape units.

Additionally to the ground based sensors telematric guided electric field sensors installed on model aircraft were used to investigate the electric field disturbances in the vicinity of trees and buildings.

The investigations were performed in connection with three different types of nelicopters:

1) ALDUETTE, 1,2 - 1,6 t, v(max) = 203 Km/h

2) UH-1D, 2,3 - 4,3 t, v(max) = 224 km/h

3) CH-53, lo,4 - 19 t, v(max)= 315 km/h

In Fig. 2 these helicopters are shown during the measuring process flying over electric field sensors installed on a meadow and hovering near the measuring vehicle equipped with instrumentation as oscilloscopes, amplifiers and magnetic tape units.

#### EXPERIMENTAL RESULTS

In the following some typical measurement results are presented which were selected out of a variety of more than 2no individual tests.

In Fig. 3 signals are shown which are produced by a helicopter type UH-ID passing different sensors with constant velocity but different flight altitudes. It is recognizable that the main signal originated by the electric charge Q<sub>0</sub> on the helicopter according Fig. 1 is modulated by the rotating rotor blades. The signals are rather atrong and reproducable.

In Fig. 4 and 5 similar results are shown concerning helicopter type CH-53 and Alouette. The signals produced by CH-53 are much stronger than the signals originated by Alouette. If the CH-53 passes with rather low distance to the measurement equipment or to the earth corona

generated noise is recognizable.

Such experimental results in connection and in comparison with theoretical computations reparding different assumptions about the electric charge distribution on the helicopter's surface lead to a model conception about the electric charging of helicopters and about the electric field distribution in the helicopter's vicinity. The model conception derived for the helicopter UH-ID is shown in Fig. 6.

Outgoing from this model conception and outgoing from the measured electric field strength originated of charges helicopters an estimation is possible about the range of the helicopters detection. For this purpose theoretical computations and additional investigations are necessary about the electric field disturbances produced in the vininity of helicopters by trees and buildings.

#### THEORETICAL COMPUTATIONS

The flying or hovering helicopter is more

or less electrically charged and produces en electrical field. Besides the helicopter generated electric field however exists the rather strong atmospheric electric field which interacts with the helicopter and e.g. the trees on the earth. The atmospheric electric field is characterized by positively or negatively values up to more than loo v/m. In fig. 7 some typical and reclistic situations are shown in principle concerning hopering helicopters with different charge values partly in the vicinity of trees.

Numerous mathematical correlations could be derived between the static field distribution on the surface of the earth ground regarding different assumptions about the presence

of trees and charged helicopters.

In Fig. 8 some examples are shown concerning a charged Selicopter flying over the ground with two different trees influenced by the atmospheric electric field (5). The variation of the electric field strength cering the helicopter's passing is clearly recognizable.

In Fig. 9 an electric field sensor is telemetric guided passing an artificial charged mast and a tree in the influence of the atmospheric electric field. The electric signal measured by the flying sensor and registered by telemetric system is shown. Additionally theoretical computations were performed concerning the electric field strength which is registered by the flying sensor.

A comparison between experimental and theoretical results gives a rough understanding about the reality concerning the electric field distribution in the Micinity of electric energed helicopters and influenced by the Almosphalic electric field in the presence of trees.

The realized computer programme allows to plot in a three dimensional manner the electric field strength distribution assuming quite different situations concerning charged half—copters flying in the vicinity of trees and buildings. Further experimental and theoretical investigations are ongoing.

#### SUMMARY AND CONCLUSIONS

The experiments and theoretical investigations lead to a good understanding about the electric field strength and distribution in the flying helicopter's withnity. The experimental results show:

dependent on their size in the range of lo
As concerning small and in the range of lo
Isrge helicopters. The charge value is moutly
positively. Rainy and det weather leads to
relatively small charge values. The charge
distributed on the helicopters surface produces
pratter strong electric field in the helicopture vicinity which is measurable by simple
sensor electrodes. The electroutatic field in
modulated by the retating mainrotor bisdes
dependent of the characteristics of the helicopter construction. This effect in particularly
strong concerning the helicopter UH-1D equipped
with only one double mainrotor bisdes.

It is possible to detect helicopters flying in an environment without trees and buildings in a range of up to 200 m by electric field measurements. This wide range is ausifable particularly when utilizing the electric field modulation effect taking in account the constant rotation frequency of the mainrotor.

However in the presence of trees and buildings strong field disturbances occur originated by the atmospheric electric field. In such disturbed emwirronment the range to detect flying helicopters by electric field measurements is diminished down to some lo m.

The theoretical computations concerning electric field distributions in the environment with trees, buildings, charged aircraft or helicopters demonstrate the possibility to get numerous informations about the structure of this environment by simple electric field measuraments. This kind of Electric Field Detection And Ranging (EFDAR) will be inquired by further experimental and theoretical investigations.

#### PEFERENCES

- Lightning and Static Electricity Conference, 12-15 Day 1972
- J.E. Nanevicz, D.G. Rouglas "Electroctatic Cischarge System", SRI-Project 1657, Menlo Park, Nov 1972
- J.L. ter Macaboad, H. Trinks "Detection of Projectiles by Electric Field Measurements" IEEE AES-16, No. 6, 750-754, 1980
- H. Trinks, J.L. ter Hassborg "Application of Charging Effects Ranging of Aircraft", Int. Assospace Conf. Lightning and Static Electricity, Oxford, 23 - 25 March, 1982
- D. Freechke "Berechnung von Feldmassungen durch vorgegebene geerdete Konturen" Dipl.Arb. USBw-Hamburg 1982

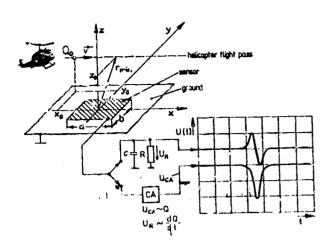


Fig. 1 - Electric signals  $U_{\rm R}(t)$  and  $U_{\rm L}(t)$  caused by an helicopter flying over the sensor

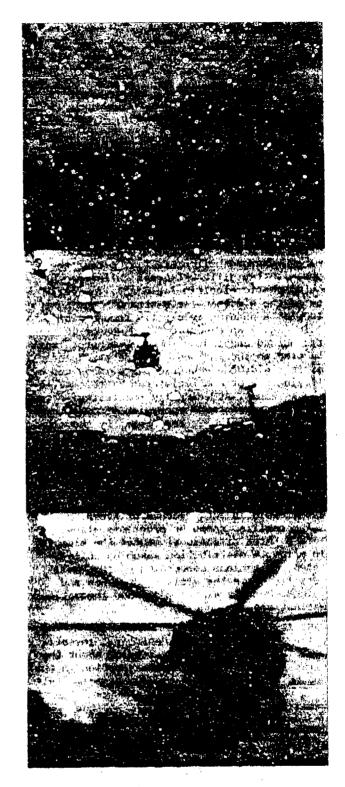
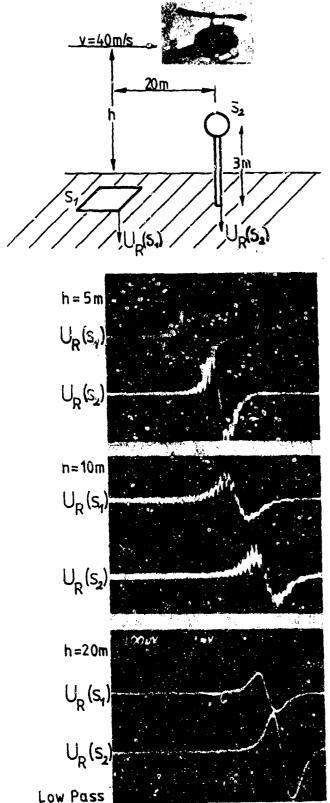


Fig. 2 - Different types of helicopters in flight over electric field sensors:

1. Alouette 2. UH - 1 D 3. CH - 53



大学 (大学 ) (

Low Pass

Fig. 3 - Helicopters UH - 1 D flying over different sensors 5 1 and 5 2

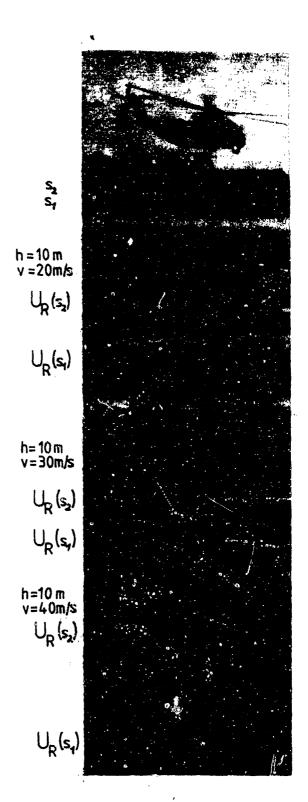


Fig. 4 - Helicopter CH  $\stackrel{\cdot}{=}$  53 flying over two sensors S l and S 2. The distance from S l to S 2 is 25 m

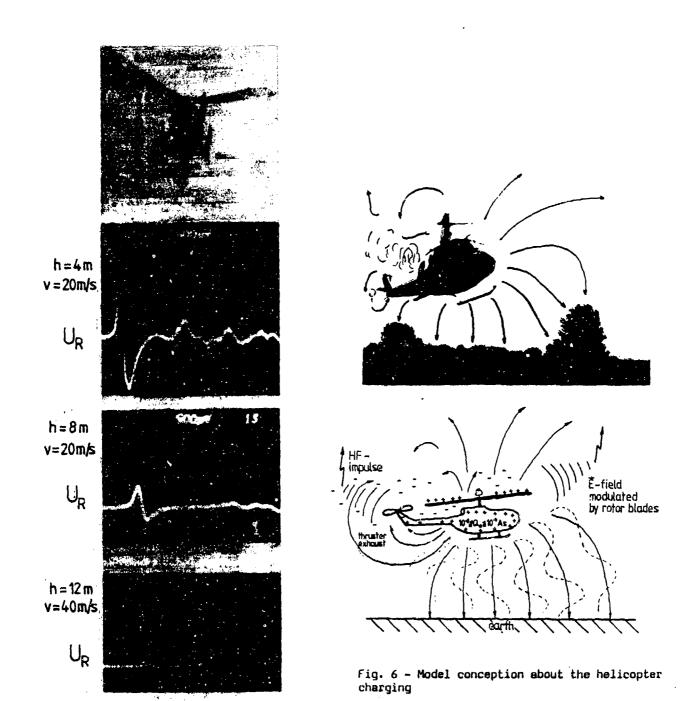


Fig. 5 - Helicopter Alouette flying over a sensor with different altitudes and velocities

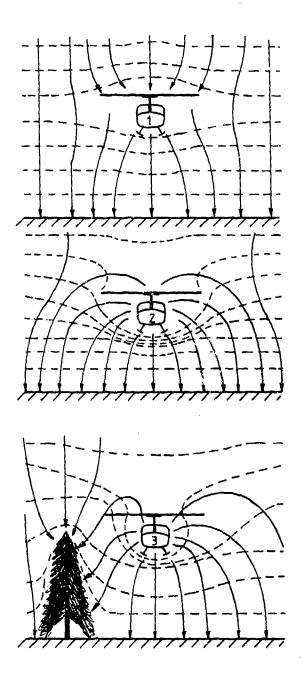


Fig. 7 - Electric field distributions in the vicinity of hovering helicopters under the influence of atmospheric positively electric fields l. Helicopter uncharged 2. Helicopter positively charged 3. Helicopter positively charged near a tree

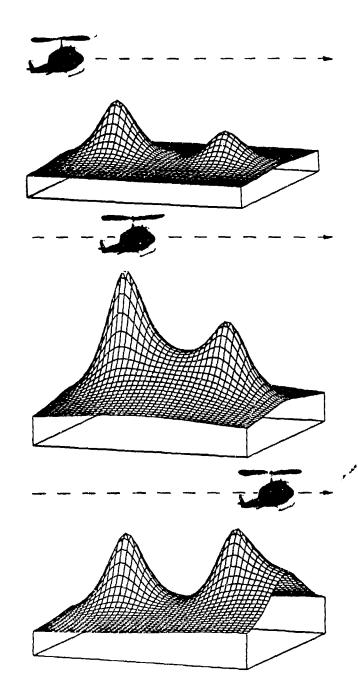


Fig. 8 - Computed plots concerning the electric field distribution generated by trees under the influence of the atmospheric electric field. A positively charged helicopter passes the trees

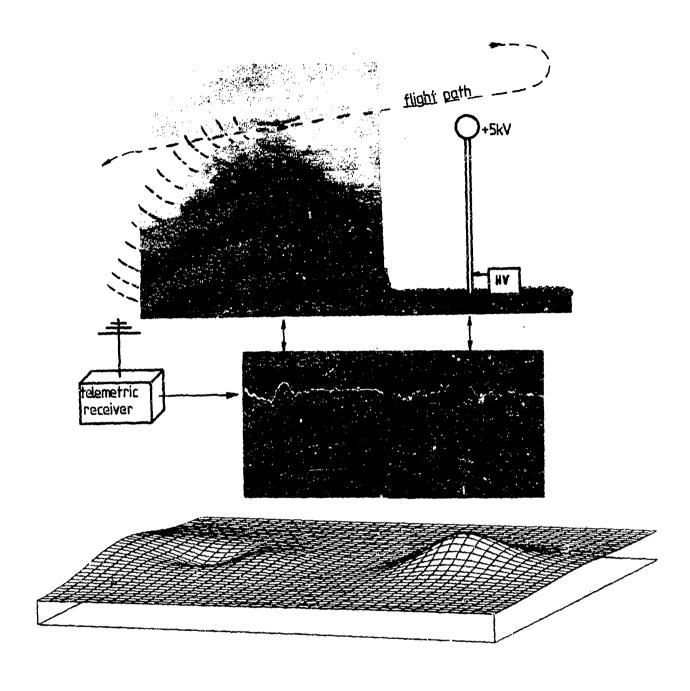


Fig. 9 - Experimental and theoretical results concerning the electric field distribution in the vicinity of trees under the influence of the atmospheric electric field



G. L. Weinstock McDonnell Aircraft Company, McDonnell Douglas Corporation

ABSTRACT

Lightning protection for fighter aircraft is presently based on the requirements of MIL-B-5087 and refined by the recently issued MIL-STD-1757. These documents specify current and energy levels sufficient to cover greater than 99 percent of the cloud-to-ground strikes. These levels are applied to aircraft according to lightning strike zones established by attach point analysis and test. The application of these specifications to aircraft is made without consideration of mission, probability of strike occurrence, or penalties associated with protective designs. Pata from recent in-flight test programs, a tabulation of aircraft strike rate per aircraft type, and an examination of strike damage records, all show that the requirements may be too stringent and that a revision to the method of applying lightning specifications to aircraft may be justified.

In conventional and V/STOL high-technology fighter aircraft, weight has a direct effect upon performance, combat effectiveness, losses, and life-cycle cost. Unnecessarily stringent lightning protection requirements can add weight out of proportion to the lightning risk. A systematic method of tailoring requirements to risk or damage probability is desirable to provide a more balanced protective design. This paper presents a probabilistic approach to the design of aircraft lightning protection which may be a useful method of avoiding conventional worst case design penalties.

THE PURPOSE OF THIS PAPER is to present a new approach to lightning protection for tactical military aircraft based upon realistic probabilities of strike parameters and damage.

In recent years, there has been an increased emphasis in providing lightning protection for tactical aircraft. New specifications of the lightning environment have been generated and some old specifications have been provided with expanded interpretations. These new lightning descriptions have generally been based upon compilations of cloudto-ground strikes gathered by Stanford Research Institute under contract to McDonnell Douglas Astronautics and published in 1972[1]. Data on frequency of strikes to aircraft has been based primarily upon commercial airline experience. Recent information and an examination of old data strongly suggests that for tactical military aircraft, the lightning specification description, the current amplitudes, and the frequency of air strikes are overly severe.

#### BACKGROUND

Based upon the in-service records of the U.S. Navy on lightning strikes to aircraft[2], the actual strike frequency is lower by more than a factor of 10 than that used for design of lightning protection for recent aircraft.

For example, the strike rate for fighter/ attack type aircraft was loss than one strike per 100,000 flight hours whereas, the rate used as a specification for protection design is on the order of one strike per 5,000 flight hours. This data clearly implies that the strike rate specification is overly severe.

#### APPROACH

A more quantitative definition of the "correct" specification can be made by applying statistical methods to the inflight strike data. Of primary interest is a definition of the probability distribution for strike frequency (i.e. strikes/flight hour) versus hours of flight. Alternatively, a definition of the average strike frequency, in terms of expected value and range, is a convenient parameter which serves the same purpose. That is, for the true (but unknown) average strike frequency,  $F_A$ , we require an estimator  $\hat{F}_A$  such that by using available data, we may bound  $\hat{F}_{A,as}$   $F_L \leq \hat{F}_A \leq F_u$  where the probability that  $F_A$  lies outside the range (FL, Fi) is less than any desired percent. Performing an accurate estimate of FA from the limited data is made even more difficult because the "population distribution" is unknown. That is, the actual distribution of strike amplitude is unknown and cannot be assumed to be "normal". Thus, special steps must be taken to circumvent this

difficulty. One possibility is to utilize non-parametric methods which can be applied to the data without regard to the population distribution. This is easily done, however, non-parametric methods tend to be "inefficient" in that it takes relatively many data points to provide an accurate estimate (i.e., to define a narrow range for the estimated value).

An alternative to the non-parametric methods is to construct a family of distribution curves for strike frequency versus conditions, aircraft type, and flight scenario. A composite cumulative distribution curve may then be determined by using a best fit of the data. Standard techniques may then be applied to this "known" distribution to establish the range for F.

This procedure was used on the Navy data [2] to find a best fit chi-square distribution which was, in turn, used to find bounds for FA. The results are as follows. For an interval which covers 99% of all strikes (i.e., only 1% of the composite distribution curve lies outside the interval), the strike frequency,  $\hat{F}_A$  was found to lie in the range  $(9.1 \times 10^{-6}, 2.8 \times 10^{-5})$ ; this corresponds to a flight hours/ strike (i.e. 1/F,) range of (36,000, 110,000). Note that this result is based upon the use of all data "lumped together" and therefore does not distinguish strike frequency versus type of sircraft. From the data available, it was not possible to make separate quantitative estimates for each aircraft type, however, it is clear that the strike frequency for non-patrol aircraft is substantially less. For example, the 99% interval for fighter/attack sircraft appears to be in the range of  $(1.3 \times 10^{-5}, 5.9 \times 10^{-6})$  for  $F_A$  with a corresponding flight hours per strike of (77,000, 169,000). Regardless of what the exact frequency may be, this data clearly says that the values typically used (~5000 hrs/strike) are too

Similar statistical procedures can be applied to strike amplitude data to determine if the ground based lightning statistics are realistic. Comparisons can be made either for worst case (99th percentile) or for average strikes (or for both). The primary difficulty in this application is the shortage of good flight date. In order to develop reasonable precise estimates (i.e., upper and lower bounds on the estimator which are relatively close), there must be a fairly large data base. This is particularly necessary for the application of non-parametric techniques where the estimators are less efficient because no knowledge of the sample distribution is presumed. Since the only flight data used for this evaluation were from the programs conducted by NASA[3, 4, 5] and the Air Force, precise confidence bounds could not be established. However, for estimation purposes,

THE CASE OF THE PARTY OF THE PA

an approximate value of the average strike amplitude can be calculated from the inflight data. If this average is used in conjunction with a strike amplitude distribution curve whitch fits ground lightning statistics, then a range can be established to include 99% of all strikes. Using this procedure, a value of approximately 6.5 kiloamperes (KA) was found for the average measured strike and the 99% range for strike amplitude was found to be (1.2KA, 65KA).

Since the accuracy of this procedure cannot be determined, it is not clear what weight to give to the results. However, the strong implication is that the inclight lightning threat is less severe than the ground based threat traditionally used for the design of aircraft protection. This agrees with a recent examination of approximately 10 strikes to fighter aircraft radomes which indicated amplitudes of 10 kiloamperes or less.

The significance of these numbers becomes apparent when compared with the typical requirement for tactical aircraft of a 200KA strike every 5,000 flight hours.

The location of strike points on an air-craft should also be considered as a probability situation. A few primary attach points (nose, wing tips, tail trailing edge) are involved in most strikes. Lightning will attach to these primary points when approaching the aircraft from wide solid angles. However, some initial attach points such as inboard pylons may have an attach window of only a few degrees wide by a few degrees long. The probability of striking these locations with a direct attach strike is small. They can be assigned a probability figure based upon the solid angle involved.

An example would be an inboard pylon that tests have shown can only be an attach point from the underneath side of the wing. If, for this inboard pylon, if we assume a solid angle corresponding to a cone of angle  $\psi$  ( $\psi$  small), the ratio of solid angle to the total sphere is  $\frac{\pi\psi^2}{\sqrt{4\pi}}$ . For  $\psi$  = 2 degrees,

(.035 radians), the ratio is  $7.6 \times 10^{-5} \pm .0008$  or, assuming both attach and exit points, the ratio is 0.00016. If we now consider that there is 1 strike every 100,000 flight hours we expect one strike each 100,000 0.00016

= 625,000,000 flight hours to the inboard pylon.

Considering a 1,000 aircraft fleet and an average life of 10,000 flight hours per aircraft there is then only a 1.6% probability that any aircraft in the total fleet life will be struck on that pylon. If it is further assumed that a 20KA strike will cause no damage, then the probability of strike amplitude and strike rate can be combined to provide a probability of damage. From previous paragraphs it could be assumed

that there is about a 5% probability (95th percentile) that any strike would exceed 20KA. This yields a probability of damage to the inboard Pylon for all aircraft of 0.05 x  $0.016 = 8 \times 10^{-4}$ . In this manner, a probability of damage or risk factor could be defined for each aircraft type and mission. In many cases it may not be advisable to incur a lightning protection penalty for such a low probability of damage.

Swept stroke areas are also affected by improbable, but possible, attach points. By eliminating an attach point based upon a low strike probability, significant aircraft fuselage areas may be exempted from swept stroke protection. Using the inboard pylon as an example, the swept stroke area could include parts of wings and stabilator. This swept stroke area should first be examined to determine if lightning protection is required and if so, what penalties are incurred. Then, a probability of damage should be computed. A trade study of risk versus penalty should then be used to decide if protection is to be applied.

The extensive use of composite materials makes the application of overly stringent requirements exceedingly expensive both in dollars and in aircraft performance. For example, our tests have shown that a typical fastener in a carbon fiber composite (CFC) structure can carry a 25KA lightning strike without strength degradation and that a bonded lap joint can transfer approximately 2KA/in<sup>2</sup> also without damage. Thus, depending upon the magnitude of this lightning strike requirement, protection may or may not be required. Approximately 5 plies of CFC cloth (0.05 inches) is required to withstand the 100KA restrike component presently specified. Many aircraft panels, doors, and fuselage sections can meet all structural requirements if made from thinner material. However, using a thinner material and the 100 KA requirement requires the application of protective coatings or layers. These added layers, of course, present a penalty (cost, weight, maintenance) that tend to negate some of the CFC advantages. If the restrike component were 10KA instead of 100KA, much thinner CFC could be used without a lightning protection penalty.

#### OTHER INFLUENCES

A significant amount of testing to define lightning strike amplitudes has been done from mountain tops. This data represents a specific geographic area, altitude and terrain. Thus, another probability that may influence the strike amplitude data is variations in the geographical distribution of strikes. It is probable that data gathered from mountain tops located in mid-continent regions may not be valid for aircraft that generally fly over water, coastal regions or deserts. This is an area that warrants future study.

#### CONCLUSIONS

It is not unusual for commercial and military aircraft to have different specifications. Rather the converse is true and there are probably more environmental and safety specifications that are different than are the same. Thus, to arbitrarily place the same requirement on a fighter aircraft with built-in-tolerance for battle damage and a large commercial passenger aircraft does not seem prudent or cost effective.

The application for tactical military aircraft of more realistic values of lightning strikes and the use of probabilities of occurrence, magnitude and damage would remove many of the penalties associated with lightning protection with only a minimum increase in risk.

#### RECOMMENDATIONS

- It is recommended that efforts be increased to gather inflight strike data.
- o The Navy study of strike occurrence should be continued and broadened to include Air Force data and military aircraft data from other countries.
- o A lightning specification should be prepared for military aircraft. Different requirements should be available for various aircraft types and missions.

#### ACKNOWLEDGEMENT

The assistance of Dr. C. D. Skouby in the preparation of this paper is appreciated.

#### REFERENCES

- [1] Cianos, N. and Pierce, E.T., "A Ground Lightning Environment for Engineering Usage", Technical Report SRI Project 1834, 1972.
- [2] Lane, R.F., United States Navy Inservice Aircraft Lightning Strike and Damage Survey, NADC, 1981.
- [3] Pitts, F.L., Electromagnetic Measurement of Lightning Strikes to Aircraft, NASA Langley, 1981.
- [4] Fisher, B.D.; Keyser Jr., G.L.; Deal, P.L., "Lightning Attachment Patterns and Flight Conditions for Storm Hazards '80".
- [5] Private Conversations with Fisher, B.D. Relating to 1981 and 1982 NASA Flight Test Program Data.



## AD P002190

CORRELATION OF SPACE SHUTTLE AS-BUILT ATMOSPHERIC CAPABILITIES WITH KNOWN ATMOSPHERIC CONDITIONS
THAT PRODUCE LIGHTNING



Tim Fitzsimmons
McDonnell Douglas Technical Services Company, Incorporated, Houston, Texas

ABSTRACT

This paper summarizes the atmospheric flight capabilities of the Space Shuttle; these capabilities are limited by vehicle systems such as structures, tiles, and RF navigation. An analysis of the storm parameters, and the launch and landing profiles at Cape Kennedy (the primary landing site) are examined. Spark-over field data for the Shuttle are calculated and coupled with electric field strengths found in Florida thunderstorms studies. Probabilities for encountering lightning strikes of varying magnitudes are proposed based on the above information and lightning amplitude statistics.

#### I. INTRODUCTION

In 1982 in anticipation of making shielding modifications to the Space Shuttle, Rockwell International began testing various Shuttle Line Replacable Units, LRUS, as well as analyzing various circuits to determine their susceptibility to the electromagnetic effects of a lightning strike. A question was raised among NASA engineers as to whether or not the Shuttle would ever encounter lightning producing weather conditions. The questions were raised because flight rules, based on known vehicle capabilities, appeared to constrain the vehicle from flying in lightning producing weather. NASA contracted McDonnell Douglas to study the flight capabilities of the Shuttle and see if they would prevent the vehicle from encountering lightning; in essence could lightning be the sole weather cause of loss of the vehicle. If possible, the probability of this cause was to be determined. Enclosed is a summary of the results of this study.

#### II. VEHICLE LIMITATIONS

The Space Shuttle has four systems that are constrained by different atmospheric conditions. Rain is a weather constraint to both the Thermal Protection System (Tiles) and the RF Navigation Aid System. The section of RF Navigation Aid affected by rain is the Microwave Scanning Beam Landing System (MSBLS). The MSBLS is a RF Navigation Aid link between the Orbiter and a transmitting/receiving installation at the landing site. In clear weather, the three signals, tracking vehicle elevation, azimuth, and distance, are acquired approximately two and one half minutes prior to touchdown. With rainfall rates between 10-50 mm/hr such as in a thunderstorm, the signal acquisition times can be reduced to much less than one minute from touchdown; this can make landing hazardous.

A more serious problem is tile damage caused by rain during launch since tile damage or erosion can cause a failure during landing. Bell Aerospace has conducted tests revealing erosion at an artificial rain rate of 1/4 inch/hour for tiles at an incident angle of 20°, 410 mph velocity for one minute; the same results for tiles at an incident angle of 40°, 350 mph velocity for 30 seconds. NASA engineers mounted tiles on the speedbrake of a T-38 and an astronaut flew an Orbiter type flight path through "moderate storms." The speed was 300 kts and the exposure time was four minutes. These tiles were eroded to an average depth of 1/4 in. This type damage can cause tile failure during reentry and requires tile repair/replacement.

The other systems constrained by atmospheric conditions are Flight Control and Structures. Landing simulations run at Ames Research Center indicate that crosswinds greater than 30 knots can easily cause loss of control of the vehicle. A crosswind in excess of 20 knots would have caused the Columbia's wheel bearings to fail. Testing at cross-winds greater than this caused the wheel bearings to grind up and start a grease fire. This crosswind capability has been increased somewhat by using a new lubricant and bearing torque up procedure.

The structural atmospheric constraint relates to the G load the vehicle can withstand in making its final turn for the runway. This limit is 2.5 Gs; is not constrained by any flight system, and could be exceeded if wind speeds of approximately 100 knots or greater exist as a tail wind for the beginning of the turn. This turn is made in the altitude range of approximately ten to fifty thousand feet, dependent on absolute approach profile.

The above mentioned are weather conditions that might very well be accompanied by lightning. It is therefore noted that avoidance of these constraints reduces the chances of encountering lightning.

#### III. SPARK-OVER FIELD VALUES FOR THE SHUTTLE

The spark-over field, an electric field of sufficient magnitude to enable a lightning discharge, of the Shuttle/Orbiter is analyzed. The method used in the determination of the spark-over field is a theoretical-calculational one found in a H. W. Kasemir study (Ref. 1, pp 5-7). The study gives a series of formulas which can be used to calculate the spark-over field at the tip of a spheroid. The Shuttle and Orbiter are modeled as spheroids letting a be the long axis of the spheroid, b be the short axis and c be the eccentricity. The field concentration at the tip is given by

$$f = (1/e(1/e^2 - 1) (tanh^{-1}e - e))^{-1}$$

where

$$e = (a^2 - b^2)^{1/2} (a)^{-1}$$

The breakdown field in air at sea level is Eb = 3000 Kv/m (Ref. 2, pp. 41-2). To find the breakdown field with the vehicle present we divide Eb by f (the field concentration factor) or.

$$Fb = Eb/f$$

This value for Fb is valid, according to

Kasemir (Ref. 1, p. 1) only when corona discharge does not precede spark-over. Corona points occur wherever the surface of the vehicle has a small radius of curvature (sharp point). For the Shuttle and Orbiter there are many of these points (External Tank lightning rod, Solid Rocket Booster skirts, Orbiter wing tips, Orbiter vertical stabilizer, and Orbiter air data probe) that will cause corona discharge for any electric field orientation across the vehicle. According to experimental results (Ref. 1, p. 17) the value of the spark-over field must be reduced by approximately 33% when corona discharge precedes the lightning discharge. Hence

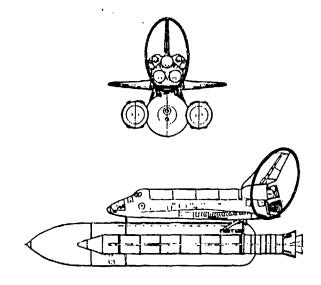
#### Fbc = .67 (Eb/f)

The final factor that must be considered in calculating the spark-over field is the altitude in question. The breakdown field varies inversely with altitude; this is due to the decreased air density (Ref. 1, pp. 6,7). Letting h stand for this fractional factor yields the final formula for the spark-over field value Fbc for a given vehicle spheroid.

#### Fbc = .67 (h) (Eb/f)

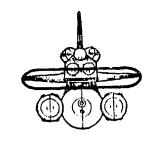
Figures 1 through 3 show the modeling of the Orbiter for various field orientations using different sizes of spheroids. The choice of size and shape of the spheroids is based upon a lightning attach point study by D. W. Clifford (Ref. 3) and upon visual inspection and fitting. Figure 1 corresponds to the top-belly direction for the electric field at the Orbiter. The attach points for this orientation (Ref. 3, p. 53; Ref. 1, Figures 7, 8) are the tip of the vertical stabilizer and the bottom of the fuselage. Figure 2 corresponds to the nose-tail field direction with one attach point being the Orbiter's nose or eyebrow (above cockpit windows) and the other being the vertical stabilizer. Figure 3 models the wing-wing field direction for the Orbiter with the wing tips being the attach points (Ref. 3, pp. 56, 57; Ref. 1. Figure 10).

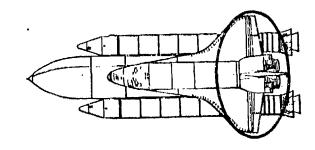
In Figures 1 and 2 one spheroid fits the geometry of both views of the Orbiter. However, in Figure 3 two different spheroids are necessary, one shown in Figure 3A and the other shown in 3B. In order to obtain one value for the spark-over field in this orientation, the long axes of the two spheroids were averaged as were the short axes (hence the designation  $\bar{a}$  and  $\bar{b}$ ) and then calculations proceeded using this averaged spheroid.



a = 7.46 m f = 5.42 b = 3.95 m Fb = 476.01 kV/m e = 0.8483158 Fbc = 318.03 kV/m

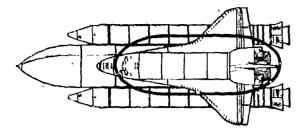
Fig. 1 - Top-belly electric field spheroid model

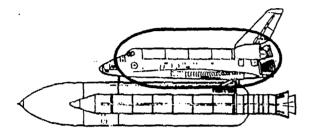




a = 12.19 m f =7.37 b = 4.89 m Fb = 350.07 kV/m e = 0.9159409 Fbc = 234.55 kV/m

Fig. 3 - Wing-wing electric field spheroid model





a = 17.54 m b = 7.02 m e = 0.9164156

f = 7.39 Fb = 349.12 kV/m Fbc = 233.91 kV/m

Fig. 2 - Nose-tail electric field spheroid model

Heinz W. Kasemir conducted experiments (Ref. 1) to determine the spark-over field for various Shuttle/Orbiter configurations. This was done by subjecting models to increasing electric field values until spark-over occured. As mentioned earlier, these tests were conducted at 1.6 Km altitude. Spark-over field values, adjusted to a 1.6 Km altitude, are calculated and appear in Figures 1-3. Table 1 compares these values to Kasemir's experimental values; the correlation is high. This calculational method is accepted as the means for calculating spark-over field values.

### IV. ELECTRIC FIELD AND LIGHTNING AMPLITUDE - VALUES

The spark-over field must exceed the surrounding electric field potential for a discharge to occur. In thunderstorms these charged fields abound (Ref. 4, p. 26; Ref. 5); the probability of encountering a field greater than the spark-over field yields the maximum probability of incurring a strike. This kind of electric field probability data is found in three sources: "JSC Thunderstorms, Experiment Results" by the Johnson Spaceflight Center Program Operations Office, "Lightning Trigger Field of the Orbiter" by Heinz Kasemir, and "Atmospheric Electricity Hazards Analytical Model Development and Application: Volume I" by Martin Uman and E. Philip Krider. The JSC data was taken from 35

Florida thunderstorms all of which were one of the following four types: developing anvil, mature anvil, dissipating anvil, or storm system. For each storm, the maximum electric field was recorded along with the altitude range flown within the storm. The average altitude at which the measurements were recorded was 10.5 km. Kasemir's data also indicates maximum electric fields within thunderstorms, but the only altitude data given is that the anvil cloud tops were typically at 28,000 feet in altitude. Uman and Krider give typical and maximum electric field values measured in thunderstorms for 7 different studies; these have no accompanying altitude data. The cumulative probability distribution functions of the data from the first two studies are found. There are three sets of data points; the Kasemir study has one set of data for positive gradients as well as one for negative gradients. These three distributions are found by fitting a line to the data points. Tables 2, 3, and 4 show the results of linear regressions performed on these three sets of points. Figures 4, 5 and 6 show graphs of the data points with the regression lines from Tables 2, 3, and 4 respectively superimposed onto them. As seen from Tables 2, 3 and 4 the linear correlation of this data is very good; this would indicate that the probability of encountering a field greater than the spark-over field decreases linearly with increasing spark-over field values.

In the review of 7 studies by Uman and Krider (Ref. 4, p. 28), presented as Table 5, the typical and maximum fields measured in thunderstorm clouds for each study are presented. The average typical field magnitude for these studies is 143 Kv/m while the average high field magnitude is 310 Kv/m. Using the fact that the JSC and the Kasemir datasets are highly, linearly correlated it seems that our model cumulative distribution function (CDF) should likewise be linear. The average typical and average high values calculated from Table 5 support this because the typical or average value (143) is about half the magnitude of the high value (310) which would be expected in a CDF of this form. Using the Uman and Krider average high field value of 310 Kv/m, the model CDF in Figure 7 is constructed giving the probability of encountering a field greater than or equal to any given spark-over field.

Now that the CDF has been determined, the probability density function (PDF) can be found by differentiating and taking the absolute value (since the CDF slope is negative) of the CDF. Since the CDF is linear, the PDF will take the form of the uniform distribu-

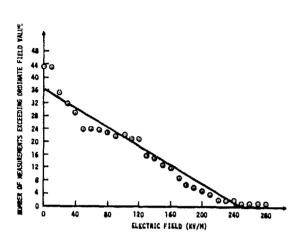


Fig. 4 - K.S.C. thunderstorm data

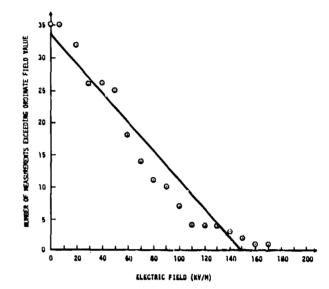


Fig. 5 - Katemir thunderstorm data - positive gradient

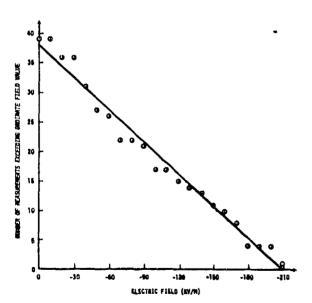


Fig. 6 - Kasemir thunderstorm date - negative

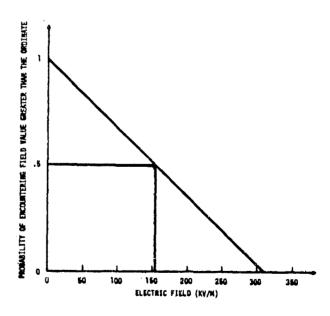


Fig. 7 - Hodel cumulative distribution function

tion with height given by the inverse of the maximum spark-over field value in Figure 7 or 1/310. A graphical representation of the PDF is shown in Figure 8. From this, the probability of encountering a field of a given value or greater is found by finding the area underneath the PDF for a chosen spark-over field and subtracting this area from one.

The next task is to calculate the mititude adjustment factor h for a given altitude. It was stated that the breakdown field varies inversely with altitude due to decreased air density; Table 6 gives these factors calculated from air densities in the summer months at the Cape.

Table 1 - Comparison of Calculated and Experimental Spark-over Field Values.

DESCRIPTION	CALCULATED SPARK-OVER FIELD (KV/M)	EXPERIMENTAL SPARK-OVER FIELD (KV/M)
FIELD ORIENTATION: TOP BELLY	318.93	311.4
FIELD ORIENTATION: NOSE-TAIL	233.91	232
FIELD ORIENTATION WING-WING	234.55	246

TABLE 2 - Regression of JSC Thunderstorm Data

#### REGRESSION TYPE NUMBER: 1

X	γ .	MODEL Y
0	35	33.3509
10	35	31.1135
20	32	28.8762
30	26	26.6388
40	26	24.4014
50	25	22.1641
60	18	19.9267
70	14	17.6894
80	11	15.452
90	10	13.2147
100	7	10.9773
110	4	8.73994
120	.4	6.50258
130	· <b>4</b>	4.26522
140	3	2.02786
150	2	209494
160	1	-2.44685
170	ï	-4.68421

A = -.223736 B = 33.3509 CORRELATION COEFFICIENT = .964706 NUMBER OF DATA POINTS = 18

TABLE 3 - Regression of Kasemir Thunderstorm Data - Positive Gradient

#### REGRESSION TYPE NUMBER: 1

X	Y	MODEL Y
0	43	36.3241
10	43	34.8601
20	35	33.3961
30	32	31.932
40	29	30.458
50	24	29.0039
60	24	27.5399
70	24	26.0759
80	23	24.6118
90	22	23.1478
100	22	21.6837
110	21	20.2197
120	21	18.7557
130	16	17.2916
140	14	15.8276
150	13	14.3635
160	12	12.8995
170	. 9	11.4355
180	/	9.97143
190	0	8.50739
200	5 	7.04335 5.57931
210	<b>%</b>	4.11527
220 230	2	2.65123
240 240	2	1.18719
250 250	7 6 5 4 2 2 2 1 1 1	276847
260 260	î	-1.74089
270	i	-3.20493
280	i	-4.66897
	•	-7.0003/

A= -.146404 B= 36.3241 CORRELATION COEFFICIENT= -.97066

NUMBER OF DATA POINTS= 29

TABLE 4 - Regression of Kasemirs's Thunderstorm Data - Negative Gradient

#### REGRESSION TYPE NUMBER: 1

x	Y	MODEL Y
-210	1	189723
-200	1 4	1.63354
-190	4 ·	3.4568
-180	4	5.28007
-170	8	7.10333
-160	10	8.9266
-150	ĨĨ.	10.7499
-140	13	12.5731
-130	14	14.3964
-120	15	16.2196
-110	17	18.0429
-100	17	19.8662
-90	21	21.6894
-80	22	23.5127
-70	22	25.336
-60	26	27.1592
-50	27	28.9825
-40	31	30.8058
-30	36	32.629
-20	36	34,4523
-10	39	36.2756
Ō	39	38.0988

A= .182326 B= 38.0988 CORRELATION COEFFICIENT = .989419

NUMBER OF DATA POINTS = 22

'Table 5 - Thunderstorm Electific Fields Measured in Airborne Experiments

Investigation	Typical (Kv/m)	High Values Occasionally Observed	Measurement Type
Winn et al (1974)	50-80	200	Rockets
Winn et al (1981)	-	140	Balloons
Rust, Kazemir (Private Comm.)	150	300	Aircraft
Kasemir and Perkins (1978)	100	280	Aircraft
Imyanitov et al (1972)	100	250	Aircraft
Evans (1969)	-	200	Parachuted Sonde
Fitzgerald (1976)	200-400	800	Aircraft

Using these h values, spark over field values are calculated for the spheroids in Figures 1 thru 3 at various altitudes. These are displayed in Table 7. Since electric field values measured in thunderstorm experiments are oriented in all different directions, spark over field values are averaged. Given this value the probability of exceeding the value, incurring a lightning strike, is determined from Figure 8.

Amplitudes of lightning strikes in a storm are now summarized. When amplitudes of strikes are considered, a distinction must be made between in cloud strikes and cloud to ground strikes; this is because cloud to ground strikes are of a much greater magnitude. In this regard, E. T. Pierce and workers at Westinghouse have independently formulated expressions that estimate the percentage of total lightning strikes that go to ground. Pierce's expression (Ref. 6, p. 13) is p = 0.1  $(1 + (\lambda/30)^2)$  where p is the proportion of lightning strikes going to ground and  $\lambda$  is the latitude of the location of interest in degrees. Using this method for KSC (latitude 28.5°) p = 0.19 which means that about 19% of all flashes go to ground. The Westinghouse expression (Ref. 6, p. 13) is:

$$p = 0.05 + \frac{(\sin \lambda + 0.05)}{((Tm + 3)^{1/2})}$$

where p and  $\lambda$  are as above and Tm is the number of thunderstorm days per month at the selected site. For KSC Tm = 6 on the average over the year, so p = .23. These two results when averaged together yield a value of 21% for the average proportion of strikes going to ground in a month at KSC.

N. Crains and E. J. Pierce have collected and summarized much data relative to cloud to ground strikes and intracloud strikes. Figure 9 is a distribution graph of these statistics for intracloud strike currents. Figure 10 is a distribution graph of these statistics for cloud to ground peak currents.

Table 6 - h Factors (Altitude Density/Sea Level Density) at Various Altitudes

<u>Altitude</u>	h factor
0 km	1.13537/1.13537 = 1
1.6 km	.976418/1.13537 = .86
5 km	.710939/1.13537 = .63
7 km	.580019/1.13537 = .51
10.5 km	.396034/1.13537 = .35

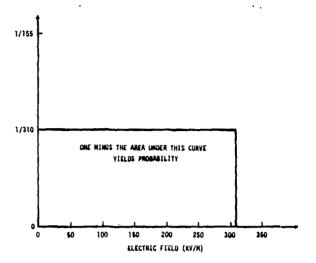


Fig. 8 - Probability density function

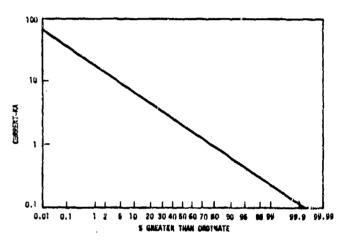


Fig. 9 - Distribution graph of intracloud strike

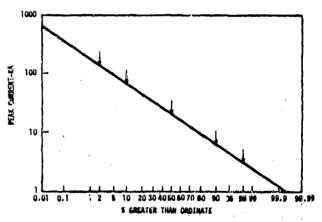


Fig. 18 - Distribution graph of cloud to ground peak currents

Table 7 - Calculated Spark-Over Field Values for Three Field Orientations at Various Altitudes

#### Altitude (M) Spark over Field Value (KV/M)

	TOP-BELLY	NOSE-TAIL	WING-WING
10,500	129	95	95
9,000	153	112	113
7,000	190	139	139
5,000	232	170	171
2,000	310	227	228

#### V. LAUNCH AND LANDING PROFILES

Due to the previously mentioned tile restrictions, the Shuttle is not to be launched in rain, hail, or sleet/snow. The Shuttle is also not to be launched with its flight path closer than 5 nautical miles to the edge of a cumulonimbus radar cell (the distance lightning may reach outside a storm), through cumulus clouds having weather radar achoes, or if the ground electric field exceeds 1 kilovolt per meter. Within ninety seconds after launch, the vehicle reaches the 80,000 ft. altitude and has traveled 15 miles along the vehicle's azimuth (either Northeast or due East). Considering these restrictions coupled with the short time span and the small area covered in the altitudes where lightning can be produced, the threat of a strike during launch is almost non existant.

The risk is increased in the landing phase. This is because where a launch can be delayed if conditions are sub-par, landing cannot be delayed once a de-orbit burn (one hour prior to landing) has been made. The Orbiter is powerless when landing; it deorbits to a particular site and must glide there. At the 80,000 ft. altitude (reached approximately six and one half minutes prior to touchdown), a runway approach must be chosen. There are four options here. The Orbiter can pass over the runway and then appreach and land from either end of the runway, or the Orbiter can glide straight to either end of the runway. Figure 11 shows the envelope of a nominal energy (approaching at nominal altitudes) approach of the Orbiter. The envelope encloses the area the Orbiter might be in, gliding in from 60,000 ft. downward. The Orbiter cannot pass over the rulway if it is low on energy. In the nominal energy case, however; the Orbiter can negotiate one of the four possible approaches. This provides the vehicle with limited weather evasive capabilities.

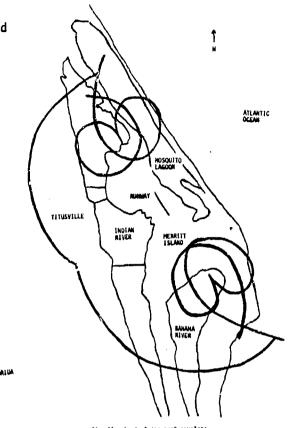


Fig. 11 - Auminal approach envelope

#### VI. SUMMARY AND PROBABILITY

In the landing phase, analysis of the vehicle's atmospheric non-lightning limitations suggest the needed avoidance of lightning producing weather conditions. Analysis of alternate landing sites, particularly Vancenberg and Edwards, indicate low probabilities of encountering lightning. Weather forecast capabilities at Vandenburg suggest the capability of completely avoiding lightning by making additional revolutions if necessary. The high risk situation is a deorbit burn to Kennedy Space Center, the primary landing site, in the summer months. This burn could be made with clear skys at Kennedy. As the runway is approached fifty minutes later, a diurnal thunderstorm may have formed. If the Orbiter is to be struck by lightning, it will probably be in this type scenario.

A method for calculating the maximum probability of receiving a strike (at a particular time at the Cape) of a given amplitude or greater is to multiply these factors.

A. The propability of a thunderstorm at the Cape.

- B. The probability of the storm being in the vehicle's flight path,
- C. The probability of the vehicle being struck in a storm (based on sparkover fields, altitude dependent),
- D. The probability of this being a cloud to ground strike of a given amplitude or greater,
- E. And the probability of the strike being a cloud to ground strike;

this probability is added to the product of these same factors except substituting "intracloud strike" for "cloud to ground strike." The formula is

P = (A)(B)(C)(D)(E) + (A)(B)(C)(D')(E')

The A factors are displayed in Table 8, the C factors are in Table 9, and D and D' factors are extracted from Figures 9 and 10 respectively. As calculated earlier, E = .21 and E' = .79. Table 8 indicates that July is the worst month and 3:00 to 5:00 PM local time is the worst time of day. That time period correlates to a 20% frequency of occurence of thunderstorms. The best time of day in July is between 3:00 and 9:00 AM, when frequency of occurrence is 0.5%. This is compared to the month of December where the time period between 9:00 AM and 5:00 PM has an associated frequency of occurrence of 0.3% to 0.4% and all other times are 0.1%. It is assumed that KSC landings will normally occur in the time period between 6:00 AM and 6:00 PM. If the frequency of occurrence is averaged for this time period for the months of June, July, and August a frequency of oc-currence of 4.7% results. Thunderstorms are recorded when thunder is heard which can be up to a distance of fifteen miles.

Considering this distance and the flight path envelop in Figure 11, a storm may "exist" at the Cape and not be near (few miles) the vehicle's flight path. Given the four approach paths, the fact that some storms are frontal and predictable, and the method used to record thunderstorms, B is estimated to be .67.

Strikes which could cause severe systems degradation were the basis for this study. A range of amplitudes thought to be potentially dangerous were defined and investigated. The range was from 2KA to 200 KA. Figures 9 and 10 show that exceedance of these amplitudes are almost exclusively cloud to ground strikes; therefore, the intracloud strikes were not considered for this particular probability calculation. The C factor of this probability equation varies from 0% to 49%

depending on the altitude for which the spark--over field is chosen. Since the Orbiter would most likely cover a range of altitudes if it encountered a storm, the probability of exceeding spark-over fields at different altitudes is averaged (Average = 24.5%). The probability equation

$$P = (A)(B)(C)(D)(E)$$

is now

$$P = (.047) (.67) (.245) (D) (.21)$$

By letting the D factor vary from 2 to 200 KA, the probability of encountering a light-ning strike less than a chosen design level is shown in Figure 12.

For the Shuttle Launch Configuration, observance of existing launch constraints should preclude exposure to lightning. Relaxation of constraints to allow launching through thunderstorms or layered clouds with freezing temperatures was not recommended because of potential TPS damage from in-cloud precipitation. In addition there is a high probabil-ity of triggering a cloud-to-ground strike during launch. Trailing wire rockets tests (comparable to the Shuttle with SRB plumes) have achieved a triggered strike rate of 68%. These tests were performed with a ground level field intensity of 10 KV/M or greater, well above the launch criteria limit of 1 KV/M. However it does suggest a high strike risk at launch. It should be noted that layered clouds can produce misleading indications from field mills on the ground at KSC because of low layers masking fields from higher layers.

The following were conclusions drawn based on the study.

- The KSC diurnal thunderstorm presents the greatest unavoidable lightning threat, given existing constraints, due to prediction limitations. This risk can be minimized by planning early morning landings.
- A lightning protection level for the Orbiter at landing of 50 KA is suggested as a goal. The flight dynamics capability of the vehicle suggests a high probability of successfully flying through a thunderstom, provided it survives lightning.
- For Shuttle at launch, TPS damage potential, as well as high triggered strike likelihood, suggest that the Shuttle should not be launched through thunderstorm or deep or layered clouds at freezing altitudes. (Near radar echoes).

Table 8 - Percent Frequency of Occurence of Thunderstorms from Hourly Observations at KSC

Month											
Hour	Feb	Mar	Apr	May	Jun	Ju 1	Aug	Sep	Oct	Nov	Dec
00-02	.3	.5	.1	.7	1.2	1.0	2.0	1.8	.7	.3	.1
03-05	.2	.6	.1	.5	.9	.5	.9	1.0	.7	.3	.1
06-08	.2	.5	.3	.2	.6	.5	1.1	.9	.5	.3	.0
09-11	.1	.5	.3	.8	1.2	1.1	1.7	1.8	.3	.2	.3
12-14	.2	1.2	.7	2.7	9.2	11.0	9.4	3.4	1.7	.1	.4
15-17	.6	1.1	1.9	5.9	13.7	20.0	15.6	7.4	1.7	.7	.3
18-20	.1	1.8	1.6	5.4	8.1	11.0	8.0	5.2	2.2	.8	.1
21-23	.4	1.3	.8	2.5	1.7	3.6	2.9	2.7	.6	.8	.1

Note: Data not available for January.

Table 9 - Probability of Exceeding Spark Over Field Values in Florida Thunderstorms

Altitude	Orbiter Probability
Below 4km	-
5km	.08
7 km	.25
9km	.39
10.5km	.49

#### Note

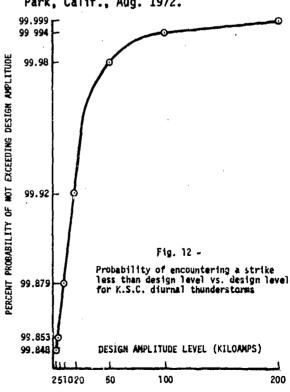
Orbiter probabilities below 4km are not indicated because the linear amplitude model stops at 310 kv/m. Actual probabilities continue to decrease with altitude.

#### REFERENCES

- H.K. Kasemir, "Lightning Trigger Field of the Orbiter," National Oceanic and Atmospheric Administration, Boulder, Co., Oct. 1978.
- H.P. Westman Ed., "Reference Data for Radio Engineers" Howard W. Sams & Co. Indianapolis, Indiana 1968.
- D.W. Clifford, "Simulated Lightning Test Shuttle .03 Scale Model," Report No. MDC A3155, McDonnell Aircraft Co., St. Louis, Mo., Dec. 1974.
- 4. M. Uman and E.P. Krider, "Atmospheric Electricity Hazards Analytical Model De-

velopment and Application: Volume 1," Air Force Wright Aeronautical Laborato-ries, Wright Patterson A.F.B., Ohio, Aug. 1981.

- J.S.C. Program Operations Office, "JSC Thunderstorm Experiment Results," Report No. JSC-12509, NASA, Houston, Tx., March 1977.
- 6. E.T. Pierce and N. Cianos, "A Ground-Lightning Environment for Engineering Usage," Technical Report 1 SRI Project 1834, Stanford Research Institute, Menlo Park, Calif., Aug. 1972.



## ATMOSPHERIC ELECTRICITY THREAT DEFINITION FOR AIRCRAFT LIGHTNING PROTECTION

 $\rightarrow$ 

Dr. B. G. Melander
The Boeing Military Airplane Company, Seattle, Washington

#### ABSTRACT

This paper describes a consistent atmospheric electricity threat: environment for use in the protection of aircraft electronic/electrical systems. The definition has evolved from many prior research efforts including measurements of direct strikes to aircraft and ground installations.

The AE threat definition includes threats of two basic types. The first includes all lightning-associated threats and the second includes static electrification threats. Cloud-to-ground lightning has been studied extensively and is used as the basis for the present lightning threat definition. The defined threat is compared to available cloud-to-ground lightning strike data. Intracloud discharges, which account for over half of all discharges, are less well studied, but usually are less severe. Direct strike measurements of intracloud lightning on an F-106 research aircraft during the NASA Storm Hazards Program are compared to the threat based on the cloud-to-ground discharges. Characterization of static electrification including streamers and corona are also included in the total atmospheric electricity threat. Static electrification is caused by both tribo electric and exogeneous charging which creates both corona and streamers.

The threat includes the best currently available data for both lightning and static charging phenomena. This threat is being used for the Atmospheric Electricity Hazards Protection Program sponsored by USAF, USN, DNA, FAA, and NASA. The threat definition will ultimately be used to define future protection and qualification requirements.

This work was sponsored by AFWAL/FIEA under Contract F33615-82-C-3406, Rudy Beavin, Project Officer.

#### INTRODUCTION

An atmospheric electricity threat is Spresented for use in the protection of aircraft electronic/electrical systems. The threat is being developed as part of the Atmospheric Electricity Hazards Protection (AEHP) Program at Boeing. The objectives of the program are to develop design criteria, guidelines, and qualification test procedures for mitigating any atmospheric electricity vulnerabilities of electronic equipment in future advanced aircraft structures. The emphasis is on indirect effects of lightning/static electrification and their induced electrical transients in aircraft wiring rather than direct arc/spark effects. The atmospheric electricity threat lightning both and static electrification phenomena. This presents the initial lightning threat compared against ground-based direct current measurements and direct strike data from NASA's F-106 aircraft. Also presented are the static electrification threats due to streamers and corona.

Potential hazards to electronics equipment within an aircraft encountering natural atmospheric electricity depends strongly on the interaction of airframe structure with a lightning strike and its associated electromagnetic fields. The physical processes whereby electrical transients are induced by lightning or static electricity within an air vehicle wiring complex are significantly different than processes previously considered for structural damage due to directly attached lightning. The most important difference for electronic effects is the need to consider rate-of-rise parameters for

currents and fields because inductive and capacitive coupling dominate internal transients when circuitry is isolated from vehicle structure. Peak values and time duration of current and fields are important in determining voltages and currents within the structure. Pulse energy is important in determining the rating for transient protective devices that may be required to absorb energy from the lightning induced transients.

Physical understanding of the data sources that define lightning and static electrification environments are important in determining the critical rate of rise parameters. These parameters are especially important for determining currents and electromagnetic fields associated with aircraft interaction with the AEH threat environments.

The problem Οť determining atmospheric electricity (AE) threat t.o aircraft in flight has been examined for many years. More recently due to research into advanced composite material having poor electrical properties compared to metals, interest has increased in better prediction the AE threat to aircraft electrical/electronic equipment. The severity of the threat will determine the equipment protection necessary for aircraft all weather operation.

Natural atmospheric electricity presents two separate hazards: lightning and static discharges due to aircraft charging. The mechanism of a natural cloud-to-ground lightning discharge is illustrated in Figure 1. When sufficient charge accumulates in the lower part of a cloud to cause an

electric field which exceeds the ionization threshold of air, an electrical discharge is initiated toward the earth. Because the discharge requires a finite amount of charge and time for the channel registance to lower to the arc phase, the discharge proceeds in a sequence of steps, pausing periodically to allow the previous channel section to become fully conducting. This mechanism is known as the stepped (or step) leader process.

The natural electrical phenomena occurring with lightning discharges vary in number and intensity. A statistical basis is needed because of this variability. A moderate level is defined as the expected levels from a typical lightning flash. Severe lightning is defined as the worst-case level expected to occur during the service life of an aircraft. The maximum rate-of-rise and peak current that represent the severe lightning threat are currently subjects of en-going current rasearch into lightning hazards to aircraft in flight.

The best available statistical data on lightning currents is data measured on the ground. Currently published data on cloudto-ground lightning currents measured on the ground show that 180 kA/µs is the largest rate of rise directly measured [1]. Recently obtained data on lightning currents inferred from measured electric fields are as high at 400 kA/us [2]. Both of these measurements are subject to uncertainties in the measuring techniques. The best engineering judgment at present is that 200 kA/ $\mu$ s adequately represents the worst-case expected for an aircraft in flight and is defined as the severe level for AEH threat. Additional research is needed to resolve the difference between the defined severe threat and the distant field measurements.

A second threat to aircraft from atmospheric electricity occurs due to aircraft charging effects. As an aircraft moves through the air, it can become charged. This can result in discharges either by streamering, corona or arcs and sparks.

Figure 2 shows these discharges from various sections of an aircraft. Arcs and sparks can create direct damage effects especially in fuel tanks. Proper grounding and bonding can usually eliminate these problems. Noise problems from corona or streamering phenomena is not so easily eliminated. These noise levels must be established as a part of the total atmospheric threat levels to aircraft.

Numbers in brackets designate References at end of paper.

Lightning and static electrification threats will be discussed separately. The second section discusses lightning and comparisons with current measurements. The third section characterizes the static electrification threat. The last section summarizes and makes recommendations for future threat characterizations.

#### LIGHTNING THREAT

Lightning is a transient, high current electric discharge. The most common source of lightning arises from the electric charge separation in ordinary thunderstorm clouds (cumulonimbus). Well over half of all lightning discharges occur within the cloud (intracloud discharges). Cloud-to-ground lightning (sometimes called streaked or forked lightning) has been studied more extensively than other forms of lightning because of its practical interest (e.g., as the cause of disturbances in power and communication systems, strikes to aircraft and the ignition of forest fires) and because it is more easily observed with optical instruments. Cloud-to-cloud and cloud-to-air discharges are less common than intracloud or cloud-to-ground lightning.

Strikes to aircraft are thought to involve both cloud-to-ground strikes (at low altitudes) and cloud events (at high altitudes). The lightning data discussed at present will include only cloud-to-ground events. This data will be used to establish a ground based lightning threat.

A typical cloud-to-ground discharge starts with a preliminary breakdown within a cloud followed by a stepped leader initiating the first stroke. Leader steps are usually  $l_{\rm HS}$  long, tens of meters in length, with a pause between steps of  $50\mu s$ . The typical leader current is the order of 1 kA [3].

As the leader nears an aircraft, it emhances the local fields. Discharges off the extremities of the aircraft are produced when the field values reach air ionization levels. When the stepped leader connects to one of the aircraft discharges, it becomes merely a part of one step as the stepped leader proceeds to ground or another charged cloud.

As the leader tip nears the ground, an upward moving discharge is initiated at the ground. The leader channel is discharged as a ground potential wave, the return stroke, propagates up the ionized leader path. The return stroke has a much higher current than a leader, an average of 20 kA with maximum up to 200 kA and a rise time of few microseconds. The return stroke may be followed

by a dart leader which initiates a subsequent stroke. Subsequent strokes have faster rise times but comparable rates of change as return strokes. Many additional complete discharges called multiple strokes can take place. In general, these subsequent strokes have smaller magnitudes. Establishing the size of these threats is the first part of establishing an AEH threat.

The AEH lightning threat defined herein will be shown to be consistent with the most recently published statistical lightning data. Two sets of parameters are used to identify a moderate or expected lightning stroke and a severe or worst-case stroke. The lightning threat is not designed to match the physical parameters of a particular lightning stroke but rather to be representative of the range of values for the many types of lightning discharges.

The parameters of most importance in this lightning threat were chosen because of their impact on aircraft electrical/ electronic systems. These parameters include maximum current rise rate, peak current and energy input (action integral). The selected values were chosen from a review of existing data. They are consistent with statistical variations of other available data. Other characteristics of the waveform (rise time and fall time) are determined uniquely by choosing the above three parameters since the threat model has only three independent parameters. Even so, both rise and fall times are well within the statistics of measured data.

The lightning threat must characterize both single and multiple stroke phenomena. The multiple stroke will be characterized by several single strokes with the addition of induced transient duration, inter-stroke time interval, total event time and total number of strokes. These parameters are listed in Figure 3.

The initial single stroke lightning threat model is a double exponential waveform representing the lightning current; the waveform and spectrum is shown in Figure 4. The parameters are listed in Figure 5. The double exponential form of the lightning threat model will be shown to adequately predict the expected electric field spectra from a combination of measured lightning discharges. This threat is to be interpreted as the current flowing in the unperturbed lightning are channel (i.e., no aircraft interaction). In applying the threat to an aircraft, an electromagnetic coupling model is needed which includes the aircraft and channel geometry and includes the threat as an incident current waveform propagating along the channel.

The double exponential waveform, which is a convenient model for engineering calculations, has a historical precedent in The waveform both lightning and NEMP. parameters are selected to include the most important features of the lightning current rather than to faithfully represent any single lightning waveform. The three lightning parameters incorporated in the threat waveform are peak rate-of-rise, peak current, and action integral. The moderate and severe threats were selected to be expected and worst-case levels of the parameters based upon review of the best available measured data. Figure 5 shows these threat parameter values and the equations for defining the doub!e exponential current waveform.

DATA SOURCES - The data desired in establishing aircraft lightning threat parameters are measurements of direct lightning strike currents and EM fields on aircraft at altitude. Strike data measured on aircraft are not yet we'l understood as regards threats to aircraft safety. Two ongoing programs to gather more strike data at altitude are the NASA F-106 and USAF C-130. This data will be used to aid in understanding the threat level at altitude.

The available data necessary to establish lightning threat characterization is limited. Of all the types of lightning processes (leader, dart leader, J & K changes, preliminary breakdown, etc.), the most critical processes to aircraft safety are thought to be first return and subsequent strokes due to high current levels, high current rise rates and high energy inputs into aircraft systems. Data on these processes are for the most part confined to ground measurements of electric and magnetic fields, current waveforms, and stroke velocities (see Reference [3] for a list of references on each type of measurement).

Ground parameters are thought to be the worst case situation for lightning threats. Current and field amplitudes and rate of rise are thought to decrease with altitude [4]. Hence, the most severe lightning threat to aircraft is a severe lightning strike on the ground.

The initial lightning threat outlined in this paper is based on these ground measurements. A final AEHP threat will take into account altitude effects including in flight data.

DATA APPLICABILITY - The present threat definition is based on ground based direct current measurements. The data sets used were taken from available statistical

studies on measured lightning current parameters [5-8]. Current parameters derived from field measurements were not used in the initial threat definition. The statistics were not yet available when establishing the threat.

Measurement errors exist associated with both direct current measurements and currents derived from field values. These uncertainties must be established before a more complete and thorough use of the presently available data can be implemented. Data limitations due to measurement techniques are listed below for the most recent statistical data sets available.

Berger, Garbagnati - Berger [5] in Switzerland and Garbagnati [6] in Italy have made a series of direct current measurements using towers on mountain tops. Berger's data is measured on a 70 m tower on top of Mount San Salvadore which is 914 m above sealevel. Garbagnati's measurements are from 40 m towers on Italian mountains near San Salvadore. Berger's latest data is comprised of 101 negative and 26 positive first strokes and 135 subsequent strokes. Garbagnati has 103 negative and 5 positive first strokes and 175 subsequent strokes.

Uncertainties associated Berger and Garbagnati's data arise from the fact that both used towers on rocky mountain The presence of the tower may have two effects on the data taken. The presence of the tower may influence the statistics of the lightning strikes. For example, larger amplitude strokes are thought to strike tall towers [1]. The distance over which a structure attracts a downward leader is a function of the charge on the leader which, in turn, is related to the amplitude of the current in the return stroke [4]. Therefore. lightning strikes to open ground should have a greater proportion of lower currents while taller structures should have a higher number of more intense currents. Another statistical fluctuation may be in the number of positive strokes seen. Evidence exists that positive flashes may increase with altitude [1, 5]. If this trend holds true to aircraft altitudes, then any statistics taken near the ground will not be the statistics at altitude. The statistics of lightning strikes to aircraft are the statistics of interest here. Any way of measuring lightning strike statistics other than to the specific aircraft under mission conditions will not reflect the true statistics of interest. Obviously, compromises on this issue will have to be made and some estimates of the errors involved must be established.

The presence of a tower in direct current measurements also affects the measurements themselves. The maximum rise rate is effected by the tower inductance and ground impedance effects. The magnitude of this effect needs to be established.

The early time portion of the waveform may also be effected due to the presence of the upward-going leaders which may lead to slower rise times for tall objects [7]. The leader effect should be more pronounced for first return strokes than for subsequent strokes since subsequent strokes are not thought to have long upward propagating leaders. Both Berger [5] and Garbagnati's [6] data show much higher rates of rise for subsequent than first return strokes while Uman [9] and Weidman and Krider [10, 11] report no difference in current rates of rise derived from fields. This difference indicates that either the leader presence does affect the tower measurements or that the current model used to derive current parameters from field data is not accurate. This discrepancy needs to be cleared up.

Uman and Krider - Uman and Krider have spent many years measuring and analyzing electric and magnetic fields of various types of lightning [9-16]. They have found much higher field rise times (under a microsecond) than have been seen in direct current measurements. The fast rise times were seen in measurements over salt water. Propagation over salt water does not attenuate the high frequencies as severely as earth. The upper frequency limit is felt to be 20 MHz [12] due to wave action influencing measurements above 20 MHz. This data is very useful in establishing validity of a physical current model from which EM fields can be calculated and compared to the measured results.

To use this data in establishment of a lightning current threat, the uncertainty associated with deriving currents from EM field measurements must be established. First, uncertainties arise from the measurements due to equipment limitations, resonance effects, propagation effects, etc. Second and more serious are uncertainties due to the assumptions in the current models and the number of parameters needed to fit the data. The first type of uncertainty can be readily quantified. The second needs to be examined. In Uman's model, current is assumed to propagate up the channel at constant velocity. The channel is taken to be vertical with the initiation of the stroke at the ground. Three types of current profiles (uniform or leader current, breakdown current and corona current) have been incorporated to fit

simultaneous electric and magnetic fields at two distances. The pulse velocity is an input to the model and is not well known. Assuming the velocity to be constant with height may also add uncertainties to the results. The corone current shape is somewhat arbitrary as stated by Lin et al [13]. The non-uniqueness of the current decomposition is a major problem and the uncertainties due to this have not yet The assumption that established. the initiation point is at the ground and not above has been argued [14] to introduce a factor of two error due to the two return front waves produced above ground. Lastly, the effect of the assumptions that the column is vertical and straight must be taken into account. Differences between current measurements on towers and those derived from field values have to be reconciled before a fully consistent ground based lightning threat can be established.

Data summerized by Cianos and Pierce [7] was used in this establishment of the initial lightning threat. The data was a compilation of work prior to 1972 and is limited by the time resolution used in the data collection. This skews the results toward longer rise times and lower rise rates.

Data collected and raviewed by Popolansky [8] include not only results obtained on tall chimneys and lightning rods but also the negative and positive first strokes recorded by Berger, totaling 624 waveforms. The resulting cumulative frequency distribution curve produces a median value of 28 kA. Berger et al [5] conclude that the median values obtained on Mount San Salvatore and on tall chimneys in open country are similar. However, slopes of Poplansky's and Berger's data curves do not coincide completely (see Figures 9 and 10).

Anderson and Erikscon [1] in South Africa measured lightning currents on a tower located in open country. Unlike Berger and Garbagnati, the measurements were taken on flat terrain. Only a small number of strokes (eleven) were analyzed with a maximum current rise rate of 180 kA/µs for a subsequent stroke. This is a higher level both in absolute value and relative percentage than Barger's or Garbagnati's measurements. With so few events, however, definite comparisons are premature.

Recently current waveforms are being measured on aircraft in flight by NASA [17, 18]. To date cloud discharges dominate their results. The 1983 program will attempt to measure some cloud-to-ground strikes.

THREAT RATIONALE - No single waveform can represent all types of lightning discharges (e.g., cloud-to-ground, intracloud, positive strokes, negative first strokes, and negative subsequent strokes). It is necessary to select parameters from particular stroke types which provide reasonably conservative threat levels for all strokes. Cloud-to-ground strokes were chosen because they are generally more severe, although a less frequent threat to aircraft, than intracloud discharges. On this basis, the threat waveform parameter values were chosen as described below.

Peak Current - The peak current was chosen from the statistical study done by Cianos and Pierce [7]. The moderate threat level of 20 kA was chosen at their 50% level for first return strokes. The severe threat of 200 kA was chosen at their upper 1% level.

Action Integral - The action integral was also chosen from Cianos and Pierce data. Peak current values and mean rise and fall times were used to determine a moderate energy input level of 1.5 x  $10^4$  Å $^2$ -s and a severe level of 1.5 x  $10^6$ Å $^2$ -s.

Rate of Rise - Rise rate data displayed by Clanos and Pierce has recently been interpreted to be too low. More recent statistical data [4, 6, 8, 13] has shown higher current rates of rise. The values for the initial threat determination were taken from Berger's [6] tower measurements. The moderate value of 50 kA/µs lie at his upper 35% mark while the severe threat of 200 kA/µs was chosen at his 1% level.

COMPARISON TO PRIOR LIGHTNING STANDARDS - In this section, the lightning threat defined in Figures 3-5 is compared against other industry lightning standards. Table I summarizes comparisons between previously used standards and the present threat definition. Only the severe throat is compared since the other standards represent severe strikes.

Current rise rate values are given in the first column of Table I. The values in parenthesis are obtained from the peak current value divided by the rise time for the corresponding standard. This gives an average rise time or a maximum rise time if the initial current waveform is a straight line. The straight line waveform for the initial current rise is used in the SAE-4L standards. The rise time for the AEH threat is the peak rate of rise, not an average. For a double exponential waveform these quantities are substantially different. The peak rate of rise, not the average, is the important quantity when specifying a lightning threat. This difference between

peak and average rate of rise leads to the AEH higher standard for rise rate.

The peak and average rate of rise definition also leads to an AEH rise time different from other industry standards. This difference is shown in column 3 of Table I. The longer AEH rise time is due to the double exponential waveform used. Other standards use ramp functions. However, the rise rate, not the rise time, is the important parameter when considering possible damage to aerospace vehicles.

The peak current and fall time are listed in columns 2 and 4. The AEH initial threat values agree with those previously used.

LIGHTNING THREAT COMPARISON TO MEASURED DATA - Comparison with available data is presented in this section. The data presented is the most recent found in the literature. Each model parameter is examined separately below. All the model parameters chosen lie within reasonable statistics of this data.

Uman-Krider Measured Field Data Comparison - A comparison is made in this section to measured electric presented by Uman and Krider [3]. fields comparison of a lightning current profile to electric radiation field data is not straightforward if lightning geometry, propagation effects, height dependence of lightning current, etc. are taken into account. Since the comparison presented here is meant to be preliminary, a simpler procedure will be followed. The magnetic radiation field is calculated from an infinite current carrying wire. This approximation is valid close to the wire (less than a wavelength away). This minimum distance is 300 km for 1KHz and goes to 3km at 100 KHz. The electric radiation field is obtained from the magnetic radiation field assuming free space radiation. The results for both moderate and severe current profiles are plotted in Figure 6 against Uman and Krider's electric field spectra for first strokes. The threat levels tend to be well above the data for low frequency and straddling the data at higher frequency. The shape of the frequency spectra of the predicted fields matches the measured fields fairly well. More recent measurements by Krider have shown higher rates of rise. The newer spectra have more high frequency content, larger than the AEHP initial threat levels.

Current Rise Rate - The single stroke threat value for maximum current rise rate is given in Figure 5 as 50 kA/ $\mu$ s for a moderate stroke and 200 kA/ $\mu$ s for a severe

stroke. These values correspond to the upper 35% and upper 1% as shown in data from Berger [5] in Figure 7. Note that no measurements were made with a rate of rise greater than 100 kA/us. Figure 7 also shows older data accumulated by Clanos and Pierce [7]. The moderate and severe threat correspond to the upper 12% and upper 0.1% values. This data is taken from average rates of rise rather than maximum values. Thus the threat values show as higher percentiles as compared to Berger's data. Data from Garbagnati [6] is shown in Figure 8. The moderate threat is at the upper 10% mark in (a) and upper 35% in (b). The severe threat is at the upper 3% in (a) and 1.5% in (b). These statistical values agree well with the choice of rise rate picked for the current threat levels. No direct current data has been directly measured showing current rise rate greater than 180 kA/ $\mu$ s. Higher current rates of rise values (up to 400 kA/ $\mu$ s) have been reported [2] but are inferred from field measurements. The choice of 200 kA/us for the severe threat level was in anticipation of using some of these higher current rise rate values derived from the field data. A study of the uncertainties inherent in both the tower measurements as well as the field derived current values may lead to a change in the final rise rate values chosen.

Peak Current - Peak current values taken from Poplansky's data [8] are shown in Figure 9. The moderate (20 kA) and severe (200 kA) threat values lie at 60% and 1% respectively. Data in Figure 10 from Berger [5] show the threat values to lie at 80% and 0.1%, respectively. Figure 11 is data from Garbagnati [6]. The moderate threat is at 60% in (a) and 45% in (b). The severe threat is less than 0.1% in both figures. The moderate threat is close to a median value in Figures 9 and 11. Figure 10 shows 20 kA to be a very optimistic moderate threat level at the upper 80% level. The severe threat amplitude shows as a very severe threat (<0.1%) in both Berger and Garbagnati's negative stroke data, but is at the desired 1% level in Poplansky's data. If one considers positive strokes, Berger's shows the severe threat level to lie at the upper 8%. Debate is ongoing as to the importance of positive strikes as a threat to aircraft.

Action Integral - The last parameter chosen in the threat definition is the energy input or action integral. Figure 12 shows the Berger data. The percentiles for the moderate threat case range from 25% to 85% for negative subsequent and first return strokes.

Figure 13 shows moderate threat levels

for these two stroke types to lie at the upper 45% and 80%, respectively. The severe threat levels show as upper 1% both in Berger's data (Figure 12) and Garbagnati's first return stroke data (Figure 13). The moderate value of the energy input is seen to be overly severe for subsequent strokes but overly optimistic for first return strokes (at least for measurements taken at the ground).

Rise Time - The rise time of the threat model is a consequence of fixing the maximum current rise-rate, the peak current and the action integral. Rise time is not fixed independently of these parameters. independently Consequently, comparing rise time to data gives an indication of the general adequacy of the form of the couble exponential used to model the lightning current. Figure 14 from Berger shows the moderate threat rise time of 2µs falling at 25% and 95% for subsequent and first strokes respectively. The severe threat value of  $4\mu s$  lies at the 6% and 70% mark respectively. Figures 15a and b show results from Garbagnati. Figure 15a shows moderate and severe percentile of 70% and 43%. Figure 15b shows values of 25% and 3%. The data is widely scattered over a large range of rise times. The values chosen fall within this middle range of the data.

Figure 16 from [11] shows results that very short rise times (<lus). These results are from field measurements taken over salt water. The relationship to data taken over land is not completely understood. This data does indicate, however, that much shorter rise times may have to be included in a future threat. The impact of short rise times on the lightning threat is through the related parameter rise rate. Generally the shorter the rise time, the higher the rise rate, although the relationship is waveform dependent. Large current rise rate values could increase the amount of protection an aircraft must have to guard against lightning strike upsets or damage.

Fall Time to Half Peak - The fall time, like the rise time, is determined by the preceeding parameters so no fit to data was done when defining the threats. Figure 17 from Berger shows the moderate and severe threat fall time of 50µs to lie at 30% and 80% for negative subsequent and negative first strokes respectively. Figure 18 from Garbagnati shows the threat value ranging from the 35% to 75% level in 18(a) and is 30% in 18(b). The threat value is well within the median range of the above data. This parameter affects the lightning threat through the energy input or action integral. The longer the fall time, the

higher the current level for a longer time. This implies more energy is available to be coupled into aircraft systems.

F-106 Comparison - During the summers of 1981 and 1982, Boeing data loggers were flown on a NASA F-106 for the purpose of obtaining data on direct lightning strikes. This was part of NASA's Storm Hazards program. One strike was recorded by the data loggers in 1981 and ten in 1982. These waveforms are thought to be all cloud to cloud or intracloud events due to the high altitude of the measurements (25 Kft in 1981 and 25-36 Kft in 1982).

The largest current amplitude recorded was 14 kA. The largest rise rate was 30 kA/µs. These amplitudes are well below the AEHP threat level. Frequency spectra were obtained for all waveform and a mean and standard deviation calculated. The 1-106 spectra are compared to the AEHP lightning threat levels in Figure 19. Up to the Nyquist frequency (30 MHz), the threat level is well above the measured strikes. The data is very limited (only eleven events) and represents intracloud rather than cloud to ground strikes. Further flights in 1963 are hoped to obtain more cloud-to-ground events.

#### STATIC ELECTRIFICATION

Static electrification of a conventional aircraft can occur in various ways as illustrated in Figure 20. Figure 20(a) illustrates frictional electrification; as uncharged precipitation particles strike the aircraft, they acquire a positive charge, leaving an equal and opposite negative charge on the aircraft and raising its potential to tens or hundreds of thousands of volts. Charging occurs both on the metal structure of the aircraft and on dielectric surfaces such as the windshield. Dielectric surfaces can thus become charged with respect to the airframe. Engine charging, illustrated in Figure 20(b), occurs when flight vehicles are operated at low altitudes. Processes as yet incompletely within occur the understood combustion chamber and cause a predominantly positive charge to be expelled with the engine exhaust. This causes an equal and opposite (negative) charge to be imparted to the aircraft charging it to potentials of tens or hundreds of thousands of volts. Exogenous charging, illustrated in Figure 20(c), occurs when the vehicle flies in a region of electric field, such as that generated between oppositely charged regions of clouds; this field can cause discharges to occur from the extremities of the vehicle.

The operational conditions under which

static electrification can occur depend somewhat on the class of vehicle. Since airplanes encounter severe charging during operation in clouds in horizontal flight, electrification can continue for considerable periods of time on all-weather missions. On jet aircraft operating at low altitude, engine charging can be an additional source of long-term electrification. Helicopters become charged while flying through naturally occurring clouds. In addition, a hovering helicopter can strup snow or dust thereby generating its own cloud of particles to produce frictional electrification. Thus, helicopters encounter static problems in regions where conventional aircraft do not.

The charging process itself produces virtually no difficulty, but vehicle voltage and electric fields can become so high after a period of time that electrical discharges occur. It is the discharge of the accumulated static electricity that generally produces the most harmful effects.

NOISE SOURCES - An important consequence of static electrification is electrical noise. The various noise mechanisms that have been identified are shown in Figure 2. As the airplane becomes charged, the electric fields at the extremities of the vehicle become sufficiently high to cause corona breakdown of the air. At the operating altitude of airplanes, this breakdown occurs as a series of very short pulses containing energy in the radio frequency spectrum. These noise pulses can couple into communication, navigation, or digital circuitry to produce interference.

Another source of noise occurs when dielectric surfaces on the front of the airplane, such as the windshield and radome, are exposed to frictional charging, as illustrated in Figure 2. These surfaces can be charged by impinging particles. Since these materials are insulators, the charge is bound at the place where it was deposited and cannot be discharged until sufficient electric charge has accumulated to produce a streamer (a spark-like discharge) across the dielectric surface to the metal airframe. Streamer discharges are slow in duration, and involve the transport of charge over a large distance. They therefore produce radio frequency interference which can couple into susceptible systems on the aircraft. In some cases, the streamering on a square inch of surface in a critical location is sufficient to disable systems.

A third source of interference that often occurs inadvertently on airplanes is associated with sparking between unbonded adjacent metal sections of the aircraft.

For example, in Figure 2, a break shows in the wing; charging processes on the airframe will raise the potential of the inboard section with respect to the outboard section until a spark occurs in the gap. This spark produces a short current pulse, which is also a source of noise. In flight, the current required for corona discharge from the isolated wing tip is supplied from the remainder of the airplane.

Finally, slowly varying induction pulses can be produced in antennas by the passage of charged particles. This noise is of importance only at VLF or ELF and does not pose much of a problem to conventional communication and navigation equipment. With the advent of systems operating at frequencies of the order of 10 kHz, however, induction noise should be considered.

CHARGING PARAMETERS — The interference problem due to any of these noise sources depends on the charging rate of the plane. The most important process as measured in flight tests is frictional charging.

The precipitation charging current to a vehicle is given by [18]

where

q<sub>p</sub> = Charge per particle
 c = Particle concentration

v = Aircraft velocity
Aeff = Effective intercepting area
of aircraft.

The various parameters in the equation and their interdependencies have been studied analytically, in the laboratory and in flight, and are generally understood for the operating regimes of current aircraft. Typical values of particle parameters for an aircraft operating in the subsonic flight regime are given in Table II for two cloud types.

Table II Precipitation Particle Parameters [19]

Cloud Type	picn Coulomb	m <sup>§</sup>
Cirrus	1 - 10	2 x 10 <sup>4</sup>
Thunderstorm Anvil	1 - 35	5 x 10 <sup>4</sup>

Laboratory experiments involving the charging of projectiles fired through ice crystal clouds were conducted to determine the relationship between the charge acquired and the impact velocity. The results of these experiments indicate that the projec-

tile charge decreases with increasing velocity. These results were further verified by flight tests. It was noted that the observed effect might be caused by the melting of the ice crystals by the energy of the impact, since flight-test experience indicates that clouds composed of water droplets tend to charge an aircraft at a much lower rate than do clouds containing ice crystals. Thus, if an ice crystal is completely melted upon impact, greatly reduced charging would result.

The effective intercepting area, A<sub>eff</sub>, as been found to be affected by aircraft speed as well as body shape. The results of studies of water droplet impingement on airfoils indicate that the effective intercepting area of a typical aircraft would increase with speed [19]. The decrease of particle change and the increase of intercepting area with aircraft speed together predict the charging current shown in Figure 21 [19]. Because of ice-crystal melting, the figure shows that the charging rate decreases rapidly at speeds above 1500 mph. The maximum charging current occurs at about 1400 mph and is only 2.6 times the charging current at 600 mph. This result is highly significant in that it indicates that precipitation static problems on highly supersonic aircraft are not appreciably more severe than they are on subsonic aircraft.

CORONA — As the static charging increases, the electric potential of regions of the aircraft increases to the point that corona discharges take place. These discharges are in the form of a series of short pulses. The precise amplitude and time structure are a function of aircraft altitude and discharge point radius. Laboratory measurements of corona discharge indicates that at atmospheric pressure, the pulse repetition frequency is the order of  $10^5$  pulses per second when the discharge current is  $100\mu\text{A}$  [20].

The corona discharge noise spectrum has been measured by Vassilades [21] and Tanner and Nanevicz [22] from 500 kHz to 12 MHz as a function of altitude and discharge current. At high values of DC discharge current, the coronal noise spectral density varies as the square root of the discharge current. Oh, et al [23] extended the noise spectrum. Measurements were made up to 1 GHz and extrapolated to 10 GHz using theoretical predictions.

Figure 22 [23] shows some characteristics of this spectrum. Note that the low frequencies are a larger threat for high altitudes. This trend with altitude changes for higher frequencies. Above about 10 MHz,

higher noise levels are present for lower altitudes.

STREAMERS - When charge is deposited on dielectric surfaces such as radomes, windshields or composite material structures, it cannot flow freely to other parts of the aircraft because of the insulating character of these surfaces. If the potential between these surfaces and the main body of the aircraft becomes too great, a surface streamer discharge will occur.

The charge transferred by a single streamer discharge is 1 to 1.5 x 10-9 Coulomb. This is roughly the same as the charge transfer in a corona pulse. The difference in pulseforms produced by the two mechanisms results from the difference in the lengths of the two discharges. The corona discharge extends to only one tip radius from the burr or other imperfection from which it occurs. A streamer on the other hand extends many inches out on to the dielectric. This long discharge length causes the streamer to contain substantial low frequency energy.

Measured streamer noise spectra [23] are given in Figure 23 as a function of sample area. The noise spectra is proportional to area since the total charge stored and thus the discharge current is proportional to area. Measurements were made to 1 GHz and extended to 10 GHz as for the coronal noise spectrum.

COUPLING OF NOISE TO AIRCRAFT SYSTEMS -In general, noise sources on an aircraft are located in one place, and the affected antenna or system are located somewhere else. To calculate the interference to a system by a noise source, it is necessary to define the coupling between the source and problem system. Measurements have been made, for example, for a Boaing 707 and a helicopter. Using the measured coupling values, noise source spectra can be calculated and measured. Examples are shown in Figure 24 [20] for given source current levels. Note that both coronal and streamer noise levels are much larger than either daytime or nighttime atmospheric noise levels. Note also that for the helicopter spectra, the low frequency streamer noise is a factor of two higher than the coronal noise.

#### CONCLUSIONS

An atmospheric electricity threat covering the lightning and static electrification threats have been presented. The lightning threat level was compared to available current measurements.

Static electrification was characterized including both steamers and corona.

The lightning threat is based on ground-based direct current tower measurements. To more correctly assess the ground lightning threat, the available data sets (including Berger, Garbagnati, Uman, Eriksson, Clanos and Pierce and Popalansky) must be critically assessed as to accuracy and limitations. The earlier data (Clanos and Pierce and Popalansky) do not reflect the recent fast rise times measured and so are biased to smaller rise rates. Both tower current data and current values derived from field measurements are subject to uncertainties. These uncertainties need to be quantitatively assessed for use in an updated current threat level.

Static electrification threat levels may change in the future as new technology (fly-by-wire) and materials (graphite/epoxy, Kevlar, etc.) are used in newer aircraft. Charging rates and location of corona and streamers may change as well as the coupling to aircraft systems. As new technology aircraft are designed, static electrification threat levels will have to be updated.

#### RECOMMENDATIONS

atmospheric electricity threat directly affects aircraft protection. Uncertainty in the threat level imposes a penalty factor for all future technology (graphite aircraft. New muterials composite, Kevlar, etc), fly-by-wire flight control and increased systems integration introduce new requirements for protection. An accurate atmospheric threat level imposes the least overprotection requirements with consequent lower cost and weight penalties. The present uncertainty in the atmospheric electricity threat is estimated to be a factor of two from the present AEH threat definition. The only way to increase the accuracy of the threat is By obtaining more data. This objective can be accomplished in the following ways:

- 1. Airborne data collection. This is the most critical need for defining an airborne threat level. Flight tests should be continued to establish a future data base. This method is expensive and will not yield a large enough volume of data for many years. The immediate benefit would be better understanding of the interaction between naturally occurring lightning and aircraft in flight.
- 2. Ground strike current measurements. Continuation of studies similar to Berger, Garbagnati and Erikason on towers. The

towers need calibration to establish effects of the tower inductance and local ground impedance on the lightning current waveforms. Geographical effects on lightning could be established by a network of towers. Rocket triggered lightning experiments offer the advantage of near certain strikes.

3. Simultaneous measurements. This would allow correlation of fields, visual pictures of the stroke, and luminosity measurements as a function of time. These would help establish a more accurate means of deriving current parameters from field data. The pictures would establish orientation and tortuosity profiles. The luminosity data would establish the velocity of propagation more accurately.

本なる

- 4. Luminosity measurements. More data is needed to establish velocities of propagation near the ground as a function of distance away from the initiation point. Velocities are needed to establish more reliable means of obtaining current parameters from field data and for checking theoretical lightning models.
- 5. Reprocess the existing data base. The most effective way to establish a more accurate AEH threat is to compile and evaluate all existing lightning data to date. This approach could bring the uncertainty down to within a factor of two from the present AEHP threat. To analyze the presently available data more appropriately:
  - a. Raw data must be collected and experimental setups and limitations established from unpublished sources.
  - b. Quantify errors/uncertainties to put the experimental data on a common basis.
  - c. Derive the statistical threat levels from the total data base accumulated.

A complete lightning definition program would pursue all the items listed above as cost allowed. The most effective approach, however, is item (5). This approach also has the possible advantage of establishing future calibration needs for various types of experiments. This could lead to better quality data being obtained from future efforts to quantify haturally occurring electricity environments.

# REFERENCES

- 1. A. J. Eriksson, "Lightning and Tall Structures", Trans. South Afrikan IEE, 69, pt. 8, 238-252, 1978.
  - 2. M. A. Uman, private communication.
- 3. M. A. Uman, E. P. Krider, "A Review of Natural Lightning: Experimental Data and Modeling", IEEE EMC Transactions; p. 79-111, May 1982.
- 4. R. H. Golde, ed; "Lightning, Vol. I: Physics of Lightning", Academic Press, 1977.
- 5. K. Berger, R. B. Anderson, H. Kroninger, "Parameters of Lightning Flashes", Electra, 89, 23-37, 1975.
- 6. E. Garbagnati, G. B. Lopipard, "Lightning Parameters Results of 10 Years of Systematic Investigation in Italy", Proceedings of International Conference on Lightning and Static Electricity; Oxford, England, March 1982.
- 7. N. Cianos, E. T. Pierce, "A Ground Lightning Environment for Engineering Usage", Stanford Research Institute Technical Report, No. 1, Project 1834, August 1972.
- 8. F. Popolensky, "Frequency Distribution of Amplitudes of Lightning Currents", Electra, 22, 139-147, 1972.
- 9. M. A. Uman, D. K. McLain, R. J. "isher, E. P. Krider, "Currents in Florida Lightning Return Strokes", JGR, 78, 3530-3537, 1973.
- 10. C. D. Weidman, and E. P. Krider, "Fine Structure of Lightning Return Stroke Waveforms", JGR, 83, 6239-6247, 1978.
- 11. C. D. Weidman, and E. P. Krider, "Submicrosecond Risetimes and Lightning Return Stroke Fields", in Lightning Technology NASA Conference Publication 2128, FAA-RD-80-30, NASA Langley Research Center, Hampton, VA, 1980.
- 12. C. D. Weidman, E. P. Krider, M. A. Uman, "Lightning Amplitude Spectra in the Interval 100 kHz to 20 MHz", GRL, 8, 931-934, 1981.
- 13. Y. T. 'M. A. Uman, J. A. Tiller, R. D. Brantley, W. H. Beasley, E. P. Krider, C. D. Weidman, "Characterization of Lightning Stroke Electric and Magnetic Fields from Simultaneous Two-Station Measurements", JGR, 84, 6307-6314.

- 14. C. Baum, private conversation.
- 15. J. A. Tiller, M. A. Uman, Y. T. Lin, R. D. Brantley, E. P. Krider, "Electric Field Statistics for Close Lightning Return Strokes Near Gainesville, Florida", JGR, 81, 1976.
- 16. D. W. Clifford, E. P. Krider, M. A. Uman, "A Case for Submicrosecond Rise-Time Lightning Current Pulses for Use in Aircraft Induced-Coupling Studies", IEEE Symposium on Electromagnetic Compatibilty, San Diego, CA, October 1979.
- 17. F. L. Pitts, "Electromagnetic Measurement of Lightning Strikes to Aircraft", AIAA 19th Aerospace Sciences Meeting, St. Louis, Jan. 1981.
- 18. F. L. Pitts, M. E. Thomas, 1981 Direct Strike Lightning Data, NASA Technical Memorandum 83273, NASA Langley Research Center, Hampton, VA, March 1982.
- 19. J. E. Nanevicz, E. F. Vance, "Studies of Supersonic Vehicle Electrification", Lightning and Static Electricity Conference, 1970.
- 20. J. E. Nanevicz, "Static Electricity Phenomena: Theory and Problems", Conference on Certification of Aircraft for Lightning and Atmospheric Electricity Hazards, ONERA ~ Chatillon, France, September 1978.
- 21. A. Vassiliadis, "A Study of Corona Discharge Noise in Aircraft Antennas", AFCRL-TN-60-1107, Technical Report 70, SRI, 1960.
- 22. R. L. Tanner, J. E. Nanevicz, "An Analysis of Corona-Generated Interference in Aircraft", Proc. IEEE, 52, 1964.
- 23. L. Oh, G. C. Huang, R. Goldman, "Natural and Induced Electrical Effects on Integrated Antennas and Circuits at Frequencies to 10 GHz", AFWAL-TR-69-210, September 1969.

Table 1. Present Industry Lightning Threats

一個神殿を大学の意思である。 しょうなおまれ こうじょう 本で

		Single Stroke Lightning Parameters	ntning Parametan	
Present Lightning Standards	Maximum Rise Rate	Peak Current	Rise Time (µs)	Fall Time to Half Peak Value
	(kA/µs)	(kA)	(0 to Peak)	(87)
Initial AEH threat definition (severe)	200	200	4	95
Bosing severe (1% exceeding) (767/757 evionics)	200	200	4	8
MIL B-5087—Bonding, Electrical and Lightning Protection for Aerospace Systems (1978)	(100)	200	8	95
SAE Committee AE-41 (1978) and MIL-STD (1980)	901	200	8	99
NASA Lightsing Protection Criteria (JSC-07k36, Space Shuttle Guidelines, 1975)	(100)	200	8	S .

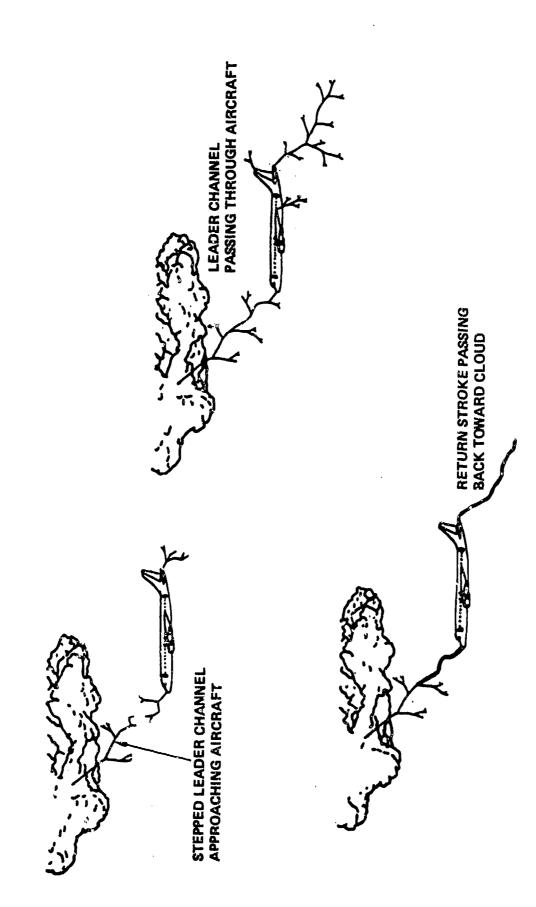


Figure 1. Lightning Flash Striking an Aircraft

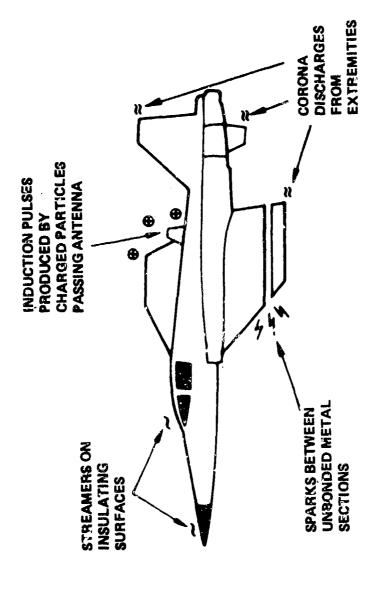


Figure 2. Noise Generation Sources

Variables	Range
• Duration of transient	50 - 5 <b>00</b> μs
• Inter-stroke time interval	10 - 100 ms
• Time duration of lightning event	0.01 - 2 sec
• Number of strokes	1 - 24

Figure 3. Multi-Stroke Threat

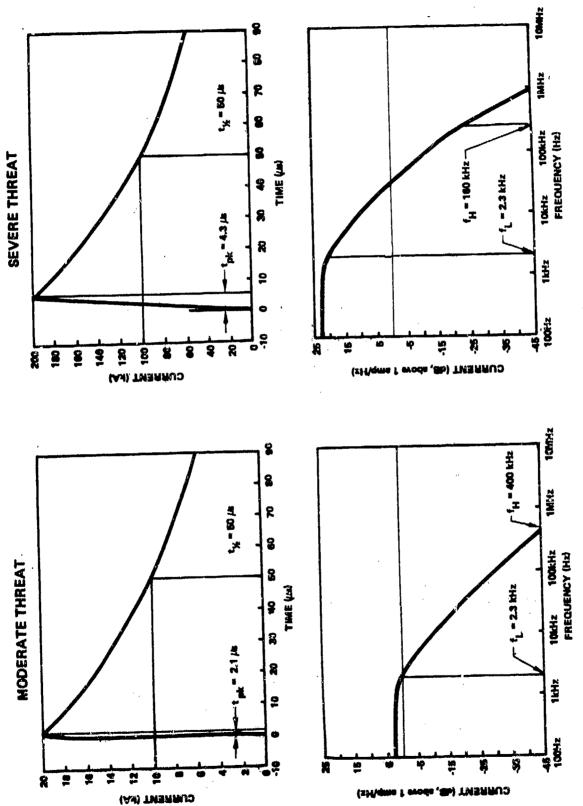


Figure 4. Single Stroke Threat Waveforms

50 µs

\$0 hs

 $I(f) = I_0(1/[a+j2\pi f]-1/[\beta+j2\pi f])$ Spectrum

Lower Turning Frequency Upper Turning Frequency 400 kHz 1.4 amps/Hz DC Limit

2.3 kHz

2.3 kHz

160 kHz

14 amps/Hz

Severe:

**Lightning Parameters** 

Action Integral	1.5 x 10 <sup>4</sup> amp <sup>2</sup> -sec	1.5 10 <sup>6</sup> amp <sup>2</sup> -sec
Peak Rate-of-Rise	$5 \times 10^{10}$ amps/sec	$2 \times 10^{11}$ amps/sec
Peak Current	20 kA	200 kA
	Moderate:	Severe:

Figure 5. Definition of Single Stroke Threat

Moderate:

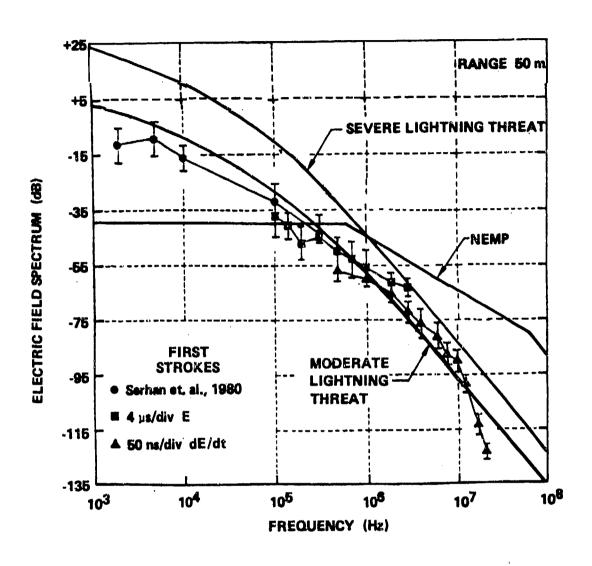
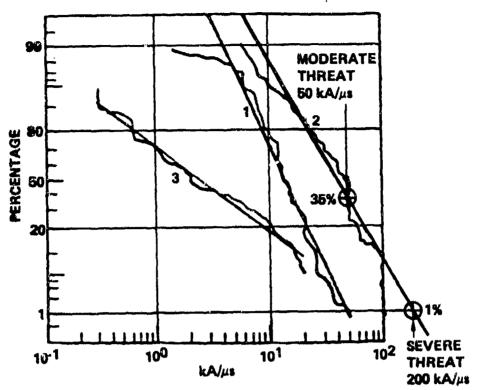
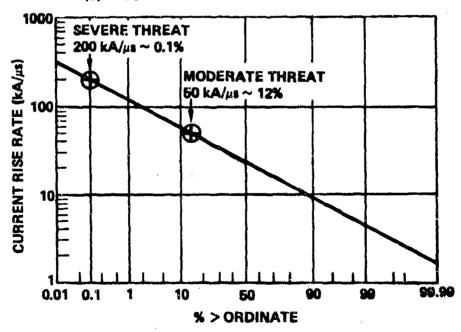


Figure 6. Comparison of Electric Field Data with Initial Threat Definitions



DISTRIBUTION OF MAXIMUM RATE OF CURRENT RISE-FROM BERGER, et al. (1975)

- (1) NEGATIVE FIRST STROKES
- (2) NEGATIVE FOLLOWING STROKES
- (3) POSITIVE STROKES

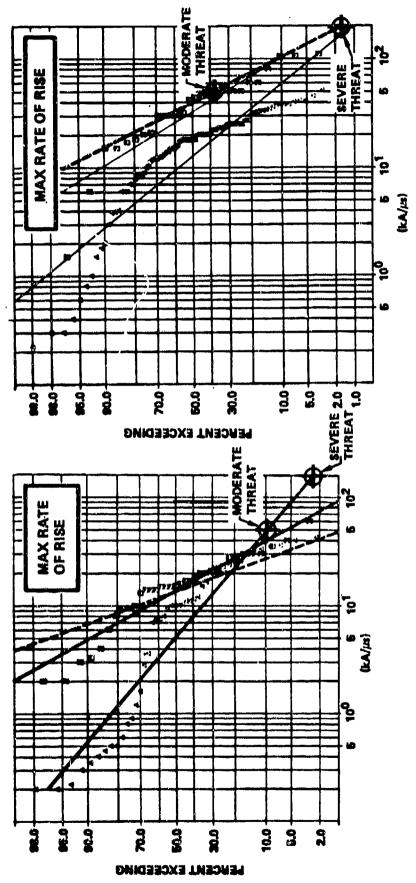


DISTRIBUTION OF AVERAGE RATES OF RISE FROM CIANOS & PIERCE (1972)

Figure 7. Comparison of Initial Threat Current Rise Rate with Available Statistical Data

☐ DOWNWARD STROKES

A UPWARD STROKES



(b) SUBSEQUENT STROKES

(a) FIRST STROKES

Garbagnati and Lopipard, 1982

Figure 8. Maximum Current Rise Rate

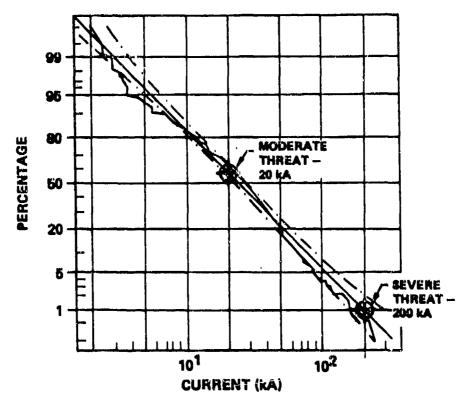
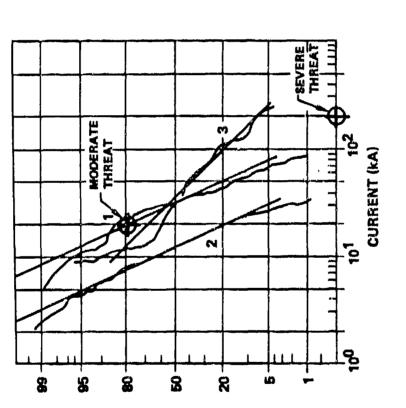


Figure 9. Current Amplitude Distributions



PERCENTAGE

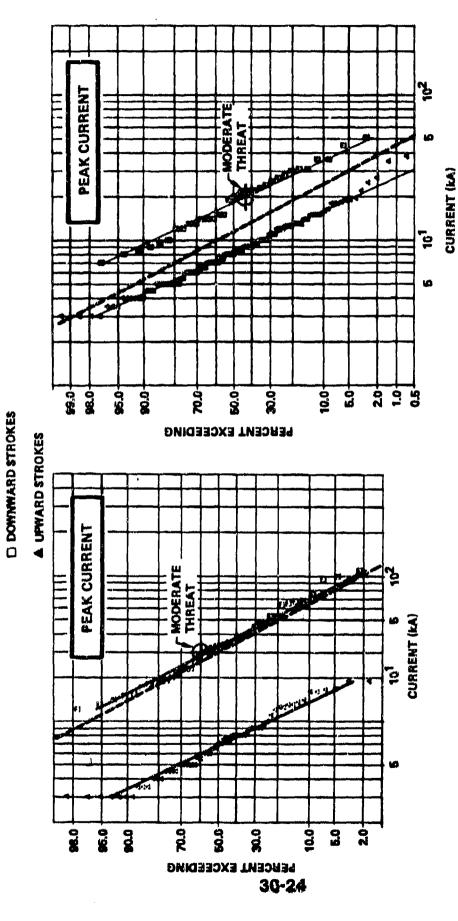
Figure 10. Current Amplitude Distributions

Negative first strokes Negative subsequent strokes

Positive strokes

**-**: ⋈ ⋈

36-23

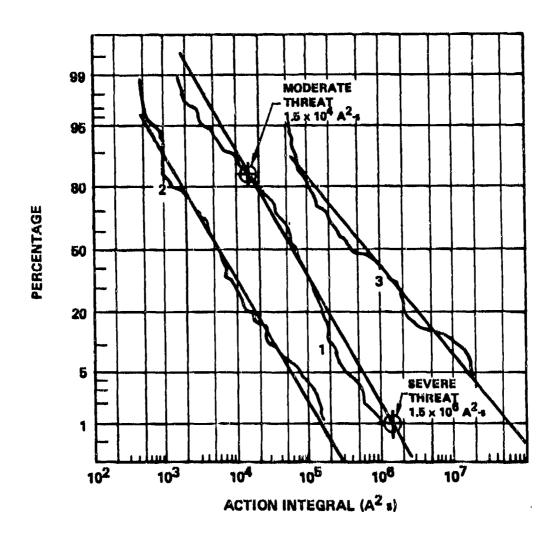


(b) SUBSEQUENT STROKES

(a) FIRST STROKES

Garbagnetti and Lopipard, 1982

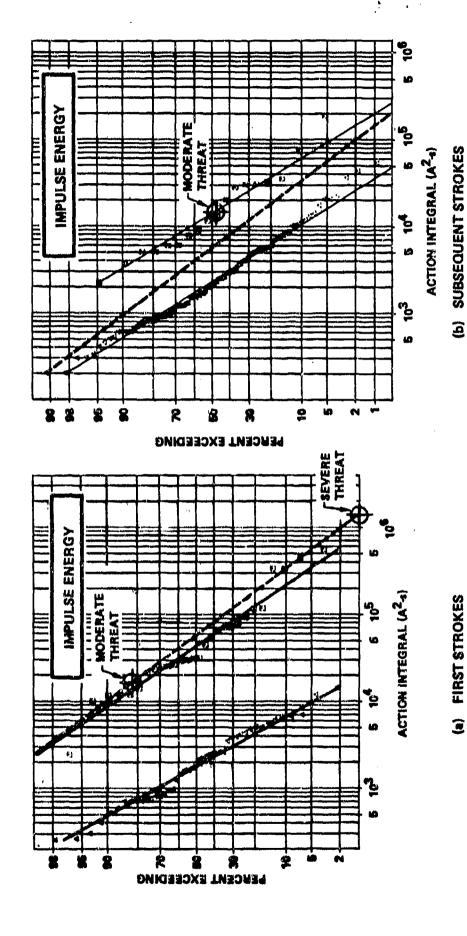
Figure 11. Current Amplitude Distributions



- 1. Negative first strokes
- 2. Negative subsequent strokes
- 3. Positive strokes

Berger, et. al., 1975

Figure 12. Energy Input Distributions

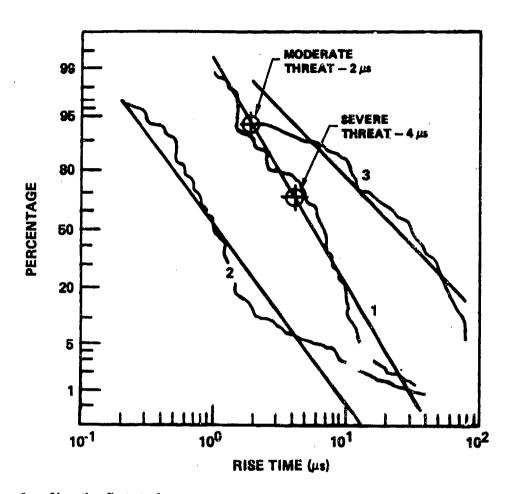


☐ DOWNWARD STROKES

A UPWARD STROKES

Garbagnati and Lopipard, 1982

Figure 13. Energy Input Distributions

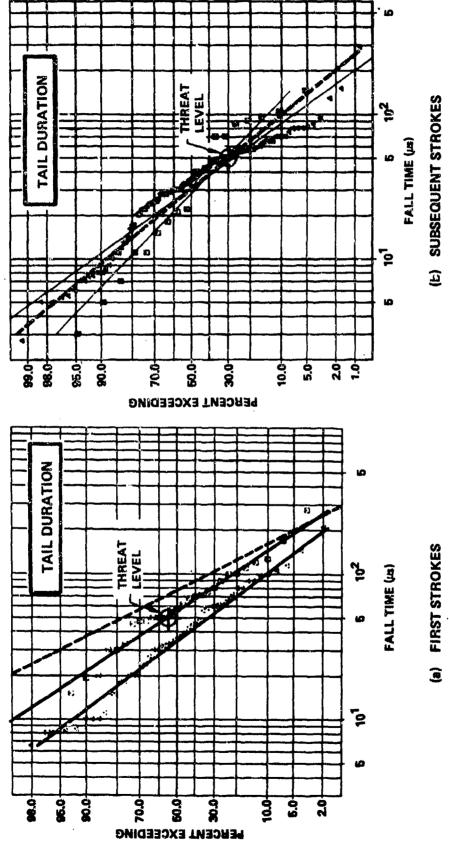


- 1. Negative first strokes
- 2. Nagative subsequent strokes

3. Positive strokes

Berger, et. al., 1975

Figure 14. Rise Time Distributions



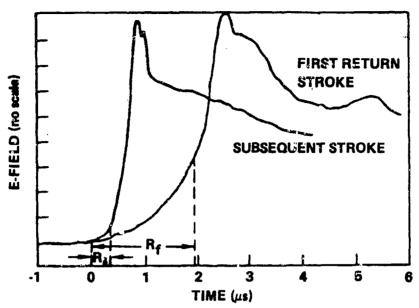
Garbegnati and Lopipard, 1982

Figure 15. Rise Time Distributions

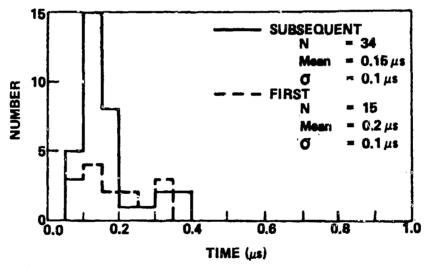
☐ DOWNWARD STROKES

▲ UPWARD STROKES

36-28

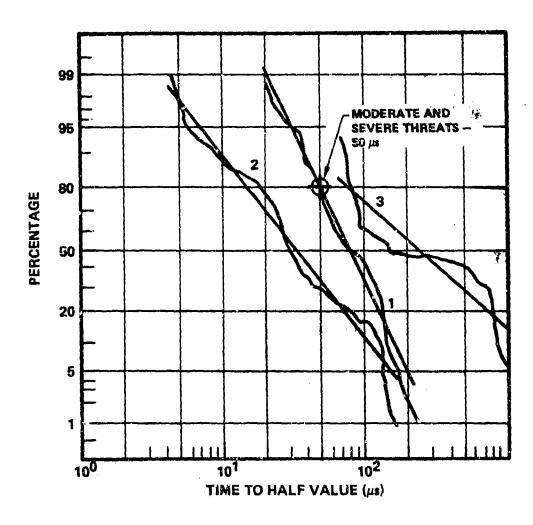


(a) CHARACTERISTIC OF FIRST RETURN STRO... FRONT RAMP ( $R_{\rm f}$ ) AND SUBSEQUENT STROKE FRONT RAMF ( $R_{\rm s}$ ) AS MEASURED BY WEIDMAN AND KRIDER (1978) E-FIELD AMPLITUDES ARE NOT TO SCALE. WAVEFORMS ARE BASED ON MEAN VALUES OF HISTOGRAMS.



(b) HISTOGRAMS OF THE 10 TO 90% RISETIMES OF THE FAST FIELD TRANSITION IN FIRST AND SUBSEQUENT STROKE FIELDS IN FLORIDA AT A DISTANCE OF 15 TO 30 km OVER SEA WATER.

Figure 16. New Data Suggestive of Very Fast Rise Times (< 1 µs)

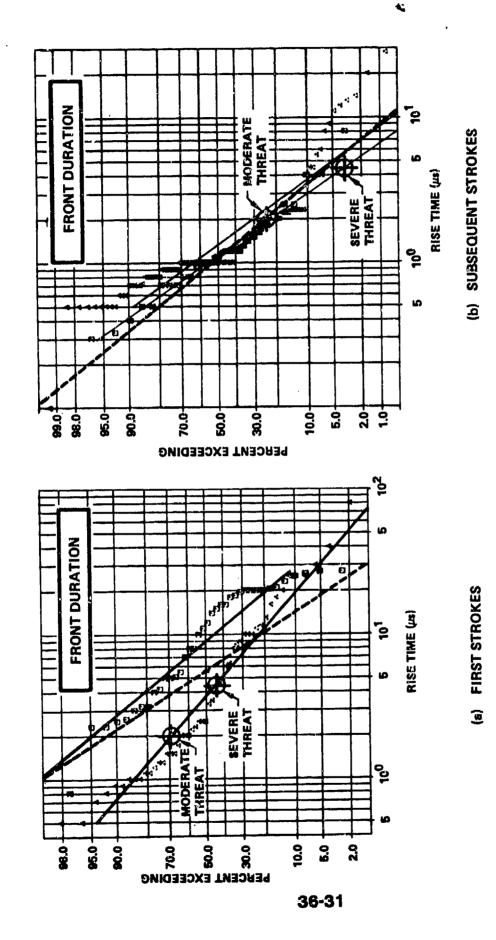


- 1. Negative first strokes
- 2. Negative subsequent strokes

Berger, et. al., 1975

3. Positive strokes

Figure 17. Fall Time to Half Peak



Garbagnati and Lopiperd, 1982

☐ DOWNWARD STROKES

A UPWARD STROKES

Figure 18. Fall Time to Half Peak

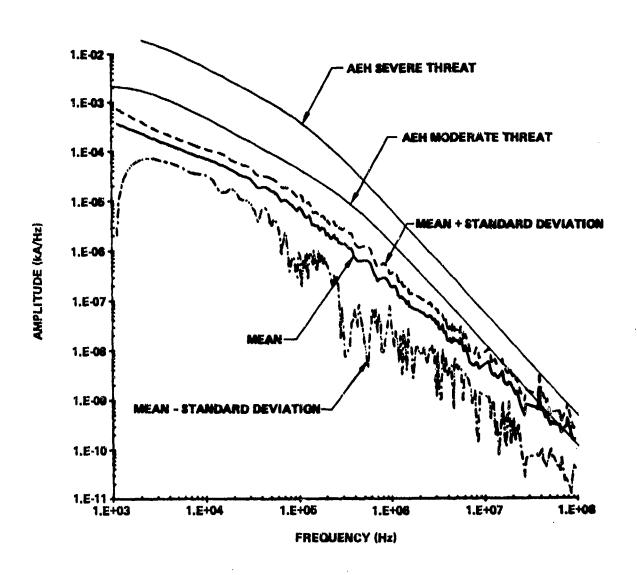


Figure 19. F-106 Statistics (Eleven Events)

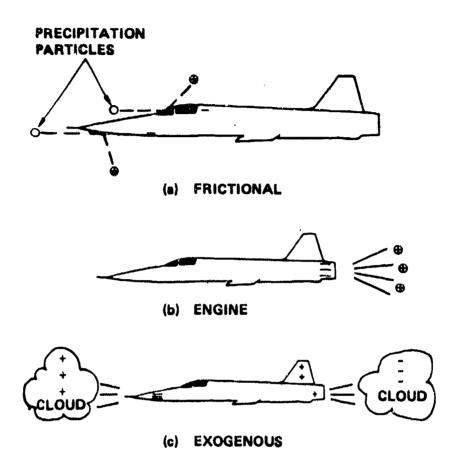


Figure 20. Charging Processes

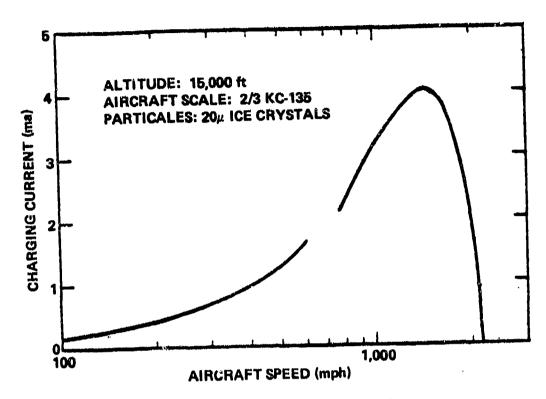


Figure 21. Predicted Charging Current for Advanced Aircraft

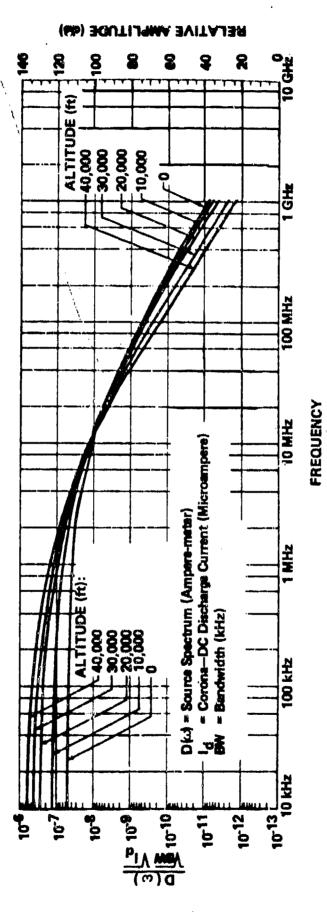


Figure 22. Measured Corona Noise Spectra

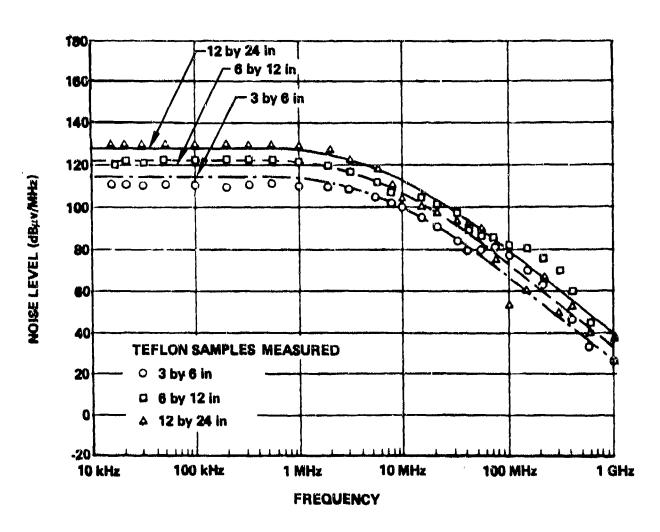
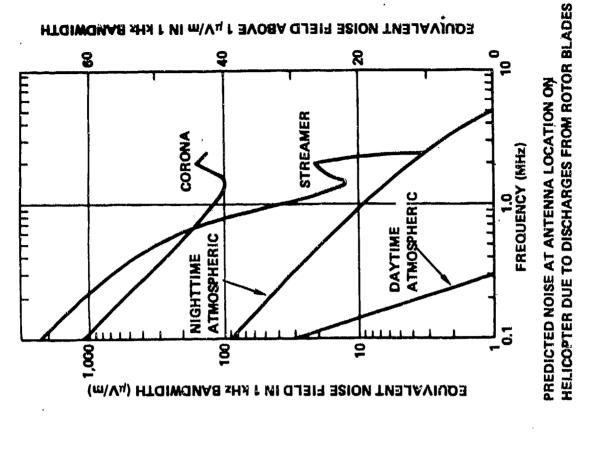


Figure 23. Streamer Noise Spectra — Messured and Calculated



O

0

MEASURED NOISE WITH

8

TOTAL CHARGING

CURRENT = 360

8

100

OTA!LCAP OBELLY I = 3.5 mA

PREDICTED

BELLY-

NOISE T

ATMOSPHERIC

DAYTIME

一年 とっま

PREDICTED
TAILCAP ...

( = 3.5 mA

I = 360 μA

1,000

3,000

Figure 24. Measured Coronal and Streamer Noise

CORONA DISCHARGE NOISE IN 707 ANTENHAS

FREQUENCY (MHz)

ATMOSPHERIC

NIGHTTIME

I = 350 μA

1

8

Equivalent moise field in 1 has bandwidth ( $\mu V/m$ )

# AD P002192

LIGHTNING STRIKES TO AIRCRAFT OF THE GERMAN FEDERAL ARMED FORCES

 $\rightarrow$ 

By

# Wilfried Ziogler

Bundesant für Wehrtschnik und Beschaffung Leiter des Musterprufwesens für Luftfahrtgerät der Bundeswehr (BWB-ML)

(Federal Office for Military Technology and Procurement Director of Aeronautical Equipment Qualification for the Federal Armed Forces)

#### ABSTRACT

A survey is given of the lightning strikes to aircraft of the Federal Armed Forces over the past 10 years, from 1973 until 1982, inclusive. About 80% of the lightning strikes involved the following 4 types of aircraft: F-104 C Starfighter, F-4 "Phantom", C-160 "Transall", BR-1150 "Breguet Atlantic." For these 4 types the annual rates of lightning strikes as well as the respective average rates over these 10 years are shown. The main locations at which lightning attached to the aircraft and damage sustained are described. Two lightning strikes are discussed in greater detail. In the one case a UH-1 D was struck during flight, and in the other case it was a Phantom where the metal wall of one wing pylon tank was malted through. Finally, the paper touches briefly on problems that are expected to result from the greater use of CFC for the airframe, the increasing employment of computers, and the electrical transmission of essential control signals.

LIGHTNING STRIKES to aircraft basically cannot be prevented, hence the individual aircraft must be adequately protected against the effects of lightning.

In a thunderstorm environment the most prevalent electrical discharge is by intracloud flashes, and only about 25 % of lightning discharges to the ground (1)\*.

Reliable measurements of the electric characteristics are available only for these claud-

to-ground flashes.

An aircraft, however, may be struck by both forms of lightning. Therefore, only analysis of a fairly large number of natural lightning strikes to aircraft allows a complete assessment of the effectiveness of lightning protection measures. If such analyses cover a longer period of time, significant findings will be gained in addition as to the rate and severity of natural lightning strikes as well as important information on possible shortcomings within lightning protection, e.g. from vibration or corrosion effects which become evident only after a fairly long in-service time of the respective aircraft.

The following data and experience gained in more than 10 years of flight operations are intended to serve as a basis to this effect.

# LIGHTNING STRIKE RATE

All reported lightning incidents have been systematically investigated and evaluated according to uniform criteria since 1975. The first lightning incidents investigated at BWB-ML date back to 1962 and concern the F-104.

From 1973 until 1982 a total of more than 260 lightning strikes have been reported about 80 % of which involved the following aircraft types:

F-104 G/TF-104 G "Starfighter"

RF-4E/F-4F "Phontom"

-Fighter/Reconnaissance Aircraft (Mach 2+)-

C-160 "Transall"
-Transport/Cargo Aircraft-

BR-1150 "Breguet Atlantic"
-Long-Range Sea Reconnaissance
Aircraft-

These 4 aircraft types are subsequently referred to in short as F-104, F-4, C-160, and BR-1150.

For these 4 types the lightning strike rates per year related to the respective flying hours and landings in that year are shown in the following Figures 1 and 2.

\*Numbers in Parentheses designate References at end of paper.

For all 4 aircraft types together it becomes apparent that the rate of lightning strikes related to landings is higher than that related to flying hours. This means that on an average more than one flight hour lies between two landings.

The great variation of the strike rate from one year to the next has no discernible relation to the number of flying hours.

Between two successive years aside from a few exceptions the number of flying hours or landings varies by ± 10 % from the respective previous value. The number of lightning strikes, in contrast, varies 5 to 6 times from one year to the next.

Thus, for example, the number of flying hours for the F-104 (Figure 1) went up by approximately 10 % from 1976 to 1977 and then went down by about 6 % from 1977 to 1978. At the same time, however, the number of lightning strikes rose by 450 %, and then dropped by 46 %. On the other hand, the number of flying hours for the F-4 aircraft increased in each of these years whereas the number of lightning strikes first dropped by 20 % and then rose by 75 %. For both types of aircraft 1980 was one of the years with the lowest number of lightning strikes, whereas in 1981 the second highest number of lightning strikes was experienced since 1973.

With respect to the C-160 -see Figure 2-, in contrast, the situation is balanced. Since 1977, the number of lightning strikes has varied by only ± 20 % max. from the respective previous value.

For the BR-1150 (Figure 2), the number of flying hours as well as the lightning strikes per year are such lower as for the other types shown in Figures 1 and 2, so that already one lightning strike has a significant influence on the strike rate.

At this point in time no definite statement can be made yet as to why there are such differences in the rate of lightning strikes between individual years in some cases. Figures 1 and 2, however, clearly show that the evaluation of lightning strikes in one single year may easily be misconstrued and lead to erroneous conclusions. Even analysis of 2 to 3 years of experience may lead to a distorted picture.

Figure 3 shows the rates averaged over a period of 10 years for the 4 types of aircraft. The differences which become evident here are attributable to the different mission conditions in each case; the influence of individual years becomes less important. The F-104 and F-4 aircraft are subject to comparable conditions; in particular, however training activities allow the meteorological conditions to be taken into account to a large extent. The respective tasks of the C-160 and EE-1150, on the other hand, do allow no or only little consideration of the

meteorological conditions with respect to possible lightning events. It becomes evident that the selection of the reference magnitude for such strike rates is quite important, as the rates related to landings are comparable for both C-160 and BR-1150, but not those ,

related to flying hours.

The lightning strike rates plotted in percent against the flight level in Figure 4 are close together for all 4 types of aircraft. The differences between the individual aircraft types cannot be definitely assigned to specific causes, the statistical basis still being too narrow. But even the extremely few lightning strikes to the BR-1150 (less than 10) fit in well. From Figure 4 it can be generalized, however, that -irrespective of the type of aircraft, type of propulsion, mission, and geographical location of the training area- the flight level is an essential factor with respect to the probability of lightning strikes. This fact receives increased emphasis when a comparison is made of the flying hours accumulated by the 4 types of aircraft over a period of 10 years (rounding ± 10 % max.): BR-1150 : C-160 : F-4 : F-104 -1 : 4 : 7 : 10: these relations do not become evident at all from Figures 3 and 4.

## ATTACHMENT POINTS AND DAMAGE

ATTACHMENT POINTS - The evaluation of the more than 260 lightning strikes has clearly confirmed the findings gained to date on the distribution of the lightning flash attachment points on the surface of aircraft as well as the resulting subdivision into the known aircraft zones.

For the F-104, F-4, and C-160 aircraft the number of lightning strikes reported within the last 5 years (1978 - 1982) alone is sufficiently large to make a statistically significant statement.

The evaluation of both F-104 and F-4 together shows the following results:

- More than 60 lightning strikes.
- Attachment points were detected in about 80 % of the cases on pitot and radome, about 35 % of the cases on wing tips, including tip tanks, about 32 % of the cases on the hori-
- zontal/vertical tail.

  In some cases no definite attachment points were detectable, or none of the three zones was affected.
- In 11 cases the aircrew felt electrical or mechanical shocks.
- In 4 cases the aircrew did not become aware of the lightning strike during flight.

The results for the C-160 aircraft were as follows:

- Nore than 45 lightning strikes.

- Attachment points were detected in about 43 % of the cases on the radome, about 36 % of the cases on the wings, about 28 % of the cases on the horizontal/vertical tail.
- In some cases no definite attachment points were detectable, or none of the three zones were affected.
- In one case the aircrew felt an electrical shock.
- In one case the lightning strike was not noticed by the aircrew during flight.

In these 5 years some a/c were hit several times:

F-104 1 4/0 2 times each 2 1/0 F-4 3 m/c 2 times each 8 times C-160 1 a/c 3 W/O 3 times each 6 a/c 2 times each BR-1150 2 m/c 2 times each

Summarised in a somewhat different way:
Considering the F-104 and F-4 sircraft together, 6 a/c were hit by 13 lightning strikes, or about 1 % of the fleet by approximately 23 % of the strikes. As to the C-160 aircraft, 10 a/o received 29 lightning strikes,
or about 11 % of the fleet approximately 64 %
of the strikes.

DAMAGE - About 90 % of the lightning strikes analyzed can be classified as normal cases, and they can be described as follows:

- The aircrew become aware of the lightning strike, e.g., as lightflash, bang, or shaking of the aircraft, but immediately following the strike no hazardous irregularities or damage regarding aircraft systems are noticed during flight, and the aircraft is subsequently landed without problems.
- The subsequent special inspection of the aircraft shows melting marks at the attachment points typical for metal surfaces, and occasionally, destroyed navigation lights, static dischargers or antennas.
- Frequently the navigation compass shows a deviation, but all systems including the aircraft electrical system function properly. This description also applies to lightning strikes not noticed by the aircraw during flight and detected only during postflight inspection.

In the remaining 10 % of the cases considerably more severe damage caused directly by lightning is found. Damage custained includes: punctures or cracks in metal surfaces, disrupted skins, electrical breakthrough in the radome wall, explosive vaporization of diverter strips on the radome and physical damage to the radome wall, burnt-through or mechanically broken grounding conductor tube between pitot and fuselage, as well as failed and partly damaged electronic equipment. But even in such cases the damaged aircraft was able to land.

Such severe damage occurs more often than would be expected in view of the respective lightning protection designs. This leads to the question whether the incidence of extremely severe lightning strikes really is not considerably greater than hitherto suspected, requiring a new discussion and determination of the present 1% probability (limit values (1) at:

Peak value  $i_{max} > 200 \text{ kA}$ , Current steepness  $\frac{di}{dt} > 100 \frac{\text{kA}}{\text{uS}}$ , Electric charge  $Q = \int idt > 400 \text{ As}$ , Specific energy  $W = \int i^2 dt > 10^7 \text{ A}^2 \text{s}$ ).

#### EVALUATION OF LIGHTNING PROTECTION

In the following paragraphs, an evaluation is made of the lightning protection of the F-104 F-4, and C-160 on the basis of experience gained to this date.

F-104 AIRCRAFT - Since the introduction of lightning protection on the radome (bonding of the pitot to the fuselage by a copper grounding conductor tube, with an electrically effective cross-section of about 50 mm<sup>2</sup> and the pitot heater wire threaded in the tube) and installation of surge protection in the pitot heater wire, no more problems have

been experienced with lightning.

F-4 AIRCRAFT - Here the situation is similar to that of the F-104. The RF-4E lightning protection system, however, has a

ning protection system, however, has a threaded joint with adverse electrophysical characteristics at the rear end of the aluminum grounding conductor tube between pitot and fuselage resulting in abrupt changes of the surge impedance. This in turn causes arcing in the threaded joint along with the danger of flashover in the radome. Therefore these items must be replaced after a lightning strike. Hence the system is not maintenance-free. In the F-4F such problems have been avoided in that the tube end transits into a flat plate which is electrically well bonded to the fuselage. This system is maintenance-free. Experience has shown, however, that both aircraft can be considered lightning hardened, the RF-4E though only with respect to one lightning strike at a time.

C-160 AIRCRAFT - As no pitot is mounted on the C-160 radome, 4 diverter strips of approximately the same length are symmetrically arranged on the exterior of the radome (top L/h and R/H, bottom L/H and R/H) extending about 2/3 forward. They have a width of 20 mm and a maximum thickness of C.14 mm, i.e., a cross-section of about 2.8 mm<sup>2</sup>. Experience gained so far has shown that these metal foil strips are unsuitable from the flight-operational and mission points of view.

In the investigations and tests from approximately 1965 on, the lightning current values assumed were too low, and as a conse-

quence the assessment indicated that this cross-section of 2.8 mm<sup>2</sup> diverts 93% of all strikes without damage to the diverter strip itzelf. A hazard to the radome from lightning effects hence was to be expected on an average only once in 10 years related to 100 aircraft.

Actual experience since 1971, however, looks different. Several times a year radomemounted diverter strips sustain severe damage at the attachment points of a lightning flash so that repair becomes necessary; once or twice a year the diverter strip is vaporized explosively as the lightning current flows through; the effect is similar to that of a linear explosive charge with the radome becoming mechanically disrupted along the strip over length up to 30 cm. The cause of these secondary effects is the method used to fasten the diverter strips on the exterior of the radome: They are glued on, in addition covered with a thin fiberglass fabric and coated with an elastic protective layer of low electrical conductivity. Repairs, therefore, may only be made at the manufacturer's plant as this cover, if it should turn out too thick, has the same effect as the confinement of an explosive charge.

It is true that such diverter strips are adequate for lightning flashes of small to medium charges or low to medium currents, but the protective effect may be reversed in the case of severe lightning strikes. Flight operations and missions are greatly impeded by the indeed frequently necessary repairs. On the other hand this type of aircraft is quite invulnerable to the effects of lightning as experience shows, and in all cases so far the aircraft, even after severe lightning strikes with serious damage to the radome, was perfectly controlled and landed.

Thus, although the lightning protection provisions on the radome show considerable design shortcomings the risk for this type of aircraft in lightning events is considered tolerable.

# TWO PARTICULAR INCIDENTS

Of the lightning incidents that occurred in the past 5 years, two extraordinary cases are reported below.

LIGHTNING STRIKE UH-1 D - This concerns the first definitely verified in-flight lightning atrike to a Federal Armed Forces helicopter. The aircrew noticed an explosion-like bang and simultaneously a glaring flash. After the emergency landing which was immediately initiated and successfully completed, and in the course of subsequent investigations, the following damage was detected:

 Main rotor blade red: Skin delaminations (about 15 cm²) on blade tip, skin delaminations on trim tab and close beside it;
 Tail rotor blades: Melting and burn marks on blade tip.
The following assemblies were out of tolerance or exhibited damage:

- primary and secondary converter

- RPM warm box
- gyro amplifier
- C 6 H indicator

- antenna of SAR intercom system.

Initially the strike was classified as not severe as the visible damage to the main rotor blade was minor, and the visual inspection of the transmission system and the flight control system disclosed no further lightning marks. The main rotor head was replaced because of the vibrations that occurred after the strike, and shortly thereafter the three hydraulic actuators for cyclic and collective pitch were replaced as well becau-

se of leakage.

The subsequent investigation of the main rotor, cyclic and collective pitch hydraulic actuators and swash plate (the latter was replaced after some further flying hours because of too high frictional resistance) along with the investigation results of the main rotor blade which had been disassembled in the meantime showed a different result: The charge transferred by the lightning discharge was about 10 times higher than was obvious from the slight damage to the main rotor blade that was visible or otherwise detectable from the exterior; so the helicopter was hit by a lightning strike of medium severity which caused direct and secondary damage to essential major assemblies of the aircraft. In the main rotor biade the conductive aluminum honeycomb structure was burnt through at several places and also showed a lot of small arc erosion points due to the high current density, though an aluminum erosion edge extends over the entire blade length which would normally provide sufficient protection against a high lightning current. Small arc erosion points were detected on the raceway surfaces of the swash plate ball bearing. During the next few operating hours of the bearing the resulting loads caused individual balls to be heated to high temperatures up to the tempering color range, with the consequence of excessive frictional resistance of boaring. Current marks also existed in several further contacting surfaces in the rotor head, where bolted joints, bushings, and bearings were involved.

The experience gained from this kind of lightning incident which was the first of its kind to occur in the Federal Armed Forces, is

as follows:

In sandwich-type components, while visible damage appears to be minor, there may exist severe hidden damage - without detailed investigation no assessment can be made of the severity and extent of the damage. The same applies to complex mechanical assemblies such as the rotor head.

LIGHTNING STRIKE F-4F - This lightning strike is an example of the fact that even severe in-flight strikes need not necessarily be noticed as such by the aircrew.

'n

As regards the attachment points, this strike represents a "normal" case, i.e., they were found on pitot, fuselage top and bottom, vertical tail light, engine R/H nozzle flaps and R/H wing pylon tank. However, the hole of about 3 x 10 mm in the wing pylon tank and the spots immediately beside it where an extreme amount of metal had melted away were unusual. The total charge transferred here was entremely large ( > 200 coulombs) and was spread over several attachment points.

Up to now the wall of such an auxiliary tank was deemed sufficiently safe against lightning, but this assumption must be corrected at least for lightning flashes with extremely large charges below the 1 % probability of occurrence. This incident, however, is the only case so far known at BWB-NL where such a tank wall had melted through.

#### FUTURE PROBLEMS

Two sectors can be foreseen at present where in the immediate future considerable problems will arise in connection with lightning protection measures:

- Use of fiber reinforced plastic, e.g., increased use of large-surface structures made of CFC and GFEP

Electronics growing more and more complex and with components with increasingly larger-scale integrated circuits as well as increasing takeover of control and monitoring functions by on-board computers.

The lightweight metal construction so far used for aircraft constitutes a structure of continuous electrical conductivity which will not be damaged even by extremely high lightning currents - except for the spots of melted-away metal in the lightning attachment points.

On such a structure the lightning current can disseminate quite uniformly so that the interior of the fuselage, wing and tail remains largely free of the magnetic field of the lightning current. In addition, the metal structure greatly damps the effects of electromagnetic fields into the aircraft.

When increasing use is made of largesurface fiber-reinforced structures adequate
conductive paths for the conduction of the
lightning current must be provided for in
the design, particularly if the fiber layers
in the plastic are conductive. In such cases
it must even be ensured that no current flows
through the fibers as otherwise current-dependent local overheating of the fibers occurs which may result in delaminations and
consequently in a reduction of the component
strength without any damage being identifiable from the outside. Furthermore, the

shielding effects against electromagnetic fields are lower, i.e., voltages are more easily induced in electrical lines (in the aircraft electrical system as well as in data and control circuits).

This leads directly to the second complex of problems mentioned, i.e., the increasing use of solid-state components and large-scale integrated circuits, and employment of on-board computers. Already in the case of metal constructions presently in use additional measures, such as against induced voltages, are required. Such induced volt ges may cause not only (temporary and pernent) damage to components, but they may also simulate control or signal impulses in the respective circuits thus triggering faulty reactions in the on-board computer or in systems - for example when operating the control surfaces electrically (fly-by-wire).

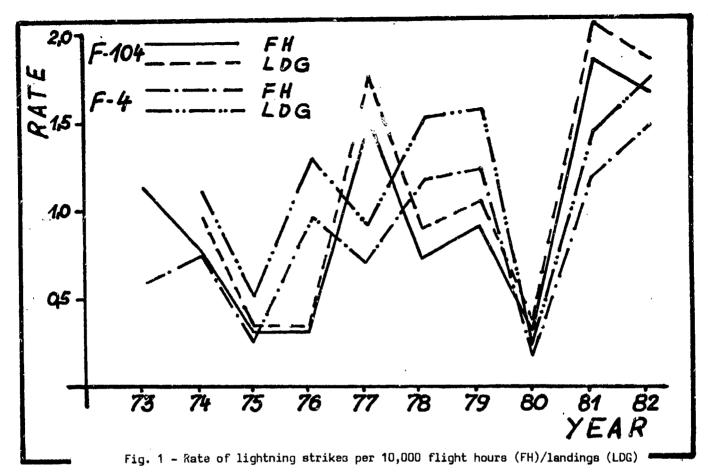
Knowledge acquired so far in solving lightning protection problems can be applied only to a very limited extent to these two complexes of problems touched, so that, besides the necessary laboratory tests, continual experience and findings regarding the effects of in-flight natural lightning strikes to aircraft must be collected and evaluated on a larger basis in the future.

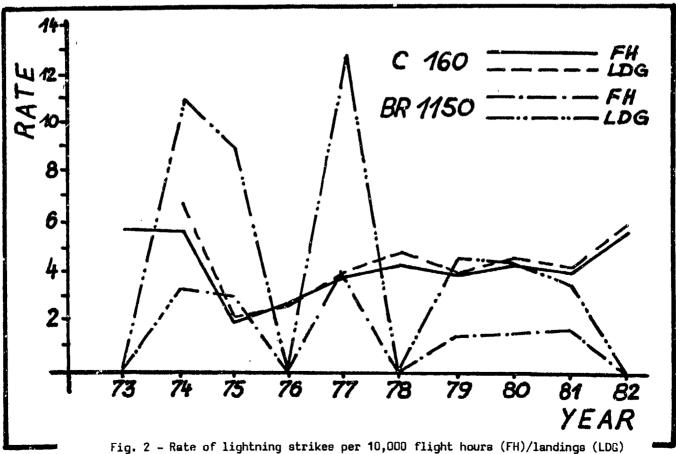
## ACKNOWLEDGEMENT

The author wishes to acknowledge the help of Mr. M. Schirp, of BWB-ML, in collecting data reported herein and preparing the graphs.

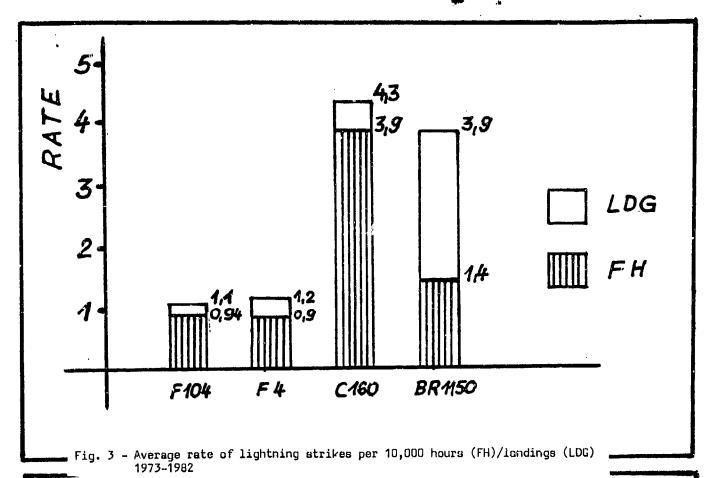
# REFERENCE

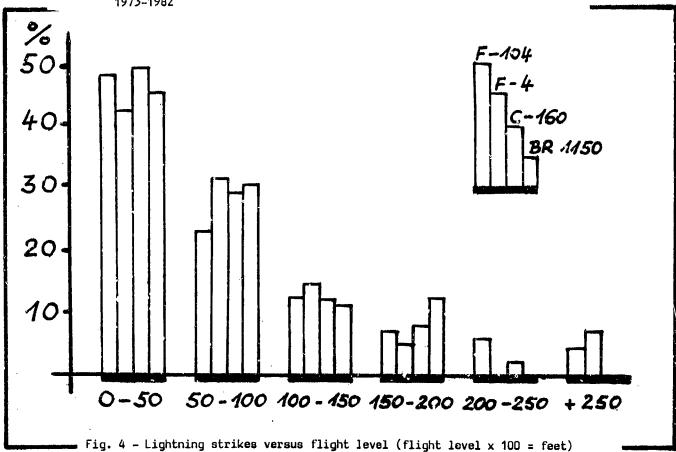
(1) Prof. Dr.-Ing. H. Baatz,
"Mechanismus des Gewitters und Blitzes Grundlagen des Blitzschutzes von Bauten."
VDE-Schriftenreihe 34.
VDE-Verlag imbH, Berzin 1978.
("Mechanism of thunderstorm and lightning Fundamentals of lightning protection of
buildings.")





ガスターニア はない 日本語の音楽 (Managaran Angaran Angaran







Effects of Simulated Lightning Current on the Tensile Strength of Graphite/Epoxy

> By William E. Howell NASA Langley Research Center Hampton, VA

#### ABSTRACT

A literature search reveals a very limited number of reports on structural tests of composite materials after a simulated lightning strike. The depth of damage for strikes of given "action integral" values has been reported, but these data do not define the structural strength degradation caused by a lightning strike. Therefore, an investigation of the strength degradation caused by strike currents was conducted.

This paper presents experimental data on the strength degradation of graphite/epoxy (Gr/Ep) caused by currents representative of lightning strikes. Tests were made on eight-ply laminates, fabricated from tape, in two ply orientations: unidirectional, (0), and quasi-isotropic, (+45,-45,0,90)<sub>8</sub>. Specimens machined from the laminates were exposed to test current and then tested to failure in tension. The data were used to determine the current density required to cause strength degradation.

The effects of moisture content and mechanical load on the strength degradation caused by test current were inventigated with quasi-isotropic specimens. Specimens of three moisture contents were tested: dry, intermediate and saturated. The quasi-isotropic laminate was chosen for the moisture tests because the effects of matrix degradation are readily detectable. For the mechanical load tests, the specimens were loaded in tension to a specified strain, exposed to current, and afterward tested to failure in tension.

Data obtained in the :resent investigation are compared on the basis of "action integrals" to previously reported data on the effects of simulated lightning strikes. The onset of significant strength degradation is compared to visual determination of ply penetrations. Also, data from the present investigation are used to define the area of structural damage to a laminate of unit thickness. This information should be useful in judging if a composite structure requires repair and the area needing repair.

This paper was not available for incorporation into this book. Therefore, it will be published at a future date.

# AD P002193

RECENT LIGHTNING INDUCED VOLTAGE TEST TECHNIQUE INVESTIGATIONS



Keith E. Crouch Lightning Technologies, Incorporated, Pittsfield, Massachusetts

#### ABSTRACT

Lightning induced voltage testing has evolved over the past several years. Recent efforts into investigating the cause/effect relationships associated with technique procedures has generated a better understanding of test circuit behavior.

The aircraft under test must have a spaced set of return conductors around the aircraft to maintain a realistic electromagnetic field condition. The aircraft, the return conductors, and the facility where the tests are conducted form sets of short transmission lines. The travelling waves propagate in a transverse electromagnetic (TEM) mode at the speed of light. However, due to reflections and refractious at the junctions of different impedance sections of the aircraft (i.e., wing and tail attachments) the bulk of the wave energy travels distances considerably farther than the nose-to-tail dimension. Consequently, the wave appears to take longer to reach the tail, which had been interpreted as a slower propagation velocity.

Travelling electromagnetic waves reflecting and refracting on the aircraft transmission lines control the response of the system during the initial few microseconds of the test. For slowly rising test current waves, (> 5 (15)) the transmission line characteristics of the test circuit can be ignored. At current risetimes of 1-5 (15), the aircraft can be represented by a single impedance transmission line which can be terminated in a characteristic resistance. At very fast risetimes (< 0.5 (15)) the aircraft system looks like a connected set of short transmission lines of different impedances. In the limit, the system itself will govern the current risetime which can be injected due to the reflection/refractions and the low pass filter characteristics of the system. With present configurations, current risetimes faster than 100ns do not appear possible.

=(microsec)

#### BACKGROUND

More and more flight critical control functions are being performed by solid state electronic systems. The effects of adverse environments on the systems has been of concern. One of the more potentially damaging environments is generated by lightning strikes to the aircraft. In addition to using micro-circuitry, many new high performance aircraft utilize advanced composite structural materials which can increase the electromagnetic levels around the aircraft electrical wiring system.

These potential problems are not aw and NASA sponsored efforts to understand and develop test techniques to measure lightning induced voltages were started almost 15 years ago. This work identified two areas of need, 1) an analytical technique which could be applied during the aircraft design phase to reveal potential problems and 2) a non-destructive test technique to verify that the aircraft met its design goals. Further work in the first areas has been carried out by a number of investigators from various organizations.

NASA sponsored work in the second area resulted in the Lightning Transient Analysis (LTA) test which has been applied to several aircraft systems. Work is still needed in both areas since the efforts to date have not resulted in techniques which are widely accepted. The work reported in this paper is in the second area.

Before exposing new aircraft systems containing advanced composite structural materials and solid state micro-circuit controls to inflight lightning, it is desirable to have some assurances in the form of test data available to indicate that the systems will survive.

The original non-destructive test technique (LTA) was published in 1974(1)\*. Measured induced voltages were extrapolated to full threat level using a ratio of the applied peak current to a selected threat level (30kA or 200kA). The applied current waveshapes were chosen to fit the average and severe current models generated by the Cianos and Pierce data. An average stroke of 30kA peak and 22kA/us rate of current rise can be represented by a current pulse rising to crest in lus. A severe stroke of 200kA peak, 100kA/us can be extrapolated from a current pulse with a 2us crest time. Data obtained from these tests showed that the peak induced voltages, especially in single point ground circuits, occurred in the first 1/2µs, considerably before the crest of the applied current (usually at 2µs). This apparent lack of correlation between the stimulus and the response caused many to question the validity of the test.

To investigate the fundamental cause/effect relationships, NASA funded further efforts in technique evaluation. The results of those efforts are contained in NASA CR 3329, 1980 (2), and LT-82-132, 1982 (3). This paper summarizes part of the work covered in those reports.

#### TEST CIRCUIT RESPONSE

The LTA test technique does not stipulate the circuit return conductor configuration. Early tests were conducted using a single return wire, usually laid under the center line of the aircraft (4). As the effects due to return wires were recognized, the returns were split and routed around the perimeter of the aircraft (5). Later work indicated that the return wires should be distributed around the aircraft in a pattern which follows the electric field lines (6). All of these changes improved

\*Numbers in parenthesis designate references at the end of the paper. the electromagnetic field configuration around the aircraft and hopefully made it more representative of the inflight fields.

In flight, the lightning current has a return which is effectively at infinity. The aircraft also exhibits a surge impedance which is governed by the physical dimensions of the aircraft alone. When the aircraft is positioned in a hangar and surrounded by return conductors, the electromagnetic environment is greatly altered. Viewed at the current input point (attachment point), the test circuit looks like a short electrical transmission line, with a surge impedance of 75 to 150 ohms. Due to the close proximity of the return conductors, this surge impedance level is probably much lower than the corresponding inflight situation. But, from a practical standpoint, not much can be done about it. If the return conductors are moved away, two problems arise. The total circuit impedance goes up, reducing the applied current, and the aircraft must be raised off of the hangar floor. The second problem will establish limits long before the first has much offect.

Unfortunitely, during the ground test more then one set of transmission lines affect the circuit response. The circuit return conductors will also set up effective transmission lines between themselves and other conductors in the near vicinity (rebar in the hanger floor, steel walls and roofs, electrical conduits and conductors in the area). All of these other conductors make up a building or facility ground

plane. Whenever a signal is introduced into the primary transmission line (between the aircraft and its return line) some response will be induced into the secondary transmission lines. As travelling waves propagate on these primary and secondary transmission lines, they interact with each other and both contribute to the final waveshapes observed in measurements taken in the primary system.

大学 の 日本の 一本の 一本の 一本の こうかん

Tests conducted on both the F-8. i the relative geometric scale model verified the transmission line performance of the test circuit. To minimize the effects of waves propagating in the secondary transmission lines, resistors were connected between the return lines and building ground. The improvement in circuit behavior is shown in Fig. 1. These termination resistors do not prevent energy coupling into the secondary lines, but they absorb it to prevent reflections.

When the swtich between the generator capacitor and the test circuit is closed, the capacitor voltage will be impressed across the circuit impedances. The voltage impressed across the primary transmission line will be a function of the transmission line surge impedance and the series impedance between the capacitor and the transmission line. At that time, voltage and current travelling waves will begin propagating down the transmission line. The voltage and current rates of rise will be a function of the switch operating time. In general, arcing switches are used and the risetimes are quite short. This means that a low magnitude current pulse (<10% of the final peak) but with a very fest rise time (<0.1µs) as shown in Fig. 2, could be inducing voltages in the electrical wiring. These voltages, due to the fast risetimes involved, could be an order of magnitude higher than the response to the 2us risetime current. This phenomena could very definitely account for the observed discrepancy between applied current risetime and the induced voltage response.

In an attempt to resolve this problem, the test circuit was redesigned to have a resistor between the aircraft and the return lines equal to the approximate surge impadance of the system as shown in Fig. 3. This provides two changes; first, the transmission line is terminated and no reflections can occur. Secondly, the series inductor value is increased (L/R = 2µs) since R increased, so the magnitude of the first current pulse is decreased. Although it may not completely eliminate the induced voltage response due to travelling waves, it will reduce it to at least the same magnitude as voltages caused by the applied current pulse.

#### TRAVELLING WAVE VELOCITIES

If the termination of the aircraft is removed and the aircraft isolated from the return lines, measurements of the travelling waves on the airframe can be made. When a transmission line is open circuited on one end and shorted on the other (source capacitor) the reflected waves will result in a damped oscillation with a frequency equal to four times the electrical transit time as shown in Fig. 4. Tests conducted on both the F-8 and the relative geometric scale model resulted in calculations predicting transit times corresponding to wave velocities less than the speed of light.

A test fixture was designed and tests apecifically conducted to measure and understand the phenomena observed. Originally, it was theorized that the diameter of the center conductor in an array of wires (fuselege) could affect the wave propagation due to its reduced inductance per unit length. Measurements of transit times on the fixture (20 ft. long, 4 ft. dis.), shown in Figs. 5 and 6, were made using a two wire system and a nine wire system (8 return wires and a center tube). The results of the tests, shown in Fig. 7 and Table I. revealed that transit times corresponded to the speed of light within the accuracy of the measurements. Table I - Summary of Transit Times Determined From Open Circuit Ringing Frequencies

Test No.	Description	Frequency MHz:	Transit Times
69	Two Wire	10.3	24.2
80	8 Wires & Center Wire	10.8	23.2
105	12.5cm & 8 Wires	10.8	23.2
_		lc. from	20.5
-	6.9m sp	eed of ght	23.0

To evaluate the response further, aluminum foil wings and a vertical fin were added to the fixture in the same proportion as the Y-8 dimensions as shown in Fig. 8. As each of the three items were added, the oscillation frequency decreased as shown in Fig. 9. The final tests showed a frequency reduction of 45%, very close to the 50% values observed during the Y-8 tests. A set of measurements were made of the time of arrival of the voltage and current wavefronts. These measurements are shown in Fig. 10 and indicate that the waves are indeed travelling at the speed of light.

The aircraft is not a constant impedance transmission line. For fast rising pulses, it probably looks more like a series of several short transmission lines of different impedance. When the generator switch is closed, the travelling waves start down the pitot boom. At the function between the boom and the forward fuselage, the impedance drops slightly. At the junction of the wings and the fuselage, a more significant impedance change occurs. The travelling waves reflect and refract at each of these junctions. The bulk of the wave energy travels down the fuselage, out of the wings, back to the fuselage, up the vertical fin and back to the tail. The total distance travelled is much longer than the length of the aircraft and the period of oscillation will be related to this length. Observations of the oscillograms in Fig. 10 does show evidence of reflections that could be associated with the wing attachment point.

#### FAST RISING CURRENT TESTS

Cianos and Pierce (7) provides data to substantiate the use of a 2 x 50µs waveshape for lightning strokes reaching the ground. Recent data has been provided by other researchers who report current risetimes of considerably shorter durations. Risetimes of 25 to 50ns have been observed using the indirect measurement technique (8,9). To generate current pulses with risetimes of these magnitudes, generators with different characteristics are required. An LC ladder network (LCLN) generator was designed to represent a portion of the lightning stroke channel and has a source surge impedance nominally equal to the aircraft test surge impedance. The generator is shown schematically in Fig. 11.

Tests conducted with this generator, which has 24 stages, resulted in current pulses with risetimes of 100 to 125ms. At high voltages, 20-50kV, considerable variation in the applied voltage waveshape was noted from pulse to pulse as shown in Fig. 12. Since the generator was configured to operate on a repetitive pulse basis of 5-20 pulses per second, variations in succeeding pulses were quite obvious in the oscillograms taken of the applied voltage and current. Tests showed that the variations appeared to be related to switch breakdown characteristics. A standard high voltage triggered sparkgap was used for this work. After triggering, the rate at which the gap switches will be a function of several variables, including spacing, voltage, air density, presence of free electrons, etc. Consequently, the closing time will be a statistical distribution about some nominal value. If that time is on the same order of magnitude as the required risetime of the current pulse, then variations will result. A study of the oscillograms show that the switch is closing faster than the risetime but not at uniform rates. Using lower voltages and a mercury wetted relay switch resulted in perfectly repeatable applied waves. However, the wave-shapes are somewhat different. Comparisons are shown in Figs. 13 and 14.

The most important point observed was the inability to inject current pulses with risetimes faster than ~100ns. It is known that a mercury wetted switch will apply risetimes well below ins. It appears that the varying input surge impedance characteristics of the airframe must be controlling the shape of the applied wave. As faster and faster risetimes are applied, reflections and refractions from aircraft structural shape changes become more pronounced. The boom to nose cone junction and the front wheel reflections must be involved in the observed waveshape. Depending on the magnitude changes involved in the surge impedances! magnitude changes of 20-50% in the applied wave will result from these reflections. Such changes will distort the wavefront and make the definition of the applied wave risetime very difficult to interpret. Secondly, and just as important, is the fact that shape of the applied current at the injection point will bear little resemblance to the wave further back along the fuselage where the wires being tested may be located. If the wave risetime has slowed to 100ns by the time it reaches the midpoint of the sircraft after starting at 20ns, what is the rate of rise of the test? The majority of the cable runs are not at the nose but further back along the fuselage. A transmission line will act as a low pass filter for fast rising injected pulses, so the rate of rise will always decrease along the length of the line.

INDUCED VOLTAGE RESPONSE TO FAST RISING PULSES

During the F-8 test technique evaluations, induced voltage measurements were taken on a pair of flight control cable wires. The wires were connected to airframe at the base of the vertical fin and measurements were made at the pailet area just aft of the cockpit. Voltages in these wires were nonitored throughout the test program using a battery powered Tektronix 475 oscilloscope installed inside the aircraft.

Measurements were made as the injected current waveshape was changed. With a 2 x 50µs waveshape applied, as shown in Figure 15, two identifiable frequencies are observed in the induced voltage oscillograms; one at 750-800kHz and a low level oscillation at 10-11MHz. Using the LCLN generator, a 120ms risatime pulse was applied. The resulting induced voltage, shown in Fig. 16, now contains a significant contribution at 10.6Miz. Modifying the LCLN generator (removing inductors) yielded a risetime of 90ns. Induced voltage measurements made with this applied pulse, shown in Fig. 17, resulted in voltages very similar to the 120ms pulse except that the 10.6MHz amplitude increased significently.

A final test was conducted using a 0.luF capacitor at 110V dc and a mercury switch. The applied current pulse was found to be double humped. The first portion raised in about 50ms. In attempting to increase the current rate of rise some changes were made in the return circuit connections. The induced voltage shown in Fig. 18 now has a predominate response 11.8MHz with low level oscillations of 40-80MHz present.

To investigate the response of the flight control wires, they were excited by pulsing them at the base of the vertical fin using the 0.1uF capacitor and the mercury relay. Except for some steps at 100ns on the front, the response shown in Fig. 19 was approximately 2.5MHz. None of these frequencies or times correspond to the responses obtained during the induced voltage tests. Therefore, it can be concluded that the cables are not excited and/ or oscillating during the induced voltage test. so they must be responding to electromagnetic fields inside the airframe. These fields are related to the sircraft external environment. It had been postulated that the aircraft dimensions would limit the upper frequency. This does not appear to be correct. CONCLUSIONS

Significant developments in the LTA test technique have evolved in the past few years. More representative electromagnetic environments can be simulated due to the use of spaced multiple return conductors around the aircraft. A better understanding of the interaction of the return conductors and the facility grounds allows steps to be taken to reduce the problems in that area.

Perhaps the most significant achievement in understanding the test has been the identification of the role played by travelling electromagnetic waves. The aircraft and its return conductors represent an interconnected set of differing impedance transmission lines. The response of these transmission lines to the applied stimulus governs the tests that can be applied successfully as well as the induced voltage responses that occur.

Specifically, the transmission line travelling wave theories have resulted in the following conclusions:

- Travelling waves do propagate at the speed of light but travel distances further than the nose-to-tail dimensions.
- The airframe appears to behave like a collection of short, different impedance transmission lines. The induced voltage frequency content will reflect these frequencies rather than a frequency related to the major aircraft dimension.
- The airframe geometry will limit the practical risetime of the applied current pulse.

 The LCLN type of generator will provide the fastest input current pulse which appears to be on the order of 100ns.

However, in light of presently available data, most lightning induced voltage tests should be conducted using a 2 x 50µs test current which can successfully be generated using the resistively terminated return circuit configuration.

## REFERENCES

- 1. L.C. Walko, "A Test Technique for Measuring Lightning-Induced Voltages on Aircraft Electrical Circuits", NASA CR-2348, 1974.
- 2. J.A. Plumer, and K.E. Crouch, "Improved Test Methods for Determining Lightning-Induced Voltages in Aircraft". NASA CR-3329, 1980.
- 3. K.E. Crouch, "Aircraft Lightning-Induced Voltage Test Technique Developments", Lightning Technologies, Inc. Report No. LT-82-132, 1982.
- 4. J.A. Plumer, F.A. Fisher and L.C. Walko, "Lightning Effects on the NASA F-8 Digital Flyby-Wire Airplane". NASA CR-2524, 1975.
- 5. J.A. Plumer, "YF-16 #1 Lightning Transient Analysis Test Report". General Dynamics Report 16PR051, 1975.
- 6. P.F. Little, A.W. Hanson, and B.J.C Burrows, "Tests Techniques for Simulating Lightning Strikes to Carbon (Graphite) Fibra Composite Structures". Proceedings of the 1979 Federal Aviation Administration-Florida Institute of Technology Workshop of Grounding and Lightning Technology.
- 7. N. Cianos and E.T. Pierce, "A Ground-Lightning Environment for Engineering Usage", Stanford Research Institute, SRI Project 1834, 1972.
- 8. M.A. Uman, et al., "Calculations of Lightning Return Stroke Electric and Magnetic Fields Above Ground". Lightning Technology, NASA Conference Publication 2128, FAA-RD-80-30, April 1980. p.21.
- 9. C.E. Baum, et al., "Measurement of Electromagnetic Properties of Lightning With 10 Nanosecond Resolution", Lightning Technology, NASA Conference Publication 2128, FAA-RD-80-30, April 1980. p. 39.

## ACKNOWLEDGEMENTS

The author would like to acknowledge the support and encouragement of Calvin R. Jarvis and Wilton Lock of NASA Ames Research Center, Dryden Flight Research Facility. Work on the Digital Fly-by-Wire F-8 Aircraft has been instrumental in the developments reported here.

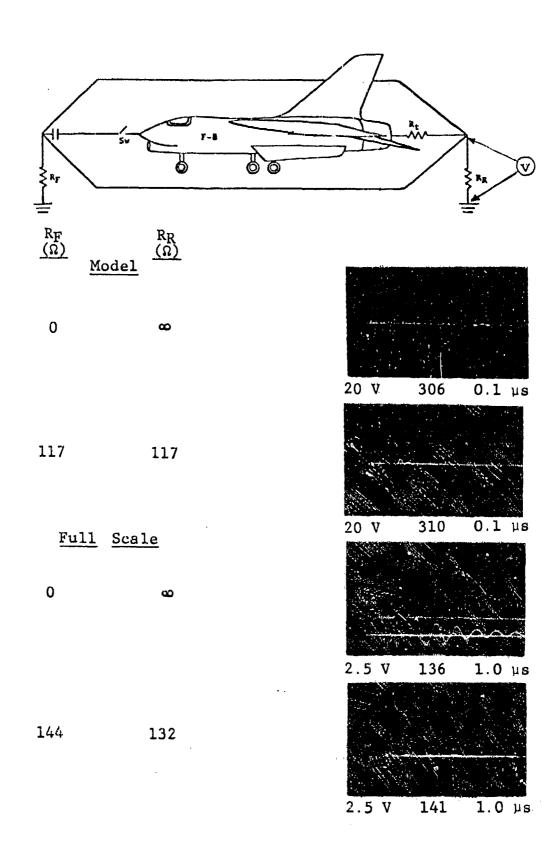
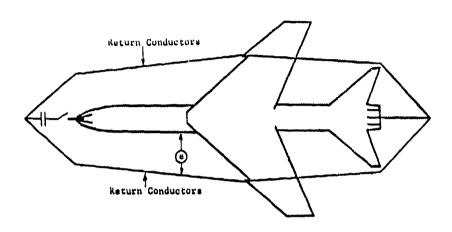


Fig. 1 - Typical return line-to-building voltages before and after termination



Idealized Test Circuit

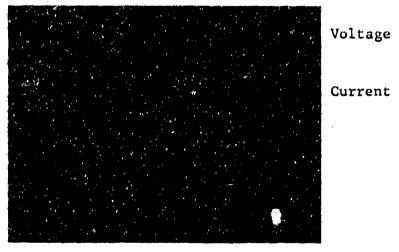


Figure 2 - Voltage and Current Travelling Waves on an Idealized Test Circuit; as Observed at the Center of the Fuselage.

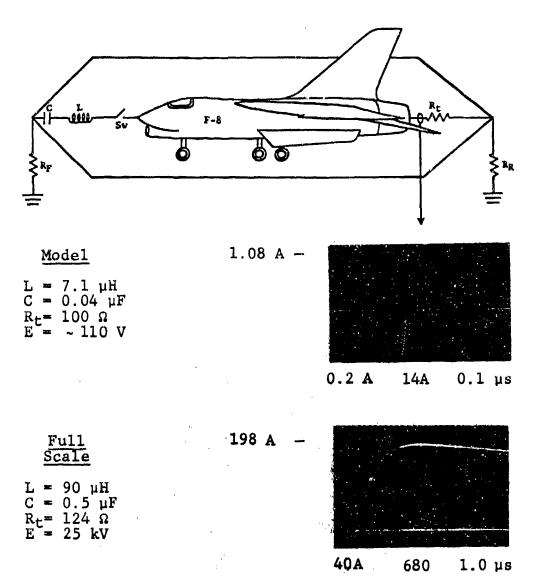


Fig. 3 - 2 x 50 $\mu$ s Return Stroke into Aircraft Terminated with R<sub>t</sub> =  $Z_0$ 

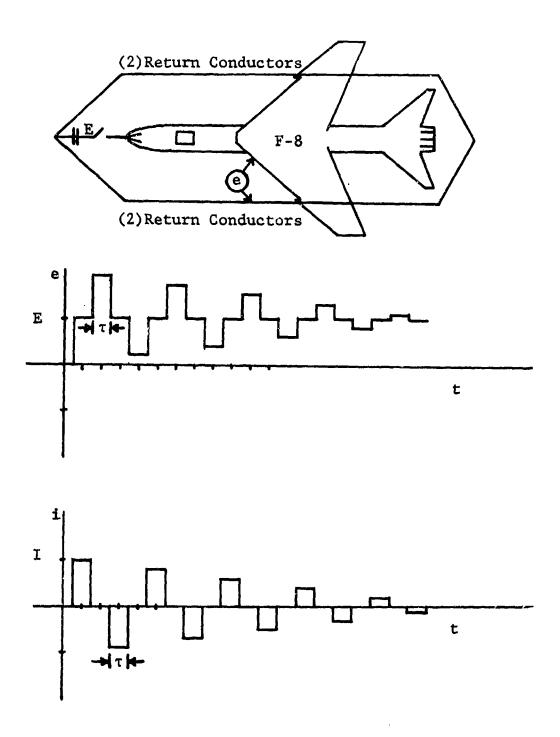


Fig. 4 - Voltage and current traveling waves on an idealized test circuit; as observed at the center of the fuselage

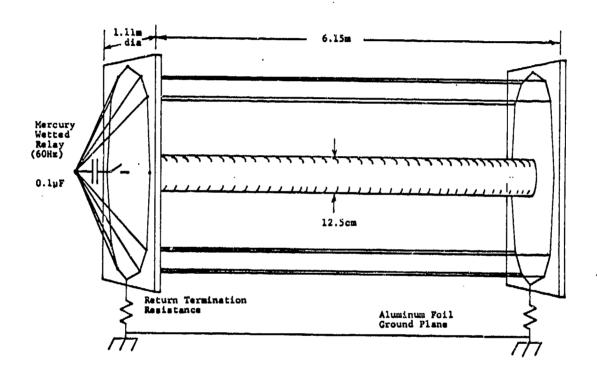
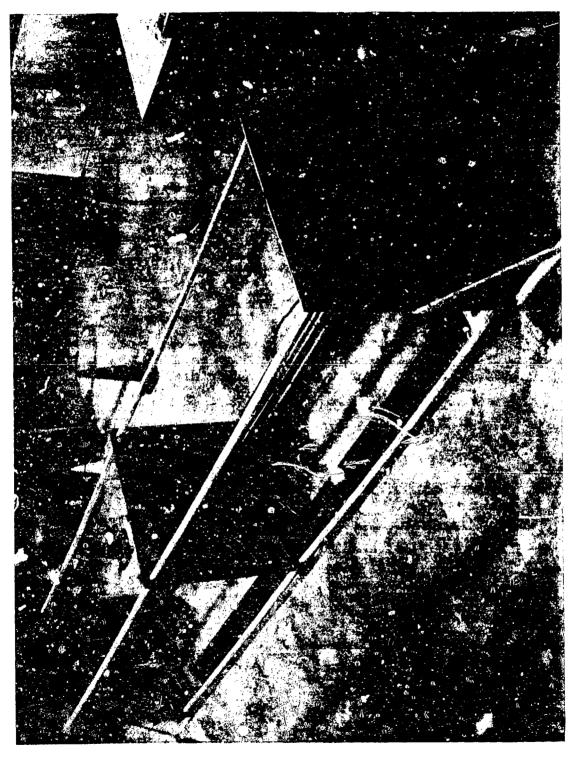


Fig. 5 - Diagram of transit time test fixture



39-11

Test 68

500x 200'S

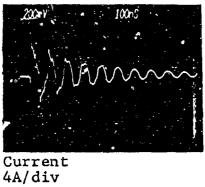
Voltage
50V/div

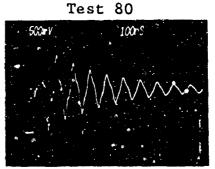
Test 69
2001/V 2007S

Current 4A/div

Measured at Center of Fixture

Test 79

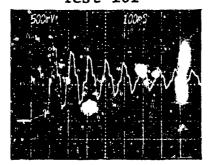




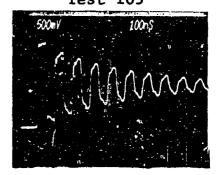
Voltage 50V/div

Measured at Center of Fixture

Test 101



Test 105



Voltage 50V/div

> Measured at Center of Fixture

Voltage 50V/div

Measured at the Far End of Fixture



Figure 8 - Transit Time Test Fixture With Simulated Aircraft Wings & Tail

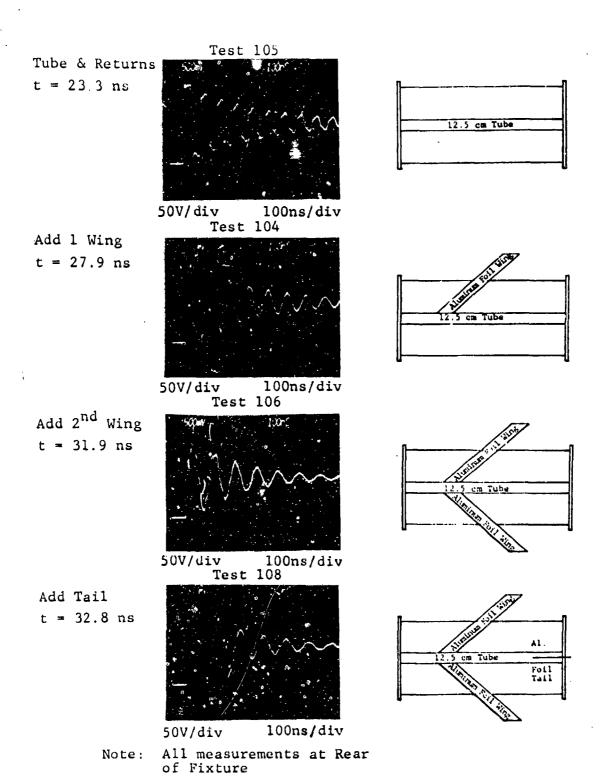
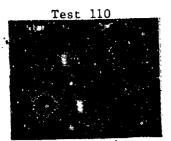
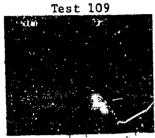


Figure 9 - Comparison of Ringing Frequencies as a Function of Added Parts



Voltage 50V/div 20ns/div

Front of the Test Fixture



Voltage 50V/div 20ns/div

Rear of the Test Fixture

Fig. 10 - Comparison of Travelling Wave Voltages at the Front and Rear of the Fixture With Simulated Wings

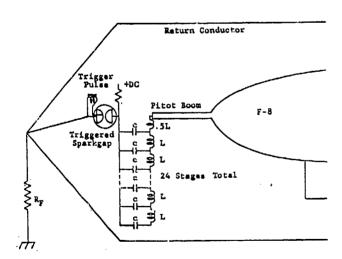
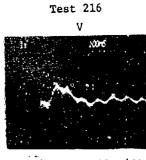
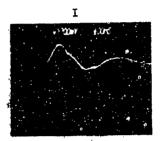


Fig. 11 - Schematic Diagram of the LCLN Repetitive Pulse Generator Configuration



4900V/div

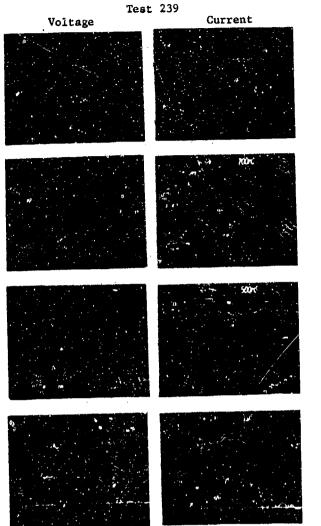
100ns/div



>200A/d1v

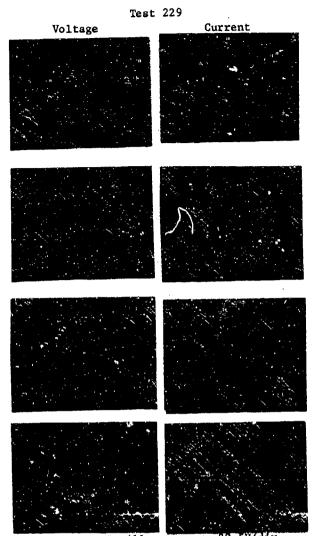
100ns/div

Fig. 12 -- Fast Rise Voltage and Current Oscillograms at the F-8 Pitot Boom  $\,$ 



Note: Voltage Oscillograms are 5190V/div Current Oscillograms are 20A/div

Fig. 13 - High Voltage Triggered Sparkgap Switch LCLN Generator Oscillograms



Note: Voltage Oscillograms are 22.5V/div Current Oscillograms are 0.2A/div

Fig. 14 - Low Voltage Mercury-Wetted Switch LCLN Generator Oscillograms

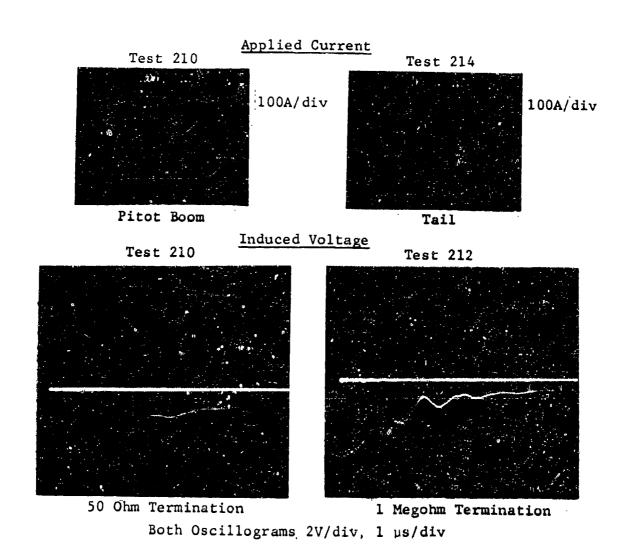


Fig. 15 - Induced Voltage Measurements 2  $\times$  50  $\mu s$  Wave

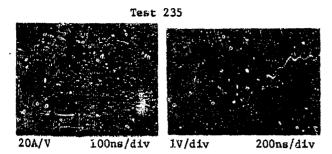
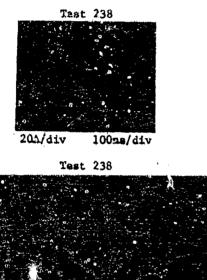


Fig. 16 - LCLN Applied Current and Induced Voltage (120 ns risetime)



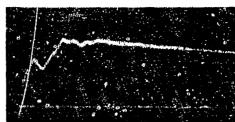
200ms/div

Test 240

1V/div lµs/div

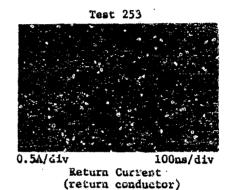
IV/div

Fig. 17 - LCLN Fast Applied Current and Induced Voltage (90 ns risetime)



Test 252

0.5A/div 100ns/div Input Current (pitot boom)



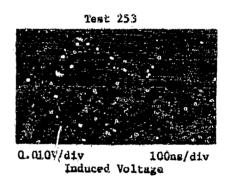


Fig. 18 - Fast Rise Current and Induced Voltage Test

Test 246

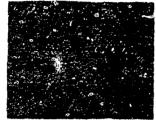


50V/div

500ms/div

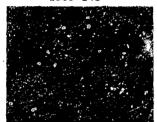
50 ohm Termination

Test 248



50V/div 500ns/div 1 Megohm Termination

Test 248



50V/div 100ns/div 1 Megohm Termination

Fig. 19 - Induced Voltage Measurement Wire Natural Frequency Tests

## NASA F-106B LIGHTNING GROUND TESTS



B. D. Heady and K. S. Zeisel

McDonnell Aircraft Company McDonnell Douglas Corporation St. Louis, Missouri 63166

## **ABSTRACT**

Lightning simulation ground tests were conducted on the NASA F-106B research aircraft prior to its 1982 flight program. The purpose of the test program was to measure the response of the aircraft's electromagnetic sensors and interior wire circuits to controlled ground test environments. Both direct attachment and radiated field lightning test techniques were used. In most cases, the F-106B's engine was running, and test data were gathered simultaneously by the on-board instrumentation system and a remote data acquisition system. The wide variety of ground test data obtained in these tests will aid the interpretation of the transient data produced by natural strikes.

NASA's LANGLEY RESEARCH CENTER is currently using a specially-instrumented F-106B aircraft to conduct a thunderstorm hazards research program. Their primary task is to measure the aircraft's response to direct lightning strikes in order to refine the characterization of the lightning environment [1]. The research is motivated by the lack of significant quantities of flight data on the lightning/aircraft interaction process. A more detailed understanding of the lightning threat at altitude is needed to optimize the protection schemes of future aircraft systems which are becoming increasingly dependent on sophisticated microelectronic circuits.

This paper summarizes the lightning simulation ground tests of the F-106B conducted under NASA contract NAS 1-16202 at NASA Langley by McDonnell Aircraft Company (MCAIR) prior to the aircraft's 1982 flight program [2]. The purpose of the ground tests was to measure the response of the aircraft's electromagnetic sensors and interior wire circuits to controlled ground test environments which simulate the electromagnetic effects of a lightning strike. Specific objectives were to (a) compare the F-106B sensor responses with those of externally-mounted MCAIR sensors, (b) determine the variation of the sensor responses for controlled input waveform changes, (c) identify the characteristic aircraft resonances, and (d) measure the interior wire responses for different test conditions. The ultimate goal of the project is to compare the ground test data to actual flight test data obtained from natural strikes in active thunderstorms. The comparison of these two sources of data will help assess the adequacy of the present lightning simulation test techniques.

Two completely different types of test configurations and aircraft stimuli were used to accomplish the test objectives. Most of the testing was conducted with the aircraft being pulsed directly by a Marx generator, and the current being returned by a coaxial wire arrangement. During the direct attachment tests, the input inductance, output configuration (hard-wired or spark gap), and the output location were varied to provide a wide variety of test conditions. In addition, radiated field tests were conducted using a long, parallel

wire transmission line to excite the natural resonant frequencies of the electrically-isolated F-106B aircraft.

### F-106B RESEARCH AIRCRAFT

The NASA F-106B contains ten specially-designed electromagnetic sensors [3] and two interior wire circuits which can be monitored in flight by either expanded-memory digital or wide-band analog data channels. Figure 1 shows the approximate sensor locations. The I and I sensors are located at the base of the nose boom. Flat phate D sensors are located on the lower forward fuselage, on the left side of the vertical fin, and under each wing near the wing tip. Semi-circular loop B sensors are located on either side of the aft upper fuselage and under the wings near the outside of the main landing gear doors. The B sensor on the right side of the fuselage is oriented to measure longitudinal current down the axis of the aircraft. The other three B sensors are oriented to measure transverse current flow.

The two interior wire circuits are each unshielded single wires that are shorted to the airframe on one end and monitored across a 50-ohm load on the other end to obtain their induced voltage responses. One circuit is shorted to the airframe near the left wing tip and runs in the leading edge of the wing to the instrumentation system. The other circuit is shorted to the nose bulkhead and runs through the lower fuselage to the instrumentation system.

The data recording system includes digital and analog transient recorders and is located in a shielded enclosure in the missile bay. The system power is isolated from the main aircraft power by a motor-generator set. Shielded coaxial cables transfer the passive electromagnetic sensor outputs to the recording system.

#### **DIRECT ATTACHMENT TESTS**

The direct attachment tests were conducted using a typical lightning test configuration (Figure 2) with the aircraft being the inner conductor of a "coaxial" transmission line which was pulsed by a Marx generator. The aircraft placement and test setup were similar to that used previously by NASA in the F-106B lightning safety tests [4], except: (a) the aircraft was isolated from ground potential by high-voltage dielectric pads beneath each landing gear wheel, (b) a high-voltage Marx generator was used to produce the system stimulus instead of a high-current capacitor system, (c) a spark gap was sometimes incorporated in the output line from the aircraft to the return conductors, and (d) the test data were gathered using fiber optic data links.

1

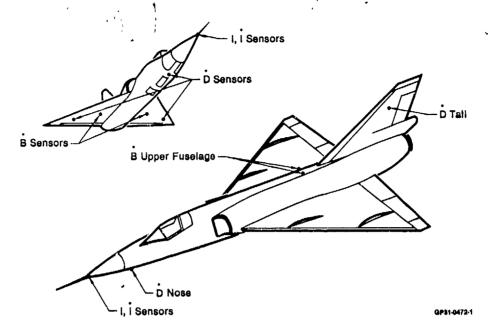


Fig. 1 - NASA F-106B sensor locations

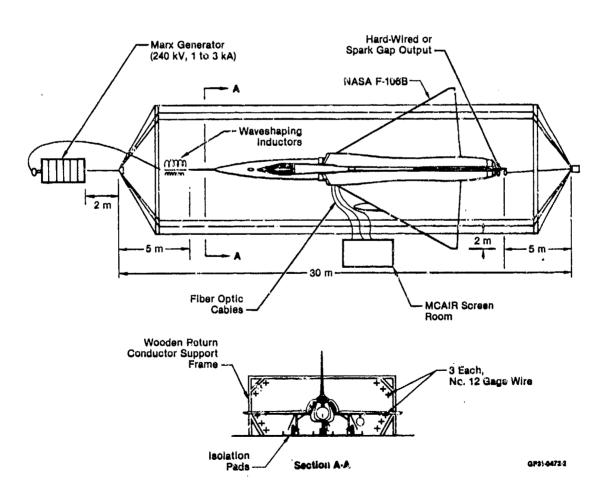


Fig. 2 - Schematic of direct test setup

The aircraft stimulus was varied by adding coil inductors and by incorporating either a hard-wire or spark gap output connection. MCAIR B and D sensors were taped to the aircraft in the vicinity of the NASA sensors so that both NASA and MCAIR sensors could simultaneously provide comparative responses. The NASA and MCAIR instrumentation systems each monitored four data channels per test. In many cases the same sensor output was monitored by both the NASA on-board and the remote MCAIR systems. The real-time MCAIR system permitted immediate observation of the sensor responses which were stored directly on magnetic tape by the aircraft system.

TIME DOMAIN RESULTS - Over 130 test shots were conducted using a wide variety of sensor and configuration combinations. The time domain results from the direct attachment tests can be summarized as follows:

- (a) The NASA sensor responses agreed well with the predicted levels and varied as expected for changes in the test conditions.
- (b) There was good agreement in the responses of the NASA flight sensors and the externally-mounted MCAIR sensors.
- (c) In most cases the sensor responses were very similar for nose-to-tail and nose-to-wing tip tests, except that the larger transverse currents in the nose-to-wing tip shots approximately doubled the wing's transverse B sensor output.
- (d) The D sensor responses at the time of spark gap breakdown increased with higher aircraft voltages and were strongly modulated by the 2 MHz transmission line frequency during the aircraft's discharge.
- (e) The interior wire responses were inductively coupled to the system current, and the fuselage wire's induced voltage was approximately 15 times larger than that of the wing wire.

Figure 3 shows a typical shot with the aircraft output hard-wired from the tail hook to the junction of the return conductors. The system current is a damped sinusoid with a peak of 2.8 kA and frequency of  $\approx$  330 kHz. The calculated system inductance is 42  $\mu$ H. The B transients from MCAIR sensors on the access door aft of the nose year and on the upper aft fuselage demonstrate that most of the current flow is in the axial direction; however, a fast transverse component is present immediately after the generator is triggered. The B response on the lower forward fuselage location agrees with that calculated for a uniform current distribution around the nose perimeter. The induced voltage on the interior fuselage wire is phase shifted by 90 degrees from the system current since inductive coupling was dominant in the common mode circuit.

Figure 4 shows a typical shot with a spark gap inserted between the aircraft output connection and the return wire conductors. In this test configuration, the aircraft is first charged by displacement currents and then discharged when the spark gap breaks down. Since the system current was measured in the output lead from the aircraft, the current trace does not include the displacement currents. Evidence of the displacement currents are seen in the NASA longitudinal B sensor on the aft upper fuselage and the interior wire responses. The B sensor response is proportional to the

derivative of the charging and the discharge currents. Like the inductively coupled wire transients, the B response is therefore shifted by 90 degrees from the current. The B sensor and wire circuit responses during the displacement current portion of the test are approximately equal in magnitude to their responses during the discharge current portion. The higher RLC resonant frequency of the displacement currents compensates for the lower current amplitudes.

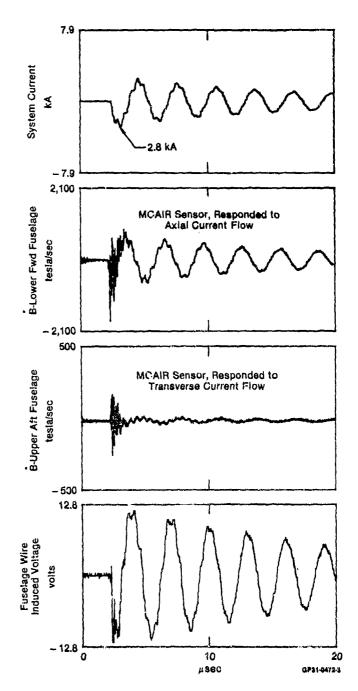


Fig. 3 - Typical test with hard-wired output

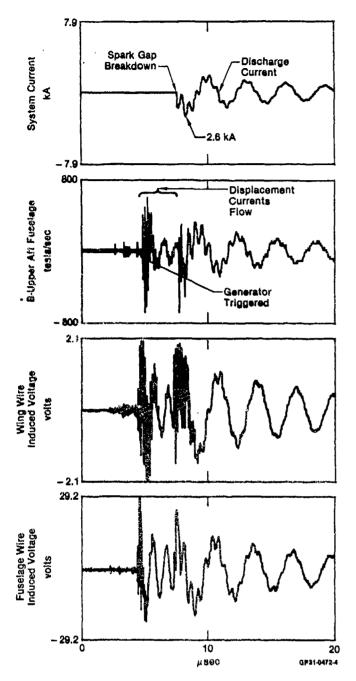


Fig. 4 - Typical test with 10-inch output spark gap

Figure 5 shows another shock-excitation type test with an output spark gap. A frequency-compensated capacitive voltage divider was used to monitor the aircraft voltage across the spark gap. With the divider in the circuit, both the aircraft-to-return conductor capacitance and the divider capacitance are charged prior to the spark gap breakdown. The addition of the divider's capacitance slows the displacement current resonance somewhat, but provides useful information on the time variation of the aircraft voltage and its relationship to the response of the other aircraft sensors. The voltage divider response is a displaced cosine waveform whose midpoint of oscillation is shifted about the steady-state voltage level that is attained if the spark gap does not break down. The aircraft

reaches its peak voltage (approximately twice the steady-state level) in a half cycle, and the 10-inch spark gap breaks down in 2-1/4 cycles. The response of the  $\dot{D}$  sensor on the vertical stabilizer is in phase with and proportional to the displacement current before the spark gap breakdown, and oscillates at a setup dependent transmission line frequency of  $\simeq 2$  MHz after the breakdown. The fuselage circuit response is very similar to that shown in Figure 4.

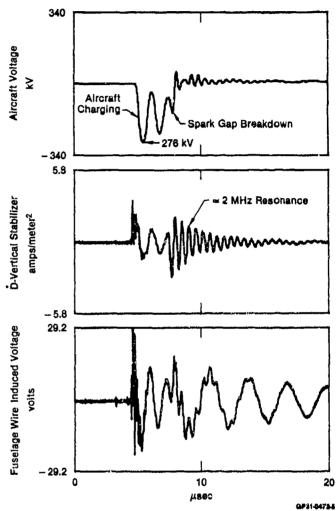


Fig. 5 - Test with spark gap output and capacitive voltage divider monitoring the F-106B voltage

FREQUENCY DOMAIN RESULTS - The measured data contained frequencies generated from three sources; the system RLC frequencies during aircraft charging and discharge, transmission line frequencies due to the test setup, and the aircraft's characteristic resonances. The RLC frequencies were dependent on the primary system components and layout. Key elements included the gener tor capacitance, the aircraft-to-return conductor capacitance, and the system inductance. The RLC frequencies were closely modeled by a series RLC circuit. When a spark gap was incorporated in the output, a single equivalent capacitance was calculated from the series combination of the generator and the aircraft-toreturn conductor capacitances to give the resonant frequency of the displacement current. The RLC resonances were less than 1 MHz and were varied during the test program by changing the circuit inductance.

The transmission line frequencies were principally determined by the physical arrangement of the test setup and the terminations at the ends of the aircraft/return conductor transmission line. Transmission line resonances were present for both the hard-wired and spark gap output configurations. However, the output spark gap case produced much larger transmission line oscillations, since the output termination was abruptly changed from an open to a nearly shorted condition whenever the gap broke down. The transmission line resonances varied between 1 and 2 MHz for the different test conditions and were not typical of the half-wave resonances which would be observed in flight.

The high-frequency aircraft resonances were dependent on the aircraft geometry and were excited during abrupt system transitions such as the generator triggering and spark gap breakdown. The aircraft resonances were quickly damped within a microsecond or two. Figure 6 shows the time and frequency response of NASA's longitudinal B sensor to a shock-excitation test. The B waveform shows the high-frequency aircraft oscillations excited at the generator firing and the spark gap breakdown. The fast Fourier transform (FFT) of the aircraft charging portion of the waveform shows resonant peaks at 7, 11, and 18 MHz. These frequency peaks were present in almost all spectra, and an additional peak was present at 14 MHz in the transverse B sensor responses.

#### RADIATED TESTS

Radiated tests were conducted to determine the characteristic aircraft resonances. For these tests the aircraft remained on the dielectric isolation pads, but the return conductor assembly was completely removed and the test setup, shown in Figure 7, constructed. The 100-meter-long by 40-meter-wide parallel wire transmission line was elevated to the height of the aircraft wings and terminated in approximately its characteristic impedance by a 1250-ohm resistor made from long, strapded carbon fibers.

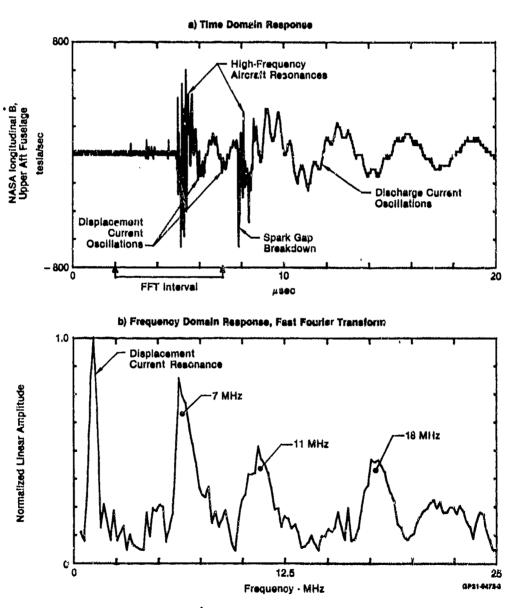


Fig. 6 - NASA longitudinal B sensor response for a shock-excitation test

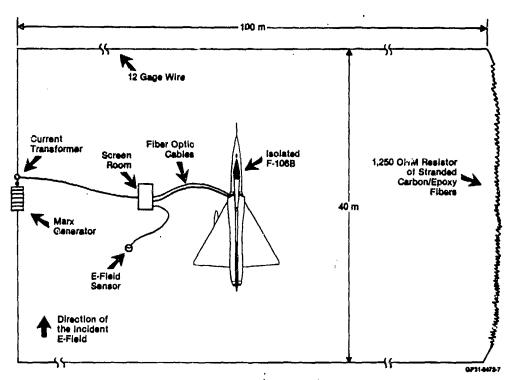


Fig 7 - Schematic of F-106B radiated test setup

When the Marx generator was fired into the transmission line, an abrupt electric field pulse was applied to the aircraft along its axis and drove longitudinal displacement currents which oscillated at the aircraft's natural frequencies. The resulting aircraft voltage variations on the NASA D sensors were monitored by fiber optic data links to the remote MCAIR data acquisition system, MCAIR sensors monitored the incident electric field and the current pulse applied to the transmission line.

Figure 8 shows the transmission line current and the D responses from the tail and left wing sensors for a radiated test. The current pulse has a rise time of 120 ns and contains a small lotch 700 ns after the start of the pulse. The timing of the notch is consistent with the down-and-back time of the 100-me er-long line. Since the amplitude of the reflected wave was small, no attempt was made to perfectly match the load termination.

The D waveforms were high-frequency transients measured with a 5-ns sampling interval and lasted only a microsecond. The amplitudes from the fuselage and tail sensors were approximately 0.30 A/m<sup>2</sup> peak-to-peak and were about three times larger than the wing sensor responses. Figure 9 shows the fuselage D response and its fast Fourier transform. The resonant peaks are only approximately identified since the frequency resolution of the FFT is only 0.8 MHz for such a short duration transient. The spectra of the derivative sensor emphasizes the higher frequencies, so that resonances were generally oberved at approximately 7, 11, 18, 23 and 26 MHz. The 7-, 11-, and 18-MHz oscillations were also observed in the direct attachment tests. The 14 MHz seen in the transverse sensors of the direct attachment case is not present in the radiated data since the excitation was primarily longitudinal. The higher harmonics in the radiated tests at 23 and 26 MHz were masked by the more dominant lower frequencies in the direct attachment tests.

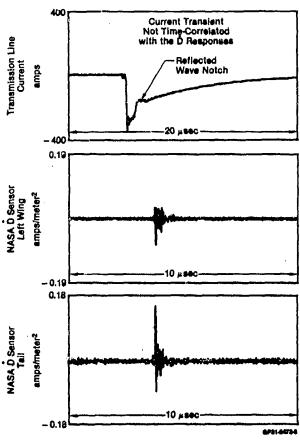


Fig. 8 - Typical radiated test transients

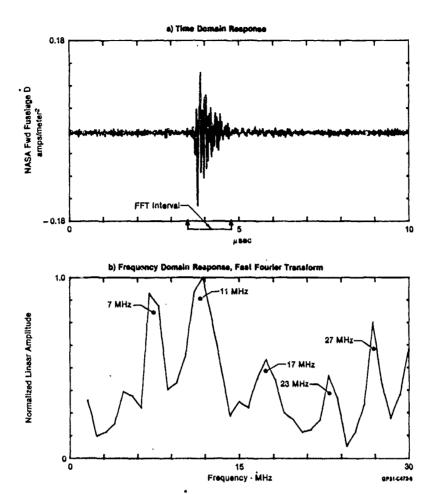


Fig. 9 - NASA Fuselage D sensor response for a radiated test

## **SUMMARY**

The lightning simulation ground tests accomplished all program objectives. All NASA sensors and interior wires were monitored for a wide variety of test conditions, and their responses were compared to externally-mounted MCAIR sensors. The sensor responses were repeatable, self-consistent, and in general agreement with values predicted in pretest calculations. The interior wire responses were inductively coupled to the circraft currents and produced sizeable induced voltages during both the displacement current (charging) and discharge phases of the shock-excitation tests.

The direct attachment tests produced three types of frequency resonances. The overall system RLC response agreed well with values predicted from RLC circuit theory. A strong transmission line resonance at  $\approx 2$  MHz was due to the physical arrangement of the test setup and the terminations at the ends of the aircraft/return conductor transmission line. Aircraft resonances were measured at 7, 11, 14, and 18 MHz, but were somewhat masked by the transmission line and RLC resonances. In the radiated tests, aircraft resonances were measured at approximately 7, 11, 18, 23, and 26 MHz. These measured aircraft frequencies generally agree with the observed flight data resonances at 7, 8, 13, and 21 MHz [5].

The ground test data have not yet been compared to the 1982 flight program data which include nose I, fuselage D, and longitudinal B sensor responses for over 150 lightning

incidents. As the 1982 and future F-106B flight data are compared to these ground test results, a more accurate assessment of the realism of indirect effects lightning test techniques will be possible.

TO THE PROPERTY OF THE PARTY OF

#### REFERENCES

- 1. N. L. Crabill, P. L. Deal, B. D. Fisher, and G. L. Keyser, "Thunderstorms Hazards Flight Research-Program Dverview," AIAA-81-2312, AIAA 1st Flight Testin; Conference, Las Vegas, Nevada (Nov 1981).
- B. D. Heady and K.S. Zeisel, "NASA F-106B Lightning Tests," NASA Report CR-166057 (Jan 1903).
- T. F. Trost and K. P. Zaepfel, "Broadband Electromagnetic Sensors for Aircraft Lightning Research," NASA Conference Publication 2:28, FAA-RD-80-30 (22-24 April 1980).
- 4. J. A. Plumer, "Lightning Safety Tests on NASA F-106B Thunderstorm Research Aircraft," I.T-81-86 (26 April 1981).
- F. L. Pitts and T. F. Trost, "Analysis of Electromagnetic Fields on an F-106B Aircraft Draing Lightning Strikes," International Agrospace Conference on Lightning and Static Electricity, Oxford, England (March 1982).

# AD P002195

INDUCED TRANSIENTS IN A SIMULATED LIGHTNING TEST OF THE FLY-BY-WIRE JAGUAR AIRCRAFT

 $\rightarrow$ 

R. H. Evans Consultant formerly at Royal Aircraft Establishment, United Kingdom J. Bishop Royal Aircraft Establishment, United Kingdom

ABSTRACT

Simulated lightning tests were performed on the Jaguar aircraft modified for demonstrating fly-by-wire technology. A pulse generator injected currents of 100 kA maximum into the fuselage; measurements were made of induced voltage and current transients in cables, currents and magnetic fields in equipment bays, current density on the fuselage and wings, and rate of change of electrical field at two locations. Full-threat estimates were obtained by extrapolation. Some remarks are included on the consistency and accuracy of the results and their realism in relation to actual in-flight strikes.

AS PART OF THE JOINT MOD AND BRITISH AEROSPACE PROGRAM to demonstrate fly-by-wire technology. a Jaguar aircrait was modified to incorporate a quadruplex igital flight control system (FCS)(1)\*. Since the system had full authority, flight safety was critically dependent on its correct operation and it was therefore important to demonstrate that such a systom could be adequately protected against sources of electromagnetic interference, including a lightning strike. Tests with simulated lightning were carried out over four weeks in 1982 as a joint exercise by BAe Warton, the Culham Lightning Studies Unit (CLSU) and the Flight Systems Department of RAE in order to assess the adequacy of the lightning protection incorporated and hence to obtain if possible a relaxation of the restrictions which were applied to test flying in lightning risk conditions.

The tests consisted of employing a CLSU transportable pulse generator to pass a damped sinusoidal current pulse through the aircraft fuselage, the current return circuit being a quasi-coaxial system of conductors similar in principle to that used previously on other aircraft (2). The resulting transieut voltages and currents in the FCS were recorded, as were the magnetic and electric fields at selected points on or in the siteraft. As far as possible, recorded peak amplitudes were extrapolated to full-threat levels, and in the case of induced voltages in the FCS these were compared with the equipment susceptibility levels determined by a separate program of analysis and tests.

An estimate of system resonances was made from frequency analysis of the waveforms, and those were further explored in subsidiary tests using a low power pulse generator in the frequency runge 3.4 to 8 MHz.

## TEST PROCEDURE

For the tests the aircraft was mounted on jacks, undercarriage up, and insulated from the earth except at a single earthing point, which was the connector for the ground electrical power supply. To minimise risk to sensitive or flight-safety critical equipment all such equipment not essential to the test of the FCS was removed or electrically disconnected. To reduce fire hazard the fuel system was drained as far as possible and was purged of oxygen by

a continuous flow of nitrogen, the level of oxygen being monitored and kept below 2% by volume.

Two alternative current paths through the fuselage were employed namely nose-to-tail (N-T) and nose-to-fin-tip-aerial (N-F), the latter simulating a commonly observed lightning attachment point to this aircraft. For most of the tests the FCS computers were removed (except for the durmy computers which were installed as part of the measurement system as described below) and no electrical or hydraulic power was applied. However, the program did include some tests at the highest current pulse level (all nose-to-tail current path) with the missing computers installed (they were 'rig standard' not 'flight standard' but were electromagnetically the same) and with electrical and hydraulic power supplied, from ground equipment. This two-stage procedure was adopted in order to ascertain the level of trensients before real computers were put at risk.

At the completion of the test program, the sircraft was cleared for flight by installing and connecting all equipment and carrying out a full series of functional checks. The 'rig standard' equipment which had been fitted for the lightning tests was also re-qualified.

The current pulse was injected into the fuselage by the CLSU pulse generator, using a solid connection. It was essentially a demond sine wave of frequency 32 kHz and decay time-constant 125 us, corresponding to a Q factor of about 13. The first current peak was proportional to the initial voltage on the 6.25µF capacitor bank of the pulse generator, being 100 kA for 80 kV, with a corresponding initial rate of current rise of 30 kA/us. Tests were performed at 20, 40 and 80 kV. Oscillograms of all current pulses were obtained in order to assess their variability; about 92% of pulses were within 20% of the nominal level and results were corrected for pulses outside this range.

## METHOD OF MEASUREMENT AND ANALYSIS

MEASUREMENT OF VOLTAGES AND CURRENTS IN CABLES - Induced transient voltages were measured at 18 selected points in the FCS by

<sup>\*</sup> Numbers in parentheses designate References at end of paper.

means of two dummy computers containing monitoring circuits, installed respectively in place of one of the four Flight Control Computers (FCG) and one of the two Actuator Drive and Monitor Computers (ADMC). As stated above, for most of the tests only these dummy computers were installed, the other computer positions being left empty.

The measurement system for voltages and cable currents is shown in Fig 1. For the voltages, three data signals could be recorded simultaneously, each channel having a fibre optical link (50 Ω input impedance) between a 6-way coaxial switch unit and a storage oscilloscope in the screened recording room. The diagnostic circuits (D) presented the correct impedance to the incoming signals and transformed them to suitable impedance and voltage levels for transmission; some were passive networks and others were active high impedance circuits using operational amplifier type LM318 having a flat frequency response to 5 MHz. Power was obtained from batteries located within the aircraft but external to the dummy amplifiers. The 18 monitoring points were chosen to represent a variety of wiring types, wiring routes and circuit types.

The transient bulk current in selected cables was measured by means of current transformers (C in Fig 1) followed by a fibre optical link.

なから

Besides the transients appearing at the computer inputs, it was decided in selected cases to assess the common-mode voltage that would stress the insulation between the air-frame and the wiring in a remote sensor feeding the FCS. For practical reasons this was achieved by grounding the sensor and measuring the voltage appearing at the computer end of the cable - referred to as 'remote earth' tests.

ANALYSIS OF VOLTAGE AND CURRENT TRANSIENTS - The transients contained one or both of the following components:

- (a) A component having the frequency and damping of the applied test pulse; referred to as the LF component (32 kHz in these tests).
- (b) A component, referred to as HT, having a complex waveform consisting of various frequencies (usually above 1 MHs) having no relation to the frequency of the applied pulse, being shock-excited oscillations related to the natural electrical resonances of the aircraft itself and its electrical circuits.

In some cases only one of these components was present, while in others both appeared, the HF being superimposed on about the first quarter cycle of the LF waveform.

Processing of the recorded waveforms took two forms:

- Measuring the peak value of the transient and extrapolating to the full-threat value. Full threat was taken to be 200 kA peak current, 100 kA/us rate of current rise and 1014 V/m per second rate of rise of electrics! field; the last figure is a value which has been discussed but not yet agreed as a severe threat level. The extrapolation factor to be applied to the measurements obtained with the most severe test pulse (80 kV on the capacitor bank) varied with the particular waveform obtained, being 2 for LF waveforms showing resistive coupling (sine wave), 5 for LF waveforms showing inductive coupling (cosine wave) and 5 for all HF waveforms, assumed to depend on either di/dt or dE/dt, the measurements of dE/dt (see below) having suggested that a common extrapolation factor would be appropriate. Ref. 3 discusses in greater detail the relationship between induced HF voltages and the various parameters of the lightning stroke.
- (ii) Digitising the recorded waveform and storing in an HP9845B desk-top computer where its frequency spectrum was computed numerically, the objective being to determine the frequencies and damping factors of the natural resonant modes of the system.

MEASUREMENT OF AIRCRAFT CURRENT, CURRENT DENSITIES AND FIELDS - The waveform of the fuse-lage current was recorded at two locations - on the port side of the forward fuselage below the cockpit and on the starboard keel. These measurements were made by fitting a current transformer around a short wire anchored between two fastoners at each location.

A current density sensor was placed in turn at various points around the fuselage at four selected cross-sections as shown in Fig 2abb. These were compared with values calculated by means of the CLSU program INDCAL. Measurements were also made of the magnitude and direction of current densities on the upper and lower surfaces of the wings (Fig 2c).

Measurements were made of the magnetic field, and the current in various structural members, inside the Navigation and Weapon Aiming System (NAVWAS) bay, partly in order to assess the gasket design on the door. Finally, measurements were made with 'total flux loops' in the NAVWAS and starboard gun bays; such a loop is achieved by running a wire around the bay near the walls in a manner that maximises the induced voltage.

In the past, assessment of lightning induced effects has concentrated on the magnetic fields, but changing electrical fields can also be important, and these were measured at two positions on the aircraft. For this purpose an

EG & G balanced D sensor was installed above the centre spine and later in the cockpit; at each location the installation was varied to detect in turn the vertical and horizontal component of flux. Transmission of data to the recording room was again through a fibre optical link. The recorded waveforms were digitised and then integrated numerically using the HP9845B computer to obtain the waveform of D or E; spectral analysis was also performed using the FFT program.

LOW POWER INJECTION TESTS AT HIGHER FREQUENCY - For some tests the CLSU pulse generator was disconnected and transients were injected by means of a lower power higher frequency pulse generator originally produced for transient testing of equipments. Its output was a damped sine wave selectable in a nominal frequency range of 3-30 MHz; it had a voltage injection mode (direct connection) and a current injection mode (through a current transformer). The instrument was used initially as a convenient and safe way of commissioning the instrumentation without having to pulse the aircraft, by direct injection into the electrical system. It was also used to measure the coupling between particularly exposed cables (for example, in the aircraft spine) and the FCS cables. At the end of the main tests it was used in place of the CLSU pulsa generator for injection into the fuselage in order further to explore resonances of the system. Both voltage and current injection into the nose were employed at nominal frequencies of 3, 5 and 7 MHz, each at two generator HT lavels, the peak injected currents being in the range 3-28 A. By means of current transformers the nose current near the injection point was measured and the skin current in the fuselage was sampled using a surface wire attached to the starboard keel. Transmission, recording and frequency analysis of data were as in the main tests.

#### RESULTS

VOLTACES AND CURRENTS - In Table 1, the 18 channels of voltage measurement are grouped according to function and type of circuit, this classification also corresponding to the type of wiring. The impedance of the circuit is also given; this affects the level of coupled voltage and the relative importance of inductive and capacitive coupling. Table 1 includes the peak induced voltages extrapolated to full—threat level, both for normal and 'remote earth' configuration, and the principal frequency of the HF transients. Sample waveforms are shown in Fig 34-c.

The above results were obtained by plotting separately the peak induced LF and HF voltages against the voltage on the capacitor hank (20-80 kV). The linearity of the curves was one measure of the confidence to be placed in the results. Separate noise tests were made

during some current test pulses, consisting mainly of measuring the voltage received when the plugs of the dummy computers were disconnected, the power cupply to the diagnostic circuits was removed or the 6-way switches were open-circuited. The general conclusion was that for those channels where the measured induced voltage was substantial the effect of noise was small and in any case pessimistic. For measured transients of small amplitude, which are not of much practical importance, the proportion of noise was high in some cases.

The highest HF voltages are in Group A, because of the routing and type of wire; channel I also shows a high 'remote earth' LF voltage which in practice would stress the remote hardware at 260 V, but this is well within withstand capability. This group has low impedance, but generally speaking in the other circuits higher voltages correspond to higher impedances. Voltages do not seem to correlate with routs length, so the shielding is probably good over most of the length.

The transient bulk current measurements indicated again that the linearity of transient peak against capacitor voltage was generally good. Noise measurements consisted mainly of occasionally triggering the bank switch with zero voltage on the bank and sometimes passing a normal test current pulse but with the current transformer disconnected from but left close to the cable to which it had been fitted. Conclusions on the noise content were similar to those for the voltage measurements. The extrapolated full-threat peak values of the translent bulk currents in selected cables are given in Table 2. In this context a cable means a bundle of wires all feeding into the same connector on a computer etc. Fig 3d shows a current waveform consisting of HF only. An example of a frequency spectrum is given in Fig 4.

The amplitudes and waveforms obtained have been a basis for formulating tests on the FCS equipments themselves and should also contribute to the discussion on standardisation of equipment test techniques taking place in Committee SAE41 (4).

During the most severe tests (100 kA test current), with all FCS computers installed and with electrical and hydraulic power on, the FCS was monitored by means of ground test equipment and no malfunctions were observed.

AIRCRAFT CURRENT, CURRENT DENSITIES AND MAGNETIC FIELDS - The recorded fuselage surface currents at two locations indicated an LF waveform with a small HF transient (about 5 MHz, Q = 30) superimposed on the first quarter cycle. The HF amplitude was such that it would be 4 kA for a 100 kA test pulse.

The measurements of current density in the fuselage (Fig 2b) showed that current flow was inductively dominated and gave a good indication of high and low current concentrations and hence guidance on the regions where any doors need to make good electromagnetic contact, for example by means of gaskets. Current density on a wing surface is shown in Fig 2c.

Magnetic field strengths in the NAVWAS bay at various points for a fuselage current of 25 kA were 55-200 A/m, the current in a particular axial struct being 96 A; both field and current were approximately doubled when the conducting door gaskets were insulated. These figures indicate that the currents flowing internally in the bay at full-threat level would be as high as 800 A even with good gasket design.

The results for the 'total flux loops' were particularly significant in the gun bay; with gasket fitted, the peak induced voltage (for 25 kA test pulse) was 5 V and the waveform was essentially resistive (proportional to test current) while with the gasket insulated the peak was 30 V and of di/dt waveform, as shown by the waveforms of Fig 3e&f. Extrapolation by factors of 8 and 20 respectively gave full—threat values of 40 V and 600 V. These results show that the conducting gasket prevented the direct penetration of flux, so that when it was fitted only diffusion flux remained.

ELECTRICAL FIELD - The waveform of E often contained a burst of 40 MHz, followed by 5 MHz, oscillations. It is thought that the former were produced by the trigger circuit of the switch in the pulse generator while the latter were characteristic of the aircraft. Integration to produce E of course attenuated the HF in proportion to the frequency. Because of errors in the vertical positioning and the levelling of the zero line of the E trace prior to integration, the waveform of E often contained a spurious ramp and other distortions. but the ramp could be allowed for. There was also a wide spread in the amplitude of E and E from shot to shot, not accounted for by instrumentation and processing errors. This is thought to have been mainly due to variability in the operation of the switch, since E is very sensitive to conditions at switch-on, and such an explanation is consistent with the variable nature of the 40 MHz content. The highest values recorded (at the cockpit sensor) were  $1.6 \times 10^{13}$  V/m per second and 360 kV/m respectively, with 40 kV capacitor bank voltage. Average values under the same conditions were 1013 V/m per second and 220 kV/m. The rise time (from 10-90% of peak) for E was about 0.06 us; this is consistent with the field rising to a peak in a half cycle of the predominant aircraft resonance (5 MHz). A sample waveform of E and E is given in Fig 5.

Although there is no agreed specification level for É, a figure of  $10^{14}$  V/m per second is often quoted - a factor of 5 up on the average level to be expected at 80 kV in these tests. This extrapolation factor of 5 is the same as for magnetic coupling, and is therefore the full-threat extrapolation factor employed in Table 1 for all the HF voltages.

1

LOW POWER INJECTION TESTS AT HIGHER FREQUENCY - In general, frequency analysis of the waveforms indicated that for each frequency setting the nose and keel currents had the same predominant frequency, of amplitude proportional to the pulse generator HT. However, it was noted that with current injection giving a nose current of 4.4 MHz, the keel current contained a substantial component at 3.6 MHz as well as at 4.4 MHz, suggesting that a resonance had been excited. Construction of the resonance curve of the eircraft and return current conductors was attempted by plotting the ratio of keel to nose current against frequency as in Fig 6. A resonance near 3.5 MHz is suggested, although unfortunately there are no results at lower frequencies, which would have identified the shape of the curve and the position of the peak more exactly.

#### CONCLUSIONS

- (1) It has been shown that it is possible to carry out a simulated lightning test on a complete FBW aircraft at a severity level requiring comparatively small extrapolation to full threat and without hazard to flight capability provided the test level and completeness of equipment fit are gradually extended as results are obtained.
- (2) In general, the measurements were repeatable and scaled linearly with pulse generator HT voltage, although there was a wide spread in È measurements which suggests a wide variation in the switch-on time of the capacitor bank.
- (3) It was possible to measure induced voltages and currents, where they were of significant amplitude, in a reasonably interference-free manner by the employment of fibre optical links and by careful attention to shielding and grounding of the instrumentation. However, in some instances it was found that HF transients were reaching the instrumentation directly (from the trigger circuit of the pulse generator) and were not actually part of the waveform being measured.
- (4) The technique of digitising waveforms for subsequent processing (eg integration or frequency analysis) proved useful although the operations were the source of some inaccuracies and require review for future work.

- (5) The low power pulse generator of frequency range 3-30 MHz provided a useful auxiliary method of test for initial commissioning of the instrumentation, for measuring coupling between cables and for investigation of aircraft resonances.
- (6) Good agreement was obtained between measurement and calculation of current densities in the fuselage and wings.
- (7) The degree of penetration of current and magnetic field into equipment bays was assessed and also the dependence of these on the degree of contact around the door edges. It was shown that the conducting door gasket prevented direct flux penetration.
- A wide variety of waveforms was experienced, both LF and HF, and indicating coupling of the resistive, inductive and capacitive type. Application of test currents in the 3.4 to 8 MHz range indicated a principal resonance of the aircraft and return current conductors of about 3.5 MHz. With the CLSU pulse generator, oscillations in skin current and electrical field were mainly at 5 MHz; this higher figure can be accounted for by the modifying effect of the lower impedance of the CLSU pulse generator. It is of interest that calculation of the natural modes of electrical oscillation of the Jaguar in free flight by the 'stick model' method gives the following values for the first eight resonant frequencies: 6.5, 10.2, 18.1, 26.4, 30.2, 31.1, 38.1 and 44.3 MHz. Measured HF oscillations in the FCS were complex, but frequencies of 5 MHz and 2 MHz were most common. The amplitudes and waveforms obtained have been a basis for formulating tests on FCS equipments.
- (9) With reference to the validity of the simulation, although the current return conductors for the test pulse were designed to cause the magnetic field distribution to approximate to that in flight, there were still significant differences between the two situations, such as the driving voltage and impedance of the pulse generator, proximity of the aircraft to earth, and spurious HF oscillations characteristic of the switch in the pulse generator. The question of better simulation of the electrical field requires further work (see for example Refs 3 and 5), as does obtaining a more representative relative timing of the peaks of current, rate of change of current, and electrical field.

#### ACKNOWLEDGMENTS

The trial was conducted under MOD contract primarily by a British Aerospace team led by Mr P.A. Doggett and the Culham Lightning Studies Unit led by Mr B.J.C. Burrows; it was co-ordinated by Mr Doggett. The work is acknowledged of Massrs J.S.P. Hardy, G.A.M. Odam, R.F. Penny and N.J.C. Sanders in the RAE contribution to the preparation of instrumentation, making the measurements and processing the results.

#### REFERENCES

- 1. P.A. Doggett and I.P. MacDiarmid, "Lightning protection design and lightning threat flight clearance of a fly-by-wire Flight Control System for an unstable aircraft." Paper at this Conference.
- 2. B.I. Wahlgren, B.A. Olsson and C.A. Luther, "Lightning testing of the Viggen Aircraft", International Aerospace Conference on Lightning and Static Electricity, Oxford, UK, March 1982.
- 3. B.J.C. Burrows, "Nanosecond resolution of E, H and I in aircraft lightning test rigs." Paper at this Conference.
- 4. SAE Committee AE4L, "Test waveforms and techniques for assessing the effects of lightning induced transients." SAE Report AE4L-81-2, December, 1981.
- 5. W.G. Butters et al, "Assessment of lightning simulation test techniques." International Aerospace Conference on Lightning and Static Electricity, Oxford, UK, March 1982.

Table 1 - Induced voltages in 18 selected channels

	į			MT - Not	tested		earth tests	facorractly carried out	-	Go - 608 of	screened	triple. Meturn twis- ted pair.	These two	a loop for Chammel 12				A-f: Bose- fin A-f: Bose- rail					
lamote earth measurements	Probable	CTRAC	Cockeit	ameodze									} Exposure	unozajun		uj sineodny -	lage joint						
Bamote eertl	Extrapolated	dI/dt (wolts)	260	Ħ	Ľ		-	,	•	E	Ľ		57	13		69	۶	Ė	Ħ	°	i i	E	Ľ.
t threat	41/4:	(walts)	9172	Lero	tero	<b>Ze</b> 70		<b>27</b>	23	æ	<b>26</b> T0		Smell or Done	<b>Zero</b>		Zero	<b>2</b>	[76@-r] [25@-rj]	2470	Small or	<b>24</b> 70		Smell.
Extrapolated full threat results	Frechence	(ME)	3.3	15,5	•	2		2	9	•	20		2	1		\$	7	•	•	•	•		ı
Extrap	h	(wolts)	210	82	155	S		*	H	3	61		;	77		86	¥	5	10	9	•	15	, "
	Input i	computer	053	450	659	2.4K		2.4K	2.4K	100	250K		180K	20		300	1001	1000	82	8	20	01	9
	Cable type		Single wire	Twisted pair	Twisted pair	Go - one of	ecremed refered sefe	Return - one of	twisted	See commut	Screened twisted		Screened single	Screened twisted	Peter	Screened twisted pair	Screenod twisted pair	Screened twisted pair	Screened twisted pair	Screened twisted pair	Screened twisted	Single wire	Single wire
	Aircraft		Cockpit	U/c bay	Cockpit	Computer	bays	Computer	Computer bays	Centre apine	Formerel		Formrd fuselage	Formere		Ling	Spine-tail	Spine-tail	Fing	Spine-tail	Spine-tail	Mctary bay	Nose wheel bay
	Chamel.		Status reset	Weight on wheels		F0C1 + F0C2		F0C3 + FCC2	FOC4 + ADMC2	Poll gyro	Incidence		Roll QPS position	Poll QPS		M spoiler rem position	LE taileron servo position	M taileron servo position	LE spoiler commund	LH talleron	Al tailaron servo position arcitation	PC busher	F2 busher
	Group		(A) Discrete		6	(B) Computar- 2	computer		E1	(C) Sensor S	inputs 8		12	~		(Di) Actuator 10 drive and	(high	<u>s</u>	(D2) Actuator 16 drive and	(low impedance)	4	(E) Power Lines 7	9

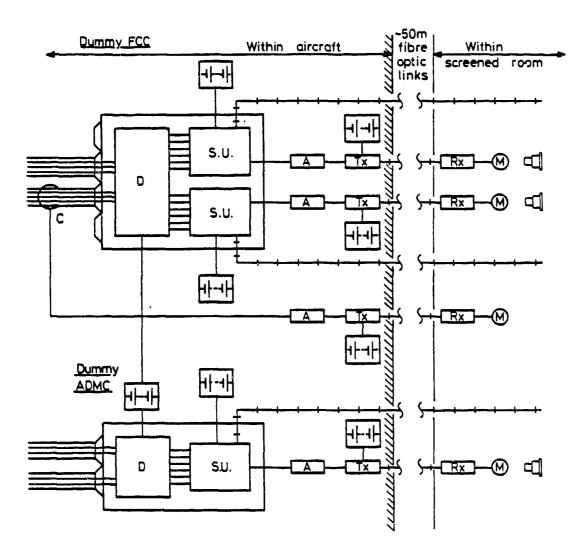
Table 2 - Bulk cable currents

Cable and	Extrapola threat pask		HF free		Waveform Figure	
test condition	LF	HF	MHz	Q		
FCC2 - J1 N-T	3.0	No reliabl	e measur	ament		
J2 N-T	Zero	1.5	5.2	11		
J3 N-T	15.0	3.0	2.3	4		
J4 N-T(P)	Zero	3.0	2.5	6	3d	
FCC4 - J2 N-T(P) J4 N-T(P)	Zero 16.5	2.0 1.25	Spread	in rang	e 1-15 MHz	
ADMC2 - J1 N-T J2 N-F	Zero Zero	1.0 2.25	10 5.5	NT 20		
V/UHF Aerial N-T Feeder*	1100	NT	NT	NT		
N-F	800	350	5.3	15		
Cockpit Whole N-T Loom 1 cable N-T (3 cables)	800 240	100 30	} 6	22		

N-T Nose-Tail N-F Nose-Fin N-T(P) Nose-Tail (Power on)

NT Not tested

\* The V/UHF aerial was the fin tip attachment point



Key: A = Attenuator

Tx = Fibre optic transmitter

Rx = Fibre optic receiver

M = Storage oscilloscope

□ = Camera

C = Bulk current detector (R.A.E)

+++ = Fibre optic link

D = Diagnostic circuits

S.U. = Switching unit

= Aircraft skin

Fig 1 Dummy computers, voltage and current monitoring systems

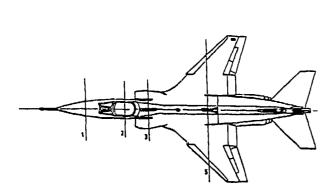
Fig 2 Current densities

Fig 3 Waveforms of transient voltages and currents

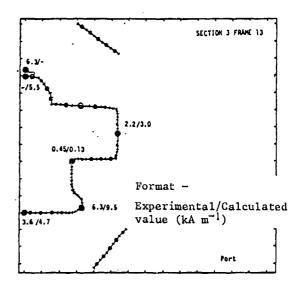
Fig 4 Bulk current (time and frequency domains) in ADMC2-J2 (40 kV bank voltage)

Fig 5 Ė and E on spine for pulse M1-14 (40 kV bank voltage)

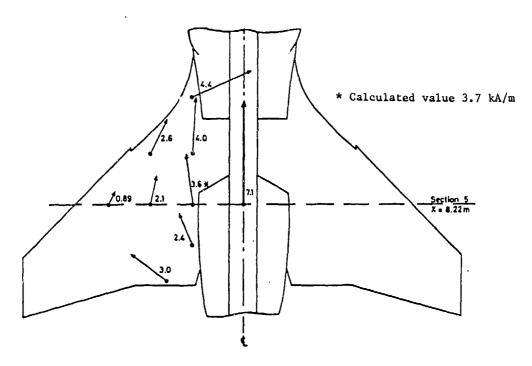
Fig 6 Frequency response of keel sensor current relative to nose current



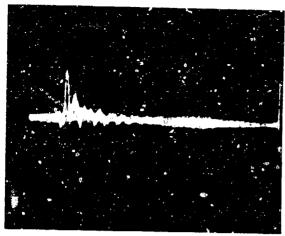
(a) Selected cross-sections



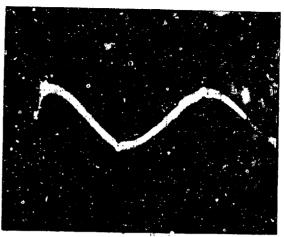
(b) Current density, section 3



(c) Current density, wing top



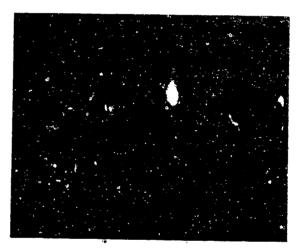
(a) Status reset (1) M/10/20 l µs/div. Induced voltage



(b) Status reset (1) F/23/8 5 μs/div (remote Earth). Induced voltage



(c) FCC3 → FCC2(3) M/5/22
2 µs/div. Computer signal
and induced voltage



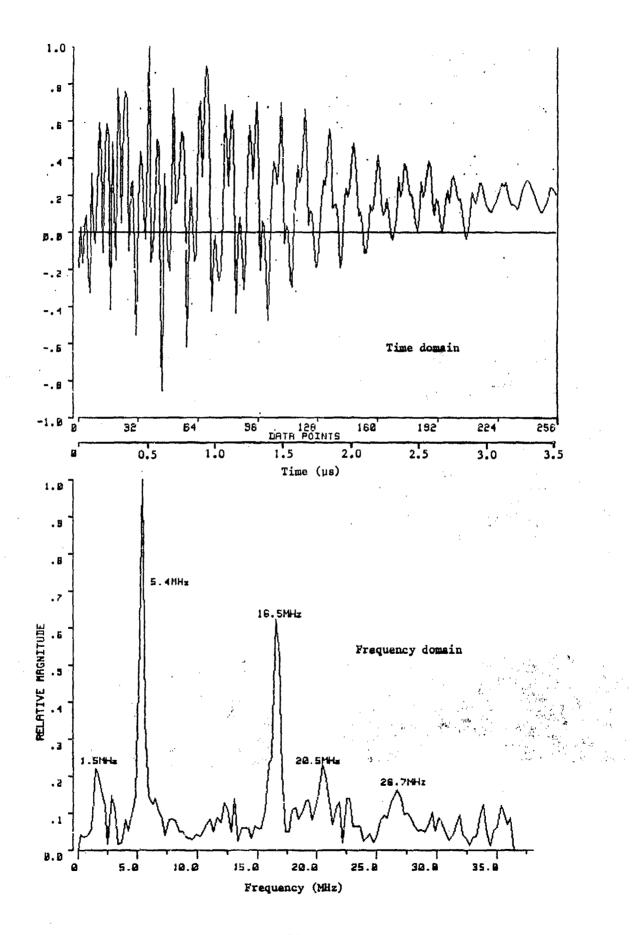
(d) 0.2 μs/div 140 mA/div FCC2-J4. Induced current

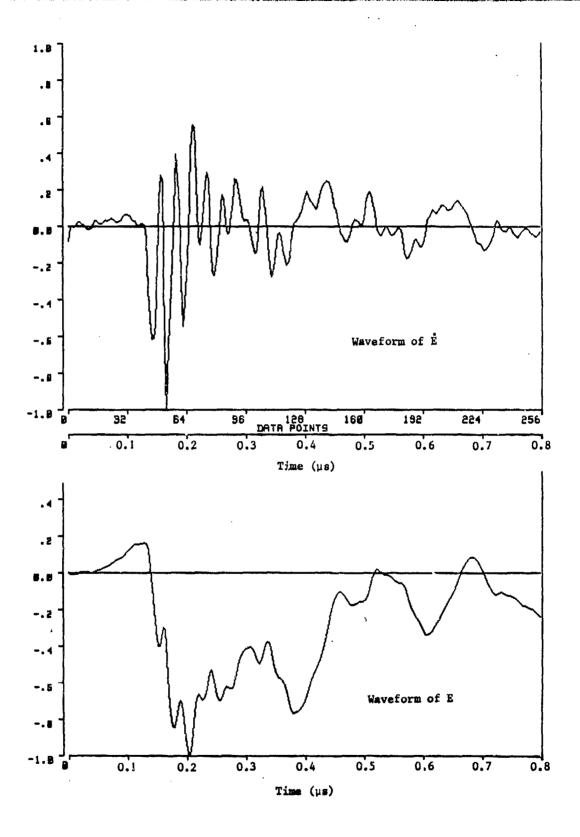


(e) Gun bay, EMC gasket normal 5 μs/div. Voltage in flux loop

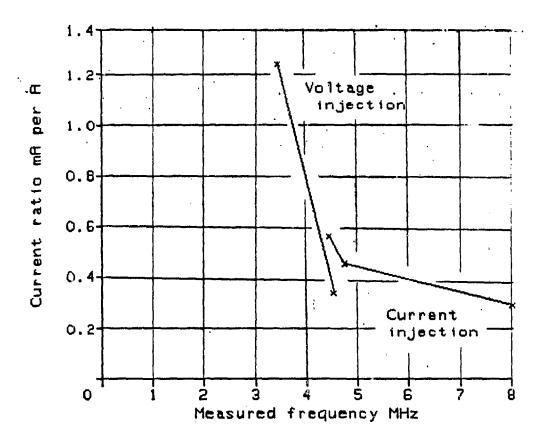


(f) Gun bay, EMC gasket insulated 5 μs/div. Voltage in flux loop





þ



The Streamer-Leader Transition in Uniform Fields

grelule,

Dr. J. A. Bicknell

Department of Physics, University of Manchester Institute of Science and Technology, P.O. Box 88, Manchester, M60 1QD, United Kingdom

#### ABSTRACT

Although the possibility of aircraft-triggered lightning is generally acknowledged, the mechanism remains unclear. Corons, which develops at suitable sites, either as a result of turboelectric charging, geometric field enhancement or both, must represent the early stage of a process which culminates in the transformation of corons streamers into a leader. Recent work on breakdown in short point-plane gaps suggests that the glow-to-arc transition is promoted once some (minimum) criterion is attained. This criterion may be current (Marode 1974) or energy (Sigmond/Goldman 1981) dependent although these parameters are not mutually exclusive.

An important feature of the corona at aircraft surfaces is the potentially large distance over which the streamers may propagate. This is a consequence of the electric field structure which resembles a locally enhanced quasi-uniform field rather than the strongly divergent fields associated with highly stressed point or rod/plane gaps. In the latter case prebreakdown currents may rise to several amperes in a few microseconds thus ensuring the requisite glow-to-arc transition on which the conversion of the corona streamsr to leader depends. craft potentials can never achieve the megavolt potentials required for such immense currents because of the dissipatory nature of the initial corons and the low charging rates produced by the triboelectric or other process. Positive corona streamers, however, can continue to grow if propagating in a uniform field greater than some critical, pressure-dependent value; these critical values have been observed on a large scale in thunderclouds and may well exist in relatively small volumes in regions where the average field is less than critical. This growth provides a possible means of achieving the current densities required for the important glow-to-are transition.

Current measurements made in an electrode configuration designed to simulate corona growth in uniform fields will be reported. The injected charge and a knowledge of the ambient electric field allow breakdown energies to be computed. These breakdown currents and associated energies will be compared with those obtained by Marode, Sigmond and Goldman in point-plane geometry. A possible model of aircraft-triggered lightning based on the comparison will be presented.

This paper was not available for incorporation into this book. Therefore, it will be published at a future date.

## AD P002196

INTRACLOUD LIGHTNING STREAMER MODELING BASED UPON IN SITU BALLOON MEASUREMENTS

G. J. Byrne, A. A. Few, M. E. Weber\*, and M. F. Stewart

Department of Space Physics and Astronomy Rice University Huston, Texas 77251

530,000

ABSTRACT

Intracloud lightning streamers have been modeled from balloon borne electric field change measurements and acoustic reconstructions of the lightning channel to approximate the streamer path. The simple model assumes the streamers extend along a straight line with constants velocity and uniform line charge concentration. Positive and negative pulsarity streamers were measured with an average velocity and line charge concentration to 5.3 x 10 ms and 6.7 x 10 CM , respectively.

A lightning-struck balloon measured field changes associated with the positive

A lightning-struck balloon measured field changes associated with the positive propagating streamer that coupled to the conducting balloon skin. The first results of these measurements are presented. The model for this streamer based on the balloon data is incomplete at the time of this writing.

0.0067/cm)

<sup>\*</sup> Now at Naval Research Laboratory, Washington, D. C. 20375

FREE BALLOONS designed to measure thunderstorm vector electric fields and vector electric field changes associated with lightning streamers were launched during the summers of 1976 and 1981 by Rice University participating in the Thunderstorm Research International Program (TRIP) at the Langmuir Laboratory for Atmospheric Research, New Mexico. During the 1981 flight, the balloon, constructed of aluminum coated mylar and 10 ft. in diameter, was struck by a lightning flash artificially triggered by a rocket fired toward the thunderstorm base. The instrument resolved field changes associated with the initial lightning streamer revealing information on the streamer propagation.

This paper presents the first results from that data analysis and recent results of modeling intracloud streamers with the 1976 data.

#### INSTRUMENTS

The operation of the balloon, Balloon Electric Field Sensor (BEFS), is described in detail by Christian and Few (1)\* and Weber et al. (2) and is shown at launch in Fig. 1. It is spherical in shape with a thin conducting outer skin. Three pairs of orthogonal surface patches (.23 m2) are isolated from the rest of the balloon skin and define the balloon coordinate axes. Each patch is electrically connected to the electronics payload inserted inside the balloon at its base. Charge amplifiers measure the amount of surface charge on each patch. Given the surface charge distribution induced by the thunderstorm electric field, assumed to be uniform, the solution for the undistorted vector electric field components in the balloon reference frame is well known for such a geometry.

Onboard inclinometers and magnetometers determine the orientation of the balloon in space giving the elements of the matrix which provides the transformation from the balloon coordinates to a stationary earth frame. The values of the electric field components calculated in this manner are then averaged over one period of the balloon rotation about its vertical axis; the rotation forced by spin paddles mounted on the balloon's equator.

The instrument is capable of resolving vector electric field changes on the order of 100 V/m. The time resolution of each component is either 2 or 4 ms, and is limited by the rate at which each charge sensor is sampled and is a function of the sampling sequence.

Altitude and atmospheric temperature are determined by an onboard pressure transducer and a thermistor. The data from each sensor is digitally encoded, multiplexed and telemetered to a ground receiving station.

#### STREAMER MODELING

From a BEFS flight on August 12, 1976 over Langmuir Laboratory, Weber et al. (2) were suc-

"Mumbers in parentheses designate References at end of paper.

cessful in modeling intracloud lightning streamers by interpreting the balloon-measured field changes (with an 8 ms resolution) as the effect of extending, unipolar streamers of constant line charge concentration as did Ogawa and Brook (3). Figure 2 illustrates the model.

The orientation and extent of the lightning channel is estimated from acoustic reconstructions of thunder sources (4). The streamer path is then approximated as the straight line that minimizes the sum of the perpendicular distances from the line to the thunder sources and that connects a source volume charge with the streamer termination point.

The balloon coordinates are provided by a directional receiving antenna (AN/GMD-2) and the atmospheric pressure measurement.

Usually, the streamer polarity and direction of propagation are clear from the basic structure of the vector field changes. To complete the streamer model, the line charge concentration and propagation velocity chosen are those that yield the best fit of the calculated vector field changes to those measured by the balloon.

Figure 3a illustrates the lightning channel reconstruction, model streamer path and the vector electric field changes for the lightning flash at 11:54:15 MST. A positive streamer, estimated to be 3.8 km in length, propagated in the direction indicated with an estimated velocity of  $2.3 \times 10^4~\mathrm{ms}^{-1}$  and line charge concentration of  $4.9 \times 10^{-3}~\mathrm{Cm}^{-1}$ . Using these model parameters, the streamer current was 110 Amperes and total charge transferred was 18 Coulombs.

Figure 3b shows the streamer model of the flash at 11:52:33 MST. In this case streamers of either polarity could reasonably fit the observed field changes; a 4.1 km positive streamer of  $14.4 \times 10^{-3}$  Cm<sup>-1</sup> (580 Amperes) moving at  $4 \times 10^{4}$  ms<sup>-1</sup> in Model 1 or a negative streamer of  $-5.7 \times 10^{-3}$  Cm<sup>-1</sup> (230 Amperes) moving at  $4 \times 10^{4}$  ms<sup>-1</sup> in Model 2.

Of the seven streamers modeled from this flight, the average propagation velocity was  $5.3 \times 10^{14} \, \mathrm{ms^{-1}}$  and average length was  $4.7 \, \mathrm{km}$ . Streamers of both polarity were found with an average absolute line charge concentration of  $6.7 \times 10^{-3} \, \mathrm{Cm^{-1}}$ , and average current and net charge transferred of 390 Amperes and 30 Coulombs, respectively.

#### TRIP 81 RESULTS

In 1981, a BEFS was launched into a thunderstorm on August 14 at 13:35 MST. The launch site is at 3.2 km altitude. Eight minutes after launch (13:43:13 MST), the balloon was struck by a lightning flash artificially triggered as a rocket was fired from the ground toward the thunderstorm base. A rapidly unspooling conducting wire connected the rocket to ground. Triggered lightning is discussed by Newman et al. (5), Figur et al. (6), and Habert and Mouget (7).

In triggered lightning, a streamer starts at the rocket wire tip when the local field

enhancement reaches the threshold for streamer initiation (rocket height of 100-300 m). The atreamer "slowly" propagates upward toward a cloud charge region which is subsequently discharged by the ensuing very fast return stroke.

Ground measurements by Laroche et al. (8) indicate the flash at (13:43:13) was initiated by an upward propagating positive streamer. Figure 4 illustrates this and the location of the balloon relative to the rocket launch site. The balloon was 1.6 km south southeast and 1.6 km above (4.8 km altitude; 0° C) the rocket site and immediately below the cloud base. The balloon measured the magnitude of the electric field at this altitude prior to the flash to be approximately 100 kV/m. The direction of the field vector indicated a negative charge center was above and to the south.

Figure 5 shows the horizontal components of the vector electric field changes associated with the initial lightning streamer as measured by the balloon. The vertical field change was relatively small compared to those in the horizontal. The trends of the field changes are consistent with a positive streamer propagating mostly horizontally and southeast toward the balloon.

A ground electric field record indicates the streamer was initiated at the rocket at 13 hours, 43 minutes, 13 seconds and 307 ms MST (9). The first resolved field change (100 V/m) measured by the balloon occurred at 316 ms. By 348 ms, the absolute value of the north-south component (Ey) had increased by approximately 50 kV/m and by 349 ms, the absolute value of the esst-west component ( $E_{\rm X}$ ) had increased by 90 kV/m before data telemetry was lost at 351 ms. We assume the telemetry loss coincides with either the time at which the streamer coupled with the balloon or the time of the lightning return In either case, the maximum time elapsed between the streamer initiation at the rocket and the coupling to the balloon was approximately 44 ms.

Unfortunately, the acoustic reconstruction of this flash necessary for modeling the streamer path, is unavailable at the time of this writing. However, the case of streamer propagation along a straight line from the initiation point to the balloon gives the minimum streamer velocity of approximately  $5.0 \times 10^{14} \, \mathrm{ms}^{-1}$ .

#### SUMMARY

Seven intracloud lightning streamers have been modeled successfully from the 1976 BEFS data. The estimated streamer velocities ranged from  $2.3\times10^4~{\rm ms^{-1}}$  to  $15.4\times10^4~{\rm ms^{-1}}$  with the mean velocity  $5.3\times10^4~{\rm ms^{-1}}$ . These measurements are consistent with those determined by Ishakaws (10);  $(5\times10^4~{\rm ms^{-1}})$ , Taylor (11);  $1.5\times10^4~{\rm to}~1\times10^5~{\rm ms^{-1}})$ , and Proctor (12);  $6\times10^4~{\rm to}~5\times10^5~{\rm ms^{-1}})$ . The absolute value of the current in the modeled streamers ranged from 70 to 1530 Amperes (average 390 A) with an average line charge concentration of  $6.7\times10^{-3}~{\rm Cm^{-1}}$ 

compared to Ogawa and Brook (120 A) and Proctor (90 to 400 A).

The Weber et al. models suggest that intracloud streamers of both polarity occur and that negative streamers may be fairly common (four were positive, two negative and one could be modeled positive or negative). This is in contrast to the conclusions of Ogawa and Brook and to the fact that since positive streamers can propagate in substantially lower fields than negative ones, they would seem to be much more likely to initiate lightning (13).

The rocket triggered flash of 1981 was determined to have an initial positive streamer velocity of at least 5 × 10<sup>4</sup> ms<sup>-1</sup>. Triggered lightning streamers have been photographically determined to have velocities between 2 × 10<sup>4</sup> ms<sup>-1</sup> and 10<sup>5</sup> ms<sup>-1</sup> (14). We hope to obtain an acoustic reconstruction of this flash in the near future in order to proceed with modeling the streamer based on the balloon field data.

This lightning struck balloon flight may afford a unique opportunity to model the influence of an airborne conductor on streamer propagation and the path of the ensuing lightning stroke as well as the coupling mechanism between the streamer and conductor.

#### **ACKNOWLEDGMENTS**

We thank A. C. Conrad and A. J. Weinheimer for their great help on this project. Special thanks to C. B. Moore and the personnel of Langmuir Laboratory for their support in 1976 and 1981 and continuing assistance. This research was supported by the Atmospheric Sciences Program of the Office of Naval Research on Contract N00014-75-C-0139 and by the Atmospheric Research Section of the National Science Foundation under Grant ATM-8016164.

#### REFERENCES

- 1. H. J. Christian and A. A. Few, "The Measurement of Atmospheric Electric Fields Using a Newly Developed Balloon Sensor," in "Electrical Processes in Atmospheres." Darmstadt, FRG, Dr. Dietrich Steinkopff Verlag, 1977.
- 2. M. E. Weber, H. J. Christian, A. A. Few, and M. F. Stewert, "A Thundercloud Electric Field Sounding: Charge Distribution and Lightning." J. Geophys. Res., 87, 7158-7169, 1982.
- ning." J. Geophys. Res., 87, 7158-7169, 1982.
  3. T. Ogawa and M. Brook, "The Mechanism of Intracloud Lightning Discharge." J. Geophys. Res., 69, 5141-5150, 1964.
- 4. A. A. Few, "Lightning Channel Raconstruction From Thunder Measurements." J. Geophys. Res., 75, 7517-7523, 1970. A. A. Few, D. R. McGorman, and J. L. Bohannon, "Thundercloud Charge Distributions, Inferences From the Intracloud Structure of Lightning Channels." "Preprint Volume: Conference on Cloud Physics and Atmospheric Electricity." Issaquah, WA, 1978.
- 5. M. M. Newman, J. R. Strahmann, J. D. Robb, E. A. Lewis, S. G. Martin, and S. V. Zinn, "Triggered Lightning Strokes at Very Close



Fig. 1 - BEFS being prepared for launch. One of the circular sensing patches and a spin paddle can be seen.

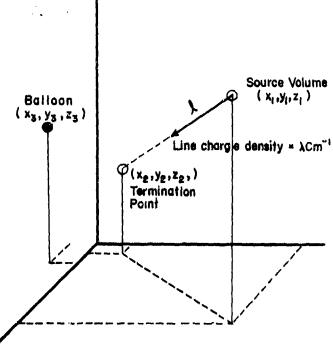


Fig. 2 — A model to interpret electric field changes during intracloud lightning. Charge is withdrawn from a spherical volume centered at coordinates  $\frac{1}{2}$ , and distributed uniformly along the line  $\frac{1}{2}$ . At time t, this "streamer" has advanced a distance 1 — vt where v is the constant velocity of propagation for the "streamer." The electric field change at the balloon's position  $\frac{1}{2}$  results from this line charge and from the withdrawal of charge from the source volume.

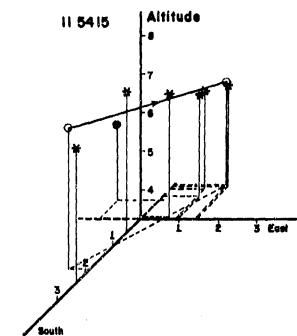
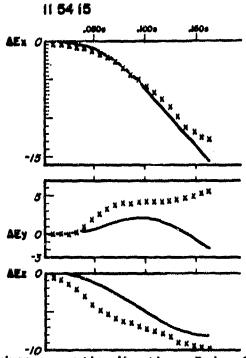
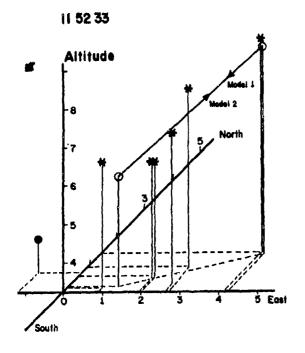


Fig. 3a — Lightning channel reconstruction and measured and calculated electric field changes for the flash at 11:54:15 MBT. Plotted are: (1) Model lightning channel relative to a coordinate system with origin at Languair Laboratory. Asterisks denote reconstructed thunder sources. Open circles are source and termination points for the model streamer; arrowhead



gives propagation direction. Darkened circle is the balloon's position at the time of the discharge. (2) Calculated electric field changes (solid lines); measured electric field changes (X characters — spacing reflects digital sampling rate). In the stationary coordinate frame the +x axis points east, +y north and +x upwards.



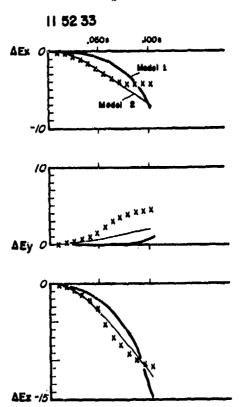


Fig. 3b — Same as Fig. 3a for the flash at 11:52:33 for a positive streamer (Model 1) or negative streamer (Model 2).

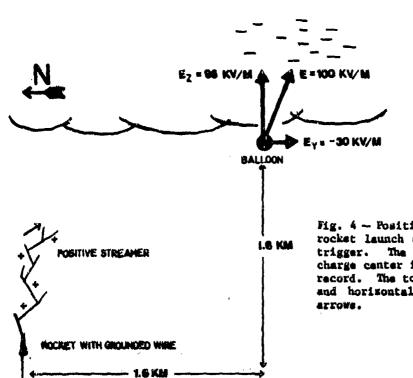
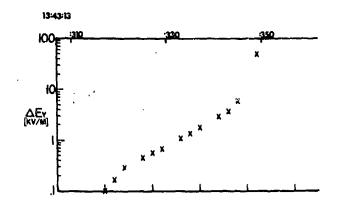


Fig. 4 — Position of the balloon relative to the rocket launch site at the time of the lightning trigger. The general location of the negative charge center is inferred from the balloon field record. The total field vector and the vertical and horisontal field components are shown by arrows.



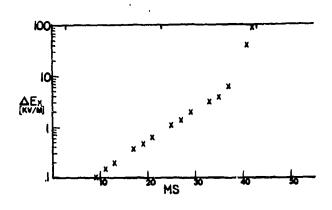


Fig. 5 — The changes in the absolute value of the east-west electric field component ( $\Delta E_{\rm X}$ ) and north-south field component ( $\Delta E_{\rm Y}$ ) with time due to a positive streamer propagating toward the balloon. The streamer was initiated at t = 0 ms (:307 ms). Telemetry was lost at t = 44 ms (:351 ms).

Range." J. Geophys. Res., 72, 4761-4764, 1967.

6. R. Fieux, C. Gary, and P. Hubert, "Artificial Triggering of Lightning Above Ground." Nature, 257, 212-214, 1975.

7. P. Hubert and G. Mouget, "Return Stroke Velocity Measurements in Two Triggered Lightning Flankes." J. Geophys. Res., 86, 5253-5261, 1981.

8. P. Laroche, P. Hubert, and A. Eybert-Berard, "Triggered Lightning Flashes at TRIP 81: First Results." Paper presented at AGU Meeting, San Francisco, December 7-11, 1981.

9. Courtesy of C. B. Moore, New Maxico Institute of Mining and Technology.

10. H. Ishikawa, "Nature of Lightning Discharges as origins of Atmospherics." Proc. Res. Inst. Atmos., Nagoya Univ. 8A, 1-274, 1961.
11. W. L. Taylor, "A VHF Technique for

11. W. L. Taylor, "A VHF Technique for Space-Time Mapping of Lightning Discharge Processes." J. Geophys. Res., 83, 3575-3583, 1978.

cesses." J. Geophys. Res., 83, 3575-3583, 1978.
12. D. E. Proctor, "VHF Radio Pictures of Cloud Flashes." J. Geophys. Res., 86, 4041-4071, 1981.

13. J. Latham, "The Electrification of Thunderstorms." Quart. J. Roy. Met. Soc., 107, 277-298, 1981.

14. J. L. Boulay and P. Laroche, "General Presentation of the ONERA Lightning Research Program." Paper presented at AGU Meeting, San Francisco, December 7-11, 1981.

# AD P002197

PROPAGATION OF DISCHARGE CHANNEL INSIDE THE CLOUD

P. P. Pathak, J. Rai and N.C. Varshneya
Physics Department
University of Roorkee
Roorkee -24767 (U.P.)
India

#### ABSTRACT

A mechanism for propagation of discharge channel inside the cloud is proposed. The mechanism is based on the motion of charged streamers under the combined influence of cloud-electric field and geomagnetic field. The mechanism gives a theoretical explanation for various experimental observations that most intracloud discharges and incloud portions of ground discharge are oriented roughly horizontally and are aligned always in the same direction.

THE MOST COMMONLY OBSERVED DISCHARGES are the intracloud (IC) type. They constitute from 60% at moderate latitudes to 90% in tropics, of total lightning (1,2). Attempts to determine their structure, though very few, gave widely varying results. From the earlier attempts (3-11), no definite conclusion can be drawn. Some of them had a better fit of their data to a vertical dipole model (4-6) while others getting vertical and horizontal separation of charge centers approximately equal (3). Among those who found considerable horizontal extent of IC channel are Takeuti (6), Workman et al. (7), Ligda (8), Nakano (9), Stanford (10) and Hughes (11). Relatively recent observations of Teer and Few (12) and Brantley et al. (13), however, conclusively confirmed that most IC discharges are horizontal and vertical cloud-to-Ground (GC) discharges become horizontal after entering the cloud. The direction of the alignment was observed to be different from the direction of motion of thunderstorm, in contrary to the observation of Ogawa and Brook (5). This lead to an end of earlier speculation that the direction of alignment is decided by the direction of motion of the thunderstorm. Therefore, there is a strong need for alignment machanism, as stressed by Teer and Few (12). Here, a me chanism of propagation of discharge channel inside a cloud is presented, which also explains the alignment of the channel.

MECHANISM OF DISCHARGE

Qualitatively, the mechanism of discharge has been explained in terms of streamer-model (14). The discharge begins with small local discharges at high field electrode. Consequently the luminous pulses of ionisation propagate towards the low-field-electrode. These pulses are named as primary streamers (15). The primary streamers propagate in groups, to form a narrow luminous channel termed as secondary streamer (15). The secondary streamer carries the potential of high field electrode and therefore, it produces a very strong field when reaches near the other electrode. As a result, a return stroke starts from there, rendering the discharge channel highly conducting. The return stroke, which may be called as resultant se condary streamer, also consists of primary streamers of opposite polarity and having speeds orders of magnitude higher than the primary streamers of previous se condary streamer.

In general, the above terminology is not used in lightning research. Therefore, for convinience, in the following text, the word streamer will be reserved for above mentioned primary streamers

and, the secondary streamers will be called as 'channel'. For the study of channel properties and its orientation, the motion of streamers is need be con-

sidered in detail.

MOTION OF STREAMERS - Streamer is a bunch of charges and it can be considered as a single body for propagation study (15). The velocity of streamers depends on strength of fields and the gaseous pressure in the medium. The two types of streamers - positive and negative, have wide difference in their propagation characteristics. The positive streamers are faster and more vigorous than the negative ones. Also, the negative streamers are quinched after propagating small distances while positive ones propagate large distances. The average charge on both types of streamers is known to be of order of tens of picocoulombs and their radii of order of tens of microns.

In the case of lightning discharge, the conditions in which the streamers move, vary with time and space. For example, the negative streamers in the stepped leader start from high field and more towards low field region (i.e. towards the ground). As they progress towards the ground, the potential gradient between the tip of channel and the ground goes on increasing. The surrounding atmospheric pressure also increases as it propagates to lower levels. Reverse is true in the case of return stroke where the streamers start in a very high field which goes on reducing as the channel propagates upward. After entering the cloud they reach in the region of low and variable fields (16). Alongwith these variable electrical fields, there exists a geomagnetic field. The geomagnetic field, though weak, is likely to influence the motion of streamers when the electrical fields are low and the two forces are comparable. In the next section, the combined influence of electrical and geomagnetic field is consi-

MOTION OF STREAMERS UNDER ELECTRIC AND MAGNETIC FIELDS - In presence of magnetic field B, a streamer of mass m and charge q experiences a Lorentz force

$$\mathbf{F} = \mathbf{q}[\mathbf{E} + \mathbf{\vec{v}} \times \mathbf{\vec{B}}] \tag{1}$$

where  $\overline{\mathbf{v}}$  is the streamer velocity and  $\mathbf{E}$ is the electric field. Due to this force the streamer starts gyrating and moves in a helical path, around the magnetic field line, with redius

$$R_{g} = \frac{mv_{\parallel}}{q(E_{\perp} + v_{\perp}B)}$$
 (2)

vi and E being the components of w and

E respectively, in the direction normal to B. Equation (2) shows that the streamers with different mass, charge and velocity components, have different radius of gyration. All of them, however gyrate around identical axis of helix. The channel therefore, propagates along the magnetic field line. Apparent radius of the channel is approximately the maximum value of Rg (Fig. 1) i.e. the radius of gyration of heaviest streamers with smallest q. The combination however, is not true. The streamers consist of charged particles and ions, the heavier streamers ought to have more charge. Thus the values are to be optimised some-

RESULTS AND DISCUSSIONS
It is difficult to evaluate the radius Rg, with accuracy as the streamer parameters m, q, v are not precisely known. A rough estimate may however be made from the values of ion density. Loeb (15) has given some representative valwes of ion density (see Table 3.3 of his book). 3.5x109 ions consisting of few protons and neutrons have a mass of order of 10-17 kg and charge of order of 10-10 coulomb (if singly ionised). The velocity component v<sub>1</sub> is expected to be a fraction of tip velocity 6x105 ms<sup>-1</sup>. If  $\theta$ , the angle between  $\overline{v}$  and  $\overline{B}$  is large  $\underline{v}$ ,  $\underline{v}$  v sin $\theta$  is of the same order as  $\underline{v}$  ( $105 \text{ ms}^{-1}$ ). With  $B = 3 \times 10^{-5}$  we ber  $\underline{m}$  and  $\underline{E}$  very small (say  $\sim 100 \text{ V/m}$  in some parts of cloud) Rg comes out to be about 300 m, similar to the observed value (13). The values of parameters, as taken above, are quite arbitrary and variable. For example some measurements (17,18) show that the charge on streamers cannot exceed more than few tens of picocoulombs. The tip velocity in the case of return stroke is very high(14). Also, the angle 0 in higher latitudes is small which reduces the component v of velocity. Taking all these factors into account one can see that Rg can exceed even more than few kilometers.

The orientation of the channel is along the geomagnetic field line. In low latitudes the geomagnetic field is nearly horizontal in north-south direction. Observations of intracloud lightnings listed in first para above, have not recorded the actual direction of horizontal channels. Although from the report of Teer and Few (12) it is evident that the channels were aligned in north-south direction. They have stated, "The horizontal portions of all channels are aligned perpendicular to storm motion" and the storm motion was reported to be from east to west. Similarly Ogawa and Brook (5) reported the direction of

horizontal intracloud channel to be in the direction of storm motion, and the storm motion was in nearly north-south direction. More recent and detailed analysis (19,20) shows maximum spreading of accoustically reconstructed channels in north-south direction. These observations clearly show the maximum speading in north-south direction. Hence it should be noted that the direction of the channel alignment is not related to the direction of movement of the storm, as has been often speculated. The horizontal stretching of the storm, making the electric field E more inclined to vertical may affect the dimensions of the channel by reducing E1. But it is not expected to affect the direction of

alignment of the channel.

The length of horizontal channel depends upon the charge distribution inside the cloud while the hieght, at which it becomes horizontal, depends upon cloud hieght and on the structure of vertical field. The horizontal branching from the vertical channel starts only where the vertical electrical field reduces to the value low enough to make the magnetic and electrical force on the streamer, comparable. The horizontal branching from the vertical channel can not be seen outside the cloud because of the following reasons: (i) The strong circular magnetic field of the channel current does not allow any horizontal motion of charges (see Pinch effect in ref. 21), (11) Vertical electrical field outside the cloud is very large. So the electrical force is a many orders of magnitudes higher than the geomagnetic force, (iii) Due to the lack of sufficleat charges in the air, outside the leader channel, the streamer cannot propagate large distances horizontally.

However, inside the cloud where electrical fields are small (16), whole channel starte gyrating with 6-component of velocity as drift velocity. The mag-netic field due to this circular current ir added to the geomagnetic field. This gives an additional magnetic force in perpendicular plane to reduce Rg. Thus the vertical channel becomes horizontal

after entering the cloud.

The experimental determination of the length in horizontal direction by optical methods cannot be expected to give actual values unless the location of the observation point is properly chosen. As we see that the orientation of the channel is in north-south direction, full length of the channel can be photographed only if it is perpendicular to the viewing direction. For this purpose the observation point should be located in the east or west from the

storm. If the storm is in far north or south from the observation point, the horizontal extent photographed would be only the diameter of the channel i.e. 2 Rg, which would not exceed more than a kilometer and its alignment would seem to be in east-west direction. Also, the horizontal extent and the vertical extent would be nearly same, as observed by Renolds and Neil (3). It is therefore, strongly anticipated that any optical observations for proper conclusions about the horizontal extent of the channels should be done from the east or west direction from the thundercloud.

The acoustic observations, however, do not involve such type of difficulty. Such observations (9,12,13,19,20) give more realistic situation and they are in accordance with this theory.

The orientation of channel inside the cloud is along the geomagnetic field Therefore, its inclination to horizontal varies with the latitude of the place of observation. In low latitudes, where magnetic field is horizontal, the channel would be horizontal. In higher latitudes, it would be inclined to the horizontal by an angle  $\lambda$  - the dip angle. At the magnetic poles ( $\lambda = \pi/2$ ) the intracloud lightning would also be vertical and cloud-to-ground lightning would remain vertical even after entering the cloud.

However, there might be some cases of a general orientation of incloud portions of the vertical channel. When the streamer parameters are such (e.g. larger m and smaller q), that the value of Eg is extremely large, say, of the order of few kilometers, one single helix of gyration is not completed. This makes the channel to appear as curved in vertical plane and in east-west direction (i.e. in a plane perpendicular to B). To say anything conclusively about this possibility, more accurate values of streamer parameters are needed.

#### CONCLUSION

From the above discussion it can be concluded that all intracloud discharge channels and the incloud portions of the vertical cloud-to-ground channel are aligned along the geomagnetic fie. d direction. Therefore they are horizontal in low latitudes, inclined in high latitudes and vertical at poles but in all the cases, in meridinal plane. Some possibilities of general orientation in the plane perpendicular to meridinal plane are also found.

Acknowledgement The work has been supported by ISRO Grant No. 750-12-61.

HE BRICKS

1. S. V. C. Aiya, Lightning and Power Systems", Electrotechnology (Banga-lore) 12, 1-12, 1968.

2. J. Galejs, "Terrestrial propagation of long electromagnetic waves"

Pergamon Press, New York, 1972. 3. S.E. Beynolds and H.W. Neill, "Distribution and Discharge of Thunderstorm Charge Centres", J. Wet., 12,1-12,

4. L.G. Smith, "Intracloud Lightning

Discharges", Quart . J. Roy. Met. Soc., 83, 103-111, 1957.
5. T. Ogawa and M. Brook, 'We chanism of Intracloud Lightning Discharge",

J. Geophys. Res. 69, 5141-5150, 1964. 6. T. Take uti, "Studies on Thunder-storm Electricity, (1) Gloud Discharge",

J. Geomagn. Geoelect., 17, 59-68, 1965. 7. E.J. Workman, R.E. Holzer and G.T. Pelsor", The Electrical Structure of Thunderstorms", NASA Technical Memo.

No. 864, 1-47, 1942.

8. M. Ligda, "The Radar Observations of Lightning", J. Atmos. Terr. Phys. 9, 329, 1956.

9. M. Nekano, Lightning Channel Determined by Thunder", Proc. Res. Inst. Atmos. Nagoya University, 20, 1, 1973.
10. J.L. Stanford, "Polarisation

of 500 Hz Electromagnetic Noise from Thunderstorms: A New Interpretation of Existing Data", J. Atmos. Terr. Phys., 28, 116-119, 1971.

11. W.L. Hughes, "Preliminary Resu-

Its of Horizontally and Vertically Polarised Spheric Field Messurements at Altitude of 15000 to 20000 Feet, Quart. Hep. to U.S. Army Electronics Commond. WP 69-1 -3, 1968.

12. T.L. Teer and A.A. Few, "Hori-zontal Lightning", J. Geophys. Res., 79,

3536-3541, 1974. 13. R.D. Brantley, J.A. Tiller and M. A. Uman, Lightning Properties in Floride Thunderstorms from Vedio Tape Records", J. Geophys. Res. 80, 3402-3406. 1975.

"Lightning" , McGraw 14. M. A. Uman,

Hill, New York, 1969.

25. L.B. Loeb, "Electrical Caronas", University of California Press, Berkeley

16. W.P. Winn, C.B. Moore and C.R. Holmes", Electric Field Structure in an Active Part of a Small Isolated Thundercloud", J. Geophys. Res., 86, 1187-1193,

17. F. Bastien and E. Morode, "The Determination of Basic Quantities during Glow-to-Arc Transition in a Positive Point-to-Plane Discharge", J. Phys. D (Applied Physics) 12, 249-463, 1979.

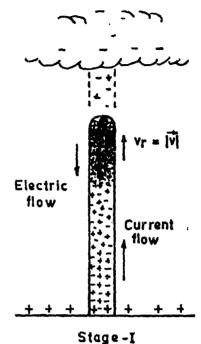
18. T.S. Verma, "A Laboratory Study of Rain-Gugh", Ph. D. Thesis, UMIST Man-

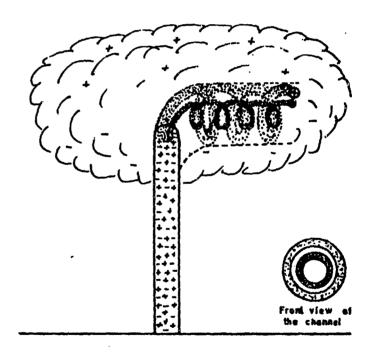
of Rain-Gush", Ph.D. Inesis, UMIST Manchester.

19. D.R. MacGorman, A.A. Few and T.L. Teer", Layered Lightning Activity", J. Geophys. Res. 86, 9900-9910, 1981.

20. P.P. Pathak, J. Rai, N.C. Varshneya and C.R. Holmes, "Orientation of Intracloud Lightning", Communicated to J. Atmos. Terr. Phys. 1983.

21. J. Rai, A.K. Singh and S.K.Saha "Magnetic Field Within the Return Stroke Channel of Lightning", Ind. J. Radio Space Phys., 2, 240-242, 1973.





Stage - II

Fig. 1 - Propagating channel before and after entering the cloud.

## ELECTROMAGNETIC MEASUREMENTS OF LIGHTNING

ATTACHMEN

ATTACHMENT TO AIRCRAFT

P.L. Rustan, B. Kuhlman, J. Shovalter
Air Force Wright Aeronautical Laboratory (AFWAL/FIESL)
Wright-Patterson AFB, Ohio 45433

and

# J. Reazer Technology/Scientific Services Dayton, Ohio 45431

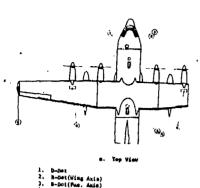
ABSTRACT - A NOAA WC-130 aircraft instrumented with electromagnetic field sensors was flown in South Florida in close proximity to thunderstorms in the summer of 1981. Electromagnetic field measurements of two direct lightning attachments to the aircraft were recorded in a continuous analog recorder with a frequency response of 2 MHz on 17 July and 26 Aug. The 17 July flash lasted 295 msec and was characterized by about 200 individual pulses with a maximum pulse repetition rate of 100 pulses/ 12000) sec. The maximum uniform current of any of the isolated pulses was 650 Amperes. The risetimes of these pulses ranged from less than 350 nsec to about 12 used. This flash had a con-(nicrosec) tinuing current of 50 A, caused eleven small burn marks along the fuselage and burned through one of two external antenna wires on top of the aircraft. The 26 Aug flash lasted 460 msec and was characterized by about 300 individual pulses with a maximum pulse repetition rate of 104 pulses/sec. The maximum uniform current of these pulses was 3 kA. The risetime of these pulses ranged from less than 350 nsec to about 10 usec. There was no evidence of a continuing current component in this flash. Two of the navigation computers experienced memory upsets during the attachment and were disabled for the rest of the flight. During both of the direct attachments, the aircraft was flying inside clouds at an altitude of about 16,000 ft and no previous lightning flashes had been observed closer than about 5 km from the aircraft. These aircraft lightning strikes and many others presented in the literature indicate that the physical mechanisms of most lightning attachments to gircraft are different than those of cloudto-ground and intracloud lightning. This paper presents an analysis of the WC-130 direct strikes and a description of a possible mechanism for lightning attachment to aircraft.

Several experimental programs (1)-(8) have been performed to determine the characteristics of lightning attachment to aircraft. Some of the electromagnetic characteristics of over 300 direct lightning strikes have been measured in various aircraft. The electromagnetic field data recorded on the aircraft during direct attachments have different characteristics than those recorded on the ground during natural cloud-to-ground and intracloud flashes. However, far-field data recorded in an aircraft at 3 to 35 km from a natural lightning flash have similar characteristics to those recorded on the ground (9). These experimental results indicate that in most cases the physical process that produces lightning attachment to aircraft is different than the process which causes natural intracloud or cloud-to-ground discharges.

Here we analyze the characteristics of the electromagnetic field measured during the two direct lightning attachments to the WC-130. Then, by comparing these results with other experimental data (1)-(7) and theoretical analysis (10)-(15), we present a description of a possible mechanism of cloud-to-aircraft lightning. On the basis of the conditions surrounding the aircraft during reported lightning attachment (16)-(19), it appears that over 95% of all lightning attachments to aircraft are produced by some type of cloud-to-aircraft discharge, usually referred to in the literature as a triggered flash (10)-(12).

#### INSTRUMENTATION

A WC-130 aircraft provided by the National Oceanographic and Atmospheric Administration (NOAA) was located at the Mismi airport and flown over South Florida during the summer of 1981. The aircraft was instrumented with 11 sensors to measure the electromagnetic fields on the surface of the aircraft. The sensors were mounted on the aircraft as shown in Figure 1. These types of sensors are designed to operate away from the main lightning channel where there is no effect



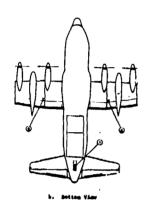


Fig 1. Sensor Locations

due to arc and corona (20). During a direct lightning attachment the conductivity of the air surrounding the sensor is likely to change and distort the electric field on the aircraft surface particularly at high frequencies. However, changes in the air conductivity do not have a significant effect on the measurements of the magnetic field (21). Since comparable magnitude electric and magnetic field pulses were recorded simultaneously on different locations of the aircraft surface and the data are well correlated, it appears that these sensors operate properly over our frequency range of near DC to 2 MHz.

Flush plate dipole (FPD) D-Dot sensors were mounted on the front upper fuselage (FUF), left wing tip (LWT), and aft lower fuselage (ALF). A hollow spherical dipole (HSD) Q-Dot sensor was located on the aft upper fuselage (AUF). Both the D-Dot and Q-Dot sensors were used to measure the time rate of change of the electric flux density. The HSD is easier to adapt to the aircraft curvature at the AUF but it produces an enhancement of about three times that of the FPD. The B-Dot sensors were oriented to be sensitive to either current flow nose-to-tail (NT) or current flow wing-to-wing (WW). The J-Dot sensors located on the wings were sensitive to current flowing on the wings and were referred

to by locations; right upper wing (RUW), right lower wing (RLW), left upper wing (LUW), and left lower wing (LLW). There was alos a J-Dot sensor located on the fuselage which was sensitive to current flow nose-to-tail; this was referred to as the J-Dot aft upper fuselage (AUF) sensor. A detailed description of the design and equivalent circuits for all these sensors can be found in the references (9), (20), and (22).

Fiber optic cables were used to transmit the detected output of the sensors to the recording equipment. A 28 channel Honeywell 101 analog recorder with a frequency response of DC to 500 kHZ on the FM channels and 400 Hz to 2 MHz on the direct channels was used to monitor the data continuously. The derivative outputs from the field sensors were hardware integrated to about 1 KHz before storage on the analog recorder channels. After the first attachment the output from the D-Dot FUF sensor was integrated down to .5 Hz to provide a low frequency electric field record of the lightning activity. Outputs from the J-Dot sansors were recorded as derivatives. In addition to the analog recorder, an eight bit resolution ten channel digital transient recorder capable of recording 8192 sample points at 20 nsec intervals was used to record chosen data windows above a pre-selected threshold level. Two or three data windows could be recorded per second with the digital system. The frequency response was about 25 MHz. For both of the direct attachments the digital system triggered hundred of milliseconds prior to the strike and remained disabled during the attachment. Therefore, the only data recorded was on the continuous analog recorder which was limited to 2 MHz. Most of the electric and magnetic field data channels of the analog recorder were calibrated to be within their dynamic range for distances up to about 35 km from the lightning discharge. Consequently, some of these channels saturated when the electric field exceeded a few hundred volts/meter. We measured the magnitude of all the small pulses and some of the large pulses in the discharge and determined the total amount of pulse activity during both attachments.

The aircraft was equipped with a weather radar from which a digital printout of precipitation echoes could be obtained. A Stormscope was also installed on the aircraft to provide information on thunderstorm location.

#### RESULTS

THE 17 JULY FLASH. On 17 July at 17:21:44.EDT, we received a direct lightning strike to the aircraft which was characterized by a bright, noisy are which was visible from the cockpit and temporarily blinded the copilot. The aircraft was flying inside the cloud in an area of light precipitation at 405 km/hour at an altitude of 17,000 ft with an outside air temperature of -0.7°C. There was no anvil above the aircraft and the cloud tops were estimated at 22,000 ft. Figures 2(a) and (b) show the ground weather radar data obtained from the National Weather

uniform current value corresponding to any of the pulses was 650 Amps, which was obtained from one of the pulses can the J-Dot AUF. The magnetic field sensor sensitive to current flow in the NT direction recorded the largest amount of pulses and they corresponded to the largest magnitude pulses from the J-Dot AUF. These results strongly suggest that attachment occurred across the fuselage.

The J-Dot sensors were calibrated for a range between 200 A and 30 kA. By correlating the pulses from the four J-Dot outputs in Figure 3, the time and relative location of the largest current flow on the aircraft was determined. There were only five current pulses above 300 Amps. Four of these occurred toward the end of the active portion of the flash and during the isolated pulses in the second phase of the flash. All of these pulses propagated along the wing, as shown by the correlated H WW records in Figure 3.

By observing smaller data windows we noted that the train of pulses during the initial active phase of the flash starts to decrease in magnitude for several milliseconds after the first 10 to 15 msec, then increases again for 10 to 15 msec. The pulse repetition rate is maximum during the first 43 msec of the flash and is near 10<sup>4</sup> pulses/sec. Defining a pulse as any spike with a magnitude of at least twice the noise level, there were about 200 pulses in this flash.

Figure 4 shows the first 4 msec window from the time just prior to the start of the flash. A slow field change of about -1800 volts/meter occurred on the FUF electric field sensor during

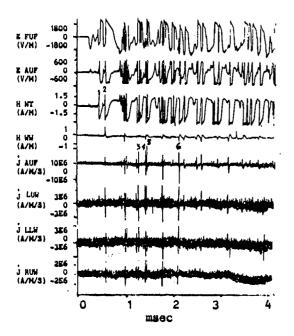


Fig 4. Electric and magnetic fields and current density for the first 4 msec of the flash on 17 July 1981.

a period of about 42 usec. Also, during this period, the AUF electric field sensor reading increased to about 200 volts/meter. These low frequency pulses suggest a leader propagation. There is some activity in the H NT sensor during this period which indicates a small current flow along the fuselage. That leader current may have propagated from the aircraft to a nearby cloud charge center. It appears that the field enhancement near the surface of the aircraft is sufficiently large to produce leader propagation. The apparent leader propagation lasts less than 200 usec which corresponds to a distance of less than 200 meters from the aircraft to the surrounding charge center. It should be noted that the frequency response of the sensors only goes down to a few kilohertz and a steady field change could not be detected with this frequency resolution. The first fast field change is shown as "1" in Figure 4 and it probably corresponds to the first time that any charge is neutralized in the discharge. Pulse "2" corresponds to the first time current flow is neutralized with a significant contribution in the WW direction. Pulses "3" to "6" have current flow along the fuselage and in the wing direction. Figure 4 also shows the structure of the type of pulses recorded during the first few milliseconds on the flash. The pulses in the J-Dot reading correspond to the largest magnitudes of the saturated pulses in the electric and magnetic field readings.

Figure 5 shows a 164 usec data window around the time of pulse 6 in Figure 4. These four pulses are obtained from the J-Dot outputs by using a software computer integration routine. A calculation of the charge transfer from this pulse using the corresponding uniform current of 815 Amps and its risetime of 10 usec is 8.15 millicoulombs. This value is somewhat larger than the maximum charge estimated for the aircraft (11).

The fastest risetime that could be measured accurately with the 2 MHz frequency response was about 350 nsec. Since most of the pulses were saturated in the electric and magnetic field sensors and the data were band-

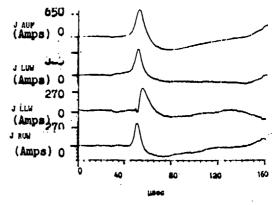
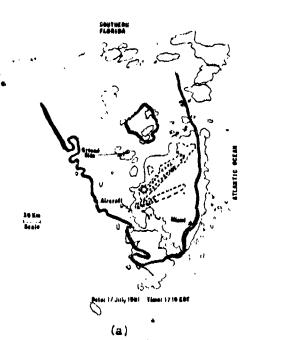


Fig 5. Integrated J-Dot outputs for pulse 6 in Figure 4.



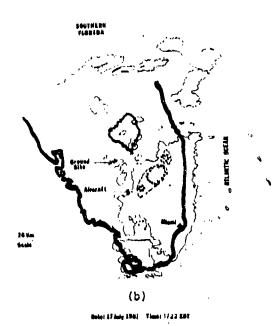


Fig 2. Weather Radar and Stormscope data (a) 5 minutes before and (b) 1 minute after the lightning attachment on 17 July 1981. The continuous lines indicate rain or clutter contours as determined by a ground weather radar at Miami. The crosses represent the regions of highest precipitation from airborne radar. The dashed lines encircle the locations of the return stroke locations obtained by the Stormscope.

Service (NWS) Office at Miami, Florida superimposed with the airborne radar and Stormscope data from five minutes before and one minute after the direct strike. The locations of the aircraft and a ground site are shown on both maps. The wideband electric field (DC to 2 MHz) and VHF radiation (60 to 66 MHz) were recorded at the ground site. At the time of the attachment the aircraft was near the edge of the cloud in an area of weak precipitation. The Stormscope showed no lightning activity within 5 km of the aircraft.

Figure 3 shows the data collected on all the sensors for the entire flash, which lasted about 300 msec. The sensors presented here are the integrated output of the D-Dot FUF, the integrated output from the Q-Dot ALF, the integrated output from the B-Dot NT and WW, and the derivative outputs from the current sensors on LUW, LLW and RUW. The first phase of the flash was very active, lasted about 76 msec and consisted of a train of pulses tens of microseconds apart, each with a duration of few micro seconds. After this fairly continuous pulse train there were a few isolated pulses spread out over 224 maec. The electric field from the FUF and AUF sensors saturated at + 2500 volts/ meter and + 500 volts/meter, respectively. The Magnetic field in the NT direction saturated at about + 1.6 Amps/meter but the magnetic field in the WW direction did not saturate. The

measurements of the magnetic field and current sensors were converted to uniform current flow using an aircraft model (23). The maximum

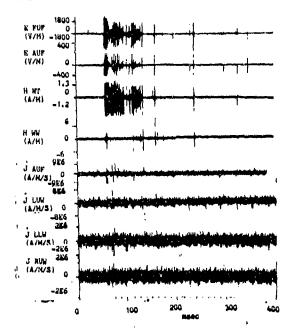


Fig 3. Electric and magnetic fields and current density for the entire flash on 17 Jul 81.

limited, no significant conclusions could be derived from rate of rise calculations.

Damage to the aircraft was caused by a continuing current as it swept across nine fastening screws spread along the upper fuselage from a spot outside the copilot's window to a spot near the wing. Also, one of two antenna wires mounted between the upper fuselage and the top of the vertical tail was burned through.

Since the instrumentation package at the time of this flash was not calibrated to measure low frequencies, a laboratory test was performed to estimate the continuing current necessary to produce the same amount of damage as seen on the aircraft. The distance between the burned rivets ranged from 33 cm to 158 cm for a total length of 5.4 meters. Since the aircraft speed was 405 km/hour, the duration of the continuing current was 48 msec and the average dwell time was about 6 msec. The charge transfer required to produce the same burn in the rivets was estimated as .315 coul and the continuing current as .315/.006 = 52.5 Amps. It is likely that continuing current existed over the entire initial phase of 76 msec but that we were able to estimate only 48 msec based on the noticeable burns on the rivets.

THE 26 AUG FLASH. On 26 Aug at 17:09:45 EDT, we received a second direct strike to the aircraft. The aircraft was flying at 333 km/hour at an altitude of 16,000 ft with an outside air temperature of -5°C. The aircraft was inside the cloud in an area of slushy precipitation in a rapidly building part of the cloud formation. There was no anvil above the aircraft and the cloud tops were estimated as 30,000 ft. The Stormscope had not shown any cloud-to-ground lightning flashes closer than about 5 km from the aircraft.

All the electric and magnetic field sensors except the E LWT were kept at the same magnitude saturation levels as in the previous flash. The E LWT sensor saturation level was changed to 320,000 volts/meter. This sensor recorded a maximum electric field of about 160,000 volts/meter but this reading might not be quire accurate because, as explained previously, this sensor is not designed for recording a direct strike.

Figure 6 shows the overall structure of the flush. The E FUF sensor was calibrated before this flash for a low frequency response less than 1 Hz. The sensor drifted and saturated a few seconds prior to the attachment. During the attachment the E FUF output oscillated between maximum positive and negative saturation levels and zero.

The flash rasted 460 msec and consisted of an initial active phase of about 220 msec and a few isolated pulses during the remaining 350 msec. The pulse repetition rate reached a maximum of 10 pulses/sec during the first 30 msec. Most of the electric field pulses were correlated with magnetic field pulses sensitive to current flow in the NT direction, which tended to indicate a direct attachment across

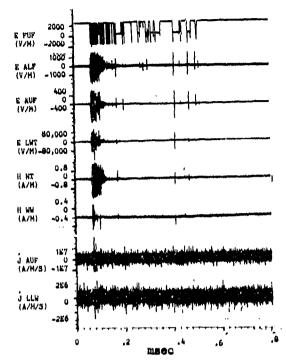


Fig 6. Electric and magnetic fields and current density for the entire flash on 26 Jul 81.

the fuselage. There were about 300 pulses in the entire flash.

Figure 7 shows the first 4 msec of the flash. The first indication of the flash can be observed on the slow electric field records obtained for all four sensors. The first fast field change occurred about 350 usec after the initial field change. As in the previous flash, this pattern suggests a leader propagation. The leader's short duration of about 350 usec might indicate that pockets of charges were neutralized just a few hundred meters away from the aircraft. Since no activity is seen in the magnetic field sensors during the slow electric field change, it can be assumed that the leader propagated from the cloud to the aircraft. As in the previous flash, the apparent leader propagation is from a charge center 100 to 200 meters away to the aircraft. Pulses 1 through 5 in Figure 7 show the first few correlated pulses during the flash. Pulse 5 is the largest in the J-Dot AUF and corresponds to a uniform current flow of about 3 kA.

Figure 8 shows a 164 usec pulse window of pulse 5 in Figure 7. This pulse was integrated to determine a uniform current of 3 kA and a charge transfer of 30 mC. This charge is about five times larger than the expected charge on the aircraft (11).

The only damage produced by the strike was to two of the computer systems on board the aircraft. Memory upsets occurred to these two computers, which were located in the forward upper fuselage behind the cockpit area. This strike did not produce any distinguishable burn marks on the skin of the aircraft. This implies

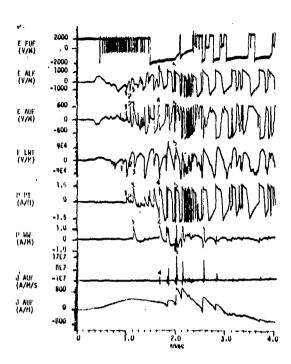


Fig 7. Electric and magnetic fields and current density for the first 4 msec of the flash on 26 July 1981. that the flash had low or nonexistent continu-

ing current flow.

#### DISCUSSION

During both lightning attachments reported here the aircraft was flying in clouds in areas of slight or slushy precipitation but at least 5 km away from the closest thunderstorm. The characteristics of the electric and magnetic field and current distribution on the sircraft rule out the possibility of a cloud-to-ground discharge. Since the aircraft was not in close proximity to any thundercloud, it is highly unlikely that the aircraft was part of an intracloud discharge. The initial slow electric field variations that resemble leader propagation suggest that a cloud-to-aircraft direct attachment occurred. From the duration of the leader propagation, it appears that the charge region neutralized by this discharge was within two hundred meters of the aircraft. The total duration and overall structure of the train of pulses obtained in these flashes are consistent with other reported aircraft lightning strikes (4), (7). If analog data had been recorded continuously in all airborne lightning characterization programs we suspect that the individual attachment pulses reported would prove to be part of a more complex process which probably involved hundreds of pulses.

The pulse repetition rate and relative amplitude of the pulses during direct attachments are not known for much of the reported lightning attachment data (2), (5)-(6). For example, Fitzgerald (2) does not show the total duration of his 55 direct lightning strikes but claims a pulse repetition rate of 10 pulses/sec.

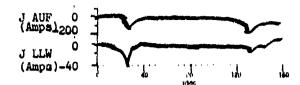


Fig 8. Integrated J-Dot outputs for one the pulses in figure 7.

The direct strike reported by Nanevicz (5) lasted 700 msec with a pulse repetition rate of 0.2 x 103 pulses/sec. Trost and Pitts (7) reported a strike to the NASA F-106 that lasted over 760 msec and had more than 100 pulses. Our maximum pulse repetition rate of 104 pulses/ sec is one order of magnitude larger than any previous reported data and is probably due to the high sensitivity of our instrumentation. The magnitude of the maximum uniform current flow of 800 A and 3 kA for any pulse in these two flashes is of lower intensity than the average reported data (2), (3), (5)-(7). The maximum reported current in a direct attachment to an aircraft is 70 kA (5) and the average is probably about 6 kA. It should be noted that lightning triggered by rockets launched from the ground has a much larger number of return strokes than natural lightning. This large number of fast rise pulses resembles the cloud-to-aircraft lightning since they are both triggered by the presence of a charged object in a high electric field.

Table 1 shows a summary of the characteristics of our two direct strikes.

Statistical data for lightning attachments to aircraft in this country (16) indicate that. for 80% of all reported direct strikes, the aircraft was in a nonthunderous cloud and at least 10 km from the closest thundercloud. In the remaining 20% the aircraft was either below or above the clouds. Reports from Australia (19) indicate that over 50% of all lightning attachments to aircraft occur in lightning-free clouds. Other types of clouds such as nimbostratus and altostratus probably have sufficient charge to produce an internal discharge to a moving charged object (19). The analysis of the data reportedhere provides additional evidence for the occurrence of cloud-to-aircraft discharges. Even though the triggering mechanism that caused these types of discharges is not fully identified, our data and analysis provide some insight into this process. During the few seconds prior to the 26 Aug flash we experienced a build-up of static charge which could be heard on the radio. Simultaneously with this build-up of the static charge, the E FUF which had a frequency response less than 1 Hz became saturated in the positive direction, which indicates a negative charge on the surface of the aircraft. Note that this sensor was saturated prior to the beginning of the discharge, as shown in Figure 7. It appears that the aircraft was charged to a level which would cause corona and the discharge of streamers. The 28 identifiable short pulses

u, o

Table 1
Comparison of the Characteristics of the
Two Direct Lightning Attachments to the WC-130 Aircraft

	17 July	26 August
Flash Duration	295 msec	460 maec
Maximum Pulse Repetition Rate	10 <sup>4</sup> pulses/sec	10 <sup>4</sup> pulses/sec
Total Number of Pulses	150 - 200	200 - 300
Maximum Uniform Current Flow in a Single Pulse	800 A	3 kA
Maximum Electric Field Change in a Pulse	2000 V/m (Saturation Level)	200,000 V/m
Maximum Magnetic Field Change in a Pulse	1.8 A/m (Saturation Level)	1.8 A/m (Saturation Level)
Risetime	Max: 12 µsec	Max: 10 psec
	Min: about 20% below BW limit of 350 naec	Min: about 25% below BW limit of 350 nmec
Continuing Current	50 A	

during the first millisecond of the E FUF record might be an indication of these streamers. The sircraft continued to accumulate negative charge throughout the strike. Since the aircraft was flying at about -5°C the aircraft charging mechanism probably involves a combination of triboelectric charging and other types of charging process which continues to build up the aircraft charge.

The duration of the entire cloud-toaircraft discharge is comparable to a natural lightning discharge and may be interpreted in a manner similar to an intracloud discharge (25). In most cases the sircraft has entered an area of high electric field which is further enhanced due to the presence of the aircraft. Since the aircraft cannot sustain additional build-up of charges, streamer propagation occurs. Simultaneously with these streamers, a leader develops and crosses the gap between the aircraft and a region of opposite charge near the aircraft. A mini-return stroke then occurs similar to those that probably occur in an intracloud discharge. As the aircraft continues to be recharged negatively (in this case) new mini-return strokes occur which keep extending the charge region of the first stroke. This process may occur hundreds of times in a cloudto-aircraft strike. The distance of the cloud charge center from the aircraft might be anywhere from a few aircraft lengths to a few hundred meters. The initial phase of the cloud-to-aircraft discharge has a duration comparable to the active phase of an intracloud discharge whereas the isolated pulses which spread out over a few hundred milliseconds after the initial phase resemble the junction phase of the intracloud discharge (26).

#### CONCLUSION

We have provided electromagnetic measurements of two direct lightning attachments to an aircraft, compared these results with other experiments and provided an explanation for the results. The data reported here agree with Schaeffer (11), who postulated that the aircraft must be adjacent to or in close proximity to a source of charge before leaders can propagate. The aircraft should not be able to divert to itself a natural discharge occurring more than a few hundred meters from the aircraft. Several articles (27)-(28) discuss the physical process of lightning attachment to an aircraft in flight as if the type of lightning were the same as that seen on the ground. Based on the U.S. Air Force lightning incident reports (16), we will speculate that well over 95% of all aircraft lightning attachments are triggered by the presence of the aircraft. However, we must not believe that there is no real threat to sircraft because the individual pulses in these flashes are of smaller magnitude than the return stroke pulses in a cloud-to-ground flash. The USAF C-130E which crashed in Charleston, S.C. in November 1978 in a lightning confirmed accident (29), was flying at the freezing level in a precipitating, nonthunderous cloud at the time of the strike. It is highly likely that this was a triggered discharge. Additional data of the electromagnetic characteristics of direct lightning attachments must be obtained to increase our understanding of the cloud-to-aircraft lightning discharge.

#### REFERENCES

1. R. Gunn, "Electric Field Intensity of Natural Clouds," J. Appl. Phys., Vol. 19, pp.

481-484, 1948.
2. D.R. Fitzgerald, "Aircraft and Rock" Triggered Natural Lightning Discharges." Lightning and Static Electricity Conference, AFAL Tech Rep 69-290, Dec 1968.

B.J. Petterson and W.R. Wood, "Measurements of Lightning Strikes to Aircraft." Final Report to Fed. Aviation Admin. under contracts FA65WAI-94 and FA66NF-AP-12, Jan 1968. J.E. Nansvicz, R.C. Adams, and R.T. Bly, "Airborne Measurement of Electromagnetic Environment Near Thunderstorm Cells (Trip-76)," Standford Res. Inst. Final Rep., Air Force (FDL) Contract NA59-15101, Mar 1977.

5. Centre D/Essais Aeronautique de Toulouse, ."Messure Des Characteristiques De La Fondre en Altitude," Essair No. 76/650000P.4 et Final July 1979.

F.L. Pitts, "Electromagnetic Measurement of Lightning Strikes to Aircraft, "AIAA Paper

81-0083, Jan 1981.

7. T.F. Trost and F.L. Pitts, "Analysis of Electromagnetic Fields of an F106B Aircraft During Lightining Strikes," Int. Aerospace Conf. on Lightning and Static Electricity, Oxford, England, March 1982. 8. P.L. Rustan, B.P. Kuhlman, G.A. DuBro, M.J. Reazer, M.D. Risley and A.V. Serrano, "Correlated Airborne and Ground Measurements of Lightning," Int. Aerospace Conf. on Lightning and Static Electricity, Oxford, Eng., March 1982. P.L. Rustan, B.P. Kuhlman, A. Serrano, J. Reazer, and M. Risley, "Airborne Lightning characterization," AFWAL-TR-3013, 11 April 1983. 10. D.W. Clifford and H.W. Kasemir, "Triggered Lightning," IEEE Trans on EMC, Vol 24, May 1982.

11. J.F. Shaeffer, "Aircraft Initiation of Lightning," 1972 Lightning and Static Electricity Conference. USAF Rep AFAL-TR-72-325, Dec 1972. 12. E.T. Pierce, "Triggered Lightning and Its Applications to Rockets and Aircraft. 1972 Lightning and Static Electricity Conference, USAF Rep AFAL-TR-72-325, Dec 1972.

13. D.W. Clifford, "Another Look at Aircraft Triggered Lightning," NASA Conf. Pub. 2128,

FAA-RD-80-30, Hampton, VA., April 1980. 14. W.E. Cobb and F.H. Holitza, "A Note on Lightning Strikes to Aircraft," Monthly Weather Review, Vol. 96, No. 11, Nov 1968. 15. H.W. Kasemir, "Basic Theory and Pilot Experiments to the Problem of Triggering

Lightning Discharge by Rockets," NOAA Tech Memo ERL APCL 12, 1971.

16. J.C. Corbin, "Lightning Interaction with USAF Aircraft," 1983 Int. Conference on Lightning and Static Electricity, Fort Worth, Texas, June 1983.

17. O.K. Trunov, "Conditions of Lightning Strike on Air Transports and Certain General Lightning Protection Requirements," 1975 Lightning and Static Electricity Conference, Culham Lab, England, April 1975.

18. H.T. Harrison, "UAL Turbojet Experience with Electrica Discharges," UAL Meterological

Circular No. 57, Jan 1967.

19. M. Darveniza, private communication. 20. C.E. Baum, E.L. Breen, J.P. O'Neill, C.B. Moore, and G.D. Sower, "Electromagnetic Sensors for General Lightning Application," NASA Conf Pub 2128, FAA-RD-80-30, April 1980. 21. C.E. Baum, "The Influence of Radiation and Conductivity on B-Dot Loop Design," Sensor and Simulation Notes 29, Kirtland AFB, Oct 1966. 22. C.E. Baum, E.L. Breen, J.C. Giles, J. O'Neill, G.D. Sower, "Sensors for Electromagnetic Pulse Measurements Both Inside and Away From Nuclear Source Regions," IEEE Trans. on Antennas and Propagation, Vol. AP-26, No. 1, Jan 1978.

23. B.J.C. Burroughs, "Absolute Calibration of B and J Sensors on FY60 WC-130 Aircraft," USAF Contract No. F61708-81-M0140, June 1981. 24. P. Hubert, "Eclairs Declenches an Laboratoire Langmuir Durant L'ete 1981." Service D' Electronique Physique, DPH/EP/81-66, Centre d' Etudes Nucléaires de Saclay, 91191 Gif-sur-

Yvette Cedex-France.

25. T. Ogawa and M. Brook, "The Mechanism of the Intracloud Lightning Discharge," J. of Geophys. Res., Vol. 69, No. 24 5141-5150, 1964. 26. N. Kitagawa and M. Brook, "A Comparison of Intracloud and Cloud-to-Ground Lightning Discharges," J. Geophys. Res., 65, 1189-1201, 1960.

27. F.A. Fisher and J.A. Plumer, "Lightning Protection of Aircraft." U.S. Dept of Commerce.

N78-11024-11041, October 1977.

28. J.A. Plumer, "Laboratory Test Procedures to Determine Lightning Attachment Points on Actual Aircraft Parts," Conference on Certification of Aircraft for Lightning and Atmospheric Electricity Hazards," ONERA-Chatillon, France, Sept 1978.

29. D.W. Clifford, "Aircraft Mishap Experience from Atmospheric Electricity Hazards," NATO AGARD Lecture Series No. 110, June 1980.



## AIRBORNE MEASUREMENTS OF THE RISETIMES IN LIGHTNING RETURN STROKE FIELDS

P. Rústan, B. Kuhiman, G. DuBro Air Force Wright Aeronautical Laboratory (AFWAL/FIESL) Wright-Patterson AFB, Ohio 45433

and

### J. Reazer Technology/Scientific Services Dayton, Ohio 45431

ABSTRACT

A WC-130 aircraft instrumented with electromagnetic field sensors was flown in South Florida in close proximity to thunderstorms. Electric and magnetic fields were measured over one thousand lightning return strokes at distances between 4 and 35 km from the aircraft. These field waveforms were recorded with a Digital Transient Recorder with a 25 MHz bandwidth which consists of 8192 samples in 20 nsec intervals.

The risetimes for over two hundred return stroke magnetic fields have been calculated. The average risetime (10 to 90%) of the entire waveform for the first return stroke was 1.78 used with a standard deviation of .87 used. Interest The average risetime for the fast portion of the first return stroke was 356 nsec with a standard deviation of 141 nsec. The average risetime for subsequent return strokes was 405 nsec with a standard deviation of 148 nsec.

From the far-field data, the average rate of rise of the current in the return stroke channel for 38 strokes was estimated as 4.39 x 10 4/sec with a standard deviation of 2.39 x 10 4/sec.

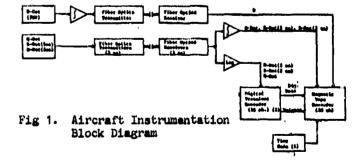
10 to the 10th)
In 1981 the Air Force Wright Aeronautical Laboratories (AFWAL) conducted a lightning characterization program in a WC-130 aircraft provided by the National Oceanographic and Atmospheric Administration (NOAA). The aircraft was instrumented with wideband electromagnetic field sensors as described by Rustan et al. (1) in a different paper of this proceeding. The gircraft flew twelve missions in South Florida and accumulated about 50 flying hours. Most of the data was collected at an altitude between 4 and 35 km from the lightning discharge. In this paper we briefly describe the procedure used to obtain the data, discuss the structure of the electric and magnetic field waveforms recorded in the sircraft, and summarize the

risetime calculations for first and subsequent return strokes.

#### AIRCRAFT MEASUREMENT SYSTEM

Eleven sensors were used on the WC-130 in 1981 (1)-(2). The measurements discussed here are the horizontal components of the magnetic field on the forward upper fuselage (FUF), and the electric field component on the FUF and on the aft upper fuselage (AUF). These waveforms were continuously recorded on an analog tape with an upper frequency response of about 2 MHz. The analog recorder step response was 350 nsec. In addition, an eight bit resolution digital recorder was used to obtain 8192 sample points at 20 nsec intervals of the derivatives of the measured quantities. Two or three data windows could be recorded per second with this system which has a frequency response of 25 MHz. The data blocks are initiated in a pre-trigger mode be any incoming signal exceeding a preset derivative threshold level.

The selected signal at the sensor outputs were transmitted using fiber optic cables, and recorded in two different forms as shown in figure 1. The derivatives of the desired mea-



sured quantities detected by setting the threshold level were logged and stored in the digital recorder. The continuous output was hardware integrated and recorded in the analog tape. The clow frequency response of the analog tape for the magnetic field on the FUF and the electric field on the AUF was 3 kHz. This low frequency response was limited by the noise level at the fiber optic receiver. Since a low frequency response of near 1 Hz is required to fully identify the different return strokes in a cloud-to-ground flash, the electric field at the FUF was hardware integrated at the sensor output, transmitted in the fiber optic cables, and recorded directly in different gain settings of the analog recorder. This channel was used to ensure that the waveforms being analyzed were indeed first or subsequent return strokes.

#### RESULTS

One of the horizontal components of the magnetic field recorded on the digital system was analyzed for 173 first return strokes and 7.1 subsequent return strokes. These data consisted of all the return strokes recorded in the digital system in three of the flights when the aircraft was located between about 10 km and 35 km from a cloud-to-ground flash. Figure 2 shows a

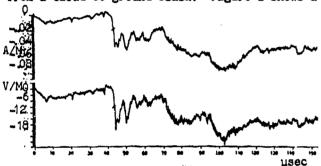
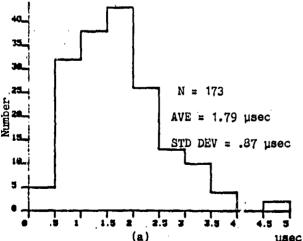


Fig 2. Typical first return stroke magnetic field (top) and electric field (bottom) waveforms about 20 km away.

simultaneous record of the electric and magnetic surface fields for a first return stroke recorded on the aircraft about 20 km away from the discharge. The return stroke occurred 43.8 usec after the beginning of the record. First return stroke waveforms usually consist of a



(b) nsec Lg 4. Histograms of the risetimes of the digital data for first return strokes (a) 10-90% overall (b) 10-90% fast portion.

slow front which rises in 2 to 8 usec to about half of the peak amplitude (3)-(9) and is followed by a faster transition to peak with a 10 to 90 percent risetime that ranges from less than 100 usec (8) to several microseconds (8), (9). There is a diagonal dash line during the return stroke in figure 2 to indicate the transition between the slower and faster portion of the waveform. Our calculated 10 to 90 percent risetimes for first return strokes were measured for both the entire waveform and the fast portion of the waveform. The transition point between the slow and the fast part of the waveform was determined using a technique similar to that of Weidman and Krider (8) and illustrated in figure 3. The zero amplitude level in figure 3 corres-

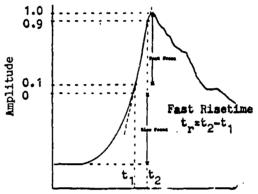
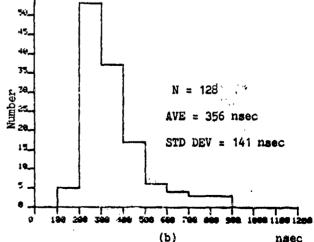


Fig 3. Typical 10-90% risetimes measurements.

ponds to the beginning of the faster portion of the waveform.

Measurements obtained from the digital data over the entire waveform for 173 first return strokes show an average of 1.79 µsec and a standard deviation of .87 µsec as shown in figure 4(a). For 128 of these 173 events the transition point from the slow to the fast front of the return stroke was easily identified. For those first return strokes the 10 to 90% risetimes showed an average of 356 nsec and a standard deviation of 141 nsec as shown in figure 4(b). After obtaining these data, it was argued



that the preset derivative threshold level might have biased the data by selecting only the faster pulses. To investigate this possibility we reviewed the records of the simultaneously recorded analog data during one of the three chosen flights for the first 48 cloud-to-ground flashes. The 10 to 90% risetime over the entire waveform for these 48 first return strokes from the analog data was 2.62 µsec and the standard deviation was 1.09 usec as shown in figure 5a. For 34 of these events the transition point in the waveform was clearly identified and the 10 to 90% risetime of the fast portion was 552 nsec with a standard deviation of 241 nsec as shown in figure 5b. The digital recorder did not have all the first return strokes observed in the continuous analog data, but for each simultaneous record the waveform was exactly the same. Since the results of taking all the return strokes over a time period were comparable to the digital data, we concluded that the averages of the digital data blocks were a fairly good representation of all the recorded data.

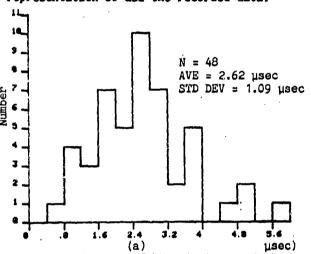


Fig 5. Histograms of the risetimes of the analog data for first return strokes (a) 10-90% overall (b) 10-90% fast portion.

Similar measurements were obtained in the digital and the analog data of subsequent return strokes for the same time period. Figure 6

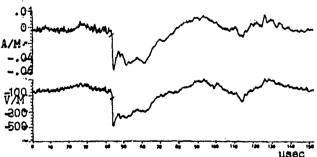
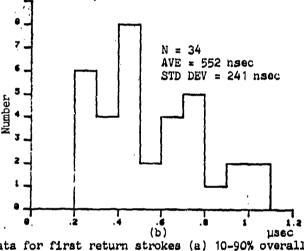


Fig 6. Typical subsequent stroke magnetic field (top) and electric field (bottom) wave-forms about 10 km away.

shows a simultaneous record of the electric and magnetic surface field for a subsequent return stroke recorded on the aircraft about 10 km away from the discharge. The return stroke occurs at the same relative location as in figure 2 because he pre-trigger mode was to 2192 samples out of the possible 8192 data points which at 20 nsec becomes 43.8 usec. The 10 to 90 percent risetime for 71 subsequent return strokes showed an average of 405 nsec and a standard deviation of 148 nsec as shown in figure 7. When 40 subsequent return strokes were analyzed over a portion of the continuous analog data, the 10 to 90 percent risetime was 436 nsec with a standard deviation of 165 nsec as shown in figure 8.

We have also calculated the rate of rise of the electric and magnetic field for 38 return strokes for which the horizontal distance from the aircraft to the discharge could be measured. These events occurred when the aircraft was located between 20 and 38 km from the discharge. For these records, there was only one small



N = 71
AVE = 405 nsec
STD DEV = 148 nsec

Fig 7. Histogram of the risetimes (10-90%) of the digital data for subsequent return strokes.

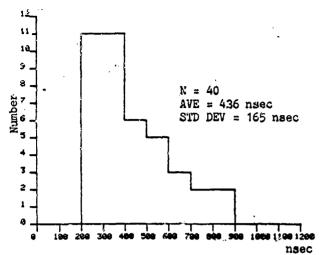


Fig 8. Histogram of the risetimes (10-90%) of the analog data for subsequent return strokes.

isolated thunderstorm cell and the distance from the aircraft to the cell could be measured accurately by using the display of the airborne radar. The calculated values for the rate of rise of the fields were converted to the rate of rise of the currents in the channel by using the results derived by Uman et al. (11) which assumes a fixed current waveshape propagating up a straight vertical channel. If D is the horizon all distance to the channel in meters and the dE/dt and dH/dt are determined in Volts/m.sec and A/m.sec, respectively, the rate of rise of the current can be calculated by the following equations:

di/dt = ((dE/dt)D)/20or  $di/dt = 6\pi D(dH/dt)$ 

We calculated the rate of rise of the current in the channel for the electric and magnetic field data. Since these data were collected in the far-field, the E and H were closely related by the impedance of free space. For first return strokes, the rate of rise was determined for both, the 10 to 90% of the entire waveform and the 10 to 90% of the fast portion of the waveform. The fastest of these two rates was the one used in our averaging. The average rate of rise of the current determined from either the electric or the magnetic field for 38 return strokes was 4.39 x 10 A/sec and the standard deviation was 2.39 x 10 A/sec. The calculated values ranged from 5.8 x 10 A/sec to 1.03 x 10 A/sec

#### CONCLUSION

We have provided risetime statistics for a sufficiently large number of first and subsequent return strokes such that some general conclusions could be established. Since the current in the channel has the same structure than the radiated fields (11), these results can be interpreted as estimates of the current in the channel. Our average calculated rise-

times (10 to 90%) for the entire first return stroke are comparable to those used for standard test waveforms, but the risetime of the fast portion of the first return stroke can produce rate of rise faster than those of the overall waveform. In addition, the subsequent return strokes analyzed here have an average risetime of 405 nsec and can produce a rate of rise larger than those of the standard 2/50 test waveform.

The average rate of rise of the current in the channel for 38 return strokes of  $4.39 \times 10^{10}$  A/sec is lower than the average  $1.5 \times 10^{10}$  A/sec estimated by Weidman and Krider (7), but considerable larger than the average measured rate of rise of the current on top of towers (9).

Two factors have not been accounted for on our measurements. First of all, over these distances of 10 to 35 km, the measured fields suffer attenuation of their high frequency components due to propagation along the earth. For a distance of about 30 km, the 1 MHz component might be attenuated by a factor of 2 with respect to the signal propagating on a perfectly conducting surface (3). Taking this problem into consideration, the average true risetime of the current in the channel might be about half of the calculated value. Furthermore, we have not considered the effect of the aircraft on the measurements. The lower aircraft resonant frequencies are 3.70 and 4.95 MHz and any measurements of the surface fields at these frequencies or higher will be affected by the presence of the aircraft. However, the frequency response of the major component of most of the return strokes analyzed here were below 3.7 MHz and the effect of the aircraft resonance for these far-field waveforms is considered negligible.

#### REFERENCES

- 1. P.L. Rustan, B. Kuhlman, J. Showalter, and J. Reazer, "Electromagnetic Measurements of Lightning Attachment to Aircraft," Int. Aerospace and Ground Conference on Lightning and Static Electricity, Forth Worth, Texas, June 21-23, 1983.
- 2. P.L. Rustan, B.P. Kuhlman, A. Serrano, J. Reazer, and M. Risley, "Airborne Lightning Characterization," USAF Technical Report, AFWAL-TR-83-3013, April 1983.
- 3. R.J. Fisher and M.A. Uman, "Measured Electric Field Risetimes for First and Subsequent Lightning Return Strokes " J.Geophys. Res.,
- vol 77, 399-407, 1972.
  4. J.A. Tiller, M.A. Umon, Y.T. Lin, R.D. Brantley and E.P. Krider, "Electric Field Statistics for Close Lightning Return Strokes Near Gainesville, Florida," J. Geophys. Res., vol 81, 4430-4434, 1976.
- 5. M.A. Uman, R.D. Brantley, J.A. Tiller, Y.T. Lin, E.P. Krider and D.K. McLain, "Correlated Electric and Magnetic Fields from Lightning Return Strokes," J. Geophys. Res., vol 80, 273-376, 1976.

6. Y.T. Lin, M.A. Uman, J.A. Tiller, R.D. Brantley, E.P. Krider, and C.D. Weidman, "Characterization of Lightning Return Stroke Electric and Magnetic Fields from Simultaneous Two-Station Measurements," J. Geophys. Res., vol 84, 6307-6314, 1979. 7. C.D. Weidman and E. P. Krider, "Submicrosecond Risetimes in Lightning Ret. Str. Fields," Geophys. Res. Lett., vol 7, 955-958, 1980. 8. C.D. Weidman and E.P. Krider, "Submicrosecond Risetimes in Lightning Radiation Fields," in Lightning Technology, NASA Conf. Pub. 2108, FAA-RD-80-30, April 1980. 9. M.A. Uman and E.P. Krider, "A Review of Natural Lightning: Experimental Data and Mcdeling," IEEE Trans. on Electromag. Comp, EMC-24, No 2, May 1982. 10. P.L. Rustan, B.P. Kuhlman, G.A. DuBro, M.J. Reazer, M.D. Risley and A.V. Serrano, "Correlated Airborne and Ground Measurements of Lightning," Proceedings of the Int. Aerospace Conf. on Lightning and Static Electricity, Oxford, England, March 1982. 11. M.A. Uman, D.K. McLain, and E.P. Krider, "The Electromagnetic Radiation from a Finite Antenna," Amer. J. Phys., vol 43, 33-38, 1975.

P002200



B. P. Kuhlman
Air Force Wright Aeronautical Laboratories, Dayton, Ohio
J. S. Reazer
Technology/Scientific Services, Incorporated, Dayton, Ohio
W. P. Geron
Boeing Military Airplane Company, Seattle, Washington
P. L. Rustan
Air Force Institute of Technology, Dayton, Ohio

LIGHTNING FIELD SPECTRA OBTAINED FROM AIRBORNE MEASUREMENTS

ABSTRACT

A WC-130 aircraft was used as an airborne platform for broadband electric and magnetic field sensors to measure the surface fields on the airframe from lightning strikes in the 7 - 35 km range. The waveforms were recorded digitally, with a sample interval of 20 nsac and a time window of 164 microseconds. Since the aircraft was above 15,000 feet, and the lightning source was relatively nearby, the effects of ground propagation were minimized. Spectra have been obtained for the stepped leader, first return stroke, and subsequent return stroke over the frequency range 100 kHz to 20 MHz. These spectra are compared to published data of lightning field spectra obtained from ground-based measurements. With airframe resonances and field enhancement effects removed, the data have two primary applications:

(1) To add to the data base for the nearby lightning strike threat; and

(2) To infer characteristics of the stepped leader, first return stroke, and subsequent return stroke processes.

Recommendations for these applications are presented.

47-1

ATTENTION HAS BEEN GIVEN in recent years to characterization of unwanted sources of electromagnetic interference, such as lightning or nuclear EMP, that may interact with aircraft and impair mission capability. The use of non-metallic airframe materials and solid-state avionics aggravates the problem by reducing electromagnetic shielding and lowering damage or upset thresholds on new generation aircraft. Measurements of lightning fields and currents, indicating the level of the hazards, have been made on the ground for several years. Recently, wide bandwidth measurements of lightning fields and currents have been recorded on aircraft in flight to obtain a more pertinent threat characterization. As a part of this characterization, it is necessary to consider the electromagnetic effect of the aircraft on the measurements so that a generic threat definition may be derived.

In 1979 the Air Force Flight Dynamics Laboratory, in conjunction with the National Oceanic and Atmospheric Administration (NOAA), initiated a three-year program to measure the properties of lightning encountered in flight (1). A NOAA WC-130 "Hurricane Hunter" aircraft was fitted with sensors for measuring nearby and direct lightning strikes. A sophisticated data acquisition system designed for repetitive wide bandwidth transient measurements was developed by the Micro Pro Company and installed in the WC-130. More than one hundred flight hours were logged over the threeyear period and several hundred wide bandwidth lightning measurements were recorded. Progress and results of this research are documented in references (1) through (4).

In this paper, we have analyzed the frequency characteristics of three lightning transients — stepped leader pulses, first return strokes, and subsequent return strokes, recorded on the WC-130. Wide bandwidth magnetic field measurements were Fourier transformed, averaged, and normalized for range. The results are compared with published frequency spectra from similar field measurements obtained on the ground.

#### INSTRUMENTATION

The sensors and instrumentation used on the WC-130 have been described in detail in reference (4). The specific equipment used to obtain the data for this study are reviewed next. Magnetic field waveforms were obtained from a single wideband sensor mounted on the centerline of the up-

per fuselage of the WC-130 approximately seven meters from the nose of the aircraft ( $\hat{B}_1$  in Figure 1). The sensor was an EG&G model CML-7 cylindrical Moebius loop B-Dot sensor (5,6) that produces an output voltage proportional to the derivative of the magnetic field over a 38 MHz bandwidth. A second B-Dot sensor ( $\hat{B}_2$ ) was positioned adjacent to the first and oriented to respond to magnetic flux parallel to the wing axis as shown in Figure 1. This sensor was used in conjunction with  $\hat{B}_1$  and an electric field sensor to assist in locating the lightning strikes. The arrows in Figure 1 indicate the direction of increasing field for a positive sensor output voltage.

B-Dot sensor outputs war ansmitted through Merit fiber optic dainks to instrumentation inside the aircraft. The signals were logarithmically compressed, digitized, and encoded on magnetic tape. A partial block diagram of the instrumentation is shown in Figure 2. The digitizing was performed with a Micro Pro model PR7901 digital transient recorder with a 20 ns sample period, 8 bit amplitude resolution and 164 µs sample window. Forty microseconds of pretrigger sampling was programmed into the ligitizer so that leader pulses preceeding return strokes could be recorded.

An electric field sensor was mounted directly ahead of the B-Dot sensors on the upper fuse-lage of the aircraft. The sensor output was integrated electronically and recorded on two wideband FM channels of a Honeywell model 101 analog tape recorder. Recorded bandwidth of the electric field was 0.1 Hz to 500 kHz. The analog recorder also recorded a logic pulse indicating the time of digital transient recorder triggering. Trigger pulse location within the overall electric field waveform was the first criteria used to categorize the digitized data (Figure 3). Refinement of the categorization was obtained through examination of the fine structure of the digitized waveform.

AIRCRAFT EFFECTS - We have simplified the interpretation of the magnetic field measurements to a certain degree by careful positioning of the B-Dot sensor. By positioning the sensor in the plane defined by the wings and upper fuselage surface, and orienting it to respond to magnetic flux parallel to the fuselage axis and perpendicular to the wing structure, we have made it in-

sensitive to magnetic fields and resonances associated with axial wing and fuselage current flow. Some coupling of resonant responses is evidenced in the time domain waveforms due to non-ideal symmetry (8).

Field enhancement due to the aircraft structure can be determined in the manner described by Taylor (9,10). The aircraft fuselage is modeled as a cylinder with the axial component of the magnetic field at the surface given by

$$H_1 \approx H_1 inc (1-j2kacos\theta)$$

where  $\rm H_1$  inc is the incident magnetic field, a is the fuselage radius,  $k=2\pi/\lambda$  and  $\theta$  is measured upward from the direction of incidence along the fuselage circumference. This equation is valid for broadside incidence where  $(ka)^2<<1$ . For most of our data, the aircraft is positioned so that the cosine function in the second term goes to zero. In the worst case,  $\theta$  would be 45° and the second term would result in an enhancement of high frequencies. This enhancement would be below 3 dR at 20 MHz, however, and less at lower frequencies. Therefore, the resultant magnetic field parallel to the fuselage axis at the  $B_1$  sensor location is approximately equal to the incident magnetic field at this point.

RANGE DETERMINATION - Distances to thunderstorms were determined from radar patterns obtained during flight. The radar data were recorded on digital tape and processed later by
computer for analysis. Lightning data were selected from storm cells that could be clearly
identified. When several storm cells were active
around the aircraft, ambiguities in locations
were resolved by examining the polarities and relative amplitudes of the B-Dot signals. Since
the precise location of the return stroke within
storm cells was unknown, lightning location accuracy deteriorated with decreasing thunderstorm
range.

#### DATA PROCESSING

The digitized lightning data was scaled, anti-logged and numerically integrated to display the field waveshape. A typical overall data window and the integration are shown in Figure 3. A 10.24 us (512 sample points) time interval containing the data of interest was selected from the overall waveform for processing. For first return strokes, the interval was chosen to include the slow front of the field waveform but to exclude stepped leader pulses. Consequently, the derivative impulse corresponding to the fast front of the return stroke was placed about 2 to 4 μs after the beginning of the interval. Figure 5 shows a first return stroke derivative waveform and the numerical integration recorded at 9 kilometers. Subsequent return stroke waveforms were positioned approximately 1 to 2 us after the beginning of the 10.24 µs interval. For stepped leader pulses, 4 us of data containing the pulse was positioned at the beginning of the interval and the remaining 6.24 us set to zero. Subsequent stroke and stepped leader waveforms are shown in Figures 6 and 7, respectively.

A fast Fourier transform of the data was calculated using a rectangular window according to the following equation:

$$X(mF) = T \sum_{n=0}^{N-1} x(nT)e^{-j(2\pi mn/N)}$$

where T is the sample interval, N is the number of samples, F = 1/NT, m = 0,1,..., N/2, x(nT)is the sampled magnetic field data, and X(mF) is the complex spectra value (7). With 512 samples and a 20 ns sample period, spectra values are calculated at discrete frequency increments of approximately 97 kHz. Since field derivatives were recorded, the time waveform was near zero at the beginning and end of the 10.24 us interval, minimizing errors introduced by abrupt transitions at the boundaries of the window. Magnitudes of the frequency spectra were normalized to a distance of 50 km assuming a 1/r relationship, where r is the distance from the thunderstorm to the aircraft, and corrected for angle of incidence to the sensor by dividing by the sine of the angle from the aircraft nose to thunderstorm location. Spectra magnitudes were then averaged at each frequency and standard deviations calculated. The derivative response of the sensor was accounted for by dividing the spectra magnitudes by radian frequency  $\omega$ . The resulting values were expressed in decibels using

$$\overline{H}$$
 ( $\omega$ )(dB) = 20 Log<sub>10</sub>  $\left[\overline{H(j\omega)}\right]$ 

where the horizontal bar denotes mean and the vertical bars | | denote magnitude. Standard deviations  $(\sigma(\omega))$  were referenced to average values and expressed in decibels using

SD (
$$\omega$$
) (dB) = 20 Log<sub>10</sub>  $\left[\frac{|H(j\omega)|}{|H(j\omega)|} + \sigma(\omega)/|H(j\omega)|\right]$ 
RESULTS

The data were recorded during several storms occurring on 25 August and 26 August 1981 at an altitude of 5.2 km. Ten first return strokes at a range of 11 km to 35 km and nine subsequent return strokes at a range of 7 km to 28 km were selected for processing. The last stepped leader pulse preceeding the return stroke was processed from nine of the first stroke waveforms. Subsequent strokes showing dart-stepped leaders were excluded from the data set.

Average spectra values for first return strokes, subsequent strokes and leader pulses are plotted in Figures 8 through 10, respectively. A linear interpolation between data points is also plotted. Spectra magnitudes at selected frequencies are tabulated in Table 1 along with standard deviations.

TREADS IN SPECTRA WITH FREQUENCY - Average spectra values at 100 kHz are -142 dB for both first and subsequent return strokes and 20 dB lower for leader pulses. All three sets of data

decrease approximately inversely with frequency (f) to about 1 MHz and decrease more rapidly at higher frequencies. Approximate trends in average spectra amplitude with frequency are summarized in Table 2.

First stroke spectra show a decrease proportional to  $1/f^2$  from 800 kHz to 5 MHz. Beyond 5 MHz there is a slight dip in the spectra and then the amplitudes tend toward 1/f dependence.

Subsequent stroke spectra maintain the initial 1/f slope from 100 kHz out to 1.2 MHz and then decrease rapidly until 3.5 MHz. This spectra also regains a 1/f slope by 20 MHz.

Leader pulses show less relative energy at low frequencies with a decrease of 16 dB from 100 kHz to 1 MHz rather than 20 dB as in the case of the return strokes. Beyond 1 MHz the spectra decreases proportional to 1/f.

Evidence of aircraft resonances is visible in the graphs in the 3 to 5 MHz region.

STANDARD DEVIATIONS - Standard deviations are greatest for leader pulse spectra and smallest for subsequent stroke spectra as indicated in Table 1. The larger leader pulse standard deviations are indicative of the more random structure of the leader waveshapes as well as a lower signal to noise ratio. Since leader pulse data were extracted from the return stroke waveforms, the signal to noise ratio would be a factor of two to five lower for leader pulses than for first return strokes (for derivative magnetic field data). Subsequent stroke standard devintions are low, particularly at lower frequencies, suggesting uniformity in different return stroke waveshapes.

COMPARISON TO PUBLISHED SPECTRA - Frequency spectra derived from broadband ground-based electric field measurements have been obtained by Serhan (11) and more recently by Weidman (12). Serhan calculated spectra from 2 kHz to 700 kHz for measurements recorded from 1.5 km to 200 km. Weidman obtained spectra of electric fields from 100 kHz to 20 MHz for measurements at 30 to 50 km where propagation was over saltwater so that the effects of ground wave attenuation were minimized.

Weidman's data for first return strokes show a spectral amplitude of about -95 dB at 100 kHz, a slope of 1/f to 2 MHz,  $1/f^2$  to 10 MHz, and  $1/f^5$  beyond 10 MHz. These trends are similar to the WC-130 data with two exceptions — the transition from slopes of 1/f to  $1/f^2$  occurs at 800 kHz rather than 2 MHz; and the data shows no rapid decrease in spectral amplitude beyond 10 MHz for the aircraft data.

A comparison in spectral amplitudes between the air and ground-based data is difficult for several reasons. For identical waveshapes, spectra amplitudes should be proportional to waveform amplitudes. With different frequency characteristics, however, the proportionality becomes a function of frequency. Also, sircraft waveforms are obtained at varying range and elevation from the return stroke which practudes a direct comparison with ground-based data at a fixed position. Examination of the first stroke data shows a ratio of 112 to 1120 for electric field

spectra on the ground versus magnetic field on the aircraft over a 500 kHz to 5 MHz frequency range. This bounds the impedance of free space  $(377\Omega)$  that would be expected for simultaneous, distant, ground-based electric and magnetic field data (13).

#### SUMMARY

We have calculated the frequency spectra of broadband lightning magnetic field measurements recorded on a WC-130 aircraft in flight. The data were recorded at a range of 7 to 35 km. Spectra values were calculated from 100 kHz to 20 MHz for stepped leader pulses, first return strokes and subsequent return strokes. Spectra amplitude trends with frequency were extracted and compared with trends of published ground based spectra. From the data we can infer the following lightning characteristics:

- 1. First and subsequent return strokes have similar energy levels in the 100 kHz to 20 MHz frequency range.
- 2. The initial transition point from slopes of 1/f to steeper slopes, occurring at 800 kHz for first strokes and 1.2 MHz for subsequent strokes, is probably indicative of faster subsequent stroke risetimes.
- 3. Leader spectra lie 14 to 20 dB below first stroke spectra at low frequencies suggesting a factor of 5 to 10 difference in magnetic field amplitude.
- 4. Subsequent stroke spectra show a relatively small standard deviation suggesting a uniformity of waveshape among independent return strokes. Although some of these characteristics could be observed from time domain waveforms, one significant feature that is extracted by Fourier analysis is the presence of high frequency energy beyond 10 MHz that is not observed with ground-based measurements. From our analysis, this does not appear to be characteristic of the recording system or sirframe enhancement but rather an inherent feature of the lightning fields.

#### REFERENCES

- 1. R.K. Baum, "Airborne Lightning Characterization." Proceedings of the NASA Symposium on Lightning Technology, NASA CP2128, April 1980.
- 2. R.K. Baum et al., "Airborne Electromagnetic Characterization of Lightning." Proceedings of the International Aerospace Conference on Lightning and Static Electricity, Oxford, England 1980.
- 3. P.L Rustan, et al., "Correlated Airborne and Ground Measurement of Lightning." Proceedings of the International Aerospace Conference on Lightning and Static Electricity, Oxford, England 1982.
- 4. P.L. Rustan, et al., "Airborne Lightning Characterization," USAF Technical Report, AFWAL-TR-83-3013, April 1983.
- 5. C.E. Baum, et al., "Sensors for Electromagnetic Pulse Measurements Both Inside and Away from Nuclear Source Regions." IEEE Transactions

on Antennas and Propagation, Vol AP-26, No. 1, January 1978.

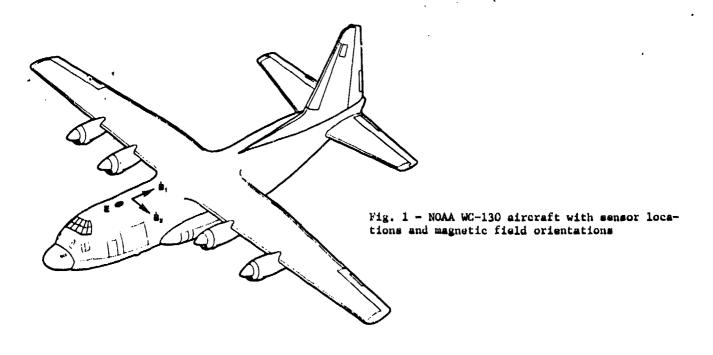
- 6. "CML B Sensors (Full Loop), "EG&G Washington Analytical Services Center, Data Sheet 1106, September 1980.
- 7. "TEK SPS Basic Signal Processing Pack-age." VO1 CP91171, SPS Information Group, February 1977.
- 8. C.E. Baum, "Interaction of Electromagnetic Fields with an Object Which has an Electromagnetic Symmetry Plane." Air Force Weapons Laboratory EMP Interaction Notes, No. 63, March 1971.
- 9. C.D. Taylor, "External Interaction of the Nuclear EMP with Aircraft and Missles." IEEE Transactions on Electromagnetic Compatibility, Vol EMC-20, No. 1, Fabruary 1978.
- 10. W.P. Geren, "Calibration of C-130 Lightning Characterization Sensors." Air Force Contract F33615-81-C-3409 Final Report, AFWAL-TR-82-3095, December 1982.
- 11. G.I. Serhan, et al., "The RF Spectra of First and Subsequent Lightning Return Strokes in the 1- to 200- km Range." Radio Science, Vol 15, No. 6, December 1980.
- 12. C.D. Weidman, E.P. Krider, M.A. Uman, "Lightning Amplitude Spectra in the Interval from 100 kHz to 20 MHz." Geophysical Research Letters, Vol 8, No. 8, August 1981.
- 13. M.A. Uman, et al., "Correlated Electric and Magnetic Fields From Lightning Return Strokes." Journal of Geophysical Research, Vol 80, January 1976.

Table 1 - Average Spectra Values and Standard Deviations in Decibels

Frequency	First S	trokes	Subsequent	t Strokes	Lead	ers
	Mean	SD	Mean	SD	Mean	BD
100 kHz	-142	2.4	-142	2.1	-162	4,2
200 kHz	-152	4.5	-146	2.2	<b>-166</b>	3.5
500 kliz	-158	3.7	-156	2.8	-172	3.1
1MHz	-170	3.1	164	2.5	-179	4.0
2MHz	-177	3.4	-177	3.0	-191	4.3
5 MHz	-196	4.2	-196	4.0	-205	4.2
10 MHz	-210	3.5	-209	3.3	-216	3.9
15 MHz	-213	2.9	-215	5.2	-220	3.6
20 MHz	-218	4.6	-221	4.6	-225	4.7

Table 2 - Variations of Spectra Amplitude with Frequency

First Return Strokes	Subsequent Return Strokes	Leader Pulses
Frequency Range Trend	Frequency Range Trend	Frequency Range Trend
0.1 - 0.8 MHz 1/f 0.8 - 5.0 MHz 1/f <sup>2</sup> 5.0 - 20 MHz 1/f	0.1 - 1.2  MHz $1/f1.2 - 3.5 \text{ MHz} 1/f^310 - 20  MHz$ $1/f$	0.1-1.0MHz -16dB/decade 1.0 - 20 MHz 1/f



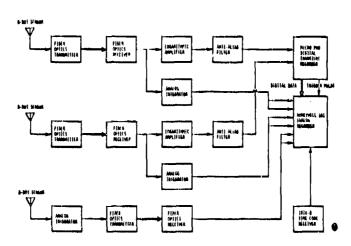


Fig. 2 - Block diagram of aircraft instrumentation

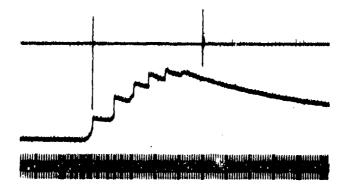
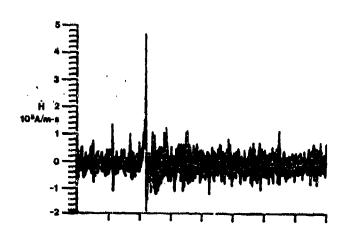


Fig. 3 - Strip chart of aircraft electric field (center trace), digital trigger pulse (first pulse on top trace) and IRIG-B time code (bottom trace)



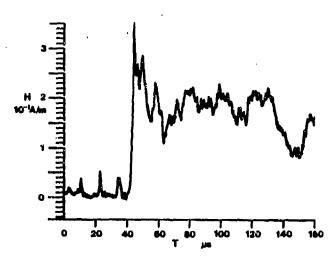
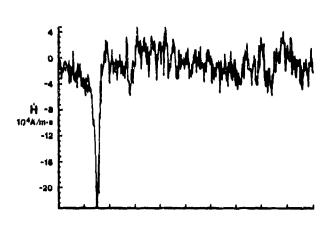


Fig. 4 - Overall graph of digital magnetic field derivative data (H, top trace) and the numerical integration (bottom trace)



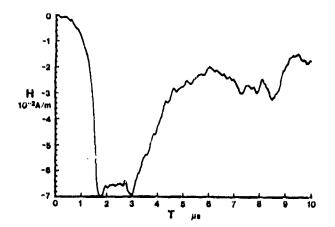
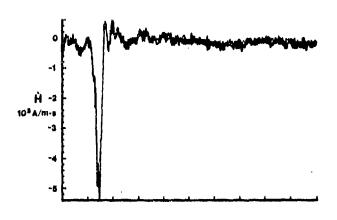


Fig. 5 - Ten microsecond data window for first return stroke waveform at 9.5 km with numerical integration



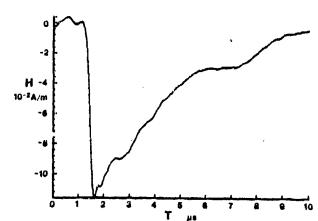


Fig. 6 - Ten microsecond data window for subsequent return stroke waveform at 10.4 km with numerical integration

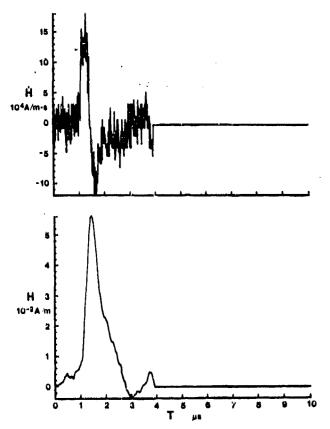


Fig. 7 - Ten microsecond data window for leader pulse waveform at approximately 11 km with numerical integration

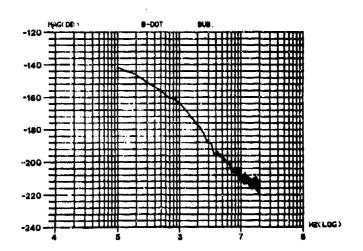


Fig. 9 - Graph showing average spectra amplitude in dicibels versus log frequency for subsequent return strokes

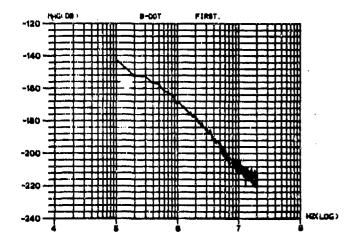


Fig. 8 - Graph showing average spectra amplitude in dacibels versus log frequency for first return strokes

THE RESERVE OF THE PARTY OF THE

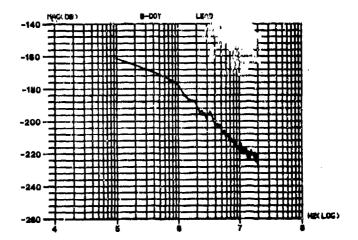


Fig. 10 - Graph showing average spectra amplitude in decibels versus log frequency for leader pulses

GROUND EVALUATION OF AN AIRBORNE LIGHTNING LOCATOR SYSTEM



William Lawis, Anthony J. Barile, Nickolus O. Rasch FAA Tachnical Center, Atlantic City Airport, New Jersey

ABSTRACT

In a ground evaluation of an airborne lightning locator system, lightning stroke rates per 4 minutes were compared with aircraft turbulence during thunderstorm penetrations. Data were taken on 3 thunderstorm days and summarized mostly into 15-minute periods consisting of three to four aircraft penetrations. Stroke rates varied considerably and did not show a linear relationship to aircraft turbulence. However, when average stroke rates for the 15-minute periods increased, aircraft turbulence increased and vice versa. It is concluded that the lightning locator system is a potentially useful thunderstorm turbulence warning device, but requires further ground/air testing.

THE FEDERAL AVIATION ADMINISTRATION (FAA) has developed a test bed at the FAA Technical Center, Atlantic City Airport, N.J., to make concurrent Doppler radar and aircraft measurements of thunderstorm turbulence. Some data have been analyzed (reference 1) and results indicate that Doppler radar has the potential to provide useful turbulence advisories for aircraft.

in the summer of 1982, a lightning locator, i.e., storm receiver, was installed at the radar site to investigate the relationship between thunderstorm lightning activity and turbulence. The investigation was carried out through an agreement with the Navai Air Development Center (NADC), Warminster, Pa., because of their interest in developing the storm receiver (see paper by E. Coleman, elsewhere in these proceedings). The FAA, as a party to this agreement, was the vehicle whereby the testing could be accomplished with existing facilities, and in conjunction with on-going work to provide useful and meaningful information to both parties.

Three concurrent data collections of lightning, aircraft turbulence, and Doppler radar data were made on separate thunderstorm days. This paper reports on the relationship between lightning activity and thunderstorm turbulence shown by an analysis of these data collections.

#### STORM RECEIVER

The storm receiver was developed by the Naval Air Development Center, Warminster, Pa., It is primarily an airborne system but can be used on the ground (see the Coleman paper, these proceedings for a complete description). storm receiver has two orthogonal loop antennas responsive to the N-S and E-W rate of change in magnetic field, and an electrically isoluted capacitive plate antenna to measure the rate of change in the electric field. Azimuth bearing to each thunderstorm electrical/magnetic discharge (stroke) is determined by sampling the three electromagnetic field time-derivative wave forms and comparing them with other submicrosecond pulses associated with each lightning stroke. Range to the discharge is computed from the ratio of the total magnetic field to the electrical field. These measurements are made on all electromagnetic discharges - ground to cloud, cloud to cloud, or within cloud. Usually three or four (but sometimes many more) strokes are required to dissipate a potential. These comprise the complete lightning event referred to as a "flash." The individual discharges (strokes) are measured in hundreds of microseconds, separated in time by 10's of milliseconds. Sometimes lightning appears to flicker as observed through the human eye. This is caused by the eye discerning the individual strokes that make up the flash.

The storm receiver measures the vertical component of the individual discharges whether ground to cloud, cloud to cloud, or within cloud. The system operates in the 1.5 kHz to

15 MHz frequency region up to a 200-nmi radius. Received signals are displayed on a PPI-type CRT with compass bearings and range rings. The display range is adjustable to 200 nmi, but was set to 50 nmi for these tests. Strokes more than 4 minutes old are automatically removed from the display, which can also be cleared manually. All data are recorded on special cassette tape for later analysis.

#### RADAR TEST BED

The instrumentation radar is one channel of a standard dual-channel Airport Surveillance Radar (ASR)-8 Interconnected to a 15-foot parabolic antenna. Peak power is 1 MW, transmittar frequency 2790 MHz, PRF 1030 pps, pulse length 0.6 µs, and antenna two-way beamwidth 1.20. The system maximum range is 60 nmi, but data are taken only to 40 nml to keep pulse volumes small. Data are taken on a grid of range-azimuth cells in a window controllable in range and azimuth dimensions, but generally set for about 10 nmi x 10 nmi. As the antenna sweeps the window, a 262K buffer memory is filled with 21-Lit digital words of 180 information from each pulse-volume. The data are read out on tape through a NOVA computer. which also computes fields of radar reflectivity factor, Doppler mean velocity, and Doppler spectrum width in terms of the cube root of & (turbulence dissipation rate) for display in the window. During these operations, the antenna is returned to the starting azimuth to await another sweep command. Time between scans is approximately 80 seconds. The stationkeeping rader is an ASR-7 (S-band, 60-nml range). Associated with it is a beacon interrogator and a precipitation contouring system to monitor storms of interest. The instrumentation radar window, aircraft beacon track, and ASR-7 precipitation contours are shown on a common display.

## AIRCRAFT EQUIPMENT

A Convair-580 turboprop aircraft was used to penetrate thunderstorms. The aircraft is equipped with a center-of-gravity (CG) accelerometer (20 samples/sec), a differential Pitot pressure transducer (100 samples/sec), an altitude transducer, Rosemount temperature probe, crystal-controlled clock, and Litton INS, ail sampling at 1/sec. Data are digitized and recorded on magnetic tape.

## DATA COLLECTION

The aircraft was launched when thunderstorms were occurring within 40 nmi of the radar. National Weather Service WSR-57 radar Video Integrator and Processor (VIP) level three and four storms (41-45 dBZ-heavy and 46-50 dBZ-very heavy, respectively) were preferred. VIP level five and six storms were avoided because of the high probability of damaging hall. The aircraft was flown in an altitude block of 3,000 to 5,000 feet to avoid encreaching on the New York Air Route Traffic Control Center airspace.

RADAR MEASUREMENTS - The 1 & Q components (196 pulses) for each pulse volume (90 m by 1.20) are recorded range sequentially. They are then reordered in azimuth and the first three autocorrelation lags determined. The lags are used to compute the corresponding Doppler moments (radar reflectivity factor, mean velocity, and spectrum width) through specific pulsepair algorithms (reference 2).

The spectrum width is converted to the following equation:

「「「「「「」」」を表現の場合で、あるではないないでは、これであった。 「「「」」」

$$e^{\frac{1}{3}} = \frac{\sigma_u}{1.352 \, a^{\frac{1}{3}}} \, (cm^{\frac{2}{3}}sec^{-1})$$
 (1)

where  $\sigma_u$  is the spectrum width (cm sec<sup>-1</sup>), and is the turbulence dissipation rate (cm<sup>2</sup> sec<sup>-3</sup>, "a" is the Gaussian half-power beamwidth (cm), and 1.352 is composed of known constants, assuming isotropic and homogeneous turbulence. Since "a" is a function of range, the cube root of E is essentially a rangeweighted spectrum width and, as such, should be superior to spectrum width as a turbulence measure.

The turbulence dissipation rate (reference 3) represents the kinetic energy converted to heat per unit mass per unit time as the larger eddies decay into progressively smaller eddies. The system is steady-state in the inertial subrange where atmospheric motions are isotropic.

The beacon track of the aircraft is smoothed and interpolated to produce positions points at one-second intervals. The radar data fields for each scan are also smoothed and interpolated. The radar moments at the locations of the 1-second aircraft position points are then extracted, allowing each radar scan to cover the period from approximately 40 seconds before to 40 seconds after scan time. This provides continuous radar data along the aircraft track during thunderstorm penetrations. (Note: Radar processing programs were not available to produce these data for the missions discussed in this report.)

AIRCRAFT MEASUREMENTS - The aircraft turbulence parameter is a combination of  $\epsilon^{1/3}$ derived both from the CG acceleromater and Pitot pressure (airspeed) fluctuations.

The value derived from the accelerometer is(reference 2):

$$\epsilon_a^{1/3} = \frac{\sqrt{3D_a^{NV}^{3/4}}}{c_{L_\alpha}Sc^{1/2}_\rho} (cm^{2/3}sec^{-1})$$
 (2)

where D is the acceleration structure function assuming isotropic, homogeneous turbulence, C is the universal constant (1.77), V is true airspeed, p is air density, M is aircraft mass, CL the wing lift curve slope, and S the wing area.

ea<sup>1/3</sup> was computed each second by continuously averaging over a 7.5-second interval using a cosine squared weighting.

The value derived from the airspeed fluctuations is (reference 2):

$$\epsilon_{\rm p}^{1/3} = \frac{\sqrt{D_{\rm v}}}{c^{1/2} r^{1/3}} (cm^{2/3} sec^{-1})$$
(3)

where  $\mathbf{D}_{\mathbf{V}}$  is the acceleration structure function assuming isotropic, homogeneous turbulence, r is the distance between successive airspeed measurements, and C the universal constant

 $\epsilon_p^{1/3}$  was computed each second by continuously averaging over a 7.5 second Interval using a cosine squared weighting.

The two 8 values were combined

into one by the following equation:

$$\epsilon_{ap}^{1/3} = \sqrt{\frac{\epsilon_a^{2/3} + (\lambda \epsilon_p^{1/3})^2}{2}}$$
(4)

was determined by minimizing are error between  $\epsilon_a^{1/3}$  and  $\epsilon_p^{1/3}$ The factor the mean

mean square error = 
$$\frac{\sum (\epsilon_{\mathbf{A}}^{1/3} - \lambda \epsilon_{\mathbf{p}}^{1/3})^2}{N}$$
 (5)

where N = number of data pairs. The minimum was determined by taking the partial derivative with respect to  $\lambda$  and setting it equal to zero. The factor \( \) was found to be 1.04 based on five 1982 thunderstorm flights with the Convair-580 aircraft. This was used in equation (4) to compute the combined aircraft turbulence parameter.

An aircraft turbulence scale based on  $\varepsilon_{ap}^{1/3}$ has been established from 1980, 1981, and 1982 data which agrees closely with recorded pilot reports of turbulence severity. This scale is shown in table 1.

STORM RECEIVER - The vertical components of ground to cloud, cloud to cloud, and intracloud discharges were detected and converted to stroke rates per 4-minutes for pie shaped wedges extending from the radar site to approximately 50 nml. The azimuth dimensions were chosen to cover the aircraft track during thunderstorm penetrations. (See Colemen paper, these proceedings, for system procedure for diagnosing discharges (strokes.)

DATA ANALYSIS

Concurrent storm receiver data, aircraft turbulence data, and ASR-8 radar data were obtained on 7/28/82, 8/17/82, and 8/23/82. A summary of these data is shown in tables 2, -3, and 4, respectively, for periods of approximately 15 minutes consisting of three to four aircraft penetrations. The aircraft turbulence is in terms of the maximum experienced during the period, either in the moderate category or the severe category (see table 1). The lightning data are the average of the 4-minute stroke rates through the period and the maximum 4-minute stroke rate. The NWS WSR-57 radar Video Integrator and Processor (VIP) thunderstorm precipitation intensity levels and cell heights in thousands of feet are also shown. These were obtained from hourly PPI plots prepared by the local NWS station. VIP levels of interest are level (L) 3: 41-45 dBZ, heavy; L4: 46-50 dBZ, very heavy; L5: 51-56 dBZ, intense; L6: 557 dBZ, very intense. The ASR-8 maximum VIP levels and thunderstorm turbulence indications for approximately the 5,000-foot level are shown. These entries were obtained from the array of dBZ and & values displayed in the ASR-8 data window during the periods. The ASR-8 VIP is less than the NWS VIP because the NWS radar probes higher altitudes where radar reflectivity is normally greater. The ASR-8 turbulence indication is approximate. pending further studies on the relationship between aircraft and radar-measured 8

The aircraft pilot reported lightning on most of the thunderstorm penetrations. The lightning tended to be associated with turbulence peaks, although there were more peaks than reports. Since reports were not given in quantitative terms and may be incomplete, they are not summarized in the tables.

MISSION OF 7/28/82 - On this day an intensifying cyclone moved eastward, well north of the area, trailing a cold front southwest-ward from the low center. Severe thunderstorms formed into squall lines in advance of the front and moved from the west at 30K through the Atlantic City area during the day. The aircraft made penetrations of three of these thunderstorms at an altitude of approximately 4,500 feet from 1018 to 1225 EDI. Table 2 is a data summary for this mission.

During period 1 the aircraft made three penetrations of a NWS VIP L5 (trending to L6) thunderstorm located about 25 nmi NNE of the radar site. The NWS radar plots showed that this storm was the second in a line extending from the radar site for 125 nmi to the NE. The southern part of the line formed between 0930 and 1000. Stroke rates were very high at the beginning of the period with a steady decline thereafter. The severe aircraft turbulence occurred early in the period at 1021, during the maximum stroke rate interval (1018-22). The ASR-8 indicated severe turbulence at the beginning of the period decreasing to moderate toward the end.

During period 2 the aircraft made three more penetrations of the same storm which was now shown by NWS to be VIP L6. However, the ASR-8 5,000-foot VIP level remained at 4. Stroke rates decreased to moderate levels through the period and only moderate turbulence was encountered by the aircraft. The ASR-8 turbulence indication was moderate.

Four penetrations of thunderstorm 1 were made during period 3. Stroke rates increased appreciably and aircraft turbulence increased to severe. This occurred at 1058 somewhat before the maximum stroke rate (79), observed in the 1101-05 interval. The ASR-8 turbulence indication increased to severe.

After period 3, storm 1 moved out of range and the aircraft was vectored to thunderstorm 2. This was a NWS L5 cell located about 15 mmi NE of the radar site. Stroke rates were quite high during the period. However, the aircraft only experienced moderate turbulence. This may be due to the fact that the aircraft flew mostly in the peripheral areas of the storm because of difficulty in obtaining the desired air traffic clearance. The ASR-8 turbulence indication was severe.

During period 5, three more penetrations were made into thunderstorm 2. Stroke rates averaged quite high and severe turbulence was experienced. The stroke rate was not recorded for the 4-minute interval (1139-43) covering this encounter due to a tape change. The ASR-8 indicated severe tubulence in the storm. The storm height was probably above 38,000 feet by the end of the period since NWS showed it to be L6 and 47,000 feet at 1230.

Meanwhile strong lightning activity was noted on th PPI display coming from a large thunderstorm located about 25 nmi to the WSW of the radar site. The aircraft was vectored to this storm and made penetrations during periods 6 and 7 as it moved toward the radar, increasing in intensity and height. Stroke rates were moderate for the first three 4minute intervals of period 6, then increased sharply (as seen on the PPI). Unfortunately, this indication was interpreted by the operator of the lightning locator system as strong radar interference prompting him to turn the system off as a safety measure. Subsequently, it was determined that the "interference" was indeed strong lightning activity and the processor was turned on again at 1225. The stroke rate for the following period (1225-29) was 290, which is near the maximum detectable with the system. The extreme turbulence experienced in period 7 was just before this interval, at 1222. The severe turbulence encountered in period 6 was just before the break at 1203. It is likely that very high stroke rates were also occurring from 1205-1225 when the storm was intensifying. After the extreme turbulence experience, the storm was considered too dangerous for further penetration and the aircraft returned to base.

MISSION OF 8/17/82 - On this day thunderstorms formed along a cold front which passed through the Atlantic City area in the early evening. Storms moved eastward at about 20K. The NWS radar was out of service and no PPI plots were available. However, the tropopause height was about 50,000 feet and it is probable the storms reached this level. The ASR-8 5,000foot V!P levels for the cells penetrated were all 4. Table 3 is a data summary for this mission.

During period 1 the aircraft made three penetrations of a thunderstorm located about 20 nmi NE of the radar site. The stroke rate was 7 at the beginning of the period, increasing to the maximum of 23 at the end. Severe turbulence occurred during the second penetration when the stroke rate per 4 minutes was 19. The ASR-8 turbulence indication was not recorded for this period.

During period 2 stroke rates increased appreciably. The maximum of 102 occurred from 1457-1501 and the aircraft experienced severe turbulence at 1500. The ASR-8 indication was moderate. After the second penetration, an overhead thunderstorm at the radar site caused a power failure and the aircraft was held outside the storm from 1504-1513.

Three more penetrations of storm 1 were made during period 3. Stroke rates decreased considerably and only moderate turbulence was experienced by the aircraft. The ASR-8 turbulence indication was not recorded for this period.

During period 4 the aircraft made 4 penetrations of a second thunderstorm located about 12 nmi east to southeast of the radar site. Stroke rates were very high, although only moderate turbulence was experienced by the aircraft. The ASR-8 turbulence indication was also moderate.

The aircraft made only one penetration of storm 2 during the last abbreviated period. Stroke rates increased and the aircraft encountered severe turbulence. The ASR-8 turbulence indication was also severe.

MISSION OF 8/23/82 - On this day semiisolated (rather than line-type) thunderstorms
formed along a cold front which passed through
the area in late afternoon. The individual
storms moved from the west at 30%. NWS showed
the storms to be L6 with tops 34,000 - 38,000
feet. The ASR-8 5,000-foot VIP levels were
mostly 4. In view of the low tops and ASR-8
VIP measurements, the L6 classification is
considered doubtful.

During period 1 the aircraft made three penetrations of an isolated NWS VIP L6 (ASR-8 VIP L4) thunderstorm located about 15 nmi WSW of the radar site. Only one lightning stroke was recorded - that in the 1401-1405 period. The highest aircraft turbulence (just in the severe category) was encountered during this interval at 1402. The ASR-8 turbulence indication was also severe.

In the second period, three more penetrations of the storm were made with stroke rates and turbulence both increasing. The peak rate

of 13 occurred in the 1420-24 interval, just proceeding a severe turbulence encounter at 1425. The stroke rate abruptly dropped to zero for the 1424-28 interval. The ASR-8 indicated severe turbulence in the cell.

Thunderstorm 1 was beginning to enter ground clutter and appeared to be weakening so the aircraft was vectored to thunderstorm 2. This was located about 20 nmi north of the radar site. Stroke rates were low through period 3 and only moderate turbulence was experienced. The ASR-8 turbulence indication was severe.

Three more penetrations of storm 2 were made in period 4 with stroke rates increasing slightly. Severe turbulence was experienced at 1443 and was associated with a stroke rate of 3 for the 1442-46 interval. The ASR-8 turbulence indication was again severe.

During period 5 the aircraft made three penetrations of a third NWS VIP L6 storm located about 20 nmi to the NW of the radar site. The ASR-8 5,000-foot VIP level for this thunderstorm was only 3. No lightning strokes were detected and only moderate turbulence was encountered. The ASR-8 turbulence indication was also moderate.

The low stroke rates for the 8/23/82 storms are thought to be due primarily to the low heights of the storms.

#### SUMMARY AND CONCLUSIONS

The d "a of tables 2, 3, and 4 do not show any linear relationship between stroke rate and turbulence for these diverse storms. It can only be said that the strongest turbulence observed was associated with a storm producing the highest stroke rate (290 with thunderstorm 3 on 7/28/82). However, all tables show that, in general, the maximum turbulence encountered increased when the average stroke rate increased, and vice versa. The maximum turbulence was not usually associated with the maximum stroke rate for a period, but was mostly within one 4-minute interval of it. It was also noted that qualitative pilot reports of lightning, when given tended to be associated with turbulence peaks.

There was generally good agreement between turbulence indicated by Doppler radar and that experienced by the aircraft. However, this must be considered preliminary, pending a more detailed analysis of the data.

It is concluded that the storm receiver is a potentially useful thunderstorm turbulence warning device for airborne or ground use. However, further ground/air testing is needed to clarify the relationship between thunderstorm lightning stroke rates and turbulence, considering such factors as storm height and size. Testing of the ranging precision of the storm receiver and the use of radar-measured turbulence fields will help in data analysis.

## REFERENCES

1. W. Lewis, R.G. Oliver, A. Delamarche, T. Y. Lee, "Test and Evaluation of the Radar Thunderstorm Turbulence Detection System (Phase I)" FAA Technical Center Interim Report, FAA-RD-82-22 (FAA-CT-82-6), July 1982.

2. M. Labitt, "Coordinated Radar and Technical Center Interim Report, TAA-RD-82-22 (FAA-CT-82-6), July 1982.

2. M. Labitt, "Coordinated Radar and Aircraft Observations of Turbulence," ATC-108, MIT Lincoln Laboratory, Lexington, Mass., (prepared for FAA System Research and Development Service). May 26 1981

Service), May 26, 1981.
3. P. B. MacCready Jr., "Standardization of Gustiness Values from Aircraft." J. Appl. Meteor, 3, pp. 439-499, August 1964.

Table 1. Aircraft Turbulence Scale

Aircraft e1/3	•
2/3 -1 cm sec	Turbulence
0 - 2	Negligible
<b>&gt;</b> 2 - 4	Light
54 - 7	Moderate
57 - 12.5	Severe
<b>512.5</b>	Extreme

Table 2 - Data Summary for 7/28/82

			No.	Max A/	C Turb.	: Strokes	/4 Min.	NWS	Data	ASR-8	Data
Period	Time (EDT)	TSTM	Pen.	Mod	Sev	Aver.	Max.	VIP	Ht.	VIP	Turb.
1	1018-1033	1	3	-	7.2	137	23;	5/6	46	4	S/M
2	1033-1049	1	3	5.7	•	26	45	6	46	4	. M
3	1049-1105	1	4	-	8.6	54	79	6	46	4	s
4	1117-1131	2	4	5.0		91	139	5	38	4	s
5	1131-1147	2	3	-	7.9	118*	127*	5 **	38**	4	S
6	1153-1209	3	3	-	9.3	55#	88#	5/6	50	4	s
7	1209-1225	3	3 .	•	13.2##	¥	#	6	55	5	s

<sup>\*</sup> No data for 1149-43

<sup>\*\*</sup> Storm increased to L6 and 47,000' at 1230

<sup>#</sup> No data from 1205-25. Stroke rate 1225-29 was 290

<sup>##</sup> in extreme category

Table 3 - Date Summary for 8/17/82

•			No.	Max. A/C	Turb.	Strokes	/4 Min.	NWS	Data	ASR-E	3 Data
Period	Time (EDT)	TSTM	Pen.	Mod	Sev	Aver.	Max.	VIP	Ht.	VIP	Turb.
1	1437-1453	1	3	-	7.5	18	23	*	*	4	-
2	1453-1504**	1	2	-	7.1	84	102	*	*	4	М
3	1513-1529	1	3	6.2	-	23	46	*	*	4	-
4	1537-1553	2	4	6.3	-	166	259	*	*	4	. м
5	1553-1559	2	1	-	8.1	194	195	*	*	4	s <sub>.</sub>

<sup>\*</sup> No NWS data. storm heights est. 50,000' based on Tropopause height.

Table 4 - Data Summary for 8/23/82

			No.	Max. A	/C Turb.	Strokes	/4 Mln.	NWS	Data	ASR-	8 Deta
Period	Time (EDT)	TSTM	Pen.	Mod	Sev	Aver.	Max.	VIP	Ht.	VIP	Turb.
1	1349-1403	1	3	-	7.0	a	1	6*	34	4	s
2	1412-1427	1	3	-	7.7	7	13	6*	35	4	S
3	1427-1442	2	3	6.8	-	2	5	6*	35	4	S
4	1442-1458	2	3	-	8.3	3	7	6*	35	4	s
5	1503-1519	3	3	5.7	-	0	0	6*	38	3	М

<sup>\*</sup> L6 classification considered doubtful due low heights and ASR-8 VIP levels



<sup>\*\*</sup> Radar power failure. A/C held outside storm 1504~13.



## A WIDEBAND AIRBORNE/GROUND LIGHTNING FLASH LOCATION SYSTEM

Ernest Coleman

Naval Air Development Center (Code 3021) Warminstar, Pennsylvania 18974

#### ABSTRACT

This paper presents the design and summary of test results of a new wideband lightning location system. Although this paper emphasizes airborne application, the design and performance of the subject system is identical for both airborne and ground applications. The unique method used for identifying, direction-finding and ranging to a lightning stroke is discussed. The lightning location system is designed to detect severe storms and to identify potentially turbulent weather. standard video display output shows the location of thunderstorms by displaying the rate of lightning stroke activity. As new lightning strokes are received, the display intensifies on the CRT to show the center of the electrical activity. provides a display of severe electrical storas similiar to the standard radar reflectivity displays. The lightning stroke data is integrated for four minutes. As the number of lightning strokes diminishes, the display decreases in brightness. A standard serial interface provides remote control and monitor capability. For the ground and airborne test programs, the serial channel is used to record all lightning data on a magnetic tape for later retrieval and display. Accurate direction findings is determined by utilizing only the peak pulses of the wideband return stroke waveform. The range estimation from a single station to each lightning stroke uses the differences between the decay of electric and magnetic fields. A single antenna unit consisting of two orthogonal wideband magnetic cross-loops and a short vertical monopole antenna. The system has adequate bandwidth (3 MHz) to detect return stroke pulses for accurate direction finding and ranging. The system has a maximum range of 120 nm radius. Tests on a number of lightning storms at distances to 75 nm indicate the angular resolution is better than \$10° and may be in the range of less than 3° with little or no systemmatic dependence on the number of active thunderstorm cells which are at different angles. The lightning location system is a modular/digital design and may easily be integrated into other digital weather systems. Test results are presented which show the accuracy of the system in locating sovers weather. Future plans for advance development of the lightning location system by the Navy are discussed.

(+ or - 10 deg



NAVY AIRCRAFT are often required to fly missions in/around adverse weather. The ability of radar to locate severe thunderstorm turbulence is inadequate (1)\*. In addition to airborne radar, there are airborne systems specifically designed to detect lightning. However the range accuracy of these lightning detection systems is poor. The range information is based on a so-called ideal lightning stroke amplitide and is determined by assuming a known propagation loss. Furthermore, the lightning data is presented to the pilot serially without adequate correlation with old data already on the CRT. The rate at which lightning data is produced is important to the pilot as a weather hazard prediction. The program reported here was established to provide an alternate and improvement over conventional storm detection systems.

Broadband measurements of the radiation fields (high time resolution) produced by lightning discharges within 120 and as close as I show that most lightning waveforms have zero-to-peak rise times of less than five microseconds. Most first and subsequent return stroke fields have several small second peaks or shoulders immediately following the first peak. The large subsidiary peaks (spaced 10-30 microseconds) in first strokes are produced by the effects of branches. Since the propagation speed of a raturn stroke up a previous leader channel is approximately 200 meters/microsecond, these peak fields are separated by 2 to 6 km. There are many reports in the literature on the electromagnetic characteristics of thunderstorm radiation for example Uman (2-6), Krider (4-6), Taylor (7), Ruhnke (8), Fisher (9), Brantley (10), Herrman (11), and Li ingston, (12).

Here, we present a new version of a lightning direction and range finder\*\* (fig. 1), which utilizes the peak of the magnetic radiation fields to provide accurate directions to the channel of individual return strokes. Range to the stroke is estimated by measuring the ratio of the low-frequency magnetic field to the electric field. The performance of the storm warning system during initial test by FAA is presented in a companion paper by W. Lewis in these proceedings. The system operated effectively for discharges as close as a few kilometers and as far away as 200 km. The signals received by a stroke are compared to other strokes within a geographical ares. The rate of stroke occurrences are calculated and used to show the intensity of the thunderstorm.

\*Numbers in parenthese designate references at end of paper. \*\*A U.S. Patent Application Serial No. 235, 168 filed February 17, 1981 entitled "Storm Warning Method and Apparatus" is pending.



Fig. 1 - Storm Warning System

### **APPARATUS**

The storm warning system (fig. 2) consists of three units; antenna, display and receiver. The antenna assembly is mounted on either the top or bottom of the aircraft. A low aerodynamic drag shape contains the basic electric and magnetic detectors. The display assembly is a standard raster display. Two size units are available (3 inch and 5 inch) but any video monitor with composite video input and 525 line display may be used. The receiver has been designed for an operation environment defined by MIL-E-5400, CLASS 2. The total weight of the receiver is 14 pounds and head dissipation is 52 watts maximum. The receiver maximum dimensions are 3.25 X 12.37 X 10.25 inches.

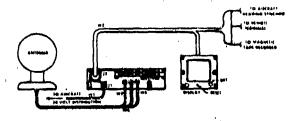


Fig. 2 - Storm Warning System Installation

ANTENNA - The antenna separately receives the electric (E) and magnetic (H) radiation fields produced by lightning. Basically, the magnetic sensors are shielded orthogonal loops with a gap in each shield. The shield around the loop improves the amplitude balance of each loop and minimizes the aircraft structure effects. The magnetic sensor output is proportional to the lightning signal multiplied by the cosine of the angle between the plane of each loop and the discharge. The electric field is sensed by a short vertical monopole. The antenna includes three low pass filters which reject high frequency signals and convert the sensor outputs to 50 ohms.

RECEIVER - The antenna signals (figure 3) go directly to the receiver which has three separate wideband, high gain amplifiers, which provide a system noise figure of 7.5dB. The amplifier gain of 26.5dB was choosen to allow the linear detection of lightning signals between 4 and 200 km. The bandwidth of each amplifier is 1.5 kHz to 3 MHz. The three amplifiers provide signals which are proportional to the time rate of change in

the radiation fields to separate integrators. The output of each integrator (decay constant of 45 microseconds) is proportional to the radiation field waveforms. These signals go directly to separate track and hold circuitry which holds the peak of each pulse in response to a sampling control signal. The control signal is provided each time the electric field value peaks after a rise time less than five microseconds. The resulting voltages (E and orthogonal H fields) are digitized and stored in a first-in-first out (FIFO) memory.

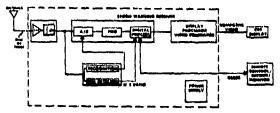


Fig. 3 - Functional Block Diagram

Recognition Circuitry - The output of the electric field amplifier is also connected to recognition circuitry. The recognition circuitry descriminates against interferring signals which are not caused by the lightning return stroke. The recognition circuitry measures two parameters-pulse width and rate of voltage change. The lightning step leader is a narrow-pulse usually on the order of several 100 nanoseconds duration and is ignored by the recognition circuitry. The time rate of change of the electric field is monitored and used to identify a return stroke signal. When the electric field has reached its peak voltage, the sample control signal is generated. After the recognition of the first lightning pulse, an integration control signal which has a duration of one lightning stroke event (approximately one millisecond) is used to interrupt the digital processor.

Low Frequency Detection - The outputs of the integrators are also provided to 1.5 KHz band pass filters which have a narrow bandwidth of 200 Hz. The narrow band signals are separately converted to a signal proportional to true RMS voltage levels. These signals are a measure of the intensity of the electric and magnetic fields. Outputs of the true RMS detector are directly connected to sample and hold circuitry. In response to the integration control signal which is generated at the end of a lightning stroke event, all three outputs are sampled by the digital processor.

Digital Processor - The digital processor digitizes the low frequency data and moves all the sample peak pulse data from the FIFO memory into random access memory (RAM). After the new data is saved, the recognition circuitry is once again allowed to detect new lightning data. The digital processor anal-

yses the sampled peak pulses to determine the general direction to each lightning stroke. First, the low frequency data is used to calculate the absolute ratio of H/E. The magnitude of the magnetic field decreases with the square of the distance from the source while the electrostatic field decreases with the cube of the distance from the source (8). The effects of this relation are clearly shown in figure 4. The amplitudes of the E to H ratio (E/H) at 1.5 KHz frequency are plotted as a function of distance. Although the assumptions of a flat, good conducting ground and a vertical lightning channel are considerable over simplifications, the digital processor algorithm corrects for many of the errors. The test results to date are encouraging as to the value of the H/E ratio to determine range. After the digital processor estimates the range to the stroke the new data is analyzed to determine the lightning stroke rate for the corresponding geographical area. The display is updated to reflect an increase in the lightning flash rate.

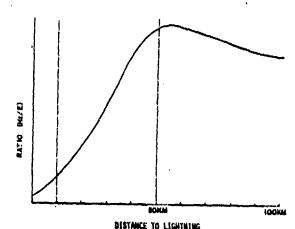


Fig. 4 - Ratio of H/E Versus Distance

TEST RESULTS

During the 1982 storm season, a total of 24 hours of lightning data was collected using the storm warning system which included 6 hours of aircraft turbulence data. National Weather Service (NWS) radar summary data was obtained for the majority of the lightning data. One storm on 28 July 1982 showed extreme turbulence along with a high lightning stroke rate. The lightning stroke rate in general indicated the severity of the storm. The lightning stroke rate appears to go from a low to a high rate in a relatively short time during storm development. The storm of 23 August 1982 represents the typical storm cell which has low lightning stroke rate and likewise, a less severe turbulence than the general storms measured during the 1982 season. The following discussion summarizes test results and shows typical storm warning

display data (see Lewis paper, these proceedings, for comparing lightning activity and turbulence). A detail report of test results may be found in reference 14.

PREFRONTAL SQUALL LINE ON 28 JULY 1982 - A prefrontal squall line of severe thunderstorm cells formed in Pennsylvania and Delaware to the north and west of Atlantic City, New Jersey at 0830 EDT. The storms formed a line about 125 nautical miles long (25 nm wide) moving from 260 deg. at 30 nm/hr. Additional squall lines of thunderstorms formed 50 nm west of the first line.

The NWS Video Integrator and Processor (VIP) contours for 0935 EDT are shown in figure 5 along with an overlay of the storm warning system display. A computer program was used to combine the storm warning data and the NWS VIP contour data. The lightning stroke data (fig. 5) is plotted as a dot for lightning stroke rates less than four strokes per four minutes and circles for lightning strokes greater than four strokes per four minutes. Note storm cell one for the test had a VIP contour level two (L2) approximately 25 nautical miles west of the test site. This cell moved from 270 degrees and, at 1008 EDT, was measured by the doppler radar to be a level four (48-50 dBZ). The doppler data showed possible severe turbulence at approximately 1019 EDT. Later at the end of test period one, the doppler data showed cell 1 to be moderate and the VIP contour leval was decreasing.

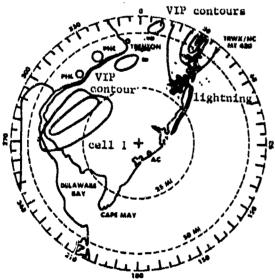


Fig. 5 - Lightning Location vs Radar Reflectivity Contours for 0935 EDT 7/23/82

The storm warning system (SWS) display showed lightning activity to be North East of the FAA Atlantic City, New Jersey, Terminal Facility of Automation and Surveillance Testing (TFAST) site between 25 nm and 50 nm.

The dark areas indicate lightning activity occurring at a rate of more than four strokes per four minutes. Storm cell one to the West of TFAST showed only two dots but the cell to the North was showing extreme lightning activity. This cell was out of range for the doppler rader. Consequently, the sircraft was not flown to the cell. Note the dark lightning cells to be leading the contour plots for the radar data (the cell was moving from West to East). There were moderated levels of lightning activity behind the storm cell. As storm cell one moved North of TFAST, the display indicated extreme lightning activity. This cell was within range of the doppler radar and the aircraft was directed into the storms center.

A new thunderstorm cell formed (cell number two) west of cell one and moved into range of aircraft at 1117 EST. The NWS data indicated a maximum VIP contour level five (L5) and cell height of 38,000 feet. The lightning stroke rate of 139 occurred at the end of test period four. The aircraft did not have clearance to fly into the storm cell and consequently, flew mostly in the peripheral areas. The aircraft did experience a turbulence level of 7.9 (see Lewis, these proceedings, for turbulence scale) during test period five and the pilot reported light hail. The lightning rate continued at a high level during test period five.

Meanwhile, a third storm cell formed due West of the TFAST sits at 1135 EDT. The display indicated the new cell to have extreme lightning activity, (fig. 6). The aircraft was vectored to cell three. At approximately 1156 EDT, the doppler radar measured a VIP level of two (39 dBZ) for cell three. Six minutes later, the doppler rader measured a VIP level five (51 dBZ) and the NWS was showing a level six. The storm cell height was now at 50,000 feet. The storm warning system recorded a maximum stroke rate of 88 about five minutes before the aircraft measured a turbulence level of 9.3. The storm warning system was not operated between 1205 to 1227 EDT. At 1227 EDT the lightning stroke rate was 290. The aircraft measured an extrame turbulence level of 13.2 about four minutes earlier. The storm height was now at 55,000 feet. Storm cell three was too severe to continue the test program. The pilot confirmed the lightning activity and messured extreme turbulence at the leading edge of the storm cell.



Fig. 6 - Lightning Location vs Radar Reflectivity Contours for 1135 EDT 7/28/82 CONCLUSIONS

The storm warning system was successfully operated as a single ground station during the 1982 storm season and detected, located and recorded over 5,000 lightning strokes. The azimuth angle resolution of the system was measured to be better than +10 degrees. The maximum azimuth angle resolution should be in the neighborhood of 20 and will be measured in 1983 storm season. The range accuracy was not easily measured; however, by comparing the thunderstorm cell radar reflectivity contours with lightning stroke data (see examples in figures 5 and 6) the range was estimated to be at least +25 percent of the measured range. The performance of the storm warning system to date has proven the feasibility of locating lightning activity.

When comparing the lightning activity with the NWS radar measurements of reflectivity, the lightning activity was not completely confined to the highest reflectivity regions; however, the lightning stroke data was easily associated with the VIP contours for individual storm cells. The lightning activity was found to occur anywhere within the thunderstorm cell. The results have shown that some storm cells (identified by NWS as severe) have high level of measured reflectivity, but produce only moderate turbulence and lightning. However, this lack of lightning activity and turbulence experienced by the test aircraft may not represent the normal convective storms. The data collected during the final Phase of the project should confirm the correlation of turbulence and lightning. As experienced during the 1982 storm season, the results have also shown that convective storms which generate severe turbulence and hail also generated electrical activity.

#### FUTURE WORK

The calibration of the range accuracy of the storm warning systems will significantly enhance the data obtained on individual storm cells. For the 1983 storm season, the storm warning system will be installed in a Navy A-7 and a FAA Convair-560 aircraft. After calibrating the range capability of the storm warning system sirborne measurement of thunderstorms will be recorded using the test methods reported in reference 14. The testing of thunderstorms will no longer be limited to the Atlantic City, New Jersey area. More data will be collected from storm cells in three geographical areas (Oklahoma, New Jersey and Florida). Of particular interest, will be the amount and time of occurrence of hail activity during the convective storm life cycle. In addition, the turbulence factor of each storm cell will be compared with the lightning stroke rate. The final report will be available by 1984.

### REFERENCES

- 1. Lewis, et al, "Test and Evaluation of The Radar Thunderstorm Turbulence Detection System (Phase 2)," FAA report DOD/FAA/RD-82/22, July 1982
- 2. Uman, et al, "Magnetic Field of Lightning Return Stroke," Journa, of Geophysical Research, Vol. 74 No. 28, December 20, 1969 pp 6899-6909
- 3. Uman, et al, "Correlated Electric and Magnetic Fields From Lightning Return Strokes," Journal of Geophysical Research, Vol. 80 No. 3, January 20, 1975 pp 373-376
- 4. Krider, et al, "Broadband Antenna Systems for Lightning Magnetic Fields," Journal of Applied Meteorology, Vol. 14, March 1975 pp 252-255
- 5. Krider, et al, "A Gated, Wideband Magnetic Direction Finder for Lightning Return Strokes," Journal of Applied Mateor-ology, Vol. 15, March 1976 pp 301-306
  6. Krider, et at, "The Electric Fields
- 6. Krider, et at, "The Electric Fields Produced by lightning Stepped Leaders," Journal of Geophysical Research, Vol. 82 No. 6, February 20, 1977 pp 951-690
- 7. Taylor, "A VHF Technique for Space-Time Mapping of Lightning Discharge Process," Journal of Geophysical Research, Vol. 83 No. C7, July 20, 1978 pp 3575-3583 8. Ruhnke, "Determining Distance to
- 8. Ruhnke, "Determining Distance to Lightning Strokes from a Single Station," NOAA TR-E-RL 195-APCL. 16, January 1971, pp 20-23
- 9. Fisher, et al, "Measured Electric Field Risetimes for First and Subsequent Lightning Return Stroke," Journal of Geophysical Research, Vol. 77 No. 3, January 20, 1972
- 10. Brantley, et al, "Lightning Properties in Florida Thunderstorms From Video Tape Records," Journal of Geophysical Research, Vol. 80, 24 August 20, 1975 pp 3401-3406

- 11. Herrman, et al, "Test of the Princi-ple of Operation of a Wideband Magnetic Direction Finder for Lightning Return Strokes," Journal of Applied Meteorology, Vol. 15,
- April 1976 pp 402-405

  12. Livingston, et al, "Electric Fields Produced by Florida Thunderstorms," Vol. 83

  No. Cl, January 20, 1978 pp 385-401

  13. Uman, "Lightning," McGraw-Hill
- 1969, pp 108
- 14. Coleman, "Investigation of the Correlations of Electrical Activity and Severe Air Turbulence During 1982 Thunderstorm Season," Report No. NADC-83003-30, 31 January 1982



WIDEBAND MAGNETIC DIRECTION FINDER NETWORKS FOR LOCATING CLOUD-TO-GROUND LIGHTNING

R. C. Binford, L. G. Byerley, E. P. Krider\*,
M. W. Maier, A. E. Pifer\*\*, and M. A. Uman\*\*\*
Lightning Location and Protection, Incorporated, Tucson, Arizona

ABSTRACT

Extensive networks of lightning direction finding stations are now operating in the United States, Canada, Mexico, Norway, Sweden, South Africa, Australia, Japan, and the Paople's Republic of China. These systems are being used to determine the location, movement, and intensity of thunderstorms; to facilitate the early detection of lightning-caused fires; to determine whether electric power outages are lightning-caused; to warn of impending lightning hazards; and for a number of other applications and basic research. Here, we describe the principles of operation of these lightning locating systems, system capabilities, typical system configurations, and system erformance factors.

### "LOCATING SYSTEM

To begin, it would be helpful to review the terminology for the physical processes which occur during a typical cloud-to-ground lightning discharge. A lightning discharge to ground, or flash, contains several large current surges of strokes (1) \*\*\*. A flash begins with a faint leader, which proceeds rather slowly from cloud to ground in a series of short luminous steps. When this stepped leader contacts the ground, a very energetic and bright return stroke propagates rapidly back up the ionized path established by the leader. After a pause of 30-50 milliseconds, a dart leader often forms and is followed by another bright return stroke propagating upward. A typical flash to ground contains three or four leader-return stroke combinations, which almost always transfer negative charge to ground. The currents in return strokes typically rise to peak values of 10-40 kA in 1-10 page or less.

Figure 2 shows a block schematic diagram of the basic LLP lightning locating system. Two, three or four direction-finding (DF) stations transmit lightning direction and signal strength data to a central positionanalyzing (PA) station via dedicated, asynchronous communications links. For larger installations, LLP offers a PA system which can accept data from up to 20 DFs via a synchronous communications network. The position analyzer (PA) receives data from the remote direction finders, calculates the lightning positions, and outputs the results in realtime to a digital x-y plotter, a magnetic tape recorder, and/or a local data terminal. The system provides the time and location of each discharge, the number of return strokes in each flash, and the peak amplitude of the return stroke magnetic field. Remote display processors are also available for plotting color TV and/or hard-copy maps of lightning locations at any number of remote sites.

DIRECTION FINDER - Each direction finder (DF) senses the electromagnetic fields radiated by lightning on two orthogonal magneticloop antennas and on a flat-plate electric antenna. The bandwidths of the antenna system are wide (approximately 1 kHz to 1 MHz) so that the shapes and polarities of the light-ning field waveforms are preserved. The voltage produced by the electronics associated with each magnetic loop is proportional to the lightning magnetic field multiplied by the cosine of the angle between the plane of the loop and the direction of the incoming field. Therefore, the direction of a lightning flash can be determined from the ratio of the signals on the two orthogonal loops, a standard technique for radio direction finding.

In order to optimize accuracy and to reduce background noise, the DF electronics are designed to respond to only those field waveshapes that are characteristic of return strokes in cloud-to-ground flashes. The DF electronics require the incident lightning field to have risetime, width, and subsidiary peak structure that is characteristic of a return stroke. The electric field must have a positive initial polarity (the polarity produced when negative charge is lowered to ground), and the field overshoot following the initial peak must not be too large relative to the first peak. The risetime and bipolar shape requirements also serve to eliminate very distant (> 400 km) lightning signals because the effects of propagation increase the field risetimes (2), and distant ionospheric reflections are often large and inverted with respect to the initial ground wave (3). A modification to the DF electronics that permits the detection of positive return strokes, as well as the negative, is also being tosted.

In order to provide an optimum detection efficiency over a wide dynamic range, the DF contains both high- and low-gain analog circuits that operate in parallel. The field shape criteria can be different in the high- and low-gain sections because the shapes of near and distant lightning signals are usually different (2)(4). Since the shapes of first

<sup>\*</sup>Also, Department of Atmospheric Physics,
University of Arizona, Tucson, Arizona
\*\*Also, Department of Physics, University
of Arizona, Tucson, Arizona
\*\*\*Also, Department of Electrical Engineering,
University of Florida, Gainesville, Florida
\*\*\*\*Numbers in parentheses designate References
at end of paper.

and subsequent stroke fields are also different, the shape criteria are sutomatically switched to values appropriate for subsequent strokes after the first stroke in a flash is detected.

When a return-stroke field is detected. the magnetic direction is determined at just the time that the radiation field reaches its initial peak. At this time, the stroke current is still within about 100 m of the ground, so that any errors in magnetic direction due to horizontal channel sections and branch currents are minimized (5)(6), and errors due to ionospheric reflections (7) are eliminated. Also, by sampling at this time, the magnetic direction indicates the location of the ground contact point rather than some elevated portion of the channel. As we shall see, the angular accuracy of a DF system is typically 1-2 degrees or better (5), a value which is usually more than adequate to resolve individual cells of electrical activity within larger cloud systems.

A photograph of the DF electronics is shown in Figure 3. The system is designed to operate either in a stand-alone mode, often in conjunction with a weather radar, or as part of a larger network with an automatic PA. In the former case, the lightning directions are plotted on an analog x-y recorder on a compass grid with the length of each vector being proportional to the peak amplitude of the first stroke field. Clusters of vectors show the directions and angular extent of individual storm cells, and if weather radar data are available, then the lightning clusters can be used to identify which achoes are producing lightning and which echoes are not. With some experience, the operator of a single DF system can often estimate an approximate range of a storm using just the average lightning signal strength within a given cell.

A microcomputer subsystem built into each DF digitizes and stores the signals for up to 14 return strokes in each flash to ground, computes the angles to each stroke, and stores the results in a buffer memory for subsequent output. The time, angle, signal amplitude, and the number of return strokes for the most recent flash are shown on a front panel LED display and can be typed on a local data terminul, if desired. Under most conditions, the amplitude of the field at a given range and the multiplicity of return strokes are good indicators of the severity of the discharge. The total number of flashes that are detected each hour, or for an operator-determined time interval, are available for display on the front panel or for typing on command. The DF microcomputer can also transmit the angle and signal strength data for each discharge to the position analyzer where individual lightning locations are computed automatically in real-time.

POSITION ANALYZER - The position analyzer (PA) is a preprogrammed microcomputer system which automatically accepts lightning angle data from a natwork of direction finders, calculates the lightning locations and generates

the appropriate outputs for both local and remote display devices. Normally, the position analyser is configured to accept data from up to four LLP direction finders. The direction finders transmit lightning data to the position analyzer via voice-grade dedicated data circuits, either land line or VHF/UHF radio. Each direction finder sends a briof message at the end of each lightning flash which contains the lightning azimuth, first stroke signal amplitude, flash polarity, number of return strokes, and the time interval from the first stroke to the time the message was transmitted. When the messages are received at the position analyzer, the absolute time which the flash occurred is calculated by subtracting the direction finder processing time from the message receipt time at the position analyzer. When the position analyzer receives two or more direction finder inputs which are time coincident it calculates the lightning location by a triangulation of the direction finder azimuth angles. When only two direction finders detect a flash and the azimuth angles are parallel or very nearly parallel, the position analyzer uses the ratio of the first stroke signal amplitudes to calculate the flash position. In all other cases the position calculation algorithm determines which combination of direction finder angles give the best solution. Prior to calculating the lightning location the position analyzer searches a table of correction factors which may be applied to the raw direction finder data. Correction factors for direction finder signal amplitude, constant angle correction, or azimuth dependent angle correction are provided to minimize the effects of incorrect direction finder gains, loop autenna alignment errors, and site errors respectively. All position calculations are done with 24-bit precision on an episoidal earth.

The lightning locations calculated by the position analyzer are output in a number of formats:

Front Panel Display - The time, szimuth angle, range and number of return strokes for the most recent discharge is displayed continuously by a series of LEDs on the front panel of the position analyzer. The origin for the azimuth and range shown on the front panel display is user definable but is usually assigned to be the position analyzer coordinates. The range units are also user definable.

Local Data Terminal - The lightning location data may also be printed in real-time on a local data terminal. For each flash the data terminal normally prints the time, coordinates, polarity, mean range normalized signal amplitude (a quantity which is related to the peak stroke current), number of return strokes, and the identification numbers of the direction finder sites which detected the flash and those which were used to calculate the flash location. Additional data terminal outputs may be selected which print all the direction finder azimuth angle, signal amplitude, and polarity data as

well as the intersection points of all pairs of direction finder azimuth angles. An example of an extended data terminal output for a positive flash detected by five direction finders in a large network is shown in Figure 4. The lightning location can be printed in latitude/longitude, angle/range, or cartesian (x-y) coordinates. The origin and units for the angle/range or cartesian outputs are user specified. The user may also control the size and location of the region for which data will be printed on the data terminal.

High-Resolution Hardcopy Graphics - The lightning locations may also be plotted in real-time in map form using a high-resolution pen plotter interfaced directly to the position analyzer. The pen plotter marks the location of each flash using different symbols or different color pens which can be set to denote flashes with different polarities or flashes which occur within different time periods. The user can select any plot region by specifying the latitude and longitude of the southwest and northeast corners of the map region. Both front penel and data terminal commands are provided to begin and end plots. The position analyzer buffers the lightning data between plots so data are not lost when maps are exchanged. The position analyzer uses a Lambert biconical map projection to convert lightning locations to plotter (map) coordinates. The biconical map parameters are input by the user to permit accurate alignment between the plotter and a user supplied, preprinted map base.

Local Video Displays - The position analyzer provides the necessary outputs to operate a remote display processor (described below) as a local video display at the position analyzer site. The remote display processor provides medium resolution color map displays which may be operated independently of the position analyzer. This allows the RDP operator to change map displays and replot older data without interrupting the collection of real-time data.

Remote Displays - The position analyzer provides outputs to drive any number of remote display processors. The position analyzer buffers the last 5700 flashes in nonvolatile memory. These data may be accessed by remote display processors via the switched (dial-up) telephone network when an auto-answer modem and phone line are connected to the remote interrogation port on the position analyzer. Remote display processors may also be connected to the position analyzer via dedicated data circuits when continuous monitoring is required.

The position analyzer also incorporates a number of test programs and diagnostic aids. For example, the direction finders are programmed to periodically transmit a confidence message which contains information on the status of the DF power supplies and clock. When either the power supply voltage or time falls out of tolerances the position analyzer prints a status message on the local data terminal so

that the system operators can take the corrective action. If direction finder confidence messages fail to be received at the regular interval, the position analyzer automatically prints another status message. The absence of periodic confidence messages usually signals he loss of the data communications circuit t ween the direction finder and position analyzer. The position analyzer also generates system summary messages on an hourly basis. daily basis, or at user request. The summary messages give the number of flashes detected by all direction finders, the number of flashes received from each direction finder that were not time coincident with a flash from at least one other site, the number of flashes which were time coincident but did not intersect, the number of overrange events, and the number of flashes which could not be printed because the printer buffer reached capacity. An example of an actual summary message for a three direction finder network is shown in Figure 5. Operators can readily diagnose system problems based upon the summary message. For example, the summary message in Figure 5 shows that direction finder number 2 was only responding to about 20% of the flashes seen by the other two sites. This message led to the discovery and repair of a sensitivity problem in direction finder 2.

The position analyzer can also be interfaced with a cartridge magnetic tape recorder to archive the lightning data. During periods when the position analyzer is not being used to process lightning data from the direction finders in real-time, the archived tape data may be reprocessed. The user specifies a time interval of interest and the position analyzer searches the tape for the data within that interval. The data may be printed on the data terminal or new lightning location maps may be plotted on the hardcopy pen plotter or the color video displays. Since the raw direction finder azimuth angle and signal strength are preserved on the tape records the position analyzer can also apply any angle or signal amplitude corrections during playback. The cartridge tape recorder can be easily interfaced to larger user-owned computer systems to transfer the lightning data to bulk tape or disk files for further post processing.

REMOTE DISPLAY PROCESSOR - In order to display the location, intensity, motion, and evolution of lightning storms in both space and time, LLP has developed a remote display processor (RDP) system specifically for lightning data. Basically, the RDP is a pre-programmed microcomputer with substantial memory that generates a high-resolution (640 x 480 pixel) color video display of the lightning locations together with geographic map detail. Lightning data are transmitted from the PA to the RDP via a dedicated or dial-up telephone circuit or via the network communications loop. The data are plotted in real-time and the last 6,000 or 12,000 flashes are also stored in a local random-access memory for subsequent play

back onto any of up to 100 different maps. The display itself can be in any of up to six operating modes, two for real-time applications and four for stored data. For example, the real-time display can be set to periodically delete lightning locations that are older than a preset time interval, and locations can also be color coded according to their absolute or relative age so an operator can easily discern old and new cells and storm motion. During playback, the operator can replot maps in an accelerated real-time mode according to a preset time factor; and, again, there can be color coding according to absolute or relative time. Black-and-white examples of the RDP hardcopy maps that were produced by an optional color dot-matrix printer are shown in Figures 6 and 7.

### NETWORK COMMUNICATIONS SYSTEM

As we indicated in the position analyzer section, the basic LLP position analyzer accepts data from two, three or four DF stations via dedicated point-to-point communications links. For larger networks, the recurring communications and operator costs can often be substantially reduced by using a multidrop communications network that is controlled by a central PA. Here, the lightning data are stored at the DF sites until they are requested by the PA, and up to 20 DFs can be operated simultaneously on up to three independent communications loops. Normally, the DF sites are interrogated by the PA at a rate of 10 sites per second. The network PA can serve as a central station for data archiving and also can act as a front-end processor for a larger host computer or to an existing data processing system.

A large network of DFs usually provides more accurate lightning locations because of the extra angle intersections and more extensive DF overlap area. If one DF should go down, a large network will usually have enough redundancy to prevent a significant loss of data.

# PERFORMANCE CHARACTERISTICS

The performance of any lightning detection system is best judged by its demonstrated ability to provide accurate and reliable data under a wide variety of operating conditions. Here, we will present some quantitative results on the lightning location accuracy, the detection efficiency, and other factors which are important in most applications.

LOCATION ACCURACY - The accuracy of lightning locations depends on at least four fac-

- 1) the accuracy of the DF antenna alignment:
- random errors in the angles to the ground strike points;
- 3) systematic angle errors that are associated with the quality of the DF sites.

Normally these so-called "site errors" are themselves a function of angle; and,

4) the location of the lightning with respect to the locations of the DF stations.

Antenna Alignment - The crossed-loop magnetic antenna must be precisely aligned North-South and East-West to obtain optimum DF accuracy. Normally, this alignment can be kept to an accuracy of ± 0.5 degrees; but in cases where a larger error occurs, the PA is programmed to automatically apply an appropriate correction. The alignment should be chacked periodically, particularly if the antennas are mounted on wooden platforms or poles which might change shape or twist when there are changes in the weather environment.

Random Errors - Small random errors are usually present in the lightning directions due to background electromagnetic fields, noise in the analog circuits, digitizing errors, and polarization errors in the lightning field itself. The LLP system has been designed to keep all these errors to a minimum. For example, there are passive and active filters to eliminate background fields; the analog section is kept inside an RF-shielded enclosure and low-noise circuits are used throughout; the analog signals are digitized with 15-bit accuracy; and the magnetic direction is determined just at the time of the initial radiation field peak to minimize polarization errors. The magnitude of the residual random errors in the system can be determined experimentally by comparing the directions to different return strokes within the same flash since these usually follow the same path to ground. Figure 8, for example, shows the angles to each of 14 return strokes within the same discharge. By analyzing several hundred such events, we have determined that the random angle errors in the DF system are distributed with a mean of zero degrees and a standard deviation of 0.9 degrees.

Site Errors - Non-uniform terrain and various conducting objects near the DF antennas can, in many cases, introduce magnetic direction errors which are a function of angle. For example, a nearby overhead electric power line can act as a large antenna loop and can raradiate a small portion of the lightning magnetic field and cause an angle error. It is best to minimize the effects of site errors by installing the DF antennas properly at good site locations. In cases where a poor site is unavoidable, the PA is programmed to correct these errors using an array of correction factors that are derived from either an objective analysis of the lightning data on a larger computer or from other independent observations. The objective analysis is an iterative procedure that utilizes the lightning signal amplitudes at all DF sites (as well as all DF angles) to determine a location, and then the computer minimizes the systematic angle differences on thousands of lightning

Figure 9 shows a plot of the angle

corrections that were derived for a DF station in Oklahoma in 1980. Thus far, there is no indication that these corrections change with time or range; and, in fact, these same correction factors have been applied successfully to data obtained in 1979.

Position Accuracy - In general, the final accuracy of a lightning location will depend on the number of DF stations that respond to the event, their separation distances and geometric placement, and the location of the lightning with respect to the stations. For example, if a flash occurs close to the baseline separating two DF sites, the associated direction vectors will be nearly parallel and the intersection accuracy will be poor. The PA is programmed to provide an optimum intersection for any combination of DFs that respond to a flash; and, in the case mentioned above, it even uses the ratio of signal amplitudes as well as the angles to provide an optimum result.

Because of the difficulty in obtaining accurate ground-truth observations of the cloud-to-ground lightning strike point, definitive data on the position accuracy of the LLP Lightning Locating System are not abundant. Piotrowicz and Maier (8) have reported accuracy data for ten flashes which occurred approximately 60 km equidistant from two direction finders in Oklahoma. Their results are reproduced in Figure 10. Two locations are shown for each flash; the ground-truth positions (based on all-sky video camera records for azimuth and thunder uelay for range) are shown with the open boxes while the direction finder intersections are shown with the shaded boxes, common events are connected. The mean horizontal distance error is 1.0 km with a range of 0.4 to 2.7 km. These accuracy figures are or matent with a 1° random direction finder erass for two direction finders at a distance of approximately 60 km (9). Most users of large lightning locating systems with well sited direction finders report location accuracies in the range of 1 to 2 km near the center of the network and 6 to 8 km at the outer edges. A comparison of radar echo and lightning location data by Holle, et. al. (19) found that only 15% of the lightning locations occurred outside of the radar echoes while over 60% occurred in or near the radar echo core.

DETECTION EFFICIENCY - A significant but often overlooked performance factor is the lightning detection efficiency. This efficiency is defined to be simply the ratio of the number of cloud-to-ground flashes which were detected to the number which actually occurred. Since lightning is highly variable a source, the detection efficiency will in general be a function of range. This is because large impulses can be detected at great distances, and even a small source close to the DF site can saturate the electronics. The detection efficiency can also be a function of

the lightning rate if there is dead time in the electronics or if there is extensive computer processing. These effects are now negligible in the LLP system, and, in fact, the LLP DY can process up to four lightning flashes which overlap in time, as long as they occur in different directions.

Figure 11 shows typical detection efficiency versus range curves for two DF stations in Oklahoma. The drops in efficiency at close distances were caused by over-range events, and the decrease at large distances is due to both the decreasing signal amplitudes and to a change in the lightning signal shape with distance. A peak efficiency of 80 to 90% occurs in the 20 to 120 km interval with a medium gain DF system, and less than half the flashes are detected beyond 350 km.

OTHER PERFORMANCE FACTORS - The long-term reproducibility and reliability of a lightning locating system depends on a number of factors. First, the electronics must be reliable and easy to maintain. Each LLP DF system contains a built-in lightning waveform simulator that can be used to check and align all system components. Thus far, the mean time between failures of the LLP DF system is at least 6,000 to 10,000 hours, and the position analyzer is approximately 18,000 hours.

As we previously mentioned in the section regarding the position analyzer, each DF automatically transmits a periodic status message to the PA to verify that the DF is functioning and that the data communications lines and modems are working properly. The PA in turn automatically types a message to the system operator if the status of a DF or the data link changes.

## ACKNOWLEDGEMENTS

We would like to thank Vicke Wood for preparing this manuscript. Special thanks should also go to the many LLP customers who have suggested and supported improvements in the LLP system during the past eight years. We would also like to thank the Alberta Forest Service for the data reproduced in Figure 4, the NOAA/PROFS Program Office for the data reproduced in Figure 5, and the U.S. Air Force Detachment 11, 2nd Weather Squadron, Patrick Air Force Base, Florida, for the data reproduced in Figures 6 and 7.

## REFERENCES

- 1. M. A. Uman, "Lightning", McGraw-Hill, New York, pp. 264, 1969.
- 2. M. A. Uman, C. E. Swanberg, J. A. Tiller, Y. T. Lin, and E. P. Krider, "Effects of 200 km propagation on Florida lightning return stroke electric fields", Radio Science, vol. 11, pp. 985-990, 1976.
- 3. W. L. Taylor, "Radiation field characteristics of lightning discharges in the band 1 kc/s to 100 kc/s", J. Res. NBS, vol. 67D, pp. 539-550, 1963.

- 4. Y. T. Lin, M. A. Uman, J. A. Tiller, R. D. Brantley, W. H. Beasley, E. P. Krider, and C. D. Weidman, "Characterization of lightning return stroke electric and magnetic fields from simultaneous two-station measurements", J. Geophys. Res., Vol. 84, pp. 6307-6314, 1979.
- 5. E. P. Krider, R. C. Noggle, and M. A. Uman, "A gated wideband magnetic direction finder for lightning return strokes", J. Appl. Meteor., vol. 15, pp. 301-306, 1976.
- 6. B. D. Herrman, M. A. Uman, R. D. Brantley, and E. P. Krider, "Test of the principle of operation of a wideband magnetic direction finder for lightning return strokes", J. Appl. Meteor., vol. 15, pp. 402-405, 1976.
- 7. F. Horner, "Very-low-frequency propagation and direction-finding", Proc. IEEE, vol. 104B, pp. 73-80, 1957.
- 8. J. M. Piotrowicz, and M. W. Maier, "Performance characteristics of a magnetic direction finder for lightning return strokes" (abstract only), Trans. Amer. Geophys. Union, vol. 61, pp. 975, 1980.
- 9. R. G. Stansfield, "Statistical Theory of D. F. Fixing", J. IEE, Part IIA, pp. 762-770, 1947.
- 10. R. L. Holle, R. E. Lopez, and W. L. Hiscox, "Relationships between lightning occurrences and radar echo characteristics in South Florida", Proceedings of the International Aerospace and Ground Conference on Lightning and Static Electricity, Fort Worth, Texas, June 21-23, 1983.

# BIBLIOGRAPHY

Principles of Operation

E. P. Krider and R. C. Noggle, "Broadband antenna systems for lightning magnetic fields" J. Appl. Meteor., 14, 252-256, March, 1975.

- E. P. Krider, R. C. Noggle, and M. A. Uman, "A gated, wideband magnetic direction finder for lightning return strokes", J. Appl. Meteor, 15, 301-306, March 1976.
- B. D. Herrman, M. A. Uman, R. D. Brantley, and E. P. Krider, "Test of the principle of operation of a wideband magnetic direction finder for lightning return strokes", J. Appl. Meteor., 15, 402-405, April 1976.
- C. D. Weidman and E. P. Krider, "The fine structure of lightning return stroke wave forms", 83, 6239-6247, December 1978.
- Y. T. Lin, M. A. Uman, J. A. Tiller, R. D. Brantley, W. H. Beasley, E. P. Krider, and C. D. Weidman, "Characterization of lightning return stroke electric and magnetic fields from simultaneous two-station measurements", J. Geophys. Res., 84, 6307-6314, October 1979.
- M. A. Uman, Y. T. Lin, and E. P. Krider, "Errors in magnetic direction finding due to nonvertical lightning channels", Radio Science, 15, 35-39, Jan-Feb 1980.
- E. P. Krider, A. E. Pifer, and M. A. Uman, "An automatic locating system for cloud-to-ground lightning', NASA Conference Publication 2128, April 1980.

- R. L. Johnson, D. E. Janota, and J. E. Hays, "A study of the comparative performance of six lightning warning systems, NASA Conference Publication 2128, April 1980.
- J. Hyypia, "Lightning new detection system: Science & Mechanics, Winter 1980.

Weather - Operations and Research

- A. G. Boulanger and M. W. Maier, "On the frequency of cloud-to-ground lightning from tropical cumulonimbus clouds", 11th Technical Conference on Hurricanes and Tropical Meteor-
- M. W. Maier, A. G. Boulanger, and J. Sarlat, "cloud-to-ground lightning frequency over South Florida", Conference on Cloud Physics at Atmospheric Electricity, Issaquah, Washington, July 31 to Aug. 4, 1978.
- "Maps of lightning strikes aid storm studies", USDC NOAA News, Vol. 5, No. 11, June 2, 1980.
- J. A. Rea and C. E. Fontane, "An automatic lightning detection system in Northern California", NOAA Technical Memorandum NWS WR-153, June 1980.
- M. W. Maier and R. L. Holle, "FACE-2 data reductions and analyses (prior to disclosure of the treatment decisions): Part VI", Cloud-to-Ground Lightning Data for FACE-2, NOAA Technical Memorandum ERL OWRM-10, October 1981.
- C. L. Crozier and J. W. Scott, "A C-band weather radar system with spherics to service multiple diverse users in the Canadian climate", 20th Conference on Radar Meteorology, Boston, Massachusetts, Nov. 30 to Dec. 3, 1981.
- R. L. Holle and M. W. Maier, "Radar echo height related to cloud-to-ground lightning in South Florida", 12th Conference on Severe Local Storms, San Antonio, Texas, Jan. 11-15, 1982.
- M. W. Maier and E. P. Krider, "A comparative study of the cloud-to-ground lightning characteristics in Florida and Oklahoma thunderstorms", 12th Conference on Severe Local Storms, San Antonio, Texas, Jan. 11-15, 1982.
- R. E. Orville, M. W. Maier, F. R. Mosher, D. P. Wylie, and W. D. Rust, "The simultaneous display in a severe storm of lightning ground strike locations onto satellite images and radar reflectivity patterns", 12th Conference on Severe Local Storms, San Antonio, Texas, Jan. 11-15, 1982.

"Experimental Lightning Detection Charts Help Locate Thunderstorms", Western Region Technical Attachment (National Weather Service), No. 82-32, July 27, 1982.

# Electric Power Utilities

M. Darveniza and M. A. Uman, "Research into lightning protection of distribution systems", II - Results from Florida Field Work 1978 and 1979. T. & D. Conference, Minneapolis, Minnesota, September 1981.

M. Darveniza and M. A. Uman, "Lightning studies of distribution lines", IEEE Power Engineering Conference on Overhead and Underground Transmission and Distribution, Atlanta, Georgia, April 1-6, 1979.

B. Fischer and E. P. Krider, "'On-Line' lightning maps lead crews to 'trouble'", Electrical World, May 1982.

Forestry - Fire Detection

R. C. Noggle, E. P. Krider, D. L. Vance, and K. B. Barker, "A lightning direction-finding system for forest fire detection", 4th National Conference of Fire and Forest Meteorology, St. Louis, Missouri, Nov. 16-18, 1976.

D. L. Vance and E. P. Krider, "Lightning detection systems for fire management", 5th Joint Converence on Fire and Porest Meteorology, Atlantic City, New Jersey, March 14-16, 1978.

E. P. Krider, R. C. Noggle, A. E. Pifer, and D. L. Vance, "Lightning direction-finding systems for forest fire detection", Bull. Am. Meteor. Soc., 61, No. 9, September 1980.

Other Applications

M. A. Uman and E. P. Krider, "A lightning locating and warning system for airports", I. E.S. Aviation Lightning Seminar, Key West, Florida, Nov. 18, 1980.

R. L. Johnson and W. M. Sherrill, Evaluation and improvement of electrical storm warning systems - Warning parameter study, supplemental report", Southwest Research Institute Report No. 16-5297, December 1981.

R. L. Johnson, D. E. Janota, and J. E. Hays, "An operational comparison of lightning warning systems", J. Appl. Meteor., 21, 703-707, May 1982.

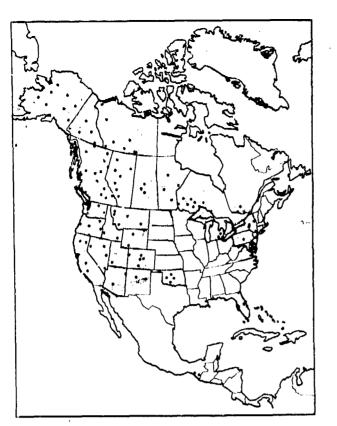


Fig. 1 - The solid dots show the locations of all LLP lightning Direction Finders installed in North America at the end of 1982. The shaded area represents the effective area covered by these systems

# A TYPICAL LIGHTNING LOCATING SYSTEM CONFIGURATION

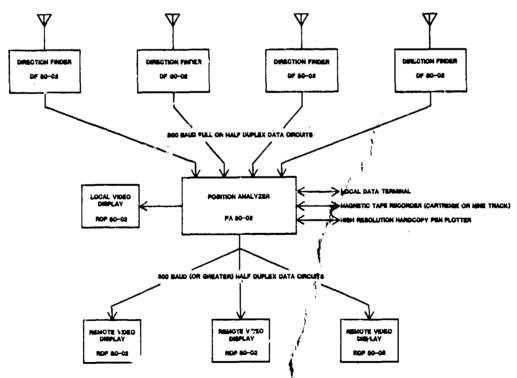


Fig. 2 - Block diagram of the basic LLP Lightning Locating System. The this example the Position analyzer drives (only three Remote Display Processors (RMP 80-02), however, any number of Remote Display Processors can access data from a Position Analyzer

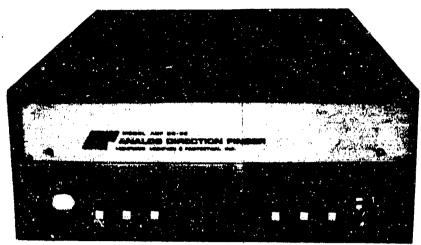


Fig. 3 - The LLP Direction Finder electronics consists of an analog and a digital signal processor. The front panel LED display shows the time, angle, signal amplitude, and number of return strokes for the last cloud-to-ground flash

```
52.59285 -111.90735
                                    94. Ú
           80.8 134.0
                       7
                              36.7
                                              52.56393 -112.26702
          80.8 134.0
                      # 5
                            110.1
                                   61.5
                                   59.9
                                              52.59615 -111.86746
                      # 4
                            146.2
          80.8 134.0
                                   33.3
                      # 2
                            195.8
                                              52.48796 -113.15148
          80.8 134.0
                                              52.50038 -112.02821
                94.0
                      # 5
                            110.1
                                   61.5
          36.7
                                              52.61151 -111.88289
          36.7
                94.0
                      # 4
                            146.2
                                   59.9
                                              51.18157 -113.68106
          36.7
                94.0
                      # 2
                            195.8
                                   33.3
                                              52.40580 -111.67734
                61.5
                      # 4
                            146.2
                                   59.9
         110.1
                                              52.76395 -113.03544
         110.1
                61.5
                      # 2
                            195.8
                                   33.3
                      # 2
                            195.8
                                   33.3
                                              53.44683 -112.74169
   45
         146.2
                59.9
                  52:35:34 -111:54:26 +380.3
                                                 1
                                                       6,7,5,4,2
59 17:39:01.79
           +586.6
                                                         1 +209.5
       1
                  # 7 1
                           +498.2 # 5
                                        1
                                            +461.4
                                                     # 4
        1
           +145.7
```

Fig. 4 - An extended data terminal message from the Position Analyzer for a flash detected by five Direction Finders. The first terlines give the azimuth angle and signal amplitude from all combinations of two Direction Finders and the latitude and longitude of the

intersection point. The eleventh line gives the flash sequence number, time, most probable latitude and longitude, polarity, mean range normalized signal amplitude, number of return strokes, polarity, and range normalized signal amplitude for each Direction Finder station

	LLP LIGHTNIN	FLASH SUMMARY
FROM	18:00:00 08/05/82	TO 06:00:00 08/06/82

STATION	DF	TOTAL	MON-	NONINTER-	OVERRANGE	POSITIVE	WITHIN
NAME		INPUTS	COINCIDENT	SECTING	INPUTS	INPUTS	REGION
BYERS	1	1022	48	17	0	0	0
MART-MAR	2	231	40	19	1	0	0
BOULDER	3	1058	1 <b>0</b> 7	13	0	0	0
~ ~ ~ ~ ~ ~ ~ ~ ~ ~ ~ ~ ~ ~ ~ ~ ~ ~ ~ ~	PA	TOTAL FLASHES	NOT PRINTED	NONINTER- SECTING	OVERRANGE FLASHES	POSITIVE FLASHES	WITHIN REGION
BUCKLEY	0	1010		21	i	0	739

Fig. 5 - A typical Position Analyzer summary message for a three Direction Finder network.

The message is printed on the local data terminal

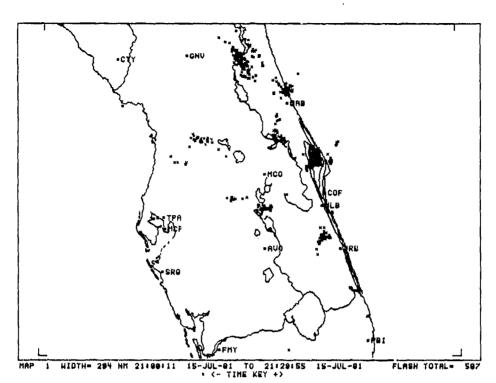


Fig. 6 - A black-and-white example of a color RDP map display for central Florida. The lightning locations during the period from

2100:11 UT to 2129:55 UT are shown by small x's. An intense storm is located over the NASA Kennedy Space Center

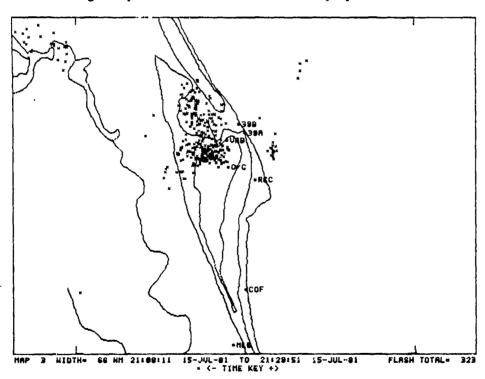


Fig. 7 - Same as Fig. 6, except for a smaller area centered on the NASA Kennedy Space Center. This figure illustrates the RDP zoom capability and increased spatial resolution provided in the small area map displays. The intense

storm at the Space Center is located over and just south of the Shuttle runway. The storm produced 294 cloud-to-ground flashes during this 30 minute map period

		₩		
16:38:39.569	245.3	97.7	1 H	14
39.569	244.8	207.7	1	WO
39.592	245.5	36.4	2	FWOH
39.610	245.4	92.4	3	FWOH
39.644	245.2	184.5	Lį	FWO
39.700	245.6	25.3	ij	FWOH
39.742	245.2	139.7	6	FWOH
39.789	245.3	65.9	7	FWOH
39.861	245.2	51.2	8	FWOH
39.888	245.3	46.4	9	FWOH
39.902	245.1	37.5	10	FWOH
39 <b>.92</b> 2	245.5	90.2	11	FWOH
39.936	245.2	23.3	12	FWOH
39 <b>.98</b> 2	245.4	159.9	13	FWO
40.001	244.8	29.6	14	FWOH

Fig. 8 - The Direction Finder output for a cloud-to-ground flash composed of 14 return strokes. The first column on the left shows the time of each stroke in seconds, the second

column shows the azimuth angle to the stroke in degrees, the third column shows the stroke amplitude, and the fourth column shows the stroke number

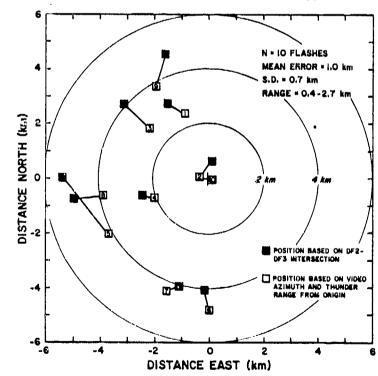


Fig. 10 - Lightning ground strike points determined by direct observation (open boxes) and corresponding locations from two Direction Finder intersections. One Direction

Finder was located about 60 km northwest of the origin and the second Direction Finder was located about 60 km southwest of the origin

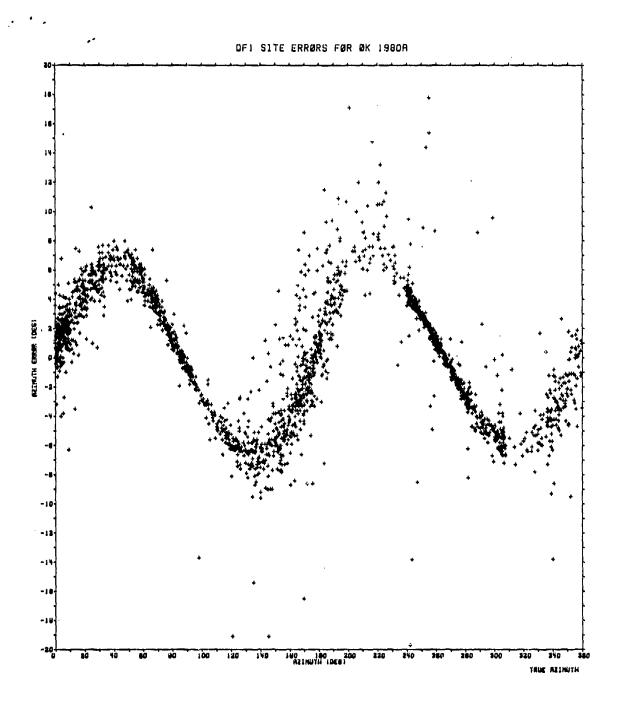


Fig. 9 - The Direction Finder azimuth corrections that were derived for an LLP Direction Finder site in Oklahoma

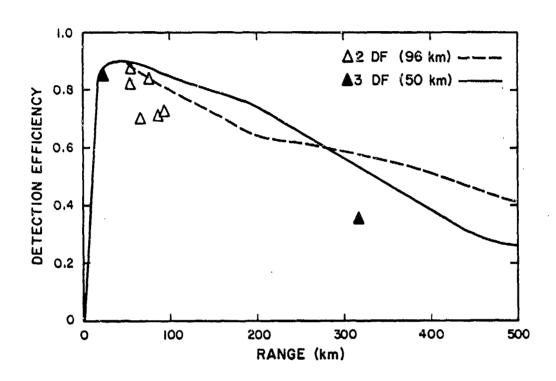


Fig. 11 - Detection efficiency versus range for two Direction Finder networks operating at medium-gain. The curves were derived from an analysis of the signal amplitude changes with distance. The triangles represent direct observations of detection efficiency. For high-gain Direction Finders multiply the range scale by two

AIRBORNE AND GROUND-BASED LIGHTNING ELECTRIC AND MAGNETIC FIELDS AND VHF SOURCE LOCATIONS FOR A TWO-STROKE GROUND FLASH

M. A. Uman and E. P. Krider
Lightning Location and Protection, Incorporated, Tucson, Arizona
P. L. Rustan, Jr., B. P. Kuhlman, and J. P. Moreau
AFWAL/FIESL, Wright-Patterson AFB, Ohio
E. M. Thomson, J. W. Stone, Jr., and W. H. Beasley
University of Florida, Gainesville, Florida

ABSTRACT

We have reduced and analyzed the data from a two-stroke lightning flash to ground which occurred in South Florida on July 16, 1981, within a network of four ground stations instrumented for VHF measurements, about 15 km from a ground station instrumented for wide-band electric field measurements, and within 10 km of a WC-130 aircraft operating at 5.2 km and instrumented for wide-band electric and magnific field measurements. The four-station ground-based VHF measurements allow a reconstruction of the geometry of the flash, which was composed of two separate channels to ground. Electric field system bandwidth for the ground measurement was from 0.02 Hz to about 2 MHz; electric and magnetic field system bandwidths on the aircraft extended to 20 MHz. Ground-based and airborne measurements of fields are presented and shown to be consistent with one another.

DURING 1979, 1980, AND 1981 THE AIR FORCE Wright Aeronautical Laboratories directed a program designed to characterize airborne lightning electric and magnetic fields. A WC-130 aircraft instrumented for electric and magnetic field measurements was flown in South Florida in the vicinity of a network of ground-based stations which provided electric field at ground level and data from which the location of lightning VHF sources could be determined. Extensive data were obtained. These will take many years to analyze fully. In this paper we briefly describe the instrumentation used during the 1981 measurement season and illustrate the potential of the data base by presenting an analysis of data from one two-stroke lightning flash to ground which occurred at 17:09:40 EDT on July 16, 1981.

### ATRBORNE MEASUREMENT SYSTEMS

The WC-130 aircraft is about 30 m from nose to tail and about 41 m in wingspan. Aircraft resonances are expected at half and integer multiples of 9.9 and 7.4 MHz. The airborne instrumentation had an upper frequency response limit of about 20 MHz so that some of these resonance effects could be observed. Three basic types of sensors, described in Baum et al. (1)\*, were used: (a) plates to measure the component of the electric field intensity perpendicular to aircraft surfaces, (b) loops to measure the magnetic field intensity parallel to aircraft surfaces, and (c) loops to measure current densities flowing in aircraft surfaces by sensing the magnetic field associated with those current densities. The latter two sensors have essentially similar principles of operation. A total of eleven sensors were used on the WC-130 in 1981. Electric field was measured on the forward upper fuselage, aft upper fuselage, aft lower fuselage, and left wing tip. Both horizontal components of the magnetic field were measured on the forward upper fuselage. Skin current density was measured on the top and bottom of each wing and on the aft upper fuselage. All measured quantities were continuously recorded on instrumentation tape with an upper frequency response limit of about 2 MHz. In addition, the derivatives of the measured quantities were sampled at 20 ns intervals for time blocks of 160 µs. Such blocks of data, with an effective upper frequency response limit of about 20 MHz, were acquired at a rate of twice a second, the data block being initiated in a pre-trigger mode by an incoming signal exceeding a pre-set thresh-hold.

### GROUND-BASED MEASUREMENT SYSTEMS

Ground-based electric field measurements are essential to proper interpretation of the airborne data since considerable information exists on the characteristics of the fields observed at ground level and the relation of those fields to their sources, whereas such information is not available for airborne fields. The ground-based electric field system was similar to that described in Beasley et al. (2). The fields were recorded on eight channels of an instrumentation tape recorder with a bandwidth in the FM mode of 0.02 Hz to 500 kHz and in the direct mode of 400 Hz to 2 MHz. A variety of gains allowed the measurement of fields between 4 V/m and 40.000 V/m. Fig. 1 shows the overall experimental setup including the location of the trailer that housed the electric field avetem.

The VHF source location system comprised four VHF stations located about 20 km apart as shown in Fig. 1. The VHF radiation at each station was (a) detected with an omnidirectional antenna, (b) passed through a filter with a center frequency of 63 MHz and a bandwidth of 6 MHz, (c) log amplified, (d) envelope detected, and (e) recorded on a modified version of the RCA VCT 201 Video Cassette Recorder. The system allows VHF locations from the measurement of the difference in the time of arrival of a given pulse at the four stations as explained in Rustan et al. (3) and Proctor (4). The time correlation necessary for this measurement, about 0.1 µs, was accomplished by using WWV for crude time correlation and the vertical and horizontal sync pulses from WINK-TV in Fort Myers (shown in Fig. 1) for fine time correlation. The horizontal sync pulses have a rate of one each 63

\*Numbers in parentheses designate References at end of paper.

A conceptual sketch of the lightning channels of a two-stroke flash occurring on July 16, 1981 at 17:09:40 EDT is shown in Fig. 1. The sketch is based on the VHF time of occurrence and location of the VHF radiation sources shown in plan view in Fig. 2a and looking north in Fig. 2b. The location and orientation of the WC-130, which was flying at 5.2 km, is also shown in both figures.

Both strokes appeared to originate from about the same region, but the second went to a different ground strike point, about 5 km north-west about 250 ms after the first stroke.

The first VHF radiation sources start about 50 ms before the first return stroke, at an altitude of about 7 km, that is, 2 km above the level of the WC-130, and about 7 km east and 3 km south of it. The source locations then spread up and down about 1 km and east to about 8 km in about 5 ms. During the last 5 ms before the return stroke, the source locations are at an altitude between 4 km and 1 km, from 7 to 10 km east and from 2 to 6 km south of the WC-130. The ground strike point of the first stroke appears to be between 7 and 8 km east and 2 to 3 km south of the WC-130. For about 0.5 ms after the return stroke. VHF sources appear between 3 and 8 km altitude, 7 to 10 km east and 1.5 to 8 km south of the WC-130.

About 200 ms later, VHF sources become active for 0.5 ms between 6 and 3 km altitudes, 5 to 9 km east and 2 to 3 km south of the WC-130. Then, 30 ms later, for about 1 ms, VHF sources appear from 5 km down to 1.5 km altitudes, 4 to 5 km east and 2 to 5 km south of the WC-130. The strike point appears to be about 5 km east of the WC-130.

Figs. 3, 4, and 5 show the vertical electric field at the ground station, the airborne vertical electric field on the aft upper fuse-lage (AUF in Fig. 1), and the magnetic field in the direction of the fuselage as measured on the forward upper fuselage (FUF on Fig. 1), respectively, for the first stroke in the flash.

The stroke which produced the electric field in Fig. 3 was at a range of 16 km from the ground station and 8 km from the aircraft. The airborne field magnitudes in Figs. 4 and 5 are not corrected for field distortion by the aircraft. The stepped leader pulses which precede the return-stroke transition and the first ten microseconds or so of the return-stroke field are essentially radiation field at these ranges; and the fields on and above the ground are expected to have essentially the same shape (5), as the results in Figs. 3, 4, and 5 confirm. After about 10 µs, the return-stroke electric fields show an electrostatic component which the magnetic field does not possess (5) (6). Additionally, the low-frequency cut off of the system used to obtain the magnetic field shown in the figure decays slightly faster than the actual field.

The first-stroke electric-field intensity measured at the ground station has an initial peak value of 50 V/m, or 8.0 V/m normalized to 100 km, a peak field typical of Florida lightning (7). The comparable field values at the WC-130 are 110 V/m, or a normalized 8.8 V/m, on the forward upper fuselage, and 32 V/w, or a normalized 2.6 V/m, on the aft upper fuselage. The second stroke peak field measured on the ground was 14 V/m, and the stroke was at a range of 14 km, resulting in a normalized field of 2.0 V/m, a relatively small value for Florida return strokes (7). The airborne second stroke fields were comparably small and difficult to make any measurements on other than amplitude. In the first stroke field records the ratios of the stepped-leader pulse heights to the return stroke peak are essentially the same, on average about 0.1, and, as expected, the stepped-leader pulses occur at the same times before the return stroke on all three records, as can be seen in Figs. 3, 4, and 5. The zero-to-peak rise-time of the first return stroke measured at the ground is about 3.0 µs, also consistent with typical values measured in Florida (7). with airborne values of 2.9 µs at the forward upper fuselage and 2.6 µs at the aft upper fuselaga. Stepped leader pulses have zero-topeak rise-times on the ground of about 1 µs and full-widths at the pulse base of about 2 µs. Comparable airborne values are 0.8 µs and 1.2 µs at the forward upper fuselage and 0.3 µs and 1.0 µs at the aft upper fuselage. All measured rise-times are well within system limits. The rise-times on the ground are expected to be longer than in the air because of the effects of groundwave propagation involving a nonperfectly-conducting earth, as discussed in Lin et al. (7), Uman et al. (8), and Weidman and Krider (9). The reason that the rise-times at the aft upper fuselage are faster than those at the forward upper fuselage is not known, but aircraft resonances may contribute to this effect. Wing and fuselage resonances are excited by the airborne horizontal electric field which is the dominant field within about 1 km of a return stroke and is comparable to the vertical field near 10 km (5). The leader pulse rise-times are somewhat slower than the typical values for 10 to 90 percent of 0.1 µs reported in Weidman and Krider (10) for lightning over salt water.

Maximum rates-of change of airborne electric field for both leaders pulses and return strokes were the same, about 40 V/m µs, or 3.2 V/m µs normalized to 100 km. These are to be compared with the normalized mean of 30 V/m µs for return strokes and 21 V/m µs for leader pulses reported in Weidman and Krider (9) (10) for lightning over salt water.

## ACKNOWLEDGEMENT

This research was supported, in part, by the Wright Aeronautical Laboratories, Wright Patterson Air Force Base, Ohio under contract F33615-79-K-0177.

### REFERENCES

1. C.E. Baum, E.L. Breen, J.P. O'Neill, C.B. Moore, and G.D. Sower, "Electromagentic sensors for general lightning application," in Lightning Technology, NASA Conference Publication 2128, FAA-RD-80-30, 1980.

2. W.H. Beasley, M.A. Uman, and P.L. Rustan, Jr., "Electric fields preceding cloud-to-ground lightning flashes," J. Geophys. Res.,

87, 4883-4902, 1982.

3. P.L. Rustan, Jr., M.A. Uman, D.G. Childers, W.H. Beasley, and C.L. Lennon, "Lightning source locations from VHF radiation data for a flash at Kennedy Space Center," J. Geophys. Res., 85, 4893-4903, 1980.

4. D.E. Proctor, "A hyperbolic system for obtaining VHF radio pictures of lightning,"
J. Geophys. Res., 76, 1478-1489, 1971.

5. M.J. Master, M.A. Uman, Y.T. Lin, and R.B. Standler, "Calculation of lightning return stroke electric and magnetic fields above ground," J. Geophys. Res., 86, 12,127-12,132, 1981.

6. Y.T. Lin, M.A. Uman, and R.B. Standler, "Lightning return stroke models," J. Geophys.

Res., 85, 1571-1583, 1980.
7. Y.T. Lin, M.A. Uman, J.A. Tiller,
R.D. Brantley, W.H. Beasley, E.P. Krider, and
C.D. Weidman, "Characterization of lightning
return stroke electric and magnetic fields from
simultaneous two-station measurements," J.
Geophys. Res., 84, 6307-6314, 1979.

8. M.A. Uman, C.E. Swanberg, J.A. Tiller, Y.T. Lin, and E.P. Krider, "Effects of 200 km propagation on Florida lightning return stroke electric fields," Radio Science, 11, 985-990, 1976

9. C.D. Weidman, and E.P. Krider, "Submicrosecond risetimes in lightning return-stroke fields," Geophys. Res. Lett., 7, No. 11, 955-958, 1980.

10. C.D. Weidman, and E.P. Krider, "Submicrosecond risetimes in lightning radiation fields," in Lightning Technology, NASA Conference Publication 2128, FAA-RD-80-30, 1980.

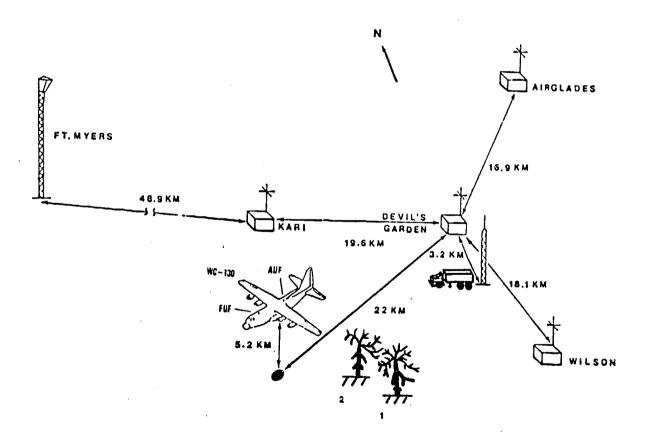


Fig. 1 - The experimental setup including the position of the WC-130 at 17:09:40 EDT on July 19, 1981 and a drawing of the two lightning channels to ground deduced from VHF time-of-arrival measurements

Fig. Captions, Kasemir, Static Discharges.

Fig. 1 - Charge distribution on charged leader
a. Stepped leader
b. After return stroke
c. Cloud discharge advancing upwards
d. Cloud discharge advandinc downwards

Fig. 2 - Charge distribution on uncharged leader
a. Stepped leader
b. After return stroke
c. Cloud discharge beginning stage
d. Cloud discharge end stage

Fig. 3 - Corona discharge on Orbiter

MADNIE ORGANICA

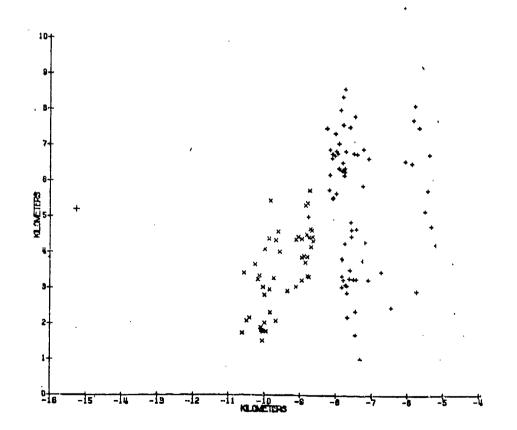
NACIONAL MADIENTICA

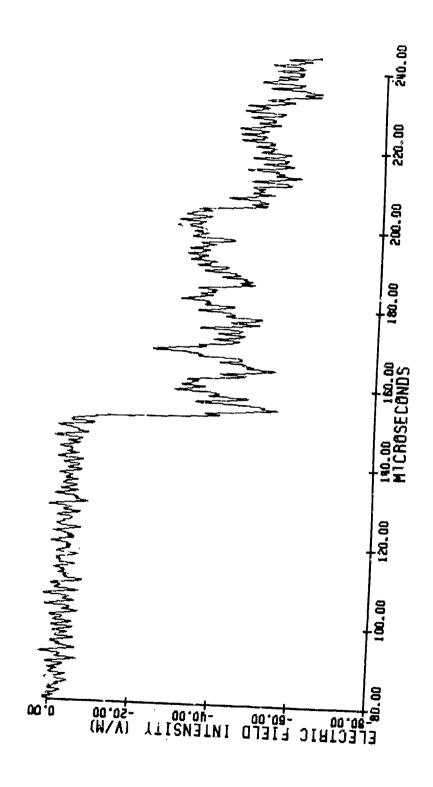
MADNIE ORGANICA

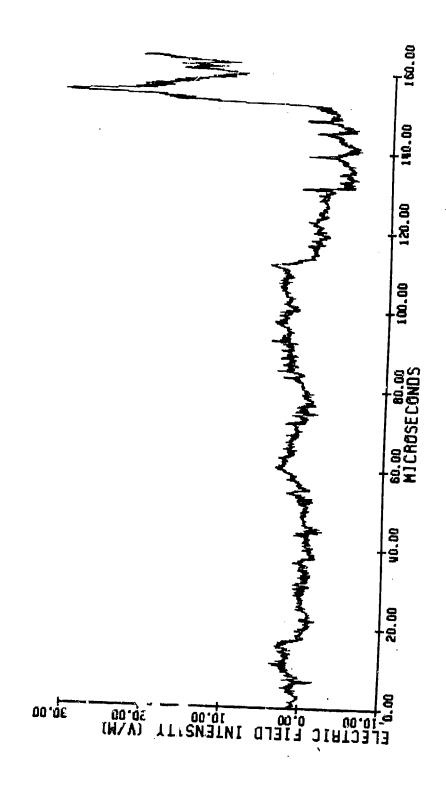
NACIONAL MADIENTICA

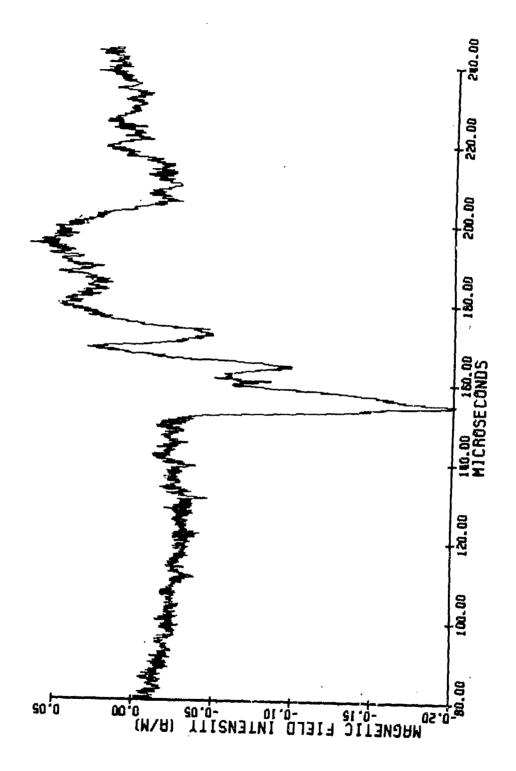
MADNIE ORGANICA

MADN









-8

51-8

LIGHTNING FLASH DENSITY VERSUS ALTITUDE AND STORM STRUCTURE FROM OBSERVATIONS WITH UHF- AND S-BAND RADARS

Vladislav Mazur Cooperative Institute for Mesoccale, University of Oklahoma, Norman, Oklahoma John C. Gerlach

NASA/Goddard Space Flight Center, Wallops Island, Virginia
W. David Rust

National Severe Storms Laboratory, Norman, Oklahoma

ABSTRACT

The UHF- (70.5 cm wavelength) and S-band (10 cm wavelength) radar at NASA/Wallopa Island Research Facility in Virginia U.S.A. have been used to relate lightning activity with altitude and with reflectivity structure of thunderstorms. Two centers of lightning flash density were found; one between 6 and 8 km altitude and another between 11 and 15 km. Our observations appear to correspond to observations by Taylor et al. (9), of two classes of discharges separated in altitude.

THE LOCATION OF lightning flashes has been examined by several investigators. The methods of such studies have utilized: 1) a network of electric field change sensors for location of charges neutralized during a flash (1); 2) three-dimensional mapping of VHF radiation sources associated with flashes (2,3); 3) mapping of strike points of cloud-to-ground flashes using two or more cross-loop magnetic direction finders (4); 4) radar indications of lightning channels in two dimensions (5,6); and 5) acoustic techniques to reconstruct structure three-dimensional lightning from thunder (7). We have found the use of radar to be most effective for determining lightning distributions in real time, and for guiding an instrumented aircraft so that it will be struck by lightning (8).

The antenna pattern and wavelength are critical factors for effective lightning location by radar. With longer wavelength precipitation reflectivity from the backscattering decreases while lightning channels increases. The combined necessity of a long wavelength radar (tens of centimeters) for better separation of lightning echoes from precipitation echo and a narrow beamwidth antenna (e.g. < 30) for greater accuracy in mapping leads to antennas of considerable sizes. Radars with such characteristics are uncommon. One such radar is the UHF-band radar (70.5 cm wavelength) at NASA/Wallops Island Research Facility in Virginia. The results of our study of lightning structure of frontal storms with that unique radar are presented here.

## EXPERIMENTAL TECHNIQUE

Prior to and during periods between storm penetrations by a F106 research aircraft, we used the 10-cm wavelength

radar 'SPANDAR') to record precipitation reflectivity while the UHF radar was used to locate lightning flashes. Table 1 shows the important specifications for these radars. Both radars were operated in an RHI (range-height indicator) mode. The UHF radar was held at a constant azimuth while its elevation was stepped in 2.50 increments, with a 30 s holding period at each elevation angle. A complete vertical scan of nearby storms at a single azimuth usually took about 5 min. The SPANDAR was scanned continuously within the 2.50 azimuth sector of the UHF radar.

Table 1 - The Operating Characteristics of UHF- and S-band Radars

	S-band (SPANDAR)	UHF-band
Peak power, MW Pulse width, us	1 1	1 1
Pulse repetition rate, 1/s Beam width, degrees Beam pattern	320,640 0.4 conical	320,640 2.6 conical
Receiver sensitivity, dBm	-119	-112

## **RESULTS**

We characterized the lightning activity by the flash density: i.e., the number of flashes per minute observed in each kilometer interval along the radar beam. Our UHF radar measurements show that returns from lightning echoes are at least 25 dBz higher than those from precipitation. The radar cross section (RCS) of lightning channels varies from about 10 m², received from regions without

any precipitation echo in UHF-band, to the maximum value of about 100 m received elsewhere. Most lightning echoes with small amplitudes (  $< 0.1 \text{ m}^2$ ) occurred at high elevation angles near the top of the storm. The number of such echoes decreased considerably at lower elevation angles, possibly due to the absence there of short, low current discharges present in the upper part of the storm, or due to echoes from small lightning discharges being indiscernible within the more intense precipitation at lower heights. Because of this uncertainty, we limited our analysis to lightning echoes with the RCS > 0.1 m which is about the minimum value detected in precipitation regions. On 11 August 1982, a storm was south of Wallops Island On 11 August and in the front part of a northeastward moving squall line. The RHI scans were made when the storm center was about 215 (SW), 187 (S), and 160 (SE) of Wallops Island. Figures 1-3 show lightning flash density superimposed on a vertical precipitation reflectivity structure of the storm.

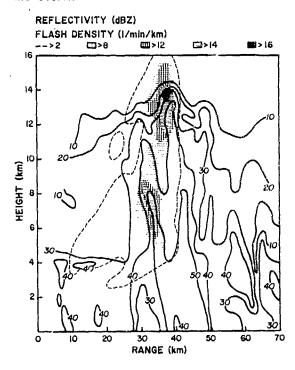


Fig. 1 - Storm structure and contoured lightning flash density on 11 August 1982, 1903.41-1908.07 UT.

Notice two 'cores' of lightning activity. Also notice that 50 dBZ precipitation core in rear (~44 km range) is devoid of lightning while front part of the same reflectivity core is within the lower lightning maximum. Azimuth is 215° from the radar.

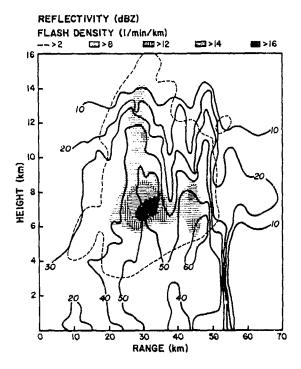


Fig. 2 - Storm structure and contoured lightning flash density on 11 August 1982, 1917.40-1923.00 UT. The upper level lightning maximum almost dissipates and its lower counterpart spreads into both lower precipitation cores. Azimuth is 187 from the radar.

In the period 1903-1908 UT two "cores" of lightning density that are vertically separated are present in the storm. The lower one is associated with the front part (relative to the storm movement) of a 50 dBZ precipitation core, while the upper maximum is near the top of the 40 dBZ reflectivity contour. During the period 1917-1923 UT, the upper lightning density maximum is decreased considerably and the top of the 40 dBZ reflectivity has lowered from 13.5 km to less than 12 km. The lower lightning density maximum is now found in both parts of the 50 dBZ reflectivity. The front part of the 50 dBZ region has increased in altitude from 8 km to 9.5 km, and a new 60 dBZ core has developed inside the rear portion of the storm. In the third period, 1951-1956 UT, the upper lightning density maximum is again present. The lower maximum has decreased about 0.5 km in altitude and now is associated with the heavy precipitation region (60 dBZ) which is elongated downward. In each of the three series of observations the highest region where lightning echoes were observed is above the upper contour of 10 dBZ reflectivity level.

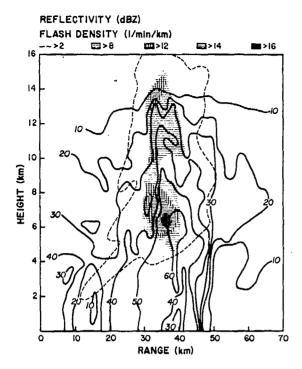


Fig. 3 - Storm structure and contoured lightning flash density on 11 August 1982, 1951.28~1956.21 UT. The upper level lightning density core is again obvious; the lower one diminishes and the heavy precipitation (60 dBZ) elongates downward.

CONCLUSIONS

The results shown here indicate clearly the presence of two centers of lightning activity located in lower (between 6 and 8 km) and upper portions (above 11 km) of the severe storm. Lightning density was greater in one center or another at different times; however, the lower maximum varied only little with time while the upper one changed significantly.

Our finding of two cores of lightning density that are vertically displaced is similar to a finding of Taylor et al. (9) in non-severe and marginally severe Oklahoma thunderstorms using a dual VHFmapping system (6) for lightning location. Taylor et al. identified a class of small intercloud flashes called minor flashes in a region centered at about 11-13 km altitude. These flashes produce only a small number of VHF radiation sources in each flash, but they occur at higher rates than the larger ones. It seems reasonable that their small size associated with small RCS. Therefore the group of echoes with the RCS less than 0.1 m<sup>2</sup> situated mostly at upper part of the storm, which we did not include in the analysis, could be echoes from minor flashes. If we had counted

these small echoes, the lightning density in the upper part of the storm would have been even greater, while that in the lower part would remain essentially the same.

#### ACKNOWLEDGMENTS

We thank the personnel of NASA/Wallops Island Research Facility for their enthusiastic support and help in data collections and reduction. This work was supported in part by National Aeronautics and Space Administration Grant No. NCC5-600.

## REFERENCES

1. P.R. Krehbiel, M. Brook and R.A. McCrory, "An Analysis of the Charge Structure of Lightning Discharges to Ground", J. Geophys. Res., 84, 1979, 2432-

2. W.L. Taylor, "A VHF Technique for Space-Time Mapping of Lightning Radar Echoes and Simultaneous Electric Field Changes", J. Geophys. Res., 83, 3575-3583,

3. D.E. Proctor, "VHF Radio Pictures of Cloud Flashes", J. Geophys. Res., 86,

4041-4071, 1981.
4. E.P. Krider, R.C. Noggle, A.E. Pifer and D.L. Vance, "Lightning Direction-finding Systems for Forest Fire Direction", Bull. Am. Meteorol. Soc., 61, 980-986,

5. V.D. Mazur and L.I. Divinsky, "The Cell Structure of Frontal Thunderstorms (in Russian), Tr. Vsesousnogo Instituta Nauchnoi i Techn. Inform., No. 1117-77, 25 pp., 1977.

V. Mazur and W.D. Rust. "Lightning Propagation and Flash Density in Squall Lines as Determined with Radars", J.

Geophys. Res., 88, 1495-1502, 1983.
7. A.A. Few, "Lightning Channel From Thunderstorm Reconstruction Measurements", J. Geophys. Res., 7517-

7523, 1970.

V. Mazur, B.D. Fisher and J.C. Gerlach, "Condition Conducive to Lightning Striking an Aircraft in a Thunderstorm",

(prasent issue).

W.L. Taylor, W.D. Rust, D.R. 9. MacGorman and E.A. Brandes, "Lightning Activity Observed in Upper and Lower Portions of Storms and its Relationship to Storm Structure from VHF Mapping and Doppler Radar", (present issue).



# LIGHTNING SHOCKWAVE EFFECTS ON AIRCRAFT FUEL VENT LINES T. S. Lee\* and J. D. Robb\*\*

#### ABSTRACT

Earlier researches have shown unusually pressures from lightning strikes into aircraft fuel vents which are effluxing flammable fuel mixtures. A combination detonation wave and shockwave has been suggested as the explanation for this damage. Recent investigations of possible lightning effects on oil tanker vents has suggested that lightning strikes close to the vent could, in fact, produce this combination shockwave and detonation wave which could, because of the high pressures involved, defeat the conventional flame arresters protection.

Investigations and calculations have disclosed that into a vent, even weak finite-amplitude acoustic waves will evolve during propagation into a full detonation wave as the pressure progressively builds up, if the vent line is sufficiently long. This distance is called the "run-up distance" and studies of conventional shockwave run-up distances have indicated the general parameters. Calculations of the run-up distances when triggered by a lighting discharge indicate that these can be fairly short if a full lightning shock pressure is present at the vent inlet. This suggests that jettison tubes or vents should be located well away from probable lightning strike points on aircraft.

- \* University of Minnesota, Lightning & Transients Research Institute
- \*\* Lightning & Transients Research Institute

This paper was not available for incorporation into this book. Therefore, it will be published at a future date.

15

THE EFFECTS OF NEW TECHNOLOGY TRENDS ON AIRCRAFT LIGHTNING VULNERABILITY AND THE CAPABILITY TO IDENTIFY TECHNOLOGY DEFICIENCIES

 $\rightarrow$ 

D. T. Auckland and R. F. Wallenberg Syracuse Research Corporation, Syracuse, New York J. A. Birken Naval Air Systems Command, Washington, D. C.

ABSTRACT

Departional aircraft representing the 1960 and 1970 technology time frames were tested in the Full-Level Lightning Aircraft System Hardening (FLLASH) program at Albuquerque, New Mexico, during the spring and summer of 1982. The direct-strike lightning threat was simulated and peak injection currents of 180 kA were achieved. A methodology was developed during this program which enables the aircraft designer to perform trade-off studies at very early design stages involving avionics packages, airframe configurations, and various threat scenarios.

DISCUSSION

NEW MATERIALS, AIRCRAFT designs, and highlevel threats are rapidly emerging which necessitate that future aircraft satisfy mission requirements from the onset of design. Mission requirements now include surviving extreme electromagnetic threat levels using low-level solid-state equipment which comprise fly-by-wire control systems, and composite materials which can compromise electromagnetic shielding. A new methodology has been developed which can aid in making a first-cut evaluation of the electromagnetic vulnerability of a new platform at a very early design stage. This methodology has been applied to low frequency threats such as lightning and the nuclear electromagnetic pulse, and is currently being extended to microwave frequencies. This ability to evaluate performance and cost impact of new technologies and modern threats has extremely high value.

To synthesize the electromagnetic protection required by new technologies such as fly-by-wire and composite material aircraft, it is necessary to generate the Fig. 1 transfer functions D(f) and  $T_1(f)$  through  $T_5(f)$  for different airframes and avionic systems.

Knowledge of the transfer functions allows evaluation of voltages and currents which will result from the different throats. Transfer functions are most easily obtained from frequency domain measurements or theoretical calculations. They may then be tabulated in several data files, which are used by a simulation program package. Fig. 2 illustrates the difference between the threat spectra, D(f), for lightning and nuclear electromagnetic pulse (NEMP). Typical point-of-entry transfer functions are illustrated in Figs. 3 and 4 for composite panels (transfer impedance) and joints (transfer admittance), respectively. More detail concerning the transfer function approach and methodology description may be found in References [1]\* and [2].

\*Numbers in brackets designate References at end of paper.

The ever increasing complexity of present and future platform designs also pushes the designer into consideration of several cross-discipline issues. These include environmental effects on new airframe materials, zerodynamic effects due to shielding improvements, and many synergistic effects which relate to overall mission performance. A general algorithm

for hardening a proposed platform against various threats, including external electromagnetic and environmental, has been developed. Each step toward the ultimate design goal may be taken by a combination of simulation techniques or test results. A feedback loop is included which incorporates the important trade-off considerations that must be made.

Measured results show that conductive coatings applied to composite material laminates provide significant protection against structural degradation during a direct lightning strike attachment as well as providing improved shielding. A feeling for the circuit-level protection afforded by various types of coating materials can be seen in Fig. 5. Here a 3m length of 100-ohm line is terminated in its characteristic impedance and a fuselage longitudinal current density of 64 kA/m is assumed to flow on the panel material exterior. This corresponds approximately to a 200 kA direct strike on a 1/2m radius fuselage. Various maximum open-circuit voltages are given from 1 to 500V for different conductive coating thicknesses using uncoated 8-ply graphite/epoxy as a baseline. Wunsch constants are given in parenthesis and represent the minimum Wunsch constant that a semiconductor junction must have if it is to survive being connected directly in the circuit. For example, 50V of open-circuit voltage protection is provided with a 45-mil coating of aluminum on 8-ply graphite/epoxy. If uncoated, the graphite/epoxy panel would have to be 30 cm thick to provide 50V protection against 64 kA of external surface current density.

Protection by costings, however, is gained at the expense of a weight penalty. Various protection techniques are also available to the aircraft manufacturer at the wire harness or circuit level. These include mismatches between source and load impedances and use of voltage limiters. A trade-off between the protection provided by these methods and that provided by conductive panel coatings is performed in Reference [3].

The mechanisms by which direct-strike lightning couples to the interior of a platform is extremely dependent on platform design (i.e., T<sub>1</sub>, T<sub>2</sub>, and T<sub>3</sub>). The material distribution of a fly-by-wire mixed metal/composite aircraft is illustrated in

Fig. 6. Experiments were conducted during the FLLASH tests to provide operational airframe data to refine/corroberate assumptions made in the methodology. Further experiments will provide additional detail.

This methodology is being applied to the analysis of the impact of advanced-concept avionics packages on new airborne weapon systems. Examples of this are the impact of airframe configuration on the all-new JVX aircraft depicted in Fig. 7 and the implementation of the Advanced Digitial Optical Control System (ADOCS) being considered for the US Army Black Hawk helicopter shown in Fig. 8. The Navy Seahawk, which is very similar, is shown for comparison of airframe material distribution.

The helicopter is a substantially poorer "Faraday shield" than the fixed-wing fighter and, consequently, interior field levels due to aperture coupling are of great concern. It can be shown that for a unit H-field incident plane wave at 1 MHz, electric field strengths inside the cockpit can be as high as 2000 V/m using the methodology. Also, for cable bundles lying outside the Faraday shield, as is the case for harnesses on the roof of the helicopter. induced voltages as high as 4000V have been predicted for 100 kA/µs rates of directstrike rotor-to-tail current rise. Voltages can be much higher if the circuit is near a concentrated current path such as the rotor shaft or if the particular circuit had a relatively large loop area. The wire bundle used in this example is shown in Fig. 9 and is located on the roof of a mixed Kevlar/ metal helicopter. These predicted levels are comparable to reported test results. Table 1 summarizes estimates of peak induced voltage for a cable on top of the helicopter when struck by a lightning waveform on the rotor blades. Waveforms of various rates of rise are considered.

## CONCLUSION

The importance of the capability to identify technology impacts in new platforms is underscored by recent lightning test results [3, 4, 5, and 6]. In particular, it was found that:

 Graphite/epoxy materials may be used in place of metal if adequate protection techniques are implemented.

 Kevlar requires protection beyond graphite/epoxy to compensate for its lack of conductivity.

 Conductive coatings can significantly improve composite material shielding properties.

 Nonconducting radomes should have lightning protection.

 Methodology allows designs to be adjusted to changing requirements, technologies, and threats.

Methodology informed sponsor of advantages and deficiencies of new

technologies, new threats, and modifications imposed on its platform.

Methodology can aid in ranking IR&D programs.

Such an integrated overview forms the basis for proposing and justifying new programs needed to overcome technical deficiencies.

In addition, tests have shown that adequately hardened subsystem boxes can significantly harden device susceptibility. Consequently, total subsystems rather than devices must be illuminated in tests.

Analysis to date has identified a number of technology voids when considering the high-level lightning threat as summarized in Fig 10. It indicates some of the areas in which technology gaps must be filled. As work continues, other voids requiring detailed analysis and experimentation will be identified.

#### REFERENCES

1. D.T. Auckland, R.F. Wallenberg, and J.A. Birken, "Modelling of Direct-Strike Lightning Coupling by a Transfer Function Technique", these proceedings.

2. R.F. Wallenberg, D.T. Auckland, and J.A. Birken, "A Transfer Function Approach to Coupling to the Interior of a Composite/Metal Aircraft Based on a Triangular Patch Model", IEEE International Symposium on EMC, Santa Clara, September 1982.

3. D.T. Auckland, et al, "Interdispline Studies on the Structural/Electromagntic Optimization of Advanced Composite Aircraft", interim report prepared by the Syracuse Research Corporation for the Naval Air Systems Command under Contract NO0019-82-C-0088, SRC TR 82-1596, December 1982.

4. FLLASH (Full-Level Lightning Aircraft System Hardening) tests performed on the F-14 and F-18 aircraft at Albuquerque, New Mexico, under the direction of J.A. Birken, Naval Air Systems Command, spring-summer 1982.

Command, spring-summer 1982.
5. R.A. Persla, "Full-Level Lightning Aircraft System Hardening (FLLASH) Test Plan for Lightning Testing of the F/A-18A", prepared for Syracuse Research Corporation under Naval Air Systems Command Prime Contract N00019-82-C-0088, March 1982.

6. R.A. Perala, "Full-Level Lightning Aircraft System Hardening (FLLASH) Test Plan for Lightning Testing of the F-14A Aircraft", prepared for Syracuse Research Corporation under Naval Air Systems Command Prime Contract N00019-82-C-0088, February 1982.

7. L.G. Riffe and W.J. Motil, "F-14 Lightning Test Report", prepared for Syracuse Research Corporation under Naval Air Systems Command Prime Contract NOO019-82-C-0088, 15 August 1982.

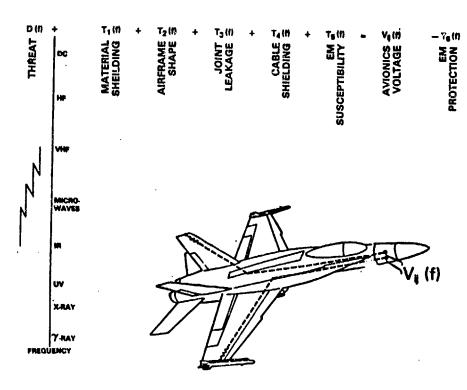


Fig. 1 - Electromagnetic harding methodology parameters

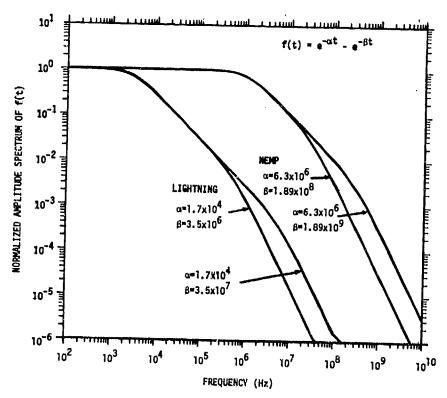


Fig. 2 - Normalized amplitude spectrum of double exponential waveform for various values of  $\alpha$  and  $\beta$ 

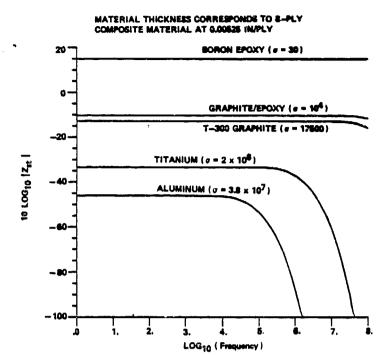


Fig. 3 - Surface transfer impedance as a function of frequency

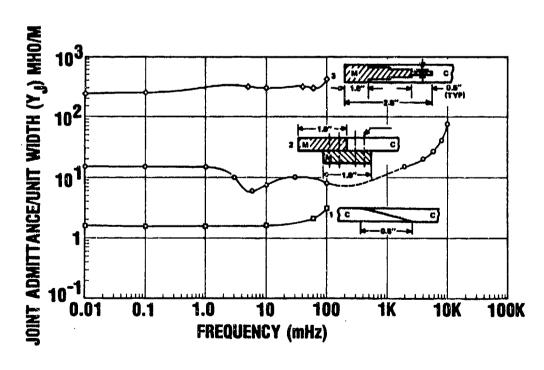


Fig. 4 - Joint admittance/unit width as a function of frequency

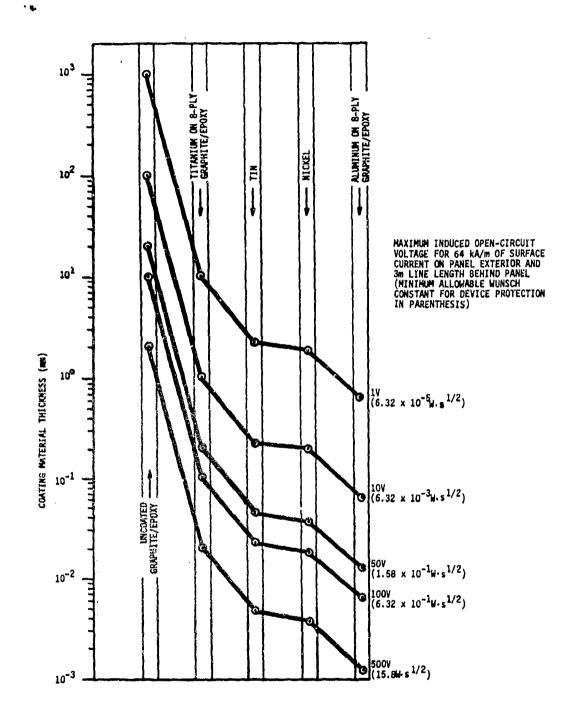
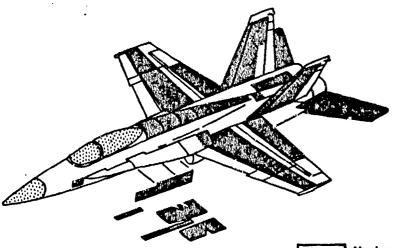


Fig. 5 - Locus of material thickness to limit  $V_{\text{oc}}$  to various voltages

## COMPOSITES APPLICATION



- Principle Coupling Through Joints and Apertures (Cockpit, Wheelwells, and Radome)
- Kevlar Appears Susceptible
- Unknown Above 18 GHz

| Weight | 50% | 10% | 60% | 10% | 40% | 40% | 40% | 40% | 40% | 40% | 40% | 40% | 40% | 40% | 40% | 40% | 40% | 40% | 40% | 40% | 40% | 40% | 40% | 40% | 40% | 40% | 40% | 40% | 40% | 40% | 40% | 40% | 40% | 40% | 40% | 40% | 40% | 40% | 40% | 40% | 40% | 40% | 40% | 40% | 40% | 40% | 40% | 40% | 40% | 40% | 40% | 40% | 40% | 40% | 40% | 40% | 40% | 40% | 40% | 40% | 40% | 40% | 40% | 40% | 40% | 40% | 40% | 40% | 40% | 40% | 40% | 40% | 40% | 40% | 40% | 40% | 40% | 40% | 40% | 40% | 40% | 40% | 40% | 40% | 40% | 40% | 40% | 40% | 40% | 40% | 40% | 40% | 40% | 40% | 40% | 40% | 40% | 40% | 40% | 40% | 40% | 40% | 40% | 40% | 40% | 40% | 40% | 40% | 40% | 40% | 40% | 40% | 40% | 40% | 40% | 40% | 40% | 40% | 40% | 40% | 40% | 40% | 40% | 40% | 40% | 40% | 40% | 40% | 40% | 40% | 40% | 40% | 40% | 40% | 40% | 40% | 40% | 40% | 40% | 40% | 40% | 40% | 40% | 40% | 40% | 40% | 40% | 40% | 40% | 40% | 40% | 40% | 40% | 40% | 40% | 40% | 40% | 40% | 40% | 40% | 40% | 40% | 40% | 40% | 40% | 40% | 40% | 40% | 40% | 40% | 40% | 40% | 40% | 40% | 40% | 40% | 40% | 40% | 40% | 40% | 40% | 40% | 40% | 40% | 40% | 40% | 40% | 40% | 40% | 40% | 40% | 40% | 40% | 40% | 40% | 40% | 40% | 40% | 40% | 40% | 40% | 40% | 40% | 40% | 40% | 40% | 40% | 40% | 40% | 40% | 40% | 40% | 40% | 40% | 40% | 40% | 40% | 40% | 40% | 40% | 40% | 40% | 40% | 40% | 40% | 40% | 40% | 40% | 40% | 40% | 40% | 40% | 40% | 40% | 40% | 40% | 40% | 40% | 40% | 40% | 40% | 40% | 40% | 40% | 40% | 40% | 40% | 40% | 40% | 40% | 40% | 40% | 40% | 40% | 40% | 40% | 40% | 40% | 40% | 40% | 40% | 40% | 40% | 40% | 40% | 40% | 40% | 40% | 40% | 40% | 40% | 40% | 40% | 40% | 40% | 40% | 40% | 40% | 40% | 40% | 40% | 40% | 40% | 40% | 40% | 40% | 40% | 40% | 40% | 40% | 40% | 40% | 40% | 40% | 40% | 40% | 40% | 40% | 40% | 40% | 40% | 40% | 40% | 40% | 40% | 40% | 40% | 40% | 40% | 40% | 40% | 40% | 40% | 40% | 40% | 40% | 40% | 40% | 40% | 40% | 40% | 40% | 40% | 40% | 40% | 40% | 40% | 40% | 40% | 40% | 40% | 40% | 40% | 40% | 40% | 40% | 40% | 40% | 40% | 4

Fig. 6 - Primary microwave coupling will occur through joints and apertures

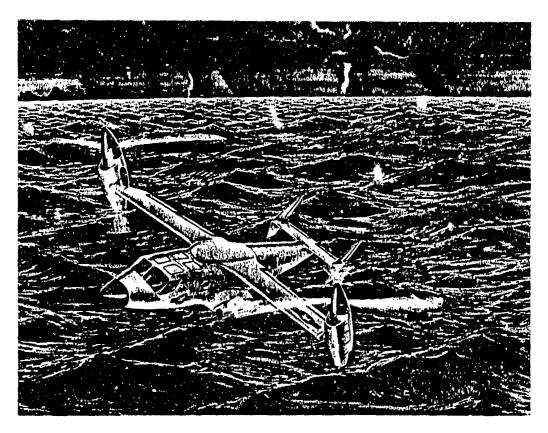


Fig. 7 - Artist rendering of JVX

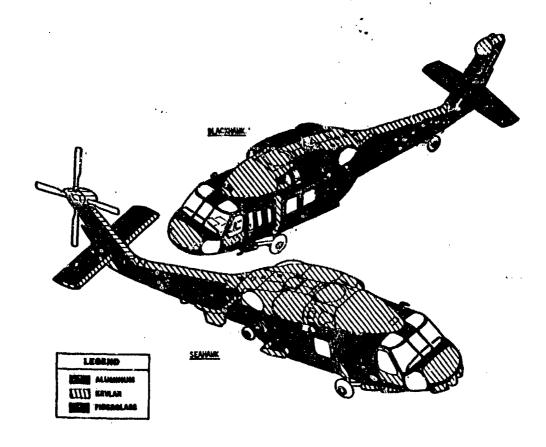


Fig. 8 - Black Hawk and Seshawk surface material description

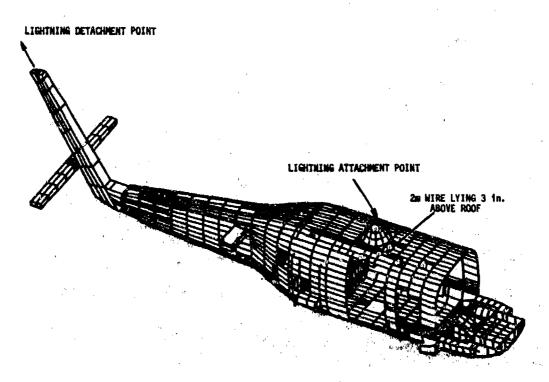


Fig. 9 - MASTRAN model of Kavlar/metal helicopter

Table 1 - Peak induced voltage on 2m cable 3 in. above Kævlar/metal helicopter roof area caused by direct strike to rotor

Direct-Strike (Injection) Current Description	Nominal Rate of Rise (kA/µs)	Peak Open-Circuit Voltage (V)
LTRI Test Waveform (Reference 5)	0.04	1.5
Full-Level Threat (Recommended SAE Waveform)	100	4000
AFFDL 1 kA FLLASH Waveform (References 3 and 4)	2.5	100
SANDIA 80 kA FLLASH Waveform (References 3 and 4)	35	1300

TUBES	DISCRETE TRAMEISTORS	INTEGRATED LARGE SCALE INTEGRATED CIRCUITS (IC) CIRCUITS (LSI)		VERY LANGE SCALE INTEGRATED CINCUITS (VLSI)	
(i)	770-8	FLATPACK	想。	CARRIER CITTLE	
I WATT/DEVICE	12V-24V 18-1-10-2 WATTS/DEVICE	VSI-VB E-01_5-01 BHAHYETTAW	6V-7V 16-3_18-4 WATTS/TRANS	1.6V-36 10-6_10-6 WATTE/TTANE	
GLAIR/ METAL/ CERAMIC	METAL/ CERAMIC	METAL/ CERAMIC/ EPOXY	METAL/ CERAMIC/ EPOXY	CERAME/ EPOXY	
F-0	F-4	F-14	F-18	vetol, JVX	
ALUMNUM	ALUMNUM	ALUMHUM/VITAN	GRAPHITE-EPOXY MUMMULA	GXAPHITE DPOXY KEVLAH	
PRC~1986's	1956's	1967)	1070%	1964)	

## CONCLUSIONS

- . COMPOSITE MATERIALS INCREASE PLATFORM SUSCEPTIBILITY
- \* DEVICE TRENDS INCREASE AVIONICS SUSCEPTIBILITY
- . HIGH THREAT LEVEL TRENDS FURTHER EXPLOIT SUSCEPTIBILITIES
- \* PLATFORM TYPE SIGNIFICANTLY APPECTS SUSCEPTIBILITY

Fig. 10 - Aerospace technology trends



# UNPROTECTED RADOME LIGHTNING TESTS AND IMPLICATIONS TO KEVLAR AIRFRAME DESIGNS

D. T. Auckland Syracuse Research Corporation Syracuse, NY 13210 J. A. Birken
Naval Air Systems Command
Washington, DC 20361

## ABSTRACT

A fiberglass radome, mounted on an operational aircraft, was subjected to a direct lightning strike attachment experiment. It was found that lightning diverter strips could be effectively used to prevent damage from occurring to the radome. Omission of any protective schere, however, resulted in burnthrough of the radome surface and arcing to the edge of the phased array radar antenna. These test results are discussed in context with the application of nonconducting composite materials, such as Kevlar, to airframe component design.

DISCUSSION

DURING THE SPRING and summer of 1982, Full Level Lightning Aircraft System Hardening (FLLASH) tests were performed on two operational aircraft at Sandia National Laboratory in Albuquerque, NM. During the end of these tests, it was attempted to get the Sandia lightning simulator to arc to the radome of one of the aircraft. The radome consists of layers of fiberglass and is nonconducting except for a metal wear tip. The test bed configuration is shown in Fig. 1. Further details concerning the test fixture and Sandia lightning facility are given in [1]\* and [2].

A combination of basis and derived parameters may be used to represent lightning flashes. Those used for the Sandia simulator are: the stroke rise time, number of strokes per rlash, peak current in a single stroke, action integral (the integral of the square of the current with respect to time), and total charge transferred.

Some simple analyses show that this set of parameters is reasonable for describing the severity of lightning effects. The rise time is important because the coupling through apertures increases with decreasing rise time and correspondingly greater high frequency content. The number of strokes is important because of the synergistic effects which may occur because the first of a series of strokes produces initial effects which allow significant damage to occur on later strokes. The peak current is important because it determines the maximum magnetic forces which a structure may The sciion integral important because when recistive heating damage effects are expected, the action integral times the resistance gives the deposited energy. Finally, the total charge transferred is important in such phenomena as burnthrough when a plasma is formed at the surface, since in this case the energy deposited in proportional to the total charge times the plasma voltage drop.

\*Numbers in brackets designate references at end of paper.

The capability to produce the levels required is made possible by a circuit concept which has not previously been used for lightning simulation, although the general concept has been studied extensively for other purposes. The key to the circuit used in the Sandia lightning

simulator is the use of a crowbar switch across the Marx generator used to supply the high voltage required to produce the high current levels in an external load. The use of a crowbar switch produces an essentially nonlinear circuit in which, before closure of the crowbar switch, the circuit is a lightly damped L-C circuit, while after closure the circuit becomes an L-R circuit. The circuit is shown in Fig. 2.

With this design, the lightning current rise time is dependent upon the product of the Marx capacitance and the total circuit inductance, which is a series combination of the external load inductance (equipment under test), the intrinsic Marx inductance, the interconnection inductance. and the deliberately added inductance to provide the desired current rise time. The decay time of the current is then determined by the ratio of the total circuit inductance to the total circuit resistance. With a total circuit inductance on the order of 9 microhenries, a total circuit revistance on the order of 0.1 ohms is required to give a decay time on the order of the desired value of 75 microseconds. This low a value turns out to be well within achievable ranges.

The nature of the circuit used in the Sandia lightning simulator obviates the requirement for a large damping resistor, and the resulting energy efficiency is approximately two orders of magnitude better than an overdamped circuit with essentially the game. output characteristics. The crowbar circuit requires a low inductance voltage source to drive the peak current through the external load inductance, Lince the peak current obtainable is the initial voltage times the square root of the C/L ratio of source capacitance to total circuit industance.

A Marx generator is a high voltage generator consisting of a number of capacitors which are charged in parallel and connected in series by spark gaps. Initially the spank gaps are open circuits, and an external power supply is used to charge the capacitors to a common voltage. When the Mark generator is fired (erected) one or more spark gaps are triggered, and the untriggered spark gaps are rapidly fired by overvoltage. The resultant configuration is a series configuration in which the capacitance is the series combination of the capacitors, and the voltage is the original charging voltage times the number of capacitors connected in

series. A voltage multiplication is thus realized, allowing high voltage output with relatively low voltage input.

During testing of the radome, one Marx generator was erected which yielded a peak current of 60 kA when the circuit was completed through the entire aircraft. No damage was incurred by the radome surface when lightning diverter strips were used as shown in Fig. 3. When the diverter strip was removed, however, no arc could be initiated to the radome surface. In order to initiate breakdown at the radome surface, a short length of copper tape was used as shown in Fig. 4. The arcs which were then initiated on the radome surface propagated from the corners of the copper tape strip back along the surface to the position of the phased array dish, located as shown in Fig. 5. Burnthrough then occurred as the arc was diverted onto the edge of the phased array and hence to the bulkhead and ground return. Figs. 6 and 7 are reproductions of pictures taken at the test site showing the phase array mounted on the sircraft and the radome damage area, respectively.

## CONCLUSIONS

THE PARTY OF THE P

It was shown that, under the relatively dry test conditions present, lightning attachment to a fiberglass radome could occur. The bulk relative dielectric constant of the radome is between 3 and 5

with negligible conductivity. These results should be directly applicable, then, to Kevlar, which has very similar electrical properties. Under more humid conditions, as would probably be present during an actual lightning strike aituation, arcing would occur much more readily along the radome surface but burnthough might be avoided altogether depending on the local atmospheric conditions at the radome surface.

The use of diverter strips has been shown to offer a significant degree of protection to non-conducting radomes. It has been shown that without them the potential for damage to a non-conducting radome due to direct lightning strike attachment is great.

#### REFERENCES

- 1. R.A. Perala, "Full Level Lightning Aircraft System Hardening (FLLASH) Test Plan for Lightning Testing of the F/A-18A", prepared for Syracuse Research Corporation under Naval Air Systems Command Prime Contract N00019-82-C-0088, March 1982.
- 2. R.A. Perala, "Full Level Lightning Aircraft System Hardening (FLLASH) Test Plan for Lightning Testing of the F-14A Aircraft", prepared for Syracuse Research Corporation under Naval Air Systems Command Prime Contract N00019-82-C-0088, February 1982.

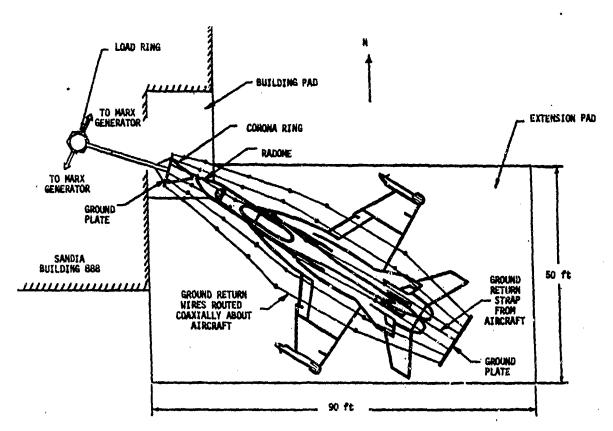


Fig. 1 - Test Bed Configuration for FLLASH Simulated Lightning Tests

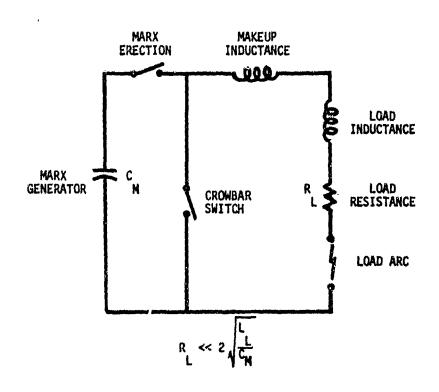


Fig. 2 - Basic Equivalent Circuit for Sandia Lightning Simulator

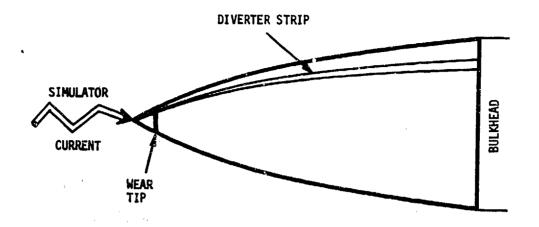


Fig. 3 - Use of Divarter Strip to Protect Radome

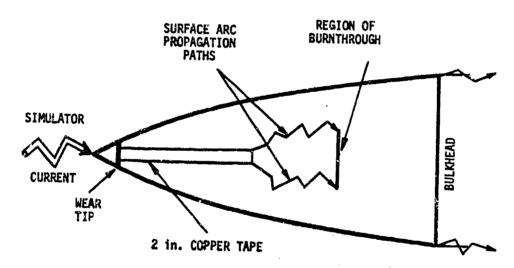


Fig. 4 - Use of Cooper Tape to Initiats Radome Surface Arc

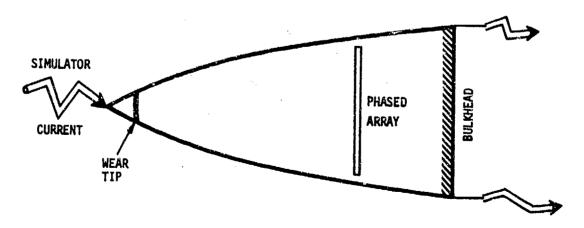


Fig. 5 - Cross Section of Radome

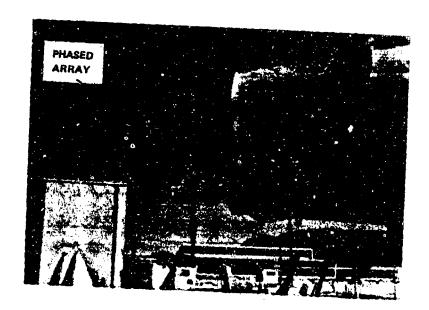


Fig. 6 - Picture of F-18 Nose Area with Radome Removed



Fig. 7 - Picture of Radone Surface Damage Region

Helister

## AN OVERVIEW OF THE F-14A AND F/A-18A LIGHTNING TESTS

R. A. Perala and C. C. Easterbrook Electro Magnetic Applications, Incorporated, Denver, Colorado

### **ABSTRACT**

During the spring and summer months of 1982, various 100 and high level current injection tests were accomplished on the F-14A and F/A-18A aircraft. The intent of this paper is to present an overview of the tests and a summary of some of the more significant results. The low level tests included swept CW, a fast (~300 ns) risetime test, and a nuclear EMP related test referred to as the Surface Current Injection Technique (SCIT). High level pulses up to 173 kA with a 10-90% risetime of 1.7 µsec were injected into a powered up active aircraft. Shock excitation tests were also performed with voltages on the aircraft on the order of 1 MV. Comparisons between low and high level, fast and slow risetime, and CW and pulse responses are summarized. In addition, because the two aircraft afford an opportunity to compare metal and carbon fiber composite (CFC) construction, comparisons between the two aircraft are given.

ERRORS IN LIGHTNING DIRECTION FINDING BY AIRBORNE CROSSED LOOPS

-

Lee W. Parker Lee W. Parker, Incorporated, Concord, Massachusetts

ABSTRACT

Analytical and commuter approaches are presented for predicting the site errors of airborne crossed loops used for lightning direction-finding. This type of azimuth error is caused by distortion of the incident field due to induced skin currents. Computer code results are presented for a T-39 and a C-130 aircraft used in flight-testing a commercial corssed-loop system. Another type of bearing error, caused by non-vertical lightning channels, is analyzed for the case where both detector and lightning source are above a conducting ground plane. Also discussed is the 180-degree ambiguity and its resolution by an electric field antenna.

AIRBORNE CROSSED LOOPS may be used to sense the azimuth of lightning discharges as an on-board aid in the avoidance of thunderstorm regions. However, the loops can be susceptible to serious sité errors in lightning direction-finding, depending on the geometry of the aircraft and the loop location on it (1, 2, 3)\*. These site errors are caused by scattering (re-radiation due to induced eddy currents) of the incident magnetic wave field by nearby conducting surfaces (the skin of the aircraft). These eddy currents produce a secondary magnetic field that results in a total magnetic vector of generally different (distorted) orientation from the incident orientation. The crossed-loop detector is "misdirected" when it senses the distorted orientation and indicates an erroneous bearing. (The term "misdirection" was used earlier in this sense, and may have been coined by A. Sommerfeld (13).) Another consequence of the site error is that it disturbs also lightning ranging systems that use relations between magnetic amplitude and distance, since the amplitude as well as the direction is distorted by the scattoring effect.

Two approaches, analytical and numerical, are presented for analyzing and predicting the site errors of airborne crossed loops. In both approaches we assume that the aircraft is small compared with the radiation wavelength (magnetostatic limit), and solve Laplace's equation to obtain the scattered magnetic field vector, for arbitrary azimuth angles of incidence of the wave from the lightning radiation source. The site error arises from the fact that the individual orthogonal magnetic field components are changed by different factors. The error analyses presented here and in Refs. (1) and (2) do not appear to have been published previously.

In the analytic approach, fuselages, wings and tails are modeled by ellipsoids. An important analytical result is that large errors in lightning direction-finding can occur (e.g., of the order of 20°) even in the case where the instrument is symmetrically located, e.g., centered on a long fuselage. The error can be still larger if the instrument is mounted near the nose or tail, or near edges. (See Ref. 3.)

In the numerical approach, the aircraft geometry is modeled realistically, and numerical solutions are obtained using a 3-D computer code. Computational results are presented for two actual aircraft, a T-39 Sabreliner and a C-130 Hercules. These aircraft have been used in flight tests to evaluate a commercially-available crossed-loop system for severe weather avoidance (4, 5, 6). The predicted errors (of the order of 10° for the T-39 and 20° for the C-130) are consistent with flight-test results for the particular mounting locations chosen. The calculations indicate that other locations would reduce the error.

By a combination of theory and experiment, one may determine correction factors for site

errors affecting crossed loops, for any given airplane geometry. The results of this determination would suggest optimum locations for the placement of the loops on the aircraft. The correction factors need be determined only once. If this is done, the site errors can be completely eliminated by suitable adjustment of the electronic amplification.

Also discussed are azimuth errors due to non-vertically-polarized lightning channels, and the 180-degree ambiguity inherent in crossed loops. A non-vertical (or "slant") lightning channel will cause a crossed loop to determine an erroneous direction, if the loop and lightning channel are at different altitudes. The effects of loop altitude above a conducting ground plane (as opposed to lightning altitude) on azimuth (or bearing) errors do not appear to have been considered in the literature. An analytical formula is derived, generalizing results obtained for zero loop altitude (9, 10) to the case of finite altitude.

The use of an electric antenna in conjunction with the loop to resolve the 180-degree ambiguity by correlating the phases of the electric and magnetic vectors is an important problem, and is considered in the Appendix. It is clear that low signal-to-noise ratios or unintentional phase shifts in the electronic amplifiers can produce 180-degree errors.

#### ANALYTICAL APPROACH

Evaluation of the scattering of incident electromagnetic waves is generally a difficult problem, even for perfectly conducting bodies of simple shape, e.g., spheres (7). If we assume that the radiation wavelength is larger than the dimension of the airplane, the problem is simplified because Maxwell's equations are replaced by the Laplace equation of magnetostatics. This approximation is valid for frequencies below the first aircraft resonance, i.e., for frequencies below about one MHz (8). In the magnetostatic limit, the boundary condition at the aircraft surface is that the magnetic field be tangent to the surface (zero normal gradient, a Neumann boundary condition). That is, the magnetic field is excluded from the interior of the aircraft by the induced skin currents. This boundary condition is justifiable based on the fact that the skin depth (given by  $66/v^{\frac{1}{2}}$  in mm for copper, where v is the frequency in Hz (7)) is only 0.3 mm at the frequency 50 kHz of interest here, and is therefore less than typical aircraft skin thicknesses (at least one mm).

In magnetostatics the magnetic field vector at any point may be expressed as the gradient of a scalar potential function  $\phi$ , where  $\phi$  satisfies the Laplace equation in the region exterior to the airplane, has a vanishing normal derivative on the airplane surface, and asymptotically approaches a linear form (constant gradient) at infinity.

For analytical purposes (as opposed to the numerical approach discussed later for realistic

Numbers in parentheses designate references at the end of paper.

geometries) it is convenient to model the aircraft by a single geometric form. Since the Laplace equation is separable in ellipsoidal coordinates, a versatile 3-D form that can be defined by one coordinate of a 3-parameter ell'osoidal coordinate system is the tri-axial ellipsoid. Here solutions are expressed in elliptic integrals, that need special tables or computer programs for numerical evaluation. However, if we specialize the ellipsoid to a biaxial (rotationally symmetric) prolate spheroid or to an elliptical cylinder, simpler solutions expressed in terms of trigonometric functions (arc tangent) are obtained. In many cases these simplified mathematical models are sufficient to study conditions on the edges of the wings and on the tail (using the elliptic cylinder) and conditions on the fuselage (using the prolate spheroid). When we specialize to a circular cylinder the difference in the induced surface fields due to the separate orthogonal components of an incident field vector (the cause of the site error) is still significant, as will be shown. However, if we specialize further to a sphere this difference vanishes because of the extreme symmetry of the sphere (see e.g. Table 1). Therefore, the sphere has no site error and cannot be used to model the misdirection effect of an airplane body.

Consider an ellipsoid representing an airplane or a part thereof. Figure 1 shows the ellipsoid projected onto the x-y plane of a cartesian coordinate system. It is aligned with the 3 axes, and has semi-axis lengths a, b, and c along the x, y and z axes, respectively. (The z axis is not shown.) We assume that the top of the airplane body points in the +z direction, and that the incident magnetic field is parallel to the x-y plane. The incident wave propagates with angle of attack  $\theta_{O}$  with respect to the y-axis as shown, and with the magnetic field lines perpendicular to this direction. One can consider the magnetic field distortions at several points, such as A, B, C, and D in the figure. These can represent for example positions along the centerline on top of a fuselage or vertical stabilizer and rudder ("tail fin"), or along a wing or horizontal stabilizer and elevator.

Later we will consider the axially symmetric case in which the y-axis is the axis of rotational symmetry. Thus we consider the solution to be a superposition of the two primary solutions: One is the "transverse" case where  $\theta_0$ =0°, the incident field being in the x-direction, perpendicular to the axis of symmetry. The other is the "axia1" case where  $\theta_0$ =90°, in which the incident field is in the y-direction, parallel to the axis of symmetry.

Before considering the spheroid, let us first consider the limit in which b becomes infinite. The ellipsoid then elongates into a long cylinder or wire parallel to the y-axis and of constant elliptic cross-section, as shown in Fig. 2.

CIRCULAR CYLINDER (c=a)

Here we treat the circular cylinder, where c=a and b=∞, first in the  $\underline{ax_1a_1}$  case where  $\theta_0$ =90°. In this case the field is parallel to the cylinder axis, and the solution becomes trivial. The field is excluded from the interior by a solenoidal sheet current in the surface, in the azimuthal direction about the axis. This current produces an internal field that cancels out the incident field, but the current produces no external field. Hence there is no distortion in the axial case,  $\theta_0$ =90°.

Next we treat the circular cylinder in the transverse case, where  $\theta_0 = 0^\circ$ . Figure 3a shows the field ("flow") lines in this case. The solution of Laplace's equation that satisfies the boundary conditions at infinity and on the surface is the potential function

$$\phi = -B_o \cdot (r + a^2/r) \cdot \cos \psi$$
 (1)

where r denotes the cylindrical radial coordinate, a denotes the cylinder radius,  $B_0$  denotes the magnetic field magnitude at infinity (large r), and  $\psi$  is the azimuthal angle about the cylinder axis ( $\psi$ =0 along the direction of  $B_0$ ). It may be readily verified that the potential defined by Eq. (1) satisfies Laplace's equation in cylindrical coordinates:

$$\frac{\partial^2 \phi}{\partial r^2} + \frac{1}{r} \frac{\partial \phi}{\partial r} + \frac{1}{r^2} \frac{\partial^2 \phi}{\partial \psi^2} = 0$$
 (2)

One boundary condition is that as r becomes large,  $\phi$  approaches

$$\phi \sim -B_o r \cos \psi = -B_o x \tag{3}$$

representing the potential of the constant field  $\vec{B}_0$  along the x-direction. On the surface the other boundary condition is that the normal component of the gradient vanishes, that is,

$$-\frac{\partial\phi}{\partial r} = +B_0(1 - \frac{a^2}{r^2})\cos\psi \tag{4}$$

vanishes for all  $\psi$  when r=a. Thus Eq. (1) satisfies both boundary conditions.

The radial and azimuthal field components,  $B_{\Upsilon}$  and  $B_{\psi}$ , are given by the components of the gradient,

$$R_{r} = -\frac{\partial \phi}{\partial r} = B_{o} \cdot (1 - \frac{a^{2}}{r^{2}}) \cdot \cos \psi$$
 (5)

$$B_{\psi} = -\frac{1}{r} \frac{\partial \phi}{\partial \psi} = -B_{o}(1 + \frac{a^{2}}{r^{2}}) \cdot \sin \psi$$
 (6)

The distorted field of interest is obtained by considering the x-component B, at r=a, namely,

$$(B_{x})_{a} = B_{r} \cos \psi - B_{\psi} \sin \psi$$

$$= B_{o} + B_{o} (2\sin^{2} \psi - 1) (a^{2}/r^{2})$$

$$= B_{o} + (2\sin^{2} \psi - 1) B_{o} \qquad (7)$$

where the first term on the right-hand side of Eq. (7) represents the undisturbed field, and the second term represents the distortion caused by the cylinder.

Thus, the perturbation field (addition to the incident field) goes from -Bo on the "side" looking into the magnetic field, to +B on the "top" of the cylinder (where the dot in Fig. 3 represents the probable position of the crossed loop), as  $\psi$  increases from 0 to  $\pi/2$ . Assuming the crossed loop to be normally positioned (at the dot position) on "top", it senses a total field value 2Bo, that is, the incident value enhanced by a factor 2.

Now we are in a position to calculate the misdirection at angle of attack  $\theta_{\rm Q}$  . On top of the cylinder  $B_{\rm K}$  is enhanced by a factor 2, while B, remains unaffected. Hence we have

$$\frac{B_{y}}{B_{x}} = \tan\theta = \frac{B_{oy}}{2B_{ox}} = \frac{1}{2} \tan\theta_{o}$$
 (8)

as the definition of the apparent angle of incidence,  $\theta$ , and therefore

$$MD \equiv \theta - \theta_{O} = \arctan(\frac{1}{2} \tan \theta_{O}) - \theta_{O} \qquad (9)$$

is the amount of misdirection or bearing error

at angle of attack  $\theta_0$ . From Eq. (9) we deduce that the bearing error is zero (i.e.,  $\theta=\theta_0$ ) when  $\theta_0=0$  and when  $\theta_0=90^\circ$ . The maximum error is -19.5° (or +19.5°) occurring when 80 is 54.70 (or its supplement 125.30). This follows from the vanishing of the derivative of MD with respect to  $\theta_{c}$ . The variation of bearing error with angle  $\theta_0$  given by Eq. (9) is shown in the "needle limit" column of Table 1. These results are consistent with ADF loop antenna calibrations shown in Ref. (3).

At arbitrary angle of attack  $\theta_0$ , the axial field component gives rise to skin currents flowing azimuthally around the cylinder, while the transverse field component gives rise to longitudinal currents, in the +y directions on the two x-sides of the cylinder. Thus the resultent skin current flow-lines are ellipses

whose planes are parallel to the z-axis and the direction of attack (i.e., skewed with respect to the cylinder axis, as shown in Fig. 2).

#### ELLIPTIC CYLINDER

In the more general elliptic cylinder case (c/a), the two principal fields are again in the x-direction ( $\theta_0$ =0°, transverse), and the y-direction ( $\theta_0$ =90°, axial). Again as in the circular cylinder, the axial field gives rise to no perturbation. In the transverse case, however, the field lines are perturbed as shown in Fig. 3, where in Figs. 3b and 3c the lines are topologically similar to the circular case, Fig. 3a. Figure 3b (c<a) can represent a flat wing, with the crossed loop (large dot in the middle) sensing relatively little field distortion. Figure 3c (c>a) can represent a tail fin, where the crossed loop (large dot on the edge) senses a large distortion.

It can be shown that for all cases in Fig. 3 the misdirection is given 17

$$MD \equiv \theta - \theta_0 = arc \tan (R \tan \theta_0) - \theta_0$$
 (10)

where the "ratio-factor" R is defined by

$$R = \frac{a}{a+c} \tag{11}$$

Thus, R reduces to 1/2 when c-a as in Fig. 3a, and Eq. (10) reduces to Eq. (9) for the circular cylinder. At the middle of a flat wing (Fig. 3b) where c<<a, R reduces to approximately unity so that the distortion is minimal. On the edge of a tail fin (Fig. 3c) where c>>a, R becomes small and  $\theta$  becomes zero (due to the dominance of  $B_{\mathbf{x}}$ which becomes large), independent of  $\theta_0$ . Thus the distortion is equal to  $-\theta_0$  and becomes large at angles near  $90^\circ$  (except at  $90^\circ$ ).

#### PROLATE SPHEROID

A prolate spheroid is a reasonable model for a fuselage of finite length. In this case (referring to Fig. 1, where y is now the axis of rotation), the radii are related by a=c, as in the circular cylinder, but b is now finite. Hence the results depend on the aspect ratio t=a/b, which is less than unity for a prolate spheroid (and greater than unity for an oblate spheroid). The incident direction angle  $\theta_0=0^\circ$ if the direction of incidence is parallel to the long axis, and  $\theta_0=90^\circ$  if the direction of incidence is perpendicular to the long axis.

It can be shown that the ratio-factor R in Eqs. (10) and (11) is now replaced by GR (see Eq. (15) below), where G is defined by

$$G(y,t) = (b^2-y^2)^{\frac{1}{2}}/(b^2-y^2+t^2y^2)^{\frac{1}{2}}$$
 (12)

where t=a/b, and y is the y-distance of the

surface point from the mid-point; and R may be defined by

$$R(t) = 0.5 (1 - 2t^2 + N)/(1 - N)$$
 (13)

with N defined by

$$\frac{t^2}{2s} \ln \left( \frac{1+s}{1-s} \right) \tag{14}$$

and  $s = (1-t^2)^{\frac{1}{2}}$ . Thus the misdirection angle is given by

MD 
$$\equiv \theta - \theta_0 = \arctan (GR \tan \theta_0) - \theta_0$$
 (15)

where G and R are given by Eqs. (12) and (13). Note that G denotes the cosine of the tilt angle B of the tangent-plane with respect to the horizontal plane. Note also that G-1 for y=0 (the crossed loop is centered on the fuselage).

As the aspect ratio varies from the "needle" limit t+0 (an infinitely-long circular cylinder) to the opposite limit t+1 (sphere), the factor R varies from 0.5 to 1.0. Assuming the crossed loop to be centered on the fuselage (G=1), the misdirection angle MD-A0 is tabulated as a function of  $\theta_o$  in Table 1, for values of t=0, 0.1, 0.2, 0.5 and 1.0. (The corresponding values of R are 0.5, 0.5207, 0.5591, 0.7100 and 1.0.) Note that MD=0 if  $\theta_0=0^\circ$  or  $90^\circ$  in all cases, and has a maximum magnitude for  $\theta_{O}$  somewhere between 0° and 90°.

As the aspect ratio t increases the largest MD magnitude decreases from its value of 19.50 for an infinitely-long circular cylinder. Thus, if the crossed loop is centered on an F-106 Delta Dart, which may be approximately modeled by a prolate spheroid with aspect ratio t=0.1, the largest MD magnitude is predicted to be 18.4° by Table 1, and occurs at  $\theta_0$ =55°. If the aircraft is a C-130, characterizable by t between 0.1 and 0.2 (but assuming t=0.2) the largest MD is  $16.4^{\circ}$ , occurring at  $\theta_0$ =55°. As t increases further (as the fuselage becomes thicker compared with its length), the maximum MD decreases toward zero, while the corresponding  $\theta_0$  moves slowly toward 45°. In all cases the errors increase if the loop position is moved off center toward the nose or tail. Reference (2) presents further tabulations of Eq. (15) for off-center positions, such as A, B, C, and D in Fig. 1.

## REALISTIC NUMERICAL MODELS

For detailed realistic geometries, computer methods must be employed. Our 3-D computer model numerically solves the Laplace equation, in integral form, by a method of moments, subject to the boundary conditions of uniform field at infinity, and zero normal gradient at the aircraft surface. The aircraft surface is approximated by a large number of small quadrilateral "panels" or "patches", as illustrated in Figs. 4 and 5. (Our code was adapted from a fluid-flow code due to J. L. Hess.) It should be noted that the problems treated here are equivalent to the problems of error compensation encountered in the calibration of low-frequency ADF antennas for aircraft (3).

In the light of data obtained in 1977 and 1981 by the Air Force in flight tests of a Stormscope crossed loop (4, 5, 6), we applied our computer code to obtain a preliminary assessment of the possible influence of site errors. The 1977 tests (4, 5) involved a T-39 Sabreliner, with the instrument installed near the leading edge of (and on the underside of) the right wingtip. The model portrayed in Fig. 4 shows the wing modeled reasonably realistically, while the fuselage, whose detailed structure should be unimportant in this case, is modeled crudely. The 1981 tests (6) involved a C-130 Hercules, with the instrument located under the fuselage near the tail and close to the cargo door. The detailed structure was modeled numerically as illustrated in Fig. 5. In this case we require realistic modeling of the fuselage and tail structure.

We consider first the T-39 results, and then those for the C-130.

T-39 MODEL - The panels in Figs. 4a and 4b are labelled by letters A-H, denoting various sections, with A and B on the fuselage, and C-G on the wing and H on the wingtip. Each section has 12 panels, with Nos. 1-6 on the upper surface and Nos. 7-12 denoting image positions on the under surface (with 7 under 6, 8 under 5, ..., and 12 under 1). The Stormscope instrument position is on Panel G-11, as indicated.

Some selected preliminary results are as follows, indicating panel location, maximum misdirection, and angle of incidence at which this occurs. For each section we give the optimum location.

- +11° at 135° (bottom of fuselage A-9: at midwing)
- (no good location, vertical plane) +16° at 30° (top of wine, behind B: ·· C-3:
  - leading edge)
- +18° at 5° (bottom of wing, behind C-10:
- leading edge) +8° at 15° (top of wing, adjecent D-2:
- D-11: +12° at 5° (bottom of wing,
- adjacent to leading edge) E-11:  $+5^{\circ}$  at  $15^{\circ}$  (bottom of wing,
- adjacent to leading edge) +10° at 160° (top of wing,
- E-2: adjacent to leading edge)
- +3° at 110° (top of wing, shead F-5:
- of trailing edge)
  F-10: +3° at 25° (bottom of wing, behind leading edge)

G-10: +4° at 80° (adjacent to wingtip, bottom, behind leading edge)

G-3: +6° at 115° (adjacent to wingtip, top, behind leading edge)

G-11: -7° at 170° (Stormscope location, bottom, leading corner of wingtip)

G-2: +10° at 95° (mirror of Stormscope location, top surface)

H: (no good location, vertical plane)
The foregoing represent optimum locations
(where the misdirections are minimal). The misdirections are larger at other locations.

The following conclusions may be drawn. The optimum fuselage location is underneath, at midwing position. The optimum locations on the wing (and in fact on the whole airplane) are near the wingtip and away from the fuselage, either on top and shead of the trailing edge, or underneath and behind the leading edge. The actual Stormscope location used was a reasonable choice (in the absence of data on site errors) but could have been improved. The reported bearing discrepancies (5) are consistent with the computed maximum misdirection near the wingtip, of the order of 10°.

It should be mentioned that these figures apply to an incident field lying entirely in the horizontal plane. The presence of a vertical field component would be associated with a slanted lightning channel. In this way the error due to slant would be coupled with site error. It is straightforward to include the vertical component in the calculations, i.e. to study the site errors associated with slanted channels.

C-130 MODEL - The geometry of the C-130 was simulated as illustrated in Fig. 5. The location of the Stormscope, just aft of the cargo door, is indicated in Fig. 5 by a darkened panel. Some detailed small structures such as engine pods have been omitted in this preliminary work on the assumption that such small structures are sufficiently remote from the particular location of interest that their contributions should be negligible.

At the Stormscope location the maximum bearing error or misdirection (MD) is predicted to be approximately 20°. This error is experienced for incident lightning wave direction 55° (left or right) from the forward direction. Although the instrument was located on a flattened area, which would be expected analytically (ellipsoid model) to result in a smaller MD, the nearby tail structure has a strong influence on the MD. With the tail structure omitted, the calculation predicts an MD value of about 120. Restoring the tail structure raises the MD to 200. Lower values of the MD are predicted at other locations on the aircraft (e.g. of order 40 just shead of the cargo door). The calculations are still in progress and further results will be reported.

The overall agreement between the analytical calculations (e.g. using cylinder and ellipsoid models) and the numbers obtained from the computer model is satisfying. However, it

is evident that more detailed information can be obtained with the computer model calculations. The analytical calculations are limited to simple analytical shapes, whereas with the computer model one can treat more realistic airplane shapes.

#### NONVERTICAL LIGHTNING CHANNELS

In this section we consider the error in magnetic direction finding due to the effect of nonvertical orientation of a radiating lightning channel, modeled by a radiating dipole tilted away from the vertical. This effect has been analyzed previously (9, 10), but only with the crossed loop detector at ground level. This situation results in important simplifications. The more general case, where the detector is not on the ground but airborne, does not appear to have been considered in the literature. We deal here with the more general case, where both source and observer are above a conducting ground plane. The magnetic crossed-loop detector is considered to be otherwise perfect (no perturbations due to the sircraft, etc.). The "misdirection" due to induced skiu currents was treated in the previous section.

Referring to Fig. 6, we consider the detector to be at altitude h above the ground plane (mounted on an aircraft). The lightning radiation source is represented by a dipole of vector dipole moment F, located at altitude H above the ground plane. Define a cartesian coordinate system, wherein the ground plane is represented by the x-y plane, and the dipole is centered on the z-axis at a vertical height z-H above the ground plane. The detector is located in the x-z plane, at a height z=h above the ground plane, and at horizontal distance x=D from the z-axis (for y=0). Thus, the coordinates of the source and detector in this system are (0, 0, H) and (D, O, h), respectively. Let R<sub>1</sub> denote the distance from the dipole to the detector, and let Ro denote similarly the distance from the dipole image (at depth H below the ground plane) to the same detector. Then  $R_1$  and  $R_2$  are given by  $R_1^2=D^2+(H-h)^2$  and  $R_2^2=D^2+(H+h)^2$ . Let the dipole be arbitrarily oriented, with components Px, F and Pg. We can then compute the magnetic field as the superposition of contributions from the 3 separate vector dipoles of moments  $P_x\hat{1}$ ,  $P_y\hat{1}$ , and  $P_z\hat{k}$ , where  $\hat{1}$ ,  $\hat{1}$ , and  $\hat{k}$  denote unit vectors in the x, y and z directions.

According to Hertz' solution of Maxwell's equations, the electric and magnetic fields due to a radiating dipole may be expressed in terms of a dipole moment vector function (11, 12). If we denote the Hertzian time-dependent function by P(t-R/c), the vector potential A may be written as

$$\dot{\mathbf{x}} = \frac{1}{2} \dot{\mathbf{y}} \ (\mathbf{t} - \mathbf{R}/\mathbf{c}) \tag{16}$$

where the argument denotes the retarded time at distance K from the dipole, and the dot denotes

Now the magnetic field intensity B is given by

$$\vec{B} = \text{curl } \vec{A}(R) = (\vec{R}/R) \times (d\vec{A}/dR)$$
 (17)

since  $\overrightarrow{A}$  is a function of R only. Differentiation yields

$$\frac{d\vec{A}}{dR} = -\frac{\dot{\vec{P}}}{R^2} - \frac{\dot{\vec{P}}}{Rc}$$
 (18)

where the second term results from the dependence of the time-like argument on R, and we obtain

$$\vec{B} = \vec{M}(R) \times \vec{R} \tag{19}$$

with

$$\vec{R}(R) = \frac{1}{R} \left( \frac{\vec{P}}{R^2} + \frac{\vec{P}}{Rc} \right) = \alpha \vec{P} + \beta \vec{P}$$
 (20)

so that  $\alpha = 1/R^3$  and  $\beta = 1/cR^2$ . In terms of our cartesian coordinates, let

$$\vec{h}_{1} = M_{1x}\hat{i} + M_{1y}\hat{j} + M_{1z}\hat{k}$$

$$\vec{h}_{2} = M_{2x}\hat{i} + M_{2y}\hat{j} + M_{2z}\hat{k}$$

$$\vec{k}_{1} = D\hat{i} - (H-h)\hat{k}$$

$$\vec{k}_{3} = D\hat{i} + (H+h)\hat{k}$$
(21)

where  $\hat{\mathbf{i}}$ ,  $\hat{\mathbf{j}}$  and  $\hat{\mathbf{k}}$  denote unit vectors in the x, y and z directions; and  $\hat{\mathbf{M}}_1$  and  $\hat{\mathbf{M}}_2$  denote  $\hat{\mathbf{M}}_1(\mathbb{R}_1)$  of the original dipole, and  $\hat{\mathbf{M}}_2(\mathbb{R}_2)$  refers to its image, respectively. In this case, the components of  $\hat{\mathbf{F}}_2$ ,  $\hat{\mathbf{F}}_2$  are related to those of  $\hat{\mathbf{F}}_1$ ,  $\hat{\mathbf{F}}_1$  by:

$$\dot{P}_{2x} = -\dot{P}_{1x} \equiv -\dot{P}_{x} \qquad \dot{P}_{2x} = -\dot{P}_{1x} \equiv -\dot{P}_{x} 
\dot{P}_{2y} = -\dot{P}_{1y} \equiv -\dot{P}_{y} \qquad \dot{P}_{2y} = -\dot{P}_{1y} \equiv -\dot{P}_{y} 
\dot{P}_{2z} = +\dot{P}_{1z} \equiv +\dot{P}_{z} \qquad \dot{P}_{2z} = +\dot{P}_{1z} \equiv +\dot{P}_{z}$$
(22)

where we identify the unsubscripted variables with the original dipole. It follows from Eqs. (19) and (21) that, at the observer's position, the magnetic field of the original dipole is given by

$$\vec{B}_{1} = [-(H-h)M_{1y}] \hat{i} + [(H-h)M_{1x} + D M_{1z}] \hat{j}$$

$$+ [-D M_{1y}] \hat{k}$$
(23)

while the magnetic field due to the image is given by

$$\vec{B}_{2} = [(H+h)M_{2y}] \hat{i} + [-(H+h)M_{2x} + D M_{2z}] \hat{j}$$

$$+ [-D M_{2y}] \hat{k}$$
(24)

Hence, the sum of the two fields is:

$$\vec{B} = \vec{B}_{1} + \vec{B}_{2}$$

$$= [(M_{2y} - M_{1y})H + (M_{2y} + M_{1y})h] \hat{I}$$

$$+ [-(M_{2x} - M_{1x})H - (M_{2x} + M_{1x})h$$

$$+ (M_{2z} + M_{1z})D] \hat{J}$$

$$+ [-(M_{2y} + M_{1y})D] \hat{k}$$
(25)

For a vertical dipole, all components of  $\mathbb{R}_1$  and  $\mathbb{R}_2$  vanish except for  $\mathbb{N}_{1z}$  and  $\mathbb{N}_{2z}$ . Then  $\mathbb{R}_1$  has only a y component, and there is no misdirection. When  $\mathbb{R}_1$  has an x-component also, the misdirection angle is given by the arc tangent of  $-\mathbb{R}_x/\mathbb{R}_y$  (Fig. 6b). Consider the ratio  $-\mathbb{R}_x/\mathbb{R}_y$ , obtained from Eq. (25):

$$-\frac{B_{x}}{B_{y}} = \frac{-(M_{2y}-M_{1y})H - (M_{2y}+M_{1y})h}{-(M_{2x}-M_{1x})H - (M_{2x}+M_{1x})h + (M_{2z}+M_{1z})D} (26)$$

Using Eqs. (20) and (22), we may rewrite Eq. (26) as:

$$-\frac{B_{x}}{B_{y}} = \frac{p_{y}E + q_{y}h}{p_{x}H + q_{x}h + p_{z}D}$$
 (27)

where

$$P_{x} = (\alpha_{2} + \alpha_{1})\dot{P}_{x} + (\beta_{2} + \beta_{1})\dot{P}_{x}$$

$$P_{y} = (\alpha_{2} + \alpha_{1})\dot{P}_{y} + (\beta_{2} + \beta_{1})\dot{P}_{y}$$

$$P_{z} = (\alpha_{2} + \alpha_{1})\dot{P}_{z} + (\beta_{2} + \beta_{1})\dot{P}_{z}$$

$$Q_{x} = (\alpha_{2} - \alpha_{1})\dot{P}_{x} + (\beta_{2} - \beta_{1})\dot{P}_{x}$$

$$Q_{y} = (\alpha_{2} - \alpha_{1})\dot{P}_{y} + (\beta_{2} - \beta_{1})\dot{P}_{y}$$
(28)

and where  $P_x$ ,  $P_x$ ,  $P_y$ ,  $P_y$ ,  $P_z$ ,  $P_z$  refer to the original dipole components. Divide through numerator and denominator by  $p_z$ D, and note that we may write:

$$\dot{P}_{x} = \frac{P_{x}}{P}\dot{P}, \qquad \dot{P}_{x} = \frac{P_{x}}{P}\dot{P}$$

$$\dot{P}_{y} = \frac{P_{y}}{P}\dot{P}, \qquad \dot{P}_{y} = \frac{P_{y}}{P}\dot{P} \qquad (29)$$

$$\dot{P}_{z} = \frac{P_{z}}{P}\dot{P}, \qquad \dot{P}_{z} = \frac{P_{z}}{P}\dot{P}$$

where  $P_x$ ,  $P_y$ ,  $P_z$  are the original dipole moment vector components, and where P and P are the time derivatives of the vector magnitude P. Then  $p_x/p_z$ ,  $p_y/p_z$ ,  $q_x/p_z$ , and  $q_y/p_z$  become, using Eqs. (28) and (29):

$$\frac{p_x}{p_z} = \frac{P_x}{P_z}, \qquad \frac{p_y}{p_z} = \frac{P_y}{P_z}$$

$$\frac{q_x}{p_g} = Q \frac{P_x}{P_g}, \qquad \frac{q_y}{p_g} = Q \frac{P_y}{P_g}$$
(30)

where

$$Q = \frac{(\alpha_{2} - \alpha_{1})\hat{P} + (\beta_{2} - \beta_{1})\hat{P}}{(\alpha_{2} + \alpha_{1})\hat{P} + (\beta_{2} + \beta_{1})\hat{P}}$$

$$= \frac{(1/R_{2}^{3} - 1/R_{1}^{3})\hat{P} + (1/R_{2}^{2} - 1/R_{1}^{2})\hat{P}/c}{(1/R_{2}^{3} + 1/R_{1}^{3})\hat{P} + (1/R_{2}^{2} + 1/R_{1}^{2})\hat{P}/c}$$
(31)

In the case of harmonic radiation, of angular frequency  $\omega$ , we may replace P by juP in Eq. (31), so that Q is given by the complex quantity, with  $k \equiv \omega/c$ :

$$Q = -\frac{(x_1^3 - x_2^3) + jk(x_1^2 - x_2^2)}{(x_1^3 + x_2^3) + jk(x_1^2 + x_2^2)}$$

$$= -\frac{a + jb}{a^2 + jb^2}$$
(32)

where

$$x = 1/R$$
  $(x_1 = 1/R_1, x_2 = 1/R_2)$ 

$$a = x_1^3 - x_2^3$$
  $b = k(x_1^2 - x_2^2)$ 

$$a' = x_1^3 + x_2^3$$
  $b' = k(x_1^2 + x_2^2)$ 

so that

$$Q = -\frac{(aa' + bb')}{(a')^2 + (b')^2} + \frac{1(ab' - ba')}{(a')^2 + (b')^2}$$

$$= Re Q + 1 Tra Q$$
 (33)

Finally, the ratio  $-B_x/B_y$  may be written:

$$-\frac{B_{x}}{B_{y}} = \frac{G\frac{P_{y}}{P_{x}}}{1 + G\frac{x}{P_{x}}} \in \tan (MD)$$
 (34)

where MD is the misdirection angle and where G is a geometrical factor:

$$G = \frac{E + Qn}{D} \tag{35}$$

If the detector is on the ground plane (h=0), the problem simplifies greatly, and we have  $\alpha_1=\alpha_2$  and  $\beta_1=\beta_2$ , so that Q=0. Then G reduces simply to G=H/D, and we have

$$-\frac{B_{x}}{B_{y}} = \frac{\frac{H}{D} \frac{P_{y}}{P_{z}}}{1 + \frac{H}{D} \frac{P_{x}}{P_{z}}}$$
(36)

which is identical to the result given by Uman et al (Ref. 10 - see plots), re-expressed in our terms, for a detector on the ground plane. An equivalent result was also given earlier for this case by Kalakowsky and Lewis (9).

If the ground plane is completely nonconducting (no image), then the case of the detector at allitude h above ground also simplifies greatly. In this case  $\alpha_2$  and  $\beta_2$  vanish, and Q=-1. Then

東京の は、 日本の は、

$$-\frac{B_{x}}{B_{y}} = \frac{\frac{(H-h)}{D} \frac{P_{y}}{P_{z}}}{1 + \frac{(H-h)}{D} \frac{P_{x}}{P_{z}}}$$
(37)

That is, H is replaced in Eq. (36) by the "net altitude," H-h.

A geometric interpretation of Eq. (36) (or (37)) is obtained by rewriting Eq. (34) in the form, assuming Q=0:

$$(D + H \frac{P_x}{P_z}) B_x + H \frac{P_y}{P_z} B_y = 0$$
 (38)

This expression implies that the "misdirection," in the plane of the observer and perpendicular to B at the observer, passes through the point whose x, y, z coordinates are  $-(P_x/P_z)H$ ,  $-(P_y/P_z)H$ , and zero. This point (indicated by the letter I in Fig. 6a) is also the intercept of the extended line of the dipole with the z=0 plane. This simple geometric interpretation for a detector on a conducting ground plane was pointed out by Kalakowsky and Lewis (9).

The correction factor for finite aircraft altitude is given by the term Qh in Eq. (35). Assuming a frequency of 50 kHz (Stormscope central frequency), a lightning distance 15 km (=D), a lightning altitude 3 km (=H), and aircraft altitude 3 km (=h), we obtain from Eq. (33) the approximate value -1/3 for Re Q. Thus, for this case the geometrical factor G is reduced to about 2/15 compared with its zero-altitude (h=0) value of 3/15.

APPENDIX. USE OF ELECTRIC ANTENNA TO RESOLVE 180-DEGREE AMBIGUITY

A simple way of seeing how correlation of the phases of the electric and magnetic vectors can be used to resolve the ambiguity is the following.

Consider one loop of a narrowband crossedloop system aligned with two sources, one in "front" and one in "back". In Fig. A-1, the plane of the loop is perpendicular to the plane of the paper and is sligned with the sources (upper dot = front, lower dot = back). The sources are assumed to be electric dipoles in the same plane as the detector, but oriented perpendicular to the plane of the paper. Four sets of vectors are shown, at (a), (b), (c) and (d), with E, H, and P in each set denoting, respectively, the electric vector, magnetic vector, and directionof-propagation vector, respectively. Sets (a) and (b) correspond to radiation from the front, while sets (c) and (d) correspond to radiation from the back. Let signs be associated with E and H, such that E pointing upward and downward denotes a positive and negative amplitude, respectively. While H pointing right and left denotes also a positive and negative amplitude, respectively (readily convertible into loop voltage signs). The four possibilities may be tabulated as follows:

	<u>E</u>	<u>H</u>	Source
a)	-	+	front
b)	+	_	front
c)	•	-	back
d)	+	+	back

It is evident from the table that E and H have opposite signs if the source is in front, while they have the same signs if the source is in back. It is not difficult to apply the same procedure to the second loop.

Thus it is readily seen why electrical noise can produce 180° errors. If the signal-to-noise ratio is too low or the electronics is ineffective, electrical noise pulses of the wrong sign can overwhelm the electric field amplitude and make it appear, say, negative when it should be positive, and vice versa. Similar errors may be caused by unintentional phase shifts in the signal amplifiers.

#### **ACKNOWLEDGMENT**

This work was supported by the Air Force.

#### REFERENCES

1. L. W. Parker and H. W. Kasemir, "Airborne Warning Systems for Natural and Aircraft-Initiated Lightning," IEEE Transactions on Electromagnetic Compatibility, Vol. EMC-24, No. 2, pp. 137-158, May 1982.

2. L. W. Parker and H. W. Kasemir, "Air-borne Lightning Warning Systems: A Survey," Lee W. Parker, Inc. Final Report to Air Force Geo-physics Laboratory, AFGL-TR-80-0226, July 1980.

- 3. These errors are equivalent to the well-known "quadrantal" bearing errors (difference between true and apparent directions) that are normally compensated in the design of low-frequency ADF loop antennas for aircraft. See for example "Antenna Engineering Handbook," pp. 27-10, 11, 12, H. Jasik, editor, New York: McGraw-Hill, 1961.
- 4. T. J. Seymour and R. K. Baum, "Evaluation of the Ryan Stormscope as a Severe Weather Avoidance System for Aircraft Preliminary Report," Report FAA-RD-79-6, pp. 29-35, FAA/FIT Workshop on Grounding and Lightning Technology, Melbourne, Florida, 1979.

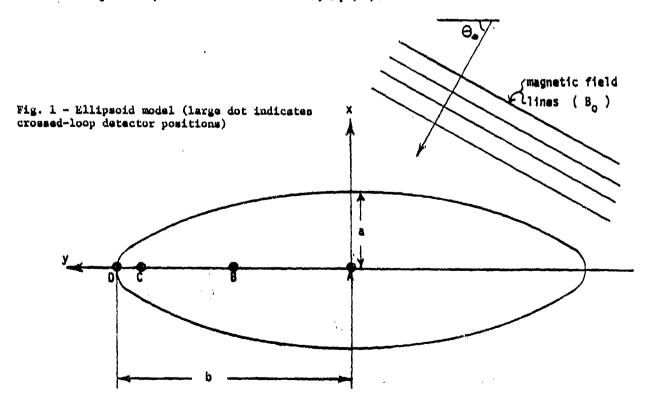
5. R. K. Baum and T. J. Seymour, "In-Flight Evaluation of a Severe Weather Avoidance System for Aircraft," Air Force Flight Dynamics Laboratory Report AFWAL-TR-80-3022, May 1980.

- 6. J. Reazer, "Data Acquisition for Evaluation of an Airborne Lightning Datection System," Air Force Flight Dynamics Laboratory Draft Report, to be published in Spring of 1983.
- 7. J. A. Stratton, "Electromagnetic Theory," New York: McGraw-Hill, 1941.
  - 8. C. E. Baum, personal communication.
- 9. C. B. Kalakowsky and E. A. Lewis, "VLF Sferics of Very Large Virtual Source Strength," Air Force Cambridge Research Laboratories Report AFCRL-66-629, 1966.
- 10. M. A. Uman, Y. T. Lin and E. P. Krider, "Errors in Magnetic Direction Finding Due to Non-vertical Lightning Channels," Radio Science, Vol. 15, pp. 35-39, 1980.
- 11. M. Abraham and R. Becker, "The Classical Theory of Electricity and Magnetism," London: Blackie and Son, Ltd., 1937.
- 12. A. Sommerfeld, "Electrodynamics. Lectures on Theoretical Physics," Vol. 3, New York: Academic Press, 1952.
- 13. A. Sommerfeld, "Partial Differential Equations in Physics. Lectures on Theoretical Physics," Vol. 6, New York: Academic Press, 1949.

Table 1 - Misdirection (Bearing Error) of Crossed Loop on Spheroidal Fuselage (MD =  $\theta$  -  $\theta_0$ )\*

Incident Angle θ <sub>O</sub> (degrees)	Needle (Cylinder) Limit t=0.0 R=0.5	t=0.1 R=0.5207	t=0.2 R=0.5591	t=0.5 R=0.7100	Sphere Limit t=1.0 R=1.0
0	0.	0.	0.	0.	0.
5	- 2.50	- 2.39	- 2.20	- 1.45	o.
10	- 4.96	- 4.75	- 4.37	- 2.86	o.
15	- 7.37	- 7.05	- 6.48	- 4.23	o.
20	- 9.69	- 9.26	- 8.50	- 5.51	ŏ.
25	-11.88	-11.34	-10.39	- 6.68	o.
30	-13.90	-13.26	-12.11	- 7.71	ŏ.
35	-15.70	-14.96	-13.62	- 8.57	ŏ.
40	-17.24	-16.39	-14.87	- 9.22	ŏ.
45	-18.43	-17.48	-15.79	~ 9.63	ō.
50	-19.21	-18.16	-16.33	- 9.76	0.
55	-19.47	-18.35	-16.40	- 9.60	Ö.
60	-19.11	-17.94	-15.93	- 9.12	o.
65	-18.00	-16.83	-14.83	- 8.30	ů.
70	-16.05	-14.94	-13.07	- 7.14	o.
75	-13.19	-12.22	-10.61	- 5.68	0.
80	- 9.43	- 8.70	- 7.51	- 3.95	o.
85	- 4.92	- 4.53	- 3.90	- 2.02	o.
90	0.	0.	0.	0.	0.

 $<sup>\</sup>theta$  = sensed angle;  $\theta_0$  = incident angle; t = aspect ratio = ratio of minor to major axes; R = misdirection factor, Eq.(13).



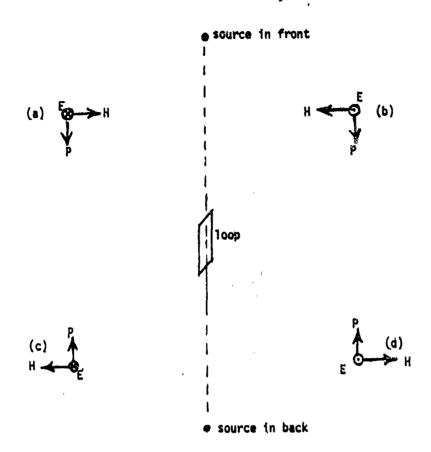


Fig. A-1 - Resolution of the 180-degree ambiguity

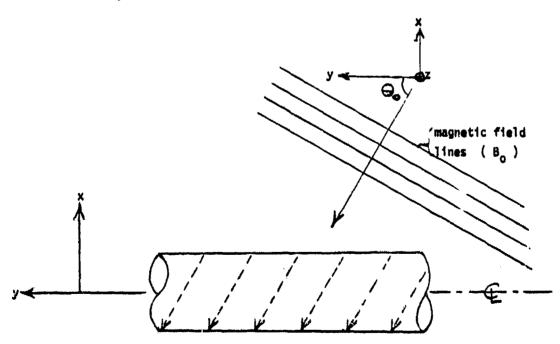


Fig. 2 - Elliptic or circular cylinder (dashed lines indicate current flow planes)

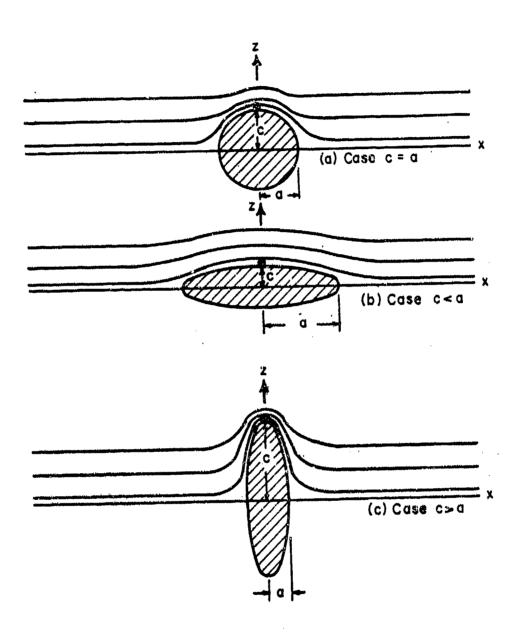


Fig. 3 - Transverse field lines around circular and elliptic cylinders (large dot indicates detector position)

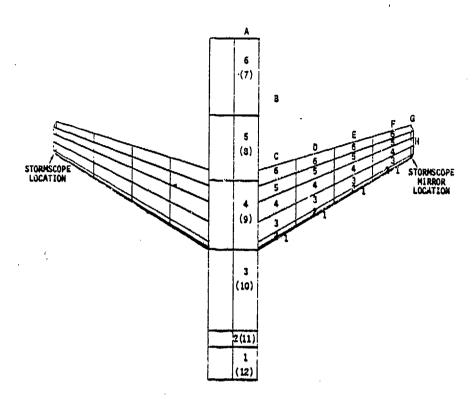


Fig. 4a - T-39 computer model, topside view (letters and integers indicate panel locations, mirror of Stormscope detector located on Panel G-11 directly under Panel G-2)

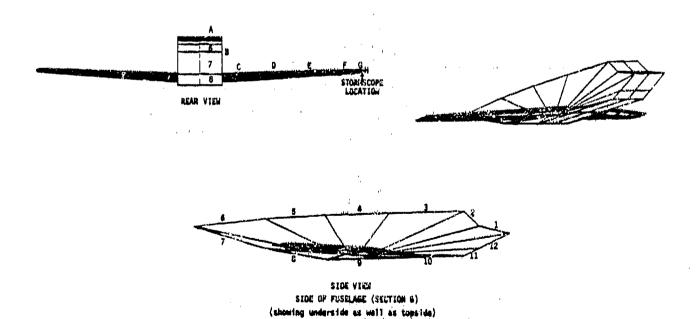


Fig. 4b - T-39 computer model, other views

STORMSCOPE LOCATION Fig. 5a - C-130 computer model, general under-side view (dark panel indicates Stormscope detector location) STORMSCOPE LOCATION Fig. 5b - C-130 computer model, underside view 57-15

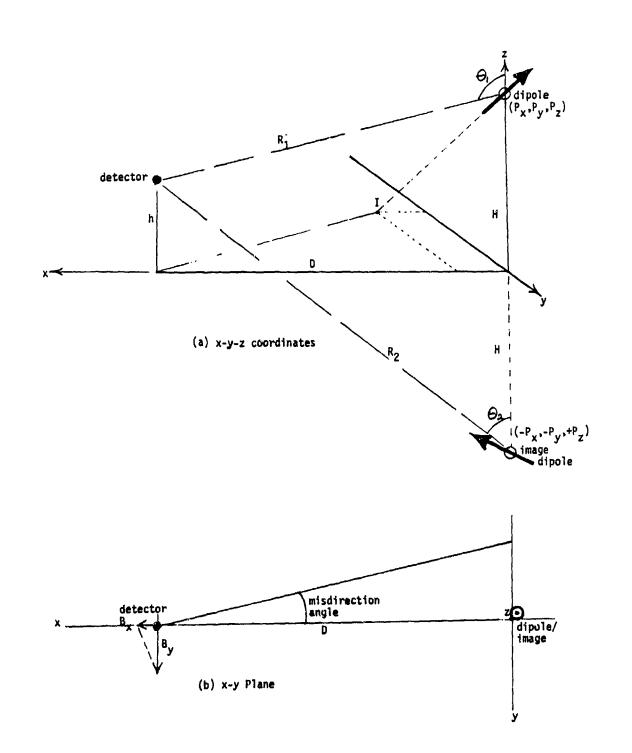


Fig. 6 - Nonvertical dipole and image in conducting ground plane (detector also above ground)

Shorman

UHF Interferometric Imaging of Lightning\*

Ву

P. Richanrd and G. Labaune

Office National d'Etudes et de Recherches Aerospatiales B.P. 72 - 92322 Chatillon - France Phone: (1) 657.11.60

# ABSTRACT

ONERA has operated in Ivory Coast in 1981 and in the United States in 1982 a lightning imaging system. This system in a UHF interferometer which gives the location of the emitting sources all along the various phases of the lightning discharge. The corresponding set-up is described with emphasis on the means used for increasing the accuracy. Examples of results obtained both with natural and triggered lightning strokes, and correlation of these results with spectral analysis of the radiation and with E field measurements will also be presented.

This paper was not available for incorporation into this book. Therefore, it will be published a a future date.

<sup>\*</sup> Research supported in part by DRET (Direction des Recherches, Etudes et Techniques de la Delegation Generale pour 1' Armement).

Eligible

# Mechanical Force Damage Resulting from Lightning Strike

C C R Jones and G W Reid, Culham Laboratory, Abingdon, Oxon, OX14 3DB, England

This paper will broadly review the mechanical force effects arising from magnetic interaction, confined and semi confined arcs producing rapid gas pressure rises, and shock waves associated with lightning strikes. Experiments will be described using arcs representing lightning channels for investigating the arc movement resulting from magnetic fields around the arc and solid conducting structures, and the subsequent damage to the solid conductors such as radome diverter strips. The impulse equivalent continuous force theory proposed by James and Phillpott will be examined and agreement with experiment explored. Finally, the design of joints and connectors, the choice of materials both conducting and nonconducting, their mechanical properties, and the effects of geometrical considerations will be discussed.

This paper was not available for incorporation into this book. Therefore, it will be published at a future date.

ELECTROSTATIC THEORY APPLIED TO HELICOPTER DISCHARGING

-

Robert V. Anderson Naval Research Laboratory, Washington, D. C.

**ABSTRACT** 

An electrostatic analysis is made of a hovering vehicle out of electrical contact with the ground. Charging of the vehicle is seen to be accomplished by a variety of mechanisms. Engine exhausts are strongly ionized; and, since they are physically localized at the stack(s), can be modulated to produce vehicle charging. Strong charging can result from the frictional contact of dust, ice, or water particles with the vehicle skin; and the processes of conduction and diffusion will operate to remove net charge from any isolated object.

The electrostatics of an isolated body above a ground plane are reviewed and developed. Expressions are presented for charge, potential difference, and current. Typical physical situations are applied to allow presentation of meaningful examples. The theory and practice of net charge control as applied to an isolated body are briefly reviewed, and it is shown that discharge impulses upon initial contact cannot be eliminated by any system contained solely within an isolated vehicle.

The dynamics of the discharge process are next addressed. The equivalent circuit of a discharge path is presented with reasonable numerical values, and discharge waveforms are calculated. By using the equivalent circuit, the effects of variation in grounding technology are evaluated. It is shown that the use of an exceptionally "good" low resistance grounding path can easily exacerbate the discharge problem.

In the process of summarizing the results presented, several possible solutions to the grounding prob! \_ are suggested. All rely on establishing initial ground contact through a controlled non-zero resistive path in order to limit the magnitude and steepness of the current discharge pulse. Upon accomplishment of this initial attachment, existing grounding techniques may be profitably employed. It is suggested that existing specifications and procedures be assessed to determine their usefulness in the light of this analysis.

ELECTROSTATIC CHARGES ON HELICOPTERS are known to present a hazard both to ground personnel and to on-board systems. Electric shocks have been reported by persons on the ground ranging from mere tickles to physiologically dangarous jolts. Cases have been reported of damage to operational systems, caused by the discharge at initial grounding, which necessitated immediate termination of the operation. There have been extensive studies of grounding procedure and of on-board helicopter charge control, but a perusal of extant literature indicates that these studies do not, in general, address all of the relevant aspects of electrostatic theory and hence often proceed in directions which are either unprofitable or even counter-productive.

Before addressing these issues, however, a brief review is presented of the mechanisms through which charge is deposited on a flying vehicle, and the limits on charge imposed by natural processes are discussed. Following the discussion of charging mechanisms, there is an analysis of the potential, charge, and capacitance of an isolated conducting body above a conducting plane. A brief catalog of active discharging techniques is given, and their ultimate inadequacy is demonstrated. The dynamics of the discharge process are studied in detail, and the effect of grounding resistance is shown to be significant. The paper is concluded with a list of possible techniques to alleviate the problems associated with electrostatic discharging.

# CHARGING MECHANISMS

The charging of an isolated body requires a process of charge separation and some means by which the separated charge is transported away from teh body. An abundant source of ions is found in the engine exhausts of powered vehicles. The exhaust gases have been ionized by combustion temperatures, and the flow rate

precludes excessive recombination. The exit velocity of the effluent stream and the vehicle motion (and/or rotor downwash) effect the required transport away from the vehicle. The actual effect of the exhaust stream is dependent on the electric field existing at the exhaust port. In the absence of any field, the ionized stream will be effectively neutral in charge and will not contribute to the charging process. A field at the exit will attract ions of one polarity and repel those of the other, producing a net charge separation. It is well known that charging currents of the order of 100 micro-amperes are achievable with high fields at exhaust ports.

The most severe commonly encountered charging mechanism is that of airborne particulates - dust, water droplets, and ice crystals. Significant amounts of charge can be transferred to the vehicle whether the particles in question are themselves initially charged or not. The primary charge separation mechanisms are friction, Volta potential differences, and particle shattering. It would be difficult to overstate the dramatic nature of this phenomenon, and it is hard to picture without a personal experience with a dust-charging situation. Measurements have been made in such diverse environments as high altitude ice crystals, helicopter downwash, and Sahara sandstorm; and in every case the electrification of bodies exposed to the particle flux has been extreme. Charging currents to airborne vehicles in excess of 1 milliampere have been frequently observed (1)\*.

Although they are not charging sources per se, brief mention should be made of corona discharge, exhaust currents modulated by vehicle charge, and ionic conduction, since they consittute the sinks against which a charging process must operate to effect the accumulation of net charge. Corona discharge will form whenever

\*Numbers in parentheses designate Meferences at end of paper.

and wherever the local electrostatic field exceeds a threshold value. As vehicle charge increases, corona becomes a dominant limit on attained total potential. As indicated above, the exhaust stream is respondent to fields at the exit port. Consequently, the existence of net charge on a vehicle leads to exit fields which modulate the exhaust stream toward vehicle discharge. Finally, ionic conduction to the vehicle skin will also operate to effect a net discharging. Turbulence in the vicinity will insure that no electrical boundary layer can exist which will somewhat facilitate the action of the conduction process.

# ELECTROSTATIC ANALYSIS OF AN AIRBORNE YELICOPTER

A consideration of the electrostatic behavior of a helicopter must include the effect of the nearby ground plane. The simplest (and most tractable) geometry to consider is that of an isolated sphere above an infinite conducting plane. If the sphere is far removed from the plane, the analysis degenerates into the well known case of an isolated sphere of radius a for which the potential is

$$V = \frac{Q}{4\pi\epsilon_0 r} \qquad r \ge a \tag{1}$$

and the capacitance to free space is consequently

$$C = Q/V = 4\pi\epsilon_0 a \tag{2}$$

At large altitudes, any valid formulation must approach this functional form as a limit. The solution is appreciably more complex for altitudes not large with respect to the radius and is most easily addressed by consideration of the sphere and its image in a bispherical coordinate system. In this system, for which the Laplace equation is separable, the charge on the sphere can be expressed as a function of its potential relative to the ground plane as (2)

$$Q = \sum_{n=0}^{\infty} \frac{2 \sqrt{b^2 - a^2}}{\left[ (b/a) + \sqrt{(b/a)^2 - 1} \right]^{2n-1} - 1}$$
 (3)

where a is the radius of the sphere and b the distance from the sphere center to the plane. From this the capacitance of the sphere to the plane is easily derived from C = Q/V as

$$C = 8\pi\epsilon_0 a \sqrt{\xi^2 - 1} \sum_{n=0}^{\infty} \frac{1}{\left[\xi + \sqrt{\xi^2 - 1}\right]^{2n+1} - 1}$$
 (4)

is rationalized MKS units where  $\xi$  denotes the ratio b/a.

A second simple model applicable to an airborne helicopter is a section of an infinitely long circular cylinder parallel to the ground plane. From the expression for an infinite line charge above a conducting plane (3) it is possible, ignoring end effects and with some algebra, to obtain an expression for the capacitance of a section of the cylinder of length L as

$$C = 2\pi\epsilon_0 L / \left[ \ln(\xi + \xi^2 - 1) \right]$$
 (5)

with \$\xi\$ defined as in the previous equation. Plots of these two functions are shown in Figure 1. It should be noted that both curves approach infinity as the isolated object nears contact with the ground plane. The sphere capacitance is asymptotic to the proper constant at large separations while the value for the cylindrical section is seen to approach aero as the spacing increases due to the neglect of end effects. Consequences of the behavior at small heights are that the capacitance increases at low slittudes, and that the variation with height is strong at helicopter cargo handling altitudes.

Another expression has been reported (4) for the capacitance of an isolated cylindrical section with diameter a and length L at a height of b in which end effects have apparently been considered. It gives

$$C = \frac{2\pi\varepsilon_{o}L}{\ln\left\{\frac{2L}{a}\left[\frac{L^{2} + 16b^{2} - L}{L^{2} + 16b^{2} + L}\right]^{\frac{1}{2}}\right\}}$$
(6)

which is valid only when a << L. Curves of this function are shown in Figure 2 for several pairs of a, L values. Although the plots extend only as low as about 10 M, the marked increase praviously noted is apparent here also. Examination of (6) indicates that the capacitance so computed at large values of b, approaches a constant value as is required.

A series of capacitance measurements has been reported using 1/50 scale model helicopters (5). Figure 3 shows the same data as Figure 1 in a full logarithmic plot along with some of these model measurements. The latter are obviously in conflict with theory since they have the wrong curvature and, rather than approach a constant value at high altitudes, they tend strongly to zero at very modest heights. It may be speculated in the absence of any report of the measurement technique that there was an over-compensation for the effect of the measuring instrumentation; but at least at lower altitudes where such an error would be small, the measured values are consistent with the model.

The possibility of controlling vehicle charge to eliminate or reduce the discharge upon ground contact has long been an obvious topic of

interest. The Army-Navy precipitation static project in the 1940's (6) addressed this issue with the development of the static discharger wicks so familiar to us all. The use of an active system on helicopters was mentioned as early as 1958 with the statement that the concept had been under study for some time (5). The use of modulated engine exhausts for charge control was the subject of a successful patent application (7) in 1962. Since that time there have been many efforts reported in this direction utilizing either exhaust modulation (8,9) or some form of nozzle discharge (10,11).

Although it is obviously quite possible to alter vehicle charge with some active controller, it is absolutely impossible to determine the earth potential without a physical ground contact because of the inherent nature of a scalar potential. This fact has been mentioned (3,8), but it does not seem to have achieved general appreciation. In a time of stormy weather it is quite possible that the potential of a hovering vehicle at 10 meters which is in perfect equilibrium (zero net charge on the vehicle) can be many tens of kilovolts relative to ground. Additionally, the equilibrium potential can be significantly increased by the thick dust often present in the downwash. Dust is often extremely active electrically (1,12), and a turbulent cloud between helicopter and ground can raise the equilibrium potential dramatically. It is therefore apparent that an effective charge control system would often maintain a potential relative to ground which is sufficiently great to be dangerous.

# DYNAMICS OF ELECTRICAL DISCHARGING

In order to assess correctly the mechanics of the discharge process, the exact configuration present should be recalled. The cargo halicopter can be thought of as a capacitor C which is charged with a charge Q to a potential V = Q/C. It must be emphasized that use of this model does not imply that zero charge on the helicopter guarantees the vanishing of the potential V. A vehicle aloft with zero net charge is in electrostatic equilibrium with its immediate environs, and hence it is at a potential with respect to ground equal to the integral of the ambient field from ground level to vehicle height. When grounding of such a vehicle is effected, a charge must flow into the vehicle to bring it from the elevated potential of its environs to ground potential. Consequently the equivalent circuit will apply whether the helicopter is charged or not as long as V in the equations is taken as the total chango in potential and Q is the total amount of charge transferred.

The grounding cable, whether it is part of the cargo sling or not, can be modelled as a conductor of zero resistance and length equal to the altitude. Finally, completing the circuit is the resistance of the grounding connection, into which can be added any non-zero resistance of the actual cable. An analysis of this series circuit with ressonable values for the circuit parameters can now be developed.

The inductance L is primarily that of the grounding cable. For a long, straight wire it is given as (13)

$$L = 2 \times 10^{-7} I \left( \ln \frac{41}{d} - .75 \right)$$
 (7)

where I is the wire length (in meters), d the diameter of its circular cross section, and the inductance L is in Henrys. The inductance of a 10 meter length of AWG #2 wire is thus 17.5 uH: while much thinner AWG #22 wire of the same length has  $\alpha$  calculated inductance of 22.1  $\mu\text{H}_{\bullet}$ The capacitance of a large helicopter hovering at 10 meters altitude can be taken to be about 1000 pF whether the model calculations or measurements are invoked. The resistance of a "good ground" in broadcast antenna usage, with 100-200 buried radials of the order of 100 meters' length, is usually taken to be in the range 2-5 ohms. The resistance of a casual ground such as a dangling conductor contacting the surface can vary from several thousand ohms to many megohms, depending on the type of surface; while the grounding resistance of a large metal ship in sea water is only a small fraction of one ohm. For illustrative purposes, therefore, consider the circuit in Figure 4 with  $C = 1000 \text{ pF}, L = 20 \mu\text{H}, \text{ and } 250, 2.5, \text{ and } 0.025$ 

Current flow in the circuit of Figure 4 is described by the well-known RLC circuit equation

$$\frac{d^{2}I}{dt^{2}} + \frac{R}{L}\frac{dI}{dt} - \frac{1}{LC}I = 0$$
 (8)

which has the solution

$$I = \frac{V}{\sqrt{\frac{L}{C} - \frac{R^2}{4}}} e^{-\frac{R}{2L}t} \sin \sqrt{\frac{1}{LC} - \frac{R^2}{4L^2}} t \qquad (9)$$

for  $1/LC > R^2/4L^2$  and the initial condition I = 0 at t = 0. This is the equation for a damped harmonic oscillation of frequency

$$f = \frac{1}{2\pi} \sqrt{\frac{1}{LC} - \frac{R^2}{4L^2}}$$
 (10)

with a damping time constant of  $\tau=2L/R$ . For R=250 ohms, the frequency is 526 KHz and the damping time constant is 0.16  $\mu S$ ; so the current oscillation is well damped within a fraction of a cycle. When we pass on to a "good" 2.5 ohm ground, the frequency increases to 1.125 MHz

and the damping time to 16 uS; there are almost 18 complete cycles of oscillation before the amplitude is reduced to 1/e of its initial magnitude. In the third case, the frequency of oscillation is essentially the same as for the 2.5 ohm ground, but the current oscillations persist for 1.6 mS. The peak currents for the 250 and 2.5 ohm cases are 70 and 26 amperes. respectively, for an initial potential difference of 10 KV.

Larger values of grounding resistance for which 1/LC < R2/4L2 have no oscillatory behavior. This may contribute to an explanation of the CH53E tests in 1977 when there was no trouble during over land trials but serious problems occurred when the same tests were repeated at sea. The solid, low-resistance ground connection which intuition says will provide the safest possible operation leads to circuit values which produce current oscillations of high frequency and long duration. The existence of such oscillatory currents introduces the possibility of damage to on-board systems through non-contacting. inductive coupling mechanisms. It is possible to use grounding resistance values much in excess of the 250 ohm value discussed to limit further the peak current (14), but there then is a possibility of large potential drops across the resistor if strong dust charging exists.

#### SUMMARY AND RECOMMENDATIONS

Atmospheric particulates are seen to be the most powerful electrification source encountered in flight. Electrostatic modulation of engine exhausts is also a generous source of charging current, and it is one which is subject to control. The capacitance of an isolated conducting body is seen to vary with height above the ground plane in a strongly non-linear manner, and the capacitance of a helicopter attains values significantly larger than in free space at typical cargo-handling altitudes. It has been demonstrated that electrostatic equilibrium with its environment is not, in general, the correct criterion for operational safety.

An equivalent circuit for the discharge process was presented in which reasonable values for the circuit parameters were employed. It was found on solution that a low resistance grounding connection gave rise to large amplitude oscillatory currents of long duration subsequent to the instant of initial grounding. Conversely, "poor" ground connection of several hundred ohms value reduced the magnitude of the initial current impulse and caused it to damp to negligible values within a small fraction of a microsecond.

In the context of the above facts, what is an appropriate response to the discharge problem? It must first be re-emphasized that a physical ground contact is mandatory to any effective solution since electric potentials are only determinable to within an unknown constant by isolated measurements, however sophisticated the instruments used. The second point which must be considered concerns the grounding resist-

ance. The requirements of safety and reliability which have led to specification of low values are in direct opposition to the problems of current pulse magnitude, oscillation, and duration which are a direct result of low resistance ground technology. The solution obviously must involve some form of ground resistance control.

There are several considerations which establish constraints on any operational discharge system. A significant level of human operation and/or intervention cannot be required. The problems of logistics and operations militate against the use of any items which might be misplaced or lost. There must be no compromise of safety or of operational affectiveness, and it is probably unwise to require the possession of any specialized apparatus by ground personnel. The effect of these considerations is to demand that the discharging system be simple, passive, and permanently attached to the helicopter.

One solution which suggests itself by its elegant simplicity is the installation of a length of semi-conducting cord (cotton and manila suggest themselves) to the helicopter with a weight at the bottom. If the cord hangs slightly below the lowest point of the cargo sling, a high resistance grounding will be effected prior to the (presumably) lower resistance achieved upon payload contact. A short such cord attached to the cargo sling might also be a practical approach. If there are objections to a non-metallic cord, an equivalent piece of steel cable could be used if a suitable lumped resistor be made a part of the installation.

Once the necessity of physical ground contact through a sufficiently high resistance is established, it is apparent that any possible discharge technique will necessarily contain many of the characteristics of the weighted string just discussed. There can be grounding cords which drop on the command of the pilot or which (to be somewhat extreme) are controlled by the radio altimeter. It is possible to conceive a system which senses the current flow and short circuits the limiting resistor upon cessation of the current. A resistive ground want operated by ground personnel would be effective, but this would violate the constraint against requiring specialized tools on the ground. In every case, obviously, a good low resistance ground must be established immediately after discharge is achieved.

Finally it must be observed that existing regulations and procedures must be examined to ascertain whether they are consistent with physical reality. At present, a grounding connection of very low resistance is required by regulation, and the utilization of higher resistences which damp both peak current and harmonic oscillations would not be permitted. Therefore, upon experimental verification of the predictions enumerated herein, it is probable that appreciable revision of pertinent documents will be required. It is urged that the entire subject of helicopter discharge be re-examined to determine if there is not now a misdirection

of emphasis and effort.

#### REFERENCES

- 1. J.E. Namevicz, "Static Charging and its Effects on Avionic Systems." IEEE Trans. EMC-24, 203-209, May, 1982.
- 2. P.M. Morse and H. Feshbach, "Methods of Theoretical Physics." New York: McGraw-Hill, 1953.
- J.R. Reitz and F.J. Milford, "Foundations of Electromagnetic Theory." Reading, Mass.: Addison-Wesley, 1967.
- 4. R. Mühleisen and H.J. Fischer, "Elektrische Aufladung von Hubschraubern." BNVg-FBWT-78-7, 1978.
- 5. "Helicopter Static Electricity Conference Notes." Sikorsky Aircraft, Div. United Aircraft Corp., August 20, 1958.
- 6. R. Gunn, W.C. Hall, and G.D. Kinser, "The Precipitation Static Interference Problem and Methods for its Investigation." Proc. IRE, Vol. 34, 156-161. April. 1946.
- Vol 34, 156-161, April, 1946.
  7. J. F. Clark, "Method and Apparatus for Discharging an Electric Charge." U.S. Patent No. 3035208, May 15, 1962.
- 8. J.E. Nanevicz, D.G. Douglas, S.B. Poteate, and B.J. Solak, "Experimental Investigation of Problems Associated with Discharging Hovering Helicopters." 1972 Lightning and Static Electricity Conference, AFAL-TE-72-325, December, 1972.
- 9. B.J. Solak, J.E. Nanevicz, G.J. Wilson, and C.H. King, "Helicopter Cargo Handling Electrostatic Considerations." 1972 Lightning and Static Electricity Conference, AFAL-TR-72-325, December, 1972.
- 10. N. Felici and S. Larigaldie, "Experimental study of a static discharger for aircraft with special reference to helicopters." Jour. of Electrostatics, Vol 9, 59-70, June, 1980.
- 11. R.G. Buser, H.M. Kaunzinger, and H.E. Inslermen, "Aerosol Discharge System for Heavy List Helicopters." 1972 Lightning and Static Electricity Conference, AFAL-TR-72-325, December 1972.
- 12. P. Borchung, W. Hilgner, G. Luttgens, B. Maurer, and A. Widner, "An experimental contribution on the question of the existence of Lightning-like discharges in dust clouds." Jour. of Electrostatics. Vol. 3, 303-310. November 1977.
- of Electrostatics, Vol 3, 303-310, November 1977. 13. F.E. Terman, "Radio Engineers' Hand-
- book." New York: NcGraw-Hill, 1943.

  14. G.J. Born and E.J. Durbin, "A Passive Discharge System for the Electrically Charged Hovering Helicopter." 1972 Lightning and Static Electricity Conference, AFAL-TR-72-325, December, 1972.

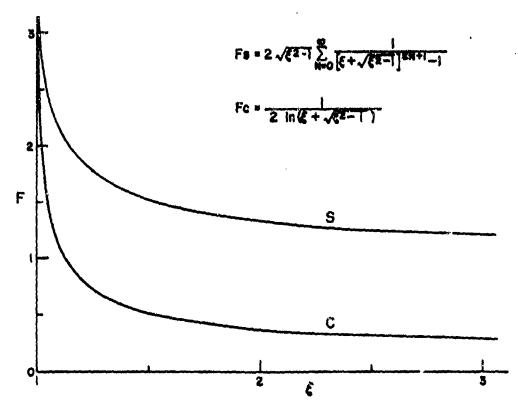


Fig. 1 - Capacitance of sphere and truncated cylinder as functions of height. The actual capacitance in each case is given by C=4 aF,

where F is the value plotted. The symbols S and C denote sphere and cylinder, respectively.

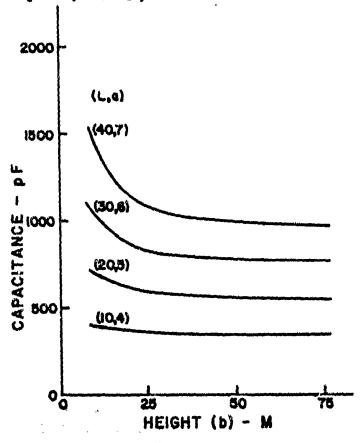


Fig. 2 - Capacitance of inité cylinder es function of height b, for several values of length L and radius a.

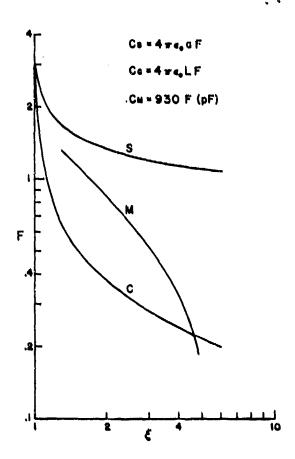


Fig. 3 - Logarithmic plot of computed capacitance values (S,C) and plot of measured capacitance (M) showing significant disagreement.

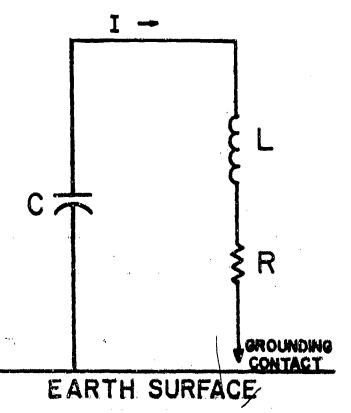


Fig. 4 - Equivalent circuit of the helicopter discharge process.

8-08

Evolude

The Lightning and Electrostatic Control Effort For the Apache/AH-64 Helicopter

> G. A. Booth and H. M. Hoffart Hughes Helicopters Inc. Culver City, CA 90230

#### ABSTRACT

The primary flight pattern of the AH-64 Helicopter will subject the vehicle primarily to cloud-to-ground lightning discharges as well as cloud-to-cloud. Other considerations are the tribo-electric effects. To effect control, a concerted review of the vehicles lightning and charging aspects was performed. Deleterious effects were examined and corrective measures described in this paper will assure greater personnel and vehicle safety while complying with the vehicles mission requirements.

The AH-64 Apache Helicopter uses a four blade main rotor and a four bladed tail rotor driven by two gas turbine engines to meet the required flight and performance characteristics. The main and tail rotors, in addition to sections of the vehicles body, include composits materials in their design and construction. Composite materials are also used for structural support as well as for serodynamic covers for some of the avionics equipment as well as for the gas turbine engines. The extensive use of composite materials in the AH-64 vehicle design impacted on the control efforts for lightning attraction and discharging plus the problems associated with possible lightning penetration into on-board avionics equipment. Other areas associated with electrostatic discharging included electromagnetic interference/slectromagnetic compatibility requirements and effective eletrical bonding control for all electrical-electronic units used in the vehicle. To effectively implement the above areas, whatever control measures were exercised, the control effort impact was considered for each of the areas outlined above. Wick static dischargers are used extensively. Including blade tip static discharge wicks, to dissipate vehicle electric potential charges to limit vehicle potential levels to only a few thousand volts. Blade wicks also reduce pulse discharge levels. The lower peak energy levels per pulse can effect a 20dB to as much as 100dB of quieting for the vehicles communications equipment. Thus, an improvement in electromagnetic compatibility is realized, though the initial effort pertained to the reduction of vehicle electrification potential levels. Streamer currents are also reduced because of the use of multiple wick static dischargers. Electrical bonding designed into the structure and surfaces and effectively implemented, will reduce arcing that would otherwise be present due to high potential levels and high level streamer currents.

The paper will therefore delineats the controls and measures employed to reduce the effects of lightning, static electrical charging and the interaction of electromagnetic interference control and electrical bonding.

This paper was not available for incorporation into this book. Therefore, it will be published at a future date.

を変え

# ADVANCE TESTING OF LIGHTNING PROTECTION SCHEMES FOR COMPOSITE MAIN ROTOR BLADES (HELICOPTER)

-

M. J. Heseltine Westland Helicopters, Ltd., Yaovil, Somernet, United Kingdom

ABSTRACT

The choice of composites, with their structural and aerodynamic advantages, for helicopter main rotor blades is briefly discussed along with some of the difficulties associated with their design, manufacturing and testing. This paper is concerned with the necessity for lightning and erosion protection for the blade's leading adge and the desire for early evaluation of projected design schemes. Attention is drawn to the lengthy lead time between the designing of a blade and the arrival of suitable, expensive tooling required to examine an actual blade specimen.

A technique has been developed which satisfies both the designer and the accountant. A blade is imagined to be cut, spanwise, from root to tip through the trailing edgs and spar regreall. The blade is then opened out like a book. If care is taken with the manufacture of the flat test specimen various lightning protection schemes can be evaluated well in advance of prototype blade specimens. The bulk of this paper examines a selection of protection schemes and the effect of varying the engineering tolerances of erosion shield assembly and the extent of damage so caused.

The information gained through this work enabled blade design to be finalized well before actual blade specimens became available for test. Testing showed close correlation to the results of their flat counterparts.

Work has now progressed into the modelling and testing of flat psnels representing complex blade planforms that do not immediately appear to lend themselves to this technique.

UP TO NOW, helicopter rotor blades have been manufactured around an aluminium extrusion or fabricated stainless steel spars. Being metallic, these presented no real problem for the passage of a lightning strike. However, in the case of a composite blade this problem is particularly acute as the fabrication material is highly resistive. Problems are compounded as the matched metal tools (dies) are not usually produced until the blade design is well established, resulting in a long period between initial design and the production of the first prototype blade. To wait for a prototype to become available to assess a protection scheme and for this to be acceptable first time is quite a gamble. It was therefore obvious that a simple, cheap, and representative method for testing proposed schemes and materials was required. The ideal test specimen would be a flat panel.

#### 1. LIGHTNING PROTECTION FOR COMPOSITE BLADES.

Flight experience has shown that the tip of a rotor blade is the most likely lightning attachment point. The strike energy then has to pass along the blade, through its mounting ouff to the remainder of the aircraft.

A composite blade spar consists of a large number of unidirectional fibres running from the tip to the root. Constructional fibres such as glass or aramid (kevlar) and the spony resin matrix are all insulators and therefore do not transfer strike energy. The unidirectional carbon fibres do however and, in traversing the full length of the spar would carry all of the energy. Unfortunately these fibres are held in an insulating matrix so damage to the structure would occur should a strike attach to this. A full-span metallic conductor that would also act as a strike plate was required.

The next step in the blade's design was to protect the composite from rain and dust erosion. Inspection of metal blades showed that erosion is greatest within 1.5 inches (40 mm) of the leading edge so our lightning conductor was now bigger and of an erosion resisting metal.

A further requirement placed upon our blade is provision for the fitment of a deicing mat, should this be required in the future. To protect these elements from lightning strike the shield was extended to 25% on both upper and lower surfaces — this being the area of heater coverage normally required.

The choice of metals available for this protection was titanium, nickel and stainless steel for their erosion and fatigue strain proper les. For the blade being considered here the decision was for titanium - high fatigue strength was of paramount importance. The blade, when fitted with an aluminium tip plate, was considered to be basically well protected though there remained several areas which required evaluation through testwork.

For various reasons it was necessary to form the erosion shield in four individual sections. When positioned on the blade electrical continuity across the full span could not be guaranteed due to adhesive flow into the joints. These joints were also required to be covered by narrow titanium strips (butt straps) to transfer flight loads from one shield section to the next. Conductive adhesives, for this application, have insufficient strength and would have been ineffectual for lightning transfer. To transfer strike energy to the aircraft the erosion shield must connect to the blade ouff. The transition area of the spar is subject to changing sections making manufacture difficult. The extent to which the leading edge balance bar might be effected was also subject to speculation.

 TEST METHOD, COUPONS AND RELEVANCE TO BLADE.

2.1 IDENTIFICATION OF PROBLEM AREAS FOR TEST - A Design decision was made, for manufacturing and repair requirements, to produce the leading edge protection of several lengths of titanium with their joints being covered by 2" wide titanium strips. The effect of discontinuity in the shield and the lightning conduction properties obviously required investigation. The blade requires to be thicker at the inner end resulting in a considerable profile change - this change would be very costly to reproduce in the metal erosion shield so other solutions needed to be investigated. Another unknown area was the tip plate and its fittings.

To encompass all these unknowns five flat specimens were devised: two for cutboard tip and butt strap damage, two with schemes for the transition area to the attachment cuff and one specimen possessing a one-piece metal shield from tip to cuff.

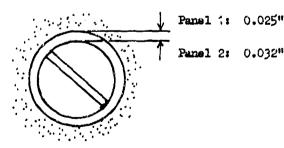
2.2 DESIGN AND MANUFACTURE OF FLAT 'SPAR'

- The blade spar in question possessed a
large proportion of unidirectional carbon and
with the tip plate and its attachment screws
passing through this conductor current sharing
with the shield would be inevitable. The spar
was therefore considered to be cut through
the spar rearwall and opened out like a book.
This cut line was chosen as the least amount
of carbon was in this area and would consequently be the least affected. The trailing
edge fairing was omitted from the model as it
was non-conductive.

The actual method of manufacture involved accurate representation of the glass and carbon materials (fibre direction/number of plies/dimensions) being laid into an aluminium 'picture frame' type tool with a pressure plate to maintain constant consolidation and flatness. These were cured in a press as a panel of 7/16" (11.2 mm) thickness would have possessed a high void count and be poorly compacted if cured in an oven under vacuum pressure. A suitable recess was formed in the panel into which a flat titanium sheet would be bonded to represent the erosion shield.

2.3 TESTING OF OUTBOARD DESIGN FRATURES Flat Panels - These panels were arranged to examine the butt straps and the extreme tip plate (light alloy) and its attachment screws which pass through the shield. Two particular unknowns were the result of not having the adjacent shield sections touching each other and the effect of a clearance hole around the tip plate attachment screws so that there would be no direct tip plate - screw - shield electrical path. For both these specimens the shield was bent up and clamped by 2 cuff bolts, which had been accurately located to simulate the cuff. For all tests the electrode was clamped to the tip plate with the cuff connected to the return circuit. Of the four components which comprise a lightning event, Component A (1)\* initial stroke was considered to be the most relevant as sufficient material was present to reduce the damage due to heating and burning, caused by the remainder of the stroke.

PAREL 1: On this panel the shields were nominally touching beneath the butt strap and 0.025" radial clearance between the tip screws and shield. When given quite a severe strike  $(207kA \ 1.76 \times 10^6 \ A^2t)$  most of the current passed through the carbon as the only visual damage arose from a tip plate to shield are and a small amount of soot blown out from under the butt strap suggesting a small manufacturing void. This are damage, being very minor, was repaired and another severe strike was applied (198 kA 1.93 x  $10^6$  A<sup>2</sup>t). The soot of the first strike encouraged the second to pass through the shield resulting in a partially debonded butt strap (less than t bond area) and surface are scorching around the tip plate screws. Fig 3.



TIP SCREW CLEARANCE

(1)*	Peak Current	200 KA
·	Action Integral	2 x 106 A2
	Pulse Length	< 500 Ps
	Rise Time	< 25 ps

PANEL 2: This panel was identical to the previous one except for a deliberate 1mm resin filled gap between the shields and a greater clearance (.032") for the tip screws. Fig. 3 and 4.

A severe strike (190kA 2.22 x  $10^6$  A<sup>2</sup>t) succeeded in arcing from the tip plate to shield producing delamination. 75% of the butt strap debonded and was bent back due to the 1 mm spacing and areas of the shield

were vapourised here. Blades - When blades were eventually produced to what was hoped to be the final standard, two specimens were despatched to Culham Lightning Studies Unit for testing. BLADE 1: A blade specimen 3 ft. in length with a central butt strap covering shields sections that were nominally touching. This specimen recieved 8 open arc strikes of increasing severity from 48 kA 4.5 x 106 A2t up to 158kA 0.6 x 106 A2t. The first 4 strikes did no damage to the joint other than barely visible soot deposits. The 5th was of moderate severity (145kA 0.98 x 106 A2t) and produced a small amount of soot from one area of butt strap. It must be remembered that this damage was accumulative. BLADE 2: This was given a moderate strike  $(173kA \ 0.6 \times 10^6 \ A^2t)$  of approx. equal intensity to that on Blade 1, and 2 of the butt strap debonded and an area was melted. This blade had a 1 mm gap between its shields.

Comparison Of Panels With Blade Tests The four samples tested demonstrated that it
is possible to obtain very good correlation
between blade and accurate representative
panels. These tests also proved early in
the design days the degree of damage likely
to be caused by a gap between adjacent shield
sections either deliberate or accidental.

Table 1: Shields Mominally Touching.

·	Severity	Damage
Panels	1 Severe strike	delamination of butt strap
Blades	1st Moderate Strike	Soot on corners of strap

Table 2: 1 mm gap between shields

	Severity	Damage
Panels	1 Severe	delamination
Blades	1 Moderate Strike	delamination

2.4 TESTING OF INBOARD DESIGN FRATURES - EARTHING SCHEMES

2.4.1 Schemes Tested - As mentioned earlier, an easier and cheaper means for connecting the parallel sections of shield to the cuff had to be found. Two most likely materials were selected and the flat panels on which to mount these were produced. PANEL 1 - HEXCEL THORSTRAND: This material is a woven glass fabric prepreg in which the individual fibres are partially coated with aluminium. The panel layout was as follows: a 10 inch length of titanium sheet to represent the parallel portion of the blade then 24 inches of Thorstrand (2 plies of T.E.F. 7). The joint between these two could best be described as nominally touching and was covered by a butt strap. The inboard end was earthed out via the close tolerance cuff attachment bolts and the simulated cuff. Incidentally, the face of the Thorstrand shield was not in direct contact with the cuff as a sheet of nylon antifret shim (approximately 0.012") was positioned in between - any strike in the shield had to pass through the end of the fibres and into the bolt shanks. Fig 6.

A severe strike was administered (202kA 1.83 x 10° A2t) with encouraging results. The butt strap debonded for 75% of its bond area, slight are damage to Thorstrand at that point and very slight pitting of the bolt shank.

PANEL 2: EXPANDED ALUMINIUM MESH: This panel was identical to the previous specimen except for the replacement of Thorstrand with Fine mesh. A strike of slightly less power (195 kA 1.75 x 10<sup>6</sup> A<sup>2</sup>t) produced an identical degree of damage. Fig 6.

PANEL 3: ONE PIECE METAL SHIELD: This specimen was to represent the ideal - if money and time were no object. We butt straps, no alternative materials, and no antifret shim to worry about - just a one piece titanium shield bolted to the ouff. A heavy strike

of :202kA 1.77 x  $10^5$  A<sup>2</sup>t produced no damage other than the usual slight superficial arcing at the tip attachment screws. Fig 5.

2.4.2. Discussion of Scheme Results — These trials demonstrate the desirability of a continuous solid metal path for the whole span but if necessary either of the two alternatives tested would give protection if the degree of damage shown could be tolerated. the first two tests on the outboard specimens showed that the results from coupons can be read across to an actual blade. Of the two substitutes examined the Thorstrand would be preferred for its ease of handling.

2.4.3. Testing of Inboard Blade Specimens - The results obtained by the 5 flat panels were particularly interesting in the areas of the tip screws and cuff. The tip screws with the larger radial clearance to the shield did not sustain any flashover damage and the Thorstrand and Mesh showed that no untoward dam're was produced by passing the conductor unds: the cuff. These two findings enabled a flight standard design to be produced. To recap, it would be very costly to produce an erosion shield formed to fit the changing spar shape of the inboard end, but, if a standard shield section had its leading edge cut away in this area the two strips left would pass up the flat sides of the spar. The strips could neatly pass under the cuff and with oversize holes to prevent arcing to the cuff bolts the lightning strike would are over the antifret shim to the edge of the cuff.

A blade was manufactured to this standard and was passed to C.L.S.U. for trials. A strike of 188kA 2.76 x 10<sup>6</sup> A<sup>2</sup>t was applied. This was in excess of the required level of 2 x 10<sup>6</sup> A<sup>2</sup>t but nevertheless damage was very minor. The only visual damage incurred was slight debonding of the butt strap (15% est.) This degree of damage would not present a flight hazard, indeed on the subsequent teardown examination the strap proved very difficult to remove.

However, further examination on the dismantled in-board cuff area of the blade specimen showed arcing from the carbon layers to the bolts had resulted in pitting of the cuff bolts. This damage would be of no immediate flight safety concern but could have long term fatigue implications. It was felt that further work was necessary to investigate and resolve this issue.

Following this discovery the flat specimens were re-examined in the pseudo-ouff area and on closer inspection, similar arcing between the carbon and the bolts was found on these specimens. This would appear to reaffirm our belief that the results obtained from flat specimens can be directly related to those produced on an actual blade and that proper interpretation of the results from flat specimens is capable of saving a considerable amount of time, finance, etc. on the re-design of the final blade.

To resolve the issue of the pitted cuff bolt holes, flat specimens have been manufactured which contain a combination of plain drilled holes and bushed holes. The philosophy of the bushes is that any arcing between the carbon layers and the cuff details will now pit the bushes which are not so critical. The strike will safely transfer from bush to bolt.

### 3. CONCLUSION

It is envisaged that this method can and will be used with greater confidence by our designers who up to now only had their basic intuition and C.L.S.U. experience to tide them over until manufacture of a blade was very far advanced and design decisions had been taken which could result in costly changes if found to be incorrect.

#### ACKNOWLEDGEMENT

The author wishes to thank Mr. R. Ellis (Westland Helicopters Limited) and Mr. C. C.R. Jones (Culham Laboratory) for their technical inputs and comments.

#### REFERENCE

1. J. Phillpott, "Recommended Practice for Lightning Simulation and Testing Techniques for Aircraft" Culham Laboratory Report CLM - R 163 dated 1977.

FIG 1. MAIN ROTOR BLADE B.I.M. Indicator Çÿ **Erosion shield** Titanium Heater mat dummy Cuff Outer Wraps Unidirectional Glass Closing Channel ADVANCE TESTING OF LIGHTNING PROTECTION SCHEMES FOR COMPOSITE MAIN ROTOR BLADES (HELICOPTERS) Carbon Nose moulding Skin Glass Inner Wraps Carbon Honeycomb Skin Gless Sidewell slab Unidirectional Carbon/Glass Unidirectional Carbon/Glass Sidewall slab Unidirectional Glass **Backwall** slab 62-6

ADVANCE TESTING OF LIGHTNING PROTECTION SCHEMES FOR COMPOSITE MAIN ROTOR BLADES (HELICOPTERS)

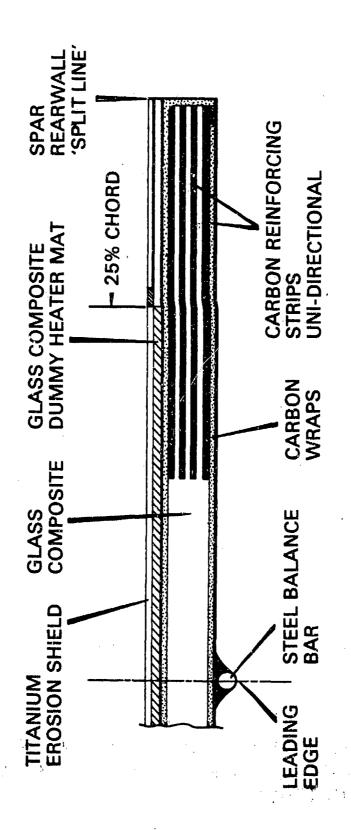
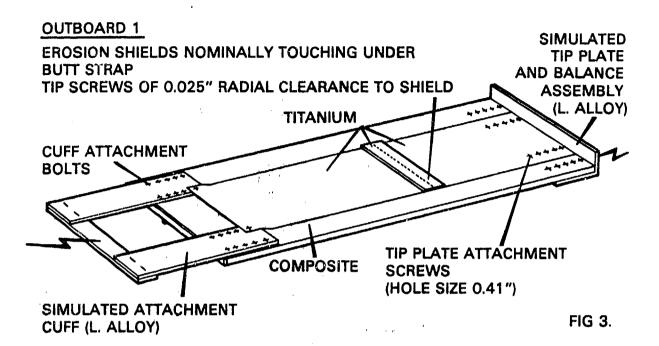
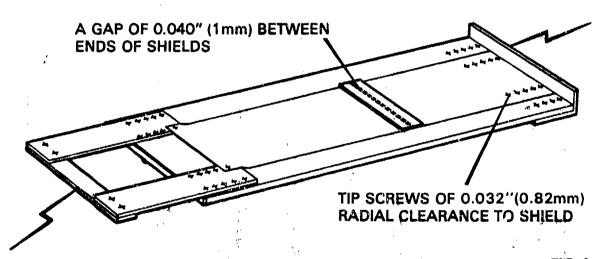


FIG. 2 DEVELOPED SPAR SECTION

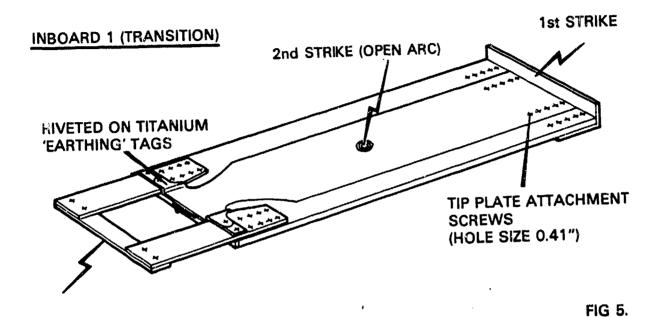


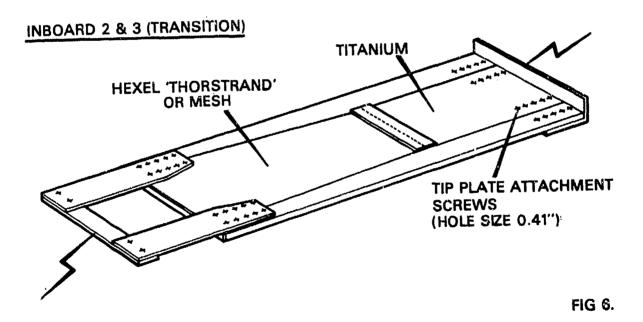
# OUTBOARD 2 IDENTICAL TO OUTBOARD 1 ABOVE EXCEPT FOR-



FIC 4.

ADVANCE TESTING OF LIGHTNING PROTECTION SCHEMES FOR COMPOSITE MAIN ROTOR BLADES (HELICOPTERS)





ADVANCE TESTING OF LIGHTNING PROTECTION SCHEMES FOR COMPOSITE MAIN ROTOR BLADES (HELICOPTERS)

62-9

K



NANOSECOND RESOLUTION OF É,H AND Î IN AIRCRAFT LIGHTNING TEST RIGS B J C BURROWS, CULHAM LABORATORY, ABINGDON, OXON OX14 3DB, ENGLAND

ABSTRACT

-> Many designs of test rig have emerged in recent years incorporating hardwired connections (Culham, LTA, etc.) and design incorporating series open arcs at each end of the aircraft (McDonnell) etc). Important characteristics of the test rigs are not specified, but these characteristics control the generation of large (and usually hf) transients through the fast coupling processes (ie D,B). Both lumped element and distributed element representation of these test rigs and the capacitor banks driving them will be given, and the effects of parameter and geometry variations will be highlighted. It will be shown that quantitative analysis of fast transients (D.B) requires much closer specification of the test rig performance including switch closure time, capacitor bank and connecting line inductance. and the transmission line impedance of the test rig. The recent tests on the Fly-by-Wire Jaguar at Warton near Preston in England showed the need for developing a quantitative relationship between hf transients and the fast coupling processes.

STUDIES OF LIGHTNING INDUCED VOLTAGES on aircraft have frequently included considerations of test methods for assessing an entire circraft in a ground test in which simulated lightning currents are passed between representative attachment points. Such tests are briefly discussed in the SAE AE4L Committee Report(1)\* and Culham Report CLMR163(2).

Many aircraft tests using somewhat different techniques from one another have been carried out in the US, UK and Europe, and in these tests it has been reported that many transients occur in the aircraft wiring which are not proportional to peak current (Î) or peak rate of rise of current (dI/dt or Î) as described in ref 1 and 2.

In particular tests on the Jaguar Fly-by-Wire(3) in England recently, and the Viggen in Sweden the previous year(4) showed that scaling some of the largest amplitude transients with dI/dt or I was not justifiable in terms of transient waveforms and the circuit types. This implies the lumped element equivalent circuit model of the high current circuit shown in figure 1 does not produce an accurate indication of the voltage and current environment for the aircraft. Also work in the US at McDonnell Aircraft Company(5) has shown that transients in

\*Numbers in parentheses designate References at end of paper.

certain types of wiring comprise bursts of decaying oscillations in the MHz range which show no resemblance to the driving current waveform which is usally a unidirectional pulse or damped sinusoid in the range 30-300kHz. These transients are due to the complex nature of real I the I waveforms in practice and the presence of large rates of change of electric field E. has also been pointed out by AFWL that field coupling to the aircraft must be considered as for NEMP. This paper presents an improved model for calculation of the aircraft test system performance which enables the peak transient values of all the relevant parameters (I, I; H, K; B,B; E,E; and D,D) to be calculated. Several important conclusions may be drawn from the improved model which affect the design of test rigs and the validity of results. Predictions from the new model are compared with results using a computer circuit code (NAP2)(6) showing that during the first 60ms very reliable indication of the initial transients of I (and hence B) and D are obtained. It will be shown that 2 distinct time constants dominate the performence of the system, determine the amplitude of the transient fields, and the oscillation frequencies; namely a source time constant to and the aircraft/return conductor two-way transient time tA. A further time constant, the switch closure time to may influence results somewhat but it is felt that this is less significant than Ta and will be considered in future work.

#### REVIEW OF LUMPED ELEMENT MODEL

An elemetary model of the high current circuit of a whole aircraft test rig for induced voltages is shown in figure 1 for a system similar to that used for most tests so far, incorporating a capacitor bank, high voltage switch(us); connecting lines, the aircraft; and return conductors. These are shown diagramatically in figure 2 (taken from ref 1).

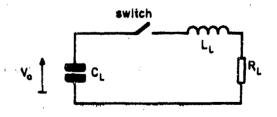


Fig.1 Lumped Element Model

 $L_{L, \nu} \ C_{L, \nu} \ R_{L, \nu}$  are the lumped element circuit values.

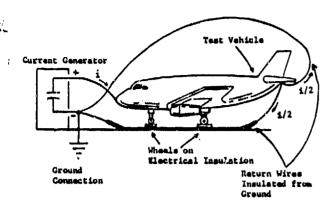


Fig. 2. Typical setups for complete vehicle tests.

Alternative but generally similar schemes are the Culham Quasi Co-axial rig and the new EMP type pulser described by Robb and Fersla(7).

In figure 1 the effective bank capacitance is shown by CL, the total effective inductance of the whole system including aircraft, return conductors, capacitor bank and transmission lines is shown by LL, and RL is the total series damping resistance caused by losses in the switch, the capacitors and inductance plus any added waveshaping resistance.

Using this model, the LF circuit performance can be calculated although it does not predict any hf transients or any hf oscillations. Assuming C<sub>L</sub> is initially

charged to Vo, at switch closure the main parameters are given by

$$\hat{\mathbf{I}} = \mathbf{K}_1 \, \mathbf{V}_0 \sqrt{\frac{C_L}{L_L}} \quad \mathbf{A} \qquad (1)$$

$$\frac{\hat{\mathbf{I}}_L}{\mathbf{I}_L} = \frac{\mathbf{V}_0}{\mathbf{I}_L} \quad \mathbf{A}/\mathbf{S} \qquad (2)$$

$$\mathbf{f} = \frac{1}{2\pi\sqrt{L_L} \, C_L} \quad \mathbf{H} \times (\mathbf{I} \mathbf{f} \, \mathbf{R} < \mathbf{R} \, \mathbf{crit} = 2\sqrt{\frac{L_L}{C_L}})(3)$$

For the purposes of example in this paper, a test rig geometry as in figure 3 is assumed where the aircraft fuselage is represented by a lm radius cylinder. (An arbitary value has been chosen in order to illustrate values of surface H and F later in the paper). The inductance and capacitance per unit length of the 'fusleage' L<sub>0</sub>, C<sub>0</sub> are given by

$$L_0 = 0.2 \log_e \frac{R_2}{R_1} \mu H/m = 0.133 \mu H/m$$
 (4)

$$C_0 = \frac{2\pi \times 8.854}{\log \frac{R_2}{R_1}} \text{ pF/m} = 83 \text{pF/m}$$
 (5)

Therefore the inductance of a 10m aircraft/return conductor system is  $\approx 1.33\,\mu H$ . A total ( $L_L$ ) of 3.8  $\mu H$  has been assumed for the calculation below, that is 1.33 for the aircraft and 2.47  $\mu H$  in the capacitor bank and connection system.

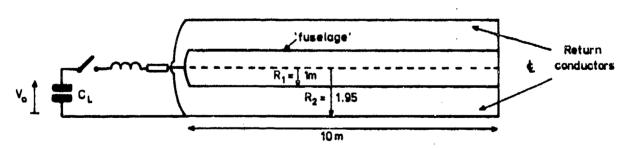


Fig. 3 Simplified 'Aircraft' geometry assumed for this paper. The aircraft fuselage is shown as a cylinder 1m radius, 10m long, with return conductors spaced at an equivalent radius of 1.95 m.

Extensive measurements on the Hawker Hunter (see for instance ref 8) show that the values of I, di/dt and f are usable if the transients occurring in the first few hundred nanoseconds are ignored. An improved model is required to compute these.

Using the values of  $L_L$  above and assuming  $C_L = 0.125\,\mu\text{F}$  and  $V_0 = 380\text{kV}$  (for a severa test), and putting  $K_1 = 0.95\,\text{g}$ 

from (1) 
$$\hat{1} = 0.95 \times 3.8 \times 10^5 \cdot \frac{125 \times 10^6}{3.8 \times 10^6}$$
  
= 66kA

from (2) 
$$\frac{61}{dt} = \frac{380 \times 10^3}{3.83 \times 10^{-6}} \approx 10^{11} \text{ A/s}$$
  
from (3) f = 230kHz

NEW LUMPED/DISTRIBUTED MODEL FOR INITIAL TRANSIENTS

The model is shown in figure 4(a) and comprises two parts: a lumped source, and a transmission line load as in 4(b). In figure 4(b)  $R_{\rm H}$  is not a physical element, it is the transmission line characteristic impedance of the aircraft/return conductor system which is seen by the source for times shorter than  $2 \, k/(3 \times 10^{8})$ . For  $k=10 \, {\rm m}$ ,  $k_{\rm A}=66 \, {\rm msec}$ .

Using this model the transients occurring on the system may be calculated by using the source model at 4(b) which itself is a simple lumped element circuit. The voltage across, and current through,  $R_{\rm s}$  determine exactly the voltage and current impressed on the end

of the transmission line. The capacitor bank and switch are shown in this model as a voltage source turning on at a time to+. It is unnecessary to use the bank capacitance here because in times as short as 60ms the capacitor bank does not discharge appreciably and behaves as an inductor in series with a voltage source, and La is that inductance together with the connecting bus-bar inductance to the load. Such a source model requires that the bank is physically small and close to the aircraft in order that the use of a lumped inductance representation is allowable. If it were physically large compared to N/4 at any frequency of interest it would have to be represented by another transmission line.

For the source model  $I = \frac{V_0}{R} (1 - e^{-t/\tau_0}) \cdot \frac{dI}{dt} = \frac{1}{\tau_0} \frac{V_0}{R} e^{-t/\tau_0}$   $= \frac{V_0}{L} e^{-t/\tau_0}$ 

$$\frac{\partial \hat{\mathbf{u}}}{\partial t} = \frac{\mathbf{v}_0}{\mathbf{L}_a} \tag{6}$$

and from V = I x R.

$$J_{*} \frac{d\hat{\mathbf{V}}}{dt} = \frac{\mathbf{V}_{0} \cdot \mathbf{R}_{u}}{\mathbf{L}_{u}} \tag{7}$$

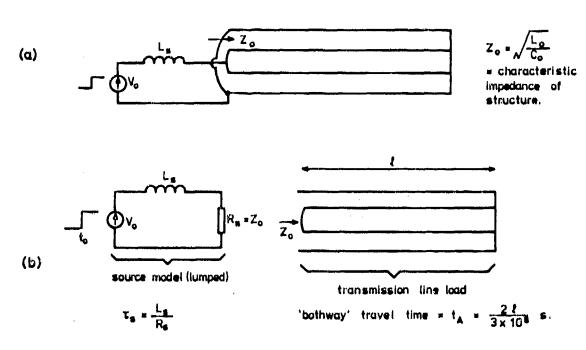


Fig. 4 Proposed Lumped / Distributed Model.

4

(Equation (6) may be compared with equation (2) which gives  $d\hat{I}/dt = V_0/L_1$ .

Thus both dI/dt and dV/dt are exponential decays, time constant  $\tau_g = L_g/R_g$  and whose peak values, occurring at time  $t_0+$  are solely dependent on  $V_0, L_g$  and  $Z_0$ , is depend upon the lumped element source model. Therefore di/dt must be larger than the simple LF lumped element model by an amount depending on the ratio of  $L_L/L_g$ . In fact, dI/dt with a physically close low inductance bank might be many times the LF value. dV/dt yields extremely large values, eg using  $V_0 = 380 {\rm kV}$  as before, let  $L_g = 2.5 \, {\rm pH}$  and  $Z_0 = 400 {\rm pfrom}$  equation (7)

$$dV/dt = \frac{380 \times 10^3 \times 40}{2.5 \times 10^{-6}} = 6 \times 10^{12} \text{ V/s}.$$

For the geometry described for fig 3. ( $r_1 = lm$ ,  $r_2 = 1.95m$ ) and from the relation

$$\underline{\mathbf{r}} = \frac{\mathbf{V}}{\mathbf{r}_1 \log_{\mathbf{c}} \mathbf{r}_2/\mathbf{r}_1} \tag{8}$$

$$\frac{dE}{dt} = \frac{6 \times 10^{12}}{\log_e 1.95} = 9 \times 10^{12} \text{ V/m/s}$$

and 
$$\dot{D} = \varepsilon \dot{E} = 80A/m^2$$

Thus, in summary, this test rig design would produce a pulse whose parameters are: - dI/dt (mean) =  $10^{11}$  A/s; di/dt (peak) =  $1.5 \times 10^{11}$  A/s and D (peak) = 80A/m<sup>2</sup>; all severe values.

To complete the summary of performance, for the structure of fig 3, and for I = 66kA (from this simple equivalent circuit).

$$\hat{H} = \frac{66 \times 10^{8}}{2 \times r_{1}} = 1.05 \times 10^{4} \text{ A/m},$$

$$\hat{H} = \frac{1.5 \times 10^{11}}{2 \times r_{1}} = 2.38 \times 10^{10} \text{ A/m/s}$$
and  $\hat{B} = \mu \hat{H} = 30.000 \text{ T/s}.$ 

The model therefore predicts that a waveform comprising peak values of I, H and D will start at the transmission line and pass down it towards the far end. This combined waveform produces the circuit excitation by combination of electric and magnetic field coupling processes depending on the wiring type and orientation.

After a period of t<sub>A</sub> (= 66ns in the above example) the lumped/distributed model of figure 4(b) is no longer applicable because the reflection from the far end of the transmission line reaches the source, so changing the apparent impedance of the line. In the following section, the initial and subsequent behaviour of the system is shown by the use of a circuit analysis code NAP2.

COMPARISON OF SIMPLE MODEL AND CIRCUIT ANALYSIS CODE PREDICTION

The NAP2 circuit analysis is used to demonstrate the performance of 2 different circuit configurations, with 3 different values of  $L_{\rm H}$ , the source inductance. A short circuited transmission line as in figures 3 and 4, was calculated with values of  $L_{\rm H}$  of 0.5, 2.5 and 10 $\mu\rm H_{\rm H}$ ; and with the same values of  $L_{\rm H}$  an open circuit line was calculated. Of particular interest is the short circuit case with  $L_{\rm H}=2.5\,\mu\rm H$  for comparison with the previous section. Figure 5 shows the system as calculated with MAP2. Calculation was made of 1, 1, V and V in the three places as shown.

Some results of these calculations are shown in figure 6. The time span of the calculation is 500ns, and the decaying exponential values of I and V derived in the previous section are also sketched on these lines. The curve of  $\mathbf{I}_1$  has been included to demonstrate the linear ramp of

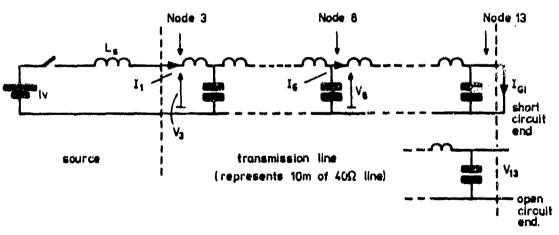


Fig. 5 Representation of aircraft test system for NAP2 calculation.

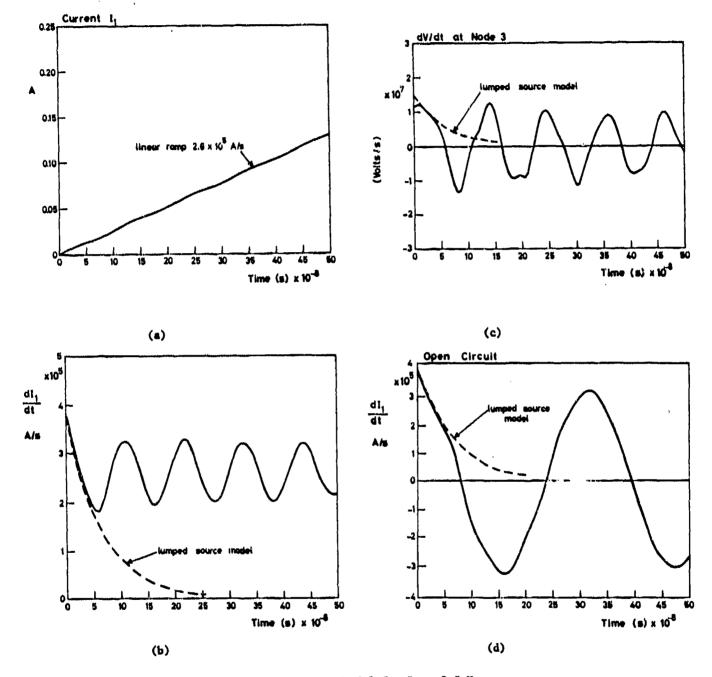


Fig 6 Waveforms from NAP2 and Lumped Source Model for L = 2.5µH

- (a) Short circuit line, current I<sub>1</sub>
  (b) Short circuit line, dI<sub>1</sub>/dt
  (c) Short circuit line, dV/dt at mode 3
  (d) Open circuit line, dI<sub>1</sub>/dt

current to be expected from simple theory on which is impressed an oscillation - frequently called 'hash', but now seen to be an inherent part of such a test system. (If a capacitor has been used for the source, the linear ramp of current would be the initially linear part of a sine wave.) The curve of dI 1/dt confirms that the peak value of di/dt is higher than the linear ramp rate; for smaller values of Lu this is even more marked as in figure 7 for La = 0.5 pH. Both curves show dI 1/dt for the open circuit line, again showing the good fit to the exponential decay until approximately 60ms. However the open circuit line then relaxes into a very low frequency oscillation ( 3MHs) which is essentially the lumped element frequency of the source inductance L resonating with the total line capacitance to ground (approx 830pF). This frequency does not have any relationship to a natural frequency of the transmission line. For the short circuit line the main resonances are 9, 22.5 and 32MHz which are much closer to the natural frequencies of the line itself (n x 7.5MHZ where n is 1,2,3 etc). Table 1 lists the values calculated by NAP2 of dI/dt and dV/dt for  $V_0 = 1$  volt.

It is also important to note that the ratio of the peak di/dt to mean becomes larger progressively further along the line with a maximum at the short circuit. In Table 2 these ratios are listed for all 3 values of  $L_{\rm g}$  for both short circuit and open circuit line.

Table 3 lists the values of dI/dt and dV/dt from the NAP2 calculation on the line together with the predicted values from the lumped source model above.

Thus the electric field (and hence D) and the current (and hence H and B) environment on the surface of the structure is defined at the 3 locations on the structure. Using the NAP2 code the values at any point along the line could be calculated. Local variations in geometry from a circular cross section can be calculated using 2D analysis techniques using a local maximum and minimum values of E and H. The oscillatory transients die away slowly beyond the 500ms time of the present NAP2 calculations. For a unidirectional, or oscillatory current pulse no further transient generation occurs except where associated with non-linearties in the structure and sparking.

# COMMENTS ON RESULTS AND CONCLUSIONS

The hf transient waveforms occurring on test rigs for induced voltage work are seen to be an inherent characteristic of the electrical design and physical size of the rig, and can not be classed as 'hash'. In fact they form an essential part of the electrical and magnetic field environment and provide severe values of D and B during testing. It has been shown that a simple lumped constant source model predicts the initial peak amplitude of the transients and compares very favourably with results from a

circuit code calculation using NAP2. In the next phase of work, experimental measurements will be performed to check the validity of this model.

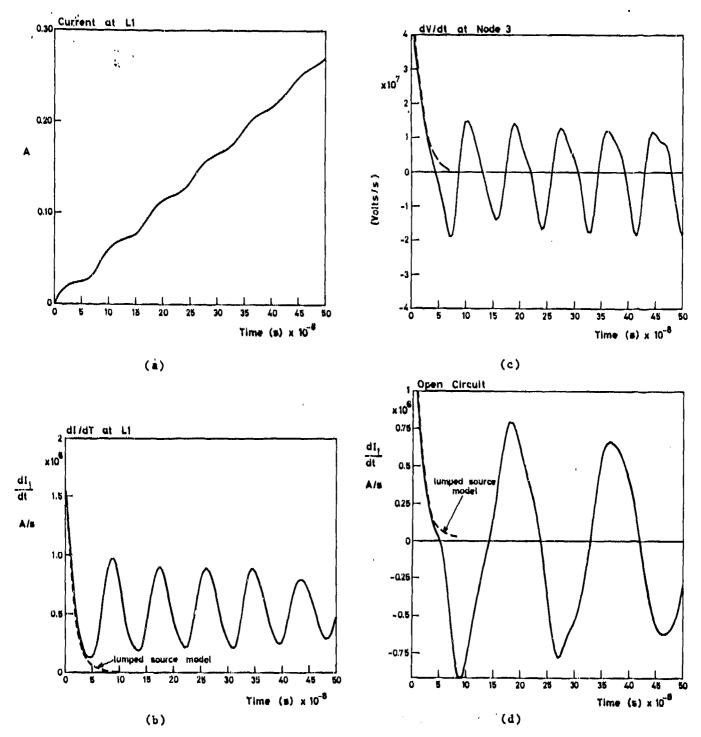
Thus it can be stated provisionally that tests reported in the literature in the past, using the close spaced low inductance test system preferred by Gulham (eg FBW Jaguar, the Hawker Hunter, the Viggen in Sweden and the F16 composite fuselage in the US) all had severe components of fast electric field as a result of the initial transient phenomena discussed in this paper, and the same would be true of tests reported elsewhere.

Moreover, pending experimental confirmation, it appears that the transient levels can be designed into the system by consideration of two time constants T. and t.

Other factors need to be considered in a physical test are those arising from closeness of the ground and the formation of another transmission line between the aircraft, its return conductors and ground. This could introduce additional hf resonances as a result of excitation of the ground/airframe system. Tests should of course be ideally done over a very dry insulating ground. However it is likely that the major excitation processes occur from the initial transient described in the previous section.

These results provide an insight into the sequence of excitation using the two arc method, is the aircraft is situated in a test rig with arc gaps at each end. When the generator fires it first sparks over the the entry gap, charges the aircraft up, and then the far end grounding gap breaks down.

The entry gap spark over is similar to the excitation described above with the transmission line open circuit at its far end. A comparatively low frequency will be excited depending on the source inductance and sircraft capacitance to ground, together with frequencies around W2 frequency of the aircraft test object. This will quickly be changed to a very different type of excitation when the far end grounding gap flashes over so becoming a short circuited structure having the sort of excitation described in an earlier section (it being of little significance in terms of the transients as to whether a voltage source is suddenly applied to the load or is discharged to ground) with different frequencies, and additionaly a steady ramping current with its associated oscillatory rise. From the NAP2 calculation it is apparent that when the spurious low frequency lumped element resonances around 1.7 to 5MHz are ignored that the B and D values are generally lower than those with a short circuited end; additionaly the open circuit case does not include the main LF current ramp (leading to the mean LV current pulse) which is important in testing GR/EP structures; hence the more severe case is the short circuit and case, where high B and D are combined with a lightning type current. This does not infer that simulation is perfect; on the



我是明天京都以外教育了是不是我是 不以及其一年人 神也是我的

Fig 7 Waveforms from NAP2 and Lumped Source Model for  $L_{\rm B}=0.5\mu{\rm H}$ 

- (a) Short circuit line, current  $I_1$  (b) Short circuit line,  $dI_1/dt$  (c) Short circuit line, dV/dt at node 3 (d) Open circuit line  $dI_1/dt$

Table 1A - Results of NAP2 Calculations for Short Circuit and Open Circuit Transmission Line Peak Values of dI/dt and dV/dt for  $L_{\rm s} = 0.5$ , 2.5 and 10 pH.

La pH	<b>s</b> c 0.5	oc	sc 2.	5 oc	sc 10	oc oc
dI <sub>1</sub> /dt A/s dI <sub>6</sub> /dt A/s dI G/dt A/s	8.3 ×10 <sup>6</sup>	7.5 x10 <sup>5</sup>	4.9x10 <sup>5</sup>	3x10 <sup>5</sup>	1.7x10 <sup>5</sup>	9x10 <sup>4</sup>
dV <sub>3</sub> /dt V/S dV <sub>8</sub> /dt V/s dV <sub>13</sub> /dt V/s	2.7 x10 <sup>7</sup>	3.2 x10 <sup>7</sup>	1.15x10 <sup>7</sup>	2.1x10 <sup>7</sup>	3.3x10 <sup>6</sup>	

Table 1B - Results of NAP2 Calculation for sc and oc Transmission Line Value of dI/dt and dV/dt of the most Predominant RF Component (but ignoring the spurious resonance for the oc case (see text)

	0.5		2.5		10	
Ls ph	8C		8C	ос	8C	oc
Frequency MHz	11.4	17	9 • 2	15	8.3	14.6
dI 1/dt A/s	5 x10 <sup>5</sup>	8 x10 4	8x10 <sup>4</sup>	very small	7 <b>x</b> 10 <sup>3</sup>	very small
dI <sub>6</sub> /dt A/s	3.7x10 <sup>5</sup>	1.9x10 <sup>5</sup>	1.7 x10 <sup>5</sup>	1.3x10 <sup>5</sup>	5x10 4	3.2x10 <sup>4</sup>
dI G/dt A/s	7.5x10 <sup>5</sup>	-	2.5 x10 <sup>5</sup>	_	9x10 4	-
dV 3/dt V/s	1.5x10 <sup>7</sup>	6.7x10 <sup>6</sup>	1.25x10 <sup>7</sup>	3×10 <sup>6</sup>	4.1x10 <sup>6</sup>	1 <b>x</b> 10 <sup>6</sup>
dV <sub>8</sub> /dt V/s	2.5x10 <sup>7</sup>	5x10 <sup>6</sup>	1x10 <sup>7</sup>	1x10 <sup>6</sup>	3 <b>x</b> 10 <sup>6</sup>	<5x10 <sup>5</sup>
dV <sub>13</sub> /dt V/s	-	≃1x10 <sup>7</sup>	~	3x10 <sup>6</sup>	_	=1x10 <sup>€</sup>

Table 2 - Ratio of Peak dI/dt to mean dI/dt for Short Circuited line; obtained from NAP2 code.

Lu při	0.5	2.5	10	
rı	2.82	1.45	1.12	
16	1.7	1.88	1.9	
IG 1	2.82	2.46	2.27	

Table 3 - Comparison of Lumped Source Model and NAP2 Calculation of Initial Peak Values of dV/dt and dI/dt

Ls µH	0.5			2.5			10		
	LS Model	NAP2 sc	NAP2 oc	LS Model	NAP2 sc	NAP2 oc	LS Model	NAP2 sc	NAF2 oc
dV 3/dt	6.3 x10 <sup>7</sup>	3.7 x10 <sup>7</sup>	3.7 x10 <sup>7</sup>	1.5x10 <sup>7</sup>	1.25x10 <sup>7</sup>	1.2 x10 <sup>7</sup>	3.9x10 <sup>6</sup>	3.6x10 <sup>6</sup>	3.3x10 <sup>6</sup>
dI <sub>1</sub> /dt	1.58x10 <sup>6</sup>	1.54×10 <sup>6</sup>	(1.54x10 <sup>6</sup> )	3.8x10 <sup>5</sup>	3.76×10 <sup>5</sup>	3.76x10 <sup>5</sup>	9.9x10 <sup>4</sup>	9.75×10 <sup>4</sup>	9.9x10 <sup>4</sup>

LS model = Lumped source model

NAP2 sc = NAP2 calculation short circuit end NAP2 oc = NAP2 calculation open circuit end.

contrary, the successive phases of natural lightning contact to an aircraft probably give high D components (and possibly high B components) at different times from the low frequency I and the main current pulse. For example D is probably at its highest at leader contact with the aircraft when currents, I and B may be comparatively small, or at least be of very short duration. It is vital for specifying a ground test adequately that the values of D, the frequency content and duration need to be obtained for inflight strikes. It is to be hoped that the NASA, US Air Force and French work on inflight measurements will yield sufficient data for the purpose of specifying test design in due course.

### REFERENCES

以原公文的 解於學者 免禁事

が不可能を対する。

1 Report of Committee SAE AE4-L, June 1978, ('Blue Book'),

2 J Phillpott, 'Recommended Practice for Lightning Simulation and Testing Techniques for Aircraft' ('Green Book'). CLM-R163 1977.

3 R H Evans, J Bishop, 'Induced Transients in Simulated Lightning Test of the Fly-by-Wire Jaguar Aircraft'. Paper at this Conference.

4 B I Wahlgren, B A Olsson, C A Luther 'Lightning Testing of the Viggen Aircraft'. Proceedings of the International Conference on Lightning and Static Electricity, Oxford, March 1982. Published by Culham Laboratory.

5 W G Butters, D W Clifford, K P Murphy, K S Zeisel, B P Zuhluan, 'Assessment of Lightning Simulation Test Techniques'.
Proceedings of the International Conference on Lightning and Static Electricity, Oxford, March

1982. Published by Culham Laboratory.

6 T Rübner-Peterson, 'NAP2 - A Nonlinear Analysis Program for Electronic Circuits' Users Manual 16/5-73. Institution of Circuit Theory Telecommunications Technical University of Denmark.

7 R A Perale, F J Erikson, P H Rudolph, 'Vol II Electromagnetic Coupling Modelling of the Lightning/Aircraft Interaction Event' EMA Report 81-R-21 Vol III.

8 B J C Burrows, C A Luther, P Pownall, 'Induced Voltages in Full Sized Aircraft at 10 ll A/s' Proceedings of IEEE Symposium on EMC Seattle Washington 1977.

9 B J Wallace, B J C Burrows, R T Zeilter, A J Ledwig, K Wiles, 'Composite Forward Fuselage Systems Integration Vol II'. AFFDL-TR-78-110 September 1978. (Report on Induced Voltage Measurements in F16 Composite Forward Fuselage with Simulated Lightning Pulses.)

## ACKNOWLEDGEMENT

The author would like to acknowledge the support given by the Procurement Executive, Ministry of Defence, UK for the work reported in this paper, and to Miss B Stone for the NAP2 analysis work.

The Sandia Lightning Simulator

Ву

James C. Bushnell and J. G. Kostas Sandia National Laboratories Albuquerque, New Mexico 87185

#### ABSTRACT

Sandia has developed a lightning simulator to produce currents equivalent to those of severe natural lightning, (99 percentile), on external loads on the order of 8 microhenries. The simulator can produce from 1 to 4 pulses, with the first pulse having peak current of 200 kiloampere, rising to this value in 2 microseconds, with an e-folding decay time on the order of 75 microseconds. The interpulse spacing may be varied over a wide range. A continuing current on the order of 300 amperes for 1 second may also be included. The total action integral is as high  $3 \times 10^6$  ampere  $^2$  - second, and total charge transfer 300 coulombs. The design and implementation of this facility and associated instrumentation will be discussed.

This paper was not available for incorporation into this book. Therefore, it will be published at a future date.

# AD P002212

FULL-SYSTEM TESTS USING THE SANDIA LIGHTNING SIMULATOR

Robert A. White Sandia National Laboratories, Albuquerque, New Mexico 2

ABSTRACT

Direct-stroke, very high-level natural lightning is simulated with a developmental lightning simulator, which has been used to apply fast-rising, high-current, high-energy outputs to full-scale operational systems. Samples of the wide range in output capabilities of this high-voltage, multiple-pulse simulator are described. Circuit considerations related to its use for testing physically large test items are discussed. The simulator is primarily used for conducting internal Sandia National Laboratories test programs, but example waveforms from direct-strike lightning simulation tests made for the Navy with functional F-14 and F/A-18 aircraft are also presented.

LIGHTNING SIMULATION TESTING of full-scale, fully operational systems at pulse levels corresponding to low-probability, maximum-threat conditions is a subject of relatively widespread interest. Severe-threat current levels as high as 200 kA peak are being specified for an increasing number of systems. High rates of rise in current are more frequently being associated with hazards to equipment from natural lightning. Simulation test current rate of rise (di/dt) as high as 2 x 10<sup>11</sup> A/s is also being specified more frequently.

The need for high-current lightning simulators has been described in numerous previous publications and conferences, and much has been written concerning natural lightning and subjects related to it. The 1982 IEEE Transactions on Electromagnetic Compatibility(1)\* contains many papers and their references which describe and summarize much of what is known about lightning and its interaction with aircraft. It includes a paper by Uman and Krider(2) that provides a good review of lightning subjects and also a comprehensive bibliography of literature related to lightning measurements and models.

This paper discusses some aspects of lightning simulation testing of items ranging in size up to that of full-scale operational military aircraft. A partial discussion of the Sandia National Laboratories, Albuquerque (SMLA) lightning simulator itself and some of its capabilities are included. Bushnell and Kostas(3) provide a more detailed description of the simulator elsewhere in this conference. Several different output pulse voltage and current waveforms related to use of the simulator for lightning simulation testing are discussed below. No attempt is made in this paper to discuss instrumentation or test item responses.

Natural lightning encompasses such a wide distribution of high-voltage, high-current characteristics that the task of simulating it is made easier by using some of the high-voltage, pulsed-power technology that has developed over the years in several of the national laboratories. A little of that technology, as related to the Marx generators and magavolt switches used in this simulator, is also mentioned.

Some of the discussion in subsequent sections is intended to support the concept that severe (high-level) lightning can be more easily simulated with physically small objects or systems having low-impedance than with large, high-impedance test items. The great majority of lightning simulation testing with this simulator is done with test systems smaller than full-scale fighter sircraft, so it is easier to do. The versatile nature of this

developmental simulator is made more apparent by describing some of the large-item high-level tests that have been made.

#### LIGHTNING SIMULATION

CROWBARRED MARX LIGHTNING SIMULATOR -Underdamped RLC capacitor discharge circuits using the crowbar technique to clamp or short out the capacitor when peak current is reached have been used for pulse stretching here for more than 25 years and also at several of the other national laboratories. This method can provide fast-rising, long-duration, unidirectional pulses. Use of crowbarred Marx surge generators was strongly supported by F. W. Neilson(4) in 1977 for simulation of very high-level lightning currents. How to crowber megavolt or higher voltage circuits was an important factor related to the success of such a simulator. Testing described by Parker(5) confirmed and demonstrated the feasibility of using a gas-dielectric, triggered-spark gap as a 1-MV crowbar switch.

Utilization and developmental operation of this new lightning simulator facility during the past year or so has confirmed the performance characteristics and capabilities predicted and described by Neilson. Once the capability of using the simulator for lightning studies was demonstrated, the request for tests became so great that continued development efforts had to be greatly curtailed. Since then, nearly constant test operation of the simulator has displaced its continued development to brief intervals between test programs.

The advantages of a crowbar-switched Mark circuit over other approaches for a simulator were described by Neilson(4) along with the important transient circuit parametric relationships for several approaches. The underdamped crowbar switched RLC circuit approach to generating a severe threat current pulse is many times more efficient than using an overdamped bank.

APPLICABLE TEST CRITERIA - The type of test and the test levels to be used need to be carefully considered relative to the nature of the item being tested. Simulation of low-occurrence-probability, severe-threat, very high-level lightning places stringent demands on lightning simulator performance and on the item being tested. The need for a high-level simulator may be very important if critical systems must be tested with severe simulated lightning environments. Very high-level testing may then be the only way of obtaining the required information.

Operational survivability or safety needed for other test items, on the other hand, may be much less critical, and/or exposure probabilities may be low. It may be important not to overdesign or overtest, especially when the relative consequences of lightning damage or service disruption are minimal. Very large,

Numbers in parenthesis designate references at the end of the paper.

unjustified costs and large design and performance penalties for normal nonlightning environments may result from providing unnecessary overprotection.

Simulation of all of the more important characteristics of natural lightning requires a versatile system with a broad range of capabilities. Simulation of simplified versions of the extreme-level high-current pulses is a smaller task but still not easy. A number of sources such as Cianos and Pierce(6), the SAE committee AE4L report(7) or MIL-STD-1757(8) propose or establish simplified pulse criteria for lightning simulation. Natural lightning characteristics and summaries of proposed or established simulation specifications are provided in many references. The papers in the proceedings of the Culham Laboratory, England 1975 Conference on Lightning and Static Electricity, including those of Pierce(9) and of Phillpott(10) give good summaries and discussion of lightning test criteria.

Even after simplification to bare essentials, a single, severe-level, return-stroke, simulated pulse is not easy to show in its entirety in a simple plot. A simulation pulse shown in Fig. 1 has an amplitude that ranges over three orders of magnitude and a time duration that ranges over seven orders of magnitude.

Simulation of just one pulse may not be enough to satisfy some test requirements. Over a decade ago, Cianos and Pierce proposed a three-pulse "Applied Model" for simulation of severe lightning. Since natural lightning often has many return strikes, several pulses are a better simulation than just one. Their severe lightning applied model has three. The first has a 200-kA peak and the two subsequent strokes each have 100 kA. More recent proposals and criteria have been in general agreement and propose two pulses with the same 200-kA and 100-kA levels. MIL-STD-1757, entitled "Lightning Test Waveforms and Techniques for Aerospace Vehicles and Hardware," specifies a 250mp to 1-second interval between pulses.

DOUBLE PULSE WITH FULL-SCALE AIRCRAFT -The majority of items tested at this facility require double-pulse simulation with continuing current at some point during the test process. Fig. 2 shows the current waveform record from one such test with the Navy F/A-18 Hornet jet sirplane made during August 1982. This record was obtained using one of the lightning facility Tektronix 7612 digitizers, which provides a split time base capability. The horizontal timebase shown is divided into five separate time intervals. Approximately 16 ms was the time interval between pulses. Time separations between pulses have been selected between 10 ms and 800 ms for other tests.

This test also included continuing current in the several hundred ampere range between pulses and continuing well past the second pulse. Time of rise for each of the two pulses was 2 µs.

Double-pulse lightning simulation with continuing current was applied several times to the F/A-18 and was also used in June 1982 for lightning testing of the Navy F-14 Tomcat jet airplane. Additional description of the use of the lightning simulator for the Navy airplane tests has been treated by Ewing(11) and by Perals and Easterbrook(12).

調源

NULTIPLE PULSE SIMULATOR ARRANGEMENT - Several different combinations of impulse generators have been used in the two main tanks of this simulator system. Using multiple sources allows multiple-stroke lightning simulation. Output pulse characteristics can also be more easily adapted to different specific test requirements using multiple sources with different inductive circuit elements to suit the test requirements. Fig. 3 shows multiple isolation spark gaps arranged to allow multiple sequential pulses during a single test. Use of the isolation gaps allows time separation between pulses to be set to any interval from microseconds to 1 second.

Most of the testing with the simulator has been done using only one crowbar spark-gap switch (GCB) and one isolation spark gap in two simulator tanks. Sometimes one each of the crowber switch is used with a single-impulse generator, and at other times, two generators are crowbarred simultaneously with a single switch. Make-up inductors (L<sub>MU</sub>) are used between a crowbarred Mark generator and its test load to provide the desired wave shape. Different inductance values are built into these coils for different generators or different combinations of generators. The product of total loop inductance and source capacitance are adjusted to make (π/2)√LC equal to the desired time to peak. Most of the tests have had

a nominal 2- $\mu$ s time to peak (t<sub>p</sub>). The very simplified diagram of Fig. 3 is not intended to be comprehensive. Many things are not shown in the diagram, including the continuing-current generator system. It is used to provide sustained current flow for durations out to about 1 s. The continuingcurrent system is also connected to the output for those tests requiring it. Since it is a lower voltage system, it is located outside of the simulator tanks. Low-level current from the continuing-current system is started with the first high-amplitude, return-stroke, current pulse and continues until the arc extinguishes between 0.5 and 1 s. The continuingcurrent component starts around 1 kA and slowly decays to about 300 A.

The oil-insulated, coaxial interconnection between simulator tanks provides a connection path to the load but also acts as a short transmission line that affects the detailed features of the output pulse. During tests with series spark gaps in the test-load circuit, the capacitance of the oil line acts somewhat like a peaking capacitor and briefly increases the initial rate of rise in current. Different kinds of terminal arrangements and

return-circuit arrangements are used to connect to the test item.

The maximum stored energy of 650 kJ from all four impulse generators combined could deliver at most  $2 \times 10^6$   $A^2 \cdot s$  action integral to a total load circuit resistance not exceeding 0.3 ohms. MIL-STD-1757 specifies a single-pulse action integral of  $2 \times 10^6$   $A^2 \cdot s$  for the initial 200-kA high-peak current component A of qualification tests for full-size hardware subject to direct-stroke attachment.

TEST SETUP PHYSICAL LAYOUT - Since the SNLA lightning simulator was originally developed to test relatively small systems, physical layouts of the facility were not oriented toward testing full-size, operational aircraft. Smaller test items are generally located indoors between the two main simulator tanks. They may be vertically supported above a vertical-axis, high-voltage terminal or may be located near it but displaced to one side. horizontal-axis high-voltage bushing can be used as an alternate terminal arrangement. It mounts on the side of an oil-filled, cross transition that allows switching to an oilinsulated dummy-load coil mounted in a horizontal cylindrical container on the opposite side.

The arrangement of the simulator tanks is shown in Fig. 4 with the cross, horizontal bushing and oil-insulated load coil. The dummy-load coil allows the simulator to be fully checked out with a representative load just prior to a subsequent shot into the real load. An Air-Launched Cruise Missile, ALCM, with its return circuit, is shown connected to the simulator output. Lightning simulation tests with the ALCM are scheduled during 1983.

The relative locations of the four separate Mark surge generators used in the simulator are also shown in the diagram. Other components used in the oil-filled simulator tanks to trigger, crowbar, waveshape, etc., are not shown in this figure.

When the full-size aircraft were tested, there was not room within the building for them. An oil-insulated, coaxial transmission line was constructed so that the horizontal high-voltage bushing shown in Fig. 4 could be located outside of the building. The ALCM tests require that portions of the missile and its return circuit be outside in an adjoining temporary addition.

RETURN CIRCUITS - Current returning to the simulator from the test object is usually routed back to the output terminal ground through multiple conductors. The conductors are positioned to provide the minimum practical value of total-load-circuit inductance and still not greatly disturb the surface currents in the test item. The return circuits are often made coaxial unless it is either impractical or no particular need to do so exists.

The return circuit needs to be adequately spaced from the test item so that unintended flashovers between them do not occur. A series spark gap is shown in the previous figure near

the tail of the missile. The test circuit is completed by breakdown of this gap between the ALCM and its return circuit. At least a small are gap is always used in any test requiring continuing current. However, it can be located at either end of the test item. Instead of using a short free-air spark gap to complete the test circuit, some setups employ a long-spark in conjunction with high-peak current tests.

The return circuit for the F/A-18 is sketched in Fig. 5, which shows the aircraft surrounded by cables. The wheels were down for both airplane tests and supported on highvoltage insulators. Twenty cables were arranged around the plane in a nearly coaxial array for both aircraft tests. The cables were supported by wooden stands and routed both to the tail and, with a branching array, to the left wing. Both the F-14 and the F/A-18 lightning tests were conducted for the Naval Air Systems Command. The overall return circuit structures and systems for both sirplanes were of similar design. The return circuits were furnished and fabricated on site by Electro Magnetic Applications, Inc. (12) An overview of the tests is provided by Perala(12) in another paper in this conference.

The inductance value of the test item and its return circuit becomes relatively high when something as large as an airplane is being tested. The simulator must have high voltage to drive high-peak currents with high-rising di/dt through the load. This is discussed further in later sections.

IMPULSE GENERATORS - The design of the four Mark generators used in this lightning simulator was adapted from a 3.2-MV design used in a number of nonlightning SNLA pulsed power applications.(13) The basic 3.2-MV arrangement was designed over a decade ago, and a number of working variations have evolved from it since then.

The physical arrangement of this multiply folded impulse generator design is shown in Fig. 6. Each generator has 32 separate energystorage capacitors arranged in a dual- polarity Marx circuit. Sixteen field- distortion, midplane, triggered spark gaps are used to switch the capacitors in series after the bipolar charging is complete. Each of the capacitors in charged to a maximum of 100 kA. Most of the lightning simulator tests have been made with less than full-charge voltage. full-charge voltage, each sulphur hexafluoride (SF6) insulated spark gap holds off 200 kV. Each of the four impulse generators used in the lightning simulator are of the same design and physical size. Each has 32 of the 100-kV capacitors, but two different values of capacitence are used. The capacitors in the lower capacity generators are a little over 0.7  $\mu F$ , and the higher capacitance units in the same size container are each nearly 1.35 µF. This provides the higher capacitance Mark generators with nearly twice the energy of the lower

capacitance units.

The Mark circuit was devised by E. Mark in Germany in 1924, and many variations have been adpaired from it in the nearly 6 decades that have passed. The dual polarity charged Marx is one of several that has been used extensively at SNLA. This bipolar design has demonstrated high reliability in PRFA-I(14) where 36 separate 116-kJ units are simultaneously erected to a circuit-driving voltage near their design rating of 3.2 MV.(15) The resultant 4-MJparallel output pulse of the PBFA-I accelerator is used for research in the Particle Beam Fusion program at SNIA. A somewhat larger 6-MV, 400-kJ generator has been designed and tested for the 14-MJ PBFA-II accelerator where 36 of them will again be used in parallel.

The impulse generators in the lightning simulator and all of the others mentioned are oil-insulated. Multiply folded, oil-insulated, bipolar generators have a desirably low source circuit inductance and furnish much higher voltage to inductance ratios than are generally possible with air-insulated impulse generators.

The bipolar Mark circuit has a number of advantages in high-energy pulsed-power applications, even though it requires both positive and negative equal-charging voltages. A simplified schematic is shown in Fig. 7 for a four-capacitor, two-spark gap circuit. Because only one-half as many spark gaps are required, maintenance is reduced and reliability improved. It is relatively easy to fold into compact, low-inductance configurations. It does not need an isolation gap between its output and the test load (for single pulses) although one may be used. The output polarity of this type generator can usually be reversed quite easily.

The basic 3.2-MV PBFA Mark generator has more voltage than was needed for lightning simulation testing with low-inductance loads. Therefore, when this 3.2-MV design was adapted for use with the lightning simulator, it was split in two. The two resultant, normally series-connected halves were then joined in parallel to make a unit with four times the capacitance and twice the current capability but with only a 1.6-MV output, i.e., one-half of the original design voltage. Fig. 8 shows the discharge circuit for this lower voltage Mark generator.

All four of the simulator generators had the same electrical design parameters for the first year of operation, which included the periods during which both of the Navy sirplanes were tested. Erected, series, output capacitance for each of the generators was 88 nF. The highest level peak currents were applied to the sircraft by combining the outputs from parallel impulse generators into a single-pulse. Two of the Mark generators have since been rebuilt to furnish more energy from the same size units. Replacement of the capacitors provided an output capacitance of about 165 nF. One high-C Mark can now supply about the same

output as two of the original generators. Low-level tests can still be furnished by using the two generators that retained their original capacitors.

CROWBAR SWITCH AND ITS TRIGGER - The performance of the simulator is very dependent upon the crowbar switch and its operating characteristics. It must reliably hold off the full-output voltage of the erected Marx, but almost immediately thereafter, it must be capable of being triggered near the time that the voltage across it passes through zero. It must pess very high currents that are even higher than that through the load. Crowbar switch current, as shown later, is the composite of load current and any Marx generator current oscillation that occurs. The switch electrodes must survive the high current and charge through it for some reasonable number of discharges.

The switch used with the lightning simulator facility was also adapted from PBFA-I and related pulsed-power technology. The PBFA switch is a 3-MV, gas-dielectric, triggeradspark-gap trigatron used for pulse forming. Electrical triggering with the switch dielectric gas composed entirely of sulphur hexafluoride is used in PBFA and most of the other pulsed-power applications of the switch. It is a larger version of an earlier (1972) 3-MV, SNLA-developed trigatron described by Tucker. (16) Thirty-six separate switches, each holding off 2.5 MV, are simultaneously triggered within about 10 ns in the PBF accelerator to dump 36 separate water-dielectric capacitors. These same switches do not have stringent timing requirements, as used in the lightning simulator, but they must be capable of being triggered at low voltage.

Crowbar switching right at peak current is difficult because switch voltage at that time is very near zero. Crowber switching within ±30° (or within (π/6)/LC) of peak current Ip, still provides 0.866 Ip. For an undamped LC oscillation, voltage at 60° or 120° is 0.5 of the initial voltage. The problem then becomes one of triggering the crowbar switch at instantaneous main-electrode voltages that do not exceed 50% of the initial peak voltage. minimum main-gap voltage at which a specified trigger mechanism will ensure reliable operation has for many years been called cutoff voltage. Cutoff voltage differs for different trigger mechanisms and also is dependent upon other dynamic conditions related to use of the gap. Low ratios of cutoff voltage to holdoff voltage (or to operating voltage) allow generation of better pulses from the simulator. Good pulses can be provided when crowbar switching occurs either before or after peak current. Switching after peak has been used for much of the development testing. Switching before peak has been investigated more recently, and it better satisfies some requirements.

Electrical triggering and SF6 gas were used with the unmodified trigatron during early

developmental operation of the simulator, and good output pulse results were obtained. It switched near peak current and permitted full 100-kV charging of the capacitors and open-circuit erection voltages near 1.6 MV. When problems were encountered with the electrical-trigger pulse generator, other crowbar triggering approaches of interest were explored.

Infrared (IR) laser triggering has been used for much of the development testing during the past year. The trigatron configuration was modified by removing the trigger pin and shaping the hole though the main electrode to allow focus of the laser beam within the main gap. The modified laser triggered switch has been used with lower dielectric strength gas compositions containing 50% nitrogen, 40% argon, and 10% SF6. Many tests have been made with the IR lsser triggering, and it has been moderately successful. Good triggering is obtained using the mixed gas, but the gas dielectric strength is much lower than it is for pure SF6. Evan with increased gas pressure, maximum holdoff voltage is reduced. Mark output and charging voltages have been limited to about 80% to avoid exceeding pressure limitations of the spark-gap housing. The lowered voltage reduces maximum stored energy in the impulse generators to about 64% of rated energy.

Work with ultraviolet (UV) laser triggering is in progress. This will permit use of 100% SF<sub>6</sub> in the crowber switch so that full-rated, 100-kV charge voltage can be used. The UV laser trigger is expected to provide very good performance and will probably be used with both simulator tanks. As time permits, any other triggering methods, such as electrical triggering, that appear to offer lower operating complexity, lower cost, or improved relia-

bility may also be investigated.

A new oil tank for developmental testing with an additional Marx generator is located near the two main simulator tanks. It is expected to be operational soon, which will then allow crowbar and triggering studies and other development activities to proceed in parallel with scheduled simulation tests. Crowbar switch and triggering development that leads to an improved cutoff-to-holdoff ratio should have a good payoff in terms of increased system versatility and reliability. Since the Mark generators are connected to provide only one-half of their normal design voltage, crowbar switch operational characteristics remain as one of the main temporary constraints to operating the simulator at higher voltages.

FAST-RISING, HIGH-CURRENT, WIDE PULSE — The simulator has the capability of providing very fast-rising, very high-amplitude, long-duration current waveforms. Waveforms of current and action (∫1²dt) are shown in Fig. 9 for a 1- by 380-µs very high-amplitude pulse delivered into a low-impedance load during development test series conducted with the simulator in the apring of 1982. Crowber was above 200 kA and the 200-kA pulse level was

sustained for over 20  $\mu s$  with a slow decay to half value of nearly 400  $\mu s$ . This pulse achieved an action integral of 1.1 x  $10^7$  (A^2-s) and delivered a unidirectional charge of greater than 300 C. This pulse would be too severe for most test items, but it illustrates possible capabilities of the simulator. Since this test series was made, two of the impulse generators are being converted to even higher energy units.

Both inductance and resistance are added to the test circuit for most tests. Inductance is usually added to slow down the current rise and provide a time-to-current peak of about 2 µs. Added resistance can be used to speed up the decay and shorten the tail of the waveform to about 50 µs at half amplitude. Usually any special pulse-shaping components that need to be added to the circuit are located within the simulator tanks below the oil fill level. This provides them with adequate high-voltage oil insulation and prevents voltage flashovers that might otherwise occur in air.

LOW-CURRENT TESTS - A broad range of output current waveforms is made possible by the arrangement of the simulator. Lower current pulses are provided by selecting only one impulse generator and lowering its charge voltage to about half of rated value. Currents down to about 50 kA peak can be provided without significant changes in circuit components. Even lower peak current was desired for the early portion of both airplane test series. Current waveforms with peaks of 10 to 15 kA were provided by shunting the inductance of the test load with an even lower inductance added to the circuit and located within the simulator tank. A schematic of this arrangement with the F-14 Tomcat is shown in Fig. 10. A bypass inductor  $(L_{\rm p})$  with an inductance value about one-fourth that of the downstream load shunted about three-fourths of the simulator current to ground. The remaining fourth of the output current provided the desired low-current pulse.

WIDE HANGE OF CURRENT PULSES - As a part of the tests with the F-14A and the F/A-18 Navy aircraft, different current levels were desired. Initial tests were commenced at relatively low currents of 10 to 15 kA peak. The test levels were increased as confidence in the instrumentation and recorded results was acquired. This is a fairly common sequence of events for most test items. The relatively high inductances of the airplanes and their return circuits constituted higher than normal load impedances for the simulator. Even so, the tests went quite well.(11)

The two example simulator pulses shown in Fig. 11 were recorded during the F/A-18 test series. The simulated lightning pulse was injected nose-to-wing in both of these tests. These particular tests did not use long-spark gaps to complete the test circuit to the aircraft. Nose-to-tail injection was also used in many of the tests. Long-spark air gaps were used to complete the test connections for a

portion of both the nose-tail and nose-wing tests. These were called E-field tests, and they allowed the field on the surface of the aircraft to build up until breakdown of the long-spark gap occurred. Charging of the oil-transmission line plus the aircraft itself acted somewhat as a peaking capacitor. Start of initial current was delayed until sparkchannel breakdown, and then current rose very rapidly during the discharge of the locally stored dielectric energy. During E-field tests, local currents generated at the aircraft would not pass through the simulator injected current monitors and would not be recorded. Since the two waveforms in Fig. 11 are not E-field-type tests, the early portions of the current rise are smoother. These sample waveforms into the F/18A show that a 10-to-1 range in peak current is available for a given test load circuit configuration.

LONG-SPARK, HIGH-CURRENT TESTING - When long-eperk gaps in free air are used to establish connections to the test load, such as in the previously described airplane tests, portions of the circuit are subjected to very high voltages. Production of open-load-circuit voltages sufficient to break down the gaps requires that comparable high voltages also be present in the simulator. Some simulators, particularly those used primarily for generating controlled specified voltage waveforms, have sufficient voltage but are not designed to also deliver high current. Partly for this reason, combination of long sparks and high current into a single test has not been considered practical at some other facilities.

This simulator emphasizes the value of using high voltage and low inductance, but the greater emphasis is put on high voltage. This makes it quite practical to combine long sparks and high current into the same test.

One of the reasons stated for long-spark tests is to furnish high-voltage shock-excitation or fast E-field changes at the test system. Long 150- to 300-mm air gaps were used for some of the tests with both Navy airplanes. This was intended to allow charging of the aircraft and then to furnish a subsequent high dV/dt when the detach are commenced. This quits likely did occur at least for portions of the airplane. However, for aircraft surfaces near the simulator terminal, the average rate-of-change in voltage was greater both in duration and in value during voltage rise than during voltage fall.

Rapid, large drops in test-item voltage occur with the long spark if subsequent L di/dt voltages are low either from low L, or from low di/dt. When breakdown current begins and the L di/dt voltage has a high value, it may approach the voltage that was required to break down the long spark path. In that case, the voltage appearing between the point of current injection and the nearest point of the return circuit may not be greatly different whether or not a long series spark path was used in the

downstream circuit. When the long-spark breakdown occurs, terminal voltage cannot fall very far before it equals the high L di/dt voltage of the load circuit.

For fast pulses and high-inductance loads, the rising voltage at the start of the pulse reaches a very high peak value with or without either long or short series spark gaps. With spark gaps, all or a portion of the voltage is applied to the gap until it breaks down. However, that may or may not exceed the subsequent L di/dt voltage, depending on gap length.

For predominately inductive loads, simulator tests in the 100-kA peak current range can produce voltage rises to 1 MV in 100 to 200 ms. This corresponds to dV/dt rates—of—rise in voltage of 0.5 x  $10^{13}$  to 1.0 x  $10^{13}$ . Local maximum values of available instantaneous current, together with local distributed capacitance, control the maximum possible value since dV/dt = 1/C. Sometimes this also can be treated as a case of pulse reflection at the junction of mismatched transmission lines.

COMBINED HIGH-VOLTAGE AND HIGH-CURRENT TESTS - Discussion in previous sections makes it apparent that fast-rising, high-current tests have much high voltage associated with them. Combined high voltage and high current have been provided in some tests, and for most test items up to several microhenrys such combinations are not greatly constrained by simulator limits.

The voltage waveform shown in Fig. 12 is one example of the terminal voltage developed during a 100-kA peak current nose-to-wing injection into the Y/A-18. The voltage spike at the front results from the oil-filled transmission line being terminated in a predominately inductive load. Most of the oil-line extension from the simulator to the sirplane has a characteristic impedance of about 40 ol**ms.** The pulse applied to the transmission line reflects and increases when it arrives at the output terminal. This explanation is somewhat oversimplified because there are other distributed circuit parameters also involved in the process. The waveform shown consists basically of L di/dt voltage components. The sharp change that occurs a little more than 3 He into the pulse is related to crowbar switching.

The voltage waveforms appearing at the input to the airplane during high-current E-field, long-spark tests are not much differant from the voltage shown in Fig. 12 for a test without the long-spark gap. Depending on the spark path length, the voltage in a long-spark test may go somewhat higher and last a little longer before the drop due to breakdown occurs, but the fast decrease only goes down to the appropriate L di/dt voltage level related to the test. Consistent results were obtained with computer circuit analysis simulations of the circuit. When a long-spark test is combined with a low-current (and/or low-di/dt) test, then the sharp voltage change related to

gap breakdown can be large.

The voltage waveform shown in Fig. 12, is composed of the sum of incremental series voltage drops along the surface of the sirplane and of those developed along the return conductors. For a true cylindrical coaxial return, almost all of the voltage drop would be associated with the length and the per-unit-length inductance only of the central conductor.

Whatever the diameter of an object struck by natural lightning, its diameter is likely to be small compared to the effective diameter of the natural system return path. Inductive voltage drop along the length of a solid metal conductor or vehicle surface subjected to a di/dt of 2 x 10<sup>11</sup> can be on the order of 200 to 300 kV/m.

Several tests were made with the F-18 in which a primary objective was to develop voltages sufficient to cause sparkover across an insulating surface. The simulator was set up to furnish a noncrowbarred damped oscillatory pulse with about one-half of critical damping resistance.

The first test developed the voltage waveform shown in the upper part of Fig. 13. This waveform resulted when a 0.7-m-long flash-over occurred between the output terminal and a return circuit cable. The local return circuit spacing was increased and the simulator voltage was lowered to produce the intended test load breakdown in the next shot. The voltage waveform in the lower half of the figure was recorded on that test. Also, some adjustment may have been made to the sparkover length of test item surface.

Peak currents for these tests are shown in Fig. 14 for the first and second tests, respectively. Nearly 90 kA was delivered in the first test with most if not all of it into the return circuit flashover. The subsequent 55-kA pulse was all delivered to the test aircraft. The difference in circuit inductance between the two tests is evidenced by the nearly 1- $\mu s$  difference in pulse periods.

The simulator system described here has been used primarily to simulate current waveforms. The majority of the tests have been with low-impedance loads, or at least they become low once current through an isolation gap is established. Load inductances are often only a few microhenrys. MIL-STD-1757 and other test criteria specifications describe both current waveforms and voltage waveforms. Very little voltage testing has been done with this simulator. Major circuit components needed for voltage simulation may be similar to that needed for current simulation. There appears to be no major reason why this simulator system cannot be also used for some types of voltage simulation if the need for it becomes more important in the future.

COMPUTER SIMULATION OF CRECUIT RESPONSE -Understanding and predicting what is going on in a simulator circuit is sided by simplified diagrams of the setup. Good rough estimates of performance can be obtained by paper-and-pencil application of basic relationships. However, the task of analysing and predicting circuit performance becomes large when there are many variations of interest or the actual circuit becomes complex.

Actual circuits may have a number of stray or second-order elements that modify or affect performance. Stray capacities, stray-inductances, sections of changing characteristic impedance transmission lines, and other such factors that can contribute to superimposed oscillations may be present. Deliberately added shunt or damping resistors may have been added to various portions of the circuit to eliminate or minimize such oscillations. The number of circuit parameter combinations can become very large when test loads and test Computer levels or conditions are varied. simulation and analysis becomes valuable when simple methods become unwieldy or ineffective in treating a complete representation of the circuit.

The Air Force SCEPTER(17)(18) program is one of several transient circuit analysis aids that has been used frequently at SNLA. It has been quite valuable for simulating many circuit variations related to use of the lightning simulator. SCEPTEE is a general transient analysis program that was developed about 15 years ago by IBM on contract to the Air Force Weapons Laboratory (AFWL).

An example current waveform computed by SCEPTRE for selected values of simulator parameters is shown in Fig. 15. Crowbar occurs 3.4 µs after peak current in this waveform. All other waveforms in the circuit being analyzed can be examined with plots available from SCEPTRE. Such examination and study can yield valuable insight and information concerning simulator operation.

The computed voltage waveform in the lower portion of Fig. 15 is that appearing across a 3-µH load inductance as a result of the upper current waveform. The synthesized simulator circuit for these two waveforms included distributed parameter elements representing the oil lines between tanks and the load terminal stray capacitance in addition to other physical elements that have been included in the simulator tanks. The initial spike on the voltage waveform is due to the peaking capacitor effect of the unmatched oil transmission line and terminal capacitance. The sharp change in voltage at crowbar switch time occurring at 3.4 µs is like that of measured simulator records. Undamped ringing similar to that appearing on the voltage waveform also appeared on the current waveforms prior to the addition of winor circuit elements. Such parasitic element oscillations have been reduced on output current waveforms by adding damping elements at various locations in the circuit. Some ringing still shows up on some of the more sensitive L di/dt waveforms. Even though natural lightning current has such unpredictable noise on it, class current pulses are often preferred for simulation purposes because the responses of the system-under-test can be more easily interpreted.

A composite of three computed simulator current waveforms is shown in Fig. 16. The upper solid trace, I, is load current. The middle trace, I, is Marx current, which continues to oscillate from energy trapped in inductance and capacitance of the Marx/crowbar shorted loop. Crowbar current, I, is then the combination of load current and the oscillating Marx current. Load current and Marx current do not exactly coincide before crowbar time because a physical resistor has been placed in the real circuit across the crowbar switch to help damp-out noise appearing on the Marx terminal voltage that is applied to the crowbar switch.

The large oscillation of Marx current after crowber can also be damped out with minimal reduction of initial peak current by additional series resistance placed in the Marx portion of the crowbar loop. This is shown in the lower portion of Fig. 16 for the same circuit parameters and the same voltage with only two changes. Crowbar timing was moved to an earlier time at 1.5 µs so that it occurred. on the front side of peak current. Also, an additional series resistance was added on the Mark generator side of the crowbar switch. The added resistance rapidly damps out the oscillation in the low surge impedance,  $(\sqrt{L/C})$ , Marx/ crowbar loop because it is a large fraction of critical damping resistance in that loop. The added I ohm has little affect on load peak current because in the load circuit loop, it is a small fraction of critical damping resistance, Rc = 2/LC.

#### SIMULATION CIRCUIT CONSIDERATION

This section discusses some elementary considerations related to simulation and natural lightning circuit parameters such as resistance, inductance, action, energy, etc. It is not intended to be comprehensive. Clifford, Crouch, and Schulte(19) review much additional information on lightning simulation and testing.

HIGH RATE OF RISE IN CURRENT - Many natural lightning events have very fast-rising currents even though inductance of an established channel can be very high. Current pulses with di/dt values of 1 or 2 x 10<sup>11</sup> A/s have been specified for some simulation testing. Clifford, Krider, and Uman(20) propose that even faster rising simulator pulses be considered for some studies.

Achieving high rates of rise in current from a lightning simulator can become a difficult development task unless the means for providing a high V/L ratio is available. Obviously, two ways are possible: the inductance must be kept low or the voltage made very high. Making inductance as low as practical

appears desirable, but with a crowbarred Mark generator simulator, increasing the driving voltage (or maximum erection voltage of impulse generator) is a better way of achieving the requisite high V/L ratios, providing that a suitable crowbar switch is available. Load/source interaction is reduced and the simulator becomes more versatile because it can furnish the required pulses for a greater variety of test item characteristics. If total loop inductance is made too low, the maximum permissible load circuit resistance must also be low if a long L/R decay time on the tail of the waveform is needed.

If the inductance of the impulse generator is permitted to constitute a significant fraction of the total inductance then a proportional fraction of  ${\rm Li}^2/2$  magnetic energy is trapped in the Mark/crowbar circuit loop. The trapped energy is unavailable to the load and oscillates back and forth between inductance and capacitance of the Mark/crowbar loop. The SNLA pulsed-power Mark, as modified for this simulator, has a very low value of source inductance, so this is not generally a problem. Each 1.6-MV impulse generator has a source inductance of about 1  $\mu{\rm H}$ .

The underdamped RLC circuit clamped or crowbarred near peak furnishes an energy-efficient way to furnish the needed high V/L ratio. With a 1.6-MV full erection voltage, di/dt of 2 x  $10^{11}$  is attainable with a total loop inductance up to 8  $\mu$ H.

HIGHER RESISTANCE LOADS - The probability of whether or not any particular natural lightning event will be high current or low current is relatively independent of the electrical impedance of any small-dimension object (airplane, building, troe, etc.) that may be encountered in the path. A given high-current natural lightning event (with its low probability of occurring at all) could well encounter either a low-impedance or a high-impedance object in its path.

Tremendous local energy deposition and damage might occur with a high-resistance object such as a tree; whereas, an event with similar electrical characteristics may have only slight effect on a heavy, low-resistance, copper grounding conductor. The tree or a moderate resistance object may shatter or disassemble with explosive violence as a result of the natural lightning stroke. Thermal damage in a good conductor would result if the stroke action integral exceeded the melting action value or the vaporization action value related to its cross section.

The greater energy deposition in highresistance materials as compared to metals was described by Plumer and Robb(21). They indicate an energy deposition in graphite composite 2,000 times greater than in aluminum in accordance with their relative resistance values.

Fortunately, test loads of interest for this simulator have had a low resistance. They generally have been all metal. Even with the nirplanes and series spark gaps, the total load circuit resistance has been low. Greater stored energy and higher load circuit inductance would be required if it became necessary for a simulator to deliver 200 kA with a half-amplitude pulse width of 50 µs into a significantly greater load circuit resistance.

Load circuit loop inductance must be made higher for high values of load resistance if pulse width is to be maintained. Over 70 µH of inductance would be required for a total load circuit loop inductance of only 1 ohm. Magnetic energy stored in 70 µH of circuit inductance at 200 kA would be 1.4 MJ. This energy would have to be initially supplied from energy stored in the impulse generators. Even with the high-efficiency crowbarred Marx system, this requires more stored energy than is presently available with this simulator.

This may be an appropriate place to note the obvious. When 1.4 MJ of magnetic energy stored in load circuit inductance is released to a total load circuit resistance of 1 ohm, the resultant action is 1.4 x  $10^6$   $\Lambda^2 \cdot s$ . If both the desired pulse action integral and effective load resistance are known, their product yields a quick estimate of the minimum  $\text{Li}^2/2$  magnetic stored energy required of a simulator.

LOAD SCALING AND SIMULATOR TYPES - Manmade objects or systems that may encounter
lightning are generally dimensionally small
compared to the dimensions of a system producing natural lightning. The small relative size
of the system struck prevents its resistance or
inductance from having any significant effect
on the action integral or other pulse parameters of the natural stroke main current path.

The dimensions of a natural lightning system can be extremely large. As a part of lightning studies being made in connection with the NASA Shuttle program, B. Vonnegut(22), with the State University of New York, has obtained photographic records of lightning with horizontal dimensions of 60 km or more. This was from a not particularly large winter storm over Brazil in June or July of 1982. NASA astronauts have visually observed single lightning events apparently spreading over several hundred kilometers.

Natural lightning is a "stiff" high-current source that is little affected by the impedance of some local object intercepted by it. This is a result of natural lightning having extremely high driving voltages and very high circuit inductances. Inductances of the cloud-to-ground portion of the current path may range from about 0.5 to 5 µH. Capacitances related to a single return stroke portion of the wave may be on the order of 10,000 nV.

Very large quantities of energy are stored in a natural lightning stroke, at peak current, in the form of Li<sup>2</sup>/2 magnetic energy. One hundred MJ of magnetic energy would be stored in a 5-µH channel (on the order of 1 km long) of a severe stroke having a peak current of 200

Total circuit electrical parameters of a lightning simulator may be significantly changed by a high-impedance load or test item. For a lightning simulator to be quite insensitive to load or test item impedance or resistance requires a "stiff" source having high voltage and the capability of driving high current through a high total circuit inductance. Such a system would provide good current waveform regulation and have charge and action integrals that were relatively independent of successively varied test item parameters.

A simulator circuit with a stiff source or a high (V)(L) product becomes increasingly important when high values of test object impedance are considered. However, practical laboratory physical constraints preclude simulating more than a tiny fraction of the high (V)(L) product of natural lightning. That is partly why different kinds of simulators have been used to simulate different aspects of natural lightning.

Low-voltage, low-impedance simulators can be used to produce high current into metal or near-short-circuit test items. Even at high current, little energy is deposited in the test item so the high current can be produced through it with modest or low driving voltages. Melting and vaporisation can not be adequately studied, however, because of the rapid increases in resistance that occur.

High-voltage, low-current (low-energy) simulators can be used to evaluate breakdown characteristics of insulators or high-resistance test items if energy dissipation occurring during the transition period that occurs at breakdown can be ignored. If the breakdown is likely to occur around the item through a medium such as air, this may still be a fair test. Combinations such as these may allow many kinds of things to be tested without the need for high-energy simulators.

The requirements on a simulator are much more demanding if it is to be used for producing high currents through high-resistance and/or high-inductance test items. If the test item can be either low impedance, high impedance, or anything in between, then the simulator system must be much more versatile. Circuit-driving voltage usually must then exceed the maximum voltage drop to be developed across the load and high energy must be svailable to the load.

Total circuit inductance is often the most important controlling consideration in simulator selection if a very high rate of rise of current and a high-peak current value are both required. Once it is established, almost all other circuit parameters are constrained.

Impulse generators using the voltagemultiplying Marx circuit furnish a good way of impedance, matching the generator to the load. Clamping the capacitor near peak current changes, the circuit into a magnetic energy source that is similar to the natural lightning circuit. Large values of charge and action are available from the slow L/R decay of the current.

There are more than enough potential test items having relatively low inductance and resistance to keep this facility busy for some time. However, if it became particularly important to test some higher impedance loads, it appears that interesting levels of simulation could be obtained. The 210-kJ generators might be reconnected in their normal 3.2-MV configuration and then both placed in parallel to provide a 3.2-MV, 83-mF source. The resulting 420 kJ arrangement could produce a single-pulse peak current near 200 kA with current rate of rise of 2 x 10<sup>11</sup> into a total circuit load of 16 µH. This would be practical only if output-pulse-related voltage insulation and crowbar holdoff voltage were adequately high.

#### SUMMARY AND CONCLUSIONS

A variety of different tests with the SNLA developmental lightning simulator has demonstrated that practically all of the important characteristics of natural lightning can be simulated during full-scale system tests. Peak current, current rate-of-change, charge, action, continuing current and high-voltage values related to severe lightning can be furmished with present technology. Using multiple, separate, Marx-circuit impulse generators crowbarred near peak current provides an energy-efficient lightning simulator with the needed characteristics. Current rates of rise of 2 x  $10^{11}$  A/s, peak currents of 200 kA, action integrals up to 10" amp2 .s. charge of 80 C, along with double pulses and continuing current, have been produced. The modular nature of the simulator has produced a versatile capability with a wide range of selectable output characteristics. Although it is still in development, it already has been valuable both for testing full-size sirplanes and physically smaller systems.

### ACKNOWLEDGEMENT

The SNLA lightning simulator facility has resulted from the contributions of many people. Numerous internal and external organizations in the U.S. Departments of the Mavy and the Air Force have cooperated or have provided specific portions of program funding.

The continued efforts and direction of F. W. Neilson have coordinated and brought together broad-base support and interest. Persons responsible for much of the development of the simulator include J. C. Bushnell, J. G. Kostas, R. J. Goode, and W. P. Brigham. Many others also contributed to the successful tests with the simulator and its operation, including

R. W. Ewing, B. Stiefeld, O. Milton, W. Vandermolen, and personnel from EG&G Kirtland Operations group.

#### REFERENCES

- 1. "Special Issue on Lightning and its Interaction with Aircraft." IEEE Transactions on Electromagnetic Compatibility, Vol. EMC-24, No. 2, May 1982.
- 2. M. A. Uman and E. P. Krider, "A Review of Natural Lightning: Experimental Data and Modeling." IEEE Special Issue, Transactions of Electromagnetic Compatibility, Vol. EMC-24, No. 2, May 1982.
- 3. J. C. Bushnell and J. G. Kostas, "The Sandia Lightning Simulator." This conference and SAND82-2274, June 1983.
- 4. F. W. Neilson, "An Extreme Lightning Test Facility." Unpublished internal report, Sandia Laboratories, 1977.
- 5. R. L. Parker, "Feasibility Studies for Crowbarring One Megavolt on the LILI Facility." Sandia Laboratories, SAND78-1700, April, 1979.
- 6. N. Cianos, and E. T. Pierce, "A Ground-Lightning Environment for Engineering Usage," Stanford Res. Inst. Tech. Rep. No. 1, Project 1834, Aug. 1972.
- 7. "Lightning Test Waveforms and Techniques for Aerospace Vehicles and Hardware." Rep. of SAE Committee AE4L, June 20, 1978.
- 8. "Lightning Qualification Test Techniques for Aerospace Vehicles and Hardware." Military Standard MIL-STD-1757, June 17, 1980.
- 9. E. T. Pierce, "Natural Lightning Parameters and their Simulation in Laboratory Tests." Lightning and Static Electricity Conference, Culham Labs, England, April 1975.
- 10. J. Phillpott, "Simulation of Lightning Currents in Relation to Measured Parameters of Natural Lightning." Lightning and Static Electricity Conference, Culham Labs, England, April 1975.
- 11. R. T. Ewing, "Performance of the Sandia Lightning Simulator during F-14A and F/A-18 Aircraft Lightning Tests." This conference and SAND82-2276, June 1983.
- 12. R. A. Perala and C. C. Easterbrook, "An Overview of the F-14A and F/A-18 Lightning Tests." This conference, June 1983.
- 13. S. A. Goldstein, G. W. Barr, J. P. VanDevender, and T. H. Martin, "Considerations for the Design, Implementation, and Effective Operation of Sandia's Super-power Generators."

  3rd IEEE International Pulsed Power Conference, Albuquerque, NM, June 1981.
- Albuquerque, NM, June 1981.

  14. T. H. Hartin, J. P. VanDevender, G. W. Barr, S. A. Goldstein, R. A. White, and J. F. Saamen, "Particle Beam Fusion Accelerator-I (PBFA-1)." 1981 Particle Accelerator Conference, Washington, DC, March 1981.
- 15. R. A. White, "Modular Accelerator Interconnecting and Operating Systems for PBFA-1." 3rd IREE International Pulsed Power Conference, Albuquerque, NM, June 1981.

16. W. K. Tucker, "A 3 Megavolt Sulphur Hexafluoride Trigatron." Sandia Laboratories, SC-DR-72 0506 September 1972.

SC-DR-72 0506, September 1972.

17. H. W. Mathers, S. R. Sedore, and J. R. Sents, "SCEPTRE Support." IBM Corp., Contract F29601-67-C-0049 for AFWL, Kirtland AFB, NM, April 1968.

18. H. W. Mathers, "SCEPTRE (System for Circuit Evaluation and Prediction of Transient Radiation Effects)." IBM Corp., included in G. W. Zobrist, "Network Computer Analysis," Boston Technical Publishers, 1969.

19. D. W. Clifford,, K. E. Crouch, and E. H. Schulte, "Lightning Simulation and Testing." IEEE Transactions on Electromagnetic Compatibility, Vol. EMC-24, No. 2, May 1982.

20. D. W. Clifford, E. P. Krider, and M. A. Uman, "A Case for Submicrosecond Rise-time Lightning Current Pulses for Use in Aircraft Induced Coupling Studies." IEEE International Symposium on Electromagnetic Compatibility, 79CH1383-9 EMC, San Diego, CA, October 1979.

21. J. A. Plumer and J. D. Robb, "The Direct Effects of Lightning on Aircraft." IEEE Special Issue, Transactions on Electromagnetic Compatibility, Vol. EMC-24, No. 2, May 1982. 22. B. Vonnegut, O. H. Vaughan, Jr., and

22. B. Vonnegut, O. H. Vaughan, Jr., and M. Brook, "Photographs of Lightning from the Space Shuttle." Bulletin of the American Meteorological Society, Vol. 64, No. 2, Feb. 1983.

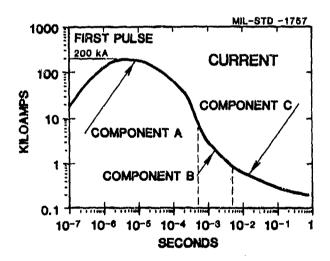


Fig. 1 - A very severe lightning stroke idealized representation. Initial return stroke component A; intermediate current component B; continuing current component C

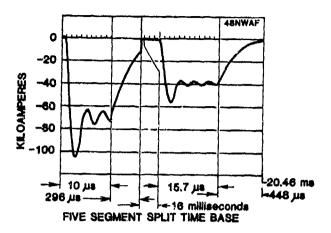


Fig. 2 - Double-pulse simulated lightning current waveform applied to full-size Navy jet airplane

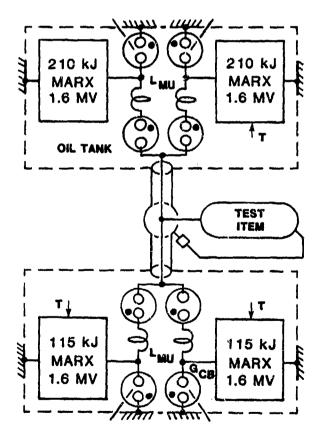


Fig. 3 - Simplified block diagram of one arrangement of lightning simulation system

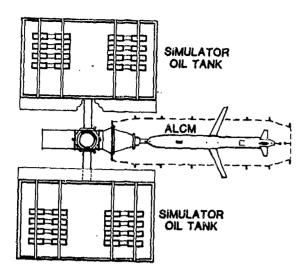


Fig. 4 - North and south oil-filled simulator tanks connected to test load and its return circuit

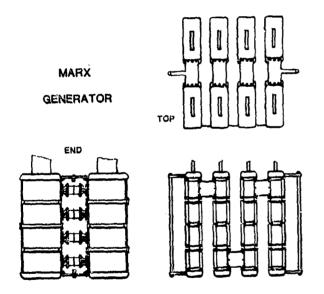


Fig. 6 - Typical SNLA pulsed-power Marx impulse generator modified for lightning simulator



Fig. 5 - Navy Hornet F/A-18 aircraft enclosed with multicable return current circuit

ğ

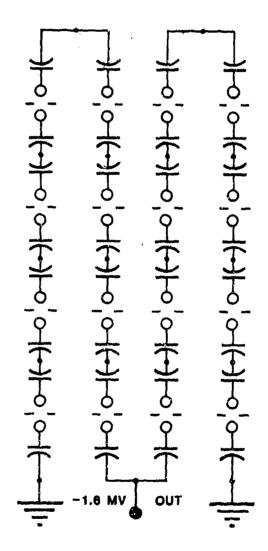


Fig. 7 - Bipolar Marx surge generator simplified charging diagram  $\mathbf{r}$ 

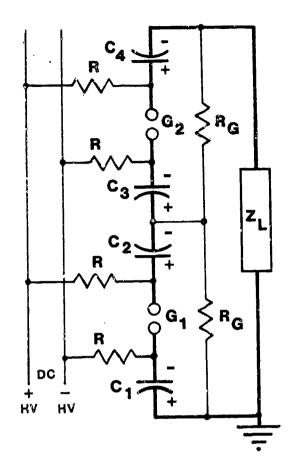


Fig. 8 - Discharge path diagram of impulse generator modified for lower 1.6-MV output

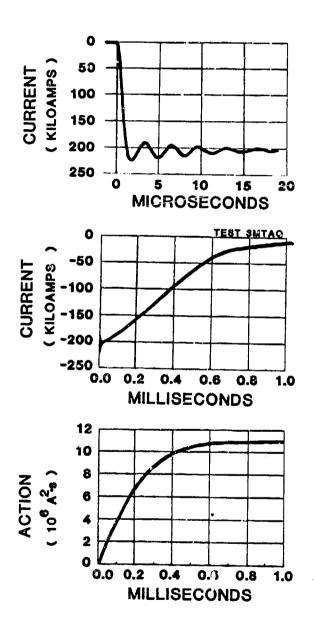


Fig. 9 - Very high 200-kA current and 1.1 x  $10^7$  A<sup>2</sup>·s delivered into low-inductance test load

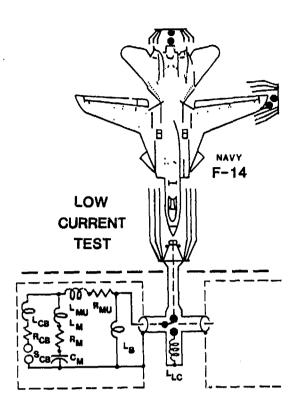


Fig. 10 - Full-size functional F-14 Navy Tomcat and crowbarred Marx simplified diagram with current bypass inductor  $\mathbf{L}_{\mathbf{B}}$  to ground

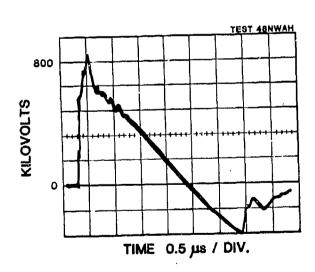
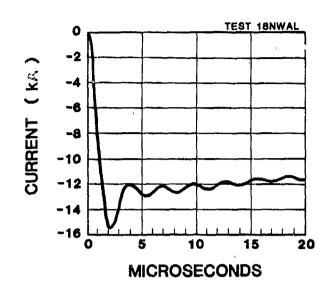


Fig. 12 - High-voltage pulse developed at nose of F/A-18 with 100-kA current pulse



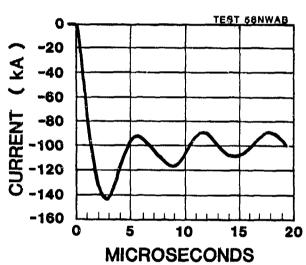


Fig. 11 - Lov-current and high-current nose-to-wing pulses into F/A-18 aircraft

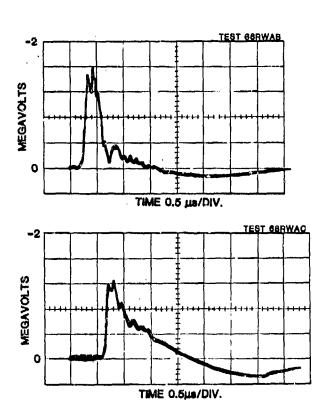
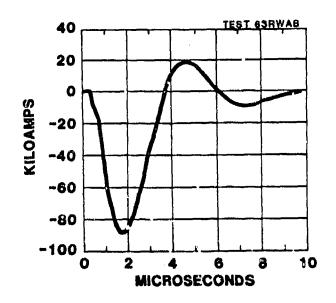


Fig. 13 - High-voltage pulses developed at full-scale aircraft



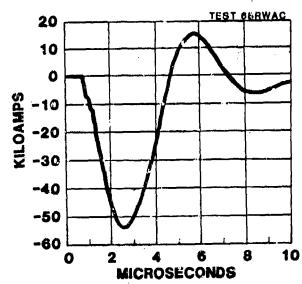


Fig. 14 - Noncrowbarred current pulses corresponding to voltage rulses shown in Fig. 13

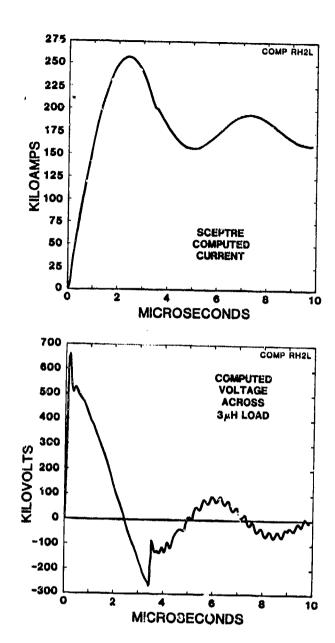


Fig. 15 - SCEPTRE-computed voltage and current for one simulator and load combination

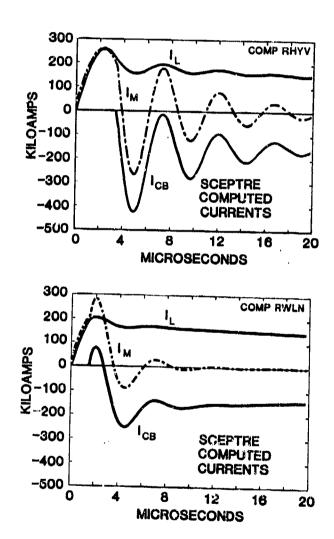


Fig. 16 - SCEPTRE-computed current waveforms for load current I, Marx current I<sub>M</sub> and crowbar switch current 1<sub>CB</sub>. (Upper) Crowbar after peak current; (Lower) Crowbar before peak current and with 1 ohm added in Marx/crowbar loop

A STATE OF THE STA

LIGHTNING INTERACTION WITH USAF AIRCRAFT

John C. Corbin, PhD Aeronautical Systems Division, Wright-Patterson AFB, Ohio

ABSTRACT

This paper categorizes and analyzes data from 877 USAF aircraft lightningrelated mishap reports involving 56 sircraft types over a 13-year period (1970-1982). Aircraft are grouped into six general classes: Attack, bomber, cargo, fighter, trainer, and helicopter. Data are tabulated under two major headings: Operational conditions at the time of the lightning strike, and the effects of the strike. Operational conditions include aircraft attitude, aircraft altitude, outside air temperature, aircraft location (with respect to clouds), precipitation/turbulence, and electrical activity prior to the strike. Effects of the strike include attachment point, interference/outage, effect on mission, effect on personnel, structural damage, electrical/electronic damage, and repair/replacement costs. Interference/outage in the form of an abnormal condition observed following a strike was experienced in 20 percent of the reported lightning incidents. Aircraft mission was affected in 37 percent of the reported incidents, but in most cases where lightning caused a precautionary abort subsequent ground inspection of the aircraft revealed only minor structural damage. Structural damage was experienced in 78 percent of the reported incidents. Electrical/electronic damage was sustained in 8 percent of the reported incidents.

A TEN-YEAR HISTORY of USAF lightning mishaps was published several years ago in a table that documented [69] separate incidents involving aircraft damage (1). The table listed four damage categories: structure, electrical/instruments, fuel, and other. Three mishap categories were listed: minor, major, and catastropic. Unfortunately, the ten-year period over which the incidents occurred was not stated.

This paper categorizes and analyzes data from 877 USAF aircraft lightning-related mishap reports over a thirteen-year period (1970-1982). The reports are on computer file at the Air Force Inspection and Safety Center, Norton 478, California. The reports stem from AF Requirements from 127-4 which establishes the requirements for reporting USAF mishaps (2). However, the regulation does not explicitly state what must be included in a lightning mishap report. As a result, the reports vary widely in content and are often remiss in reporting useful lightning-related information.

## LIGHTNING MISHAP REPORTS

Fifty-six different aircraft types (including helicopters) were involved in the 877 reported USAF lightning-related mishaps over the thirteen-year period (1970-1982). In some instances, only a single aircraft of a raticular type was involved in a lightning incident over this period. To preclude disclosure of information relating to a particular aircraft, the fifty-six separate aircraft types have been grouped into six general classes: attack, bomber, cargo, fighter, trainer, and helicopter. In the grouping, the FB-111 aircraft is classed as a fighter and the E-4 as a cargo aircraft.

Table 1 lists reported USAF lightning mishaps by aircraft class over the 1970-1982 period. Mishap data for 1982 are incomplete since not all reports are yet on file as of this writing. Each aircraft loss is denoted by an asterisk. Cargo aircraft comprise almost half of the total number of mishaps, fighters about thirty percent, and bombers and trainers about ten percent each. Attack aircraft and helicopters total about two percent.

Table 2 lists reported USAF lightning mishaps by year. More mishaps occurred in the early 1970's than in later years because the increased cost of fuel resulted in fewer flights and flight hours. Table 3 lists reported USAF mishaps by month. The most mishaps occurred from March through October; the least occurred from November through Zebruary. Again, an asterisk denotes one aircraft loss.

#### DATA CATEGORIES

In analyzing the information contained in each lightning wishap report, the lightning

\* Numbers in parentheses designate References at the end of the paper.

strike incident report form which has been used by U.S. commercial sirlines was used as a guide (3). Two major categories were established under which data could be recorded: operational conditions at the time of the strike, and the effects of the strike.

OPERATIONAL CONDITIONS - This category was divided into six subcategories: sircraft attitude, sircraft altitude, outside air temperature, aircraft location (with respect to clouds), precipitation/turbulence, and electrical activity prior to the strike.

Attitude - The attitude was divided into four conditions: climb, level flight, descent, and approach. Over ninety-six percent of the reports stated the attitude.

Altitude - The aircraft altitude was divided into four ranges: less than 5,000 feet, 5,000 to 9,999 feet, 10,000 to 15,000 feet, and greater than 15,000 feet. Seventy-five percent of the reports stated the altitude.

Outside Air Temperature - The outside air temperature was divided into three ranges: less than -5°C, -5°C to +5°C, and greater than +5°C. Only fifteen percent of the reports stated the outside air temperature.

Location - The aircraft location with respect to clouds was divided into four categories: above clouds, within clouds, below ceiling, and between clouds. Only forty-nine percent of the reports explicitly stated the location with respect to clouds.

Precipitation/Turbulence - Weather that the aircraft was experiencing was divided into: rain, hail/snow, turbulence, and clear. Only thirty-seven percent of the reports explicitly stated the immediate weather at the time of strike.

Electrical Activity - Electrical activity appears in such forms as static buildup on additional receivers and interphones, interference on scope displays, or visible St. Elmo's fire. Only seven and one-half percent of the reports explicitly referenced electrical activity prior to the strike.

EFFECTS OF THE STRIKE - This category was divided into seven subcategories: attachment point, interference/outage, effect on mission, effect on personnel, structural damage, electrical/electronic damage, and repair/replacement costs.

Attachment Point - Lightning attachment to the aircraft was divided into seven locations: nose, wing, fuselage, tail, antenna, external tank/stores, and other. Attachment points are normally determined by ground inspection after landing. Eighty-one percent of the reports explicitly stated at least one attachment point location.

Interference/Outage - Lightning strikes to aircraft can cause a variety of effects on aircraft systems. In many cases, the effects are temporary and can be remedied in-flight by the crew. These effects are divided into seven categories: communications, navigation, flight instrumentation, engine, electrical, fuel, and

other. Communications includes VLF, HF, VHF, and UHF radio transmitters/receivers. Navigation includes OMEGA, LORAN, ADF, VOR, ILS localizer/marker beacon, ILS glideslope, TACAN, DME, weather radar, navigation computer, and compass. Flight instrumentation includes various flight indicators (altimeter, angle-of-attack, airspeed), CADC, and autopilot. Engine includes flameout, rollback, compressor surge or stall, rpm gauge, and engine warning light. El atrical includes generator, circuit breaker, fuse, warning/caution light, EED, transformer, aircraft power, pitot and windshield heater, and internal lights. Fuel includes explosion/fire, flow/ quantity gauges, and venting. "Other" includes EW jammers, radar warning receivers, IFF, and environmental controls/instrumentation. Interference/outage was experienced in twenty percent of the reported lightning incidents.

Effect on Mission - The effects of lightning on the sircraft mission were divided into four categories: none, precautionary abort, emergency landing, and loss of aircraft. Aircraft mission was affected in thirty-seven percent of the reported incidents. In most cases where the mission was aborted, subsequent ground inspection of the aircraft revealed only minor structural damage.

Effect on Personnel - The effects of lightning on personnel were divided into five categories: not stated/none, flash blindness (momentary), electrical shock, crew ejection, and fatality. Only six percent of the reports explicitly stated that lightning had an immediate affect on personnel.

Structural Damage - Damage to structure/external components caused by lightning was divided into nineteen categories: nose (pitot, radome, other), wing (skin and tip, control surfaces, other), fuselage (skin, canopy/windshield, other), tail (horizontal fin/stabilizer, stabilstor/control surface, vertical fin/stabilizer, rudder, other), antenna, engine/propeller/blade, external tank/stores, loss of structure/stores, and loss of sircraft. "Other," depending upon location, includes external lights, static dischargers, diverter strips, lightning arrestor/coupler, and antenna covers. Structural damage was experienced in seventy-eight percent of the reported incidents.

Electrical/Electronic Damage - Damage to electrical/electronic equipment or components caused by lightning was divided into six catagories: communications, navigation, flight instrumentation, engine, electrical, and other. The categories are those discussed under "interference/outage." Electrical/electronic damage was sustained in eight percent of the reported incidents.

Repair/Replacement Costs - The estimated costs to repair/replace aircraft damage were divided into six categories: less than \$5K, \$5K to \$20K, \$20K to \$100K, \$100K to \$300K, \$300K to \$1M, and greater than \$1M (lose of sircraft). Although there appears to be a fairly good correlation of estimated repair costs to

to damage incurred, the reports indicate that inflation has escalated damage repair costs in recent years. Nevertheless, seventy-eight percent of reported repair costs were less than \$5K per aircraft. Ninety-three percent of the reports explicitly stated the estimated costs.

#### DATA ANALYSES

OPERATIONAL CONDITIONS - Aircraft operational conditions at the time of the strike were tabulated under the headings: attitude, altitude, outside air temperature, location, weather, and electrical activity.

G.

4

Attitude - Over half of the aircraft were in level flight when struck. This is borne out in all six classes. About one-sixth of the aircraft were climbing, about one-sixth were descending, and about one-tenth were on landing approach when struck.

Altitude - Aircraft altitude was tabulated in feet above mean sea level (MSL) rather than above ground level since this was the number given in almost all mishap reports. The data indicate that over half of the aircraft were struck at altitudes above 10,000 feet and over one-fourth above 15,000 feet. The data would be representative for aircraft flying over oceans and low-lying regions of the world, but would not be representative over mountainous or high plateau regions. Therefore, it is difficult if not impossible to draw any hard-and-fast conclusions from these data.

Outside Air Temperature - Pilots are generally warned not to fly in precipitous weather at or near the freezing level since these conditions increase the probability of a lightning mishap. Thus, outside air temperature (OAT) was a parameter of interest in evaluating the above statement. Unfortunately, the OAT was only stated in about fifteen percent of the reports. Of the fifteen percent, about two-thirds were within +5°C of the freezing point, one-sixth were less than -5°C, and one-sixth were greater than +5°C.

Location - Of the reports that stated the aircraft location with respect to clouds, over eighty percent of the aircraft were within clouds when struck. About one-tenth were below a cloud cailing, one-tenth were between clouds, and one percent were above clouds when struck. Again, these data reflect only explicit statements in the reports of aircraft location. It should be noted that pilots went to great lengths in most of the reports to explicitly state that they were many miles away from any heavy thunderstorm areas being painted on their weather radar screens at the time of lightning strike.

Weather - Of the reports that stated weather, about two-thirds of the aircraft were experiencing rain when struck. Only twenty percent were experiencing turbulence. About five percent were experiencing hail or snow. And for the remaining ten percent of the aircraft that were in clear weather, a lightning strike must have come as quite a surprise to the crew.

Electrical Activity - Only a very small percentage of reports mentioned the buildup of electrical activity prior to the strike. However, several reports indicated that electrical activity in the form of static on radios, interference on scopes, etc. persisted for up to saveral minutes after a strike had caused some form of interference or outage. More explicit information in this area is needed to aid the analyst in his attempt to understand and explain the lightning-aircraft interaction processes.

EFFECTS OF THE STRIKE - The effects of a lightning strike were tabulated under the headings: attachment point, interference/outage, effect on mission, effect on personnel, structural damage, electrical/electronic damage, and repair/replacement costs.

Attachment Point - From 707 reports that explicitly stated one or more attachment points, a total of 979 attachment locations were tabulated. Half of all the reported attachment points could be identified with the nose area, fourteen percent the wing, fourteen percent the tail, ten percent an antenna, seven percent the fuselage, three and one-half percent the external tank/stores, and less than two percent "other." Cargo aircraft reported sixty percent of all attachments to the nose area whereas trainers reported less than fifteen percent. Trainers reported a third of all attachments to the tail. Fighter and bomber aircraft each reported between seven and eight percent of all attachments to external tanks/stores.

Interference/Outage - From 180 reports that explicitly stated at least one happening or event that could not be considered normal operation following a lightning strike, a total of 236 events were tabulated and summarized in narrative form for reference. Thirty percent of all events affected navigation, twenty-five percent flight instrumentation, twelve percent engines, ten percent communications, eight percent electrical, three percent fuel, and eleven per-cent "other." Fighters and trainers appeared to be more susceptible to temporary disruptions than cargo or bomber aircraft. Abnormal events were reported in thirty-five percent of fighter mishaps, twenty-six percent of trainer mishaps, thirteen percent of bomber mishaps, and twelve percent of cargo mishaps. Flight instrumentation and navigation were most affected in fighters (thirty-eight percent and twenty-two percent, respectively) while navigation was predominantly affected in cargo aircraft (fifty-six percent). These percentage differences can in part be explained in terms of lightning attachments to the pitot system and air data sensors on fighter aircraft (which impacts flight instrumentation indicators) and a high percentage of attachments to the nose radome on cargo sircraft (which impacts weather/navigation radar). Engines were affected in fighters (thirteen percent) and trainers (thirty-eight percent), but were not a factor in cargo aircraft.

Effect on Mission - The effect of a lightning strike on mission was not stated or had no effect in sixty-three percent of the reports, caused a precautionary abort in thirty-five percent, an emergency landing in less than one percent, and loss of aircraft in less than one percent. A considerably higher percentage of fighter aircraft missions were affected (fifty-six percent) than cargo aircraft (twenty-three percent). As previously stated, mission abort was taken as a precautionary measure. In most cases, subsequent ground inspection revealed only minor structural damage to the airframe.

Effect on Personnel - Of the 52 reports that explicitly stated an effect of lightning on personnel, thirty percent listed momentary flash blindness, fifty-five percent electrical shock, six percent crew ejection, and nine percent fatalities (accompanied by loss of aircraft). A much higher percentage of fighter and trainer aircraft reported effects on personnel (12.4 and 12.3 percent, respectively) than any other class. Only 2.4 percent were reported by bombers, 3.7 percent by cargo, and none by attack or helicopter aircraft.

Structural Damage - From 687 reports that explicitly listed structural damage, 1003 tabulations were made under nineteen categories. Damage areas correlated very closely with attachment point areas. In almost all cases, some repair was required to return the aircraft to its previous pre-lightning strike condition. The severity of the damage usually correlated closely with the estimated repair/replacement costs.

Electrical/Electronic Damage - From 68 reports that explicitly listed damage to electrical/electronic equipment or components, 81 listings were tabulated and summarized in narrative form for reference. Forty percent of the listings involved navigation, mineteen percent flight instrumentation, fourteen percent electrical, ten percent communications, less than three percent engines, and sixteen percent "other." Damage was reported in twelve percent of fighter mishaps, 4.8 percent of bomber mishaps, and 6.8 percent of cargo mishaps. Most of the equipment/component damage appeared to be the result of the lightning energy directly impacting affected items rather than indirect coupling of lightning energy.

Repair/Replacement Costs - Of the 818 reports that explicitly stated estimated repair/replacement costs, seventy-eight percent were less than \$5K, seventeen percent were between \$5K and \$20K, three and one-half percent were between \$20K and \$100K, and 1.4 percent were above \$100K (which included the loss of seven aircraft). Repair/replacement costs above \$5K involved 20.4 percent of cargo mishaps, 28.7 percent of fighter mishaps, and 28 percent of bomber mishaps.

## SUMMARY AND CONCLUSIONS

Aircraft, when struck by lightning, will generally sustain some minor structural damage, may have temporary interference or outage of a

normal operational function, and in less than ten percent of all strikes will sustain damage to electrical/electronic equipment or components. This damage will not be critical to flight safety due to backup instrumentation and equipment, but may require mission abort if primary flight indicators, navigation or communications are lost. In the few instances where aircraft have been lost due to lightning, four were related to fuel vapor explosions and three to flight control or instrumentation malfunctions. Fighter and trainer aircraft are probably more susceptible to lightning effects than bomber or cargo aircraft because of their smaller size (thus higher lightning current densities), entry points (pitot system, open canopy areas), engine locations (subject to overpressure effects), and external tanks/stores (additional attachment locations). Newer aircraft are designed to be and are less susceptible to lightning-related effects because of increased awareness and application of good lightning protection practices, application of more stringent lightning qualification tests and test procedures, and a better understanding of lightning-aircraft interactional processes.

#### REFERENCES

- 1. P. B. Corn, "Lightning Hazards Overview Aviation Requirements and Interests," Proceedings of the Workshop on the Need for Lightning Observations from Space, NASA Conference Publication CP-2095, NASA-Marshall Space Flight Center, Alabama, February 13-15, 1979.
- 2. Air Force Regulation 127-4, "Safety: Investigating and Reporting U.S. Air Force Mishaps," 18 January 1980; revision AFR-127-4(C1), 22 February 1982.
- 3. J. A. Plumer, "Data from the Airlines Lightning Strike Reporting Project," Lightning and Static Electricity Conference, Las Vegas, Nevada, December 12-15, 1972; Air Force Avionics Laboratory Technical Report No. AFAL-TR-72-325.

Table 1 - USAF Lightning Mishap Reports by Aircraft Class (1970-1982)

Aircraft Class	Mishap Reports
Attack	13
Bomber	83
Cargo	429***
Fighter	274****
Trainer	73
Helicopter	5
Total	877

Note: Asterisk denotes loss of one aircraft

Table 2 - USAF Lightning Mishap Reports by Year (1970-1982)

Year	Mishap Reports
1970	67*
1971	87*
1972	78
1973	103*
1974	83
1975	83*
1976	64
1977	53
1978	51**
1979	54
1980	65 <b>*</b>
1981	53
1982	36
M-4-4	
Total	877

Note: Asterisk denotes loss of one sircraft

Table contains only partial listing of 1982 reports

Table 3 - USAF Lightning Mishap Reports by Month (1970-1982)

Month	Mishap Reports
-	
Jan	28
Feb	40
Mar	87* <del>*</del>
Apr	102*
May	130*
Jun	95*
Jul	86*
Aug	97
Sep	71
Oct	66 -
Nov	44*
Dec	31
m - 4 1	
Total	877

Note: Asterisk denotes loss of one aircraft

Brelide

COMPONENT LIGHTNING TEST FOR THE AFTI/F-16 DIGITAL FLY-BY-WIRE SYSTEM

K. G. Wiles and R. T. Zeitler

General Dynamics P. O. Box 748 Ft. Worth, TX 76101

ABSTRACT

ころをはは 本本ない のまかぬ

The Advanced Fighter Technology Integration/F-16 aircraft (or AFTI/F-16) utilizes a digital fly-by-wire flight control system with triple-redundant computer implementation. Since flight safety is contingent on a complex array of electronic circuitry, comprehensive lightning susceptibility testing was performed on flight control interface circuits to design-in protection against lightning induced transients. Criteria designation for this program was patterned after circuit-level testing completed on the F-16 aircraft (analog system) but was expanded in scope and depth to include the functional requirements of a digital system. The fundamental principle underlying the criteria was therefore protection against damage, permanent upset and temporary upset beyond safe recovery.

In order to determine circuit susceptibility and achieve the desired protection, the criteria and test procedure were designed to measure damage threshold levels and response characteristics and to assure proper protection. brief summary of the component lightning susceptibility test and criteria is given as follows:

- o All interface circuits in the Flight Control System were reduced to a worst-case generic form.
- o Damage threshold levels were measured by subjecting test circuits (power-on) to four 500-volt/5 microsecond rectangular pulses in all directions. Hardening techniques were evaluated and proven on susceptible circuits.
- o Response characteristics were measured by subjecting test circuits (power-on) to 500-volt/5 microsecond damped sinusoidal pulses. Response waveforms were than analyzed relative to the function requirements of the interfacing system.

The objective of this paper is to present an overall summary of the component lightning susceptibility test program performed for the AFTI/F-16 Digital Flight Control System. The summary will include a description of the test criteria and procedure, an overview of test results and a discussion of our conclusions and recommendations for future testing. In this manner, we hope to provide an insight into lightning susceptibility testing and hardening techniques for sensitive aircraft equipment.

This paper was not available for incorporation into this book. Therefore, it will be published at a future date.

USAGE OF THE SYSCAP II CIRCUIT ANALYSIS PROGRAM TO DETERMINE SEMICONDUCTOR FAILURE THRESHOLD LEVELS CAUSED BY LIGHTNING/EMP TRANSIENTS

D. L. Rusher and C. T. Kleiner

Rockwell International Corporation Autometics Strategic Systems Division AD P002214

湯湯

大学の大学

3370 Miraloma Avenue Anaheim, CA 92803

ABSTRACT

This paper describes an improved technique for calculating semiconductor junction heating resulting from arbitrary time-varying source terms. A FORTRAN subroutine is developed which permits solution of the convolution integral in the SYSCAP\* circuit analysis program which will simulate the thermal transient for each semiconductor of interest in a circuit subject to lightning/EMP disturbances. An example circuit is used to demonstrate the techniques; the results compare favorably with laboratory test data.

INTRODUCTION

Lightning-induced cable currents can cause semiconductors located within interface circuits to fail because of severe thermal transients. These cable currents are generated when lightning/EMP interact with the structure and couple to the cables. Predicting the exact nature and path of this coupling is difficult, and test validation is even more challenging. For some time, predicting failure levels at the semiconductor level has been performed using rectangular (single pulse) waveforms in conjunction with simplified semiconductor damage models. In many cases, a wide variation between test results and predictions has been observed and reported in actual system tests. Although some of this variation can be attributed to inadequate model data or even the model itself, a considerable error can occur if the analysis does not properly sum the thermal heating caused by the "real" stimulus to a system. Lightning/EMPinduced currents/voltages that appear as drivers to interface circuits are complex damped sinusoids [1]. The component data base is obtained by step-stressing a number of parts (eg, 25 total sample size with a 5 sample per pulse width selection ) to failure with an attempt to use constant amplitude and pulse widths over several

\*The SYSCAP II program is available on the Control Data Corporation CYBERNET system and is licensed to CDC by Rockwell International. (See SYSCAP II "System of Circuit Analysis" Program user information manual, Publication No. 76070600 Data Services Publications, P.O. Box HQCO2G, Minneapolis, Minnesota 55440).

decades of equivalent pulse width or frequency. These data are plotted and a "damage equation" is developed [2], [3]. When the test is performed with sufficient care and with a known semiconductor family (including supplier and lot number) as described in [4], the results generally validate the theory described in [2]. However, thermal failure is not the only possible failure mode. Anomalies occur, as was indicated in [4], which are usually caused by dielectric breakdown and not thermal failure. This paper only addresses thermal failure.

Given, then, that the thermal failure model is the one that is of prime concern, it is still important to resolve the rectangular pulsa test data versus actual damped sinusoidal disturbance. A means for converting the damped sinusoids to a series of equivalent pulses is needed that includes the generation of junction temperature.

A method for accomplishing this procedure was described in an earlier paper [5] by one of the authors; however, this method involved building a thermal ladder network for each p-n junction and proved impractical for large scale implementation.

The technique reported by Williams [6] basically solves the model size problem, and it was possible to easily implement this method via the FORTRAN Function capability in SYSCAP.

The following discussions will describe (a) the semiconductor failure model, (b) linear network failure models, (c) the convolution integral method including the SYSCAP FORTRAN function subroutine, and (d) application to an actual circuit with comparison to test data.

## SEMICONDUCTOR THERMAL FAILURE MODEL

Component tests to measure device damage threshold consist primarily of step-stressing a number of parts to failure with constant amplitude pulses of various widths. After curve fitting the data, a plot of typical power  $P_{\rm D}$  for damage is found as a function of pulse width  $\tau$ . From the work of Wunsch, Bell, and Tasca [2,3], the general form of these data has been well established to be:

- (1) A region for short pulses less than  $\tau_0$  (10 to 100 ns) where  $P_D$  depends on  $\tau^{-1}$  and energy is constant. This is the adiabatic region.
- (2) A region for long duration pulses

greater than  $\tau_1$  (10 µs to 1 s) where heat flow out of the device has stabilized. Here  $P_D$  is no longer dependent on  $\tau_2$ 

(3) A transition region where  $P_D$  depends on  $\tau^{-1/2}$ .

In the transition region where  $\tau_0 < \tau < \tau_1$ , the classic Wunsch-Bell relation applies,

$$P_{D} = K_{D} \tau^{-1/2} \tag{1}$$

where  $K_{D}$  is the damage constant. Then for the adiabatic region, ie, for  $\tau < \tau_{o}$  ,

$$P_{D} = K_{D} \tau_{O}^{1/2} \tau^{-1}$$
 (2)

Since currents of sufficient duration to cross into the equilibrium region are very unlikely in the lightning or EMP environments, the thermal response for long duration pulses ( $\tau > \tau_1$ ) were not modeled. Equations (1) and (2) represent failures caused by excessive localized temperature in the device. A case exists [4] where an integrated circuit failed at a lower power level than prediced by equation (2). For pulses shorter than 0.5  $\mu$ s, nearly constant power caused failure because of voltage-sensitive surface breakdown. However, for pulses of 0.5  $\mu$ s to 20  $\mu$ s duration, power at failure was observed to follow equation (1).

#### LINEAR NETWORK FAILURE MODELS

An approximate enalysis of the threshold cable current for failure is frequently made in the following manner [7].

- Reverse junction breakdown of the part selected for analysis is modeled by a surge resistor, R<sub>B</sub>, in series with measured breakdown voltage V<sub>BD</sub>.
- (2) The Wunsch failure model is utilized and,

$$P_D = I_F V_{BD} + I_F^2 R_B$$
 (3)

An approximate conversion to the frequency domain is made,

$$\tau = 1/nf \tag{4}$$

where n is chosen to represent a typical damped sinusoid. A standard value of 2.2 to 3.0 is generally used for all circuits.

(4) Substitution of equation (4) into equation (1) produces the following estimate of failure current and voltage when the resulting quadratic equation is solved,

$$I_{F} = \frac{-V_{BD} + \left[V_{BD}^{2} + 4 R_{B} K_{D} \sqrt{nf}\right]^{1/2}}{2R_{B}}$$
 (5)

$$V_{p} = V_{BD} + I_{p} R_{R} \tag{6}$$

(5) The part failure current and voltage from equations (5) and (6) are then converted to connector pin current and voltage by linear circuit analysis. This step is done by hand in simple cases or a program such as HANAP2 [7] may be used. The result is a prediction of the connector pin current and voltage required for failure of the part selected for analysis.

Several approximations which may seriously affect accuracy are often required with frequency-domain failure analyses. For example, with the HANAP2 program, there is a limitation of one semiconductor per model. Consequently, each junction of each part in an interface circuit must be examined separately, with all others ignored or roughly represented by a resistor and/ or capacitor. The large currents present at interface circuits often switch devices ON and OFF, so that a linear model is a poor approximation to the actual circuit behavior. Circuits with rectification may convert the frequency of current at the interface connector to a lower frequency. This cannot be handled with linear analysis techniques. Use of the Wunsch model in the adiabatic region (frequencies above about 5 MHz) produces an estimate of failure current which is in error on the low side. Finally, it is difficult to justify a standard value of n for use in equation (5) which will represent all circuits and cable current waveforms.

Linear analysis techniques provide a reans of quickly estimating the failure levels for interface parts. However, numerous assumptions have been noted which will degrade accuracy. A general purpose, time-domain simulator such as SYSCAP provides the means of eliminating many of these assumptions.

#### CONVOLUTION INTEGRAL METHOD

equation (7) to give,

A convolution integral was developed by Williams [6] which relates arbitrary device power waveforms to pulse power for failure and generates the junction temperature rise versus time. This technique is based on the Wunsch-Bell model [2] for pulsed semiconductor failure, as modified by Tasca [3] for the adiabatic region. Utilizing classical Laplace transform theory, the normalized temperature rise (I) of a device is computed in the following manner:

$$I(t) = \int_{0}^{t} P(\tau) \frac{d}{d(t-\tau)} \left[ \frac{1}{P_{D}(t-\tau)} \right] d\tau \qquad (7)$$

Since simulated part temperature is normalized to that required for failure, a peak value of unity typically represents failure. Pulse power for failure  $(P_D)$  need not be determined explicity. Instead, the general expressions for  $P_D$  from equations (1) and (2) are substituted into

$$I(t) = \begin{cases} \int_{0}^{t} \frac{P(t')}{K_{D}\sqrt{\tau_{0}}} dt' & t \leq \tau_{0} \\ & \ddots & \\ \int_{0}^{t-\tau_{0}} \frac{P(t')}{2K_{D}\sqrt{t-t'}} dt' + \int_{t-\tau_{0}}^{t} \frac{P(t')}{K_{D}\sqrt{\tau_{0}}} dt' & t > \tau_{0} \end{cases}$$
 (8)

Since instantaneous device power dissipation P(t') is a standard feature of the SYSCAP II program for arbitrary driving functions, the implementation of equation (8) is not difficult. The numerical method used by Williams to solve equation (8) has been tested on a number of circuits. In general, a favorable comparison between the damage threshold obtained by the convolution integral and test data or other analytic methods has resulted. However, it was observed that the peak value of I(t) is quite dependent on the solution time-step size. For example, an unprotected 1N4148 diode was driven by a 1.5 MHz sinusoidal current with an initial peak of 200 mA, decaying to zero in 10 cycles. The average value of the Wunsch-Bell damage constant is 0.0113 based on pulse tests. The normalized temperature response was simulated using the TRACAP transient analysis option of SYSCAP. With a solution time-step of 0.3 ns (or 2222 per cycle), I(t) reaches 63 percent of typical failure temperature on the sacond cycle. With 667 solutions per cycle, this value increases slightly to 63.7 percent. However, at 67 solutions per cycle (10 ns time-step), the peak on the second cycle increases further to 85 percent of the failure level. For comparison, linear analysis based on equation (5) infers that 255 mA is typically required for failure (where n was presumed to be 2.25).

Williams computes equation (8) by means of trapezoidal integration. Because two relations for I(t) are used (depending on whether integration time exceeds  $\tau_0$ ), an error in integration occurs unless solution happens to occur exactly at elapsed time minus  $\tau_0$ . Since this situation holds at each time step, errors are cumulative.

An alternate method of solving equation (8) has been obtained by assuming that the power, P(t), is a straight line between t and  $t_{n+1}$ ,

$$P(t) = P(t_n) + (t - t_n)Q_n$$
 (9)

for

$$t_n \le t \le t_{n+1}$$

where

$$Q_n = [P(t_{n+1}) - P(t_n)]/(t_{n+1} - t_n)$$

the integral from  $t_n$  to  $t_{n+1}$  has an exact explicit solution which can be used to replace the approximate trapezoidal integration. This is also true if  $t-\tau_o$  is contained in some  $t_n$  to  $t_{n+1}$  interval. The mathematical steps required to carry out this method of solution are straightforward. The final form is presented in Fig. 1. This figure is a listing of the FORTRAN subroutine which, in conjunction with SYSCAP,

provides I(t) for all parts of interest in a specific interface circuit.

```
FUNCTION FUNCTION, CDO, WATTO, AI, PTS, X)
   REAL TE, TIME, PUR, DAMP, TO, CD, WATT
   COMMON/FIXCON/JCONT(100),TE
   DIHENSION DAMP(800,4), PUR(800,4), TIME(800)
   DATA H/1/
   KEPTS
   I=A1
   T0=T00
   CD=CDO
   UATT=UATTO
   IF(ICONT(9).NE.4)GD TO 200
   IF(TE.LE.O..DR.M.GE.1000) GO TO 200
   PUR(N.I)=UATT
   IF(I.EQ.1)TINE(N)=TE
   IF(M.EQ.1) GU TO 190
   IF(TIME(H).LE.TIME(H-1)) GO TO 200
   SID=SORT(TO)
   TH=TIME(H)
   DAMP(M, I)=0.
   DO 10 J=2.K
    TJ=TIME(J)
   TJ1=TIHE(J~1)
    PURJ=PUR(J,I)
    PURJI=PUR(J-1,I)
    Q=(PURJ-PURJ1)/(TJ-TJ1)
    IF(TM-TJ.LT.TO) GO TO 5
    STJ=SURT(TM-TJ)
    STJ1=SQRT(TH-TJ1)
    DAMP(M,I)=DAMP(M,I)+(PURJ1-Q+TJ1)+(STJ1-STJ)/CD+
   19+((TJ1+2.+TM)+STJ1-(TJ+2.+TM)+STJ)/(3.+CD)
    GD TD 10
 5 IF(TH-TJ1.LE.TO) GO TO 6
    DAMP(M,I) *DAMP(M,I)+(PURJ1-Q*TJ1)*(STJ1-STQ)/CD+
   1Q+((TJ1+2.+TH)+STJ1-(3.+TM-TO) +STO)/(3.+CD)+
  2(PURJ1+Q+(TK-TO-TJ1)+PURJ)+(TJ-TH+TO)/(2.+CB+STQ)
    80 YO 10
 4 DAMP(M,I)=DAMP(M,I)+(PURJ(+PURJ)+(TJ-TJ()/(2.+CD+8TQ)
10 CONTINUE
190 FUNC1=DAMP(H,I)
    IF(I,EO,K)N=H+1
    X=FUNC1
    RETURN
200 FUNC1=X
    RETURN
    END
```

Fig. 1 - Listings of subroutine for convolution integral solution

The simulations previously described involving a 1N4148 diode were repeated using this revised integration technique. For very small time steps, the peak value of I(t) is asymptotic to 0.63 as with trapezoidal integration. However, as illustrated in Fig. 2, accuracy is considerably improved for larger (and more economical) values of the time-step. For example, with 22 solutions per cycle (30 ns time-step), the revised integration technique computes a peak value of I(t), which is 9.1 percent in error, while the numerical technique of Williams appears to have a 140 percent error. (It is assumed that this has been improved.)

An estimate of unnormalized temperature response can be obtained by assuming that failure occurs at the intrinsic temperature (550 to 650°C depending on the doping level). At this temperature, the junction properties revert to those of

undoped silicon [0]. This results in localized increased discipation which may cause these areas to reach the melting point of silicon (1410°C).

"Li. "positive feedback" effect is rarely included in the semiconductor may also of the various circuit analysis programs.

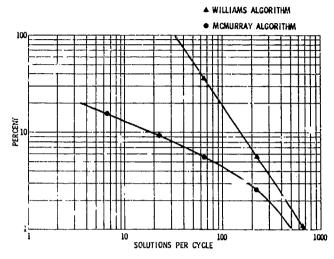


Fig. 2 - Error in predicted maximum temperature versus solutions per cycle

#### APPLICATION TO A SPECIFIC CIRCUIT

The convolution integral model was applied to a PNP apitaxial planar filicon transistor (2N3051) which had been tested in its circuit to burnour. The circuit is shown in Fig. 3. The test pulse was of 100 µs duration with a constant amplitude over the interval. The pulses, separated by a time interval to permit cooling, were repeated with an increasing magnitude of negative voltage until failure occurred. The voltage at the Q10 transistor emitter was monitored as was the current from the emitter to the pulser. Test to burnout was performed five times, using the came circuit and replacing the transistor [5].

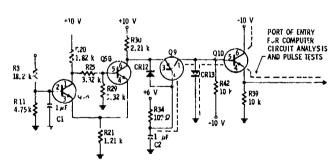


Fig. 3 - Test circuit schematic

The negative pulse drives Q10 into the inverted mode with the base-emitter diode near avalanche breakdown. However, most of the test current traverses from collector to emitter. Failure analysis revealed that a collector-emitter short was present and that base-collector and base-emitter diode action still existed.

Alloying was noted at the edge of the emitter and beneath the emitter contact.

The SYSCAP coding used to model the example circuit is shown in Fig. 4. In addition to standard device model parameters, the damage constant  $\mathbf{K}_{D}$  and the adiabatic transition pulse width  $\tau_{o}$  are required for each part of interest.

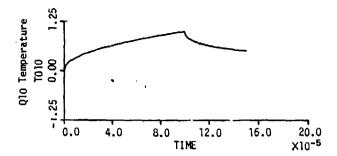
```
EXAMPLE CIRCUIT OUTPUT B/C HODEL
R30(1,2)2.21K
R34(3,4)100
R42(5,6)10K
R39(7,0)10K
C1(1,2)5P
C2(4,0)1U
C3(2,4)5P
C4(5,0)10P
C5(5.4)8P
Q9,PNP(B4,C5,E2)P,
25,0,.5,10U,.5,.1,4,1,.1,.05,.1P,.89,56G,65,10N,3.1,20P,
.75,.5,46.7N,0,0,0,0,00017P,.89,.056G,6.6,10N,3.1,9P,.75,.5,
.336N,0,0,0,0
Q10,PNP(B5,C6,E7)P,IC,Q9
D13(A5,C0)P,
1.25,1.896N,1.8077,9.8G,90,10H,10,1.9P,.75,.5,2.16K,0,0,
D12(A4,C2)P,D13
E1(+1,-0)10.
E2(+3,-0)6.
E3(+6,-0)-10.
E4(+7,-0)POINTS,0.0,0,-17.43,.10,-17.43,1000,0.0,1010,0.0,1
TQ10=FUNC1(50N, 10424, Q10PT, 1, 4, 0.0)
TQ9=FUNC1(50N,.0424,Q9PT,2,4,0.0)
TD12=FUNC1(50N,.12,B12PD,3,4,0.0)
TD13=FUNC1(50N,.12,D13PD,4,4,0.0)
FINIS
INITIAL =COMPUTE
CALC/PLT=2
TIME=.5U.150U
PLOT, HIGHRES, 3=NODE7, Q9PT, Q10PT, D12PD, D13PD, T010, T09, TD12,
TD13,010IC
```

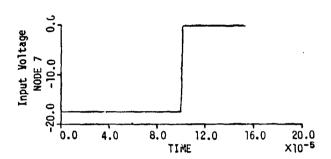
Fig. 4 - SYSCAP coding of example circuit

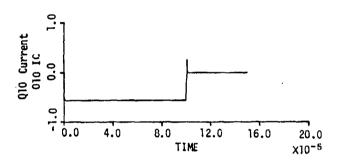
The temperature rise for transistors Q9 and Q10 and diodes CR12 and CR13 was simulated for several amplitudes of a 100 µs pulse. The response at Q9, CR12, and CR13 was several orders of magnitude below that of transistor Q10. Fig. 5 presents transistor Q10 power, current, and normalized temperature for the -17.43 V input amplitude which just causes normalized peak temperature to reach unity. Table 1 compares the tested failure threshold of the five samples with the model. Simulated power, current, and input voltage are within 4.3 to 5.1 percent of the test average.

Table 1. Model Comparison to Test Data for Example Circuit

Transistor Q10 Power	Interface Voltage	Interface Current	Description
2.5 W	-15 V	0.5 A	Test of Part 035
4.9 W	-17 V	0.7 A	Test of Part 029
2.8 W	-17 V	0.4 A	Test of Fart 006
6.4 W	-18 V	0.8 A	Test of Part 030
3.0 W	-16 V	0.5 A	Test of Part 008
3.92 W	-16.6 V	0.58 A	Test Average
4.12 ₩	-17.43 V	0.555 A	Nominal Model
+5.1 X	+5.0%	-4.3%	Difference







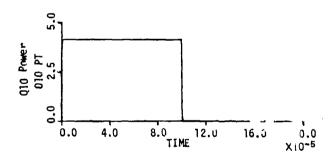
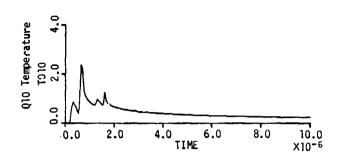
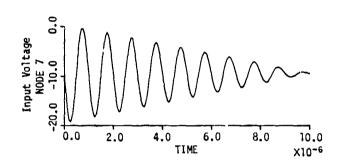


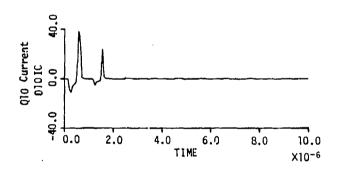
Fig. 5 - Simulated thermal response of example circuit at failure threshold

Figures 6 and 7 show simulation waveforms when the circuit is in the other logic state, and the input is a damped voltage or current sinusoid at 1 MHz. The incident cable voltage decays from 9 V to near zero in 10 cycles, producing a peak

temperature change of transistor Q10 on the second cycle of about twice that needed typically for failure. With a 5 A damped current source, a peak temperature change of 65 percent of that required for failure occurs.







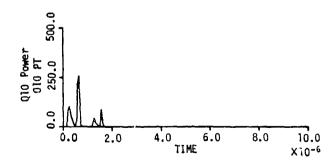


Fig. 6 - Thermal response of example circuit with damped sine input

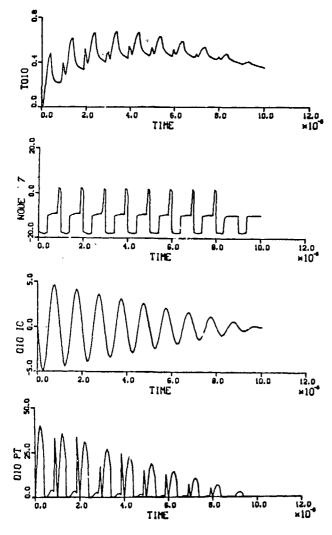


Fig. 7 - Thermal response of example circuit with damped sine input current

#### SUMMARY

A technique which properly accounts for thermal failure of semiconductor devices caused by damped sinewave disturbance akin to lightning/EMP cable transients has been described. Exceptional accuracy was established on sample parts and a circuit that had a well-conducted test. The authors believe that this technique (as embodied in the SYSCAP program) should dispel any

reasonable conjecture about "unknowns" when predicting component failure levels in hardware subject to lightning/EMP disturbances. This does not imply that it is "easy" to obtain such accuracy, rather it points out that the inherent accuracy is there if enough time and effort are devoted to the prediction and the laboratory tests. The significance of this paper is that the technique described herein is readily available to the lightning/EMP community via the SYSCAP program.

#### ACKNOWLEDGEMENT

The authors wish to thank Dr. L. R. McMurray for providing the mathematics and FORTRAN coding of the convolution integral solution. Dr. McMurray is with the Autometics Strategic Systems Division of Rockwell International.

#### REFERENCES

- 1. R. A. Perala and T. H. Rudolph, "The Interaction of Electromagnetic Fields with Aircraft During a Lightning Event", 1982 Conference of Lightning and Static Electricity, Culham Laboratory, p. C3, March 1982.
- 2. D. C. Wunsch and R. R. Bell, "Determination of Threshold Failure Levels of Semiconductor Diodes and Transistors Due to Pulse Voltages", IEEE Trans. on Nucl. Sci., Vol. NS-15, p. 244, December 1968.
- 3. D. M. Tasca, "Pulse Power Failure Modes in Simiconductors", IEEE Trans on Nucl. Sci., Vol. NS-17, p. 364, December 1970.
- 4. C. T. Kleiner, J. Nelson, F. Vassallo, and E. Heaton "Integrated Circuit Model Development for EMP," IEEE Trans. on Nucl. Sci., Vol. NS-21, p 323, December 1974.
- 5. L. R. McMurray and C. T. Kleiner, "Adaptation of the P-N Junction Burnout Model to Circuit Analysis Codes," IEEE Trans. on Nuclear Science, Vol. NS-19, No. 6, December 1972.
- 6. R. L. Williams, "Semiconductor Device Damage Assessment for the INCA Program A Prohabilistic Approach", Harry Diamond Laboratories, HDL-TR-1833, March 1978.
- 7. EMP Assessment Handbook, APWL-TR-78-60, April 1980.
- 8. P. B. Budenstein, D. H. Pontius, and W. B. Smith, "Second Breakdown and Damage in Semiconductor Junction Devices," RG-TR-72-15, dated April 1972.

# AD P002215

THE SUBMICROSECOND STRUCTURE OF LIGHTNING RADIATION FIELDS

Institute of Atmospheric Physics, University of Arizona Tuscon, Arizona 85721

ABSTRACT

those from return strokes.

The EM fields radiated by the preliminary cloud breakdown, leader steps, and the return strokes in cloud-to-ground lightning all exhibit large submicrosecond variations. Values of the maximum dE/dt during return strokes range from 7 to 76 V/m/us; when rangenormalized to 100 km, with a mean and standard deviation of 33 - 14 V/m/microsec + 14 V/m/us). If this return stroke field is produced by a single current pulse propagating upward at a speed of 108 ms, then the above values of dE/dt imply that the maximum dI/dt ranges from 35 to 355 kA/us with a mean of 154 770 kA/us? Leader steps just above the ground and the fast components of large cloud pulses produce dE/dt signatures that are often surprisingly similar to

(+ or --)

ALTHOUGH THE INTERACTIONS of lightning with aircraft, space vehicles, power systems, ships, and other structures are critically dependent on the risetimes and the maximum rates of change of the lightning fields and currents, there are relatively few fast time-resolved measurements of these quantities in the published literature (1)\*. For the past several years, the University of Arizona has ten attempting to measure the E and dE/dt signatures produced by various lightning processes with submicrosecond resolution. A description of the apparatus used to make these measurements and examples of the data have been given previously by Weidman and Krider (2,3,4) and Weidman (5). Here, we will present some inferences of the maximum rates of change of the channel currents that have been derived from the E and dE/dt fields.

#### I. EXPERIMENT

We have endeavored to measure the E and dE/dt signatures produced by known discharge processes under conditions where the results would not be significantly affected either by the response time of the measuring equipment or by ground wave propagation. Two experiment sites were chosen where the lightning and the field propagation were over salt water so that the effects of propagation were minimal. One site was near Tampa Bay, Florida, and the other was at the NASA Kennedy Space Center, Florida. A commercial lightning locating system (6,7) provided the locations of most cloud-to-ground flashes within about 100 km of each site. The field sensors and recording equipment were placed within a few meters of the shore, again so that the field propagation would be almost entirely over salt water to the recording equipment.

E signatures were recorded on both a slow and a fast time scale so that the type of lightning impulse which produced the dE/dt signature, and the precise time within the E signature that the dE/dt occurred, could be determined. The E field measuring system had a 10 to 90% risetime of about 40 ns, and the dE/dt system had a risetime of about 10 nsec.

#### II. RESULTS

RETURN STROKES - In general, the shape of the electric fields radiated by a return stroke depends on whether it is the first return stroke in a flash, a subsequent return stroke, or a subsequent return stroke that is preceded by a dart-stepped leader (2). First stroke fields begin with a relatively slow "front" which rises for 2 to 8 µs to about half of the peak field amplitude. This front is followed by a fast transition to peak, and it is this fast transition which is of primary interest in this report. Subsequent strokes produce "Numbers in parentheses designate References at end of paper.

fields that have fast transitions very similar to first strokes, but the fronts last only 0.5 to 1 us and rise to only about 20% of the peak field amplitude.

A reproduction of the fast field transition produced by a first return stroke, and a histogram of measured 10 to 90% fast transition risetimes are given in Fig. 1. Note that the mean risetime is only 90 ns and that the standard deviation is only 40 ns.

The width of the fast initial peak produced by return strokes is surprisingly narrow. Fig. 2 summarizes the full width of this peak measured halfway between the onset of the fast transition or breakpoint and the peak (FWHM). Note that the mean and standard deviation of this width are only  $360 \pm 140$  ns.

The maximum slopes of the fast field transitions produced by return strokes are summarized in Fig. 3. Here, all data have been range-normalized to 100 km assuming there is a simple inverse distance dependence in the amplitude of the fast transition,  $\Delta E$ . The values of  $\Delta E/\Delta t$  in Fig. 3 range from 7 to 76 V/m/µs, and the mean and standard deviation are 33 ± 14 V/m/µs. These data are plotted for different range intervals, and from these results we infer that the range-normalized values do not have a significant dependence on distance.

Fig. 4 shows a plot of the range-normalized values of the maximum field slope,  $\Delta E/\Delta t$ , versus the associated range-normalized  $\Delta E$ . There is a rather large scatter in the points, but the best linear fit to these data has a slope of 9.1  $\mu s^{-1}$ , and the correlation coefficient is 0.71. The implications of Figs. 3 and 4 for the maximum current derivative in return strokes will be given in the Discussion.

STEPPED-LEADER - The overall shapes of the fields radiated by individual steps of the stepped-leader have been discussed by Krider and Radda (8) and Krider, et. al. (9). As the leader nears the ground, the amplitude of individual step impulses increases, and occasionally such a step triggered our E or dE/dt recording system just before there was a return stroke. The maximum dE/dt occurs during the initial rise of the step waveform. and values of this quantity derived from the initial slopes of E data have a mean and standard deviation of 27 ± 9 V/m/µs for 18 steps. The shapes of the leader dE/dt signatures are very similar to those from return strokes, and the maximum dE/dt values for 3 leader steps just before return strokes ranged from 30 to 45 V/m/usec at 100 km. The submicrosecond structures of leader fields have also been measured by C. E. Baum and associates (10,11).

CLOUD PULSES - The overall shapes of the larger radiation field impulses produced by the intracloud discharge processes that initiate cloud-to-ground lightning and also by isolated cloud flashes have been discussed by Weidman and Krider (12) and Beasley, et. al. (13). In general, the shapes of these

pulses tend to be bipolar with several fast, unipolar impulses superimposed on the initial half-cycle. The unipolar structures have fast risetimes, and the shapes of the dE/dt signatures during these transitions are very similar to the shapes of the signatures radiated by return strokes. Values of the maximum dE/dt produced by 11 cloud impulses have a mean and standard deviation of 16 ± 8 V/m/µs at 100 km.

FIELD AMPLITUDE SPECTRA - The dE/dt signatures radiated during the fast return stroke transition have been Fourier analyzed to provide field amplitude spectra over the frequency interval from about 1 to 20 MHz. The results for 24 first and 5 subsequent strokes are shown in Figs. 5 and 6, respectively, together with previous spectra published by Serhan, et. al. (14) and Weidman, et. al. (15). Here, the mean spectral amplitudes are given in dB from a reference level of 3 V/m/s, and all data have been range-normalized to 50 km.

Fig. 5 shows three curves; Curve [1] represents the mean spectrum of 24 first stroke signatures that have not been corrected for any truncation of the records at the end of the finite recording interval. In Curve [2], any truncations have been corrected by multiplying the records by a cosine windowing function. Curve [3] shows the mean spectrum of 6 strokes that did not require any truncation correction. Clearly, Curves [2] and [3] are probably the best approximation to the true return stroke source spectrum.

Fig. 6 shows the mean spectrum of 5 subsequent return strokes. Curve [1] is the spectrum of data that have not been corrected for truncation errors, and Curve [2] is the spectrum of the same data after multiplication by a cosine windowing function. Again, Curve [2] is undoubtedly the best approximation to the true subsequent scroke source at the higher frequencies.

#### DISCUSSION

Lightning current models and the implications that lightning fields have for lightning currents have been discussed by Uman and Krider (1), and by Baum, et. al. (10). If we assume that the initial, fast-rising portions of the fields produced by leaders, return strokes, and cloud impulses can all be described by a form of the transmission line model (1), then the maximum rate of change of the source current is related to the maximum field derivative through the relation:

 $\frac{dI(t)}{dt} = \frac{2\pi \text{ Dec}^2}{v} \frac{dE(t+D/c)}{dt}$ 

where D is the range to the discharge, v is the velocity of the current pulse, and where the ground has been assumed to be flat and perfectly conducting. This relation also assumes that the measured field is produced by a single current pulse propagating in a single channel.

Fig. 7 shows a cumulative distribution of the maximum dI/dt values that have been

computed for return strokes using the above equation and the field derivatives plotted in Figs. 3 and 4. The values are plotted for a velocity of 10<sup>8</sup> m/s, and the dashed lines show velocities of 0.6 X 10<sup>8</sup> m/s and 1.4 X 10<sup>8</sup> m/s. Fig. 7 also shows the maximum current derivatives measured during lightning strikes to instrumented towers by K. Berger in Switzerland, as reported by Anderson and Eriksson (16), and by Garbagnati, et. al. (17) in Italy. Fig. 8 shows estimates of the maximum dI/dt in leader steps that occur just prior to a return stroke and in the fast structures on cloud impulses.

It should be noted that the maximum current derivatives that are inferred from the E and dE/dt data in Figs. 3 and 4 tend to be substantially higher than those in the tower data. This might be because the towers, which are located on mountains of rock, or the upward connective leaders which originate from the towers, limit the maximum rate of rise of current that can be measured. Another reason might be that the E and dE/dt data have been obtained with a triggered oscilloscope recording system that may not have recorded all of the smaller signatures, and this might have biased the statistics toward larger values. Finally, if the fast field transitions are produced by more than one current pulse radiating simultaneously, then our inferred dI/dt values will overestimate the true value for one pulse. Since the dI/dt values in Figs. 7 and 8 are larger than the dI/dt used in most lightning test standards. we think these problems clearly warrant further study.

#### ACKNOWLEDGEMENT

This research has been supported in part by the Office of Naval Research, Contract N00014-81-K-0175.

標

#### REFERENCES

- 1. M. A. Uman and E. P. Krider, "A Review of Natural Lightning: Experimental Data and Modeling", IEEE Trans. on EMC, Vol. EMC-24, pp. 79-112, 1982.
- 2. C. D. Weidman and E. P. Krider, "The Fine Structure of Lightning Return Stroke Wave Forms", J. Geophys. Res., Vol. 83, pp. 6239-6247, 1978.
- 3. C. D. Weidman and E. P. Krider, "Submicrosecond Risetimes in Lightning Return Stroke Fields", Geophys. Res. Lett., Vol. 7, pp. 955-958, 1980.
- 4. C. D. Weidman and E. P. Krider, "Submicrosecond Risetimes in Lightning Radiation Fields", in Proc. Lightning Technology, NASA Conf. Pub. 2128 and FAA-RD-80-30, pp. 29-38, April, 1980.
- 5. C. D. Weidman, "The Submicrosecond Structure of Lightning Radiation Fields", Phi Dissertation, Univ. of Arizona, 1982. Available from University Microfilms, Ann

Arbor, Michigan.

- 6. E. P. Krider, R. C. Noggle, A. E. Pifer, and D. L. Vance, "Lightning Direction-Finding Systems for Forest Fire Detection", Bull. Am. Met. Soc., Vol. 61, pp. 980-986, 1980.
- 7. E. P. Krider, A. E. Pifer, and M. A. Uman, "An Automatic Locating System for Cloud-to-Ground Lightning", in Proc. Lightning Technology, NASA Conf. Pub. 2128 and FAA-RD-80-30, pp. 205-214, April, 1980.

8. E. P. Krider and G. J. Radda, "Radiation Field Waveforms Produced by Lightning Stepped Leaders", J. Geophys. Res., Vol. 80, pp. 2653-2657, 1975.

9. E. P. Krider, G. J. Radda, and R. C. Noggle, "The Electric Fields Produced by Lightning Stepped Leaders", J. Geophys. Res.,

Vol. 82, pp. 951-960, 1977.

10. C. E. Baum, E. L. Breen, D. L. Hall, C. B. Moore, and J. P. O'Neill, "Measurements of Electromagnetic Properties of Lightning with 10 Nanosecond Resolution", in Proc. Lighting Technology, NASA Conf. Pub. 2128 and FAA-RD-80-30, pp. 39-82, 1980.

11. C. E. Baum, E. L. Breen, F. L. Pitte, G. D. Sower, and M. E. Thomas, "The Measurement of Lightning Environmental Parameters Related to Interaction with Electronic Systems", IEEE Trans. on EMC, Vol. EMC-24, pp. 123-137, 1982.

12. C. D. Weidman and E. P. Krider, "The Radiation Field Waveforms Produced by Intracloud Lightning Discharge Processes", J. Geophys. Res., Vol. 84, pp. 3159-3164, 1979.

13. W. Beasley, M. A. Uman, and P. L. Rustan, Jr., "Electric Fields Preceding Cloud-to-Ground Lightning Flashes", J. Geophys. Res., Vol. 87, pp. 4883-4902, 1982.

14. G. I. Serhan, M. A. Uman, D. G. Childers, and Y. T. Lin, "The RF Spectra of First and Subsequent Lightning Return Strokes in the 1 to 20 km Range", Radio Science, Vol. 15, pp. 1089-1094, 1980.

15. C. D. Weidman, E. P. Krider, and M. A. Uman, "Lightning Amplitude Spectra in the Interval from 100 kHz to 20 MHz", Geophys. Res. Lett., Vol. 8, pp. 931-934, 1981.

16. R. B. Anderson and A. J. Eriksson, "Lightning Parameters for Engineering Application", Electra, No. 69, pp. 65-105, 1980.

17. E. Garbagnati, F. Marinono, and G. B. LoPipero, "Parameters of Lightning Currents, Interpretation of the Results obtained in Italy", 16th Conf. on Lightning Protection, Szeged, Hungare, July, 1981.

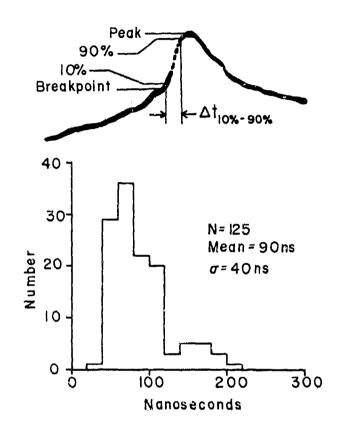


Fig. 1 - A histogram of the 10 to 90% risetime of the fast transition in return stroke E fields

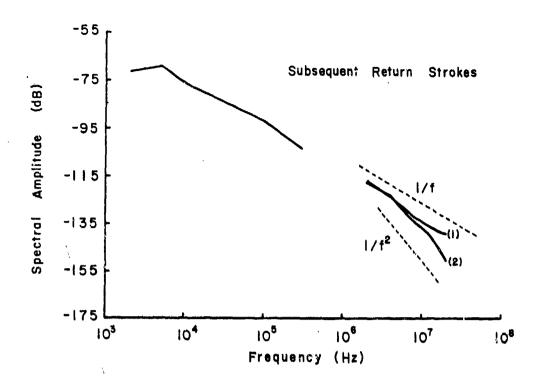


Fig. 6 - The mean amplitude spectrum of 5 subsequent return strokes range-normalized to 50 km. Curve [2] is the best approximation of the true source

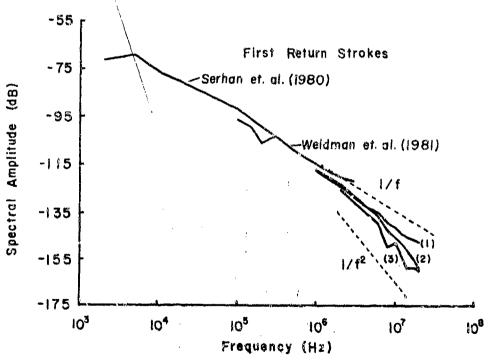


Fig. 5 - The mean amplitude spectrum of 24 first return strokes range-normalized to 50 km. Curves [2] and [3] are the best approximation to the true source at higher frequencies

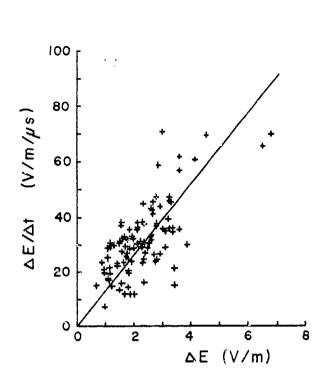


Fig. 3 - A histogram of the maximum rate of rise of the fast transition in return stroke E fields range-normalized to 100 km

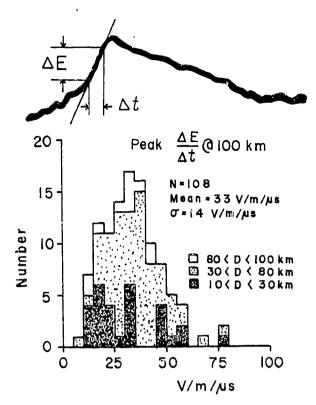


Fig. 4 - Maximum  $\Delta E/\Delta t$  during return strokes vs. the associated  $\Delta E$ 

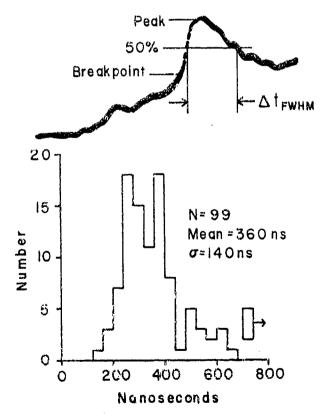
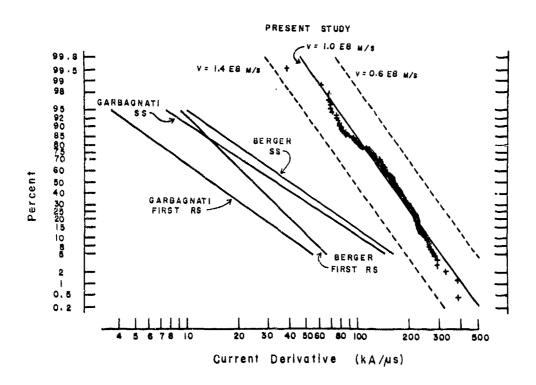


Fig. 2 - Histogram of the rull width at half maximum of the fast peak in return stroke  $\Xi$  fields.



ここのでは、大きなないのでは、大きなないのでは、大きなないのでは、大きなないのでは、大きなないのでは、大きなないのでは、大きなないのでは、大きなないのでは、大きなないのでは、大きなないのでは、大きなないのでは、

Fig. 7 - Cumulative distribution of the maximum dI/dt during lightning return strokes derived from measured dE/dt fields

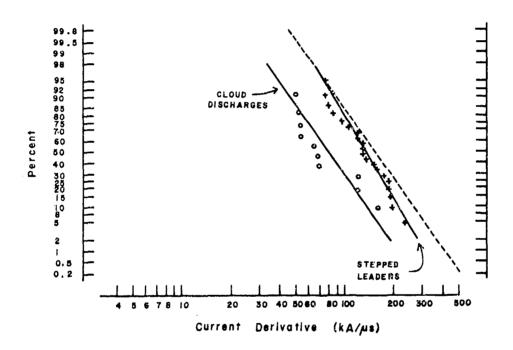


Fig. 8 - Cumulative distribution of the maximum dI/3t during leader steps and the fast components of cloud impulses. These data assume the current propagates at a speed of  $10^8$  m/s

69-8



D. M. Le Vine and R. Meneghini Goddard Space Flight Center Greenbelt, MD 20771

## AD P002216

#### ABSTRACT

A solution is presented for the electromagnetic fields produced by a current pulse propagating along a filamentary path apropos of lightning return strokes. This solution includes the effects of charge transfer by the pulse. It is obtained following traditional procedures but modifying the electric scalar potential to insure conservation of charge at the filament's ends and employing a relativistically correct relationship between charge and current. Conventional solutions can be obtained from this solution by employing conservation of charge to rewrite it in terms of current only; however, this form has computational advantages over other formulations very close to the channel.

#### INTRODUCTION

Determining the electromagnetic fields radiated from a current pulse propagating along a linear filament is a classic problem in electromagnetic theory with a long history of association with the analysis of linear antennas [1, 2, 3, 4]\*. It is also a problem relevant in contemporary atmospheric science to describe radiation from lightning return strokes [5, 6, 7]. In the analysis of antenna performance the statics (d.c.) component of the solution is generally not of concern; however, in the lightning discharge large quantities of charge are transferred by the propagating pulse and so to properly describe the fields it is necessary to predict not only the transient behaviour of the fields but also to obtain the net change in the electrostatic field when the transient is complete.

Properly including electrostatic effects in the solution to Maxwell's equations involves some subtleties. In particular, to properly predict electrostatic effects it is necessary to have a relationship between the sources of the fields, charge and current, which reduces to the proper statics value of the quantity when there is no time variation. Although it may not be possible to explicitly obtain such a relationship in general, the required relationship can be obtained in the special case of charge and current which propagate at constant velocity along current filaments. In this case a coordinate transformation (the Lorentz transformation) exists which converts the problem to a purely statics situation where only one source quantity, charge density, needs to be specified (for example, an observer running beside the pulse at exactly the velocity of propagation sees only a static charge distribution along the filament, not charges and currents). Hence, to obtain a consistent relationship between charge and current, one postulates the charge distribution in the frame of the running observer and then transforms back to the coordinate frame of the fixed observer.

In this paper, a solution will be obtained for the electromagnetic fields close to a lightning return stroke by using the preceding procedure to relate charge and current. The return stroke will be modelled as a pulse propagating along a filament. The charge and current on the filament will be determined by specifying charge density in the frame in which the pulse is at rest. Transforming back to the coordinate system of the observer determines the actual charge and current on the filament. The relationship for current density and charge density so obtained is then used to obtain electric scalar and magnetic vector potentials and the electromagnetic fields are obtained from them in the usual manner. It will be shown that the conventional forms for the fields radiated from return strokes using the transmission line model can be obtained from this formulation; however, the solution presented here has the advantages of explicitly identifying the contribution due to charge accumulation at the channel end points, an effect which is dominant for observers

very close to the channel. In addition, the form of the solution to be presented here has some computational advantages over other formulations for observers very close to the channel.

#### RADIATION FROM A FILAMENT

Until relatively recently the lightning discharge was modelled as an electric dipole and the electromagnetic fields were obtained assuming the dipole to be a point source. Such a solution is called a moment appearamenton in the lightning literature. This model is good for very low frequencies and very distant discharges [7, 8]; however, it is inadequate to predict modern wideband measurements of the transient radiation from return strokes [7]. Models developed to predict modern day measurements assume that the discharge consists of a current pulse propagating along the discharge channel (and for sake of simplicity, it is generally assumed that the channel is a filament). This model is sometimes referred to as a "transmission line" model [6] and was suggested by Dennis and Pierce [5] and developed formally by M. Uman and colleagues [8, 9, 10] who also demonstrated a first order agreement with data [8]. In this section a solution will be presented for the electromagnetic fields radiated by such a model discharge, and in subsequent sections this solution will be compared with other solutions which have appeared in the literature.

Consider sources  $\overline{J}$  and  $\rho$  of arbitrary shape propagating along a straight filament at constant velocity,  $\overline{V}$ . Letting  $\widehat{V}$  be a unit vector along the filament in the direction of propagation, the current density  $\overline{J}$  and charge density  $\rho$  can be written in the form:

$$\overline{J(r,t)} = \hat{\ell} \overline{J(t-\frac{\hat{\ell} \cdot \overline{r}}{v})}$$
 (1a)

$$p(\overline{t},t) = \rho(t - \frac{\hat{\ell} \cdot \overline{t}}{v})$$
 (1b)

A solution for the electromagnetic fields  $\vec{E}$  and  $\vec{B}$  radiated by these sources can be obtained in terms of the magnetic vector potentials  $\vec{A}$  and the electric scalar potential  $\phi$  following standard procedures [11, 12, 13]. In the absence of boundaries one obtains:

$$\vec{B} = \vec{\nabla} \times \vec{A}$$
 (2a)

$$\overline{E} = -\nabla \phi - \frac{\partial \overline{A}}{\partial t}$$
 (2b)

where

$$\overline{A} = \frac{\mu_0}{4\pi} \int \frac{[\overline{y}]}{R} d\overline{r}'$$
 (3a)

$$\phi = \frac{\mu_0 c^2}{4\pi} \int \frac{[\rho]}{R} d\overline{r}'$$
 (3b)

<sup>\*</sup>Numbers in parentheses designate References at end of paper.

In Equation 3, the square brackets, [], denote "retarded" quantities: time is replaced by t-R/c where  $R=|\overline{\tau}-\overline{\tau}'|$  is the distance between the source point  $\overline{\tau}'$  and the observation point,  $\overline{\tau}$ . For example, the retarded current density is  $[J] = RJ(t-R^{\circ}\overline{\tau}'/v-R/c)$ .

Equations 2 and 3 are not a complete solution for the fields because the sources J and  $\rho$  and the potentials  $\overline{A}$  and  $\phi$  are not independent quantities (i.e., cannot be independently specified).  $\overline{J}$  and  $\rho$  must satisfy conservation of charge  $\overline{\nabla} \cdot \overline{J} + \partial \rho / \partial t = 0$  on the filament and the potentials  $\overline{A}$  and  $\phi$  are related by the Lorentz gauge condition  $\overline{\nabla} \cdot \overline{A} + 1/c^2 \ \partial \phi / \partial t = 0$ . It is common practice to use conservation of charge or the Lorentz gauge to remove the explicit dependence on  $\rho$  from the solution [11, 13]. However, the approach in this paper will be to determine the relationship between  $\overline{J}$  and  $\rho$  explicitly and to keep both in the solution.

In order for the solution to be correct for both time varying and stathe fields, a relationship between  $\overline{J}$  and  $\rho$  is required which satisfies cures restion of charge and also reduces to the correct current and chests when there is no time variation. Although it may not be possible to obtain such a relationship in general, the required relationship can be obtained for pulses propagating on linear filaments. In this case a transformation of coordinates (the Lorentz transformation) exists which converts the problem into a purely statics problem where only one source quantity, charge density, needs to be specified. In particular, an observer summing beside the pulse at exactly the velocity of propagation sees only a static charge distribution along the filament, not charges and currents. Figures, to obtain a consistent relationship between charge and current one need postulate only the charge distribution in the frame of the running observer (statics) and then transform back to the laboratory coordinate frame to obtain J and p. The relativistically correct way of doing this is by means of a Lorentz transformation. One obtains:

$$\rho(\overline{t},t) = \frac{1}{\sqrt{1-(v/c)^2}} \rho_0 \left[ -\frac{v}{\sqrt{1-(v/c)^2}} \left(t - \frac{v \cdot \overline{t}}{v}\right) \right]$$
(4)

$$\overline{J}(\overline{r},t) = \overline{v} \rho(\overline{r},t) = \hat{\ell} v \rho(\overline{r},t)$$
 (5)

where  $\rho_0(T)$  is the electrostatic charge distribution on the filament which must be specified. It is easy to see that this result satisfies conservation of charge and clearly it reduces to the electrostatic result,  $\rho_0(t)$ , when t = 0.

 $ho_{\rm O}(r)$ , when v = 0.

If the filament is infinitely long then this is all that is required to complete the solution. However, if the filament is finite, additional conditions are required to guarantee conservation of charge at its ends. For this purpose assume that at the ends current is converted to charge and for simplicity that the charge is located in a single point right at the end of the filament. To find the appropriate relationship between T and  $\rho$  conservation of charge can be applied at these end points. To do so imagine a small sphere centered at the end point. Integrating over the volume of the sphere and using the divergence theorem, one obtains:

$$\iint \mathbf{T} \cdot \mathbf{d} \mathbf{s} = -\frac{\partial}{\partial t} \iiint \rho d\mathbf{v}$$
sphere
$$= \mathbf{T} \cdot \mathbf{\hat{v}} \tag{6}$$

and letting  $Q = \iiint \rho dv$  one can write:

$$\frac{\partial}{\partial t}Q = -\hat{k}\cdot \hat{\gamma} \tag{7a}$$

OF

$$Q = -\int_{t_0}^{t} \hat{\mathbf{l}} \cdot \mathbf{J} dt$$
 (7b)

where the integration in Equation 7b starts when the current pulse reaches the end point and it has been assumed that there is no charge at the end point before the pulse arrives. Q is a point charge at the end of the filament and the electric scalar potential  $\phi_{\rm end}$  associated with this charge can be obtained from Equation 3b using a delta function distribution. One obtains:

$$\phi_{\text{and}} = \frac{\mu_0 c^2}{4\pi} = \frac{Q_e (t - R_e/c)}{R_e}$$
 (8)

where  $R_e$  is measured from the end point to the observer and  $Q_e(t)$  is zero until the pulse reaches the end point (at  $t = t_e$ ).

A complete solution for the case of pulses propagating along a current filament can now be constructed. It consists of Equations 2 and 3 subject to the constraints between J and  $\rho$  given in Equation 5 and with the addition of Equation 8 to the electric scalar potential to account for the end points. Two terms of the form given in Equation 8 are required, one at each end of the filament. The complete solution for E and E is:

$$\overline{\mathbf{B}} = \nabla \times \overline{\mathbf{A}} \tag{9a}$$

$$\overline{E} = -\nabla \phi - \frac{\partial \widetilde{A}}{\partial t}$$
 (9b)

where

$$\overline{A} = \frac{\mu_0}{4\pi} \int_{\text{filament}} \frac{\overline{J}[t - \frac{\widehat{R} \cdot \overline{\Gamma}'}{v} - \frac{R}{c}]}{R} d\overline{\tau}'$$
 (10a)

$$\phi = \frac{\mu_0 c^2}{4\pi} \int_{\text{filament}} \frac{\rho[t - \frac{\hat{k} \cdot \vec{r}'}{v} - \frac{R}{c}]}{R} d\vec{r}'$$

$$+ \frac{\mu_{0}c^{2}}{4\pi} \left\{ \frac{Q_{a}[t - R_{a}/c]}{R_{a}} + \frac{Q_{b}[t - R_{b}/c]}{R_{b}} \right\}$$
 (10b)

and

$$\overline{J} = \overline{v} \rho \tag{11a}$$

$$Q_{a,b} = -\int_{a,b}^{t} (\hat{k} \cdot \hat{J}) d\hat{r}$$
 (11b)

where a, b denote the two ends of the filament and  $t_{a,b}$  are the times when current arrives at the end point. The sign in Equation 11b has been chosen so that the charge is positive if current flows into the end point and negative if current flows away.

Equations 9-11 satisfy Maxwell's equations, satisfy conservation of charge, and reduce to electrostatics when v=0. In addition, it will be shown below that the more traditional forms of the solution can be derived from them. It is interesting to note that Equations 10 for  $\overline{A}$  and  $\phi$  satisfy the Lorentz condition, but only with the correction term  $\phi_{\rm ends}$  added to the scalar potential. In fact, it can be shown that the Lorentz gauge condition implies the end conditions deduced here to satisfy conservation of charge (see Appendix A).

The electromagnetic fields E(r,t) and B(r,t) can be obtained from Equations 9-11 by substituting the potentials  $\overline{A}$  and  $\phi$  into Equation 9. The electric field intensity,  $\overline{E}(r,t)$  can be obtained in terms of  $\overline{J}$ , (the most common form) by substituting Equation 10 into Equation 9 ard then using Equation 11 to eliminate  $\rho$ . One obtains:

$$\begin{split} \overline{E}(\overline{r},t) &= -\frac{\mu_{o}}{4\pi} \int_{\text{filament}} \hat{R} \hat{J}[t - \frac{\hat{R} \cdot \overline{r}'}{v} - \frac{R}{c}] \frac{1}{R} d\overline{r}' \\ &+ \frac{\mu_{o}c^{2}}{4\pi} \int_{\text{filament}} \left\{ \frac{1}{R} J[t - \frac{\hat{R} \cdot \overline{r}'}{v} - \frac{R}{c}] \right\} \\ &+ \frac{1}{c} \hat{J}[t - \frac{\hat{R} \cdot \overline{r}'}{v} - \frac{R}{c}] \right\} \frac{\nabla R}{vR} d\overline{r}' \\ &+ \frac{\mu_{o}c^{2}}{4\pi} \left\{ \frac{1}{R_{b}} Q_{b}[t - \frac{R_{b}}{c}] + \frac{1}{c} J[t - \frac{R_{b}}{c}] \right\} \frac{\nabla R_{b}}{R_{b}} \\ &- \frac{\mu_{o}c^{2}}{4\pi} \left\{ \frac{1}{R_{a}} Q_{a}[t - \frac{R_{a}}{c}] + \frac{1}{c} J[t - \frac{R_{a}}{c}] \right\} \frac{\nabla R_{a}}{R_{a}} \end{split}$$

where it has been assumed that current starts at the "a" end of the filament and propagates to the "b" end and the sign from Equation 11b has been included explicitly by letting  $Q_{a,b}$  both be positive. The magnetic flux der—ity, B(r,t) can be obtained by substituting Equation 10a into Equation 9a to obtain:

$$\overline{B}(\overline{r},t) = \frac{\mu_0}{4\pi} \int_{\text{fillment}} \left\{ \frac{1}{R} J \left[ t - \frac{\hat{\ell} \cdot \overline{r}'}{v} - \frac{R}{c} \right] - \frac{1}{c} \dot{J} \left[ t - \frac{\hat{\ell} \cdot \overline{r}'}{v} - \frac{R}{c} \right] \right\} \frac{\hat{\ell} \times \nabla R}{R} d\overline{r}' \tag{12b}$$

The solutions above apply to arbitrarily oriented filaments in the absence of boundaries. In application to lightning, and in many other engineering applications, the filament is above a ground plane. When the ground plane is perfectly conducting (not unreasonable for the earth at frequencies of interest in studies of lightning) the boundary can be taken into account by adding image sources to the solution. The solution for images has the form given above with  $R_I = R - 2\left(R \cdot 2\right) 2$  and  $R_I = r + 2$  z  $\frac{1}{2}\left[14\right]$ . The examples to be presented later are of the fields radiated from filaments above a perfectly conducting ground plane and have been obtained by including image sources in this manner.

#### OTHER FORMS OF THE SOLUTION

Several different forms of the solution for the electromagnetic fields produced by the transmission line model for the lightning discharge have appeared in the literature [7, 10, 14, 15, 16]. These solutions differ in the form given for the electric field,  $\overline{E}(\overline{\tau},t)$ . It will be shown in this section that Equation 12a for  $\overline{E}(\overline{\tau},t)$  is equivalent to these other more traditional forms.

One alternate form for the electric field intensity, E(T,t), can be obtained by substituting Equations 3 into Equation 2b and then using conservation of charge to eliminate the derivative of charge density which appears. This is a procedure described by Panofsky and Phillips [11] and permits explicit identification of the "radiation" terms in the solution for the fields. In recent work, Leise and Taylor [16] adopted this form of the solution to study radiation from lightning return strokes Unfortunately with this solution, if one does not start with an electric scalar potential modified to ensure conservation of a charge at the ends of the filament, the form obtained does not properly predict the electrostatic components of the fields. A correct form of this solution will be presented below by starting with the properly modified form of the electric scalar potential (Equation 10b) and the errors that can occur when end effects are neglected will be pointed out. Another form for the electric field intensity E(7, t) can be obtained by using conservation of charge to completely eliminate charge density,  $\rho$ , from the solution. In this case an expression for E(T,t) is obtained in terms of current density, I, with no explicit dependence on and conditions. In the frequency domain, this solution is the traditional form obtained from the magnetic vector potential, A, by using the Lorentz gauge condition to eliminate the electric scalar potential,  $\phi$ , from the solution [13, 17]; or equivalently this is the solution obtained using the free space dyadic Green's function to express E in terms of J [18]. This is the form of the solution which has been used most extensively in the study of radiation from lightning [6]. It correctly accounts for electrostatic effects because the Lorentz gauge condition, which is used to obtain this form of the solution, is equivalent to the end conditions deduced in the preceding section (see Appendix A). However, the end conditions are not explicit in this solution and it is not readily apparent that the underlying model to which this solution pertains is that of a current pulse which propagates up the channel and then deposits charge in a point at the channel terminus. These two alternate forms of the solution will be discussed in detail

The form for E(T,t) obtained by Panofsky and Phillips [11] to explicitly separate "radiation" terms can be derived by beginning with Equations 2 and 3 and then using conservation of charge to eliminate the derivative of charge density  $\rho$  which appears when Equation 3b is substituted into Equation 2b. A similar procedure will be followed here but beginning with Equations 9 and 10 to insure that conservation of charge is satisfied at the filament's end points. The required manipulations are accomplished most conveniently in the frequency domain. Thus, Fourier transforming Equations 9 and 10, one obtains:

$$E(\vec{r}, \nu) = -\nabla \phi + jkc \vec{A}$$
 (13a)

THE PARTY NAMED IN COLUMN TWO IS NOT THE PARTY OF THE PAR

$$\phi(\tilde{r},\nu) = \frac{\mu_0 c^2}{4\pi} \int_{\text{filament}} \rho(\tilde{r}',\nu) \frac{e^{jkR}}{R} d\tilde{r}'$$

$$+ \frac{\mu_0 c^2}{4\pi} \left[ Q_b(\nu) \frac{e^{jkR_b}}{R_b} - Q_a(\nu) \frac{e^{jkR_a}}{R_a} \right] \qquad (13b)$$

$$\overline{A}(\overline{r},\nu) = \frac{\mu_0}{4\pi} \int_{\text{filament}} \overline{J}(\overline{r}',\nu) \frac{e^{jkR}}{R} d\overline{r}'$$
(13c)

where  $k = \omega/c$  and it has been a sumed that the pulse propatages from end (a) to end (b). Substituting Equations 13b-c into 13a yields

$$\overline{E}(\overline{r}, \nu) = \frac{\mu_0 c}{4\pi} \int_{\text{fixament}} \left\{ c \rho \frac{\nabla R}{R^2} + j k c \left[ \frac{1}{c} J - \rho \nabla R \right] \right\}$$

where

$$\tilde{E}_{end}(\nu) = \frac{\mu_0 c^2}{4\pi} \left\{ \left[ \frac{Q_a(\nu)}{R_b} + \frac{1}{c} J(\nu) \right] \frac{e^{jkR_b}}{R_b} \nabla R_b - \left[ \frac{Q_a(\nu)}{R_a} + \frac{1}{c} J(\nu) \right] \frac{e^{jkP_a}}{R_a} \nabla R_a \right\}$$
(14b)

Now using conservation of charge, which in the frequency domain is  $\nabla\cdot\overline{J}$  — jkc  $\rho=0$  to eliminate the jkc  $\rho$  term in Equation 14 in terms of  $\nabla\cdot\overline{J}$  one obtains

$$\overline{E}(\overline{\tau}, \nu) = \frac{\mu_0 c}{4\pi} \int_{\overline{Bk} \to cnt} \left\{ c \rho \frac{\nabla R}{R} + jk\overline{J} - (\overline{\nabla}' \cdot \overline{J}) \nabla P \right\}$$
(15)

$$\times g d\overline{r}' + \overline{E}_{end}(\nu)$$

where  $g = (1/R) \exp{(jkR)}$ . Now consider the term  $(\nabla' \cdot \overline{J}) g \nabla R$ . Using the relationship  $\nabla \cdot (g \overline{J}) = g \nabla \cdot \overline{J} + \overline{J} \cdot \nabla g$  and introducing the notation  $R_i = x_i \cdot \nabla R$  one obtains

$$(\nabla' \cdot \overline{J})_g \nabla R = \sum_{\text{all } i} \widehat{x}_i [\nabla' \cdot (\overline{J}_g R_i) - \overline{J} \cdot \nabla' (g R_i)] \qquad (16)$$

and noting that

$$\sum_{\mathbf{g},\mathbf{g}} \hat{\mathbf{x}}_{i} [\overline{\mathbf{J}} \cdot \nabla'(g\mathbf{R}_{i})] = -[\overline{\mathbf{J}} - (j\mathbf{k} - 2/R)(\overline{\mathbf{J}} \cdot \nabla R)\nabla R]g \qquad (17)$$

one obtains

$$\overline{E}(\overline{\tau}, \nu) = \frac{\mu_{o}c^{2}}{4\pi} \int_{\text{filament}} \rho g \frac{\nabla R}{R} d\overline{\tau}' \\
+ \frac{\mu_{o}}{4\pi} \int_{\text{filament}} jkc \overline{J} \cdot [\overline{\overline{I}} - \nabla R \nabla R] g d\overline{\tau}' \\
- \frac{\mu_{o}c}{4\pi} \int_{\text{filament}} \overline{J} \cdot [\overline{\overline{I}} - 2 \nabla R \nabla R] \frac{g}{R} d\overline{\tau}' \\
- \frac{\mu_{o}c}{4\pi} \sum_{\text{all i}} \hat{\chi}_{i} \int_{\text{filament}} \overline{\nabla}' \cdot (\overline{J}gR_{i}) d\overline{\tau}' + \overline{E}_{efid}(\nu) \tag{18}$$

None of the manipulations done so far depend on the specific form of  $\overline{J}$  or  $\rho$  or whether or not the sources propagate on filaments. However, by restricting the result to the specific case of filaments additional simplification can be obtained. For currents propagating on filaments  $\overline{J}=$  & J and so  $\overline{\nabla}' \cdot [\overline{J}gR_i]= \hat{k} \cdot \nabla'(JgR_i)$  and one can we write:

$$\int_{\text{filament}} \overline{\nabla}' \cdot [\overline{J}gR_i] d\overline{\tau}' = \int_{\text{filament}} \hat{\ell} \cdot \overline{\nabla}' (JgR_i) d\overline{\tau}'$$

$$= \int_{\text{filament}} \overline{\nabla}' (JgR_i) \cdot d\overline{\ell}'$$

$$= JgR_i = Jg_b R_b - Jg_a R_{a_i} \quad (19)$$

where  $g_{C,b}=1/R_{a,b}e^{jkR_{a,b}}$  and where  $d\ \overline{\ell}'$  is a differential length along the filament. Consequently, in the case of filaments, the last integral in Equation 18 becomes  $(\mu_{oc}/4\pi)\ \bar{\ell}[Jg_b \nabla R_b - Jg_a \nabla R_a]$ . This term cancels one of the terms in  $E_{ext}(\nu)$  due to the charge build-up at the filament ends, and one obtains

$$\overline{E}(\overline{\tau},\nu) = \frac{\mu_0}{4\pi} \int_{\text{filtiment}} j \, k \, c \, \overline{J} \cdot [\overline{\overline{I}} - \nabla R \, \nabla R] \, g \, d\overline{\tau}'$$

$$- \frac{\mu_0 c}{4\pi} \int_{\text{filtiment}} \overline{J} \cdot [\overline{\overline{I}} - 2 \, \nabla R \, \nabla R] \, \frac{g}{R} \, d\overline{\tau}'$$

$$+ \frac{\mu_0 c^2}{4\pi} \int_{\text{filtiment}} \rho \, \frac{\nabla R}{R} \, g \, d\overline{\tau}'$$

$$+ \frac{\mu_0 c^2}{4\pi} \left\{ Q_b(\nu) \, \frac{\nabla R_b}{R_b} \, g_b - Q_a(\nu) \, \frac{\nabla R_a}{R_a} \, g_a \right\} \tag{20}$$

Inverting the Fourier transfer in yields the time dependent form of the solution:

$$\overline{E}(\overline{\tau},t) := -\frac{\mu_{o}}{4\pi} \int [\overline{J}] \cdot [\overline{\overline{I}} - \nabla R \nabla R] \frac{dr'}{R} \\
-\frac{\mu_{o}c}{4\pi} \int [\overline{J}] \cdot [\overline{\overline{I}} - 2 \nabla R \nabla R] \frac{d\overline{\tau}'}{R^{2}} \\
+ -\frac{\mu_{o}c^{2}}{4\pi} \int \frac{[\rho]}{R^{2}} \nabla R d\overline{\tau}' \\
+ \frac{\mu_{o}c^{2}}{4\pi} \left\{ \frac{[Q_{b}]}{R_{b}^{2}} \nabla R_{b} - \frac{[Q_{a}]}{R_{o}} \nabla R_{a} \right\}$$
(21)

Several comments are in order. First, Equations 21 as they stand do not represent a complete solution for  $\overline{E}(\overline{x},t)$  because the relationship between  $\overline{J}$  and  $\rho$  has not been specified. If  $\overline{J} = \rho \overline{v}$  is used, then the solution is complete and is just a rearrangement of Equation 12a. (The equivalence of Equations 21 and 12s has been verified numerically and examples will be presented below.) Second, Equation 21 is almost, but not quite, the form obtained by Panoisky and Phillips [11]. The difference is the last term  $\mu_0 c^2 / 4 \pi \{ [Q_b] \nabla R_b / R_b \dots [Q_a] \nabla R_a / R_a \}$  which is not present in the Panofsky and Phillips solution. In deriving their solution for  $\overline{E}(\overline{\tau},t)$  Panofsky and Phillips follow a procedure identical to that outlined above except that they begin with Equation 3b for  $\phi$  and not Equation 10b as was done here (that is, end conditions to guarantee conservation of charge are not included). Also, in their derivation, Panofsky and Phillips set the summation in Equation 18 equal to zero using an argument (see reference 11 page 297) which is not true for filaments of finite length. Both assumptions are valid in the case of currents which are continuous and differentiable; however, for filaments of finite length, end conditions and the summation in Equation 18 must he included.

The net effect of taking end conditions into account and evaluating the summation in Equation 18 for filaments is the last term in Equation 21. This term has the form of a statics electric field due to a point charge Q located at the ends of the filament. Clearly it will be important for observers close to the filament's end points and it will be important at times after current stops propagating along the channel. In fact, when  $t \to \infty$  this term is just the static electric field due to a charge

$$Q = -\int_{1}^{\infty} \overline{J} \cdot \hat{I} dt$$
 transferred by the current from one end of the fila-

ment to the other. In contrast the first three terms in Equation 21 go to zero as  $t \rightarrow \infty$  because by then J=0. The relative importance of these terms is illustrated in the numerical results (Fig. 3) to be presented in the following section.

A second form for  $\overline{E}(\overline{\tau},t)$  can be obtained by using conservation of charge to eliminate the remaining dependence on charge density in Equation 21. The substitution is also most reasily done in the frequency domain (Equation 20). Thus substituting  $\rho = \nabla \cdot \overline{J}/\mathrm{jkc}$  into the second term in Equation 20 one obtains:

$$\frac{l'_{O}c^{2}}{4\pi}\int \rho g \frac{\nabla R}{R} d\vec{r}' = \frac{\mu_{O}c}{4\pi} \frac{1}{jk} \int (\vec{\nabla}' \cdot \vec{J}) g \frac{\nabla R}{R} d\vec{r}' \qquad (22)$$

and now using Equation 16 with g replaced by g/R, noting that

$$\sum_{\mathbf{a}|\mathbf{i}|\mathbf{i}} \hat{\mathbf{x}}_{\mathbf{i}} [\overline{\mathbf{J}} \cdot \overline{\nabla}' (\frac{g}{R} R_{\mathbf{i}})] = [J/R - (jk - 3/R)(\overline{\mathbf{J}} \cdot \nabla R) \nabla R] \frac{g}{R}$$
(23)

and using Equation 19, one obtains

$$\frac{\mu_{0}c^{2}}{4\pi}\int\rho\,g\,\frac{\nabla R}{R}\,d\,\overline{r}' = -\frac{\mu_{0}c}{4\pi}\int\left\{\left[\overline{J}\cdot\nabla R\right]\,\nabla R\right] + \frac{\overline{J}}{jk}\cdot\left[\overline{\overline{I}}-3\,\nabla R\,\nabla R\right]\frac{1}{R}\right\}\frac{g}{R}\,d\,\overline{r}'$$

$$+\frac{\mu_{0}c^{2}}{4\pi}\left\{\frac{i}{jkc}\left(\overline{J}\cdot\hat{R}\right)\right\}$$

$$\times\left[\frac{\nabla R_{b}}{R_{b}}\,g_{b}-\frac{\nabla R_{a}}{R_{a}}\,g_{a}\right]\right\}$$
(24)

Substituting this into Equation 20 leads to the frequency domain form:

$$\overline{E}(\bar{r}, \nu) = \frac{\mu_0 c}{4\pi} \int_{\text{filament}} j \, k \, \overline{j} \cdot \left\{ \left[ 1 - \frac{1}{jkR} - \frac{1}{(kR)^2} \right] \, \overline{\overline{l}} \right\}$$

$$- \left[ 1 + \frac{3}{jkR} - \frac{3}{(kR)^2} \right] \, \nabla R \, \nabla R \left\{ \frac{e^{jkR}}{R} \, d \, \overline{r}' \right\}$$
(25)

and transforming back to the time domain yields:

$$\overline{E}(\overline{\tau}, t) = -\frac{\mu_0}{4\pi} \int_{\text{filament}} [\overline{J}] \cdot [\overline{\overline{I}} - \nabla R \nabla R] \frac{d\overline{\tau}'}{R} 
- \frac{\mu_0 c}{4\pi} \int_{\text{filament}} [\overline{J}] \cdot [\overline{\overline{I}} - 2 \nabla R \nabla R] \frac{d\overline{\tau}'}{R^2} 
+ \frac{\mu_0 c}{4\pi} \int_{\text{filament}} \{ ([\overline{J}] \cdot \nabla R) \nabla R 
- \frac{c}{R} \int_{\text{filament}} [\overline{J}] \cdot [\overline{\overline{I}} - 3 \nabla R \nabla R] dt \} \frac{d\overline{\tau}'}{R^2}.$$
(26)

where the square brackets (e.g., [1]) mean the retarded form. Equation 25 is a standard result found in many textbooks on electromagnetic theory, and its Fourier transform, Equation 25, is the form of the solution employed extensively to study radiation from lightning return strokes by Uman and colleagues [6, 8, 9, 19, 20]. Notice that Equation 25 can be written in the form

$$\overline{E}(\overline{\tau}, \nu) = j \omega \mu \int \overline{J} \cdot \overline{\overline{G}} (\overline{\tau}/\overline{\tau}') d\overline{\tau}' \qquad (27)$$

where  $\overline{G}(r/r')$  is the conventional form for the free space dyadic Green's function [18]. Also notice that auxillary conditions necessary to guarantee conservation of charge at the filament ends no longer appear explicitly in the solution for  $\overline{E}(\overline{r},t)$ . However, clearly they are included in Equations 25 and 26 because these equations were obtained starting with an electric scalar potential (Equation 10b) which included contributions at the ends. Equation 25 can also be obtained in an alternative more direct manner without reference to end conditions at all. One car begin with the definition  $\overline{E} = -\nabla \phi - d\overline{A}/dt$  and then use the Lorentz gauge condition  $\overline{\nabla} \cdot \overline{A} + 1/c^2 - \partial \phi/\partial t = 0$  to eliminate  $\phi$ . Doing this in the frequency domain yields

$$\overline{E} = -jkc[\overline{A} + \frac{1}{k^2}\nabla(\overline{\nabla}\cdot\overline{A})]$$
 (28)

Substituting for  $\overline{A}$  from Equation 9b yields Equation 25, and inverting the Fourier transform leads to Equation 26. Special conditions to guarantee conservation of charge at the filament end points are never explicitly required in this approach. However, they are implicit in the Lorentz gauge condition as is shown in Appendix  $F_{A}$ .

#### NUMERICAL RESULTS

In the preceding sections several different forms have been obtained for the electric field radiated by a pulse propagating along a filament. These are Equation 12a which was obtained directly from the electromagnetic potentials after modification to include end conditions; the Panofsky and Phillips form of the solution which is obtained by using conservation of charge to eliminate certain terms involving charge density and which is given in its complete form by Equation 21 and in the form appearing in the literature by the first three terms of Equation 21; and finally the "classical" form of the solution (Equation 26) which is the most common form for  $\overline{E}(\overline{r},t)$  and which was obtained here by using conservation of charge to eliminate all explicit dependence on charge density. The classical solution can also be obtained from the magnetic vector potential by using the Lorentz gauge condition to eliminate the scalar potential from the expression for the electric field (Equation 2b) and can even be derived directly in the time domain following a procedure outlined by Uman, McLain and Krider [15]. Examples of  $\tilde{\mathbb{C}}(\bar{\tau},t)$ predicted by these solutions will be presented in this section.

Example: of  $\overline{E}(\overline{r},t)$  have been obtained by computing the electric field at a fixe I observation point for filaments representative of lightning return strokes. An example filament is shown in Fig. 1. This tortuous path was created by connecting short straight segments end-to-end in a random walk in a manner suggestive of the way the stepped leader forms the channel in cloud-to-ground lightning discharges [14]. To obtain  $\overline{E}(\overline{r},t)$  for the tortuous path, the solution for electric field (Equations 12a, 21 or 26) is applied to each linear segment separately and the results added, keeping track of phase as the pulse advances up the filament. The filament is assumed to be above a perfectly conducting ground plane with the lower end touching the plane. The effect of the ground plane is handled by including appropriate image currents and charges [14]. The pulse propagating up the channel was chosen so that the current on the filament is representative of the current in lightning return strokes. In particular, the exponential model suggested by Bruce and Goide [21] and subsequently modified to include additional terms [22, 23] has been adopted for the current J(t) or, the filament in the following form:

$$J(t) = I_0(e^{-\alpha t} - e^{-\beta t}) + I_1(e^{-\gamma t} - e^{-\delta t})$$
 (29)

The parameters were chosen to be representative of first return strokes  $[5]: I_0 = 30 \text{ kA}; I_1 = 2.5 \text{ kA}; \alpha = 4 \times 10^4 \text{ sec}^{-1}; \beta = 8 \times 10^5 \text{ sec}^{-1}; \gamma = 10^3 \text{ sec}^{-1}; \delta = 2 \times 10^4 \text{ sec}^{-1}.$  The current pulse is assumed to propagate up the channel at constant velocity, v, and in the case of the tortuous channel shown in Fig. 1, the value  $v = c/3 = 10^8 \text{ m/s}$  was used.

Fig. 2 shows the electric field seen by an observer on the ground at several distances from the channel shown in Fig. 1. Very far from the channel, the radiation term in the solution (first term in Equations 21 and 26) is dominant. In this case, one can show [7, 14] that each of the kinks in the tortuous path behaves like a radiating source and as a result, the observer sees the irregular waveform evident in the lower panel in Fig. 2 (500 km). When the current pulse reaches the top of the channel (in about 20 µs) an electric field waveform having the shape of the current pulse is radiated, resulting in the smooth overshoot evident in the example. These far field characteristics of the radiated field can be established independently using a fraunhofer approximation to obtain the solution [7, 14]. As one moves closer to the channel other terms in the solution become more apparent. For example, at 5 km from the channel the radiation terms are still clearly apparent in the early portions of E(t) while the pulse propagates up the channel, but after it reaches the top of

the channel an electrostatic term due to charge deposited at the channel end point becomes evident. At 1 km from the channel the radiation terms are still noticeable but are only a small perturbation on the total electric field seen by the observer, and at 500 m from the channel the radiation terms are virtually unidentifiable. By the time the observer is 50 m from the channel the character of  $\overline{E}(\overline{\tau},t)$  has changed completely from its far field form which was dominated by radiation terms to a shape which can be explained quite well with purely electrostatic arguments. For example, one can obtain the waveform at 50 m by neglecting currents and imagining a pulse of charge which moves up the channel. Initially, as the charge emerges from the channel base, there is a rapid increase in the electric field both because an increasing length of channel is becoming charged (the pulse has finite width) and because the vector from the location of the charge to the observer changes from purely horizontal at the channel base to a vector having a vertical (zdirected) component. Then as the charge moves up the channel, the distance between observer and charge increases and as a result the electric field decreases. This trend continues until eventually the charge reaches the top of the channel. The final value is the electric field predicted by a point charge at the tip of the channel. This behaviour is clearly evident in Fig. 2 at 50 m from the channel and is apparent even in the case of an observer 500 m from the channel. For closer observers the amplitude grows but the overall shape of  $\overline{E}(\overline{r},t)$  is as seen in the example at 50 m. An important consequence of the electrostatic nature of  $\overline{E}(\overline{\tau},t)$  when the observer is close to the channel is that the rate of change of the electric field early in the waveform (e.g.,  $t \approx 20 \,\mu s$ ) can be very large. This is due to the increasing amount of charge on the filament but also because of the rapidly changing vertical component of the vector from the location of charge on the channel to the observer. The change in this vector component is a purely geometric phenomena and can be very large. As a result, observers close to the channel can experience larger values of the rate of change of electric field (dE/dt) than appear in the radiation fields or are implied by the current wateform propagating up the channel.

It was pointed out in the preceding sections that the version of the Panofsky and Phillips form for E(T,t) that appears in the literature (first 3 terms in Equation 21) does not properly predict electrostatic conditions at the filament ends. This is illustrated in Fig. 3 which shows the complete solution (Equations 12a, 21 or 26) and the uncorrected Panofsky and Phillips form at several distances from the tortuous channel (Fig. 1). The solid line is the complete solution and the dashed line is the uncorrected Panofsky and Phillips form. Both forms are correct initially  $(0 < t < 20 \mu s)$  because in this time period, the current has not yet reached the top of the channel. However, once the current pulse reaches the top of the channel charge builds up there, and the contribution of this charge to E(T,t) is not included in the uncorrected from of solution. This is clearly evident in Fig. 3 where it is seen that the uncorrected solution goes to zero after the current pulse reaches the top of the channel because current ceases to flow, but the complete form of the solution (all terms in Equation 21) goes to a non-zero static value which is just the contribution due to a point charge at the top of the channel.

It was shown in the preceding section that all complete forms of the solution (Equations 12a, 21, and 26) are mathematically equivalent. That is, they predict the same  $\overline{E}(\overline{r},t)$ . In particular, the curves shown in Fig. 2 can be obtained with any of them. However, the solutions aren't equally convenient to use in computations of the electric field. In particular, for observers very close to the channel, the common, "classical". form of the solution (Equation 26) frequently predicts very misleading results unless special attention is paid to perform especially accurate numerical integration. An example of the problems which can be encountered is shown in Fig. 4 which shows the electric field at 1 m from a long (1 km) straight vertical channel (Fig. 5). The solid curve was obtained from Equations 12a and 21 and the dashed curve was obtained using the classical form of the solution (Equation 26). Three cases are shown which differ only in the size of the increments used to compute the integrals in the various solutions. The increments were 0.67 m, 0.50 m, and 0.40 m, respectively (1.0 m = 1000 samples per l km channel). Clearly, the  $E(\bar{r},t)$  obtained from Equations 12a and 21 are relative insensitive to the increments used. Changes in the second or third significant figure for  $\overline{E}$  ( $\overline{r}$ ,t) were observed. With sufficiently accurate numerical integration, the classical form of the solution also predicts the same electric field waveform (top curve in Fig. 4). However, with larger increments in the numerical integration, the classical solution can

predict radically incorrect waveforms. The problem with this form of the solution is not just with errors in  $\overline{E}(\overline{r},t)$  but in the fact that the entire shape of the waveform can change dramatically. This difficulty with the classical form of the solution appears when the observer is close to the filaments and the last term in Equation 26 is important.

#### CONCLUSIONS

A solution has been presented here for the electromagnetic fields produced by a current pulse propagating along a filamentary path. This solution reduces to the proper statics solution if the velocity of propagation goes to zero and includes the effects of charge transfer by the current pulse from one end of the filament to the other. It was obtained following traditional procedures but by modifying the electric scalar potential to insure conservation of charge at the filament's ends and by employing a relativistically correct relationship between charge density,  $\rho$ , and current density,  $\overline{J}$ .

It was shown that this solution is equivalent to more conventional forms for the electric field. In electromagnetic theory, one of two approaches is generally followed for determining the fields from given sources  $\overline{J}$  and  $\rho$ . One approach involves the introduction of potentials as an intermediate step to simplify the vector complexity of the problem. This was the procedure adopted here. It is also the procedure adopted by Panofsky and Phillips to 'erive a rearrangement of this basic solution by using conservation of charge to eliminate the derivative of charge density which occurs when the electric scalar potential is substituted into the expression for electric field intensity. In the case of current pulses on fliaments, this rearrangement is equivalent to the solution derived here if one properly accounts for the discontinuity at the filament's ends. If not, this form of the solution will not correctly predict the final electrostatic helds when the current pulse reaches the end of the filament. The error which results manifests itself close to the channel. The second approac!, common in electromagnetic theory is to solve for the fields directly by in troducing dyadic Green's function [18] or by using the Lorentz condition to eliminate the electric scalar potential from the expression for electric field. It was shown that this is equivalent to using conservation of charge to eliminate charge density  $\rho$  completely from the solution by potentials. This form of the solution is the one which has been used most extensively in the study of radiation from lightning. However, this particular form of the solution has draw Lacks. First, since the explicit dependence on tharge density has been eliminated from the solution, the electrostatic character of the fields close to a channel aren't readily apparent. This problem is exacerbated ir the conventional derivation of this form of the solution (e.g., by using the Lorentz gauge condition to eliminate for electric scalar potential from the solution) because no coplicit reference is required to the conditions imposed at the end of the filament. As was shown here these conditions require the conversion of current to charge at a point at the filament ends and are imposed by the Lorentz guage condition itself. That is, the standard transmission line model used in lightning studies, when used with a solution such as Equation 16, implies specific end conditions at the channel reminus even though these are not generally mentioned explicitly in the statement of the model. Secondly, the classical form of the solution is difficult to evaluate numerically when the observer is very close to the filament. This is due to the integral required to account for charge on the channel. Unfortunately, when the observer is close to the channel, this solution can predict dramatically different forms for  $\mathbb{E}(\overline{r},t)$  depending on the accuracy with which the integral is computed. The other forms of the solution for  $\overline{E}(\overline{r},t)$ derived here tend to converge to the correct answer in a much more uniform manner with less computer time.

### APPENDIX A: IMPLICATIONS OF THE LORENTZ GAUGE CONDITION

It is the purpose of this appendix to show that the potentials  $\widetilde{A}$  and  $\phi$  as given in Equations 10 satisfy the Lorentz gauge condition, and in particular that  $\widetilde{A}$  and  $\phi$  satisfy the Lorentz gauge condition only if the terms  $\phi_{\rm end}$  (Equation 8) are added to the scalar potential to account for conservation of charge at the filaments ends.

To demonstrate this, Equations 10 are substituted into the Lorentz gauge condition:  $\nabla \cdot \vec{\Lambda} + 1/c^2 - \partial \phi / \partial t = 0$ . This is most conveniently done in the frequency domain in which case the potentials have the form:

$$\bar{A}(\bar{\tau}, \nu) = \frac{\mu_0}{4\pi} \int \bar{J}(\bar{\tau}', \nu) \frac{e^{jk \cdot R}}{R} d\bar{\tau}'$$
(A1)

$$\phi(\overline{\tau},\nu) = \frac{\mu_0 c^2}{4\pi} \left\{ \int_{\text{filament}} \rho(\overline{\tau},\nu) \frac{e^{ikR}}{R} d\overline{\tau}' + \frac{\hat{\varrho} \cdot \overline{\jmath}}{jkc} [g_b - g_a] \right\} (A2)$$

where  $g_e = e^{jkR}e/R_e$  and where it has been assumed that the current propagates from the end e = "a" to the end e = "b"; and Equation 11b has been used to express the charge at the filament's ends in terms of current. The Lorentz gauge condition in the frequency domain is:

$$\nabla \cdot \overline{A} - j - \frac{k}{c} \phi = 0$$
 (A3)

Now substituting Equations A1 and A2 into Equation A3, one obtains

$$\int_{\text{filament}} \overline{\nabla} \cdot [\overline{J}g] d\overline{r}' - jkc \int_{\text{filament}} \rho g d\overline{r}' + \hat{\ell} \cdot \overline{J}[g_b - g_a] = 0 \quad (A4)$$

where  $g = e^{jkR}/R$ . Note that  $\nabla \cdot [g\overline{J}] = \overline{J} \cdot \nabla g$  and that  $\nabla g = -\nabla' g$ . Then using  $\nabla \cdot (A\overline{B}) = \overline{B} \cdot \nabla A - A \overline{\nabla} \cdot \overline{B}$  one obtains:

$$\int_{\text{filament}} \overline{\nabla} \cdot [\overline{J}g] : J \overline{r}' = \int_{\text{filament}} [g \overline{\nabla}' \cdot \overline{J} - \overline{\nabla}' \cdot (\overline{J}g)] d \overline{r}'$$

$$= \int_{\text{filament}} [g \overline{\nabla}' \cdot \overline{J}] d \overline{r}' - \hat{\ell} \cdot \overline{J} [g g - g_a] \tag{A5}$$

where the last result follows from Equation 19 in the text and applies for currents on filaments. The end condition in Equation A5 cancels the last term on the right in Equation A4. Hence, using Equation A5, the I orentz condition (Equation A4) can be written in the form:

$$\int_{\text{fill-ment}} \left[ \nabla' \cdot \mathbf{J} - jkc\rho \right] g d \mathbf{r}' = 0 \tag{A6}$$

The term in brackets in the integrand in Equation A6 is just a statement of conservation of charge and is zero on the filament because I and  $\rho$  satisfy conservation of charge there. Hence  $\phi$  and  $\overline{A}$  as given in Equations 10 satisfy the Lorentz gauge condition. Clearly if the end condition it. Equation 10b (or equivalently Equation A2 in the frequency domain) is omitted, the Lorentz gauge condition will no longer be satisfied because the last term, on the right in Equation A5 will not be concelled. Hence for flaments the end conditions are implicit in the Lorentz condition in the sense that the scalar potential obtained from the Lorentz gauge condition  $(\phi=-j(c/k)\ \vec{\nabla}\cdot\vec{A})$  is equivalent to that given by Equation 10b.

#### REFERENCES

- 1. C. Mannehack, "Radiation from Transmission Lines," Trans. J. AIEE, Vol. 42, pp. 289-300, 1923.
- 2. A. A. Pistolkors, "The Radiation Resistance of Beam Antennas", Proc. IRE, Vol. 17 (No. 3), pp. 562-579, 1929.
- 3. S. A. Schelkunoff, "Advanced Antenna Theory", John Wiley, New York, 1952.
- 4. D. L. Sengputa and C-T. Tai, "Radiation and Reception of Transients by Lineau Antennas", Chapter 4, Transient Electromagnetic Fields, L. B. Felsen, Ed., Springer-Verlag, 1976.
- 5. A. S. Dennis and E. T. Pierce, "The Return Stroke of the Lightning Flash to Earth as a Source of VLF Atmospherics", Radio Science,
- Vol. 68D (No. 7), pp. 777-794, 1964.6. M. A. Uman, "Calculation of Electric and Magnetic Fields Produced by Close Lightning", in Electrical Processes in Atmospheres, Procedings, 5-th International Conf. on Atmospheric Electricity,
- H. Dolezalek and R. Reiter, Ed., Verlag, pp. 597-600, 1977.
  7. D. M. Le Vine and R. Meneghini, "Electromagnetic Fields Radiated from Lightning Return Strokes: Application of an Exact Solution to Maxwell's Equations", J. Geophys. Res., Vol. 83 (No. C5), pp. 2377-2384, 1978.
- 8. M. A. Uman, D. K. McLain, R. J. Fisher and E. P. Krider, "Electric Field Intensity of the Lightning Return Stroke", J. Geophys. Res., Vol. 78 (No. 18), pp. 45, 3523-3529, 1973
- 9. M. A. Uman and D. K. McLain, "Magnetic Field of Lightning Return Stroke", J. Geophys. Res., Vol. 74 (No. 28), pp. 6899-6910,
- 10, D. K. McLain and M. A. Uman, "Exact Expression and Moment Approximation for the Electric Field Intensity of the Lightning Return Stroke", J. Geophys. Res., Vol. 76 (No. 9), pp. 2101-2105, 1971.
- 11. W. K. H. Panofsky and M. Phillips, "Classical Electricity and Magnetism, Addison-Wesley, (Section 14-3), Second Edition, 1962.
  - 12. J. A. Stratton, "Electromagnetic Theory", McGraw-Hill, 1941.
- 13. D. S. Jones, "The Theory of Electromagnetism", Pergamon Press, 1964
- 14. D. M. Le Vine and R. Meneghini, "Simulation of Radiation from Lightning Return Strokes: The Effects of Tortuosity", Radio Science, Vol. 6, October, 1978.
- 15. M. A. Uman, D. K. McLain and E. P. Krider, "The Electromagnetic Radiation from a Finite Antenna", Amer. J. Phys., Vol. 43, pp. 33-38, 1975.
- 16. J. A. Leise, and W. L. Taylor, "A Transmission Line Model with General Velocities for Lightning", J. Geophys. Res., Vol. 82 (No. 3), pp. 391-396, 1977.
- 17. M. Born, and E. Wolf, "Principles of Optics", Pergamon Press, 1959.
- 18. C-T. Tai, "Dyadic Green's Functions in Electromagnetic
- Theory", International Text Book Co., 1971.

  19. Y. T. Lin, M. A. Uman, and R. B. Standler, "Lightning Return Stroke Models", J. Geophys. Res., Vol. 85 (No. C5), pp. 1571-1583, 1980.
- 20. M. J. Master, M. A. Uman, Y. T. Lin, and R. B. Standler, "Calculation of Lightning Return Stroke Electric and Magnetic Fields Above Ground", J. Geophys. Res., Vol. 86 (No. C12), pp. 127-132,
- 21. C. E. R. Bruce and R. H. Golde, "The Lightning Discharge", J. Inst. Elec. Eng., London, Vol. 88, (No. 11), pp. 487-505, 1941.
- 22. M. A. Uman, "Lightning", McGraw-Hill, 1969. 23. R. H. Golde, "Lightning Currents and Related Parameters" Chapter 9, Lightning, Vol. 1, Academic Press, R. H. Golde, ed., 1976.

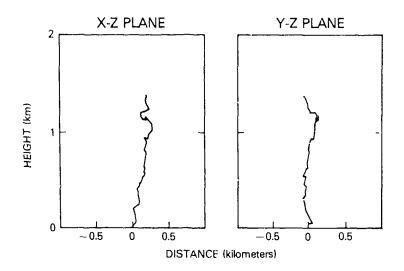


Figure 1. Tortuous channel made up of straight filaments placed end-to-end in a random pattern.

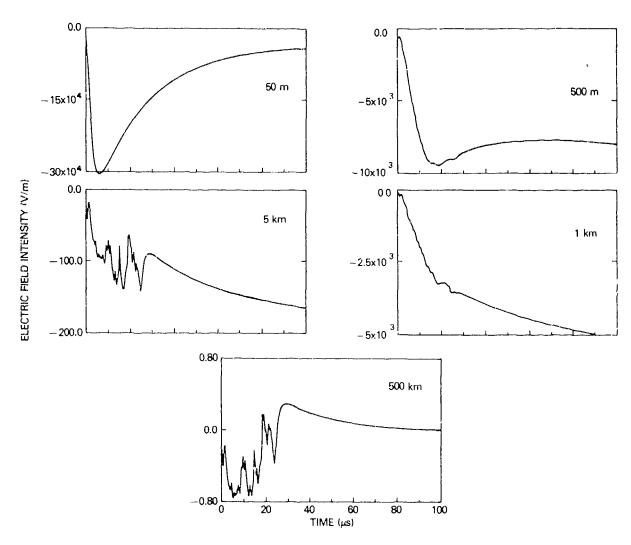


Figure 2. The electric field seen by an observer at several distances from the tortuous channel shown in Fig. 1.

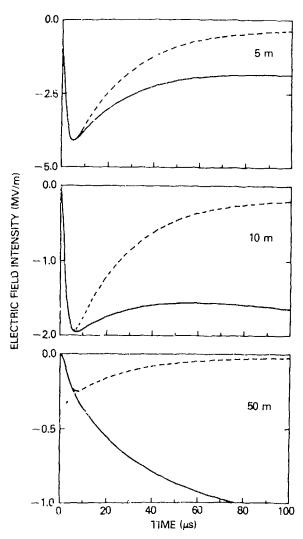


Figure 3. Illustration of the effect of not properly including electrostatic effects (dashed curve) at the end of the channel in the Panoisky and Phillips form of the solution.

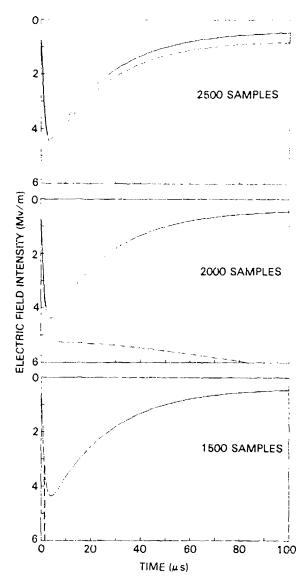


Figure 4. Illustration of the computational problems encountered with the classical solution (broken line) for observers close to the channel. The observer is 1 meter from the 1 km long straight channel shown in Fig. 5.

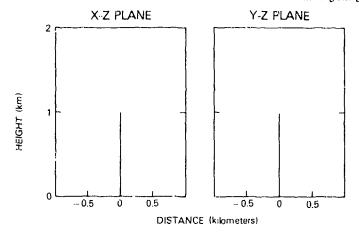


Figure 5. One kilometer long straight channel used to illustrate problems with the classical form of the solution.

## TROPICAL LIGHTNINGS: ELECTROMAGNETIC CHARACTERIZATION C.O.P.T. 81 EXPERIMENT (TROPICAL DEEP CONVECTION)

C. LETEINTURIER - J. HAMELIN - M. LE BOULCH

-

CENTRE NATIONAL D'ETUDES DES TELECOMMUNICATIONS LANNION - FRANCE

# AD P002217

#### Abstract :

In 1981, the National Telecommunications Research Center (C.N.E.T.) participated in the characterization of the tropical lightnings in the IVORY COAST.

In this communication, we present all the electromagnetic measurements results. Two methods were used during this campaign.

- a time-domain analysis (already used in temperate country, more particulary in ST. PRIVAT D'ALLIER), allowed to characterize the radiated signals by lightnings return-strokes and these emitted by intra-cloud discharges, in secure the most numerous ones in the ics). From the results obtained, we can exercively define the two types of discharges.

- an-harmonic analysis was used to know the instantaneous spectrum evolution during the different lightning phases. During this COPT campaign, we perfected the measurement method for future campaigns, as TRIP 82 (Thunderstorm Research International Program); the first results of which are presented. The data obtained allow to understand better the physical lightning discharge process and to define the VHF-UHF environment of electronical equipment.

#### Introduction :

In 1981, a variety of experimental measurements were performed on the Ivory Coast (Africa), with the intent of studying thunderstorm convection in a tropical region. These experiments, collectively entitled COPT (Convection Profonde Tropicale), grouped together several different organizations from France and the Ivory Coast interested either in thunderstorm dynamic and thermodynamic

processes or their electrical properties and characteristics of lightning. The objectives of the CNET (Centre National d'études des Télécommunications), working in association with the Office National d'Etudes et de Recherches Aérospatiales (France), the Laboratoire de Physique Atmosphérique (Université de Toulouse, France), and the Laboratoire de Physique de l'Atmosphère de l'Université d'Abidjan (Ivory Coast), were to characterize lightning discharges on both a phenomenalogical level (identily distinguish between different stages in discharges, studies of discharge channel propagation, types and nature of leader discharge processes, comparisons with lightning properties observed in temperate regions) and a quantitative level (current amplitude as a function of time, estimates of charge transfer, location and tracking of discharge sources, and electromagnetic field measurements).

In this publication, we will discuss the ensemble of wideband (150 Hz - 20 MHz) magnetic field measurements collected during the COPT campaign. The measurement campaign has permitted a characterization of intracloud discharges, the preponderant discharge process in tropical countries. These signals from intracloud lightning are also compared with those produced during cloud-to-ground discharges.

In addition, in view of the disparity between measurements of RF radiation made by different researchers in the VHF and the poor understanding of the processes which produce these emissions, the CNET has undertaken a program of studies in this domain. The second part of this publication presents some of the

very first results of narrow band RF measurements made during the TRIP 82 (Thunderstorm Research International Program) Campaign. Measurements were made at six frequencies between 60 and 900 MHz using tuned receivers with 350 kHz bandwidths.

## -I- 150 NZ - 20 MHZ ELECTROMAGNETIC FIELD STUDIES

#### I.1 - DATA COLLECTION AND PROCESSING

#### - Experimental means

Measurements of thunderstorm discharge electromagnetic fields were made using magnetic field sensors with a 150 Hz - 20 MHzpassband. These sensors were connected to two sets of recording instrumentation. Each set consisted of both a video tape recorder (VTR) (upper frequency response 3 MHz) and an oscilloscope equipped with a camera with continuously moving film which permitted the recording of fast field variations. The two chains of recording equipment had the following characteristics:

chain 1:
oscillo. + camera:
trigger level: 45 %
(1 %=10 Wb/m<sup>2</sup> or T)
maximum signal: 800 %
VTR: dynamic range: 40 % - 400 %

chain 2 :
oscillo. + camera :
trigger level : 150%
maximum signal : 1600%
VTR : dynamic range : 40% - 1000%

The magnetic field sensors /1/ were placed horizontally in a direction perpendicular to the preferred direction of movement of thunderstorm fronts.

The different sensitivities chosen for the two chains of recording instrumentation permitted simultaneous measurements of fields from both near and distant discharges (knowing that all of our measurements would have to be made on natural lightning).

#### - Limits on the interpretation of results

Some of the equipment operating during these experiments, notably a field mill network, VHF interferometry and Doppler radars,

had allowed us to hope to be able to locate and track all of the discharges observed during the campaign. For our application this would have given an accurate distance to each discharge, as well as the orientation of the discharge channel with respect to the magnetic field antenna. However, the enormous task of processing the data collected by the different organizations has allowed the localization of only a few events. Knowing only rarely the distance to a discharge it has not been possible to determine lightning current amplitudes using field measurements. Also, for the oscilloscope records of magnetic fields, a delay line ought to have allowed us to record the beginning of the signal which was below trigger threshold. For some of the slower events, though, the delay time wasn't sufficient. In these cases, a readjustment of signal amplitudes was necessary.

#### - Processing and analysis of the data

Despite the limitations described above, it is possible to give some general results concerning the parameters which characterize an electromagnetic field impulse.

The video tape recordings were displayed on an oscilloscope and photographed, and have been used to determine the time evolution of the discharges, notably the repetivity and duration of the events.

The film records best characterize the rapid changes in the field, notably the slopes, amplitudes, and pulse durations. Each waveform was manually digitized and the data were stored in the memory of Tektronix 4081 graphics computer. Data were subsequently transferred to a CII IRIS 80 computer for analysis.

#### I.2 - RESULTS OBTAINED

## - Classification of intracloud and cloud-to-ground discharges

A field mill network, operated by the ONERA (Office National d'Etudes et de Recherches Aérospatiales (ONERA) permitted the simultaneous measurement, at 10 locations, of electrostatic field variations at the ground. These data allowed us to identify whether a field change appeared to involve charge neutralization of only one polarity, or both positive and negative charge, descriptions which are often used to model cloud-to-ground

and intracloud discharges, respectively. Also, sequences of impulses of mixed polarities are more likely to be produced by intracloud discharges, because the large amplitude signals radiated by return strokes during a cloud-to-ground discharge are ordinarily all of the same sign. (see photos 1 and 2).

## - Characteristics of tropical lightning intracloud discharges

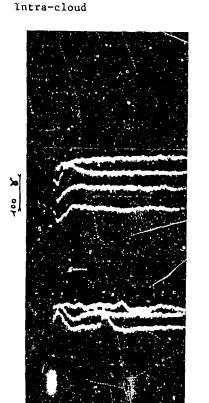
We have studied the following parameters:

- 1. Maximum amplitude
- 2. Slope during fast field transitions
- Pulse width (between t = o and the half peak amplitude point following the peak)
- 4. Sequences of impulses within a discharge

l) Because of the limitations discussed earlier (I.1), it is difficult to present conclusion results regarding intracloud and cloud-to-ground discharge field amplitudes. Nonetheless the table below gives peak amplitudes and the number of events recorded (N) (see reservations in section I.1):

- Intracloud: N = 109;
mean peak amplitude: 96 %;  $\sigma$  = 49 %
- Cloud-to-ground: N = 33;
mean peak amplitude: 120 %;  $\sigma$  = 64 %

For some of the intracloud discharges (N = 35), the location of high reflectivity zones in the storm clouds by radar has given an estimate of distances (2 < D < 20 km) between the field measurement station and the discharges. For these discharges, the mean peak amplitude is 70 Y . If we apply theory developed for return stroke discharges /3,4/





Photos 1 and 2

Streak camera records of successive oscilloscope triggers produced by magnetic field impulses:

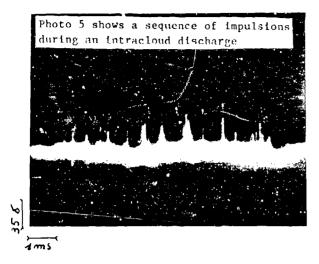
film transport speed 5 cm/s trigger level : 45 Y inhibition time between successive triggers : 5 ms

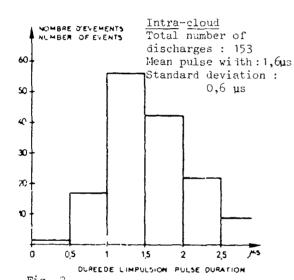
4 h 56' 24''

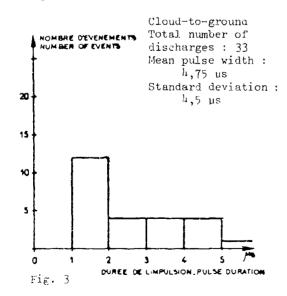
18 MS

4 h 55' 28''

22 june 1981





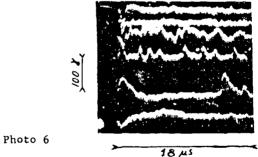


#### - Detailed study of one discharge

#### 22 june 81 - 4 h 53' 08''

This event is one of the complicated to analyse because of the large number of impulsions recorded. Figure 4 shows the time evolution of this discharge, as inferred from the video tape recording. A large amplitude pulse is present near the center of this record which, in contrast with the other impulses which were produced by intracloud processes, was radiated by a return stroke. This discharge was located (5km away from the measurement station) by the VHF interforemeter being operated by the ONERA. The amplitude of the magnetic field exceeded 1000 Y during one 80 µs period (the VTR record was saturated), which, we note implies a peak current of about 60 kA, much larger than the mean peak return stroke current observed in temperate regions (Berger /2/ gives a mean peak current value of 12 kA).

For the intracloud impulses produced during this discharge, which were also located by the VHF interferometer, we have observed both large numbers of isolated impulses, with durations which range from a few tens to a few hundreds of microseconds, as well as sequences of very narrow impulses (pulse widths of a few microseconds). The duration of these pulse sequences was typically 50-60 ms.



In photo 6, we can see some examples of sequences of very narrow impulses, with pulse widths and interval times of the same order, 1 or 2 microseconds. These sequences are one particular characteristic to intracloud discharges and have been observed to occur during different discharges.

The peak amplitudes of the intracloud impulses during this discharge ranged from a few tens of Y to 300 Y .

to these discharges, the value of the peak current, taking into account the distance, is between 2 and 20 kA.

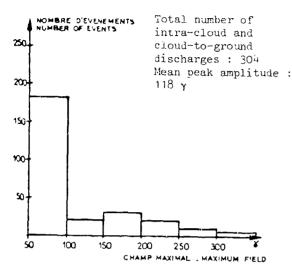


Fig. 1

Figure 1 gives a histogram of peak magnetic field amplitudes, intracloud and cloud-to-ground discharges combined, observed during the course of the COPT campaign.

2) The slope between 10 and 90 percent of peak during rapid field transitions has been calculated fo all digitized waveform data using the method of least squares. The values obtained for intracloud and cloud-to-ground discharges are comparable.

```
~ Intracloud : N = 153 ;
mean slope : 71 \chi /µs \sigma = 40 \chi /µs ~ Cloud-to-ground : N = 33 ;
mean slope :76 \chi /µs \sigma = 53 \chi /µs
```

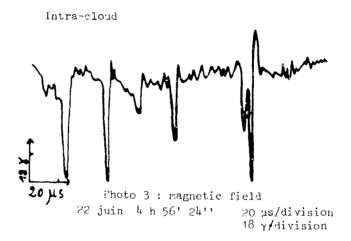
3) The most notable difference between the impulses radiated during intracloud and cloud-to-ground discharges is in the pulse widths, here, the time between t = 0 and the half amplitude point following the peak. This difference is obvious in photos 1 and 2. Figures 2 and 3 present histograms of measured pulse widths. Mean values are summarized below

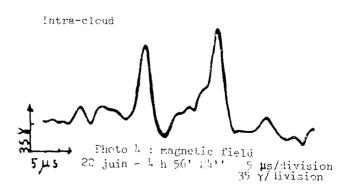
```
- Intracloud : N = 153 ;
Mean pulse width 1,6 \mu s ;
\sigma = 0,6 \mu s
- Cloud-to-ground : N = 33 ;
Mean pulse width 4,75 \mu s ;
\sigma = 4,54 \mu s
```

The intracloud discharge pulses are much narrower than those radiated during cloud-to-ground discharges.

4) With the video tape records we have been able to observe that during an intracloud discharge; impulses often occur very quickly in sequence, that is with interval times ranging from a few microseconds to a few tens of microseconds (see, for example, photos 3 and 4).

Repetition frequencies of this order, which have been observed in different intracloud discharges, are much higher than are found during a cloud-to-ground flash. Berger /2/, for example, gives a mean interval time between return strokes of 33 ms.





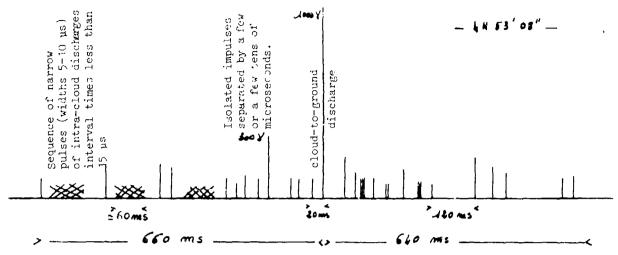


Fig. 4: Chronology for the discharge of 22 jun 81 - 4 h 53' 08''

#### 1.3 - DISCUSSIONS AND CONCLUSION

until the present experimental studies of thunderstorm discharges have been confined to cloud-to-ground flash /2, 5, 6, 7/. As a result, we have in hand a considerable amount of data characterizing the different aspects of that process. comparison, when one considers the intracloud discharge process, there is a very real shortage of data. The intracloud discharge is also very complex /8/. Electromagnetic field measurements, with which it is possible to compare our results from the COPT campaign, have been made in Florida by /9, 10/. Those anthors have also observed isolated large impulses, amplitude during intracloud discharges, with durations which range from 10 to about 200 µs, as well as trains of narrow pulses (widths of 2-3 µs). They note also that the risetime of the fast pulses is comparable (ie, less than a microsecond) to that found in return stroke fields.

#### -II- NARROW-BAND RF MEASUREMENTS 60-900 MHZ

#### II.1 - BIBLIOGRAPHIC ASPECT

A considerable amount of work has been done with the intent of quantifying the energy radiated by the electrical processes of a lightning discharge. A review and synthesis of results has been published by /11/ and more recently by /12/. Among the outstanding points considered were the following.

#### - Form of the spectrum

Two types of representation of the radiation as a function of frequency are used.

- The first consists of expressing the spectral amplitude density of the radiation beginning with continuous recordings of signals from a battery of tuned narrow-bandwidth receivers. Integration of these data, the exact form of which depends on the shape of the impulses recorded, is then necessary. This method has been employed by /13/. The mean spectral amplitude density from several discharges and normalized to a distance, d = 10 km, is proportional to f<sup>-1</sup> in the range 10 KHz to 100 MHz.

- The other method adopted by /11/ gives directly the mean peak amplitude, an average of observations from several flashes, as a function of the receiver frequency and bandwidth. Disparate measurements normalized to a distance, d = 10 km from the flash and to a bandwidth of 1 KHz. If for frequencies from 10 kHz to 10 MHz there appears to be concordance among the results published by different anthors, for a 1/f decrease in the spectrum with increasing frequency, outside of that interval there is a large dispersion in the data, which is all the more difficult to interpret because of its limited number. One can only remark that there is a tendency for the amplitude to vary more slowly with frequency. Results published by /14/ show an increase of amplitudes beginning at and continuing above 300 MHz and suggest that this turning point in the spectrum appears to be due

to the intervention of a different discharge process. More recently /15/ have observed a similar phenomenon beginning at 50 MHz, with the RF emissions showing a maximum around 100 MHz.

#### - Temporal structure

While strong RF emissions associated with intracloud discharges and the stepped leader, dart leader, and K change phases of a cloud-to-ground discharge have been observed, the time evolution of the radiation produced during a return stroke is still a subject of controversy. For example, /16/ as well as /17/, have mentioned a delay of a few tens of microseconds between the VHF radiation and the abrupt fast electric field change associated with the beginning of a return stroke. The explanation given for this delay is that the return stroke current which propagates from the the cloud towards does radiate at VHF frequencies, but that these radiations are due to the branches of the return stroke channel and due to junction processes once the current wave has entered the cloud /16, 17/. This explanation, which leaves the impression that VHF radiation does not accompany the creation of the return stroke current wave, seems to be contradicted by observations made at 3 MHz by /18/. Here, in 90 % (54 of 61) of the records examined, a large impulse (in 25 of the 54, the largest) was observed at the beginning (time synchronization accuracy 1 µs) of the first return stroke. A large impulse (the peak in the RF emissions in 99 % of more than 100 observations) was observed to occur at the beginning of subsequent strokes also.

#### II.2 - EXPERIMENTAL MEANS

Six receivers with 350 kHz bandwiths and central frequencies of 60, 100, 175, 300, 500 and 900 MHz have been used during the experimental campaigns COPT 81 and TRIP 82. Each receiver was equipped with a logarithmic amplifier which gave an 80 dB dynamic range.

The front end of each receiver was connected to a vertically polarized half wave dipole antenna, the ensemble of which were mounted on a mast in a fashion that would minimize mutual coupling between antennas.

The signals thus obtained were recorded wit' a 400 kHz bandwidth magnetic tape recorder

operating in the FM mode.

Signals from a capacitive electric field antenna (BW 400 Hz - 2 MHz) were recorded simultaneously to permit precise temporal location of the different phases of a discharge, most notably the return stroke. To achieve the maximum possible bandwidth, the recorder was operated at peak tape transport speed, which, with 14 inch tape reels, allowed about 15 minutes of continuous recording.

The campaign COPT 81 at Korhogo, on the Coast, permitted us to test the Ivorv functionment of the bank of receptors and to put the system into an improved configuration during the TRIP 82 campaign. These data are presently in the process of being digitized. The use of digitized data will permit an investigation more detailed than the preliminary approach to be presented here. For these initial studies, the analog tape data were played back using an optical (UV) chart recorder, permitting a reconstitution of the time evolution of the signals with a bandwidth of 128 kHz. The fastest time scale achievable was 156 µs/cm.

should Ιt bе noted that time displacements between channels due to misaligned magnetic recorder heads as well as time scale changes due to capstan fitter and stretching of the tape, allow us resynchronize the signals with an accuracy of the order of 10 µs. After digitization, the use of time synchronization signals which were superposed on all data channels on a second magnetic tape recorder, wi11 nermit synchronization of better than 1 µs.

#### II.3 - TRIP 82 RESULTS

During the course of the TRIP 82 Campaign, which was conducted at Socorro, New Mexico, about ten triggered discharges and a large number of natural flashes have been studied; a total of about 1 hour of thunderstorm activity was recorded.

During the remainder of this publication we intend to describe in detail, observations based on two discharges - one triggered and one natural discharge.

#### II.3.1 - Shape of the spectrum

Figure 5 presents the peak signal

levels observed during each of the two flashes at the different frequencies and normalized to the Pierce curve /11/, that is normalized to a

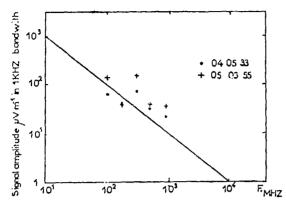


Fig 5: Peak received amplitude at 10 Km

1 kHz bandwidth and a distance of 10 km. We can remark that there is reasonable accord between the observed peak amplitudes and the Pierce curve.

#### II.3.2 - Radiation macrostructure

Figures 6 and 7 reproduce, totally, the signals recorded during the triggered event 04-05-33 and the natural discharge 05-03-55, respectively. In these two figures one can see clearly the simultaneous evolution of the VHF radiations at the six frequencies studied, and the signal from the capacitive antenna.

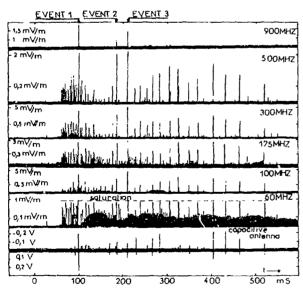


Fig.6: Signatamplitudes in 128KHZ, bandwith-Lightning 04-05-33

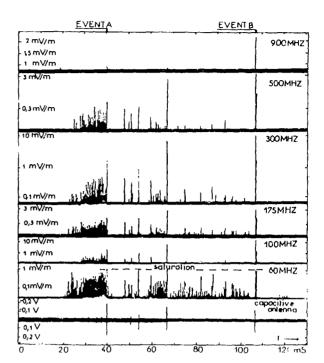


Fig 7: Signal amplitudes in 128kH7 bandwith 11 ahming 05 (B.55

One can observe that in both cases, the beginning of the discharge is indicated by continuous VHF activity, which persists for a few tens of milliseconds and ends with a brutal increase of radiation associated with a change on the capacitive antenna signal. This initial radiation corresponds with preliminary breakdown processes within the cloud, as well as the development of a stepped leader which initiates the first stroke in a cloud-to-ground discharge.

If for the natural discharge 05-03-55 this phase has a very regular evolution, corresponding to the creation of a stepped leader which continues to develop up until the return stroke, for the triggered discharge 04-05-53 the appearance is much more disturbed. We see here an abrupt beginning of a stopped leader which stops 20 ms later and is followed, during the next 30 ms, by perhaps ten intracloud events visible at the different frequencies. It is only after a second stepped leader of very short duration (1,7 ms) that the return stroke is initiated. The short duration of this leader can be explained perhaps by the existence of a non-radiating, continuously moving upward discharge initiated by the wire pulled upward from the ground by the rocket.

The stepped leader doesn't intervene until after the end of the triggering phase of the discharge.

During the following phases of the two discharges, the VHF radiation appears as abrupt impulses with durations of less than 1 ms and mean interval times on the order of 10 ms.

For the event 04-05-53, the capacitive antenna record shows roughly a dozen large amplitude impulses indicating significant currents flowing within the cloud or between the cloud and ground. There are roughly 20 large impulses visible on the VHF records, however, which leads us to conclude that the VHF radiation isn't associated exclusively with the cloud- to-ground discharges, nor with K change processes within the cloud.

These emission sequences last for about 500 ms in the case of discharge 04-05-33 and for about 100 ms for event 05-03-55. There is no radiation afterwards and for the several seconds preceding the next discharge.

#### II.3.3 - Radiation microstructure

#### (a) First return stroke

The fine structure of events (1), (2) and (3) of discharge 04-05-33 as well as that of events (A) and (B) of discharge 05-03-55 are presented in figures 8, 9 and 10.

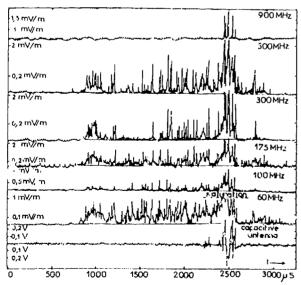


Fig.8: Signal amplitudes in 128 KHZ bandwith-Lightning 04 05 33 - Event 1 -

Figure 8 and figure 10 (a) show the radiation associated with the propagation of the stepped leader and the initiation of the first return stroke for the two discharges.

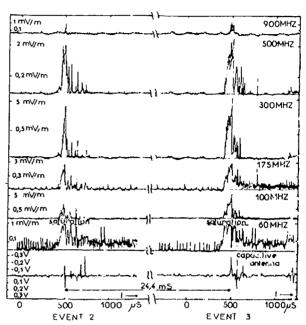


Fig 9: Signal amplitudes in 128KHZ bandwith - Lightning 04: 0533-Events 2, 3

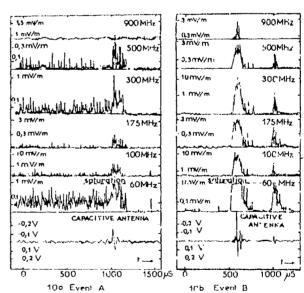


Fig. 10. Signal amplitudes in 128KHZ bandwith-Lightning 05-03-55

While figure 10 (a) represents only the final part of the leader associated with event (A), figure 8 shows all of the radiation from the leader of event (1). We note that the

beginning of this leader is indicated by a burst of ladiation which lasts for about 200 µs. In both cases one can observe that the radiation consists of a large number of impulses with pulse widths and interval times less than the 3 µs time constant of the receiver producing more slowly varying features. Despite this effect, the largest impulses have mean interval times of a few tens of microseconds and could correspond with steps of the leader process.

The end of the leader phase occurs in conjunction with an abrupt transition on the capacitive antenna record and is caracterized by a sharp increase in the level of RF radiation at all frequencies. These emissions persist for a few hundreds of microseconds and are followed by a quiet period of a few milliseconds duration.

#### (b) Subsequent events

Figures 9 and 10 (b) show the fine structure of events (2) and (3) of discharge 04-05-33 and of event (B) of discharge 05-03-55.

These events occur simultaneously with abrupt changes of level on the capacitive antenna record. They are not preceded by VHF emissions, except at 60 MHz, where the radiation might be due to corona discharge off the end of the antenna. It should be noted that none of the subsequent events in these 2 flashes is preceded by VHF radiation which could be identified with a dart leader, thus it seems to us that this process might not radiate at the frequencies studied.

In the case of the event in figure 9, the initial envelope of radiation seems to provoke a persistant radiation indicated by the offsets visible at 60 MHz for event (2) and at 60 and 175 MHz for event (3). This radiation might be produced by micro-discharges which follow an abrupt field change produced by an intracloud discharge. This phenomenon does not appear in the case of event (B) in figure (6) which seems to be a subsequent stroke.

The envelopes of VHF radiation are composed of a multitude of impulsions which occur more frequently and have larger amplitudes than found during the leader phase. One can frequently distinguish between successive groups of impulses which are separated by a few tens of microseconds, such as seen in figures 8, 9 and 10. The suggestion

given by /16/ and /17/ is that this radiation is produced by the branches in the first return stroke channel as well as junction processes within the cloud. To support this hypothesis it is interesting to note the compact appearrance of event (B) in keeping with an absence of branches and a minimum of micro discharges associated with subsequent strokes.

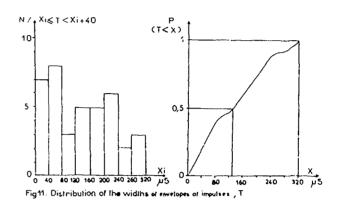


Figure 11 gives the distribution of the widths, T, of the envelopes of impulsions based on about 40 events from the two flashes. The mean width obtained, "T mean", is  $132~\mu s$ .

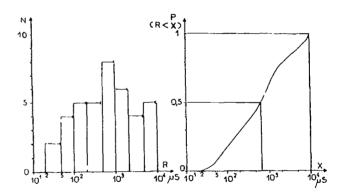


Fig 12 - Distribution of the delay R. between two successive envelopes of Impulses

For each of the events presented in figures 8, 9 and 10 we observe a second narrow envelope of impulsions which appears a few hundreds of microseconds after the principal packet of impulsions. For the event (B) this second burst of radiation is itself accompanied by an appreciable capacitive antenna change. The phenomenon has also frequently been observed to occur without a capacitive antenna change. Figure 12 presents the distribution of separation times between two successive impulse groups based on about 40 measurements. In 50 % of the cases the separation time is less than 680 ms.

The second burst of radiation which we have observed could be generated by the current flowing from a charge induced in the cloud following a return stroke or a K change process.

#### 11.4 - CONCLUSION

Continued reduction and analysis of data from the TRIP 82 campaign will permit us to verify and explore in more detail the considerations given here which were based on two discharges, and will allow a better characterization of the radiation from different phases of a discharge. With the digitized data and sufficiently precise synchronization between channels, we will be able to reconstruct the temporal evolution of the spectrum and the capacitive antenna record on a microsecond time scale. Like /19/, we can already say that the forms of the signals recorded at different frequencies are not identical. This puts into evidence the existence of numerous different discharge processes during a lightning flash.

Additional narrow-band RF measurements will be made 3 km from a discharge triggering point during the campaign to be held june-september, 1983, at the experimental station at St-Privat-d'Allier, "rance. Based on these early studies, it appears necessary to increase the sensitivity of the 900 MHz receiver, which was insufficient for detailed study except during very energetic phases of a discharge. The saturation of the 60 MHz receiver must be attributed to an incorrect choice of the terminating resistance, the receiver doesn't require any modification. During the course of the next campaign, to remove any ambiguity concerning the type of radiating process, a wideband magnetic field sensor (150 Hz - 20 MHz), as well as an optical sensor which will point a couple of hundred meters above the rocket launching point, will be recorded in addition to the signal from the capacitive antenna.

Finally, in order to begin studies of lightning emissions at microwave frequencies, a 4,6 GHz signal from a microwave horn antenna, pointing at the triggering site, will be recorded alongside the six RF frequencies already studied.

#### COMMENTARY

The results presented in this communication treat two particular aspects of thunderstorm electromagnetic emissions - the radiation produced by intracloud discharges and the radiation in the VHF-UHF band.

Despite the fact that these data can have important consequences for the development of telecommunications systems whether situated in a high risk area (tropical region) or because they involve new techniques (numerically encoded radio wave transmission for example), very few studies of this kind are found in the literature.

From this initial work we can say :

- that, based on the amplitudes measured at the ground and the frequency of occurence, the influence of electromagnetic field impulses produced by intracloud discharges in a tropical region on a telecommunication network, particularly a digital system, cannot be neglected.
- that our understanding of the physical processes and the possible consequences that lightning radiation in the VHF-UHF band may have on new radio wave transmission systems (digital systems, for example) is still too limited.

#### ACKNOWLEDGEMENTS

The work presented in this publication has been supported in part by the ONERA, contract  $\pi^{\circ}$  19500 / SAT.2. / CT.

#### BIBLIOGRAPHY

- /1/ J. HAMELIN, and al.

  "Sonde de mesure du champ magnétique dû
  à une décharge orageuse".

  Annales des Télécommunications janvier février 1978.
- /2/ K. BERGER, and al.
  "Parameter of lightning flashes".
  Electra n° 41 1975.

- /3/ M.P. UMAN, and al.

  "Correlated electric and magnetic fields from lightning return-strokes".

  J.G.R. vol. 80 n° 3 january 1975.
- /4/ C. LETEINTURIER, and al.

  "Electromagnetic field emitted by lightning stroke. Theoritical model taking into account the ground conductivity.

  Comparison with experimental measurement made at Saint-Privat-d'Allier".

  "5ème International Wroclaw Symposium on Electromagnetic Compatibility 17-19 sept. 1980.
- /5/ Y.T. LIN, and al.

  "Characterization of lightning electric and magnetic fields from simultaneous two station measurements".

  J.G.R. 8th 6307-6314 1979.
- /6/ SAINT-PRIVAT-D'ALLIER RESEARCH GROUP,

  "Eight years of lightning experiments
  at Saint-Privat -d'Allier".

  Revue générale de l'électricité sept.
  1982. n° 9.
- /7/ E. GARBAGNATI G.B. LOPIPARO,

  "Lightning parameters Result of 10
  years of systematic investigation in
  Italy".

  International aerospace conference on
  lightning and static electricity march 1982 Oxford ENGLAND.
- /8/ T. OGAWA A. BROOK,

  "The mechanism of the intracloud
  lightning discharge" J.G.R. vol. n°
  24 december 1964.
- /9/ E.P. KRIDER, and al.

  "Regular radiation field pulses
  produced by intracloud lightning
  discharges".

  J.G.R. vol. 80 n° 27 sept. 1975.
- /10/ C. WEIDMAN E.P. KRIDER,

  "The radiation field wave forms produced by intracloud lightning discharge processes".

  J.G.R. vol. 84 n° 66 juin 1979.

- /11/ E.T. PIERCE,
   "Atmospherics and radio noise in lightning".
   vol. 1, Golde, R.H., Ed., Academic Press, New-York, 1977.
- /12/ E.A. LEWIS,

  "Highfrequency radio noise in handbook of atmosphe- rics".

  vol. 1, Volland, H., Ed., CRC Press,
  Inc., Boca Raton, Florida, 1982.
- /13/ F. HORNER P.A. BRADLEY,

  "The spectra of atmospherics from near lightning discharges".

  J. of Atmospheric ant Terresterial Physics, 1964, vol. 26, pp. 1155-1166
  Pergamon Press. L.t.d.
- /14/ E.L. KOSAREV V.G. ZATSEPIN A.V. MITROFANOV,

  "Ultrahigh frequency radiation from
  lightning".
  J. Geophysic Res. 75 (36), 7524, 1970.
- /15/ Z.G. KACHURI. M.I. KARMOV Kh.Kh. MEDALIYEV,

  "The principal characteristics of the
  radio emission of convective clouds".
  IZV, Atmos. Oceanic Phys. 10 (11) 1163,
  1974.
- /16/ M. BROOK N. KITAGAWA,

  "Radiation from lightning discharges in
  the frequency range 400 to 1000 MC/S".
  J. Geophys. Res., 69 (12), 2431, 1964.
- /17/ D.M. LEVINE E.F. KRIDER,

  "The temporal structure of HF and VHF radiations during Florida lightning return strokes".

  Geophys. Res. Lett. 4, 13-16, 1977.
- /18/ C.D. WEIDMAN,

  "The submicrosecond structure of lightning radiation fields".

  Ph. D. Dissertation, University of Arizona, Tucson, AZ, 1982.
- /19/ G.N. OETZEL E.T. PIERCE,

  "The radio emissions from close
  lightning, in "Planetary
  electrodynamics".

  (S.C. Coronici and J. Hughes, Eds), vol.
  1, pp 543-571. Gordon and Breach,
  New-York, 1969.



# AD P002218

THE EFFECT OF PROPAGATION ON ELECTROMAGNETIC FIELDS RADIATED BY LIGHTNING

Louis Baker and Robert L. Cardner Mission Research Corporation, Albuquerque, New Mexico

#### ABSTRACT

The model of Gardner (Radio Science 16, 377-384, 1981) is used to study the attenuation of lightning fields with distance over a variety of propagation paths. The lightning channel may consist of an arbitrary arrangement of linear segments, each with a different propagation velocity. The effects of an imperfectly conducting, anisotropic ionosphere and a lower surface of earth or water (including sea state) are studied.

"It is of great interest to deduce the properties of lightning, such as the current profile as a function of time, from remote measurements of the radiated fields. For this reason, distortion of the signal by propagation path effects must be understood quantitatively. The study of the distortion of electromagnetic transient fields as they propagate over the earth's surface has a long history; Sommerfield (1)\* considered the propagation of radio waves over an imperfectly conducting earth in 1909, and a number of recent texts (2,3,4) review more recent developments. In general, the signals are attenuated, the attenuation increasing with frequency and decreasing as the surface conductivity increases. This presupposes smooth surfaces; corrugated surfaces (5,6,7) have also been studied in connection with propagation over a sea surface covered by waves. When the ocean waves have lengths small compared to the radio wavelength, a "trapping" of the surface wave is possible (8) which results in an increase in signal, while at higher frequencies an increased attenuation results. The attenuation dces not increase monotonically with frequency, as Barrick (7) notes, but rather a saturation sets in, with the greates losses for frequencies in the range 10-15 MHz for typical ocean wave spectra...

In this paper, we use the computer model developed by Gardner (9,10), extended using the results of Barrick (6), to evaluate the role of propagation effects on lightning signals.

THEORY

First we will briefly review the theory; a more complete discussion will be found in references 2-10. The lightning channel is treated as a dipole source with specified current, with triple exponential form:

$$I(t) = [A(exp(-at) - exp(-bt)) + B exp(-ct)] U(t)$$
 (1)

where U(t) is the Heaviside step function, A = 30 kA, B = 2.5 kA, a =  $2 \times 10^4 \text{ sec}^{-1}$ , b =  $2 \times 10^5 \text{ sec}^{-1}$ , c =  $1. \times 10^3 \text{ sec}^{-1}$ . The term proportional to A has an inverse rise time of roughly b, or about 10 microseconds, and a fall time of roughly 1/a or about 100 microseconds. The term

\*Numbers in brackets designate References at end of paper.

proportional to B represents the 'continuing current" and constitutes a slow "tail" to the current pulse, falling off over several milliseconds. While such a form for I(t) is not perfect (e.g., its behavior at t=0), it is often used [12] and we will follow custom for ease of

comparison with other references.

We will work in frequency domain rather than time domain, and assume the fields have time dependence exp (iwt). This will both facilitate analysis and comparison with observation. We can in principle inverse Fourier transform into time domain if desired. The lightning channel is treated as a chain of dipole sources, and the Hertz potential [13] may then be used to find the fields at any point. The Hertz vectors have simpler expressions in terms of the sources than the vector and scalar potentials and therefore simplify calculations. For example, the electric field due to a vertical electric dipole dipole may be written in terms of the vertical component of the electric Hertz vector as:

$$\dot{E} = \nabla \nabla \cdot \pi + k^2 \pi \tag{2}$$

where  $\pi$  is the Hertz vector and  $k = \omega/c$  is the wavenumber. Expressions for general dipole source orientation will be found in Balos [2]. Cylindrical coordinates  $(\rho,\phi,z)$  will be used [10], with the source centered above the origin, as shown in Fig. 1. Wait [7,8] shows that the Hertz vector due to a vertical dipole at any point above the surface may be written as:

$$\pi = \frac{Ids}{4\pi i \epsilon \omega} \int_{0}^{\infty} \left[ e^{xp} \left[ -u | z + h | \right] + R(\lambda) e^{xp} \right] \left[ -u(z - h) \right] \frac{\lambda}{u} J_{0}(\lambda_{\rho}) d\lambda$$
 (3)

where c the speed of light, ds is the length of the dipole carrying current I (resulting in a dipole moment of Ids),  $u = (\lambda^2 - k^2)^{\frac{1}{2}}$ , and

$$R(\lambda) = \frac{u - ik\Delta}{u + ik\Delta} \tag{4}$$

is a reflection coefficient, expressed in terms of the normalized surface impedance  $\Delta$  which we will define shortly. By use of the identity

$$exp - ikr/r = \int_{0}^{\infty} exp[-u(h-z)] J_{0}(\lambda \rho) d\lambda \qquad (5)$$

where

$$r = (\rho^2 + (h-z)^2)^{\frac{1}{2}}$$

We may put this in the form:

$$\pi = \frac{Jds}{4\pi i \varepsilon \omega} \left[ \frac{e^{ikr'}}{r'} + \frac{e^{-ikr}}{r} - 2P \right]$$
 (6)

with

$$r = (\rho^{2} + (z-h)^{2})^{\frac{1}{2}}$$

$$r' = (\rho^{2} + (z+h)^{2})^{\frac{1}{2}}$$

$$P = \int_{0}^{\infty} \frac{ik\Delta \exp - u(h-z)}{u_0 + ik\Delta} \frac{\lambda}{u} J_0(\lambda \rho) d\lambda$$
 (7)

We clearly have a direct wave of the form:

$$\pi_d = Ids/(4\pi i \varepsilon \omega) \exp(ikr)/r$$
 (8)

with a reflected wave:

$$\pi_r = Ids/(4\pi i \epsilon \omega) [exp(ikr')/r' - 2P]$$
 (9)

(where r' is the distance to the image dipole source). Note that for a perfectly conducting, smooth ground P=0. The quantity  $\Delta=z/\eta$  in the above is the surface impedance normalized by the free space value  $\eta=120$  ohms. The surface impedance is the wave impedance, that is the ratio of fields z=E/H, at the surface. For a smooth homogeneous surface it is given by:

$$\Delta = u_1 / (\sigma_1 + i \varepsilon_1 \omega) \tag{10}$$

where

$$u_1 = (k^2 - k_1^2)^{\frac{1}{2}}$$
,  $k_1 = (\omega^2 u_1 \epsilon_1 - i \omega \mu_1 \sigma_1)^{\frac{1}{2}}$  (11)

 $\mathbf{k}_1$  as the wavenumber below the surface,  $\omega$  the frequency,  $\sigma_1$  the conductivity,  $\epsilon_1$  and  $\mu_1$  the dielectric permittivity and the permeability, respectively, with Refs. 6, 7 giving corrections for corrugations. Note that it is in general a complex number; the real part represents a resistive component while the imaginary part represents a reactance and gives rise to the wave trapping discussed previously. The integral may be evaluated using the asymptotic methods, yielding an expression containing the complex error function. We found it simplest and most accurate to include the results of Ref. 6 by simply calculating the transmission for a smooth surface and then correcting this result for the changed attenuation, interpo-

lating from a table in frequency, range, and sea state from the results of Barrick. His data show little effect below frequencies of 3 MHz for propagation ranges below 50 km. Enhancements in signal due to trapping are typically only fractions of a dB for such ranges and are therefore much smaller than other effects. Finally, integrating along the length of the finite channel segments, taking into account the finite signal velocity, results in the factor ds being replaced by terms of the form

$$Lsinc(kL/2 (v - \nabla r)_{7})$$
 (12)

where L is the length of the segment, and V = v/c is the normalized propagation velocity and

sinc(z) = sin(z)/z.

We will refer to the signal discussed above as the "ground wave". In addition, there is a "sky wave" due to reflection by the ionosphere. Its treatment is analagous, the "single bounce" approximation of Wait [11] being used to find the reflection coefficient. References 9 and 10 give the details of the method used. The sky wave is typically unimportant except at the lowest frequencies. Finally, we note that at frequencies below 1 kHz it is most appropriate to treat the propagation as occurring in a waveguide formed by the ground and the ionosphere. This is discussed in Ref. 9 and will not be discussed here.

RESULTS

Fig. 2 compares the results of Ref. 13 with our calculations, for a pulse propagating at the speed of light along a vertical channel with a length of 1500 m at a distance of 50 km. We show results for propagation over moist ground (the lowest curve), calm sea, and sea in "sea state 6", corresponding to a wind of 30 knots. We note that agreement with the propagation over water is excellent for frequencies below 10 MHz. It would seem that the assumed form for the current I(t) possesses too high a content of high frequencies, possibly due to the "continuing current" term which is discontinuous near t=0. Note that attenuation over the land is somewhat higher than over the highly conductive sea water, but that this is significant only for the higher frequencies. Note also that sea state has an almost indiscernable effect.

Figs. 3-4 presents results for similar calculations for a tortuous channel, both for pulses propagating at the velocity of light and 1/3 that velocity. As the travel time of the pulse down the channel increases, due either to the lengthening of the channel or the slowing of the propagation along the channel, the resonances shift downward in frequency and the structure of nulls in the  $E(\omega)$  curve shifts downward. The slower propagation velocity reduces the high frequency component somewhat. Hence the gross features of the curve, along with the location of the resonances in frequency space, tell us the gross properties of the stroke--its length and propagation velocity.

Note that we do not include effects of branching, there being only one current-carrying channel, although it need not be a straight line. Additional branches can be treated with a fairly straightforward modification of the code, how-

Unfolding the pulse shape would be quite a bit more difficult. The pulse shape may be expected to change with propagation [9]. The pulse shape and the precise geometry of the channel would interact to give the fine structure of  $E(\omega)$  at higher frequencies. We could hope to extract the current as a function of space and time only with both optical measurements to supply channel geometry and an array of electromagnetic observations to enable us to separate signals from different portions of the stroke. Note that even the rolloff of signal with frequency is a function of both propagation velocity and pulse shape, and therefore it would be useful if the optical observations would give us the former. There is some hope that in the near future experiments in New Mexico may provide us with such correlated measurements.

#### REFERENCES

l. A. Sommerfeld, "Uber die Ausbreitung der Wellen in der drahtlose Telegraphie", Ann. Physik 28, 665-737 (1909). 2. A. Baños, Jr., "Dipole Radiation in the

Presence of a Conducting Half-Space," Oxford:

Pergamon Press, 1966.

3. J. R. Wait, "Electromagentic Waves in Stratified Media," New York: Pergamon Press, 1970.

4. J. R. Wait, "Wave Propagation Theory", New York: Pergamon Press, 1981. 5. D. E. Barrick, "Theory of HF and VHF propagation across the rough sea, 1, The effect of surface impedance for a slightly rough highly conducting medium at grazing incidence", Radio Science 6, pp. 517-526, 1971.
6. D. E. Barrick, "Theory of HF and VHF

propagation across the rough sea, 2, Application to HF and VHF propagation above the sea, " ƙadio

Science 6, pp. 527-533, 1971.

7. J.R. Wait, "Perturbation analysis for reflection from two-dimensional periodic sea waves," Radio Science 6, pp. 387-391, 1971.

- 8. J. R. Wait, "Electromagnetic Surface Waves," in Advances in Radio Research, J. A. Saxton, ed., Vol. 1, pp. 157-217, New York: Academic Press, 1904.
- 9. R. L. Gardner, "A model of the lightning return stroke," Thesis, U. of Colorado, 1980.
- 10. R. L. Gardner, "Effect of the propagation path on lightning-induced transient

fields," Radio Science 16, pp. 577-384, 1981.

11. J. R. Wait, "Introduction to the theory of VLF propagation," Proc. IRE, 50, pp. 1624-47, 1962.

12. D. M. LeVine and R. Meneghini, "Electromagnetic fields radiated from a lightning return stroke: Application of an exact solution to Maxwell's equations, "J. Geophys. Res., 83(c5), 2377-84, 1978.

13. J. B. Marion, "Classical Electromagnetic Radiation," New York: Academic Press, 1965, pp. 227ff.

14. M. A. Uman and P. Krider, "A Review of Natural Lightning: Experimental Data and Modeling," IEEE Trans. Electromag. Compat., EMC-24, pp. 79-111, 1982.

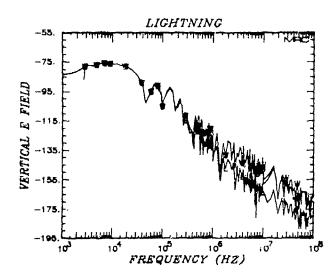
FIGURE CAPTIONS

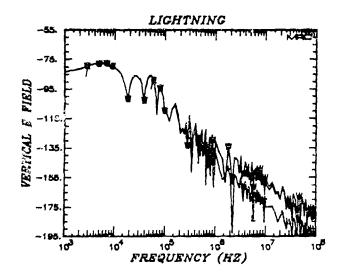
Fig. 1 - Geometry for a point source

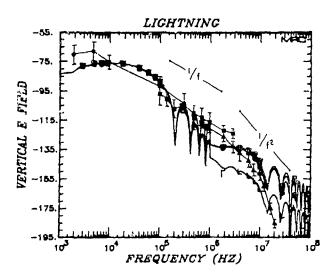
Fig. 2 - Vertical electric field just above the surface, as a function of frequency, for a vertical channel 1500 m long, carrying the standard current pulse propagating along the channel at the speed of light. The curves are, from bottom to top, for propagation over moist ground, ocean water in sea state six, and a smooth ocean surface

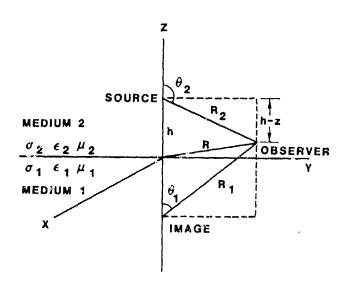
Fig. 3 - Same as Fig. 2, but for a channel with three straight line segments connecting the following points in Cartesian coordinates: (0,0,0), (500,500,500), (-500,-500,1000), (0,0,1500) where all lengths are in meters

Fig. 4 - Same as Fig. 2, but for a current pulse along the channel with a propagation velocity of 1/3 the speed of light









# AD P002219

PERFORMANCE OF THE SANDIA LIGHTNING SIMULATOR DURING F-14A AND F/A-18 AIRCRAFT LIGHTNING TESTS



Ronald I. Ewing Sandia National Laboratories Albuquerque, NM 87185

#### ABSTRACT

Two Navy Aircraft (F-14A and F/A-18) were subjected to high-level lightning tests using the Sandia Lightning Simulator. The peak pulse currents applied were varied from 9 to 170 kiloamperes. The nominal rise time to peak was 2 microseconds. Double-pulse and continuing currents were also applied. Several high current, high voltge pulses were also obtained. Ninety-six test pulses were applied to the F-14A and sixty-four pulses were applied to the F/A-18. Approximately eighty percent of these pulses met the test specifications and essentially all pulses produced useful data.

THE F-14A and F/A-18 AIRCRAFT were tested as part of Operation FLLASH (Full Level Lightning Aircraft System Hardening) sponsored by the Naval Air Systems Command of the U. S. Department of the Navy. This paper will present a summary of the performance of the Sandia Lightning Simulator during these tests. The results and interpretation of the tests and measurements made on the aircraft will not be discussed here.

#### FACILITY DESCRIPTION

The purpose of the Sandia Lightning Simulator is to provide a facility for studying the effects of lightninglike currents on components and systems of interest to the weapons community. Use of the Sandia Lightning Simulator is described in detail elsewhere in these proceedings (See: White, R. A., Full Systems Tests Using the Sandia Lightning Simulator.). The electrical currents are designed to simulate an extremely severe (up to 99th percentile) lightning ground return stroke. In addition, a multistroke capability and a continuing current component are provided. The simulator is in the development stage, and all tests are considered to be emperimental.

The current pulses are provided by oil-insulated Marx generators located in two separate tanks, each containing about 16,000 gallons of oil. Two Marx generators are located in each tank. In most tests, the object to be tested is suspended in a coaxial fashion over the output terminal, located between the tanks. The continuing current is produced by a motorgenerator set built from modified diesel-electrical traction motors. The operation of the simulator is controlled from an adjacent shielded control room that also serves as the data collection center.

#### AIRCRAFT TEST CONFIGURATIONS

The aircraft were located outdoors, on a concrete pad adjacent to
the building housing the simulator.
An oil-filled coaxial line and high
voltage bushing were constructed to
connect the output terminal of the
simulator to the nose of the aircraft,
located over twenty feet apart. The
outer conductor of this line served
as the ground return path for the
injected current. The coaxial line
also contained a dummy load coil that
could be switched into the circuit
for the purpose of adjusting the

simulator parameters without applying pulses to the aircraft. The high voltage bushing used two atmospheres of  $\rm SF_6$  gas for electrical insulation.

The aircraft test fixture arrangement is shown in Figure 1. The output of the high voltage bushing was hardwired to the nose of the aircraft. The aircraft was insulated from ground by resting the landing gear on individual insulating pads. The current could be extracted from the tail, wing tip, or fins of the aircraft, depending upon the particular test. The extraction point could be hard-wired or an air gap provided. Air gaps up to eleven inches were used to cause the aircraft to charge up to several hundred thousand volts prior to breakdown and current discharge. A system of cables around the fuselage and wing of the aircraft was used as the ground return system to provide an approximately coaxial arrangement.

#### SIMULATOR OUTPUT

The peak current output of the simulator was varied from 9 to 170 kiloamperes by controlling the charge voltage applied to the Marx generators and by connecting one, two or three Marxes in parallel. The lowest currents were obtained by using a single Marx generator and shunting part of the current away from the aircraft. The simulator current was measured using a five milliohm current viewing resistor in series with the ground current return circuit. Three current waveforms obtained during these tests are shown in Figures 2, 3 and 4. The negative going currents are shown here as they were displayed on the recording digitizers.

Figure 2 shows a low current test using a single Marx with a shunt located in the oil tank. The current reaches peak value, about 15 kilo-amperes, in just under 2 microseconds. A laser-triggered gas discharge switch ("crowbar") located at the output of the Marx, is triggered about one microsecond after peak current. This crowbar switch changes the circuit to produce an exponentially decaying current that falls to half value in about 100 microseconds.

Figure 3 shows the current waveform obtained by using three Marx generators in parallel. The time to peak is just under 3 microseconds, and the crowbar switches were triggered at about 3.8 microseconds.

Double pulses were also produced in these tests, using two Marxes to

produce the first pulse, and a single Marx for the second. Figure 4 shows one such result on a variable time base as it appeared on the digitizer display. The time intervals between time scale changes (vertical lines) are indicated. The first pulse and crowbar are shown in the initial 10 microsecond interval. The time sweep was then slowed down to show the exponential decay of the current. A further reduction in sweep speed shows the 16 millisecond interval between pulses. The sweep is then switched to the original speed to show the second pulse and crowbar. The final 448 microsecond interval shows the decay of the second pulse.

A continuing current that averaged about 300 amperes for a duration of 1 second was added to both ringle and double pulses for some tests.

For one series of high voltage tests the simulator was configured as an underdamped circuit without the crowbar switch. This produced the current waveform shown in Figure 5, with a peak current of about 54 kilo-amperes. A capacitive divider was used to measure the voltage at the end of the high voltage bushing, producing the result shown in Figure 6. The peak voltage obtained was about 1.2 million volts.

SIMULATOR PERFORMANCE SUMMARIES

The F-14A was tested over a two week period in April 1982. Tests were accomplished in 9 days. Two night operations with extensive photographic coverage were completed. The aircraft was passive for these tests; that is, no on-board systems were functioning. The number of test attempts and successes are shown in Table 1 for each of the three current levels. Only single pulses were used in these tests, and continuing current was provided on two tests. A test was considered a success if the desired current level was attained and the level at which the crowbar switch operated was at least 70 percent of the peak level.

The F/A-18 was tested over a four week period in August 1982. Tests were accomplished in 18 days. One night operation was completed. On sixty percent of the tests, the auxiliary power unit of the aircraft was operating and the on-board aircraft systems were functioning. In addition, two motion picture cameras were photographing the cockpit display area during these active tests. The attempts and successes are tabulated

in Table 1. The high current tests are subdivided into single pulse, double pulse, double pulse and continuing current, and triple Marx with continuing current.

#### CONCLUSIONS

Essentially all of the test objectives for the Sandia Lightning Simulator were achieved during these tests. This includes low, intermediate, and high level pulses, double pulses and continuing current. In addition, several high current, high voltage (1.2 megavolt) tests were achieved, and two pulses in excess of 140 kiloamperes were applied. Of the 160 test pulses applied to the aircraft, 129 (about eighty percent) were successful, where success indicates that the desired peak current level was attained and the crowbar, or exponentially decaying current, was obtained. Most of the pulses that did not meet the success criteria still produced useful data. A successful night operation with extensive photographic coverage was carried out on each aircraft.

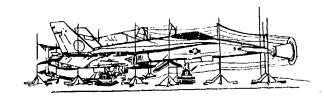


Fig. 1 - F/A-18 test arrangement

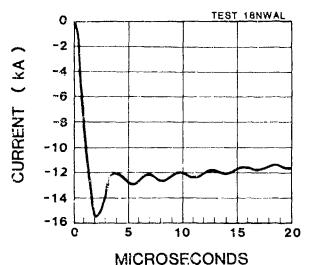


Fig. 2 - Current vs time, low level test

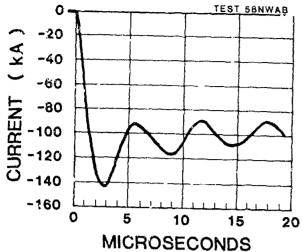
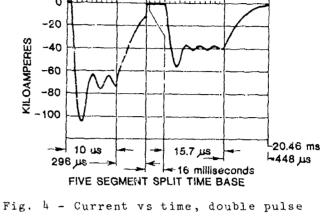


Fig. 3 - Current vs time, high level



48NWAF

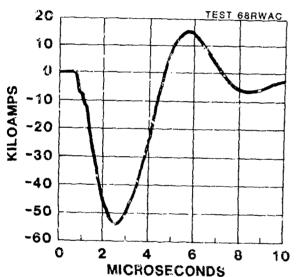


Fig. 5 - Current vs time, high voltage

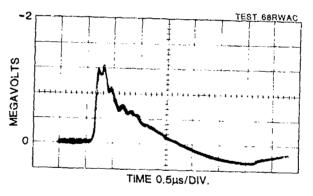


Fig. 6 - Output voltage vs time, high voltage test

Table 1 - Sandie Lightning Simulator Aircraft Tests, 1982

F-14A	Current Level (kA) Low (10) Intermediate (40) High (80)	Attempts 66 24 6 96	Successes 54 21 _3 78
T/A 3.0	Low (15) Intermediate (<100) High (>100)	26 9	25 9
F/A-18	Single Double Double + CC 3 Marx + CC High Voltage	11 3 8 3 4 64	5 2 5 2 3 51

AN IMPULSE GENERATOR TO SIMULATE LIGHTNING EFFECTS ON AIRCRAFT



E. GOCKENBACH, M. MODRUSAN, H. SUTTER Emile Haefely & Company LTD, Basel, Switzerland

ABSTRACT

Lightning flashes mainly differ in current amplitude, in the transferred charge, and the impulse shapes of the lightning current. A mobile impulse generator has been developed for the simulation of the lightning flash characteristics. The main parameter of this newly developed lightning current simulator is the possibility of simulations the different waveforms of the indirect current effects with one test equipment. It can produce unipolar currents up to 50 kA with a rate of rise of 35 kA/us for at least 1,0 us. With the same equipment oscillating current waves can be simulated with peak values up to 120 kA or at frequencies of roughly 40 kHz or few kA at frequencies up to 130 kHz. Furthermore, an optimal combination of test sets is presented to simulate the direct current effects.

GREAT DIFFICULTIES are encountered when a complete natural lightning flash must be simulated in the laboratory, because the natural lightning is a very complex and variable phenomenon.

Most of the voltage and current characteristics of lightning can be effected reparatly with relatively simple impulse generators, but the simulation of the complete lightning process necessitates an extensive equipment. These characteristics are of two broad categories

- the voltages, produced during the lightning flash and
- the currents that flow in the completed lightning channel.

The simulation of the voltage waveforms, described in (1)\* can be effected very easily with a standard impulse generator (2). This generator produces high voltage by charging a number of relatively low voltage capacitors in parallel and then discharging them in series through a spark gap switching arrangement.

The simulation of the current waveforms has to consider two components

- the simulation of the direct current effects and
- the simulation of the indirect current effects.

The latest researches (3) and (4) have shown that the effects of a lightning stroke can be represented through 4 parameters, namely:

- the current peak amplitude
- the max. current slope di/dt
- the action integral ∫i dt and
- the charge transfer ∫i dt.

Each of these parameters is responsible for a certain effect of the lightning impulse and therefore must be taken into consideration when simulating the lightning current in the laboratory.

#### CURRENT WAVEFORMS

As mentioned above the effects of the lightning current are classified in two groups

- the direct current effects
- the indirect current effects considering the level of the influence parameter and the effects of the parameter in practice. Table 1 shows the main parameters of the lightning currents. For both groups idealized current waveforms have been considered, which simulate in each case definite parameters of the natural lightning.
- \* numbers in brackets designate references at end of paper

The ideal current waveform for direct current effects is shown on fig. 1. The current waveform is divided into 4 components. Component A (initial stroke) Peak amplitude - 200 km ± 10% Action integral - 2x10 A - 1 - seconds ± 20% Time duration - < 500 µs Component B (intermediate current) Maximum charge transfer - 10 Coulombs Average amplitude - 2 kA ± 10% Component C (continuing current) Charge transfer - 200 Coulombs ± 20% Amplitude - 200-800 A Component D (restrike) Peak amplitude - 100 kA ± 10% Action integral -  $0.25 \times 10^6$  A<sup>2</sup> Time duration - <500 µs The components take into account the statistic values taken from table 1 concerning the current peak amplitude, the action integral and the charge transfer. These 3 influences parameters are responsible for the direct effects. For the indirect effects the current slope is first of all decisive, thus it determines the test currents of fig.2. Waveform E - Peak amplitude 50 kA, rate of rise 25 kA/µs for at least 0,5 µs Waveform F - T1 = 2  $\mu$ s ± 20%, T2 = 50  $\mu$ s ± 50 % Peak amplitude = 250 A Waveform Gl - 2 kHz ±50%, minimum 20 kA peak Waveform  $G2 - 100 \text{ kHz} \pm 30\%$ , min. 10 kA peak

#### TEST EQUIPMENT

The impulse generator for simulating the indirect current effects is housed in an insulating cabin and placed on a trailer with the dimensions of 10 m length, 2,5 m width and 3,5 m height. Figure 3 shows an outdoor photograph. All accessories, which are necessary for producing the different current waveforms, and all measuring and control devices can be stored in the cabin. Figure 4 shows the simplified construction of the test equipment. It can be divided in three main parts, the charging circuit, the high voltage circuit and the intermediate circuit. Figure 5 shows the simplified block diagram.

The charging circuit is composed of an ac voltage transformer with Joo kV (rms), a full-wave rectifier and a high-impedance voltage divider. The control of the charging voltage occurs with a solid state controller.

The high voltage circuit is composed of two standard impulse generators in parallel with 3 stages. Each stage has a charging voltage of 200 kV and an energy of 30 kJ.

The connection between the charging circuit and the high voltage circuit, that means the impulse generator, is done with a polyethylene cable. The charging circuit is equipped with one magnetically actuated grounding switch, the high voltage circuit with two grounding switches in the bottom stage. In addition the high voltage circuit is provided with a flexible strip - half conducting, half insulating - which directly grounds all impulse capacitors. The high voltage output is on the top of the cabin. Fig. 6 shows an indoor photograph of the high voltage circuit. The two control units are placed in a small control box with 0,3m height, 0,5 m width and 0,5 m depth. The impulse rate comes to one impulse every two minutes, when the full impulse energy is necessary. Standard shunts together with an impulse oscilloscope are used for measuring the different currents.

The intermediate circuit is necessary to produce the various current waveforms with one high voltage circuit. It consists of a resistor and capacitor (Waveform E), resistor and inductance (Waveform F), an other inductance (Waveform G1) and a capacitor (Waveform G2).

#### TEST RESULTS

WAVEFORM E - the current waveform E has the following main parameter:

peak value 50 kA, rate of rise 25kA/µs for at least 0,5 µs. Figure 7 shows the schematic diagram of the high voltage circuit. The connection between the intermediate circuit and the test object is a 1 m rod-to-plane spark gap. According to Fig.8 the breakdown voltage of this spark gap is about 500 kV, so that the maximum voltage of the high voltage circuit was chosen to 600 kV. The shape of the current can be calculated with the following equation

i (t) = 
$$I_0$$
 (e<sup>-t/Ta</sup> - e<sup>-t/Tb</sup>) (1)  
with  $I_0 = \frac{U\sqrt{C/L}}{2\sqrt{x^2-1}}$   $X = \frac{R}{2}\sqrt{\frac{C}{I_0}}$ 

Ta : 
$$\sqrt{LC} (x + \sqrt{x^2-1})$$

Tb = 
$$\sqrt{LC}$$
  $(x - \sqrt{x^2 - 1})$ 

R,  $\mu$ , C are the parameters of the series resonant circuit. The maximum rate of rise is given by the equation Smax  $=\frac{U}{L}$ 

with U = total charging voltage L = circuit inductance The calculation does not consider the influence of the spark gap. The inductance of the high voltage circuit is about 7  $\mu\text{H}$ , the inductance of the total test circuit about 20  $\mu\text{H}$ . That means about 12  $\mu\text{H}$  for the test object. For example a plane of roughly 40 m length, with a fuselage diameter of 3-5 m and a medium height about the ground of 4-6 m has an indunctance of about 12  $\mu\text{H}$  with a simple bright return line on the ground. For usually used coaxial return-lead arrangement a further reduce of the test circuit inductance—can be achieved.

Figure 9 shows the oscillogram of the current waveform E. The result of this test is a peak value of about 50 kA and a rate of rise of about 22 kA/µs. According to equation (1) the expected peak value should be about 52 kA and the expected rate of rise about 28 kA/µs. The reasons of the deviation is due to neglecting the spark gap. With the above mentioned intermediate circuit the rate of rise can be increased. Figure 10 shows the current wave with the intermediate circuit. The interpretation of the oscillogram results in a peak value of 52 kA and a rate of rise of 35 kA/µs.

WAVEFORM F - the main parameters of the current waveform F are the peak time  $T_1$  of 2  $\mu s \pm 20\%$ , the decay time to half amplitude  $T_2$  of 50  $\mu s \pm 50\%$  and the minimum amplitude of 250 A. To produce this waveform only one stage of the high voltage circuit is necessary. Figure 11 shows the schematic diagram.

The waveform can be calculated also with equation (1). The time to crest can be estimated

$$t_{\rm cr} = \frac{\sqrt{LC} \ln (x + \sqrt{x^2 - 1})}{\sqrt{x^2 - 1}}$$
 (2)

Figure 12 shows the oscillogram F the current waveform F. The peak value is about 0,6 kA, the time  $T_1$  = 1,8  $\mu s$  and the time  $T_2$  = 65  $\mu s$ .

With this test equipment a peak value between 100 A and 1,5 kA can be obtained. A comparison between calculation and measuring results in a very good correspondence.

WAVEFORM G - the waveform G is divided into two oscillating current waveforms with different frequencies and peak values. The current waveform Gl has a frequency of 2 kHz  $\pm$  50% and a minimum peak value of 20 kA, the current waveform G2 a frequency of 100 kHz  $\pm$  30% and a minimum peak value of 10kA.

For the current waveform Gl Figure 13 shows the schematic diagram. The stages of the impulse generator are all connected in parallel. The expected peak value can be verified with the equation

$$\hat{\tau} \approx \eta \cdot \upsilon \cdot \sqrt{\underline{c}}$$
 (3)

 $\eta = \text{utilization factor } (0.8..0.95)$ 

with U = charging voltage

C = impulse capacitance

L = inductance cf the total test circuit

This impulse has a very high charge, which can be expressed by equation

$$Q = \frac{2}{\omega} \frac{I_1}{1-K} \tag{3}$$

with

This waveform caused a strong stress of the capacitors, because of large voltage reversal.

In Figure 14 the measured current waveform Gl is shown. The frequency is about  $2.5~\mathrm{kHz}$  and the peak value of the current about  $20~\mathrm{kA}$  and the charge value about  $40~\mathrm{As}$ .

For the current waveform G2 Figure 15 shows the schematic diagram. There is only required a half stage of the impulse generator.

With a charging voltage of 100 kV a peak value of 12 kA can be reached. The frequency can be charged in a few steps between 80 and 130 kHz. Figure 16 shows the oscillogram of the current waveform G2. The frequency is 122 kHz and the peak value 10 kA.

Also with the current waveform G the agreement between the measured and calculated parameters is very good.

With the above mentioned test equipment the current waveforms E to G can be simulated with one night voltage circuit. Only the intermediate circuit has to be adapted to the different waveforms. For practical purposes it has mentioned, that the test equipment is available on site in less than half an hour. Only the connections of the power supply and the control box are necessary. The time to convert the test equipment from one current waveform to another is in the range between 15 and 30 minutes.

Table 2 shows together all the results of the simulating indirect current effects with the different waveforms.

#### WAVEFORMS A - D

The simulation of the direct current effects necessitate extensive equipments.

The current waveform shown in fig. 1 can be realized by means of an installation, composed of several sectional installations, being controlled by a single control device. Thereby, for economical reasons, it is important to generate the required unipolar impulses using for example a crowbar system as an intermediate circuit. The high voltage circuit with the impulse generator remains naturally.

Oscillograms, measured in a coupling arrangement with crowbar system are given in fig. 17. Thereof it is noticed that in this circuit an unipolar steep front pulse with a long time on half-value can be generated. This connection corresponds to the most economical solution for component A and D of the impulse. By shifting the trigger instant of the crowbar switch, the pulse length and consequently the charge as well as the action integral can be varied.

For the present installation a 100 kV crowbar switch was developped. Depending on the instant of short-circuiting the crowbar switch features a triggering range of approx. 30% to 50%. The large triggering range of the discussed Growbar for 100 kV was realized by means of a longitudinally triggered multiple spark gap. built of 5 partial spark gaps.

The equivalent circuit of an installation for the current component B is given in fig. 18. A typical current waveform is presented in fig. 19. The duration of the square wave current  $T_D \simeq 1.75 \sqrt{\Sigma L \Sigma C}$  and the amplitude of the peak value of the current I = U/(R + Z), whereby  $Z = \sqrt{L/C}$ , are adjustable by the intermediate circuit elements. A practical execution of an installation, suitable for current component B, is shown in fig. 20.

The partial component C of the lightning current is generated most aconomically by a battery, being connected through a thyristor switch. Fig. 21 shows an installation carried out for current components A and C. Thereby the charge stored in the accomulator battery is 500 Coul, i.e. 100 A can be delivered up to max. 1 sec.

Fig. 22 gives the circuit diagram of a complete installation, being capable to yield a lightning current according to fig. 1 for the simulation of the direct effects. The lightning current generator can be optimized to a further extent by choosing the most adequate charging voltage. The level of the charging voltage mainly depends on the inductance of the test object and on the required impulse waveform /6/. The smaller the charging voltage can be chosen, the more favorable are the expenses for the whole installation.

Owing to the high current impulses, the installation in question was built to a charging voltage of 100 kV. If a lightning impulse simulator is to be optimized with regard to the direct current effects, a lower charging voltage will be chosen.

Table 3 summarizes the characteristic values of a lightning current simulator, which ones can be achieved at a charging valtage of 20 kV. For simulating the direct effects, this proposed generator is considered to be an optimal solution.

#### SUMMARY

- The test equipment for the simulation of indirect current effects is placed on a trailer and therefore very mobils
- 2. The current waveforms can be simulated with one high voltage circuit
- Only the intermediate circuit has to be adapted to the requested waveform
- 4. With the waveform E a peak value of more that 50 kA, a rate of rise of 35 kA/μs and a decay time to the half value of about 10 μs was reached with a 1 m spark gap
- 5. The time to convert the test equipment is in the range of approx. ten minutes
- For all current waveforms measuring and calculations agree very well
- 7. The simulation of the direct current effects needs extensive test equipments
- 8. An optimal solution for simulating direct effects is proposed

#### REFERENCES

- /l/ Lightning test waveforms and techniques for aerospace vehicles and hardware Rep. of SAE Committee AE4L, June 20,1978
- /2/ A. Rodewald, K. Feser: The generation of lightning and switching impulse voltages in the UHV range with an improved Marx circuit

  IEEE Trans.Pow. and App. Syst. Vol 93
  (1974) p. 414 417
- /3/ H. Prinz: Die Blitzentladung in Vierparameterdarstellung. Bull. SEVIVSE 68 (1977) S. 600 - 603
- /4/ F.A. Fisher, J.A. Plumer: Lightning
  Protection of Aircraft
  NASA Reference Publication 1008
- /5/ M. Modrusan: Normalized calculations of impulse current circuits for given impulse currents
  Bull, SEV/VSE 67 (1976) 22
- /6/ M. Modrusan: Long-duration impulse current generator for arrester tests according to IEC recommondations
  Bull. SEV/VSE 68 (1977) 24

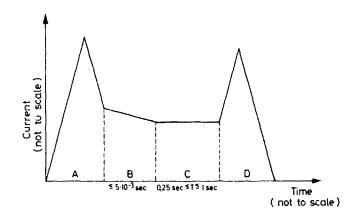


Fig. 1 - Idealized current test waveform components for evaluation of direct effects

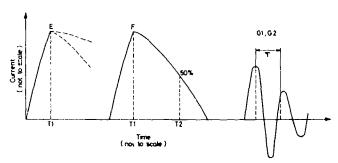


Fig. 2 - Idealized current test waveforms for evaluation of indirect effects

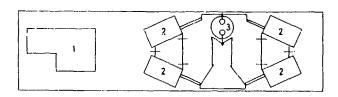


Fig. 4 - Top view of the charging and high voltage circuit

- 1 Charging circuit
- 2 Impulse capacitor
- 3 Spark gaps

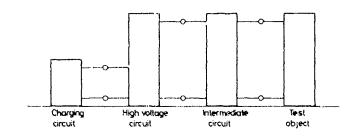


Fig. 5 - Block diagram of the complete test circuit

Table 1 - Influence parameters of lightning currents

	neg. F	olarity	pos. Polarity		
Parameter	5 % value	50 % value	5 % value	50 % value	
i in kA	80	30	250	35	
$(\frac{di}{dt})$ in $\frac{kA}{\mu s}$	120	40	32	2,4	
fi <sup>2</sup> dt in A <sup>2</sup> s	0,55.10	0,055.10 <sup>6</sup>	15 . 10 <sup>6</sup>	0,65 . 10 <sup>6</sup>	
∫i dt in As	40	7,5	350	80	

Table 2 - Results of the simulating indirect current effects

Waveform Type	Charging voltage kV	Energy kJ	Current Peak value kA	di/dt bei 0,5 μs kA/μs	Tl µs	T2 µs	T μs
E	600	180	52	35	2 ·	10	
F	40	15	0,6		1,8	65	
G1	185	155	20				400
G2	200	30	10			}	8

Component of current waveform (fig.1)	U kV	E kJ	I max kA	T <sub>D</sub>	T s µs	Τ r μs	∫i dt As	∫i <sup>2</sup> dt A <sup>2</sup> s
	}					 	min	min 6
A	20	100	200	- '	15	50500	10	2.10
В	20	100	2	5ms	-	-	10	-
C	3,5	-	0,5	ls	-	-	500	-
D	20	25	100		8	25500	min 2,5	min 0,25.10

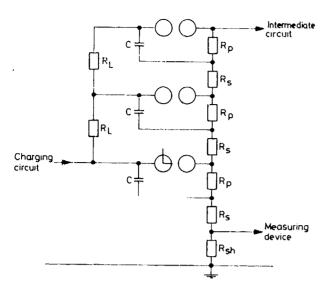


Fig. 7 - Schematic diagram of the high voltage circuit (waveform E)

R<sub>L</sub> charging resistor

Rp parallel resistor

Rs series resistor

C impulse capacitor

Rsh measuring shunt

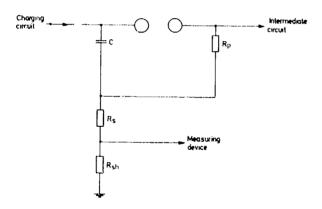
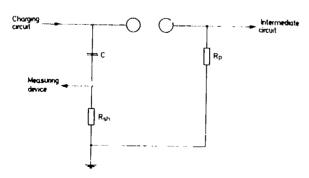


Fig. 11 - Schematic diagram of the high voltage circuit (waveform F)

Designation of the elements see Fig. 7



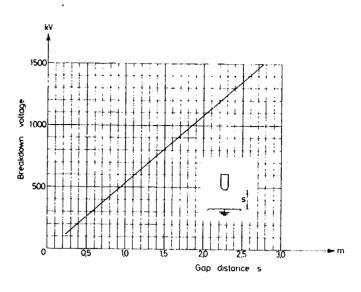


Fig. 8 - Breakdown voltage of a rod-toplane spark gap as a function of the gap distance at standard atmospheric conditions (20°C, 1013 mbar 11 g/m3)

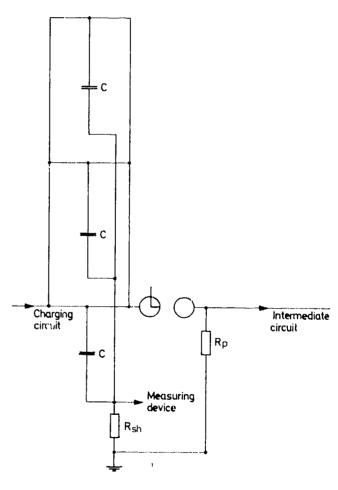


Fig. 13 - Schematic diagram of the high voltage circuit (waveform Gl)
Designation of the elements see fig. 7

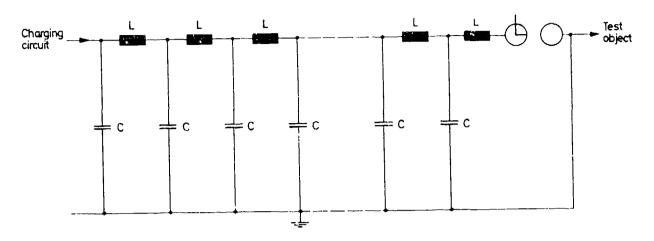


Fig. 18 - Schematic diagram of square wave generator

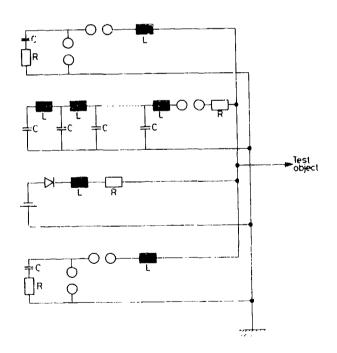


Fig. 22 - Schematic diagram of complete lightning stroke test equipment for direct current effects

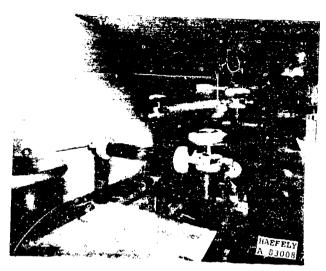


Fig. 6 - Indoor photograph of the test equipment

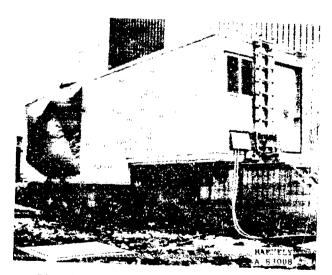


Fig. 3 - Outdoor photograph of the test equipment

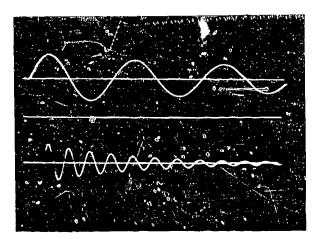


Fig. 16 - Oscillogram of the current waveform G2 Peak value: 10,2 kA Lower beam: 2,5 µs Frequency: 122 kHz Upper beam: 10 µs

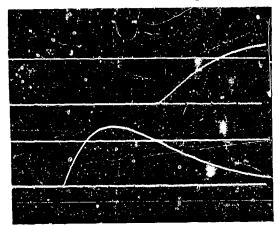


Fig. 9 - Oscillogram of the current waveform
E without intermediate circuit

Peak value: 50 kA Upper beam: 1 μs/div
Rate of rise: 22 kA/μs Lower beam: 2,5 μs/div

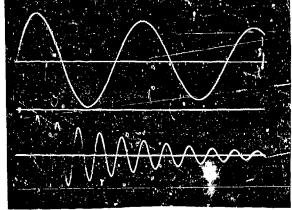


Fig. 14 - Oscillogram of the current waveform Gl Peak value: 20,5 kA Lower beam: 100 µs Frequency: 2,5 kHz Upper beam: 500 µs



Fig. 12 - Oscillogram of the current waveform
F
Peak value: 580 A

 $T_1$  1.8  $\mu s$   $T_2$  65  $\mu s$  Upper beam: 1  $\mu s$  Lower beam: 10  $\mu s$ 

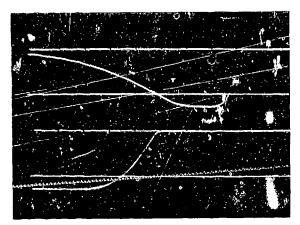


Fig. 10 - Oscillogram of the current waveform
E with intermediate circuit
Peak value: 52 kA
Rate of rise: 35 kA/µs
Upper beam: 1 µs
Lower beam: 2,5 µs/div

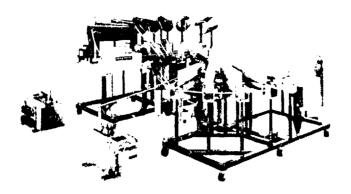


Fig. 21 - Impulse current generator for component A and C

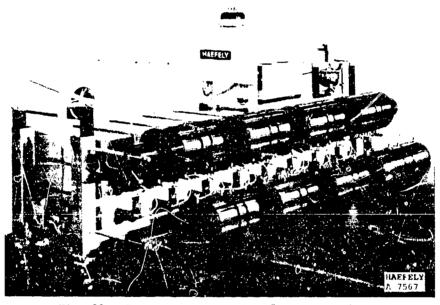


Fig. 20 - Square wave generator for component  $\ensuremath{\mathtt{B}}$ 

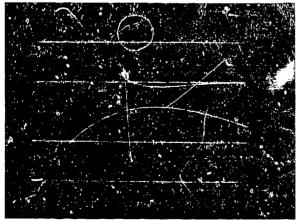


Fig. 17 - Oscillogram of the current waveform with a crowbar system as intermediate circuit

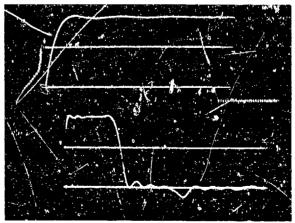


Fig. 19 - Oscillogram of square wave current

# AD P002221

MEASUREMENTS AND THEORETICAL ANALYSIS OF A FULL SCALE NEMP



TYPE LIGHTNING SIMULATOR FOR AEROSPACE VEHICLES

J.D. Robb, Lightning & Transients Research Institute

R. A. Perala, Electro Magnetic Associates

In an earlier paper, it was suggested that peaking capacitors as are used in nuclear simulators be electromagnetic pulse used to supply the fast current rise times which have been indicated in recent researches in the field of spherics and lightning lightning aircraft. strikes to Α experimental quantitative and analytical study has been undertaken to examine the feasilibility and the significant parameters for such a system. The results of the studies have indicated that average lightning currents of 20,000 to 40,000 amperes with moderately fast rise times of 100 nanoseconds (which is an order of magnitude improvement ). can achieved fairly economically, but that rise times of the order of 30 to 50 nanoseconds would increase the cost and design difficulties significantly. What remains to be determined is the statistical distribution of currents and risetimes in strikes to aircraft. A number of flight research programs currently underway which are accumulating data for establishment of new rise time test standards.

THE RECENT WORK done in the characterization of lightning by the Flight Dynamics Laboratory and NASA has revealed that the risetimes of lightning return stroke components are on the order of 100 nanoseconds. This is an order of magnitude faster than the previously accepted risetime of one microsecond. The faster risetime produces more energy at frequencies of than previously aircraft resonances anticipated. Energy coupling to the aircraft interior can be due to both and magnetic field electric apertures and penetration of the faster risetimes increase coupling. At present, most impulse generators for lightning simulation are designed to generate one to two microsecond risetimes and simulate the newly-revealed threat. Modifying present generators

achieve the fast risetimes and large voltage levels is not a simple task because inherent generator resistances and inductances limit the magnitude and risetime of generator output.

### ANALYSIS

It is therefore desirable to design a new type of simulator suitable for testing aircraft to this new threat. Design of such a simulator involves both analysis and test. The objective of the analysis phase as discussed in this section is to provide analytic (numerical) results to support the design of such a simulator.

The analytic results fall into three areas:

- o QUANTIFICATION of the results for a test cylinder
- o QUANTIFICATION of results for an F-16 in a proposed simulator
- o INVESTIGATION of pulse generator shielding requirements.

test cylinder 30' long and 6' used as both an diameter is experimental and numerical test bed for investigating the basic simulator concepts. Parameter studies of the cylinder response are accomplished for variations in geometry, pulser elements, termination waveshaping impedances, and spark configurations.

These cylinder results are then used to provide insight into the response of a full size aircraft (the F-16) in the proposed full scale simulator design. Parameter studies are also done in this case for variations similar to that in the cylinder case. It was found that the valves of injected current and its derivative were greatly dependent upon the size of the peaking capacitor which was used. The size of this

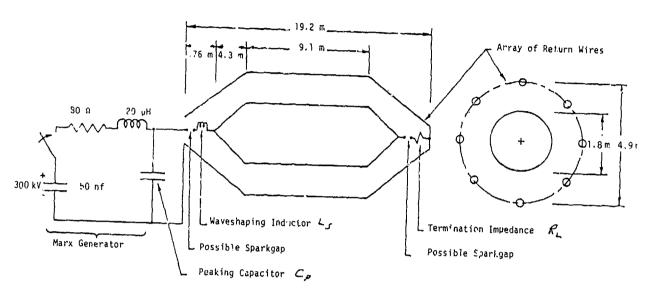


Figure 1 Basic Cylinder Configuration

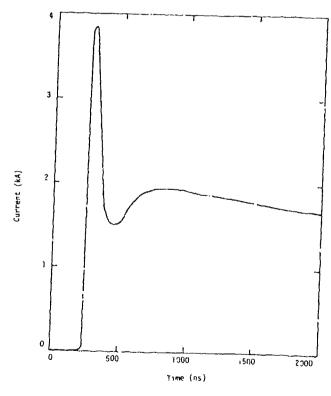


Figure 2 Injected Current for Baseline Configuration

capacitor is greatly determined by economic factors but a modest investment in a 1000 pf. capacitance can provide currents on the order of 35-40 KA with rise rates exceeding 5X10" A/m/s.

One item of concern is the potential need for shielding the Marx generator. This is a great cost item, and it is worthwhile to determine the extent to which a shield is needed. It was found that construction of an expensive quality overall shield is not warranted, although an inexpensive isolation flat screen would be desirable. Signal to rise ratios of 45 dB are expected.

RESPONSE OF THE RIGHT CIRCULAR CYLINDER

#### MODELLING APPROACH

A right circular cylinder test bed is used to provide basic configurations. The basic cylinder configuration is shown in Figure 1, which includes the Marx generator, measurement point locations, geometry, and spark gaps and terminations. This geometry is solved by treating it as a nonuniform transmission line.

The model combines the solutions for the telegrapher's equations in the test fixture itself with the solutions for the circuit which represents the Marx generator. The solution is accomplished in the time domain using finite difference techniques (1).

The geometrical inputs for the model are the per unit length capacitance and injuctance which are simply related to the characteristic impedance Zo (2,3). The transmission line is nonuniform in that Zo is different on the end cones from that on the cylinder. It is not possible to taper the conic sections so that Zo is preserved, because of the requirement to have feed points and terminations which occupy finite amounts of space.

The cell size used was .0762 m

### RESULTS

A considerable number of parameters were varied to quantify the response of the cylinder in the test fixture. The parameters considered are listed in Table I.

and the time step was 100 ps.

### TABLE I PARAMETER VARIATIONS

- o Gap Locations: Front, Back, Both
- o Characteristic Impedance: No. of Wires, Distance from Cylinder, Size of Wires (6 Cases)
- o Termination Load: Open, Short, Matched, 10 Ohms
- o Series Inductance J.s: 50 nH, and for 30 ns and 300 ns Risetimes
- 0 Peaking Capacitance: 1 nf, e nf, 5
  nf

RESPONSE OF THE BASIC configuration includes the Marx generator of Fig. 1., a peaking capacitance of 1 nf, a transmission line characteristic impedance Zo of 71.4 n, a gap at the front, a termination impedance equal to the characteristic impedance, and a series inductance which gives a risetime of 30 ns. The output spark gap fires when the voltage on the peaking capacitor reaches 300 kV.

THE INJECTED CURRENT is shown in Fig. 2.

One may observe that for this case, the response can be thought of as the sum of initial short fast and a long risetime pulse risetime pulse. These two pulses are relatively independent of each other and can be closely calculated by simple analytic formulas. Each pulse can be thought of as coming from an RLC the circuit made up of series combination of the peaking capacitor, waveshaping inductor, and a resistor equal to the characteristic impedance. The long pulse comes from the series RLC circuit made up of the Marx capacitance, the sum of the Marx resistance ard the characteristic impedance. It is easily seen

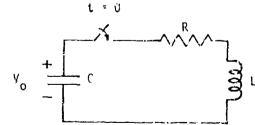


Figure 3 Simple RLC Circuit Model

$$Z_{0} = \sqrt{L/C^{1}}$$

$$\omega_{0} = \frac{1}{\sqrt{LC}}$$

$$\zeta = \frac{R}{2 Z_{0}}$$

$$\alpha = \omega_{0} \left(\zeta + \sqrt{\zeta^{2} - 1}\right), \zeta > 1$$

then the current I(t) is given by

$$a_{t} - a_{t}$$
 -a\_t [(t)=V/L(a<sub>t</sub>- a\_))(e -e ).(2)

Thus each of the pulses of Fig. 2 is double exponential described by equation  $2. \ \ \,$ 

VARIATION OF CHARACTERISTIC IMPEDANCE

A parameter study of the of the characteristic impedance of the cylinder in the wire cage was done. Wire spacing (i.e., distance from the cylinder), the number of wires, and the wire size was varied. The results are summarized in Table 2. It can be seen that the results vary from 67 to 130 n, a span of a nominal factor of 2.

TABLE 2 CYLINDER PARAMETERS Wire Wire No. of Surge Size Space Wires Imped 8 102.0 . 1 32 .1 67.4 10 109.0 . 1. 16 130.3 64.8

### VARIATIONS IN INJECTED CURRENT

The variation in injected current as a function of Zo and peaking capacitance is given in Fig. 4 and Fig. 5 respectively. It is noted that the rear gap case results in less injected current, although the exit

current would be greater in this case. Currents well over 4000 A are possible, for a drive voltage of 300 kilovolts and the importance of having as large a peaking capacitance and as small a characteristic impedance as possible is evident.

THREE DIMENSIONAL AIRCRAFT RESPONSE IN A FULL SCALE SIMULATOR

Modelling Approach - The three dimensional finite difference techniques (1) is used to model the response of a full size aircraft in a full scale simulator. The configuration is shown in Fig. 6. The large clearances are required to provide sufficient voltage stand off such that arcing of the aircraft to the outer wire grid does not occur. Voltages exceeding 6 MV are expected on the aircraft.

The aircraft is an F-16, and shape of the computer model is shown in Fig. 7. The cell size is I meter in the longitudinal direction, and is 1/2 meter in the other directions. The time step is 2 ns. Because approximately 5 cells are required to resolve a wavelength, the upper frequency limit of the computation is 60 MHz. The erected Marx voltage is MV. Measurement points include the injected current and E and H fields near the cockpit.

### RESULTS

Results for 1000 pf peaking capacitance, a waveshaping inductance of 2 uH, and a /8 ohm temination resistor are illustrated in Fig. 8. The peak initial current of about 45 unchanged with is various termination resistances, but the late time responses are quite different, as expected. The giraraft resonates with the peaking capacitor initially and then with the Marx generator in the late time phases. The same basic frequency of about 5 MHz is again excited, as was the case for 200 pf peaking capacitance. Again, the late time increase in currents for the lower are caused by the resistances discharge of the Marx generator. Other oscillations at 10 MHz are evident for higher termination resistances, corresponding to the half wave the aircraft resonance of fixture.

Parameter studies were done for various combinations of peaking

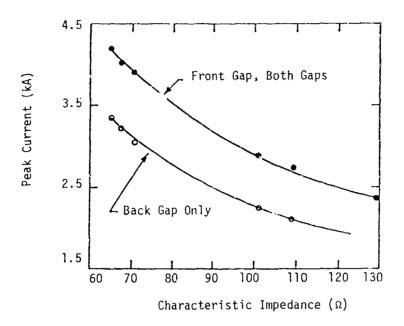


Figure 4. Variation of Peak Injected Current With Characteristic Impedance;  $C_p = 1$  nf;  $\tau_r = 30$  ns

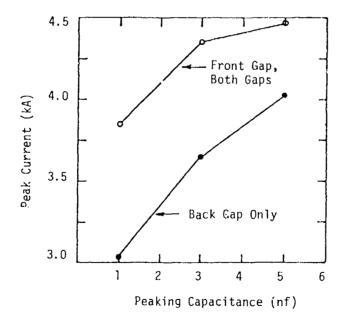


Figure 5. Variation of Peak Injected Current With Peaking Capacitance;;  $Z_0$  = 71.4  $\Omega$ ;  $\tau_r$  = 30 ns

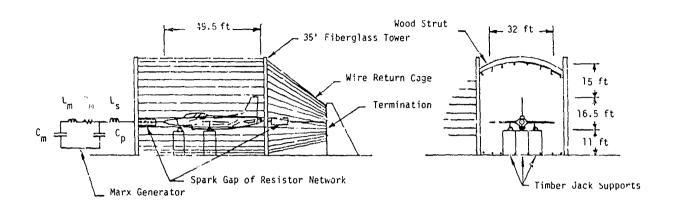


Figure 6 F-13 Aircraft in Full Scale Simulator

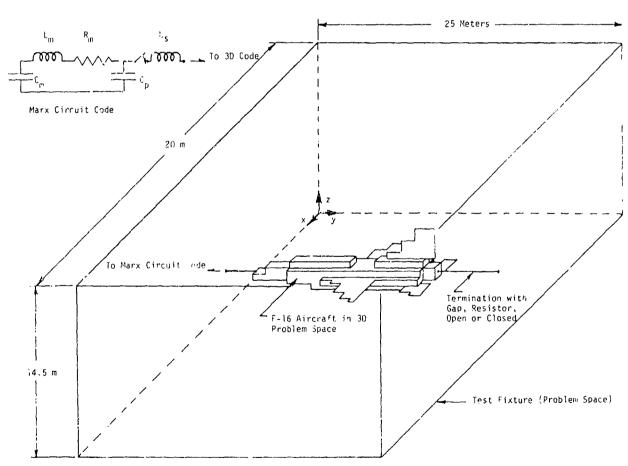


Figure 7 Three Dimensional Finite Difference Model of F-16 Aircraft in Test Fixture

TABLE 3
SUMMARY OF PARAMETER STUDY RESULTS FOR FULL SCALE SIMULATOR

¢ p	Ls	t <sub>r</sub>	k.J	1 × 10 <sup>11</sup>	k x 100	и х 10 <sup>10</sup>	E kV/m	C x 1913
1000	2	107	45	30	68	47	1600	13
	8	125	37	7.5	51	15	1600	4.2
	20	178	29	3	45	7	1200	2
200	2	34	27	30	44	47	1300	13
	10	100	22	6	38	12	425	3.5

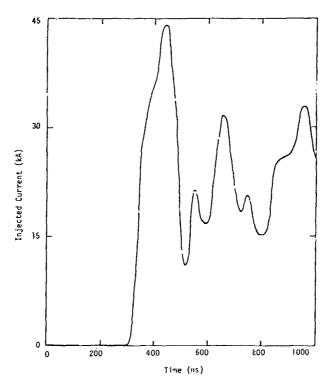


Figure 8 Injected Current for C  $_{p}$  = 1000 pf, L  $_{s}$  = 2  $\nu H$  , and R  $_{L}$  = 78  $\Omega$ 

capacitance and waveshaping inductance. The results are summarized in Table 3, which shows the rise time and injected current, magnetic field, electric field, and their derivatives. The fields are measured at the test point shown in Fig. 7.

Several things are evident from this data:

The level of peak injected current is greatly dependent upon the value of the peaking capacitance. This is primarily an economic decision, because large night voltage capacitors are expensive. Because Ls probably cannot be made much less than 80H, peak currents of about 35 kA are to be expected from a 1000 pf capacitance.

VALUES OF 1 OVER 5 X 10" A/m/sec should be obtainable with the simulator. This is in the range of values presently inferred from recent LEMP field measurements.

VALUES OF E AND H on the same order of that caused by nuclear EMP (> 1.0 V/m/sec and 10" A/m/sec respectively) are possible to achieve.

AIRCRAFT RESONANCES are excited. Their amplitudes are of course dependent upon the risetime. If the minimum achievable inductance of the peaking capacitor output circuit is on the order of 8-louh, then minimum risetimes on the order of 100 ns are probably the best one can expect.

### EXPERIMENTAL STUDIES

the Based on analvtical investigations, a nominal system was selected for the low level experimental tests with voltage scaling of about 10 percent and size scaling of approximately full scale. The test voltage was 200 to 300 kilovolts using a Marx generator drive. The resultant data was to be used along with the analytical data to design the full scale four megavolt system. The test arrangement is shown in Fig.9. It consists of the Marx generator, the peaking capacitors, the feedpoint sparkyap, all housed in a weather shelter, the test object, in this case the 6-foot diameter by 30-foot long cylinder, and the downstream sparkgap or termination resistor. Plywood and 2 x 4 lumber were used in fabricating the test arrangement. The tests were carried out with the variation basically in the terminations at the far end of the array.

The result of the tests are presented in Table 4 and in the oscillograms of Fig. 10a, and b for a terminated line and a line with a far end sparkgap output. As shown in Fig. 10a, the current waveform of the experimental test arrangement showed a rise time of approximately 100 nanoseconds on the linear portion of the front of wave followed by the more slowly rising pulse from the Marx generator drive. The time duration of the impulse was approximately three microseconds. The array spacing was 5 feet from the cylinders to the wires and with 300,000 volts applied, this resulted in a radial electric field of about 150,000 volts per meter. With the 70 ohm termination, the current peak was approximately 4,000 amperes. With the far end output gap, the current oscillogram is less smooth throughout the entire duration of the wave. One of the aims in the design was to investigate the feasibility of using a non-EMP peaking capacitors in order to reduce the cost of the system and in the test arrangement, standard energy storage capacitors were used. The addition of inductance to the input of the vehicle was suggested on the basis of the analysis for cleaning up the wavefront. The solution of using additional inductance suggests that if inductance is added to the input to the vehicle, then there is no requirement for providing special low inductance peaking capacitors, and this was found to be the case, but only if a 100 nanesecond rise time is adequate. If the faster risetimes of 30 to 50 ranoseconds are required, then the input inductance must be reduced and the capacitors must be the higher cost low inductance capacitors, at the expense also of a less clean

### FULL SCALE DESIGN

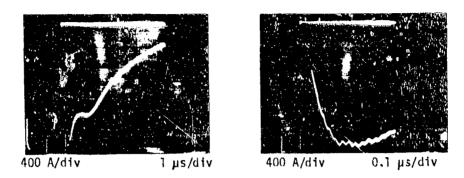
wavefront.

The full scale test arrangement is shown in Fig. 6. The vehicle being tested is set up on wood block for insulation and the array grid is supported by fiberglass lamp posts. A simple lumber structure is used for support of the EMP peaking capacitors and these in effect act as the high voltage bushing to equalize (linearize) the voltage equally across the entrance to the transmission line array. High voltage input bushing

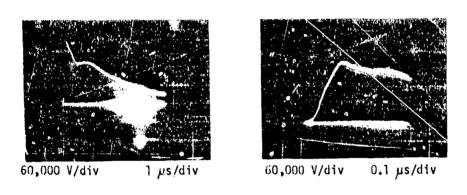


Figure 9 Photograph of Test Arrangement Showing Cylinder and Wood Support Structure Along with Wood Weather Housing For Marx Generator.

### Drive Current



E-Field



H-F1e1d

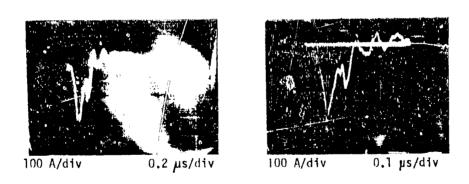
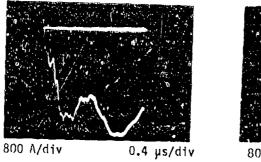
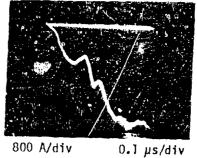


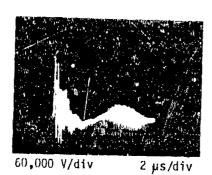
Figure 10a. Oscillograms for Terminated Array.

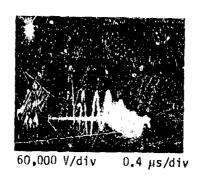
### Drive Current



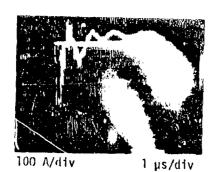


E-Field





H-Field



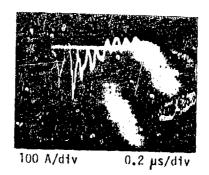


Figure 10b. Oscillograms for Array With Spark Gap Termination.

design is always a difficult problem for high voltage systems. The peaking capacitors are in effect also used to equalize the voltage across the array input to help in solving this problem.

The output firling gap and the downstream gap or termination resistor are fabricated of fiberglass gasoline storage tanks supported on a wood structure. Simple plumbing hardware is used for the sphere gaps in order to minimize the system cost.

### CONCLUSIONS

The analytical and experimental studies have verified that the NEMP peaking capacitor approach can be used for lightning simulators to provide an order of magnitude improvement in current rise times over existing current rise times over existing lightning simulators and with relatively clean wavefronts. electric and magnetic field rise times and magnitudes comparable to the magnitudes measured in flight data can be obtained. Risetimes of the order of 100 nanoseconds can be obtained relatively easily, but risetimes of the order of 30 nancseconds would be more expensive and difficult to obtain. The remaining ouestion will be to decide what rise times should be used. Current Flight Dynamics Laboratory and NASA flight programs should help to provide data for this purpose.

### ACKNOWLEDGEMENT

This paper is based on the work carried out under contracts sponsored by the Flight Dynamics Laboratory of the USAF Wright Aeronautical Laboratories, Wright Patterson AFB, Ohio.

### REFERENCES

- 1. Merewecher, D. E. and R. Fisher, "Finite Difference Solutions of Maxwell's Eduations for EMP Applications," Electro Magnetic Applications, EMA-79-R-4, 24 July 1980.
- 2. Licking, Leonard, "Capacitance Analysis for Arbitrary Cylindrical Geometries Application to Electromagnetic Coupling into Subsystems Through Cables," Sandia aboratories, SC-RR-72 0299, May 1972.

- 3. Rudolph, T. H., "User's Manual for EXEC and PROP Internal Propagation Codes," EMA-81 R-22, April 1981.
- 4. Babcok, L. F. and R. L. Cloe, Jr., "Measurement of Rocket Engine Spark Gap Ignition EMC, "Measurement of Rocket Engine Spark Gap Ignition EMC," IEEE Transactions on Electromagnetic Compatibility, May 1971
- 5. Huang, G. C., R. Goldman and R. B. Schulz, "Interference Characteristics of Streamer Discharges," IEEE Transactions on Electromagnetic Compatibility, Vol. EMC-12, No. 2, May 1970.
- 6. Klapas, D., R. H. Apperly, R. Hackam and F. A. Benson, "Electromagnetic Interference From Electric Arcs in the Frequency Range 0.1-1000 MHz," IEEE Transactions on Electromagnetic Compatibility, Vol. EMC-20, No. 1, February 1979.



## UPDATING THE MCAIR LIGHTNING SIMULATION LABORATORY

E.H. Schulte

# AD P002222



#### ABSTRACT

The goal or lightning simulation testing of aircraft is to ensure flight safety. The realism of each simulation is limited by the complexities of both the lightning environment and the aircraft itself. As the natural threat becomes better understood and improved test techniques are developed, the modern lightning laboratory must continually upgrade its equipment and facilities to meet the need for more accurate test simulation. This paper describes the major test improvements incorporated in the McDonnell Aircraft Company (MCAIR) lightning laboratory.

THE MCDONNELL AIRCRAFT COMPANY lightning simulation laboratory was initially developed in 1968 to provide the minimum test capability needed to qualify fighter aircraft under then existing military specifications. Over the years, the laboratory has been gradually upgraded and enlarged to include the simulation of all the important aspects of the natural lightning environment, as well as other related high-voltage and high-current phenomena. This paper summarizes the major laboratory improvements which have been implemented during the past five years to keep pace with the expanding threat definition and advanced design trends.

### REASONS FOR UPDATING

Several factors have influenced the continued updating of the MCAIR lightning laboratory:

- (1) Knowledge of the natural lightning characteristics has improved.
- (2) Lightning qualification test specifications have changed. (References to lightning test components listed in this paper refer to MIL-STD-1757).
- (3) Advanced microetectronic systems pose new lightning susceptibility problems which must be evaluated by test.
- (4) New composite materials and construction techniques must be tested to verify design concepts and safety margins.
- (5) Better test realism is needed to ensure that all important test parameters are simulated.

Natural lightning is a complex and variable phenomenon which is not easily characterized. The advancements in electronic instrumentation, fast transient recorders, radar, and computing systems have enabled researchers to obtain better information about the natural lightning environment. Research flight programs and computer modeling are further extending this knowledge to encompass the interaction of lightning with aircraft in flight. One significant result of the recent research is that very fast ( $\simeq 90$  ns) rise times have been observed for the fast portions of some return strokes [1].

These submicrosecond current and field changes may present a significant hazard to aircraft because they can efficiently excite aircraft resonances which could be coupled into sensitive interior electronic systems. Flight programs have confirmed that aircraft resonances are excited by direct and nearby lightning strikes. Lightning test techniques must therefore be modified to both excite and measure the impact of such resonances.

As a result of the better understanding of lightning and its interaction with aircraft, lightning testing specifications have been revised in recent years. The major aircraft/ spacecraft specifications are now MIL-STD-1757 for military aircraft [2], JSC-07636 Rev A for NASA spacecraft [3], and AC 20-53 for civilian aircraft [4]. Although these documents impose new testing requirements not previously required, they do not stipulate all of the testing which may be necessary to verify a specific protection system. A large number of tests are for research or development purposes for which test procedures and waveforms other than qualification specifications are used. Table 1 lists the vide variety of lightning tests which are conducted in a comprehensive lightning laboratory [5]. When test facilities and equipment are updated, system versatility and flexibility must be stressed so that the modified equipment can be used in a variety of tests without major changes.

Modern aircraft are becoming much more complex and sophisticated electronically. New solid-state microelectronic circuits are very sensitive to damage or upset by transients, and they are used in almost all flight control and weapon systems. In addition, the advanced composite materials used in modern aircraft have higher electrical resistances and lower electromagnetic shielding capability. The increased sensitivity of the avionics and the reduced shielding protection afforded by the aircraft structure complicate the design of lightning protection schemes. Therefore, lightning tests are required to evaluate proposed designs and to verify the protection of the final design.

The newer aircraft are using composite materials in ever increasing amounts for skins and other structural components. Airframes are thus becoming mechanically simpler because there are fewer components to be bolted, riveted, and welded together. However, they are still very complicated to design because there are now numerous selections of composite materials and layups available. There are bonded (glued) composite to composite joints, and there are bolted and riveted composite to metal joints. These new construction techniques pose new lightning protection problems not only at the strike point but all along the lightning current path through the composite and metal airframe. Although lightning protection schemes can usually be developed to protect the various composite structures, they must be evaluated by test, and the test must be closely controlled because of the different damage mechanisms of composites as compared to metals [6].

Table 1 - Lightning Simulation Test Issues

Type of Tesi	Test Issues	Diagnostics Required
Model Attach Point Test	Voltage Rate-of-Rise; Polarity; Gap Size; Scaling	Voltage Waveform, Photography
Full-Scale Hardware Puncture/Flashover Test	Voltage Waveform; Number of Shots; Gap Size	Voltage Waveform, Photography
Corona/Streamering Test	Voltage Waveform; Film Sensitivity; Electrode Geometry	Voltage Waveform, Photography
High-Current Damage Test	Peak Current; Action Integral; Gap Size; Electrode Geometry	Current Waveform
Continuing Current Test	Electrode Geometry; Spacing; Field Interaction; Action Integral	Current Waveform, High-Speed Photography
Swept-Stroke Test	Airstream Quality; Restrike Waveform; Continuing Current Decay	Air Uniformity; Restrike/Continuing Current Waveforms; Still/ High-Speed Photography
Fuel Ignition/Sparking Test	Film Sensitivity; Current Waveform; Fuel/Air Ratio	Current Waveform, Photography; Fuel/Air Mixture
Indirect Effects/Components	Peak Current; di/dt; J <sub>tn</sub> ; Scating; Component Installation; Noise-free Instrumentation; Load Impedance	Current Waveform, Induced Voltage/Current
Indirect Effects/ Full Vehicle	Vehicle Isolation; di/dt; dV/dt; Scaling; Diagnostic Technique; Arc Channel Impedance; Wire Access	Current, Voltage Waveforms, Induced Voltage/Current

P21 0762-2

In lightning simulation testing, the desire is always to make the test as realistic as possible. This has practical limitations, but the test must at least simulate the natural environment well enough to assure confidence in the test conclusions. Several examples of improving test realism are: (1) combining high current components A, B, C and D into one test waveform (as opposed to applying them individually to a test sample and allowing the sample to cool between tests), (2) combining components A and E or D and E (to evaluate non-linear effects such as arcing between adjacent sections on a test sample resulting from the fast rate-of-rise of the current waveform), (3) using unipolar test waveforms (as opposed to oscillatory waveforms to evaluate damage), and (4) using long arcs to the test sample (to eliminate probe effects caused by the probe being too close to the test sample).

The desire for realism has also led to the use of large aircraft sections or complete aircraft for simulated lightning tests. The use of the whole aircraft is often necessary in order to evaluate resonance effects. This has meant increasing the size of test areas to accommodate larger test sections. It has also resulted in the construction of portable generators so that tests could be conducted at remote sites when it was not possible to accommodate the aircraft in the laboratory.

A further desire of realism is to combine environments in a test. This has led to the construction and modification of equipments to obtain this test realism. For example, a swept stroke test combines the lightning arc and air blown over the aircraft surface. The lightning current should encompass the full-width current components, and the wind source should provide iaminar air flow along the aircraft surface. As another example, live fuel has been used to evaluate hot spot and sparking of integral fuel tank skins struck with simulated lightning.

The MCAIR lightning laboratory has met the changing test specifications and the need for more realistic test simulation by modifying existing generators, developing and procuring new generators, developing new test methods, procuring new electronic and photographic instrumentation, and enhancing the lightning test facilities [7]. A condensed listing of generators and equipment is given in Tables 2 and 3. The more prominent changes are described in the following sections.

### ONE-MEGAJOULE/THREE-MEGAWATT LIGHTNING SIMULATOR

High-current testing at MCAIR has undergone extensive changes since it began in 1968 with only one 30-kJ, 12-kV capacitor bank. The one-megajoule/three-megawatt lightning simulator in use today is the result of gradual improvements in high-current simulation of both direct damage and induced voltage effects. Some of the simulator modifications during the past five years have included: (1) expanding individual generators and improving their operation, (2) coupling several capacitor systems together to produce the combined high-current threat waveform, (3) adding a fast current rise time to the high-peak current pulse, and (4) adding a large, pulsed DC power supply for continuing current simulation. The individual improvements are not historically described, but, instead, the operation of the present system is detailed.

The 1-MJ (actually 1.4-MJ)/3-MW lightning simulator consists of four capacitor banks (660 kJ, 192 kJ, 72 kJ, and 486 kJ) and a 3-MW pulsed DC power supply. The separate generators and the power supply are extremely versatile. They may be operated individually or in many combinations. When they are all coupled together, they readily meet or exceed the requirements of the complete MIL-STD-1757 direct-damage waveform in a single test. Figure 1 is a schematic of the combined operation. After all capacitor banks are charged and the 3-MW supply turned on, the 660-kJ bank is triggered and presents a high-voltage at its output spark gap. This spark gap closes and applies the high-voltage to the output probe. As the arc from the output probe propagates to the test sample, the 72-kJ bank triggers, so that the output of these

Table 2 - MCAIR Lightning Simulation Sources

				High Current Generators <sup>1</sup>	
Energy (kJ)		Voltage Current (kV) (kA)		Usage and Characteristics	
660 2		40 300		High Peak Current Damage Tests <sup>2</sup>	
192		96	150	High Peak Current/Restrike Tests; Portable <sup>2</sup>	
72 4		480	200	Fast-Risetime, High-Current Tests; Portable <sup>2</sup>	
480		12 10		Intermediate and Continuing Current Tests <sup>2</sup>	
			ا	High Voltage Generators	
Voltage (kV)	Current (kA)		Energy (kJ)	Usage and Characteristics	
4,000	15	1	40	Fuli-Scale Component and Large Model Tests; 20 ft Soark; Outdoor	
1,650	5		4	Induced Voltage Studies; Portable	
1,500	500 10		2.4	Remote Site induced Voltage Tests; M. Hular Construction	
800	25		24	Arc Attach Point Tests; Adjustable 38 Ramp	
480	30		240	Higher-Current induced Molfage Tasis; Portable	
400	2 1		1	General Lab Use	
				Swept Stroke Testing	
				not Swept Stroke Facility apacitor Bank and Pertable High Current Generators	
				(not Blower for Low Speed Testing High Current Gererators	
				DC Power Supplies <sup>3</sup>	
Voltage (kV)	Curren <sup>†</sup> (A)	Pov	ver Plating (kW)	Principal Usage	
6	500		3 000	Continuing Current Damage Tests (High Coulomb) for Large Composits Structures	
0.3	300		90	Continuing Current Damage Tests for Conductive Test Articles	
				Static Electricity Equipment	
French Injeco Device			- Compressed Air Charge Spray Gun, Up to 80ஓA Current		
Blown Dust			— Dry Nitrogen Driven, Triboelectric Charging of Panels		
₹00 kV DC Rectifier			— Corona Spray for Electro Static Charging		

- Notes

  1) Smaller high current generators are evailable for general lab use
- Generators can be integrated together to provide combined current component A. B. C and D full-threat waveform with 2 μsec risetime.
- 3) Generator charging power supplies up to 120 kV are also available

GP31-0471-1

Table 3 - MCAIR lightning laboratory instrumentation and data processing equipment.

ltem	Characteristics		
Pulse Sensors • EG&G: MGL-S7, MGL-6.	Skin Current, B, Ď, i Sensors		
HSD-4, CFD-1, CPM-1.  Pearson Current Transformers: 110A, 411, 1025, 1049, 3025	5 kA to 250 kA		
<ul> <li>Bell DC Current Transformer</li> <li>T&amp;M Research Coaxial shunts:</li> </ul>	1 kA, 150μs Response Time		
F-5000-20, F10000-40	0.001, 0.0005 ohm		
Fiber Optic Data Links  Six MCAIR Built Units	Battery Powered Transmitter; 25 MHz Bandwidth; Differential, High Impedance Input; Variable Voltage Gain to 150 X; Receiver Drives 50 S2 Load		
Transient Recorders			
<ul> <li>Biomation 8100</li> </ul>	8 Bit Resolution, 2,048 Data Points, 10 ns Minimum Sampling Interval		
<ul><li>Biomation 6500 (2 Each)</li><li>Tektronix 76120 (2 Each)</li></ul>	6 Bit Resolution, 1,024 Data Points, 2 os Minimum Sampling Interval 2 Channels, 8 Bit Resolution, 4,088 Data Points, 5 os Minimum Sampling Interval		
• Tektronix 7912	512 x 512 Point Matrix, 200 MHz Bandwidth		
Laboratory Computers			
<ul> <li>Hewlett Packard (HP) 9825</li> <li>with Floppy Disk Storage,</li> <li>Plotter, and Printer</li> </ul>	64 K Bytes of Memory; Integrated with Fiber Optic and Transient Recording Systems to Provide Computer Controlled Data Acquistion; Modern to DEC PDP 1 i/40 Computer		
<ul> <li>Hewlett Packard (HP) 9825 with Plotter, and Printer</li> </ul>	64K Bytes of Memory; Integrated with Transient Recorders for Automated Data Acquisition.		
North Star	16 K Bytes of Memory; Disk Storage		
Photographic Equipment			
<ul> <li>Cordin Model 200</li> </ul>	High-Speed Streak and Framing; 1 μs Interframe I terval		
<ul> <li>Cardin Model 351/326</li> </ul>	Streak and Framing Camera; 25,000 Frames/sec		
<ul> <li>Image Converter System</li> </ul>	Electronic Image Intensifier Camera Both Streak and Framing Modes; (in Procurement)		
<ul> <li>Photec IV</li> </ul>	Movie Camera, 10,000 Frames/sec		
<ul> <li>Four Still Cameras</li> </ul>	4 in. x 5 in. Frame Size, Numerous Lenses and Associated Equipment		

Note. Besides the above listed specialized equipment, the lightning laboratory has a large quantity of gene- is purpose text equipment such as oscilloscopes, pulse generators, time domain reflectometers, etc.

GP31-0471-6

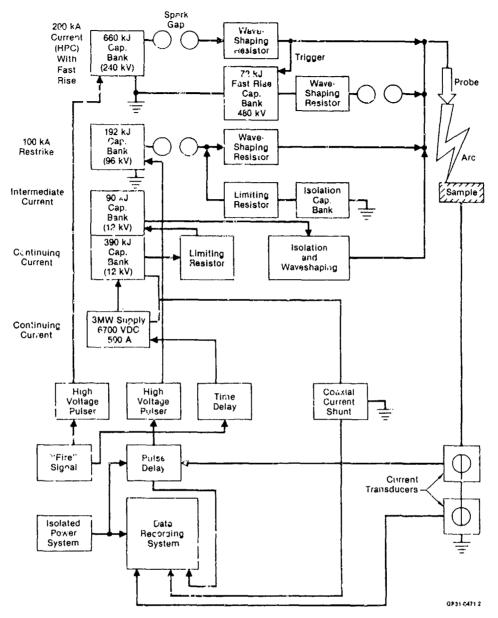


Fig. 1 · 1MJ/3MW high current simulator configured for multicomponent strike

two banks reaches the test sample at the same time. The segmented 480-kJ bank and the 3-MW supply then discharge through the established are to the sample. The 192-kJ restrike bank is fired upon command after a preset time delay. Its output spark gap breaks down, and the generator also discharges into the test sample through the established are path.

660-kJ CAPACITOR BANK — The 660-kJ capacitor bank consists of 270 energy storage capacitors (each 42  $\mu$ F, 12 kV) connected in a Marx surge arrangement. Normally the bank is used as a ten-stage Marx generator with a per stage capacitance of 231  $\mu$ F and a charge voltage of 24 kV, yielding an output voltage of 240 kV. The generator output is, however, not restricted to these values. Capacitors, or whole

stages, are easily disconnected from the electrical circuit to permit extreme flexibility in obtaining a full range of output voltages, peak currents, and pulse width:

Because of the layout of the capacitors, the 660-kJ bank is easily separated into two five-stage Marx generators which may be used individually or paralleled to increase the output capacitance four-fold over the ten-stage configuration. The paralleled configuration (Figure 2) produces the 200-kA, 2 x 106 A<sup>2</sup>s (Component A) pulse with the total energy being delivered in the first half cycle. The high output voltage of the generator permits the use of added damping resistance to control the peak current and waveshape regardless of the test article's size or resistance.

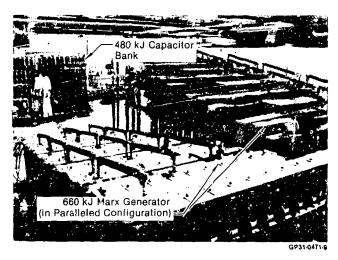


Fig. 2 · High current generators and test area

192-kJ CAPACITOR BANK - The 192-kJ (96-kV) capacitor bank is essentially a smaller portable version of the 660-kJ bank and uses the same capacitor type, charge voltage, and triggering methods. This capacitor bank is principally used to provide the 100-kA restrike current pulse (Component D) and is often combined with the 72-kJ generator when a fast current rise time is needed. Each of the generator's four stages is assembled on its own cart, so that the generator may be transported to any test location.

72-kJ FAST RISE CAPACITOR BANK — The 72-kJ, 480-kV capacitor bank is a low inductance, portable Marx generator. Each of its eight stages contain three 15  $\mu$ F 20-kV capacitors connected in series. When operated independently, the 72-kJ generator can delive a 200-kA pulse with a 2- $\mu$ sec rise time. However, this generator is normally operated in a combined mode with either the 660- or the 192-kJ generator to provide a fast rising high-energy pulse. This bank is also useful for induced coupling tests at medium-current levels where a moderately wide waveform is needed.

480-kJ CAPACITOR BANK — The 480-kJ capacitor bank consists of 160 high-energy capacitors connected in parallel. Thirty of the capacitors are normally used to provide the intermediate current portion of a simulated lightning strike (Component B) with the remainder being used to provide a portion of the continuing current (Component C). As with the other capacitor banks, not all the capacitors or the maximum charge voltage need be utilized in all applications. The 480-kJ bank may be used independently, but it is usually utilized in conjunction with the 660-kJ bank.

3-MW POWER SUPPLY - The 3-MW high-voltage/high-current supply has a floating 6700 V DC output and is capable of providing an output of 500 amps for one second or up to 1500 coulombs in five seconds. This supply is located near the 1-MJ facility and is normally used in conjunction with it, but it can also be used independently.

The 3-MW supply requires large external resistors for current limiting. This has the advantage of making the supply appear as a constant current source to more closely approximate the characteristics of a natural lightning strike. Because of the high voltage available from this supply, the test probe can be located several inches from the test sample. The long

are eliminates erroneous results which may be encountered when the probe is located too close to the test sample.

### REMOTE LOCATION HIGH-CURRENT TESTS

High-current tests in locations other than the I-MJ/3-MW test cell have been necessary for very large test articles or when other specialized test environments have been required. For many of these remote applications, the combination of two portable generators (the 192- and 72-kJ banks) has met the test needs. The combined system produces a 100-kA restrike pulse (Components D and E) with a 2-µs rise time.

Figure 3 shows a portion of the high-current test setup used in tests of a full-scale mock-up of the MX missile's post-boost vehicle. (The 9-m-tall missile mock-up was housed in the large coaxia! current return structure partially shown at the far right of the photo.) The purpose of the tests was to measure the external current distribution, the interior magnetic field distribution, and the induced voltage on the antennas when the missile was hit with a fast-tising, 100-kA strike.

The combination of the 192- and 72-kJ banks has also been beneficial in remote swept stroke and live fuel tests. Although the sleept stroke facility and the explosion-proof test ceil are located in the same building which houses the 1-MJ/3-MW simulator, safety considerations and the long cable lengths prevent the effective utilization of the 660-kJ bank with these facilities. Full-threat restrike tests (Components D, B, and C) are conducted in these facilities using the portable generators for the high-current pulse in combination with the 480-kJ bank and the 3-MW supply for the intermediate and continuing current components.

### HIGH-VOLTAGE/INDUCED-VOLTAGE SIMULATORS

Although numerous high-voltage generators have been added to the lightning laboratory through the years, only the 1500-kV modular generator and the 800-kV Haefely generator are recent additions. The 1500-kV generator was developed to conduct shock-excitation induced-voltage tests on full aircraft at remote sites. The 800-kV generator was procured to conduct variable waveshape attach point tests.

1500-kV MODULAR GENERATOR - The modular Marx generator is used in induced-voltage tests and has produced 10-kA current pulses with 200 ns rise times on test articles as large as the MX missile mock-up and the AV-8B carbon epoxy wing The generator (Figure 4) is built in 100-kV modules with each shelf being an interchangeable generator stage. Up to 15 stages can quickly be assembled using only the shelves and nylon rods for mechanical support. Each shelf contains a capacitor, three resistors, a spark gap switch, a trigger electrode, and a grading ring. Interchangeable 40-ka copper sulfate resistors interconnect the capacitor terminals and trigger electrodes from one stuge to the next. Each stage is triggered with an electrode biased at approximately half the potential between the copper-sphere spark gap electrodes. A grading ring is used on each shelf to suppress corona and produce a smoother electric field distribution. Control of the generator system is provided by a pneumatically-operated charge/dump switch which totally isolates the generator from ground potential during firing. This switch minimizes ground loops and coupling to the power supply and provides excellent operator safety.

The property of the second second

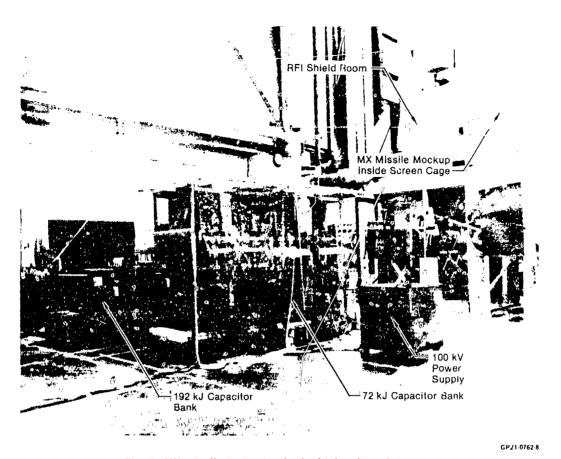


Fig. 3 - MX missile test setup in the high voltage laboratory

800-kV HAEFELY GENERATOR — Lightning model attach point studies continue to be a controversial area of lightning testing. Many test parameters such as electrode potarity and shape, model size, are distances, and voltage waveshape are known to affect the test results. The Haefely generator was resigned to study are propagation and the statistical are attachment distributions as a function of the voltage rate-of-rise. The generator uses a capacitive waveshaping/voltage divider and various inductors to adjust the voltage rate-of-rise over a wide range.

### REMOTE LOCATION INDUCED-VOLTAGE TESTS

In the late 1970's, the MCAIR lightning laboratory developed the shock-excitation test technique to more realistically simulate the induced-voltage responses of interior aircraft circuits to a lightning transient. The shock-excitation test technique differs from other induced-voltage test methods in that both high-voltage and high-current stimuli are applied. In the test setup, an output spark gap is inserted between the test article and the current return conductors. The test article is first charged to a high potential by a high-voltage Marx generator. Once the test article is charged, streamers form and then break down the output spark gap which quickly discharges the test article and allows the generator current to flow through the test article. The charging/discharging sequence better simulates the natural lightning strike process of the stepped leader attachment followed by a current return stroke.

The early test development centered on equipment needs, such as high-voltage dielectric insulators to isolate the test article from ground potential and fiber optic data links to measure millivolt induced-voltage responses in a test article charged to several hundred kilovolts. After this equipment was built and the test technique demonstrated in our laboratory, NASA and the US Air Force wanted several aircraft tested at remote locations. The need to conduct tests outside our laboratory required the development of the 1500-kV modular Marx generator (to replace our large highvoltage generators) and a computer-controlled data acquisition system (to simplify data taking and storage). The completely portable induced-voltage test system has been used to test the space shuttle orbiter [8], YF-16 [9], F-106B [10], and C-130 aircraft at remote locations ranging from Florida to California. The system is readily assembled in a day and is highly flexible to meet diverse test requirements.

### FACILITIES AND INSTRUMENTATION

The MCAIR lightning simulation laboratory is separated into two areas. The high-voltage facility is primarily housed in a 17x26 meter high bay area of a large hangar building. With the exception of the outdoor 4-MV generator, all the generators used in this facility are movable so that facility modifications have not been required to meet changing test needs. The high-current test facility is located in a nearby building and includes the 1-MJ/3-MW test cell, a 250-knot swept stroke facility, and an explosion-proof test cell.

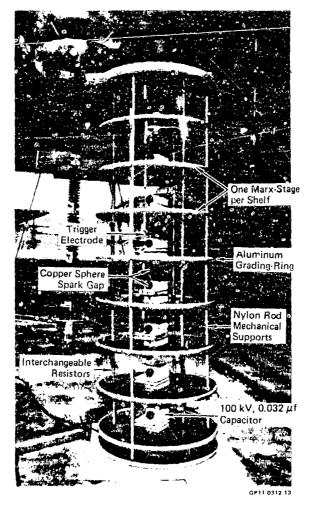


Fig. 4 - Modular high-voltage generator

The high-current lightning test area is presently being modified and enlarged to that shown in Figure 5. The facility changes are necessary to accommodate additional capacitor banks and power supplies and to increase the floor area available for large test setups. The lab area is being increased to 13x17 meters, and a 3.6 m wide door is being added to permit direct access of large test articles.

Figure 5 also shows the location of the explosion-proof test cell which is utilized when lightning tests require the use of live fuel. For these tests the portable 192- and 72-kJ high-current generators are moved to the screened test area, and the generator power supplies are moved into the test cell control room. The output of the 480-kJ capacitor bank and the 3-MW power supply are routed overhead to the screened area to provide the continuing current component of the waveform.

The 250-knot outdoor, swept stroke test facility with its 25- x 76-cm output nozzle area has not been changed. However, a portable blower system has been built for low-speed swept stroke tests up to 160 knots. The new system is powered by a 50-hp electric motor and has a large stilling chamber with a 30- x 30-cm fiber glass output nozzle. This portable system has recently been used in conjunction with the

1-MJ/3-MW lightning simulator to conduct full-energy restrike swept sti-ke tests on composite and aluminum wing skin panels.

The lightning laboratory has also continually updated its test instrumentation. A large variety of electromagnetic sensors, high-frequency oscilloscopes, and digital transient recorders are available. The test instrumentation is housed in either permanent or portable RFI shielded enclosures and run on isolated power lines. Still and high-speed movie cameras with numerous lens systems are used for photographic data, and computer-based acquisition systems are used for transient data taking and storage.

### SUMMARY

As the knowledge of the lightning threat improves and more realistic test simulations are desired, the laboratory must change to meet these needs. The MCAIR lightning simulation laboratory has continually been upgraded to meet these needs both in the generation of the lightning test waveforms and in the measurement of the responses of the test samples.

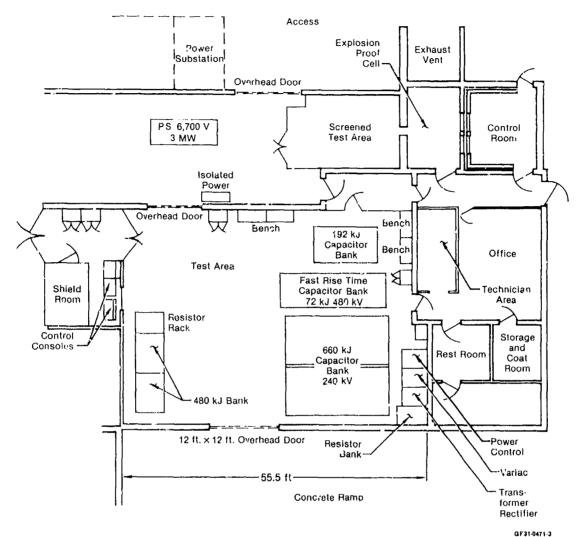


Fig. 5 - High current test areas

REFERENCES

- 1. E. P. Krider and C. D. Weidman, "Submicrosecond kise Times in Lightning Return-Stroke Fields," Geophysical Research Letters, Volume 7, page 955, November 1980.
- "Lightning Qualification Test Techniques for Aerospace Vehicles and Hardware," MIL-STD-1757, June 17, 1980.
- "Space Shuttle Program Lightning Protection Criteria Document," JSC-07636, Revision A, November 4, 1975.
- 4. "Protection of Aircraft Fuel System: Against Lightning," FAA Advisory Circular 20-53, October 1967.
- D. W. Clifford, K. E. Crouch, and E. H. Schulte, "Lightning Simulation and Testing," IEEE Transactions on Electromagnetic Compatability, Vol. EMC-24, No. 2, May 1982.

- 6. E. H. Schulte, "Effects of Lightning Waveform Components on Graphite/Epoxy Material" Society for the Advancement of Material and Process Engineering, 23rd National Symposium, Anaheim, California, May 1978.
- E. H. Schulte, "The MCAIR Lightning Simulation Laboratory," MCAIR Report, Revised October 1982.
- W. G. Butters, D. W. Clifford, J. E. Lenz, and K. P. Murphy, "OV101 Orbiter Lightning Test," Report MDC A6547, August 1980.
- W. G. Butters, D. W. Clifford, K. P. Murphy, and K. S. Zeisel, "Assessment of Lightning Simulation Test Techniques," USAF Report AFWAL-TR-3075, August 1981.
- B. D. Heady and K. S. Zeisel, "NASA F-106B Lightning Tests," NASA Report CR-166057, January 1983.

VULNERABILITY ASSESSMENT OF ELECTRICAL/ELECTRONIC SUBSYSTEMS
AND EQUIPMENT TO ATMOSPHERIC ELECTRICITY



Jack R. Lippert

Air Force Wright Aeronautical Laboratories AD P002223

### ABSTRACT

During Phase I of the Atmospheric Electricity Hazards Protection (AEHP) Program, the sensitivity of several generic classes of electrical/electronic subsystems and equipment will be assessed to electrical/electromagnetic threats associated with atmospheric electricity; e.g., lightning and precipitation static generated currents, fields, and potentials. This will be accomplished through the utilization of appropriate atmospheric electricity simulation and various test vehicles for flight/mission critical subsystem/equipment evaluation for operation in atmospheric electricity generated electrical/electromagnetic environments.

This paper will discuss simulation techniques contemplated for use on this task as well as specification of the environmental parameters to be simulated. In addition, the testbeds planned to be used, including advanced composite skin modifications, for both Phase I and Phase II of the AEHP Program will be identified. These vehicles will be appropriate for assessment of the EM threat to electrical/electronic subsystems and equipment for different classes of aircraft; e.g., fighters, bombers/transports, helicopters, cruise missiles.

This paper will outline vulnerability assessment procedures to be used on the AEHP Program and afford an opportunity for contributions from the technical community regarding the adequacy of the proposed assessments. The assessments planned for Phase I will be presented more completely than those for Phase II, but the genre of the total AEHP Vulnerability Assessment Program will be displayed. It is anticipated that valuable contributions to understanding of the AEHP Advanced Development Program by the technical community will result from this presentation. The continuing review of and contributions to the planned AEHP Program by appropriate members of the technical community is desired so that the AEHP Program's contribution to increased operational effectiveness for both military and commercial scenerios may be maximized.

### INTRODUCTION

The AEHP Advanced Development Program enjoys the application of financial and program

resources by an assembly of Military/Civilian agencies. This support is suggested on the Logo for the ADP shown as Figure 1. The Flight Dynamics Laboratory of the Air Force Wright Aeronautical Laboratories (AFWAL/FI) provides the ADP office for interagency coordination and AEHP Program direction. Other Federal Military Agencies contributing to the Program include other Air Force Laboratories and the Aeronautical Systems Division, as well as the Army, the Navy Air Systems Command and the Defense Nuclear Agency. In addition, the Federal Aviation Administration and the National Aeronautics and Space Administration are participating in the Program, while the Boeing Military Airplane Company (BMAC) is the Prime Contractor for the Program. The general program overview is discussed in an earlier paper of the conference. This paper will highlight and concentrate on the experimental equipment procedures used to assess the aircraft system vulnerability to ultimately develop the definition of balanced protection concepts.



Figure 1 - AEHP ADP LOGO

This will in turn provide confidence for all-weather application of advanced avionic and structural concepts in military and civilian scenarios. These results of Phase I will then be incorporated into interim design guides for dissemimation to industry early in the program activities.

Currently, Phase II is anticipated as having a January 1984 start with the technical investigations program being completed by October 1986 (33 months). During that period, it is planned to configure modified YUH-61 Helicopter and F-14 testbeds with representative advanced electrical/electronic systems and advanced structural concepts to demonstrate the effectiveness of the balanced AEHP defined during Phase 1. The testbed A/C, together with protected electrical/electronic systems representative of A/C of the 1990's will be subjected to interaction with simulated lightning flashes which will be representative of the AE threat determined during the ADP. The results of these tests will be evaluated and appropriate adjustments made to the protection schemes employed. In addition to the demonstration of balanced protection effectiveness, techniques for qualification of protection and continued assessment of the integrity of the AEHP provided will be identified and demonstrated.

Atmospheric Electricity Threat Definition - The characterization of the atmospheric electricity threat environment imposed on flight and

mission critical electrical/electronic elements aboard A/C is important for the AEHP Program. The "initial" threat is based on three major sources of lightning current measurement which have an adequate statistical base; e.g., Berger in Switzerland, Garbagnati in Italy, and Uman, Weidman and Krider in the United States. From these measurements there is sufficient evidence to demand the increase of the prior accepted lightning maximum rate of current rise by a factor of two which has been included in the initial characterization of the AEHP threat to A/C.

The "initial" single stroke lightning threat has been characterized by double exponential current waveforms. The severe threat for the AEHP Program has a maximum rate of rise cf 200 kA/ $\mu$ s with a peak current of 200kA, a falltime to half-peak value of 50 $\mu$ s, and an action integral of 1.5 x 10  $^{\rm h}{\rm A}^{\rm 2}{\rm -sec}$ . The moderate threat has a 20kA peak current with a maximum rate of rise of 50kA/µs, a fall-time to half-peak value of  $50\mu s$  and an action integral of  $1.5 \times 10^{4} A^{2}$ -sec. Although the moderate and severe lightning flashes consist of multiple strokes, this feature is difficult to simulate, and therefore the test generators are designed for single stroke operation. In addition, the double exponential nature is not obtainable at these levels, but the crowbar-type generator has an acceptable representation sine wave rise with exponential tail as shown in Figure 2.

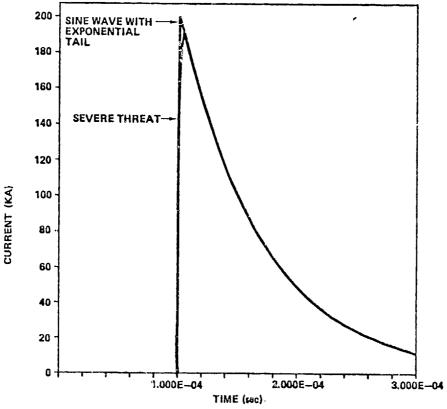


Figure 2 - LIGHTNING WAVEFORM

Electronic Susceptibility - The interest of the AEHP ADP is in providing effective protection for flight/mission critical electrical/ electronic systems of the 1990's, anon. Many of the devices/systems of interest will not be available for direct investigation, but as a first step in determining the protection which must be afforded, the historical record has been examined to identify damage mechanisms for various types of semiconductors and other components. The sensitivity to upset has been assessed from manufacturer's data sheets and the necessity of testing to evaluate system upset effects roted. Some device upset evaluation by lightning transient testing will also be performed to assist in system upset consideration. Both bench tests and installation in mock-up/testbed for moderate level impulse tescing are being used for this purpose.

<u>Vulnerability Assessment</u> - This requires a substantial degree of experimental work. The main purpose is to obtain generic data on the susceptibility of components/subsystems in various generalized configurations when subject jected to the defined lightning threat. This investigation is being accomplished via two different testbeds (YG-16, ALCM) at two different facilities (BMAC, Sandia).

The YG-16 testbed consists of an advanced composite forward fuselage section mated to a mock-up representing the remainder of the F-16 aircraft. The forward fuselage is 78% GR/EP with some aluminum support structure and two Kevlar non-conducting panels. The mock-up is sheet aluminum over a wood frame in the general F-16 shape to preserve electrical lengths ar

resonances appropriate for the fighter aircraft. The entire testbed is supported above the ground plane by non-conducting wood bracing. A picture of the YG-16 testbed is shown in Figure 3.

The YG-16 test series is designed to: a. Characterize the induced transients in aircraft wiring due to lightning attachment to the aircraft. b. Determine upset and damage sensitivities of advanced technology subsystems when exposed to moderate level lightning environments. c. Provide low level CW and moderate level pulse test data for comparison with analytical calculation.

Of the two test techniques employed, the Swept Continuous Wave (Swept CW) technique injects a low level current onto the aircraft skin/structure and measures the output voltage/ current at wiring/equipment stations as a function of frequency. This results in definition of the transfer functions the frequency domain which may be used to determine coupling effectiveness and as an analytical tool. The other technique, pulse injection, applies a unipolar current impulse to the aircraft with response measurements taken in the time domain. This test generates information concerning susceptibility levels and interaction mechanisms. The pulse waveform used is the moderate level threat representation defined as a double exponential current waveform with the following parameters:

- a. Peak Current 20kA
- b. Peak Rate of Rise 5 x 10 A/sec.

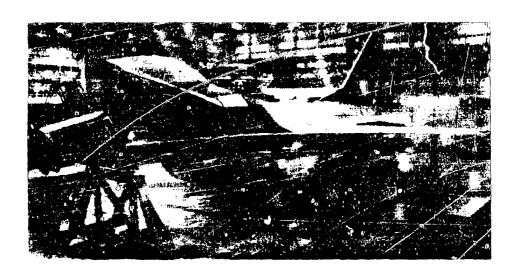


Figure 3 - YG-16 TZSTBED

c. Action Integral - 1.5 x  $10^{11}$ A<sup>2</sup>-sec.

. BMAC has designed and is fabricating an impulse generator capable of subjecting the YG-16 testbed to a current pulse with the above parameters. A block diagram of the generator configuration is shown in Figure 4.

Three levels of complexity are structured into the YG-16 test series: a. Simple, point to point wiring configurations with no operating subsystems. b. Generic installation of wiring with dummy loads which are electrically representative of advanced avionics (Figure 5). c. An operating subsystem with an airborne computer, appropriate power, control, and display equipment.

The general procedure for testing first involves modeling the YG-16 mock-up for the WIRANT and TRAFFIC computer codes. Their outputs are predictions of the expected L1 threat levels in the testbed's equipment and will be correlated with the experimental results to determine validity and worth as an analysis tool. These tests are scheduled through the August 1983 time period. The information gained from these tests feeds into protection concept development and tradeoffs for total system balanced protection which will also be evaluated via testbed experimentation. These tests should be completed by October 1983.

The Air Launched Cruise Missile (ALCM) testbed is a prototype version of the production AGM-86B which has undergone skin panel(s)

modification/removal and cable shield alteration to yield generic data for the general missile configurations. The pulse of this test series is being conducted at the Sandia Lightning Facility in Albuquerque N.M., shown in Figure 6. This facility is capable of subjecting the ALCM to current waveforms corresponding to the defined severe lightning threat:

- a. Peak Current 200kA
- b. Peak Rate of Rise  $2 \times 10^{11} A/S$
- c. Action Integral 1.5 x  $10^6 \text{A}^2$ -s

This severe threat coupled to a vehicle as small as the ALCM will result in a very strong current density on the vehicle.

The objectives of the ALCM test series are as follows: a. To characterize the EM coupling paths from the lightning attachment point to mission critical equipment interfaces; b. To determine stress levels at selected equipment from various pulse levels; c. To determine upset and damage effects of simulated full threat lightning current pulses on operating avionics. Testing will be accomplished in three parts as follows:

Part 1 - Low level CW test will be used to characterize EM coupling paths to mission critical equipment interfaces. CW testing will be accomplished with the missile in the power off mode. CW testing will be performed in the EMI laboratory at Seattle, Washington.

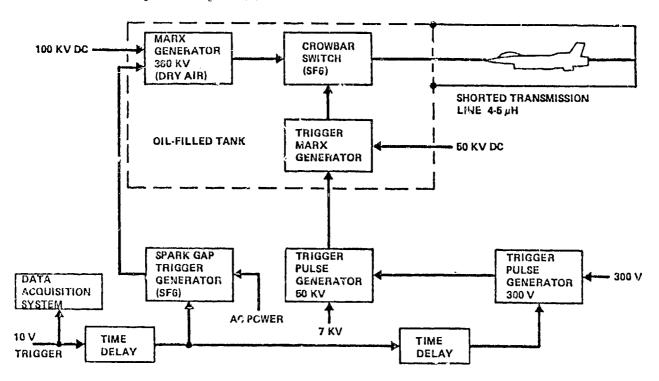


Figure 4 - CROWBAR PULSE GENERATOR EQUIPMENT

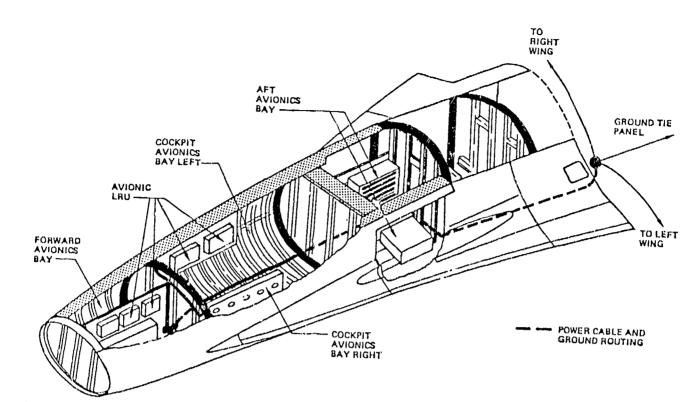


Figure 5 - GENERIC INSTALLATION CONCEPT

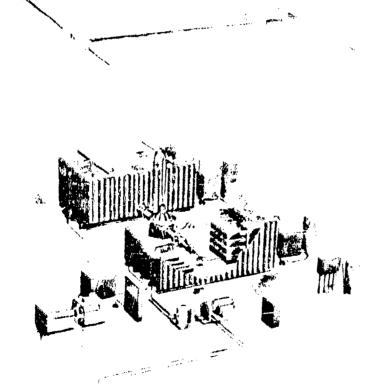


Figure 6 - SANDIA LIGHTNING SIMULATOR

Part 2 - During this part, missile power will be on, and the missile will be operated in a simulated free flight mode. High level pulses will be applied to determine sensitivity of ALCM mission critical equipment to simulated lightning strikes. The testing will be accomplished in the Sandia Laboratory at Albuquerque, New Mexico.

Part 3 - This part will also be accomplished at Sandia. Missile power will be off, a dummy warhead will be installed in the missile, and selected missite equipment will be replaced by instrumentation to measure voltage and current transients at interfaces. Various pulse levels will be used with Sandia responsible for testing of the dummy warhead. The warhead test will be performed to evaluate lightning effects on the warhead. However, this testing is part of Sandia mission and performed in conjunction with the AEHP program. These tests are scheduled during July-August 1983, and the information gained will complement that from the YG-16 test series for use during Task V efforts.

Protection Evaluation/Tradeoffs - The objective of this Task is to evaluate and establish practical effective protection concepts. These concepts will minimize cost, weight, power, reliability/maintainability requirements. The Task V trade study is to develop a specification for balanced protection for advance (1990-95) airframes and associated electronic/electrical systems. The trade studies will be primarily analytical, but when required, concepts will be evaluated experimentally on the YG-16 testbed to determine hardness effectiveness. At completion of Task V, the protection concepts will have been developed and evaluated parametrically. information will then be assembled and correlated into the interim design criteria and used as the basis for the Phase II plans for full scale demonstration of these protection concepts.

Interim Design Criteria - Near the conclusion of Phase I, interim design criteria for Atmospheric Electricity Hazards Protection will be provided to the Aerospace Community for review and comment. It is important that the results of this ADP are effectively communicated to A/C and Systems producers so the AEHP from the ADP may have an early introduction to the Military/Commercial A/C fleets.

#### PHASE TWO (II)

The AEHP ADP is configured as a two phase effort with Phase I being directed toward the development/design of effective AEHP for the four classes of flight vehicles; i.e., fighters, transports/bombers, cruise missiles, helicopters. In Phase II the effectiveness of the AEHP Interim Design Criteria and initial AEHP concepts will be demonstrated on fullscale A/C testbeds using ground-based, fullthreat Atmospheric Electricity Simulators. Presently, existing simulators are not capable of subjecting a complete F-14 size A/C to severe threat parameters. One of the programs subcontractors, Lightning and Transients Research Institute (LTRI), is developing such a simulator based on the Sandia-type crewbar impulse generator for Phase II. The generator/ test configuration presently envisioned is shown in Figure 7. At this time it is contemplated that the testbeds to be used will be derived from a YUH-61 Helicopter and an F-14 A/C. Although the YUH-61 already has substantial composite structure, as shown in Figure 8, the basic vehicles will likely be extensively modified through application of advanced composite and other poorly conducting material as vehicle surface cover, as well as installation of electrical/electronic systems employing operational concepts representative of those anticipated for the 1990's.

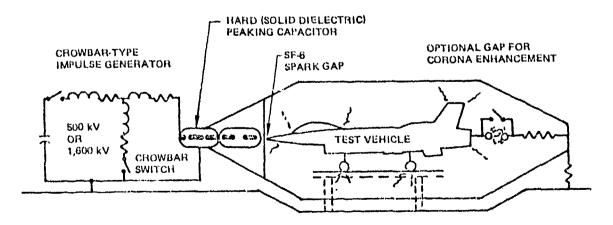


Figure 7 - PHASE 11 - SIMULATOR/TESTBED

It is believed that this procedure will permit the evaluation of many electrical/electronic system protection concepts, including structural aspects and topological shielding as well as AEH. tolerant electrical concepts, in configurations which are representative of those which will be encountered in future  $\lambda/C$  of the four classes being considered. Figure 9 shows the F-14 and the amount of skin panels that would be available for replacement with

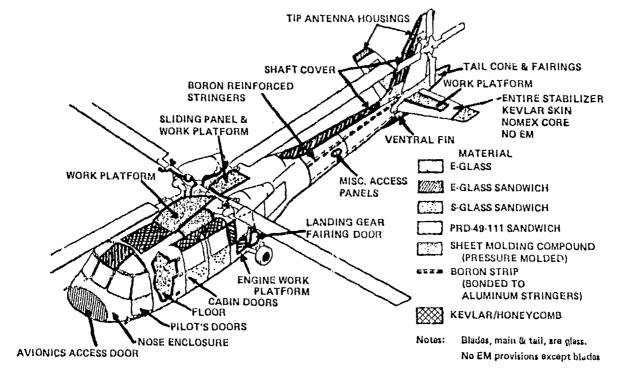


Figure 8 - YUG-61 HELICOPTER

## VIEW LOOKING INBOARD LEFT SIDE

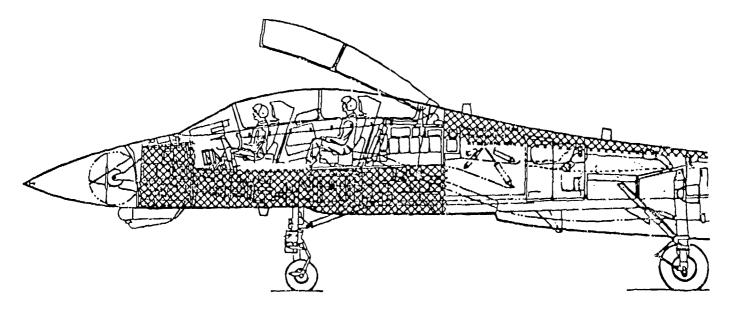




Figure 9 - F-14 SKIN PANELS

composite/nonmetallic samples. The details of the Phase II Program to be conducted will be documented as part of the Phase I activity on the AEHP contract, but one of the underlying goals is to develop a standardized hardness assurance test technique that can be easily and inexpensively performed to routinely verify incorporated AEHP as the system ages.

### CONCLUSION

The AEHP program depends on threat level experimental testing to develop and evaluate hardening/protection concepts, correlate the worth and reasonableness of analytical tools, and proof demonstrate the developed, balanced AEHP for the total system. After these accomplishments, it is anticipated that the basis for a reasonable hardness assurance test technique will be understood.



Monitors for Upset Detection in Computer Systems



M. E. Schmid, R. L. Trapp, \*G. M. Masson, A. E. Davidoff

Department of Electrical Engineering and Computer Science, The Johns Hopkins University, Baltimore, MD., 21218

The Johns Hopkins University

Applied Physics Laboratory

Johns Hopkins Rd., Laurel, MD. 20707

### Abstract

An upset is a deviation of system performance based on apriori knowledge of the system application task. There has heretofore been little experimental work reported in the literature regarding characterizations of upsets in computer systems. This problem was addressed in the research reported in this paper with two series of fault injection experiments on a representative microprocessor-based system. In the first series, the system executes a small machine language program; in the second series, a much larger software environment consisting of a Pascal

interpreter running a general applications program is used. each case, a broad spectrum of fault conditions is utilized for the fault injections. An extensive instrumentation complex has been developed to record microevent data associated with the upsets resulting from the injections. This data is used to characterize upsets in computer-based systems. It also serves as a benchmark for the performance of candidate upset monitors in the sense that coverage and latency figures for such devices can be deduced from this data.

THE MCNITORING OF COMPUTERBASED SYSTEMS by simple external
devices is a frequently suggested
solution to increasing system
reliability (1), (2). A
comprehensive overview of the primary
issues associated with this approach
has been provided by Avizienis (2).
Highly ranked among such issues are
characterizations of system
performance deviations to which
monitors can be sensitized, and
assessments of the effectiveness and

complexity of such monitoring devices. This paper reports on an experimental investigation of these issues.

The monitoring devices considered in this paper are sensitized to the type of system disturbance known as an upset (1). An upset is a deviation of system performance based on apriori knowledge of the system application

task. An overview of upset phenomena is described in a companion paper (1).

There has heretofore been little experimental work reported in the literature regarding characterizations of upsets in computer systems. This problem was addressed with two series of fault injection experiments on a representative microprocessor-based system. In the first series, the system executes a small machine language program; in the second series, a much larger software environment consisting of a Pascal interpreter running a general applications program is used. For each case, a broad spectrum of fault conditions is utilized for the lault injections. An extensive instrumentation complex has been developed to record microevent data associated with the pages resulting from the injections. This data is used to characterize upsets in computer-based systems. It also serves as a benchmark for the performance of candidate upset monitors in the sense that coverage and latency figures for such devices can be deduced from this data.

In both experiment series, one particular class of upsets is seen to be dominant. However, full, rigorous designs of monitoring devices sensitized to such upsets are in general prohibitively complex and/or memory intensive. Hence, there is motivation to consider more practical alternative upset monitor designs. This is done for a particular class of upsets in the form of compressed

upset monitors. Here, the complete database that characterizes the upset is reduced; then a menitor is considered that would only be sensitized to the upset to the extent that the reduced or compressed database characterizes it.

Interestingly, rather significant compressions yield upset monitors with coverage and lacency figures which approach those of a full, rigorous implementation.

The second secon

FAULT INJECTION-DATA RECORDING EXPERIMENTS

Beyond the three general features of system performance (program flow, memory access, and instruction repertoire) described in the companion paper, it is difficult to apriori characterize the forms that upsets can take. Yet, doing so is obviously the first step toward the assessment of monitors that can be used for their detection. Hence, there was motivation to develop an experimental testbed for the purpose of injecting faults into a representative computer based system and recording data so that such upset characterizations can be made. A block diagram of our experimental testbed is shown in Figure 1.

The testbed contains a representative computer-based system (Z80) running applications programs Faults are injected into the representative computer-based system under a wide range of conditions. Indeed, because so little is actually known about the details of faults, a set of approximately 700 fault injection

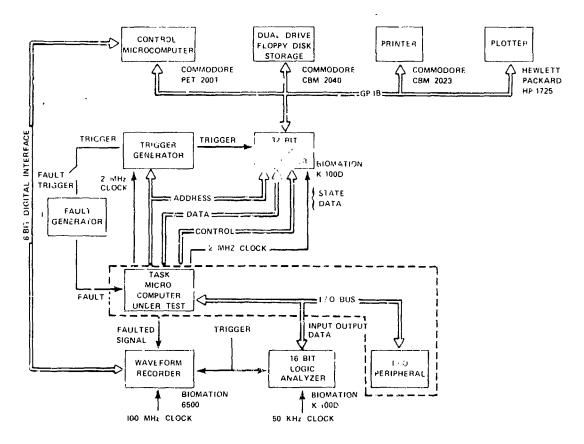


Fig. 1 Upset detection experiment configuration.

conditions are used for each of the two experiment series. These conditions, outlined in Table 1, include variations in target microprocessor line, target instruction, fault duration, fault type, and relative fault timing. can be seen from the table, for the reported experiments, faults are injected into data, address, or control lines of the target microprocessor. Both transient and permanent faults are injected. The transient fault durations are such that they correspond to the duration of a machine cycle, a single instruction, or multiple instructions.

Data are collected from separate gold and faulted test runs

as illustrated in Figure 2. A gold run is initiated by starting testbed execution from a known state.

Microevents (e. g. CPU cycle states) and macroevents (e. g. input/ouptut) are recorded at a predetermined time from the test start. Faulted runs occur on the same testbed under identical conditions except that a fault is injected during the run in a precise, reproducible manner.

Computer events are recorded as in the gold run.

The fault injection - data collection scenario can be summarized as follows. Upon occurence of a precisely timed trigger, a transfent or permanent fault is generated on the target line and monitored with a wide bandwidth waveform recorder.

Table 1
FAULY INJECTION PARAMETERS

Microp	rocessor Line Types	Durations		
Addres	s (AO,A5,A10,A15)	Machine Cycle -		
	Ì	1 usec		
Data (1	DO,D4,D7)	Instruction -		
		5 usec		
Contro	1 (M1, MREQ, IORQ, RD, WR)	Multi-Instruction -		
		100 usec		
		Permanent -		
		10 sec		
Z80 In	structions	Fault Types		
LD	A, (MEMADR)	Latch-up		
ADD	A, L	Latch-down		
RET				
CALL	SUB			
JЯ	START	Fault Relative Timing		
JP	LOOP			
EXX	j	At start of specified		
IN	A, IOADDR	mechine cycles within		
PUSH	DE	target instruction		
BIT	FLAGA, A			

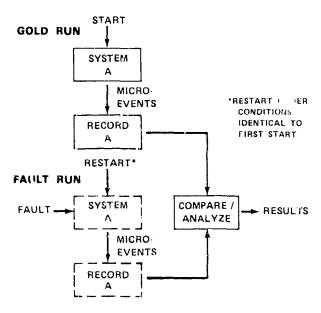


Fig. 2 Experimental procedure series comparison of gold and faulted runs.

Transient single line foults are injected primarily because they may cause more subtle perturbations of computer operation than permanent and multiple line faults. Detection of an upset caused by such a fault is indicative of upset monitor sensitivity. Three logic analyzers, sampling at different rates, record microprocessor state responses and input/output responses. A control microcomputer and supporting peripherals collect and permanently record the measured data. Thus the experiment configuration enables the detailed and voluminous collection of data necessary to effectively

classify upsets and analyze the performance of upset monitors.

Experiment series are run with two software environments. For the first experiment series, the representative computer-based system is executing a small machine language program. This program consists of two parts: a shell program and a target instruction area. The shell program remains unchanged throughout the experiment series and provides a constant environment for evaluating the effect of injected faults on a variety of target instructions. The target instruction area is located at a fixed location within the shell program; different instructions are inserted into this location for the fault injection. The fault is injected during various states relative to the execution of the target instruction. Although other software is co-resident, only the shell program is executed (in faultfree operation) during the window of data recording.

In order to verify that the classification of upsets and assessments of upset monitors is not unduly influenced by the size and functional simplicity of the assembly language program used for the first experiment series, a second experiment series was run w. h a much different and larger software environment (while still using essentially the same fault injection parameters as listed in Table 1). The second software environment consists of a Pascal interpreter running a general applications program. The interpreter requires over 3K bytes of program area,

approximately 8K bytes of intermediate code storage area, and 2K bytes of data storage.
Furthermore, another 4K bytes of system software are active. Finally, in centrast to the utilization of a shell program, the fault injection region varies considerabley depending upon the target instruction.

### UPSET CLASSIFICATIONS

For each experiment series upsets are characterized by means of a cycle by cycle comparison of the recorded data for gold and faulted operation. When differences exist, their primary features are extracted, and an attempt is made to associate them with one or move upset classes. The classes that are of most interest are, of course, those that can be described in terms of highly observable features of operation, since these correspond to the potentially most promising upset monitors. With this observation criterion in mind, as injection experiments are performed, it is seen that certain upset classes tend to cover a significant majority of the upsets observed. Conversely, some recorded upsets cannot be classified because they correspond to differences between the gold and faulted runs that are unique/complex to the extent that a classification is not realistic from the point of view of external monitoring. Indeed, for some injectious which cause microevent diff: rences, there are no perceivable differences from a macroevent perspective. Fortunately such cases are the exception. For

both of our experiment series, consisting of over 700 runs each for the first series (involving the machine language program) and the second experiment series (involving the Pascal interpreter running a general application program), only 27% of the runs were unclassifiable.

On the basis of these two experiment series, eight monitorable upset classes were identified. These classes are listed and explained in Table 2. Figure 3 shows the extent to which each upset class covered the upsets produced by an injection for each experiment series. Also reported is the average time of

emergence for each class. Given that an upset is classifiable, the time of emergence is the average time in microseconds between the fault injection and the accumulation of sufficient data to so classify the upset. Time of emergence is obviously related to latency of detection by associated upset monitors.

From Figure 3, it is seen that the results of both experiment series are relatively consistent. The predominant type of upset observed is invalid program flow. The most notable differences in coverage between the experiment series are for

Table 2

### UPSET CLASSES

IPF (invalid program flow)	<ul> <li>improper sequence of instructions</li> </ul>
IOA (invalid opcode address)	fetch of an instruction from a non-instruction address
UNM (unused memory)	<ul> <li>memory access to an existent but unused memory area</li> </ul>
IRA (invalid read address)	read access (for data) to an instruction area, or unused or non- existent memory
IOC (invalid opcode)	fetch of an illegal instruction, or an instruction not part of the subset used in the specific task software
(IWA (invalid write address)	<ul> <li>attempt to write into memory not designated as alterable</li> </ul>
NEM (non-existent memory)	- access to a location with no memory

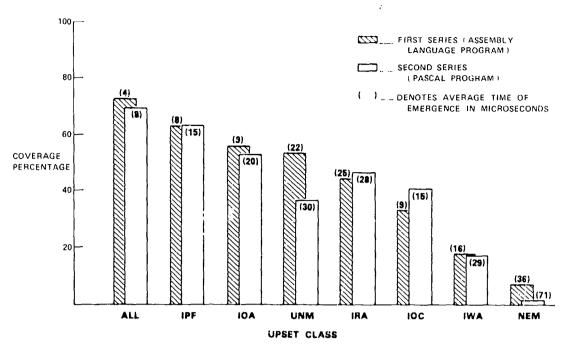


Fig. 3 Coverage by upset class.

the classes of unused memory, invalid opcode, and nonexistant memory. The variations in coverage of the unused memory and nonexistent memory classes are readily explained by the large increase in the amount of memory present and used in the second experiment series. The increased invalid opcode coverage in the second series is largely due to improved analysis techniques that allowed full checking of both single and double byte opcodes. (The first experiment series analysis did not fully check double byte opcodes.) The times of emergence for the second experiment series are generally twice that of the first series. This effect appears to be the result of differences between the execution style of the interpreter and the functionally simpler assembly language program. The loops and code sequences in the interpreter tend to be longer than those in the assembly language program. Thus, faulty data

and operations in the interpreter often take longer to emerge as classifiable upset conditions.

#### FULL PROGRAM FLOW MONITORS

In both series of experiments, invalid program flow (PF) characterized the greatest number of observed upsets and also had the minimum time of emergence. This provided strong motivation for an investigation of practical and efficient implementations of program flow monitors (PF monitors). In general, the flow or sequence of instructions executed by a processor is unambiguously specified by the program it executes and the current state of the computer (assuming selfmodifying code is not used). This flow is characterized by the execution sequence of instruction and operand addresses. An execution sequence is described with sourcedestination address pairs, where the destination address is a program counter value that can immediately precede the fetch of that instruction. A given destination address may have more than one possible source address (e. g. the first instruction of a subrout ne), or a given source address may be paired with multiple destinations (e. g. a return instruction). Thus a PF monitor compares source-destination address pairs of fault-free program execution with actual execution to verify correct operation.

Clearly it is crucial to construct a monitor that does not allow false alarms; in other words, valid program flow must not be interpreted as invalid. Thus any PF monitor considered must utilize a database of information that includes every valid combination of source and destination addresses. Although most of this information can be obtained by extracting source-destination address pairs from assembly listings, there are cases for which sourcedestination address pairs can be difficult, if not impossible, to determine. For example, register indirect branch instructions have next addresses that depend on the state of the computer. In a general sense the address following an indirect branch is unconstrained. However, a programmer always intends for a limited number of valid next addresses to exist, and hence those addresses are determinable. In contrast, "unconstrained" situations can also exist where a next address truly may be anywhere in the address

space and therfore unspecifiable. A return from interrupt is an example of such a situation. Since in such cases a PF monitor is ineffective, a preferred approach is to disable the monitor at such points, rather than contribute an inordinately large number of source-destination combinations to the information base.

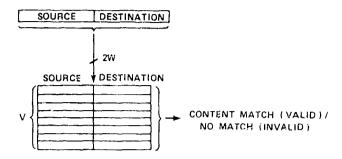
 $\label{eq:hence, a PF monitor consists} \mbox{ of: }$ 

- the representation of all valid sourcedestination address pairs:
- 2. a mechanism to determine the validity of observed address pairs;
- 3. a monitor disable function to accomodate unspecifiable addresses.

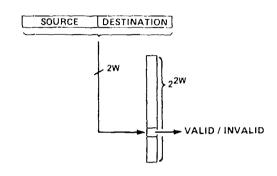
Figure 4 depicts realizations of a full PF monitor. The term "full" is used to describe these realizations because they are straightforward relative to Point 1. and Point 2. above. That is, no significant attempt has been made to condense the databases that fix the memory and complexity requirements of the realizations. In the figure, the number of valid address pairs is represented by v, and the number of bits in an address specification is w. The monitor disable function has been excluded since it can be simply implemented in a number of ways, such

A STATE OF THE STA

# (a) CONTENT ADDRESSABLE (2W x V BITS)



# (b) TABLE OF ADDRESS UNIVERSE (22 BITS)



# (c) INDEXED (2W log 2 V + VW BITS)

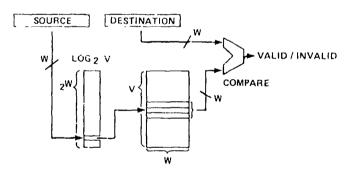


Fig. 4 Fall program flow monitors.

as tagging unspecifiable addresses with an extra bit.

# Content Addressable PF Monitor

Figure 4(a) illustrates perhaps the simplest full PF monitor in concept, but one that is difficult in practice to implement. The valid source-destination pairs are

concatenated and entered into a memory that is content addressable. An observed source-destination pair "addresses" the memory to determine whether the pair is valid. Although this method requires the least memory of the depicted realizations (v2w bits), it poses the greatest complexity on the mechanism that validates an observed address pair.

## Address Universe PF Monitor

Figure 4(b) displays a memory intensive realization of a full PF monitor. A one bit wide memory table of all possible combinations of source and destination addresses (22w bit memory) is used to represent the valid address pairs. Valid combinations are denoted by 0's and invalid combinations by 1's. Observed source and destination addresses are concatenated to form an index into the table, and the memory output directly indicates the validity of the address pair.

### Indexed PF Munitor

figure 4(c) is a compromise that uses indexing to reduce the valid pair representation. Here a source address is used to find a pointer to a set of associated valid destination addresses. An observed address pair is tested by using the source

address to find the start of a set of valid destinations. The valid destinations are compared to the observed destination to determine the observed pair's validity. Such a realization of a full PF monitor requires  $2^{v}\log_{2}v + wv$  bits.

#### COMPRESSED PROGRAM FLOW MONITORS

The full PF monitor
realizations described in the
previous section have problems
related to the extensive memory or
device complexity required. In
general, these represent major
drawbacks to their utilization.
Hence, an investigation of more
practical PF monitors is warranted.
Such PF monitors will be referred to
as compressed PF monitors. The term
"compressed" is used because the
databases which the designs utilize
are condensed relative to that of
full PF monitors.

a compressed PF monitor is illustrated in Figure 5. Note the similarity to the address universe full PF monitor (Figure 4(b)) in the use of a bit map to indicate the validity of source-destination address combinations. However, instead of having a valid/invalid entry in the bit map for all possible source-destination address combinations, the compressed PF monitor uses a compression or coding scheme to reduce the domain of combinations over which valid/invalid entries must be provided. For the compressed PF monitors to be evaluated, each individual source-

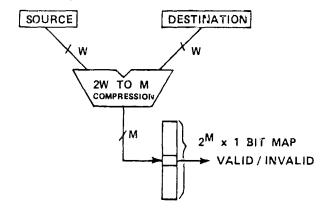


Fig. 5 Compressed program flow monitor.

destination address combination was compressed to a representation of length of  $m \leq w$ , (where w is the number of bits in one address specification), resulting in a bit map of 2<sup>m</sup> bits. As a benchmark, it is interesting to compare the memory requirements of such compressed PF monitors with that of the indexed full PF monitor of Figure 4(c) (which is apparently the most practical in terms of memory intensity and complexity of all the full PF monitors). Again assuming that there are w bits in the address specification, if the source address is used to index a memory table and if the number of valid and specifiable address combinations is v, then the memory required for an indexed full program flow implementation is  $vw + 2^{w} (log_{2}v)$ bits. Since the number of valid address combinations may indeed approach or exceed the size of the address space, the memory required can be on the order of w2w bits, which is often the size of the entire computer-based system's memory. Hence, a compressed PF monitor requiring only  $2^m$ ,  $m \leq w$ , bits

compares quite favorably, assuming, of course, that it can be shown to have similiar coverage and larency figures. As will now be discussed, this is, indeed, the case.

The six compression methods listed in Table 3 have been evaluated for monitor effectiveness. This evaluation utilized the generated data described previously. Thus the wide variety of fault conditions given in Table 1 were used in assessing the performance of these compressed PF monitors. The crucial issue of monitor performance vs. bit map size was examined by specifying different bit map sizes in the analysis software. For a representative program with approximately 8K bytes of code area within a 64K address space (much of the used address space was filled with data due to the use of the

aforementioned interpretive Pascal system), six bit map sizes were used, ranging from 29 to 216 bits. The coverage of upsets by the compressed PF monitors were viewed relative to the ratios of bit map size to program size in words. For the 8K bytes of code area in the representative program, an 8K x 1 bit map would have a ratio of 1; a 4K x 1 bit map would have a ratio of ½; and a 16K x 1 bit map would have a ratio of 2.

Of the six compression methods evaluated for monitor effectiveness, the simplest are certainly the valid start address method and valid destination address method. The valid start monitor uses the program counter value preceding each instruction fetch to indicate locations that are valid to "leave" (source address) in arriving at a new

Table 3
Program Flow Compression Methods

Туре		Function
valid start	-	check source address
valid destination	-	check destination address
difference	-	check difference between source and destination
concatenate	-	check concatenation of lower half of source and destination addresses
swap exclusive-or	-	check exclusive-or of byte swapped source with destination
parity coding	-	check parity generated from concatenated source and destination

program counter value. Similarly, the valid destination monitor indicates the addresses that are valid arrivals for tetching a new instruction (destination address).

All other monitors are based on combining source-destination address pairs in various ways. Within this class, the most straightforward is the difference monitor which uses the difference between source address and destination address to specify valid combinations. For example if a combination of source address = 0001000, and destination address = 000110, occurred, then 111110, (2's complement form) would represent a valid source-destination pair. This compression is intriguing because while it can map many valid address combinations to the same point, it nevertheless resulted in a reasonably effective monitor.

The next two compression methods involved swapping and exclusive-or operations on portions of the valid source and valid destination addresses. The concatenated monitor utilizes a compression which is a concatenation of the w/2 bits of the source address with the lower w/2 bits of the destination address. The swap exclusive-or monitor is based upon a compression wherein the lower w/2 bits of the source address is first swapped with the upper w/2 bits, then an exclusive-or of the swapped source and destination addresses is performed.

In the above compression methods, representations of less than

bits are obtained by masking off order bits as necessary.

nethod is

encoding monitor,  $2w_{tm}$  of bits are combined to create each of the marity bits. Alternating bits are taken from source and destination addresses, starting with the high source bit and low destination bit, to get an interleaving effect. For example, again suppose that the source address is  $000100_2$  and the destination address is  $000110_2$ . If m=4, then three bits at a time are combined, resulting in  $0010_2$  as the representation.

Figure 6 shows the experimental results for the six different compressed program flow monitors for various bit map size to program size ratios. As is seen, although the absolute performance for the different compressions varies, all asymptotically approach the coverage of the full PF monitor. The parity coding and swap exclusive-or compressions demonstrated moderately higher coverage, and although not indicated in Figure 6, also exhibit the minimum latency figures. As points of reference, the memory requirements for the three different full PF monitors illustrated in Figure 6 are also shown on the horizontal axis. (For our 8K representative program, y was approximately equal to 3K.) With the possible exception of the content addressable full monitor, these memory requirements are excessive.

Mowever, as mentioned earlier, the primary disadvantage of a content addressable PF monitor is its sign ficant hardware complexity.

Combinations of compressed program flow monitors were also studied. Figure 7 shows the results of combining all the compressed

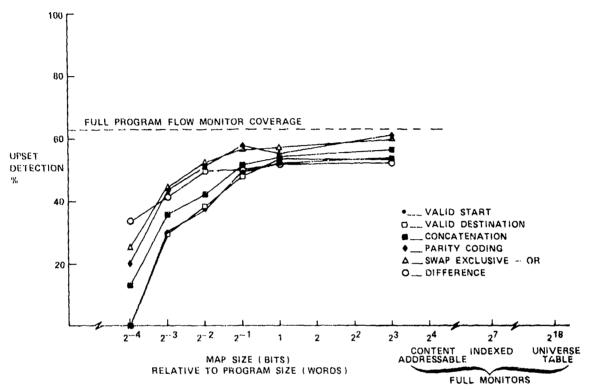


Fig. 6 Compressed program flow detection versus map size.

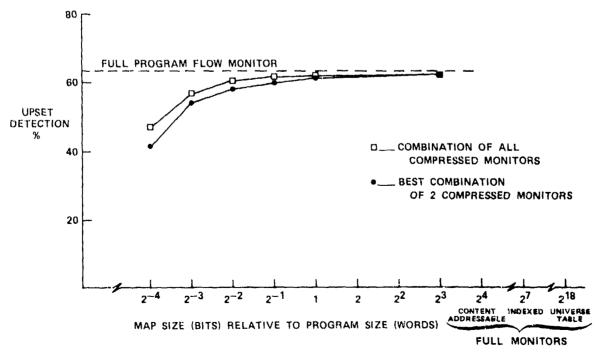


Fig. 7 Compressed program flow combinations detection versus map size.

monitors and of the best combination of two monitors at each map size.

#### CONCLUSIONS

In this paper we have presented a new class of simple external upset monitors. These monitors are compressed versions of complete program flow monitors. The motivation for considering these monitors emanated from two extensive series of fault injection experiments. Overall, program flow upsets were shown to be the predominant lass of disturbance produced by widely varying experimental fault injection. Moreover, while other classes of observed upsets (memory access, instruction repertoire) are easily monitored by relatively straightforward devices, a complete program flow monitor requires memory that usually exceeds that of the monitored computer system.

The six compressed program flow monitors studied all utilize collapsed source-destination address spaces to detect irregularities in program flow. The differences in these compressed program monitors correspond to the collapsing techniques.

While the parity coding PF monitor demonstrated the best detection capability, all of the compressed PF monitors approached the detection capability of a full PF monitor as bit map size was increased. Indeed, using a combination of swap-exclusive-or and parity coding PF monitors results in

coverage that is barely distinguishable from complete program flow monitoring for relative map sizes of one or greater.

Compressed program flow monitors could conceivably provide an enhancement to computer system reliability at a relatively insignificant cost. Their performance can be expected to exceed that of a watchdog timer, but certainly be less than that of a replicated system. The inclusion of these monitors is transparent. In practice, their integration into a system can be acheived without any significant complications, or required modifications of the applicable code. Finally, while an implementation of a compressed program flow monitor with on the order of ten SSI chips is easily acheivable, custom VLSI design would enhance its simplicity.

#### Acknowledgment

The authors wish to acknowledge contributions of Cheryl Gira, Duke University, and Ken LaBel, the Johns Hopkins University.

This work was supported as an Independent Research and Development Project under general contract N00024-81-5301 with the Department of the Navy.

#### REFERENCES

(1) G. M. Masson, "Upset
Experimentation for Computer
Systems", Interchange
Conference on Lightning and
Static Electricity, June, 1983.

(2) A. Avizienis, "Fault Tolerance by Means of Extended Monitoring", American Federation of Information Processing Conference, May, 1981.



# AD P002225



LIGHTNING PROTECTION DEVICES FOR HIGH FREQUENCIES EQUIPMENTS

Jean Pierre SIMI

LES CABLES DF LYON Division H.F., 35, rue Jean-Jaures 95871 BEZONS

#### INTRODUCTION

Lightning protection of any equipment involves :

- elimination of the undesirable surges, and this at each connection of all external wires,
- . connection to a good ground. This point supposes a good high frequency comportment of the reference is not the matter of this paper.

Good elimination of undesirable surges is now well known for low frequencies signals (i.e. < 1 megahertz). For those it is often realized with non linear volt/amp. characteristic components, like spark gaps, zener diodes or variable dependant resistor.

But those, or more generally assemblies of those, always appear as a capacitance which is put between the line to be protected and ground. So, you cannot use such a protection on an high frequency wire, for example an antenna feeder. In order to realize a good protection in regard of lightning and a quite "transparent" protection for antenna frequencies, you can use square-waves properties.

For example, you will be allowed to put first (from antenna to ground) a parallel square-wave short in the line, and so, get a "te" of protection which will appear regarding lightning frequencies as a short circuit between inner and outer conductor of the coaxial.

You will then also put a serie-square wave open circuit in your feeder and get, for lightning frequencies, an open way towards ground.

Those two ways will be developed in this paper. They allowed to get a catalogue of "tees" and "decoupling lines" of protection, now largely used to protect H.F. equipments from lightning effects coming from feeder.

Next slide shows a current family of tees, and especially clockwise from top:

the 25 + 125 MHz (L 3028), the 80 + 640 MHz (L 3233), the 400 + 900 MHz (L 3097), the 100 + 500 MHz (L 3030).

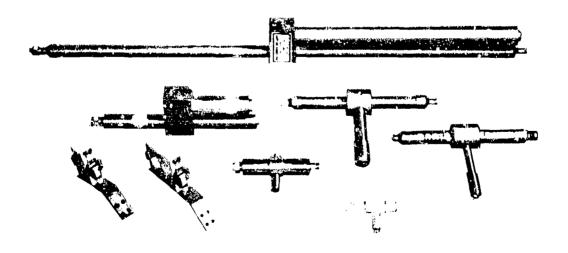
and to rapid attaches for masts.

#### CHAPTER ONE

MECHANISM OF A LIGHTNING STROKE FROM ANTENNA TO GROUND

Before introducing lightning protection devices for such applications, you must take in account some points:

- . In the main cases, it is always the inner conductor which is connected both to the hot point of the antenna and to the electronic components of the equipment.
- . Generally, the cuter conductor is connected to the cold point of the antenna and to the box of the equipment, itself connected to ground, so, the box itself eliminates to ground a part of the captured lightning stroke which is a bad situation.
- . When lightning strikes an antenna, the current which downs through the inner conductor is largely dependant of two factors which are first the type of antenna, and also the quality of the coaxial outer conductor.



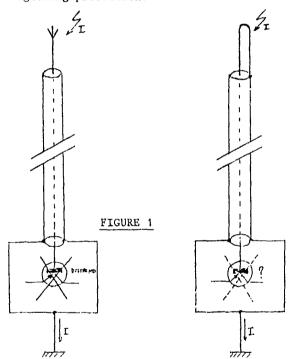
We shall rapidly developp those two points :

#### 1. Influence ot the type of antenna:

For antenna you can chose either an opened or a closed antenna. The first is equivalent to a metallic piece following the inner conducter.

The second is an accorded short circuit between inner and outer conductor. Because it is accorded for an higher frequency, it looks like a strip regarding lightning.

So, you can think that the level of lightning current will be greater on the inner conductor if you use an opened antenna, which is shown on the following schemes (figure 1). In other words, you can say that choice of antenna is the beginning of your lightning protection.



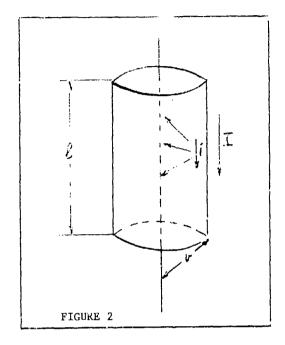
## 2. Influence of the feeder itself :

The level of current downing the inner conductor is also largely dependant of the characteristics of the outer shield.

Indeed, downing the outer conductor, the lightning current induces more or less energy toward the inner, that is dependent of its transfer impedance characteric.

Regarding figure 2, you can write :

$$\mathbf{Z} \mathbf{t} = \frac{1}{\mathcal{L}} \times \frac{\mathbf{v}}{\mathbf{I}}$$



where £ is the length of the sample (meter)
v is the overvoltage (in volts)
for a I (Amps) of lightning downing outside
the outer conductor
Zt is given in ohms/meter

For example, transfer impedance for low frequencies can take a value of  $10^{-3}$  ohms/m for a multi-wire shielded cable, and a value of about  $10^{-4}$  to  $10^{-5}$  ohms/m for a full shielded cable (i.e. cable where external is a copper tube).

But when frequency increases, a multi-wired cable is worst and worst (the wave length is coming smaller and smaller and goes to the distance of the size of the holes), but a full shielded cable becomes better and better (you benefit of skin effect and i becomes << I).

So, you can tell like the choice of antenna the choice of the feeder itself can minimize the level of lightning current on the inner conductor, and be considered as the beginning of lightning protection

#### CHAPTER TWO

PRINCIPLES OF PROTECTION DEVICES FOR FEEDERS

From what has been just written, we can tell that lightning protection of a coaxial feeder consists in minimizing the current level from lightning on the inner conductor.

You can approach that through the choice of antenna type and of coasial feeder. But that generally does not involves to you and of course it is not always sufficient.

You can complete that:

- by increasing the feeder impedance between the antenna and the equipment to be protected,
- by short circuiting the inner conductor with the ground,
- . by realizing a parallel low impedance way for the lightning surge to the ground.

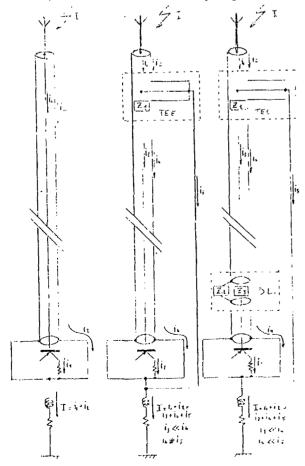
Lightning protection devices we shall now present have the two first characteristics and allow to connect the parallel ground wire of the third.

The figure 3 explains what you get without and with more and more protection:

3A → without protection,

 $3B \rightarrow with a tee,$ 

3C - with a tee and a decoupling line



### CHAPTER THREE

ELECTRICAL CHARACTERISTICS OF H.F. PROTECTION DEVICES'

In order to give a good protection regarding lightning frequencies, such devices must have a great value for the 21 to 23 elements shown on figure 3, but only for those frequencies. Indeed those impedances must be quite small according to antenna frequencies. In addition, the short circuit of the tee (3B and 3C) must be a square wave of antenna frequency.

In theory, that only allows one frequency for the device and we shall have to make it for a larger wideband: both because of stock and applications problems.

Then, the device must be quite transparent on the feeder and so it must have a correct impedance adaptation with the feeder and a small insertion loss.

REMARK: it is of course supposed that the parallel ground wire (is) is itself a low impedance way to ground, and for example that it is straight and build with a good copper wire, the section of which is greater if higher.

When we write (figure 3B) i4 ≠ i5, it is pessimist, in fact, it must be i4 < i5.

#### CHAPTER FOUR

ELEMENTS OF CALCUL OF H.F. PROTECTION DEVICES'

Figures 4 and 5 below show some parameters we can choice when we intent to build such a device.

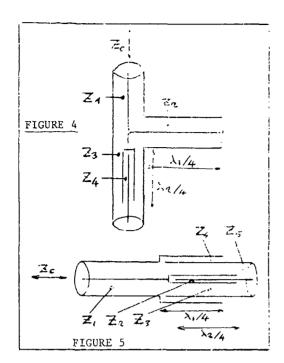
In fact, and considering the mechanical smallnest when frequencies are higher and higher, we don't make or sell tees with a decoupling inner conductor if frequency is higher than 1 GHz (see next table).

But for lower frequencies you can play with 4 different impedances for a te and 5 for a line. And more, according to the classic I.F. video transformers in superheterodyn receivers you are allowed not to chose a  $\lambda$  1/4 equal to  $\lambda$  2/4 and even equal to the  $\lambda$ /4 of the real central frequency of your expected wideband. This is a way to get a wideband device!

Now, we can, on a H.P. calculator, enter only three information which are:

- . line impedance,
- . wideband expected,
- . maximum VSWR,

It will give us all parameters to build the device and even if the demand is realist



In fact, we manufacture three classes of such equipments :

- . if K is smaller than 0,8, we get very performant devices, the VSWR of which is lower than 1,15 (below 1 GHz),
- . if K is between 0,8 and 1,3, we get good devices, with a VSWR lower than 1,30 (below 1 GHz).

For some wideband antennas, we had to developp special devices with a K > 1,50. There the VSWR can be greater that 1,50.

Nota: the end connector is also very important.

#### CHAPTER FIVE

 CATALOGUE DEVICES FOR HIGH FREQUENCIES \* PROTECTION \*

We have now been working in this way since ten years. At the beginning, we only concepted narrowband devices, for example the first which had an up-to-day mechanical design was the 900 ± 40 MHz. Machin-calcul help allows us to-day to get very large band devices.

This can be characterized through the ratio  $\frac{F2-F1}{F0}=K$ , where F2, F1, are the lowest and highest frequency between 25 MHz and 18 000 MHz we can make a device where K is greater than one.

The next table shows some examples of our up-to-day catalogue for the 50  $\Omega$  devices (tees and decoupling)

REMARK: We also have devices for 60 and 75 obms/line

REF. NUMBER	(MHz)	FOR VSWR MAX	VALUE OF K	DECOUPLING OF INN. COND.	α (dB) AT 100 kHz	TYPE OF CONNECTOR
Tee 3928	25 - 125	1,25	1,33	YES	80	N
Tee 3029	50 - 250	1,25	1,33	YES	80	N
Tee 3030	100 - 500	1,25	1,33	YES	80	N
Tee 3445	100 - 500	1,15	1,33	YES	j 80	EIA
Tee 3233	80 - 640	1,50	1,56	YES	80	N
Tee 3190	125 - 1000	1,50	1,56	YES	80	N
Tee 3001	400 900	1,15	0,77	YES	80	N
Tee 3097	400 900	1,18	0,77	YES	80	EIA
Tee 2905	1000 - 4000	1,35	1,20	NO	60	N
Tee 3039	2500 - 7000	1,40	0,94	NO	60	N
Tee 4270	10000 18000	1,50	0,57	NO	60	N
D.L. 3033	25 - 125	1,30	1,33	/	40	N
D.L. 3035	100 - 500	1,30	1,33	/	40	EIA
D.L. 3037	470 - 860	1,15	0,61	/	40	E1A

#### CHAPTER SIX

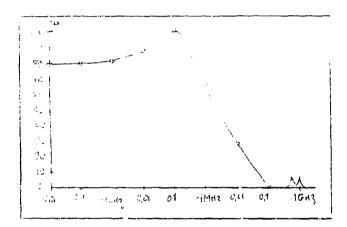
SOME MEASUREMENT RESULTS FOR TEES

We have a large choice to show measurement results of those devices. We decided to show results of a middle-range device, which is one of the more used, because it is the number L 3030 which is used, between 100 and 500 MHz:

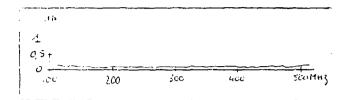
- . for civil VHF aviation (118 136 MHz),
- . for UHF military aviation (220 400 MHz),
- . for O.M. 144 MHz.
- . for 150 and 450 MHz applications,
- . for T.V. (band II and III 175 220 MHz).

Next figures show both attenuation (lightning and antenna frequencies) and VSWR (antenna wideband), and slides show the device itself and you can see on the family slide, on the low-left side, the rapid-froggy pieces to hold such a device on a mast.

REMARK: Note, for highest frequencies, outside the antenna band, some secondaries possibilities of using, in a more narrow band, such a device. They correspond to the other electrical combinations of the  $\lambda$ 1/8,  $\lambda$ 2/8,  $\lambda$ 1/16 and so on...



 $\underline{\text{FIG. 6}}$ : Tee L 3030 - Attenuation between 100 Hz to 1 000 MHz



 $\underline{\text{FIG. 7}}$  : Tee L 3030 - Attenuation in the antenne band

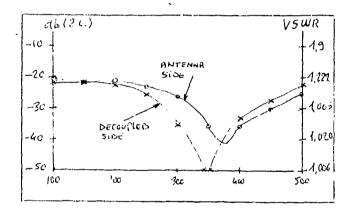


FIG. 8: Tee L 3030 - VSWR in the antenna band

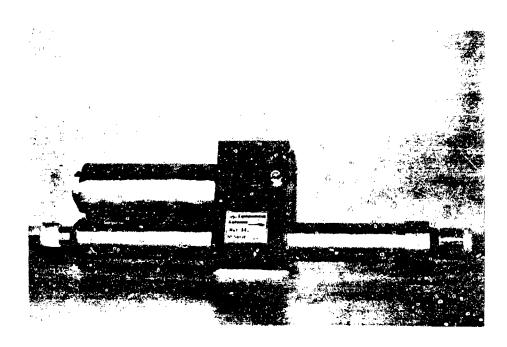
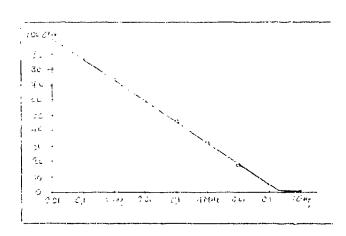


FIGURE 9 - TEE L 3030

#### CHAPTER SEVEN

MEASUREMENT PESULTS FOR DECOUPLING LINF DEVICES:

We chose for example a largely used device in TV - UHF band, largely used for the decoupling of TV retransmiters and for powers lower than 2,5 kW in band TV 1,5 kW in band TV (with EIA-END connectors).



L . '' - Decoupling line L 3037

Whole band attenuation

FIG.

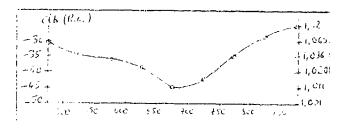


FIG. 11 - Decoupling line L 3037 VSWR in antenna band



FIGURE 12 - DECOUPLING LINE L 3037

#### CHAPTER EIGHT

INSTALLATION OF HIGH FREQUENCY DEVICES ..

Despite those devices don't give special installation problems, we describe below three typical cases which will show for example the advantage of the decoupling line or the recommended situation of the tee.

REMARK: Never forget that those devices only protect the receiver or transmitter and never the antenna itself:
scmetimes you can have an antenna electronic (i.e. antenna preamp.)
which will remain exposed, despite this H.F protection.

<u>First example</u> - antenna over a small size shelter

In this case, you will only put a ter, outside the shelter and connected outside ground reference.

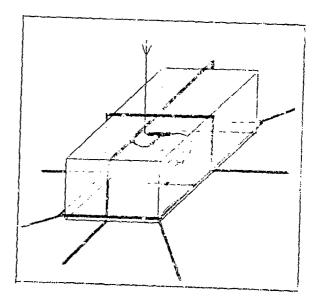


FIGURE 13

Second example - antenna over an high structure

In this case, you can see the great advantage of the insertion of the decoupling line which will make of the feeder the worst way to ground.

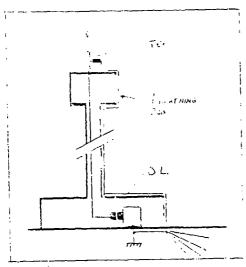
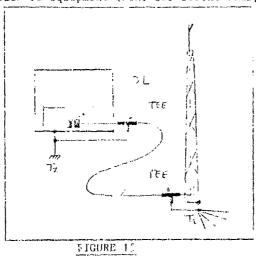


FIGURE 14

Third example - antenna over a separated mast

If equipment is in a shelter far from the mant you have to put:

- . first a tee on the lowest part of the mast, near ground reference,
- eventually a tee outside the shelter, and especially if the distance is great enough not to be allowed to consider ground reference of the mast is the same of the shelter's one,
- , if shelter is large, a decoupling line at the back of equipment (!ike for second example).



#### CONCLUSION

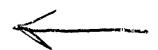
Lightning protection of an high frequency equipment supposes in theory one own reference for antenna, feeder and equipment.

But when we look at that more attentively, we find more efficient solutions, some of them showing the need of a decoupling part (outer and inner conductor of feeder) between feeder and equipment;

in this case, the way from antenna to ground for lightning is no more the equipment itself (hot entry or box).

In order to realize such arrangements, you need both very efficient tees of protection, which will allow to throw to ground inner and outer conductor surges, and decoupling devices, in order to separate feeder potential from equipment.

Such devices are now industrially developped and we can tell with very interesting characteristics, regarding lightning frequencies and quitely no perturbance for the transmitter or receiver equipment.



The state of the s

LIGHTNING TESTS OF AN ELECTRONIC ENGINE CONTROL
WITH ASSOCIATED WIRING
J. Robb, D. Loncrini, H. Ogasian and P. Geren

#### ABSTRACT

Impulse and swept CW Lightning tests have been carried out as part of a developmental program on a new Electronic Engine Control (EEC) for the next generation of transport aircraft. The tests were made using an experimental engine as a test bed, and were carried out with the controller and with a variety of wiring harnesses.

Digital electonic engine controls are generally used on modern high bypass engines which have relatively poor shielding. The controller is mounted on the fan case and because of the requirements for easy maintnance and quick access, only a few attachment points, such as hinges and latches, can be used for the fan cowl. This lack of bonding points greatly reduces its shielding effectiveness.

The tests on the Electonic Engine Control (EEC) included (a) both impulse and swept CW tests with open and short circuit measurements of the induced voltages and currents at the controller to determine the basic coupling parameters, (b) low level tests with dummy loads at the controller to provide estimates of the voltages which would actually be seen at the pins of the EEC as a function of lightning current amplitude and rate of raise and (c) upset and damage tests of an operating EEC. Bulk cable currents and magnetic fields about the engine were also measured for correlation with the cable conductor measurements.

Single and double shielded cables and cables with both pigtail and 360 degree backshell to shield connections were studied. The impulse tests were performed with an impulse generator connected both as a simple capacitor bank and as a high voltage Marx impulse generator. The drive current was a 230-kHz damped sinusoid with currents ranging from 200 to 23,000 amperes crest current.

The basic problem and the solution may be summarized as follows. With the fan cowls which have only a few attachment points, the EEC and the wiring are in effect on the electromagnetic exterior of the aircraft and therefore the extra 25 to 45 db of shielding, which would be provided by the aircraft skin if the wiring were inside the aircraft or were under a peripherally bonded metal engine cowl, must be obtained for the exposed wiring on the engine. This can be done by either using double shielding or by adding peripheral bonding and improved shielding to a composite fan cowl.

# AD P002226

DEVELOPMENT OF A HUMAN ELECTROSTATIC DISCHARGE MODEL IN RELATION TO ELECTRONIC SYSTEMS

William W. Byrne, Senior Research Scientist Southwest Research Institute, San Antonio, Texas

ABSTRACT

Electrostatic Discharge (ESD) in this paper pertains to understanding the processes of electrical charge buildup on a human being or other conductive shape, followed by a discharge into another conductor such as an electronic device. Several megawatts of peak power may be involved.

In order to design and test for ESD, it is necessary to establish the electrical characteristics of the electrostatic buildup and discharge circuit. Crude models of a human being/electronic equipment system for ESD are developed by the author in references (1)\* and (2). This paper further develops the modeling process to include a large metallic ground plane, under the facility floor covering, connected to earth. Also, the effects of hand-held sharp radii metallic objects are examined. From the circuit parameters, approximate wave shapes of the discharge are computed for various cases.

Much work has been done it actual laboratory measurements of electrostatic discharge phenomena, in order to properly design test equipment to simulate an actual discharge as accurately as possible. However, it is believed by the author that mathematical modeling of the system is essential.

\*Numbers in parentheses designate references at end of paper.

ELECTROSTATIC DISCHARGE (ESD) may be considered similar in cause and effects to lightning. The observed arc in the ESD process behaves like a lightning arc. ESD, in this paper, is limited to the buildup and flow, or redistribution, of charge between a human being, an electronic system, a ground plane and earth. Flow of the charges takes place slowly during the charging phase, and very rapidly during the charge redistribution phase. Charges are built up on the person usually as a result of triboelectric action between the shoe soles and the floor covering.

The sudden release of built-up electrostatic energy from high to low potentials in the system causes potentially devastating voltages, currents and electromagnetic fields to occur in vulnerable components in the electronic system. Upon ionization and air dielectric breakdown (arcing), the rapid redistribution currents easily propagate down interconnecting cables and other units before finally bleeding off through the higher RF impedance (inductance) of the ground connection. A person has a strong capability to retain the built-up charge due to his high degree of insulation from the floor covering and earth.

Microcircuits may be destroyed or altered 1 either low voltage, long duration pulses, as in the case of RF interference, or with high voltage, short duration pulses. Typically, in ESD, several thousand volts may be applied to a system housing, resulting in short duration pulses on the order of 100 volts applied to the microcircuits, reference [2]. End item users of these sensitive circuits can be damaged or destroyed, or electronic data may be altered by the unwanted interference. The effects upon a person with various inplanted biomedical devices is as yet unknown.

#### ELECTROSTATIC DISCHARGE MODEL

Figure 1 demonstrates a typical setup for the charge buildup on a person in a room with an electronic system. The person is insulated from the ground plane while the machine is connected to earth through a safety ground. In this model, the earth is relatively far from the person and the machine, while the ground plane is close to the system. Both the person and the machine, for equal shapes, in accordance with our model, have relatively small equal capacitances to earth, but significantly greater capacitance to the ground plane and to each other. The earth is taken as reference potential (0 volt).

For simplicity, the cylinder is used for both the model of the person and the machine. The person's arms are assumed, for capacitance simplification, to be at his sides.

The person is assumed to be fairly large, 113 kilograms (250 pounds), and 1.9 meters (6 ft, 3 in.) in height. Considering that the mass for unit volume of a person is roughly that of water, the resulting volume is 0.1 cubic meters (4 cubic feet). A cylinder of equal size is chosen for the electronic machine. The radius, therefore, of each cylinder is approximately 13.8 centimeters (5.4 in.). The two cylinders are upright and parallel to each other.

In Figure 1, the person on the left is several feet away from the machine. At this distance, the person/machine capacitance is relatively small. The amount of charge that can be accumulated on the body surface is determined by the geometry of the person as related to corona effects, and primarily by the person/ground plane capacitance. The earth is relatively far removed. The model for the case without a ground plane is shown in reference [2].

For examination of the theoretical and actually measured values of voltage that can be sustained on the person's body, see reference [2], and Appendix A of this paper.

The dotted body on the right of Figure 1 is the new position of the person who has approached as near to the machine as possible before arcing occurs and before touching the machine. The person is also capacitively coupled to the grounded machine in a configuration equivalent to a person brushing by the machine with his body. At this point, the person/machine insulation fails by the air dielectric breakdown and arcing occurs, setting up rapid redistribution transient currents in the person and the machine, followed by slower current drain back to earth through the safety ground wire.

The electrostatic portion of the problem to be solved involves determining the total amount of energy that can be built up in the system before discharge. In a system of conductors in space, a matrix (determinants) is used for the number of conductors in the system. The charge on the conductor is proportional to the voltage on the conductor. The proportionality factors are called coefficients of capacitance if the indices are alike, for example,  $C_{1,1}$ , or coefficients of induction if unlike, such as  $C_{1,2}$ .

The equations for the four bodies (person, machine, ground plane, and earth) are as follows:

Person 
$$q_1 = C_{1,1}V_1 + C_{1,2}V_2 + C_{1,3}V_3 + C_{1,4}V_4$$
 (1)

Machine 
$$q_2 = C_{2,1}V_1 + C_{2,2}V_2 + C_{2,3}V_3 + C_{2,4}V_4$$
 (2)

Ground Plane 
$$q_3 = C_{3,1}V_1 + C_{3,2}V_2 + C_{3,3}V_3$$

$$+ C_{14}V_4$$
 (3)

Earth 
$$q_4 = C_{4,1}V_1 + C_{4,2}V_2 + C_{4,3}V_1 + C_{4,4}V_4$$
 (4)

For example,  $C_{1,1}$  is a constant which relates the charge  $q_1$  on body i (person) to the voltage  $V_1$  on body 1.  $C_{1,2}$  relates the charge  $q_1$  on body 1 to the voltage  $V_2$  on body 2 (machine), etc. The q's are solved by employing determinants. Since the machine, ground plane, and earth are all at zero potential before discharge,  $V_2 = V_3 = V_4 = 0$ . Therefore, the equations reduce to:  $q_1 = C_{1,1}V_1$ ,  $q_2 = C_{2,1}V_1$ ,  $q_3 = C_{3,1}V_1$ ,  $q_4 = C_{4,1}V_1$ . The induced charge on the machine is  $q_2$ ,  $q_3$  is the induced charge on the ground plane, and  $q_4$  is the induced charge on the earth resulting from the process of giving up charge to the person and to the machine.  $C_{1,1}$  is the coefficient of expactance of the person,  $V_1$  is the potential of  $V_2$  c person,  $V_3$  is the coefficient of induction between the machine,  $C_{3,1}$  is the coefficient of induction between the

person and the earth, and  $C_{4,1}$  is the coefficient of induction between the person and the ground plane. Simply stated, the net charge on each of the bodies is proportional to the voltage of the person.

The potential on each body of an electrostatic system may be expressed in terms of the charge on each body. The proportionality constants  $P_{1,1}$ ,  $P_{1,2}$ ,  $P_{1,3}$ ,  $P_{1,4}$ , etc., are called the coefficients of potential.

The equations are as follows:

$$V_1 = P_{1,1}q_1 + P_{1,2}q_2 + P_{1,3}q_3 + P_{1,4}q_4$$
 (5)

$$V_2 = P_{2,1}q_1 + P_{2,2}q_2 + P_{2,3}q_3 + P_{2,4}q_4$$
 (6)

$$V_3 = P_{3,1}q_1 + P_{3,2}q_2 + P_{3,3}q_3 + P_{3,4}q_4$$
 (7)

$$V_4 = P_{4,1}q_1 + P_{4,2}q_2 + P_{4,3}q_3 + P_{4,4}q_4$$
 (8)

Since  $V_2 = V_3 = V_4 = 0$ ,  $V_1 = P_{1,1}q_1 + P_{1,2}q_2 + P_{1,3}q_3 + P_{1,4}q_4$ . This says that the potential on the person is related to induced charges on the entire system, as well as to his own charge; for example,  $P_{1,2}$  is the coefficient of potential relating the voltage on body 1 (person) to charge on body 2 (machine), etc. Circuit parameters are developed in later paragraphs.

#### **ESD PHASES**

Three phases of the ESD process are examined: (1) initial charge buildup, (2) induction and (3) discharge.

PHASE 1, INITIAL CHARGE BUILDUP — By walking across a floor, a person can build up very high potentials before corona ionization causes leakage of charge to the atmosphere. For worst case analysis, the user has taken no steps to control factors which lessen the severity of ESD ionization. The carpet is a highly insulating material. Under these conditions, charges can accumulate on the human body to result in voltages in excess of 25,000 volts. The average value of voltage generated is typically 5,000 to 12,000 volts, reference [3]. The magnitude of the voltage depends primarily upon the material of the shoe soles, the type of carpet fiber, type of carpet backing, wear on the carpet, human walking characteristics, the sharpness of radii of various parts of the human body, and the temperature and humidity of the room.

At this remote position, as shown in Figure 1, the person shares the built-up charge with all conductors in contact with him, such as ionized atmospheric particles. Should he stop walking, the voltage drops off at a rate called the relaxation time.

Once a charge is built up on the human body and sustained, all of the free charge on the body resides on its surface. Since the charges are essentially at rest, the electric field for the static condition is perpendicular to the body surface, and for irregularly snaped surfaces, the surface charge density and the electric field intensity vary with the geometry of the surface. For a given electrostatic charge on a body, the charge density is greater for the sharper surfaces. Appendix A (taken from reference [2]) shows why this is true, and how the corona discharge voltage, approximately  $3 \times 10^6$  volts per meter, limits the

amount of voltage that can be sustained on a human body. The technique involves distorting a single charged conductive sphere to two spheres of unequal radii, connected together by a very thin wire. It is shown that corona discharge will occur from a sphere of 1 centimeter radius when the voltage reaches 30,000 volts. The human thumb tip is approximately 1 cm in radius and is fairly well isolated from the rest of the hand so that the electric field is enhanced at the tip. Hence, it is reasonable to expect that levels as high as 30,000 volts may occur, and this level should be used in the worst case ESD modeling process.

Under these conditions, the electrostatic energy may be calculated by applying the relationship  $E_s = 1/2 \text{ CV}^2$  where C is the capacitance of the cylindrical man in relation to the nearby ground plane at his feet.

Reference [4] shows the capacitance of an upright cylinder above a horizontal ground plane to be:

For 
$$\frac{L}{r} \gg 1$$
,  $C = \frac{2\pi\epsilon_0 \ell}{\ln\left[\left(\frac{\ell}{r}\right)\left(\frac{4h+\ell}{4h+3\ell}\right)^{\frac{1}{2}}\right]}$  (9)

C = the capacitance in farads,

r = the radius of the cylinder in meters,

L = the height of the cylinder in meters,

h = the distance from the bottom of the cylinder, to the ground plane in meters, and

 $\epsilon_0$  = the permittivity of free space or air = 8.85 ×  $10^{-12}$  farads per meter.

Applying this formula for the person/ground plane separation distances of 1 centimeter to 1000 meters results in the curve shown in Figure 2. The maximum capacitance for either the cylindrical model person or the machine to the nearby ground plane at a 1-centimeter distance is approximately 51 picofarads. The capacitance reduces to 41 pf at a distance of 100 meters or at remote earth.

The total capacitance of the person to the ground plane and to earth is therefore 51 pf + 41 pf = 92 pf, neglecting the relatively large capacitance  $C_{3,4}$ , between the ground plane and earth. Reference [4] shows the capacitance of a horse above a ground plane to be 180 pf. Reference [5] shows the measured capacitance of a human, 1.75 meters tall, weighing 68 kg, to ground at 60 Hz as 100 pf, and higher values for vehicles such as automobiles, etc.

The maximum electrosic tic energy on the person, at the remote distance from the machine, is therefore 1/2 CV<sup>2</sup> or  $1/2 \times 92 \times 10^{-12} (30 \times 10^3)^2 = 41.4$  millijoules. The maximum charge that can be stored on the person in the remote position is  $Q = CV = 92 \times 10^{-12} \times 30 \times 10^3 = 2.8$  microcoulombs.

PHASE 2, INDUCTION PROCESS — A charged body affects the potentials of all other bodies in its vicinity as shown in Equations (1) thru (4). It shows that the charge on the machine is:  $q_2 = C_{2,1}$ ,  $V_1$ . The capacitance  $(C_{2,1})$   $(C_{1,2})$  between the person and the machine varies as a function of the geometry of the person and the machine, and the distance between them. As the person approaches the machine, the capacitance increases.

However, the capacitance  $C_{1,3}$ , (51 pf) and  $C_{1,4}$ , (41 pf) between the person and the machine to the ground plane and earth, respectively, and the capacitances  $C_{1.4}$ , (51 pf) and C<sub>2,3</sub>, (41 pf) between the machine to the ground plane and to earth, respectively, remain unchanged as the person moves toward the machine. These capacitances result in an additional effective capacitance of 46 picofarads between the person and the machine through the earth and ground plane for the very rapid transient currents. Since the earth and the ground plane are relatively large, their resistances and inductances are ignored in this study for reasons of simplification. In addition, C<sub>3,4</sub>, the relatively large distributed capacitance between the ground plane and earth, will have a tendency to short circuit the very small inductance of the ground plane (see Figure 3 for the equivalent ESD circuit).

Reference [2] shows how the capacitance C<sub>1,2</sub> between the person and the machine is calculated by using two identical cylinders whose axes are parallel to each other. The results of the calculations are shown in Table 1 of reference [2]. We will use the maximum calculated capacitance of 200 picofarads for  $C_{1,2}$ . This results in a total effective capacitance of 246 picofarads between the person and the machine. The machine for this model is grounded to earth, hence  $q_2$ , the charge on the machine, is constantly changing as the charged person approaches. However, the potentials V<sub>2</sub> on the machine and V<sub>3</sub> on the ground plane remain zero. For our model, it is assumed that triboelectric charging will continue until arc discharge takes place. In other words, the 30 kV is maintained on the person. This will cause the effective person-/machine capacitance (246 pf) to be charged to its maximum of C = CV = 7.4 microcoulombs, with an electrostatic energy of 1/2 CV<sup>2</sup> = 111 millijoules. This compares to 89.9 millijoules without the ground plane.

For this model, with about a 1-centimeter gap between the person's body or his fingertip and the machine, discharge will take place for the 30 kV on the person. The electric field of corona discharge, or when the air ionization process takes place, is  $3 \times 10^6$  volts per meter. At this point, the maximum surface charge density on the person and the machine is  $\rho_1 = \epsilon_0$   $E = 2.66 \times 10^{-6}$  coulomb/meter<sup>2</sup>, where  $\epsilon_0$  is the permittivity of free space (or air), or  $8.85 \times 10^{-12}$  farads per meter, and E is the electric field, or  $3 \times 10^6$  volts per meter. A very large ground plane under the system may completely shield the system from the earth, hence the capacitances  $C^{1.4}$  and  $C^{2.4}$  may vanish.

If a positive charge is assumed to accumulate on the person at the remote position, the charge will tend to be packed or concentrated in the region of the bottom of the feet, especially if a ground plane is used. As the person approaches the machine, the charge will have a tendency to be stored predominantly on the surfaces of the person

and the machine which are mutually facing each other. This means that some charges are going to travel much farther than others when arcing occurs.

Reference [1] shows that if the person is positioned at about 15.3 cm (6 in.) away from the machine with his hands at his sides, the mutual capacitance  $C_{1,2}$  is reduced to 48 picofarads. However, the effective capacitance between the two bodies, for determining the electrostatic energy in the system, and the total discharge circuit impedance is 48 pf + 46 pf (the capacitance between the person and the machine through the ground plane and earth) = 94 pf. If a person is positioned away from the machine but reaches out with his hand to touch the machine, the capacitance between his arm, hand, and finger to the machine would also be considered. We are now ready to consider Phase 3, or electrostatic discharge of the stored electrostatic energy.

PHASE 3, ELECTROSTATIC DISCHARGE — Everyone has emperienced the very unpleasant sensation of ESD shock. We would like to know just how severe the energy density really is in order to design electronic equipment to withstand the shock and also protect the person from potential harm. The most usual discharge into an electronic device is that of a human being, however, other bodies may be much more severe from the standpoint of discharged power, such as a charged metallic cart, chair or table pushed against an electronic device. Not only will the capacitance be significant, but the resistance of the discharge path will be lower than through a human body.

The pulse shapes upon discharge have been characterized by W. Michael King and David Reynolds for various human and hardware models in reference [6]. The study includes measurements of the waveforms of discharges to simulated electronic systems through mobile office furnishings and hand-held metallic objects. From this paper, it is clear that the waveform rise times and the discharge current levels vary greatly, depending upon the setup used in the testing. We now proceed to characterize the discharge circuit parameters and wave shapes.

Figure 1 shows the position of the person with respect to the machine at the moment of arcing. The worst case situation would be a person brushing against the machine. A very large electric field between the two bodies causes the air in the gap to ionize, thus drastically reducing the insulation resistance between them at the point of the arc. This essentially causes the virtual short circuit through the arc. The equivalent circuit is shown in Figure 3. Electrons in the machine are drawn with a strong force of attraction by the electric field toward the positive charges on the person, hence, the large electrostatic energy stored in the person/machine capacitor is suddenly dissipated in the circuit with the current flow in the form of an arc. It is this initial rapid redistribution of charge which is of the most interest because of the severity of the conducted power between the two conductive objects. The arc continues until the voltage across the person/machine capacitor reaches a sufficiently low level to quench itself through the arc. The current during this rapid equalization phase is governed by the R, L, C of the conduction path. The resistance and inductance are derived primarily from the high-frequency characteristics of the person's body and the machine. During the initial charge redistribution, the bulk of the current is flowing from the person to the machine. Before arcing, all of the available free charge resides on the person's skin. The general circuit parameters are shown in Figure 3.

The inductance of the green wire to earth impedes the higher-frequency components of the current, hence, these currents flow in a common mode manner into the low-impedance structure. A slower discharge to earth through the safety wire takes place for the lower-frequency components of the spectrum. At arcing, the distribution current flows as a pulse having a very fast wave front or rise time.

The discharge phase is seen as three subphases: (1) the very fast charge redistribution between the person and the machine through a relatively low-impedance path, (2) a high-frequency coupling between the remaining person/machine capacitance to earth and the ground plane, and (3) the much slower bleed-off of the built-up net charge of the system to earth.

In order to create a circuit schematic for determining the wave shapes, we must determine the electrical characteristics of the person and the machine. The following discussion of the human body is taken generally from reference [2].

The electrical impedance of the human body is very complex, as man is composed of materials of varying resistivity, such as tissue, supporting structure, and outer covering. Within the body, inside the outer covering, resistivities vary from approximately 100 ohm cm (1 ohmmeter), for most vascular tissue, up to 900 ohm cm for bone, and as great as 5000 ohm cm for fatty tissue. The live body, because of the effect of saline liquids, can be viewed, for very low-frequency considerations, to be a uniform mass with an approximate resistivity of 100 ohm cm and a dielectric constant no greater than unity [7]. The dielectric constant changes greatly at higher frequencies.

In vivo (living body) experiments performed upon cats by Maria Stuchly, et.id. [8] show that the value of approximately 1 ohmmeter resistivity, taken on the average of organic tissue, is satisfactory at 1 to 2 GHz. From the foregoing, we will use a value of resistivity of 1 ohmmeter. The dielectric constants at 1 GHz varied over the range of 43 for kidney to as high as 59 for skeletal muscle. [8]

The effect of the permittivity or dielectric constant of the body upon the current is not considered in this paper. It is a subject of further investigation.

The model of the main frame of the body for the purpose of capacitance calculation is shown under "Electrostatic Discharge Model." The capacitance was estimated under "Phase 1, Initial Charge Buildup" and is summarized for various conditions in Table 1. Figure 4 shows the possible current flow routes in parts of the human body for two conditions of discharge: (1) midsection body discharge, and (2) discharge through the finger. The shape of the body suggests the cylinder as a basic building block for the parts of the body through which current may flow.

For the discharge electrical impedance, we now determine the estimated resistance and inductance of the parts of the body most likely to influence the discharge current. These are the main frame, the arm and the finger, all modeled as cylinders.

In order to determine the impedance of the human body we must determine the "skin depth," or limit of depth within the body tissue through which current can flow. Because of the fast rise times involved, some in the order of a few nanoseconds, we must consider the frequency for the ESD currents to be as high as 1 to 2 GHz. Some rise times as fast as 500 ps have been observed. The frequency is needed to determine the skin depth for the currents in the body. Rutherford Peck [9] shows the skin depth in meters for a conducting media to be S =  $\sqrt{2/\mu g\omega}$  where  $\mu$  is the permeability or  $4\pi \times 10^{-7}$  H/m, or the same as free space; g is the conductivity in mhos per meter, and  $\omega$ , the angular velocity =  $2\pi f$ . For 1 ohmmeter resistivity, this results in 1.12 × 10<sup>-2</sup> meters at 2 GHz, and  $1.59 \times 10^{-2}$  meters at 1 GHz. We will use 1 cm since the faster rise time of 500 ps has been observed.

The resistance and the inductance of the human body main frame depend upon the point of discharge as suggested by Figure 4. The body is modeled as a hollow cylinder with a shell thickness of 1 centimeter, as shown in Figure 5 for the finger or arm discharge. The cylinder is divided into two half shells because the current, in this case, will have the tendency to take parallel paths around each side of the body while traveling from the feet to the shoulder, arm and fingertip. Refer to the specific discharge, Cases 1 through 6, for determining the discharge path and resulting conditions, series or parallel arrangements, for resistance and inductance calculations.

In the case of a human midsection discharge, the model is shown in Figure 6. Here, the current has generally four parallel current paths; from the head downward to the midsection, from the feet upward to the midsection, and around each half perimeter of the body. Hence, 4 half shells, each 1 cm thick, are used.

For the model of the human arm, refer to Figure 7. The resistance is determined by calculating the resistance of a hollow cylinder where the thickness of the shell is 1 centimeter (the skin depth).

For the model of the human finger, refer to Figure 8. The resistance is determined by calculating the resistance of a solid cylinder, since doubling the skin depth exceeds the diameter of the finger. The skin depth is 1 centimeter. The resitance of the components may be calculated by  $R = \rho(\ell/A)$ , where R is the resistance in ohms,  $\rho$  is the volume resitivity (1 ohmmeter),  $\ell$  is the length of the component in meters and A is the cross-sectional area in (meters). [10]

The resistance of the finger was determined by considering the resistance of the finger bone in parallel with the more conductive outer sheath of the finger, taken as 1/8 in thick.

The outer skin layer, the epidermis, has a resistivity of up to 106 ohm cm and may be taken as about 1 mm thick. [7] For this reason, it will be considered a thin layer of insulation carrying relatively little current.

An area of uncertainty lies in the effect of the relatively high resistive epidermis portion of the skin. Just

before discharge, the free charge resides on the surface and the electric field is perpendicular to the skir. At discharge, the current takes the path of least relistance, which is below the skin in the region of the saline structure. The skin is only 1 mm thick, hence the charge would be influenced by the skin for only a very short portion of the rise time, considering the length of the discharge path for each charge. If the skin resistance effect were continuous, the resistance of the skin over the body surface would be  $R = \rho(\ell/A) = 55.7$  ohms, where  $\rho$  is the resistivity of the skin or  $10^4$  ohmmeter,  $\ell$  is the skin thickness or 1 mm, and A is the surface area of the body or  $1.8 \times 10^{-1}$  m<sup>2</sup> for a cylinder. It appears, therefore, that the skin acts only as a delaying factor, and not as a continuous circuit resistance during the discharge process.

The self inductance is determined by considering each component as a cylindrical conductor. Terman [10] shows the inductance of straight round wires for intermediate frequencies as  $L = 0.00508\ell$  (2.303  $\log_{10} (4\ell/d) - 1 + \mu \delta$ ) microhenries, where  $\ell$  is the length in inches, d is the diameter in inches,  $\mu$  is the permeability, and  $\delta$  is a skin depth factor, which, for higher frequencies, is inversely proportional to the square root of frequency, and for very high frequencies approaches zero. Hence, the term  $\mu \delta$  will be taken as zero, since the frequency (2 GHz) is very high. Terman states that "the changes of inductance with frequency are comparatively small." [10] Therefore, the value of inductance used is:

$$0.00508\ell \left( 2.303 \log_{10} \frac{4\ell}{d} - 1 \right) \tag{10}$$

H.C. Barnes, et al. [7] arrived at values of 0.1 microhenry for inductance and 1 ohmmeter resistivity for the human body, modeled as a prolate spheroid, at 60 Hz. These compare favorably with our values. Ronald J. Spiegel [11], uses various cylinders for parts of the human body in his work relating to current induced into the body for high voltage power lines.

In this paper, there are 6 specific conditions taken for discharge. (The case of a metallic intervening object, e.g., a person seated in a metal chair or pushing a metal cart of some configuration are not included in this paper.) The values of resistance, inductance, and capacitance for each case are shown in Table 1. The cases are as follows:

Case 1. A charged person with 30 kV on his body approaches a large, low-resistive machine such as in Figure 1, with his arms close by his body, and he brushes up against the machine (see Figure 10 for the wave forms).

Case 2. This case is similar to Case 1, which is for a person approaching within a very close distance from the machine, e.g., 1 cm, (0.4 in.) allowing the full capacitance development between the person and the machine. The difference is that he touches the machine with his finger instead of brushing by it (see Figure 11).

Case 3. This is the same as for Case 2, except the person is about 15.3 cm (6 in.) away from the machine when he reaches out to touch it with his finger (see Figure 12)

Case 4. This is the same as Case 3, except the machine has a high resistance, chosen as 10<sup>6</sup> ohms (see Figure 13).

Case 5. In this case, a person standing 15.3 cm (6 in.) from a low-impedance machine is holding a sharp object such as a key with a radius of 1 millimeter. His body has only 3 kV on it. He then reaches out to touch the machine with his finger (see Figure 14).

Case 6. This is a rerun of Case 4 in reference [2] for the condition of no ground plane, but including the capacitance from the person to the machine through earth (see Figure 15 for the wave forms).

The resistance of the machine was chosen as the relatively low value of 1 ohm for a metal chassis, or  $10^6$  ohms for an insulated chassis. The inductance of the machine is taken to be the same as the human main frame, both modeled as cylinders. For calculating the predicted wave form, the simplified circuit is shown in Figure 9. The charged capacitance serves as the voltage source. With the current flowing upon arcing,  $R_T$  and  $L_T$  are the total circuit resistance and inductance, respectively, and C is the capacitance.

In the simplified schematic for the series circuit, the capacitor is the storage element for the initial voltage  $V_0$ . When the circuit is completed by closing the switch (low resistance arc), the Kirchhoff voltage law may be used to set up the differential equation:

$$L \frac{d^2i}{dt^2} + R \frac{di}{dt} + \frac{1}{C} i = 0,$$
 (11)

where i is the instantaneous current.

The solution of this equation and discussion of the factors controlling the wave shape are shown in Reference [2]. The voltage, current and time curves are shown in Figures 10 through 15 for the six cases. These curves were obtained by using an HP 21 MX Minicomputer and an HP 9872A Plotter. Conditions described in the six cases determine whether the curves are overdamped, or underdamped. Case 1 is an example of an underdamped case due primarily to the low value of resistance R in the system. The wave snapes are shown in Figure 10. This shows a rise time of about 6 ns for the "brush by" or midsection discharge case. Case 2 is an example of an overdamped case due to the higher resistance of the finger and the are, as compared to the body.

Recommendations for designing and testing electronic equipment to meet the conditions of ESD are shown in reference [2].

### CONCLUSIONS

The results show that Case 1 for the midsection discharge is far more severe than the others from the stand-point of electrical power to be absorbed by the system. The current approaches 589 amps. This represents a peak power of  $589^2 \times 11.3$  ohm = 3.9 megawatts. The peak power released for, e.g., Case 3 is  $27^2 \times 1083$  ohm = 0.79 megawatts.

The use of the ground plane increases the peak current for Case 1 from 573 amps to 589 amps, as shown in

Figure 10. Hence, it appears that the insertion of the ground plane does not appreciably increase the current and power in the case of a human discharge into a large machine. This is because of the relatively higher capacitance between a person and the large machine, as compared to the capacitance between either the person or the machine to the ground plane.

The current wave form shown in Figure 14 shows that if a person is carrying a sharp object such as a key and discharging with either the key or a finger, the worst case peak power to be absorbed by the system is reduced to  $(2.7)^2 \times 1083 = 7895$  watts. Discharge through a sharp object is also much less uncomfortable than through the nerve sensitive finger tip. It is believed by the author that an arc discharge from the body actually burns a small hole through the skin due to the very great current density.

It is apparent that ESD poses a threat to all sensitive electronic equipment, whether enclosed in an electronic machine or present in the human body in the form of biomedical implants. Fortunately, the threat may be greatly reduced through analysis, design and test of systems.

#### REFERENCES

- 1. William W. Byrne, "Development of an Electrostatic Discharge Model for Electronic Systems." IEEE International Symposium on Electromagnetic Compatibility, September 8-10, 1982, Santa Clara, California
- 2. William W. Byrne, "Development of Design and Fest Procedures to Meet Electrostatic Discharge (ESD)." MIDCON 82, Nov. 30, 1982, Dallas Texas, Professional Program Session Record 28, p. 28/4.
- 3. Edward Nakauchi, "Static Discharge Problems on Data Processing Equipment." 1975 IEEE Electromagnetic Compatibility Symposium Record, San Antonio, Texas, October, 1975.
- 4. Reilly, J. Patrick, "Electric Field Induction on Sailboats and Vertical Poles." IEEE Transactions on Power Apparatus and Systems, Vol PAAS97, No. 4, July/August 1978.
- 5. O.P. Gandi and I. Chatterjee, "Radio Frequency Hazards in the VLF to MF Band." Proceedings of the IEEE, Vol. 70, No. 12, December, 1982.
- 6. W. Michael King and David Reynolds, "Personnel Electrostatic Discharge: Impulse Waveforms Resulting from ESD of Humans Through Metallic-Mobile Furnishings Intervening in the Discharge Path." 1982 IEEE International Symposium on EMC, September 8-10, 1982, p. 212.
- 7. H.C. Barnes, A.J. M Elroy and J.H. Charkow, "Rational Analysis of Electric Fields in Live Line Working." IEEE Transactions on Power Apparatus and Systems, Vol. PAS-86, No. 4, April 1967.
- 8. Maria Stuchly, T. Whit Athey, Stanislaw S. Stuchly, George M. Samaras and Glen Taylor, "Dielectric Properties of Animal Tissues in Vivo at Frequencies 10 MHz-1 GHz." Journal of the Bioelectromagnetics Society, Volume 2, Number 2, 1981, Alan R. Liss, Inc., New York.

- 9. Edson Ruther Peck, "Electricity and Magnetism." New York: McGraw-Hill Book Co., Inc., 1963.
- 10.Frederick E. Terman, ScD. "Radio Engeineers Handbook." 1st Edition, New York: McGraw-Hill Book Co., Inc., 1943.
- 11. Ronald J. Spiegel, "High Voltage Electric Field Coupling to Humans Using Moment Method Techniques." IEEE Transactions on Biomedical Engineering, Vol. BME-24, No. 5, September 1977.

# APPENDIX A — POTENTIAL AND CHARGE ON A NONUNIFORMLY SHAPED BODY

The field strength at the surface of a charged conductor is geometry dependent. Figure 16 shows a charged body on the left with a nonuniform surface such as would be the case of a person with an appendage of relatively sharper radius, such as a finger, or if he were holding a metallic object such as a kev. Charge is free to migrate from point to point on the surface. The surface is equipotential in the static case; however, the electric field and surface charge density will be more intense at the sharper radii. It will be shown that the upper limit of voltage that can be sustained on the human body is approximately 30 kV based upon the radius of, e.g., an icolated fingertip which forms a hemisphere with a radius of roughly 1 cm.

The body on the left may be simplified by compressing the neck of the appendage to a short, very small diameter conductive wire connecting two conducting spheres of unequal radii of a and b, respectively.

Since the wire length is held to a small length equal to the approximate length of the neck, the potential of the system will not be appreciably changed. In other words, negligible work is expended in the charge redistribution process. The two spheres are at the same potential  $V + V_a = V_b$ . The potential on the surface of an isolated sphere is

$$V = \frac{Q}{4\pi\epsilon_0 \text{ radius}}$$

where Q is the charge on the sphere [9] and  $\epsilon_0$  is the permittivity of free space (or air). The total charge on the wire is held negligible since it is relatively small. Also, the spheres are assumed to have a negligible effect on each other since sphere radius a is much larger than sphere radius v. It follows that:

$$\frac{Q_a}{4\pi\epsilon_0 a} = \frac{Q_b}{4\pi\epsilon_0 b}$$

Since radius a is much larger than radius b,  $Q_a$  is much greater than  $Q_b$ . The electric field at the surface of the sphere

$$E = \frac{Q}{4\pi\epsilon_0 r^2} = \frac{\sigma}{\epsilon_0}$$

is derived from the Gauss law of electrostatics.  $\sigma$  is the surface charge density. It follows that:

$$E_a = \frac{Q_a}{4\pi\epsilon_0 a^2} = \frac{\sigma_a}{\epsilon_0}$$

$$E_b = \frac{Q_b}{4\pi\epsilon_0 b^2} = \frac{\sigma_b}{\epsilon_0}$$

Since E = V/r for a sphere,

$$\frac{V_a}{a} = \frac{\sigma_a}{\epsilon_0} \frac{V_b}{b} = \frac{\sigma_b}{\epsilon_0}$$

ог

$$V_a = \frac{\sigma_a a}{\epsilon_0} = V_b = \frac{\sigma_b b}{\epsilon_0}$$

Since a is much larger than b,  $\sigma_b$ , the surface charge density on the smaller sphere b, is much larger than that on the larger sphere a. From the rationship  $E = \sigma/\epsilon_0$ , it follows that the electric field is much greater at the surface of the smaller sphere than that at the larger sphere and is inversely proportional to the radius.

From the foregoing, assuming a radius of a typical fairly uniform appendage such as a fingertip of approximately 1 cm, and considering the Corona breakdown of the electric field  $E = 3 \times 10^6 \text{ V/m}$ , V = Er = 30 kV. If the body of the cylindrical model had no sharp radii appendages, a much higher voltage could be maintained on the body. This shows the importance of the natural body appendage or added conductor to the body such as, e.g., a handheld object. If the object were, e.g., a key with a radius of 1 mm, the highest voltage that could be maintained would be 3 kV. Hence, it appears reasonable that the highest voltage to use for the model is approximately 30 kV.

Fable 1
Discharge Circuit Characteristics

# Resistance—Ohms (1 Ohm Resistivity et 2 GHz)

Inductance—Microhenries at 2 GHz

Case	Voltage kV	Body	Arm	Finger	Machine	Total Circuit	Body	Arm	Finger	Machine	Total Circuit	Capacitance Picofarads
1	30	11.3		-	2	12.3	0 16			0.16	0.32	246
2	30	22.7	211.7	848	1	1083	0.89	0.27	0.054	0.16	1.37	246
3	30	22.7	211.7	848	1	1083	0.89	0.27	0.054	0.16	1.37	94
4	30	22.7	211.7	848	106	1C6	0.89	0.27	0.054	0.16	1.37	94
5	3	22.7	211.7	848	{	1083	0.89	0.27	0.054	0.16	1.37	94
6*	30	22.7	211.7	848	1	1083	0.89	0.27	0.054	0.16	1.37	69

<sup>&</sup>quot;This is a rerun of Case 4 in reference [2] for the condition of no ground plane, but including the capacitance from the person to the machine through earth.

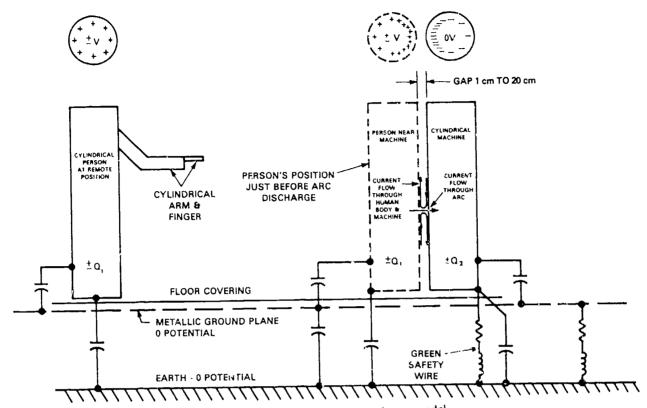


Fig. 1 - Electrostatic buildup and discharge model

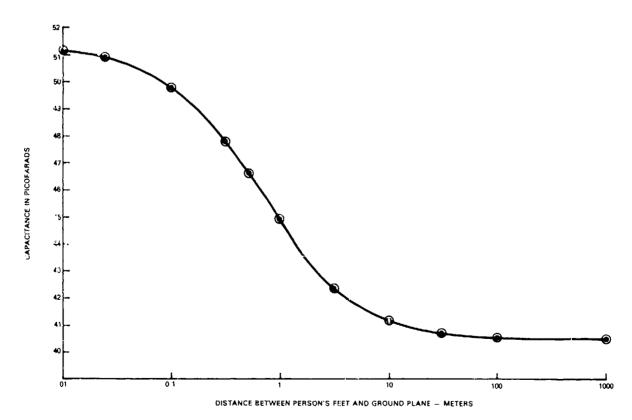


Fig. 2 - Capacitance between simulated person and ground plane

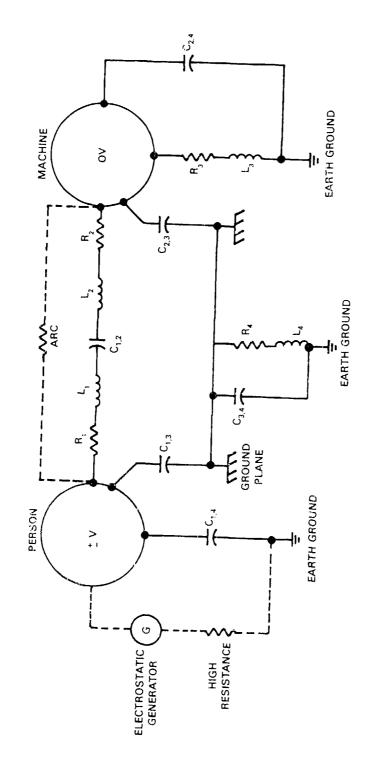


Fig. 3 - Equivalent ESD circuit

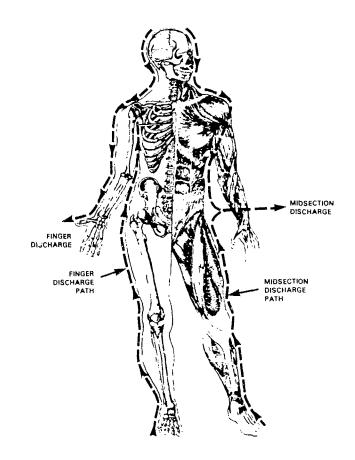


Fig. 4 - ESD current flow through a human body

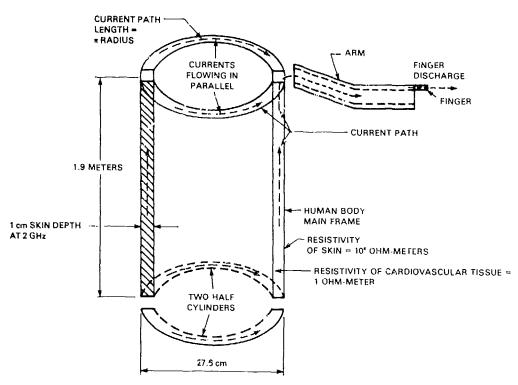


Fig. 5 - Cylindrical model of human body for finger or arm discharge

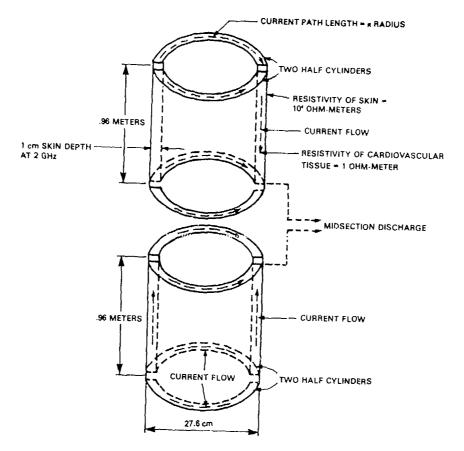


Fig. 6 - Cylindrical model of human body for midsection discharge

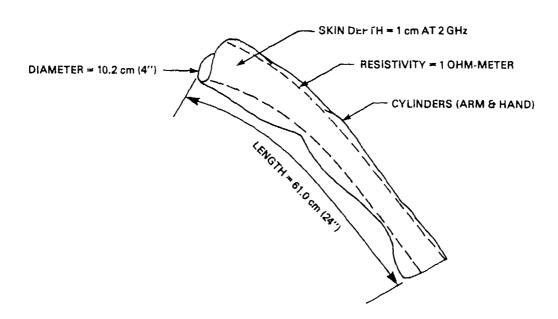


Fig. 7 - Model of human arm

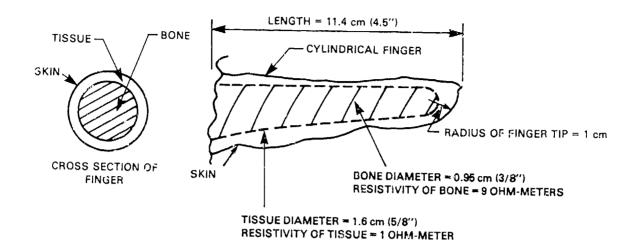


Fig. 8 - Model of human finger

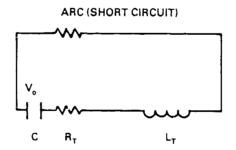
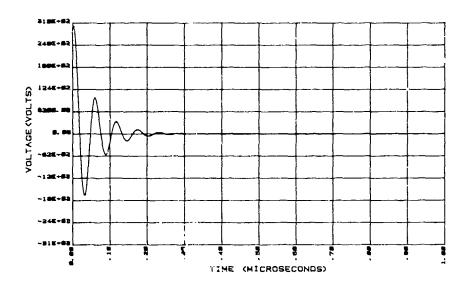


Fig. 9 - Simplified circuit schematic

# VOLTAGE VS. TIME



# CURRENT VS. TIME

(a)

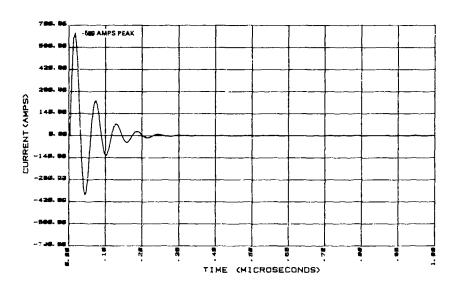
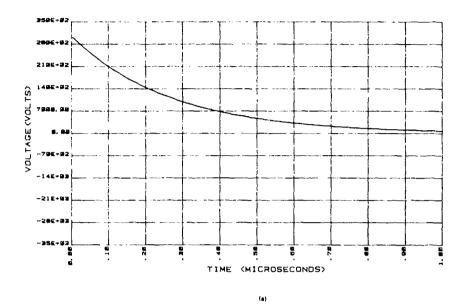


Fig. 10 - Case 1 — "brush by" — underdamped —low-impedance machine

# VOLTAGE VS. TIME



### CURRENT VS. TIME

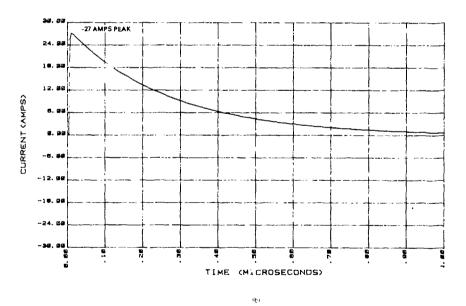
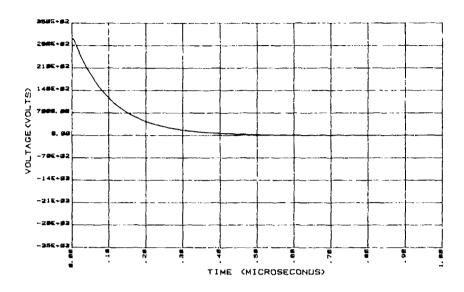


Fig. 11 - Case 2 — contact with finger — person close to low-impedance machine

### VOLTAGE VS. TIME



# CURRENT VS. TIME

(a)

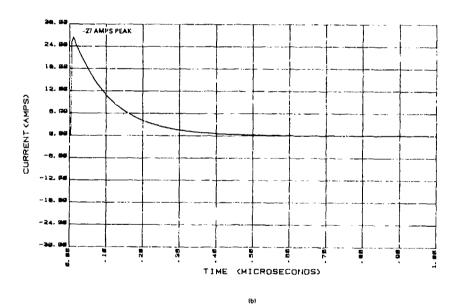
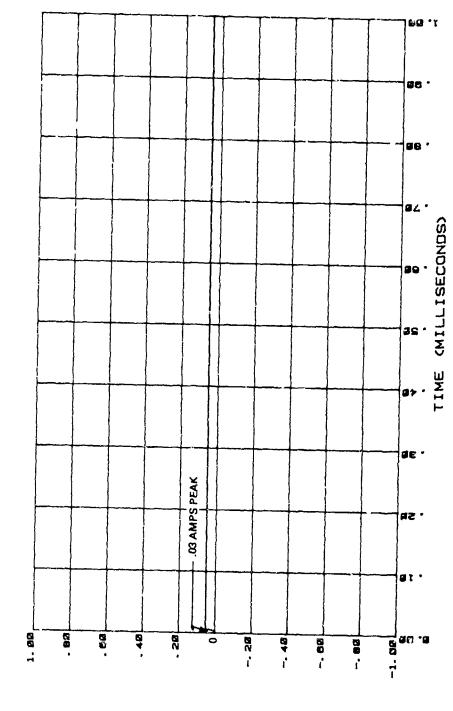


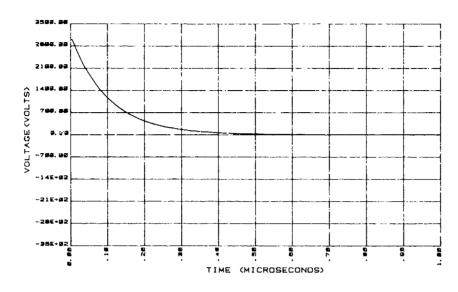
Fig. 12 - Case 3 — contact with finger — person standing away from low-impedance machine



CURRENT VS.

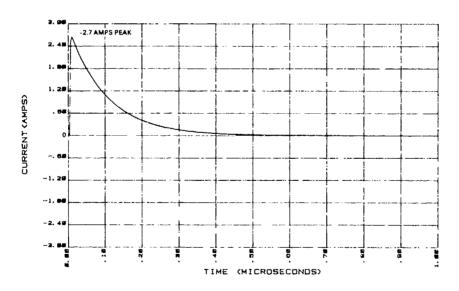
Fig. 13 - Case 4 — person standing away from nighimpedance machine

## VOLTAGE VS. TIME



(a)

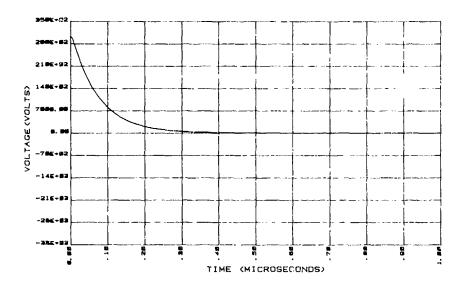
# CURRENT VS. TIME



(b)

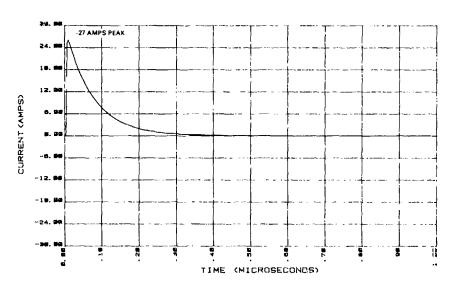
Fig. 14 - Case 5 — contact with finger — person standing away from low-impedance machine — 3kV

## VOLTAGE VS. TIME



## CURRENT VS. TIME

(a)



(6)

Fig. 15 - Case 6 — contact with finger — person standing away from low-impedance machine — no ground plane

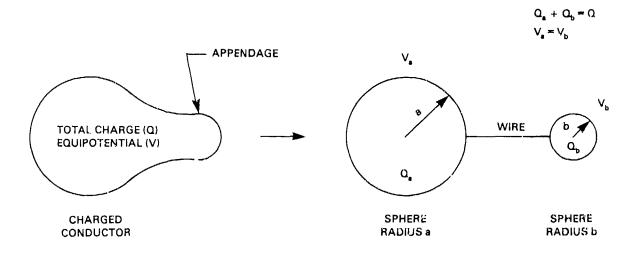


Fig. 16 - Potential and charge on nonuniformly shaped body



# FAST FIELD CHANGES PRODUCED BY POSITIVE GROUND STROKES

AD P002227



Masaru Ishii, Junichi Hojo and Tatsuo Kawamura

Institute of Industrial Science, University of Tokyo 22-1, Roppongi 7 Chome, Minato-ku, Tokyo

Kazuo Fujikake

Tohoku Electric Power Co. Inc. 7-2, Nakayama, Sendai

### ABSTRACT

Fast electric and magnetic field changes produced by positive ground strokes in Japan were recorded with the output of a slow antenna. High rate of positive ground flashes was recorded not only in winter but also in spring, and the fraction of positive ground flashes in a storm was known to correlate with the radar echo top instead of the vertical wind shear. The characteristics of the wave shape of the fast field changes of a positive ground flash and the difference from that of a negative ground stroke is stated, and the possible causes are discussed.

POSITIVE GROUND FLASHES that lower positive charge to the ground have drawn attention in recent years. They are few in summer, but it is known that about half of the ground flashes are positive for Japanese winter thunderstorms, and they are also not rare for thunderstorms in cold regions even in summer (1)\*. It is natural that lightning parameters of those positive flashes may be different from those of negative flashes, and it is necessary to know about them for lightning protection or warning in areas where positive flashes frequently occur.

In Japan, lightning current is observed at tall structures in winter thunderstorm areas (2); however, almost all those ground flashes that strike such tall structures in winter are believed upward flashes, and their lightning parameters must be different from downward flashes. The authors have observed fast electric and magnetic field changes produced by lightning flashes together with slow electric field changes. The aim is to know parameters of positive downward flashes, believed to be the majority of the positive flashes, details of

\*Numbers in parentheses designate References at end of paper.

which have not yet been reported. The result of the observation of positive flashes in all seasons in Japan, comparing them with fast field changes of negative flashes, is reported, and a possible cause of the difference in field changes between positive and negative flashes is discussed.

### MEASUREMENT

Electric field was measured by a slow antenna and a fast antenna having time constants of 4.2 s and 5 ms respectively. Each antenna was a hemisphere with the diameter of 27 cm and was lifted about 1.5 m from the ground. They were calibrated using a VLF broadcasting signal The highest frequency recorded by the (3). fast antenna system was 1 MHz. Fast magnetic field change was measured by a crossed-loop antenna comprised by coaxial cable with an active integrater (4) having the time constant The step response of this system was of 1 ms. measured by injecting rectangular current into a nearby wire loop as seen in Fig. 1. above trace is the waveshape of the injected current and the bottom is the output of the integrater showing rise time of 0.3  $\mu s$  which means that the measurable highest frequency was about 1 MHz.

Fast field change signals were digitized every 0.2 µs with the resolution of 8 bits and the length of 2 KW, and was recorded by a floppy The system was triggered by the magnetic field changes, so usually the field change caused by a first stroke was recorded. the end of 1982, the resolution was improved to 10 bits and up to 7 electric field changes of subsequent strokes were made possible to record. Slow electric field changes and the trigger signal of the fast field system were recorded by an analog data recorder with the frequency range from DC to 2 kHz. The distance between the recording site and the lightning flash was estimated from the wave shape of field changes, direction and the radar echo.

It was reported that there exist fast components with rise times of less than 0.1 µs in the field changes produced by lightning (5), and such very fast field changes could not be

recorded in our measuring system. Fig. 2(a) is electric field change for a first negative return stroke at the distance of about 15 km, and Fig. 2(b) is the one at about 50 km, both recorded at Tokyo propagating over land. Little difference is seen in the high frequency component of these figures, and it is also clear that the waveshapes were not affected by the response of the recording system. Thus it is known that in the waveshapes propagated more than about 15 km over land, high frequency component higher than 0.5 MHz is almost lost, and lower frequency is hardly attenuated up to about the distance of 50 km in Tokyo area. This is the same tendency as the observation at Florida (6). From this result, the discussion on the fine structure of field changes in this paper was decided to be based on the data of ground flashes at the distance of about 15 to 60 km. In Niigata area, high frequency component was more attenuated for some field changes propagated about 50 km over mountainous region, which were eliminated from our statistics of leader activity.

## RATIO OF POSITIVE GROUND FLASHES

Numbers of clearly recorded flashes in each season at Niigata and Tokyo are shown in Table 1. Few negative ground flashes were recorded at Niigata in winter, and the majority was also positive in spring at Tokyo. On the contrary, almost all ground flashes in August were negative at Tokyo. Among about 1000 clear records of ground flashes from winter to summer, 25% were positive. Most of the thunderstorms in winter and spring were frontal.

The unusual high rate of positive ground flashes was reported for Japanese winter and Swedish summer thunderstorms (7), and it was proposed that this was caused by strong vertical wind shear making the dipole in the thundercloud tilt (1). Another type, denoted 'second type' here, of the source of positive flashes is the

decaying stage of severe thunderstorms (8)(9). The positive flashes observed by the authors in winter and spring are believed to belong to the first type, and those observed in August are believed second type, as the ratio of positive flashes to the total is 3.6% and they did not occur randomely but in groups.

To check the hypothesis of the tilted dipole, the correlation between the wind shear and the rate of positive flashes was examined for thunderstorms from May to July in Tokyo area. The wind shear was based on the data available twice a day from the meteorological observatory, and was defined here as the difference of the wind speed at the cloud base and the altitude of the radar echo top normalized by the distance between these two altitudes. The result is shown in Fig. 3 which shows poor correlation with the correlation coefficient of 0.33. The dotted line in Fig. 3 is the regression line adopted from ref. (1).

It was common in the thunderstorms of the first type that the temperature at the ground was relatively low, resulting the altitudes of the freezing level were also low. same thunderstorms of Fig. 3, correlation between the radar echo top and the rate of positive flashes was examined and the result is shown in Fig. 4. Strong negative correlation exists, and it is known that the rate of positive flashes reduced with increasing height of the radar echo top. The correlation coefficient was -0.76. This suggests that the low altitude of the positive charge center is significant for the occurrence of the high rate of positive flashes, which seems also true for the second type thunder clouds.

In Table 2 are shown parameters for several thunderstorms from May to July in Tokyo area. Distinct changes in the ratio of positive flashes to the total are seen from storm to storm. The freezing level itself does not show correlation with this ratio.

Table 1 - Numbers of Recorded Flashes

Period	Ground +	Flashes -	Cloud Flashes	Unidentified	Total
Dec.'81-Mar.'82	42	1	32	2	77
Dec.'82-Feb.'83	89	24	55	7	175
May '82	33	3	5	3	44
June '82	13	75	2.7	17	132
July '82	58	196	42	8	304
Aug. '82	1.7	453	4	1	475

Table 2 - Parameters of Thunderstorms in Tokyo Area (1982)

	ers of ash	Wind Shear (m/s/km)	Maximum Radar Echo Top (km)	0°C Isotherm (km)
30				
30	2	4.7	6.5	3.4
0	34	1.2	12.0	3.5
5	19	1.2	9.0	4.0
13	2	1.5	8.0	4.4
2	88	2.6	12.0	4.4

## FINE STRUCTURES

Marked difference in the field changes of positive first return strokes from negative is that many positive strokes showed no activities caused by the leader propagation. characteristics is that the period of gradual rise before the fast transition in the beginning of positive first return stroke, denoted 'slow front' in ref. (10), is rather long. Fig. 5(a) is the typical electric field produced by a positive first return stroke with no leader The other typical waveshape is Fig. 5(b) showing leader activity similar to those of negative ground flashes reported earlier (11). There also existed waveshapes in which no activity of leader pulse was seen except the leaderlike pulses superposing on the beginning of the slow front. For the present, we do not regard these superposing pulses as the leader activity.

In the discussion of fine structures of field changes, waveform distortion caused by the propagation and the recording system should always be kept in mind. The fast transitions of recorded negative return strokes within about 50 km were between 0.4 and 1.4  $\mu s$ . The actual time of fast transition may be less than 0.2  $\mu s$  (10), and the elongation of the recorded fast transition is supposed due to the propagation over land. Thus for slower phenomena takes more than 2  $\mu s$ , the influence of the waveform distortion becomes negligible.

In Table 3(a) is summarized the 10-90% rise times of first return stroke fields in each polarity. The data were consistent in all seasons and the rise time of positive return

Table 3 - Averaged Rise Times of Field Change for First Return Strokes

## (a) 10-90% Rise Time

	Polarity	Rise Time (us)	Number of Data
Niigata	+ -	8.7	32
'82 Dec'83 Feb.		3.9	8
Tokyo	+	7.2	42
'82 May - Jul.		3.6	60

#### (b) Zero-peak Rise Tima

			Polarity	Rise Time (us)	Number of Data
	Niigata		+	23.3	24
182	Dec'83	Feb.	-	7.5	8
	Rust (12)		+	6.9	31

strokes was about twice of the negative. This eharacteristic was further enhanced in the 'slow front'. Table 3(b) is the average of zero to peak rise times in each polarity. This value for positive first return strokes is three times as long as negative, resulting from the difference in the slow front. Another data for summer thunderstorms (12) shown in the table is supposed to correspond to 10-90% rise time due to the poor S/N ratio.

The long slow front is not observed in laboratory long spark and the mechanism is not clear, but the difference between positive and negative return strokes must come from the difference of the leader polarity, downward or upward. Following the slow front, fast transition similar to negative strokes occurs as seen in Fig. 5. Concerning the positive subsequent strokes, few data are available and will be discussed in the next chapter.

Table 4 shows the percentages of the existence of the leader activity at first return strokes. The leader pulse is susceptible to

Table 4 - Existence of the Leader Pulses before First Return Strokes

	Polarity	Leader Pulse Existed	No Leader Pulses	Percentage of the Existence of Leader Pulses
Niigata	+	7	16	30 %
'82 Dec'83 Feb.	-	19	0	100
Tokyo	+	9	25	26
'82 May - July	-	7	e	100

the waveform distortion by propagation and various noise. Therefore, the field change records used in Table 4 are limited to those suffering from small distortion and noise, and the number of data is reduced from Table 3. In spite of this selection, leader pulses having the amplitude of less than 1% of the associated return stroke peak could no longer be distinguished from noise, which may result lower than real percentage of the existence of leader pulses. But in Table 4, distinct difference is seen between the positive and negative strokes. All the negative first return strokes were associated with leader pulses, whereas they were observed at only about 30% of the positive ones. This means that the majority of the positive downward leaders propagate continuously.

Table 5 shows the averages of the largest leader amplitude divided by the associated return stroke peak. For pulses with small amplitudes, digitizing error becomes significant, and pulses with the amplitudes within 3 digits were eliminated from Table 5, which further reduced the number of the data and made the averaged amplitude of positive leader pulse larger. The difference between positive and negative is not so remarkable as in Table 4, but the averaged amplitude of the positive leader pulse is smaller than the negative. The largest amplitude of positive leader pulse was 22% of the return stroke peak, about the same level as the negative leader.

Fig. 6 is the time interval between positive leader pulses observed at Niigata in winter. Influence of various errors are small in this data. This result is similar to those of negative leaders observed in Florida (11).

The most distinct difference in the field changes of positive and negative first return strokes is the activity of leader pulses. At laboratory long sparks, the positive leader may propagate continuously or stepwise, depending on the applied impulse voltage waveshape and the absolute humidity (13). The negative leader always propagates stepwise because of the mechanism of its extension (14). These characteristics seems qualitatively common in the propagation of lightning downward leaders. For the positive long gap discharge in the laboratory, the applied impulse voltage controls the leader tip potential, which decides the propagation of the positive leader whether continuous or step-

Table  $\bar{\textbf{5}}$  - Averaged Lar est Leader Pulse Amplitude Divided by the Associated Return Stroke Peak

		Polarity	Amplitude	Number of data
	Niigata	+	u.n8	9
'82	Dec'83 Feb.	-	0.12	2
	Tokyo	+	0.05	4
182	May - Jul.	-	0.11	14

wise. In the lightning positive leader, the mode of the propagation is supposed also controlled by the leader tip potential, which may be influenced by the charge transportation, leader conductivity and so on. So it is quite natural that the activity of field changes of lightning leaders considerably differ according to their polarities.

#### MULTIPLE FLASHES

Observed multiplicity of positive ground flashes was low in all seasons as was reported for summer thunderstorms (15). The maximum multiplicity in winter observed at Niigata using a magnetic direction finding system (16) was 3, but only 2 field change records of positive flashes with the multiplicity of 2 are available for the present. The electric field changes shown in Fig. 7 is similar to negative multiple flashes both in slow and fast field. The first stroke shows leader activity, and the rise time of the subsequent stroke is faster than the first stroke. The amplitude of fast field change for the subsequent stroke is 40% of the first.

The flash shown in Fig. 8 is somewhat different. In the slow electric field, first return stroke preceded by the leader is clearly seen. The second stroke is difficult to identify from the slow field only, and we knew it from the data of the recording system of fast field changes. So it is difficult to know the multiplicity of positive flashes from the slow field change only. The second stroke in Fig. 8 also seems to be preceded by the leader, but the direction of the leader field change is opposite to the first stroke. If the stroke channel of the first and sec and were same, the first stroke was initiated by an upward leader. But in the fast field changes, the rise times were 7.9 and 7.2 µs for the first and the second stroke respectively, and the amplitudes were about the same. The waveshapes after the main peaks were somewhat different, which may indicate that these two strokes had different return stroke channels. So there exists the possibility that these two positive return strokes were individual single strokes.

As stated above, the interpretation of Fig. 8 is not clear. The number of ground flashes recorded by the magnetic direction finding system with the nominal range of 200 km was 17 in 20 minutes around the time of the flash of Fig. 8. The interval between these two strokes was 194.2 ms. Considering such low flash rate and the time interval it is unlikely that these strokes were two individual single strokes. The relatively long interval between the two strokes or different channel might explain the waveshape of the second stroke.

## SUMMARY

 The ratio of positive ground flashes to total ground flashes in a storm varies according

- to the season in Japan. In winter and spring, high rate of positive flashes were observed and in summer, most of the ground flashes were negative. In spring, the ratio had strong negative correlation with the altitudes of the radar echo top, whereas poor correlation with the vertical wind shear was seen.
- 2. About 250 fast field changes of positive return strokes were recorded with the frequency range of up to 1 MHz. Typical waveshapes are presented, and the rise time of the main pulse was known to be about twice of the negative stroke. The 'slow front' was about 3 times. No seasonal variation was observed in the fast field changes.
- 3. In the fast field records, only about 30% of positive first return strokes were preceded by the leader pulses. This means that the majority of the positive leader propagates continuously to downward. The average of the amplitudes of positive leader pulses are small compared with negative. The intervals between pulses were about the same as the negative. These are qualitatively explained from the characteristics of leaders in long laboratory sparks.
- 4. Both multiple flashes and multiplicity in positive ground flashes were small in number in all seasons. One example comprised two return strokes showed similar characteristics to a negative multiple flash.

### REFERENCES

- (1) M. Brook, et al., 'The Electrical Structure of the Hokuriku Winter Thunderstorms.' J. Geophys. Res., Vol. 87, C2, pp1207-1215, Feb. 1982
- (2) K. Nakahori, et al., 'Characteristics of Winter Lightning Currents in Hokuriku District.' IEEE PES paper 82 WM 205-3, Feb. 1982
- (3) M. Ishii, et al., 'Calibration of Electrostatic Antennas Using Broadcast Signal.' Res. Lett. on Atmospheric Electricity, Vol. 1, 1, pp45-48, Mar. 1981

- (4) E. P. Krider, et al., 'Broadband Antenna Systems for Lightning Magnetic Fields.' J. Appl. Met., Vol. 14. pp252-256, Mar. 1975
- (5) C. E. Baum, et al., 'Electromagnetic Sensors for General Lightning Application.' NASA Conf. Pub. 2128, pp85-118, Apr. 1980
- (6) G. I. Serhan, et al., 'The RF Spectra of First and Subsequent Lightning Return Strokes in the 1-200 km Range.' Radio Sci., Vol. 15, 6, pp1089-1094, Nov./Dec. 1980
- (7) T. Takeuti, et al., 'On Thunderstorms Producing Positive Ground Flashes.' Abstracts of 4th Int. Conf. on Atmospheric Electricity, Manchester, XI-12, Jul. 1980
- (8) M. Brook, et al., 'Positive Ground Stroke Observations in Japanese and Florida Storms.' ibid., VII-6
- (9) R. E. Orville, et al., 'An East Coast Lightning Detection Network.' 5th Symp. on Met. Obs. and Instrumentation, Toronto, Apr. 1983
- (10) C. D. Weidman, et al., 'The Fine Structure of Lightning Return Stroke Wave Forms.' J. Geophys. Res.: Vol. 83, Cl2, pp6239-62-7, Dec. 1978
- (11) E. P. Krider, et al., 'The Electric Field Produced by Lightning Stepped Leaders.'
  J. Geophys. Res., Vol. 82, 6, 951-960, Feb. 1977
- J. Geophys. Res., Vol. 82, 6, 951-960, Feb. 1977 (12) W. D. Rust, et al., 'Positive Cloud-to-Ground Lightning Flashes in Severe Storms.' Geophys. Res. Lett., Vol. 8, 7, pp/91-794, Jul. 1981
- (13) Les Renardieres Group, 'Positive Discharges in Long Air Gaps at Les Renardieres. 19/5 Results and Conclusions.' Electra, No. 53, Jul. 1977
- (14) Les Renardieres Group, 'Negative Discharges in Long Air Gaps at Les Renardieres. 1978 Results.' Electra, No.74, Jan. 1981
- (15) D. M. Fuquay, 'Positive Cloud-to-Ground Lightning in Summer Thunderstoims.' J. Geophys. Res., Vol.87, C9, 7131-7140, Aug. 1982
- Res., Vol.8/, C9, 7131-7140, Aug. 1982
  (16) M. W. Maier, et al., 'Locating Cloud-to-Ground Lightning with Wideband Magnetic Direction Finders.' 5th Symp. on Met. Obs. and Inscrumentation, Toronto, Apr. 1983

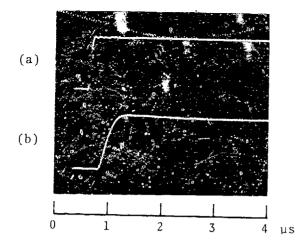


Fig. 1 - The response of the magnetic field measurement system  $% \left( 1\right) =\left( 1\right) +\left( 1\right) +\left($ 

- (a) current waveform producing input magnetic field
- (b) output of the system

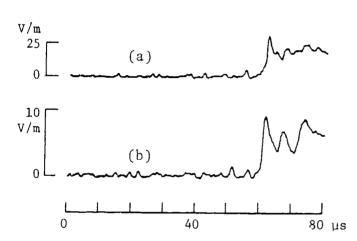


Fig. 2 - Electric field waveforms for leader steps and associated negative return strokes at about 15 km (a) and 50 km(b)

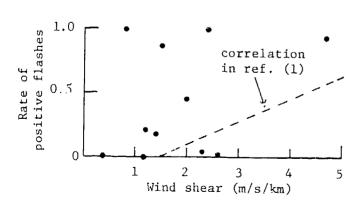


Fig.  $\beta$  - Plot of the rate of positive flashes versus wind shear in the cloud

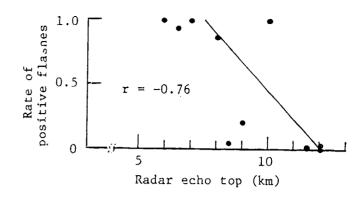


Fig. 4 - Correlation between the rate of positive flashes and highest radar echo tops (r: coefficient of correlation)

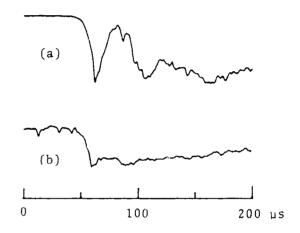


Fig. 5 - Typical electric field waveforms of positive first return strokes

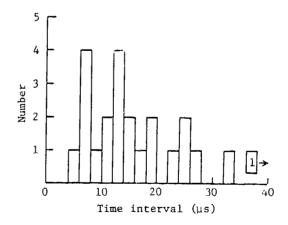


Fig. 6 - Histogram of the time intervals between leader pulses before positive first return strokes  ${\sf S}$ 

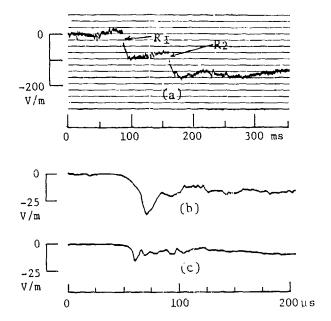


Fig. 7 - Electric field changes due to a positive multiple flash on Jan. 26, 1983

(a) output of a slow antenna

(b) electric field change of first return stroke  $(R_1)$ 

(c) field of subsequent stroke  $(R_2)$ 

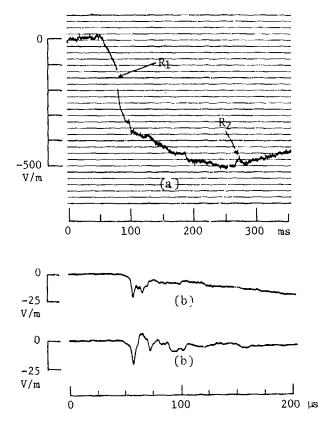


Fig. 8 - Electric field changes due to a positive multiple flash on Feb. 6, 1983

(a) output of a slow antenna

(b) electric field change of first return stroke  $(\ensuremath{\mathtt{R}}_1)$ 

(c) field of subsequent stroke  $(R_2)$ 

ON THE OSCILLATING BIPOLAR RETURN STROKE CURRENT



Tosio Takeuti, Nobuyuki Takagi, and Minoru Nakano The Research Institute of Atmospherics, Nagoya University, Toyokawa, Japan

## ABSTRACT

Oscillating bipolar field changes due to nearby lightning return strokes (up to 25 km distance) were sometimes recorded during winter thunderstorms in Japan together with ordinary unipolar field changes as recorded in summer thunderstorms. In order to understand the reason for the appearance of an oscillating field change, we calculated the return stroke current along a lightning channel with a transmission line model. The calculation shows that the return stroke current oscillates because of the relatively small volume of the winter thundercloud.

IT IS GENERALLY BELIEVED that the change in sign of the electric field from a distant return stroke, called a bipolar field change in this paper, is due to the predominant radiation component. However, in winter thunderstorms oscillating bipolar field changes due to return strokes in very nearby region were often recorded (1) \*. Weidman and Krider (2) \* reported unipolar oscillating field changes. They suggested that the oscillating components were produced by a reflection current at channel branches. It is difficult to understand how oscillating bipolar field changes could be caused by reflections from branches. An aperiodic bipolar current was measured by Huse in the lighting to a high tower(3) \* Accordingly we must discard the idea that the lightning current is always unipolar, i.e., direct current. In order to understand the oscillating bipolar field change, we calculate the return stroke current with a transmission line model and also calculate the electric field changes associated with the current.

OBSERVATION SITES AND INSTRUMENTATION

The electric field changes of winter thunderstorms for the discussion herein were recorded since 1979 in the Hokuriku area with a fast antenna system.

The block diagram of the field change recorder system is shown in Fig.1. The upper part of the Figure is called a slow antenna, frequency range from 0.016 Hz to 1 kHz, and the lower part a fast antenna, 160 Hz to 1 MHz.

The field changes due to lightning discharges are detected with 30 cm diameter disks which are placed at about 50 cm from the ground. The signals from the disks are fed into the slow and the fast antenna. For the details of the system, see Takeuti et al. (4)\*.

Time response of the fast antenna system was checked by the following way. A 1 kHz square wave with rise time of about 50 ns. was fed into the antenna input, a in Fig.1. The output signals from the amplifier, b in Fig.1, and from the modified VTR, video taperecorder, c in Fig.1, were recorded by photographing the displays on a oscilloscope. These

results are shown in Fig.2. Response times of both output signals shown in (b) and (c) are less than 0.3 Ms. It is obvious from Fig.2 that the electronics did not produce the oscillating waveform in the frequency range 10 kHz to 100 kHz, that is, the oscillation frequency range of the field changes due to the return strokes discussed here. We checked further that an oscillating wave was not produced, even if a surpassing input signal were applied. Therefore the instrument itself did not cause the oscillating waveforms discussed here.

#### DATA

Examples of the electric field change due to a negative ground flash and a positive one are shown in Fig.3 and Fig.4 respectively. In both figures (A) shows the field changes recorded by the slow antenna. L denotes the beginning of the leader stroke and R the return stroke. The waveforms from (B) to (D) were recorded by the fast antenna. Time expansions of (B) are given in (C) and (D). (D) in Fig.4 shows the oscillating bipolar field changes due to return strokes are shown in Fig.5.

#### RETURN STROKE MODEL

Many models of the return stroke channel have been proposed to calculate the lightning return stroke current. In the lumped circuit model composed of inductance, resistance and capacitance the current can be very easily calculated. There are other models such as a lumped parameter ladder network model (5)\*, a wave guide model (6)\*, and a model that the lightning current is composed of a breakdown pulse current, a uniform current, and corona current (7)\*.

We use a model in which the main discharge channel is represented by a transmission line terminated in the thundercloud with a capacitance. This capacitance supplies charge to the channel. The channel is terminated at the ground with a resistance. We compute the current using this model. On the transmission line model, refer the papers by Oetzel (8)\*and Price and Pierce (9)\*.

<sup>(1)</sup> Takeuti et al., 6th International Conf. on Atmospheric Electr., Manchester, England, 1980

<sup>(2)</sup> Weidman et al., J.G.R., 83, 6239-

<sup>(3)</sup> Huse, personal communication, 1978

<sup>(4)</sup> Takeuti et al.,J.G.R.,83,2385-2394 1978

<sup>(5)</sup> Little, J. Phys. D,11,1893-1910,1978

<sup>(6)</sup> Volland, J.A.T.P., 43, 191-204, 1981

<sup>(7)</sup> Lin et al., J.G.R., 85,1571-1583,1980

<sup>(8)</sup> Outzel, J.G.R., 73, 1889-1896, 1968

<sup>(9)</sup> Price et al., Radio Science, 12-3,

<sup>381-388,1977</sup> 

Fig. 6 shows a model of the leader stroke and charged region in the thundercloud. An upper sphere with radius a represents the charged region of cloud. This approximates the actual situation in a thundercloud of many branched channels. We define the radius such that its capacity relative to the ground equals the total capacity of many branched channels in the actual cloud. From the charged sphere, a leader stroke progress straight and vertically toward the ground. I in Fig. 6 indicates final step length of the leader channel. The connecting leader stroke from the ground is neglected. I +1 indicates the height of lightning channel.

This model is shown in (A) of Fig. 7. The capacity of a charged sphere, c<sub>1</sub>, is given by c<sub>1</sub>=4\(\text{R}\_0\)a(1-k+k')/(1-k)\) where \(\text{t}\_0\) is the permittivity of free space and k=a/2h, h being the center height of the sphere (10)\*. The line is held at uniform potential V by the charges in the thundercloud and in the leader channel. The return stroke is formed by switching S on. The lumped capacitance of the charged sphere C<sub>1</sub> can be replaced by an equivalent transmission line in which the line capacitance is C<sub>1</sub> and the line inductance L<sub>1</sub> is very small. Then the propagation time T<sub>1</sub> and the surge impedance Z<sub>1</sub> of the equivalent line are given by T<sub>1</sub>=(L<sub>1</sub>C<sub>1</sub>) and Z<sub>1</sub>=(L<sub>1</sub>/C<sub>1</sub>)/2, so that Z<sub>1</sub>=T<sub>1</sub>/C<sub>1</sub>. The accuracy of this approximation increases with decreasing L<sub>1</sub>, and hence decreasing T<sub>1</sub> and Z<sub>1</sub> (11)\*. We found that T<sub>1</sub>=Z C<sub>1</sub>/15 gives a good approximation to the current waveform, where Z is the surge impedance of the lightning channel. The surge impedance, Z , is etermined by Z = [(R + 1.0 L )/(G + 1.0 C )] where P is the channel resistance per unit length, \(\omega\$ the angular frequency, L and C the inductance and capacitance of the channel per unit length respectively, G the leakage conductance per unit length. G=0 in this model. We assume a distortionless line in the calculation as a first approximation, because L<sub>1</sub>(C) R/2L is less than unity(12).

(10) Takayama, Electromagnetic phenomenon theory, (in Japanese) 147, Maruzen Press, Japan, 1973.
(11) Sekine, Analytical theory of the electric power system, (in Japanese) 388-392, Denkisyoin Press, Japan, 1975.
(12) Moriwaki, Calculation method on transient phenomena, (in Japanese), 350-360, Syoukohdo Press, Japan, 1952.

For the distortionless line, the surge impedance is independent of  $\omega$  and  $Z = (L_{c}/C_{c})^{1/2}$ . Assuming that the channel is cylindrical conductor,  $L_{c}$  and  $C_{c}$  are given by

$$L_0 = \frac{M}{2} (\log \frac{21_c}{r} - 1) [H/m]$$
 (1)

$$C_o = 2\pi \xi_c / \log \left[ \frac{1_c}{r} \left( \frac{41_g + 1_c}{41_g + 31_c} \right)^{1/2} \right] [F/m]$$
 (2)

where  $\mu_c$  is the permeability of free space and r the radius of return stroke channel. In (A) of Fig.7, when the swithch S is turned on at t=0, the current I =V /(Z +R\_E) flows into the transmission line from its sendingend. The equivalent circuit at t=0 is shown in (B) of Fig.7.

RESULTS OF CALCULATION

LIGHTNING CURRENTS-In order to obtain the discharge current from the transmission line, we used lattice diagram method (See Fig. 8). Since 1 (L C) R/2L is less than unity in the present study, a damping factor, R/2L, is added to lossless solution (12). The current at x and t in Fig. 8 is calculated using

$$I(x,t) = (I_1 + I_2) \exp[(-R_0/2L_0)t]$$

$$= (1+b_1) I_0 \exp[(-R_0/2L_0)t]$$
(3)

Fig.3 shows the computed current pulses at the ground, the middle point of the  $% \left( 1\right) =\left( 1\right) ^{2}$ channel, and the top. We used  $l=4~\rm km$ ,  $l=50~\rm m$ ,  $r=3~\rm cm$ ,  $a=100\rm m$ ,  $R_p=100~\rm \Omega$ ,  $R_p=0.08~\rm cm$ ,  $V=5~\rm MV$  as typical values for a ground stroke in winter. Using the above values we find that  $L = 2.50 \, \text{MH/m}, C = 9.87 \, \text{pF/m}, Z = 503 \, \text{Ohm},$  and that the propagation velocity of the current along the channel is  $V_c=2.01 \times 10^8$  m/s. Ordinarily the lightning current decreases remarkably withn 200 Ms, because the channel resistance increases due to recombination of electrons and ions. Accordingly, the following discussion is limited to times less than 200 /s. The current wave forms shown in Fig 9 seem to be somewhat different from the actual current. The computed waveforms have overly steep changes and pulses. This is caused by the step function inflow current and the approximation by step functions for reflected waves at

the receiving end. These artifacts of the calculation should therefore be neglected. It is seen in Fig.9 that the current pulse propagates upward and reflectes from the cloud. The reflected downward currents are furthermore partly reflected again at the ground. The amplitude of current gradually decreases because of channel resistance and mismatching. We do not consider in Fig.9 the effect of increasing channel resistance with time by the recombination of ions and electrons so that the actual current should decrease more rapidly than the current shown in Fig.9. Fig.10 shows the current pulse with a=3 km and all other parameters remaing the same. It is seen by comparsion between Fig.9 and Fig.10 that the oscillation frequency of the current decreases with increasing radius a. In the case cf Fig. 10, assumed to be a typical summer discharge, the current at ground crosses the base line, that is, changes polarity, at about 160 Ms. The channel resistance is very high by this time in actual lightning, which nearly dissipates the current. This is apparently why most observed currents are directional ones.

ELECTRIC FIELD CHANGES-If current i(z,t), where z is height from ground and t time, flows from the ground into a linear vertical channel on the ground, the vertical electric field change E(D,t) on the ground, assumed to be a perfect conductor at a distance D from the bottom of the channel, is given by Uman et al. (13)\* as

$$E(D,t) = \frac{1}{4\pi\xi_{\xi}} \left\{ \int_{0}^{H} \frac{2-\sin^{2}\theta}{r^{3}} \int_{0}^{t} i[z, t-(r/c)]dt dz \right\}$$

$$+\int_{0}^{H} \frac{2-3\sin^{2}\theta}{cr^{2}} i[z,t-(r/c)] dz$$

$$\int_{0}^{H} \frac{\sin^{2} \theta}{c^{2}r} \frac{\partial i[z, t-(r/c)]}{\partial t} dz \qquad (4)$$

where H is the length of the lightning channel (=1 +1 ),  $r=(z^2+D^2)^{1/2}$ , and  $\theta=\pi_--\tan^{-1}(D/2)$ .

(13) Uman et al., J.G.R., 80, 373-376, 1975

Field changes at D=5,10,20 km are calculated by Eq.4 using the currents calculated with the above transmission line model for a=0.1 km and 3 km. In the calculation process, the current values are used at 100 m height intervals, The results are shown in Fig.11 and 12. In the Figures, very steep pulses are caused by the calculating process, and should be ignored. We see the oscillating bipolar field changes at D=10 km and 20 km in Fig.11, but not see in Fig.12.

Table 1 indicates the occurrence of oscillating bipolar field changes as a function of the radius of charged sphere, a, and the distance from lightning channel, D. It is clear from Table 1 that the oscillating bipolar field changes appear in the case of very small radius, that is, less than 0.2 km for D=10 km and 2 km for D=20 km.

#### DISCUSSION

It is believed that oscillating bipolar electric field changes are only observed at distance more than about 50 km where the radiation field is predominant. However, we have observed oscillating changes within 25 km in winter thunderstorms. The oscillating field changes due to close lightning return strokes were observed both positive and negative lightnings. However at first, let us discuss on positive lightning. Table 2 is occurrence percentages of the oscillating field change by nearby positive return strokes. More than half of field changes are oscillating change in the range between 15 and 25 km. The height of positive charges in the winter is roughly same as that of negative charges in summer, so that there is no large difference between the return stroke channel length in the winter and that in the summer. The oscillating field changes in winter storms are therefore not a result of different channel Jengths. The most significant difference between winter and summer storms is the size of thundercloud. Summer thunderclouds in Japan range from 1.5 km cloud base to 10 km cloud top while Japanese winter thunderclouds range typically from 0.3 km to 6 km (4). The volume of winter clouds is thus smaller than that of summer clouds. Hence the volume of the charged region in winter is likely to be smaller than that in the summer. The smaller charged volume implies a smaller radius and hence a smaller capacitance for the charged sphere. We might be able to infer by comparison Table 1 and 2 that the effective radius of positively charged sphere in winter thundercloud could roughly be estimated as 0.5 km.

We have too little number of data to make similar table for negative ground discharges in winter thunderstorms. In general, negative charge locates under positive one, so that length of negative return stroke channel is shorter than that of positive stroke channel. Accordingly, it is thought that the negative ground discharge in winter has higher occurrence probability for the oscillation. Actually, we recorded some oscillating field changes due to close negative ground discharges in winter.

#### CONCLUSION

The oscillating bipolar electric field change at distances less than 25 km from a ground discharge, both positive and negative, is caused by the current oscillation through a lightning channel. The calculation makes it clear that the current oscillation producing the oscillating field change occurs in small thundercloud in the winter. We will measure in a further study the current by means of magnetic field measurement to compare with the above discussed results.

#### REFERENCES

1.T. Takeuti, S. Israelsson, S. Lundquist, E. Astrom, and M. Nakano, "Fine structures of field changes due to positive ground flashes." 6th International Conference on Atmospheric Electricity, Manchester, England, 1980.

2.C.D.Weidman and E.P.Krider, The fine structure of lightning return stroke wave forms. "J.Geophys. Res. 83, 6239-6247,1978.

3.J.Huse, "personal communication."1973. 4.T.Takeuti, M.Nakano, M.Brook, D.J. Raymond and P.Krehbiel, "The anomalous winter thunderstorms of the Hokuriku Coast."J.Geophys. Res. 83, 2385-2394, 1978.

5.P.F.Little, "Transmission line representation of a lightning return stroke." J.Phys.D, 11, 1893-1910, 1978. 6.H.Volland, "A wave guide model of lightning currents." J.Atmos.Terr.Phys., 43,191-204, 1981.

7.Y.T.Lin, M.A.Uman and R.B.Standler, "Lightning return stroke models." J. Geophys.Res., 85, 1571-1583. 1980. 8.G.N.Oetzel, "Computation of the diameter of a lightning return stroke." J. Geophys. Res., 73, 1889-1896. 1968. 9.G.H.Price and E.T.Pierce, "The modeling of channel current in the lightning return stroke." Radio Science, 12-3, 381-388,1977.

10.E.Takayama, Maruzen Press, Tokyo, Japan, "Electromagnetic phenomenon theory" (in Japanese) 147,1973.
11.T.Sekine, Denkisyoin Press, Tokyo,

Japan, "Analyti al theory of the electric power system." (in Japanese) 388-392, 1975.
12. Y.Moriwaki, Syoukohdo Press, Tokyo, Japan, "Calculation method on transient phenomena." (in Japanese), 350-360, 1952.
13.M.A.Uman, R.D.Brantley, Y.T.Lin, J.A.
Tiller, E.P.Krider and D.K.McLain, "Correlated electric and magnetic fields from lightning return stroke." J.
Geophys. Res., 80, 373-376, 1975.

Table 1-Appearance of the Oscillating Bipolar Electric Field Changes Within 200 /4s.

Radius of a charged sphere	Distance 5 km	from a 10 km	channel 20 km
0.02 km	х	0	0
0.05	x	0	0
0.1	x	0	0
0,2	x	0	О
0.5	х	x	0
1.0	x	x	0
2.0	x	x	0
3.0	x	x	x
4.0	x	x	x
5.0	x	x	x

o:oscillating bipolar; x:unipolar

Table 2-Two Types of Field Change Due to Positive Return Strokes

Distance from a channel (km)	0-7.5	7.5-15	15-25	
Oscillating bipolar	1	2	3	
Unipola	11	2	2	-

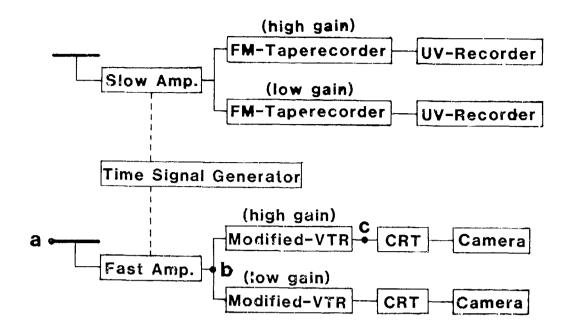


Fig. 1 - Block diagram of the field change recorder system.

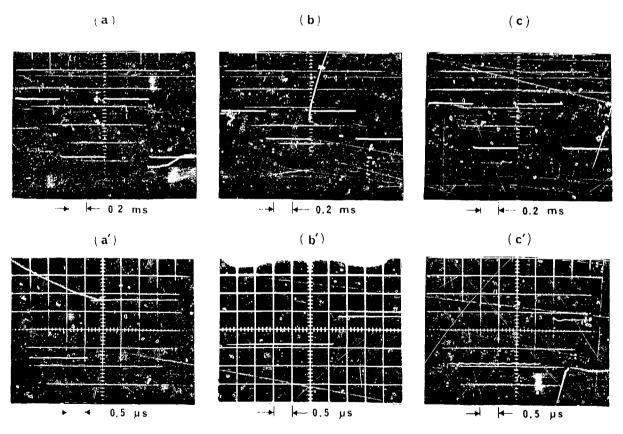


Fig. 2 - The time responses of the fast antenna: (a) input signal, (b) output signal of the amplifier, and (c) output signal of the modified-video taperecorder; (a'), (b'), and (c') show time expansions of (a), (b), and (c) respectively.

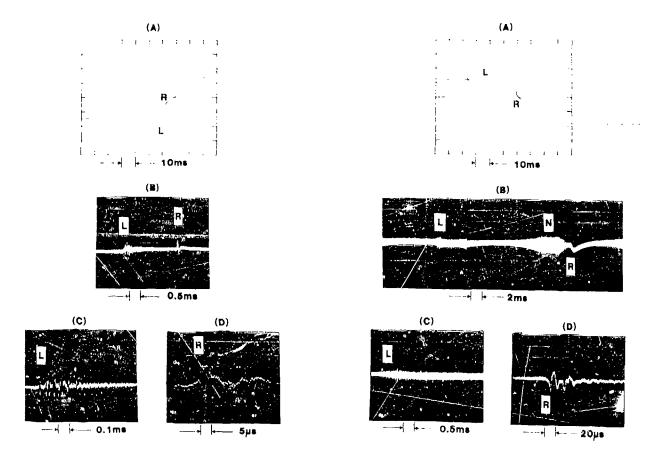


Fig. 3 - An example of the electric field change due to a negative ground flash.

The state of the s

Fig. 4 - An example of the electric field change due to a positive ground flash, N denotes instrumental noise.

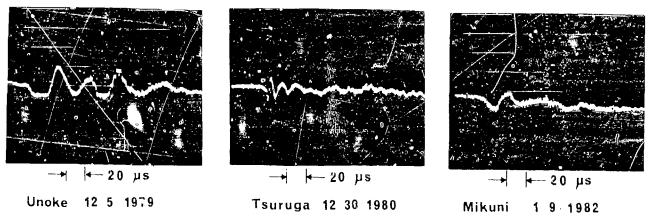


Fig. 5 - Examples of the oscillating bipolar field changes due to return strokes.

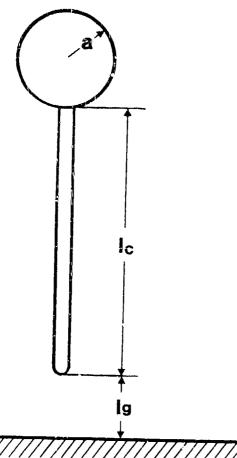


Fig. 6 - Model of lightning stroke.

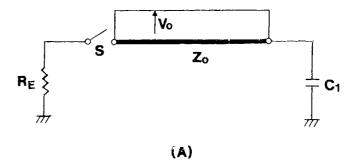
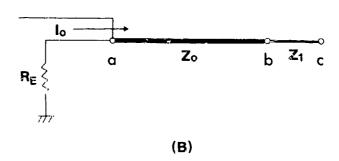


Fig. 7 - Transmission line model of lightning return stroke: (B) is an equivalent model to (A); Z: surge impedance of the lightning channel, R<sub>E</sub>: earth resistance, C<sub>1</sub>: capacitance of the charged sphere, V: initial potential, I: initial current, Z<sub>1</sub>: surge impedance of line equivalent to  $c_1$ .

THE RESIDENCE OF THE PROPERTY OF THE PROPERTY



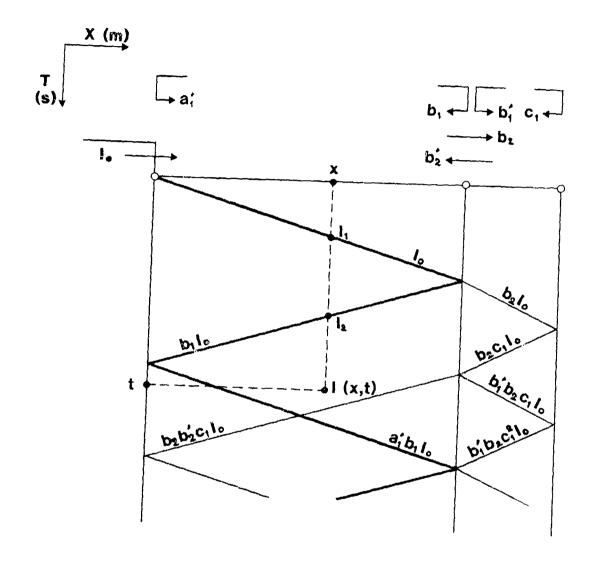


Fig. 8 - The lattice diagram method; a', b', b', c'; reflection coefficient at point a, b and c in (B) of Fig.7; b, and b': transmission coefficient at point b.

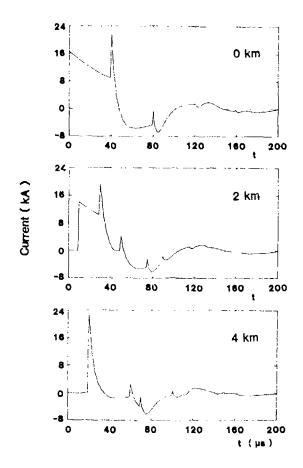


Fig. 9 - Computed lightning current at height, 0, 2, and 4 km, respectively (a=100m, 1 =4 km); the return stroke current originates at ground level at t=0.

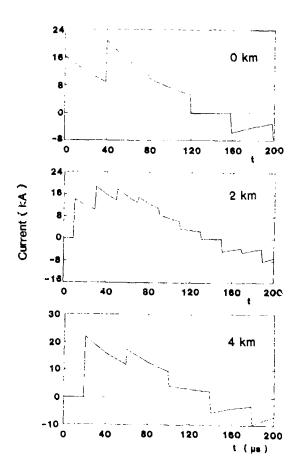


Fig. 10 - Computed lightning currents at height, 0, 2, and 4 km, respectively (a=3 km, 1=4 km); the return stroke current or ginates at ground level at t=0.

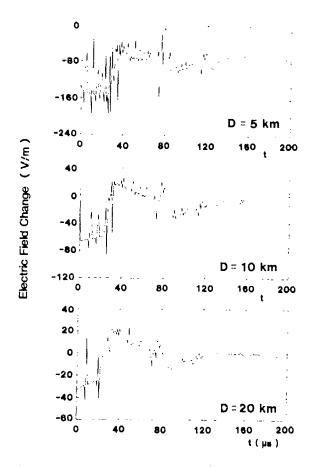


Fig. 11 - Computed electric field changes at distance, 5, 10, and 20 km, respectively (a=100 m, 1 =4 km); the electric field changes begin at each distance at t=0.

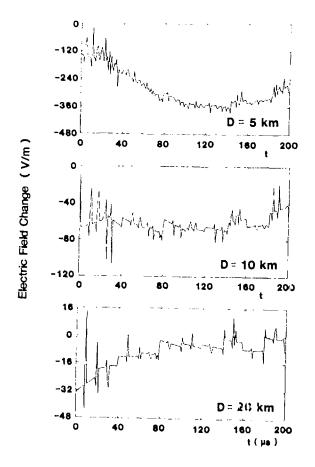


Fig. 12 - Computed electric field changes at distance, 5, 10, and 20 km, respectively (a=3 km, l=4 km); the electric field changes begin at each distance at t=0.



P-Static Flight Evaluation of a Large Jet Aircraft

 $\rightarrow$ 

Charles H. King

Boeing Commercial Airplane Company Seattle, Washington 98124

## ABSTRACT

The use of static dischargers to reduce "P-static" interference in radios is universal in large modern aircraft. These devices, although they quietly discharge the aircraft, represent drag and weight penalties and can delay dispatch of a flight if dischargers at key locations are missing.

Flight tests were conducted on a modern jet transport to determine the location and number of dischargers required for dispatch. Traditionally the minimum complement is based upon "engine charging"; i.e., only those dischargers required to quietly discharge the current produced by operating the engines in clear air would be required for dispatch. The aircraft was instrumented to measure charging current, discharge current, ADF radio noise and field potential.

The data from this instrumentation was recorded on a system which sampled data at a rate of 5 times per second. Data plots obtained during various charging conditions are presented.  $\tilde{\beta}$ 

THE ELECTROSTATIC CHARGING AND DISCHARGING CHARACTERISTICS of a modern large jet transport were investigated. In-flight charging data was recorded over a wide range of p-static flight conditions ranging from clear air cruise to penetration into icing and lightning environments.

INSTRUMENTATION - Four basic parameters were instrumented on the aircraft for flight measurements. The positions of the various sensors on the aircraft are shown in Figure 1. All parameters were recorded on a flight test multiplexed data recording system and presented for real time viewing at a seat location.

AIRCRAFT POTENTIAL - A field meter located just aft of the nose wheel well was used to measure relative aircraft potential. The field meter is of the rotating blade type where a sense element is located beneath a spinning aperture (1)\*. The sense element is alternately exposed and shielded from electric field lines which terminate on the aircraft.

CHARGING CURRENT PATCH - A 2' x 1' aluminum foil patch was installed on the leading edge of the right wing to sense the relative p-static charging current seen by the aircraft. The foil was isolated from the wing leading edge with a thin layer of dielectric material. The patch was connected to ground through an ammeter (for real time observation) and through a series resistor (which acted as a voltage source for the on-board flight test data recording system).

STATIC DISCHARGERS - Two static dischargers were instrumented during the initial flights: a tip type on the right wing and a trailing type on the left wing. Discharger instrumentation was achieved by isolating the resistive element at the base of the discharger and attaching a wire from the resistive element to ground via an ammeter and resistor.

ADF RECEIVER - A standard ADF receiver was modified to allow relative measurement of the noise intensity. The receiver squelch was deactivated and the AGC voltage was made available at a connector. In addition, audio lines were connected to the receiver output and were wired to the monitoring console along with the AGC voltage. A digital voltmeter was used to monitor AGC voltage at the instrument console. A calibration of field strength in microvolts per meter vs. AGC voltage was conducted and used to convert AGC voltage co dB above microvolts/meter by the data recording system.

Flight data from the aircraft's on board data system was also available. The parameters usually presented with the p-static data were: indicated air speed, pressure altitude and ambient air temperature.

### DISCUSSION

MINIMUM DISCHARGER COMPLEMENT FOR DISPATCH - Discharger configurations are designed to provide protection from p-static noise under the most severe charging The number of trailing conditions. dischargers required on a particular aircret is a function of the vehicle's frontal surface area and varies approximately with the three halves power of the wing spread (2). The number of tip type dischargers on each air foil is less well defined and varies from 1 to 3 depending upon the size of the tip of the air foil. Table I shows some typical aircraft and their discharger locations.

Dischargers are occasionally broken off since they extend beyond the extremities of the air foil. They are occasionally dislodged from their mountings by mechanical and aerodynamic forces. For normal operations a full complement of dischargers is seldom required and aircraft may be dispatched with several dischargers missing.

A minimum complement of dischargers required for dispatch is established for each aircraft. In theory, this minimum dispatch complement would dissipate "light-to-medium" charging without causing a radio noise source. Unfortunately, it is not always possible to find "light-to-medium" charging conditions for a test aircraft. In the past it's been noted that jet engines charge the aircraft appreciably when the engines are operated near maximum rated thrust. A minimum discharger complement was often determined to be that which would dissipate the "engine charging" (usually during climb out) without causing noise in the ADF receivers.

Early in our flight tests it became apparent that engine charging on the test vehicle was not characteristic, even at the high thrust levels typical of climb out. Figure 2 shows a data record typical of low altitude flight with ambient temperature near or above freezing. This plot was obtained during a cloud penetration during climb out. Manual notes indicated no ADF noise. No particle charging was evident even though the ambient temperature was slightly below zero.

A cloud penetration at a higher altitude is shown in Figure 3. In this case, the ambient temperature was well below freezing and partial charging is evident. Notes show that p-static noise was prevalent during the time there was activity on the charging patch.

 $<sup>\</sup>boldsymbol{\star}$  Numbers in parentheses designate references at end of paper.

Figure 4 is the record from a low altitude cloud penetration with all but the instrumented discharger removed from the aircraft. The characteristics were: no particle charging, no ADF noise, high "engine" charging during the time the aircraft is in the cloud,

Figure 5 is a high altitude encounter with particles and all dischargers removed from the aircraft. ADF noise was noted whenever charging patch current was present. Since the noise occurred even when the aircraft potential was relatively low, the source was believed to be other than corona from the aircraft extremities. This belief is re-enforced by the fact that similar p-static noise occurred on flights where dischargers were installed.

P-STATIC NOISE INVESTIGATION - The source of the p-static noise was thought to be a dielectric surface with frontal area exposure to particle impingement. An electrostatic charging device, INJECO<sup>R</sup> (3), was used to charge all suspicious areas on the aircraft while the ADF receiver system was being monitored. Also, a resistance meter was used to check bonding. Figure 6 shows the areas on the aircraft which were investigated and include:

Nose radome
Nose radome lightning diverter
strips
Window and frames
Anti-collision light
VHF blade
Wing/body fairing
Static dischargers (all
extremities)
ADF antenna radome
HF notch

The only condition that would produce noise in the ADF receiver system was when the ADF radome was charged. A data plot of the ADF receiver noise taken during the noise installation is shown in Figure 7.

Two additional flight tests were conducted on the instrumented aircraft with a conductive coating installed over the ADF antenna radome. Unfortunately, conditions for charging were not encountered. However, shortly thereafter a dual ADF antenna system experienced extreme p-static noise. INJECO was used on an ADF System test setup to demonstrate the effect of p-static charging on the radome and the resulting noise in the system. Noise identical to that encountered during the earlier flight was produced (the RDMI needle swung wildly and the identification of an ADF station was swamped out by the noise). The antenna was then coated with conductive paint with 10 to 20 megolms per square inch resistance and then re-tested with  ${\rm INJECO}^{\rm C}$ . The RDMI needle was unaffected by the charging and the station identification was clear; however, some p-static noise could still be heard in the background.

ADDITIONAL P-STATIC FLIGHT TEST DATA -Data samples were collected from additional flight tests conducted in a variety of atmospheric conditions. Figure 8 shows charging conditions during climb out through a cloud layer at 5000 feet (1524 meters) altitude. The aircraft potential was sufficient to saturate the most sensitive scale on the field meter. Some charging was evident on the charging patch even though the ambient temperature was well above freezing; however, ADF noise was extremely slight. Figure 9 is a similar take-off through cloud layers at 2500 and 5000 foot (762 and 1524 Again the ambient meters) altitude. temperature was above freezing, the charging slight and the noise minimal.

The rest of the data to be shown were obtained when the test aircraft was looking for natural icing conditions.

Heavy charging conditions are shown in Figure 10 where the aircraft dipped into a cloud at 14,000 feet (4267 meters) with an ambient temperature of -10°C. Patch charging rates up to 20 microamperes were observed with ADF noise levels 40 dB above ambient. At 13:02 and 45 seconds a lightning discharge occurred to the aircraft. The data during this time period is shown in Figure 11. The ADF noise was on the order of 70 dB above ambient just before the incident. Rapid changes in the potential of the aircraft one or two seconds before the strike are thought to cause the non-tracking of the two field meter scales. A flash was seen a few minutes later (13:06 and 38 seconds) but was not accompanied by the characteristic sound associated with lightning. The extreme fields experienced in this time frame are shown in Figure 12.

Figure 13 shows a condition where the aircraft was operating in a cloud. The aircraft potential was relatively high and the temperature was  $-12\,^\circ\text{C}$  but there was no particle charging and no noise. Later at a similar altitude and temperature (Figure 14) the ADF experienced 20 dB of noise above ambient.

The final flight was totally conducted in a cloud. During climb out the ADF noise was relatively low at temperatures above freezing, but as the temperature dropped below freezing the ADF noise rose to 40 dB above ambient. The patch indicated charging to 10 microamperes, and the next to most sensitive scale on the field meter saturated. These conditions prevailed during the remainder of the flight, with the highest charging levels recorded at 16:02 when patch charging levels reached 22 microamperes and the noise was 60 dB over ambient.

#### RESULTS AND CONCLUSIONS

One must be careful in drawing conclusions from test data when conditions cannot be completely controlled or well defined. It a unfortunate that more flight tests could not have been conducted with instrumented dischargers and that flight tests into charging conditions were not encountered when the ADF antenna was protected with antistatic coating.

In spite of this, some conclusions can be drawn:

- The jet engines on the test aircraft did not produce static charging when operated in clear air. Similar testing conducted on earlier aircraft types has shown that aircraft charging in clear air was dependent upon engine thrust settings. It is the opinion of this investigator that the emphasis on cleaner burning, more efficient engines has greatly reduced the particle content of the exhaust and hence greatly reduced triboelectric charging due to engine operation. The aircraft charging experienced in clouds, where particle impact charging is zero, is believed to be due to less complete combustion in the engine because of the presence of water vapor.
- When operating in clear air, the engines tended to act as a resistance to their surroundings. The aircraft has an approximate free space capacitance of 1000 microfarads. When the aircraft exited a cloud the aircraft potential rapidly returned to zero and exhibited relaxation times of from 2 to 6 seconds. Considering an RC time constant, this indicates that the aircraft's resistance to its surroundings is in the order of 2 to 6 x 10 ohms. Aircraft potentials are known to be in the order of 200,000 volts (1) before extremities unprotected by static discharges are known to go into corona discharge. The maximum current to which "engine resistance" could be counted upon to discharge the aircraft before the extremities go into corona is therefore about 100 microamperes. This source is not only small but under conditions when it is needed (during cloud penetration) the engine may become a charge source because of the pressure of the water vapor in the cloud.

The dominant ADF noise source appears to be the radome of the ADF antenna. This is believed since the presence of ADF noise is more a function of patch current than of the aircraft potential. ADF noise in the absence of patch charging (Figure 14) at time 11:55:20 and time 11:59:10 is bolieved to be corona discharge at the aircraft's extremeties. ADF noise in the absence of particle charging occurred only when the aircraft potential was in excess of 25 kV/meter (corrected to sea level).

### REFERENCES:

- J. E. Nanevicz et. al., "Development and Testing of Techniques for Precipitation Static Interference Reduction," Stanford Research Institute Final Report ASD-TDR-62-38, January 1962.
- R. L. Tanner and J. E. Nanevicz, "An Analysis of Corona-Generated Interference in Aircraft," Proceedings of the IEEE, January 1964.
- Joseph Taillet, "Aircraft Static Charging Testing," Office National D'Etudes et de Recherches Aerospatiales, AGARD Lecture Series No. 110.

Table I - Number of dischargers used on commercial aircraft

TIP TYPE
5
4
16
10
10
18

Fig. 1 - P-Static sensor position on test aircraft

Fig. 2

Fig. 3

Fig. 4

Fig. 5

Fig. 6 - Major areas of noise source investigation

Fig. 7 - Ground test of uncoated ADF antenna using INJECO, R to charge dielectric surfaces

Fig. 8

Fig. 9

Fig. 10

Fig. 11

Fig. 12

Fig. 13

Fig. 14

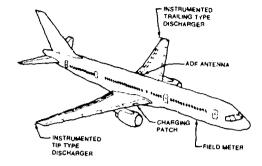


Figure 1 P-Static Sensor Positions on Test Aircraft

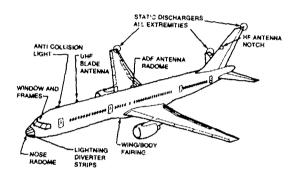
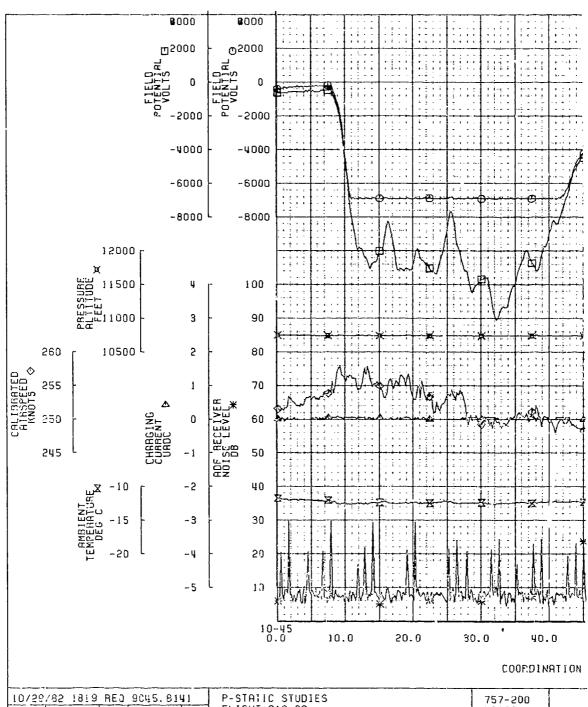
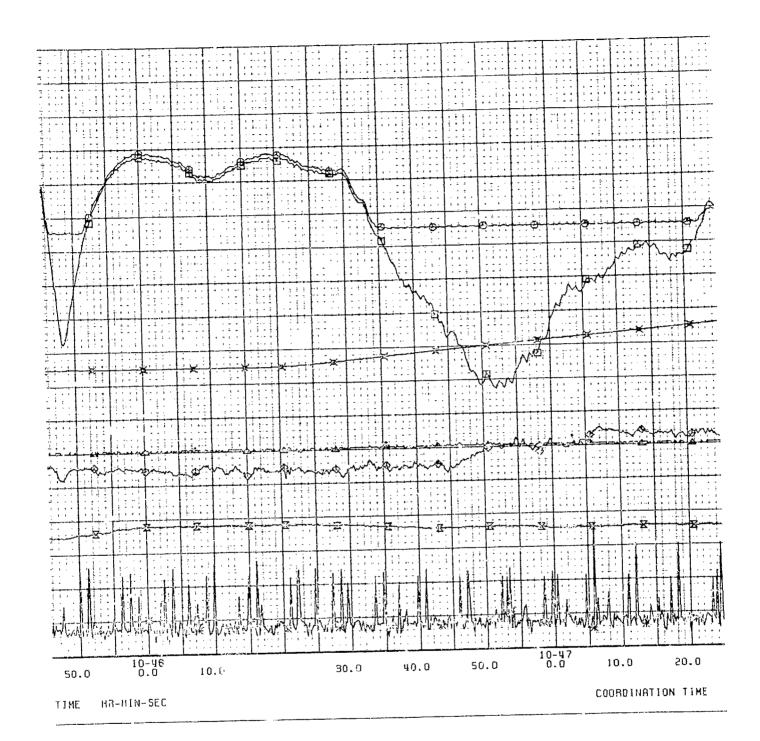


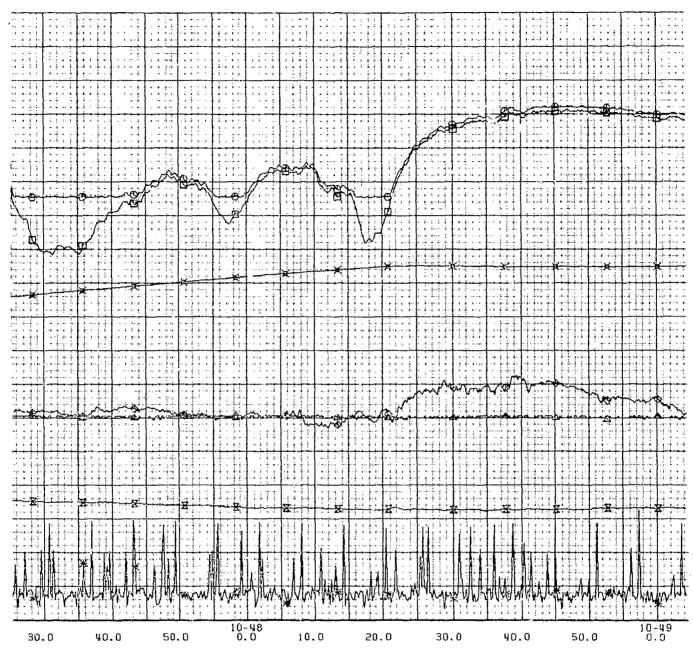
Figure 6 Major Areas of Noise Source Investigation



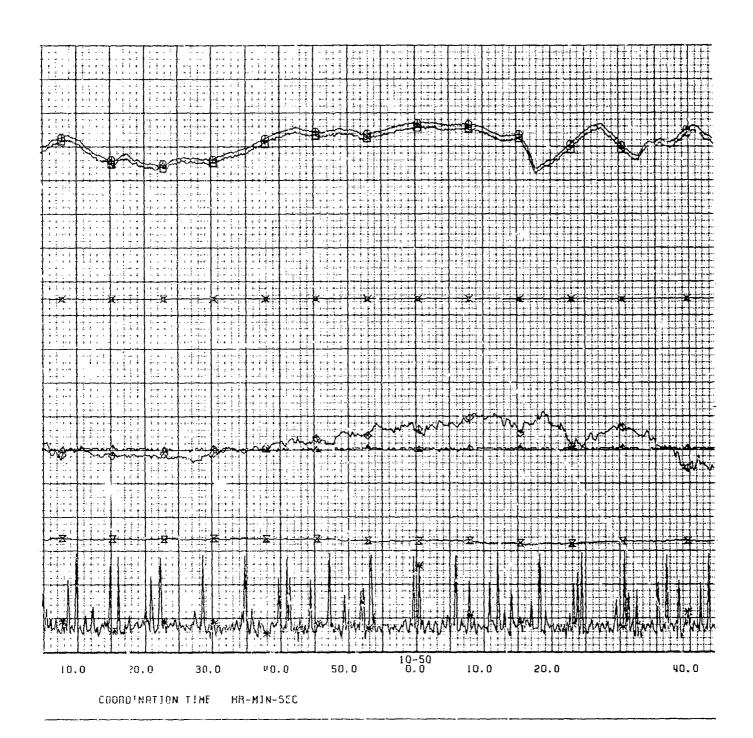
| 10/29/82 1819 RED 9045.8141 | P-STATIC STUDIES | 757-200 | NA003 | P-STATIC STUDIES | FLIGHT 012-02 | P-STATIC STUDIES | P-ST

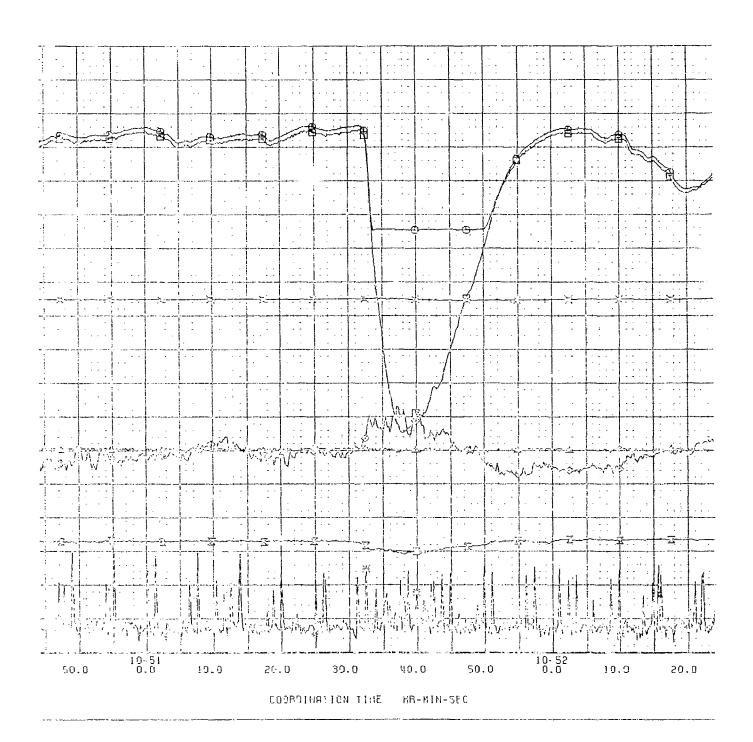
FORMAT 1 P-STATIC STUDIES





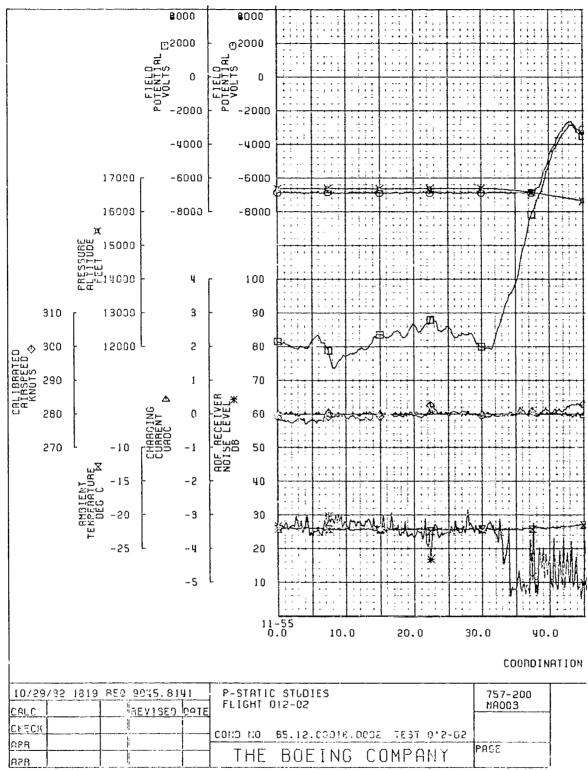
HR-MIN-SEC



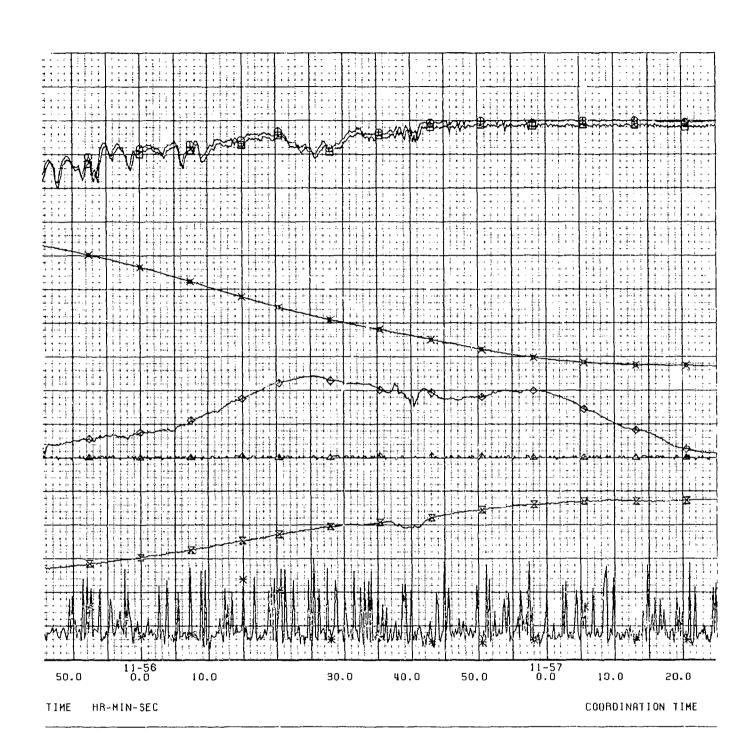


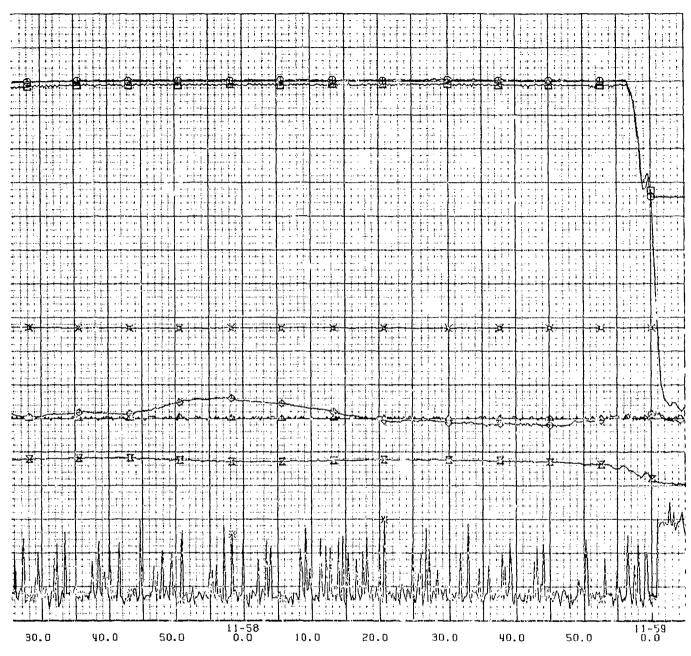
84-10

	1	
1 ::.		١
	l '	
	L	. ' '
	1 1	
1		
1	!	
	;	
1		
1	1	
1	1 ' ' !	
- i	1	
1		
المتعلق المستعمل الم	)	
80	! !	
	•	
1	, ,	
1		
*		
1		
1		
1	,	
	1	
		-
1		
	:	
1 1		
1		
	, . !	
3.4	, ,	
	. !	
	٠,	
	•	
<del></del>	-	
· i	:	
	:	
1 1		
1 1 1 1 1		
	:	
: :		
	'	
i :		

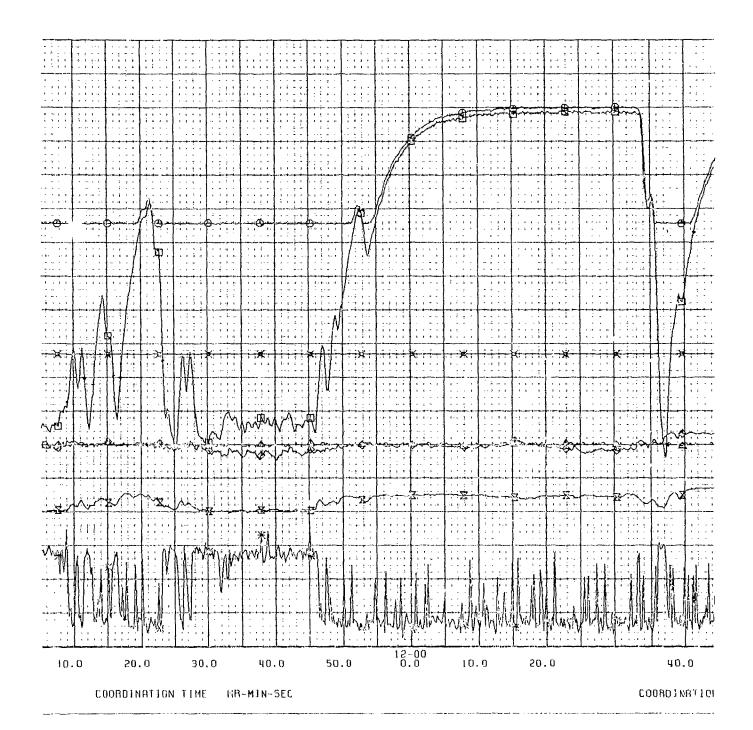


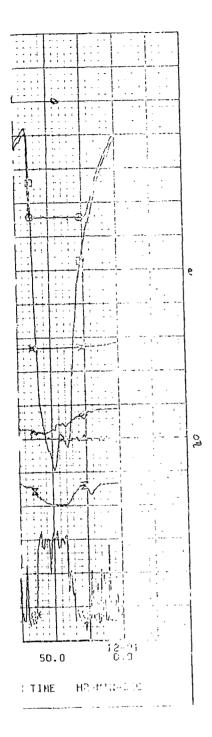
FORMAT 1 P-STATIC STUDIES

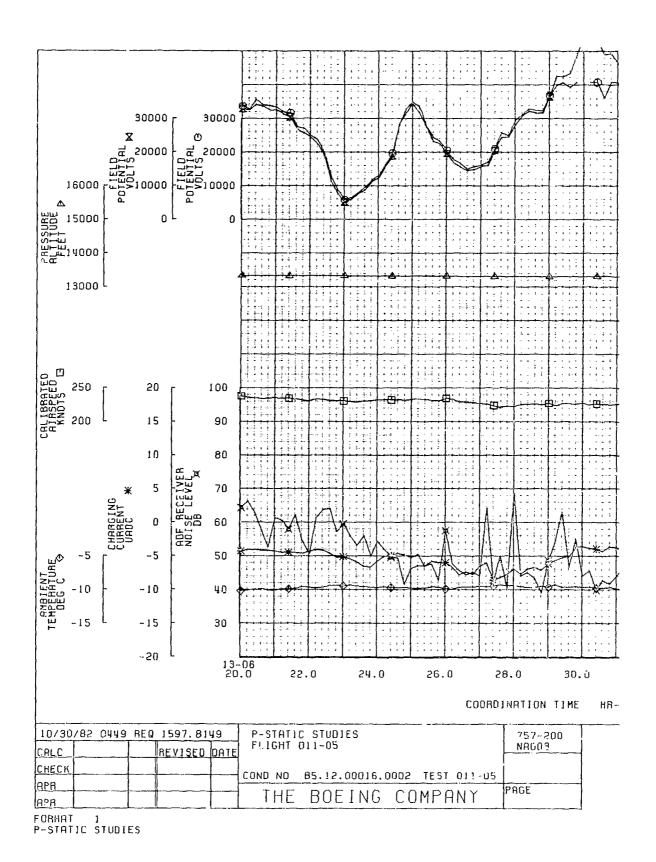




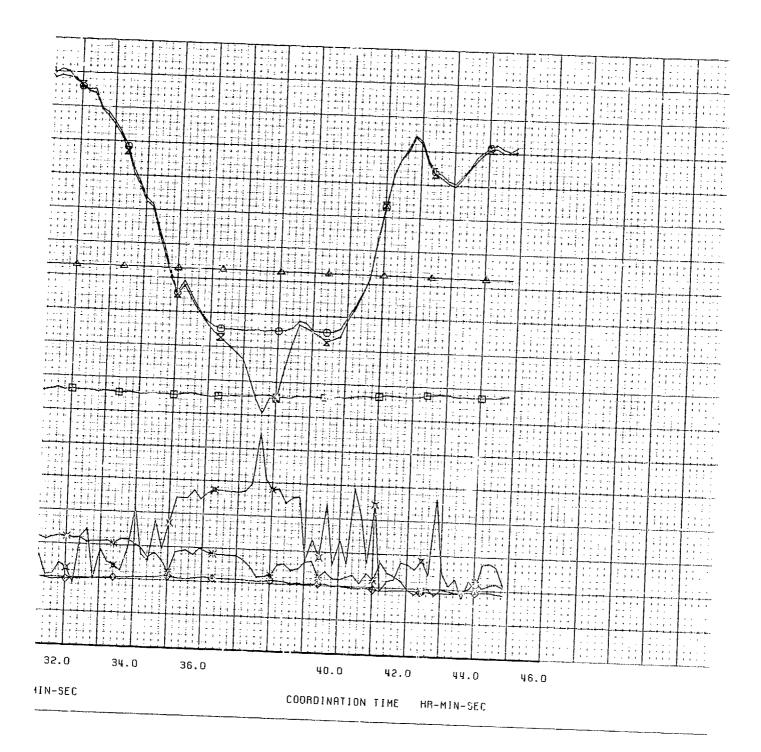
AR-MIN-SEC



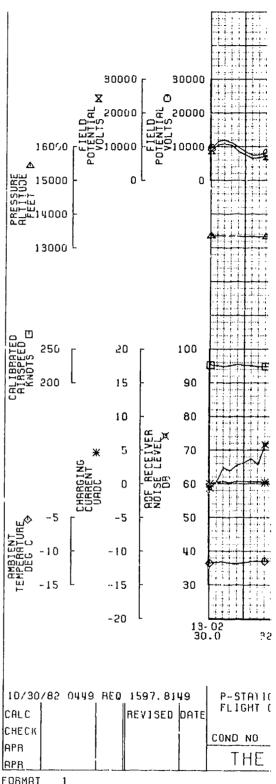




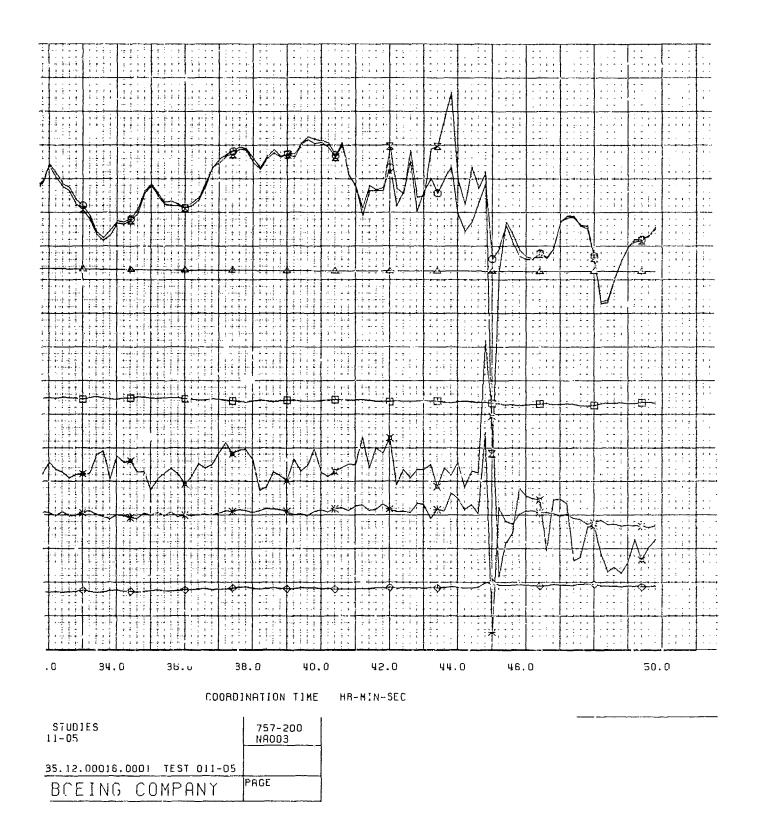
84-17



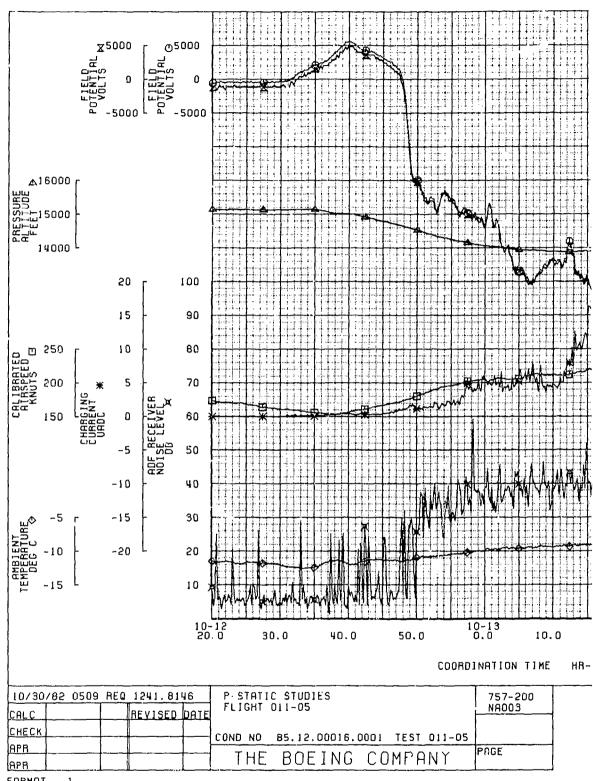
1				: : : :					
				, , :		_			
1						, , , ,			
				1 ( ) 2 ( ) 1	- 1	1 1 ·			
		1111		1 10 4 1	* * * * * * * * * * * * * * * * * * *	1111			
1 7 1 1						, , , ,			
			.,		2 3 4 4				
			* * * * * * * * * * * * * * * * * * * *		1 - 1				
	1					,			
			1 1						
11:1									
				- L			1 j + 1		
1 7 2 1			1 1 1 1 1 1 1 1 1 1 1 1 1 1 1 1 1 1 1		in a fi graph and a kapangananan				
	Activities	,,,,,,	1	1	* * : * : * : * : * : * : * : * : * : *	i I U			
1 1 2 1 2		1111	1 1 1 1 1 1 1 1 1 1 1 1 1 1 1 1 1 1 1	1					
				1 . 7					
1 1 2 1		3 1 1 7			F 1 1 1	3 1 1 2			
4		3 / 2 4		1 1		. 1 1		,	
				1   1   1   1   1   1   1   1   1   1	- 1 - 1 - 1 - 1 - 1 - 1 - 1 - 1 - 1 - 1			· ·	
1:::	Lili		1 1 1	11.5					



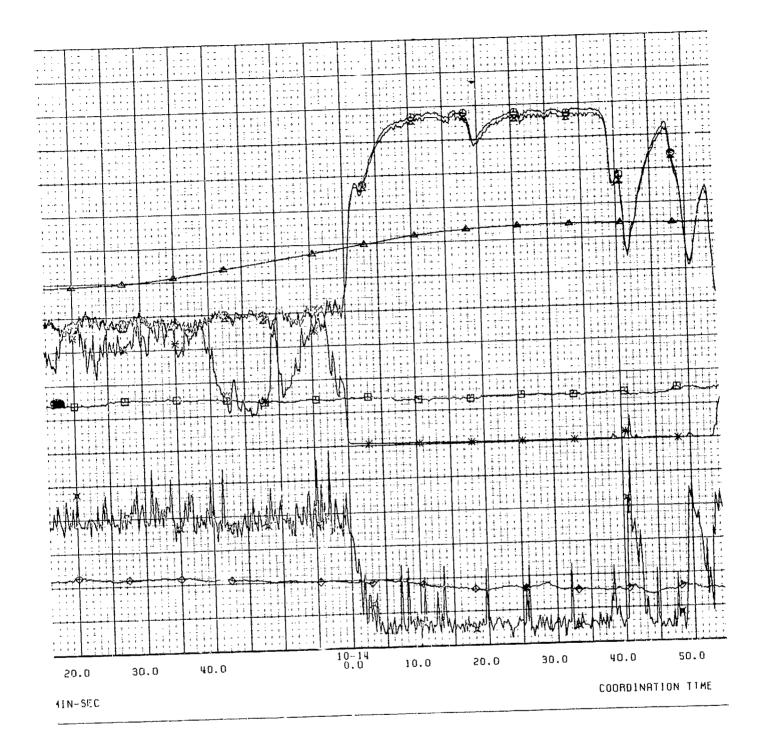
FORMAT 1 P-STATIC STUDIES

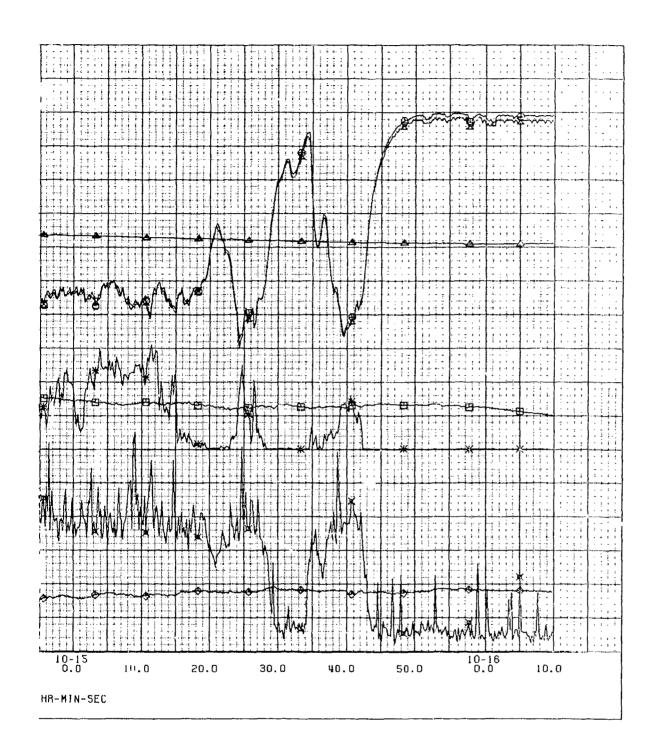


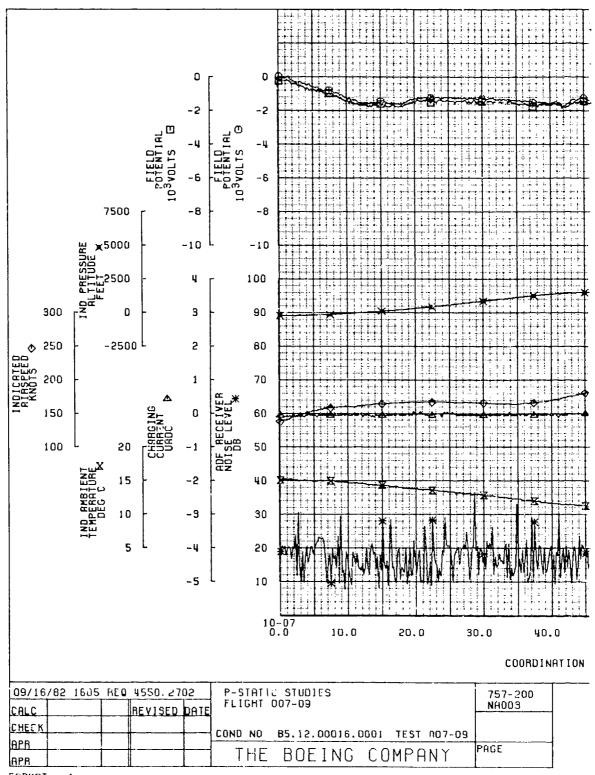
. ;		; ; ; ; ; ; ; ; ; ; ; ; ; ; ; ; ; ; ;	1 2 2 2 2 2 2 2 2 2 2 2 2 2 2 2 2 2 2 2	+		7 T T	1			1 2 2 3	÷ ; ;		1	- i :				
			2	12.11.1		· · · · ·		1 1 1 1 1 1									1 2 2 1 1 1 1 1 1 1 1 1 1 1 1 1 1 1 1 1	
									1 1 1 1 1 2	5. 2. 1 1. 2. 1 1. 1 2. 1			1.1.1.1	- 3 1 1		1		1 1 1
		1				1 1 2 1 1 1 1 1 1 1 1 1 1 1 1 1 1 1 1 1												
	:	1	<del>   </del>					1 4 8 4							<del> </del>			
	1	E E	* * * ; ; ; ; ; ; ; ; ; ; ; ; ; ; ; ; ;		<del></del>										1 1 1 1 1 1 1 1 1 1 1 1 1 1 1 1 1 1 1			
						*												4 1 1 1 1 1 1 1 1 1 1 1 1 1 1 1 1 1 1 1
			7 2 1 1 1 1 1 1 1 1 1 1 1 1 1 1 1 1 1 1				1111		1 - 1 - 1 - 1									
			<del></del>															
			** 1 1 1 4 4															
												1 1 1 1 1						
3 4 4 4						4 4 4									1 1 1 1 1		1	
						1 1 1 1 1 1 1 1 1 1 1 1 1 1 1 1 1 1 1			17						1 ( 4 4 4			
										T 1 1 1 1 1			1111				1 :	- 1
				1 1 4 1 2														[



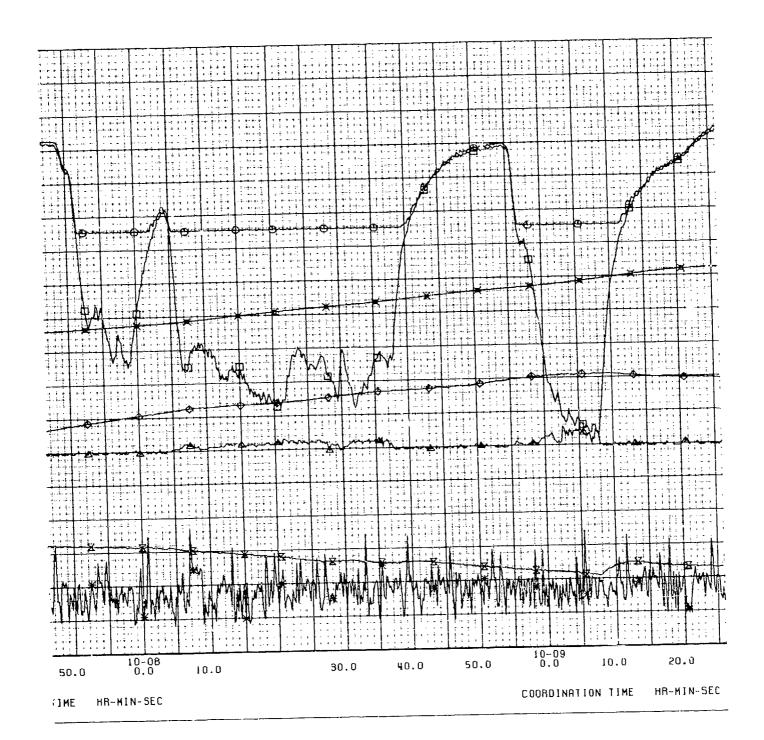
FORMAT 1 P-STATIC STUDIES

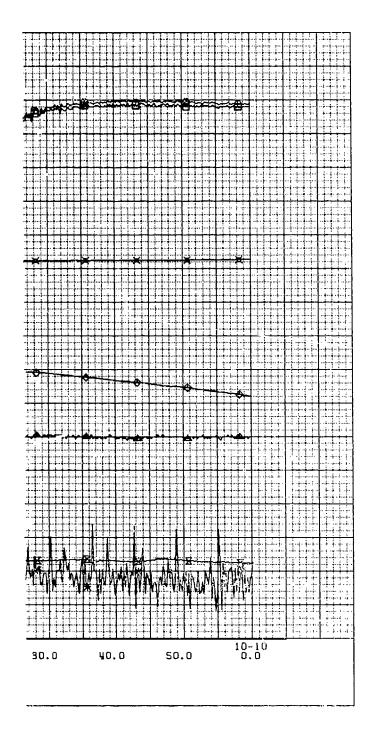


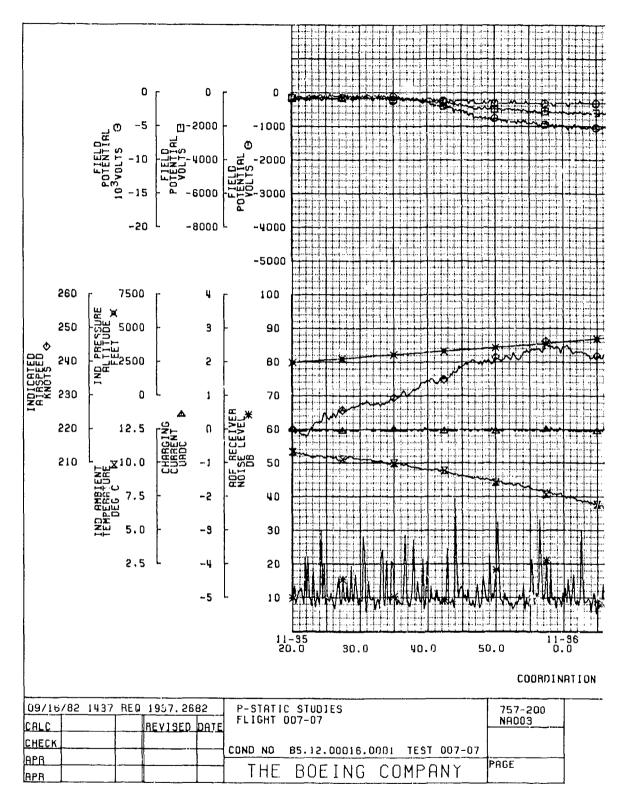




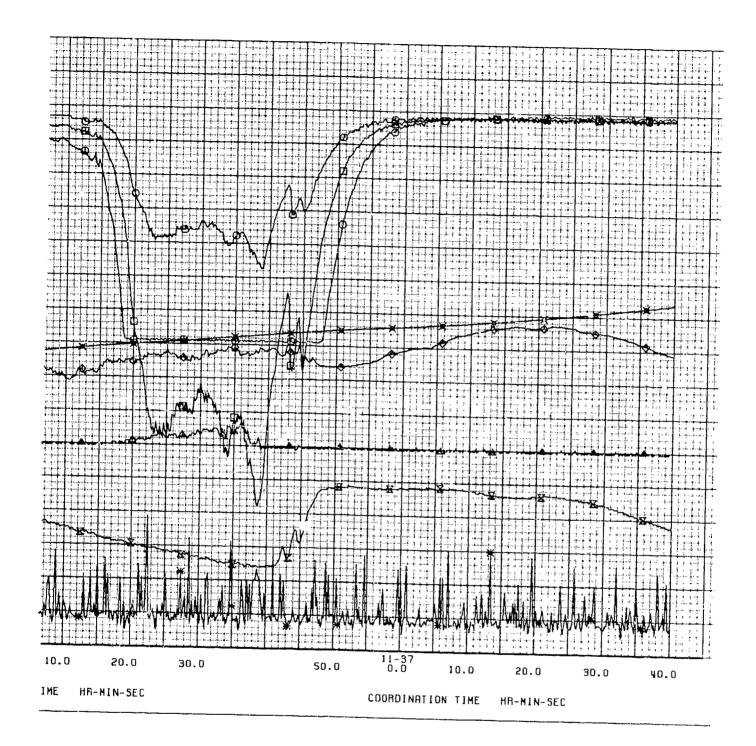
FORMAT 1 P-STATIC STUDIES



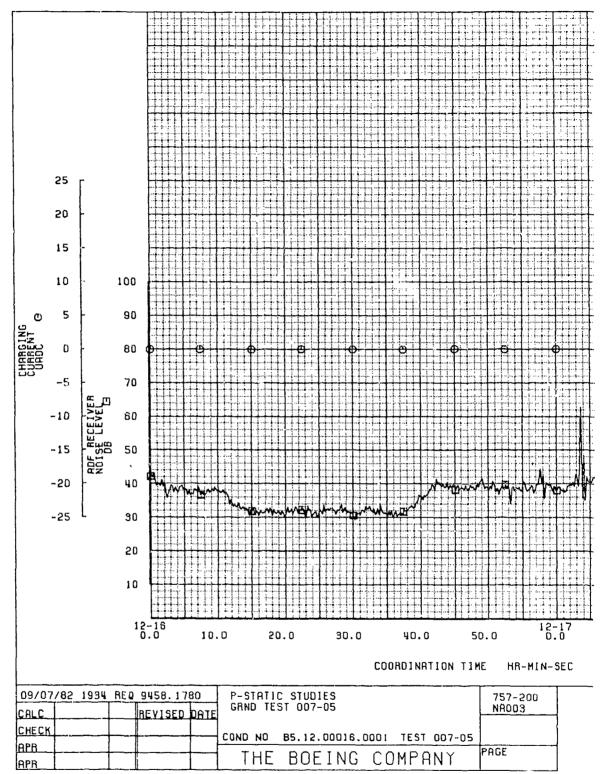




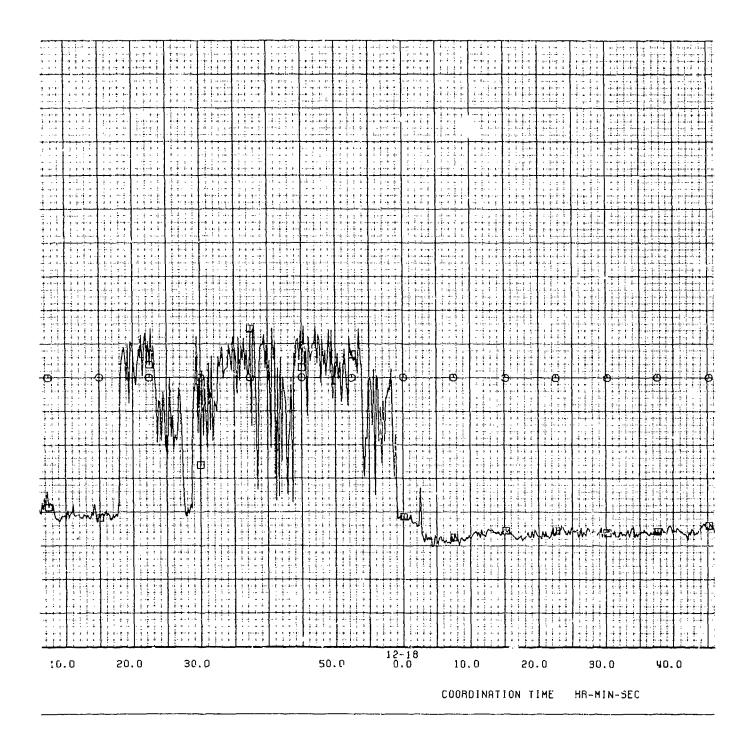
FORMAT 1 P-STRTIC STUDIES



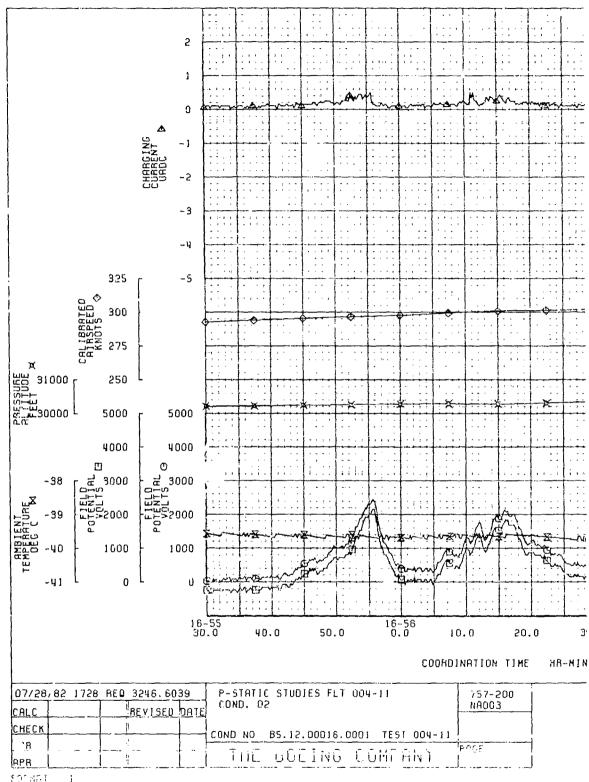
		. [. [. [. [. [. [. [. [. [. [. [. [. [.		ППППП
<del></del>	11111111			
		minimum de la		أماسانية والمرابطة
		<del></del>		+++++++
	<del> </del>		<del>++++++++</del>	
4-1-1-1-1-1-1-1-1-1-1-1-1-1-1-1-1-1-1-1				
	{ <del>                                    </del>		<del></del>	
4				
				المالية استشعابها
		1.1.1 (1.1.1 ) (1.1.1 )		
<u> </u>	<u> </u>			
-3				
	the state of the s			
	1 ( ) . [ ] . [ ] . [ ] .			
	14.4 + + 1 + 1 + 2			



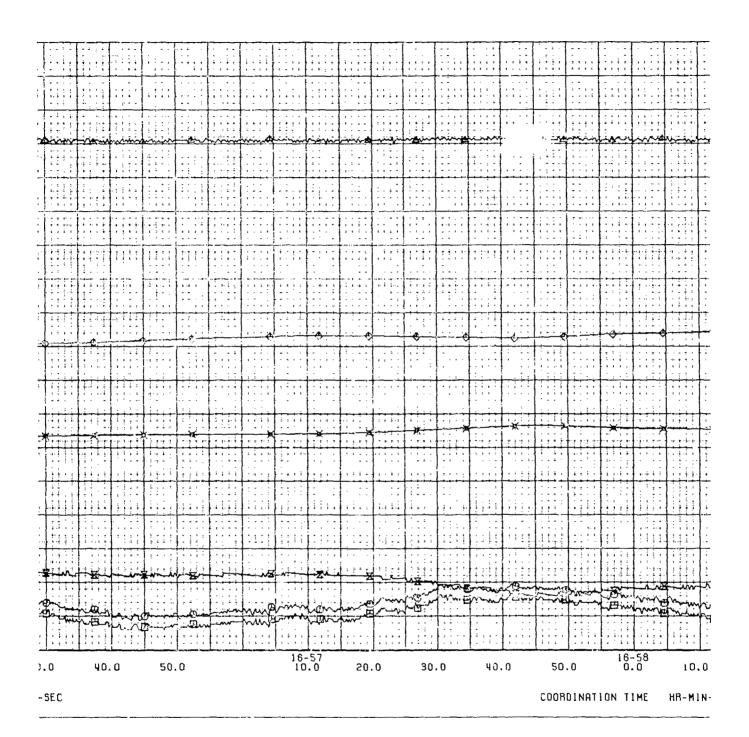
FORMAT 1 P-STATIC STUDIES

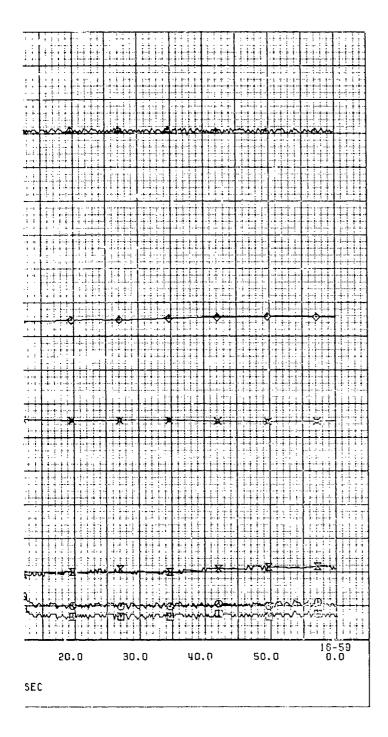


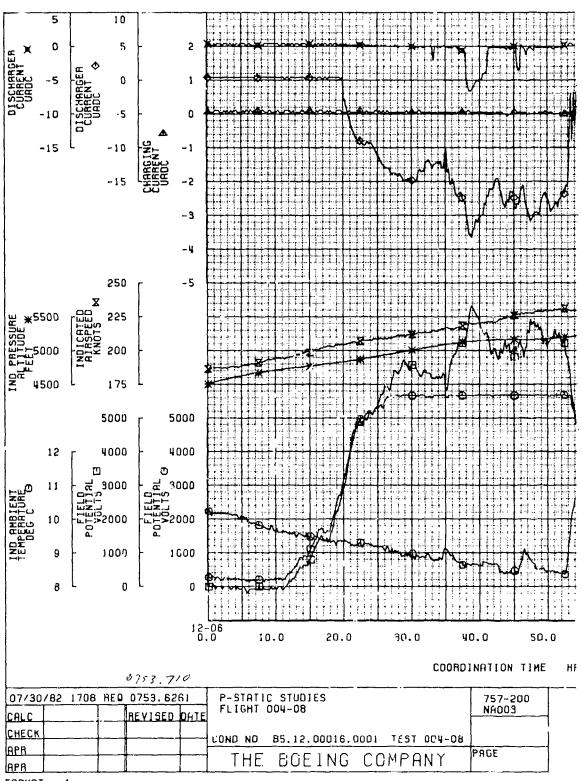
	<del></del> -1								
									·
. ; ; ]						1111	: ' '		
					-				
. , .		`:::.	1::.	1	- :::			1111	2.1
	50 L 1		7.1		111			1.33	
					2.1.1			'	. : "
	. 1 1						7777		
					·		·	•	-
					~				
:	• •	1		- 11		. ::			:
				1 . 2 .	. 177	3	11.1		7 7 7 7
				~					
7 : ]			1111						.311
:[	· ·								
:::			11111	1		3 1 1 1			
	• • • • •	1. 1. 1				1: ::			1:: .
				1 , 2 2		771	1 4 1 7		, , ,
		1		:					[::
						1111		,	
111		1:1:	1			1 1 1 1	::	: : : .	[ ]
	1 1 1 1	1111		1.23	7:11	1::::			} ' , ; ;
		:							
1 1 1		1111		1		1: 1			1:::::
	0		ļ : <u></u>			1::::			
	1::74	1 111	127	1 - 1 1	^ ' ; ;	2 1 1 2	1:1::		
		1111	1 ::::	:::::		:			1
, ,	-	7 4 4 4	1167					E / , 1	, , , , ,
٠.					1 :	1		] : : : .	
	1		1			1	<b> </b>	- ii.	
			1::.:	1.11	] : : ' : :	1 : : :	]	' '	]: '''
: ;			1	1				:::::	11,
	1								
		1.11	11,71		1771	1,11	. :	: : : :	
<u></u>			1	}	1 1 1	ļ <u>.</u>	<u> </u>		
			1::::		]			j : : :	177
Such	1 400	min	]	1711	,:::	1.2 1.2	[ ' : ' '		-:::
	f		1,	1		1	1		
, , ,		1 . ". "	1 ' : : : :		]:::'	1.11	1,	1 : : :	]:::::
<del>+-</del>			ļ	<u> </u>					
:::	.	] - ' ' :	1::::	1:::"			] [ ]	: : : :	1::
: : .	1							1.	17.
		7	1	1		T	T		1:
			11.73	1.11.			1000		1
	L	1	1	<u> </u>	1,	1	_1	L	T
50.	. 0	12: n	-19 .0						
50.		Ü	• •						



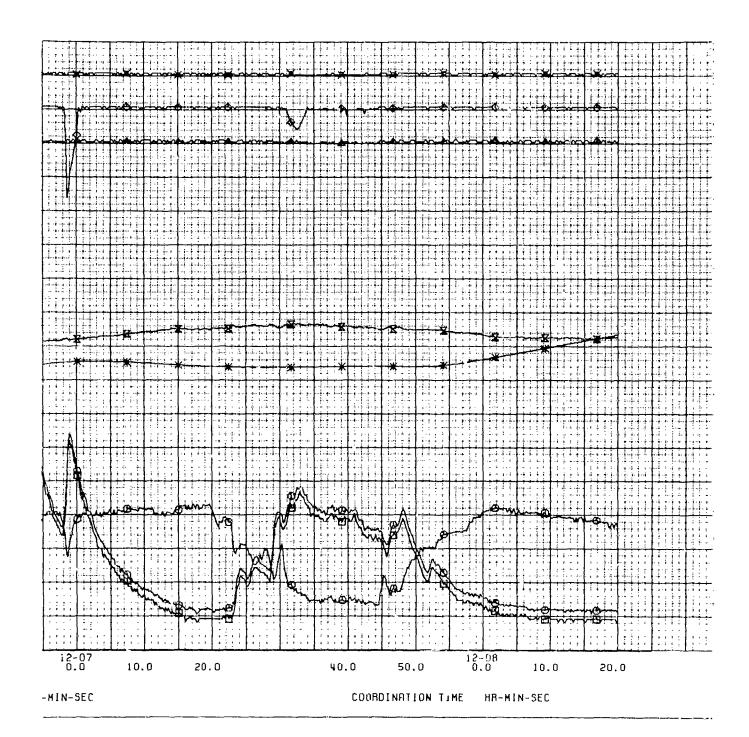
SOTMAT : 1 P-STRITE STUDIES FLIGHT 004-11

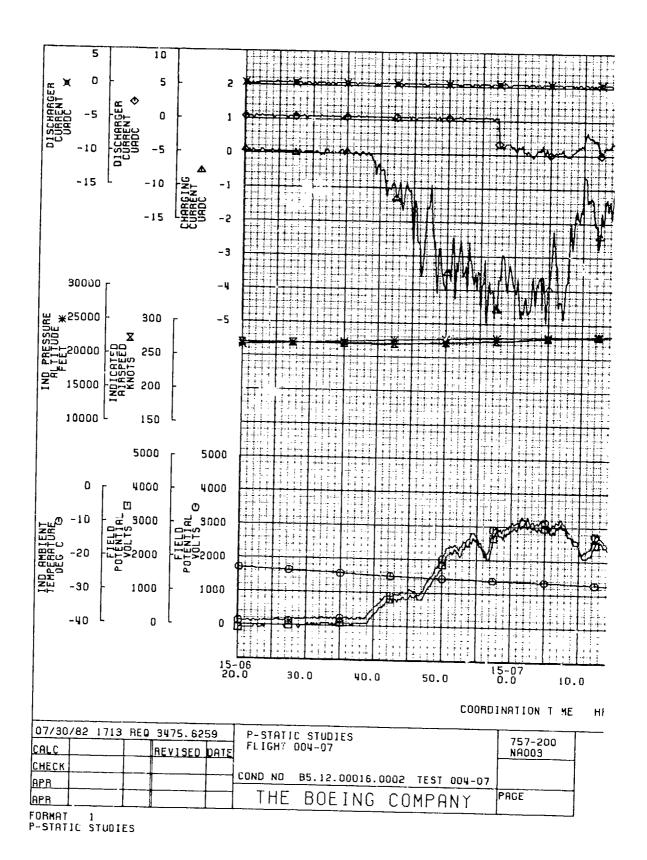






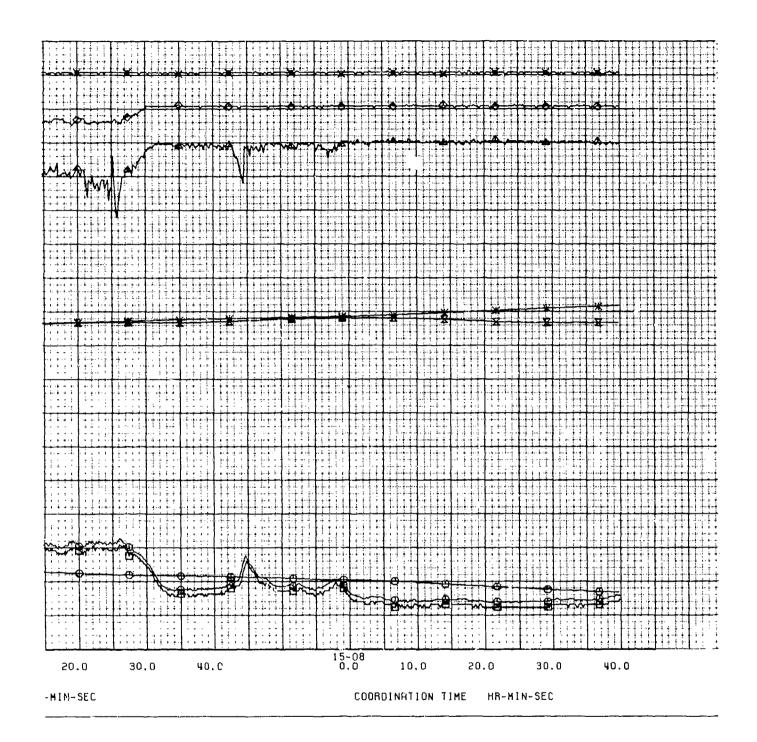
FORMAT 1 P-STATIC STUDIES

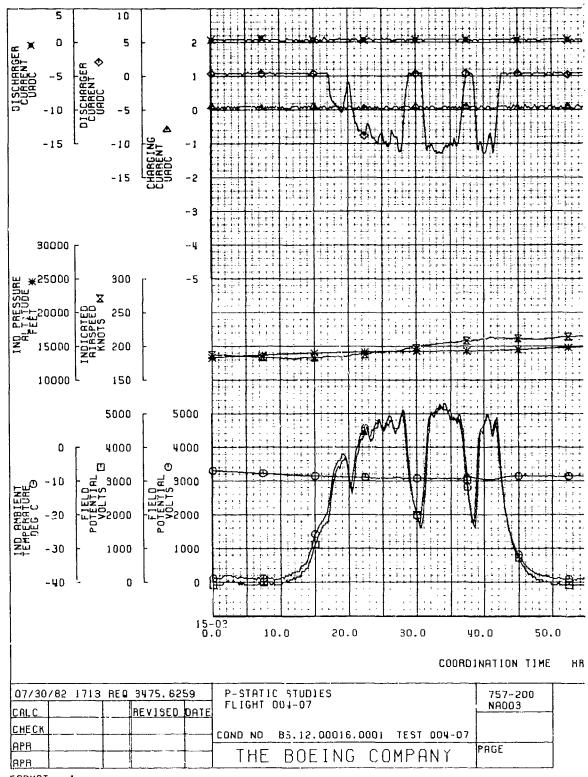




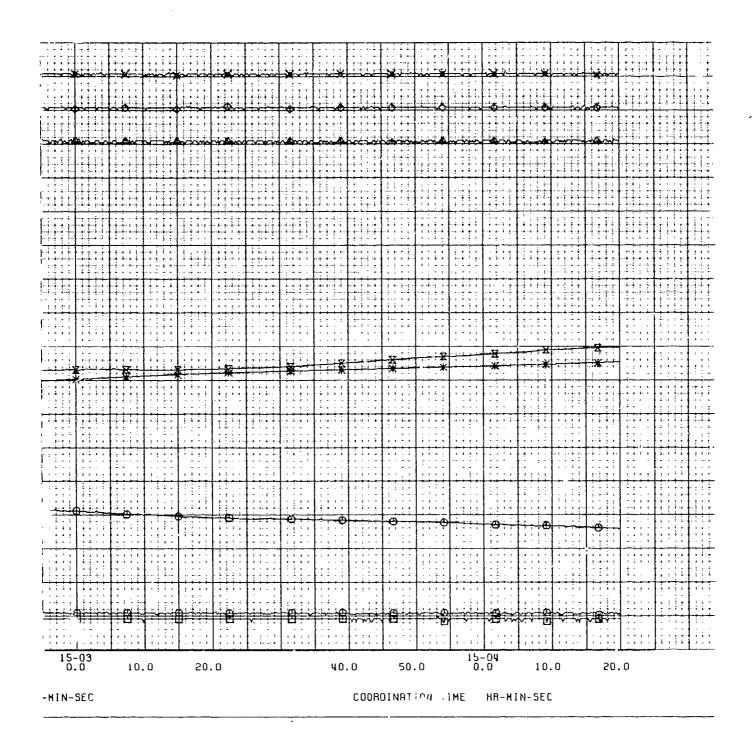
THE RESIDENCE OF THE PROPERTY OF THE PROPERTY

84-40





FORMAT 1 P-STRIIC STUDIES



ELECTRIC CHARGING BY IMPACT OF HAILSTONES AND RAINDROPS

H. Trinks\* and J. L. ter Haseborg\*\*

\*Technical University Hamburg-Harburg, Hamburg, Germany

\*\*German Federal Armed Forces University Hamburg, Hamburg, Germany

ABSTRACT

Hailstones, raindrops, and particles are electrically charged with charge values of  $(10^{-14}~10^{-1})$  As. When the particles strike the surface of aircraft or rockets, charge transfer processes occur. Expecially impacting particles with high velocity generate small clouds of dust or water vapor. This effect is accompanied by strong electric charge separation processes. An impacting hailstone with a primary charge of about  $Q_0 = 10^{-13}$  As generates a secondary electric charge transfer of up to  $Q=10^{-13}$  As. Waterdrops and ice particles were shot against target plates. By electric field measurements and shorttime shadow photographs, the impact processes were investigated experimentally. Model computations were performed.

regarding day

ELECTRICAL CHARGING PROCESSES have been investigated by numerous authors concerning contact electrification when insulators are involved. But the mechanism responsible for charge transfer and the accompanying dissipation processes of air breakdown are still not fully understood. Many of the studies concerning contact electrification are engaged in measuring the charge produced by rolling or sliding contact e. g., between a metal or plastic sphere, and a dielectric sheet. In most cases, the charging processes during long-term lengths of some seconds as well as low velocities between the different materials have been investigated.

The effects concerning the interaction between impacting bodies of various kinds of material during short-time lengths of about lo-loo as accompanied by a strong mechanical disturbance are interesting concerning the charging effects of aircraft in flight through clouds of raindrops and hailstones.

Studies on precipitation static charging have been carried out both in the laboratory and on aircraft in flight - see e.g. (1,2). The charge separation effect and the charge transfer during the impact of hailstones at various velocities were tried to be explained by the Workman-Reynolds effect (3), by thermoelectric effects (4) and finally by inductive mechanism (5). In (2) is suggested that the charge transfer is dependent on the work function of the metal and the surface or contact potential of ice.

The different explanations and mechanism take in account mostly low impact-velocities below 20 ms. However at high velocities up to looo ms. the fracturing of the impacting material e. g. the ice crystals will occur accompanied by heavy charging effects.

To produce strong mechanical interactions under controlled conditions, different targets were bombarded by projectiles, waterdrops and ice crystals simulating hailstones. The charge transfer process was investigated by antennas and electric field measurement systems installed in the vicinity of the breakdown. Additionally the impact process was studied by shorttime shadow photographs.

# EXPERIMENTAL DESCRIPTION

The experimental set-up is illustrated in Fig. 1. Projectiles or accordingly waterdrops or ice bullets simulating hailstones are accelerated by air gun or by similar weapon systems to velocities of about 35 ms<sup>-1</sup> up to looo ms The bullet passes through light barriers, different kind of charge measuring sensors and finally it impacts or penetrates a target plate. During this process the velocity of the bullet is measured. To measure the primary charge  ${\mathbb Q}$  on the projectile or hailstone different electric field sensors are placed parallel to the projectile's trajectory. During the charge  ${\bf Q}$  passes without touching the sensor, the charge  ${\bf Q}$  are induced on the surface of the metal sensors. These effects are observed by charge amplifiers or by a resistor R coupled to the electric field sensors.

As shown in (6,7,8) it is possible to derive the value of the primary charge Q outgoing from the measured electrical signals  $U_R^0(t)$  and  $U_{CA}^{-1}(t)$ . During the impact of the projectile or hail-

During the impact of the projectile or hailstone on the target plate, electrically charged clouds of dust and scraps of material are produced. The electric fields thus originated induce electric charges on the metal sensors placed near the location of the impact. The measured time dependent signals give informations about the impact process itself and about the strength of the accompanied charge transfer.

Additionally to the electric field measurements shorttime shadographs were taken in different moments during the impact process.

#### EXPERIMENTAL RESULTS

In the following some typical examples are shown demonstrating impact processes concerning projectiles, waterdrops and finally hailstones. fig. 2 shows some typical experimental results produced by different types of projectiles while penetrating a metal foil. Electric current on the target was recorded, too. One of the projectiles (cal. 20 mm, v = looo ms<sup>-1</sup>) is illustrated by a short ime shadowgraph which shows the breakdown of the target material.

A special series of investigations under well-defined conditions was performed to clearly understand the physical mechanism of the electric charge separation and the origination of the electric fields. Electric field measurements and shorttime shadowgraph observations were made of the impact of air gun pellets on paper, of ice particles simulating artifical hailstones on different metal targets, and finally of water droplets or water jets on targets. To eludicate the complex and high dynamical impact process some shorttime shadowgraphs are compiled in Fig. 3 and 4. Particularly the clouds of vapor and particles are recognizable which were generated during the impact process accompanied by strong electric charge separation processes.

Fig. 5 represents results of measurements which were obtained by an experimental set-up similar to that shown in Fig. 1. These experiments have been conducted by four different velocities of air gun bullets which penetrate a paper sheet. The signals  $U_{\rm R}(t)$  were registered. The results illustrate, that the exchange of electric charges increases with the intensity of the impact.

Fig. 6 represents results of measurements concerning an artificial hailstone which impacts on a metal target plate. The hailstone is primary charged with  $Q = + 10^{-11}$  As. During the impact process however a charge transfer of  $Q = -10^{-1}$  As to the target plate can be observed by the generation of clouds of dust and water vapor according Fig. 3.

### COMPUTATIONS

A pisysical model of the effects during the impact was developed by computing the electric field distribution under certain assumptions. The theoretical results were compared with the experimental results. In the following one example concerning such computations is explained.

Fig. 7 shows a schematic illustration of a projectile penetrating a target viewed at two different moments. The impact between projectile and target causes partial destruction of the target material. Thus, a cloud of dust particles is generated which expands in the direction of the trajectory. The velocity of the cloud decreases.

The impact and the mechanical destruction of the target material result in an intensive exchange of electric charges between projectile and dust particles. Fig. 7 shows the oscillograms  $U_p(t)$  and  $U_A(t)$ . The signals  $U_p(t)$  and  $\mathsf{U}_{\mathtt{A}}(\mathsf{t})$  wêre derived experimentally using resistor R'and charge amplifier coupled to metal sensors placed near the location of the impact. The negative doublepeak at the beginning of the oscillogram  ${\rm U}_{\rm p}(t)$  marks the penetration through the target and is caused by the top and driving band of the bullet. Contact between bullet top and target, and driving band target both generate dust particles of the target material. Here, the particles are negatively charged. The negative double peak is then followed by that part of the signal produced by the positive charged projectile. When the projectile passes the sensors, the oscillogram  $U_R(t)$  falls to approximately zero and whereas the oscillogram  $U_A(t)$  shows a quasi constant value caused by the decreasing drift velocity of the particle cloud.

Outgoing from the model shown Fig. 7 it is possible to compute the charge Q(t) produced on the sensors and registered as signal  $U_A(t)$ . Q(t) is caused by the projectile charged positively during the impact process and the cloud of negatively charged dust particles. The projectile velocity is assumed to be constant while the velocity for the particle cloud may decrease with time

The following equation is valid:

$$Q = \frac{1}{2\pi} \sum_{i=1}^{n+1} Q_i \left[ \text{arc tan} \frac{(b/2 - y_i) (a/2 - x_i)}{z_i \sqrt{(a/2 - x_i)^2 + (b/2 - y_i)^2 + z_i^2}} + \text{arc tan} \frac{(b/2 + y_i) (a/2 - x_i)}{z_i \sqrt{(a/2 - x_i)^2 + (b/2 + y_i)^2 + z_i^2}} + \text{arc tan} \frac{(b/2 - y_i) (a/2 + x_i)}{z_i \sqrt{(a/2 - x_i)^2 + (b/2 - y_i)^2 + z_i^2}} + \text{arc tan} \frac{(b/2 - y_i) (a/2 + x_i)}{z_i \sqrt{(a/2 + x_i)^2 + (b/2 - y_i)^2 + z_i^2}} + \text{arc tan} \frac{(b/2 - y_i) (a/2 + x_i)}{z_i \sqrt{(a/2 - x_i)^2 + (b/2 - y_i)^2 + z_i^2}} \right]$$

a,b; dimensions of antennas, see Fig. 7.

 $x_i$ ,  $y_i$ ,  $z_i$ : coordinates of the projectile and the dust particles

n: number of the dust particles

 $Q_1$ : projectile charge (positive)

 $Q_2-Q_{n+1}$ : dust particle charge (negative)

The computed and plotted curve  $\rm U_A$  (computed) shows clearly the origin of the particle cloud according to the experimental derived signal  $\rm U_A$  (measured).

By variation of the different assumptions concerning the charged cloud distribution and the drift velocities it is possible to refine the model conception about the impact and the penetrating process.

## CONCLUSIONS

During impact and breakdown processes electrical charged dust is originated and in this connection characteristic electric fields can be observed. It seems that this effect may lead to a further understanding of the physical mechanism concerning contact electrification processes between different kinds of materials interacting with rather high velocities.

Particularly the charging process concerning aircraft flying with velocities of  $v=50-150~\text{ms}^2$  through clouds of hailstones seems to be affected.

The results described are based on a first series of investigations, further experiments and computations must be conducted. In particular investigations are planned concerning the dependence of the electromagnetic radiation effects of the kind of material and of the interacting velocity.

## REFERENCES

- 1.J.E. Nanevicz, E.F. Vance, Ligthning and Static Electricity Conference San Diego (1970)
- J. Caranti, A.J. Illing worth, Lightning and Static Electricity Conference Oxford (1982)
- E.J. Workman, S.E. Reynolds, Phys. Rev. 78, 254-259 (1950)
- 4. J. Latham, B.J. Mason, Proc. Roy. Soc. A 260, 523-536 (1961)
- J. Latham, B.J. Mason, Proc. Roy. Soc. A 266, 387-401 (1962)
- J.L. ter Haseborg, H. Trinks, IEEE, AES-16, No. 2, 227-232 (1980)
- J.L. ter Haseborg, H. Trinks, IEEE, AES-16, No. 6, 750-754 (1980)
- H. Trinks, J.t. ter Haseborg, IEEE, AES-18, No. 3. 268-274 (1982)

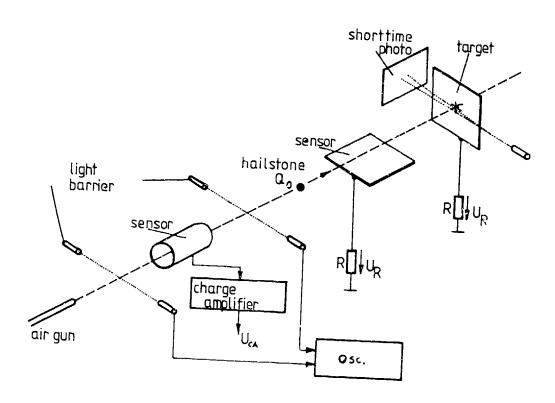


Fig. 1 - Experimental set up

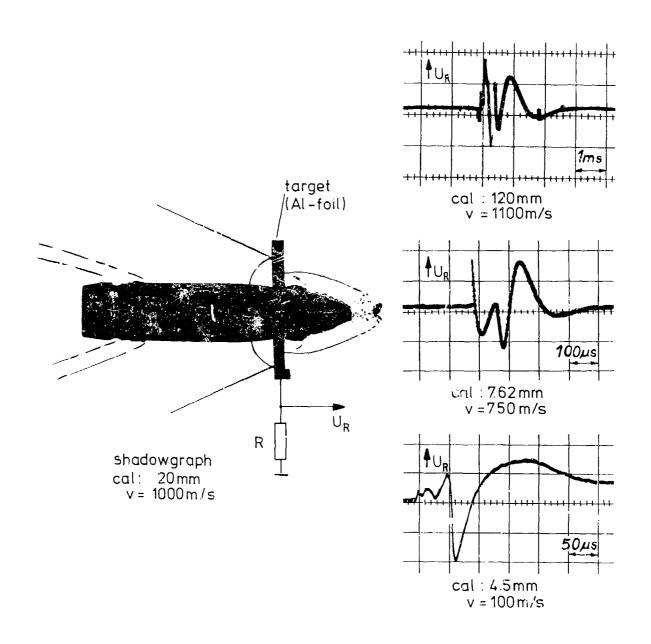


Fig. 2 - Projectiles penetrate a target (AL-foil)

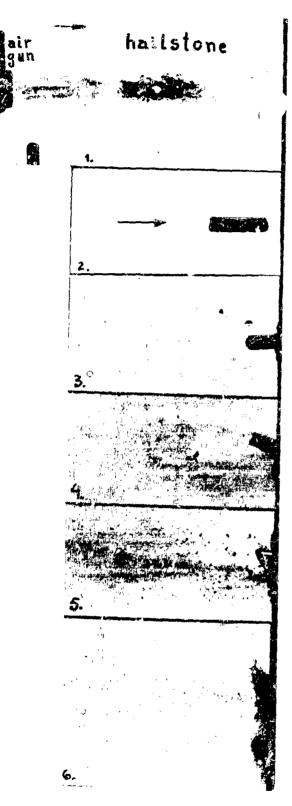


Fig. 3 - An artificial bailstone impacts a target plate (v =  $loo\ m/s$ )

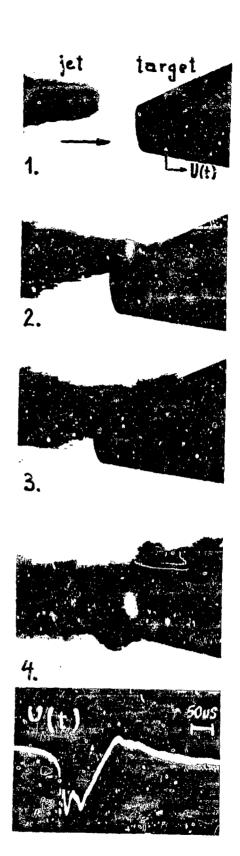
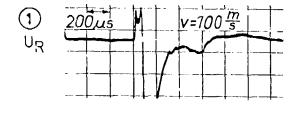
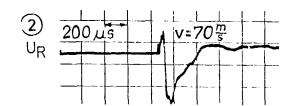
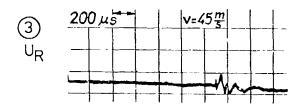


Fig. 4 - A water jet hits on a meta: target surface (v = 1.400m/s)







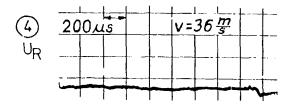
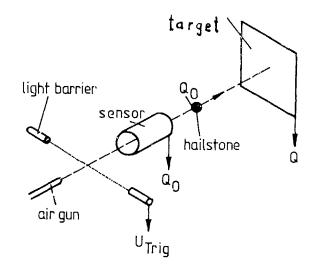


Fig. 5 - Air gun  $\beta$  ellets penetrate a sheet of paper with different velocities



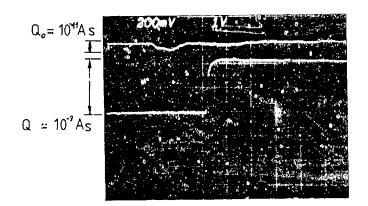
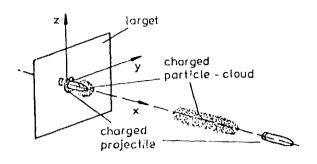


Fig. – An artificial hailstone impacts on a metal target plate and produces charge transfer



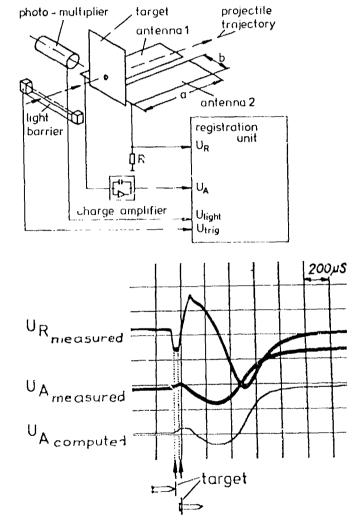


Fig. 7 - Experimental and theoretical results results concerning projectiles or artificial hailstones penetrating a target



THE EFFECTS OF PRECIPITATION STATIC : D LIGHTNING ON THE AIRBORNE RECEPTION OF LORAN-C

James D. Nickum, P.E. Avionics Engineering Center, Ohio University, Athens, Ohio

# ABSTRACT

The results of ground charging tests and airborne biased-discharger flight tests are presented to indicate the p-static noise performance improvement obtained by using static-wick dischargers on an aircraft for the reception of LORAN-C. An instrumented aircraft was flown near areas of thunderstorm conditions to collect data on noise due to p-static discharging. The data indicate that significant improvement in p-static noise reduction is possible by using static-wick dischargers on the airframe to maintain adequate LORAN-C signal-to-noise in p-static discharging conditions.

LORAN-C NAVIGATION EQUIPMENT is finding its way into more and more aircraft as an effective area navigation system. With Loran-C operating at 100 Khz the reception of the signals in the presence of triboelectric airframe discharging noise can cause a degraded signal-to-noise situation. This discharging noise is much less of a problem at VHF frequencies and therefore is less noticeable to the pilot for a given discharging condition. At VLF frequencies the noise produced by p-static discharging is less tolerable.

This paper will outline the results of three types of tests made using a Douglas DC-3 (N7AP) equipped with data collection equipment to measure discharging currents and measure noise generated at 100 Khz to evaluate the improvement that static-wick dischargers provide for Loran-C reception. The three different tests include a ground charging test, a flight test using a biased discharger to simulate in-flight triboelectric charging and flights into natural charging conditions near thunderstorm activity. This work was performed for the Federal Aviation Administration under contract DTFA01-81-C-10007. (1)(2)\*

# GROUND P-STATIC CHARGING TESTS

In order to measure the noise produced by discharging triboelectric charge accumulation on the airframe, a ground test procedure\*\* has been used to simulate the triboelectric charging of an aircraft in flight (3). First, the aircraft is placed in a hangar such that the minimum lateral and overhead clearance is 5 feet (3.05 meters). The aircraft landing gear are positioned on acrylic sheets of at least 0.25 in. (6.35mm) thickness. This is done to insulate the aircraft electrically from ground. As shown in Fig. 1, ion flood fixtures made up of static-dischargers are connected to the high voltage power supply (HVPS) and placed in front of, but not touching the wings. Ion collection fixtures were placed behind the areas of the aircraft where the static-wick dischargers are attached (trailing edges of wings, elevator and rudder), with the ion collection fixtures connected to the opposite polarity of the HVPS through a current monitor meter. The current monitor is always placed in the HVPS line that is at the same

potential as safety ground to simplify current measurements. If the ion flood fixtures are connected to the negative lead of the HVPS and the ion collection fixtures are connected to the positive lead of the HVPS, then negative-point corona will be produced at the tips of the static-wick dischargers mounted on the aircraft. By interchanging the HVPS connections, positive-point corona car also be produced. In the results illustrated in the ground charging data, both positive-point and negative-point corona were considered.

To measure the current that flows through aircraft-mounted dischargers, each mounting base was insulated from the airframe and a single wire returned to the cabin area from each discharger mounting plate. Each wire was connected to a 10k current-sensing resistor with the opposite end of the resistor grounded to the airframe. The voltage across each resistor is instrumented and represents 10 mv per microampere (µA) of discharger current. Each of the 12 dischargers on the aircraft was instrumented in this way and recorded on the data collection system. Fig. 2 indicates the placement of the 12 instrumented dischargers for all of the tests described. The noise amplitude above the ambient at  $100\ \mathrm{Khz}$ , as measured by the EMC-25,\* was recorded along with the output of a field mill calibrated to measure aircraft potential. All this data was recorded for later data reduction. To assure that all of the charge that was placed on the aircraft by the ion flood fixtures was removed by the ion collection fixtures, the total current measured on board the aircraft, leaving through the dischargers, was compared by the current monitor placed in the HVPS lines. In all of the tests conducted, the two currents agreed within a few uA even at high current levels. Further, in order to determine if currents are leaking across the surface of the acrylic sheets, a metallic guard ring was placed across the top perimeter of the sheet with this connection returned to a sensitive ammeter. If any current were to leak across the surface, this meter would detect the current flow.

The ground tests were conducted by gradually increasing the voltage on the HVPS over a period of 3 to 5 minutes until a discharge current of 700 to 750  $\mu$ A was observed on the current monitor. During this time, the data collection equipment on board the aircraft recorded all data as described above. The ground charging tests included corona points and two different manufactured

<sup>\*</sup> Numbers in parentheses designate References at end of paper.

<sup>\*\*</sup>Patent Application Pending, R. L. Truax, TCO Manufacturing Corp., Ft. Myers, FL.

<sup>\*</sup> Electro-Metrics EMC-25 Interference Analyzer used with a 1/2 meter whip antenna and coupler mounted on underside of DC-3 aircraft.

types of static-wick dischargers. The corona points were used to determine the worst case noise situation for aircraft p-static discharging. The noise vs. discharge current performance with the manufactured static-wick dischargers was very similar; therefore, the results using only one of the dischargers will be demonstrated. Both of the discharger types and the corona points were tested in both positive-point and negative-point corona.

Fig. 3 indicates the noise levels obtained by using the corona points as  $\frac{1}{2}$ dischargers for both positive- and negativepoint corona. Notice the very rapid rise in the noise levels for relatively small discharger current levels. Essentially, the noise begins promptly at the point where corona begins and rises very quickly for both positive- and negative-point corona. This demonstrates quite well the noise problems encountered by aircraft not properly equipped with static-wick dischargers, especially if the aircraft is using Loran-C or Omega for navigation. These graphs indicate that noise levels can approach almost 40 db above the ambient noise levels at 100 Khz for 100  $\mu A$ discharge rates. This could very easily swamp a good signal-to-noise level for Loran-C reception and completely eliminate otherwise usable reception. Note also that negative-point corona seems to reach a maximum 'level at approximately 33 db, but that positive-point corona also rises very rapidly then continues at a fairly linear rate. The reason for the differences in the behavior is not fully understood, but these trends have been noted by other investigators (4). Positive-point corona appears to be a much more energetic process than negative-point corona with negative-point corona more common in triboelectric charging of the airframe. Positive-point corona can be induced on the airframe in flight near thunderstorm activity where the aircraft encounters areas of highstatic fields that can charge the aircraft depending on its location relative to these charged clouds.

Using static-wick dischargers can improve the noise performance as indicated by Fig. 4. These data, taken from the ground tests, indicate that for negative-point corona, a noise rise above ambient of 6 to 7 db will result, even at high charging rates of 700  $\mu \, \text{A}_{\odot}$ . This is a significant decrease as compared to noise generated by the corona points. There is also an improvement in positive-point corona noise performance as indicated by the data in Fig. 4 compared to Fig. 3. In comparing the noise level of the corona point in Fig. 3 to that of the discharger in Fig. 4, a reduction of

approximately 28 to 30 db is achieved for positive-point corona.

The sudden rise in noise level at approximately 250  $\mu$ A is due to a problem in the instrumentation, but jumps in noise levels have been observed in the past when testing with positive-point corona.

As can be seen from the material presented so far, the reduction in corona discharge noise when using static-wick dischargers is not trivial. With the proper testing, any airframe can be improved with respect to corona discharge noise performance. This improvement is especially necessary if the aircraft is equipped with Loran-C or Omega for navigation.

#### BIASED DISCHARGER FLIGHT TESTS

The procedure used to perform p-static charging flight tests in clear air involves equipping the aircraft with a biased discharger. Fig. 5 illustrates how the biased discharger is installed on the aircraft. Essentially, the setup involves mounting four static-wick dischargers on an insulated rod approximately 12 inches (30.5 cm.) long mounted on the tail of the aircraft. One of the HVPS leads is connected to the dischargers and the other grounded to the airframe. As the HVPS potential is increased, an electric field results between the dischargers and the airframe, causing ions to be formed at the discharger tips. If the aircraft were stationary, the ionized molecules would try to follow the lines of electric field back to the aircraft, but since the aircraft is moving through the air, the ions are swept away from the aircraft leaving the airframe with a net charge. In all of the biased discharger tests, negativepoint corona was produced at the biased dischargers which produces positive-point corona on the airframe static-wick dischargers.

All of the biased discharger tests performed were conducted along a closed course in the southeastern Ohio area and were conducted in clear weather conditions. potential of the HVPS for the biased discharger was increased in 5 Kv steps from 0 to 65 Kv over a period of 16 minutes. At the end of the data run, the supply voltage was reduced to 0 and another 2 minutes of data taken. This method produced a stepped ramp of biased discharger potential that causes the airframe to discharge as if flying into triboelectric charging. Fig. 6 indicates the envelope of 95% of the noise vs. current data points for the aircraft equipped with corona points as dischargers. This graph indicates the worst case noise examples for the biased

discharger tests, to which the static-wick dischargers will be compared. It can be seen that the aircraft was discharging a maximum of 7 to 8 db above the ambient moise level. The corona points did not begin discharging current until the biased discharger voltage was increased to 20-25 Kv.

The aircraft was then outfitted with static-wick dischargers in place of the corona points and the flight test resumed. Fig. 7 indicates the envelope of 95% of the points for this test. The noise plot of Fig. 7 indicates no significant rise in the noise level. The biased discharger voltage for the start of discharge current was 15 Kv which was less than for the test with corona points. This demonstrates some of the mechanisms employed in designing static-wick dischargers to reduce corona noise by reducing the potential at which the corona discharge begins, thereby reducing noise levels (5). The discharge current levels experienced in the biased discharger flight tests are indicative of the levels that could be expected in a small aircraft operating in light p-static charging conditions. The noise reduction, even at these low discharge current levels, are enough to maintain a low background noise level for Loran-C reception.

# NATURAL CHARGING FLIGHT TESTS

Several flight tests were conducted in the vicinity of thunderstorm conditions to determine the effects, if any, of p-static discharge noise and sferics noise generated by these conditions on the reception of Lorar-C. One particular flight indicated some interesting results. The flight was made along the same closed route used in the biased discharger flights. For all of the natural charging flights, the biased discharger was not used. The aircraft was equipped with a TI-9900, Loran-C receiver that has the capability of providing digital position data for recording during the flight. Fig. 8 is a plot of the ground track data of the TI-9900 as recorded during this flight. The flight was conducted during cold frontal passage through the southeastern Ohio area, generating thunderstorm activity throughout the area of flight. After takeoff, the data collection system was started at the point indicated in Fig. 8. Figs. 9, 10 and 11 are data plots for noise vs. discharger current, noise vs. time and discharger current vs. time, respectively, from the test. The times referred to in Figs. 10 and 11 are relative to the data collection start time in occasis indicated in  seconds, after which the TI-9900 then reacquired the Loran-C stations. Again at 2280 seconds track was lost for 2 minutes. During these lost track times, the aircraft was encountering heavy rain with lightning around and above. Fig. 10 indicates that during those times significant noise was being generated by the high discharge currents indicated by Fig. 11. This noise level persisted long enough to cause the TI-9900 to lose lock on the received Loran-C stations used for navigation output.

Fig. 9 indicates the envelope of plot points of noise vs. discharge current. This plot is of interest because it illustrates the difference in characteristics of the noise levels generated by negative-point and positive-point corona and supports the data taken in the ground charging tests. Notice the trend toward higher noise levels for a given discharge current in the positive-point corona case as compared to the negative-point case. Referring back to the results of the ground charging tests (Fig. 4), this same trend is observed. The explanation for the high noise level (in Fig. 9) for zero discharger current is that the EMC-25 interference analyzer also responds to the sferic noise occurring near the aircraft due to the thunderstorm activity.

One additional problem that could produce increased noise during this test was that sometime during the flight, the two dischargers mounted on the left elevator were lost from the aircraft. In examining the discharge current data for each discharger as recorded, the currents through these two dischargers stopped at approximately 1625 seconds. It is not clear that this was the actual time the dischargers separated, but there was very little discharge current at those discharger positions after that time.

Some other interesting observations can be made with regard to Fig. 11. Note that at approximately 1600 seconds there is a large current excursion from discharging negativepoint corona to discharging positive-point corona in a relatively short time. This is characteristic of the type of airframe charging encountered near thunderscorm activity. The aircraft is moving through ereas that have significant potential differences causing the aircraft to accumulate one polarity of charge then moving into an area of opposite charge causing the aircraft to discharge and charge to the new potential. It is even possible for the dischargers on one wing to discharge positive-point corona while the other wing is discharging negative-point corona. As the figures presented here indicate, the problem of aircraft p-static discharging near thunderstorm conditions

is a very dynamic situation with the ability to produce noise due to p-static airframe discharging along with the sferic noise associated with the thunderstorms.

#### SUMMARY

With more and more aircraft being operated in instrument meteorological conditions and the increasing use of Loran-C on boald these aircraft, the noise produced by airframe triboelectric charging needs to be minimized to assure adequate signal-to-noise environments.

This paper has presented data collected during three different test situations to obtain information regarding both controlled and actual p-static charging conditions. The ground p-static charging tests provided insight into the controlled relationship of discharge current and the noise produced at Loran-C frequencies. It was shown that the use of quality static-wick dischargers can produce significant reductions in the p-static discharge noise for the positive-point corona as well as the more common negative-point corona.

The blased discharger flight tests allowed another controlled examination of the improvement of p-static discharge noise using static-wick dischargers in actual flight conditions. The results obtained in the flight tests supported the data collection from the ground charging tests.

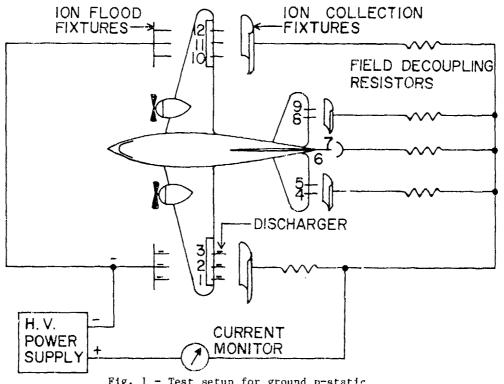
Finally, flight tests performed in actual p-static charging conditions near thunderscorm activity clearly indicate the magnitude of the problem. The effect noise, along with the p-static discharge noise, can cause problems for Loran-C equipment but with proper p-static wick dischargers placed on the aircraft, the effects of the p-static noise can be reduced.

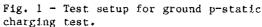
Additional work should involve more flights near thunderstorm activity to build a better data base on which to provide static-wick manufacturers and airframe manufacturers the necessary information to build the best equipment to make the aircraft quiet enough for the use of Loran-C in triboclectric charging conditions. The increased use of Loran-C for navigation in instrument meteorological conditions will indicate the need for more research in this area.

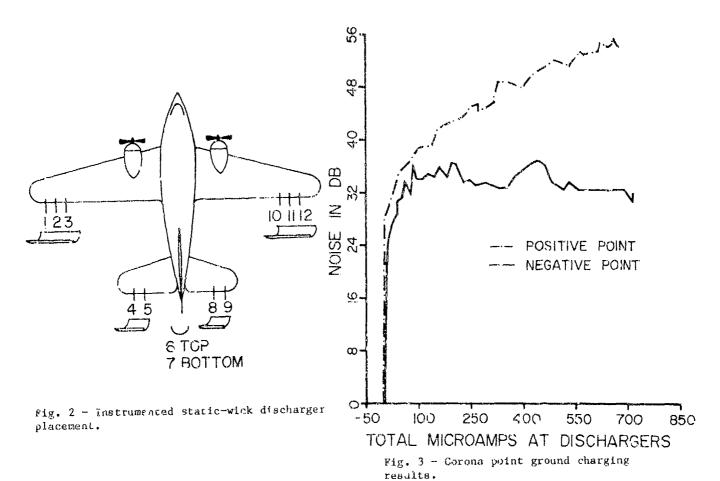
# REFERENCES

- 1. J. D. Nickum, "The Effects of Precipitation Static and Lightning on the Airborne Reception of Loran-C." Final Report, Volume I: Analysis, FAA Contract DTFA01-C-83-10007, April 1982.
- 2. J. D. Nickum, "The Effects of Precipitation Static and Lightning on the Airborne Reception of Loran-C." Final Report, Volume II: Appendices, FAA Contract DTFA01-C-83-10007, August 1982.
- 3. R. L. Truax, "Dielectric Electrostatic Charge Reduction." Paper \$10571 presented at Business Aircraft Meeting, Wichita, Kansas, April 1981.
- 4. R. L. Truax, "Electrostatic Charging and Noise Quieting." Paper 700926 presented at SAE Lightning and Static Electricity Conference, December 1970.
- 5. R. L. Tanner and J. E. Nanevicz, "Precipitation Charging and Corona-Generated Interference in Aircraft." AFCRL 336 technical report 73 under Contract AF 19(604)-3458, Stanford Research Institute, April 1961.

いるというできない。これはいいないできない。これではいいできない。







88.6

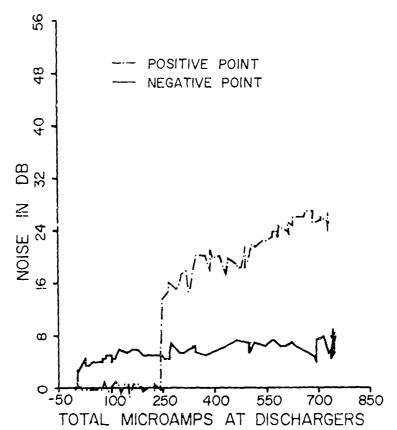


Fig. 4 - Static-wick ground charging results.

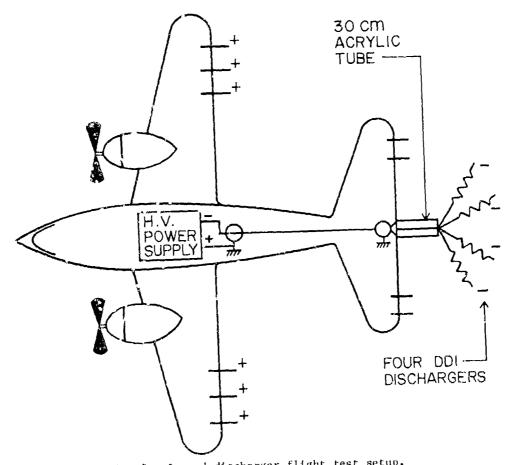


Fig. 5 - Brased discharger flight test setup.

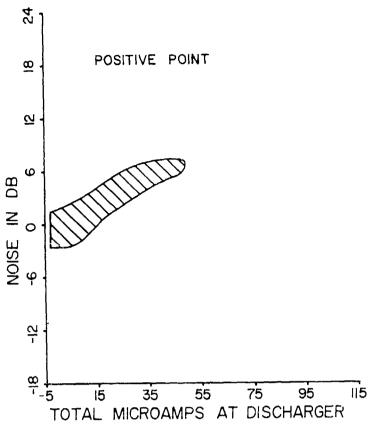


Fig. 6 - Corona point, biased discharger noise flight test results.

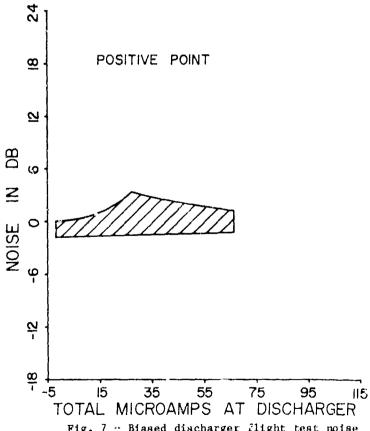


Fig. 7 " Biased discharger flight test noise results using static-wick dischargers.

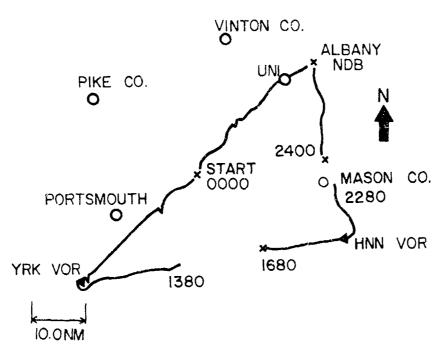


Fig. 8 - Loran-C ground tr...k, actual weather flight test.

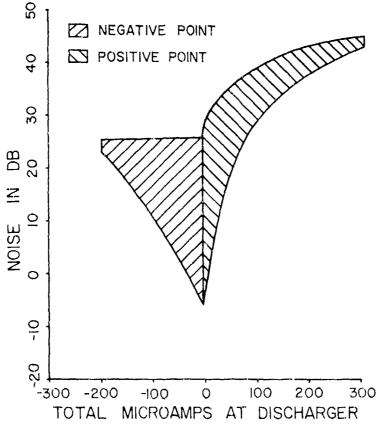


Fig. 9 - Noise vs. current results for actual weather flight test.

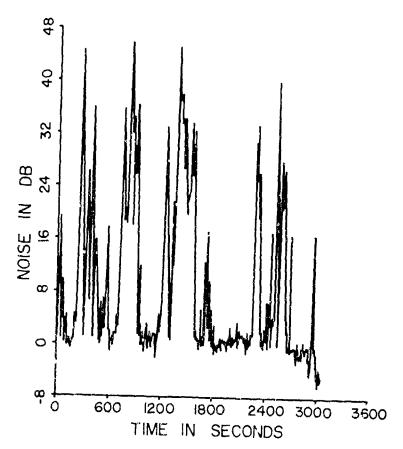


Fig. 10 - Noise vs. flight track time, actual weather.

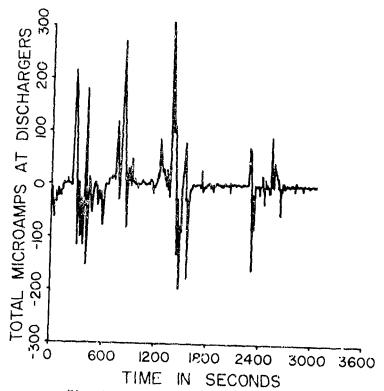


Fig. 11 - Total microamps vs. flight track time, actual weather flight test.

# AD P002232

DIGITAL SYSTEM UPSET--THE EFFECTS OF SIMULATED LIGHTNING-INDUCED TRANSIENTS ON A GENERAL PURPOSE MICROPROCESSOR



Celeste M. Relcastro NASA-Langley Research Center Hampton, Virginia

#### ABSTRACT

Flight-critical computer-based control systems designed for advanced aircraft must exhibit ultrareliable performance in lightning-charged environments. Digital system upset can occur as a result of lightning-induced electrical transients, and a methodology has been developed to test specific digital systems for upset susceptibility. Initial upset data indicates that there are several distinct upset modes and that the occurrence of upset is related to the relative synchronization of the transient input with the processing state of the digital system. A large upset test data base will aid in the formulation and verification of analytical upset reliability modeling techniques which are being developed.

#### INTRODUCTION

ADVANCED AIRCRAFT of the 1990's will be designed with composite structures and computer-based digital control systems capable of performing flight-critical functions. These digital systems will be required to be ultrareliable whether the aircraft is flying through a normal or adverse environment—such as a thunderstorm. There is, therefore, a need for a better understanding of the inflight lightning—charged environment as well as the development of techniques for assessing the performance/reliability of digital systems on composite aircraft in that environment.

When an aircraft is struck by lightning, exterior electromagnetic fields are formed that are dependent on the geometry and structural material of the aircraft. These exterior fields are coupled to the interior of the aircraft causing transient voltages and currents to be induced on electrical cables throughout the aircraft. Onboard electronic equipment are subjected to the analog electrical transients that manage to propagate to interface circuitry, power lines, etc., despite shielding and protection devices (1)\*.

Lightning-induced electrical transients can impair the operation of digital systems by either damaging components or by causing functional error modes -- or upsets -in which we component damage is involved. Digital system upset is permanent in that it requires corrective action, such as resetting the system or reloading the software, to restore normal system function. Upset can be viewed from a hardware or software perspective. The hardware viewpoint is in terms of logic states, whereas the software viewpoint is in terms of program flow. There has been some ongoing work for several years to predict erroneous loop program execution using linear difference equations (2). However, there are no standard guidelines or criteria for performing upset tests or analysis of digital systems.

This paper describes a methodology whereby a microcomputer is tested in the laboratory for its susceptibility to entering upset modes and presents data obtained to date. The objectives of these tests are to investigate the statistical

nature of digital system response to analog transients and to verify potential analytical techniques for generating upset statistics for use in upset reliability models. An analytical approach for generating such statistics is based on the utilization of a special-purpose computer specifically designed to emulate and perform error mode diagnostics on a target computer (3). Once these statistics are generated and an upset model is designed, a reliability prediction can be made for the performance of the target computer, assuming that lightninginduced transients have entered the system. This reliability prediction could be generated by using existing reliability estimation programs, such as the ComputerAided Reliability Estimation code, CARE III (4). In order to predict the reliability of the target system on an aircraft flying in a lightning-charged environment, in-flight data is needed to aid in defining the characteristics of that environment. This data is currently being obtained by tests in which a specially-instrumented aircraft is flown through thunderstorms to illicit lightning strikes (5). This lightning data, as well as data obtained through upset testing described in this paper, will aid in providing a basis from which analytical reliability prediction techniques can evolve.

# UPSET TEST METHODOLOGY

The digital unit under test is the Intel Intellec 8/Mod 80 microcomputer. It is based on an 8080 microprocessor and was chosen because it is a typical, generalpurpose microcomputer and comprises a small enough network to facilitate instrumentation. A simplified block diagram of the digital unit under test is shown in Figure 1. The analog electrical transients being input into the digital unit under test are designed to model voltages and currents that are likely to be induced by electromagnetic fields in a lightning-charged environment; the waveshapes are based on those recommended for direct application to electronic equipment pins by avionics subcommittee AE4L of the Society of Automotive Engineers (6). These waveshapes,

<sup>\*</sup>Numbers in parentheses designate References at end of paper.

shown in Figure 2, are representative of lightning-induced voltages and currents and it is recommended that both positive and negative polarity versions of the waveforms be applied to the test unit. The amplitude of these waveforms is restricted, in this case, by the damage threshold of components within the unit under test. The analog transients are input into the digital unit under test randomly with respect to time and with respect to internal processing state of the unit being tested. Randomness is desired so that transient signal inputs are not synchronized with processing activity -thus, more realistically simulating the random process that might take place in the actual lightning-charged environment. Upset statistics collected under these conditions will enable statistical cross-tabulations to be made and will enhance a stochastic upset model in which digital system response to lightning-induced transients is modeled statistically.

The upset test hardware configuration shown in Figure 3 is based on comparison monitoring of two identical Intel microcomputers that are synchronized and executing the same program code concurrently. One microcomputer, the unit under test, is perturbed by analog electrical transients while the second one serves as an unperturbed reference unit. Thirty-two of the forty pins from each microcomputer's central processing unit (CPU) are compared via error detection circuitry, in a bitwise fashion. These lines include the 8-bit bidirectional data bus, the 16-bit address bus, and eight CPU control lines. The analog electrical transients are generated when a relay is opened causing a capacitor in an RLC circuit to discharge; closing the relay causes the capacitor to again become charged, which is required for generating another transient signal. The random generation of the electrical transient is provided by circuitry that controls the opening and closing of the relay independently of either the unit under test or the reference unit. Transient signals can also be generated in a free-running manner in which the time between transients varies pseudo-randomly from about 5 seconds to 1.5 minutes with a resolution of approximately 350 ms. This time interval between transients can be adjusted and was chosen somewhat arbitrarily. The lower limit of 5 seconds, however, was chosen to provide enough time for a program of moderate size (about 500 instructions) to be executed in a continuous loop at least 1000 times. It is assumed that if the unit under test can correctly execute the program code 1,000 times, once the transient signal has entered the system, then an error due to that transient signal will probably not occur. If no

error is detected, the electrical transient is again input to the unit under test. If an error is detected, no more transient signals are generated, error data is recorded, and the test is finished.

The error data being recorded is obtained from the CPU lines that are monitored from the unit under test. These data comprise the memory addresses accessed, instructions fetched from memory, CPU data input/output (I/O),, eight CPU control signal logic states during CPUmemory data bus transactions, and the CPU status signal. The status signal is output onto the data bus by the CPU to identify the subsequent machine cycle. The 8080 microprocessor machine cycles and corresponding 8-bit status signals are shown in Table 1.

In order to statistically evaluate the effects of analog transients on the unit under test, data is generated and recorded to provide a means of determining the CPU processing state when each electrical transient was input into the test unit. This data is obtained using a 28-bit counter that is clocked by  $\mathfrak{D}_1$  from the reference unit. Since processing activity is organized in the 8080 as shown in Table 2 (7), a count of the number of clock cycles that occur between transient signal inputs can be used to determine the instruction, machine cycle, and machine cycle state in progress when each transient input occurs. The clock cycle count is initialized when the microcomputers begin executing the program code. When the electrical transient is input into the unit under test, the clock cycle count is latched, the counter is reinitialized, and the clock cycle data is recorded. This process continues until an error is detected. Once the detection of an error occurs, the number of clock cycles that clapsed since the electrical transient was input into the test unit is latched, and the error data described previously is recorden.

Clock cycle data and error data are recorded on 8 x 8K bit nonvolatile raniom access memory cards. After each test is completed, the data on these memory cards is transcribed for permanent record onto magnetic tape and become data files. The data in these files is then processed using a specially written FORTRAN program. Error data from the CPU data bus, address bus, and control lines of the unit under test are disassembled, formatted, and listed so that concurrent activity on these lines can be tracked. Clock cycle data is used to calculate the 8080 instruction, machine cycle, and machine cycle state in progress when each transient signal was injected and when the error was detected.

Upset tests completed to date have been performed utilizing a 1-MHz damped sinusoid of negative polarity as the perturbing electrical transient. No provisions have been made, at this time, to achieve the rise time of the S.A.E. recommended waveform. During each individual test, the analog transient signal was input on a single line in the unit under test, rather than on multiple lines throughout the unit. The program being executed in a continuous loop by the microcomputers during each test is shown in Table 3; the machine cycle, machine cycle states, and control signal corresponding to each instruction are indicated. The program causes data byte (CB)<sub>16</sub> to be retrieved from random access memory location (0011)<sub>16</sub> and input into the accumulator register of the CPU. The data byte is then stored in random access memory location (0023)<sub>16</sub>. This program is extremely simplistic and was chosen to minimize the number of processing states to which the input of electrical transients could be correlated in a statistical analysis. Minimizing the number of processing states reduces the amount of data needed for a statistically significant data base. Thus, a precursory analysis can be performed in a relatively short period of time to determine whether or not a correlation may exist.

The transient signal has been input into the unit under test 1101 times on lines MDI<sub>0</sub>, MDI<sub>3</sub>, and MDI<sub>7</sub> of the input data bus. DB of the output data bus, D of the bidirectional data bus, and MAD of the memory address bus. Thirty-five of these of the analog transient inputs caused the unit under test to exhibit anomalous behavior, and in 30 of these cases the system was upset. The remaining five cases involved errors that have been termed as benign. Benign errors include contaminated data, temporary divergence from correct program flow, and slight instruction changes that do not prevent the system from performing the desired activity. Data recorded during the 30 tests in which the unit under test was operating in an upset mode can be categorized into three types. Type I upset data is characterized by the CPU data bus, and sometimes the address bus and/or control lines, being "stuck" at some valid or invalid equence. Type II upset data indicates that the CPU of the unit under test was "babbling" erroneous information on the data bus, control lines, and usually the address bus as well. Table A of the appendix shows Type II upset data. Type III urset data suggests that the CPU exhibits a

pattern of behavior during which it completes several program cycles correctly and then "babbles" or becomes "stuck" during several cycles. The amount of processing activity, such as CPU-RAM interaction, taking place during each upset mode is yet to be determined. The number of times that the transient signal was input on each line in the unit under test as well as the corresponding number of anomalies, benign errors, upset modes, and upset types detected are shown in Table 4.

Several general observations can be made from the upset data recorded thus far. Eight-bit signals are input into the CPU during some instruction fetch cycles that do not correspond to instructions in the test program or even represent the op-code for any of the 8080's 244 instructions. Similarly, the CPU issues status signals that do not correspond to the machine cycles which constitute execution of the test program and often do not signify any of the ten 8080 machine cycles. The CPU also issues signals on the address bus which represent memory locations in RAM other than those that should be accessed during execution of the program, memory locations in ROM, and sometimes locations outside the boundary of available hardware. In addition, control signals are issued by the CPU that either should not occur during execution of the test program or that should not occur during CPU-memory data bus transactions. This undefined CPU activity has not yet been investigated. In 18 of the 30 upset cases recorded, normal function was restored by resetting the system. In the remaining 12 cases, some or all of the memory locations allocated for the test program were overwritten requiring that the program be reloaded and initialized to restore normal system function. This information, as it relates to the number of upsets detected and the number of times the transient was input on each line of the unit under test, is included in Table 5.

The data base obtained to date is insufficient for performing a comprehensive statistical analysis to determine if the occurrence of upset can be correlated to the 8080 processing state in progress when the analog transient signal is input into the system. Nonetheless, several rudimentary cross-tabulations were performed in which the number of observed upsets was arranged in contingency tables with several processing state subdivisions and the occurrence or nonoccurrence of upset as the random variables. The initial hypothesis being tested by each cross-tabulation is that the occurrence of upset is equiprobable for each processing state in progress when the electrical transient was input into the system.

Calculating the chi-square statistic and comparing it to the appropriate value of the chi-square distribution decermines whether or not the initial hypothesis should be rejected (8). Since the occurrence, rather than nonoccurrence, of upset is of primary interest, the chi-square statistic for the data in each contingency table was calculated using only the number of upsets observed and the number of upsets that would be expected to occur under the initial hypothesis for each processing state. An assumption that is implicit in the chi-square calculation for the data in each contingency table is that upset occurred with equal probability for each transient signal input point that yielded an observed upset. This assumption cannot be tested at this time due to the small quantity of data that has been obtained thus far. Tables 6-10 show the nurver of observed upsets, the number of upsets expected under the initial hypothesis, the calculated chi-square statistic, and appropriate values of the chi-square distribution as applied to various processing levels. Since the calculated chi-square statistic for the data in contingency Table 6 is less than the value of the chi-square distribution for an  $\alpha = 0.10$  level of significance, the initial hypothesis-that the occurrence of upset is equi-probable when the transient signal is input during execution of any instruction of the test program--cannot be rejected. On the other hand, the calculated chi-square statistic for the data as arranged in contingency Tables 7, 8, and 9 for various machine cycle categories indicates that the initial hypothesis of there being an equal probability that upset will occur when the transient signal is input during the various machine cycles, irrespective of the assoclated program instruction being executed, can be rejected at an  $\alpha = 0.005$  level of significance. This level of significance means that the probability of having rejectad the initial hypothesis when, in actuality, it should not be rejected is 0.005. Rejecting the initial hypothesis for the data in contingency Table 7 cam primarily be attributed to the much smaller than expected number of observed upsets that occurred when the transient signal was input during memory write machine cycles. Rejection of the initial hypothesis for the data as arranged in contingency Tables 8 and 9 can primarily be attributed to the larger than expected number of upsets observed when the transient signal was input during instruction fetch machine cycles. The chi-square statistic calculated for the data in contingency Table 10 indicates that there is no basis on which to reject the initial hypothesis of there being an equal probability of upset

occurring when the transient signal is input during various machine cycle states, irrespective of the associated machine cycle or instruction. A more complete statistical analysis associating instruction, machine cycle, and machine cycle state will be performed once a larger data base has been obtained.

A preliminary upset model has been developed and is presented in Figure 4. The probability of being in each of the defined states can be determined once the probability density functions (pdf's)  $\rho(t)$ ,  $\alpha(t)$ ,  $\beta(\tau)$  and  $\sigma(\tau)$  are determined for a specific digital system being considered. Function  $\rho(t)$  is the pdf of the time it takes for upset to occur, once the transient signal has entered the system. Similarly,  $\alpha(t)$  is the pdf of the time required, once the transient signal has entered the system, for benign errors to be generated. Functions  $\alpha(\tau)$  and  $\beta(\tau)$  are the pdf's of the time required for system rec very or system failure, respectively, once system upset has occurred. Probability density functions  $\rho(t)$  and  $\alpha(t)$  will be determined for the 8080-based microcomputer using upset test data currently being obtained. The clock cycle counter in the upset test circuitry is reinitialized when the transient signal is input into the test system, and the clock cycle count is latched and recorded upon detection of an error. Since the clock frequency is 2 MHz, the time required for upset to occur or benign errors to be generated, once the transient signal has entered the system, can be calculated by multiplying the clock cycle count by 506 ns. The upset propagation times calculated from each test in which upset occurred will be used to generate a histogram showing frequency of upset occurrence versus various upset propagation time intervals. Function o(t) is then determined by approximating the histogram with a known distribution or deriving the equation of the curve Which best fits the envelope of the histogram. Figure 5 shows the upset propagation time histogram formulated from the upset data obtained to date. Since the data base is small, no attempt has yet been made to determine  $\rho(t)$ . Probability density function  $\alpha(t)$  for benign error generation time will be determined in a similar manner. The pdf's  $g(\tau)$  and  $g(\tau)$  for recovery time and failure time, respectively, cannot be determined unless upset recovery mechanisms are designed and implemented in the microcomputer system. If this is undertaken, pdf's  $\sigma(\tau)$  and  $\ell(\tau)$  will be determined similarly.

#### SUMMARY AND CONCLUSIONS

A methodology has been developed to test a general-purpose microcomputer for susceptibility to upset caused by analog transient signals which model lightning induced effects waveforms. Upset data has been obtained during 30 of 1101 transient signal injection tests and indicates that there are several distinct upset modes. Type I upset involves CPU lines and/or buses being stuck at some logic state sequence whereas, during Type II upset, the CPU "babbles" erroneous and/or undefined information on its lines and buses. Type III upset occurs when the CPU exhibits a pattArn of behavior during which it completes several program cycles correctly and then "babbles" or becomes "stuck" during several cyclec. Processing activity taking place during upset modes is yet to be investigated. Statistics performed thus far do not refute the claim that upset occurs with equal probability when the transient signal is input during each instruction cycle. However, there is evidence against the occurrence of upset being equiprobable when the transient signal is input during the machine cycles that occur throughout execution of the test program, irrespective of the instruction cycle in progress. At this time, there is no evidence to disclaim the assertion that upset occurs with equal probability when the transient is input during the various machine cycle states, irrespective of the associated machine cycle or instruction cycle. A more comprehensive statistical analysis will be performed once a sufficient data base has been obtained. Upset test data will also be used to determine probability density functions of the time it takes for upset to occur and benign errors to be generated in the 8080-based wicroccaputer, once the analog electrical transient has entered the system. These probability density functions will be used to determine the upset susceptibility of the 8080 microcomputer via a preliminary upset reliability model that has been developed. although extensive upset testing has not been completed, the primary conclusion that can be made at this time is that digital system upset may best be characterized at the machine cycle level of processing activity.

#### REFERENCES

1. Rodney A. Perala, Terence Rudolph, and Frederick Eriksen, "Electromagnetic Interaction of Lightning with Aircraft." IEEE Transactions on Electromagnetic Compatability, Vol. EMC-24, No. 2, May 1982.

- 2. Gerald M. Masson and Robert E. Glaser, "Intermittent/Transient Faults in Digital Systems." NASA CR 169022, May 1982.
- 3. "Digital Avionics Design and Reliability Analyzer." Martin Marietta, MCR-81-515, NASA Report NAS1-15780, February 1981.
- 4. J. J. Stiffler and L. A. Bryant, "CARE III Phase II Report, Mathematical Description." Raytheon Co., Sudbury, Ma., NASA CR-3566, 1982.
- 5. Felix L. Pitts, "Electromagnetic Measurement of Lightning Strikes to Aircraft." AIAA Journal of Aircraft, Vol. 19, No. 3, March 1982, pp. 246-250.
- 6. "Test Waveforms and Techniques for Assessing the Effects of Lightning-Induced Transients." AE4L Committee Report AE4L-81-2, Society of Automotive Engineers, December 1981.
- 7. Intellec 8/Mod 80 Microcomputer Development System Reference Manual, Intel Corp., 1974.
- 8. S. Wilks, "Mathematical Statistics." John Wiley and Sons, Inc., New York, 1962.

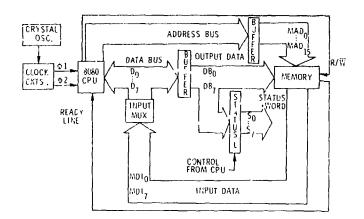


Fig. 1 - Overview of digital unit under test (8080-based microcomputer)

Table 1 - 8080 Machine Cycles and Corresponding 8-Bit Status Signals in Hexidecimal Format

MACHINE CYCLE	STATUS SIGNAL
INSTRUCTION FETCH	A2
MEMORY READ	82
MEMORY WRITE	00
STACK READ	86
STACK WRITE	04
INPUT	42
OUTPUT	10
INTERRUPT	23
HALT	8A
INTERRUPT WHILE HALT	28

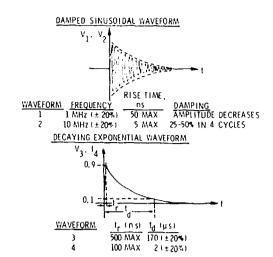


Fig. 2 - S.A.E. waveforms recommended for lightning-induced effects testing

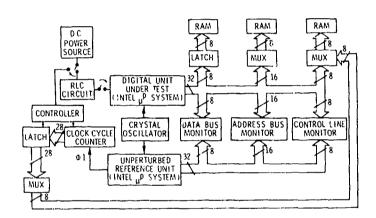


Fig. 3 - Overview of upset test hardware configuration

Table 2 - Processing Levels for the 8080 Microprocessor

PROCESSING LEVEL	COMMENTS
INSTRUCTION CYCLE	<ol> <li>Defined by op-code for each 1-3 byte instruction</li> </ol>
	2. Consists of 1-5 machine cycles
MACHINE CYCLE	<ol> <li>Identified by status signal for type of CPU-memory or CPU-I/O port transaction</li> </ol>
	2. Consists of 3-5 states
MACHINE CYCLE STATES	1. Defined by single cycle of clock signal $\phi_1$
	<ol><li>Smallest unit of processing activity</li></ol>

Table 3 - Address Bus, Data Bus, and Control Signal Activity During Execution of the Upset Test Program Code

ADDR.		DATA BUS	No on			CPU C	ONTROL	SIG	NAL		
BUS	OP.CODE/INST	STATUS SIG./MACH. CYC.	NO. OF STATES	WAIT	RDY	HLDA	SYNC	WR	DBIN	INTE	HLD
0010	3E: MVIA	A2: INST. FETCH	5	1	1	0	0	1	i	0	0
0011	CB: CB	82: MEM. READ	4	1	1	0	0	1	1	0	Ο
0012	32: STA	A2: INST. FETCH	5	1	1	0	0	1	1	0	0
0013	23: 23	82: MEM. READ	4	1	1	Ü	0	1	1	0	0
0014	00: 00	82: MEM. READ	4	1	1	0	0	1	1	0	0
0023	CB	00: MEM. WRITE	4	1	1	0	0	0	0	0	0
0015	C3: JMP	A2: INST. FETCH	5	1	1	0	0	1	1	0	0
0016	10: 10	82: MEM. READ	4	1	1	0	0	1	1	0	0
0017	00: 00	82: MEM. READ	4	1	1	0	0	1	1	0	0

Table 4 - Breakdown of System Anomalies Observed Per Number of Transient Signal Inputs at Each Input Point in the Unit Under Test

TRANSIENT INPUT POINT	NO. OF TRANSIENT INPUTS	SYSTEM ANOMALIES	BENIGN ERRCRS	TOTAL	SYSTI TYPE I	EM UPSETS TYPE II	TYPE III
MDI <sub>O</sub> (MEM. DATA IN'.SB)	11	11	3	8	2	4	2
MDI <sub>3</sub> (MEM. DATA IN4th LSB)	11	11	0	11	0	11	0
MDI <sub>7</sub> (MEM. DATA INMSB)	11	11	1	10	i	9	0
D <sub>O</sub> (CPU DATA BUS-LSB)	2	2	1	1	0	O	1
DB <sub>O</sub> (DATA BUS OUTLSB)	720	0	0	0	0	0	0
MAD <sub>O</sub> (MEM. ADDR. BUS-LSB)	346	0	0	O	0	0	0

Table 5'- Upsets Involving Overwritten Program Memory
Per Total Number of Upsets Observed from
Transient Signal Inputs at Each Input Point in
the Unit Under Test

TRANSIENT INPUT POINT	NO. OF TRANSIENT INPUTS	TOTAL NO. OF UPSETS	UPSETS INVOLVING OVERWRITTEN PROGRAM MEMORY
MDI <sub>0</sub>	11	8	3
MDI <sub>3</sub>	11	11	2
MDI <sub>7</sub>	11	10	7
DO	2	1	0

Table 6 - Contingency Table and Chi-Square Statistic for the Occurrence of Upset When the Transient Signal is Input During Instruction Cycles

,	MVIA	STA	JMP	
NO UPSET	245	473	353	1071
UPSET (EXPECTED)	12 (10.0)	9 (10.0)	9 (10.0)	30
TOTAL	257	482	362	1101

CALCULATED 
$$\chi^2 = 0.6$$

$$\chi^2_{\alpha = 0.10} = 4.61$$
  $\chi^2_{\alpha = 0.05} = 5.99$ 

Table 7 - Contingency Table and Chi-Square Statistic for the Occurrence of Upset When the Transient Signal is Input During Machine Cycles

	INST. FETCH	MEM. READ	MEM. WRITE	
NO UPSET	392	562	117	1071
UPSET (EXPECTED)	15 (10.0)	14 (10.0)	1 (10.0)	30
TOTAL	407	576	118	1101

CALCULATED 
$$\chi^2 = 12.2$$

$$\chi^2_{\alpha = 0.05} = 5.99$$
  $\chi^2_{\alpha = 0.005} = 10.6$ 

Table 8 - Contingency Table and Chi-Square Statistic for the Occurrence of Upset When the Transient Signal is Input During Machine Cycles (Memory Read Cycles are Subclassified Into Data and Addresses Read from Memory)

	INST. FETCH	MEM. RD. (DATA)	MEM. RD. (ADDR.)	MEM. WRITE	<b>-</b>
NO UPSET	392	110	452	117	1071
UPSET (EXPECTED)	15 (7.5)	(7.5)	8 (7.5)	(7.5)	30
TOTAL	407	116	460	118	1101

CALCULATED 
$$\chi^2 = 13.43$$

$$\chi^2_{\alpha = 0.05} = 7.81$$
  $\chi^2_{\alpha = 0.005} = 12.8$ 

Table 9 - Contingency Table and Chi-Square Statistic for the Occurrence of Upset When the Transient is Input During Machine Cycles (Memory Read Cycles are Subclassified into Data, Low Address Bytes, and High Address Bytes Read from Memory)

	INST. FETCH	MEM, RD. (DATA)	MEM. RD. (LOW BYTE OF ADDR.)	MEM. RD. (HIGH BYTE OF ADDR.)	MEM. WRITE	_
UPSET	392	110	218	234	117	1071
NO UPSET (EXPECTED)	15 (6.0)	(6.0)	(6.0)	(6.0)	1 (6.0)	30
TOTAL	407	116	221	239	118	1101

CALCULATED 
$$\chi^2 = 19.37$$

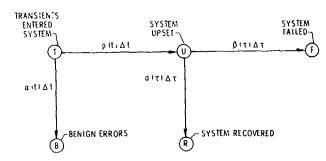
$$\chi^2_{\alpha = 0.05} = 9.49$$
  $\chi^2_{\alpha = 0.005} = 14.9$ 

Table 10 - Contingency Table and Chi-Square Statistic for the Occurrence of Upset When the Transient Signal is Input During Machine Cycle States

	T1	Т2	TW	T3	T4	-1
NO UPSET	249	268	255	223	76	1071
UPSET (EXPECTED)	9 (6.0)	(6.0)	6 (6.0)	(6.0)	(6.0)	30
TOTAL	258	275	261	228	79	1101

CALCULATED 
$$X^2 = 3.34$$

$$\chi^2_{\alpha = 0.1} = 7.78$$
  $\chi^2_{\alpha = 0.05} = 9.49$ 



 $\begin{array}{l} \rho(t) \Delta t = \text{PROBABILITY THAT ERRORS CAUSE SYSTEM UPSET IN TIME } \Delta t \\ \sigma(t) \Delta t = \text{PROBABILITY THAT ERRORS WILL BE BENIGN IN TIME } \Delta t \\ \sigma(\tau) \Delta \tau = \text{PROBABILITY THAT SYSTEM WILL RECOVER IN TIME } \Delta \tau \\ \beta(\tau) \Delta \tau = \text{PROBABILITY THAT SYSTEM WILL FAIL IN TIME } \Delta \tau \end{array}$ 

Fig. 4 - Preliminary stochastic upset model

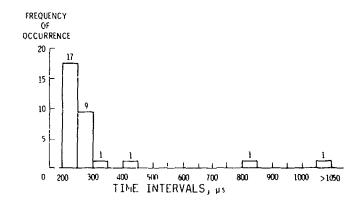
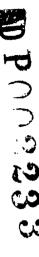


Fig. 5 - Upset detection/propagation time histogram

APPENDIX : TABLE A -	UPSET TYPE II DATA EXCERPT (TRANSIENT INPUT POINT - HOIO; CPU
	STATE DURING TRANSIENT INPUT - JMP 0010, INST. FETCH. TWO UPSET
	DETECTION/PROPAGATION TIME - 224.5 US: PROGRAM MEMORY HAS NOT
	Auto, Deament

	MEMORY				<del></del>		OL BIGN		*	
STATUS MORD	ADDRESS	DATA RUS 1/0	WAIT	RDY	HLDA	SYNC	MRNCT	DRIN	INTE	HL
			·							
BZI MEM. READ	0014	On: NOP	0	i	U	<u> </u>		0	0	0
OOL MEM, WHITE	0023	CH: ****	<del>''</del> 0	1	0	<del>0</del>	1 -	1	<del>- 0</del>	- 0
AZI INST FETCH	0015	C3: JMP	1	0	<u> </u>		<del>;</del>	<del>-</del>	- 0	
HZ: MEM HEAD	0016	101 *****	<del>-i-</del>	0	<del>0</del>	1		1	<del></del>	<u> </u>
821 MEM, READ	0017	001 KOP	<u> </u>	0	0	1	0	0	0	0
AZI INST FETCH	0018	201 *****	<del>-i-</del>	<del>- <u> </u></del>	<u> </u>	<del></del>	0	<u> </u>	0	1
AZI INST.FETCH	0019	Ols LXT B	<del>- i-</del>	0	0	1	0	0	0	0
FF1 *******	0500	201 *****	<u>I</u>	0		1	0	1	0	1
BRI MEM. READ	011H	CII LXI B	1	Ų	0	1	0	0	0	Ü
AZ: INST.FETCH	0016	501 *****	1	Ø.	0	1.	0	i	0	1
FF: nundantes	0010	011 LX1 B	1	0	0_	1	0	0	0	0
FD) ********	0010	821 ADD D	i	0	0	1	0	1	0	1
AEr ******	0018	CII LXI B	1	0	0	11		0	0	0
FF: *******	0015	CH 2 米米米米市	1	0	0	1	0	1	0	1
CA1 #******	0050	0 00A 158	1	0	0	1	0	0		0
CR: *******	0021	CR\$ ######	1	0	0		0	1	0	1
CH: *******	0022	FF: RST 7		0	0		0	0	0	0
FFE ******	0004	DUE THE B		0	0		0		0	1
CH1 *******	2109	041 THR 8		0	0	!	0	0	0	- 0
CC: *********	21CA	FFI HST 7	1 1	0	0	<del></del>	0		0	1
01: ******	211A 0039	FF1 AST 7	<u>1</u>		0	1	<del>0</del>	0		1
20: *******	0034	201 ****	<del>1</del>	<del></del> 0			0		0	
01: ******	0038	00: NOP		Ŏ.	0		<del></del>	<del></del>		1
501 *******	0030	FF1 RST 7	<u>i</u>	<del>ŏ</del>	ŏ		0	· <del>.</del>	<del>ŏ</del>	
011 *****	0030	OOL NOP	<del>- i -</del>	<del> ў</del> :			·· <u>"</u>		<del>-</del>	<u>Ť</u>
20: *******	001F	201 4***	<del>-</del> i	0	0		0	<del>.</del>	0	·
011 *****	903F	UO! NOP	<u> </u>	0	0	<del>i</del>	0	1	ō	1
201 *****	0040	201 *****	1	U	0	1	0	0	0	0
AZI INST FRICH	0041	001 NOP	i	0	0	1	0	1	0	1
AZ: INST. FETCH	0042	501 #***	1	0	0	1	0	Ô	0	0
FF8 *******	0038	Olf FXI B	1	U	0	1	0	1	0	1
FES ARRESTAN	0043	AZI ANA D	1	0	0	1	00	0	0	0
AF1 *******	0044	D ANA 15A	1	1	0	0	11	1	0	0
01: *******	0045	FFE RST 7	1	0	0	1	ņ	n	0	0
20: ********	0046	C DDA 158	1	0	0	1	0	i	0	1
201 *******	0047	AZI ANA D		0	Ú		<u> </u>	- 0	<u>0</u>	- 0
01: ******	0048	UO1 NOP	1	0	<del></del>		- 1	<del>}</del>		0
201 *******	0044	201 *****		0	<del></del> -	1			0	- 1
AZ: INST_FETCH	0048	01: LXI B	<u>1</u>	<del></del>	0		<del></del>	1	0	
FF: *****	0020	201 *****		<u>i</u>	<del>-</del> 0		1	1	<del></del>	- <del>-</del>
821 HEM READ	0140	001 NOP	<del>:</del>	<del></del>		<del></del>		<u> </u>	0	- 0
AZI INST. FETCH	004E	201 *****	<del></del>		<del></del>	<del>1</del>	0			
AZ, INST.FETCH	004F	001 NOP	<del></del>	0	0	1	0	0	0	<del>- ;</del>
FF1 ******	0038	201 *****	<del>i</del>	0	0	<del></del>	<del></del>	<u> </u>	0	<u>`</u>
AE1 *******	U 0 5 0	O AVA 15A	<u> </u>	0	0	<u> </u>	<u>ò</u>	<del>-                                    </del>	0	<del>:</del>
ON; MEM, WRITE	0.051	FFI HST 7	0	0	<del></del>	0	0	U	0	0
201 *******	0052	G GGA 158	1	0	0	1	0	0	0	0
01: *******	0.053	AZ; ANA D		1	0	0	1	1	0	0
201 *******	0.051	FFI RET 7	1	0	0	1	0	0	0	0





LIGHTNINC PROTECTION DESIGN AND LIGHTNING THREAT FLIGHT CLEARANCE OF A FLY-BY-WIRE FLIGHT CONTROL SYSTEM FOR AN UNSTABLE ATRORAFT



P. A. Doggett and I. P. MacDiarmid British Aerospace PLC, Lancashire, United Kingdom

ABSTRACT

The rapid growth in autonic flimt sarety critical systems coupled with large scale use of poor ', conducting structurel materials has made essential a deliberate and consistent design and test philosophy for aircraft lightning strike protection.

The paper discusses the design measures taken in the installation of a fly-by-wire (F&W) system in a Jaguar aircraft to be used as a technology demonstrator. The whole aircraft simulated lightning strike tests carried out are briefly described, together with complementary bench tests.

The experience gained is reviewed and used to provide a basis for a consistent philosophy of design and test for any future FBW aircraft.

l. IN A 'FLY BY WIRE' (FBW) aircraft, the traditional cables and rods of the flight control system are replaced by electronic circuits linking central computers to inceptors such as pilot's stick, and to actuators to move the control surfaces. The trend in military aircraft flight control systems is now firmly towards digital electronic FBW technology. Six years ago the most advanced production aircraft incorporated quadruplex analogue control systems; today quadruplex digital systems are developed and in production. Future projects use digital techniques with no backup system and also complete integration with avionic navigation and attack systems.

A parallel trend in aircraft production has been the increasing use of composite materials. Five years ago the use of Carbon Fibre Composite (CFC) in aircraft at BAe (Warton) was limited to a small number of access doors manufactured as replacements for metal doors on existing aircraft. Since then, a front fuselage, a wing and a taileron set have been built, and aircraft under development incorporate more than half of the structure in CFC. This usage of CFC is in common with the majority of other major manufacturers.

Although the use of digital techniques minimises EM Interference the greater dependance on continuous system functioning for safety, and the change in structural material which reduces shielding of systems from external EM effects (such as lightning) make it necessary to take deliberate action to identify and prove protective measures and design procedures. The continuous and safe functioning necessary is best illustrated by the fact that future aircraft are being designed with deliberate longitudinal instability to maximise aircraft performances. Only a high speed computer can effect the control inputs necessary to maintain controlled flight. It follows therefore that if control were to be lost, the aircraft could divergently depart from controlled flight and break up. With such an unstable airframe no manual reversion is possible and very high electrical integrity is essential.

Lightning strike represents the severest naturally occurring electromagnetic threat and furthermore, the unpredictability of the characteristics of a possible strike, necessitate always considering the worst case conditions. It is of great importance that a safe and realistic flight clearance with respect to lightning is generated for a particular aircraft type, but the problems in doing so are considerable.

Considerable programmes of whole aircraft simulated lightning testing have been

conducted in recent years, and much has been learnt about correct design and protection of systems to minimise induced transients and also to test them correctly, such that an unrestricted Ilight clearance may be confidently given. This paper reviews the experience gained in these areas by British Aerospace PLC (Warton Division) with the Jaguar fly by wire reserach aircraft. In each of these areas BAe (Warton) have been greatly assisted by the Culham Lightning Studies Unit (CLSU).

#### 2. FBW JAGUAR DESIGN

The FBW Jaguar was originally a standard production Jaguar strike aircraft and served with the RAF for three years before being delivered to BAe Warton for conversion as an Active Controls Technology Demonstrator, under contract to the UK Ministry of Defence.

Since it was always intended to fly the FBW Jaguar in unstable configurations, no form of reversionary control was retained and the original flight control system was entirely replaced by a quadruplex digital FBW system together with associated sensors and actuators. The overall objective of the project was for the aircraft to be a technology demonstrator, and thus throughout the project all aspects of equipment build and flight clearance have been to normal production standards. Therefore, in effect, the system could be fitted and flown in a future aircraft with only those changes that apply to the different aircraft layout and role.

The aircraft first flew as a FBW Demonstrator on 20 October 1981.

2.1 THE FLIGHT CONTROL SYSTEM (FCS) - Figure 1 gives a schematic illustration of the installation of the FCS into the aircraft, and major components of the system comprise:

Flight Control Computer (FCC) - (4 off) - these computers house the control laws, and each one has at its disposal the information available to the others, such that it can generate a consolidated command to the control surface actuators.

Actuator Drive and Monitor Computer (ADMC) - (2 off) - these computers each produce a further consolidated command to the control surface actuators from information received from the 4 FCCs. In addition they monitor the FCCs and generate the failure warnings as necessary.

Quadruplex Position Sensors - (5 off) - these are basically potentiometers and are used to measure pilot's stick, rudder pedal and trim settings. A separate lane is used for each FCC.

Rate Gyro Units - (3 off) - these are quadruplex gyro packs and send aircraft rate responses to each FCC.

Primary Flight Control Units - (5 off) - these comprise a separate actuator for each control surface. Each actuator receives 6 control signals on a 'duo-triplex' basis. The actuators send ram position and ram rate of travel feedbacks to the computers.

Airstream Direction Detection Probes - (4 off) - from these four probes triplex incidence and sideslip signals are generated for transmission to the FCCs.

<u>Triplex Transducer Unit</u> - from the pitot static probes triplex pitot and static signals are generated for transmission to the FCCs.

Airbrake and Flap Position Indicators te generate compensation of airbrake and flap effects, a duplex position signal is sent to 2 FCCs.

Autopilot - signals from the Jaguar Nav Attack system (NavWass) are provided to one FCC for use as an autopilot facility.

The system architecture is outlined in Fig (2) and principal components of the above system will apply equally to any future aircraft although a much greater amount of integrated avionics is to be expected with increased use of databus systems.

2.2 FCS PROTECTIVE DESIGN - The general installation techniques and design policies for the FCS equipment and wiring runs are outlined below.

Equipment - Each FCC powers its own sensors and all signal earth references are via the FCC to system star ground. Separate OV 'busbars' are provided within the computer for different signal types and all earth references exit from the box on one connector pin to the star ground. The cases of each computer and each sensor are bonded to airframe.

Traditional "transorb" devices for transient overvoltage protection are used to protect the outputs from the FCC to remote components eg Linear Variable Differential Transducer (LVDT) excitation, servo command signal. Most sensor inputs to the FCC are protected by a high resistance which limits any transient current.

Standard anti-EMI manufacturing techniques are used in the box construction eg overlapping lids and hele sizes only below a certain value.

FCC4 is an exception in that its system earth is not the star ground but a remote NavWass earth. This results from its NavWass sourced autopilot inputs which necessitated using the NavWass system earth. However, this situation was deemed acceptable since each FCC is optically coupled and electrically isolated (500V optical coupler) and therefore any resultant noise due to the remote earth is limited to one box.

The software inside each FCC is identical to enable any box to be used in any position.

The original system specification called for 500v insulation to ground for wiring and sensors and this is generally met.

Wiring Runs - The major wiring runs are illustrated in Fig 1. A specific design constraint was that all FCS wiring was to be segregated from standard Jaguar wiring, with cross overs at 90°.

EMC considerations defined which circuits required use of screened wires. These screens were earthed only at the FCC end to avoid earth loops.

Approximately 75% of FCC inputs/outputs are so screened. The screen carthing is generally by pigtail to the airframe, although 5% are earthed via the FCC to star ground.

For lightning protection it was decided to segregate mechanically the FCS wiring runs with a combination of aluminium trunking (or conduit) and mesh braid, either heavy duty braid or light gauge knitted mesh as required. These screens were all earthed multiply on an opportunity basis to reduce enclosed loop area.

The wiring, as far as possible, avoided the areas of the fuselage which were of small radius of convex curvature. These areas often carry high current densities, and thus give rise to high levels of electromagnetic coupling. The FCS computers themselves are sited approximately halfway along the fuselage in an area of low current density due to large effective fuselage diameter.

To attempt to keep lightning currents on the aircraft skin, certain equipment and gun bay doors were provided with ZM sealing. This took the form of a knitted mesh gasket which was electrically bonded to the bay door and allowed to contact the metal 'land' around the aperture in the airFrame.

#### 3. WHOLE AIRCRAFT SIMULATED LICHTNING TEST

The FBW Jaguar is the first British aircraft to rely entirely on a digital electronic flight control system and thus presented a novel problem with respect to clearing the aircraft for flight in possible lightning conditions.

The principal objective of the simulated lightning test was to demonstrate the efficacy of the protective measures and thus achieve a relaxation or abolition of the initial restrictive clearance imposed.

3.1 TEST PHILOSOPHY - To achieve an unrestricted flight clearance, confidence must be gained that if a full threat lightning strike were to occur, the flight safety critical elements of the FCS would survive and maintain control throughout. The unpredictability of interference mechanisms necessitates a practical test. So much can generally be readily agreed, but definition of a sufficient and satisfactory test is more difficult and subject to various opinions.

The test rig used in the FBW Jaguar whole aircraft simulated lightning tests is shown in Fig 3; the capacitor bank and charging equipment were provided by CLSU and the return conductors were manufactured by BAe to a CLSU design. The circuit inductance was  $\approx 4 \mu$ H and the equipment produced maxima of 100kA; 80kV; 20kA/ $\mu$ sec. Two aircraft configurations were tested; Nose to Tail and Nose to Fin Tip

aerial, including tests with aircraft fully powered electrically and hydraulically.

The values produced by the rig, although not full threat, are equivalent to a moderate to severe scrike and a flight ready aircraft cannot be put into the rig and tested without risk of expensive damage to sensitive equipment.

It was important to achieve valid test techniques whereby an aircraft in the middle, or, in future, at the beginning of its flight programme, could be subjected to meaningful tests and yet be recleared for flight with a minimum of delay after the testing. Table 1 shows how this was achieved for the FBW Jaguar. Each change was considered for its effects on the test validity. No difficulties were encountered in reclearing the aircraft for flight. The good segregation between FCS and other systems was greatly beneficial in these respects.

The principal means of data gathering were two dummy computers (one FCC, one ADMC) which were wired to receive a total of 18 circuits and terminate these with their correct impedance. A list of these circuits is given in Table 2 and it can be seen that they are representative of all major wiring routes, circuit types and sensor types.

The test philosophy anticipated basing any eventual clearance on the results of these measurements but to utilise fully the unique opportunity that the tests offered, a range of additional measurements was made. An outline of all test techniques employed is given in Table 3. Fuller details of all test measurements and techniques may be found in the complementary paper given by RAE at this Conference. Ref (1)\*

The additional measurements made were of particular use in determining the representation of the test environment. Critical in this respect are the E field surrounding the aircraft, the peak current, current waveform, dl/dt, dE/dt and current distribution. The test rig caters for all these explicitly except dE/dt. This is an area of increasing importance, and valid test techniques and agreed criceria are required.

A brief summary of aircraft test results is given in Table 4.

3.2 ROLE OF BENCH TESTS - The aircraft itself could only be used to obtain the essential database rather than extend the test duration and variety of tests to include all desirable measurements. Furthermore, it would not be possible to expose any 'flight-realy' aircraft to repeated simulated full threat strikes. Thus bench tests are essential to provide the range of data required for full confidence in the system, particularly safety margins and inter-component variation.

\*Numbers in parentheses designate References at end of Paper

Generally, two options are available to provide this data, either equipment qualification test results or specific tests based on aircraft test data. In both cases, careful consideration is required to ensure that all measurements are in the optimum format for cross comparison. Particular attention must be paid to the read across of bench test results to the real environment.

Bench tests for a particular channel were not necessary if the FBW Jaguar results when extrapolated to full threat conditions were within known tolerance levels is manufacturers specifications. However, the generally limited extent of manufacturers' specifications and, in particular, the lack of agreed lightning qualification test criteria, meant that testing outside known levels was required.

These tests are currently being carried out, therefore, it is not possible to quote results.

To minimise the risk to flight cleared units, the majority of the tests are being carried out on a combination of rig standard units and breadboard circuits. The breadboard circuits allow great flexibility in repeat testing to enlarge the sample of components and to overtest as required. The breadboard circuits are commissioned by ensuring that the 'transfer function' between input wire and monitored component was the same as for the actual computer circuit. Since the tests are designed to clear one particular aircraft, testing to full threat criteria is sufficient and overtests are made solely to investigate circuit capability.

Finally, proof tests will be carried out on flight boxes at full threat levels for 10 examples of each input type.

# 4. LESSONS LEARNED

It must be emphasised that the many valuable lessons learned from the FBW Jaguar tests were due to a consistent approach to the problem as if for a production aircraft and a full flight clearance.

4.1 DESIGN ASPECTS - From the results of the lightning tests one design features are critically assessed below.

Access Loor Gasketting - Magnetic fields in the NavWass bay were measured with the knitted mesh gasket around the door both insulated and operating normally. The results are illustrated in Table 4. It can be seen that the magnetic fields (& dI/dt) are reduced by a factor of approximately two to four by using a conducting gasket around the bay door. It should also be noted that waveforms with a very high HF concent were recorded. These arose as a result of sparking at the interface between the gasket and the aperture "law!" This did not arise in the Gun Bay door which was such that the gasket provided good continuous contact around the door.

As a comparison between the performance of the gasketting on the Gun Bay door and the NavWass Bay door, loops were placed in each bay and the voltage induced in the loops, with the gaskets operating normally or insulated, was recorded and compared. The results are given in Table 4.

It can be seen that the performance of the gasket in the case of the Gun Bay door is far superior, giving a reduction of induced voltage in the region of 15 times.

It is clear that it is extremely beneficial to provide good RF bonding around the periphery of access doors. This should be engineered with some care, and included as a feature at the earliest stages of design. Knitted mesh gaskets are far from ideal, they are not particularly durable and do not provide a weather seal. However, conducting rubber gaskets are now available which promise to have sufficient performance.

Cockpit Wiring - An mentioned earlier, a certain amount of FCS wiring was exposed in the cockpit, and was therefore protected using an overall knitted mesh screen on the loom. Subsequent to the testing, Culham Laboratory carried out an assessment of various loom shielding materials, the results of which are given in Table 5. It can be seen that most of the knitted loom shielding material offered little or no protection to the contained wiring.

In addition, the constraints of the installation allowed only fairly long "pigtail" termination of the braid, also some side console panels were manufactured in fibreglass.

These three factors combined to produce the highest induced voltages measured on the aircraft during the lightning strike tests, these were of the order of 200 V (extraplicated to full threat levels).

Wiring Installation - Many of the wiring installation design features incorporated in the FBW Jaguar have been shown to be successful in so much as the majority of voltages measured at the computer inputs were less than 50 V. Those voltages which were higher were as a result of a recognised engineering limitation, either a poorly chosen wiring run or unsatisfactory earth bonding at the ends of the screen. As a result of experience gained on FBW Jaguar the following installation aspects are highlighted:

(a) Screening should be earthed at both ends via the connector obviating the need for "pigtails".

(b) Conduit or ducting is preferable to knitted mesh loom screening braids. If the latter must be used, then only the heavy duty variety is of any value. Both conduit and braid should be multiply bonded to airframe.

(c) Major attenuation of the induced effects of lightning can be obtained by suitable routing of wires close to the metal work of the airframe.

(d) Wires crossing major stillctural joints in the airframe (eg wing/fuselage) should cross the join in conduit if no integral screening is available, and be routed close to major current paths in order to minimise loop area.

(e) Low impedance termination of input wires should be used to minimise E dot

coupling.

- 4.2 AIRCRAFT TESTING The whole aircraft simulated lightning tests on the FBW Jaguar went extremely well and yielded an extensive set of valid data. However, the difficulties of simulating the full threat lightning environment, made it impossible to demonstrate practically sufficient immunity to lightning effects to allow a clearance on the basis of simple test measurements. Therefore the analysis of, and conclusions from, these test measurements must consider the following aspects:
- (a) Interpretation of measured response to simulated test pulses with regard to response to natural lightning strike at full threat level.
- (b) The effects of possible lightning attachment points other than those tested.
- (c) The representation in the monitored circuits of all other FCS circuits.
- (d) Threshold effects with extrapolated results and also hardware variability between units tested and those used for flight.
- (a) The efficiency of the various protective measures incorporated into the aircraft design and the maintenance of this efficiency.

Interpretation of Test Results with regard to Full Threat Natural Strike differences between the simulated pulse and a full threat natural strike are in the inter-relation and magnitudes of the main electromagnetic parameters (dI/dt, I peak, dE/dt). Provided that the individual effects of these parameters can be identified from the measured waveform, the full threat environment can be accounted for by extrapolating the test responses to full threat level and combining them in correct relation to each other. The only difficulty encountered here in the FBW onally agreed full threat dE/dt
The 10<sup>14</sup> V/m/ser volume Jaguar tests was the internationally values. probably over severe.

Other Attachment Points - A lightning clearance must reflect the possibility of a strike between any two aircraft extremities. The FBW Jaguar tests covered Nose - Tail and Nose - Fin and thus consideration of a wing tip to wing tip strike was necessary. Investigation of the wiring at risk revealed a possible weakness in the Wing/Fuselage junction, and extra screening was defined for this crossover as a result. Due to the good segregation between FCS and standard Jaguar wiring, no further problem areas were found.

Adequacy of Representation of Monitored Circuits - The 18 monitored FCS circuits included representatives of all types of inputs to the computer and wiring routes plus sensor types in the aircraft. Thus it is considered that the measurements made are valid representations of the highest possible induced effects on the FBW aircraft. Therefore, the essential database has been obtained, but bench tests are necessary to enlarge this database and extend it to cover adequately variation between similar circuits and components.

It was accepted that FCC4 may be a special case due to its interface with FTI and Autopilot and its remote earthing. However, the Bulk Current Detector (BCD) measurements revealed no substantial variations in results for FCC4, and it is a design principle that one FCC (or two if not simultaneous) may be lost without effect.

Threshold Effects and Inter Box Variability - With all extrapolations beyond actual tested levels, there is a danger that at a given threshold some untoward effects may have occurred. Similarly, it is possible that a tested unit might be hard (or soft) compared to other units of the same nominal standard.

It is only the FCS computers themselves that are likely to have such threshold effects, the aircraft wiring and sensors are not at risk as the 500 V insulation specification adequately covers the extrapolated levels for Common Mode effects. Some analytical assessments of Differential Mode effects was necessary however. The threshold effects on the computers will be fully covered in the bench tests, as will be the variations between circuits and components of nominally similar characteristics.

Screening Efficiency - Insofar as an eventual flight clearance with regard to lightning is dependent upon the effectiveness of the screening measures employed, it is important to have confidence in their continued effectiveness.

As a result of the limited efficiency of the knitted mesh screening, some of the aircraft test extrapolated results are higher than need be. It is considered, from comparison of standard Jaguar and FCS measurements, that the main screening effect on the FBW Jaguar airframe came from the aluminium skin, and that cable screening is only of crucial importance (apart from EMC considerations) in exposed areas.

There are at present no defined procedures for confirming the continued effectiveness of screening. On a single research aiccraft, such as the FBW Jaguar, this is not a problem, and occasional visual inspection of critical areas will suffice. A more thorough procedure including initial calibration of screen effectiveness, would be required for future fleet aircraft.

#### FUTURE AIRCRAFT

5.1 IMPACT OF CARBON FIBRE COMPOSITE (CFC) - Because CFC has significant structural benefits over aluminium, its use in aircraft manufacture in significant quantities is here to stay, and the installation of electrical and avionic systems in an airframe consisting of large amounts of CFC must be designed accordingly.

Electrically, CFC has two undesirable properties. Firstly, it is not a good conductor, the conductivity of CFC is ~ 1/1000 that of aluminium. Secondly, because the manufacturing process leaves a non-conducting layer of epoxy resin on the surface it is extremely difficult to make good electrical contact to the material.

The problems associated with the poor conductivity of the material, and the poor bonding of any joints made, are:

(a) Reduced shielding against HF electromagnetic energy (eg lightning, EMP and on-board and external HF transmitters).

(b) Implementation of Power Earth Returns 5.2 DESIGN PHILOSOPHIES CONSISTENT WITH LARGE SCALE USAGE OF CFC - To date aluminium alloy aircraft have had an electromagnetic performance which was reasonably well assured to be adequate against the induced effects of lightning, irrespective of configuration, installation design, etc. In an aircraft consisting of large quantities of CFC, the electrical avionic system design must be linked strongly with the structural design at the earliest stages, in order to avoid incurring expensive inefficient design modifications.

Detailed work has been carried out at BAe (Warton) and general solutions to the problems outlined above have been developed. The specific procedures to be adopted on a future aircraft are outside the scope of this paper but depend strongly on the location of the CFC structure eg flying surfaces or fuselage. The options to be considered include metallisation of the inner surface of the areas of CFC; cable looms to run in a combination of conduit and heavy duty braid; improved induced transient protection within equipment. Each of these options has its own particular advantages and corresponding cost and weight implications. Correct combination of the options will be a vital management role.

5.3 EQUIPMENT QUALIFICATION TESTING - It is vastly more efficient to establish the required levels of equipment immunity to lightning strike effects during qualification tests, rather than have to define extensive dedicated tests after the whole aircraft simulated strike tests. The whole aircraft tests should rather be seen as a final 'proof test' of the system capability.

The problems associated with specifying such qualification tests are as follows:

- (a) There is remaining disagreement among lightning specialists as to the parameters of natural lightning at the altitudes at which aircraft generally get struck. In particular, the severity and importance of the E field effects need to be established.
- (b) The threat levels to a particular piece of equipment contained in the aircraft depend not only on the natural lightning parameters, but also on the configuration of the airframe and the system and the materials used. Detailed analysis is extremely complex and few computer aided schemes have been validated.
- (c) The spread in probability of failure of a component for a given transient overstress is large enough to invalidate "one-shot" testing and thus a suitable sample of components must be tested.
- (d) The absence of information on the capability of a particular electronic component (resistor, etc) to withstand likely lightning induced transient overstress makes it impossible to compare measurements of induced effects inside equipment to realistic failure levels.

In view of the above difficulties, it remains an important management function to specify the qualification test criteria for EMI induced effects. Initial bench test specifications for future BAe (Warton) aircraft have been defined but again detailed consideration of these is outside the scope of this paper.

5.4 SUMMARY: GENERATING A FLIGHT CLEARANCE - The next generation of military aircraft will demonstrate hitherto unattainable performance characteristics by utilising the manifold benefits of fly by wire flight control systems, composite structures and unstable airframes. There is no reason why these aircraft of the future need be hampered by a prohibition to fly in certain areas for fear of lightning strikes or external transmissions; provided that known design procedures are adhered to, and carefully considered test programmes are carried out.

The design procedures must give particular attention to wiring routes and screening as outlined in section 4.1. Design control procedures similar to those presently used in structural design will be necessary. Such careful electrical design combined with improved protective measures will allow full utilisation of the structural benefits of composite materials without undue degradation of electrical integrity.

The aircraft manufacturer will specify the RF interference and transient capability required of each item of aircraft equipment, in the absence of appropriate agreed qualification test criteria.

Whole aircraft testing will be required to determine the precise characteristics of the electrical systems as installed in the

These tests must obtain the airframe. essential representative database on which the eventual clearance will be based. It is unlikely that the test rig will be capable of achieving full threat levels for all relevant criteria, and also it would not be acceptable to expose a flight ready aircraft to the repeated high level testing necessary. Consequently, some extrapolation of results will be necessary; a maximum factor of to is suggested if extrapolated results are to be considered reliable. The analysis of, and conclusions from, the test results must include the considerations outlined in section

To allow for production variation and degradation in bonding through service life an appropriate safety margin should be demonstrated between the extrapolated aircraft test results and susceptibility levels demonstrated during the equipment qualification tests.

Many lessons have been learnt in each of the above areas from the FBW Jaguar programme of simulated lightning cesting and are currently being put into practice at BAe (Warton) in the Agile Combat Aircraft Demonstrator programme.

#### REFERENCES

l. R H Evans, J Bishop, "Induced Transierts in Simulated Lightning Test of the Fly by Wire Jaguar Aircraft, Paper at this Conference

# ACKNOWLEDGEMENTS

The authors wish to thank British Aerospace TLC, Warion for the encouragement and permission to publish this paper. Thanks are also due to RAE Farnborough and Culham Laboratory, Oxfordshire for permission to use data from their experimental work.

TABLE 2 PCS COMPUTER CHANNELS MONITORED

51GMAL TYPE	SIGNAL	SENSOR	ALBCRAFT MOUTING	CABLE TYPE	INPUT IMPEDANCE	T
A Discrete	Status Reset	4 pole pushburto)	Cockpit to FCCs	<del></del>	(A)	CCHORDAL
	Spin Mecovery	d pole manual switch		Single Wire Twisted Pair	450 450	Used to reset transient failures
8 Computer	Metayt on Wheels	Potentiomter	U/C BRY to 2 x FCC +	Twisted Pair	450	recovery mode theed in control in
Digita: Crosstalk	FCC1 - FCC2 FCC3 - FCC4 FCC4 - ADMC2	) Optical // Coupler // Receiver	) Transverse across ) Aircraft Vertical meparat.on	Go - one of   screened twistwd   pair	2.4x 2.4x 2.4x 2.4x	mode selection    Each FCC powers is own optical   receiver in remote   pox
Inputs	Incidence Poll Ops Poll Ops Excitation	Oyroscope Potentiometer Potentiometer DC Excitation	Mid Spine to FCCs Nose to FCCs ) Forward Fuselage , to FCCs	Screened twisted pair Screened twisted triple Screened single Screened twisted pair	100k 250k 180K 50	I These two circuits I form a loop for th
Drive and Monitor	ram position eft Taileron	LVOT	Starboard Wing to PCCs And ADMCs	Screened twisted pair	30K	Ram position facture
,	ight Taileron servo position	LVOT	Hear Fuselage to FCCs Hear Fuselage to FCCs	Screened twisted pair Screened twisted pair	100k	go to FCCs & ADMCs; Control valve feed- Packs go to FCCs
	eft Spoiler	servo valve input	Don.		100K	mly
Monitor L			Port Wing	Screened twisted pair	100	
:	ight Taileron	Vive	rear fuselage	Screened twisted pair	100 50	
Pover . FC		<del></del>			{	
Supplies   P2	Bushar	1	FUCE and ATMCs	Single wipe	10	
	·		FCCs and 1 ADMC	ingle wire	10	1

# TABLE & SUMMARY OF MESULTS

TEST TYPE	EXTRAPOLATED RESULTS AT FULL THEFT				
	status Reset 210V NF Component ( 3.) MFz dominant frequency Spin Recovery 155V NF Component ( 5.0 MFz dominant frequency) Weight on Mheels 82V NF Component (15.5 MAz dominant frequency)				
	Computer Cross Talk 24V to 20WF Component (10 or 20 MHz dominant frequence				
FCS CIRCUITS (Refer to Table 2)	Roll Gyro 669 Hr Component (9.0 Mix dominant frequency) Incidence 199 Hr Component 170.0 Mix dominant frequency) Roll Gyrs 640 Hr Component 110.0 Mix dominant frequency; Roll Gyrs Execu 284 Hr Component 110.0 Mix dominant frequency;				
	Actuator Feedbacks 839 to 989 MF Component  (5 to 20 MFz dominant frequency)  % V d1/dt Component				
	Artuator FreeDacks 109 HF Component (100 Importance) (10.0 MHz dominant frequency)  Power lines 2V and 15V				
BULK CURMENTS	FCC Cables 16.5A LF: ).CA By ADM: Cables 2.3A HF V/URF Feeder 1100A LF: 100A HF Corchpit Looms 800A LF: 100A HF				
ELECTRIC FIELD	Cocppit - 16x10 <sup>12</sup> V/M/S a 350 XV/m (Wertical Field) ) Mesults Spint : 6x10 <sup>12</sup> V/M/S a 30 XV/m (Wertical Field) ) are for 3x10 <sup>12</sup> V/M/S (Transwrise Field) : 40 XV 1 test				
TOTAL FLUX MEASUMEMENTS	Hawkass Bay : 2009 with gasket: 6709 without gashet Starboar 1 Gur. Bay : 409 with gasket; 6009 without gasket				
AMARZ BAL H. SIETO INCYTE	Centre of Bay 200 Am with gashet: 410 Am without gashet bower Surface : 55 Am with gashet: 410 Am without gashet bear Surface : 6.1 Am with gashet: 14 Am without gashet Am edge of Bay : 2.0 Am with gashet: 34 Am Without fashet with gashet: 34 Am without fashet with gashet in sulling sefected by sparking at gashet)				

Table 5 - Relative Shielding Performance of Various Types of Loom Shield

Specimen	Volts	Туре
Cu Tube 1-5mm wall	<0.5	Resistive
01mm Alfoil	11	
Metex shield wrap Ferrex 05-0860-0432-01	250	" but phase
RFI Shieldmesh A 0004-0254	500	edvanced "
* " " "	420 (vrapped)	-
" M 0004-0254+	550	Nearly 6/ds
Open wire in same location  **Alummum wire + M	560	₫⁄8 <i>l</i>

#### TABLE 1 NUMBER OF TEST HEASUREMENTS

TEST TECHNIQUE	TRANSMISSION OF DATA	DISPLAY AND RECORDING
. 16 PCS circuits terminated with correct impedance in dummy computers	Two 6 channe; switching units inside FCC One 6 channel switching unit inside Alex. Three Fibre Optic trans matters inside airframe Three Fibre Optic Links to screened room	Three Fibre Optic receivers and channel selectors Three storage oscillanceoper plan compatible Cammid
2 A5 above with selected aircraft sensors earthed to maximis: induce3 voltages at computer input	As above	As above
) Bulk Current Detectors on selected FCS looms V/UHF berial feeder inside NavMass bay, on short test wire installed on air- craft skin to measure skin current waveform	Coax cable to fibre optic transmitter inside mirframe. Then via fibre optic link to screened room	Fibre Optic receiver Storage oscillorcope plus camera
4 Skin Current mapping using current probe to measure transverse and longitudinal currents at multiple rejected aircraft stations	Screened twisted pair taped to aircraft skin, exit via earth connection, taped to earth pair to screened room	Storage oscillos ape plus cammira
5 D Measurements ysing EG and G probe	Alternate use with	BCD System
o Standard Jaquar cacles- two circuits carthed at sensor end and induced voltage measured at cockpit instrumentation	Via screened twisted pair from cucapit, then as for 4	Alternate use with 4
7 Total flux measurements using single unscreened wire loop in position of saxisum pixkup ar loss bay door	Via screened twisted pair from tested bay then as for 4	Alternate use with 4
E Time Domain Reflectometer, used to assess probable altframe resonances	8/4	Self contained pen chart
9 Cths Coupling checks using a portable EMP generator. Checks made between standard cabling and FCS 100ms	Bulk current injection and detection	Storage Oscilloscope plus camera

IT: X	SUSCEPTIBILITY	COMEST
THE POLLOWING EQUIPMENT WAS I	TEMOVED AND RELEVIANT CONNECTORS	STORED INSULATED FROM AIRPAAN
Tacan Mecelver	Cable pickup and irput e'ectronics	Well seuregated from FCS
Crash Recorder	Extensive sensor cab'ing	Well's gregated from FCS
NavMans	Precautionary measure due to multiple electionic ci. cuitry	Affects FCC4 inputs
Main Compars Detector Unit and Standby Compass	Magnetic residuals	Megligible electrical change
Teleme'ry Multiplemer	Cable pickup ard input electronics	Wel: segregated from PCS
LOX container	1,	10
Ejection Sest Canopy (incl Micro detonating cord)	) possibily explosive	removed for test safety
FTI Data Chilector and Tape Recorder	Sensitive electronics	Interfaces with FCC4
FCS Computers	Not Known	Replaced with rig standard units
Battery 1		Space required for test instrumentation
V/UHF Antennae Cover	•••	Fin tip used as alternative attachment point
THE POLLOWING EQUIPMENT N VS	ELECTRICALLY DISCONNECTED AND C	ONNECTORS STONED INSULATED
Telepatry Transmitters	Cable Pickup	Well segregated from FCS
Nozzle position indicator potentiometers TOT Amplifiers Fire protection control boses	Precautionary measures to protect engine control circuitry	 
V/UHF feeder cable. Inner and outer carthed HF feeder cable at amplifier	V/LHF fueder cable used ) in fin attachment tests; ) HF fueder table as ) precautionary measure	) Well segregated from FCS
PTI strain gauges ETI fuel flow rellys FTI long q visual warning	Trials equipment, known fisceptibility to transients	)
THE POLLOWING EQUIPMENT WAS	REPLACED BY #16 STANDARD UNITS	
Pilote Switch and Control Panel Rate Gyro Units FCS Computers (Part time fit	Electronic circuitry and flight wafety critical	) J Removed to avoid risk of , affecting flight clearance

nb F" - Flight Test instrumentation FCS - Flight Control System TOT - Turbine Gas Temperature Navigation and Meapon Alm Sho System

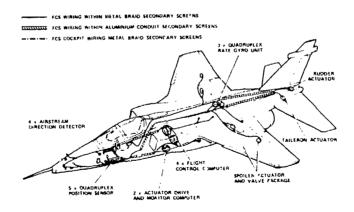
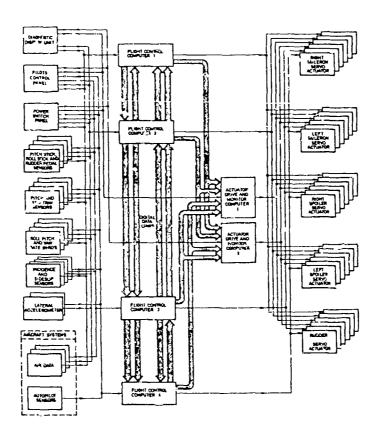


FIG 1 FBW Jaguar - Schematic of FCS equipment location and wiring routes



F1G 2 FBW Jaguar flight control system architecture

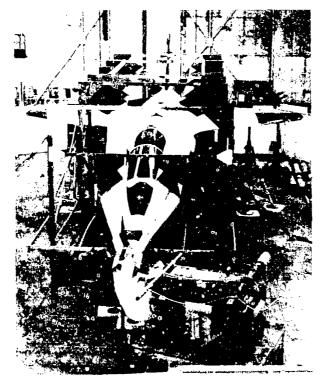


FIG 3 General test layout for FBW Jaguar simulated lightning tests

88-10

# AD P002234

#### UPSET EXPERIMENTATION IN COMPUTER-BASED SYSTEMS\*

Gerald M. Masson

Department of Electrical Engineering and Computer Science The Johns Hopkins University Baltimore, Maryland 21218

# ABSTRACT

Computer system operation can be adversely affected by physical disturbances emanating from a wide variety of sources. These disturbances, often transient in nature, are manifested in computer systems as upsets. An upset of a computer system is defined as a performance deviation that is based on a-priori operation knowledge of the computer system's task. The results of a computer system upset can be as obvious as a complete system crash or as intermittent computational errors. Hence, there exists a need to access computer system susceptability/resilience relative to transient disturbances with systematic experimentation. This paper will discuss general issues relevant to that experimentation. In a companion paper (4), some actual fault injection experimentation will be detailed relative to a particular microprocessor-based system.

<sup>\*</sup> The mesearch reported in this paper was funded by NASA Grant NSG1442.

#### UPSETS

A properly functioning computer-based system executing an applications program will have various operational features that can be used to characterize its fault-free performance. Three such features are the following:

memory access - a characterization of the memory usage;

An upset is a deviation of system performance relative to a known application tack. Upsets can be described in terms of the above features. As an illustration of this, Figure 1 shows the effect of a one microsecond fault injected on the "Read" control line of a 280 microprocessor-based system executing a simple assembly language program. It is seen that from the perspective of that control line, the injected transient fault produces a series of incorrect signals, usually referred to collectively as an error. But in terms of monitoring a system so as to detect/characterize upset phenomena, such an error would usually be at too low of a level within the context of system operation to be of use. A higher level perspective of the disturbance is necessary for such monitoring. Figure 2 shows the results of the injected fault from a program flow upset perspective. It is seen that subsequent to the injection, a code sequence that is unrelated to that observed in fault-free performance is executed by the microprocessor. Such a code sequence could actually be a paid of the applications program, and is now being executed only because the microprocessor-based system when disturbed by the injected fault has incorrectly jumped to it. Such a code sequence could also be an invalid embedded code sequence (involving, perhaps, the execution of data) into which the system has jumped because of the fault. In either case, the system has undergone what can be referred to as a program flow upset (i.e., invalid program flow).

To detect an event such as a program flow upset by the monitoring of the computer-based system, the monitoring must be done with an awareness of all valid execution sequences of instruction and operand addresses. Figure 3 illustrates one approach to the design of such a program flow monitor. Variations in the design

of the program flow monitors will be discussed in detail in a companion paper (1). The key point here is that instead of utilizing deviations caused by the fault from the exact series of signals that should be present on (in the case of the example) the control line, monitoring upsets can (and should) take a higher level perspective and utilizes information regarding a more general feature of performance. The immediate questions that this perspective raise regard detailed descriptions of types of upsets that are produced by faults and the complexity of monitoring at such a level.

#### CHARACTERIZATIONS

Since an upset is a system level phenomenon in a computer system, it follows that the details of such an event must go beyond the hardware realm of the system. Indeed, fundamental to the details of an upset is the application task of the system and its implementation as described by the operational software. In other words, two identical hardware systems with different software implementations of the same application task should be expected to have different upset characteristics. To form a framework so as to be able to quantitatively compare upset characteristics, five categories of slightly more detail than that described in the previous section have been identified:

Program Flow - the proper sequences of instructions to be executed by the program.

Opcode Set - the set of valid instructions to be executed in the program.

Opcode Address Domain - the memory locations of instructions that can be fetched in the execution of the program.

Read Address Domain - the Valid memory

locations that can be used
for non-opcode read operations in the execution of the
program.

Write Address Domain - the memory locations
that can be used for write
operations in the execution
of the program.

In experimental results regarding the operation of a Z80 microprocessor-based system and an INTEL 8085 microprocessor-based system,

(1)-(5) approximately 75% of the upsets observed fell into one or more of these five categories. Those upsets (approximately 25%) that could not be so characterized stand as a clear indication of how near the surface the study of upsets remains. But even so, as described in (1), it is still possible to build effective external monitoring devices based on the above characterizations to serve as indicators of a computer systems susceptability/resilience to a fault phenomena.

The most common class of upset seen in the reported experimentation to date is invalid program flow (1)-(6). But any straightforward attempt to externally monitor system operation in a rigorous way for program flow upsets proves to be memory intensive. The predominance of this class of upset has thus motivated the study of alternative, more abstract momitoring approaches. In the settings in which they have thus far been studied (1), these alternatives have proven to be quite effective. This suggests that upsets can potentially be viewed in more abstract terms than has heretofore been attempted. And this stands as a challenging problem for future research.

#### EXPERIMENTS

Given a computer system, to measure its susceptability/resilience to upsets, fault injection experiments must be performed. In such experiments, a baseline of information describing the system's fault-free performance must be available. This can be accomplished by running two identical systems in parallel with only one of the systems being subjected to the fault injections, and then using explicit comparisons of operational microevent data to study upset phenomena. However, since this requires the availability of two systems, it is usually impractical. Alternatively, "gold runs" and "fault runs" can be made on the same system. This is illustrated in Figure 4. In the gold run, no fault is injected and the data recorded forms the microevent baseline for comparison with that of the fault run.

It is crucial that sufficient detail be available in the recorded microevent to reconstruct the upset, but too much detail can confound the analysis. Usually, bus (data, address, and control) signals relative to the clock together with fault insertion parameters must be recorded. Fault insertion parameters include physical placements (single or multiple insertions on address, data, or control lines, power supply noise), durations (clock cycles), amplitude, types (latch-up, latch-down, noise), and program placement (points within a program state (i.e. loop) or slots within a shell program).

The recording of microevent data or even the indicating of an upset must be accomplished by means of external monitoring. It is not realistic to expect the system into which the faults are being injected to also observe and record its own upset data. This clearly follows from the observation that since the upset is a system level

event, it can certainly affect whatever software that has been integrated into the system for its observation/detection. However, in the companion paper (1), it is seen that rather simple devices for external monitoring are feasible for at least the detection of upsets. Such devices could be attached to, say, the bus lines and be transparent to overall system operation.

For fault injection experimentation, there should be some apriori knowledge of all possible valid and invalid states that a system can be driven into by a fault. If there is no sense of such a containment set of possible operation, the analysis of data to characterize susceptability/ resilience of the system to upsets can be prohibitively complex. The concept of a containment set relative to a computer system has been presented previously (5), (6) and will not be reviewed here. Suffice it to say that the containment set for a computer system represents all possible operational states. The existence of such a containment set can be enforced in a system (5) by adherence to software design rules and modest hardware modifications. If this is done, upsets can be significantly limited, so much so that their detection can be greatly simplified.

As an example of the simplification provided in the analysis of a system when a containment set is known, an INTEL 8085-based system (5) has been developed in which the only type of upset that can take place is invalid program flow. To demonstrate upset analysis with a contained system, a simple program was written so that there were only eight functional states. In other words, when not being driven by a fault, it can be verified that the system was always in one of these eight states. Upsets in the form of invalid program flow could then be measured in terms of invalid transitions among these eight states. Pigure 5 to Pigure 10 show transition matrices that indicate invalid program jumps. For these experiments, bursts of power supply noise was used as the fault source. It was generated by a reverse biased emitter junction and amplified for superposition on the five volt power supply.

In each transition matrix, the diagonal entries indicate the number of times the system was started in a state and after a transient fault (noise burst on the power supply) was injected, remained in that state. Every other entry, say, the entry in row i and column j, is the number of times an invalid program flow took place from state j to state i. For example, in Figure 5, consider row 2:

In this eight state system, this row indicates that when the system was initialized 10,000 times in state 2, and then a noise burst was injected at a random time, 259 times an invalid program flow took place to state 0, 185 times an invalid program flow took place to state 1, 9,263 times the system remained in state 2, 185 times an invalid program flow took place to state 3,...,66 times an invalid program flow took place to state

7. In summary, for this particular eight state system (i.e., this integrated hardware and software complex) and this particular injected fault (the details of the noise burst (i.e., amplitude, duration, frequency spectrum) are not important for this discussion), it is seen that 92.63% of the injections did not produce an invalid program flow upset from state 2. Moreover, when the system was in state 2 and an invalid program flow upset took place, the system was most likely to jump to state 0, 1, or 3 . Figure 6 is simply the transition matrix resulting from a repeat of the experiment that produced the transition matrix in Figure 5. It is meant to demonstrate the reproducibility of the experimental data. Although not identical, the two transition matrices of Figures 5 and 6 are quite similar.

Figures 7, 8, 9, and 10 are meant to indicate that the details of the injected transient fault do, indeed, have an impact on the system response. Using the same eight state system described above, two types of noise bursts were injected on the power supply line. Again, details of these two noise bursts are not crucial to the discussion and, furthermore, would be meaningless without an extended explanation of the system's operational specifications. Suffice it to say that the injected noise burst was higher in amplitude and longer in duration for the injections that produced the transition matrices of Figures 7 and 8 than for the injections that produced the transition matrices of Figures 9 and 10. It should also be stressed that unlike the injections that produced the transition matrices of Figures 5 and 6 which were randomly distributed throughout each state, the injections for the transition matrices of Figures 7, 8, 9, and 10 were all restricted to one particular but arbitrarily chosen point within each state.

Figures 7 and 8 correspond to repeated experiments that again show reproducibility for the "high amplitude-long duration" (HALD) experiments. Figures 9 and 10 correspond to repeated experiments for the "low amplitude-short duration" (LASD) injections. For each of these repeated run experiments, it should be kept in mind that the injection was always triggered at precisely the same point in a given state. Clearly, the difference in the transition matrices for the HALD experiments and the LASD experiments are dramatic. Such differences strongly underscore the notion that the details of the injected faults are highly important in experiments to assess a computer system's upset susceptability/resilience. It furthermore stands as a testimonial to the necessity of fault modeling research, for without accurate models of the perturbing fault phenomena, experimentally assessing the susceptability/ resilience of a computer system to upsets seems quite difficult. Finally, the possibility of "tuning" an external monitoring device so that it is sensitive to a particular upset characteristic (for example, given that the system is in a particular state, an invalid program flow monitor might give a high priority to checking

whether the system has made an invalid jump to one of those states that are most likely to be so jumped into as indicated by the transition matrix) is seemingly quite dependent on the fault model.

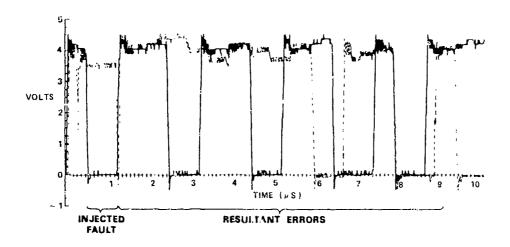
#### SUMMARY

Upset experimentation in computer systems is still very much in its developmental stages. However, a number of important factors that should be taken into account for such endeavors to be successful are now known. To begin, there is a need to have some apriori knowledge of features of upsets. These features are usually associated with operational aspects of the system being studied and its task. On the other hand, there is a danger of only finding what one is looking for that must be balanced with this perspective. It is usually impractical to have duplicate systems for direct comparison, so the actual monitoring of the system must be done with external devices. These external monitors must transparently observe a wide variety of operational parameters. However, there is now evidence (1) that such monitors can be rather simple in design. The details of the injected faults are apparently crucial to the system responses. Hence fault modeling research and efforts to extract generic features of the potentially disturbing fault source are extremely important. For without realistic injections, the susceptability/resilience data that is collected might be irrelevant. Finally, the apriori design of the system so that upset activity can be contained is exceedingly useful and worthy of further research.

#### REFERENCES

1. M. Schmid, R. Trapp, G. Masson, and A. Davidoff, "Monitors for Upset Detection in Computer Systems," Proceedings of the 1983 International Aerospace Conference on Lightning and State Electricity, June, 1983. 2. M. Schmid, R. Trapp, A. Davidoff, and G. Masson, "Upset Exposure by Means of Abstraction Verification," Proceedings of the 12th Annual International Symposium on Fault Tolerant Computing, June, 1982. 3. R. Glaser and G. Masson, "Transient Upsets in Microprocessor Controllers," Proceedings of the 11th Annual International Symposium on Fault Tolerant Computing, June, 1981. 4. R. Glaser and G. Masson, "The Containment Set Approach to Crash-Proof Microprocessor-Based System Design," The Proceedings of the 12th Annual International Symposium on Fault Tolerant Computing, June, 1982. 5. R. Glaser and G. Masson, "The Containment Set Approach to Upsets in Digital Systems," IEEE Transactions on Computers, July, 1982. 6. G. Masson and R. Glaser, "The Containment Set Approach to Digital System Tolerance of Lightning-Induced Transients, Proceedings of the International Aerospace Conference on Lightning and Static Electricity, March, 1982.

# EFFECT OF TRANSIENT INJECTED ON THE "READ" CONTROL LINE



--- GOLD RUN
--- FAULTED RUN

Fig. 1 - The effect of one microsecond transient fault on the "READ" control line of a 8085-based system.

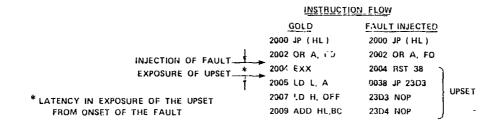


Fig. 2 - The results of the injected fault of Figure 1 from an upset perspective.

An invalid program flow has taken place.

### PROGRAM FLOW VERIFICATION

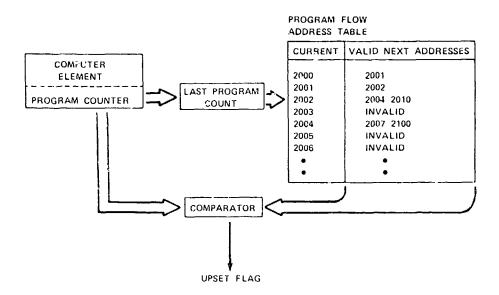


Fig. 3 - A schematic of a complete implementation of a program flow monitor that would externally monitor a computer system for such upsets.

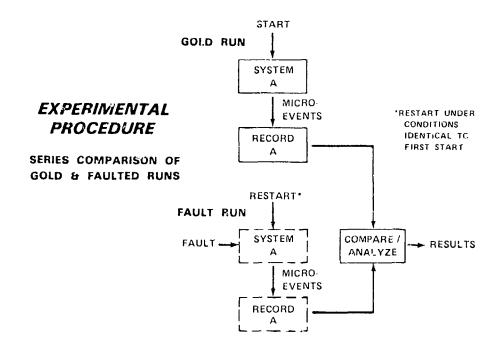


Fig. 4 - A "gold run" - "fault run" approach to fault injection experimentation of a computer system.

	0	1	2	3	4	5	6	7
0	9370	247	98	148	12	33	13	80
1	275	9365	92	143	16	23	8	79
2	259	185	9263	185	16	17	10	66
3	254	204	71	9347	20	24	14	67
4	253	262	83	136	9158	29	8	72
5	217	145	82	192	21	9248	28	68
6	229	224	74	170	13	20	9173	93
7	259	199	88	183	21	26	9	9216

Fig. 5 - A transition matrix of an INTEL 8085-based system with a containment set consiting of eight states. The transition matrix was produced using power supply noise injections randomly distributed throughout each operational state.

	0	1	2	3	4	5	6	7
0	9375	260	100	139	14	24	8	81
1	286	9368	84	167	16	13	19	48
2	<b>29</b> 0	212	9193	188	10	25	12	70
3	276	203	31	33دو	23	21	9	55
4	255	226	54	125	9235	28	11	67
5	284	119	73	213	17	9199	35	61
6	245	219	77	150	18	27	9208	<b>57</b>
7	271	228	61	153	14	23	10	9243

Fig. 6 - A transition matrix resulting from a second experimental run using the same system and fault source as that used to obtain the transition matrix of Figure 5.

	0	1	2	3	4	5	6	7
0	4885	5	24	26	1	5	3	52
1	9	4966	24	37	1	4	4	56
2	8	9	4900	31	0	2	0	51
3	4	39	29	4872	3	4	5	45
4	2	7	32	19	4877	2	3	59
! [								
5	14	9	19	28	1	4872	2	55
6	4	11	27	25	0	2	4891	41
7	9	8	15	16	4	3	2	4944

Fig. 7 - A transition matrix for an eight state containment set £085-based system. The injected fault is a burst of power supply noise. For a given state each injection takes place at the same point. Relative to the injections corresponding to Figures 9 and 10, the noise burst is of high amplitude and long duration.

	0	1	2	3	4	5	6	7
[			<del> </del>	<del></del>				
0	4870	12	26	23	0	3	2	65
1	5	4878	23	26	0	ó	0	63
2	4	6	4905	28	3	4	1	50
3	6	28	14	4884	2	4	2	61
4	4	12	23	20	4887	3	1	51
5	4	10	24	38	0	4879	1	45
6	5	11	21	25	1	7	4869	62
7	5	8	23	24	3	0	1	4937

Fig. 8 - A transition matrix resulting from a second experimental run using the same system and fault source as that used to obtain the transition matrix of Figure 7.

	0	1	2	3	4	5	6	7
0	4829	122	14	16	1	2	1	16
1	82	4883	9	13	ı	1	1	11
2	124	159	4681	21	2	2	1	11
3	91	157	ρ	4727	3	2	1	12
4	75	174	15	42	4675	1	1	18
5	267	34	1.3	27	3	4632	22	3
6	39	171	7	26	5	6	4671	16
7	89	177	17	29	0	3	0	4686

Fig. 9 - A transition matrix for an eight state containment set 8085-based system. The injected fault is a burst of power supply noise. For a given state each injection takes place at the same point. Relative to the injections corresponding to Figures 7 and 8, the noise burst is of low amplitude and short duration.

	n	1	2	3	4	5	6	7
0	4788	152	16	21	1	4	1	1/8
1	90	4845	14	26	2	1	1	22
2	117	144	4673	34	4	5	4	22
3	80	162	14	4716	4	4	1	20
4	66	146	14	35	4720	6	0	14
_								
5	249	37	21	30	ზ	4633	13	7
6	118	177	20	33	2	9	4624	18
7	105	153	12	46	1	5	1	4678

Fig. 10 - A transition matrix resulting from a second experimental run using the same system and fault source as that used to obtain the transition matrix of Figure 9.

CONDITIONS CONDUCIVE TO LIGHTNING STRIKING AN AIRCRAFT IN A THUNLERSTORM

Vladislav Mazur Cooperative Institute for Mesoscale Meteorological Studies University of Oklahoma Norman, Oklahoma 73019

> Bruce D. Fisher NASA/Langley Research Center (lampton, Virginia 23665

John C. Gerlach NASA/Goddard Space Flight Center Wallops Flight Facility Wallops Island, Virginia 23337

### ABSTRACT

The UHF band radar at NASA/Wallops Island Research Facility was used for guiding the NASA F106 research aircraft chrough the upper regions of storms with lightning activity in them so that the aircraft would be struck by lightning. The radar was used also as a rool to study nature and the characteristics of direct lightning strikes on the aircraft, and to determine the environmental conditions favorable to such strikes. The analysis of lightning echoes at the moments of the strikes strongly indicates that the aircraft itself triggers the lightning, rather than intercepting a naturally produced flash. The lightning echo characceristics of the strikes are similar to those of intracloud flashes, and led us to believe that the aircraft is most of the time part of the lightning channel. The probability of a direct strike during a storm penetration (PDS) is defined here as the racio of the number of direct strikes on the aircraft to the total number of flashes occurring in the radar resolution volume containing the mircraft. Correlations between the IDS and the intensity of rain and turbulence, temperature, and lightning flash rate in the scorms penetrated were investigated. The trends in these parameters indicate that the highest risk of the aircraft being struck by lightning during a penetration in the upper regions of thunderstorms is when 1) there are temperatures of -40°C and lower, 2) there is little or light precipitation, 3) there is light or no turbulence, and 4) there is a lightning flash rate of 10 per min.

IN OUR STUDY OF THE ELECTRICAL INTERACTION between aircraft and clouds, we are trying to find answers to the following questions: 1) Does the aircraft trigger lightning or does it intercept a naturally produced lightning channel? and, 2) What are the environmental conditions in the cloud that lead to a direct strike to the aircraft? For reasons of safety, the flying conditions have been divided into two categories: non-electrically active clouds which are considered to be safe, and electrically active storms which are considered to be risky. However, sizable data has been collected on direct strikes to aircraft under flying conditions of the first type. Several reports (1, 2, 3, 4) have shown that the most probable region for such strikes is at or near the freezing level. The circumstantial evidence, including synoptic conditions and radar observations has strongly suggested that the clouds in which the aircraft were struck had no previous lightning activity, and that therefore the direct strikes were triggered by the aircraft itself (5). A few research programs that have used specially instrumented aircraft for flying in stormy clouds have focused mostly on measuring the electrical parameters of direct otrikes and nearby flashes, rather than on the systematic study of conditions generally conducive to lightning strikes on aircraft in thunderstorms.

There is little evidence to suggest that strikes to the aircraft in non-stormy and stormy clouds are different. A "static discharge" often characterized by preliminary display of corona or by huildup of radio interference is typical in non-stormy clouds, while an abrupt and fairly severe discharge occurs in stormy clouds. Because of the possible difference in the type of discharge and conditions leading to it, it seems logical to study the electrical interaction of aircraft with non-stormy and stormy clouds separately. While measuring the parameters of direct strikes is necessary for designing and testing the aircraft, understanding the conditions of direct strikes is important to avoid lightning hazards to aircraft. We think it is necessary to identify and determine the probability of a dia rect strike to an aircraft, which may be different when flying through non-stormy and stormy clouds.

In this report, we describe some preliminary results of the NASA/Langley storm hazards program conducted in the Summer of 1982. Our emphasis will be on lightning redar echo parameters of direct strikes to the NASA F106 research sircraft, and the conditions under which the aircraft was struck during penetrations of thunderstorms.

#### EXPERIMENTAL PROCEDURE

The NASA/Wallops Island Research Facility in Virginia has been used to provide guidance to the F106. The facility includes a UHF and an S-band (SPANDAR) radge with the capability of aircraft tracking. The operational characteristics of these radars are described in (6). The UHF radar was used to detect the range, azimuth, and elevation angle of echoes from ionized lightning channels. A special device was designed to count the number of lightning echoes in a selectable range interval along the radar beam. This allowed us to determine in real time the location of a lightning activity core. A storm's reflectivity and lightning activity observed prior to and between storm penetrations were used for selecting the storm and the altitude of the next penetration. The initial assumption for the aircraft guidance was that the storm regions with the most intense lightning activity are the most likely regions where the FlO6 would be struck. Accordingly, the F106 was guided through the upper core of lightning flach density (i.e., flashes per min per km of range) in the storm, which is usually above -30°C level (6). The advantages of flying at these altitudes are that there is only a minimal risk of hail damage to the aircraft and there is less turbulence. The method of guiding the Fl06 research aircraft with the SPANDAR and the UHF radars has proven to be very effective. During the 44 penctrations conducted with this method in the Summer of 1982, the F106 was struck 49 times, i.e., an average of about one strike per penetration. The maximum number of direct strikes during the penetration of a single storm (cell) was 4. By tracking the aircraft in the storm with both radars, we obtained data of lightning echoes for strikes to the aircraft as well as the cloud reflectivity level within the aircraft vicinity.

# TRIGGERING LIGHTNING BY THE F106

In every case of a direct lightning strike to the aircraft when the F106 was tracked by the UHF radar, there was a lightning echo recorded. In only one of these events did other lightning echoes exist in the vicinity of the aircraft within 500 ms before the strike to the aircraft. The on-

ly case was a flash, which occurred about 1.8 km from the F106, that was followed by the direct strike 190 ms later. Based on both radar data and the visual observations by the crew, the lightning flashes were separate events. We analyzed the echo development of flashes that struck the aircraft with a time resolution of 16.6 ms (i.e., of one TV field), and found that every lightning echo starts directly from (on top of) the F106 echo. Fig. I shows a typical example of such an echo. If the strike to the aircraft were caused by a naturally occurring flash, i.e., the aircradt intercepted an existing flash, we would expect to see: 1) the echo in the radar beam at some distance from the aircraft, 2) progression of this echo toward the aircraft, and 3) the lightning echo spreading across the aircraft at the instant of the strike. However, none of the lightning flashes with this pattern of echo development (Fig. 2) ever struck the F106. Thus, the analysis of the UNF radar data of direct strikes to the sircraft strongly in. dicates to us that the direct strikes were triggered by the aircraft ilself.

ECHO CHARACTFRISTICS OF DIRECT STRIKES TO THE F106

The maximum radar cross section (RCS) of each lightning echo, its duration, and range-time variation for each direct strike to the F106 have been analyzed. The F106 echo itself was always at least 20 dBZ less than that from a lightning flash, i.e., its contribution to RCS of a flash is negligible. We have characterized the range-time variation of echoes by their continuity in time and movement of the echo along the radar beam. In the first category, we separated cases of single cycle echo development from the multicycle one with time intervals between cycles 4170 ms (7), by analogy with single and multistroke cloud-to-ground flashes. In the second category, we identified three different types of echo development: 1) stationary, 2) bidirectional, which progresses in both directions from the F106, and 3) unidirectional, which moves in only one direction from the F106. The majority of direct strikes are the single cycle (98%) and bidirectional (79%) in range development. The lightning echo wnich begins at the aircraft and simultaneously moves toward and from the radar with a continuously high RCS at the aircraft is indicative of the aircraft being a part of the lightning channel during the entire flash. From the histograms of echo duration for both direct strikes to the aircraft and naturally occurring flashes, which are probably intracloud (IC) due to the high altitude (Fig. 3a,b), we find no substantial difference in flash duration. A comparison of

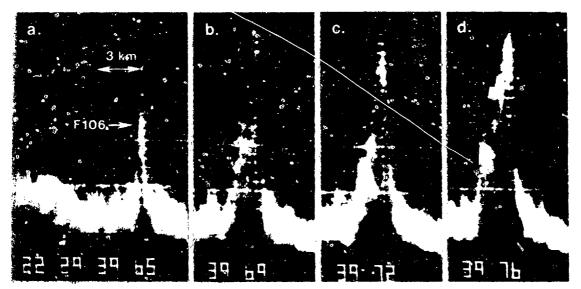


Fig. 1 - Radar echo development of a direct strike to the F106 research aircraft. Photographs are made from TV screen in sequence with time resolution of 30-40 ms. Notice the build-up of lightning echo above aircraft echo, which is typical of direct strikes

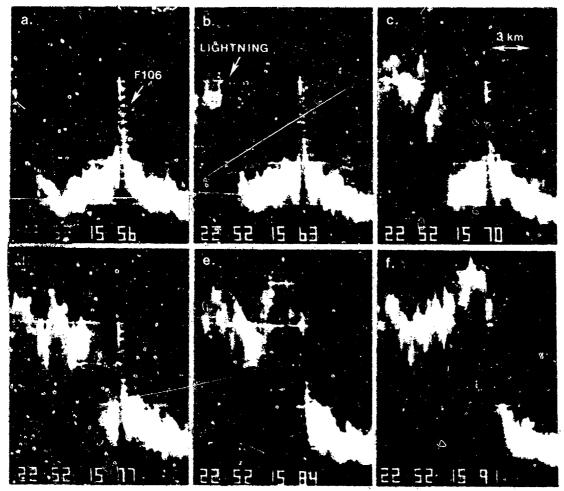


Fig. 2 - Radar echo development of a lightning flash propagated in space, which passed by the F106 research aircraft without striking it. The lightning echo appears at the left side of picture A, and propagates in range from the radar (to the right) with an average radial velocity of  $2.2 \times 10^5$  m/s

the RCS of the naturally occurring lightning flashes and direct strikes also shows no apparent difference between them. Thus, based on our radar measurements, we believe that flashes triggered by the aircraft penetrating the upper region of a storm are not much different from natural IC flashes. However, we do find a difference in the range development of direct strike and IC flash. Very often an echo from an IC flash moves along the radar beam as a sea wave, the crest of which is the maximum RCS at any given moment. On the contrary, the direct strikes (85% of cases) commonly have their maximum RCS at the aircraft while the echo itself propagates uni- or bidirectionally in range. For comparison we present in Fig. 3c the histogram of the single-cycle echoes from cloud-to-ground flashes (CG). The CG flashes were verified by the electric field changes (8). The radar echo of CG flashes and its peak (the maximum RCS) is stationary in range in most cases (96%). very much like the maximum RCS of a direct strike. However, the average echo duration of CG flashes (390 ms) is much shorter than that of direct strikes to the aircraft (630 ms). This difference in durations indicates to us the presence of continuous current in the direct strike to the aircraft. Such a suggestion was made in an earlier study in France (9), based on records of the current flow along the aircraft skin.

### PROBABILITY TO BE STRUCK BY LIGHTNING

In determining the conditions of direct strikes to the aircraft, we looked at environmental parameters such as rain, turbulence, and lightning flash rate, as well as the number of direct strikes during storm penetrations. In addition, we thought it was important to determine the factor of risk for the aircraft being struck. We define this risk factor as the probability of a direct strike while penetrating the storm (PDS), which is the ratio of the number of strikes to the F106 to the total number of lightning flashes in the radar resolution volume of a length of 150 m which contains the aircraft echo. The latter flashes have echoes spread across the aircraft echo. The concept of the probability of a direct strike was introduced first by Fitzgerald (10). However, Fitzgerald measured the PDS as a ratio of the number of strikes to aircraft to the total number of flashes in the storm determined from electric field changes recorded on an aircraft flying above the storm. As recent studies (6, 11) show, the lightning activity in some storms tends to be separated into an upper and a lower center. Therefore it seems reasonable to include in our PDS only the flashes in the upper region of the storm penetrated by the F106.

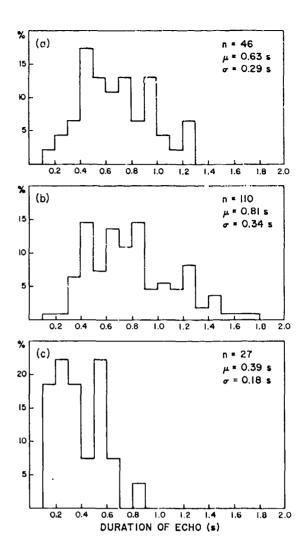


Fig. 3 - Histograms of radar echo duration of a) direct lightning strikes to the F106 measured at the aircraft; b) naturally occurring lightning flashes at high altitudes, presumably intracloud in the majority; c) naturally occurring cloud-to-ground flashes verified by the electrical field changes. Population includes single stroke CG flashes and first strokes of multistroke CG flashes

The beginning and the end of penetration were found in the UHF radar data, when possible. Otherwise, we used the crew's visual observations from the voice log to determine these times. In most cases, a penetration was through a single storm or cell in a squall line, and lasted less than 1.5 min. During two of thirty-eight penetrations, the UHF radar indicated no lightning activity in the storm prior to penetration, and the direct strikes to the F106 were the only lightning flashes that occurred. In the remaining 36 cases, the storms contained lightning before the F106 entered them. The PDS and its dependence on environmental conditions in the storms was

determined for these penetrations. Fig. 4 shows that the PDS is not much different for regions containing no or light-to-moderate precipitation, but it decreases considerably for heavy precipitation. The PDS tends to decrease with the increase in turbulence (Fig. 5). We have some doubt as to the accuracy of estimates of the precipitation and turbulence intensity by the aircraft crew, especially in distinguishing between light and moderate. However, the trend mentioned above is very noticeable when we compare the PDS in the category without rain (turbulence) to that in the category of heavy rain (turbulence). From the recorded temperature inside the storm measured on board the F106, we find that the PDS increases steadily with decreasing cloud temperature, or increasing altitude (Fig. 6). We also examined the flash rate which characterizes the lightning activity in the storm penetrated by the aircraft. The average PDS for storms with different flash rates is shown in Figure 7. From this we see that the average risk of being struck by lightning, i.e., trigger a flash to the aircraft, decreases in storms with higher rates of naturally occurring lightning.

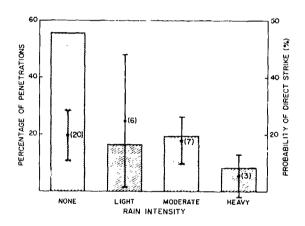


Fig. 4 - Rain intensity in storms penetrated by the F106 aircraft and the probability of direct strike. The total number of penetrations is 36.

The shaded columns are the percentage of all penetrations that were made versus the level of rain intensity reported by the aircraft crew during the penetration. The dots are the average probability of direct strike (PDS) for the number of penetrations shown in parentheses. The vertical bars are the 90% confidence intervals

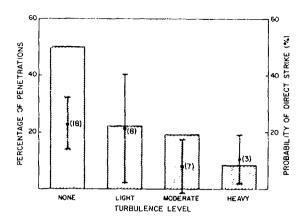


Fig. 5 - Level of turbulence within the storm penetrated by the Fl06 aircraft and the probability of direct strike. The total number of penetrations is 36. The shaded columns are the percentage of all penetrations that were made versus the level of turbulence reported by the aircraft crew during the penetration. The dots are the average probability of direct strike (PDS) for the number of penetrations shown in parentheses. The vertical bars are the 90% confidence intervals

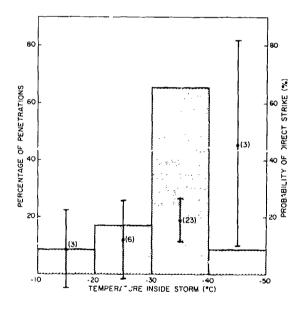


Fig. 6 - Temperature inside the storms penetrated by the Fl06 aircraft and the probability of direct strike. The total number of penetrations is 35. The shaded histogram is the percentage of all penetrations that were made versus the temperature inside the storm during the penetration. The dots are the average PDS for the number of penetrations shown in parentheses. The vertical bars are the 90% confidence intervals

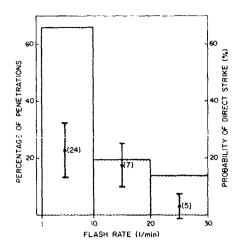


Fig. 7 - Lightning flash rate in storms penetrated by the Fl06 aircraft and the probability of direct strike. The total number of penetrations is 36. The shaded histogram is the percentage of all penetrations that were made versus the flash rate during the penetration. The dots are the average PDS for the number of penetrations shown in parentheses. The vertical bars are the 90% confidence intervals

### CONCLUSIONS

The UHF-band radar with its conical antenna pattern is an effective tool for the study of direct strikes to aircraft. It has provided us with the observational evidence that the aircraft actually triggers lightning in the upper regions of storms. The radar technique described here can be used in future studies to determine: 1) the PDS in storms at different altitudes as a function of environmental parameters and storm development, and 2) the nature of direct strikes to the aircraft in nonstormy clouds.

Our observations that the highest strike rate occurs at the -40°C level agrees with those by Fitzgerald (10) and by Fisher and Plumer (12). The suggestion about similarity between direct lightning strikes to the aircraft and natural intracloud flashes made by Clifford and Kazemir (5) is supported by our measurements of radar echo parameters. The relatively long duration of the echo from direct strikes to the aircraft is good evidence for the presence of a continuing current in strikes reported by French scientists (9).

We discovered that the PDS in storms with a flash rate of > 20  $1/\min$  is very low, while the PDS in storms with a rate of < 5  $1/\min$  is much higher than that in the active storms. The observation of a similarly small number of strikes in regions of extensive lightning activity was reported by Newman et al. (13).

In the absolute majority of penetrations, visual observations of flashes by the aircraft crew coincided with the UHF radar data. The exceptions were a few cases with high reflectivity levels in the cloud.

We believe that the probability of direct strike (PDS) to aircraft in thunderstorms, which takes into account only lightning flashes occurring in the vicinity of the aircraft, can serve as an estimate of the risk factor of lightning hazards to aviation. The trends in the relationship between the PDS and environmental parameters of the storm, determined as a result of this study, indicate that the upper regions of thunderstorms 1) at temperature levels of -40°C and lower, 2) with light or no precipitation, 3) with light or no turbulence, and 4) with a lightning flash rate of <10 1/min hold the highest risk for aircraft to trigger lightning during the penetration.

### REFERENCES

- 1. F. A. Fisher and J. A. Plumer, "Lightning Protection of Aircraft". NASA Ref. Public. 1009, ch. 3, Oct., 1977.
- 2. I. M. Imyanitov, "Aircraft Electrification in Clouds and Precipitation". USAF Foreign Tech. Div. Rep. FTD-HC-23-544-70, Apr., 1971. Published originally in Electrizatsiya Samoletov v Oblakach i Osadkakh, pp. 1-211, 1970.
- 3. W. E. Cobb and F. H. Holitza, "A Note on Lightning Strikes to Aircraft". Monthly Weather Review, 96, No. 11, Nov., 1968.
- 4. I. I. Kamaldina, "Lightning Strike to Aircraft in Nonstormy Regions", (in Russian). Tr. Glavnoi Geophys. Observat., 301, 134-141, 1974.
- 5. D. W. Clifford and H. W. Kazemir, "Triggered Lightning". IEEE Trans. on Electromagn. Compat., EMC-24, No. 2, 112-122, 1982.
- 6. V. Mazur, J. C. Gerlach and W. D. Rust, "Lightning Flash Density Versus Altitude and Storm Structure from Observations with UHF- and S-band Radars", (present issue).
- 7. V. Mazur and W. D. Rust, "Lightning Propagation and Flash Density in Squall Lines As Determined With Radar". J. Geophys. Res., 88, 1495-1502, 1983.
- 8. D. M. LeVine and V. Mazur, "Correlated Measurements of UHF Radar Signatures, RF Radiation and Electric Field Changes from Lightning", (present issue).
- 9. Centre d'Essais Aeronautique de Toulouse, "Mesure des Characteristiques de la Foudre en Altitude". Essais No. 76/650000P.4 et Final. July, 1979.

- 10. D. R. Fitzgerald, "Probable Aircraft Triggering of Lightning in Certain Thunderstorms". Monthly Weather Review, 95, p. 835, 1967.
- 11. W. L. Taylor, W. D. Rust, D. R. Mac-Gorman and E. A. Brandes, "Lightning Activity Observed in Upper and Lower Portions of Storm and its Relationship to Storm Structure from VHF-Mapping and Doppler Radar", (present issue).
- 12. B. D. Fisher and J. A. Plumer, "Lightning Attachment Pattern and Flight Conditions Experienced by the NASA F106B Airplane, (present issue).
- 13. M. M. Newman, J. R. Stahman, J. D. Robb, E. A. Lewis, S. G. Martin and S. V. Zinn, "Triggered Lightning Strokes at Very Close Range". J. Geophys. Res., 72, 4761, 1967.

### ACKNOWLEDGEMENTS

We are indebted to the personnel of the NASA/Langley Storm Hazards Program and the NASA/Wallops Island Research Facility, whose cooperation in data collection as well as data reduction made this study possible. We wish to express our appreciation to Mr. Norman Crabill for his receptiveness and support during the experiment. We thank Mr. Dale Sirmans at the National Severe Storms Laboratory in Norman, Oklahoma, for his generous help in designing and building the device for counting echoes from lightning in real time. We are grateful to Dr. W. David Rust for his helpful suggestions and productive discussions in the process of preparation of this paper.

This work was supported in part by National Aeronautics and Space Administration Grant No. NCC5-600.

# LIGHTNING INITIATION IN THUNDERCLOUDS

E STAR COPPLY . If )

J LATHAM

, nicroA

Epube)

ABSTRACT

Experiments have been carried out to determine the electric field,  $E_c$ , required to obtain coronn from both ice particles and colliding drop-pairs. In the former case it was found that corone currents of about 0.140 and above could be obtained from ice particles a few millimetres in length for  $E_c$   $4 \times 10^{5}$ V m<sup>-1</sup> for values of temperature and pressure likely to occur in the mid-regions of a thundercloud. These currents were drastically reduced if temperature was below  $-18^{4}$ C, owing to the reduction in surface conductivity suffered by the ice sample. In the second set of experiments, a pair of water drops, of radii R=2.7mm and r=0.65mm, collided with a relative velocity of  $5.8 \text{m/s}^{-1}$ . Values of  $E_c$  ranged from  $\sim 5 \times 10^{5}$ V m<sup>-1</sup> for glancing collisions which produce, momentarily, long liquid filaments.

10/2

106/10 (m)

aprox. There is in it.

A MAJOR DIFFICULTY in explaining the initiation of lightning lies in the fact that in order to account for the development of the stepped leader one requires the existence of electric fields of about  $2 \times 10^{6} \text{V} \text{ m}^{-1}(1)^*$  whereas the largest reliably measured values of the electric fields existing in the mid-regions of a thundercloud do not exceed a value of  $4 \times 10^5 \text{V}_{\text{m}}-1$ (2). Clearly, some means of intensifying the ambient field is required in order to explain this discrepancy. Many investigators have favoured the suggestion that lightning is triggered by corona discharges emanating from the surfaces of raindrops that are highly deformed by electrical forces. This mechanism was investigated experimentally by Richards and Dawson (3) who suspended large drops in a vertical wind tunnel at a pressure of about one atmosphere in the presence of an electric field, and found that corona was induced by hydrodynamic instability at the top surface of the drop under the influence of the electrical forces. For uncharged drops of radii greater than 2mm the critical field for corona onset was  $\sim 9.5 \times 10^{5} \text{V m}^{-1}$ . If the drop carried a large charge of the appropriate sign, this value was reduced to  $\sim 5.5 \times 10^{-5} V \ m^{-1}$  . Further support for the suggestion that corons could be the triggering mechanism came from the work of Phelps (4,1) who showed that, at NTR positive corona streamers will propagate indefinitely if the ambient electric field is  $\sim 4 \times 10^{5} \text{V m}^{-1}$ and will intensify if the field exceeds this value. In the lower pressure environment of the thundercloud, the value of the field required to just permit propagation is probably around 3  $\times$  10 $^{5}$ V m<sup>-1</sup>,

### LABORATORY EXPERIMENTS

In this section we describe experiments designed to investigate the conditions under which corona may be produced from two further possible sources. The first involves the collision of a pair of raindrops in a strong electric field, producing, temporarily, an elongated filament of water, which provides a favourable site for the initiation of corona. The second examines the conditions under which corona may be initiated from the extremities of ice hydrometeors. These studies have been described in full by Crabb and Latham (5) and Griffiths and Latham(6).

In the first set of experiments, conducted at a pressure of one atmosphere, pairs of water drops were caused to collide in a region of strong vertical electric field between two parallel plate electrodes. The larger of the two drops was

allowed to fall vertically through a hole in the upper electrode. The release of this drop was used to trigger the ejection of a smaller drop upwards through a hole in the lower electrode from a small wind tunnel located beneath the electrode system. The two drops could be made to produce different types of callision by varying the relative trajectories. Measurements were made of the value of the electric field,  $E_{c}$ , required to initiate corona from the colliding pair. For two drops of radii R=2.7mm and r=0.65mm, colliding with a relative velocity of 5.8m s<sup>-1</sup> (a value close to the difference in terminal velocities for drops of these sizes falling in air) it was observed that the large drop went into the "wag-mode" for central collisions, whilst for more glanccollisions a liquid filament, typically several times R in length, was drawn out between the separating drops and eventually collapsed. The values of  $E_{\rm C}$  decreased with increasing values of  $E_{\rm C}$  the length of the combined drop-pair in the direction of the field at the moment of separation - which itself increased as the collisions became less central. Ec ranged from about 5 x  $10^{5}$ V m<sup>-1</sup> for head-on collisions to about 2.5  $\times$  10<sup>5</sup>V m<sup>-1</sup> for glancing collisions producing the longest filaments. A small number of corona pulses, each carrying about  $10^{-10}\mathrm{C}$  of charge, accompanied each corona-producing collision.

The experiment on corona from ice particles were performed in a low-pressure chamber in which the ice sample under test could be suspended by freezing it onto a quartz fibre which was located so that the ice sample was centrally located between two parallel-plute electrodes across which a known voltage could be maintained, thereby providing a region of uniform electric field. The temperature and pressure within the chamber could be maintained at any desired values in the ranges  $0^{\circ}\text{C}$  to  $-80^{\circ}\text{C}$ , and 2 x  $10^4$  to  $10^4\text{Pe}$  respectively. The ice samples were grown from the vapour in diffusion chambers, and particular crystels could be selected for investigation. Artificial hailstones could be produced by freezing successive layers of water onto an ice pellet which had been attached to the quartz fibre. Having located the ice crystal, which was typically a few millimetres in length, the electric field was slowly increased until the point was reached at which corona was initiated from the extremities of the ice sample. The value of this field, Ec, was noted. The corona discharges could be monitored on either an oscilloscope or a sensitive ammeter, and could also be seen with the darkadapted eye, the experiments being

\*Numbers in parentheses designate References at the end of the paper

performed in a darkened room. Using this method, values of  $E_{\rm C}$  were determined for a large number of ice crystals of various types (needles, prisms, plates and dendrites) and rough ice spheres approximating hailstones, as a function of pressure and temperature. Other variables studied included, size, shape, purity, and orientation in the field. It was found that the current at the onset of corona was about 0.1uA in all cases studied, independent of pressure, and also of temperature in the range OOC down to -18°C; below which temperature a drastic reduction in the magnitude of the corona current was observed. This was examined in some detail and it was concluded that this effect was due to the fact that at this point the surface conductivity of the ice sample fell below the value required to permit the currents needed for continuous coruna, the bulk electrical conductivity being inadequate at all temperatures to permit such currents to flow. It was found that En was a linear function of pressure for any particular ice sample, typical values being about 4 x  $10^5$ V m<sup>-1</sup> at 5 x  $10^4$ Pe pressure, and 8 x  $10^5$ V m<sup>-1</sup> at  $10^5$ Pa for crystals of a few millimetres in length. No clear-cut relationship between  $E_{\mathbf{c}}$  and crystal length was found, and it was concluded that the surface structure at the discharging tips of the ice crystal on the microscale was more important than length in determining the value of  $E_c$ .

### DISCUSSION

These experiments demonstrate that both colliding water drops and ice crystals can give rise to corona discharge in conditions likely to occur in the mature stages of thundercloud growth. Of course, not all corona discharges will necessarily lead to a lightning stroke. The fate of ions produced by corona that do not subsequently give rise to lightning will be to affect the ionic conductivity of the cloud. Griffiths, Latham and Myers (7) have shown that in the case of corona from ice crystals, a concentration of one discharge site per metre<sup>3</sup> will be sufficient to increase the equilibrium ion concentration within the cloud to values comparable with those in clear air at the same altitude. However, in the case of colliding drop-pairs, the \*requency of collisions and the quantities of charge released per event are not sufficient to affect the ionic conductivity significantly.

On the question of lightning initiation, the types of corona event described here have a number of features which appear to be particularly conducive to the production of systems of propagating and growing of positive structures that probably constitute the embryo lightning struke. Collid-

drop-pairs can give corona in fields considerably less than those required by any other known mechanism that could occur in a thundercloud. However, the quantities of charge released are restricted to values similar to those released by single-drop corona. Additionally, a considerable fraction of such discharges will occur in fields which are less than those required to permit positive streamer propagation. On the other hand, it is evident that where fields greater than the propagation field exist, colliding drop-pairs can give rise to very vigorous discharges, since the ambient field must then be considerably in excess of the minimum corona onset field.

In considering the properties of ice particles as corona sources, one of the most important features is the fact that both polarities of discharge can occur simultaneously, so that the quantity of charge released is not limited either by the accumulation of charge on the hydrometeor, as it is in the case of a single drop, or by the short duration of the source's existence, which may be a limiting factor for colliding drop-pairs. Because of this property, ice particles can produce large numbers of the highly mobile positive streamers at one end, whilst the less mobile negative ions are produced at the other end.

These experiments indicate that corora discharges from both hydrometeors and colliding drop-pairs are of primary importance in lightning initiation.

### REFERENCES

- 1. C T Phelps, "Positive streamer system intensification and its possible role in lightning initiation", J Atmos & Terr Phys, (1974), Vol 36, pp103-111
- 2. W P Winn, G W Schwede & C B Mcore, "Measuremente of electric fields in thunderclouds", JGR, (1974), Vol 79, pp. 1761-1767.
- 3. © N Richards & G A Dawson, "The hydro-dynamic instability of water drops falling at terminal velocity in vertical fields", JGR, (1971), Vol 76, pp 3445-3455
- 4. C T Phelps, "Field enhanced propagation of corona streamers", JGR, (1971), Vol76, pp 5799-5806.
- 5. J A Crabb & J Latham, "Corone from colliding drops as a possible mechanism for the triggering of lightning" Q J Roy Met Soc, (1974), Vol 100, pp 191-202.
- 6. R F Griffiths & J Latham, "Electrical corona from ice hydrometeors", Q J Roy Mat Soc, (1974), Vol 100, pp163-180.

7. R F Griffiths, J Latham & V Myers, "The ionic conductivity of electrified clouds", Q J Roy Met Soc, (1974), Vol 190, pp 181-190

## ACKNOWLEDGEMENTS

My colleagues Dr John Crabb and Dr Richard Griffiths made major contributions to the research described in the paper.

# AD P002237

THE ORGIN OF

THUNDER TORM - ELECTRICITY

by Anton PUHRINGER

Austria

### ABSTRACT

Since BENJAMIN FRANKLIN, it has been known that lightning bolts are enormous electrical sparks. For over 230 years, many efforts have been made in vain to explain the production of thunderstorm-electricity. All known physical methods have been utilized except one: the generation of electricity by electromagnetic induction (e.m.i.) has hitherto not been used as a basis for a thunderstorm theory.

All presuppositions for the application of the e.m.i. to a cloud are present, because there exists electrical conductors in form of water droplets which are moved by winds in the magnetic field of the earth.

The new theory, giving the possibility of involving new parameters - the wind and the geomagnetic field - in the research programs, is substaintiated in many points by observations.

### A) THUNDERSTOPM RESEARCH DURING ANTIQUITY

The first attempts at explanation were made in the sixth and fifth centuries B.C. by the "Ionic" natural philosophers ANAXIMANDER, EMPEDOKLES, ANAXAGORAS and others. Some of them thought lightning to be flaming gas ignited by the collision and friction among clouds, others thought it to be fire criginating from the sun or the stars. Although their ideas appear to us to be somewhat fantastic - - these were still the first courageous steps taken against the hitherto prevailing mythological concepts.

LUCIUS ANNAEUS SENECA, in his effort to summarize all the scientific knowledge of his time in his "Naturales Quaestiones" (65 A.D.) compared lightning to small sparks similar to those produced by flints. Some 1700 years later lightning was again compared to a small spark.

B) THUNDERSTORM RESEARCH IN MODERN TIMES

The discovery of electrical sparks in 1671 by G.W. LEIBNITZ with the aid of an electric generator - a rotating sulphur ball which was frictioned by the hand - built by OTTO VON GUERICKE provided the basis for further progress. Soon thereafter, in the first half of the eighteenth century, the assumption was repeatedly expressed that lightning is an electric spark.

In 1749 BENJAMIN FRANKLIN described in an article sent to P. COLLINSON, London, methods by which he could prove the presence of electrical charges in thunderclouds.

On 10 May 1752 DALIBART - a French botanist who translated the papers of B. FRANKLIN - succeded in proving the electric nature of lightning by installing a tall isolated mast in Marly-la-Ville, near Paris, while B. FRANKLIN duplicated this soon after in June 1752 in Philadelphia, with the aid of a kite.

B. FRANKLIN established that thunderclouds are generally negatively charged but sometimes also positively charged.

Based on these discoveries it became possible to formulate the basic problem of thunderstorm research more specifically; i.e. to what type of generation of electricity may the existence of thunderstorm electricity be attributed?

This clarification of the problem formed the basis for the advancement of numerous thunderstorm theories, and thunderstorm research entered a new phase reaching into present.

C) THUNDERSTORM THEORIES IN PRESENT TIME

The greater part of current theories dealing with thunderstorm, suppose that the separated electric charges are produced by various powers and mechanisms, e.g. friction, induction, splintering of ice, spattering of water-droplets etc., resulting in charges of one polarity appearing more frequently on the smaller particles of clouds, whereas the opposite charges appear on the larger

particles. As a consequence of air-resistance in the earth's gravitational field, heavier particles fall quicker than lighter and it is supposed that this leads to a charge-separation and to the formation of space-charges within the thunder cloud.

However a high-voltage charge necessary for the formation of a thunderstorm, cannot possibly develop in this way, because by reason of the COULOMB-forces, it gradually becomes more and more difficult and finally impossible to imbody charged particles of the same sign into a growing space-charge. Besides that, a high-voltage space-charge is not stable because of its dispersion by the forces mentioned above.

A theory not incompatible with these difficulties ist the thunderstorm-theory which takes into consideration the electromagnetic induction in the magnetic field of the earth. (1) \*

When a cloud moves by the velocity  $\nu$  across the geomagnetic field  $\Gamma$ , an electric field  $\Gamma$  is induced within the particles of this cloud as a vector-product:

$$E = v \times T \tag{1}$$

The electric field-vector is perpendicular with respect to the direction of the geomagnetic field and perpendicular to the direction of the motion of the cloud.

All cloud particles therefore become unidirectional electric dipoles. The material of which the cloud particles are formed is of no importance, provided the requirement has been met that conductivity of the air is less than that of the cloud particle. This theory, therefore also applies for example to clouds made up of volcanic ash.

The cloud particles can be considered as a system of parallel- and series-connected capacitors. If discharges appear between the cloud particles, nevertheless the charges at the border of the cloud remain there and will even grow on by repeated charge-separations between the particles until the breakdown voltage is attained. W. NAUMANN (2) has assumed that such discharges can propagate within the cloud like a chain reaction. Such discharges in a prevailing horizontal direction could be observed by weather radar.

The high-voltage electric charges appear as area-charges at two opposite edges of the cloud.

Fig. 1 shows the electrification of a thunder-cloud in middle northern latitudes with a drift from SW to NE . I stands for the vector of the geomagnetic field and E stands for the direction of the induced electric field if we look in the direction the cloud is moving. The negative high voltage appears in this case at the right-hand lower border of the cloud, the positive high voltage lies

\* Numbers in Parantheses designate References at the end of paper

diametrically opposite at the left-hand upper border of the cloud. The production of the high voltage resembles that of the "VAN DE GRAAF-Generator", where the charge is carried from the inside of the conductor to its surface.

- D) PROOFS FOR THE VALIDITY OF THE NEW THEORY BY OBSERVATIONS
- 1. THE POWER OF THUNDERSTORM An important result of the "Thunderstorm Project" (3) at the end of the first half of this century was the statement that the motion of a thunder-cloud is retarded, i.e. the cloud is drifting about 10 % slower than the air in which it is imbedded. The wind thus passes a part of its kinetic energy to the thunder-cloud. According to the law of conservation of energy that no energy can be lost, but, only be turned into another kind of energy we may expect that the apparent lost of windenergy will reappear as electrical energy.

Therefore the power (P) of a thunderstorm (1) can be calculated by the following formula:

$$P = d.S.v.v_0^2 \tag{2}$$

d is the average density of the air, S is the side of the cloud which is facing the wind, v is the cloud-velocity and  $v_{\alpha}$  is the

velocity -difference between air and cloud.

Applying this equation 2 on evaluation of the power of a medium size thunderstorm with a cloud-cube of 7 km edges, a horizontal speed of 10 m/sec results in 250 MEGAWATT.

R.R. BRAHAM Jr. calculated 225 MW and HANS ISRAEL 300 MW by other methods.

Equation 2 shows that we need first a large cloud (a large S) and second, that the velocity v of the cloud must have a value greater than zero. In addition we can assume that electrification only can begin with a certain cloud velocity. Therefore a minimum speed for thunderstorm clouds should exist. The magnitude of this minimum speed will depend on the size of the cloud, the strenght of the geomagnetic field, the direction of cloud movement relative to the magnetic field vector, and as we will see later, also on the orography.

The magnetic field strenght does not appear in equation 2, but is hidden in the velocity-difference  $\mathbf{v}_0$  between cloud and air, because this difference will be greater when the magnetic field is stronger and proportionally smaller when the magnetic field is weaker.

2. DIFFERENCES BETWEEN THE CLOUD AND AIR MOVEMENT - The exact measurements during the "Thunderstorm Project" (3) yielded the interesting result that the direction of motion of the cloud and the mean direction of the air in which the cloud is imbedded, can differ up to an angle of 30°.

The new thunderstorm theory can provide a simple explanation for this phenomenon. The cumulo-nimbus which is retardet by the

geomagnetic field, has the tendency to go the way of least resistance und therefore veers, when it has the possibility, partially in the direction of the magnetic lines of force.

3. THE OCCURENCE OF SUPERBOLTS - In the temperate northern zones, where the clouds travel mostly from  $\ensuremath{\mathsf{W}}$  to E, the right hand lower part of the thunderclouds are mostly negatively charged and as can be seen from Fig. 1 , the positive charge is located diametrically opposite at the left upper border of the cloud. These positive flashes therefore must cover a larger distance to the earth. Consequently they are rarer, but have an essentially greater intensity of current. This fact agrees very well with the results of KARL BERGER who measured on the Monte San Salvatore in Switzer ' more than 400 kA for positive flashes. Fig. shows such a superboit which seems, by the perspective distortion, to exit from the side of the storm cloud and then cuts to ground. This thunderstorm took place west of Fort Worth in September 1977 and was photographed by the National Weather Service meteorologist ALAN MOLLER (4). The storm led to a tornado that touched down near Valley View.

The situation resembles "e condition in Fig. 1 and it is obvious that this flash exited from the upper border of the cloud.

4. A MINIMUM DRIFT-VELOCITY FOR THUNDER-STORMS - The theory demands that the cloud be moved in the magnetic field of the earth and the discussion of equation 2 resulted in the postulation of a minimum speed for the thundercloud. Observations confirm the existence of such a minimum speed (see Table 1).

In Austria the author precisely tested this phenomenon. Plotting the number of lightnings of a thunderstorm as the ordinate and the average horizontal wind velocity as the abscissa as in Fig. 3, one obtains an interesting dot-cloud (5). The electrification of the thundercloud can start only when the horizontal wind velocity exceeds 4 m/sec. A linear relationship between the electrical power generated in a thunderstorm and the horizontal wind-speed as it is expressed in equation 2, seems to be obvious.

The lightnings plotted here were recorded in 1957-58 at the Zentralanstalt für Meteorologic und Geodynamik in Vienna, Austria. The wind-velocity was measured at the same place at altitudes of 1 - 12 km by radio-sondes and wind radar.

5. A MINIMUM THICKNESS OF THUNDER-CLOUDS - A Russian team of investigators (6) found out that a minimum of vertical dimensions for thunderstorm-clouds exists. As it is evident in Table 2, this minimum thickness presents an interesting dependence on the geographic latitude.

The theory of the e.m.i. can give here a plausible explanation. As the induced electric fields stand vertically to the geo-

magnetic fields, and such electric fields in lower geomagnetic latitudes lie more towards the vertical, than those in higher geomagnetic latitudes where the electric fields are more horizontal, the thickness of the cloud is greater in the lower geomagnetic latitudes.

The postulation of a minimum thickness of thunderclouds underscores also the claim of a large cloud volume as it is expressed in Equation 2.

It can also be seen from Table 2 that the most important dimension of the cumulo-nimbus is the length of the cloud in the direction of the induced electric field (see Fig. 1 ) and that this length must be a minimum of about 12 km.

6. FLASHES IN HIGH GEOMAGNETIC LATITUDES - When the induced electric field lies almost horizontally, we may expect that the number of positive and negative flashes is nearly the same.

This assumption is confirmed by the results of measurements obtained by ISRAELSSON and others (7) in the far North of Sweden. Moreover we may expect that no superbolts can occur in such places.

7. THUNDERSTORMS NEAR THE MAGNETIC EQUATOR - ALEXANDER VON HUMBOLDT and many other authors report that in some regions in the tropics no flashes between cloud and ground occur, and that in consequence of this fact the native population there is not in the least afraid of flashes. Moreover HUMBOLDT also describes the fascinating displays on these places, produced by the flashes ascending to the zenith.

On the Magnetic Equator only the Horizontal-Intensity of the geomagnetic field exists. The induced electric field stands vertically and the high-voltage charges are situated at the bottom and the top of the cloud. Therefore the electric field in the inside of the cloud is higher than electric field between cloud-bottom and ground.

We may therefore expect, that there exists a small zone north and south of the Magnetic Equator of approximately  $5^{\circ} - 6^{\circ}$ , where no discharges between cloud and ground occur. Furthermore, no thunderstorm should originate in this zone when the cloud is moving in the direction of the magnetic force lines, i.e. in the direction of the Magnetic Meridian

When we assume that electricity is the cause of tornadoes, we may expect no tornadoes to occur in this zone near the Magnetic Equator.

8. THE DISCOVERY OF AN ORIENTATION-LAW FOR TORNADOES - If we assume an electric origin of tornadoes as do B. VONNEGUT (8), JEAN LACAZE (9) and many other authors, we may expect their development in places where the strongest electric fields occur between cloud and ground. The transformation of electric energy into the kinetic energy of the tornado can happen by acceleration of charged

particles in this strong electric field; thus the tornsdo is a continuous discharge between thundercloud and earth.

In Fig. 4 we may recognize the places where the strongest electric fields occur by different drift-directions. We may therefore expect that tornadoes in the northern hemisphere which are drifting with their mother-cloud from W to F. (see Fig. 4 m) originate under the right-hand lower side of cloud when we look into the drift-direction. In Fig. 4 b are depicted the conditions occuring in a drift-direction from E to W. In this case the left-hand lower side of the cloud is charged positive and the tornadoes originate at the left-hand lower side of the cloud.

The conditions in the Southern Hemisphere are reversed. There, the tornadoes drifting from W to E are leftsided, and those drifting from E to W - rightsided.

This prediction of an orientation-law which was made in 1963 (10) has meanwhile been confirmed by many observations in the northern, and by two observations in the southern hemispheres (11).

This orientation-law for tornadoes is a very important proof for the validity of the e.m.i. as the origin of thunderstorm-electricity and simultaneously a proof for the electric origin of tornadoes.

9. THE DERIVATION OF AN ELEMENTARY BUILDING BLOCK FOR THE THUNDERCLOUD - According to the e.m.i. theory, cloud particles are made into electric dipoles with parallel dipole-axes by their travel through the geomagnetic field. Thus electric forces come into play between the cloud particles which lead to a stabilization of the cloud, so that it cannot be dispersed by the divergent winds at various heights because the dipoles will have the tendency to form chains in the direction of the induced electric field (see Fig. 5). This also makes it reasonable to suppose a minimum-length of the cumulo-nimbus exists in this direction.

A new impulse to further development gave the picture (see Fig. 6 ) of a square-shaped tornado-producing cloud which was observed by Tiros I (12). After rectification the cloud was the shape of a rhombus which was moving from SW to NE in the direction of the long diagonal (see Fig. 7). This regular shape is reminiscent to crystals in which the atoms and molecules arrange themselves in a space lattice. We may therefore assume that such a space-lattice will have been developed in the thundercloud.

Two dipoles ( 1 and 2 in Fig. 8 ) will seek a position such that the negative half of one faces the positive half of the other. Two additional particles ( 3 and 4 ) will seek a symmetrical plane with respect to the first two particles and form a rhombus whose long axis lies in the direction of motion. The similarity to Fig. 7 is surprising.

The transition to the three-dimensional

space matrix model can be made by the requirement that each dipole within the cloud be faced by the same environment. This gives only one possibility. The result is an elementary building block consisting of six cloud particles arranged at the corners of a quadratic double pyramid which has three orthogonal axes. Each point in the matrix is characterized by the fact that the dipules are located at a minimum potential energy level. This means that if a dipole is slightly displaced, it tends to return to its matrix point. This satisfies a necessary theoretical condition for the formation of a stable space matrix

The electrification by e.m.i. thus acts as a control on precipitation. During the early phases of a thunderstorm it acts as a precipitation inhibitor and during the final phase it results in intensive precipitation with large drops of water.

The best condition for the formation of the space-matrix is a laminar streaming of the the cloud which occurs over plains, and this areas have the most frequent and also the most intense thunderstorms.

Over mountainous terrain, where turbulences are carried into the cloud level, the formation of the matrix is more difficult. The minimum-velocity for thunderclouds should for that reason be higher there than over plains.

The postulation of the elementary building block consisting of six cloud-particles was made in 1963 (10). Five years later the proof literally fell out from a thunder-cloud.

In 1968 spiked hailstones reached the ground in Oak Ridge, Tenn. (13). Practically all of the stones had some spike-development, the number of spikes ranging from one to six, and most of the stones had two, four or six spikes. Some of the stones also had lobes on the end of the spikes. The spikes were generally coplanar and remarkably symmetrical (see Fig. 9)

The shape of these spiked hailstones is practically identical with the shape of the elementary cloud building block (see Fig. 8 ), consisting of six droplets with three axes at right angles to each other.

The formation of these spiked harlstones can be imagined as follows: The COULOMB-forces appearing between the droplet-dipoles became so strong that the droplets were deformed and coalesced in the center of the building block. Due to the shock caused by the coalescence and the electric discharge, the supercooled droplets suddenly hardened into ice and the spiked hailstone fell to the ground.

And now there is a reason too for the need of a large cloud volume: As the induced electric field E (see Equation 1 ) is very small, a cloud of large capacity is required so more charges can be separated in the

dipoles and the COULOMB-forces demonstrated by the production of the spiked hail-stones can deform the water droplets.

10. THE INFLUENCE OF THUNDERSTORMS ON THE MAGNETIC DECLINATION - If the magnetism of the earth is the cause of the electrification of the thunderstorm cloud, then conversely the cloud, to some extent, should influence the geomagnetic field in the neighbourhood of the thunderstorm.

From the Magnetic Declination - the deviation of the magnetic needle to geographic north - we would expect that thunderstorms travelling from the north or the south, i.e. moving in the Magnetic Meridian, have no influence. But if the thunderstorms come from west or east and pass an earthmagnetic observatory in the north or south, a deviation of the magnetic needle from the normal value should be observed.

Fig. 10 shows the deviations of the hourly values of the Magnetic Declination from the normal value at the observatory Wien-Kobenzl during thunderstorms in the years 1957-59. On the left side of the abscissa are marked the West-components, and on the right side the East-components of the middle wind-velocities in m/sec. The winds were averaged in the altitudes of 1 - 12 km. The oedinate shows the deviation of the Declination from the normal value.

The daily and the yearly variations were carefully eliminated and the disturbed days were not registered in the statistics.

The dot cloud in Fig. 10 indicates that there is no change in the Magnetic Declination in the case of North- and South-winds. With increasing West- or East-components of the wind, the deviation from the normal value increases and gains considerable values, reaching over four arc-minutes.

The distribution of the points is exactly of the character required by the theory and confirms - this time from the magnetic aspect - the efficacy of the e.m.i. for the electrification of thunderclouds.

E) CONCLUSION AND PROPOSAL FOR FURTHER RESEARCH

We have seen that this new thunderstormtheory with electromagnetic induction as its basis is substantiated many points by observations and it seems therefore that the problem of the origin of thunderstorm electricity is solved.

Nevertheless there are still many questions to be answered and more observations are needed, especially in the region of the Magnetic Equator.

REFERENCES

1. A. Pühringer, "Die elektromagnetische Induktion als Grundlage einer Gewittertheorie." Arch.Met.Geoph.Sickl. A 12, 262-270, 1961

duction as a Basis for a Thunderstorm Theory." U.S.Dep. of Commerce, Office of Techn.Serv., JPRS 20, 686, August 1963

2. W. Naumann, "Gewitterentstehung." Elektrie 8/81, 395-399

3. H. R. Byers and R. R. Braham Jr., "The Thunderstorm." Washington, D. C., 1949

4. Alan Moller, "Cover Picture." Weatherwise, Vol. 32 No. 1, February 1979

5. A. Pühringer, "Comment." S. C. Coroniti, "Problems of Atmospheric and Space Electricity." Elsevier Publishing Company, 312, 1965

6. I. M. Imyanitov, B. F. Evteev and I. 1. Kamaldina, "A Thunderstorm Cloud." Planetary Electrodynamics, 423

7. Sven Israelsson, Stig Lundquist and Hans Lufke, 14. Europäische Blitzschutzkonferenz, Bericht 1. 9, Gdansk, 1978

ferenz, Bericht 1. 9, Gdansk, 1978 8. B. Vornegut, "Electrical Theory of Tornadoes." J.Geoph.Res. 65, 203-212, 1960

9. J. Lacaze, "Sur la Théorie des Tornades de Pühringer." Arch.Met.Geoph. Biokl., A 18, 377-390, 1969

10. A. Pühringer, "Beiträge zu einer elektrischen Tornadotheorie." Arch.Met.Geoph. Biokla. A 13. 450-460. 1963

Biokl., A 13, 450-460, 1963

----- "Contributions to an Electrical Theory of Tornadoes." U.S.Dep. of Commerce, Office of Techn.Serv., JPRS 21, 343 October 1963

11. A. Pühringer, "Ein Orientierungsgesetz für Tromben." Arch.Met.Geoph.Bickl. A 20, 6/-77, 1971

12. L. F. Jr. Whitney and S. Fritz,
"A Tornado-Producing Cloud Pattern Seen from
Tiros I." Bull.Amer.Met.Soc. 42, 603, 1961

13. Gary A. Briggs, "Hailstones, Starfish and Daggers-Spiked Hail Falls in Oak Ridge, Tennessee." Monthly Weather Rev. 96, 10, 744-745, 1968

Table 1 - Minimum Speed for Thundercloud

Category	Author	Country	m/sec
	<del></del>		
1	G. SCHOU	Norway	7,0
2	A. SCHÖNROCK	U.S.S.R.	5,8
3	A. PÜHRINGER	Austria	4,0

Table 2 - Minimum Thickness for Thunderclouds

Category	Region of investigation	Minimum thickness in Meters
1	Leningrad (U.S.S.R.)	5100
2	Cape Murotomisaki (Japan)	7500
3	Florida (U.S.A.)	7900
4	New Delhi (India)	9400

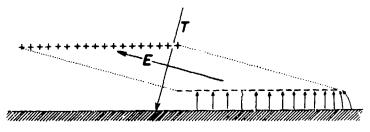


Fig. 1 - The electrification of a thunder-cloud by the e.m.i.

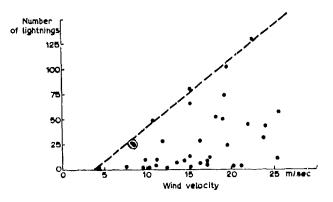


Fig. 3 - Relationship between wind velocity and the number of lightning flashes

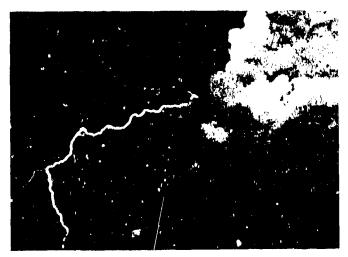
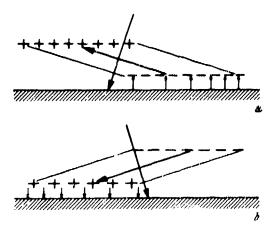


Fig. 2 - A lightning bolt emerging from the upper border of the thunder-cloud



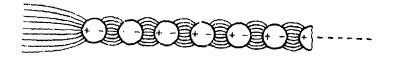


Fig. 5 - The formation of dipol-chains in the cloud



Fig. 6 - A symmetrical cloud observed by Tiros !

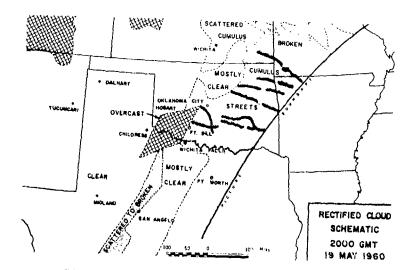


Fig. 7 - The same cloud as in Fig. 6 after rectification

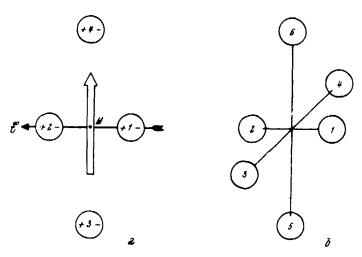


Fig. 8 - The construction of an elementary building block for the thunder-cloud



Fig. 9 - Sp.ked hailstones. Note the regular form!

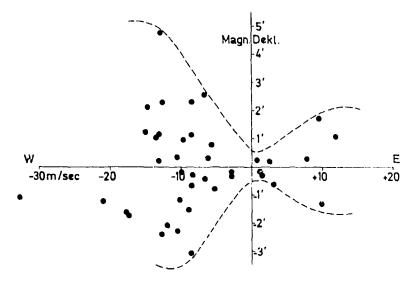


Fig. 10 - The variation of the Magnetic Declination by westerly and easterly winds during thunderstorms

92-9

AD P002238

AEROSPACE VEHICLES CHARGING BY THRUSTER PLUMES

H. Trinks
Technical University Hamburg-Harburg, Hamburg, Germany

ABSTRACT

Aerospace and spacecraft charging is a cause of a number of operational problems. Some satellites are equipped with numerous small thruster engines to stabilize and to correct their position. Particularly thruster plumes produced by small bipropellant engines consist of electrically charged clouds of drop lets, moisture and ions. A lo N engine in connection with the GALILEO spacecraft configuration was installed in a large high vacuum measuring plant equipped with electric field measurement devices suitable for the investigation of plume charging effects. A stream of charged particles leaving the thruster and interacting with spacecraft surfaces could be observed. The results are discussed.

AEROSPACE AND SPACECRAFT CHARGING causes a large number of operational problems. Such problems are e. q. the anomalous operation of on board electronic systems.

During the past several years, theoretical, analytical and experimental effects by many agencies have significantly increased the available knowledge in this aera. Several reports have been published concerning spacecraft charging - see e.g. (1.2,3). However, at present the phenomena of spacecraft charging is not yet completely understood, and a considerable amount

of work remains to be done.

Particularly the charging effects caused by bipropellant thruster plumes have not been discussed yet. Such small thruster engines are installed on the satellite surface to control and to correct the satellite position during its mission in flight. In Fig. 1 for example is shown in principle the GALILEO spacecraft configuration equipped with numerous lo Newton thruster engines. During thruster operation an interaction between the thruster plume flow field and the satellite structure takes place. Earlier performed investigations concerning bipropellant lo N thruster engines have shown that thruster plumes, indeed, consist of electrically charged clouds of droplets and moisture (4).

The numerous existing reports concerning spacecraft charging indicate the intense interest on charging effects on satellite surfaces. A systematic investigation of charging effects, produced by bipropellant thruster plumes seems to be important. In this connection basic investigations have been performed concerning the bipropellant lo Newton engine of MBB for the GALILEO spacecraft configuration. In the following the measuring plant for the plume investigation is described. The electric field measurements in the vicinity of the plume under high vacuum condition give occasion for the plume structure analysis, for velocity measurements of the particles in the plume and finally for contamination investigations on the satellite surface.

### MEASUREMENT DEVICE

The investigated MMH/N $_2$ O $_{/_1}$  thruster engine lo Newton from MBB workes in Steady state or in pulsed mode with pulse duration down to 20 ms. In Fig. 2 is shown a series of shorttime shadowgraphs during the thrusters start phase. The pictures were taken however not in high vacuum but in normal air. Simultaneously is sketched in Fig. 2 the model conception about the electrical charge distribution in the plume flow field.

Performing the investigation concerning the charging effects the thruster engine is installed in the test facility which consists of the highvacuum chamber, different pumping systems and of a number of special test instrumentations - see Fig. 3. The stainless steel chamber with a length of 2 m and a diameter of 1,2 m is well equipped with numerous flanges, feed through connections, and windows for all kinds of observations. The lo N thrusteris installed

axially in the centerline of the cylindrical vessel. The vacuum chamber is pumped by oil diffusion pumps, liquid No cryo-systems, and liquid He cryo-systems. The pump capacity of all pumping systems is about 14.000 1/s . The pressure in the chamber before thruster operation is about lo b.

The test facility is equipped with test instrumentation concerning high speed photography, mass spectrometry, velocity, heat flux distribution and particularly electric charging effects. Most of the measuring techniques were developed especially for the small thruster plume investigations. They are suitable to measure simultaneously transient parameters concerning gaseous as well as condensed reaction products with high time resolution.

In Fig. 4 the electric field sensors for the plume investigation installed in the vacuum test facility are shown. The electric charged particles are identified either contactless via influence effects when flying past field sensors, or when impinging on electrical sensor plates. When striking they release their electrical charge to the sensor and every droplet produces an electrical pulse according to its charge value.

By the installation of these rather simple electric field sensors and by evaluation of the strong electric signals it is possible to get manifold information about plume flow field structure, droplet outflow rate, plume velocity and particularly charging effects by the plume interacting with the satellites surface.

### EXPERIMENTAL RESULTS AND DISCUSSION

In Fig. 5 - Stypical results are shown measured by electric field sensors equipped with different electric resistors R. The value of the electric resistor grounding the sensor is essential for the nature of the registered signals:

- large resistor values (R = 1 MΩ) mean, that the sensor is able by influence effects to detect and to register electric fields produced by clouds of charged particles even at relatively large distances
- small resistor values (R = 1 K $\Omega$ ) mean, that the sensor is able to detect the charged droplets which hit directly on the sensors area.

In Fig. 5 is clearly recognizable the change of the plume shape with time. In the first moment after thruster start the plume is wide spread, later on the plume flow field is more narrow.

In Fig. 6 typical results are shown concerning droplet outflow measurements by electric field sensors. The signals demonstrate the good agreement between these experimental and theoretical results which has been computer generated by the CONTAM III computer code (5).

In Fig. 7 the plume velocity measurement method by electric field sensors is shown. In this case the electric field structure of the plume flow field is measured by two different

sensors arranged in a distance of  $l=110\,$  mm one behind the other. The time phase difference D between the two registrated signals gives the velocity of the plume flow field in the sensors vicinity. It is about  $v=1/D=3.000\,$  m/s.

In Fig. 8 is demonstrated that quantitative contamination measurements are possible using electric field sensors. The comparison between the results from the Quartz-Crystal-Microbalance sensor (QCM) and the electric charge sensor Q(t) shows good agreement. This effect can be explained by the assumption that the electric charge transported on one particle or droplet is proportional to the particles size or mass.

By numerous experiments and signals evaluation it could be shown that the plume flow field is characterized by strong charging effects. The core of the plume seems to be charged strong positively by the presence of positively ions and particles or droplets with a diameter of about  $10-100\,\mu$ . This positively charged core seems to be surrounded by negatively charged clouds consisting of mostly electrons—see Fig. 2. The total charge flow outgoing from the 10 N thruster during steady state operation is measured under these experimental conditions to be about  $1 = 10^{-4}$  A.

### CONCLUSIONS

The experimental investigations clearly showed that the plume flow field consists of strongly electrically charged clouds of reaction products. It seems to be possible that the charge separation process in connection with the thruster operation and the origination of the strong electrical fields in the plume field vicinity lead not only to a charging of the

satellite structure but also lead to backflow and self contamination effects. These question must be investigated by further experiments.

On the other hand the performed investigations demonstrated that the electric field measurements in the vicinity of the plume give occasion for a number of new interesting measurement methods such as plume structure, velocity and contamination analysis. It should be discussed in the installation of electric field sensors near the thruster engine during the satellites flight is recommendable for controlling the thruster engine operation.

### REFERENCES

- R.C Adamo, et al., "Spacecraft charging protection for future space systems", Lightning and Static Electricity Conference, Oxford, 23 25 March 1982
- J.E. Nanevicz, et al., Spacecraft Charging Technology, Colorado Springs, Colorado, 12 - 14 November 1980
- A. Rosen, "Spacecraft Charging by Magnetospheric Plasmso", AIAA, N.Y., 225 - 235, 1976
- H. Irinks, "Experimental Exhaust Plume Investigation with MBB lo N Thruster V Experimental Results", ESA Contract No. 4886/81/NL/Ak (SU), 1982
- H. Trinks, R.J. Hoffmann, "Experimental Investmation of Bipropellant Exhaust Plume Flow 1d, Heating and Contamination, and Cormon inson with the Contam Computer Model Predictions" AIAA 18 th Thermophysics Conference, Montreal, Canada, 1 3 June, 1983

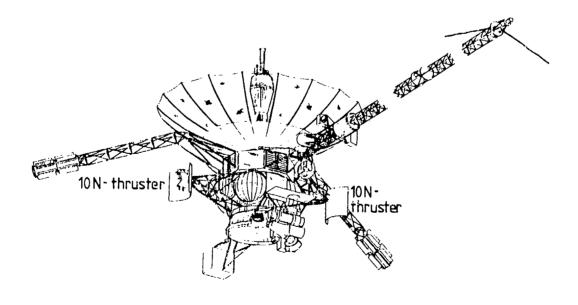


Fig. 1 - GALILEO Spacecraft with lo N thruster engines



Fig. 3 – Vacuum chamber and measurement device for the thruster plume investigation

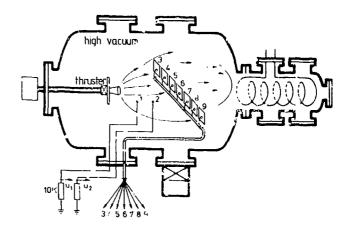


Fig. 4 - Electric field sensors for plume charging investigations

Fig. 2 - Shadow photographs of the lo N thruster plume  $% \left( 1,2,...,N\right) =0$ 

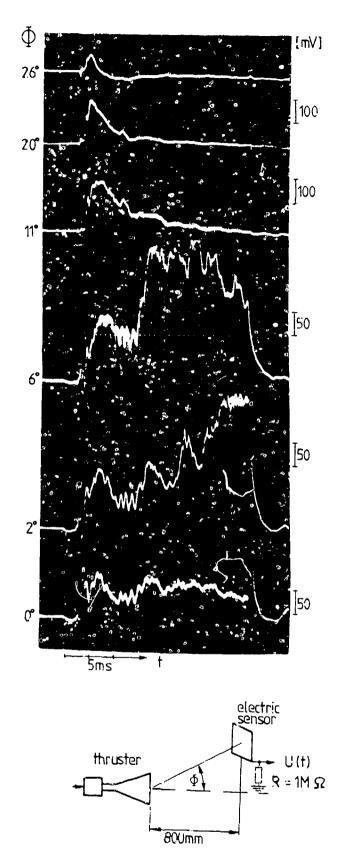


Fig. 5 - Electric charge measurements in the chruster plume flow field

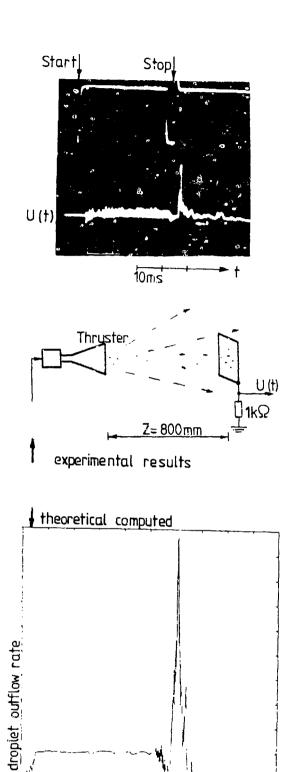


Fig. 6 - Droplet outflow measurement and computation

10 ms

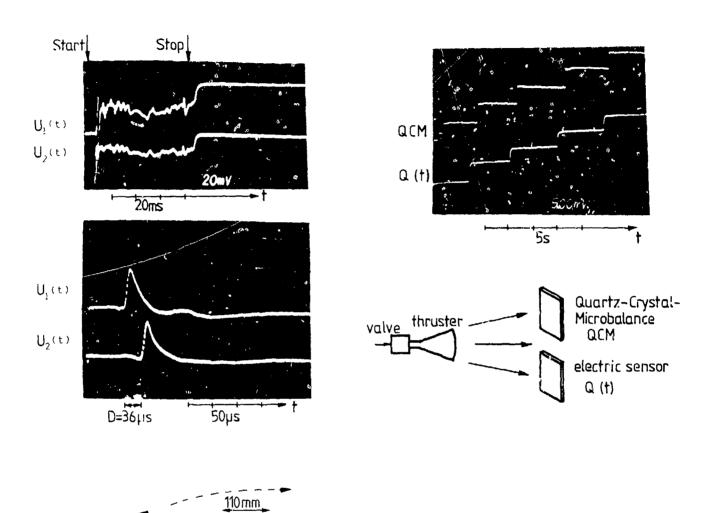


Fig. 7 - Plume velocity measurement by electric field signals



Fig. 8 - Plume contamination measurement by electric field and QCM-sensors

Laboratory and In-Flight Evaluation of Passive Dischargers\*

Etelige)

J. L. Boulay

Office National d'Etudes et de Recherches Aerospatiales B.P. 72 - 92322 Chatillon - France Phone: (1) 657.11.60

ABSTRACT

Reduction of p-static interference associated with corona discharges can be obtained by improving the passive dischargers as well as by optimizing their distribution over the aircraft structure.

Assessment of the noise reduction obtained by modifications of the individual dischargers has been performed in the laboratory. The principles used for reducing the noise, as well as the method of measurement, are described, with emphasis on a novel type of passive discharger which takes advantage of the physical mechanism of uncorrelated corona micro-discharges produced at the tip of a bunch of high resistivity carbon fibers.

To analyse the optimization of dischargers distribution, in-flight experiments have been performed on a Meteor aircraft. The total electric charge of the aircraft and the atmospheric E field have been evaluated from the measurements obtained with five field-mills. Triboelectric currents and discharger currents have also been measured, as well as the p-static noise level on various receivers between 10 kHz and 300 MHz.

The paper analyzes the following points:

- (a) relationship between impact current and aircraft charge (or potential);
- (b) evolution of the threshold of corona emission of the dischargers as a function of aerodynamic parameters (ambient pressure, air speed, nature of the local flow);
- (c) efficiency of the dischargers as a function of aircraft potential; effect of the space charge environment;
- (d) role of the atmospheric E field on parasitic corona location; its influence on the overall efficiency of noise reduction.

As a conclusion, the noise reduction expected from an optimized arrangement of passive dischargers is evaluated as a function of the external conditions.

This paper was not available for incorporation into this book. Therefore, it will be published at a future date.

<sup>\*</sup> Research supported in part by DRET (Direction des Recherches, Etudes et Techniques de la Delegation Generale pour l'Armement).



### ALLOCATION OF PROTECTION

E. F. Vance, J. E. Nanevicz, W. Graf, and J. M. Hamm SRI International, Menlo Park, California

### ABSTRACT

A procedure for determining how much protection is needed between the external lightning environment and the circuits inside equipment is developed on the basis of nested shields or electromagnetic barriers. Part of this protection is usually placed at the system level (at the aircraft skin or at a facility shield) and part may be placed at the equipment level. Four distinct allocations of protection are defined and their implications on electromagnetic compatibility and protection against lightning and other external sources are discussed. In two of these, all of the protection is allocated to one level and none is allocated to the other. When all protection is allocated to the system level, all internal cabling and equipment is protected, and no configuration control or lightning requirement on equipment is needed inside the system-level barrier to maintain the protection. When all protection is allocated to the equipment or box level, however, unprotected cabling and other system structure may remain outside the protected space (i.e., outside the boxes). When the protection is distributed between the system-level barrier and the equipment-level barrier, all of the system inside the system-level barrier has some protection. There are two methods of allocating the protection that have distinctly different ramifications on the ability to verify and maintain the protection. When the lightning stress induced inside the systemlevel barrier is the largest stress on this part of the system, then the response of the internal structure to lightning must be understood (through test or analysis) and the equipment must have a lightning tolerance requirement. On the other hand, if the stress induced by the external source is not the dominant stress inside the system barrier, no lightning requirements on the internal structure and equipment are necessary. The implications of these allocations on system protection design and maintenance are discussed in detail,

TWO KEY QUESTIONS ARISE in developing protection against the effects of lightning on electronic systems: how much protection is needed, and how protection should be allocated to the various levels of the system. In this paper we attempt to develop bounds on the answer to the first question. We also discuss four possible protection allocations between system-level barriers and bux-level barriers to demonstrate some of the consequences of these allocations. fundamental approaches to protecting a circuit from a source of transients outside the circuit include (1) eliminating the source, (2) eliminating the sensitive circuit, (3) separating the source and the circuit by an infinite distance, (4) orthogonalizing the source and the circuit so that they do not interact, or (5) enclosing either the source or the circuit in an impervious electromagnetic barrier. However, if we do not control the source and cannot eliminate the sensitive circuit, the only applicable protection approach is an electromagnetic barrier about the circuit.

In general, the electromagnetic barrier must be impervious to all electromagnetic waves -- those that propagate through space as well as those that propagate along wires or other conductors. Although a closed metal shield is very effective in excluding electromagnetic waves from the volume enclosed by the shield, almost all practical applications of shields require that power and signal wires pass through the shield and that openings be made for ventilation and visibility. As illustrated in Figure 1, penetrating conductors can reduce the "shielding effectiveness" of the shield to 0 dB, since the wire current and the magnetic field about the wire are the same inside the shield as they are outside the shield at frequencies where the wire to-shield capacitance is negligible. Where the aperture dimensions are large (in terms of wavelength), incident space waves can propagate through the apertures virtually unattenuated. Hence, signal and power wires negate the shield at low frequencies, and vents and windows negate the shield at high frequencies.

Because a practical shield with penetrating conductors and apertures is usually ineffective in excluding electromagnetic waves, we have adopted the term "electromagnetic barrier" to describe a surface that is impervious to both space and guided waves at all frequencies of The electromagnetic barrier usually contains a shield to exclude space waves, but it also contains devices, such as filters on penetrating wires, to exclude waves guided along these conductors, and various aperture treatments, such as waveguide-beyond-cutoff structures, to exclude waves propagating through these openings. Thus a closed barrier usually consists of a shield and penetrating wire treatments and aperture treatments so that both space waves and guided waves are excluded from the protected space. The shield alone, without the wire and aperture treatments, is seldom an effective barrier to broad-spectrum transients

such as lightning.

In practice, none of the elements of the barrier is perfect. The finitely conducting metal shield allows some of the electromagnetic waves to penetrate to the interior; the filter allows some out-of-band signal to pass through; and the waveguide beyond cutoff allows some of the external field to penetrate to the interior. These imperfections, combined with imperfections in assembly and carelessness in usage, often combine to make the protection of one shield inadequate. In addition, it is usually desired to use the existing structural metal to provide electromagnetic shielding when possible. Thus, we rely on the equipment housing to act as a box-level shield, and we use the skin of metal aircraft as a system-level shield. Because of these imperfections, and to avoid the expense of producing and maintaining very high quality shields, two nested barriers are frequently employed between a strong source such as lightning and sensitive digital electronic circuits.

This paper addressess the allocation of protection in a two-barrier protection system. One of the barriers is at the system level and the other is at the box or LRU level. The system-level barrier may have any shape, so long as it encloses all the system circuits and structure that need to be protected. The box-level barrier may be partitioned into many subbarriers (e.g., one for each box).

### SINGLE BARRIERS

Let us consider first a condition in which all of the protection is allocated to the system-level barrier. This case is represented by the bold outer contour of the aircraft in Figure 2 and by the dashed equipment boxes inside the aircraft.

This allocation might be used if the internal equipment had no specified tolerance for transients, or if the tolerance were unknown, so that all protection had to be placed at the sys'em level. In such a case, the system-level barrier would be required to reduce the lightning-induced transients inside the barrier to a known circuit tolerance level, such as the circuit operating level or the system-generated transient level. Whatever threshold is chosen, the lightning-induced transient would not be the dominant transient inside the barrier lest it exceed the circuit threshold. In addition, if lightning is not the dominant stress, we need to understand neither its interaction with the complex structure inside the barrier nor the circuit responses for all of its many modes of excitation and states. For modern avionics with thousands of input pins and much greater numbers of states, it is practically impossible to determine the system response to broad-spectrum, high-amplitude transients with sufficient accuracy to evaluate system performance.

Thus, although the system and all of its internal components can be protected with a single barrier, this allocation scheme recognizes no benefit from the equipment-level bar-

rier and is somewhat vulnerable to compromise because all the protection is vested in the single barrier — if this barrier fails the entire protection fails.

Now consider the opposite extreme, in which all protection is allocated to the box level, and no protection is provided at the system level. This condition is illustrated in Figure 3 by the bold outline of the equipment boxes and the dashed outer contour of the aircraft. This allocation is sometimes proposed in the belief that all lightning protection can be incorporated into the box requirements by upgrading MIL-STD-461 to include lightning requirements.

A more careful look at the implications of this allocation leads to the conclusion that if no protection is provided at the system level, the boxes must be required to withstand the full lightning stress. If the criterion is to withstand a 200 kA direct strike, then the boxes and their interconnecting cables must tolerate this threat, since no protection is allocated to the system structure. This is believed to impose a severe cost and weight penalty on avionics equipment. In addition, all our protection is again vested in a single barrier that can easily be compromised. No systems have been developed using this allocation.

Instead, it is frequently argued that there is always system structure present to reduce lightning effects somewhat; hence, the boxes need not tolerate the direct strike. However, if we accept this argument, we leave the single-barrier allocation and enter a two-level (or more) protection system, since part of the protection is now being allocated to the system structure outside the boxes. We discuss this allocation in the following section.

### PROTECTION WITH TWO BARRIERS

The protection approach using two barriers allocates part of the protection against lightning (or other external sources) to the system-level barrier and the remainder to the box or internal equipment barrier. The major issue in these allocations is how the protection should be apportioned between these two barriers. It would appear that there is a continuum of allocations between the two extremes discussed above, but there are in fact two distinctly different allocations in this continuum. The difference lies in whether or not the lightning-induced stress is the dominant stress inside the first barrier.

Let us assume that the outer barrier permits the lightning-induced transient to be the largest stress ever experienced by the internal structure and equipment. This might be the case suggested above, in which it is argued that the system-level structure reduces the lightning transient somewhat, even though we are primarily using only box-level protection. In this case (depicted in Figure 4), the lightning transient inside the system-level barrier dominates all internal interference sources.

One important consequence of this alloca-

tion scheme is that the internal equipment, its interconnecting cables, and perhaps other internal structure must meet lightning-specific requirements, because lightning is the dominant transient impressed on these parts of the system. In addition, we must be able to estimate the lightning stress applied to the cables and boxes in order to meet the lightning requirement; hence, we must understand how broad-spectrum, large-amplitude transients interact with the electromagnetically complicated internal structure to produce the stress seen by the box or circuit deep inside the system. Inasmuch as many of the boxes are used in many different systems, these difficult analyses would have to be made for all foresecable systems using the boxes to obtain an envelope of the stress the boxes must tolerate.

This allocation has several serious short-comings:

- (1) The boxes muct withstand lightning stresses larger than any other stress they are ever exposed to.
- (2) The interaction of lightning with very complex system structures and internal cabling must be well understood.
- (3) Those who specify box requirements must foresee all future applications of the box and understand how lightning will stress the box in all these applications.
- (4) To maintain the protection, the configuration of the system inside the outer barrier must be controlled to ensure that the lightning stresses remain within the tolerance of the boxes.
- (5) When a system modification changes the internal configuration, the effectiveness of the protection must be reevaluated.
- (6) It is extremely difficult to evaluate the protection because of the number of responses deep in the system that must be verified.

Some of these difficulties can be overcome by overprotecting the boxes and internal equipment. A major problem with applying this idea is that it presumes one has a sufficiently refined solution to the interaction problem that the amount of protection required is known well enough to determine that overprotection has been provided. Because of this circular logic, attempting to overprotect at the box level is often an exercise in self-delusion.

A more appropriate place to provide overprotection is at the system level. However,
when the overprotection reaches the point where
lightning is no longer the dominant stress
inside the system-level barrier, we enter the
domain of our final allocation: sufficient
protection at the system-level barrier that the
lightning-induced stress is smaller than the
transient stress produced by the system as a
result of normal operation. With this condition
(depicted in Figure 5), the dominant electromag-

netic stress at all points inside the systemlevel barrier is produced by the system itself. These transient stresses are produced by power switching, rectification, load regulation, relay coils, solenoids, and many other devices and functions routinely operating on any aircraft and in any facility.

We have coined the term "effectively impervious" to describe the effectiveness of an electromagnetic barrier that excludes external sources, so that inside the barrier the transient environment is determined by the internal sources and is unaffected by the external sources. In our final allocation scheme, the system-level barrier is made effectively impervious, so that lightning is not the dominant stress inside the system.

When lightning is not the dominant stress inside the system, the six shortcomings listed above vanish. No lightning-peculiar requirements are necessary at the box level; no detailed understanding of the transient response of complicated internal structure is required if lightning is not the principal stress; no lightning-dependent configuration control is required inside the barrier; and the protection can be evaluated at the system-level barrier—the responses of thousands of internal circuits for millions of circuit states and modes of excitation need not be verified.

The use of an effectively impervious system level barrier provides all of the advantages of the single outer barrier, but it also takes advantage of the inherent transient tolerance of the boxes. Thus, although the boxes need not have a lightning-unique specification, they must have a tolerance for system-generated transients, and the protection provided at the system level depends on this system-generated transient level. Hence, the protection has truly been apportioned between the system and box level parriers, but all lightning-peculiar requirements have been allocated to the system-level barrier.

### CONCLUSIONS

Of the four approaches to allocating lightning protection between the system and the boxes or LRUs, those that depend on lightning-unique requirements at the box level are the most cumbersome in terms of implemenation and maintenance. This is because implementing the lightning-unique box allocation requires a detailed understanding of lightning interaction with very complex structures and very large numbers of circuits, states, and modes of excitation; and maintaining this allocation requires control of the internal system configuration. In addition, it is very difficult to assess the protection, again because of the complexity of the responses and the number of conditions that must be evaluated. Finally, the protection must be reevaluated with each modification of internal equipment or structure, because these modifications can affect the internal responses to lightning, and lightning is the dominant stress inside the system.

Those allocations that do not permit the lightning-induced stress to be the dominant stress inside the system-level barrier do not suffer from these shortcomings, since no lightning-unique requirements exist inside this barrier. Since lightning is basically a system problem rather than a box problem, it must penetrate the system to reach the coxes. Hence, the protection should be applied at the system level. In contrast, intrasystem compatibility is basically a box problem - noise generated in one box affecting another box, or noise generated in the system affecting the boxes -- and it is properly treated at the box level. However, any interference-control proposal that requires the designer to evaluate the penetration of high-level, broad-spectrum sources through two layers of protection and through the complex structure between the layers should be questioned.

We conclude that the appropriate allocations of protection for lightning, nuclear EMP, and other external sources are those that prevent these sources from producing the dominant stresses inside the system-level barrier.

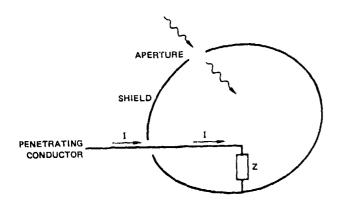


Fig. 1 - Shield with aperture and penetrating conductor.

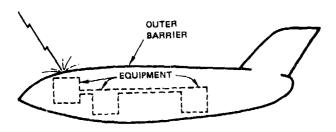


Fig. 2 - All protection allocated to system-level barrier

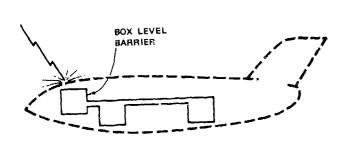
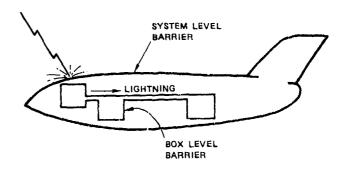


Fig. 3 - All protection allocated to box-level barrier



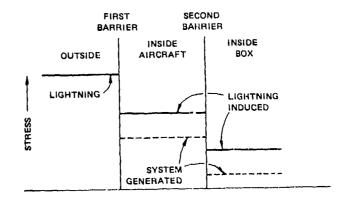
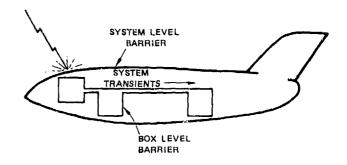


Fig. 4 - Distributed stress allocation



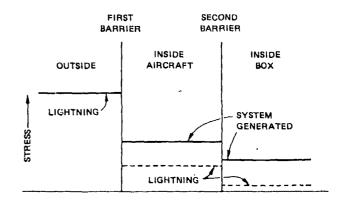


Fig. 5 - Effectively impervious barrier

## THE LIGHTNING SPARK BARRIER



by
M. P. Amason
and
M. C. Hofmeister

# AD P002240

Douglas Aircraft Company
McDonnell Douglas Corporation
Long Beach, California

#### ABSTRACT

-> Lightning protection of modern aerospace vehicles must prohibit sparking in critical fuel vapor areas. In the past, it has been particularly difficult to keep mechanical fasteners from sparking during a lightning event. Attempts to seal off the fasteners from the critical fuel vapor area by manual application of sealant material have proven to be ineffective due to gaps and voids produced by the application process. A technique was developed by Douglas Aircraft Company to control the application of dielectric sealant material to isolate the mechanical fastener sparking from the critical fuel vapor area. The technique consists of a specially designed dielectric cap that fits over the fastener, providing uniform and controlled application of dielectric filler material. An adequate thickness of filler material provides a barrier that prevents the sparks from entering the critical fuel vapor area. The Lightning Spark Barrier is applicable to a wide variety of installations, including those with composite materials. A patent has been applied for.

THE MECHANICAL FASTENERS are used extensively in modern aerospace vehicles to secure doors, access covers, and other hardware. A typical fastener in a cross section view is shown in Figure 1.

The mechanical fasteners are installed primarily to carry structural loads. The fasteners are usually

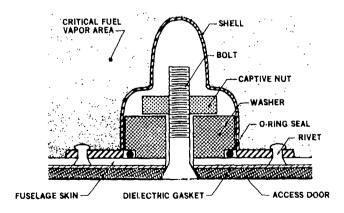


FIGURE 1. CROSS SECTION OF TYPICAL FASTENER

chosen from a vendor's pre-existing inventory; the shape and design are not directly related to preventing sparking. Sparking of mechanical fasteners in a critical fuel vapor area of an aircraft must be prevented during a lightning event. A critical fuel vapor area is defined as an area where fuel vapor and air exist in a stoichiometric mixture that can be ignited by a low-intensity spark. (1)\*

Typically, hardware is attached by a bolt through a hole into the mechanical fastener. The hardware is usually electrically grounded to the aircraft fuselage through the attachment bolts into the mechanical fastener. Dielectric paint and gaskets typically prevent the hardware from making electrical contact to the fuselage other than at the fasteners. Therefore, during a lightning event, when the lightning discharge channel contacts the external hardware, the discharge current must flow through the bolts and then through the mechanical fasteners. Sparking occurs when there is a contact resistance at the interface between two adjacent conductors in the current flow path. The current flow path in a typical fastener during a lightning discharge is shown in Figure 2.

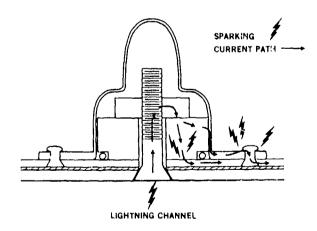


FIGURE 2. CURRENT PATH AND SPARKING IN TYPICAL FASTENER DURING LIGHTNING DISCHARGE

<sup>\*</sup>Numbers in parentheses designate references at end of paper.

Typical fastener installations were subjected to lightning simulation testing to determine the portions of the fasteners that spark. Microscopic examination of the fasteners revealed that the areas of sparking were numerous, even with proper electrical bonding at interfaces. The areas of sparking on the fastener were dependent upon the exact physical construction of the mechanical fastener, and its interface with the fuselage.

## THE LIGHTNING SPARK BARRIER

Many investigators have examined the problem of sparking of mechanical fasteners in critical fuel vapor areas (2, 3, and 4). Several researchers have attempted to use sealant material around the fastener to prevent the sparks from entering the critical fuel vapor area, but abandoned this method when it failed in lightning simulation testing. The reason for failure in all cases was small gaps, voids, and variations in thickness from the manual application of the sealant material. Douglas lightning simulation testing with manual application of sealant material around the fasteners duplicated the results of previous investigators (Figure 3).



FIGURE 3. PHOTOGRAPHIC EVIDENCE OF MECHANICAL FASTENER SPARKING DURING LIGHTNING SIMULATION TESTING

Douglas has recently developed an effective solution to overcome the difficulties previously encountered in using dielectric sealant material. A technique was developed to apply dielectric sealant in a controlled manner to prevent the voids, gaps, and variations in thickness found in other techniques. This technique is the Lightning Spark Barrier.

The technique consists of a specially designed dielectric cap that is placed over the mechanical fastoner in the critical fuel vapor area. It controls the thickness of the applied dielectric sealant and eliminates voids and gaps (Figures 4, 5, and 6). The cap can use exter-



FIGURE 4. FASTENER WITH CUTAWAY SHOWING INTERIOR OF LIGHTNING SPARK BARRIER



FIGURE 5. FASTENER WITH CUTAWAY SHOWING INTERIOR OF LIGHTNING SPARK BARRIER

nal portions of the fastener, such as the crimp shoulder, to align the cap over the fastener. Although proper alignment is not necessary in the design of the cap, a cap designed to align itself properly over the fastener saves weight and space.

The dielectric filler material inside the cap can be applied in two ways: (1) The cap is first placed over the fastener and the dielectric filler is injected through small holes in the cap, or (2) the filler material is first placed in the cap and then the cap and sealant are placed over the fastener. Both methods have proven to be satisfactory. The choice of either is dependent upon installation conditions.

After the dielectric filler material has cured and hardened over the fastener, it acts as a barrier and prevents sparks from physically entering the fuel vapor area. The dielectric barrier material must be of sufficient thickness around the sparking areas of the fastener to provide an adequate barrier against the



FIGURE 6. FASTENER AND LIGHTNING SPARK BARRIER ON ACRYLIC SHEET SHOW DIELECTRIC FILLER MATERIAL IS FREE OF VOIDS AND GAPS

sparks and the joule heating pressure of the sparking. This thickness dimension will depend on both the shape of the fastener and the dielectric filler material chosen. Lightning simulation testing in accordance with known spark detection techniques (5) is always necessary to verify the design of the lightning spark barrier for each type of fastener. Theoretical predictions with formulas are not practical because of the complex geometries involved. The dielectric filler material does not have to be a scalant. A patent application for the Lightning Spark Barrier was filed in December of 1981.

## ADVANTAGES OF THE LIGHTNING SPACK BARRIER

Previously, large, heavy mechanical fasteners were used in critical fuel vapor areas to carry the lightning discharge current without sparking. With the addition of the Lightning Spark Barrier, smaller mechanical fasteners can be chosen based on structural criteria alone. The Lightning Spark Barrier adds little weight to an aircraft, and actually saves weight over present designs.

The Lightning Spark Barrier works with either anodized or alodine coated fasteners. This gives the structural designer more latitude in corrosion prevention in the applications using mechanical fasteners.

The Lightning Spark Barrier can be installed any time during the life of an aircraft. An aircraft can be retrofitted with the Lightning Spark Barrier if a critical fuel vapor is defined after the airframe is in production. The straightforward design of the Lightning Spark Barrier requires minimal skills for installation, making it easy for airline service personnel to retrofit the aircraft.

The dielectric filler material of the Lightning Spark Barrier can also serve as a pressure seal. In many cases, sealant material would be applied around the fastener for pressure containment reasons alone. The Lightning Spark Barrier can be used as a pressure seal also.

The dielectric cap for the filler material not only provides some protection against sparking, but, when left in place after the filler has cured and hardened, the cap provides protection against mechanical damage to the barrier material by maintenance crowmen. In access doors, it is especially important to prevent service personnel from accidentally gouging the dielectric filler material of the spark barrier.

One of the most promising applications of the Lightning Spark Barrier is in semiconductive composites. Due to the semiconductive nature of the composite, the interface between the mechanical fastener and the composite will have a high contact resistance, giving rise to sparking during a lightning event. The Lightning Spark Barrier is potentially the only solution available to prevent mechanical fasteners from sparking in a critical fuel vapor area where semiconductive composites are involved.

## CONCLUSION

Sparks from a mechanical fastener cannot be allowed to enter a critical fuel vapor area during a lightning event. The Lightning Spark Barrier employs a dielectric cap that controls the application of a dielectric barrier material that prevents sparks from entering the critical fuel vapor area. The Lightning Spark Barrier has many advantages over other techniques, especially in composite installations.

## REFERENCES

1. F. A. Fischer, and J. A. Plumer, Lightning Protection of Aircraft, NASA RP-1008, October 1977.

2. M. M. Newman, J. D. Robb, and J. R. Stahman, Lightning Protection Measures for Alecraft Fuel Systems, FAA ADS-17, May 1364.

3. Composite Forward Fuselage Systems Integration, Volume 1, General Dynamics, AFFDL-TR-78-110, September 1978.

4. G. Olson, R. Force, and J. Lauba, Ignition Hazard Study of Advanced Composite Fuel Tank, Boeing Military Airplane Company, Report D180-25598-1, May 1980.

5. Lightning Hazards to Fuel Systems, LTRI, L&T Report No. 649, November 1977.



## AD P002241

PROTECTING THE WORLD'S LARGEST COMMERCIAL HELICOPTER FROM ATMOSPHERIC HAZARDS

 $\Rightarrow$ 

Gerald A. Heiderscheidt Boeing Vercol Company, Philadelphia, Pennsylvania

## ABSTRACT

The paper provides an in-depth look at the lightning protection features of the world's largest commercial helicopter, the Boeing 234. This aircraft regularly carries 44 passengers over 580 nautical miles across water, in IFR and VFR flight conditions, at altitudes consistently placing it in foul weather conditions. The aircraft is examined from the viewpoint of systems and system protection, composite external fuel pods, composite crew nose section, radome protection and, where appropriate, specific subsystem protection.

Inservice lightning strike experience is presented as well as future plans for the aircraft.

THE REGULAR OPERATION OF FARE EARNING ROTOR-CRAFT to a published schedule places demands upon the availability of a helicopter never experienced in nonscheduled service. The aircraft must be invulnerable to environmental effects or the helicopter very soon becomes a nonproductive piece of inventory best gotten rid of prior to tax assessment time. Accordingly, the airframe designer is challenged to minimize the nonproductive (nonflying) time that each indivisual airframe might experience. It then falls upon the electro magnetics engineer or the atmospherics hazards engineer to protect this machine so that it does not lose revenue service due to unnecessary repairs or aborted scheduled trips. This paper traces the development of, and delineates the atmospheric hazards protection features of, the world's largest commercial helicopter in regularly scheduled service. The service history of the aircraft is presented along with the reasons for certain design decisions.

#### BASIC AIRCRAFT

The basic fuselage of the Boeing 234 (see Figure 1) is of conventional sheetmetal, rib, frame and stringer construction, with windows, doors, and escape hatches as required by certifying authorities. The crew section is primarily Kevlar <sup>®</sup> and glass over a metal skeleton. The rotor blades are fiberglass, the only metal being the leading edge erosion protection strips. Hubs and main rotor shafts are of conventional metal construction. The aircraft is powered by twin Lycoming A5512 engines mounted in the rear of the aircraft in external engine pods. Fuel is carried externally in pods of composite construction.

#### THE EXPECTED ENVIRONMENT

The first customer was British Airways Helicopters and the aircraft was scheduled to service oil rigs in the North Sea from a home base in Aberdeen, Scotland. This involves extended flights over the North Sea, at altitudes generally below 8,000 feet (2,438.4 m) (the aircraft is not pressurized) for times approximating two hours and a half from takeoff to landing. Further, during some seasons of the year this involves extended flight in a lightning exposure environment. Accordingly, the lightning protection of the aircraft was designed to withstand multiple 200,000 ampere strikes without structural failure in critical flight components such as rotor blades, structure and fuel pods.

#### **DESIGN DEVELOPMENT**

In designing aircraft to fly in the lightning environment, the design must first satisfy the certifying agencies by meeting certain design and test standards. The documentation which served as guidelines for performance criteria are many and varied (1-9).\*

A search of existing regulations regarding the lightning protection of rotorcraft was conducted. It was quickly concluded that existing regulations were not explicit or did not apply directly to the Model 234 Aircraft. After consultation with other Boeing divisions, design changes specifically oriented to lightning protection were made to the aircraft. Following this, a consultant was hired to evaluate our designs and his recommendations incorporated. The resulting design is that reported in this paper. Each major section of the aircraft is delinested.

### DEFINITIONS OF LIGHTNING STRIKE ZONES

The referenced documents served as guidelines in selecting the general zones of probable lightning attachment, and the probable nature of the stroke attachment. Selection of the zones shown was made by judgment and comparison with known lightning strike behavior as related to fixed wirig aircraft, and Heavy Lift Helicopter model studies made with the model rotors turning. The zones shown in this paper should be considered as an indication of where lightning strikes are most likely to attach, rather than as a definition of locations where the Model 234 helicopter will and will not receive a strike.

## The general zones are defined as follows:

- Zone 1 Surfaces of the vehicle for which there is a high probability of direct lightning-flash attachment or exit
- Zone 1A Initial attachment point with low probability of tlash hang-on, such as a nose.
- Zone 1B Initial attachment point with high probability of flash hang-on, such as a tail cone or aft ramp.
- Zone 2 Surfaces of the vehicle across which there is a high probability of a lightning flash being swept by the airflow from a Zone 1 point of direct flash attachment.
- Zone 2A A sweµt-stroke zone with low probability of fiash hang-on, such as blade trailing edge or landing gear.
- Zone 3 Surfaces of the vehicle for which there is a low probability of flash attachment.

#### Zones related to the 234 are as follows:

- Zone 1A Encompasses the forward most projections of the airframe, the sync shaft cover from forward pylon to aft pylon, the blade leading edges (entire span) and upper and lower fairings from the blade tip inboard 18 inches (45.72 cm).
- Zone 1B Includes the fuselage bottom from the front to the aft most extremity until just below the APU exhaust stack and from the bottom of the aircraft to approximately haifway up the fuel pods.
- Zone 2 Extends from just behind the forward pylon aft, excluding the sync shaft cover.
- Zone 3 The vertical surfaces of the aft pylon.
- \*Numbers in parentheses designate References at end of paper.

® E. I. DuPont De Nemours, Wilmington, Delaware

## FORWARD FUSELAGE PROTECTION

The forward fuselage is considered to run from the forward most portion of the pitot booms to the production splice located at Station 160 (see Figures 2 and 3)

The cone of protection available from the forward hub is 45 degrees in total breath and affords adequate protection for all nose areas while the aircraft is on the ground. The blades, due to the metal leading edges, extend this cone of protection around the hub, 120 degrees apart. It is anticipated that all on the ground strikes will enter or exit from the blades or hub for the upper portion of the airframe, and from the landing gear on the bottom surface. There is a remote possibility that a flash can exit the VHF antenna blade. The more likely path, however, is the landing gear since the impedance of the arc channel from the gear will be much less there than to arc to ground from the antenna. All on-the-ground strikes experienced in service have entered one or more rotor blades and exited via the landing gear.

AIR DATA SYSTEM — The pitot tubes are installed as indicated in Figure 4. Lightning which attaches to the tube tip, has the available metal pitot head, the metal tube outer body and the inner metal air data tube to travel to the skin of the aircraft. The pitot boom outer tube is grounded to the mounting base by metal to metal contact. The metal base is physically close to the 120 by 120 aluminum mesh screen (Figure 3) and metal to metal contact is also made through the pitot tube base mounting hardware. The aluminum mesh screen is bonded to metal structure at the rear most attachment for the fiberglass nose piece by rivots and other metallic fasteners. Via this path, the principle lightning current can travel from the strike attachment point - assumed to be the tip of the p!tot tube - and travel via metallic paths to the main fuselage structure surrounding the cockpit. The current then flows via metallic skin and structure to the strike exit or har g-on point. The pneumatic lines within the pitot boom are metallic through the boom assembly and change to plastic immediately at the base of the boom mounting flange. The rest of the air data system is nonconductive 1/4-inch tubing (6.35 mm) and is, therefore, not endangered by a lightning strike to the pitot boom assembly.

The electrical wiring is routed through a protective copper braid. The wires exit the braid near structure. One is grounded at that point (power return); the other is routed to control circuitry. The copper braid eliminates most of the voltage or current that could be induced in the heater power circuit

RADOME — The radome is of fiberglass and Nomex® honeycomb sandwich construction. Both inner and outer skins are fiberglass. The radome is finished on the exterior surface with a black anti-static paint system. It is attached to the main fuselage using a metal channel closeout ring and hinges and striker plates with metallic guard pins and latches (see Figure 5). The outer surface also has six strike guard tapes. These are installed and grounded as shown in Figure 5. The typical current path in a strike is quite definite. The strike will follow the path of least impedance and form an ionized path on the surface of the strikeguard. Upon reaching the metal plates at the rear of the radome, the current will take two paths. Some small portion will arc from these baseplates to metal skin and hence on out of the airframe through the exit point. The larger balance will go from the baseplate through the fasteners to the metallic channel closeout ring to the striker

plates and guidepins to airframe and the exit point (see Figure 4). These components are massive and numerous (8 pins, each 1/4-inch (6.35 mm) in diameter) and the damage expected is cosmetic in a 200,000 ampere strike.

BLADES AND HUB — The rotor hub is all metal and massive, it is solidly attached to the main rotor shaft in order to transmit the drive forces necessary for flight and is considered massive enough to carry the lightning currents into the main drive system without damage. In the drive system, the gears, bearings and other metallic components are large enough and with sufficient contact area to carry the lightning current without catastrophic results. No testing is considered necessary in this area.

The rotor blades are of fiberglass and graphite construction with Nomex honeycomb to maintain the airfoll in the aft fairing area. These blades were successfully strike qualified to the waveforms recommended by the report of SAE Committee AE4L.

AIRCREW AND CABIN STRUCTURE — The aircrew and cabin structures are located in Strike Zone 1A (Figures 1 and 2). As such, we can expect flash attachments, but little or no flash hang-on. The structure in this area is metal, except for windows and windscreens. This is considered adequate protection as the aircrew in effect sits inside a cage formed by aircraft structure and skin with apertures. The die-electric strength of windscreens and windows precludes are entry as metallic structure and framing in close proximity provides a lower impedance path to primary structure and the arc exit point. To protect from the effects of flash blindness, bright cockpit storm lights are provided.

CENTER FUSELAGE PROTECTION (Excluding Fuel Pods —Figure 6)

CONVENTIONAL FUSELAGE SECTION — The center fuselage (except for windows, doors and the sync shaft tunnel cover) is metal skin on metal ribs and stringers. These structural components are assembled using standard aircraft fabrication techniques and quality control safeguards. Minor burning can be anticipated at the points of arc attachment. The severity would, of course, vary with skin thickness.

NONCONVENTIONAL FUSELAGE SECTIONS — Several areas of the fuselage are not of conventional rib, stringer, and skin construction.

Sync Shaft Tunnel Covers — The sync shaft tunnel runs the length of the fuselage from the aft pylon to the forward fuselage above the normal cabin structure (see Figure 6). This sync shaft is the drive system link from the engines and is safety of flight critical. As such, the tunnel covers which enclose the sync shaft are metal skinned, metal core honeycomb (see Figure 7). The lightning currents which attach to the tunnel cover are conducted off around the sync shaft through metal piano type hinges on one side, and metal to metal contact, secured by 1/4-turn fasteners on the other. The sync shaft tunnel floor and side walls are also niuminum. With the tunnel covers closed and secured, the shaft runs essentially inside a rectangular metallic cage and, as such, is not threatened by the lightning environment.

Windows and Exits — The windows consist of Plexiglass , surrounded by gaskets which retain the transparent Plexiglass in the metal skin structure (Figure 6). No lightning protection is added for the small windows. This is consistent with successful commercial designs on FAA and CAA certified passenger airliners. Additional protection is considered not necessary for passenger windows of this size.

® Rohm and Haas, Philadelphia, Pennsylvania

The exits represent a larger broak in the configuous aircraft skin. Some exits have windows in addition. Most exists are constructed of fiberylass or fiberglass with a paper Nomex core for rigidity. In all cases, the fiberglass portions of the quors are completely covered with aluminum mesh screen (120 by 120 or 100 by 120 mesh). In turn, all are retained in the fuselage using metal latches and pins and in the case of normal exits, metal hinges. All metal attachment hardware is in intimate metal to metal contact with the aluminum mech screen since the metallic fasteners (rivets, screws and bofts) go directly though the aluminum mesh screen. Latches, bofts and binges are considered adequate to prevent the lightning currents from entering the fuselage interior and threatening occurants.

Wiring — The wising runs are, without e otion, located within the metallic fuselage on the inner su uces of the main fuselage formers. As such, they are protected from all lightning direct effects since they are surrounded with metallic structure. For a general arrangement, see Figure 8. No other special consideration is given to wiring except local shielding and standard decoupling techniques.

Occasionally, it is necessary to exit this fuselage to route wiring to equipment bays, fuel pods, landing gear, etc. Where this happens, the wire runs are still located within metal fuselage extensions, consisting primarily of fiberglass skin entirely covered with aluminum mesh screen and firmly attached to the metal airframe via metallic fasteners or bolts; or aluminum skins and fairings, solidly attached to the main fuselage. No further protection was incorporated.

#### AFT FUSELAGE PROTECTION

AFT RAMP AND PYLON (See Figure 9) — The aft ramp on the commercial helicopter is all metal, including the sliding tongue. Consequently, lightning current exiting the aircraft through the air ramp is no more serious than an exit point through any bottom skin.

The lower trailing edge of the aft pylon, while labeled as a Zone 2B, may be 1B or 2A. There is a probability of flash hang-on on the metal portions just above the aft ramp and very little probability of flash hang-on on the fiberglass portions of the pylon. Neither condition affects safety of flight.

The aft pylon vertical skin areas (see Figure 9) are generally considered to be Zone 3, an area of very low probability of direct arc attachment. The rotor hub, blades, etc., will tend to protect this area even in a swept stroke phenomenon where the blades and hub present a much more attractive attachment point.

LANDING GEAR — The aft landing gear is solidly attached to primary structure with massive bolts and large contact surface area. This represents the most logical exit point on the bottom half of the aft pylon section. Military CH-47C Chinook helicopters have had lightning exit the landing gear without structural damage. The landing gear used on the Model 234 is similar to the military Chinook. Minor struct changes are made to accommodate a commercial type mission.

## FUEL PODS

ELECTRICAL EQUIPMENT BAYS, FORWARD AND AFT (See Figure 10) — The equipment pods are of metal skinned Nomex honeycomb shalves and bulkheads. The aluminum screened glass and Nomex skins are bonded to main airframe using rivets, bolts and screws, installed using conventional aircraft techniques. These skins react much like metal skins with the added advantage of quick repairability.

This protection method will withstand direct stroke attachment and has been used on the lightning qualified rotor blades. No further protection of the equipment bays is used.

FUEL PODS -- EXTERIOR (See Figure 11) — The fuel pods which extend up to 36 incres (91.44 cm) outside the fuselage mold line, are constructed of fiberglass, Kevlar, Nomex core, Kevlar and glass, and completely covered aluminum mesh screen on their outer wetted areas. Selected portions of the pods use graphite, particularly splices.

The pods are constructed of three curved pieces (see Figure 12) which, when spliced together, form the cylindrical fuel pod. The splices run parallel to the long axis of the fuel pod. The bulkheads at either end of the pod are fastened to the end of the pod tube. The graphite used in the pods is separated from free stream air by several layers of fiberglass which, in turn, is completely covered by aluminum mesh screen. The portions of the pod next to airframe skin do not have aluminum screen to avoid potential arcing in an inaccessible area (see Figure 12). Splices are povered again with aluminum mesh screen, which overlaps the entire joint and adjacent screen (Figure 12). The use of aluminum screen greatly reduces the induced voitage on internal components, relative to strip or bar or wire grid protection.

Any lightning currents, induced in or attached to the pod skin, will be conducted through the mesh screen to the bonding plate located on the forward and aft extreme end of the pod bottom (see Figure 12). From this bonding plate, three bonding braids, 3/4-in. (1.905 cm) minimum width, run over to main airframe attachment points. Each braid exceeds the CAA and FAA requirements for lightning bonding jumper cross section. Six per pod are provided to ease maintenance requirements and to make certain of excess multiple strike capacity.

The bonding plate concept used to transfer current from the aluminum screen to the bonding jumper without excessive damage to the aluminum screen, was shown to be successful on the rotor blades and is, in fact, used from the trailing adge trim tabs to the metal leading edge. These blade tests showed that the surface areas used provide adequate surface area between the wire mesh and the bonding plates.

FUEL PODS — INTERIOR (See Figure 13) — The primary objective within the fuel pods is to eliminate the possibility for sparks. Without sparks, fuel/air mixtures are not going to ignite when the aircraft is subjected to high skin currents, such as during a lightning strike. This was accomplished by never allowing a continuous current path within the fuel pod by using nonmetallic hose braids, and other materials exhibiting sufficient physical strength and high dielectric and high resistance. Some examples are teflon and teflon based materials, nylon braids, rubber, etc. Several examples are shown in Figure 13.

As shown in Figure 13, pipe (A) is metal, grounded only at one end to the metal flange/pump housing using a braided bonding jumper assembly. Both hoses, one at each end, are nonconductive, nonmeta!lic, nylon overbraid type assemblies. Other hoses marked (B), which run from one end of the tank across the length on top and connect to the respective vent boxes, are nonmetallic.

All wires carrying signals or power are insulated from fuel pod exterior skins by the normal resistance to case and dielectric of the powered components. Examples are: valve coils, motors for fuel pumps, capacitance type fuel probes and isolated from ground (i.e., 2-wire) thermistor sensing circuits.

With the bonding jumper arrangement, all metals for piping or housings within the fuel pods are grounded to the pod exterior at only one point along that piece of metal. This eliminates any ground or current loops, giving only the exterior surface of the pod as the contiguous current path. The

one exception is the electric bundle carrying boost pump motor power. The existing parallel lightning current path is via the outer stee! braid of the boost pump cable assembly. To preclude arcing, this cable is spark tested under lightning current conditions. The arc test required during qualification is as follows:

"Arc Test" With hard connections to the shell of each connector, the entire cable assembly shall be subjected to a 1,000 amp impulse test of 10 x 20 current wavaform. This test is to be monitored with cameras with the shutters open during the test. Any sparks, as evidenced by exposed film is cause for rejection."

<u>Fuel Pod Penetrations</u> — The fuel pod is penetrated in four areas (see Figure 13):

- At the forward bulkhead where the pressure refueling fittings are located as we'l as a manhole for insertion and removal of fuel system components
- At the aft bulkhead where the fittings for the fuel lines to the engine are located in a manhole cover and the fuel jettison fittings which go overboard and vent lines going to vents in the aft pod fairing
- At the gravity fill panel, which contains the gravity refuel provisions and equipment, and the center fuel quantity measurement probe
- At the locations for the forward and aft fuel quantity probe.

These penetration fittings are behind aluminum skin or wire mesh covered fiberglass skins. As such, these fittings are not likely to experience direct stroke attachment. Hose assemblies for pressure refueling (forward penetrations) and engine fuel feeds (aft penetrations) are nonconductive rubber with a conductive steel outer braid. All gaskets to seal metal hatch covers are standard commercial sizes and have lightning scallops. This standard configuration (Figure 14) is used on all gasket seals on the Model 234, except for man hele covers where a larger gasket is required. In that case, a Boeing designed gasket using similar protection techniques (i.e., lightning scallops) is used. Penetration covers of the bulkheads are metallic. Inside the fuel tank the fittings attach to rubber hoses with steel braid. The forward and aft penetrations do not in themselves present a hazard in the lightning environment, as they are shielded by metal skins or screen covered skins.

Fuel Quantity Probes — The pod is penetrated in three places for the installation and removal of fuel quantity measurement probes (Figure 13). One is shared with the gravity refueling port and the manual fuel level probe. The remaining two are identical; one in the forward quarter of the tank and one in the aft quarter of the tank. All three are mounted as shown in Figure 15. The lightning integrity is maintained by metal to metal contact, all the way across the penetration. All potential spark areas are:

- . Designed to isolate the spark from the pod interior
- Designed to isolate potential interior sparks from the fuel, or fuel/air vapor.

Figure 15 shows in detail how the fuel is contained within a reinforced rubber bag and all metal joints are kept outside the fuel bag. This keeps sparks which may occur, away from the hazardous environment. The sensitive areas of the fuel probe are in turn, isolated by hylon assemblies from the exterior mounting flange, thus controlling arc over. The hylon insulation is 1 inch (2.54 cm) long and is considered to be the minimum recommended. Such currents as caused by induction are routed over low resistance paths to main airframe. Mechanical joints are large enough to eliminate the potential arcs. Current loops are broken by insulators.

Drain and Pump Mounting Flanges (Typically Aft) — These flanges are on the bottom aft of the fuel tank and

represent a very probable stroke entry or exit point. These fittings are again designed to keep sparking out of the fuel bag (see Figures 13 and 15). Fuel pumps are recessed, the drain is flush. This makes the most probable attachment point the mounting hardware. The outer surface (next to freestream air) is in all cases metal, providing a contiguous path on the pod outer surface.

Boost Pump and Vent Valve Installation (Typically and) (See Figure 13) — These flanges are on the bottom in 1.d of the fuel tank and represent a probable stroke entry or exit point. These fittings, too, are designed to keep sparking outside the fuel bag. They provide a contiguous current path on the exterior of the pod with metal surfaces exposed to free stream air. The pump is recessed. The most probable attachment point is on the vent valve body or the flange attaching hardware.

Gravity Fill Adapter (See Figure 13) — The gravity fill adapter is the access to the fuel bag for the following components:

- 3. Gravity Fuel Filler Cap
- b. Probe Assembly, Fuel Gaging System
- c. Manual Fuel Level Dip Stick
- d. Automatic Fuel Shutoff for Pressure Refueling.

All four items are firmly attached to the metal adapter plate using metal bolts. The tops or exposed portions of items a through d above are metallic. For additional protection:

Item a is lightning qualified.

Item b has insulating nylon between the exposed cap and any inetal system elements.

Item c has fiberglass and other nonmetallic materials below the upper cap, isolated metal items in this probe are separated from the cap by fiberglass and other nonmetallic insulators.

Item d is isolated from other internal tank components since nonconductive hoses are used to attach to it.

Accordingly, all items connected to the gravity fill adapter are electrically connected only to the pod exterior or have sufficient nonconductors to isolate other attached conductive components from direct strike current and do not provide a current path for direct or induced currents.

## FUEL JETTISON SYSTEM (See Figure 16)

The Fuel Jettison System is all metal. The hose connecting the tube control and guide module to the valve on the aft pod wail is steel braid over rubber. The jettison system tube storage housing is attached to main airframe. The tube guide is attached to a fiberglass sandwich skin covered with aluminum mesh. The valve at the rear of the tank is isolated from all other metal conductors within the tank, but is solid! connected to airframe via jettison hose assembly.

When activated, the tube extends beyond the airframe 40.8 inches (1.04 m) minimum, such that fuel does not impinge on any portion of the cirframe. No flame arrestors are used.

The fuel jettison system is normally fully retracted. The system is used only in the event of an emergency requiring a rapid loss of airframe weight to effect an abnormal landing. The LOW FUEL caution light is nominally at the 30 minute level. Operationally, the pilot will close the jettison system at the illumination of LOW FUEL caution light. Flame propagation in the jettison system is a problem only when the tube is extended; the valve is open and a fuel air mixture is present (i.e., fuel flow has stopped) and the jettison tube experiences lightning are attachment. By closing the valve when fuel stops flowing, the risk of expusure to flame propagation is sufficiently small so that additional flame arresting paraphernalia is not required.

The main lightning protection features of the fuel jettison system are its bonding and current paths. The only situation requiring more explanation is the sequence of events in the event of a lightning strike to the extended jettison probe after fuel jettison has been completed and a combustible mixture is present in the jettision system.

To recap, while jettisoning, the system is full of fluid, no air is present and the mixture is not explosive. When the LOW LEVEL fuel light illuminates, the pilot will select Jettison OFF. At this point, we assume an explosive mixture is present in the jettision and fuel tank systems.

Upon selecting Jettison OFF, the jettison valve closes, isolating the fuel tank from the jettison tubes. A lightning strike any time after this valve closing may or may not ignite the fuel/air mixture in the tube. If ignited, the flame wall will propagate up the tube, through the tube adaptor, up the steel braid over rubber hose to the valve body. At the valve body, the flame will extinguish as it has nowhere else to go.

#### FUEL VENTS (See Figure 17)

The fuel vent exit is on the aft inboard end of the pod, on the exterior. The vent opens into the space between the aft pod bulkhead and the forward bulkhead of the aft equipment bay. This area is exposed to rotor downwash and is open to purge the fuel vapors out. Under worst case conditions, the size of the purge slit is 40 square inches (258.08 sq cm). With maximum production tolerances, it may be as much as 60 square inches (387.12 sq cm).

Lightning attachment to the fuel vent system is quite unlikely. In the event that it does attach, the covering from the aft fairing is coated with aluminum mesh which is in turn fastened to the shell of the aft equipment areas and again to fuselage metal — all with matallic fasteners. Lightning will attach either to the pod or to the aft fairing. In addition, all piping external to the fuel pods is nonconductive hosing and offers no conductive path. A schematic representation of the fuel vent protection is shown in Figure 17.

## INSERVICE STRIKES

Several strikes have been experienced by 234s while enroute from point to point. Customers using the Chinook military version of the 234 with the same rotor blade design, have had similar experiences. In all cases, the rotor blades were returned to service or placed in the customer's stores inventory with only several hours elapsed shop repair time.

Of special interest is the first reported Boeing 234 in-air strike. While enroute from Aberdeen, Scotland to an oil rig in the North Sea, a Boeing 234 was struck by lightning while cruising approximately at 125 knots indicated at a bar metric altitude of approximately 4,000 feet (1,219 m). The pilot reported seeing a bright flash at his 11 o'clock position. No other effects were immediately noticed. It was noted a short time later that the ADF was not functioning. No instability or other avionics system glitches were noticed. No other manifestations of electrical system upset or overload were noted. The aircraft continued to its destination and returned to Aberdeen where a post strike inspection was conducted. The bright flash seen by the pilot was an arc attachment to the forward rotor near a blace tip.

Of the blades involved, three were forward rotor blades, and one was an aft blade. The two remaining aft blades were not is volved sufficiently to produce visible evidence of involvement. Of the three forward rotor blades involved, one blade sustained the greatest tell-tale damage. It is therefore concluded that this blade was the initial stroke attachment point.

The most probable stroke configuration and sequence of events follows, with graphic representation of arc channel configurations and relative positions of the arc channel, blades and airframe in 10th second intervals being presented in Figures 18 and 19. The total involvement time was something less than 3/10th of a second. In this period, all three forward rotor blades were involved and one aft rotor blade, with the channel extinguishing prior to the involvement of the remaining two. The reader should keep in mind, that at the approximate cruise speed and rotor rpm, the aircraft advances approximately 21.1 feet (6.4313 m)in a tenth of a second, and the rotor rotates approximately 132 degrees.

The advancing aircraft probably first contacted a new channel being formed with the green blade in the approximate 11 o'clock position. This was during the stepped leader phase where the stepped leader was almost but not yet in contact with the rising dart leader from the ground. Before flying another 18 inches (45.7 cm) forward, the return stroke contacted the blade on the tiedown fitting causing the flash at 11 o'clock visible to the pilot, but since the blade was rotating rearward, away from the channel, the arc hung on to the trailing edge. This would account for the tiedown fitting damage and the trailing edge damage on the green blade. Peak currents are estimated at much greater than 10,000 amperes and probably less than 90,000 amperes. The primary current path was from the tiedown fitting rearward across the blade (blade is covered with 120 by 120 aluminum mesh at this point) to the trailing edge where it rejoined the stepped leader. Eventually the blade cleared the channel and its involvement ended; however, during its involvement, some current want from the tiedown fitting, inboard to the hub, through the rotor shaft, thrust bearing and transmission, airframe to finally exit via the left forward landing gear jack pad located between and behind the wheels. This caused the tell-tale jumper strips to loosen and show signs of high current and the bottom one to be blown off the aircraft. The peak current through the drive system and airframe from this blade is estimated at less than 30,000 amperes but more than 6,000 amperes. In addition, this blade was not involved with the lightning flash a second time since with the combination of rotor rpm and forward valocity, the blade rotor disk was clear of the arc channel by the time this blade was again in close proximity to the channel (see Figures 18 and 19).

CH-47 AND CTHER HELICOPTER STRIKE EXPERIENCE—Only two documented strikes are known on U.S. Army CH-47 helicopters (parent model of the 234). Both strikes were on the ground with eyewitnesses located away from the aircraft. Both strikes were from blade to gear via transmission, etc. On one strike, a detailed visual inspection of hub components could find no evidence of arcing or burning. In neither case were major components (save blades) replaced. No service difficulties are traceable to these incidents. Several strikes have been reported on RAF CH-47's (HC Mk 1) with similar minor results.

In 1970, the British presented a paper, Report Number 700936, at the 1970 "Lightning and Static Electricity Conference" authored by Breland, Quinlivan and Kuo which reports on tests of full size helicopter transmission components and suggests that no permanent damage results during a lightning strike. This is due to the large number of multiple paths, large size of the gear and bearing contact surfaces and the high preload on these surfaces, particularly when flying. This has been the situation experienced by CH-47's in service to date.

Testing (since 1965) of bearings and gears at Vertol indicates that if any arcing occurred across gear teeth or

bearings while in flight, said arcing is in the primary load path and if any damage rosults would only contribute to spalling on the load surface. Such foilures, however, are not catastrophic in nature and are generally detectable prior to becoming serious.

Both of the remaining forward blades (yellow and red, respectively) show signs of carrying considerably less current into the airframe. After the green blade breaks contact with the arc channel, there is an interval of approximately 0.091 seconds prior to contact with the arc channel by the following blade. It is uncertain whether the branch channel from the main arc to the jack pad (Figure 18) could be maintained by residual temperature and no current flow until current could be supplied by the second blade followed by another interruption of 91 milliseconds followed by the third current pulse from the third blade. It is more likely that the branch extinguished prior to the second blade contacting the channel. Accordingly, the remaining two forward blades and the one aft blade were probably involved on the initial return stroke, via branched channel, where a portion of the current went from the main channel below the aircraft via two paths, the branch to the jack pad and the main channel to the tiedown fitting, via the airframe to the main channel via the green blade trailing edge and via the airframe and remaining three involved blades to three additional branch channels to the main channel. This is the only current path which is supported by the tell-tales and damage assessment and known entry/exit points.

The forward yellow and red and the aft blade were each involved once more with the lightning channel. This was as each blade swept through the main channel. Since the channel branch to the jack pad was probably extinguished, these encounters went traveling inboard to the airframe. If the branch channel was not extinguished, minor currents would have followed the previous path to the huu; however, considerably less than on the initial return stroke.

STRIKE SCENARIO SUMMARY — The major current was confined to the forward green blade. A smaller portion traveled to the airframe/drive system where it exited via branch streamers to two other forward blades, one aft blade and the forward left gear scissors jack pad. The current estimate in the forward hub is less than 30,000 amp peak. This current is split three ways, two forward blades, one aft blade. The jack pad acted as a current source, contributing to the input from the green blade root end. Damage to blades consisted of cosmetics and replacement of tell-tale jumpers.

The analysis sequence exhibited in the report of this experience is an example of the logical approach required in lightning strike investigations. Such attention is basic to insuring that all exit and entry points are repaired and repainted prior to the aircreft's re-entry into service.

The ADF failure was repaired by replacing an open ADF sense antenna. There was no evidence of arcing on the antenna, antenna base or fuselage skin near it. The ADF failure may be due to an unrelated antenna mechanical failure. The antenna is being returned to the manufacturer for failure analysis by the aircraft operator. This failure report is not available at this time. All other ADF components and controls functioned normally.

## **FUTURE PLANS**

Much research and development work is being done by various manufacturers in the area of composite rotor hubs, composite rotor shafts and composite transmissions. We are also active in many of these areas. Composite rotor shaft design concepts have already met or exceeded mechanical, dynamic and lightning survivability criteria. Composite rotor hubs are under development. The electromagnetic achievements and characteristics will be reported in subsequent publications.

#### REFERENCES

- 1. Title 14, Chapter 1, Part 25, Federal Aviation Agency.
- 2. Title 14, Chapter 1, Part 29, Federal Aviation Agency.
- "Protection of Aircraft Fuel Systems Against Lightning," Advisory Circular 20-53, Federal Aviation Agency, 6 October 1967.
- 4. "Composite Aircraft Structure," Advisory Circular 20-107, Federal Aviation Agency, 10 July 1978.
- 5. BCAR Subsection G4, Chapter G4-6, Civil Aviation Authority.
- BCAR Subsection G4, Chapter G4-6, Appendix I, Civil Aviation Authority.
- "Lightning Protection of Aircraft," F. A. Fischer and J. Anderson Plumer, NASA Reference Publication 1008.
- 8. "Test Methods and Waveforms for Aerospace Vehicles," Report of SAE Committee AE4L.
- "Aircraft Related Lightning Mechanisms," J. F. Shaeffer and G. L. Wierstock, McDonnell Douglas Corporation for U.S. Air Force AFAL-TR-386, P21, January 1973.

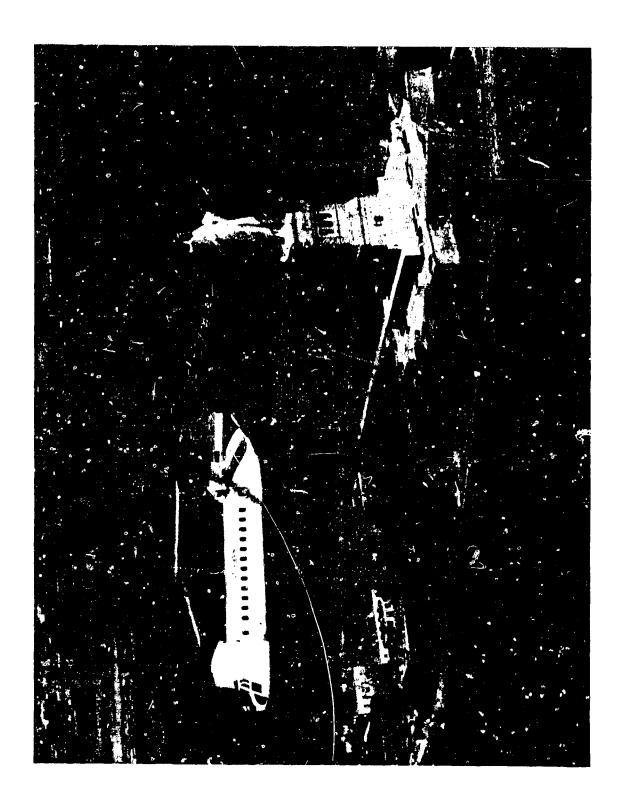


Fig. 1 - Boeing 234

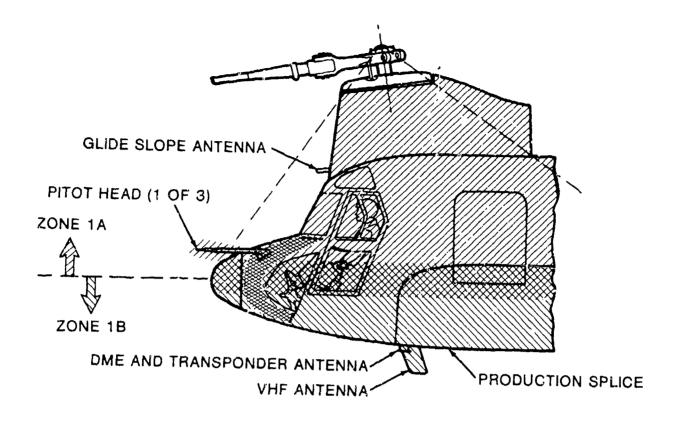


Fig. 2 - Forward fuselage

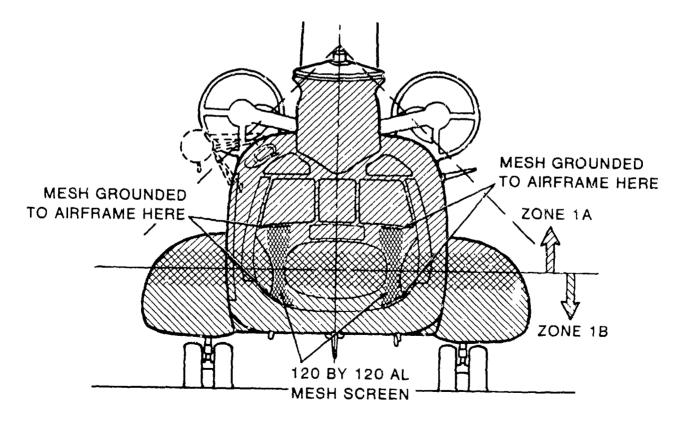


Fig. 3 - Forward fuselage - front view

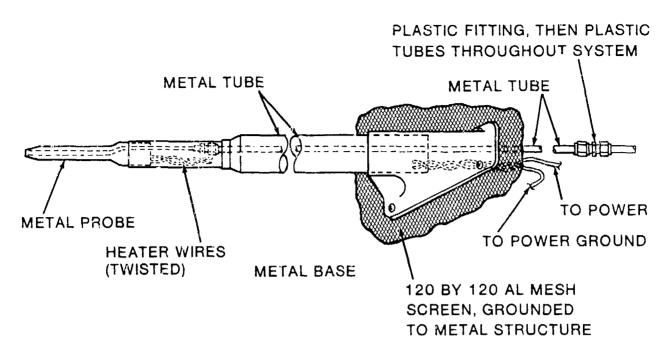


Fig. 4 - Pitot static probe

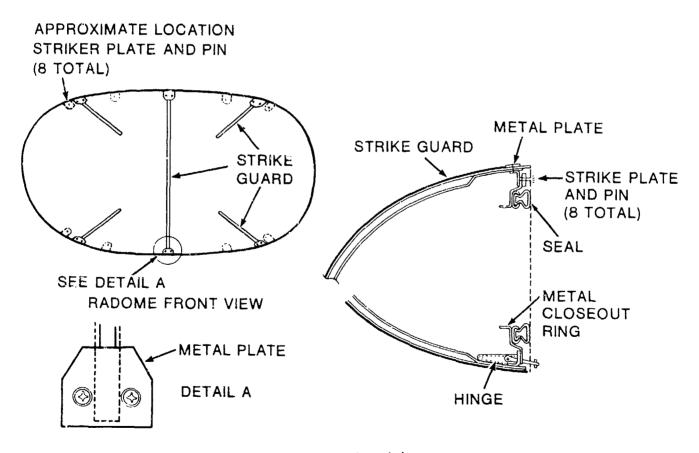


Fig. 5 - Radome design

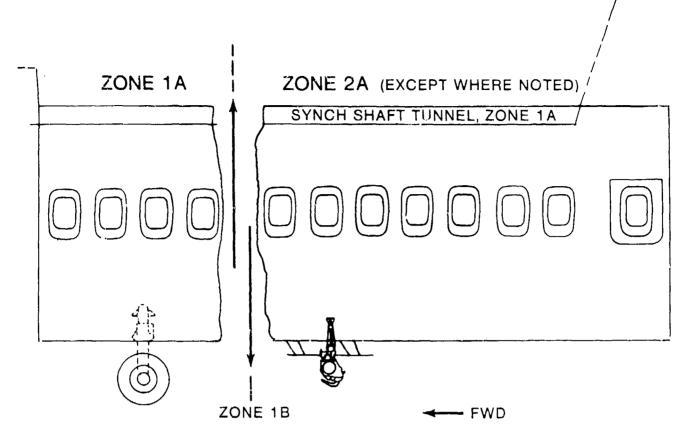


Fig. 6 - Center fuselage

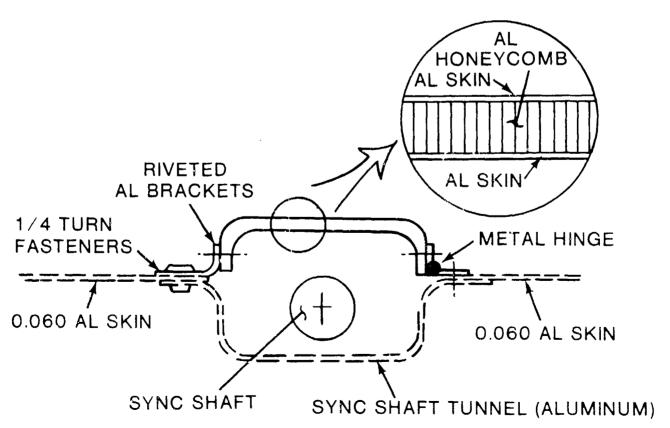


Fig. 7 - Sync shaft tunnel cover

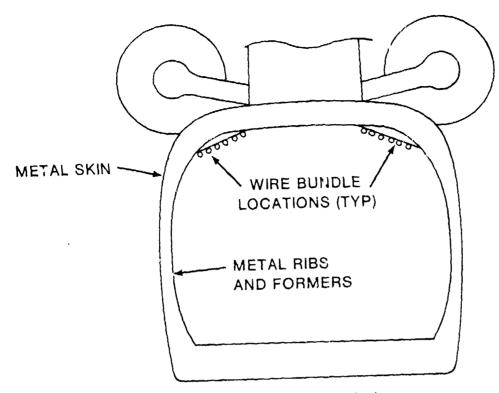


Fig. 8 - Wire routing in center fuselage

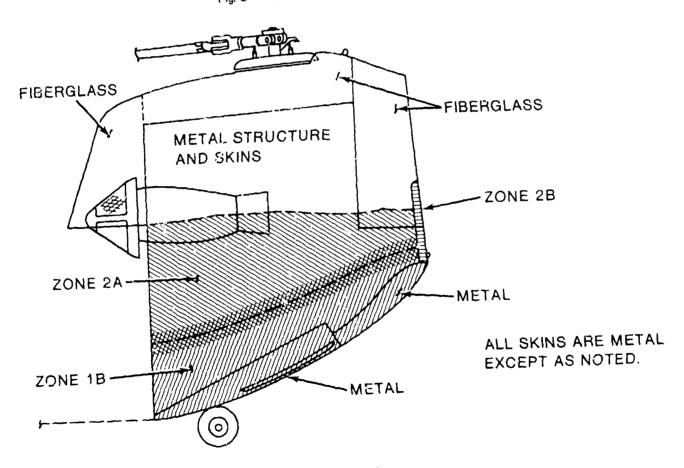


Fig. 9 - Aft fuselage

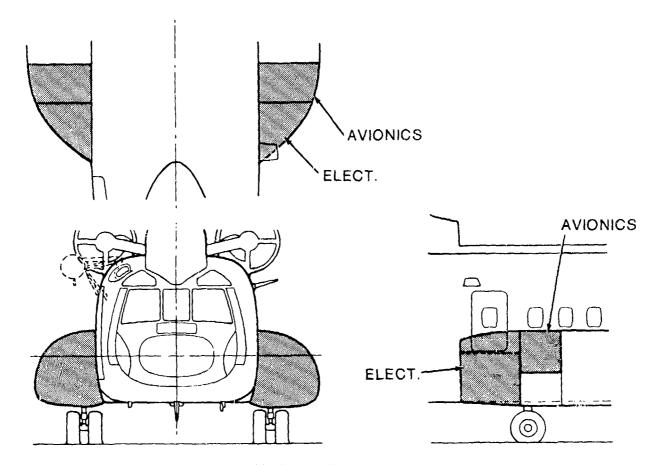


Fig. 10 - Equipment pods

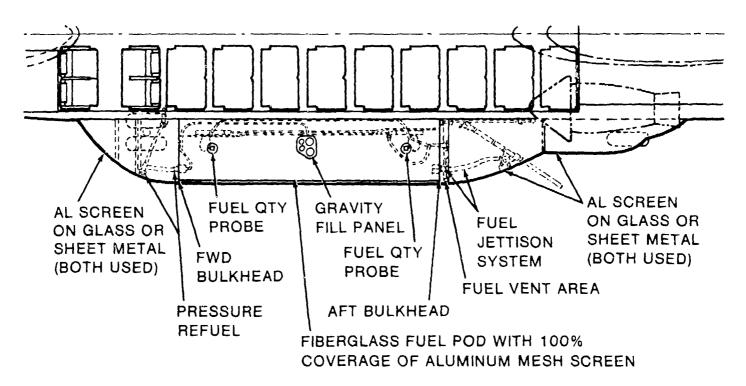


Fig. 11 — General fuel system arrangement

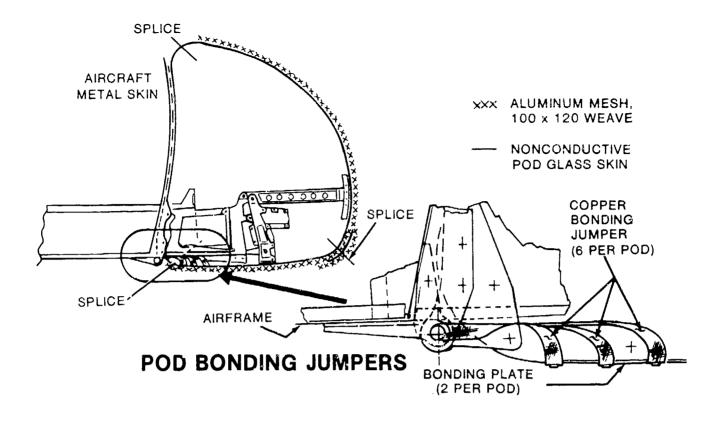


Fig. 12 — Pod bonding jumpers

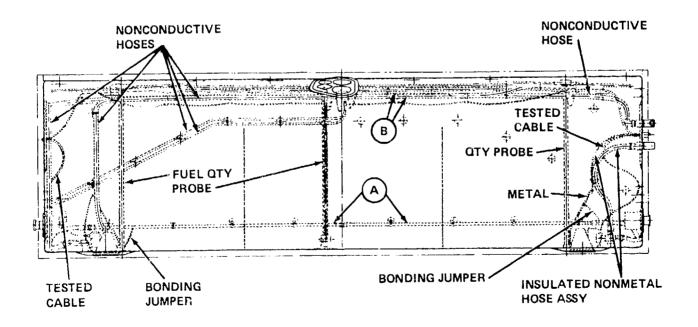


Fig. 13 - Fuel pod interior

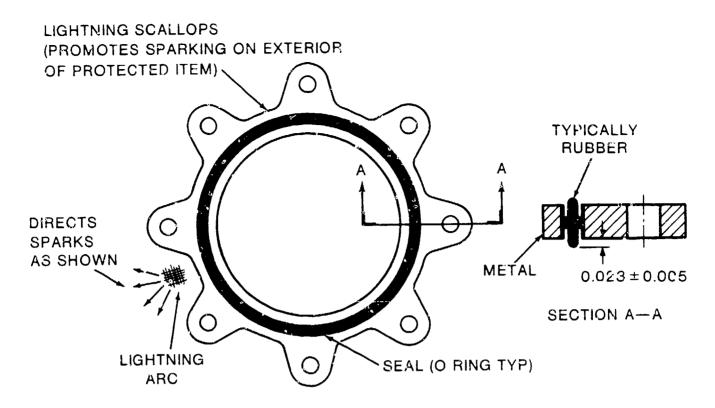


Fig. 14 - Gasket with lightning scallops

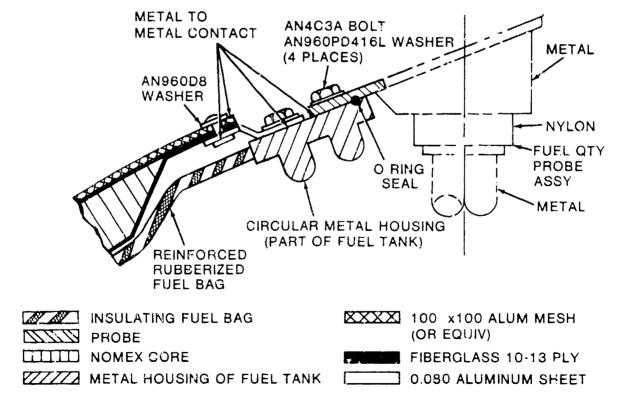


Fig. 15 - Fuel probe mounting

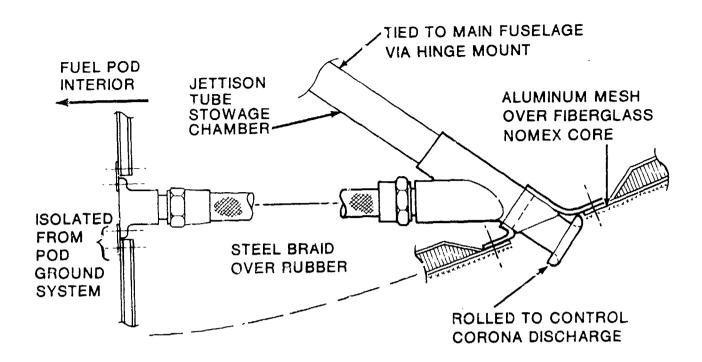


Fig. 16 - Fuel jettison - representative sketch

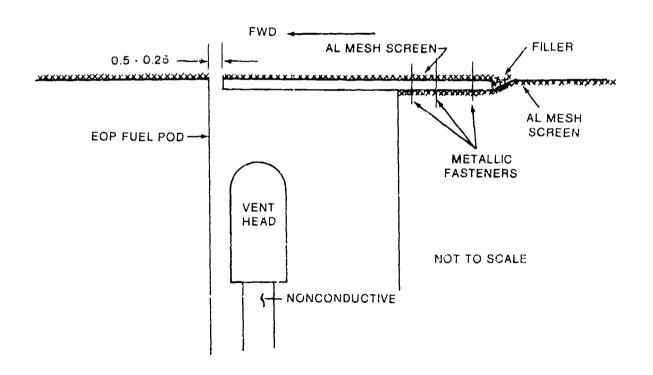


Fig. 17 - Fuel cell vent

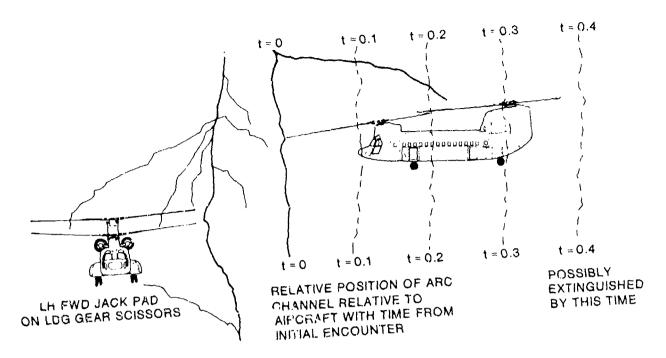


Fig. 18 — Arc channel configuration — side view

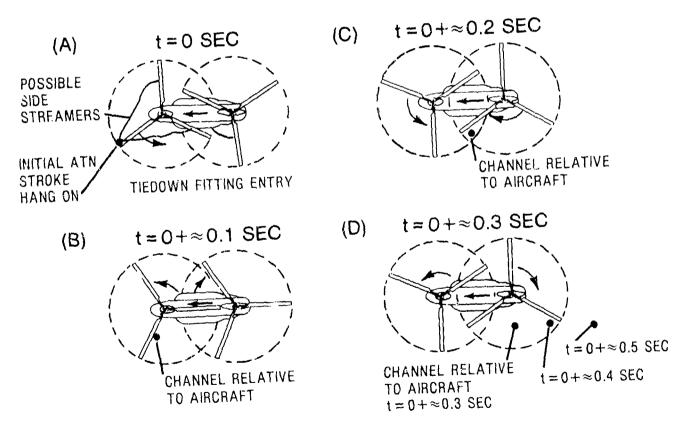


Fig. 19 - Arc channel configuration - top view

## **Author's Index**

Amason, M. 96 Anderson, R. 60 Arnold, R. 1, 5, 52 Aucr. and, D. 16, 54,55

Barile, A. 48
Beavin, R. 2
Belcastro. C. 87
Bicknell, J. 42
Binford, R. 50
Birken, J. 16, 54, 56
Bishop, J. 4!
Booth, G. 61
Boulay, J. 94
Bushnell, J. 64
Burrow, B. 63
Byerley, L. 50
Byrne, G. 43
Byrne W. 81

Coleman, E. 49 Corbin, J. 66 Crawford, S. 3 Crouch, K. 39 Davidoff, A. 78 Devarc, P. 12 Doggett, P. 88 Dougherty, J. 32 DuBro, G. 46 Duff, B. 31

Easterbrook, C. 56 Edlin, G. 21 Evans, R. 41 Ewing, R. 73 Few, A. 43 Fisher, B. 26, 90 Fitzsimmons, T. 35

Gardner, R. 72 Geren, W. 47, 80 Gerlach, J. 90 Gockenbach, E. 74 Geodman, S. 1, 5 Graf, W. 8, 9, 18

Halle', J. 25 Hamm, J. 18, 95 Haseborg, J. 11, 33, 85 Haseltine, J. 62 Heady, B. 40 Heiderscheidt, G. 97 Hiscox, W. 14, 15 Hoffart, H. 61 Hofmester, M. 96 Hogberg, R. 10 Hojo, J. 82 Holle, R. 14,15 Howell, W. 38

Ishii, M. 82 Jamelin, J. 71 Jones, C. 59

Kasemir, H. 24 Kawamura, T 82 Khemoni, L. 12 King, C. 84 Kinoshita, K. 23 Kleiner, C. 68 Koide, T. 23 Konigtein, D. 7 Krider, E. 50, 51, 69 Kuhman, B. 45, 46, 47

Labaune, G. 58 Laroche, P. 22 Latham, J. 91 LeBoulch, M. 71 Lee, T. 53 Leteinturier, J. 71 Lewis, W. 48 LeVine, D. 13, 70 Lippert, J. 77 Loncrini, D. 80 Lcpez, R. 14, 15 Lorstrand, K. 10 Lundquist, S. 10

MacDiarmid, I. 98
MacGorman, D. 1, 5
Mahoney, T. 19
Maier, M. 6, 50
Manohar, G. 12
Masson, G. 78.89
Mazur, V. 1, 5, 13, 52, 90
Malander, B. 36
Meneghini, P. 70
Millard, D. 28
Modrusan, M. 71
Menin, G. 12
Murakami, A. 20
Murty, V. 12

Nakano, M. 83 Nagai, Y. 23 Nanevicz, J. 9. 95 Nickum, J. 86 Ogasian, H. 80

Parker, L. 57 Pathak, P. 44 Perala, R. 56, 75 Pifer, A 50 Pinckney, K. 20 Piotrowicz, J. 6 Plumer, A. 26 Puhringer, A 92

Rasch, N. 48 Reazer, J. 45, 46 Reid, G. 59 Richard, P. 58 Robb, J. 21, 53, 75, 80 Rusner, D. 68 Rust, D. 1 Rustan, P. 45, 46

Saunders, C. 25 Schmid, M. 78 Schulte, E. 76 Selvam, M. 12 Showalert, J. 45 Simi, J. 79 Stahmann, J. 27 Stewart, M. 43 Sutter, H. 74

Takagi, N. 83 Takeuti, T. 93 Taylor, W. 1, 4, 5, Tranbarger, O. 31 Trapp R. 78 Trinks, H. 11, 35, 85, 93 Trost, T. 17

Uman, M. 50, 51

Vance, E. 8, 18, 95 Velkoff, H. 32 Vorgucic, A. 30

Wallenberg, R. 54 Watts, L 29 Weber, M. 43 Weidman, C. 69 Weinstock, G. 34 White, R. 65 Wiles, K. 67

Ziegler, W 37 Zeitler, R. 67